Xuecheng Bian
Yunmin Chen
Xiaowei Ye   *Editors*

Environmental Vibrations and Transportation Geodynamics

Environmental Vibrations and Transportation Geodynamics

Xuecheng Bian · Yunmin Chen
Xiaowei Ye
Editors

Environmental Vibrations and Transportation Geodynamics

ZHEJIANG UNIVERSITY PRESS
浙江大学出版社

Springer

Editors
Xuecheng Bian
Department of Civil Engineering
Zhejiang University
Hangzhou, Zhejiang
China

Xiaowei Ye
Department of Civil Engineering
Zhejiang University
Hangzhou, Zhejiang
China

Yunmin Chen
Department of Civil Engineering
Zhejiang University
Hangzhou, Zhejiang
China

Preface

The 7th International Symposium on Environmental Vibration and Transportation Geodynamics (ISEV2016) held in Hangzhou, China, from October 28 to October 30, 2016, is organized by the Zhejiang University under the auspices of ISSMGE-TC202 Transportation Geotechnics technical committee and its corresponding partner of the Chinese Society of Civil Engineering.

The ISEV conference series was initiated by Prof. H. Takemiya of Okayama University, Japan, and Prof. Yunmin Chen of Zhejiang University, China, and held in Zhejiang University, Hangzhou, China, in 2003, for the first time. The subsequent five symposia were successfully convened in Okayama University, Japan (2005), National Taiwan University, Taipei (2007), Beijing Jiaotong University, China (2009), Southwest Jiaotong University, China (2011), and Tongji University, China (2013), respectively. Following the previous ones, the topics of the conference cover, but not limited to, environmental vibrations induced by industrial, civilian, and transportation activities, and dynamics problems and related settlement deformation and performance degradation issues of transportation infrastructures (roads, rails, airports, subways, and other ground transportation infrastructures). It serves as a unique platform for academic exploration, experience exchange, and thought inspiration amongst the researchers and practitioners engaged in research, management, design, and construction of large-scale civil and transportation infrastructures.

Totally, more than 90 papers have been received by the conference organizer. After technical review, more than 70 papers have been accepted to be presented at the conference and also included in the conference proceedings co-published by Springer and the Zhejiang University Press. These papers have covered a wide range of issues concerning on environmental vibration and transportation geodynamics. Showcasing diversity and quality, these papers report the state of the art and point to future directions of research and development in this exciting area. We are also honored to have distinguished speakers to deliver keynote and invited speeches at the conference.

The success of the Symposium is due to the dedication and support of many individuals and organizations. On behalf of the Organizing Committee, I would like

to thank all authors for careful preparation of their papers, and all speakers for sharing their work, experience, and insight at the conference. All full papers submitted were reviewed by the members of the Scientific Committee and the Organizing Committee. We are grateful to all of them for their important contributions to the Symposium.

Hangzhou, China   Prof. Xuecheng Bian
October 2016   Chairman of the Organizing Committee of ISEV2016

Proceedings of the 7th International Symposium on Environmental Vibration and Transportation Geodynamics (ISEV2016)

28–30 October 2016, Zhejiang University, Hangzhou, China
Edited by
Xuecheng Bian, Yunmin Chen and Xiaowei Ye
Zhejiang University, Hangzhou, China
Organized by
Zhejiang University, Hangzhou, China
Under the auspices of
The International Society for Soil Mechanics and Geotechnical Engineering (ISSMGE)
TC202 Transportation Geotechnics Committee
Sponsor
Transportation Geotechnics Committee of Chinese Soil Mechanics and Geotechnical Engineering Association
Co-sponsor
Nanchang Institute of Technology, Nanchang, China

Scientific Committee

Honorary Chairmen
Prof. Emeritus Hirokazu Takemiya, Okayama University, Japan
Prof. Yeongbin Yang, National Taiwan University, Taipei
Prof. Wanming Zhai, Southwest Jiaotong University, China
Prof. Guotang Zhao, China Railway, China
Chairman
Prof. Yunmin Chen, Zhejiang University, China
Members
Lutz Auersch, Federal Institute for Materials Research and Testing, Germany
Dimitri E. Beskos, University of Patras, Greece

António Gomes Correia, University of Minho, Portugal
Jinchun Chai, Saga University, Japan
Renpeng Chen, Hunan University, China
Yujun Cui, Ecole des Ponts ParisTech, France
Yuanqiang Cai, Zhejiang University, China
Geert Degrande, University of Leuven, Belgium
Guangyun Gao, Tongji University, China
Liang Gao, Beijing Jiaotong University, China
Hai Huang, Pennsylvania State University, USA
Hong Hao, Curtin University, Australia
Hugh Hunt, University of Cambridge, UK
Jie Han, University of Kansas, USA
Maosong Huang, Tongji University, China
Toshiki Hamamoto, University of Toyama, Japan
Buddhima Indraratna, University of Wollongong, Australia
Tatsuya Ishikawa, Hokkaido University, Japan
Jianqun Jiang, Zhejiang University, China
Shenghao Ju, National Cheng-Kung University, Tainan
Songyu Liu, Southeast University, China
Xiaoyan Lei, East China Jiaotong University, China
Xianzhang Ling, Harbin Institute of Technology, China
Andrei V. Metrikine, Delft University of Technology, Netherlands
Jin Y Ooi, The University of Edinburgh, UK
Taesoon Park, Seoul National University of Science and Technology, South Korea
William Powrie, University of Southampton, UK
Yonglin Pi, The University of New South Wales, Australia
Jiping Ru, Natural Science Foundation of China, China
Ted Sussmann, United States Department of Transportation, USA
Erol Tutumluer, University of Illinois at Urbana-Champaign, USA
Fumio Tatsuoka, Tokyo University of Science, Japan
Fuming Wang, Zhengzhou University, China
Linbing Wang, Virginia Polytechnic Institute and State University, USA
Ping Wang, Southwest Jiaotong University, China
He Xia, Beijing Jiaotong University, China
Weiping Xie, Wuhan University of Technology, China
Yangping Yao, Beihang University, China
Bin Xu, Nanchang Institute of Technology, China
Youlin Xu, The Hong Kong Polytechnic University, HK
Haisui Yu, The University of Nottingham, UK
Jongdar Yau, Tamkang University, Taipei
Jun Yang, The University of Hong Kong, HK
Franz Ziegler, Vienna University of Technology, Austria

Organizing Committee

Chairman
Prof. Xuecheng Bian, Zhejiang University, China
Secretary in General
Prof. Xiaowei Ye, Zhejiang University, China
Members
Xiaobin Chen, Central South University, China
Xuanming Ding, Chongqing University, China
Qingsong Feng, East China Jiaotong University, China
Bo Huang, Zhejiang University, China
Hongguang Jiang, Shandong University, China
Linggang Kong, Zhejiang University, China
Jiangu Qian, Tongji University, China
Liang Tang, Harbin Institute of Technology, China
Hong Xiao, Beijing Jiaotong University, China
Junhua Xiao, Tongji University, China
Bin Zhu, Zhejiang University, China
Changbin Yan, Zhengzhou University, China
Chunfa Zhao, Southwest Jiaotong University, China
Wanhuan Zhou, University of Macau, Macao, China
Yanguo Zhou, Zhejiang University, China

Contents

Evaluating Fatigue Resistance of FRP-Strengthened RC Bridge Decks Subjected to Repeated Wheel Load

Hwa Kian Chai, Hiroshi Onishi and Shigeyuki Matsui

Introduction

In countries with increased number of aging infrastructures, maintenance and rehabilitation have become part of the critical routine in asset management practices. In the case for steel reinforced concrete (RC) road bridges, deterioration is principally caused by corrosion of reinforcements, degradation of concrete quality and unanticipated increase in traffic load requirements. The last one, which occurrence is on the rise because of the marked increase in modern traffic volume, could possibly lead to several modes of failure if neglected, including fatigue failure of bridge deck panels. As the element that receives direct loading from traffic, a RC bridge deck that suffers from serious deterioration would initiate function loss of the entire bridge infrastructure. Beside, deterioration of bridge deck is usually associated with increase of residual deformation and crack occurrence, which eventually reduce the stiffness and fatigue life if no remedial action is adopted timely [1–4].

H.K. Chai (✉)
School of Engineering, The University of Edinburgh,
King's Buildings, Edinburgh EH9 3FB, Scotland, UK
e-mail: hwakian.chai@ed.ac.uk

H. Onishi
Department of Civil and Environmental Engineering,
Iwate University, 3-18-8 Ueda, 020-8550 Morioka, Iwate, Japan
e-mail: onishi@iwate-u.ac.jp

S. Matsui
Structural Research Centre, Osaka Institute of Technology,
Ichinotani Minoyama, Yawata-shi, Kyoto 614-8289, Japan
e-mail: shigeyuki.matsui@oit.ac.jp

H.K. Chai · H. Onishi · S. Matsui
Department of Civil Engineering, Osaka University,
1-1, Yamadaoka, Suita, Osaka 565-0871, Japan

Over the past decades, application of fiber reinforced polymer (FRP) in rehabilitation scheme of concrete structural members has gained popularity owing to the excellent material characteristics, fast and simple installation as well as minimal intervention to structure's usage during installation work [5–8]. The design for strengthening RC bridge decks with FRP laminates is based on the allowable stress approach resembles that of a flexural member, e.g. a beam. It is common in considering that the improvement in flexural stiffness is always associated with the improvement in fatigue durability. However, in actual scenario when crack occurs, a deck no longer responds elastically towards load. Furthermore, under repetition of loading by traffic movements, complex combinations of stresses cause abrasion between crack surfaces, accelerating crack propagations. Consequently, a deck could fail in fatigue by repetitions of loads that are smaller than the design load. Therefore, it is vital to ensure that the strengthening not only restore or upgrade a deck's flexural stiffness, but also extend its fatigue life to an adequate level. Improvement in the fatigue durability of a deteriorated bridge deck by FRP strengthening is associated with confinement of cracks by the FRP laminates that helps in minimising crack propagation in events of traffic loading. Therefore, the tensile property of FRP, namely the tensile stiffness is regarded as one of the important parameters that determine the effectiveness of strengthening in improving fatigue life span of bridge deck.

This paper discusses collective findings from a series of experimental studies undertaken at Osaka University for investigating the performance of RC bridge decks strengthened with unidirectional aramid fiber reinforced polymer (AFRP) laminates and carbon fiber reinforced polymer (CFRP) laminates [9–11]. Large-scale fatigue tests of deck specimens were conducted using a specially developed test facility known as the wheel running machine. Parameters of the studies include thickness and reinforcement design of slab specimens and tensile stiffness of the FRP laminates. Comparison between the fatigue durability and fatigue life extension of the deck specimens was carried out via analysis of S-N relationship.

Fatigue Failure Mechanism of RC Bridge Decks

Fatigue loading on RC bridge decks is caused by moving wheels, characterised by a high number of load cycles which may exceed 100 millions over the fatigue life of a bridge [4]. It is discovered that the ultimate fatigue damage of RC slabs due to horizontal, repeated movements of load is scaling out of tension side concrete cover or partial falling out of concrete [1, 12, 13]. Observations also revealed that fracture of reinforcement seldom occurs in the event of fatigue failure. The failure mechanism has been investigated by fatigue tests with a moving wheel loading as reported in several researches [13, 14]. It is also reported that the fatigue strength of a deck subjected to wheel load is reduced to approximately half of that obtained from conventional fatigue tests with fixed pulsating load [14]. The ultimate failure

of deck is associated with development of punching shear cracks at concrete cross section perpendicular to traffic direction [14, 15]. A model for punching shear failure was proposed by Maeda and Matsui [14] to suggest computation of punching shear capacity of deck subjected to a uniformly distributed load acting on a rectangular contact area, resembling that of the contact by a wheel. As illustrated in Fig. 1, τ_{smax} and σ_{tmax} represent the ultimate shear strength and tensile splitting strength of concrete, respectively, X_m and X_d are the effective concrete depth at the main bar and distributing bar cross sections, respectively when concrete at tension side is ineffective, C_m, C_d are the concrete covers between the tensile main bar and distributing bar to the bottom of deck, respectively, a and b are the width and length of the loading area imposed by wheel, respectively, and d_m as well as d_d are the effective depth of the tensile main and distributing bars, respectively. Equations (1–5) as shown below were proposed:

$$P_{sx} = 2B \left(\tau_{smax} X_m + \sigma_{tmax} C_m \right) \tag{1}$$

where B is the width of the effective loading area extended to the neutral axis. Calculations for τ_{smax}, σ_{tmax} and B were proposed with the following empirical equations:

$$\tau_{s\,max} = 0.00026\sigma_{ck} - 2.51 * 10^{-7}(\sigma_{ck})^2 \tag{2}$$

$$\sigma_{t\,max} = 0.00059(\sigma_{ck})^{2/3} \tag{3}$$

Fig. 1 Punching shear model subjected to wheel load

(a) Cross section

(b) Stress distribution
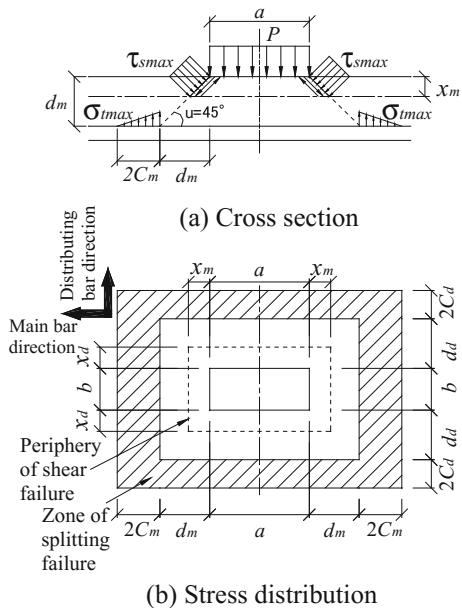
$$B = b + 2d_d \tag{4}$$

where σ_{ck} is the concrete compressive strength. An *S-N* equation that considers the relations between punching shear capacity of RC decks (*S*) and the total number of loading passages required to reach failure (*N*) was derived and expressed as follows:

$$\left(\frac{P_o}{P_{sx}}\right) = -0.07835 N_{eq} + 1.520 \tag{5}$$

where P_o is the reference load; P_{sx} is the punching shear strength for fatigue failure of RC deck and N_{eq} is the total equivalent number of loading passages under P_o. At the start of wheel running test, the magnitude of load is usually set to a minimal value as not to introduce impact that could result in pre-mature failure of deck. Attempting to optimise the period and cost of testing, the load magnitude can be gradually increased in stages at specified load passage. To obtain the equivalent number of load passages by a load magnitude, the following equation is used for the conversion:

$$N_{eq} = \sum \left(\frac{P_i}{P_o}\right)^{\frac{1}{m}} * N_i \tag{6}$$

where P_i is the load during fatigue test at respective stages, N_i is the total loading passages that corresponds with P_i and *m* is the slope of the *S-N* relation given in Eq. (5).

Experimental Program

Ten 2000 mm × 3000 mm RC deck specimens were prepared with different thicknesses of 150, 160, 180 and 220 mm. The specimens were designed in accordance with the Japanese Specification for Highway Bridges. Example layout of specimens is as given in Fig. 2. The specimens were labeled in accordance with cross sectional thickness and type of strengthening material. Table 1 summarize the designations of specimens as well as the properties of concrete and FRP laminates. The two Control specimens, namely t15-N and t22-N were not strengthened.

Concrete was designed to achieve an average 28-day compressive strength of 28 MPa in accordance with JIS A1132 (1999). For reinforcement, all specimens were reinforced with SD295A bars with design yield strength of at least 295 MPa except t22-N, which was reinforced with SD345 bars that have design yield strength of 345–440 MPa as prescribed in JIS G3112 (2004).

Several types of standard unidirectional FRP laminates were used for the strengthening. The FRP laminates were bonded to the tension face of the specimens in grid pattern by wet lay-up procedure. The width of each strip was 250 mm. The
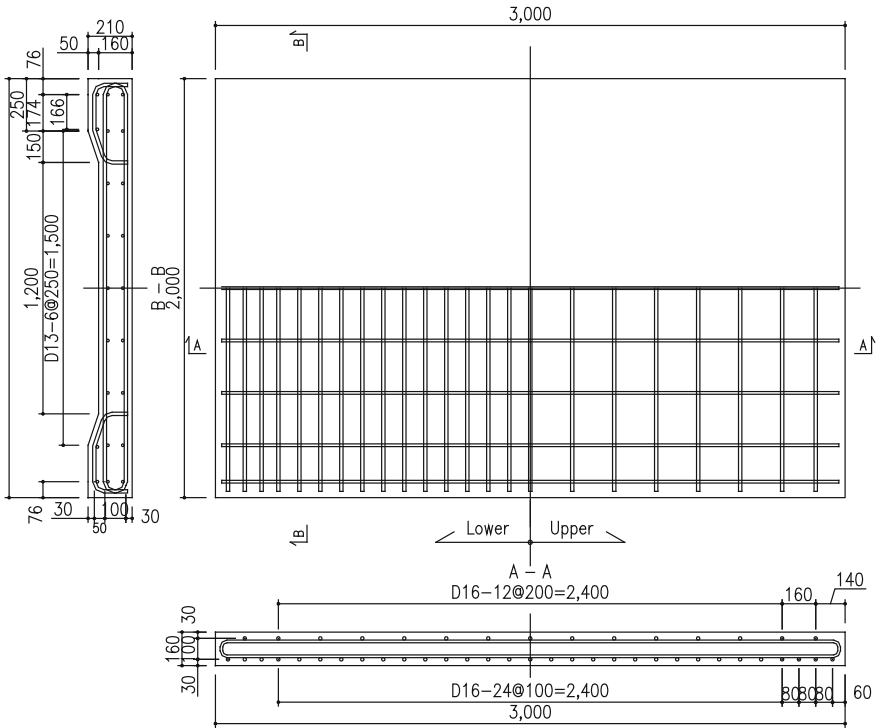
Fig. 2 Specimen layout (160 mm thick)

gap between two FRP laminate strips was 100 mm for the t15 and t16 series and 150 mm for the t18 series. The tensile stiffness, S_f of FRP laminates applied to each specimen was determined by the following equation:

$$S_f = \frac{t_f E_f b_f}{b_f + g} \tag{7}$$

where t_f, E_f and b_f are the design thickness, Young's Modulus and width of FRP laminate strip, respectively, while g is the gap between two FRP laminate strips.

A schematic diagram of the testing machine is shown in Fig. 3. The testing machine was dedicatedly developed to provide experimental simulations of a moving wheel load on decks. In this study, the moving wheel load was applied at the center of the specimens so the wheel would traverse to-and-fro in the longitudinal direction between the two ends of specimen.

All the specimens except for t15-N and t22-N were subjected to preliminary loading to induce initial deterioration before strengthening. The loading was progressively increased after specific number of passages, e.g. in the case of t16-C30, the preliminary loading was applied at 100 kN for 60,000 passages. After

Table 1 Details of specimens

Specimen	Design thickness (mm)	Concrete		FRP					
		Compressive strength (N/mm^2)	Young's modulus (kN/mm^2)	Type	Fiber mass (g/m^2)	Tensile strength (N/mm^2)	Young's modulus (kN/mm^2)	Design thickness (mm)	Tensile stiffness (kN/mm)
t15-N	150	33.5	27.7	–	–	–	–	–	–
t22-N	220	33.4	28.6	–	–	–	–	–	–
t15-C68	150	32.8	28.7	CFRP	400	2400	440	0.217	68
t15-C80	150	33.4	28.4	CFRP	470	2400	440	0.255	80
t16-C30	160	34.8	32.4	CFRP	200	2900	390	0.111	30
t16-C45	160	35.7	31	CFRP	300	2900	390	0.165	45
t16-A24	160	47	37	AFRP	415	2060	118	0.286	24
t16-A36	160	43.4	36.7	AFRP	623	2060	118	0.403	36
t18-C60	180	36.2	28.6	CFRP	400	2400	440	0.217	60
t18-C70	180	36.3	29.8	CFRP	470	2400	440	0.255	70
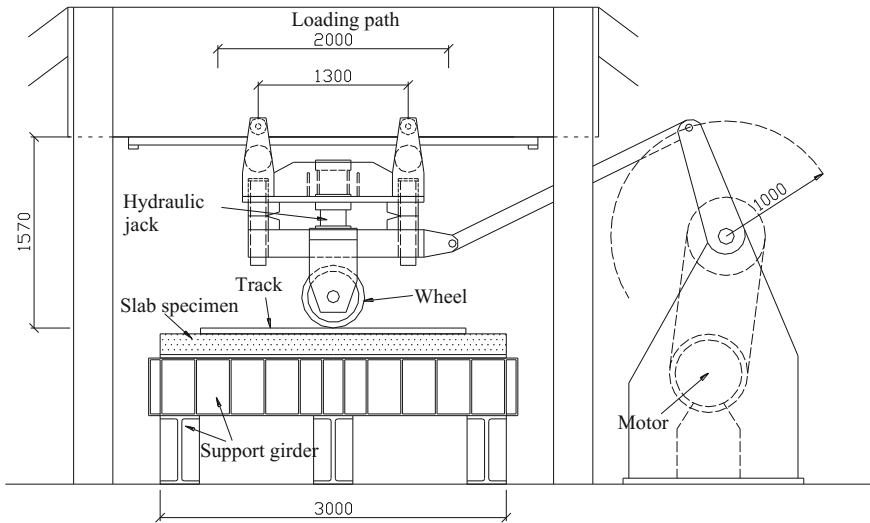
Fig. 3 The wheel running machine

strengthening, loading was resumed at 100 kN for 100,000 passages, followed by 120 kN for 100,000 passages, 150 kN for 100,000 passages and finally 170 kN till fail. At fixed intervals, the fatigue loading would be stopped to make way for static loading in order to measure vertical displacement, which was done via dial gages arranged on the specimen soffit along the longitudinal and transverse mid-spans. The measured displacements were classified into three types, namely residual displacement, live-load displacement and total displacement. Residual displacement represents the permanent deflection of the specimens due to loss of stiffness; live-load displacement indicates the elastic respond of specimens when loaded statically; the total displacement is the sum of residual and live-load deflections. The bond condition of FRP laminates was constantly inspected throughout the testing by tapping the surface of the laminate by a ball hammer to identify change of sound that signified occurrence of debonding.

Results and Discussion

Fatigue Behavior and FRP Debonding

After the preliminary loading, cracks were found on the soffit of specimens as exemplified in Fig. 4. For the two Control specimens, continuous loading increased both the density and vertical movement of cracks. Specimen t15-N developed punching shear fracture, manifested by an abrupt drop in vertical displacement that forced the test machine to halt. Specimen t22-N, on the other hand, did not failed

Fig. 4 Cracks on deck soffit after preliminary loading

after 1,000,000 load passages and the test was ended. For the strengthened speci-
mens, large vertical gaps and scaling out of concrete were found on the soffit at the
end of fatigue tests. Furthermore, significant cracks could be seen on the upper face
of specimens along the edges of loading path, in addition to numerous transverse
cracks. Shear cracks that penetrated the full depth of the cross section was found
from the cut cross sections.

Debonding of FRP laminates did not occur until the final stages loading, where
considerable increase in displacement was noted in a highly nonlinear manner as a
result of steel reinforcement yield. High shear stress concentration resulting from
vertical crack movements followed by punching shear fracture resulted in
debonding, which was located 300–500 mm from the longitudinal mid-span. These
are also the locations where critical shear cracks were found. It can be deduced that
progressive development of shear cracks on decks loaded in fatigue is the major
cause for debonding of FRP laminates.

Figure 5 shows examples of total deflection transition of measured under a static
load of 100 kN. The total loading passages, including the number of passages
during preliminary loading for the FRP-strengthened specimens, are presented in
Table 2. The equivalent number of loading passages under the load of 100 kN are
also given in the same table. The efficiency of FRP-strengthening in improving the
fatigue resistance is indicative from the results of t15 specimens, where both
t15-C400 and t15-C80 attained higher number of load passages than t15-N. It is
also noted that t15-C80 achieved lower N_{eq} than t15-C68 despite the higher tensile
stiffness of FRP used. This was probably due the greater damage that was induced
onto the specimen by higher magnitude of preliminary loading. In the case of
t22-N, the specimen exhibited steady development in deflection with slight

Fig. 5 Total deflection developments of t16 series specimens

Table 2 Total experimental loading passages, N_{eq} and failure mode

Specimen	Total load passages ($\times 10^3$)[a]	N_{eq} ($\times 10^3$) (at 100 kN)	Failure mode
t15-N	410	2649	Punching shear
t22-N	1000	3,869,069	Did not fail
t15-C68	456	33,035	Punching shear
t15-C80	344	20,365	Punching shear
t16-C30	1056	277,986	Punching shear
t16-C45	1150	366,273	Punching shear
t16-A24	1036	261,236	Punching shear
t16-A36	1060	281,517	Punching shear
t18-C60	944	2,407,374	Punching shear
t18-C70	1006	2,470,986	Punching shear

[a]For strengthened specimens, total preliminary loading passages are included

increment until the end of fatigue test. In fact the deflection of t22-N was the lowest throughout the test compared with the other specimens. On the other hand, although the FRP-strengthened t18 specimens were subjected to similar loading program as that of t22-N after strengthening, both the specimens failed, with respective N_{eq} at least 55% lower than that of t22-N. The reinforcement ratios of t22-N and the two t18 specimens were very similar. It was a typical inference that thickness of a deck governs its fatigue resistance. Within the four t16 specimens, no significant variation was observed for the development of their total displacement. However, the total number of loading passages was found to increase with the tensile stiffness of the FRP laminates, a justification of the increase in fatigue resistance with tensile stiffness.

Evaluation of Fatigue Life

Table 3 shows the results of experiment and theoretical calculated properties. The theoretical fatigue life of the specimens under the presumed unstrengthened condition was evaluated by computing N_{eq} using Eq. 5, re-defined as N_{eqo} for clarity. On the other hand, the experimental N_{eq} (for the strengthened specimens) was obtained by converting the total number of load passages from experiment using Eq. 6. In the computation, the reference load P was taken as 150 kN. The fatigue life extension ratio, α was then acquired by dividing N_{eqi} with N_{eqo}. The lower value of α for t15-C80 compared to t15-C68 was evident as the consequence of high containment of damage by the specimen after preliminary loading, in such way that higher tensile stiffness of FRP (80 kN/ mm compared to 68 kN/ mm) was not able to offset this effect. In principle, the current arrangement for FRP strengthening could not provide significant contribution in restraining vertical shear and torsion caused by wheel load. On the other hand, the α value of t18-C70 approximately doubles that of t15-C80, further justifying that strengthening effect would increase with the thickness of deck. It is also interesting to find that the specimens with thickness of 160 mm (t16) gave α values comparable to that of t15-C68. This could be due to the lower FRP tensile stiffness for the t16 specimens, despite their higher thickness to resist fatigue.

Figure 6 presents the S-N plots of the specimens. While the data of t15-N fits well into the S-N curve proposed previously for unstrengthened RC decks, the data for the strengthened specimens deviate positively from the curve with good correlation, consistently reflecting the improvement of fatigue life as a result of strengthening. Although there is significant increase in N_{eq} after FRP-strengthening, the increase in punching shear strength as calculated is insignificant, as suggested by λ values in Table 3. Theoretically, the change in P_{sx} is associated with C_m and in the case of FRP strengthening, there will only be slight change to the deck's main bar cross section neutral axis that results in increase of C_m value. In actual, there are

Table 3 P_{sx} and N_{eq} (at 150 kN) of CFRP-strengthened specimens

Specimen	Unstrengthened		FRP-strengthened		$\lambda = \frac{P_{sx}}{P_{sxo}}$	$\alpha = \frac{N_{eq}}{N_{eqo}}$
	P_{sxo} (kN)	N_{eqo} ($\times 10^3$)	P_{sx} (kN)	N_{eq} ($\times 10^3$)		
t15-N	211	15	–	–	–	–
t22-N	405	>21,912	–	–	–	–
t15-C68	208	14	226	187	1.09	13.36
t15-C80	211	16	231	115	1.09	7.19
t16-C30	265	295	272	1574	1.03	5.34
t16-C45	264	280	275	2074	1.04	7.41
t16-A24	257	257	265	1479	1.03	5.75
t16-A36	253	213	265	1594	1.05	7.48
t18-C60	276	491	296	13,634	1.07	27.77
t18-C70	276	512	300	13,994	1.09	27.33
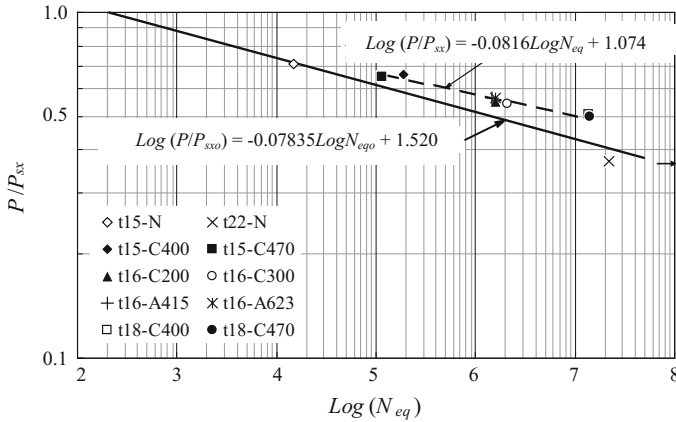
Fig. 6 *S-N* relations

other aspects that benefit from FRP strengthening, such as the degree of crack confinement and stress distribution on deck, which are worth studying for quantitative estimations.

With good correlation established for the FRP-strengthened specimens, one can predict the performance of strengthening in terms of fatigue life extension by adopting the new *S-N* equation. It is worth to mention the good compatibility of data with aramid FRP-strengthening (the two t16 specimens) into the new curve, implying the possibility of adopting a uniform equation for evaluating fatigue resistance regardless of fiber type.

Conclusions

(1) For RC deck specimen strengthened with FRP laminates relatively low tensile stiffness (30–45 kN/mm), fatigue life extensions of 5–7 times were yielded. For decks strengthened with FRP laminates of 60–80 kN/mm, fatigue life extensions of 7–27 times were obtained. The extension was reduced by a large margin for specimen that has undergone high damage in preliminary loading.

(2) The importance of deck thickness in determining the fatigue durability is justified. Bridge decks that have sufficient thickness can sustain fatigue wheel loading longer than FRP-strengthened decks with lower deck thickness. In the case of strengthening with similar type of FRP laminate, the lifespan extension of decks increases with the thickness of deck.

(3) An *S-N* relation for FRP-strengthened decks based on the punching shear capacity of RC decks can be obtained, making it possible to estimate the fatigue life extension.

References

1. Okada, K., Okamura, H., Sonoda, K. (1978). Fatigue Failure Mechanism of Reinforced Concrete Bridge Deck Slabs, Transportation Research Record No. 664, Transportation Research Board, pp. 136–144.
2. Takeshi, H. (1994). An Outline of the Repairing and Strengthening of RC Deck Slabs, Bridge and Foundation Engineering, 26(8): 105–108.
3. Mufti, A. A., Jaeger, L. G., Bakth, B., Wegner, L. D. (1993). Experimental Investigation of Fiber-Reinforced Concrete Deck without Internal Steel Reinforcement, Canadian Journal of Civil Engineering, 20(3): 398–406.
4. Schläfli, M., Brühwiler, E. (1998). Fatigue of Existing Reinforced Concrete Bridge Deck Slabs, Engineering Structures, 20(11): 991–998.
5. Teng, J. G., Chen, J. F., Smith, S. T., Lam, L. (2002). FRP-strengthened RC Structures, John Wiley & Sons, Ltd., Chichester, England, pp. 1–8.
6. Mori, N., Wakashita F., Matsui S., Nishikawa K. (1995). Reinforcing Effect of Carbon Fiber Sheet on Damaged Bridge Slabs, Bridge and Foundation Engineering, 95–3, pp. 41–48.
7. Rizkalla, S., Hassan, T. (2002). Effectiveness of FRP for Strengthening Concrete Bridges, Structural Engineering International, V. 2, pp. 89–95.
8. Clarke J. K., Waldron P. (1996). The Reinforcement of Concrete Structures with Advanced Composites, Structural Engineering, 74(17/3): 1996.
9. Chai, H. K., Nakajima, N., Onishi, H., Matsui, S., (2005). Proceedings of the Japan Concrete Institute, Japan Concrete Institute. (CD-ROM).
10. Okada, M., Onishi, H., Matsui, S., Kobayashi, A. (2003). Stiffening Effect with CFRP Sheets Arranged in Grid Pattern on RC Decks, Proceedings of 3rd Symposium on Decks of Highway Bridges, Japan Society of Civil Engineers, pp. 175–180.
11. Kobayashi, A., Chai, H. K., Shimonishi, M., Matsui, S., (2005). Fatigue Durability of RC Slabs Strengthened by CFRP Sheet in Grid Pattern, Proceedings of the Japan Concrete Institute, Japan Concrete Institute. (CD-ROM).
12. Matsui, S. (1991). Prediction of Bridge Lifespan-Fatigue Lifespan Prediction of RC Decks of Highway Bridges, Safety Engineering, 30(6): 432–440.
13. Sonoda, K., Horikawa, T. (1988). Low Cycles Fatigue Characteristics of Bridge Deck RC Slabs Under the Repetition of Wheel Load, Journal of Civil Engineering, Japan Society of Civil Engineers, 390/V-8: 97–106.
14. Maeda, Y., Matsui, S. (1984). Study on Fatigue Behavior of Highway Bridge Slabs by Wheel Running Machine, Proceedings of the 6th Annual Concrete Engineering Conference, Japan Concrete Institute, pp. 221–224.
15. Matsui, S. (1987) Fatigue Strength of RC Highway Bridge Slabs under Moving Loads and The Influence of Water, Proceedings of the Japan Concrete Institute, Japan Concrete Institute, 9–2: 627–632.

Vibration Measurements for the Control of Damaged and Repaired Railway Tracks

Lutz Auersch and Samir Said

Introduction, Experimental Methods of Multi-sensor Vibration Measurements

This contribution presents experimental methods to detect track damage. At BAM (Federal Institute of Material Research and Testing), a measuring car with a measuring system of 72 channels, geophones, mountings, cables, harmonic and impulsive exciters is used for dynamic measurements of the track, the soil and buildings (Fig. 1). An instrumented hammer allows force measurements and to evaluate transfer functions of the track, and the soil. Wave measurements are used to identify the soil characteristics [1, 2]. Train passages are measured at the track [3] and for the train induced ground vibrations [4, 5].

In addition to these in situ options, tests of tracks or track elements can be performed in a large laboratory [6, 7].

Calculations by the Three-Dimensional Finite-Element Boundary-Element Method

The track-soil systems are calculated in full detail by the combined finite-element boundary-element method [3, 8]. The track including the rails (beam elements), the rail pads (truss elements), sleepers, ballast or plate (volume elements) is modelled by the finite element method (Fig. 2) whereas the homogeneous or layered soil is

L. Auersch (✉) · S. Said
Federal Institute of Material Research and Testing BAM, 12200 Berlin, Germany
e-mail: lutz.auersch-saworski@bam.de

S. Said
e-mail: samir.said@bam.de

Fig. 1 Measuring system (*left*) in the measuring car (*right*)

calculated by the boundary element method. The dynamic stiffness matrix of the soil is established by using the Green's functions of an elastic layered half-space [9]. All calculations (Green's functions, boundary matrix and dynamic finite element matrices) are performed in frequency domain. The track is excited by a dynamic axle load (a pair of vertical forces, which acts on the rails above the central sleeper), and the frequency dependent displacements (compliances) are calculated. It is worth to notice that the important base of the finite-element boundary-element method, the point load solution for the layered soil, is established in wavenumber domain just as in the simplified method of the next section.

Calculations by the Simplified Two-Dimensional Wavenumber Domain Method

The slab tracks can also be modelled as multiple-beam systems: The first beam represents the two rails, and the second beam represents the track plate including the sleepers and the base layer. Additional beams have to be modelled if elastic elements lie between sleepers and track plate or between track plate and base plate.

Each beam is described by the bending stiffness EI_j and the mass per length m'_j which are assembled in a diagonal stiffness matrix $\mathbf{EI}$ and a diagonal mass matrix $\mathbf{m'}$. The global stiffness matrix $\mathbf{K'}$ is a nxn matrix assembled from the 2×2 dynamic stiffness matrices of each support section. The multi-beam system fulfils the set of differential equations for the beam displacements $\mathbf{u}$ under the track load $\mathbf{F_T}'$

$$\mathbf{EIu}'''' + \mathbf{m'\ddot{u}} + \mathbf{K'u} = \mathbf{F'_T} \tag{1}$$

The dynamic stiffness of the multi-beam track model in the frequency-wave-number domain reads as
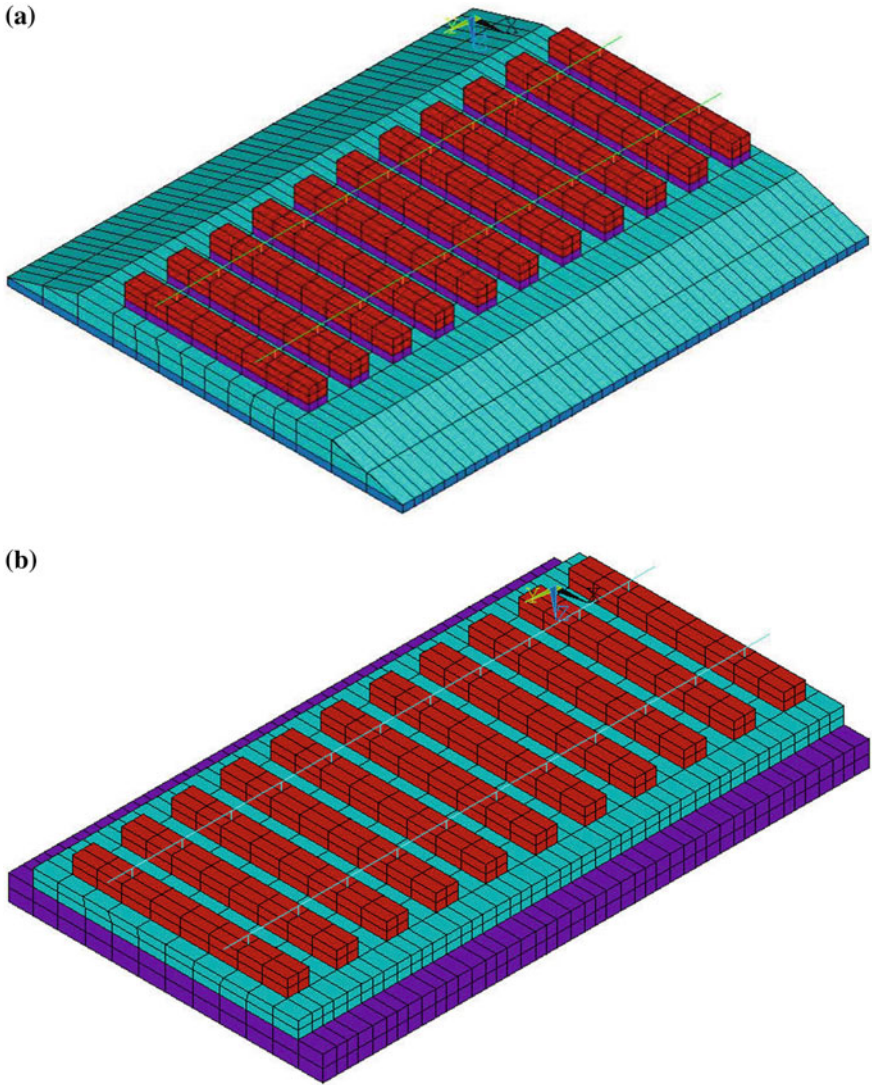
Fig. 2 Finite element model of the railway track, **a** ballast track with rail and sleeper pads, **b** slab track with rail pads, track plate and base layer

$$\mathbf{K_T} = k_y^4 \mathbf{EI} - \omega^2 \mathbf{m}' + \mathbf{K}' \tag{2}$$

where k_y is the wavenumber along the track axis and $\omega = 2\pi f$ is the circular frequency. In order to couple the track and the soil, the dynamic soil stiffness $\mathbf{K_S}$ for harmonic waves along the track [10] is added to the track stiffness $\mathbf{K_T}$ and the dynamic stiffness matrix $\mathbf{K_{TS}} = \mathbf{K_T} + \mathbf{K_S}$ of the track-soil system is established.

The displacements in the frequency-wavenumber domain are calculated by the inversion of this matrix, and the displacements along the track can be calculated by the inverse Fourier transformation as

$$\mathbf{u}\left(y, \omega\right) = \frac{1}{2\pi} \int\limits_{-\infty}^{+\infty} \mathbf{K}_{TS}^{-1}(k_y, \omega)\, \mathbf{F_T}\, e^{ik_y y} dk_y \tag{3}$$

see [10] for details.

Theoretical Results for Intact and Damaged Slab and Ballast Tracks

At first, the theoretical results for intact slab and ballast tracks with standard parameters (Table 1) are presented in Figs. 3–5. Figure 3 shows the frequency dependant displacements (compliance transfer functions u_0/F as amplitude and phase) for the different track elements. All transfer functions typically decrease with frequency f except the rail of the slab track which is almost constant. The phase delay is smallest for the rail, $-20°$ for the slab track and $-40°$ for the ballast track. The lower track elements reach higher negative phase values, $-60°$ for the sleeper of the ballast track and more than $100°$ for the other track elements. The amplitudes of the ballast track elements are not so different whereas the rail amplitude of the slab track is much higher than the amplitudes of all other track elements. The high rail amplitudes are due to the soft rail pads which are usually installed in a slab track to provide some resilience.

Figure 4 shows the frequency-dependent sleeper displacements for different soils. The stiffness of the soil has a strong influence on the static and low-frequency amplitudes. The static sleeper displacement depends mainly on the sub-soil of the track and is

u_0/F = 4.7, 2.4, 1.4, 0.7 $\times 10^{-9}$ m/N for shear wave velocities of
v_S = 100, 150, 200, 300 m/s.

for the slab track. On the other hand, the influence of the height of the track plate on the static displacement is weak [10].

The corresponding results for a ballast track are

u_0/F = 7.4. 3.9, 2.5, 1.4 $\times 10^{-9}$ m/N for shear wave velocities of
v_S = 100, 150, 200, 300 m/s.

The displacements of the sleeper of a standard ballast track are up to 100% greater than the displacements of the track plate of a slab track.

Table 1 Standard parameters of the ballast and slab tracks

UIC60 rail	Flexural stiffness	$EI_R = 2 \times 6.4 \times 10^6$ N m^2
	Mass per length	$m'_R = 2 \times 60$ kg/m
Rail pads (slab track)	Stiffness per support	$k_R = 2 \times 60$ kN/mm
Rail pads (ballast track)	Stiffness per support	$k_R = 2 \times 300$ kN/mm
	Hysteretic damping	$D = 0.1$
Sleeper	Mass	$m_S = 340$ kg
	Length	$a_S = 2.6$ m
	Width	$b_S = 0.26$ m
	Distance	$d = 0.6$ m
Track plate	Modulus of elasticity	$E_P = 3 \times 10^{10}$ N/m^2
	height	$h_P = 0.2$ m (0.15, 0.3 m)
Base layer	modulus of elasticity	$E_L = 5 \times 10^9$ N/m^2
	height	$h_L = 0.3$ m
Ballast	shear wave velocity	$v_{SB} = 300$ m/s
	height	$h_B = 0.3$ m
Soil	shear wave velocity	$v_S = 200$ m/s (100, 150 m/s)
Soil and ballast	mass density	$\rho = 2000$ kg/m^3
	Poisson's ratio	$\nu = 0.33$
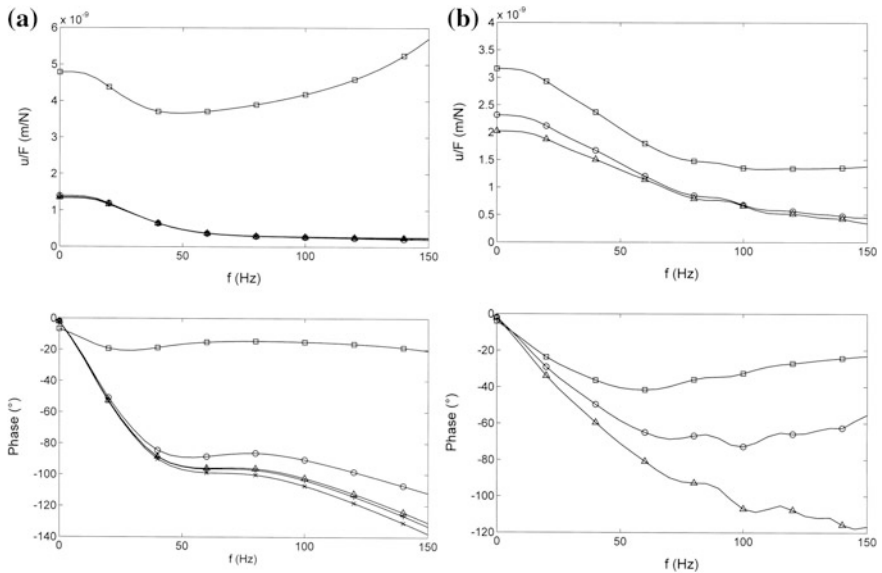
Fig. 3 Calculated compliances of tracks without damage (amplitude top, phase bottom), **a** slab track, □ rail, ○ sleeper, △ plate, + base layer, × soil, and **b** ballast track, □ rail, ○ sleeper, △ ballast
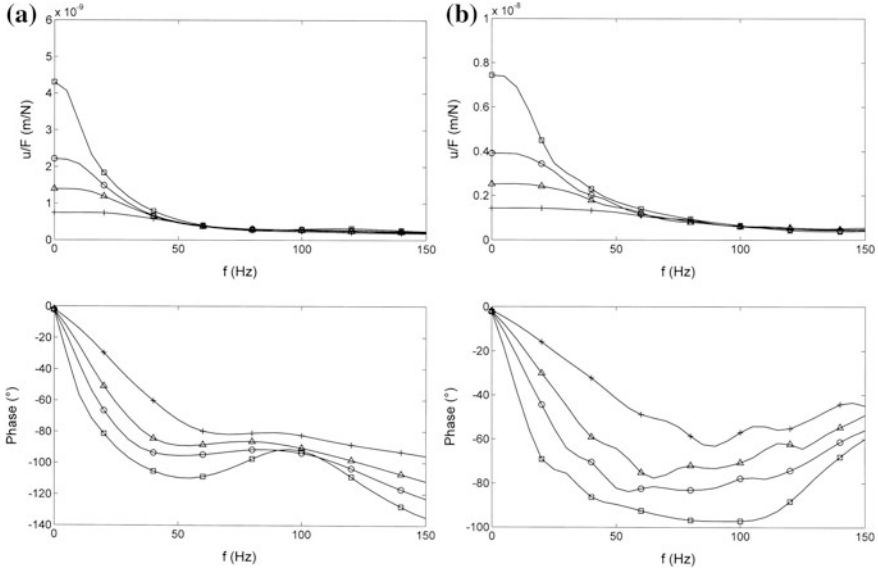
Fig. 4 Sleeper compliances for different soils v_S = $\square$ 100, $\bigcirc$ 150, $\triangle$ 200, + 300 m/s, **a** slab track with h_P = 0.3 m, **b** ballast track

The time histories of the sleeper displacements and velocities are presented in Fig. 5 for two slab tracks and two ballast tracks when an ICE train with 12 carriages (axle loads 160 kN) passes with a speed of 200 km/h. The simplest pattern can be found for the stiff slab track where each bogie yields one minimum for the displacement (Fig. 5a bottom) and one min-max combination for the velocity (Fig. 5a top). The most contrary behavior can be found for of the ballast track in Fig. 5c. The main difference compared to the slab tracks is the clear distinction of the two axles of a bogie. Two clear min-max combinations occur for the velocities and, correspondingly, two minima for the displacements. The maximum displacement between the axles is 30% higher than the minimum at each axle. The maximum between two following bogies is also higher, −0.1 mm instead of −0.2 mm for the slab tracks. These characteristics mean that the deformation of the ballast track is more local, on a shorter track length. The maximum displacements, however, are almost the same (0.5 mm) for the ballast and slab track.

If the stiffness of the plate is reduced (Fig. 5b shows a slab track with half of the height, that is 12.5% of the bending stiffness), small changes can be observed. The velocities display two min-max combinations which are shifted in amplitudes. They relate to the two close-by minima of the displacements which belong to the two axles of a bogie. The displacement between the two bogies of two following carriages is little smaller (0.18–0.2 mm) for the thick plate whereas the maximum displacement is almost the same for the thick and the thin plate. These observations mean that the thin plate has a more local response to the axle loads.
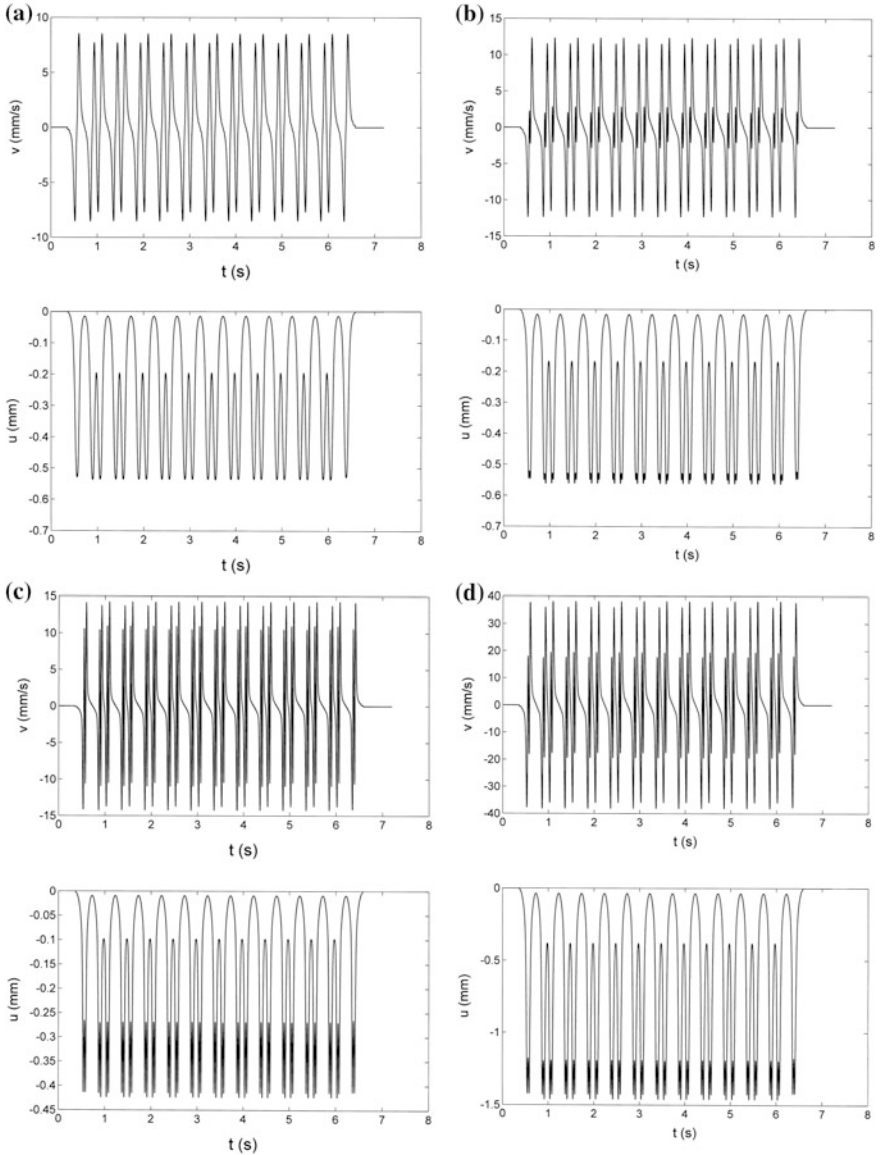
Fig. 5 Sleeper velocity (*top*) and displacement (*bottom*) due to a train passage over a slab track ($v_S = 150$ m/s) of height $h = 0.3$ m (**a**) and of $h = 0.15$ m (**b**) train passage over a ballast track on a medium stiff soil (**c**, $v_S = 200$ m/s), and on a soft soil (**d**, $v_S = 100$ m/s)

If the ballast track lies on a softer soil (Fig. 5d), the displacement and velocity amplitudes are 3 times higher. The response is less local, the two peaks of the two axles of a bogie are not so clearly separated as in Fig. 5c. The two corresponding

min-max combinations of the velocity are not as symmetric as for the stiffer soil where the peaks are almost the same for both axles and for plus and minus.

To sum up, a reduced bending stiffness of the (slab) track yields a more local behavior of the track without an important influence on the displacement amplitudes. A reduced soil stiffness will considerably increase both, the displacement amplitude and the deformation length of the (ballast) track (less local track behavior).

Looking at the damaged tracks, results of the combined finite element boundary element method are presented in Fig. 6. If a sleeper has lost the contact to the plate (Fig. 6a), the sleeper has the same high static amplitude as the rail or even higher dynamic amplitudes. An additional track resonance (here at 70 Hz) can be possible. If the plate has lost contact to the base layer on a length of three sleepers (Fig. 6b), the response of the plate and the sleeper are somewhat increased but not reaching the rail amplitude. A resonance occurs at 100 Hz, but it is strongly damped.

The amplitudes of the sleeper have also been calculated for different intensities of the track damage (Fig. 7). The sleeper amplitudes strongly increase if more than one sleeper is without contact. If the contact is lost at only the half of the sleeper (x ≤ 0.625), the amplitudes are almost the same as for the intact track (x = 0).
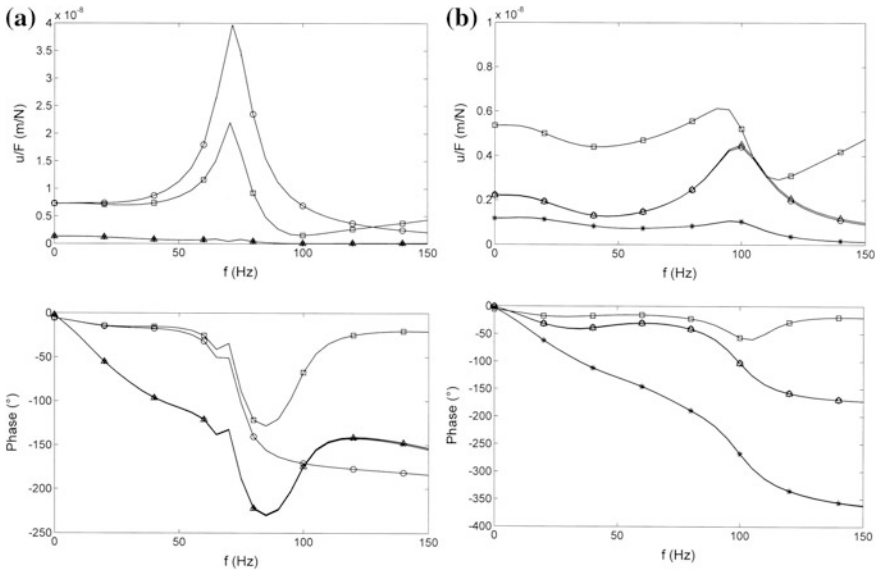
Fig. 6 Calculated compliances of a slab track with damage, **a** central sleeper without contact to the plate, **b** plate without contact to the base layer along 1.8 m, □ rail, ○ sleeper, △ plate, + base layer, × soil
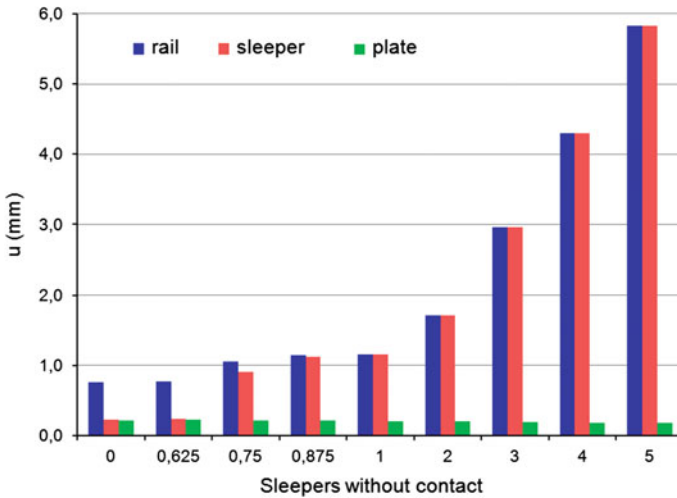
Fig. 7 Calculated static displacements of the slab track depending on the number of sleepers without contact, rail (*dark blue*), sleeper (*light red*), and plate (*green*)

Measured Train Passages at Intact, Damaged and Repaired Tracks

The passages of trains have been measured by geophones which yield the particle velocities of certain track elements. These velocity results have to be corrected for the dynamic characteristics of the geophones (eigenfrequency of 4.5 Hz). The velocities can be integrated to displacements which often need a manual baseline correction. The resulting time histories can be evaluated for maxima and minima or interpreted as the specific deformation of the intact or damaged track.

The two slab track defects of the preceding section have been analyzed experimentally. At sites of the German high-speed railway net, the defects have been found visually. The dynamic behavior (the particle velocities) of the different track elements of different track sections without and with damage have been measured before and after repair. A slab track with possible damage, a slab track on a problematic soil, and a ballast track on a very soft soil have been investigated by comparing different track sections.

Loss of Contact Between Plate and Base Layer

A track with known loss of contact between plate and base layer has been measured before and after repair. Figure 8a shows the measured response of the intact (repaired) track whereas Fig. 8b shows the response of the damaged track. The particle

velocities (*top*) and the displacements (*bottom*) of the sleeper are shown for a passage of an ICE3 train. The responses for all 12 carriages are very similar. The train passage on the intact track is close to the theory in Fig. 5a, mainly for the displacements. The measured velocities, however, include some dynamic components presumably from track irregularities which are not present in the theory. Compared to the intact track, the time history of the damaged track displays some other characteristics. In Fig. 8b, the displacement between two neighboring bogies is much smaller compared to the measured and calculated results for an intact track. Displacements and particle velocities differ considerably in amplitude between intact and repaired slab tracks. These amplitudes have been evaluated for all measuring points (Fig. 9a). The missing contact between plate and layer yields high amplitudes of 80 mm/s for all three plate measuring points whereas an intact track would show much lower amplitudes of 15 mm/s for the plate and the layer.

Loss of Contact Between Sleeper and Plate

At another site, a slab track with loose sleepers has been measured, also before and after repair. The response of the sleeper to the passage of a ICE3 train is presented in Fig. 8c and d as particle velocities and displacements. The intact (repaired) track shows results similar to the theory and to the intact slab track at site G (Fig. 8a). The damaged track in Fig. 8d exhibits more specific characteristics of the time history of the displacements like a mid-way distortion and a downward peak for each bogie. Besides these strong changes of the displacement histories, the amplitudes show an extreme increase (Fig. 9b). The velocity amplitude of the left sleeper reaches the high value of the rails of 130 mm/s. whereas a value of about 15 mm/s would be normal for an intact slab track.

Check of the Contact Between Base Plate and Base Layer

At site S, several slab track sections have been investigated for track errors, namely for the loss of contact between base plate and base layer. Track sections with expected track errors have been compared with reference track sections which are assumed to be intact. Figure 10 presents for two pairs of critical and reference track sections the velocity response of the track plate and the displacement response of the track plate, base plate and base layer due to the passage of a four unit ICE test train. A strong difference between the displacements of the track plate on one hand and the small displacements of the base plate and base layer can be observed which is due to a resilient layer between the track plate and the base plate. Two items indicate that there is no damage between the base plate and the base layer. First, the response of the critical and the reference section are very similar in time history and amplitudes. Second, the displacements of the base plate and the base layer are very
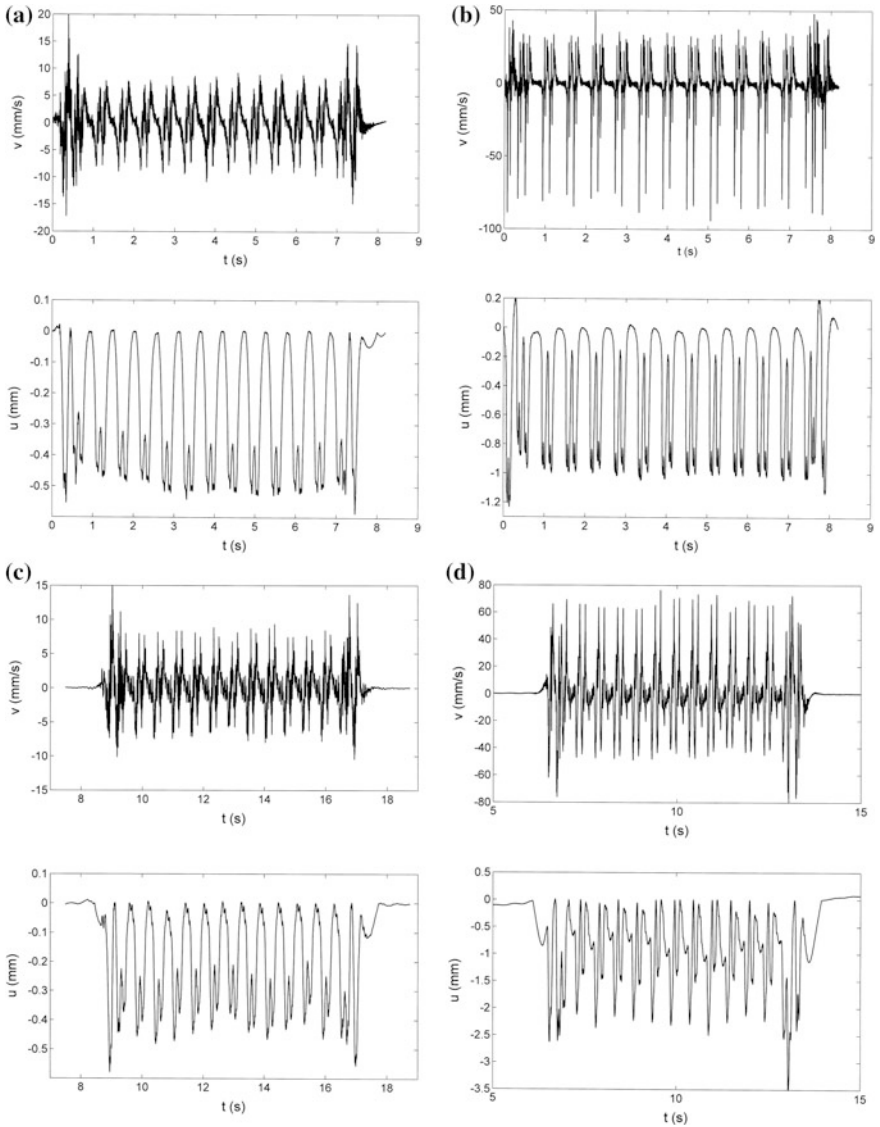
Fig. 8 Train passage over a slab track, measured particle velocities (*top*) and displacements (*bottom*) of the plate/sleeper, **a** repaired track, **b** damaged track, plate without contact, site G, **c** repaired track, **d** damaged track, sleeper without contact, site W

close together for all slab track sections. There is a difference of the track plate amplitudes for the different sections. The displacement at the end of a track plate (Fig. 10a and c) is approximately twice the displacement of the mid-side of the
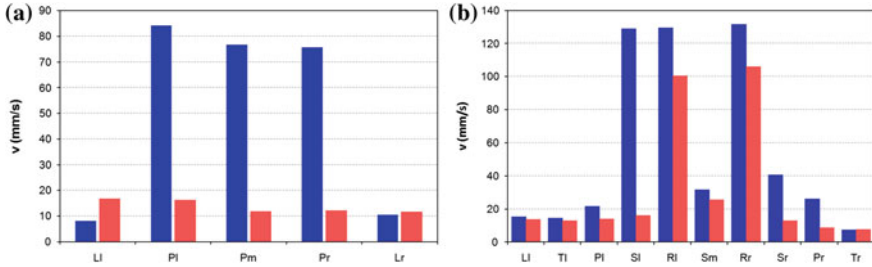
Fig. 9 Train passage over a slab track without (*light red*) and with damage (*dark blue*), **a** plate without contact to the base layer, **b** sleeper without contact to the plate; measured maximum velocities of the base layer left and right (Ll, Lr), the trough left and right (Tl, Tr), the plate left, middle and right (Pl, Pm, Pr), the sleeper left, middle and right (Sl, Sm, Sr), and the rail left and right (Rl, Rr)

track plate (Fig. 10b and d). The specific behavior of this type of slab track has also been analyzed by the hammer tests which is shown in the hammer impact section.

Check of a Soft Sub-soil of a Slab Track

At site E, a problem with the soil under the track was assumed because of a temporary high water content. The vibrations due to train passages have been measured at different slab track elements and also in the soil. In Fig. 11a and b, the velocity and displacement response of a set of measuring points from top to bottom is shown. The considerably higher amplitudes of the rails have been omitted for a better reading. The displacement amplitudes attenuate from 0.5 mm for the plate to 0.1 mm for the soil. The amplitudes of the plate as well as the time history are quite normal for a slab track on a medium stiff soil. Moreover, wave velocity measurements [2] have been performed on the soil along the track. The Rayleigh wave velocity has been determined at about 200 m/s which also indicates a sufficiently stiff soil.

Check of a Soft Sub-soil of a Ballast Track

Measurements of a ballast track have been performed at site A where a soft soil is assumed to yield safety problems. The velocity and displacement responses are given in Fig. 11c and d for two different track sections and the slow passage of a heavy locomotive for goods traffic. The displacement amplitudes of the sleepers are at about 1.7 mm which are much higher than the 0.5 mm measured at the intact slab tracks. These high amplitudes are partly due to the ballast track (see Fig. 3). But in addition, the displacement histories show minima for each bogie which are weakly
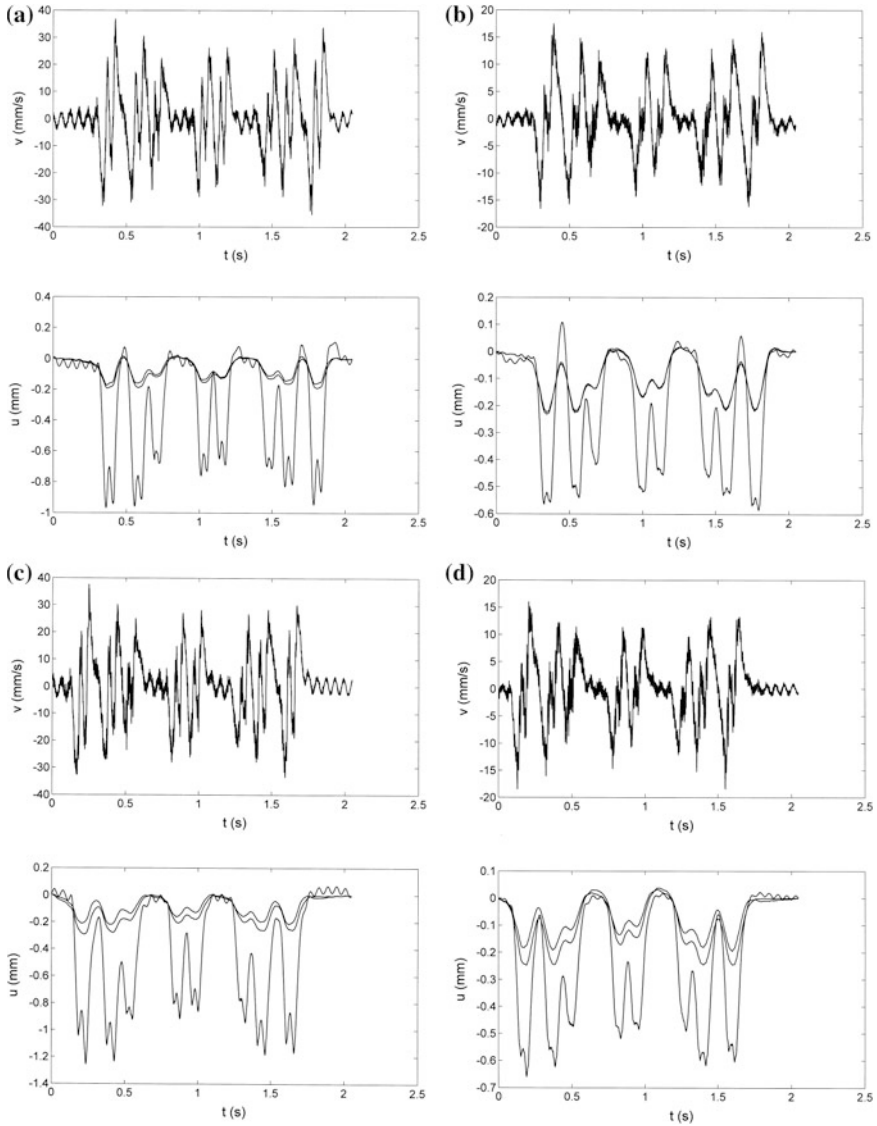
Fig. 10 Train passage over a slab track at site S, measured particle velocities of the track plate (*top*) and displacements of the track plate, base plate and base layer (*bottom*), **a** end section, and **b** mid section of the problematic track, **c** end section, and **d** mid section of the intact reference track

separated. This is also a characteristic of soft grounds. From the calculations, it could be concluded that these amplitudes are related to a very soft soil of $v_S = 100$ m/s. The small differences between Sect. 1 (on a low dam, Fig. 11c)
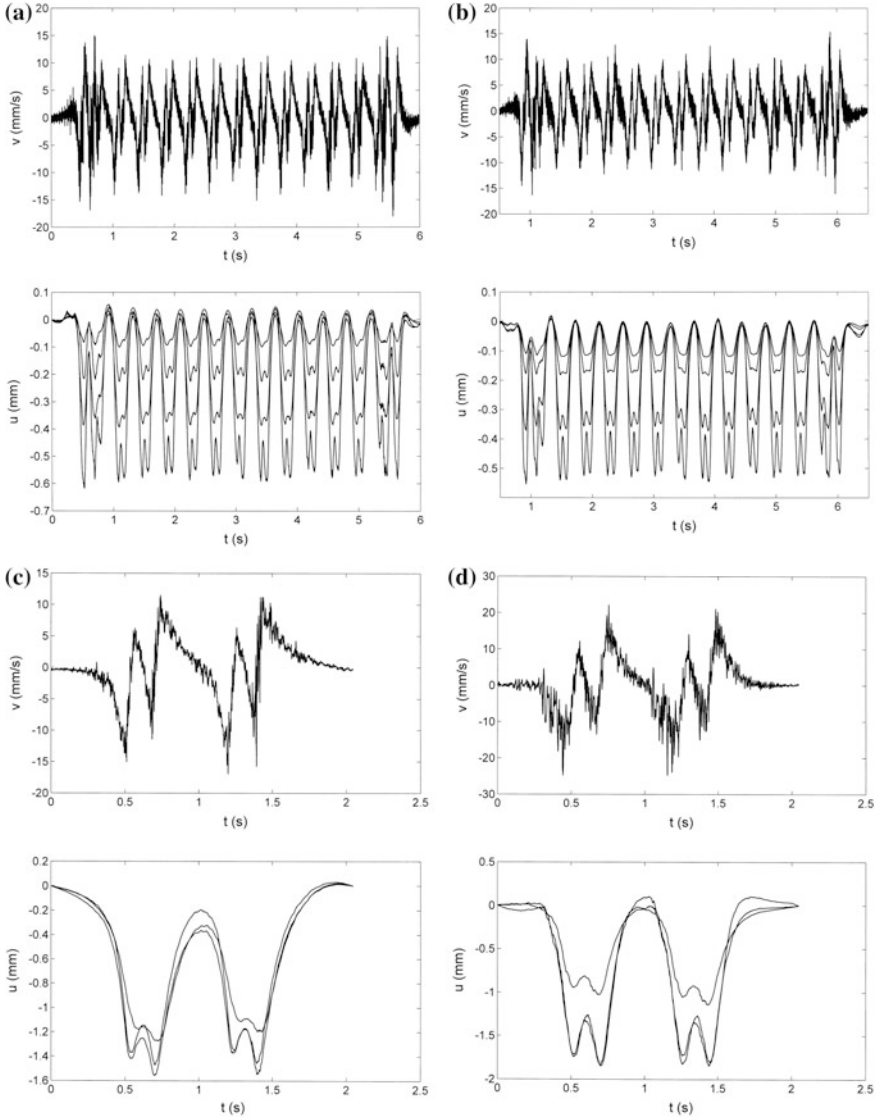
Fig. 11 Train passage over tracks on soft soil, measured particle velocities of the sleeper (*top*) and displacements of different track elements (*bottom*), **a** Sect. 1 and **b** Sect. 2 of the slab track at site E, plate, base layer, top soil, deeper soil, **c** Sect. 1, and **d** Sect. 2 of the ballast track at site A, left sleeper, right sleeper, ballast

compared to Sect. 2 (without dam, Fig. 11d), lower sleeper displacements (1.6–1.8 mm) and higher ballast displacement (1.2–1.0 mm) should be interpreted carefully. The main conclusion is the very soft soil at this site.

Track-Soil Compliances by Hammer Impact Measurements

Hammer impacts have been applied by an instrumented hammer. The measurement of the force allows to calculate the transfer function between velocity or displacement and the force (admittance or compliance spectra). These spectra are shown as

Check of the Contact Between Base Plate and Base Layer

Some results of the hammer tests at site S are shown in Fig. 12. The transfer functions of the different track elements (Fig. 12a and b) are similar for the problematic and the intact reference section. The amplitudes of the track plate are almost constant and much higher at about 5×10^{-3} mm/kN than the amplitudes of the base plate and the base layer. The transfer functions of the base plate at six different track sections in Fig. 12c show falling amplitudes from 1×10^{-3} to 0.2×10^{-3} mm/kN at high frequencies. The base layer (no figure) shows similar amplitudes and a some-what higher phase delay of $-70°$ (under hammer excitation on the base plate). These results demonstrate that the contact between base plate and base layer is satisfying. Whereas the results for the base plate and the base layer do not vary with the track sections, the transfer functions of the track plate are strongly dependent on the track section (Fig. 12d). The amplitudes are higher at the end of the plate, almost twice compared to the mid section of the plate. In addition, a smooth resonance can be observed at about 125 Hz. All these characteristics can be explained by the elastic support of the track plate and have no relevance for the damage control.

Loss of Contact Between Sleeper, Plate and Base Layer

Figure 13 shows experimental results of hammer tests on an intact and a damaged slab track. The responses of the different track elements of the intact track are very similar to the theoretical results in Fig. 3a. All elements are close together with small amplitudes except for the rail which has much higher amplitudes. The sleeper, plate, base layer, and soil have a higher phase delay similar to the theoretical prediction. The damaged slab track shows higher amplitudes and a smaller phase delay for the sleeper and the plate measuring points. According to the theoretical results in Fig. 6b, this is an indication of a plate with a lost contact to the base layer. If the impact on the sleeper is evaluated for the same track section (no figure), the loss of the contact between the sleeper and the plate can be identified by clear differences between the corresponding amplitudes and phases.
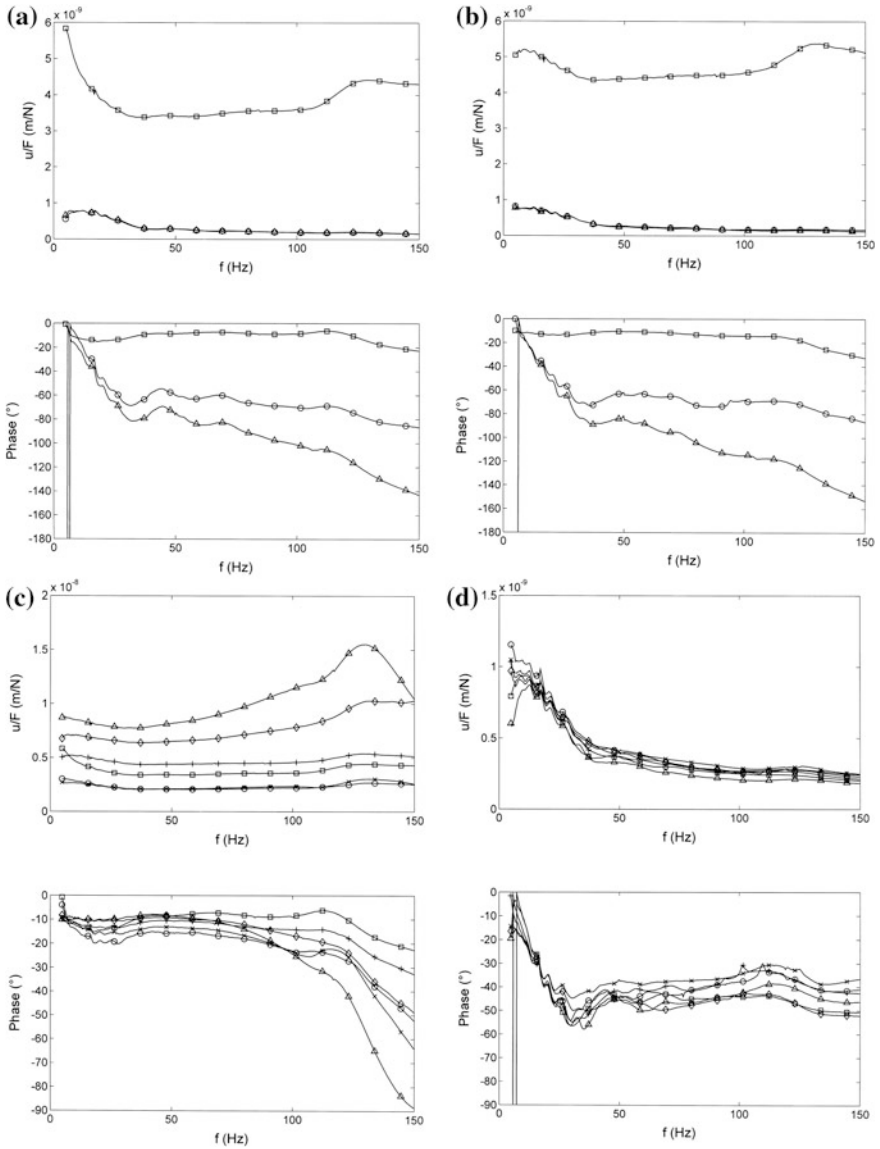
Fig. 12 Transfer functions of slab tracks at site S, amplitude and phase, **a** Sect. 1 with problematic track, and **b** Sect. 2 with intact reference track, hammer excitation on track plate, □ track plate, ○ base plate, △ base layer, **c** six sections response of track plate due to excitation on track plate **d** six sections response of base plate due to excitation on base plate amplitude and phase for frequencies up to 150 Hz in the same way as the theoretical results
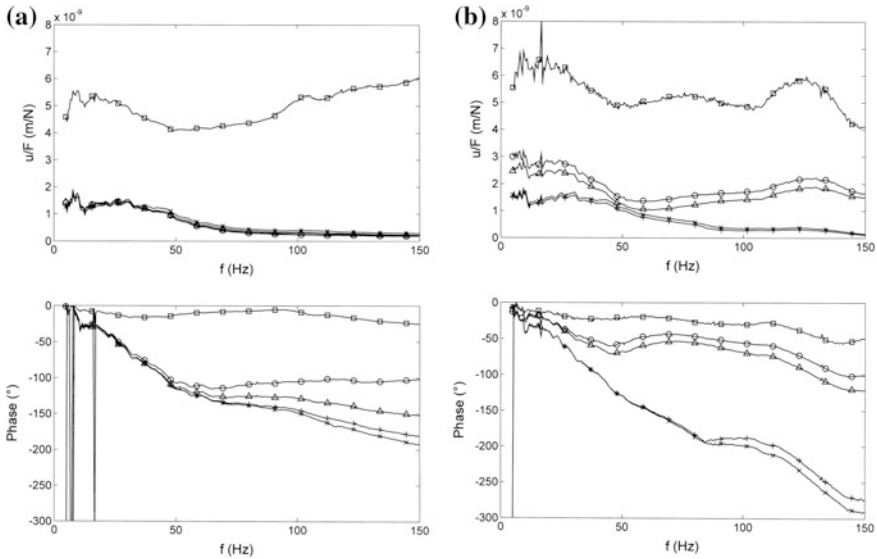
Fig. 13 Transfer functions of slab tracks at site W, amplitude and phase, **a** repaired section, and **b** damaged section, □ rail, ○ sleeper, △ plate, + base layer, × soil

Conclusion

Several tests with intact and damaged tracks have been presented. The following items have been found of importance for a successful damage detection.

– The best results can be achieved for the case of two separate measurements of the same track in damaged and repaired condition. For the normal case of a single measurement, the problematic track section should be compared with a reference section which is not far away and has a similar sub-soil. The reference track must be without damage, and to be sure, a second reference section would be helpful. The track behavior must be homogeneous along the track to get a meaningful comparison.
– Measured particle velocities include more noise (due to track irregularities), and displacements are more significant for damage detection. Nevertheless, some problems of the time integration from velocities to displacements must be solved. Sensors at different track elements and soil positions are useful to determine track characteristics (elastic elements, soil stiffness). They also allow to calculate strains and corresponding damaging criteria.
– Hammer tests can be used for quite local investigations. It must be observed that hammer tests have normally no pre-load and are highly dynamic whereas the train passage is a low-frequency excitation with the strong pre-load of the train. Moreover, the difference between the two-sided symmetric train excitation and the one-sided asymmetric hammer excitation must be observed.

– If only the problematic track section is measured, the identification of a damage should be supported by theoretical calculations of intact and damaged tracks.

The present results, the observed agreement between impulse and train passage, experimental and theoretical results are encouraging for developing a monitoring concept for railway tracks.

References

1. Auersch, L., Said, S. (2015). Comparison of different dispersion evaluation methods and a case history with the inversion to a soil model, related admittance functions, and the prediction of train induced ground vibration. Journal of Near Surface Geophysics, 13(2): 127–142.
2. Auersch, L., Said, S. (2011). Experimental soil parameters by different evaluation methods for impulsive, train and ambient excitation. In W. Zhai (ed.) Advances in Environmental Vibration, Proc 5th Int. Symposium. on Environmental Vibration (ISEV), Chengdu, Science Press, Beijing, pp. 3–9.
3. Auersch, L. (2005). Dynamics of the railway track and the underlying soil: the boundary-element solution, theoretical results and their experimental verification. Vehicle System Dynamics, 43(9): 671–695.
4. Auersch, L., Said, S. (2010). Attenuation of ground vibrations due to different technical sources. Earthquake Engineering and Engineering Vibration, 9(3): 337–344.
5. Auersch, L., Said, S. (2013). The influence of soil properties on the ground vibration due to railway traffic and other sources – the comparability of different sites. Proc. 6th Int. Symposium on Environmental Vibration (ISEV), Shanghai, Tongji University Press, pp. 175–186.
6. Rücker, W., Rohrmann, R., Limberger, E., Said, S., Schmid, W., Holtzendorff, K., Krüger, M. (1998). Investigation on ballast behaviour on bridges due to high acceleration on a test rig. Report for the European Rail Research Institute (ERRI), BAM, Berlin.
7. Auersch, L., Said, S., Knothe, E., Rücker, W. (2014). The dynamic behavior of railway tracks with under sleeper pads, finite-element boundary-element model calculations, laboratory tests and field measurements. Proc. 9th European Conference on Structural Dynamics (EURODYN 2014), Porto, pp. 805–812.
8. Auersch, L., Schmid, G. (1990). A simple boundary element formulation and its application to wavefield excited soil-structure interaction. Earthquake Engineering and Structural Dynamics, 19(7): 931–947.
9. Auersch, L. (1994). Wave propagation in layered soil: theoretical solution in wavenumber domain and experimental results of hammer and railway traffic excitation. Journal of Sound and Vibration, 173(2): 233–264.
10. Auersch, L. (2012). The dynamic behavior of slab tracks on homogeneous and layered soils and the reduction of ground vibration by floating slab tracks. J. of Engineering Mechanics, 138(8): 923–933.

2D and 2.5D Responses of Long Underground Tunnels to Moving Train Loads: A Comparison Study

Y.B. Yang, Xujie Liang, Hsiao-Hui Hung and Yuntian Wu

Introduction

In analyzing the dynamic response of tunnels to moving train loads, the 2D model [1, 2] has often been used, due to its simplicity and lower cost in modeling. However, the 2D model suffers from the lack of ability to simulate the effect of wave transmission along the tunnel axis. It is generally agreed that the 2D result is qualitatively good and can be used in the initial design of tunnels. In contrast, to account for the variation in geometry and materials of the half space, 3D models have also been attempted [3–5]. However, the 3D approach has been criticized for its relatively high computational cost, which is prohibitive for use is daily design.

In order to deal with the wave transmission along the tunnel axis, while reducing the time spent on 3D computing, Yang and Hung proposed the 2.5D analysis concept through the Fourier transformation for the excitation loads [6, 7]. For long tunnels embedded in soils with uniform materials along the tunnel direction, the 2D profile of the half space, with two in-plane degrees of freedom (DOFs) and one

Y.B. Yang (✉) · X. Liang · Y. Wu
MOE Key Laboratory of New Technology for Construction of Cities
in Mountain Area and School of Civil Engineering,
Chongqing University, 400045 Chongqing, China
e-mail: ybyang@cqu.edu.cn

X. Liang
e-mail: 380263568@qq.com

Y. Wu
e-mail: yuntianw@cqu.edu.cn

H.-H. Hung
National Center for Research on Earthquake Engineering, 106 Taipei, Taiwan
e-mail: hhung@narlabs.org.tw

31

out-of-plane DOF, can be used to simulate its 3D behavior. Using such an approach with finite/infinite elements, the effects of various parameters, such as those of the soil, tunnel and train, as well as rail roughness, on the soil vibrations due to underground railway were analyzed [8, 9].

Previously, few researches have been carried out to compare the results obtained by the 2D and 3D models. In general, the 2.5D approach is an effective tool for simulating the 3D response of the soil-tunnel system to moving trains, and thus can be considered as a reasonable substitute of the 3D approach. To realize the limitation of the 2D approach, both the 2D and 2.5D responses of soil-tunnel system to moving train loads will be studied and compared, considering the effects of train speed and rail roughness in both time domain and frequency domain.

Formulation and Basic Assumptions

Using the finite/infinite element approach, the half-space in Fig. 1 is divided into two regions as the *near field* and *far field*. The near field is modeled by the finite elements, to cope with the irregularities in geometry and materials of the soil-tunnel system. The far field extending to infinity is simulated by the infinite elements, which can duly account for the radiation effect of the infinite domain. By performing the standard finite element procedure, the equation of motion in frequency domain can be expressed as

$$\left([\mathbf{K}] - \omega^2[\mathbf{M}]\right)\{\mathbf{D}\} = \{\mathbf{F}\} \tag{1}$$

where ω is the frequency of concern, $\{\mathbf{F}\}$ and $\{\mathbf{D}\}$ denote the vector of external loads and nodal displacements, respectively, and $[\mathbf{K}]$ and $[\mathbf{M}]$ the global stiffness and mass matrices, respectively. All of these terms can be obtained by assembling the corresponding matrices of the constituting finite and infinite elements. The displacement vector $\{\mathbf{D}\}$ solved from Eq. (1) represents exactly the frequency response function (FRF) for the 2D or 2.5D approach, which are crucial to the numerical simulation in this paper.

Fig. 1 Typical model of analysis
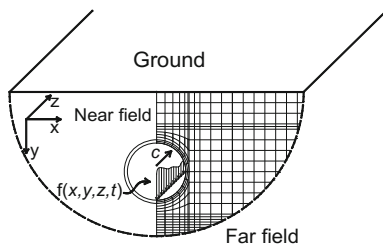
No attempt will be made herein to derive the FRFs for the 2D and 2.5D approaches using the finite/infinite elements, as they are available in Refs. [1] and [6], respectively. To obtain the load vector {$\mathbf{F}$} for use in Eq. (1) with account taken of the axle loads of each carriage of the moving train, the procedure presented in Ref. [10] should be followed.

In Ref. [9], a technique is also presented for inclusion of the effect of rail roughness. By using the cosine-shaped functions to represent the rail roughness, it was shown in Eq. (25) of Ref. [9] that the wheel-rail interaction force in the Fourier transformed domain is composed of three parts, i.e., the *static weight* of the moving wheelset, the *roughness-induced dynamic force*, and the *conjugate* of the dynamic force. In this paper, the results obtained by the 2D and 2.5D approaches will be compared, with focus on the roughness effect. For further details, the readers should be referred to a complete version of the present paper to be published in Ref. [11].

Numerical Studies

The vibrations induced by the Beijing metro Line 4 have been studied by Gupta et al. [12] to evaluate their influence on some sensitive equipment housed in one laboratory of Beijing University located near the Chengfulu Station. The same problem is analyzed here, with the properties of materials, including the soil, tunnel and track listed in Table 1. Following Ref. [12], the train adopted is composed of 6 cars of identical configurations, each of 19 m long, travelling at a speed of 60 km/h (16.67 m/s). For the tunnel, the centroid is at $h = 13.5$ m beneath the ground, the inner diameter is 5.4 m, and the wall thickness is $t = 30$ cm. Only half of the system is considered due to symmetry of the problem in geometry. The finite/infinite element mesh adopted for the following study is shown in Fig. 2, along with two observation points, OP-1 and OP-2.

Table 1 Materials properties of soil, tunnel and track

Material	Young's modulus E (MPa)	Poisson's ratio v	Mass density ρ (kg/m^3)	Damping ratio β
Concrete tunnel lining	35,000	0.25	2500	0.02
Concrete slab	28,500	0.2	2500	0.02
Elastic foundation	0.5	0.25	150	0.1
Fill material	116.6	0.341	1900	0.05
Silty clay	289	0.313	2023	0.04
Gravel and pebble	704	0.223	1963	0.03

Fig. 2 Finite/infinite element mesh
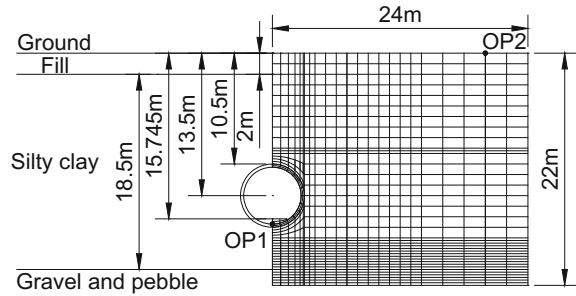
Effect of Train Speed

Three train speeds $c = 16.67$, 50, and 70 m/s and smooth rails are considered herein. Figure 3 shows the displacement responses of observation points OP-1 and OP-2, in which parts (a), (b) and (c) represent the responses in time domain for three different train speeds. It is observed for the train moving over *smooth rails* that: (1) *The trends of oscillation of the soil obtained by the two approaches get closer for the train moving at higher speeds, albeit higher amplitudes exist for the 2D result;* (2) *The trends of oscillation of the soil obtained by the 2D and 2.5D approaches match more at the invert of the tunnel (OP-1) than on the free surface in the far field (OP-2);* (3) *No oscillation occurs for the 2.5D results for any train speed for the free surface in the far field (OP-2), though the same is not true for the 2D result.*

To explain the phenomena observed in Fig. 3, the FRFs computed for the 2D and 2.5D approaches under unit harmonic load at different speeds over smooth rails are plotted in Fig. 4. Clearly, the FRF computed for the 2D approach are *much larger* than that for the 2.5D approach for the entire frequency range of concern when the train moves at normal speeds, and they become coincident when the speed approaches infinity. Consequently, the 2D result based on plane strain condition can be regarded as the limit of the 2.5D analysis with infinite train speed. Furthermore, the relatively *larger amplitude* of the FRF for the 2D analysis in the high frequency range with respect to the 2.5D analysis accounts for the high-amplitude oscillation of the 2D result at the tunnel invert (OP-1) in time domain in Fig. 3. The fact that the FRF decreases drastically for the 2D analysis for the far field (OP-2) in the high frequency range, while the one for the 2.5D analysis simply vanishes, explains clearly the drop in oscillation level for the far field response predicted by the 2D approach and the smooth, flat result by the 2.5D analysis in Fig. 3. This can also be regarded as the effect of attenuation of the high-frequency waves.

In the presence of rail roughness, due to the interaction between the wheels and rails, the deformation of the soil won't approach the plane strain condition, even for the same train under fast-moving conditions. From an analytical perspective, for the velocity and acceleration of the soil vibrations associated with the 2nd and 3rd terms (roughness-induced dynamic forces) on RHS of Eq. (25) of Ref. [9], in which
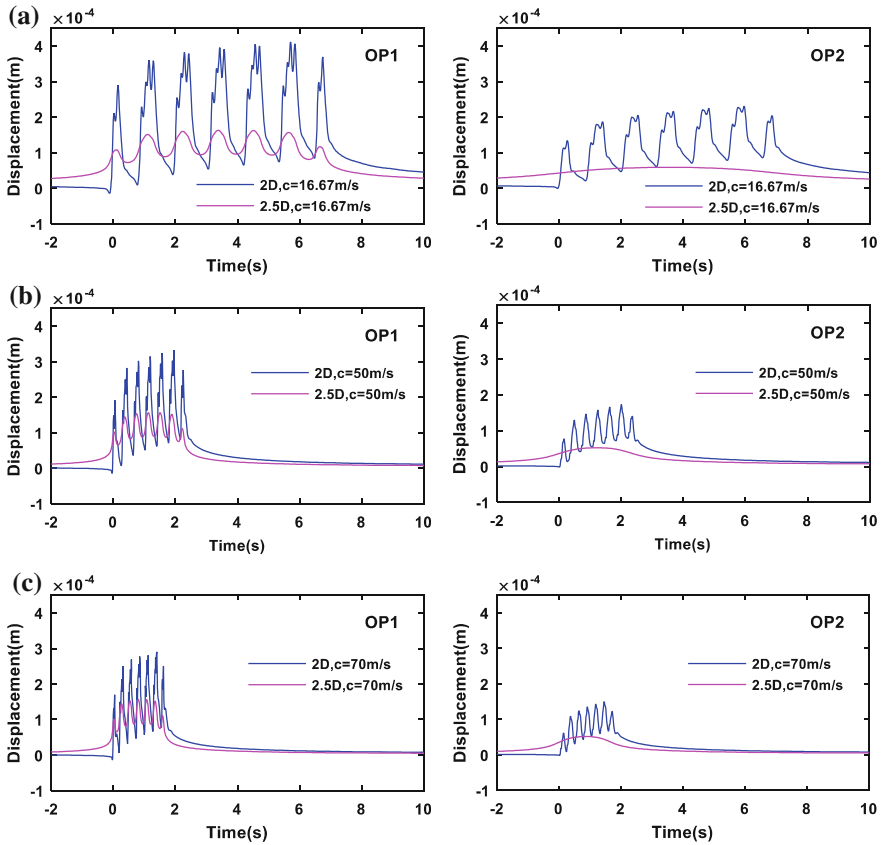
Fig. 3 Displacement responses in time domain over smooth rails with $c = 16.67$ m/s (**a**), 50.0 m/s (**b**), 70.0 m/s (**c**)
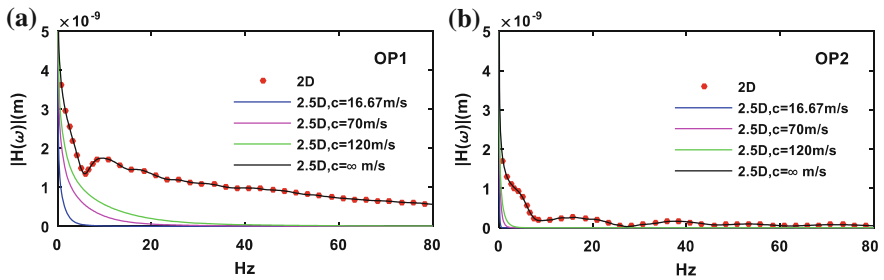
Fig. 4 Response functions for unit load at different speeds over smooth rails due to static weight: **a** tunnel invert (OP-1), **b** far field OP-2 (20 m, 0)
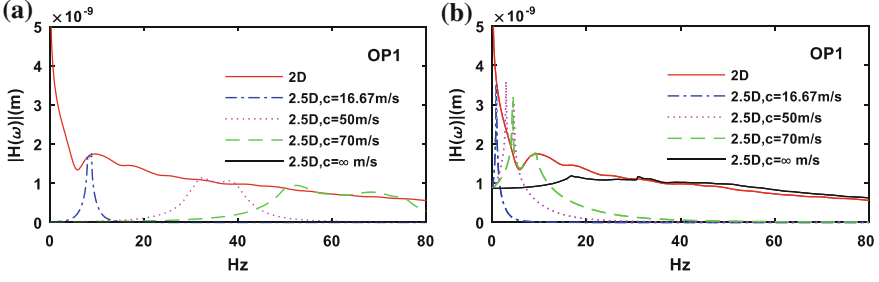
Fig. 5 Response functions due to 2nd term (roughness-induced dynamic forces) on RHS Eq. (25) [9] for unit load at different speeds over rough rails: **a** $\lambda = 2$ m, **b** $\lambda = 20$ m

the wavenumber k_z equals $-(\omega - \omega_i)/c$ and $-(\omega + \omega_i)/c$, respectively, and ω_i equals $k_i c$, the wavenumber k_z will approach $\pm k_i$ (the wave number of the ith cosine-shaped rail surface), rather than zero, when the train speed c gets close to infinity. For the roughness-induced dynamic forces (2nd term) on RHS of Eq. (25) of Ref. [9] under unit harmonic load, Figs. 5a, b show the corresponding FRFs computed by the two approaches for the track with irregularity of constant amplitude 2.0 mm and wavelength $\lambda = 2.0$ and 20.0 m, respectively. As can be seen, *when the irregularity wavelength λ gets larger (approaching the condition of smooth rails), the responses obtained by the 2D and 2.5D approaches become closer in the high frequency range for increasing train speeds*. The same phenomenon can be observed for the conjugate of roughness-induced dynamic force (3rd term) on RHS of Eq. (25) of Ref. [9].

Effect of Rail Roughness

The same train speed of $c = 70$ m/s is adopted, along with the same finite element mesh. To further evaluate the effect of rail roughness on soil vibrations, three track irregularity profiles of the cosine form with amplitude 2.0 mm and wavelengths $\lambda = 2.0$, 3.5 and 20.0 m are considered, corresponding to roughness frequencies of 35, 20, and 3.5 Hz, respectively. The velocity and acceleration responses computed for OP-1 and OP-2 in time domain are plotted in Figs. 6 and 7, respectively, in which parts (a), (b) and (c) represent the responses for three different wavelengths. Here, it is observed that: (1) *The oscillational trends of the velocity and acceleration responses obtained by the two approaches get closer for shorter irregularity wavelengths, although higher levels of oscillation always exist for the 2D results.* (2) *The vibration level of the soil surface in the far field (OP-2), either for velocity or acceleration, is much smaller than that at the tunnel invert (OP-1), due to the effect of attenuation for high-frequency components.*

Some reasonings will be given for the phenomena observed from Figs. 6 and 7. For the 2D approach, since the FRF is not affected by the wave number k_z, the FRF remains the same (as in Fig. 4) for all the three RHS terms of Eq. (25) of Ref. [9], which means that the soil responses computed by 2D approach will be affected the by all the three terms i.e., the static and dynamic forces, given in Eq. (25).

As for the 2.5D approach, in order to grasp which term affects mostly the soil response, the velocity response at OP-1 caused by each of the three RHS terms of Eq. (25) of Ref. [9] in frequency domain has been plotted in Fig. 8. Clearly, the velocity response of OP-1 is dominated mainly by the roughness-induced dynamic forces (2nd term) of Eq. (25) in the frequency range of 30–40 Hz for shorter rail wavelengths (for $\lambda = 2$ m), thereby making the contributions of the other two terms invisible. In fact, the contribution by the static weight (1st term) of Eq. (25) remains constant for the three wavelengths. It becomes dominant for medium and long wavelengths (for $\lambda = 3.5$ and 20 m) due to the vanishing contribution of the
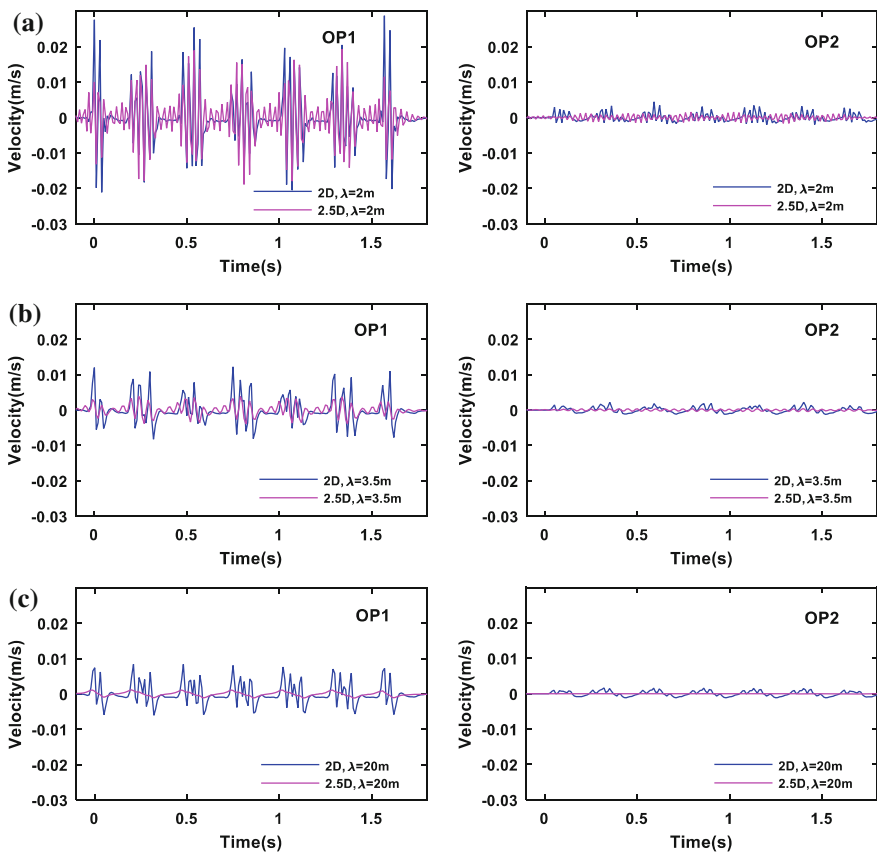
Fig. 6 Velocity responses of OP-1 and OP-2 in time domain for rough rails, $c = 70$ m/s: **a** $\lambda = 2$ m, **b** $\lambda = 3.5$ m, **c** $\lambda = 20$ m
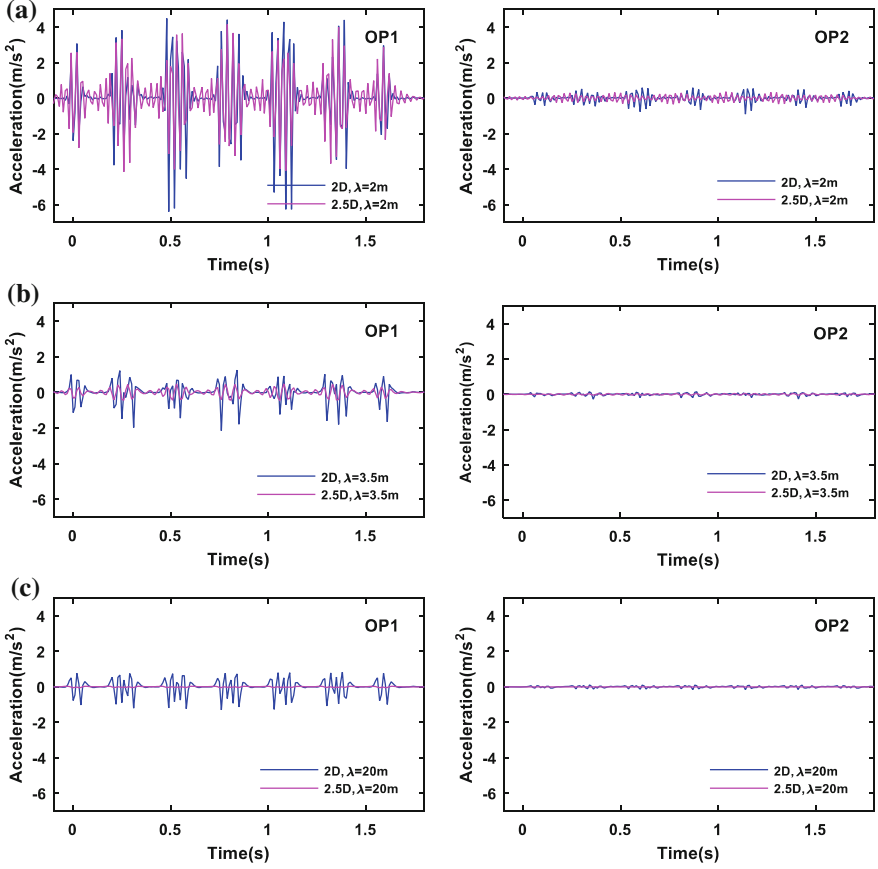
Fig. 7 Acceleration responses of OP-1 and OP-2 in time domain for rough rails, $c = 70$ m/s:
a $\lambda = 2$ m, **b** $\lambda = 3.5$ m, **c** $\lambda = 20$ m

roughness-induced dynamic forces (2nd RHS term). Besides, one observes the relatively high amplitude of the frequencies of 35 and 20 Hz induced by the 2nd RHS term for the three wavelengths in Fig. 8a, b, respectively.

For the reason that short rail wavelengths induce larger velocity and acceleration responses, while the 2nd RHS term (roughness-induced dynamic force) of Eq. (25) of Ref. [9] is dominant for rails with short wavelengths, only the 2nd RHS term (roughness-induced dynamic force) of Eq. (25) is adopted for the 2.5D analysis in studying the effect of rail wavelength. In this regard, we shall study the total force (Force1) and roughness-induced dynamic force (Force2) that dominate the velocity and acceleration responses of the 2D and 2.5D approaches, respectively, and plot them in frequency domain for various wavelengths in Fig. 9. The following are observed: (1) For all three wavelengths, the total force (Force1) for the 2D approach has some *major* low frequency components (<5 Hz), and some moderate ones for
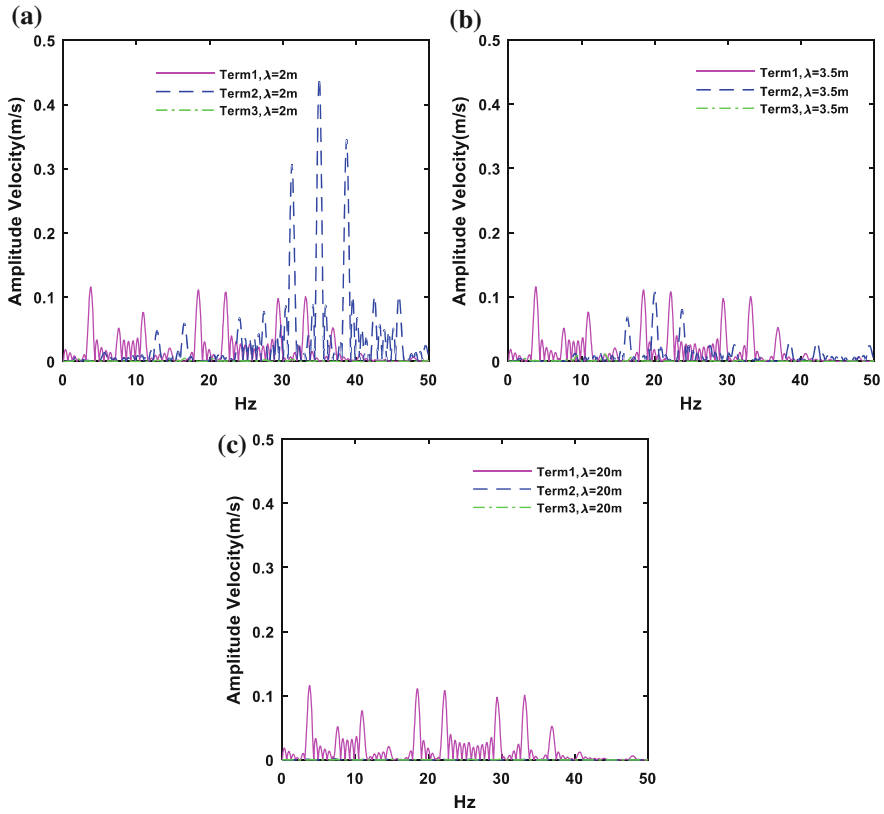
Fig. 8 Contribution of each RHS term of Eq. (25) of Ref. [9] for OP-1 in frequency domain by 2.5D approach: **a** $\lambda = 2$ m, **b** $\lambda = 3.5$ m, **c** $\lambda = 20$ m

medium and long wavelengths (with $\lambda = 3.5$ and 20.0 m) for frequencies ranging from 5 to 40 Hz. (2) For short wavelength ($\lambda = 2.0$ m), the total force (Force1) and roughness-induced dynamic force (Force2) have some *significant* higher frequency components in the range from 30 to 40 Hz. (3) For medium wavelength ($\lambda = 3.5$ m), the roughness-induced dynamic force (Force2) is visible only for 15–25 Hz, while for long wavelength ($\lambda = 20.0$ m), it vanishes virtually for the entire frequency from 0 to 50 Hz. (4) The three frequency components 35, 20, and 3.5 Hz in Fig. 9a–c, respectively, should be regarded as those induced by rail roughness.

The FRFs computed by the 2D and 2.5D approaches for the roughness-induced dynamic force (2nd RHS term) of Eq. (25) of Ref [9] under unit harmonic load for three different rail wavelengths have been plotted in Fig. 10a, b for the tunnel invert (OP-1) and the free surface in the far field (OP-2), respectively. The following are observed for the velocity and acceleration responses: (1) For the tunnel invert (OP-1), the 2D result has a uniform but slightly decaying response as the frequency
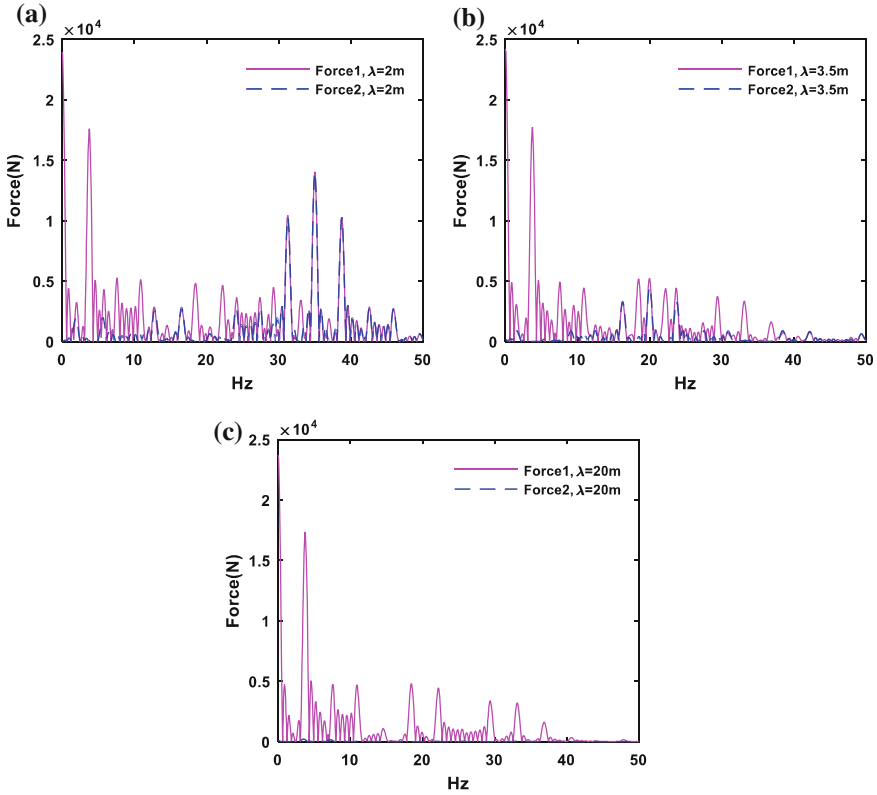
Fig. 9 Force1 (total force) and Force2 (roughness-induced dynamic force) in frequency domain: **a** $\lambda = 2$ m, **b** $\lambda = 3.5$ m, **c** $\lambda = 20$ m
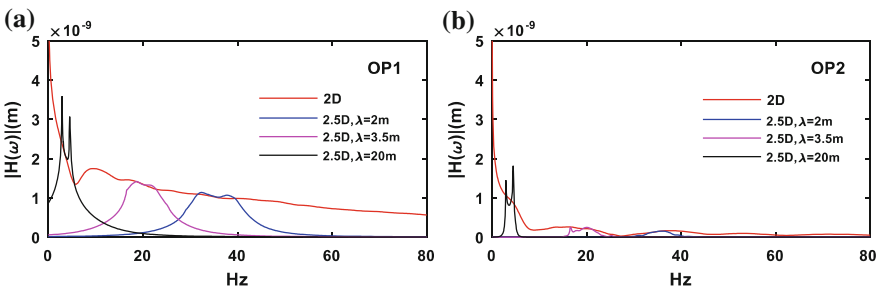
Fig. 10 Response function due to roughness-induced dynamic force of Eq. (25) under unit load for different wavelengths: **a** tunnel invert (OP-1), **b** free surface in far field (OP-2)

increases. In contrast, the 2.5D result shows that *the shorter the track irregularity wavelength is, the higher the response frequencies are*, consistent with our common understanding. (2) For the free field in far field (OP-2), there are some small peaks

existing in the low-frequency range (<10 Hz) for both the 2D and 2.5D results. However, the amplitudes for frequencies greater than 10 Hz are generally small due to the attenuation effect. (3) Relatively large amplitudes can be observed for frequencies around 3.5, 20, and 35 Hz, corresponding to rail roughness wavelengths of 20, 3.5, and 2 m, respectively, for the 2.5D response.

As a matter of fact, rails with shorter wavelength induce more high frequency components, which tend to affect much more the velocity and acceleration responses of the soils. This also explains why the oscillational trends of the velocity and acceleration responses of the soil obtained by the two approaches get closer when the track irregularity wavelength decreases. The other observation from Figs. 6 and 7 is that the vibration level of the soil surface in the far field (OP-2) is much smaller than at the tunnel invert (OP-1), which can be attributed to the low attenuation rate of low-frequency waves and the high attenuation of high-frequency waves [9]. In other words, the responses of the high-frequency components decrease more significantly with the increase in distance.

The difference between the responses of frequencies computed by two approaches is explained as follows. First of all, Fig. 10a indicates that *the 2D FRF for the tunnel invert (OP-1) is generally not affected by the composition of roughness frequencies*, namely, the *whole range* of *frequencies contribute to the response regardless of the variation in roughness frequencies*. In contrast, the 2.5D FRF is "*concentrated*" around the roughness frequencies. Figure 10a also indicates that for the 2D FRF, the low frequency components have larger amplitudes compared with the high frequency ones. From Fig. 9, we see that the total force in the low frequency range (<20 Hz) for the 2D case, i.e., Force1, shows basically the same amplitudes regardless of roughness frequencies, which is caused mainly by the moving tributary weights of the train cars. Particularly, the relatively high amplitude at the frequency $c/L \approx 4$ Hz is caused by the driving frequency, if one notes that $L = 19$ m is the length and $c = 70$ m/s is the car speed. It goes without saying that the frequencies in the range of 30–40 Hz are roughness frequencies, as was noted previously.

Conclusions

In this paper, a comparative study has been conducted for the responses of underground tunnels to moving train loads using the 2D and 2.5D finite/infinite element approaches, considering the effects of train speed and rail roughness. The 2.5D approach can be regarded as a 3D simulation for tunnel-soil systems that are uniform along the tunnel axis. Based on the numerical analyses conducted and the material and geometric properties assumed, the following conclusions are drawn:

- For all the cases studied, whether for smooth or rough rails, the soil response predicted by the 2D approach is always higher than the 2.5D approach, indicating that the former is a conservative tool for use in the initial design of

soil-tunnel systems. The 2D frequency response function is not affected by the roughness frequencies. It is contributed by the whole range of frequencies regardless of the variation in roughness frequencies.

- Effect of train speed: The trends of oscillation of the soil obtained by two approaches match more at the near field than far field, and they get closer when train moves at higher speeds over smooth rails. The 2D result (with plane strain condition) can be regarded as the limit of the 2.5D analysis with infinite train speed for smooth rails, which is not true for rough rails.
- Effect of rail roughness: The 2D FRF is contributed by frequencies of the whole range of the soil-tunnel system, but less sensitive to the variation in roughness frequencies. In contrast, the 2.5D FRF is concentrated around (and sensitive to) the frequencies of rail roughness.
- The 2D approach is good for predicting the natural frequency of the floating slab track, a property essential to selection of suitable elastic foundation for reducing the train-induced vibrations.

The 2D approach saves considerable computation time when more frequency components need to be computed, since the system matrices are much smaller in size. But the 2.5D approach is more realistic, since it can duly account for factors such as train speed, rail roughness, elastic foundation, and mechanism of wave transmission along the tunnel axis.

References

1. Yang, Y. B., Kuo, S. R., Hung, H. H. (1996). Frequency-independent infinite elements for analyzing semi-infinite problems, International Journal for Numerical Methods in Engineering, 39: 3553–3569.
2. Yang YB, Hung HH (1997), A parametric study of wave barriers for reduction of train-induced vibrations. International Journal for Numerical Methods in Engineering, 40, 3729–3747.
3. Mohammadi, M., Jarabalis, D. (1995). Dynamic 3-D soil-railway track interaction by BEM-FEM. Earthquake Engineering and Structural Dynamics, 24: 1177–1193.
4. Gardien, W., Stuit, H. G. (2003). Modelling of soil vibrations from railway tunnels. Journal of Sound and Vibration, 267: 605–619.
5. Ju SH, Lin HT (2004). Analysis of train-induced vibrations and vibration reduction schemes above and below critical Rayleigh speeds by finite element method. Soil Dynamics and Earthquake Engineering, 24: 993–1002.
6. Yang YB, Hung HH (2001). A 2.5D finite/infinite element approach for modelling visco-elastic bodies subjected to moving loads. International Journal for Numerical Methods in Engineering, 51(11): 1317–36.
7. Yang YB, Hung HH (2009). Wave propagation for train-induced vibrations – a finite/infinite element approach. Singapore: World Scientific, Singapore.

8. Yang YB, Hung HH (2008). Soil vibrations caused by underground moving trains. Journal of Geotechnical and Geoenvironmental Engineering, ASCE, 134(11): 1633–44.
9. Hung HH, Chen GH, Yang YB (2013). Effect of railway roughness on soil vibrations due to moving trains by 2.5D finite/infinite element approach. Engineering Structures, 57: 254–66.
10. Hung HH, Yang YB (2001). Elastic waves in visco-elastic half-space generated by various vehicle loads. Soil Dynamics and Earthquake Engineering, 21: 1–17.
11. Yang YB, Liang XJ, Hung, HH, Wu YT (2016). Comparative study of 2D and 2.5D responses of long underground tunnels to moving train loads. To be Submitted.
12. Gupta S, Liu WF, Degrande G. Lombaert G, Liu WN (2008). Prediction of vibrations induced by underground railway traffic in Beijing. Journal of Sound and Vibration, 310(3): 608–30.

Out-of-Plane Parametric Resonance of Arches Under an In-Plane Central Harmonic Load

Airong Liu, Hanwen Lu, Yong-Lin Pi, Youqing Huang and Jing Li

Introduction

Arches have been widely used in infrastructures such as bridges. When an arch is subjected to in-plane dynamic loading, it may lose stability in the plane of loading or out of the plane of loading in a dynamic instability mode [1]. Investigations have been focused on the in-plane dynamic instability of different arches that are subjected to various in-plane loads. Although investigations on the in-plane dynamic instability of arches have been extensive and static out-of-plane instability of arches has also been studied by a number of researchers [1–7], no research on the out-of-plane dynamic instability of arches under in-plane dynamic loading has been reported in the literature hitherto. It is not known what the frequency region of the in-plane harmonic load is that can induce out-of-plane resonance of the arch leading to dynamic out-of-plane instability of the arch. It is also not known how the amplitude of the excitation load and the damping of the arch influence the

A. Liu (✉) · H. Lu · Y. Huang · J. Li
Guangzhou University-Tamkang University Joint Research Center
for Engineering Structure Disaster Prevention and Control,
Guangzhou University, 510006 Guangzhou, China
e-mail: liuar@gzhu.edu.cn

H. Lu
e-mail: hanwenlo@foxmail.com

Y. Huang
e-mail: yqhuang@gzhu.edu.cn

J. Li
e-mail: lijing-7youyou7@hotmail.com

Y.-L. Pi
School of Civil and Environmental Engineering,
UNSW, Sydney, NSW 2052, Australia
e-mail: y.pi@unsw.edu.au

out-of-plane dynamic instability. In addition, arches may have some additional concentrated weights at their crown. It is not known how the additional weights influence the out-of-plane dynamic stability of arches.

This paper presents an experimental investigation on out-of-plane instability of shallow circular arches owing to parametric resonance.

Test Set-up

The test set-up is shown in Fig. 1. The systems of APS Dynamics Inc. [8] were used to generate excitation loads in the swept frequency vibration tests. The systems consist of the vibrator (model APS113), the power amplifier (model APS125) and the vibration control system VCS201. The systems can generate controlled sinusoidal loads under a constant frequency or swept frequencies with a maximum load of 113 N. The armature of the vibrator APS113 was connected to a rectangular steel frame using four bolts. A steel dowel bar fixed to the frame was connected with the central steel plates at the crown of the arch. The periodic excitation generated by the vibrator will be transferred to the arch through the frame, dowel bar and concentrated plate(s). A sensor mounted on the vibrator was connected to the vibration control unit (VCU113), which can control the vibration error.

The out-of-plane displacement, velocity, and acceleration of the arch during out-of-plane vibration and parametric resonance were measured using the vibration measurement system of Brüel and Kjær [9]: accelerometers, charge amplifiers, front-end module, and vibration analysis software. Accelerometers were firmly mounted on the arch in the lateral direction of the crown and quarter points of the arch (Fig. 1).

Fig. 1 Setup of vibration tests for circular swallow arch
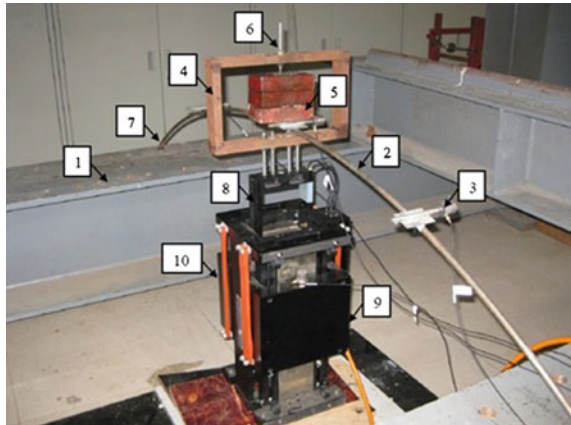
1 Counterforce frame; 2 Shallow arch; 3 Acceleration sensor; 4 Steel frame; 5 Central weights; 6 Dowel bar; 7 Ends- fixed boundary; 8 Armature; 9 Reaction block; 10 Vibrator.

Instability Regions of Excitation Frequencies

In tests, the central harmonic load was taken to be proportional to the static out-of-plane buckling load P_{cr} of the arch [5]. Swept frequencies of the central harmonic load were in the interval of the analytical solution of the critical frequency ± 0.5 Hz for out-of-plane instability and the amplitudes of the excitation force were increased in a stepwise fashion with each step of 10 N. The load was applied in the plane of the arch and exactly through the centroid of the central cross-section of the arch. It was observed from the response measurement and analysis by the system PULSE [9] that when the amplitude was small, the arch vibrated in the plane of the periodic load and due to extremely small initial out-of-plane imperfections, the arch also vibrated in a very small out-od-plane transient irregular fashion. When the frequency and amplitude of the excitation load reach certain values, the out-of-plane vibration of the arch suddenly changed from the transient irregular state to a steady state of out-of-plane parametric resonance. The frequencies at which the amplitude of the out-of-plane vibration suddenly has a significant increase or the out-of-plane vibration changes suddenly from the irregular transient state to the regular steady-state were recorded as the critical frequencies. The recorded critical frequencies of the excitation load were used to verify the analytical solution of the region of critical frequencies for out-of-plane dynamic instability of the arch.

The swept frequency tests were performed first for the arch with a central concentrated weight of 5.1 kg. The out-of-plane natural frequency of the arch was obtained by the hammer test as $f_n = 3.54$ Hz. When the amplitude of the central periodic load is 10 N, the analytical solution predicts that the arch does not vibrate in the out-of-plane direction. However, because the tested arch has inevitable initial out-of-plane geometric imperfections, the swept frequency test results for the time history of out-of-plane displacements of the arch shown in Fig. 2a indicate that

(a) With excitation amplitude of 10N

(b) With excitation amplitude of 80N
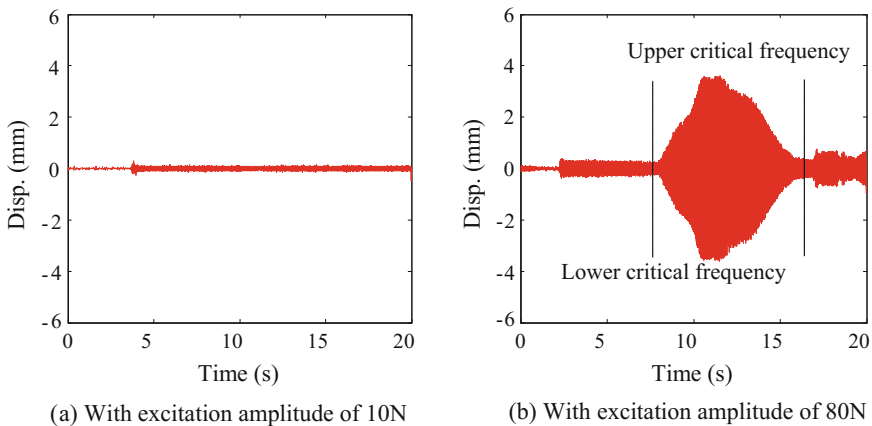
Fig. 2 Lateral displacement responses to in-plane harmonic load with swept frequencies

there is very small irregular out-of-plane vibration caused by the initial out-of-plane geometric imperfections of the arch. In spite of this, it can be seen from Fig. 2a that there is no sudden increase in amplitudes of out-of-plane vibration even when the excitation frequency is nearly twice of the out-of-plane natural frequency of the arch (±0.5 Hz), indicating that the parametric resonance did not occur.

However, when the amplitude of the periodic load increases to 80 N, the time history of out-of-plane displacements of the arch obtained by the swept frequency test is much different as shown in Fig. 2b. It can be seen from Fig. 2b that the amplitude of out-of-plane vibration of the arch increases significantly when the excitation frequency enters the analytical critical frequency region for out-of-plane dynamic instability of the arch. It can also be observed that as the excitation frequency moves out of the critical frequency region, the amplitude of out-of-plane vibration of the arch suddenly decreases.

Effects of Load Amplitude on Critical Frequencies

To investigate effects of the amplitude of the excitation load on the critical frequency of excitation, swept frequency tests were carried out by increasing the amplitude from 10 to 90 N with a step of 10 N. The critical frequencies for different values of dimensionless excitation amplitude β are listed in Table 1, in which $\beta = P_{cr}/P_{max}$ with $P_{max} = 100$ N being the maximum load used in the test. The analytical solutions [10] are also shown in Table 1 for comparisons.

It can be seen from Table 1 that test results agree well with their analytical counterparts. The effects of the amplitude of the excitation load on bounds of the critical frequency region were further investigated by swept frequency tests on arches with different central concentrated weight. The test results are shown in Fig. 3a, b for arches with no central weight and with a central weight of 5.1 kg.

It can be seen that when β is lower than a certain value, for example $\beta < 0.176$ in Fig. 3a, no out-of-plane parametric resonance occurs. When β exceeds a critical value, the parametric resonance occurs. The bandwidth of the region of critical frequencies of the excitation force increases with an increase of β. The increase of the bandwidth of the region of critical frequencies of the excitation force indicates that the possibility of occurrence of out-of-plane dynamic instability of the arch increases. It can also be seen from Fig. 3 that the bandwidth of the region of critical

Table 1 Critical frequencies of the arch with a central weight of 5.1 kg

Dimensionless excitation amplitude (β)		30%	40%	50%	60%	70%	80%
Lowest critical frequency (Hz)	Analytical	7.06	7.04	7.02	7.00	6.98	6.96
	Test	7.01	7.00	6.98	6.95	6.92	6.92
	Error (%)	0.71	0.57	0.56	0.71	0.85	0.57
Highest critical frequency (Hz)	Analytical	7.12	7.14	7.16	7.18	7.20	7.21
	Test	7.15	7.17	7.19	7.20	7.20	7.22
	Error (%)	0.39	0.39	0.41	0.30	0.55	0.09

(a) No concentrated weight (b) Central concentrated weight of 5.1kg
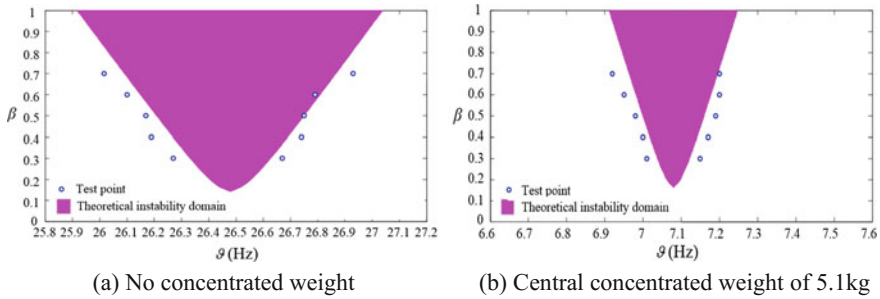
Fig. 3 Effect of central weight on critical frequencies

frequencies without the central plate is wider than that with a central plate of 5.1 kg. This is because the damping decreases with a decrease of the central weight. Hence, the possibility of occurrence of out-of-plane dynamic instability increases with a decrease of the central weight.

Effects of Excitation Frequency on Out-of-Plane Vibration

Variations of the amplitude of out-of-plane vibration with the excitation frequency for an arch having a central concentrated weight of 5.1 kg under a central periodic load with an amplitude of 80 N are shown in Fig. 4, where the solid and dashed lines represent the analytical stable and unstable solutions [11] respectively. It can be seen that there are four regions of out-of-plane vibration. In region "A", the frequency is much lower than the critical frequency for parametric resonance, thus, there is only small out-of-plane vibration. In region "B", there is steady state "traction" vibration with large amplitudes, as the excitation frequency is close to the critical region "C". In region "C", excitation frequency enters the critical region and there is beat vibration with large amplitudes. In region "D", the excitation frequency exceeds the critical region and there is steady state vibration with small amplitudes.

It can also be seen from Fig. 4 that the lowest and highest critical frequencies for out-of-plane dynamic instability of the arch are 6.95 and 7.20 Hz. When the

Fig. 4 Comparison of experimental and analytical amplitudes
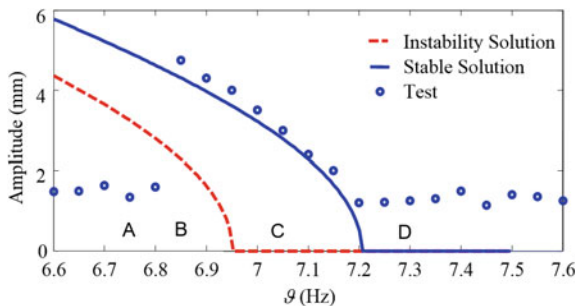
excitation frequency is lower than 6.95 Hz, it is usually thought that the out-of-plane dynamic instability of the arch cannot occur. However, because the curve of the amplitudes of out-of-plane vibration with the excitation frequency bends toward the low frequency region (Fig. 4), a "traction" mode of out-of-plane dynamic instability under an excitation frequency in the region "B" is still possible. When the excitation frequency is initially in the region "C" (6.95–7.20 Hz) and then decreases in a stepwise fashion with each step of 0.05 Hz until the excitation frequency (for example 6.9 Hz) enters the region "B", the "amplitudes" of out-of-plane vibration in the region "C" exert perturbation to the arch, the "traction" out-of-plane dynamic instability occurs although the excitation frequency has entered the region "B".

Conclusions

This paper investigated the out-of-plane dynamic instability of a shallow circular arch subjected to an in-plane central concentrated periodic load experimentally. It was shown that when the excitation frequency of the in-plane central periodic load is about twice of the out-of-plane natural frequency of the arch, the out-of-plane parametric dynamic instability of the arch occurs. In addition, the investigations demonstrated that the amplitude of the excitation load influences the out-of-plane dynamic instability of arches significantly. As the amplitude of the excitation load increases, the bandwidth of the critical region of excitation frequencies becomes wider leading to higher possibility for an arch to lose its stability in an out-of-plane dynamic instability mode. It was also demonstrated that the central concentrated weight contributes to the out-of-plane dynamic instability of arches. As the central weight decreases, the bandwidth of the critical frequency regions and the possibility of the occurrence of out-of-plane parametric resonance increase. Finally, it was shown that when perturbation is sufficient large, the "traction" mode of out-of-plane parametric dynamic instability is possible even when the excitation frequency is out of the lower bound of critical frequency regions.

References

1. Bolotin, V.V. (1995). Dynamic Stability of Structures, Nonlinear Stability of Structures. Springer, Vienna.
2. Huang, C.S., Nieh, K.Y., Yang, M.C. (2003). In-plane free vibration and stability of loaded and shear deformable circular arches. Int. J. Solids Struct. 40(22): 5865–5886.

3. Simitses, G. J. (2012). Dynamic Stability of Suddenly Loaded Structures. Springer, Berlin.
4. Pi, Y.-L., Bradford, M.A. (2008). Dynamic buckling of shallow pin-ended arches under a sudden central concentrated load. J. Sound Vib. 317(3–5): 898–917.
5. Pi, Y.-L., Bradford, M.A., Tong, Q.-S. (2010). Elastic lateral-torsional buckling of circular arches subjected to a central concentrated load. Int. J. Mech. Sci. 52: 847–862.
6. Liu, A.R., Huang, Y.H., Yu, Q.C., Rao, R. (2014). An analytical solution for lateral buckling critical load calculation of leaning-type arch Bridge. Math. Probl. Eng., 578473.
7. [7] Liu, A.R., Huang, Y.H., Fu, J.Y., Yu, Q.C., Rao, R. (2015). Experimental research on stable ultimate bearing capacity of leaning-type arch rib systems. J Constr Steel Res. 114, 281–292.
8. [8] APS Dynamics. (2014). Systems for Generating Controlled Vibration: APS 113 ELECTRO-SEIS® Long Stroke Shaker with Linear Ball Bearings, APS Dynamics Inc., Dresden Germany.
9. [9]Brüel & Kjær. (2003): PULSE-Getting Started: An Introduction to PULSE. Brüel & Kjær Sound & Vibration Measurement A/S, Nærum Denmark.
10. Liu, A.R., Lu, H.W, Fu, J.Y., Pi, Y.-L., Huang, Y.Q, Li, Jing, Ma, Y.W. (2016).Analytical and experimental studies on out-of-plane dynamic instability of shallow circular arch based on parametric resonance. Nonlinear Dynamics.
11. Liu, A.R., Lu, H.W. (2014). Investigations of out-of-plane dynamic buckling of arches under concentrated forcer. Report, Guangzhou University, Guangzhou.

Surface Vibration of a Layered Saturated Ground Subjected to an Embedded Moving Load

Anfeng Hu, Yijun Li, Bo Sun and Kanghe Xie

Introduction

The dynamic response of a soil medium subjected to moving loads has received considerable attention over the past decades. Research activities in this area have been motivated by the rapid development of mass rapid transit systems and high speed railways worldwide. It's worth mentioning that the elastic or visco-elastic half-space [1–3] and Biot's poroelastic saturated half-space [4–16] are the most widely used models in the analytical studies of the dynamic response of the ground.

In practical, it is well known that most subgrades consist of several layers. Thus, a layered model is more appropriate for inhomogeneous soil. So far, there are several main methods dealing with the layering of the medium: the propagator matrix method [17], the finite element method [18], the exact stiffness matrix method [19], and the transmission and reflected matrix (TRM) method. The TRM

A. Hu · Y. Li (✉) · B. Sun · K. Xie
Research Center of Coastal and Urban Geotechnical Engineering,
Zhejiang University, 310058 Hangzhou, China
e-mail: yijunli@zju.edu.cn

A. Hu
e-mail: anfenghu@zju.edu.cn

B. Sun
e-mail: bosun20041016@163.com

K. Xie
e-mail: zdkhxie@zju.edu.cn

A. Hu · Y. Li · B. Sun · K. Xie
MOE Key Laboratory of Soft Soils and Geoenvironmental Engineering,
Zhejiang University, 310058 Hangzhou, China

A. Hu · Y. Li · B. Sun · K. Xie
China Railway Siyuan Survey and Design Group Co., Ltd., Wuhan 430063, China

method is first established by Luco and Apsel [20, 21]. The advantage of this method is that the mismatched exponential terms are eliminated in all the terms of the TRM. As a result, the TRM method can be valid in the cases of high frequency and large layer thickness, which is very difficult to be solved by the conventional propagator matrix method. Xu et al. [22, 23] studied the dynamic response of a layered poroelastic half-space under the surface moving load with the TRM method. Studies addressing the dynamic response of a layered water-saturated poroelastic medium to buried moving loads are rather limited until now. Solutions for the internal moving load can be used in the study of dynamic response of embedded foundations, anchors, and underground structures (e.g. subway tunnels, defence related structures, etc.).

In this paper, the layered poroelastic half-space subjected to a buried moving strip load is considered to be a plain-strain problem. Based on the Biot's wave equations, the general solutions in wavenumber domain are derived by the Fourier transform. By decomposing the general solutions, the TRM method is developed. Combined the boundary conditions with the continuity conditions between each layer, the transmission and reflected matrices of each layer are obtained recursively. The solutions in time-space domain are obtained by the inverse Fourier transform. The validity and accuracy of the proposed methodology (TRM) and numerical integration scheme are confirmed by comparison with the existing result. By analyzing the three different cases in time domain and frequency domain, the characteristics of the surface vibration are discussed.

Governing Equations

The constitutive relations for a poroelastic medium based on Biot's theory can be expressed as [4]:

$$\sigma_{ij} = \lambda \delta_{ij}\theta + \mu(u_{i,j} + u_{j,i}) - \alpha \delta_{ij}p \tag{1}$$

$$p = -\alpha M\theta + M\zeta \tag{2}$$

where σ_{ij} is the total stress of the bulk material and p is the excess pore fluid pressure (suction is considered negative); $\theta = u_{i,i}$ is the dilatation of the solid skeleton; $\zeta = -w_{i,i}$ is the volume of fluid injection into a unit volume of the bulk material; u_i and w_i denote the average solid displacement and the pore fluid displacement relative to the solid matrix in the i-direction $(i = x, z)$, respectively; The subscripts $(\ )_{,i}$ denotes spatial derivatives; δ_{ij} is Kronecher delta; λ and μ are Lame constants; and α and M are Biot's parameters accounting for compressibility of the poroelastic medium.

The equations of motion for the bulk material and pore fluid can be expressed as [5]:

$$\mu u_{i,jj} + (\lambda + \alpha^2 M + \mu)u_{j,ji} + \alpha M w_{j,ji} = \rho \ddot{u}_i + \rho_f \ddot{w}_i \tag{3}$$

$$\alpha M u_{j,ji} + M w_{j,ji} = \rho_f \ddot{u}_i + m \ddot{w}_i + b \dot{w}_i \tag{4}$$

where the dot over a variable denotes the time derivative; ρ and ρ_f are the mass densities of the bulk material and the pore fluid, respectively $(\rho = n\rho_f + (1 - n)\rho_s)$, ρ_s is the density of solid skeleton and n is the porosity; m is a density-like parameter $(m = \rho_f/n)$; b is a parameter accounting for the internal viscous friction $(b = \eta/k)$.

In the plane-strain model, the displacement vector $u_i, w_i (i = x, z)$ can be decomposed by introducing four potentials ϕ_1, ϕ_2, φ, Φ as the following:

$$u_i = grad\phi_1 + curl\varphi, \quad w_i = grad\phi_2 + curl\Phi \tag{5}$$

By substituting Eq. (5) into Eqs. (3) and (4), a group of equations about ϕ_1, ϕ_2, φ, Φ are obtained.

The double Fourier transform and the double inverse Fourier transform of function $f(x, z, t)$ with respect to time t and horizontal coordinate x are defined:

$$\hat{\bar{f}}(\xi, z, \omega) = \int\limits_{-\infty}^{\infty} \int\limits_{-\infty}^{\infty} f(x, z, t)e^{-i\xi x}e^{-i\omega t}dxdt \tag{6a}$$

$$f(x, z, t) = \frac{1}{(2\pi)^2} \int\limits_{-\infty}^{\infty} \int\limits_{-\infty}^{\infty} \hat{\bar{f}}(\xi, z, \omega)e^{i\xi x}e^{i\omega t}d\xi d\omega \tag{6b}$$

Making use of the double Fourier transformation, the general solutions in frequency-wavenumber domain for displacements u_i and w_i, stresses σ_{ij} $(i, j = x, z)$ and pore fluid pressure p can be obtained.

The Layered Ground Model

The two-dimensional model is illustrated in Fig. 1.

The boundary and continuity conditions can be expressed as:

$$\sigma_{xz}(x, 0) = 0 \tag{7a}$$

$$\sigma_{zz}(x, 0) = 0 \tag{7b}$$

Fig. 1 A layered poroelastic half-plane subjected to an embedded moving load
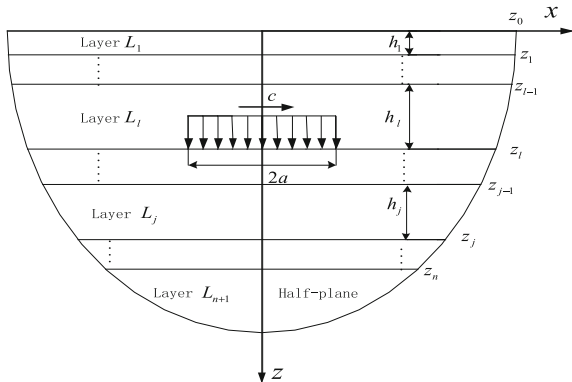
$$p(x, 0) = 0 \tag{7c}$$

$$u_x^{(j)}(x, z_j) - u_x^{(j+1)}(x, z_j) = 0 \quad j = 1, 2, \ldots, N-1 \tag{7d}$$

$$u_z^{(j)}(x, z_j) - u_z^{(j+1)}(x, z_j) = 0 \quad j = 1, 2, \ldots, N-1 \tag{7e}$$

$$w_z^{(j)}(x, z_j) - w_z^{(j+1)}(x, z_j) = 0 \quad j = 1, 2, \ldots, N-1 \tag{7f}$$

$$p^{(j)}(x, z_j) - p^{(j+1)}(x, z_j) = 0 \quad j = 1, 2, \ldots, N-1 \tag{7g}$$

$$\sigma_{xz}^{(j)}(x, z_j) - \sigma_{xz}^{(j+1)}(x, z_j) = 0 \quad j = 1, 2, \ldots, N-1 \tag{7h}$$

$$\sigma_{zz}^{(j)}(x, z_j) - \sigma_{zz}^{(j+1)}(x, z_j) = \frac{P_0 e^{i\omega_0 t}}{2a} H[a^2 - (x - ct)^2] \quad j = l \tag{7i}$$

$$\sigma_{zz}^{(j)}(x, z_j) - \sigma_{zz}^{(j+1)}(x, z_j) = 0 \quad j \neq l \tag{7j}$$

where P_0 and ω_0 denote the amplitude and the circular frequency of the vertical moving load, respectively; when $t = 0$, the center of the moving load acts on the point $x = 0$; c is the velocity of the moving load and $H[\ldots]$ denotes the Heaviside step function, which is defined as: $H[\vartheta] = \begin{cases} 1, & \vartheta > 0 \\ 0, & \vartheta < 0 \end{cases}$

If the bottom layer (i.e. the $n+1$-th layer) is a half-plane, because of the radiation conditions at infinity, the exponentially increasing terms of the $n+1$-th layer will be discarded. While, if the $n+1$-th layer is the rigid bedrock, the boundary conditions are:

$$u_x^{(n)}(x, z_n) = 0 \tag{8a}$$

$$u_z^{(n)}(x, z_n) = 0 \tag{8b}$$

$$w_z^{(n)}(x, z_n) = 0 \tag{8c}$$

It is noted that, in total, the number of the boundary and continuity conditions is equal to the number of the unknowns for the layered half-plane. Therefore, the solutions for $A^{(j)}$, $B^{(j)}$, $C^{(j)}$, $D^{(j)}$, $E^{(j)}$, $F^{(j)}$ are, in principle, subsistent.

Solutions for a Layered Poroelastic Half-Space

The general solutions in the transformed domain for the jth layer can be expressed as follows:

$$\psi^{(j)}(\xi, \omega, z)_{6\times 1} = \begin{bmatrix} D_d^{(j)}(\xi, \omega) & D_u^{(j)}(\xi, \omega) \\ S_d^{(j)}(\xi, \omega) & S_u^{(j)}(\xi, \omega) \end{bmatrix} \times \begin{bmatrix} W_d^{(j)}(\xi, \omega, z)^T & W_u^{(j)}(\xi, \omega, z)^T \end{bmatrix}^T \tag{9a}$$

$$\psi^{(j)}(\xi, \omega, z)_{6\times 1} = \begin{bmatrix} i\hat{\bar{u}}_x^{(j)} & \hat{\bar{u}}_z^{(j)} & \hat{\bar{w}}_z^{(j)} & i\hat{\bar{\sigma}}_{xz}^{(j)} & \hat{\bar{\sigma}}_{zz}^{(j)} & \hat{\bar{p}}^{(j)} \end{bmatrix}^T \tag{9b}$$

$$W_d^{(j)}(\xi, \omega, z) = \begin{bmatrix} B^{(j)}e^{-\gamma_1^{(j)}(z-z_{j-1})} & D^{(j)}e^{-\gamma_2^{(j)}(z-z_{j-1})} & F^{(j)}e^{-\gamma_3^{(j)}(z-z_{j-1})} \end{bmatrix}^T \tag{9c}$$

$$W_u^{(j)}(\xi, \omega, z) = \begin{bmatrix} A^{(j)}e^{-\gamma_1^{(j)}(z_j-z)} & C^{(j)}e^{-\gamma_2^{(j)}(z_j-z)} & E^{(j)}e^{-\gamma_3^{(j)}(z_j-z)} \end{bmatrix}^T \tag{9d}$$

where $W_d^{(j)}(\xi, \omega, z)$, $W_u^{(j)}(\xi, \omega, z)$ are termed as down-going and up-going wave vector and the matrices.

From Eqs. (9c) and (9d), we can obtain the following equations:

$$W_d^{(j)}(\xi, \omega, z) = E^{(j)}(z - z_{j-1})W_d^{(j)}(\xi, \omega, z_{j-1}) \tag{10a}$$

$$W_u^{(j)}(\xi, \omega, z) = E^{(j)}(z_j - z)W_u^{(j)}(\xi, \omega, z_j) \tag{10b}$$

where $E^{(j)}(\hbar) = \begin{bmatrix} e^{-\gamma_1^{(j)}\hbar} & 0 & 0 \\ 0 & e^{-\gamma_2^{(j)}\hbar} & 0 \\ 0 & 0 & e^{-\gamma_3^{(j)}\hbar} \end{bmatrix}$

The continuity conditions in frequency-wavenumber domain are:

$$\psi^{(j)}(\xi, \omega, z_j) = \psi^{j+1}(\xi, \omega, z_j), \quad (j \neq l) \tag{11}$$

Substituting Eqs. (9a–9d) into Eq. (11) yields:

$$\begin{bmatrix} W_d^{(j+1)}(z_j) \\ W_u^{(j)}(z_j) \end{bmatrix} = \begin{bmatrix} T_d^{(j)} & R_u^{(j)} \\ R_d^{(j)} & T_u^{(j)} \end{bmatrix} \begin{bmatrix} W_d^{(j)}(z_j) \\ W_u^{(j+1)}(z_j) \end{bmatrix} \tag{12}$$

where $\begin{bmatrix} T_d^{(j)} & R_u^{(j)} \\ R_d^{(j)} & T_u^{(j)} \end{bmatrix} = \begin{bmatrix} -D_d^{(j+1)} & D_u^{(j)} \\ -S_d^{(j+1)} & S_u^{(j)} \end{bmatrix}^{-1} \begin{bmatrix} -D_d^{(j)} & D_u^{(j+1)} \\ -S_d^{(j)} & S_u^{(j+1)} \end{bmatrix}$

The 3×3 matrix $R_d^{(j)}(\xi, \omega)$ and $R_u^{(j)}(\xi, \omega)$ in Eq. (12) represent reflection matrices for down-going and up-going P_1, P_2, S waves that incident on the jth interface, while $T_d^{(j)}(\xi, \omega)$ and $T_u^{(j)}(\xi, \omega)$ denote transmission matrices for the down-going and up-going P_1, P_2, S waves that incident on the jth interface.

Firstly, the bottom layer of the soil is assumed to be the rigid bedrock. The boundary conditions of the nth layer in frequency-wavenumber domain can be expressed as follows:

$$D_u^{(n)} W_u^{(n)}(z_n) + D_d^{(n)} W_d^{(n)}(z_n) = 0 \tag{13a}$$

Then the following equation can be obtained:

$$W_u^{(n)}(z_n) = R_d^{g(n)} W_d^{(n)}(z_n) = R_{de}^{g(n)} W_d^{(n)}(z_{n-1}) \tag{13b}$$

where $R_d^{g(n)} = -\left(D_u^{(n)}\right)^{-1} D_d^{(n)}$.

When

$$j = n-1, \quad \begin{cases} W_d^{(n)}(z_{n-1}) = T_{de}^{g(n-1)} W_d^{(n-1)}(z_{n-2}) \\ W_u^{(n-1)}(z_{n-1}) = R_{de}^{g(n-1)} W_d^{(n-1)}(z_{n-2}) \end{cases} \tag{14}$$

where $\begin{cases} T_{de}^{g(n-1)} = \left(I - R_{ue}^{(n-1)} R_{de}^{g(n)}\right)^{-1} T_{de}^{(n-1)} \\ R_{de}^{g(n-1)} = R_{de}^{(n-1)} + T_{ue}^{(n-1)} R_{de}^{g(n)} T_{de}^{g(n-1)} \end{cases}$.

Then, the general transmission and reflected matrices for soil layers below the buried moving load (i.e. $l < j < n$) can be deduced in the same way.

According to the boundary conditions on the free surface, the following equation is obtained:

$$W_d^{(1)}(z_0) = -\left(S_d^{(1)}\right)^{-1} S_u^{(1)} W_u^{(1)}(z_0) = R_{ue}^{g(0)} W_u^{(1)}(z_1) \tag{15}$$

When

$$
j = 1, \quad
\begin{cases}
W_u^{(1)}(z_1) = T_{ue}^{g(1)} W_u^{(2)}(z_2) \\
W_d^{(2)}(z_1) = R_{ue}^{g(1)} W_u^{(2)}(z_2)
\end{cases}
\tag{16}
$$

where
$$
\begin{cases}
T_{ue}^{g(1)} = \left(I - R_{de}^{(1)} R_{ue}^{g(0)}\right)^{-1} T_{ue}^{(1)} \\
R_{ue}^{g(1)} = R_{ue}^{(1)} + T_{de}^{(1)} R_{ue}^{g(0)} T_{ue}^{g(1)}
\end{cases}.
$$

Similarly, the general transmission and reflected matrices for soil layers above the buried moving load (i.e. $0 < j < l$) can be deduced.

When $j = l$, the wave vectors can be obtained based on the continuity conditions:

$$
\begin{bmatrix}
W_u^{(l)}(z_l) \\
W_d^{(l+1)}(z_l)
\end{bmatrix}
=
\begin{bmatrix}
D_d^{(l)} R_{ue}^{g(l-1)} E^{(l)}(h_l) + D_u^{l} & -(D_u^{(l+1)} R_{de}^{g(l+1)} E^{(l+1)}(h_{l+1}) + D_d^{(l+1)}) \\
S_d^{(l)} R_{ue}^{g(l-1)} E^{(l)}(h_l) + S_u^{l} & -(S_u^{(l+1)} R_{de}^{g(l+1)} E^{(l+1)}(h_{l+1}) + S_d^{(l+1)})
\end{bmatrix}^{-1}
\begin{bmatrix}
O \\
Q
\end{bmatrix}
\tag{17}
$$

where $O = \begin{bmatrix} 0 & 0 & 0 \end{bmatrix}^T$, $Q = \begin{bmatrix} 0 & \widehat{\overline{F}} & 0 \end{bmatrix}^T$, $\widehat{\overline{F}} = 2\pi P_0 \frac{\sin(\xi a)}{\xi a} \delta(\omega - \omega_0 + c\xi)$, and $\delta(\ldots)$ is the Dirac's function.

After $W_u^{(l)}(z_l)$ and $W_d^{(l+1)}(z_l)$ are determined, as discussed above, it is straightforward to obtain all the wave vectors of arbitrary layer. Then, the displacements, stresses and pore fluid pressures can be obtained.

By performing the double inverse Fourier transform, the solutions in time-space domain are presented as:

$$
\Omega(x, z, t) = \frac{1}{(2\pi)^2} \int_{-\infty}^{\infty} \int_{-\infty}^{\infty} \delta(\omega - \omega_0 + c\xi) \overline{\widehat{\Omega}}(\xi, \omega, z) e^{i\xi x} e^{i\omega t} d\xi d\omega
\tag{18}
$$

Taking advantage of the characteristics of the Dirac's delta function, the formula (18) can be reduced as:

$$
\Omega(x, z, t) = \frac{1}{(2\pi)^2} \int_{-\infty}^{\infty} \overline{\widehat{\Omega}}(\xi, \omega_0 - c\xi, z) e^{i\xi(x - ct)} d\xi
\tag{19}
$$

Numerical Results and Analysis

The fast Fourier transform (FFT) method is adopted to perform the inverse Fourier transform [24]. According to Cai et al. [14], an FFT algorithm over a grid of 2048×2048 points with a range of $-16 \, \text{m}^{-1} \leq \xi \leq 16 \, \text{m}^{-1}$ can meet the accuracy requirements.

Senjuntichai and Rajapakse [25] investigated the dynamic response of a homogeneous poroelastic half-plane under an embedded harmonic stationary (i.e. $c = 0$) load. And the load is buried at depth $z = a$. Figure 2 gives a comparison of non-dimensional displacements $\left(u_z^* = \frac{\mu u_z}{P_0 a} \right)$ obtained from the present study with those based on Senjuntichai and Rajapakse [25]. It is clear that the two results are in excellent agreement.

Choosing the point $(x = 0, z = 0)$ as the observation point, the vertical displacements of this point can be obtained according to Eq. (19):

$$u(0,0,t) = \frac{1}{(2\pi)^2} \int_{-\infty}^{\infty} \widehat{\overline{u}}(\xi, \omega_0 - c\xi, 0) e^{-ic\xi t} d\xi \tag{20}$$

Consequently, the amplitude spectra of vibrations in this point reads:

$$u_f(f) = \int_{-\infty}^{\infty} u(0,0,t) \, e^{-2\pi i f t} dt = \frac{1}{2\pi} \overline{\overline{u}}\left(\frac{f_0 - 2\pi f}{c}, 2\pi f, 0 \right) \tag{21}$$

The values of soil mechanical parameters and load characteristics are given as: $\mu = 2.237 \times 10^7 \, \text{N/m}^2$, $\lambda = 4.472 \times 10^7 \, \text{N/m}^2$, $\eta = 0.05$, $\rho_s = 2650 \, \text{kg/m}^3$, $\rho_f = 1000 \, \text{kg/m}^3$, $n = 0.388$, $b = 1.0194 \times 10^8 \, \text{kg}^{-1}\text{m}^3\text{s}$, $M = 5.173 \times 10^9 \, \text{N/m}^2$, $\alpha = 0.998$, $P_0 = 1 \, \text{N}$, $f_0 = 10 \, \text{Hz}$, $2a = 0.6 \, \text{m}$. In order to describe the visco-elastic
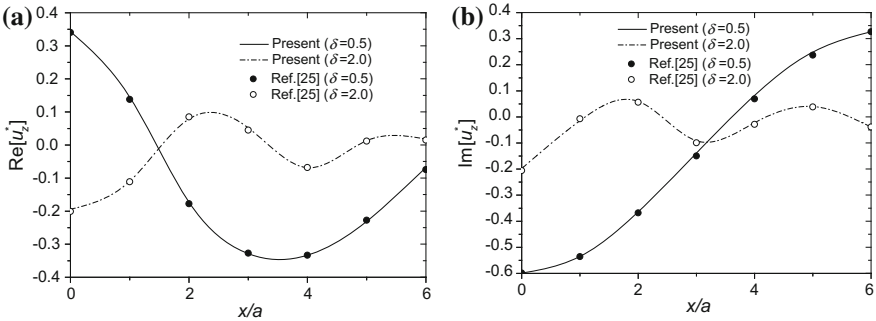
Fig. 2 **a** the real part of u_z^*; **b** the imaginary part of u_z^*

behavior of soil, a modified hysteretic damping model [15] is adopted: $\lambda^* = \lambda(1 + i\eta\text{sigh}(\omega - c\xi))$ and $\mu^* = \mu(1 + i\eta\text{sigh}(\omega - c\xi))$, where η denotes the hysteretic damping ratio.

Results for a Homogeneous Poroelastic Half-Plane to a Surface Moving Load

As mentioned above, when $l = 0$, Eq. (25) represents the vertical displacements in the case of surface moving load. Figure 3 plots the amplitude-frequency curves. It can be observed that there are two noticeable maxima located at $f_1 \approx 6.67\,\text{Hz}$, $f_2 \approx 20\,\text{Hz}$ for the case $c = 0.5c_R$. However, for the super-Rayleigh case $(c = 1.5c_R)$, there is only one noticeable maximum in the positive frequency regime at $f_3 \approx 4\,\text{Hz}$. The frequency of these waves can be determined by the following equations:

$$\omega = |\omega_0 - c\xi|, \quad \omega = c_R\xi \tag{22}$$

where the first equation reflects the equality of the phase of the radiation Rayleigh wave and the vibration phase of the moving load. The second equation is the formula for phase velocity of Rayleigh wave. The solution of Eq. (22) is:

$$\omega = \frac{\omega_0}{1 \pm M_R} \tag{23}$$

i.e.

$$f_{fro} = \frac{f_0}{1 - M_R}, \quad f_{beh} = \frac{f_0}{1 + M_R} \tag{24}$$

(a)

(b)
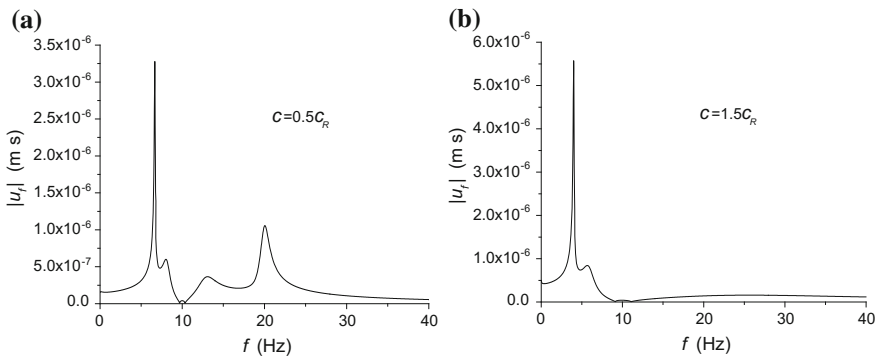
Fig. 3 The amplitude spectra

(a)

(b)
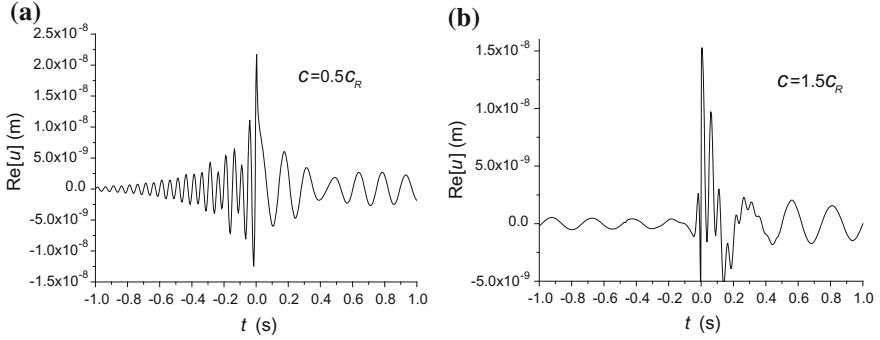
Fig. 4 The curves of surface displacement versus time

where M_R denotes the Mach number, which is defined as $M_R = c/c_R$. Substituting $f_0 = 10$ Hz, $M_R = 0.5$ or 1.5 into Eq. (24), we get the frequency $f_1 = 6.67$ Hz, $f_2 = 20$ Hz for $M_R = 0.5$ and $f_3 = 4$ Hz for $M_R = 1.5$ in the positive frequency regime. It is found that the calculated frequencies values are consistent with the observed ones.

The curves of displacement versus time are plotted in Fig. 4. In the sub-Rayleigh case depicted in Fig. 4a, the wave pattern for $t < 0$ has a higher frequency ($f_2 = 20$ Hz), while for $t > 0$, the frequency is smaller ($f_1 = 6.67$ Hz), while the vibration frequencies are both $f_3 = 4$ Hz whether $t < 0$ or $t > 0$ in Fig. 4b, which coincides with the resonance frequencies shown in Fig. 3. What's more, it can be seen in Fig. 4a that the wave attenuates more quickly when the load moves towards the observation point. And in Fig. 4b, there is almost no obvious displacement when $t < 0$, since when the load speed is beyond the Rayleigh wave, only P_1 wave propagates in front of the load.

Results for a Homogeneous Poroelastic Half-Plane to a Buried Moving Load

Figure 5 illustrates the influence of the depth of load buried (h_1) on the surface vibration of a homogeneous half-plane. It can be seen that the influence of the depth focuses on two aspects: Firstly, as the depth increases, the surface displacement amplitude decreases; secondly, the phase of the vibration experiences a delay as the depth increases.

(a)

(b)
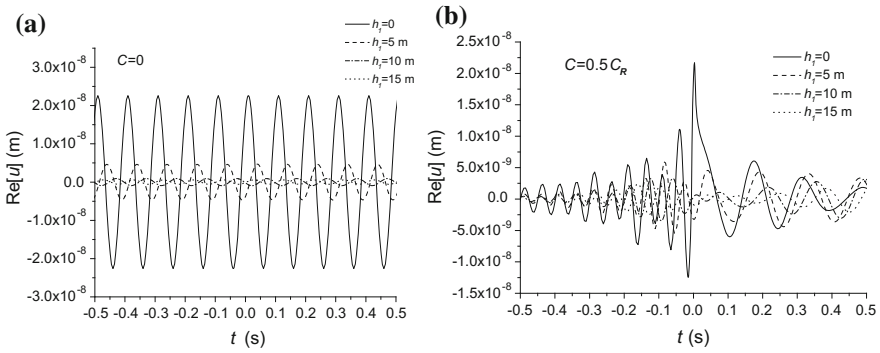
Fig. 5 The surface displacement to the buried moving load: **a** $c = 0$; **b** $c = 0.5c_R$

Results for a Multi- Layered Poroelastic Half-Plane to a Buried Moving Load

The soil parameters of the upper layer (the thickness of this layer is taken as $h = 10$ m) are selected the same as given before. For the overlaying half-plane, the soil is stiffer ($\mu = 2.237 \times 10^8$ N/m^2, $\lambda = 4.472 \times 10^8$ N/m^2). Due to the different soil characteristics of the two layers, the waves will undergo a complicated reflection and transmission procedure at the interface. Thus, the spectra of surface vibration contain more resonance frequencies as shown in Figs. 6 and 7.

Fig. 6 The amplitude spectra
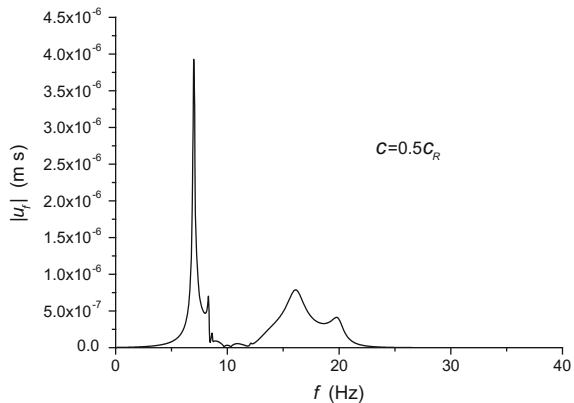
Fig. 7 The curve of surface
displacement versus time
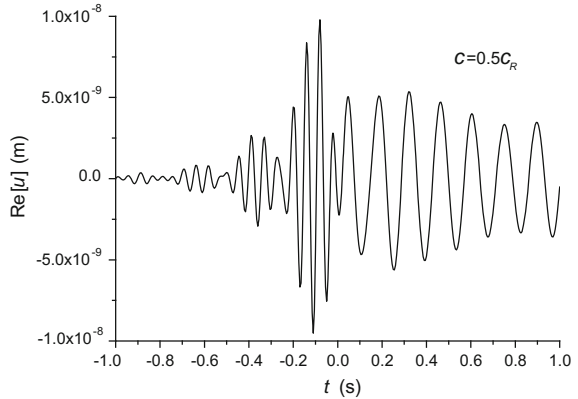
Conclusions

This paper provides an appropriate method to deal with the surface vibration problem of a multi-layered poroelastic half-plane subjected to a moving strip load. Some features of the surface vibration are presented to illustrate the complex characteristics of the wave propagation in the layered media.

(1) In the case of surface moving load in sub-Rayleigh regime, the observed wave possesses a higher frequency when the load moves towards the observation point; while the wave has a smaller frequency when the load moves away from the observation point (this is Doppler Effect).
(2) As the depth of the load buried increases, the surface displacement amplitude decreases and at the same time, the phase of the vibration experiences a delay.
(3) For the multi-layered half-plane, the reflection and transmission of the waves are complicated at the interface. As a result, the spectra of surface vibration contain more resonance frequencies.

References

1. Sneddon I N. (1952). The stress produced by a pulse of pressure moving along the surface of a semi-infinite solid. Rendiconti del Circolo Matematico di Palermo, 1(1): 57–62.
2. Eason G. (1965). The stresses produced in a semi-infinite solid by a moving surface force. International Journal of Engineering Science, 2(6): 581–609.
3. Hung H H, Yang Y B. (2001). Elastic waves in visco-elastic half-space generated by various vehicle loads. Soil dynamics and earthquake engineering, 21(1): 1–17.
4. Biot M A. (1956). Theory of propagation of elastic waves in a fluid-saturated porous solid. I. Low-frequency range. J. Acoust. Soc. Am, 28(2): 168–178.
5. Biot M A. (1962). Mechanics of deformation and acoustic propagation in porous media. Journal of applied physics, 33(4): 1482–1498.

6. Burke M, Kingsbury H B. (1984). Response of poroelastic layers to moving loads. International Journal of Solids and Structures, 20(5): 499–511.

7. Siddharthan R, Zafir Z, Norris G M. (1993). Moving load response of layered soil. I: Formulation [J]. Journal of engineering mechanics, 119(10): 2052–2071.

8. Theodorakopoulos D D. (2003). Dynamic analysis of a poroelastic half-plane soil medium under moving loads. Soil Dynamics and Earthquake Engineering, 23(7): 521–533.

9. Lu J F, Jeng D S. (2007). A half-space saturated poro-elastic medium subjected to a moving point load. International Journal of Solids and Structures, 44(2): 573–586.

10. Hu A F, Sun B, Xie K H. (2012). Dynamic response of saturated subgrade with rock substratum subjected to moving loads. Journal of Vibration and Shock, 31(4): 151–156 [In Chinese].

11. Bo J. (2004). Dynamic responses of a poroelastic half space generated by high speed load. Chinese Quarterly of Mechanics, 25(2): 168–174.

12. Jin B, Yue Z Q, Tham L G. (2004). Stresses and excess pore pressure induced in saturated poroelastic halfspace by moving line load. Soil Dynamics and Earthquake Engineering, 24(1): 25–33.

13. Zhou Y, Zhang R Y, Liu G B. (2011). Dynamic response of elastic layer on transversely isotropic saturated soil to train load. Rock and Soil Mechanics, 32(2): 604–610.

14. Cai Y, Sun H, Xu C. (2007). Steady state responses of poroelastic half-space soil medium to a moving rectangular load. International Journal of Solids and Structures, 44(22–23): 7183–7196.

15. Lefeuve-Mesgouez G, Mesgouez A. (2008). Ground vibration due to a high-speed moving harmonic rectangular load on a poroviscoelastic half-space. International Journal of Solids and Structures, 45(11–12):3353–3374.

16. Lefeuve-Mesgouez G, Mesgouez A. (2012).Three-dimensional dynamic response of a porous multilayered ground under moving loads of various distributions. Advances in Engineering Software, 46(1): 75–84.

17. Ghislain R. Franssens (1983). Calculation of the elasto-dynamic Green's function in layered media by means of a modified propagator matrix method. Geophysical Journal International, 75(3):669–691.

18. Zienkiewicz O C, Taylor R L, Zhu J Z. (2013). The Finite Element Method: Its Basis and Fundamentals (Seventh Edition), McGraw-Hill Book Company, UK.

19. Senjuntichai T, Rajapake R. (1995). Exact stiffness method for quasi-statics of a multi-layered poroelastic medium. International Journal of Solids and Structures, 32(11):1535–1553.

20. J.E. Luco, R.J. Apsel. (1983). On the Green's functions for a layered half-space. Part I. Bulletin of the Seismological Society of America, 73(4): 909–929.

21. R.J. Apsel, J.E.Luco. (1983).On the Green's functions for a layered half-space. Part II. Bulletin of the Seismological Society of America, 73(4): 931–951.

22. Xu B, Lu J F, Wang J H. (2008). Dynamic response of a layered water-saturated half space to a moving load. Computers and Geotechnics, 35(1): 1–10.

23. Xu M Q, Jian L H, Li J H. (2009). Dynamic response of a layered saturated soil subjected to harmonic horizontal loads. Rock and Soil Mechanics, 30(9): 2633–2642 [In Chinese].

24. Sneddon I N. (1951). Fourier transforms. New York: McGraw-Hill Book Company.

25. Senjuntichai T, Rajapake R. (1994). Dynamic green's functions of homogeneous poroelastic half-plane. Journal of Engineering Mechanics, 120(11): 2381–2404.

Vibration Impact of Freight Train on the Tunnel Base Rock Mass

Bin Li, Xiaojing Sun, Zhongsheng Tan and Chang Yu

Introduction

Development of economic makes a higher demand of carrying capacity of freight train. According to figures released by the relevant departments, the fill rate of requesting vehicles has only 35%, thus great demand of freight transportation had not been satisfied [1]. World experience of heavy haul railway shows that improving axle load is the most effective way to improve transport capacity and efficiency [2, 3]. Shen-Shuo Railway is the main trunk of coal transportation in China, the axle load of freight train should be increased from 25t to 30t to meet the great demand of freight train. However, the tunnel base diseases appearance in many tunnels of Shen-Shuo Railway, long-term freight train vibration load effect is the main reason [4, 5]. The freight train load can accelerate the development of tunnel base concrete cracks, which results in the damage of tunnel base diseases [6]. The freight train vibration load effect will be more serious with the increasement of axle load. So research must be taken to guarantee the safe operation of freight transportation.

B. Li · X. Sun (✉) · Z. Tan · C. Yu
School of Civil Engineering, Beijing Jiaotong University, 100044 Beijing, China
e-mail: xjsun1@bjtu.edu.cn

B. Li
e-mail: 14121029@bjtu.edu.cn

Z. Tan
e-mail: zstan@vip.sina.com

C. Yu
e-mail: 15125901@bjtu.edu.cn

This paper researched the influence law and scope of the tunnel base rock mass under the effect of freight train vibration load, research results could provide evidence for the disease treatment of tunnel base. The tunnel in this paper is Huojialiang Tunnel of Shen-Shuo Railway.

Influence Mechanism of Freight Train Vibration Load Effect on the Tunnel Base Rock Mass

In the process of tunnel construction, there will be a gap between the tunnel structure and the tunnel base rock mass if construction method is not correct. Under the circumstances, there will be high flexural stress in the tunnel base under the effect of freight train vibration load, which results in a cracking failure. If there is a hole in tunnel base, positive moment occurred in the tunnel base under the rail, and negative moment occurred in the tunnel base in the center of track bed, the tunnel base is more likely to be damaged due to the uneven distribution of stress [7]. When train vibration load transmit to the tunnel base rock mass from the tunnel base, tunnel structure and the surrounding can not deform in a same way because of the gap between them. If there is a microcrack in the tunnel base, the repeating freight train vibration load will accelerate the development of crack, at the same time, the rock mass is under the effect of freight train vibration load, relative displacement may occur in some rocks, the rock will be crushed because of the effect of friction, slide and grinding, which makes the force condition of the tunnel base worse [8, 9]. The Huojialiang Tunnel was built in 20 years ago, the concrete used is low-grade concrete, so the compressive strength is low, with the train vibration load increased gradually, the tunnel base would have fatigue failure. In the joint development zone, groundwater invades the tunnel base through the cracks. softened mud and water are extruded through the cracks as the freight train passes. After the train passed, the cracks of tunnel base are empty, and soon the surrounding water and softened mud invades the cracks. The repeating in and out of softened mud and water is the cause of tunnel base mud pumping defects [10, 11].

Introduction of Huojialiang Tunnel

Huojialiang Tunnel is located in Baode County, Shanxi, which is a double track tunnels of Shenshuo Railway. The tunnel completed in 1995, many tunnel diseases such as tunnel base mud pumping and ballast bed settlement have appeared under the effect of freight train vibration load and groundwater after two decades of operations. The tunnel was built by moulded lining. The length of Huojialiang Tunnel is 4727 m, the maximum burial depth is 160 m. Huojialiang is loess ridge, gully lies in either side of the hill, the gully is narrow, and its cutting depth is 50–80 m. The stratum which the tunnel crossed is mainly Permian mudstone and

Fig. 1 The picture of Huojialiang Tunnel

sandstone, the thickness of weathered zone of mudstone and sandstone is 3–15 m, it could be 20 m in some areas. The picture of Huojialiang Tunnel is showed in Fig. 1.

The Simulation of Freight Train Vibration Load

The simulation of freight train vibration load is always a difficult question because of its randomness, and there are three different methods to simulate the train vibration load in current study, which are model analysis method, test analysis method and empirical analyzing method, respectively. The frequency band of train vibration load deduced by model analysis method is wider, and the model analysis method take fully into account the effect of track irregularity, wheel flats, eccentric wheel and rail wear, etc. In this paper, the model analysis method is used to simulate the freight train vibration load. On the basis of field test, the mathematical expression of rail vertical acceleration was obtained, and then, the simplified model of freight trains was established and the freight train vibration load was obtained [12].

Freight train can be simplified as a combination of a series of secondary spring mass system model if just the vertical vibration is considered, assuming that the combination evenly distributed in vertical direction along the tunnel. One of simplified model of freight trains is showed in Fig. 2.

Fig. 2 Simplified model of
freight trains
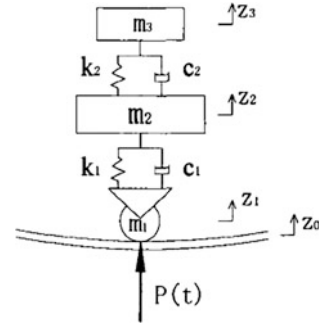
The vertical motion equation of freight train was obtained by direct balance method, the equation is showed as follows:

$$\begin{cases} m_3\ddot{z}_3 + c_2(\dot{z}_3 - \dot{z}_2) + k_2(z_3 + z_2) = 0 \\ m_2\ddot{z}_2 + c_1(\dot{z}_2 - \dot{z}_1) + k_1(z_2 - z_1) - k_2(z_3 - z_2) - c_2(\dot{z}_3 - \dot{z}_2) = 0 \end{cases} \quad (1)$$

The relative displacement of mass blocks are $\xi_1 = z_1 - z_0, \xi_2 = z_2 - z_1, \xi_3 = z_3 - z_2$, respectively, interaction force between the wheel and rail can be obtained according to D'Alembert's principle, the interaction force is showed as follows:

$$P(t) = (m_1 + m_2 + m_3)g + m_1\ddot{z}_1 + m_2\ddot{z}_2 + m_3\ddot{z}_3$$

$$= (m_1 + m_2 + m_3)g + [m_1 \quad m_2 \quad m_3]\left[\begin{bmatrix} 1 \\ 1 \\ 1 \end{bmatrix}\ddot{z}_0 + \begin{bmatrix} 1 & 0 & 0 \\ 1 & 1 & 0 \\ 1 & 1 & 1 \end{bmatrix}\begin{bmatrix} \ddot{\xi}_1 \\ \ddot{\xi}_2 \\ \ddot{\xi}_3 \end{bmatrix}\right] \quad (2)$$

The line vibration load of freight train can be calculated by the following equation:

$$F(t) = K \cdot n \cdot M \cdot P(t)/L \quad (3)$$

where the *F(t), K, n, M, L* are line vibration load, correction factor, number of bogie of each carriage, number of carriage, and length of carriage.

The simulated freight train vibration load was obtained by specific calculation software, as showed in Fig. 3. The axle load of freight train is 25t, the speed is 70 km/h.

(a) Time history of train load   **(b)** Frequency spectrum of train load
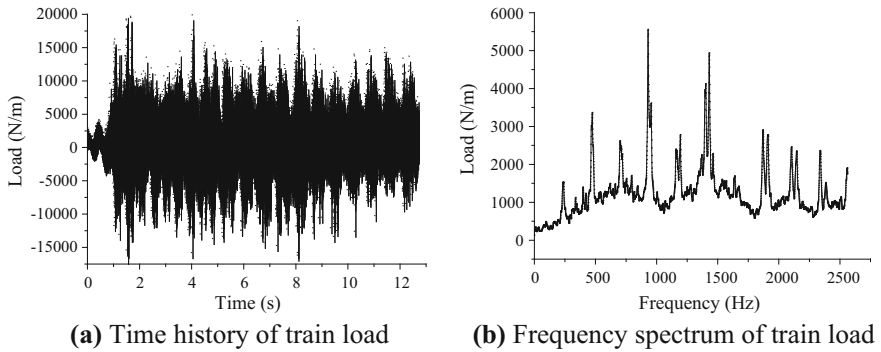
Fig. 3 Train load of freight train with 25t axle load

Influence Analysis of Freight Train Vibration Load Effect on the Tunnel Base Rock Mass

Establishment of Dynamical Finite Element Model

The tunnel section of field test was selected. The tunnel lining of Huojialiang Tunnle is monolithic lining, the concrete grade of tunnel lining is 200 concrete, the concrete grade of tunnel base is 100 concrete. The track in tunnel is ballast track, the rail is 60 kg/m rail. The rock mass is mainly mudstone and sandstone, the rock mass grading is level III. The cross section of tunnel is showed in Fig. 4, and the physical and mechanical parameters are showed in Table 1.

In the dynamic calculation, the calculation results are precise when the horizontal extent of finite element model is 8–10 times of diameter of tunnel [13]. So the horizontal extent of finite element model in this paper is 120 m, the longitudinal extent of finite is 100 m, the depth of tunnel is 42.9 m. Consistent viscous-spring artificial boundaries were applied in the finite element model. The dynamical finite element model is showed in Fig. 5.

Influence Analysis of Freight Train Vibration Load Effect

The 25t axle-load freight train vibration load was applied on the rail in the tunnel, the vibration response of model was calculated. 4 sections were chosen in the tunnel base rock mass, each section has a series of points, the vibration acceleration data of these points were extracted. The propagation rule of freight train vibration was analyzed, and then sphere of influence of the tunnel base rock mass under the effect of freight train vibration load was analyzed. Diagram of cross section is showed in Fig. 6.
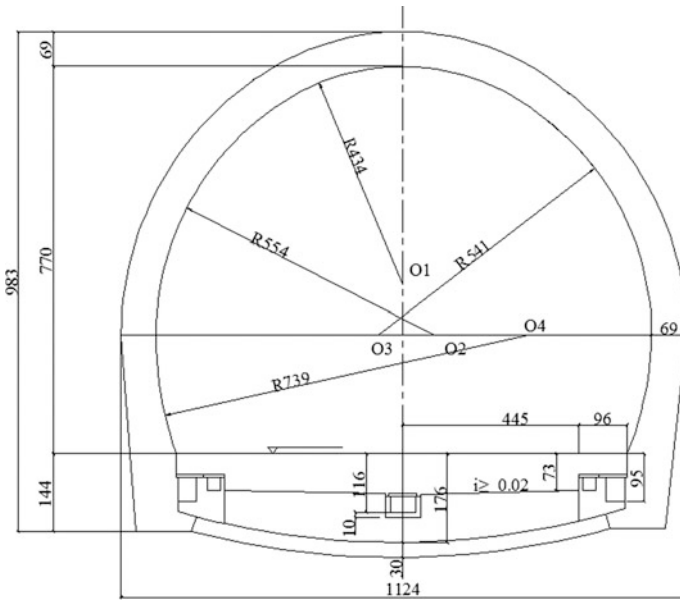
Fig. 4 Cross section of tunnel

Table 1 Physical and mechanical parameters

Species		Dynamic elasticity modulus E(MPa)	Poisson's ratio μ	Unit weight W (KN/m³)
Mudstone	/	1800	0.35	1800
Sandstone	/	3800	0.3	2200
Tunnel lining	200 concrete	2.55×104	0.2	2.37
Tunnel base	100 concrete	2.20×104	0.2	2.36
Ballast	Crushed stone	200	0.3	1.8
Sleeper	YII-F	4×104	0.2	2.68
Rail	60 kg/m	2.1×105	0.3	7.83

Root Mean Square (RMS) of acceleration was obtained. The square of RMS of acceleration objectively reflects the vibration energy magnitude in a period of time, so the vibration response of the tunnel base can be reflected by the RMS of acceleration [14, 15]. The RMS of the discrete time sequence can be calculated as follows:

$$a_{rms} = \sqrt{\frac{\sum_{i=1}^{N} x^2}{N}} \tag{4}$$
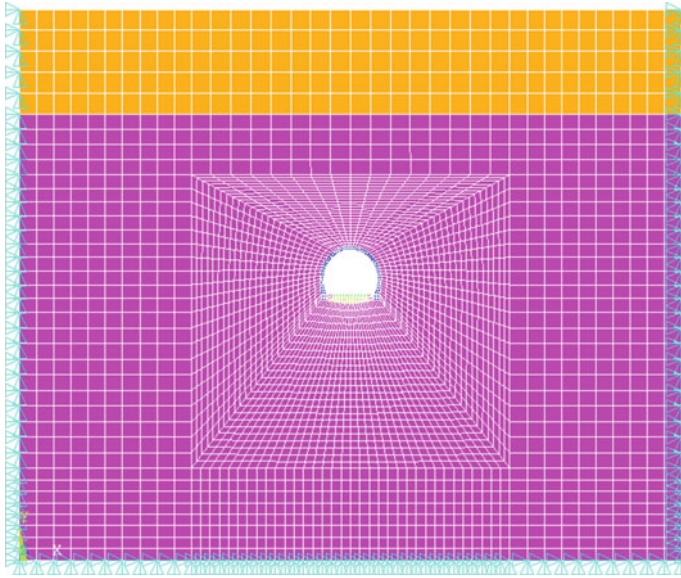
Fig. 5 The finite element model including trail, tunnel structure and rock mass

Fig. 6 Diagram of cross section
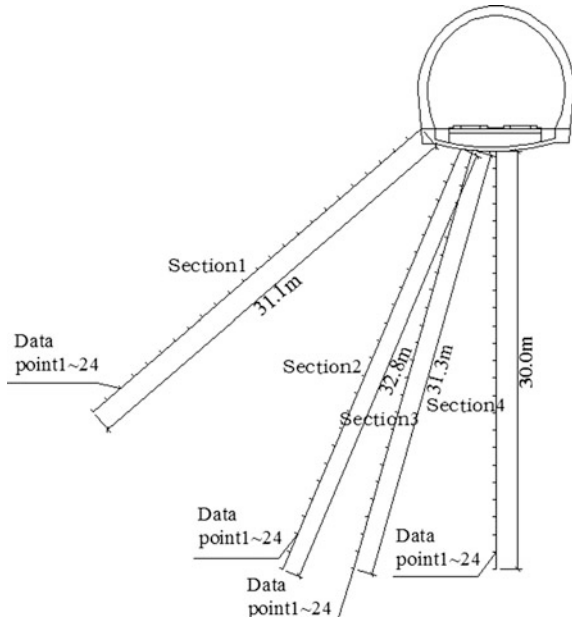
Decrement curve of vibration of tunnel base rock mass under the effect of freight train vibration load was drawn by the RMS of acceleration calculated. The decrement curve of each section is shown in Fig. 7.

As is shown in Fig. 7, the vibration response of the tunnel base rock mass becomes increasingly weaker with the increase of distance, and the rate of decay of near-field rock mass is much higher than far-field rock mass, which show up as RMS of acceleration of near-field rock mass decay rapidly, but RMS of acceleration of near-field rock mass decay slowly and tend to be stable. The influence of freight train vibration load is regarded as small if the vibration response tend to be stable, so the sphere of influence of the rock mass under the tunnel under the effect of freight train vibration load can be determined. Obtaining the following conclusions: the rock mass within 6.8 m away from tunnel invert is obviously influenced by the train vibration load, and in the section of center of tunnel invert, the rock mass within 10 m away from tunnel invert is obviously influenced by the train vibration load, the other rock mass is less influenced by the train vibration load.

One-third octave band RMS spectrum of each section under the vibration load of freight train with 25t axle load is shown in Fig. 8.

As is shown in Fig. 7, the vibration response of the rock mass becomes increasingly weaker with the increase of distance, and the rate of decay of high frequency is higher than low frequency. The peak value of vibration response of rock mass under the tunnel appears at about 250 Hz, the peak value of vibration response of each section is 93.3, 108.2, 109.9, 102.8 dB, respectively, after the
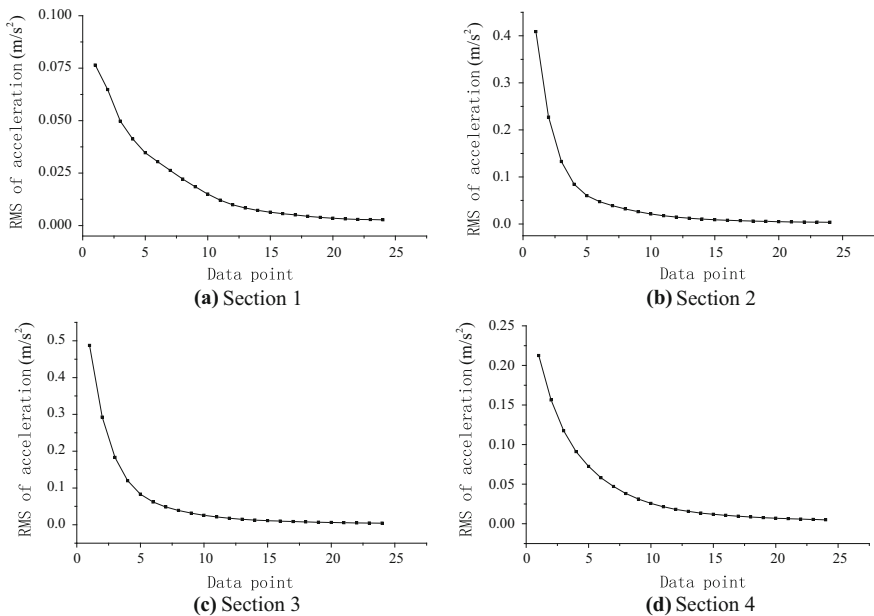
Fig. 7 Decrement curve of vibration of tunnel base rock mass
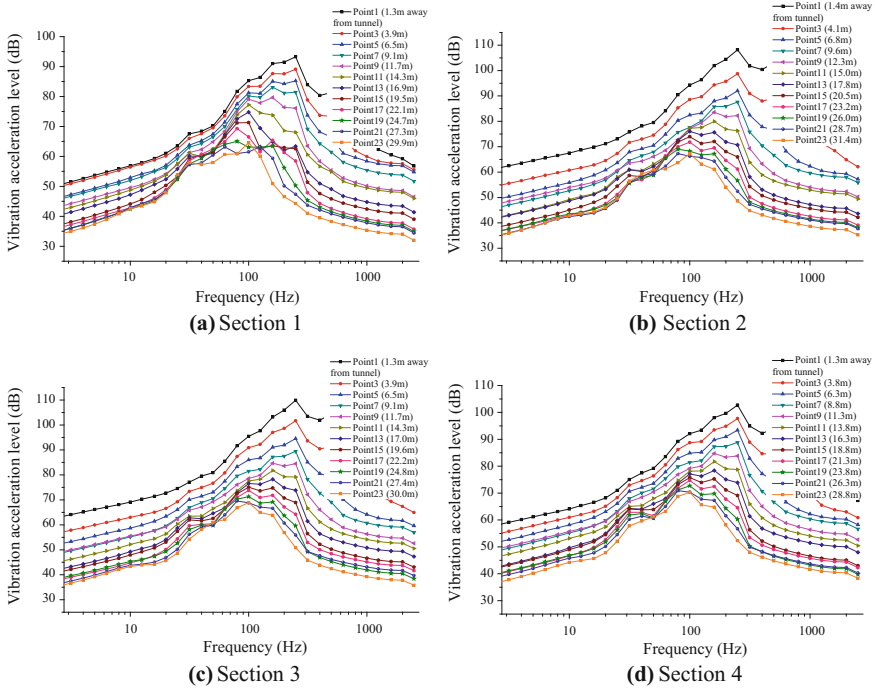
Fig. 8 One-third octave band RMS spectrum of each section under the vibration load of freight train with 25t axle load

decay in the soil, the peak value reduces 51.5, 59.2, 59.6, 51.8 dB, respectively. By comparison of vibration acceleration level of each section, the vibration response of Sections "Influence Mechanism of Freight Train Vibration Load Effect on the Tunnel Base Rock Mass" and "Introduction of Huojialiang Tunnel" are found much larger than Sections "Introduction" and "The Simulation of Freight Train Vibration Load". So conclusion could be drawn that the vibration response of the rock mass right under the rail is larger than the rock mass under the both side of the rail.

Conclusions

Several conclusions were drawn in this paper:

(1) The simulated 25t axle-load freight train vibration load was obtained by mathematical method on the basis of field test.
(2) The rock mass within 6.8 m away from tunnel invert is obviously influenced by the train vibration load, and in the section of center of tunnel invert, the rock mass within 10 m away from tunnel invert is obviously influenced by the train vibration load, the other rock mass is less influenced by the train vibration load.

(3) The vibration response of the rock mass under the tunnel becomes increasingly weaker with the increase of distance, and the rate of decay of high frequency is higher than low frequency. The peak value of vibration response of rock mass under the tunnel appears at about 250 Hz, the peak value of vibration response of each section is 93.3, 108.2, 109.9, 102.8 dB, respectively, after the decay in the soil, the peak value reduces 51.5, 59.2, 59.6, 51.8 dB, respectively

(4) The vibration response of the rock mass right under the rail is larger than the rock mass under the both side of the rail.

(5) The sphere of influence of the tunnel base rock mass under the effect of freight train vibration load was determined in this paper, which could provide a basis for regulation scope of tunnel base, and protect the safe operation of the heavy haul railway.

References

1. Duan Jia-ying, He Shi-wei, Shen Yong-sheng. (2012). Study on the Railway Increasing Freight Carrying Capacity of the Existing Busy Main-line After the Completion of Passenger-only Line. Journal of Wuhan University of Technology, 36(2):378–381
2. Niu Ya-bin. (2013). The heavy haul railway tunnel diseases mechanism and remediation technology research. Beijing: China Academy of Railway Sciences: 1–2
3. Wang Xiu-ying, Gong Zeng-jin, Liu Wei-ning. (2009). Research on the Tunnel Technical Standard under 30t Axis Load. Journal of Railway Engineering Society, 05:54–58
4. Shi Cheng-hua, Peng Li-min, Huang Juan. (2005). Study on Mechanism and Treatment Measures of Foundation Base Disease in Railway Tunnel. China Railway Science, 26(4):62–67
5. Yin Cheng-fei, Fu Bing-xian, Ma Wei-bin. (2013). Analysis on Dynamic Stress of Tunnel Structure under Heavy Haul Train. China Railway Science, 34(3):47–52
6. Zhu Wan-ting, Li Lan-qin. (2001). Base Diseases in Tunnels and Their Cause Analysis[J]. Modern Tunnelling Technology, 38(5):42–44
7. Li Li. (2014). Study on Strengthening Technology Used in Tunnel Foundation Base of Ballastless-track Heavy-haul Railway. Railway Standard Design, 58(5):95–99
8. Niu Ya-bin, Zhang Qian-li, Ma Wei-bin, Cheng Yuan-shui. (2012). The heavy haul railway tunnel diseases mechanism and treatment measure. Railway Engineering, 07:34–37
9. Ding Zu-de, Xie Hong-tao, Peng Li-min. (2013). Dynamic Response Properties of Soft Bedrock of High-Speed Railway Tunnel. Journal of Kunming University of Science and Technology (Natural Science Edition), 38(3):36–41+79
10. Fu Xiao-kang. (2014). Study on the Dynamic Response Properties of the Foundation Structure in Heavy-Haul Railway Tunnel. Hunan: Central South University: 50–51
11. Chang Wei-hua. (2009). Mechnical Properties Study of 30t Axle Load Heavy-haul Railway Track Structure. Beijing: Beijing Jiaotong University: 7–9
12. Sun Xiao-jing. (2008). Prediction of Environment Vibrations Induced by Metro Trains and Mitigation Measures Analysis. Beijing: Beijing Jiaotong University: 105–109
13. Lu Ai-zhong, Jiang Bin-song, You Chun-an. (1999). Study on range of mesh about finite element for back analysis of displacement. China Civil Engineering Journal, 32(1):26–30

14. Liu Wei-ning, Ma Meng, Wang Wen-bin. (2013). Prediction Method for Subway Train-Induced Environmental Vibration Responses. China Railway Science, 34(4):110–117
15. Liu Wei-ning, Ma Meng. (2014). Subway Train-Induced Environmental Vibration Responses. Beijing: China Science Publishing: 19–20

Establishment of Finite Element Model for Wide Steel Box-Girder Bridge by Modal Test

Boqiang Xiao, Weiping Xie, Haiqing Liu and Xiaoyu Cao

Introduction

Wide steel box-girder bridge with large width span ratio, center support, relatively light weight and other characteristics, so the effect of space, torsion modal contribution to vertical dynamic response of the bridge is larger than the traditional bridge, bridge model commonly used (such as single beam [1], grillage model [2] and finite segment method [3]) is difficult to accurately simulate the modal space. At present, in view of the city wide steel box-girder viaduct construction, the static research work is relatively more [4, 5], in view of the wide field measurement and analysis of the dynamic characteristics of the steel box-girder bridge, less work was done. Wide box girder bridge finite element model is set up by some scholars [6, 7], but lack experimental data to prove. In this paper, modal tests in various stages of construction are carried out based on the field ambient vibration, and a sophisticated finite element model is presented for the wide steel box-girder bridge.

B. Xiao · H. Liu
CCCC Second Harbour Engineering Co., Ltd.,
No. 6 Branch, 430070 Wuhan, China
e-mail: 401223514@qq.com

H. Liu
e-mail: 913165607@qq.com

W. Xie (✉) · X. Cao
School of Civil Engineering and Architecture,
Wuhan University of Technology, 430070 Wuhan, China
e-mail: wpxie@sina.com

X. Cao
e-mail: 595084019@qq.com

Project Summary

The viaduct under construction is composed by three span continuous steel box girders with eight lanes, and its construction method uses factory prefabrication and assembling on site. The span of bridge is 58 + 89 + 58 m; the width of bridge deck is 33 m; the cantilever end of the bridge length is 3.695 m. The upper structure of the bridge is the single enclosed box with six rooms, and the roof from down to up in turn is paved steel fiber reinforced concrete (8 cm) and asphalt concrete (9 cm). The lower part of bridge uses entity pier from H-type double column by C40, the height of pier is 9.894, 8.491, 9.081 and 11.106 m, respectively. The center spacing of pier is 8.5 m. Bridge applies the low pile caps, whose size is $10 \times 8.5 \times 3$ m. The type of foundation is bored cast in place pile whose length is 50 m. SF320 type expansion joint is used on both ends of the bridge and JQGZ universal spherical bearing is adopted for the bridge bearing (Fig. 1).

Modal Testing and Analysis of the Bridge

In view of the bridge in different construction stages of modal test has carried out three times, each test all uses the same instrument and measure point layout scheme. First test is along with the completion of the lower structure and the upper main girder, in this condition, the guardrail has been seated but the deck of the bridge has not yet been paved; Second test has been paved steel fiber reinforced concrete in 8 cm based on the first test condition; Third test is after the completion of the whole bridge. All the measure points are arranged on the top plate of the bridge, which has the transverse diaphragm deck of the bottom, and the test time is not less than 20 min, the sampling frequency is 200 Hz. Field test is respectively carried out from the vertical, horizontal and longitudinal directions, and the arrangement of measure points is shown in Fig. 2.

Fig. 1 Diagram of the bridge's cross section on the bearing
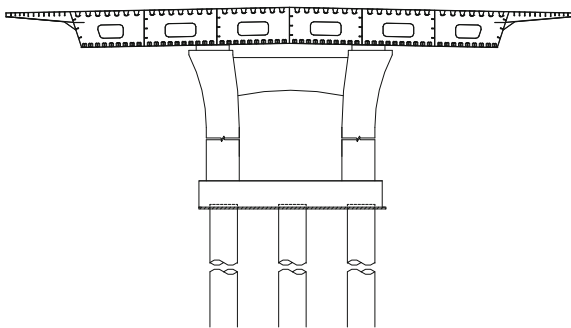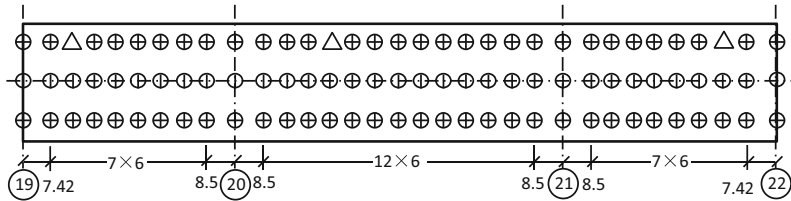
Remarks: △ Represents a fixed reference point, measures the vertical, horizontal and longitudinal acceleration of the bridge response; ⊕ Represents a moving point, measures the vertical and horizontal acceleration of the bridge response; Ⓘ Represents a moving point, meas res the ertical acceleration of the bridge response

Fig. 2 Arrangement of test point (Unit: m)

Using the method of stochastic subspace identification (SSI) and peak picking (PPI) to identify the modal of the bridge, the frequency and damping of the identification of the bridge under different conditions are shown in Table 1 (Fig. 3).

Due to the construction disturbance on Stage 1, only the vertical bending modes in first four order and the torsional modes in first order can be identified effectively. From Table 1, (1) In contrast to Stage 2 and Stage 3, the first twelve frequencies of the structure (except eighth order) were significantly reduced, and the first order frequency was reduced by 15.6%. (2) The first order damping ratio of the structure under the field ambient excitation is only 0.6%, and the damping ratio should be carefully chosen for the dynamic analysis of the large span steel structure under the

Table 1 Modal test results for various conditions (the unit of frequency: Hz)

Order	Stage 1 Frequency	Stage 2 Frequency	Stage 3 Frequency	Damping ratio (%)	Modal shape
1	1.565	1.419	1.320	0.60	1st vertical bending
2	–	1.900	1.705	–	1st longitudinal
3	–	2.238	2.064	1.78	1st transverse bending
4	2.755	2.580	2.409	1.08	2nd vertical bending
5	–	2.844	2.582	2.90	1st transverse bending + torsional
6	3.312	2.989	2.794	1.42	3rd vertical bending
7	3.796	3.325	3.151	1.99	1st torsional
8	–	3.649	3.683	1.20	2nd torsional
9	–	3.958	3.787	1.53	3rd torsional
10	5.487	4.849	4.415	2.66	4th vertical bending
11	–	5.567	4.901	1.55	2nd transverse bending + torsional
12	–	6.438	5.706	1.41	4th torsional

(a) The vertical reference point (b) The transverse reference point
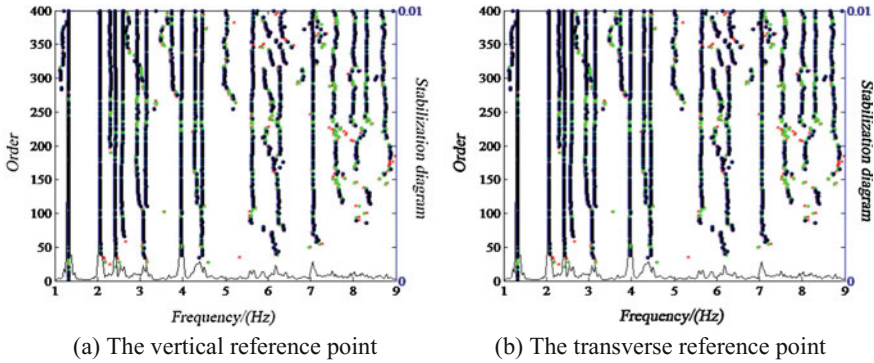
Fig. 3 The stabilization diagram of reference point

condition of weak vibration. (3) For this kind of bridge structure, bridge modal present the characteristics that the frequency is low and dense, torsional modal is much and top, the lateral bending modal coupled with the torsional modal.

Finite Element Model of the Bridge

Because the bridge structure is a thin wall structure with wide span ratio and long cantilever structure, and the shear lag effect is obvious in the structure [8]. Taking into account the ANSYS library provides rich and effective elements, which can be used to simulate the characteristics of thin-walled structures, so the finite element model of the bridge was established by different elements combined in ANSYS.

The specific treatment methods for each part of the bridge are as follows: (1) In the upper main beam, using shell181 element to simulate the top slab, bottom slab and web, and using the custom section function of beam188 to simulation U, T and rectangle stiffening rib. (2) In the lower part of the structure, the SOLID65 is used to simulate the pier and pile cap, and the beam188 is used to simulate the group pile foundation. (3) The paving layer is simulated by shell181 which have the layer characteristic, giving different material properties and thickness in the definition of the bridge roof. (4) The spherical bearing is simulated by combin14. Because there is no relevant calculation formula of bearing stiffness and the spherical bearing has the characteristics of large rotation ability and capacity, whereby the translational spring stiffness (UX, UY, UZ) and rotational stiffness (ROTY, ROTZ) with a large value, at the same time, given zero to ROTX. (5) The linear spring is used to simulate the interaction between pile and soil, the mass and damping of soil mass are neglected and the value of concrete rigidity and calculation formula are calculated according to the standard [9] and the literature [10]. (6) The longitudinal one-dimensional linear spring is used to simulate the expansion joint of the bridge, and the spring stiffness is adjusted to the reality value according to the measured

value. (7) In the anti-collision guardrails, the custom of beam section from beam188 is used to simulate the middle of the crash barrier, boundary fence using beam188 cooperated with shell181 to establish. (8) When the degree of freedom between different elements is not matched, the CE constraint equation is used to deal with the relationship between different elements. The finite element model of the whole bridge is shown in Fig. 4.

Modal analysis of the L7 finite element model is established and the comparison of the modal frequency and the measured frequency is shown in Table 2.
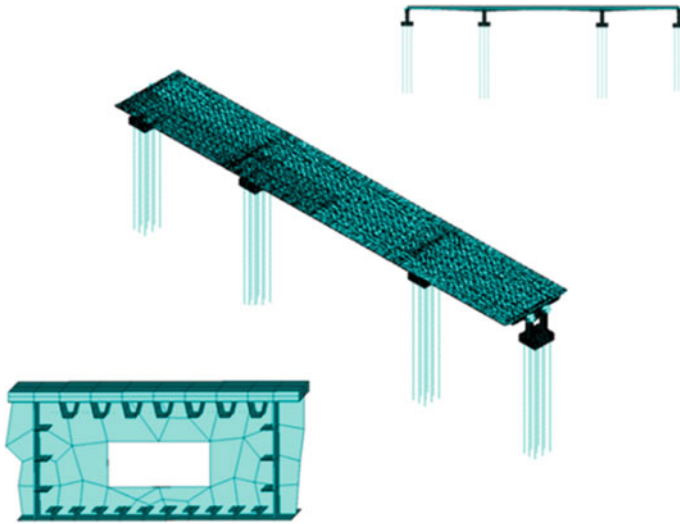
Fig. 4 The finite element model for bridge

Table 2 The identified frequency compared with the calculated frequency

Order	Test value (Hz)	ANSYS (Hz)	Relative error (%)
1	1.320	1.367	3.58
2	1.705	1.723	1.04
3	2.064	1.970	−4.5
4	2.409	2.438	1.18
5	2.582	2.650	2.63
6	2.794	2.881	3.12
7	3.151	3.244	2.96
8	3.683	3.749	1.80
9	3.787	3.887	2.64
10	4.415	4.601	4.21
11	4.901	4.985	1.72
12	5.706	5.990	4.98
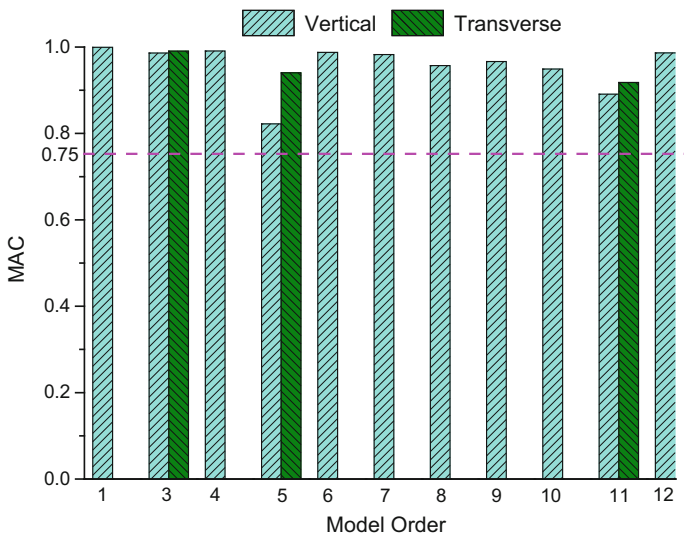
Fig. 5 Modal assurance criteria

By comparing the bridge vibration model obtained by numerical simulation with the measured vibration mode, the correlation degree measured by the modal confidence value (MAC) is shown in Fig. 5.

From Table 2 and Fig. 5, the relative error of frequency between finite element analysis and field test are less than 5%, the values of MAC are greater than 0.75. It is shown that the correlation is very well for the bridge modal between by the field test and by finite element analysis. The finite element model has high accuracy.

Conclusions

In this paper, modal tests in various stages of construction are carried out based on the field ambient vibration, and a sophisticated finite element model is presented for wide steel box-girder bridge. The conclusions are as follows:

(1) The modal frequencies of wide steel box-girder bridge under different working conditions with differing greatly, surfacing and crash barrier all can affect the dynamic performance of the bridge.
(2) The modal of wide steel box-girder bridge present characteristics that the frequency is low and dense, torsion modal is much and top, lateral bending modal coupled with torsional modal and the first order of the damping ratio is small.
(3) Comparing the finite element simulation with modal identification, the finite element model established in this paper has high accuracy and can provide reference for the modeling of such bridges.

References

1. Zhang, Q., Shi, J.J., Hu, Z.D. (2003). Coupled interaction analysis on vehicle-bridge system. Chinese Quarterly of Mechanics, 24(4): 577–584.
2. Han, W.S., Wang, T., Li, Y.Q., et al. (2011). Analysis System of vehicle-bridge coupling vibration with grillage method based on model updating. China Journal of Highway and Transport, 24(5): 47–55.
3. Wu, Y.P., Liu, S.Z., Zhu, Y.L., et al. (2003). Matrix analysis of shear lag and shear deformation in thin-walled box beam. Journal of Engineering Mechanics, 129(8): 944–950.
4. Guo, T.J. (2009). Wide steel box girder pushing construction technology. Railway Standard Design, 5(26): 56–58.
5. Chen, X.L. (2013). Research on intensity of steel box girder under combined bending and torsion. Changsha: Hunan University.
6. Cui, J.G. (2014). Analysis on the vehicle-bridge coupled vibration of the wide box girder detailed bridge model. Chongqing: Chongqing Jiaotong University.
7. Liu, H.X. (2011). Analysis of vehicle-bridge coupling vibration of wide continuous box-girder bridge. Xi'an: Chang'an University.
8. Reissner, E. (1946). Analysis of shear lag in box beams by the principle of minimum potential energy. Quarterly of Applied Mathematics, 5(3): 268–278.
9. Ministry of Transport of the People's Republic of China. JTG D63-2007. (2007). Code for Design of Ground Base and Foundation of Highway Bridges and Culverts. Beijing: China Communications Press.
10. Zhan, J.W., Xia, H., Li, Z.X., et al. (2013). A method for dynamic characteristic analysis of roadway bridge piers considering soil friction effects. China Civil Engineering Journal, 46 (10): 74–80.

Study on the Vibration of Geosynthetic Reinforced Cushion in Pile Supported Embankment

Changjie Zheng, Xuanming Ding, Lubao Luan and Hui Yu

Introduction

In recent years, high-speed trains have developed at full speed and received more and more concerns, which play an important role in promoting the development of economy. However, trains running faster brings some problems such as the safety and stability of trains and environmental vibration. Many railways are lined through deep soft soil area, the settlement of which increases with the increase of speed of trains. In a field test conducted by Swedish National Railway Administration, the settlement of railway was found larger than the limit to ensure the safety of the operation of railway [1]. Moreover, the vibration has been considered as one of the seven environmental hazards on the international. According to statistics, besides the vibration caused by the factory and constructional engineering, the vibration caused by high-speed train has been one of the strongest environmental vibration hazards. Therefore, it's significant to make a study on the vibration caused by high-speed train.

C. Zheng (✉) · X. Ding · L. Luan
School of Civil Engineering, Chongqing University, Chongqing 400045, China
e-mail: zhengchj1989@163.com

X. Ding
e-mail: dxmhhu@163.com

L. Luan
e-mail: 136417061@qq.com

C. Zheng · X. Ding · L. Luan
Key Laboratory of New Technology for Construction of Cities in Mountain Area,
Chongqing University, Ministry of Education, Chongqing 400045, China

H. Yu
ShangHai Xian Dai Architectural Design Group ShenYuan
Geotechnical Engineering Co., Ltd., Shanghai 200031, China
e-mail: 80164348@qq.com

Li et al. [2] conducted a numerical analysis on vibration characteristics of pile-supported embankment due to high-speed train loading by assuming the train load as a dynamic load made up of a stationary load and three sinusoidal loads. Hung and Yang [3] investigated the waves induced by various train loads such as centralized moving load, evenly distributed wheel loads, elastic distributed wheel loads. Amir et al. [4] assumed the high-speed train load as a series of centralized loads, the rail and ballast bed as well as the embankment as beams on a layered foundation, the foundation as viscoelastic half space, to investigate on the displacement response of different train speed.

Most of the previous studies [5–8] regarded the subgrade as homogeneous soil, but in pile-supported embankment there are piles and geosynthetic-reinforced cushion under the track, which can largely decrease the vibration of the subgrade caused by high-speed train. How the cushion vibrates under high-speed train load is still unknown. The objective of this paper is to propose an analytical solution of the displacement response of cushion under high speed train load. Numerical examples are given to analyze the vibration characteristics of cushion and provide some guidance for preventing disaster due to high-speed train.

Equation

The high-speed train load is considered as a dynamic load made up of a stationary load and three sinusoidal loads named $F(t)$ [9]:

$$F(t) = P_0 + P_1 \sin \omega_1 t + P_2 \sin \omega_2 t + P_3 \sin \omega_3 t \tag{1}$$

where P_0 is the static load of a train carriage; ω_1, ω_2 and ω_3 are the low frequency, medium frequency and high frequency, respectively; P_1, P_2 and P_3 are the dynamic loads corresponding to ω_1, ω_2 and ω_3, respectively.

$$\omega_i = 2\pi v / L_i, \quad i = 1, 2, 3 \tag{2}$$

where L_i are the wavelengths, v is the speed of the train.

$$P_i = M_0 a_i \omega_i^2 \tag{3}$$

where M_0 is the unsprung mass of a train carriage, a_i are the amplitudes of the rail (Fig. 1).

The computational model is shown in Fig. 2. End-bearing piles are assumed as simple supports of the cushion, and the embankment soil is considered as Kelvin foundation of the cushion which provides upward supporting load to the cushion. Then the motion equation of the cushion can be expressed as:

Fig. 1 The high-speed train load when the train speed is 60 m/s
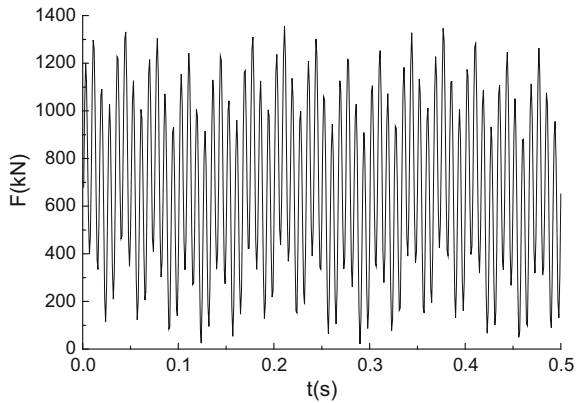
Fig. 2 Schematic diagram of computational model
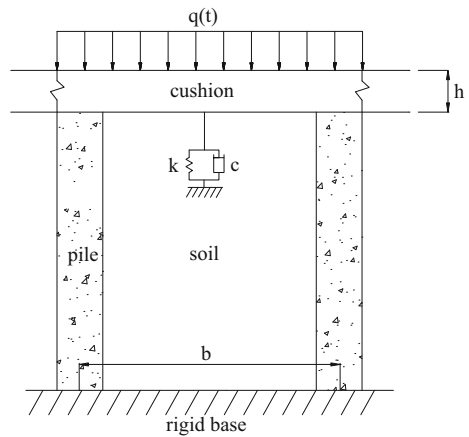
$$D\nabla^2\nabla^2 w(x,y,t) + \rho h\frac{\partial^2 w}{\partial t^2} + c\frac{\partial w}{\partial t} + kw = q(t) \tag{4}$$

where $D = Eh^3/12(1 - \mu^2)$ is the bending rigidity of cushion; ∇^2 is the Laplace operator; $w(x,y,t)$ is the deflection of cushion; k and c are the stiffness and damping coefficients of the embankment soil, respectively; ρ, h, E and μ are the density, thickness, modulus of elasticity and Poisson's ratio of cushion, respectively; $q(t) = F(t)/HW$; H is the length of the train and W is the width of the embankment.

The boundary conditions of cushion can be expressed as:

$$\begin{cases} w|_{x=0,b} = \dfrac{\partial^2 w}{\partial x^2}\Big|_{x=0,b} = 0 \\ w|_{y=0,b} = \dfrac{\partial^2 w}{\partial y^2}\Big|_{y=0,b} = 0 \end{cases} \tag{5}$$

where b is the pile spacing.

The initial conditions can be written as:

$$w|_{t=0} = \left.\frac{\partial w}{\partial t}\right|_{t=0} = 0 \tag{6}$$

Solution for the Equation

According to Eq. (5), the vibration function of cushion can be expressed as:

$$w(x, y, t) = \sum_{m=1}^{\infty} \sum_{n=1}^{\infty} T_{mn}(t) \sin \alpha_m x \, \sin \alpha_n y \tag{7}$$

where $\alpha_m = \frac{m\pi}{b}$; $\alpha_n = \frac{n\pi}{b}$.

$q(t)$ can be written as:

$$q(t) = \sum_{m=1}^{\infty} \sum_{n=1}^{\infty} Q_{mn}(t) \sin \alpha_m x \, \sin \alpha_n y \tag{8}$$

where $Q_{mn}(t) = \frac{4(1-\cos m\pi)(1-\cos n\pi)q(t)}{b^2 \alpha_m \alpha_n}$.

Substituting Eqs. (7) and (8) into Eq. (4) results in:

$$T''_{mn}(t) + 2AT'_{mn}(t) + B^2 T_{mn}(t) = Q_{mn}(t) \tag{9}$$

where $A = \frac{c}{2\rho_c h}$; $B^2 = \frac{D}{\rho_c h}\left(\alpha_m^4 + 2\alpha_m^2 \alpha_n^2 + \alpha_n^4 + \frac{k}{D}\right)$.

The general solution of Eq. (7) can be written as:

$$T_{mn}(t) = C_{1mn}e^{a_1 t} + C_{2mn}e^{a_2 t} \tag{10}$$

where $a_1 = -A + \sqrt{A^2 - B^2}$; $a_2 = -A - \sqrt{A^2 - B^2}$. C_{1mn} and C_{2mn} are undetermined coefficients.

The special solution of Eq. (9) can be expressed as:

$$T^*_{mn}(t) = D_{mn} + E_{1mn}\cos \omega_1 t + E_{2mn}\sin \omega_1 t + F_{1mn}\cos \omega_2 t \\ + F_{2mn}\sin \omega_2 t + G_{1mn}\cos \omega_3 t + G_{2mn}\sin \omega_3 t \tag{11}$$

The substitution for Eq. (11) into Eq. (9) leads to:

$$D_{mn} = \frac{4(1 - \cos m\pi)(1 - \cos n\pi)q_0}{B^2 b^2 \alpha_m \alpha_n} \tag{12}$$

$$E_{1mn} = -\frac{8A\omega_1(1 - \cos m\pi)(1 - \cos n\pi)q_1}{((B^2 - \omega_1^2)^2 + 4A^2\omega_1^2)b^2\alpha_m\alpha_n} \tag{13}$$

$$E_{2mn} = \frac{4(B^2 - \omega_1^2)(1 - \cos m\pi)(1 - \cos n\pi)q_1}{((B^2 - \omega_1^2)^2 + 4A^2\omega_1^2)b^2\alpha_m\alpha_n} \tag{14}$$

$$F_{1mn} = -\frac{8A\omega_2(1 - \cos m\pi)(1 - \cos n\pi)q_2}{((B^2 - \omega_2^2)^2 + 4A^2\omega_2^2)b^2\alpha_m\alpha_n} \tag{15}$$

$$F_{2mn} = \frac{4(B^2 - \omega_2^2)(1 - \cos m\pi)(1 - \cos n\pi)q_2}{((B^2 - \omega_2^2)^2 + 4A^2\omega_2^2)b^2\alpha_m\alpha_n} \tag{16}$$

$$G_{1mn} = -\frac{8A\omega_3(1 - \cos m\pi)(1 - \cos n\pi)q_3}{((B^2 - \omega_3^2)^2 + 4A^2\omega_3^2)b^2\alpha_m\alpha_n} \tag{17}$$

$$G_{2mn} = \frac{4(B^2 - \omega_3^2)(1 - \cos m\pi)(1 - \cos n\pi)q_3}{((B^2 - \omega_3^2)^2 + 4A^2\omega_3^2)b^2\alpha_m\alpha_n} \tag{18}$$

So the solution of Eq. (9) can be expressed as:

$$\begin{aligned} T_{mn}(t) = {} & C_{1mn}e^{a_1t} + C_{2mn}e^{a_2t} + D_{mn} + E_{1mn}\cos\omega_1 t + E_{2mn}\sin\omega_1 t \\ & + F_{1mn}\cos\omega_2 t + F_{2mn}\sin\omega_2 t + G_{1mn}\cos\omega_3 t + G_{2mn}\sin\omega_3 t \end{aligned} \tag{19}$$

Substituting Eq. (19) into Eq. (6), the constants C_{1mn} and C_{2mn} can be determined as follows:

$$C_{1mn} = \frac{a_2(E_{1mn} + F_{1mn} + G_{1mn}) - \omega_1 E_{2mn} - \omega_2 F_{2mn} - \omega_3 G_{2mn}}{a_1 - a_2} \tag{20}$$

$$C_{2mn} = \frac{\omega_1 E_{2mn} + \omega_2 F_{2mn} + \omega_3 G_{2mn} - a_1(E_{1mn} + F_{1mn} + G_{1mn})}{a_1 - a_2} \tag{21}$$

Substituting Eq. (19) into Eq. (7), the solution of Eq. (4) is obtained.

Numerical Examples and Analysis

Vibration Characteristics of Cushion

Unless otherwise specified, the following parameter values are used: $P_0 = 680$ kN, $M_0 = 8$ t, $L_1 = 10$ m, $a_1 = 5$ mm, $L_2 = 2$ m, $a_2 = 0.6$ mm, $L_3 = 0.5$ m, $a_3 = 0.1$ mm, $v = 60$ m/s, $H = 26$ m, $W = 20$ m, $E = 45$ MPa, $\mu = 0.33$, $\rho = 2000$ kg/m³, $h = 0.4$ m, $k = 2000$ kN/m³, $c = 100$ kNs/m³, $b = 2.5$ m.
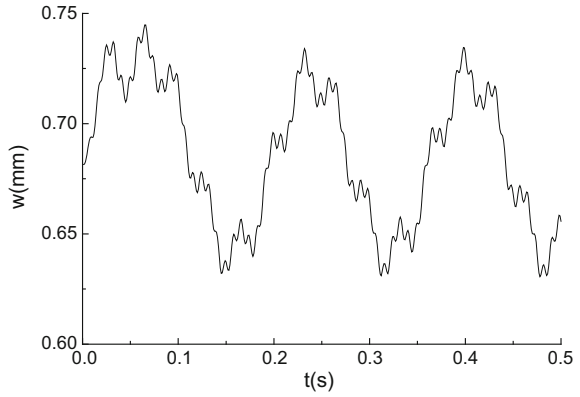
The displacement response of cushion at the center is shown in Fig. 3. The displacement oscillates along with the load. At the beginning, the high frequency and medium frequency loads have marked influence on the displacement. When the cushion comes to steady state response status, the displacement is mainly influenced by the low frequency load.

Parametric Study

The effect of the train speed on the displacement response of cushion at the center is shown in Fig. 4. It is noted that the peak value of the displacement increase and the resonance frequencies decrease with the increase of the train speed. Furthermore, the influence of high-frequency load on displacement decreases as the train speed increases. When the train speed reaches to 90 m/s, the displacement response is

Fig. 4 The effect of train
speed on the displacement
response of cushion
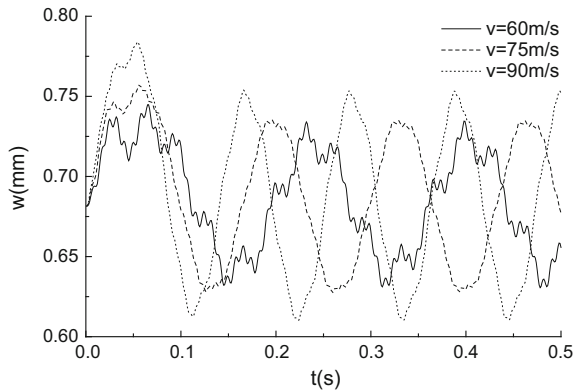
mainly influenced by the low-frequency load. The effect of damping on the displacement response is shown in Fig. 5. The peak value of displacement increase steeply with the decrease of damping. The influence of high-frequency load increases as the damping decreases.

The variations of displacement response of cushion with different thickness and modulus of elasticity at time 0.1 s is shown in Figs. 6 and 7. The thickness and Young's modulus have marked influence on the displacement response. The displacement response decreases with the increase of the thickness and Young's modulus of cushion. Properly increasing the Young's modulus and thickness of cushion can effectively reduce the deformation of cushion.

Fig. 5 The effect of damping on the displacement response of cushion
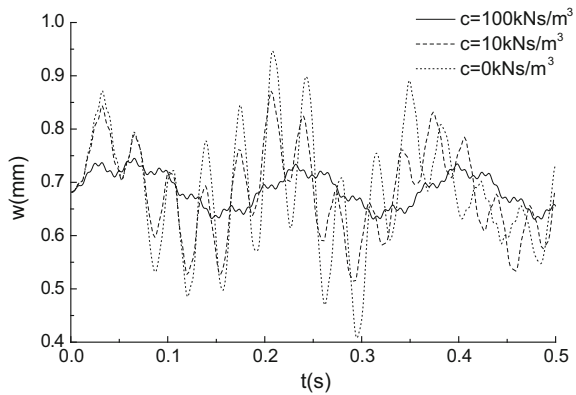
Fig. 6 The effect of Young's modulus of cushion on the displacement response
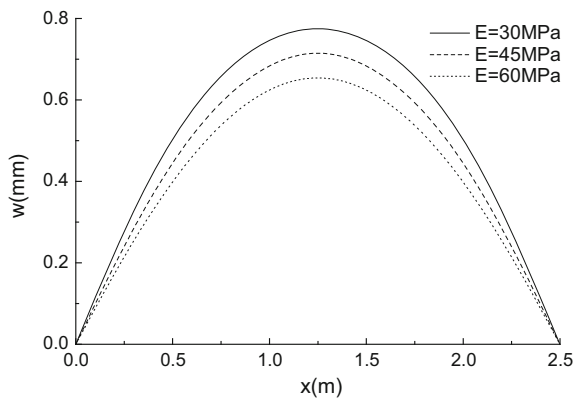
Fig. 7 The effect of thickness on displacement response
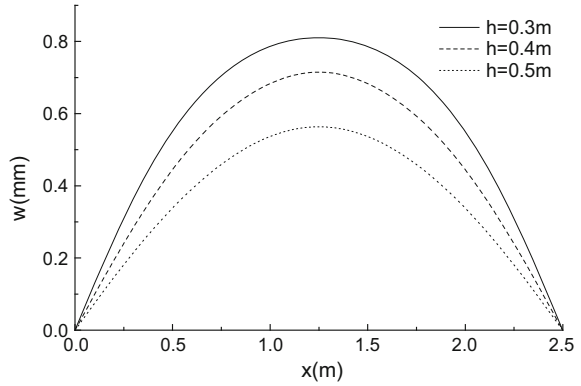
Conclusions

By considering the high-speed train load as a dynamic load made up of a static load and three sinusoidal loads and the cushion as a thin plate, an analytical solution of displacement response of cushion under high-speed train load has been derived. A parametric study has been conducted to investigate the vibration characteristics of cushion. Parametric study has been performed to analysis the effect of the train speed, damping, thickness and Young's modulus of cushion on the displacement response, velocity response. The following conclusions have been obtained:

(1) The displacement oscillates along with the load. The high frequency and medium frequency loads influence obviously on the displacement response at the beginning, but the displacement is mainly influenced by the low frequency load later.
(2) The oscillation amplitudes of the displacement increase and the resonance frequencies decrease with the increase of the train speed. With the increase of the train load, the influence of high-frequency load on the displacement decreases.
(3) The peak value of displacement increase steeply with the decrease of damping. The influence of high-frequency load increases as the damping decreases.
(4) Properly increasing the Young's modulus and thickness of cushion can effectively reduce the deformation of cushion.

References

1. Lars, H. "Simulations and analysis of train-induced ground vibrations, A Comparative Study of Two-and-Three- Dimensional Calculations with Actual Measurements." Department of Civil and Environmental Engineering, Royal Institute of Technology, Sweden. **(2000)**
2. Li, X.-B., J.-Y. Wu, and F. Qi, "Stress transfer mechanism of geosynthetic reinforced pile supported embankment due to high-speed train loading." Chinese Civil Engineering Journal, 44(supp.), 55–59. **(2011)**
3. Hung, H.-H. and Y.-B. Yang, "Elastic waves in visco-elastic half-space generated by various vehicle loads." *Soil* Dynamics and Earthquake Engineering, 21,1–17. **(2001)**
4. Amir, M.-K., M. Christian, and Z. Peter, "Ground vibration from high-speed trains: prediction and countermeasures." *Journal of Geotechnical and Geoenvironmental Engineering, 126* (6),531–537. **(2000)**
5. Fryba, L. "A rough assessment of railway bridges for high speed trains." *Engineering Structures.,* 23(5), 548–556. **(2001)**
6. Takemiya, H. "Simulation of track-ground vibrations due to a high-speed train: the case of X-2000 at Ledsgard." Journal of Sound and Vibration, 261, 503–526. **(2003)**
7. Tan, H.-M. and H.-L. Liu, "Theoretical analysis of combined action of cushion and embankment fills in pile-supported embankment." Rock and Soil Mechanics, 29(8), 2271–2276. **(2008)**
8. Xia H. and N. Zhang, "Dynamic analysis of railway bridge under high-speed trains." Computers and Structures, 83, 1891–1901. **(2005)**
9. Pan, C.-S. and G.-N. Pande, "Preliminary deterministic finite element study on a tunnel driving in loess subjected to train loading." Chinese Civil Engineering Journal, 17(4), 54–55. **(1984)**

Strength and Deformation Behavior of Roadbed Aggregate by Large-Diameter Triaxial Test

Dongdong Sun, Xuecheng Bian and Wei Li

Introduction

Graded aggregates are composed of aggregates which have different sizes. Graded aggregates are widely used in the roadbed of high-speed railway. Some scholars have studied the strength and deformation characteristics of graded aggregates. For the shear strength of graded aggregates, Yao [1] through large-diameter triaxial test to study in the condition of different confining pressure, degree of compaction, moisture state, and drainage condition, how the shear strength of graded aggregates behaviors, the experimental results show that the shear strength of graded aggregates increased with the increase of confining pressure and degree of compaction. Li and Li [2] also discuss the physical properties of graded aggregates and the factors which influence the mechanical properties of graded aggregates.

In the construction of high-speed railway, local materials are often used to fill roadbed. Resulting in the gradation is often difficult to completely maintain the same. It is necessary to study the effect of gradation on the graded aggregates.

But there is a lack of accumulation of large-diameter triaxial test result, it is difficult to form a unified and in-depth understanding. At the same time, in the actual engineering, some gravel in the foundation part of the subgrade is often broken by the upper load, which leads to the decline of the bed performance. The study of the crushing deformation of graded crushed stone is rare in the literature.

D. Sun (✉) · X. Bian · W. Li
Department of Civil Engineering, Zhejiang University, Hangzhou 310058, China
e-mail: sdd@zju.edu.cn

X. Bian
e-mail: bianxc@zju.edu.cn

W. Li
e-mail: zjulw222@zju.edu.cn

Anderson and Fair [3] proposed a method to quantify particle breakage and a conceptual model to explain the combined effects of shearing and breakage on observed specimen behavior. Indraratna et al. [4] performed a series of static triaxial tests on ballast and found that ballast particles' breakage is related to the deviator stress, the confining pressure and the excessive interaction between angular particles, while the friction angle of ballast decreases with the increase of confining pressure.

The large-diameter triaxial tests are carried out on two typical graded aggregates and two single-size gravels, to study the effects of different gradations, different densities, different loads (confining pressure and axial loading) on the strength and deformation characteristics of graded aggregates. Particle breakage and its corresponding volume strain behavior are also discussed.

Test Apparatus

Figure 1 shows the TAJ-2000 large-diameter triaxial testing apparatus utilized in this study. The test apparatus are mainly composed of six parts: the triaxial chamber, axial loading device, confining pressure boosting system, servo oil sources, loading control system, and corresponding data acquisition system. The confining pressure was applied to the specimen by a confining pressure–boosting system. To keep the loading stable and accurate, an electrohydraulic servo program with a closed-loop control system was used in the apparatus. Axial load, axial deformation and confining pressure of the specimen are measured by axial force sensor, axial displacement sensor and confining pressure sensor, and the variation of the specimen's volume was measured by the change of water volume in the triaxial chamber. In the process of monotonic static loading test, the data acquisition frequency is 2 Hz.

1. Lateral hydraulic cylinder
2. Lateral water cylinder
3. Series water cylinder
4. Axial hydraulic cylinder
5. Apparatus rack
6. Pressure transducer
7. Triaxial chamber
8. Slideway
9. Back pressure hydraulic cylinder
10. Back pressure water cylinder
11. Axial displacement LVDT
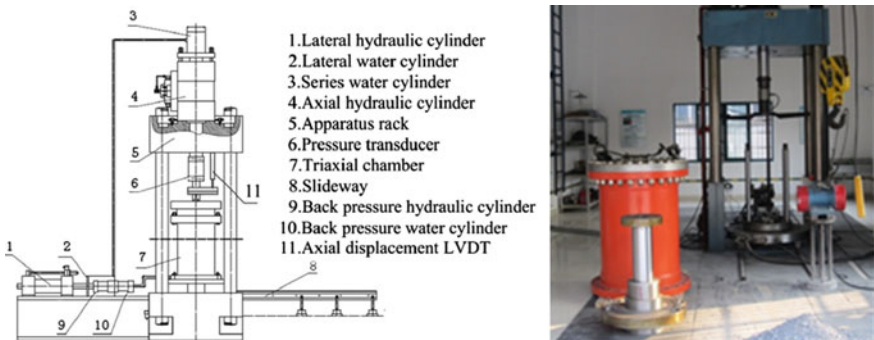
Fig. 1 Large-diameter triaxial testing apparatus

Fig. 2 Grain-size distribution of subballast materials
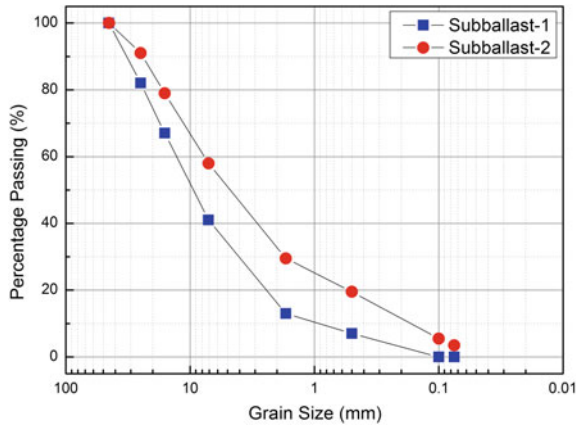
Test Procedures

In this experiment, four kinds of gravel specimens were subjected to monotonic loadig triaxial tests. Two kinds of them are graded aggregates with different graduation, subballast-1 and subballast-2. Figure 2 shows grain-size distribution of subballast materials. Other two kinds of them are single size gravels, one is 16–25 mm gravels, the other one is 25–45 mm gravels.

Each of them has identical dimensions of 300 mm in diameter and 600 mm in height, and they were compacted following the same control standard during the preparation process.

In the triaxial tests, several cases for subballast material with different compactions and confining pressures were studied. The compaction of the gravel materials is defined as the ratio of the actual density to the maximum dry density.

The mechanical behaviors of granular materials strongly depend on compaction and confining pressure. In the tests, three initial compactions were chosen as 90, 95 and 98%, three initial confining pressures were chosen as 20, 40 and 80 kPa.

In the monotonic loading triaxial tests, the axial load was controlled by the displacement, the loading speed is 5 mm/min. When its axial strain reached 10% in the tests, the specimen was regarded as failed.

Experimental Results of Monotonic Tests

Effect of Confining Pressure and Compaction on Test Results

In order to study the mechanical behavior of graded aggregates under different confining pressures, the specimens of subballast-1 and subballast-2 are subjected to monotonic loading test under confining pressures of 20, 40 and 80 kPa respectively. Figure 3 shows a typical subballast specimen before and after loading.
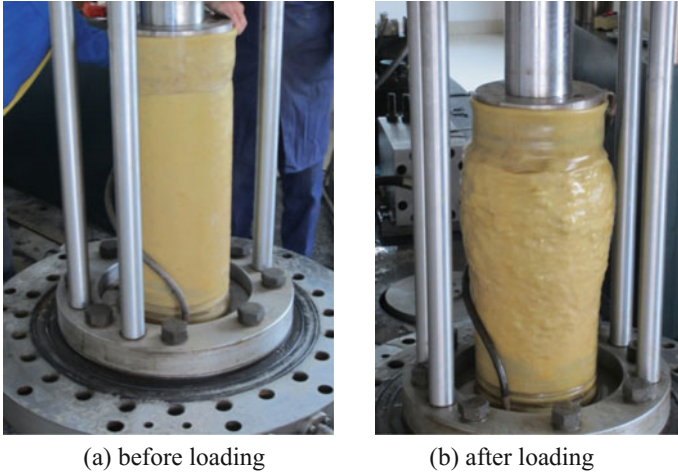
(a) before loading (b) after loading

Fig. 3 Specimen before and after loading
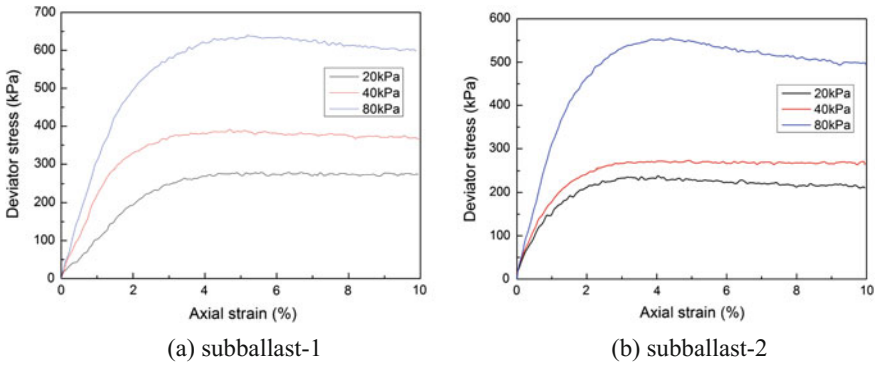
(a) subballast-1 (b) subballast-2

Fig. 4 Relationships between deviator stress and axial strain under different confining pressure

Figure 4 shows the relationship between the deviator stress and the axial strain, when the compaction is 95% for subballast-1 and subballast-2 specimen. From the test results, we can see there is a peak deviator stress during the test. When the confining pressure is low (20 and 40 kPa in this paper), the strength of specimen is almost constant after loading to the peak deviator stress. For the case of high confining pressure (80 kPa in this paper), stress softening phenomenon can be observed. The stress softening phenomenon of subballast-2 is more obvious than subballast-1.

Figure 5 shows the relationships between volumetric strain and axial strain under different confining pressure. At the beginning of loading, the volume of the specimen shrink, then the volume of the specimen increase.
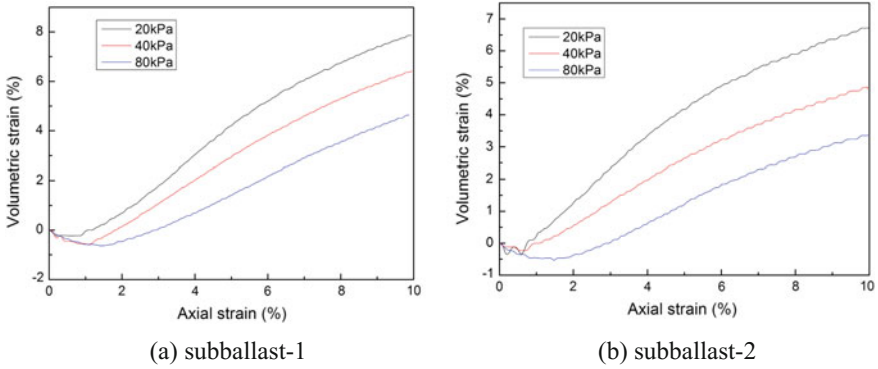
(a) subballast-1   (b) subballast-2

Fig. 5 Relationships between volumetric strain and axial strain under different confining pressure

(a) subballast-1   (b) subballast-2
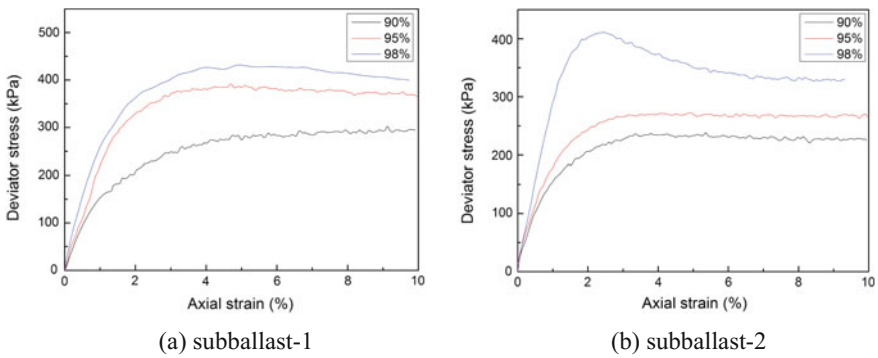
Fig. 6 Relationships between deviator stress and axial strain under different compaction

Figure 6 shows the relationship between the deviator stress and the axial strain, when the confining pressure is 40 kPa for subballast-1 and subballast-2 specimen. For subballast-1, when the compaction degree of the specimen reaches 95%, the shear strength of the specimen is almost the same as the specimen with 98% compactness. When the degree of compaction reaches a certain degree, its shear strength has little relation with the compaction degree of the specimen. For subballast-2, when the compaction degree is 90 and 95%, the shear strength of the sample is relatively low. When the compaction degree is increased to 98%, the maximum shear strength of the specimen can be increased by about 60%.

Figure 7 shows the relationships between volumetric strain and axial strain under different compaction. The volume expansion of the specimen increases with the increase of the specimen compactness. More experimental results are shown in Tables 1 and 2.

(a) subballast-1   (b) subballast-2
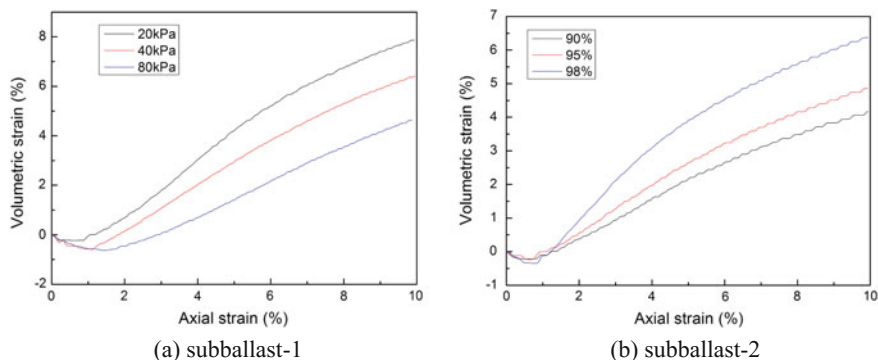
Fig. 7 Relationships between volumetric strain and axial strain under different compaction

Table 1 Monotonic loading tests results of subballst-1

Compaction (%)	Confining pressure (kPa)	Modulus E_t (MPa)	Maximum $(\sigma'_1 - \sigma'_3)_f$ (kPa)	ϕ'°_t	$\Delta V\%$ at 1% axial strain	$\Delta V\%$ at 6% axial strain
90	20	6.67	214.8	57.5	−0.12	4.28
	40	12.74	308.8	52.6	−0.34	2.2
	80	26.01	522.7	50	−0.69	−0.23
95	20	8.00	289.8	61.5	−0.11	5.2
	40	20.79	404.2	56.6	−0.57	3.82
	80	30.71	644.3	53.2	−0.58	2.2
98	20	14.78	285.6	61.3	0.35	5.9
	40	25.50	441	57.8	−0.34	4.17
	80	33.19	676.9	54	−0.46	2.77

Table 2 Monotonic loading tests results of subballst-2

Compaction (%)	Confining pressure (kPa)	Modulus E_t (MPa)	Maximum $(\sigma'_1 - \sigma'_3)_f$ (kPa)	ϕ'°_t	$\Delta V\%$ at 1% axial strain	$\Delta V\%$ at 6% axial strain
90	20	5.60	130.0	49.9	0.46	2.89
	40	14.49	247.2	49.1	−0.12	2.66
	80	26.00	401.1	45.6	−0.58	0
95	20	14.09	246.0	59.3	0.23	4.98
	40	17.05	282.6	51.2	−0.11	3.24
	80	30.79	558.0	51.0	−0.46	1.85
98	20	17.00	302.6	62.0	0.46	5.44
	40	28.74	415.5	57.0	−0.12	4.51
	80	41.45	763.2	55.8	−0.92	1.39

Particle Breakage

After the monotonic loading tests, the specimens were opened and checked for particle breakage. The particle breaking phenomenon is not obvious in subballast specimens. In order to investigate the effect of particle breakage on the strength and deformation characteristics of gravels, two single-size gravel specimen (16–25 mm gravels and 25–45 mm gravels) were used to carry out the loading test at the same compaction 98%. The shear strength of 16–25 mm gravel is obviously higher than that of 25–45 mm gravel under the same compactness (98%) and same confining pressure (40, 80, 120 kPa) (Fig. 8).

The particle breaking phenomenon is obvious in gravel specimens, especially in 25–45 mm gravels. According to the catalogs defining particle breakage proposed by Anderson and Fair [3], typical breakage forms of ballast particles observed in tests are shown in Fig. 9 and can be cataloged into five types.

Indraratna and Salim [5] examined the influence of particle degradation on the shear strength of coarse aggregates by considering the energy consumption by particle breakage during monotonic shearing, and recognized that both dilatancy and particle breakage must be taken into account when considering volume changes during shearing. McDowell and Daniell [6] stated that where there is a large particle with a low coordination number i.e., few particle contacts, there are large void spaces surrounding that particle, and when there is a low coordination number, the particle is more susceptible to breakage.

By using the following formulation 1, the total volumetric deformation caused by particle breakage in the ballast specimens can be calculated:

$$\Delta V_b = -\sum_{i=\Pi}^{i=V} \left[\sum_{j=1}^{N_i} \left(\frac{(h_{ij}T_i)^3}{3} \right) \right] \tag{1}$$

(a) 16 ~ 25mm gravels   (b) 25 ~ 45mm gravels
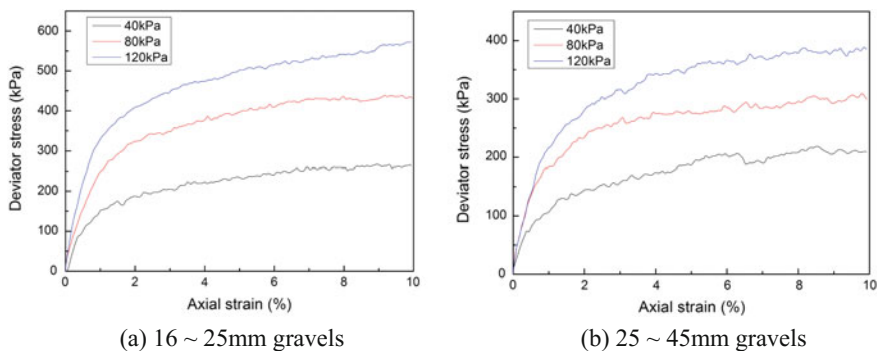
Fig. 8 Relationships between deviator stress and axial strain
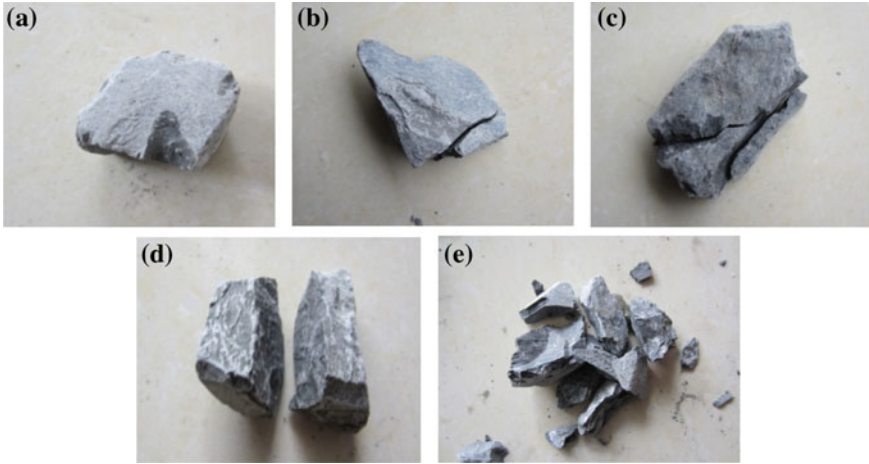
Fig. 9 Typical patterns of particle breakages in the tests: **a** Type I; **b** Type II; **c** Type III; **d** Type IV; **e** Type V

where ΔV_b = total volumetric deformation caused by particle breakage; h_{ij} = pyramid height of jth broken particle in Type i (i is from Type II to Type V); N_i = number of broken particles in type i; T_2, T_3, T_4, and T_5 = reduction factors of different types of particle breakage. The values of T_2, T_3, T_4, and T_5 were given by Anderson and Fair [3]. Broken particles in Type I have very little volume loss; hence they are not taken into account in Eq. (1). The broken particles in these specimens were counted and summarized in Table 3. Since broken particles of Type I do not cause a noticeable change in the volume of the specimens, broken particles of this type are not included in Table 3. It is calculated that the volume deformation attributable to particle breakage of the 25–45 mm gravel specimen under the confining pressure of 40 kPa is about 12,894 mm³, which is about 0.9% of the total volume change observed. The volume deformation attributable to particle breakage of the 25–45 mm gravel specimen under the confining pressure of 80 kPa is about 5% of the total volume change. The volume deformation attributable to particle breakage of the 25–45 mm gravel specimen under the confining pressure of 120 kPa is about 10% of the total volume change. It can be seen that the volumetric strain caused by particle breakage can not be ignored.

Table 3 Volume deformation attributable to particle breakage

$\Delta V_b/\Delta V$	Type II	Type III	Type IV	Type V
Confining pressure 20 kPa (%)	50.4	25.2	22.7	1.7
Confining pressure 80 kPa (%)	48.8	28.0	20.2	3.0
Confining pressure 120 kPa (%)	48.5	31.6	18.9	1.0

Conclusions

Through the large-diameter triaxial test of two kinds of graded aggregates and two kinds of single-size gravel, combined with the theoretical analysis, we can draw the following conclusions:

1. Shear strength of graded aggregates increased with the increase of confining pressure and degree of compaction. Graded aggregate has yield strength. When the confining pressure is low, the strength of the sample is basically unchanged when it is loaded to the yield strength. For the case of high confining pressure, the phenomenon of shear softening is obvious. Graded aggregate with more small size particles shows more obvious softening phenomenon.
2. For graded aggregates with more large size particles, when the degree of compaction reaches a certain degree, the strength of the graded aggregates have little relation to the compaction degree of the sample. For the graded aggregate with more small size particles, under the condition of a high degree of compaction, its strength can be fully brought into play.
3. For large size particles, at relatively low confining pressures, damage can also occur. At higher compaction, the particle breakage increases with the increase of confining pressure. The volumetric strain caused by particle breakage is a non-negligible part of the total volume strain of gravel, and can reach 10% especially under high confining pressure.

References

1. Yang Yao, Luo Qiang, Chen Zhan (2010). Experimental Study on Shear Strength of Graded Crushed Stone for Passenger Dedicated Line, Subgrade Engineering, (4), 75–78.
2. Li Hongchuan, Li Zhimin (2008) Study on Compaction Characteristics of Graded Aggregate, East China Highway, (1): 64–66.
3. William F. Anderson and Peter Fair. (2008) Behavior of Railroad Ballast under Monotonic and Cyclic Loading [J]. Journal of Geotechnical and Geoenvironmental Engineering, 134(3): 316–327.
4. Indraratna, B., Ionescu, D., and Christie, H. (1998). "Shear behavior of railway ballast based on large-scale triaxial tests." J. Geotech. Eng., 10.1061/(ASCE)1090-0241(1998)124:5(439), 439–449.
5. Indraratna, B., and Salim, W. (2002). Modelling of particle breakage of coarse aggregates incorporating strength and dilatancy. Geotech. Eng.,155(4): 243–252.
6. McDowell, G. R., and Daniell, C. M. (2001). Fractal compression of soils. Geotechnique, 51 (2):173–176.

Spatial Rotations of Principal Stress Axes in Infrastructures on High-Speed Railway

Fuchun Xue

Introduction

The change of stress state includes the variation of stress magnitude and its direction. If the stress magnitude and its direction are changed due to external effects at the same time, this may result in a phenomenon which can be regarded as the rotation of principal stress axes. The rotation of principal stress axes can be induced by wave load [1], running of train [2] and excavation [3].

The rotations of principal stress axes indicate the differences of principal stresses, it can be treated as some special king of "shearing effect". Particles may be rotated, slid or crushed under this action. It has been proved that the deformation caused by the variation of stress direction is at same level as caused by the stress magnitude [4, 5]. Correct results can only be obtained when the rotations of principal stress axes are considered in deformation analysis. Residual settlement may be induced by long-term rotation of principal stress axes coupled with the temperature and humidity effects.

F. Xue (✉)
State Key Laboratory Breeding Base of Mountain Bridge and Tunnel Engineering,
Chongqing Jiaotong University, Chongqing 400074, China
e-mail: ocean2008xfc@163.com; 1023476875@qq.com

F. Xue
School of Civil Engineering, Chongqing Jiaotong University,
Chongqing 400074, China

Rotations of Principal Stress Axes in Semi-infinite Foundation

Prior to the investigations into the rotations of principal stress axes in infrastructures on high-speed railway, it is necessary to numerically study the rotations of principal stress axes in single-phase, isotropic infinite foundation with only one soil layer. The model used is shown in Fig. 1.

The parameters of the soil are listed in Table 1.

The compression and shear wave speed of foundation soil can be calculated as $c_p = 122.3$ m/s and $c_S = 65.4$ m/s from Table 1, respectively. On this basis the Rayleigh wave speed is approximately estimated by:

$$c_R = \frac{0.862 + 1.14\upsilon}{1 + \upsilon} c_S = 60.6 \text{ m/s} \tag{1}$$

In this analysis, the speeds of the moving constant pressure applied directly to foundation surface are set to 50 and 100 m/s, which is 0.825 and 1.650 times of Rayleigh wave speed of foundation soil. Two elements namely Element 1 and Element 2, which are located 0.5 and 5.0 m below loading area respectively, are selected to compare the effects of principal stress axes rotations.

The rotations of principal stress axes for the two selected elements are shown in Fig. 2 [6].

(a) The whole model   (b) Loading condition and selected elements
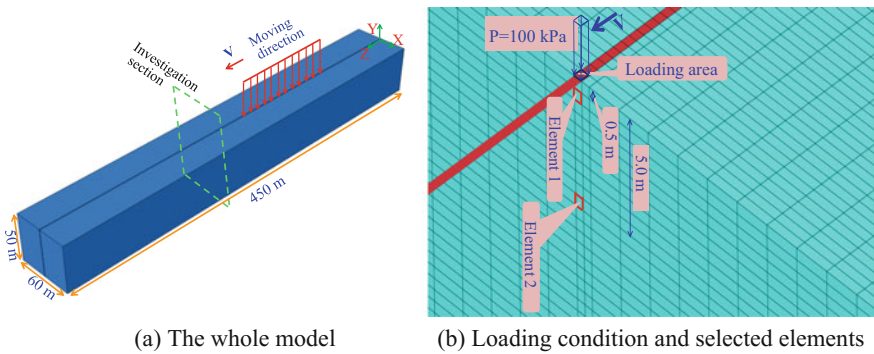
Fig. 1 Numerical model and loading condition

Table 1 Parameters for foundation soil

Unit weight (kN m^{-3})	Elastic modulus (MPa)	Poisson's ratio (–)	Cohesion (kPa)	Angle of internal friction (°)	Damping ratio (–)	Coefficients of Rayleigh damping	
						α/s^{-1}	β/s
18.0	20.0	0.3	26.8	22.0	0.08	0.239	0.010
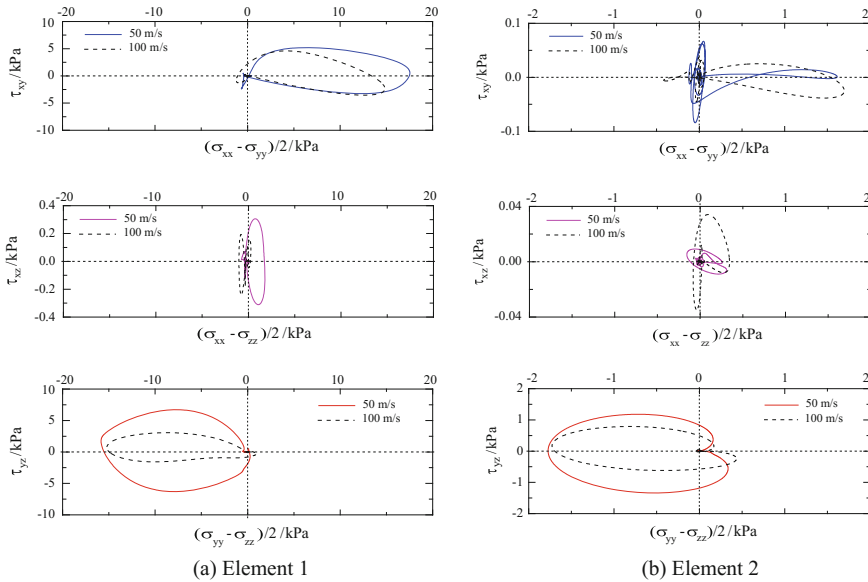
Fig. 2 Rotations of principal stress axes for selected elements

It can be seen from Fig. 2 that the axes of principal stress for element 1 and 2 rotate simultaneously and continuously in XY, XZ and YZ plane. The rotation in YZ plane has the highest intensity, whereas it is weakest in XZ plane due to the vertical response is predominated under pressure. The rotations in most planes corresponding to moving load with speed of 50 m/s are larger than those of 100 m/s because the lower moving speed of 50 m/s is nearly 0.825 times of Rayleigh surface wave speed, which to some extent causes the foundation soil to relatively low level resonance, so the soil responses are correspondingly amplified.

Two type waves, namely the P-wave and S-wave, are generated in foundation by the movement of pressure. The interaction of P-wave and S-wave leads to the generation of surface wave, which propagates in topsoil of the foundation. For this reason, it is difficult to find clear laws according to the rotations of principal stress axes for element 1. But for element 2, which is located relatively far away from loading area, it is affected less by the surface wave. So the rotation in YZ plane clearly appears some pattern, but it is not symmetric about the horizontal axis.

If attention is paid to the rotations near the origin of coordinates, it can be found that the rotations are much more complex, as shown in Fig. 3. When the load is far away from the elements selected, the equilibrium of stress state of soil elements is disturbed firstly by wave motion rather than the moving load itself because the wave speed in foundation soil is larger than the speed of moving load. With the distance between the load and the elements becomes closer and closer, the load effects play more and more significant role. After the load leaves the location of
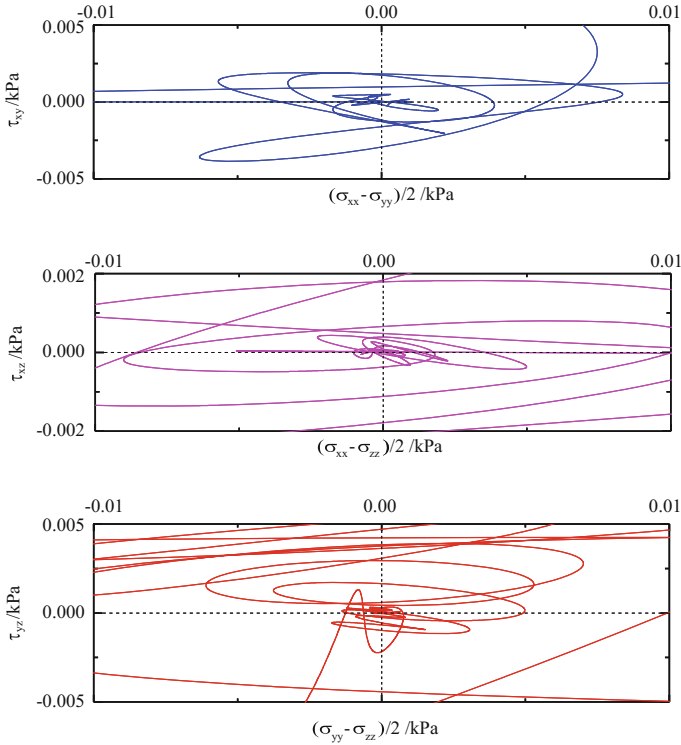
Fig. 3 Rotations near the origin of coordinate

selected elements, the load effects decrease and the surface wave becomes more important, the response intensity of soil gradually weaken due to the damping of the soil.

The rotations of principal stress axes due to moving load is usually obtained using analytical method based on assumptions such as elastic half space hypothesis, as plotted in Fig. 4. This method just solves the soil stresses in static state, the dynamic effects of high-speed moving load and nonlinear factors cannot be considered, so it cannot describe the wave motion process of foundation soil [7].

Rotations of Principal Stress Axes in Infrastructures

The typical infrastructures, including embankment, embankment-bridge transition zone and tunnel on high-speed railway, are chosen to study the rotations of principal stress axes generated by moving impulse pressures. Due to the high rigidity of pile group foundation of bridge, the deformation caused by the rotations of principal stress axes is infinitesimal and can thus be neglected, so the analysis of bridge is not covered in this paper.
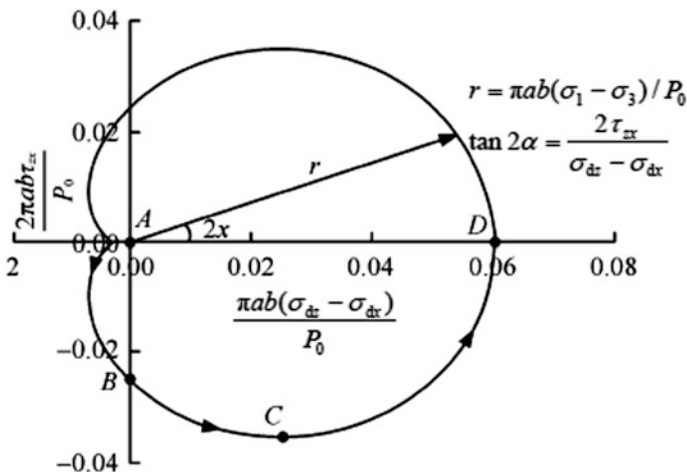
Fig. 4 Rotation from analytical solution [7]

Rotations of Principal Stress Axes in Embankment

The three dimensional elaborate numerical model is established and is shown in Fig. 5. In this analysis, the material nonlinearity, the generated geometry nonlinearity and contact nonlinearity are taken into consideration. The three-dimensional viscoelastic static-dynamic unified artificial boundaries are adopted to model the elastic recover property and radiation damping of infinite domain. The movement of pressure applied to rail top is controlled by a special algorithm and the moving speed can arbitrarily be specified. In this analysis the moving speed of pressures is set to 97.2 m/s (350 km/h). The selected elements are located below one of the loaded rails.

The rotations of principal stress axes for the two selected elements are plotted in Fig. 6.

The principal stress axes of the elements in upper layer of formation and subgrade below formation rotate in XY, XZ and YZ planes synchronously and continuously during the passage of the applied pressure. The rotations in YZ plane are the main components. The rotation intensity attenuates with the increasing of depth. Differences between the two rotation patterns can be found especially in XZ plane, the reason is that the element in upper layer of formation is closer to the loads and is greatly affected by surface wave [6].

It can be seen in Fig. 6 that the rotations of principal stress axes are much more complicated than those in Figs. 2 and 4. There are many sleepers with irregular shape in the model, the rails has also irregular section. Stress waves caused by moving pressure are reflected and transmitted at the interfaces of different materials. The stress waves interact with each other during propagation and the interactions
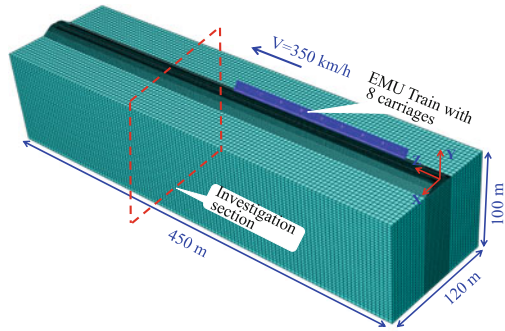
(a) The whole model
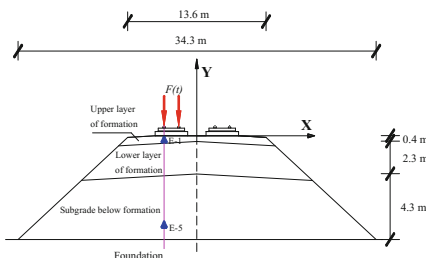
(b) Position of selected elements
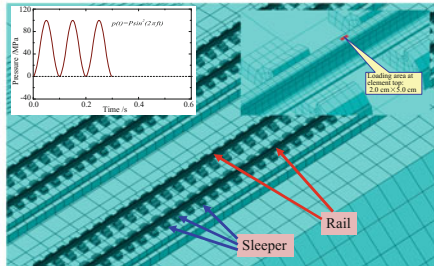
(c) Location of model and loading conditions

Fig. 5 Numerical model for embankment on high-speed railway and loading conditions
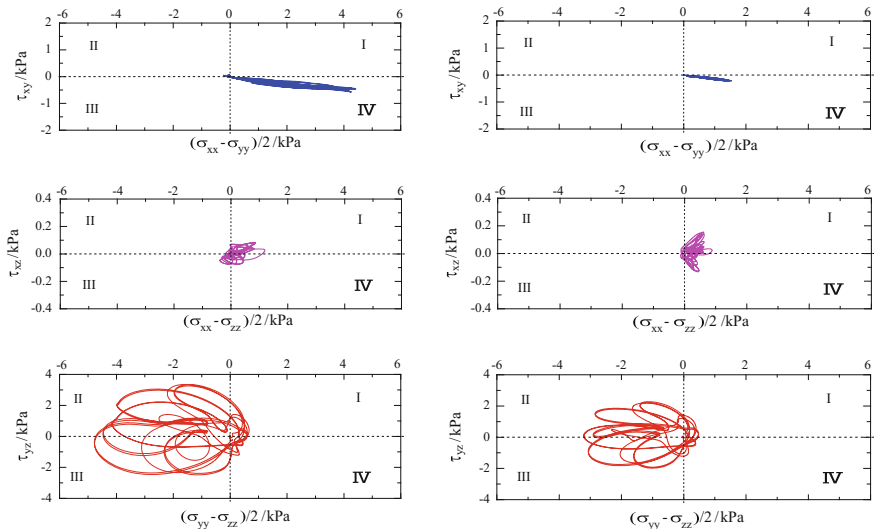
(a) Element in upper layer of formation

(b) Element in subgrade below formation

Fig. 6 Rotations of principal stress axes for selected elements

are severely distorted by the irregular shapes of the parts in the model. In addition, the embankment has limited dimensions and the inner stress cannot be obtained via Boussinesq theory because the prerequisite of the theory cannot be met.

Rotations of Principal Stress Axes in Embankment-Bridge Transition Zone

The three dimensional nonlinear numerical model for embankment-bridge transition zone is constructed as illustrated in Fig. 7. The nonlinear factors and infinite boundaries mentioned before are treated in the same way. The moving speed of pressure is set to 97.2 m/s. Two elements located below one of the loaded rails are selected for further analysis. One is in the upper layer of formation and the other is in transition zone, as plotted in Fig. 7. The rotations of principal stress axes for the two elements are demonstrated in Fig. 8.

(a) The whole model

(b) Location of investigation section

(c) Position of selected elements
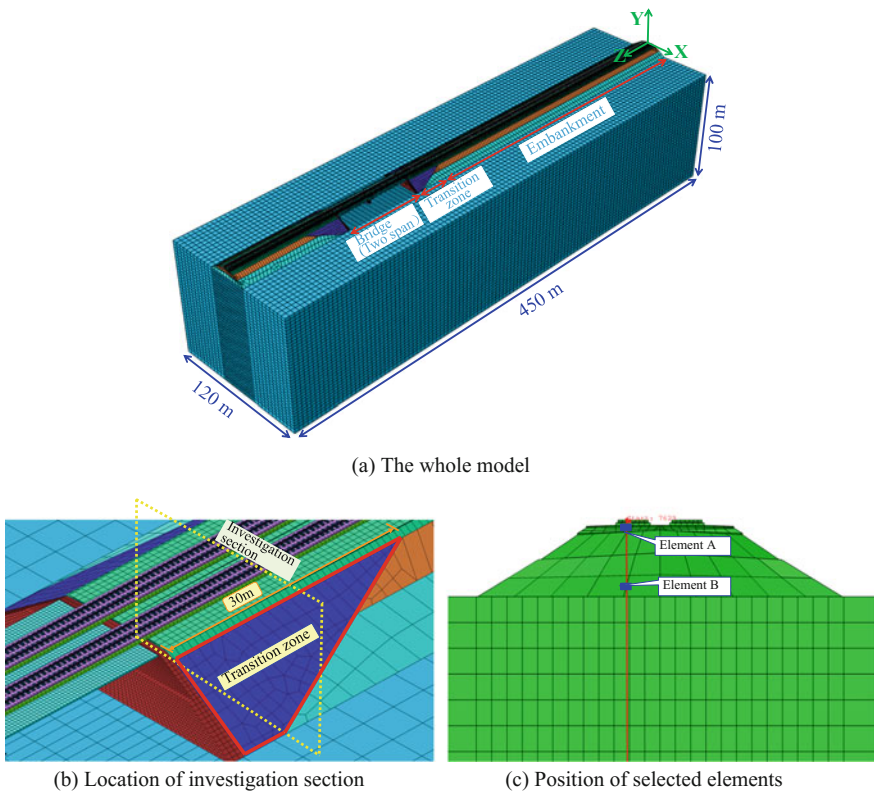
Fig. 7 Numerical model for embankment-bridge transition and the selected elements

(a) Element in upper layer of formation   (b) Element in transition zone
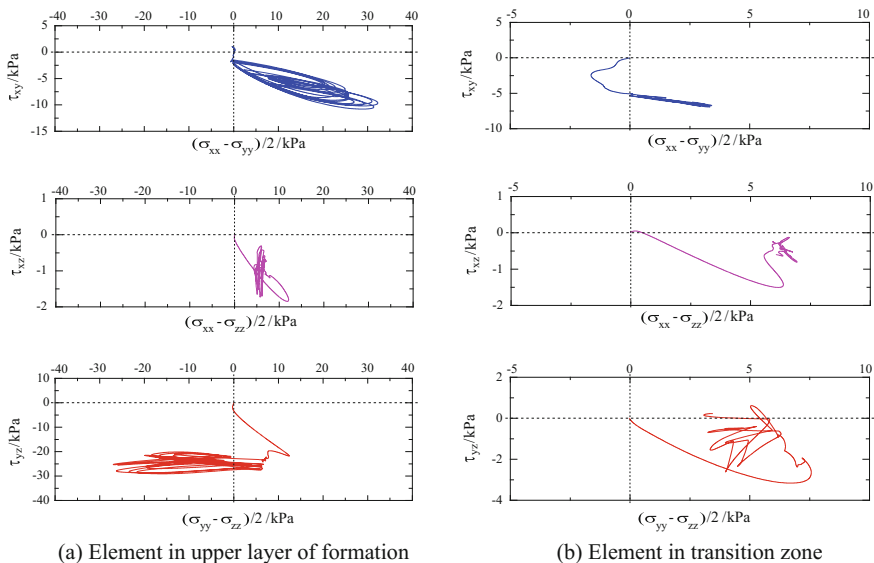
Fig. 8 Rotations of principal stress axes for selected elements

Although the rotations of principal stress axes in XY, XZ and YZ planes are synchronously and continuously during the load passage, great differences are found from Fig. 8.

On the one hand, the main parts of the rotations are severely deviated from the origin of coordinate, the reasons for the deviations are the intensive interactions of P-wave and S-wave due to the lack of the same media for them to propagate as in embankment near the transition zone. There are large free surfaces between the transition zone, the pier, the foundation and the bridge, which leads to seriously stress concentration around them, so the stress states of the adjacent elements are greatly affected and the wave fields are much more complex and in state of disorder. On the other hand, no clear rotation patterns can be obtained due to the interaction of different stress waves, the rotation laws remain to be solved.

Rotations of Principal Stress Axes in Tunnel Base

The nonlinearly coupled rail-tunnel-foundation model for double line high-speed railway tunnel is developed and is shown in Fig. 9. The nonlinear factors and infinite boundaries mentioned before are dealt with in the same way. The moving speed of the pressures is 97.2 m/s. The rotations of principal stress axes for the two selected elements are plotted in Fig. 10.

(a) The whole model

(b) Location of the cross section

(c) Position of selected elements
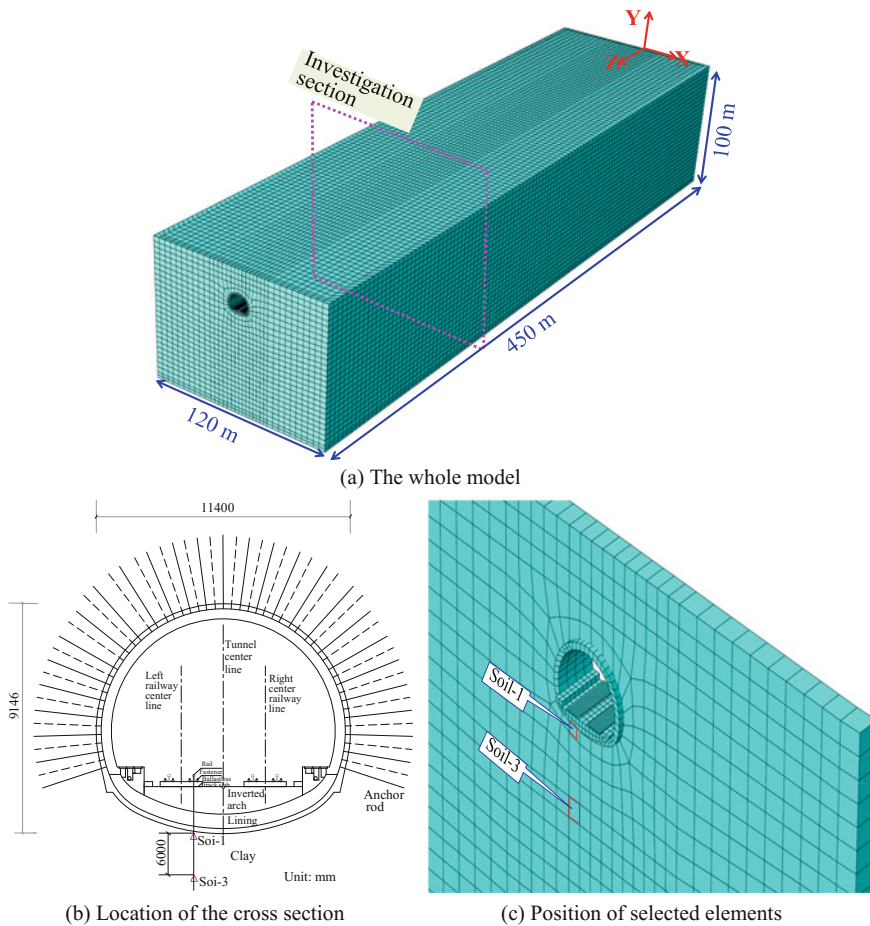
Fig. 9 Numerical model for tunnel and the selected elements

As can be seen in Fig. 10, the rotations of principal stress axes in XY, XZ and YZ planes occur synchronously and continuously during the pressures passing the investigation section. The rotation in YZ plane is predominant at different depths. At the lower depth the rotation in XY plane has the same intensity level as in YZ plane for soil-1, while at more depth it accounts for only a small part of the rotation intensity in YZ plan for soil-3, indicating the great influence of surface wave on shallow soil element.

(a) Rotations for element Soi-1   (b) Rotations for element Soi-3
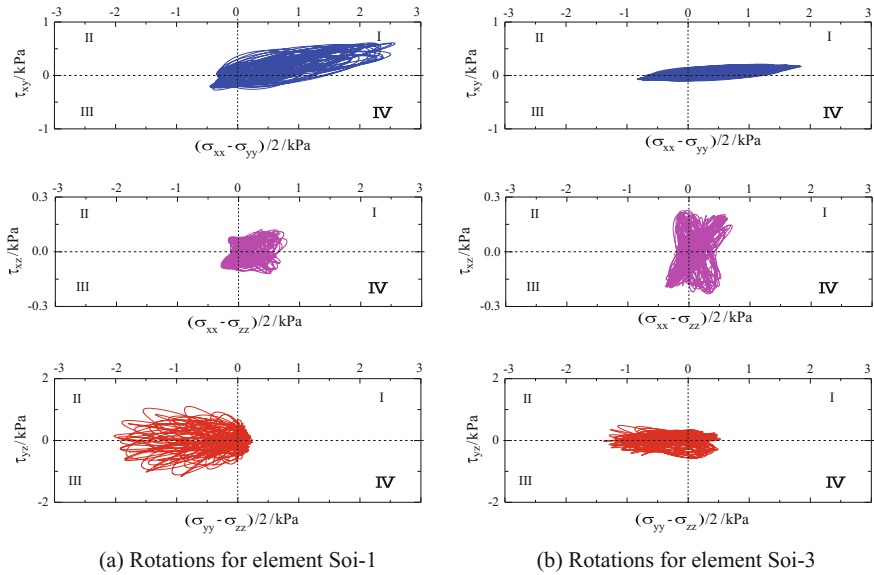
Fig. 10 Rotations of principal stress axes for selected elements

Conclusions

The rotations of principal stress axes in semi-infinite foundation caused by a moving constant pressure and in infrastructures on high-speed railway under moving impulse pressures are numerically investigated considering the nonlinear factors, the analyses result in the following conclusions:

1. The principal stress axes rotate in XY, XZ and YZ plane synchronously and continuously, and the rotation in YZ plane is the main component.
2. The rotation patterns in infrastructures on high-speed railway are much more complicated than those in semi-infinite foundation.
3. Surface waves have great influences on the rotations of principal stress axes, severely stress concentrations are found around the embankment-bridge transition zone due to the existing of large free surfaces.

References

1. Ishihara, K. (2003). Soil Behaviour in Earthquake Geotechnics. Oxford: Clarendon Press.
2. Hu, Y.F., Li, N.F. (2010). Theory of ballastless track-subgrade for high-speed railway. Beijing: China Railway Publishing House.
3. Cui, W., Wang, N. (2014). Principal stress axis rotation and effect on failure model of surrounding rock during tunneling. Journal of Central South University (Science and Technology), 45(6): 2062–2070.
4. Tong, Z.X., Zhang, J.M., Zhang, G. (2009). An elastoplastic constitutive model of sands considering cyclic rotation of principal stress axes. Chinese Journal of Rock Mechanics and Engineering, 28 (9): 1918–1927.
5. Tong Z.X., Zhang, J.M., Zhang, G. (2009). Effects of principal-stress-axis rotation on the deformation of a dam under wave loading. Engineering Mechanics, 26(10): 67–73.
6. Xue, F.C., Zhang, J.M. (in press). Effects and laws of spatial rotations of principal stress axes in embankment due to moving loads on High-speed railway, Journal of The China Railway Society.
7. Wang, C.J., Wen, R.K., Chen, Y.M. (2008). Discussion on laboratory test simulation of principal stress axes rotation induced by traffic loading. Rock and Soil Mechanics, 29(12): 3412–3416.

Field Measurement and Analysis of Ground Vibration Induced by High-Speed Train

Guangyun Gao, Juan Chen, Jian Song, Jun Yang and Shaofeng Yao

Introduction

Ground vibration induced by moving high-speed trains has received increasing attention in recent years. The dominant frequency of the induced ground vibration ranges from 5 to 150 Hz, which may cause vertical resonance and damage to nearby structures and discomfort to inhabitants in the surrounding areas of the HSR (High Speed Railway) line [1, 2]. It is therefore needed to develop effective methods to predict the ground vibration induced by high-speed trains and to reduce the vibration when necessary.

During the past decades, various analytical, semi-analytical and numerical methods with different accuracies have been developed to investigate train-induced ground vibrations [3, 4]. Among the numerical methods for analyzing ground vibrations under moving train loads, the so called two-and-a-half-dimensional finite

G. Gao (✉) · J. Chen · S. Yao
Department of Civil Engineering, Tongji University, Shanghai 200092, China
e-mail: gaoguangyun@263.net

J. Chen
e-mail: 2014chenjuan@tongji.edu.cn

G. Gao · J. Chen · S. Yao
Key Laboratory of Geotechnical and Underground Engineering
of Ministry of Education, Tongji University, Shanghai 200092, China

J. Song
College of Civil and Transportation Engineering,
Hohai University, Nanjing 210098, China
e-mail: jiansonghh@163.com

J. Yang
Department of Civil Engineering, The University of Hong Kong, Hong Kong, China
e-mail: junyang@hku.hk

element method (2.5D FEM) gained its popularity recently [5–8]. This method is computational effective in that the 3D problem is solved by using a 2D plane model for which the applied load is along the direction out of the plane.

Meanwhile, in situ tests for high-speed train-induced ground motions have been conducted for a better understanding of the high-speed train induced vibrations and for the verification of the proceeding numerical methods [9, 10]. However, these testing data are rather limited at present, especially when regarding the influence of train speed on the vibration amplitude.

European researchers have published a series of experimental data from tests of railway, intercity express and metro lines. In Germany, Auersch [11] performed three series of measurements during the test runs of the ICE (Inter-City-Express) on the newly built ballasted track near Würzburg, with the train operating at a speed of 100–300 km/h. Degrand, Lombaert and Galvin [12–14], carried out a comprehensive in situ measurements on the Thalys HST (High Speed Train) lines connecting Brussels and surrounding cities such as Brussels-Paris with the train moving speed of 223–314 km/h, Brussels-Köln with the train running at the speed of 156–307 km/h, and Córdoba-Málaga (in Spain) with the train speed of 151–298 km/h. In France, Galvin et al. measured the free field vibrations during a passage of the TGVA at a site in Reugny with a running speed of 255 km/h, and used the measured data to certificate a newly established 2.5 D FE-BE model [7]. In Sweden, the vibration test conducted by BANVERKET (Swedish National Railway Administration) is one of the earliest tests data on the X2000 train at Ledsgard on the West Coast Line between Gotenborg and Malmo [15–18]. The train experienced a very large track vibration at the speed of 200 km/h. The investigation noted significant differences in the ground vibrations as train speeds increased, and a significant response occurred when the train speed approached and just crossed over the expected Rayleigh wave velocity of the site.

Chinese researchers used to cite results of the X2000 train in Sweden to verify their numerical or analytical models [19–21], owing to the lack of open access to in situ data. However, this would cause subtle loss of rigor, since the afterwards numerical simulations would be performed on our trains moving on soils with different geological characteristics. It is thus desirable to have the test results in China. Zhai had performed series of in situ measurements on China's non-ballasted HST lines, including a 200 km/h speed level test in Suining-Chongqing line [22], a 300 km/h speed level test in Beijing-Tianjin line [23], a 350 km/h speed level CRH train test in Wuhan-Guangzhou line [24], and a recently released experimental results on a so-called 'very high speed (300–425 km/h)' train in China's Beijing-Shanghai line [25]. All these results on HSR lines with non-ballasted track provided a good source of reference for Chinese researchers.

Though non-ballasted track is becoming a dominant track type in China, ballasted track still plays an irreplaceable role in some specific geological conditions [26, 27]. Besides, when cracks appeared in non-ballasted tracks after operation [28], the bearing mechanism of non-ballasted tracks degraded to that of ballasted track. Consequently, it is still of vital importance to have tests results on China's HST operating on ballasted tracks published.

In this paper, field measurements of the ground vibrations induced by high-speed trains at a site of the Qin-Shen Line are presented. This test is initiated to assure the train running safety at a high speed of 250 km/h. The measurements were undertaken at different distances from the track center during the passage of a high-speed train at a speed varying from 230 to 250 km/h. Though the test results have been partially utilized to verify numerical models in the author's previous papers [29–31], they have never been published in detail. These materials could be a valuable complimentary data to Zhai's tests results on the non-ballasted tracks and provide a valuable reference to peer researchers in China for their establishment of numerical models.

The In Situ Experiment

Basic Information of the Test Line and the Experiment Setup

Qin-Shen Line is the first high-speed passenger railway line established in China, connecting Qinhuangdao and Shenyang, with a total length of 404.64 km. Our measurement of ground vibration is a branch of the second time comprehensive test before the commercial operation, with the purpose to provide first-hand data for analyzing ground vibrations induced by high-speed trains. The test site is at Suizhong, 44 km away from the Shanhaiguan Railway Station, as is shown in Fig. 1. Qin-Shen Line adopted double-line railway embankment. The designed cross-section of the railway embankment is shown in Fig. 2 [32]. The double-line spacing is 4.6 m. The width of the foundation bed is 12.5 m, with a 1 m-width shoulder on both sides. The embankment slope is 1:1.75.

Fig. 1 Route map of Qin-Shen Line in China
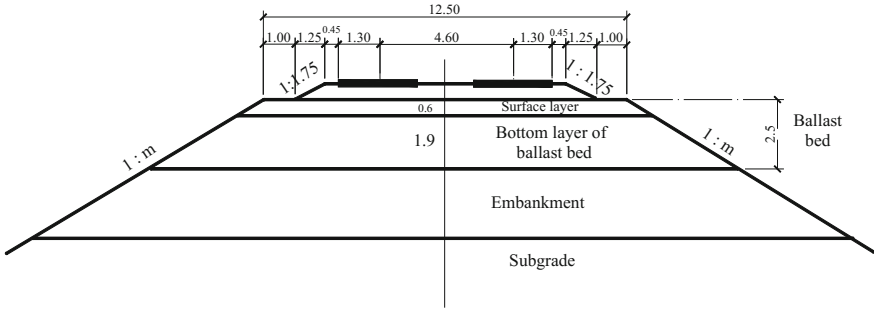
Fig. 2 The standard cross-section of the double-line highway embankment (*unit* m)

In each run of testing, the train travelled at a constant speed, and several speeds ranging from 230 to 250 km/h were tested. Generally, the ground motions at a given position are composed of vertical, transversal, and longitudinal components (ISO-2613-1; GB/T 13441-92). In this study, the focus is placed on the vertical component. The monitoring system included twelve electronic accelerometers which were located at different distances on the left side of the left track, up to 33.5 m from the track center, as schematically shown in Fig. 3. PCB acceleration sensors with a sensibility of 10 V/g and a frequency range of 0.1–1000 Hz were used. Note that the low-pass filtering is applied in the measured data. The sample frequency is set to be 512 Hz, so as to take into account the effect of high frequencies up to 256 Hz.
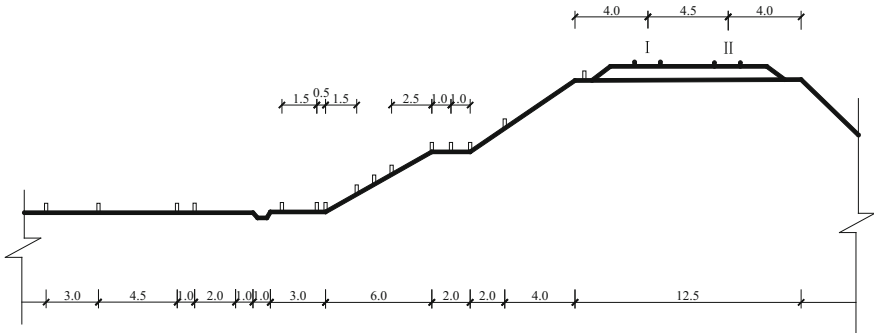
Fig. 3 Schematic illustration for positions of vibration pickups in the field test (*unit* m; not to scale in the vertical direction)

Characteristic of the Train, Track and Soil

The train running on the tested line is developed by Chinese researchers and technicians. The high-speed train consists of two units, and each includes two motor vehicles and a trailer as shown in Fig. 4. The train has 12 pairs of wheel sets and the total length is 158 m. The wheelbase is 2500 mm. The mass of the carriage, bogie and wheel set is 52,000, 3200 and 1400 kg, respectively. Detailed parameters of the high-speed train are listed in Table 1.

The HSR line adopted the 60 kg/m steel rails, Type II and Type III fasteners in different conditions according to Chinese standards. The sleeper paved is Type III concrete sleeper, with 1680 sleepers each kilometer. The track bed used the Type I ballast bed. The thickness of the ballast layer is 30 cm in soil sub-grade, and 35 cm in rock sub-grade. The Thickness of the ballast bed and embankment is 2.5 and 2.0 m, respectively. The sub-grade soils consisted of a shallow top silty clay layer (with a thickness of approximately 2.0 m) over a medium-dense fine sand layer. The parameters of the track, ballast bed and sub-grade soils are listed in Tables 2, 3 and 4. Table 5 provided a reference range for rail and track parameters that cannot be found in Tables 2 and 3, but may be desired in numerical simulation.
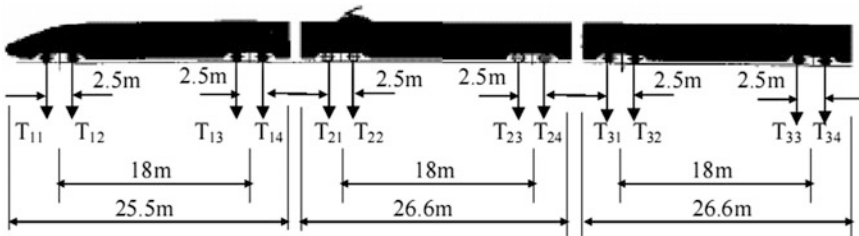
Fig. 4 One element of the high-speed train

Table 1 Vehicle parameters of the testing train

Trailer	Carriage length (mm)	25,500
	Carriage width (mm)	3105
Motor	Carriage length (mm)	26,200
	Center distance of bogie (mm)	18,000
	Wheelbase (mm)	2500
	Wheel diameter (mm)	457.5
	Carriage mass (kg)	52,000
	Bogie mass (kg)	3200
	Wheel mass (kg)	1400
	Average axle load (kg)	12,674.46

Table 2 Material parameters of rail structure and ballast bed

Material type	Elastic modulus E (MPa)	Poisson ratio v	Density ρ (kg/m^3)
Steel track	2.1×10^5	0.30	7800
Sleeper	1.5×10^4	0.30	2800
Ballast	150	0.27	2500
Sub-ballast	50	0.35	2000

Table 3 Basic parameters of railway line with 60 kg/m-track in China

	Quantities	Magnitude	Unit
Steel track	Railhead diameter	300	mm
	Mass	60.64	kg/m
	Section area	77.45	cm^2
	Horizontal moment of inertia	3217	cm^4
	Elastic modulus	2.06×10^5	MPa
Rail plate	Stiffness	78	MN/m
	Damping ratio	50	kN s/m
	Mass	3.0	kg
Sleeper	Spacing	0.568	m
	Mass	250	kg
	Length	2.60	m
	Width	0.25	m
	Height	0.20	m
	Bottom area	0.6525 (Sleeper) 0.5073 (Loading)	m^2
Ballast bed	Density	2500	kg/m^3
	Stiffness coefficient	180	MN/m
	Damping ratio	60	kN s/m
	Thickness	0.35	m
	Pressure angle distribution	35	°
	Mass	560	kg

Table 4 Soil parameters in the field test

Soil layer	Mass density ρ (kg/m^3)	Shear velocity c_s (m/s)	P-wave velocity c_p (m/s)	Poisson's ratio v	Damping ratio β
Embankment	2200	170	298	0.25	0.25
Silty clay	1700	150	270	0.30	0.25
Half-space (fine sand)	1800	280	490	0.25	0.25

Table 5 Value ranges of track related parameters

Parameters	Value range
Stiffness of sleeper plate	50–100 MN/m
Stiffness of rail fastener (clip)	2.94–3.92 MN/m
Stiffness of rail fastener	53–104 MN/m
Damping of rail fastener	30–63 kN s/m
Stiffness of ballast bed	165–220 MN/m
Damping of ballast bed	55–82 kN s/m
Stiffness of railway foundation	40–133 MN/m
Damping of railway foundation	90–100 kN s/m
Combined stiffness of ballast bed and railway foundation	40–60 MN/m
	80–100 MN/m
Rigidity of single track	14.4–23 MN/m (Wood sleeper)
	34.5–48.9 MN/m (Concrete sleeper)
	40.25–57.5 MN/m (Wider sleeper)
Spring stiffness of wheel-track interaction	1225–1500 MN/m
Horizontal spring stiffness of track sleeper	402.5 MN/m
Horizontal spring stiffness of ballast bed	11.5 MN/m

Results Analysis

Vertical ground accelerations resulting from the high-speed train moving at speeds of 230, 240 and 250 km/h were recorded respectively at the different distances from the track center. Both time domain and frequency domain analyses were performed on the recorded data. In the time-domain analysis, time histories of vertical acceleration on the measured points during the passage of train with different operation velocities are shown in Fig. 5, and the variation of the peak accelerations with distance from the track center is depicted in Fig. 6. In the frequency-domain analysis, Fourier spectral of the detected signals is shown in Fig. 7, as is corresponding to the time-domain results in Fig. 5. The one-third octave spectral plots of vertical accelerations at different distances from the track center at the train speed of 250 km/h are presented in Fig. 8.

Time-Domain Analysis

Vertical acceleration time histories at several distances from the track center for train speeds of 230, 240 and 250 km/h are depicted in Fig. 5a–c. From these figures, it can be observed that, the amplitudes of the vertical time history under the three speeds generally attenuated with distance. Besides, the periodic exciting
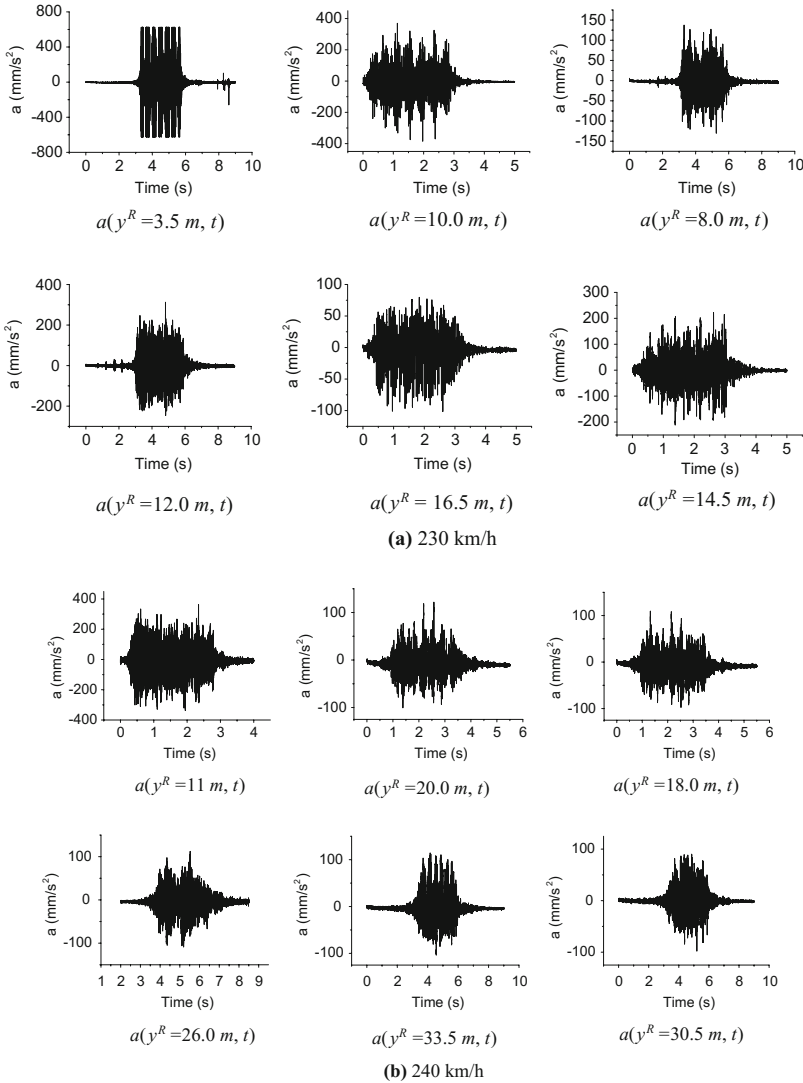
Fig. 5 Measured time histories of vertical accelerations at different distances from the track center at various train speeds

action of the train wheel-set can be identified in the time history of vertical acceleration when the testing point is near to the centerline, e.g. when yR = 3.5 m in Fig. 5a, c. In addition, the time duration of the train induced vibration is about 2.5–3.0 s, and the duration of vibrations decreases with the train speed increasing (still less than the shear wave velocity of surface layer, that is 170 m/s or 612 km/h as is measured).

$a(y^R = 3.5\ m, t)$ $a(y^R = 12.0\ m, t)$ $a(y^R = 8.0\ m, t)$

$a(y^R = 15.5\ m, t)$ $a(y^R = 18.5\ m, t)$

$a(y^R = 25.0\ m, t)$

(c) 250 km/h
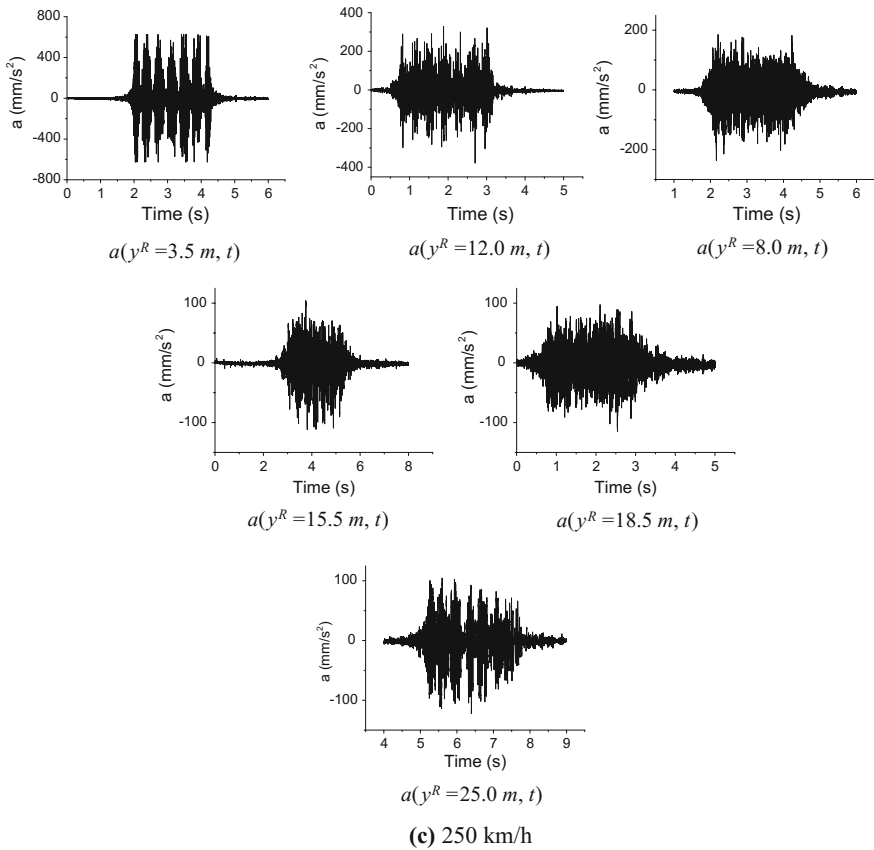
Fig. 5 (continued)
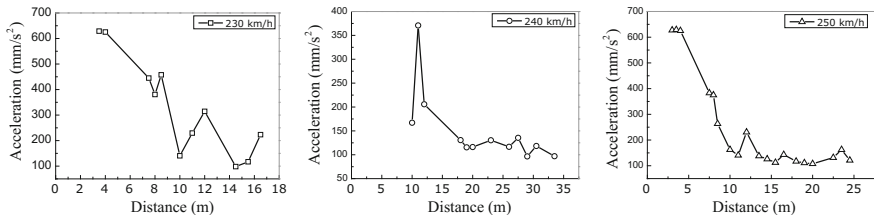
Fig. 6 Attenuation of measured peak vertical accelerations with distance from the track center at different train speeds

Figure 6 shows the observed attenuations of peak vertical acceleration with distance for the three tested train speeds. The attenuation appears to be much more significant in the vicinity of the track. This is likely due to the fact that the body waves (P wave and S wave) induced by the passage of high-speed train greatly

(a) 230 km/h

(b) 240 km/h
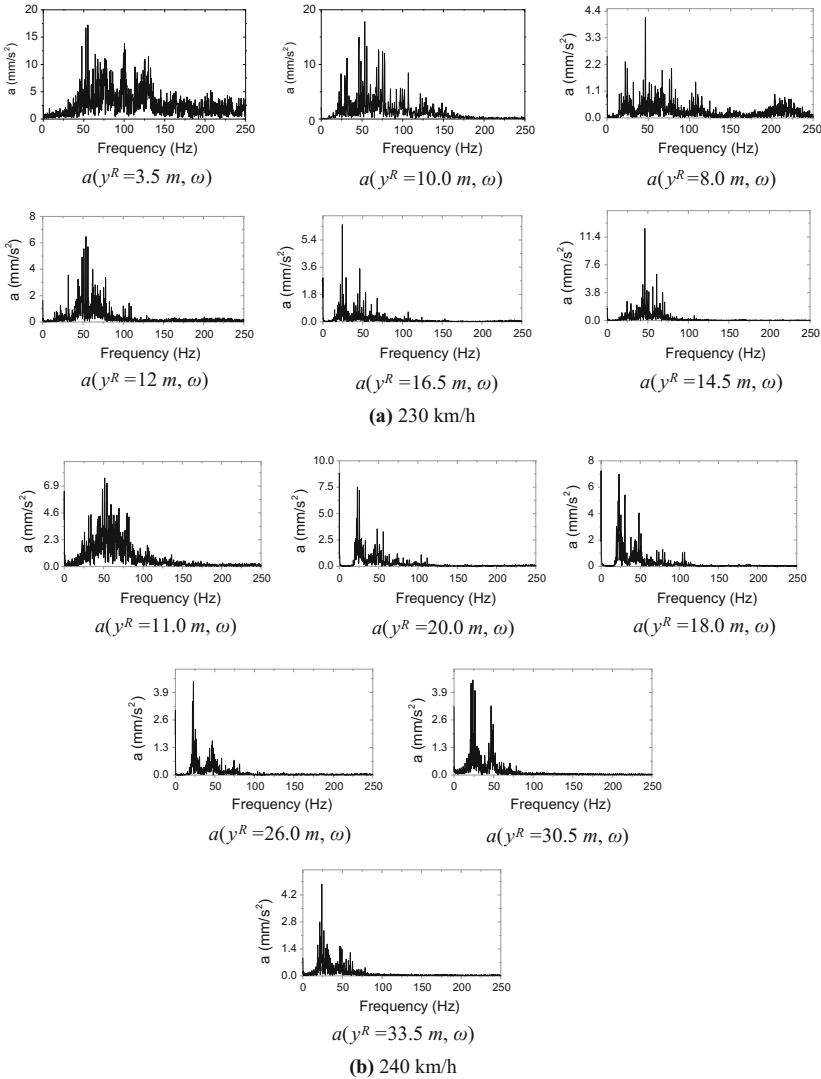
Fig. 7 Fourier spectra of the signals given in Fig. 5

contributes to the ground vibrations in the vicinity of track, but this effect decreases quickly with increasing the distance away from the track center. There is a significant change in the rate of peak acceleration reduction at the distance of about 15 m. This is likely a manifestation that the Rayleigh wave (R-wave) tends to dominate beyond this distance (about $3\lambda R$ where λ_R is the R-wave length of the soil, see Ref. [33]). Take the case of 250 km/h as an example, the fundamental axle passage frequency is 27.8 Hz, the R-wave velocity is about 156.4 m/s, the

$a(y^R = 3.5m, \omega)$ $a(y^R = 8m, \omega)$ $a(y^R = 12m, \omega)$

$a(y^R = 15.5m, \omega)$ $a(y^R = 18.5m, \omega)$ $a(y^R = 25.0m, \omega)$
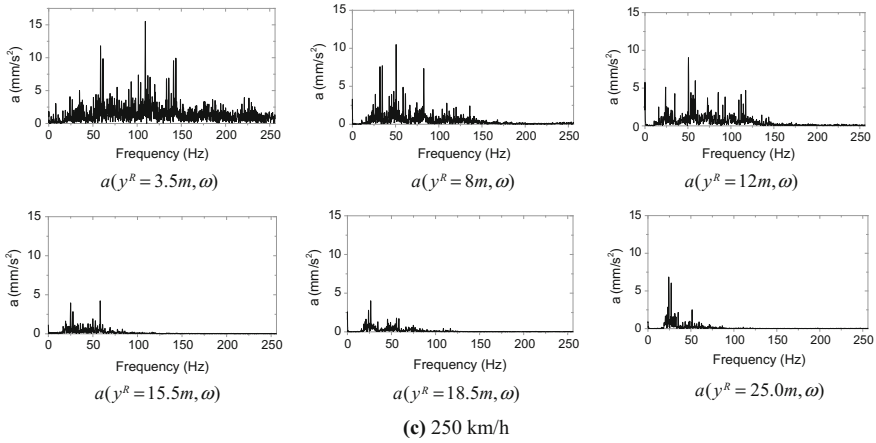
(c) 250 km/h

Fig. 7 (continued)

Fig. 8 One-third octave spectra of vertical accelerations at different distances from the track center at the train speed of 250 km/h
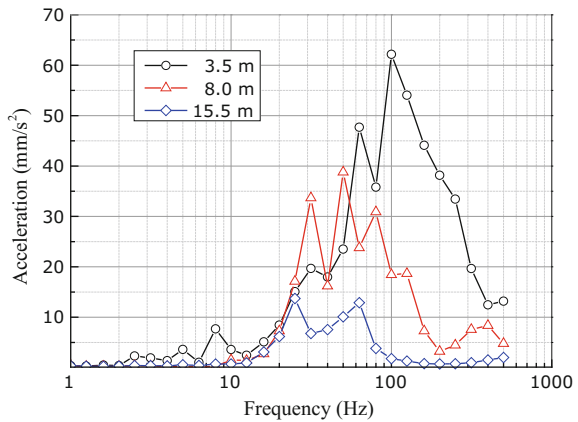
wavelength is about 5.63 m, and $3\lambda_R$ is about 16.88 m. This suggests that the contributions of the body waves to the ground vibrations should be considered in the vicinity of the track within the distance of about $3\lambda_R$.

In addition, the recorded results in Fig. 6 show that a vibration boom occurs at the distance of 12 m. This is the result of wave reflection within soil layers. Only a slight increase is observed in the peak ground acceleration, and this is likely the result of similar train speed considered in the test.

The Frequency-Domain Analysis

The Fourier spectra of the vertical accelerations corresponding to Fig. 5 are shown in Fig. 7. According to Fig. 7, the general range of vibration frequencies for the embankment is between 0 and 200 Hz, and the bandwidth of the response frequency narrowed down when the distance to track center increases since higher frequencies disappeared. It can also be observed that there are several spectral peaks in the measured spectra, among which there are two dominant frequencies at around 26 and 51 Hz, respectively.

The frequency of about 26 Hz is related to the axle-load with an axle-base of 2.5 m (the fundamental axle passage frequencies associated with train speeds of 230, 240 and 250 km/h are 25.6, 26.7 and 27.8 Hz). The other dominant frequency (around 51 Hz) increases slightly from 45 to 55 Hz as the train speed increasing from 230 to 250 km/h, this and other spectral peaks in the measurements may be related to soil layering and other non-homogeneity.

Figure 8 displays the one-third octave spectra of the measured vertical accelerations at different distances from the track center at the train speed of 250 km/h. It can be observed that the attenuation of the vibrations with higher frequencies is more rapidly than those with lower frequencies. This reduces the contribution of the high-frequency vibrations at certain distances away from the track, indicating the visco-elastic properties of the ground.

Conclusions

In this paper, field measurements of ground vibrations induced by high-speed trains at a site on the Qin-Shen Line in China are presented. The measured results are analyzed both in time and frequency domain to reveal the free field ground vibration characteristics under the train speed of 230, 240 and 250 km/h.

The time domain analysis indicates that, the duration of the train induced vibration with speed of 230–250 km/h is 2.5–3.0 s. This time duration decreases with increasing the train speed, while the vibration amplitude increases slightly. When the testing site is 3.5 m away from the track centerline, the periodic exciting action of the train wheel-set can be identified in the vertical acceleration time-history. This phenomenon cannot be observed when the distance increases. The attenuation of vibrations is more significant in the vicinity of the track and becomes less significant with further increasing the distance. In the vicinity of the track the contributions of the body waves (P wave and S wave) to the ground vibrations should be considered. There is a vibration boom appeared at the distance of approximately 12 m.

The frequency domain analysis shows that, the range of the free field vibration frequencies is between 0 and 200 Hz; and there is a dominant frequency associated with the axle passage (25.6–27.8 Hz), and other dominant frequencies resulting

from track irregularity and soil non-homogeneity. Moreover, the attenuation of the vibrations with higher frequencies is more rapidly than those with lower frequencies.

The measured data is available to other researchers. Researchers who request using this data can contact the corresponding author.

References

1. Xia, H. (2010). Traffic induced ground vibrations and controls. China Science Press, Beijing (in Chinese).
2. Thompson, D. (2009). Railway noise and vibration-mechanics, modelling and means of control. Elsevier, Oxford.
3. Connolly, D., Giannopoulos, A., Forde, M.C. (2013). Numerical modelling of ground borne vibrations from high speed rail lines on embankments. Soil Dynamics and Earthquake Engineering, 46(0): 13–19.
4. Kouroussis, G., Connolly, D., Verlinden, O. (2014). Railway-induced ground vibrations–a review of vehicle effects. International Journal of Rail Transportation, 2(2): 69–110.
5. Yang, Y.B., Hung, H.H., Chang, D.W. (2003). Train-induced wave propagation in multi-layered soils using finite/infinite element simulation. Soil Dynamic Earthquake Engineering, 23(4): 263–278.
6. Takemiya, H., Bian, X.C. (2005). Substructure simulation of inhomogeneous track and layered ground dynamic interaction under train passage. Journal of Engineering Mechanics Division, ASCE, 131(7): 699–711.
7. Galvin, P., François, S., Schevenels, M., Bongini, E., Degrande, G., Lombaert, G. (2010). A 2.5 D coupled FE-BE model for the prediction of railway induced vibrations. Soil Dynamics and Earthquake Engineering, 30(12): 1500–1512.
8. Gao, G.Y., Chen, Q.S., He, J.F., Liu, F. (2012). Investigation of ground vibration due to trains moving on saturated multi-layered ground by 2.5D finite element method. Soil Dynamics and Earthquake Engineering, 40: 87–98.
9. Kouroussis, G., Verlinden, O., Conti, C. (2011). Free field vibrations caused by high-speed lines: Measurement and time domain simulation. Soil Dynamics and Earthquake Engineering, 31(4): 692–707.
10. Alves Costa, P., Calçada, R., Silva Cardoso, A. (2012). Track-ground vibrations induced by railway traffic: In-situ measurements and validation of a 2.5D FEM-BEM model. Soil Dynamics and Earthquake Engineering, 32(1): 111–28.
11. Auersch, L. (2005). The excitation of ground vibration by rail traffic: theory of vehicle–track–soil interaction and measurements on high-speed lines. Journal of Sound and Vibration, 284 (1–2): 103–132.
12. Degrande, G., Schillemans, L. (2001). Free field vibrations during the passage of a THALYS high-speed train at variable speed. Journal of Sound and Vibration, 247(1): 131–144.
13. Lombaert, G., Degrande, G. (2009). Ground-borne vibration due to static and dynamic axle loads of InterCity and high-speed trains. Journal of Sound and Vibration, 319(3–5): 1036–1066.

14. Galvín, P., Domínguez, J. (2009). Experimental and numerical analyses of vibrations induced by high-speed trains on the Córdoba–Málaga line. Soil Dynamics and Earthquake Engineering, 29(4): 641–657.
15. BANVERKET. (1997). Evaluation and analyses of measurements from the West Coast line. Technical Report. Sweden: The Swedish National Railway Authority.
16. BANVERKET. (2000). Dynamic soil-track interaction and ground borne vibration. Technical Report. Sweden: The Swedish National Railway Authority.
17. Adolfsson, K., Andreasson, B., Bengtson, P.E., et al. (1999). High speed lines on soft ground-evaluation and analysis of measurements from the west coast line. Technical Report. Banverket, Sweden.
18. Takemiya, H. (2003). Simulation of track–ground vibrations due to a high-speed train: the case of X-2000 at Ledsgard. Journal of Sound and Vibration, 261(3): 503–526.
19. Gao, G.Y., Li, S.Y. (2015). Dynamic response of CFG pile composite subgrade induced by moving train loadings. Journal of Vibration and Shock, 34(24): 274–278 (in Chinese).
20. Ba, Z.N., Liang, J.W., Jin, W. (2014). Dynamic responses of layered ground-track coupled system under the moving loads from high-speed train. China Civil Engineering Journal, 47(11): 108–119 (in Chinese).
21. Bian, X.C., Chen, Y.M. (2016). Ground vibration generated by train moving loadings using 2.5D Finite Element, Method. Chinese Journal of Rock Mechanics and Engineering, 25(11): 2335–2342 (in Chinese).
22. Zhai, W.M., He, Z., Song, X. (2010). Prediction of high-speed train induced ground vibration based on train-track-ground system model. Earthquake Engineering and Engineering Vibration, 9(4): 545–554.
23. Zhai, W.M., Wang, S., Zhang, N., et al. (2013). High-speed train-track-bridge dynamic interactions Part II: experimental validation and engineering application. International Journal of Rail Transportation, 1(1–2): 25–41.
24. Zhai, W.M., Liu, P., Lin, J., et al. (2015). Experimental investigation on vibration behaviour of a CRH train at speed of 350 km/h. International Journal of Rail Transportation, 3(1): 1–16.
25. Zhai, W.M., Wei, K., Song, X., et al. (2015). Experimental investigation into ground vibrations induced by very high speed trains on a non-ballasted track. Soil Dynamics and Earthquake Engineering, 72: 24–36.
26. Feng, Q.S., Cheng, G., Lei, X.Y., et al. (2015). Influences of ballasted track and slab ballastless track structures on ground vibration of high speed railway. Journal of Vibration and Shock, 34(24): 153–159.
27. Ma, C.S., Xiao, H., Gao, L. (2015). Experimental study on mechanical characteristics of elastic sleeper ballast track on high-speed railways. China Civil Engineering Journal, 48(S2): 81–87 (in Chinese).
28. Zhai, W.M., Zhao, C.F. (2016). Frontiers and challenges of sciences and technologies in modern railway engineering. Journal of Southwest Jiaotong University, 51(2): 209–226 (in Chinese).
29. Gao, G.Y., Li, Z.Y., Feng, S.J., et al. (2007). Experimental results and numerical predictions of ground vibration induced by high-speed train running on Qin-Shen Railway. Rock and Soil Mechanics, 28(09): 1817–1822 + 1827 (in Chinese).
30. Chen, G.Q. (2015). Ground vibration analysis induced by high-speed train based on in-situ data. Chinese Journal of Rock Mechanics and Engineering, 34(03): 601–611 (in Chinese).
31. Gao, G., Song, J., Chen, G., et al. (2015). Numerical prediction of ground vibrations induced by high-speed trains including wheel-rail-soil coupled effects. Soil Dynamics and Earthquake Engineering, 77: 274–278.
32. Chang, J.F. (2002). The main technical standard and design for subgrade of Qin-Shen dedicated passenger railway. Subgrade Engineering, (05): 6–12 (in Chinese).
33. Gao, G.Y., Song, J., Yang, J. (2014). Identifying boundary between near field and far field in ground vibration caused by surface loading. Journal of Central South University, 21(8): 3284–3294.

Micro-analysis of Ballast Angularity Breakage and Evolution by Monotonic Triaxial Tests

Guixian Liu, Guoqing Jing, Dong Ding and Xiaoyi Shi

Introduction

Ballasted track commonly used in rail transportation considering speed and cost of construction and adaptability in all conditions. However, ballast bed needs periodic maintenance because of deformation and degradation in terms of degradation and ballast fouling, which costs a lot of money and track occupation [1]. Recent results indicated that ballast degradation involves in ballast breakage and wear, the former results from contact force exceed the aggregates strength, while the latter is universal effects of inter-particle interactions, due to the angularity is easily damaged [2, 3]. It should be noted that the ballast aggregates fracture of angularity occurs even during the initial stage of service [1]. Chrismer and Selig [2, 3] concluded that angularity reduction and abrasion results in degradation, which is the primary cause of contamination, and results in fines up to 70% of fouled materials. Too much angularity breakage and fines accumulation prevents ballast from fulfilling its functions. Firstly, drainage characteristics may be severely weakened in some fouled tracks. Secondly, resilient modulus is modified due to angularity reduction and fines fill in. Lastly, the shear strength or the sleeper resistance is consequently

G. Liu · G. Jing (✉) · D. Ding
School of Civil Engineering, Beijing Jiaotong University,
Beijing 100044, People's Republic of China
e-mail: gqjing@bjtu.edu.cn

G. Liu
e-mail: guixian.liu@etu.unistra.fr

D. Ding
e-mail: 347270686@qq.com

X. Shi
Suzhou Rail Transit Group Co., Ltd., Suzhou 215000, People's Republic of China
e-mail: cexwye@zju.edu.cn

reduced as ballast aggregates become less angular, where rounded ballast aggregates result in less interlock and friction ability with sleeper and ballast aggregates. Hence, study for ballast aggregates angularity evolution under various confinements is increasingly pressing and important for ballast bed management.

Triaxial test is commonly conducted as an effective method to study the mechanical properties of ballast [1, 4–8]. In the study of Indaratna [4], monotonic triaxial test simulations using breakable and unbreakable assemblies were carried out under a range of confining pressures (15–240 kPa). In his research, a numerical model of ballast was built using DEM in 3 dimensions, which was unbreakable regular tetrahedron attached with small spheres that could break apart to model angularity reduction, where the influence of particle size distribution is ignored.

It should be noted that, the breakage in condition of multi-direction stressing is a complicated mechanism that usually starts at the contacts of adjacent particles (i.e. breakage of asperities and sharp angle) [9]. Lees and Kennedy [10] concluded that the breakage and degradation of granular materials may occur in three ways: (a) the breakage of angular corners or projections, (b) the grinding or attrition of asperities, and (c) the splitting of particles into two or more approximately equal parts. Therefore, breakage mainly occurs in manner of sharp-angle breakage and abrasion, which provides a key micromechanical explanation for the deformation and change of ballast strength. Here for simplification, the ballast angularity reduction is the topic of the paper investigation, and the breakage of sharp angle was mainly concerned. Ballast triaxial test was performed under different confining pressure and it was further investigated in DEM for micro-analysis. The loss and evolution of angularity under monotonic loading was recorded and analyzed. The numerical model of ballast was built with a center sphere and some small attaching spheres to model the sharp angle breakage of ballast. The monotonic loading was applied because the particle breakage taking place under static loading as the preliminary modeling step of repeated loading would improve insight into and understanding of the behavior of ballast under complex cyclic loading [9, 11].

Material and Method

Triaxial Test

In the laboratory test, the cylindrical ballast samples were made for monotonic triaxial test with size of 450 mm in height and 300 mm in diameter, corresponding to an aspect ratio of H/D = 1.5. The aspect ratio of 1.5 enabled an easier and more economical design of the cells [12]. In this paper, D/dmax ratio was 6, where D is specimen diameter and dmax is maximum particle size. According to Skoglund [13], the typical value of D/dmax ratio is 5–7 to ensure that there are enough particles across the diameter to give a sufficiently representative sample. The samples were wrapped with rubber membrane. After sample preparation, the

sample was fitted in the inner and outer cells with the selected cell pressure and a seating load of 1kN. Series of monotonic triaxial tests were carried out, with the confining pressure of 10, 30 and 60 kPa. After the instrumentation installation, the sample was then loaded at 1 mm/min. All these tests were continued up to axial strains of 12%. During loading, the data of stress and strain was recorded for analysis. The triaxial apparatus is shown in Fig. 1.

Modelling Method

In this paper, laboratory tests were further investigated by PFC3D, which is a discrete element program that can be used to model ballast aggregates abrasion and breakage [2]. In simulation, a cylindrical wall was built for confining pressure and two plane walls were built at the top and bottom for axial pressure. The coefficient of friction for the walls was set to 0.5 following Lim and McDowell [4, 14, 15]. In the simulation, the normal and shear stiffness of the balls were 1e9 N/m and the density of the particles was 2600 kg/m [3, 4].

Two bonding models are supported in PFC3D: contact-bond model and parallel-bond model [18]. Parallel-bond was chosen for the inner contact of the clusters, considering the difference in failing mode between these two bonding models and way of ballast breakage. Parameters for Parallel-bond were set referring
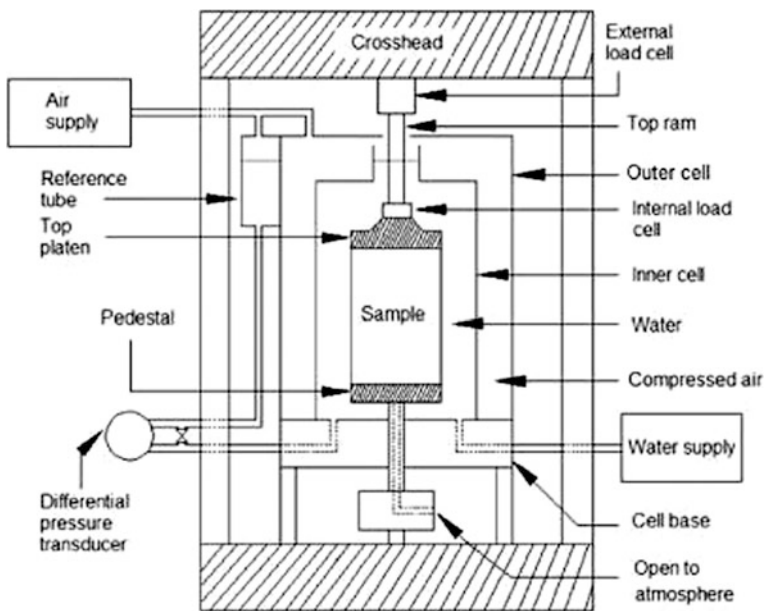
Fig. 1 Stress-controlled large scale ballast triaxial apparatus

to Indraratna and McDowell [14–18] and fine adjusted based on the test results. More details of parameters are listed in Tables 1 and 2. It should be noted that the stiffness of cylinder walls was set to 1/10 of that of balls to simulate the flexible rubber membrane.

A new modeling method was developed in order to simulate the angularity breakage, and the clusters were created to model ballast which can break apart if they are subjected to forces large enough. Firstly, the center sphere was created, then the attaching spheres externally tangent with the center sphere were randomly created to represent the sharp corner and asperity. Taking center of sphere as original point, points of tangency were along 14 vectors including $(\pm1,0,0)$, $(0, \pm1,0)$, $(0,0,\pm1)$ and $(\pm1, \pm1, \pm1)$. Visual detail for points of tangency is showed in Fig. 2. Based on the statistic data in tests, the ratio of radius between center sphere and attaching spheres are stochastic ranging from 3:1 to 7:1 to model real shape of ballast. The numerical models for ballast particle individual are shown in Fig. 3.

The assemblies were generated using the dynamic method as McDowell described [4]. An assembly of spheres was generated without overlapping with half their final diameter which was related to the particle size distribution of ballast

Table 1 Basic parameters for balls and walls

	Normal stiffness (N/m)	Shear stiffness (N/m)	Friction
Cylinder wall	1×10^8	1×10^8	0.5
Top and bottom walls	1×10^9	1×10^9	0.5
Ball	1×10^9	1×10^9	0.5

Table 2 Parallel-bond between balls inside of cluster

Normal stiffness (N/m^2)	Shear stiffness (N/m^2)	Normal strength (N/m^3)	Shear strength (N/m^3)	Radius multiplier
1×10^{12}	1×10^{12}	1×10^7	1×10^7	2
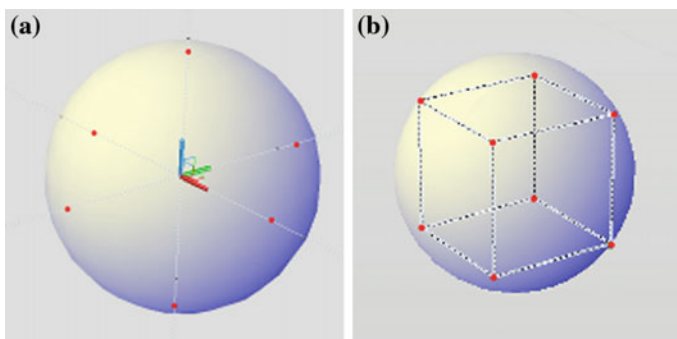
Fig. 2 Contact point of attaching sphere presented by *red points*. **a** 6 spheres attaching on the center sphere; **b** 8 spheres attaching on the center sphere
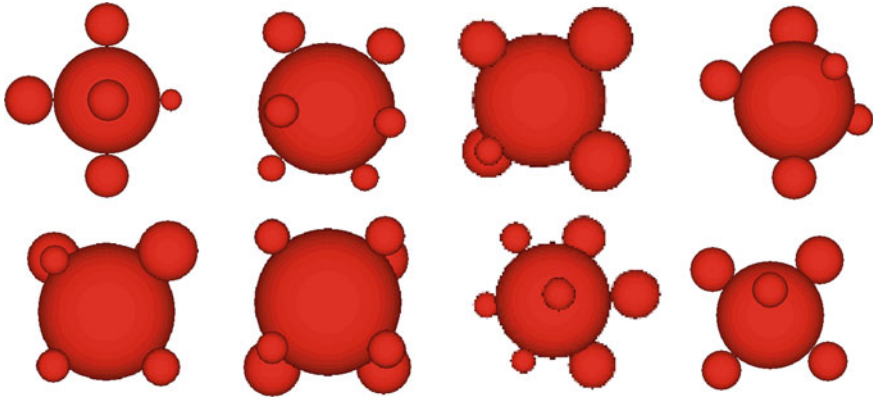
Fig. 3 Two patterns of clusters with 6 or 8 attaching balls

using by laboratory test. The particle size distribution of ballast is shown in Fig. 4. The spheres were then exaggerated to their final size and the system was cycled to equilibrium with the locations of walls remaining fixed. The system was cycled to final equilibrium before they are subjected to confining and suppressing. Steady-state solution was detected when either the maximum or the average unbalanced-force ratio reached 0.01 [18]. Numerical model for triaxial test is shown in Fig. 4. Particle size distribution of the laboratory test and simulation is shown in Fig. 5.
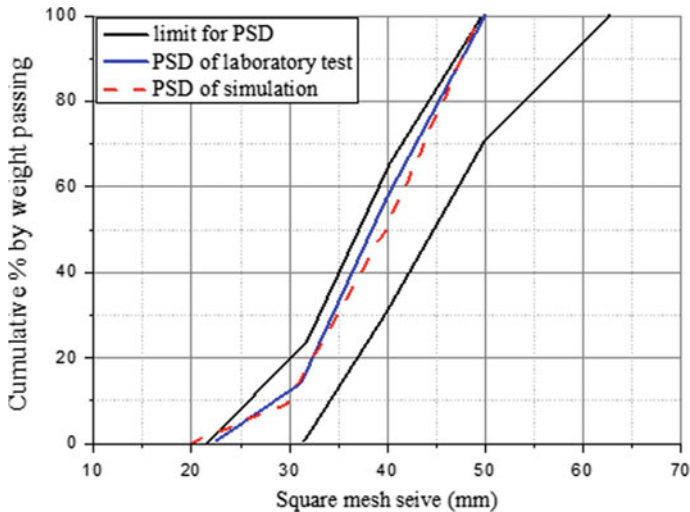
Fig. 4 Particle size distribution (PSD) for laboratory and simulation

Fig. 5 Numerical model for triaxial test

After the specimen generate procedure was completed, compression was applied to achieve the required stress state. A servo-control was applied to all the walls [4, 18, 19]. The servo-control system was designed to be invoked in every time-step so that the velocity of cylindrical wall displacement can be control and adapted to a proper value to ensure a constant confining pressure. The model was compressed until the axial strain reached 12%.

Results and Discussion

In this paper, different data was recorded for deformation and breakage analysis both in laboratory test and simulation. Simulations were performed for laboratory tests with confining pressure of 10, 30 and 60 kPa. During the loading, the required data (e.g. axial strain, volume strain, deviator stress, breakage number and breakage location et al.) were measured and recorded. The results of laboratory test and simulation are compared and analyzed in the following.

The variation of deviator stress versus the axial strain of ballast under monotonic triaxial loading and the numerical method is shown in Fig. 6. It can be seen from Fig. 6 that the deviator stress increases as confining pressure increases both in test
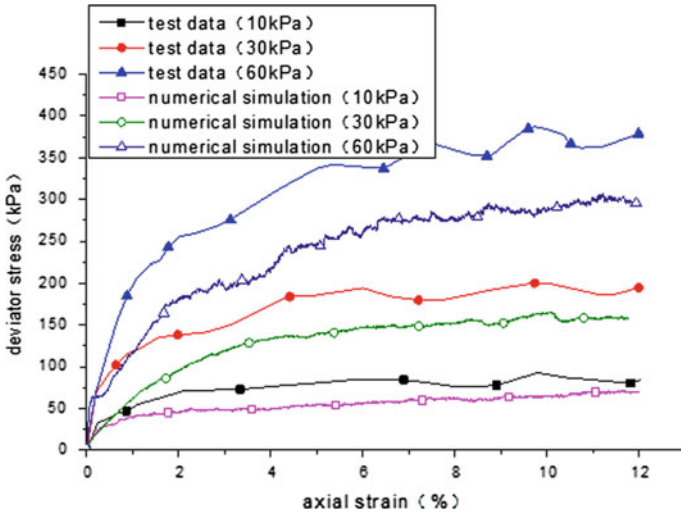
Fig. 6 Deviator stress versus axial strain

and numerical method. The value of deviator stress eventually reaches peak which can be regarded as failure for ballast samples.

The value of peak deviator stress at different confining pressures for both laboratory tests and numerical method are shown in Fig. 7. Obviously, higher confining pressure leads to higher deviator stress and it can be described as an approximate linear relation between two items.
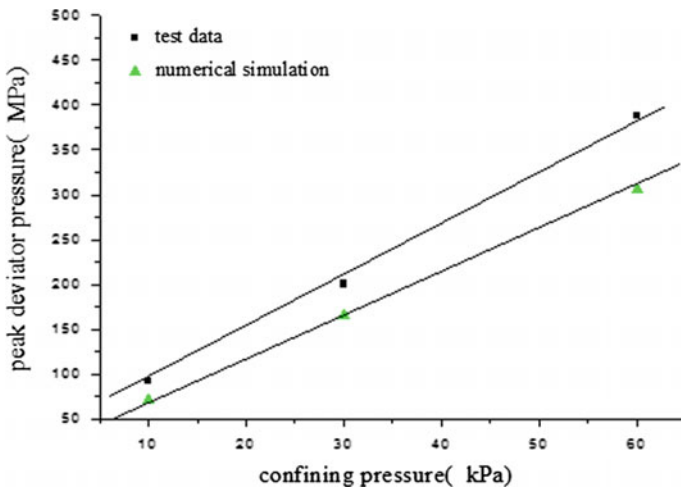
Fig. 7 Peak deviator stress versus confining pressure

The variations of volumetric strain with the axial strain of ballast are shown in Fig. 8. It shows that the volume of the ballast sample decreases firstly (compression, represented by positive volumetric strain). After short-term compression, the volumetric strain shifted towards dilation. The largest dilation occurs in the test with 5 kPa confining pressure. Meanwhile, the dilation angle, which demonstrates material shearing strength, could be calculated from the volume change behavior of ballast under monotonic loading which is gained from the slope of the expansive portion of volumetric strain versus axial strain increase. Dilation angle reveals the material shearing behavior. The calculation method is described in Eq. (1).

$$\psi = \frac{d\varepsilon_v}{d\varepsilon_a} \tag{1}$$

Dilation angle in numerical method is close to that in laboratory test. The average dilation angle gained in laboratory tests is 33°, while that in numerical simulation is 36.7°. The dilation angle is slightly larger under lower confining pressure for both laboratory tests and numerical method as shown in Fig. 8.

Ballast samples were sieved again to calculate the amount of particle breakage after each test. In the simulations, the mass and number of small spheres broke from the center body spheres were also calculated shown in Table 3.

Figure 9 shows the mass of particles smaller than 22.4 mm in tests and simulation. Results show that the mass of broken angularity in laboratory test and
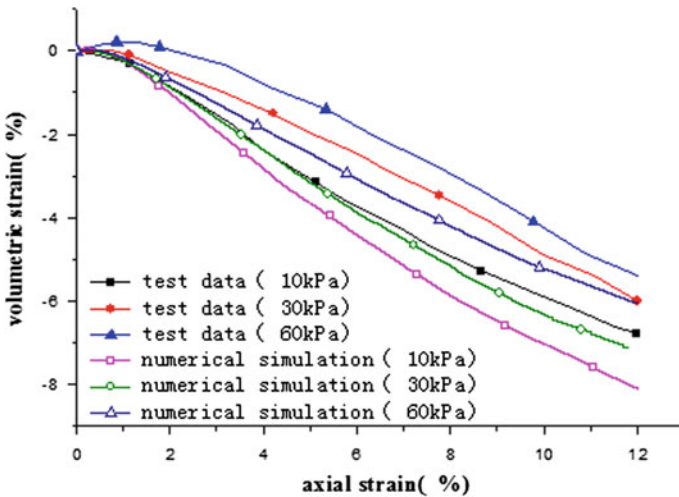
Fig. 8 Volumetric strain versus axial strain

Table 3 Number of breakage in numerical method

Radius (m)	Axial strain (%)			
	2	4	8	12
0.0016	368	1904	4208	5872
0.0025	16	192	464	688
0.003	6	27	41	43
0.007	5	9	14	17
0.01	3	6	8	9
0.01125	0	0	1	5

Confining pressure: 30 kPa
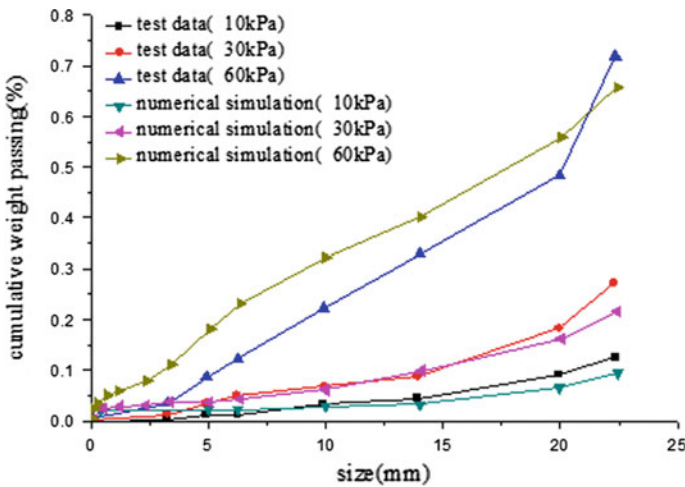
Fig. 9 Particles smaller than 22.4 mm from the monotonic triaxial tests and simulation

numerical simulation is consistent. An obvious increase of angularity breakage can be seen with increasing confining pressure, and results agreed with Key and Indraratna et al. [19, 20].

In this paper, distribution of particles breakage location was recorded in simulation as well. Figure 10 shows the breakage distribution with different axial strains for 30 kPa confining pressure. It reflects that breakage firstly occurred near the bottom and top planes, maybe due to more relative displacements occurred in these regions. Then particles break in a moderate velocity and eventually distributes within the model overall.

| Strain: 2% | Strain: 4% | Strain: 8% | Strain: 12% |
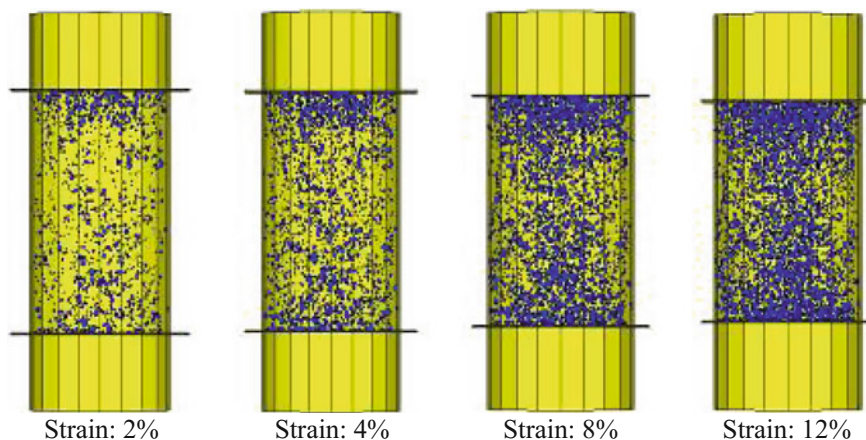
Fig. 10 Distribution of breakage particles location

Conclusion

Ballast triaxial test under different confining pressure has been performed and ballast breakage and deformation are studied. A new modeling method in DEM with a center ball and some attaching balls was developed to simulated ballast breakage especially for sharp-angle breakage and abrasion. Both the stress-strain behavior and volumetric response under different confining pressures could be achieved effectively using breakable assemblies. The results indicate that numerical method can well agree with laboratory test in terms of stress, strain and breakage. The conclusions are listed as follows:

1. The simplified cluster for ballast particle individual is reliable to model triaxial test. The results are in accordance with laboratory tests and effective in terms of the breakage, stress and strain characteristics. The parameters applied for the model is suitable for numerical method, which is helpful for cyclic triaxial tests.
2. Confining pressure plays a significant role for ballast breakage. As the confining pressure increases, more angularity corners break from ballast main body. Ballast breakage will produce small particles which lead to void clogging with fines and ballast fouling happens subsequently.
3. The deviator stress increased initially and remained stable eventually, as the confining pressure increases in monotonic triaxial tests. Short-term compression firstly occurred and soon after that, the volumetric strain shifted towards dilation. The dilation angle is slightly larger under lower confining pressure for both laboratory tests and numerical method. Higher dilation was observed with low confining pressure both in laboratory test and numerical method.

4. In simulations, it can be observed that the breakage firstly happened near the top and bottom plane wall as more displacement and interaction between clusters occurred at this zone.

It should be noted that monotonic triaxial tests act as basic foundation for cyclic triaxial test. Subsequent work is to investigate ballast aggregates angularity evolution in cyclic triaxial test, as well as modulus of resilience and permanent deformation.

References

1. Indraratna, B., Nimbalkar, S., Christie, D. (2009). The performance of rail track incorporating the effects of ballast breakage, confining pressure and geosynthetic reinforcement. 8th International Conference on the Bearing Capacity of Roads, Railways, and Airfields, London, pp. 5–24.
2. Chrismer, S. M., Read, D. M. (1994). Examining ballast and subgrade conditions. Railway Track and Structure, AREA, pp. 39–42.
3. Selig, E. T, Waters, J. M. (1994). Track geotechnology and substructure management. London. Thomas Telford, pp. 54–55.
4. Lu, M., McDowell, G. R. (2010). Discrete element modelling of railway ballast under monotonic and cyclic triaxial loading. Géotechnique, 60(6): pp. 459–467.
5. Indraratna, B, Salim, W. (2002). Modelling of particle breakage of coarse aggregates incorporating strength and dilatancy. Proc Instn Civ Engrs Geotech Engng, 155, pp. 243–252.
6. Huang, H., Tutumluer, E. (2011). Discrete element modeling for fouled railroad ballast. Construction and Building Materials, 25(8): pp. 3306–3312.
7. Shenton, M. J. (1975). Deformation of railway ballast under repeated loading conditions. Kerr A. D. Railroad track mechanics and technology, USA, Pergamon Press, pp. 387–404.
8. Raymond, G. P, Bathurst, R. J. (1994). Repeated-load response of aggregates in relation to track quality index. Canadian geotechnical journal, 31(4): 547–554.
9. Indraratna, B., Salim, W. (2002). Modelling of particle breakage of coarse aggregates incorporating strength and dilatancy.
10. Lees, G., Kennedy, C. K., (1975). Quality, Shape and Degradation of Aggregates. Journal of Engineering Geology, 8, pp. 193–209.
11. McDowell, G. R., de Bono, J. P. (2013). On the micro mechanics of one-dimensional normal compression. Géotechnique, 63(11): pp. 895–908.
12. Aursudkij, B. (2007). A laboratory study of railway ballast behaviour under traffic loading and tamping maintenance. PhD diss., University of Nottingham.
13. Skoglund, K. A. (2002). A study of some factors in mechanics railway track design. PhD Dissertation, Norwegian University of Science of Technology.
14. Lu, M., McDowell, G. R. (2006). Discrete element modelling of ballast abrasion. Géotechnique, 56(9): pp. 651–655.
15. Lim, W. L., McDowell, G. R. (2005). Discrete element modelling of railway ballast. Granular Matter, 7(1): pp. 19–29.
16. Indraratna, B, Ngo, N. T., Rujikiatkamjorn, C. (2012). Deformation of Coal Fouled Ballast Stabilized with Geogrid under Cyclic Load. Journal of Geotechnical and Geoenvironmental Engineering, 139(8): pp. 1275–1289.

17. Indraratna, B, Nimbalkar, S. S., Rujikiatkamjorn C. (2014). Enhancement of rail track performance through utilisation of geosynthetic inclusions. Geotechnical Engineering Journal, 45 (1): pp. 17–27.
18. PFC3D Users' Manual (version4.0). Minnesota: Itasca Consulting Group Inc. September, 2008.
19. Key, A. (1998). Behaviour of two layer railway track ballast under cyclic and monotonic loading. PhD Dissertation, University of Sheffield.
20. Indraratna, B., Ionescu, D., Christie, H. D. (1998). Shear Behaviour of Railway Ballast Based on Large-scale Triaxial Tests. Journal of Geotechnical and Geoenviromental Engineering, 124 (5): pp. 439–449.

Shaking Table Experiment on Soil-Micropile Interaction of Semi-integral Abutment Bridge

Haimin Qian, Yizhou Zhuang and Yun Chen

Introduction

In recent two decades, soil-pile interaction problems have been paid a lot attention [1, 2], because of the significant influences on dynamic response of the superstructure. Soil-pile interaction is a special issue in soil-structure interaction problems, which is also can be divided into three parts when analyzing [3]: (1) site response analysis (free field response analysis), (2) "Kinematic" analysis, (3) "Inertial" analysis. Enormous shaking table experiments have been conducted to investigate the dynamic responses of superstructure and the pile foundation, in which laminar soil containers were employed most frequently [4, 5], even the laminar container is expensive to manufacture. However, the biggest advantage of using laminar container most researchers thought is the effective elimination of seismic wave reflection, which is the key point of conducting soil-pile interaction shaking table experiment [6–8]. But so far, there is no unified conclusion on which is the best soil container for shaking table test.

A new type of semi-integral abutment bridge was presented in this paper, which is shown in Fig. 1. In this case, a row of micropiles are additional comments in the bridge. Because of the micropiles, however, there will be strong interaction between the micropiles and soil under seismic excitation.

H. Qian · Y. Zhuang (✉) · Y. Chen
College of Civil Engineering, Fuzhou University, Fuzhouzhou 350116, China
e-mail: 478372092@qq.com

H. Qian
e-mail: 350635311@qq.com

Y. Chen
e-mail: 314650842@qq.com
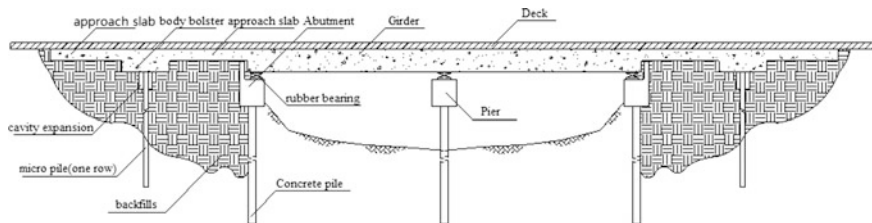
Fig. 1 Semi-integral abutment bridge using micro piles

p-y curve method [9, 10] and nonlinear Winkler beam method [11] are employed to analyze the soil-pile interaction frequently in the past 10 years. In dynamic analysis, however, *p-y* curve method cannot give an accurate result [6, 12]. Therefore, some researchers presented the opinion of studying dynamic *p-y* curves [13]. To study soil-micropile interaction, dynamic response and dynamic *p-y* curves, shaking table tests are conducted.

Shaking Table Test on Soil-Micropile Interaction

Soil and Soil Container

Min River sand are employed, via particle grade tests, it shows the sand has a good uniformity and the non-uniformity coefficient is 3.17 (C_u = 3.17 < 5). In addition, d_{60} and d_{10} are 0.57 mm and 0.18 mm, respectively I (see Fig. 2). Geotechnical test shows the Min River sand has a density of 1.712 g/cm^3, internal friction angle of 34°, relative denseness of 43%, void ratio of 0.663 and moisture content of 2.1% (see Table 1).

Fig. 2 Particle size distribution curve of Min River sand
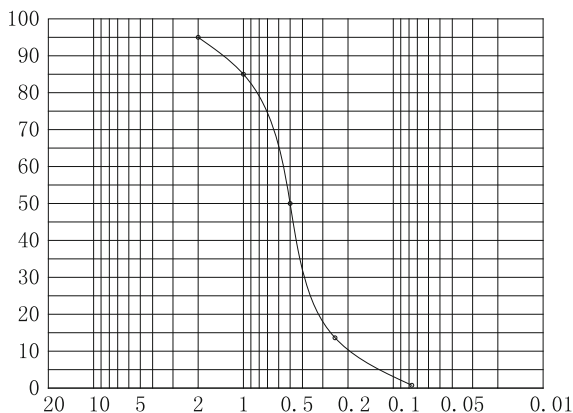
Table 1 Physical parameters of Min River sand

ρ (g/m^3)	ω (%)	D_r (%)	Φ	E
1.712	2.1	43	33	0.663

Model Pile

Steel pipe piles are employed in shaking table test, which has 2.3 m length, 5.4 cm inner diameter and 6 cm outer diameter. In test, the length of pile above the soil is 0.4 m. Additional parameters, elastic module, Poissons' ratio and flexural stiffness are shown in Table 2. In addition, the model pile is welded with bottom of the soil container.

Boundary Condition

Rigid steel box with 10 cm foam both side of box wall in loading direction and in size of 2 m × 2 m × 2.1 m (length × width × height) are employed (see Fig. 3), considering experiment cost. The soft material, foam, is used to reduce energy reflection and stress wave reflection. Compared with laminar shear box, the

Table 2 Parameters of piles

Material	Inner diameter (cm)	Outer diameter (cm)	Elastic module (GPa)	Poissons' ratio	Flexural stiffness (kN m^2)
Steel	5.4	6	207	0.3	45.3

Fig. 3 Inner view of soil container

foam

mechanism of reducing energy reflection of rigid box with soft material is different. However, rigid box with soft flexible boundary (soft material) has a good simulation result [14].

Measurements and Loading Cases

Along the pile, strain gages are installed on both side of the pile with an equal spacing of 10 cm, totally 38 strain gages on each model pile. In the direction of loading, 3 accelerometers are set in the embedded depth of 0.35, 0.95 and 1.55 m.

Sinusoidal waves of various frequencies are applied in shaking table tests. Besides the excitation frequency, the influence of mass at pile head and peak acceleration are also investigated (Fig. 4; Table 3).

Fig. 4 Setup of shaking table test on soil-micropile interaction

Table 3 Loading cases

Case	Frequency (Hz)	Mass at pile head (kg)	Peak acceleration (g)	Wave type
1	2\8\15	60/120/180	0.05\0.1\0.2\0.3\0.4	Sine wave
2	1\2\5\8\9\10\15\20\25	60	0.4	Sine wave
3		60	0.05\0.1\0.2\0.3\0.4	El-centro

Experimental Results

Natural Frequency of Soil-Pile System

Via white noise excitation, results shows that the natural frequency of soil-pile system is 8.38 Hz (see Fig. 5).

Acceleration Amplification Coefficient

Figures 6, 7 and 8 show the acceleration versus time data under 2, 8 and 15 Hz of 0.1 g sinusoidal wave, and curve of acceleration amplification coefficient is shown in Fig. 9.

From Figs. 6, 7 and 8, it shows that acceleration of table-board are 0.104, 0.113 and 1.08 g under 0.1 g sine waves, which is very close to 0.1 g. Peak accelerations of 1.55 m embedded depth is lowest, and even smaller than that of table-board, which illustrate dynamic response of this layer is weak. Peak accelerations of 0.95 m embedded depth is largest, which illustrates soil response of middle depth layer is significant and strong soil-pile interaction may happen in this layer.

Figure 9 shows the curves of acceleration amplification coefficient under 2, 8 and 15 Hz of 0.1 g sine waves. It is obvious that acceleration response of pile head under 8 Hz sine wave is the most significant, because natural frequency of soil-pile system is very close to that of excitation.

Fig. 5 Spectrum of soil-pile system
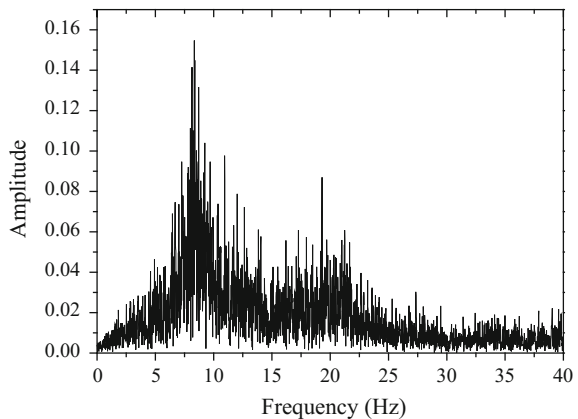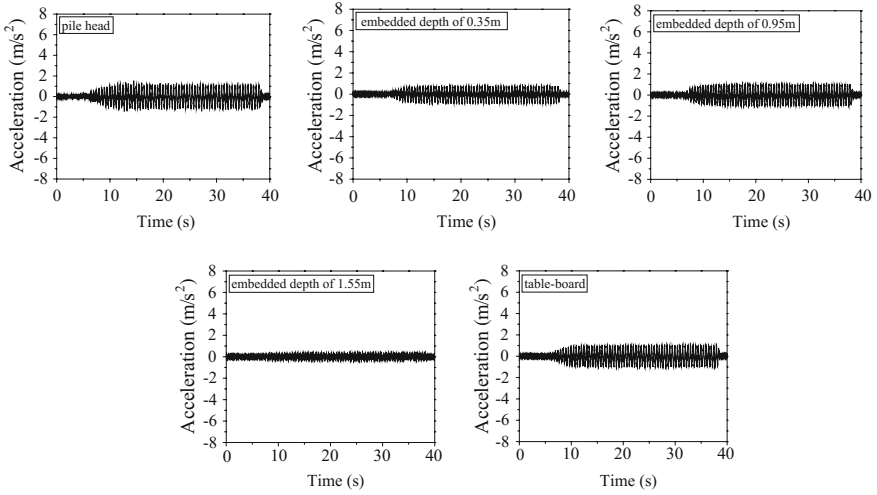
Fig. 6 Accelerations under 2 Hz of 0.1 g sinusoidal wave
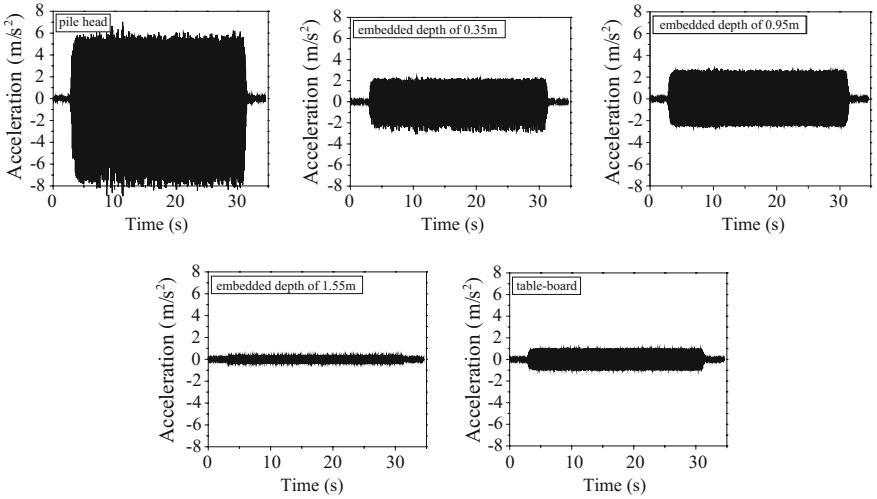
Fig. 7 Accelerations under 8 Hz of 0.1 g sinusoidal wave

Response of Displacement and Bending Moment

Figures 10 and 11 show the displacement and maximal bending moment response of model pile, it shows that under 1, 2 and 5 Hz sine waves, displacement of pile reach maximum at the pile head, while displacement below pile head decrease gradually and reach almost zero near pile bottom. Under 8, 9 and 10 Hz sine waves,
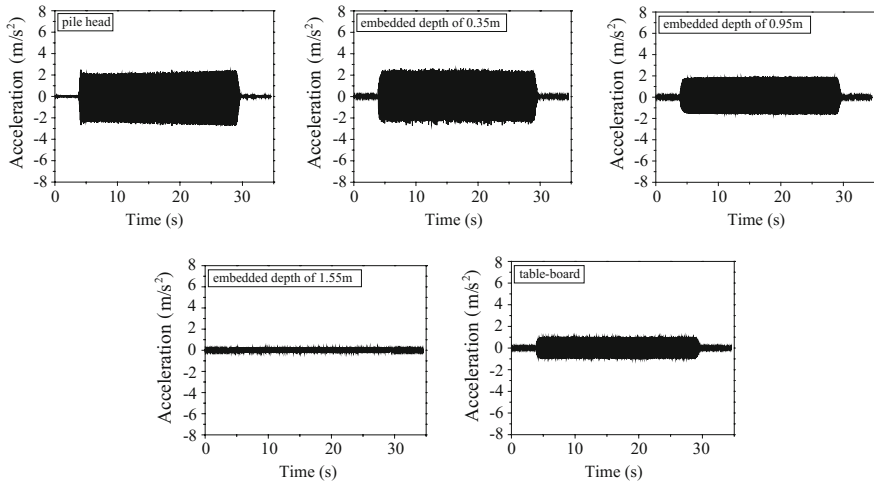
Fig. 8 Accelerations under 15 Hz of 0.1 g sinusoidal wave

Fig. 9 Curves of acceleration amplification coefficient
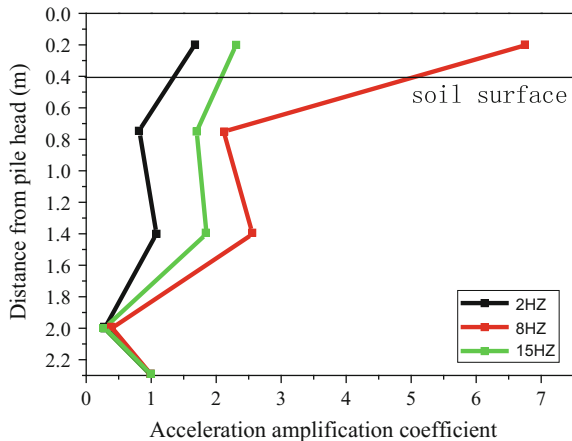
displacement of pile reach maximum at the pile head, however, inverse displacement occurs, which is about tenth of maximal displacement at pile head. Under 15, 20 and 25 Hz sine waves, displacement of pile reach maximum at about 60 cm embedded depth, which illustrates the higher mode shape of pile is excited.

Location of maximal bending moment is a key point in dynamic analysis of pile foundation, which is also a direct reference for engineers. Figure 11 shows that under low frequency excitation (frequency under natural frequency, such as 1, 2 and 5 Hz), maximal positive moment is at the embedded depth of 3.3 times pile diameter (20 cm) and bending moment at the embedded depth of 170 cm (28.3D, 28.3 times diameter) is also large. While, maximal negative bending moment is at
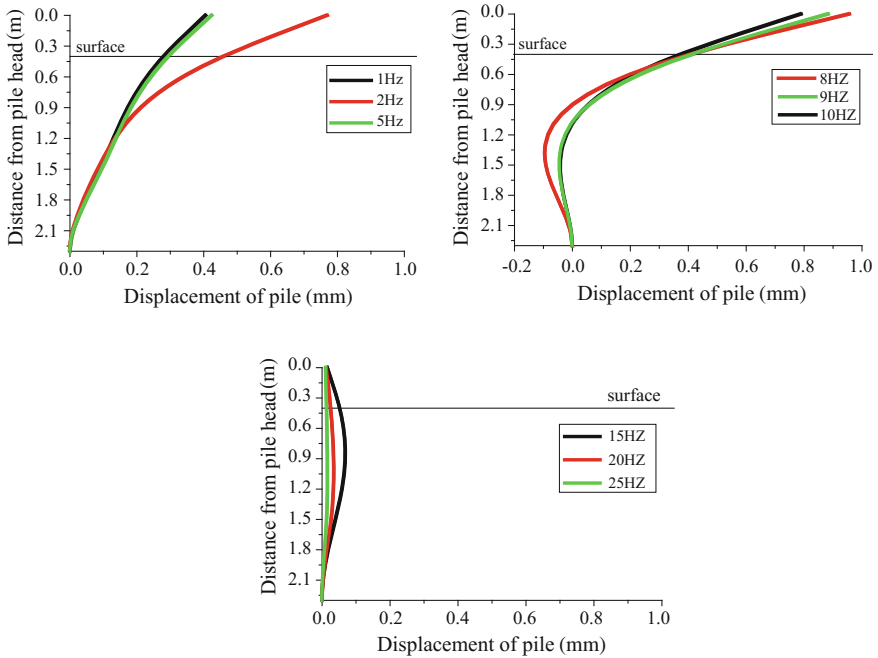
Fig. 10 Displacement of pile

the embedded depth of 18.1 times pile diameter (about 110 cm). When the frequency of excitation is close to natural frequency of soil-pile system, maximal positive moment is at the embedded depth of 3.3 times pile diameter (20 cm), which is same as the bending moment response under low frequency excitation. However, the maximal negative bending moment is at the embedded depth of 28.3 times pile diameter (near pile bottom). Moreover, the absolute value of maximal positive bending moment is much larger than that of maximal negative bending moment.

When the frequency of excitation reach 15, 20 Hz and 25 (higher than natural frequency), positive moment is not large, which is much smaller than negative moment which is at the embedded depth of 28.3D (170 cm).

Dynamic p-y Skeleton Curve

Based on Hyperbolic Function for *p-y* skeleton curve presented by Kondner [15], skeleton curves of 30, 50 and 70 cm embedded depth is presented. The function is shown as follow
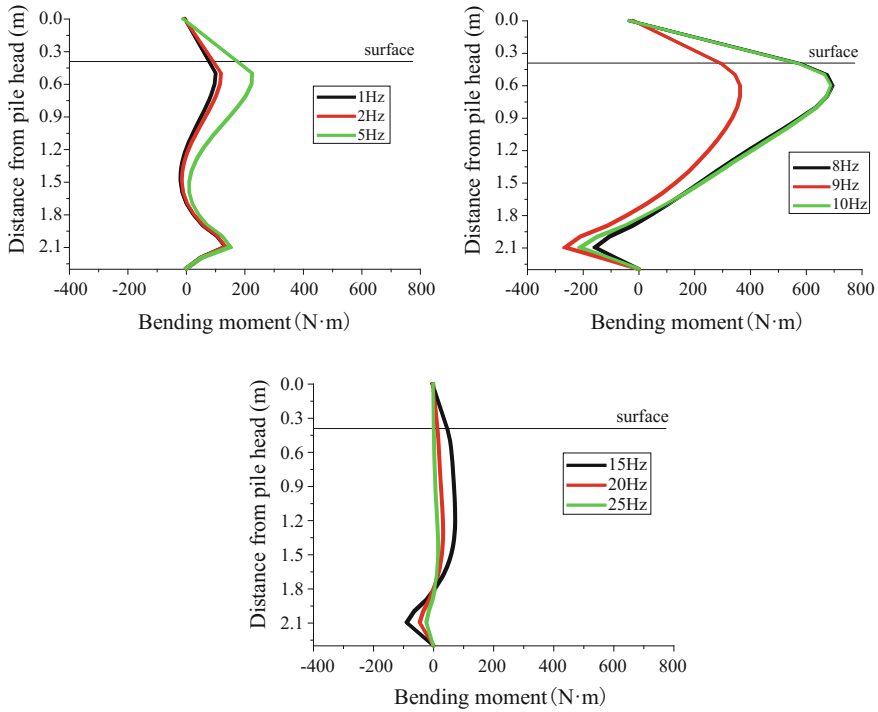
Fig. 11 Bending moment of pile

$$p = \frac{y}{\frac{1}{k_{ini}} + \frac{y}{p_u}} \tag{1}$$

where p = soil pressure, k_{ini} = initial subgrade modulus, y = lateral displacement of pile, and p_u = ultimate soil resistance.

Calculation of initial subgrade modulus is based on the following equations [16]

$$K = AP_a \left(\frac{\delta}{P_a}\right)^{0.5} \tag{2}$$

$$\frac{P}{0.01D} = \frac{1}{\frac{1}{k_{ini}} + \frac{0.01D}{p_u}} = K \tag{3}$$

$$\delta = \frac{\mu}{1 - \mu} \gamma z \tag{4}$$

where A = fitting constant, P_a = the standard atmospheric pressure, δ = lateral gravity stress, K = subgrade modulus, γ = soil weight, D = pile diameter, and μ = Poisson's ratio.

Based on the strain data, model pile was not in nonlinearity, therefore, displacement of pile can be calculated from the strain data using theory of elasticity. Soil pressure, p, can be calculated by using central difference method on time history curve of bending moment. Figure 12 shows the p-y curves of 30 cm embedded depth under various peak acceleration sine waves.

Figures 13, 14 and 15 are p-y skeleton curves at 30, 50 and 70 cm embedded depth respectively, based on Eqs. (1)–(4).

From Figs. 16, 17 and 18, it illustrates that dynamic p-y skeleton curves are much different from that provided by API and Reese which is widely used in static analysis. When the soil-micropile system is excited by dynamic load, soil stiffness and soil shear strength performs much larger, because of the kinematic effect, which is the most important point different from the static analysis. Dynamic p-y skeleton curves presented in this paper may give a reference for engineer.
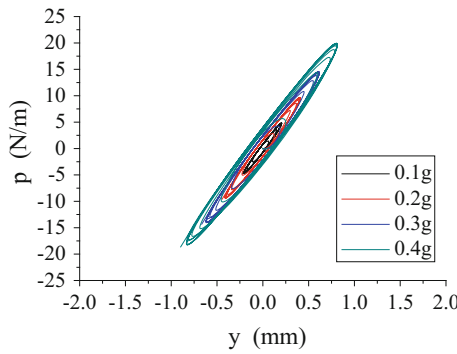
Fig. 12 p-y curves under various peak acceleration at 30 cm embedded depth
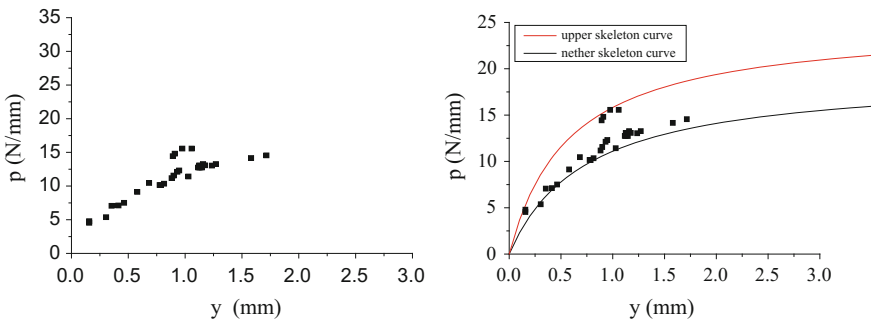
Fig. 13 p-y skeleton curves at 30 cm embedded depth
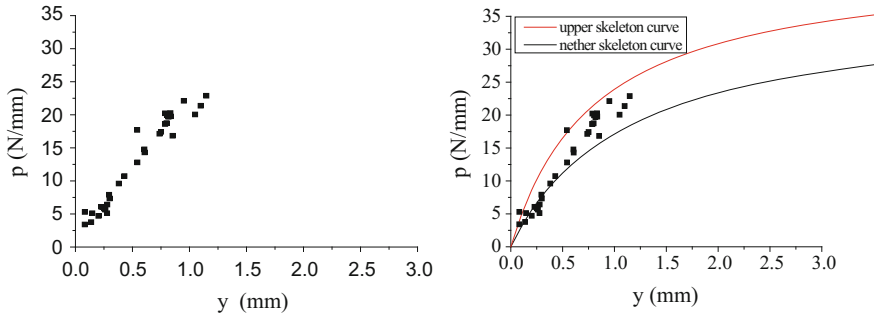
Fig. 14 p-y skeleton curves at 50 cm embedded depth
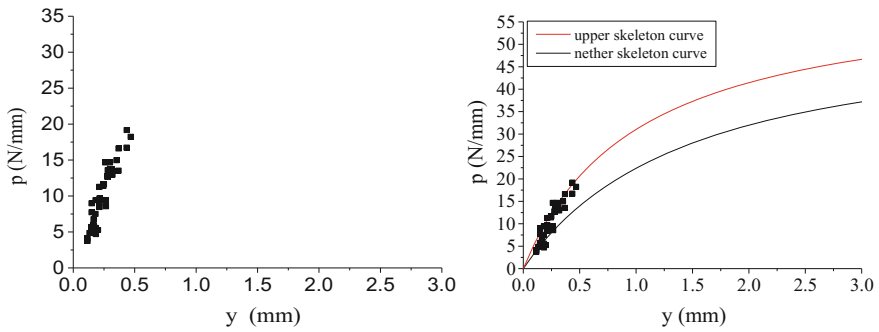
Fig. 15 p-y skeleton curves at 70 cm embedded depth

Fig. 16 comparison of p-y curves at 30 cm embedded depth
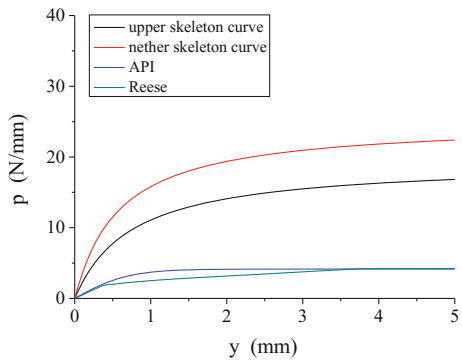
Fig. 17 comparison of p-y
curves at 50 cm embedded
depth
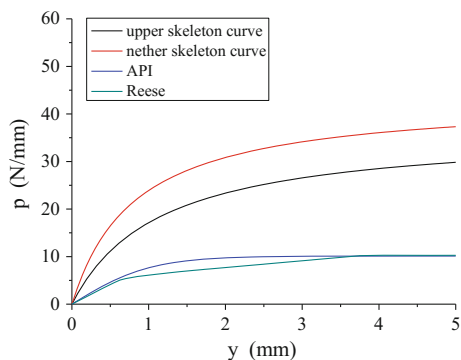
Fig. 18 comparison of p-y
curves at 70 cm embedded
depth
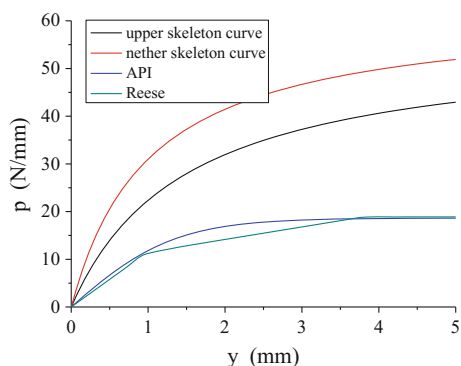
Conclusions

Natural frequency of soil-micropile system is 8.38 Hz, the maximal bending
moment distribution is highly affected by excitation frequency as well as pile
displacement distribution. Attention should be paid on the cases under excitation
frequency which is close to the natural frequency of soil-pile system. In this cases,
maximal bending moment is around the embedded depth of 3.3 times pile diameter,
and maximal displacement is at pile head. Under dynamic load, stiffness and shear
strength of sand perform much larger. Dynamic p-y skeleton curves presented in
this paper provide idea and reference for design.

References

1. Makris, N., Gazetas, G. (1992). Dynamic pile-soil-pile interaction. Part II: Lateral and seismic response. Earthquake Engineering and Structural Dynamics, 21(2): 145–162.
2. Kampitsis A E., Giannakos S., Gerolymos N., et al. (2015) Soil–pile interaction considering structural yielding: Numerical Modeling and Experimental Validation, Engineering Structures, 99: 319–333.
3. Mylonakis, G., Nikolaou, A., & Gazetas, G. (1997). Soil-pile-bridge seismic interaction: kinematic and inertial effects. Part I: soft soil. Earthquake Engineering and Structural Dynamics, 26(3): 337–359.
4. Turan, A., Hinchberger, S. D., and El Naggar, H. (2009). Design and commissioning of a laminar soil container for use on small shaking tables. Soil Dynamics and Earthquake Engineering, 29(2): 404–414.
5. Chen, G. X., Wang, Z. H., et al. (2010). Development of laminar shear soil container for shaking table tests. Chinese Journal of Geotechnical Engineering, 32(1): 89–97.
6. Boulanger, R. W., Curras, C. J., Kutter, B. L., Wilson, D. W., and Abghari, A. (1999). Seismic soil-pile-structure interaction experiments and analyses. Journal of Geotechnical and Geoenvironmental Engineering, 125(9): 750–759.
7. Chau, K. T., Shen, C. Y., and Guo, X. (2009). Nonlinear seismic soil–pile–structure interactions: shaking table tests and FEM analyses. Soil Dynamics and Earthquake Engineering, 29(2): 300–310.
8. Yao, S., Kobayashi, K., Yoshida, N., and Matsuo, H. (2004). Interactive behavior of soil–pile-superstructure system in transient state to liquefaction by means of large shake table tests. Soil Dynamics and Earthquake Engineering, 24(5): 397–409.
9. Reese, L. C., Cox, W. R., and Koop, F. D. (1974). Analysis of laterally loaded piles in sand. Offshore Technology in Civil Engineering Hall of Fame Papers from the Early Years, 95–105.
10. Ashour, M., Norris, G., and Pilling, P. (1998). Lateral loading of a pile in layered soil using the strain wedge model. Journal of Geotechnical and Geoenvironmental Engineering, 124(4): 303–315.
11. Yankelevsky, D. Z., Eisenberger, M., and Adin, M. A. (1989). Analysis of beams on nonlinear winkler foundation. Computers and Structures, 31(2): 287–292.
12. Naggar, M. H. E., and Bentley, K. J. (2000). Dynamic analysis for laterally loaded piles and dynamic p-y curves. Canadian Geotechnical Journal, 37(6): 1166–1183.
13. Yoo, M. T., Choi, J. I., Han, J. T., and Kim, M. M. (2013). Dynamic PY Curves for Dry Sand from Centrifuge Tests. Journal of Earthquake Engineering, 17(7): 1082–1102.
14. Philip Meymand. (1998). Shake table tests: Seismic soil-pile-superstructure interaction. PEERCenter News, 1(2): 1–4.
15. Kondner, R. L. (1963). Hyperbolic stress-strain response: cohesive soils. Journal of the Soil Mechanics and Foundations Division, 89(1): 115–144.
16. Tak Kim, B., Kim, N. K., Jin Lee, W., and Su Kim, Y. (2004). Experimental load-transfer curves of laterally loaded piles in Nak-Dong River sand. Journal of Geotechnical and Geoenvironmental Engineering, 130(4): 416–425.

Dynamic Shakedown Analysis for Anisotropic Material Under Traffic Moving Loading

Han Lin, Jiangu Qian and Yonggang Wang

Introduction

With the further pavement engineering research, how to predict the failure of pavement structure induced by repeat traffic load is strongly important. However, long-term stability of pavement cannot be predicted exactly by considering the elastic response of pavement structure layer simply, in which irrecoverable strain accumulates and may result in breakdown of pavement [1–3].

The shakedown theorem is firstly proposed by Melan in 1938 [4]. And then kinematic shakedown theorem is proposed by Koiter in 1960 [5]. In 1984, Sharp and Booker firstly applied the shakedown limit to estimating the maximum traffic load for the pavement system, which considered Mohr-Coulomb materials into shakedown analysis [6]. Recently, Yu and Wang proposed a method to calculate the rigorous shakedown limit using Mohr-Coulomb yield criteria [7]. After that, Wang and Yu developed their method into anisotropic half-space system [8]. Previous research is concerned with shakedown theorem under static traffic loads. However, traffic loads is a typical moving load, different from static load. Moving loads are hardly concerned in previous researches. Therefore, it's significant to calculate traffic-induced dynamic elastic stress under various speeds of moving loads. Although the lower-bound shakedown analysis for isotropic system under different moving speed had been proposed, the anisotropic material failed to be considered in shakedown analysis [6–8].

H. Lin · J. Qian (✉) · Y. Wang
Department of Geotechnical Engineering, Tongji University, 200092 Shanghai, China
e-mail: qianjiangu@tongji.edu.cn

H. Lin
e-mail: kdmugm@tongji.edu.cn

Y. Wang
e-mail: 1310008@tongji.edu.cn

In this paper, the anisotropic lower-bound theorem is introduced. Firstly, an analysis method is proposed to calculate shakedown limit for anisotropic material. Then a FE–IE model is established to compute dynamic response under moving loads. The comparison of static and dynamic solutions is also proposed to verify the validity of this method, besides, the effects of elastic cross-anisotropic parameters and plastic anisotropic cohesive parameters are investigated.

Anisotropic Shakedown Theorem

The Melan's lower-bound shakedown theorem states that it's a sufficient condition for occurrence of shakedown under repeated or cyclic loads. A time-independent, self-equilibrated, residual stress field ρ_{ij} can be found. When ρ_{ij} is added to the elastic stress field σ_{ij}^e, it produces a combined stress field that nowhere and at no-time violates the yield condition [4]. The Lower-bound shakedown theorem hence can be described as:

$$\max_{\lambda}\left\{f(\lambda\sigma_{ij}^e + \rho_{ij}) \leq 0, \ \lambda \geq 0\right\} \tag{1}$$

where λ is a dimensionless factor, for which the elastic stress field $\lambda\sigma_{ij}^e$ is induced by λp. f is the yield criterion. In this paper, an anisotropic Mohr-Coulomb yield criterion is adopted, as addressed below.

If Mohr-Coulomb criteria is used to define the yield strength of isotropic pavement materials, (1) can be written as follows [7]:

$$f = (\rho_{xx} + M)^2 + N \leq 0 \tag{2}$$

But for an anisotropic material, it's no longer valid. According to Wang and Yu, the shakedown condition for an anisotropic material should be defined as follows [8]:

$$f = (\rho_{xx} + M)^2 + N + P \leq 0 \tag{3}$$

where M, N and P are in the following form:

$$M = \lambda\sigma_{xx}^e - \lambda\sigma_{zz}^e + 2\tan\varphi\,(c_h - \lambda\sigma_{zz}^e\tan\varphi) \tag{4a}$$

$$N = 4(1 + \tan^2\varphi)\left[(\lambda\sigma_{xz}^e)^2 - (c_h - \lambda\sigma_{zz}^e\tan\varphi)^2\right] \tag{4b}$$

$$P = 4(c_v - c_h)\left[\lambda\sigma_{xz}^e - (c_h - \lambda\sigma_{zz}^e\tan\varphi)\right] \tag{4c}$$

where c_h and c_v are the values of horizontal cohesion and the vertical cohesion, φ is the internal friction angle.

In order to satisfy (3), the overall shakedown condition of (5) for the half-space must be met:

$$N + P \leq 0 \Rightarrow \lambda \leq \lambda_{sd} = \frac{c_h}{\max \left[\max_{case1}(a), \max_{case2}(b), \max_{case3}(a,b) \right]} \qquad (5)$$

where a and b are in the following form:

$$a = \sigma_{zz}^e \tan \varphi + \sigma_{xz}^e \qquad (6a)$$

$$b = (\sigma_{zz}^e \tan \varphi - \sigma_{xz}^e) \frac{1 + \tan^2 \varphi}{c_v/c_h + \tan^2 \varphi} \qquad (6b)$$

For positive a and negative b, (5) turns to *case1*. For negative a and positive b, (5) turns to *case2*. And for positive a and positive b, (5) turns to *case3*. Inequation (5) shows the maximum boundary to the lower-bound shakedown limit. As well known, the residual stresses are constant in the moving direction at the same depth. According to (3), the residual stresses ρ_{ij} at point i along moving direction x at the same depth must be between the larger root and smaller root:

$$-M_i - \sqrt{-N_i - P_i} \leq \rho_{xx} \leq -M_i + \sqrt{-N_i - P_i} \qquad (7)$$

Obviously, $-N_i - P_i$ must be non-negative in (7), because it has to satisfy the shakedown condition (5).

The residual stresses ρ_{ij} at the same depth $z = j$ vary with the change of position, according to the self-equilibrium condition. Thus the possible residual stress ρ_{ij} must meet the following condition:

$$\max_{z=j} (-M_i - \sqrt{-N_i - P_i}) \leq \rho_{xx} \leq \min_{z=j}(-M_i + \sqrt{-N_i - P_i}) \qquad (8)$$

According to (8), the critical residual stress field ρ_{ij} at same depth with a given shakedown parameter λ is unique. If λ is larger than the shakedown limit, the maximum value of f at depth j calculated from (3) will be larger than zero, and if λ is smaller than the shakedown limit, the maximum value of f at depth j will be negative.

The lower-bound shakedown limit at the specific depth can be obtained if λ_{sd} calculated by (5) matches self-equilibrium condition (refer to (3)). However, if the λ_{sd} calculated by (5) does not match self-equilibrium condition at that depth, the problem will be changed to find variable λ only for given materials of pavement and the load form.

$$\begin{aligned} &\text{maximum } \lambda \\ &\text{subjected to } f(\lambda) \leq 0 \end{aligned} \qquad (9)$$

By using the optimal method to find the maximum load parameter λ at the same depth. The real shakedown limit for anisotropic material is the minimum shakedown limit among the shakedown limit of each depth in the half-space.

FE–IE Model

In numerical model, stress waves will occur when the traffic moving load travels from one side to another side. However, if the fixed boundary is used in the numerical model, strong stress waves will reflect on the boundary of this model, and causes the energy in model to increase factitiously. In this model, a three-dimensional coupled Infinite Element–Finite Element analysis using ABAQUS is performed to provide realistic estimation of traffic-induced dynamic stress in the pavement [9, 10]. As shown in Fig. 1, the size of this simulated region is 30 m (maximum length) $\times$ 5.5 m (maximum width) $\times$ 6.25 m (maximum height).

In the numerical model, the simulated traffic moving load moves from -10 to 10 m along the moving direction on the ground by a user subroutine VDLOAD. And artificial boundaries of Infinite Element (CIN3D8) are built for simulating unbounded domains, similar to Connolly et al. [11].

The traffic load is defined as Hertz distribution, which matches better vehicles wheel loading, and it can be defined as follows [6]:

$$p = \frac{3P}{2\pi a^3}(a^2 - x^2 - y^2)^{1/2}, \quad (x+vt)^2 + y^2 < a^2 \tag{10a}$$

$$p_0 = \frac{3P}{2\pi a^2} \tag{10b}$$
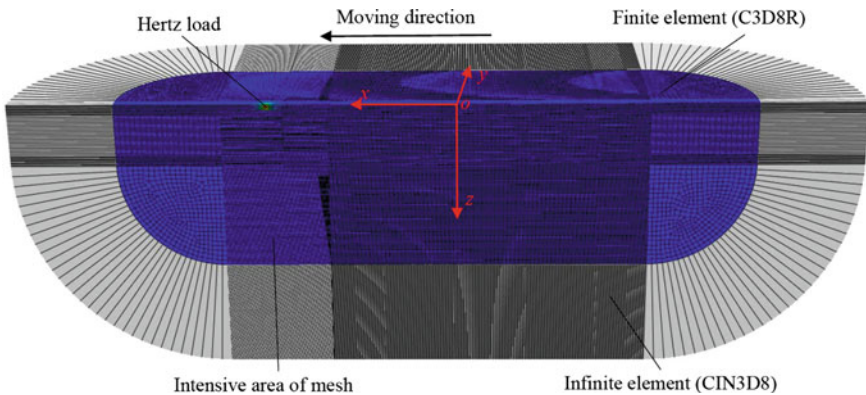
Fig. 1 Finite element model with infinite element boundaries

where a is the radius of the contact area with a = 12.5 cm in this model. x, y, z represent Cartesian coordinates (x-axis is the travel direction). P is the resultant of 3D Hertz distribution load, and p_0 is the peak pressure.

Numerical Analysis

Isotropic Half-Space System

To verify the validity of this shakedown solution, the isotropic half-space system at an extreme low speed (v = 1 m/s) has been assumed. As shown in Fig. 2, the results of present study are close to the static isotropic solution [7]. The shakedown limit is represented by a dimensionless factorλ'p0/c.

The effects of moving speed on shakedown limits are shown in Fig. 2b. It is clear that the shakedown limit decreases gradually to the minimum as the moving speed increases to the Rayleigh wave speed. Subsequently, the shakedown limit tends to increase with increasing moving speed when moving speed exceeds the Rayleigh wave speed. It has been discussed that failure tends to occur when the moving speed reaches the Rayleigh wave speed.

Influence of Elastic Cross-Anisotropic Parameters

The elastic cross-anisotropic half-space system at an extreme low speed (v = 1 m/s) has been assumed for validation of this shakedown solution, compared with the static solution [8]. As shown in Table 1, the elastic stress field of this system

(a) Static Solution   (b) Moving speed (φ= 0°)
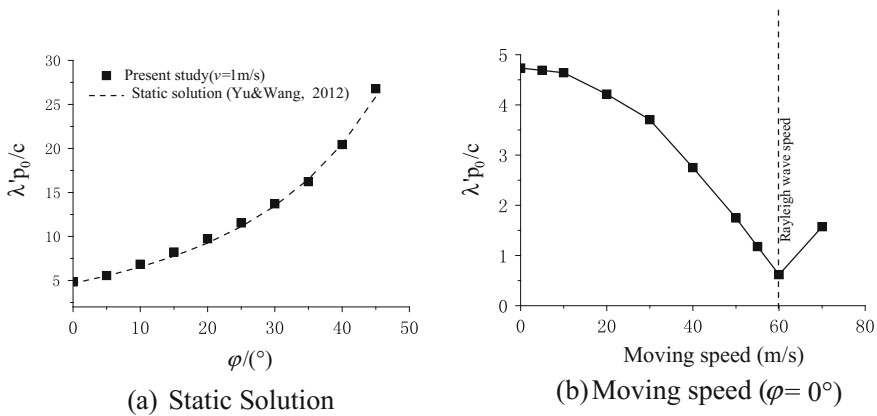
Fig. 2 Comparisons with static isotropic solution (E = 20 MPa, μ = 0.2, ρ = 1800 kg/m^3)

Table 1 Elastic cross-anisotropic solution

Case	E_h(MPa)	E_v/E_h	G_{vh}/G_h	μ_h	μ_{vh}	Static (Ref. [8])	Dynamic (v = 1 m/s)
1	9.35	0.53	0.73	0.17	0.23	4.00	4.075
2	6.96	0.41	0.64	0.08	0.12	3.74	3.817
3	7.67	0.52	0.72	0.17	0.23	3.97	4.051
4	5.76	0.76	0.87	0.23	0.27	4.37	4.454
Isotropy	10	1	1	0.2	0.2	4.68	4.73

depends on five cross-anisotropic parameters: E_h (Young's modulus in horizontal direction), E_v/E_h (E_v is Young's modulus in vertical direction), G_{vh}/G_h (Ratio of shear modulus ratio in VH plane with horizontal plane), μ_h (Poisson's ratio for horizontal strain on complementary horizontal strain), μ_{vh} (Poisson's ratio for vertical strain on horizontal strain). The five parameters are independent with the following relations:

$$G_h = \frac{E_h}{2(1 + \mu_h)} \tag{11a}$$

$$\mu_{vh}/\mu_{hv} = E_v/E_h \tag{11b}$$

As for the effect of Poisson's ratio, it has a slightly effect on the shakedown limits, as shown in Fig. 3.
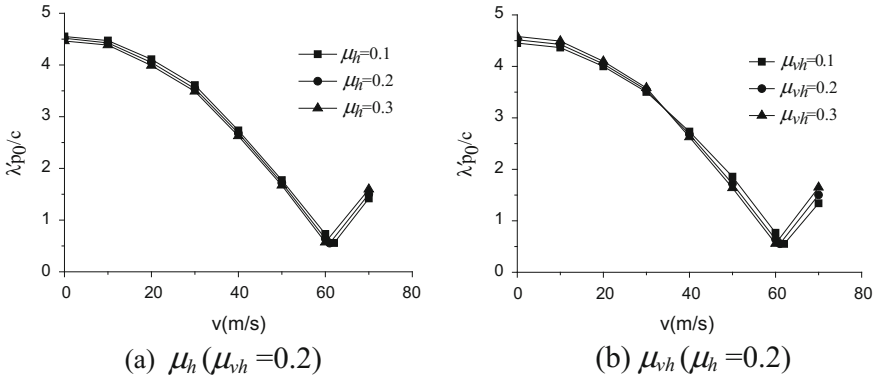
Fig. 3 Influence of shakedown limit with moving speed at different Poisson's ratio. (E_h = 20 MPa, E_v/E_h = 0.9, G_{vh}/G_h = 0.9, ρ = 1800 kg/m^3, φ = 0°)

(a) Static solution   (b) Moving speed ($\varphi=0°$)
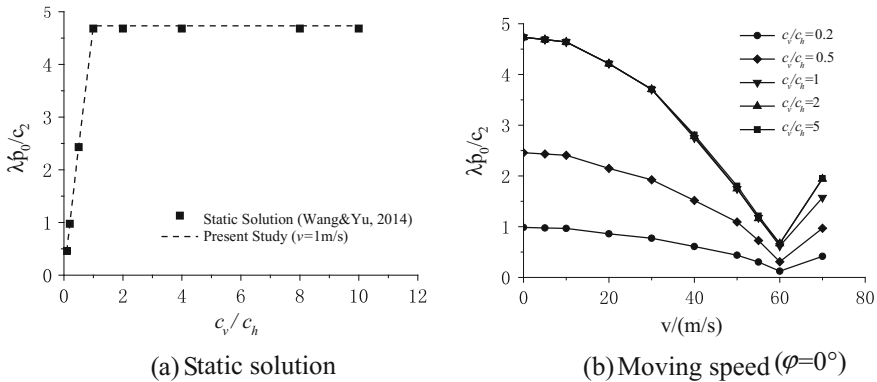
Fig. 4 Variations of shakedown limit with moving speed at different cohesion ratio. ($E_h = 20$ MPa, $E_v/E_h = 1$, $G_{vh}/G_h = 1$, $\mu_h = \mu_{vh} = 0.2$, $\rho = 1800$ kg/m^3)

Influence of Plastic Anisotropic Strength

As shown in Fig. 4a, the comparison of shakedown limits of present and previous study shows good consistence between static and dynamic solutions. Shakedown limit rises with the increasing cohesion ratio c_v/c_h, otherwise, when the lower-bound shakedown limit is controlled by $1/b$ (refer to (6b)). If the cohesion ratio is large enough, the shakedown limit will be controlled by $1/a$ (refer to (6a)) [8].

The variations of shakedown limit with moving speed at different cohesion ratios are illustrated in Fig. 4b, similar to the isotropic solution. However, the maximum shakedown limit tends to rise slightly when moving speed is below Rayleigh wave speed. But it rises significantly when over the Rayleigh wave speed.

Conclusions

The shakedown limits for anisotropic half-space system under moving loads has been explored in this paper. The elastic stress in anisotropic half-space system under moving loads is computed by proposed coupled FE–IE model with subroutine in ABAQUS. The present FE–IE method is validated by comparison with traditional static method. The proposed optimization technique has provided an effective way to find the exact solution to critical residual stresses in the numerical shakedown analysis.

The shakedown limits strongly depend on the moving speed of the traffic load. It has been found that the shakedown limit reduces with the moving speed control when the moving speed is close to Rayleigh wave. Although the cross-anisotropic parameters define the elastic anisotropic response, the Poisson's ratio μ_h, μ_{vh} only affect slightly on the shakedown limit.

For plastic anisotropic strength, shakedown limit rises with the increasing ratio c_v/c_h, but the maximum shakedown limit is limited by a specific cohesion ratio. When c_v/c_h is larger than this cohesion ratio, the shakedown limit reaches maximum value. With the increase of moving speed, the maximum shakedown limits only rise slightly before moving speed reaches Rayleigh wave speed, while significant raise is found in the maximum shakedown limit when moving speed exceeds Rayleigh wave speed.

References

1. Werkmeister, S. (2003). Permanent deformation behavior of unbound granular materials. University of Technology, Dresden.
2. Werkmeister, S., Dawson, A., Wellner, F. (2004). Pavement design model for unbound granular materials. Journal of Transportation Engineering, ASCE, 130(5): 665–674.
3. Chen, H. S., Liu, S. H. (2009). Inelastic damages by stress wave on steel surface at the incubation stage of vibration cavitation erosion. Wear, 266(1–2): 69–75.
4. Melan, E. (1938). Der spannungsgudstand eines Henky-Mises schen Kontinuums bei Verlandicher Belastung. Sitzungberichte der Ak Wissenschaften Wie (Ser. 2A), vol. 147, pp. 73.
5. Koiter, W.T. (1960). General theorems for elastic–plastic solids. In: Sneddon, I.N., Hill, R. (Eds.), Progress in Solid Mechanics, North-Holland Pub. Co., Amsterdam, pp. 165–221.
6. Sharp, R.W., Booker, J.R. (1984). Shakedown of pavements under moving surface loads. Journal of Transportation Engineering, ASCE, 110: 1–14.
7. Yu, H. S., Wang, J. (2012). Three-dimensional shakedown solutions for cohesive-frictional materials under moving surface loads. International Journal of Solids and Structures, 49(26): 3797–3807.
8. Wang, J., Yu, H. S. (2014). Three-dimensional shakedown solutions for anisotropic cohesive-frictional materials under moving surface loads. International Journal for Numerical & Analytical Methods in Geomechanics, 38(4): 331–348.
9. Achenbach, J.D. (1980). Wave propagation in elastic solids, North-Holland, Amsterdam.
10. Kouroussis, G., Verlinen, O., Conti, C. (2001). Finite-dynamic model for infinite media: corrected solution of viscous boundary efficiency. Journal of Engineering Mechanics, 137(7): 509–11.
11. Connolly, D.N., Giannopoulos, A., Forde, M. C. (2013). Numerical modelling of ground borne vibrations from high speed rail lines on embankments. Soil Dynamics and Earthquake Engineering, 46: 13–19.

Field Test Study on Influence of Undercrossing Construction on Safety of Existing High-Speed Railway

Hong Xiao, Xing Ling and Song Lv

Introduction

High-speed railway has the advantages of higher speed, safer and smoother when running [1].

The construction in CuiHeng Road starts from QianJin Road in the north, which is located in WuQing District, TianJin city of China, and crosses YiZhi canal southward, then crosses under a 16 m–20 m–16 m continuous steel frame bridge of BeiJing-TianJin Inter-city Railway and BeiJing-ShanHaiguan Railway, as shown in Fig. 1. CuiHeng Road is an urban arterial road, and its planned driving speed is 40 km/h, full-length of the construction segment is 459.34 m, clearance height of vehicle lanes is 4.5 m, clearance height of bicycle lanes is 2.5 m. BeiJing-TianJin Inter-city Railway is the first railway in China to be built for operational speeds at 350 km/h, and its operation safety is extremely important. According to the design requirements, the construction undercrossing the railway should not affect its operation safety.

According to geological survey, groundwater level of the construction segment is very high, whose buried depth is 1.65–2.6 m, and soil is mainly soft-plastic clay, whose allowable bearing capacity is as low as 85 kPa. In order to meet the design requirements of CuiHeng Road, it is planned to strengthen the foundation

H. Xiao (✉) · X. Ling · S. Lv
Beijing Key Laboratory of Track Engineering,
Beijing Jiaotong University, 100044 Beijing, China
e-mail: mgubao@163.com

X. Ling
e-mail: 15121172@bjtu.edu.cn

S. Lv
e-mail: 16121203@bjtu.edu.cn
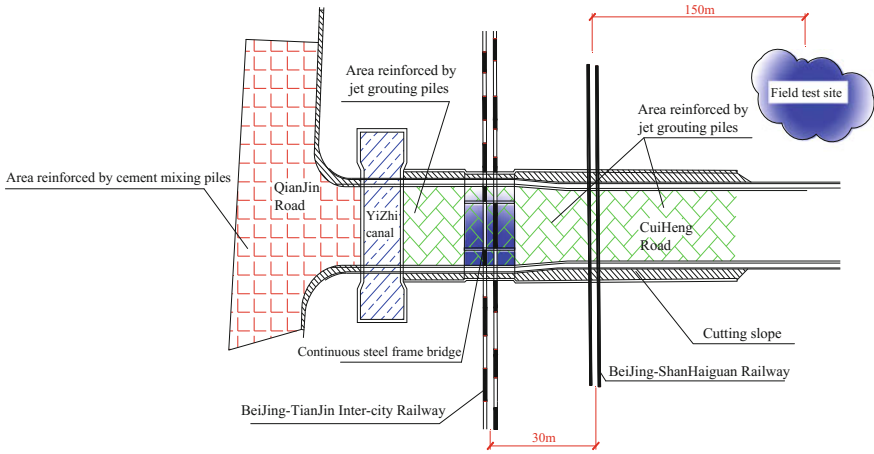
Fig. 1 Plan of the construction site

with JGP (high-pressure jet grouting piles) under and on both sides of the reserved continuous steel frame bridge of BeiJing-TianJin Inter-city Railway. However, the construction of JGP has a compacting effect on surrounding soil, causing additional settlement and lateral displacement of embankment, bridge, transition section and track, which will affect operation safety. In addition, high-speed railway is a premium risk source according to rules [2], and there has not been any experience of construction close to or undercrossing an high-speed railway previously in China. Therefore, to minimize security risks, it is necessary to figure out what influence the construction with JGP will have on operation safety of the railway. So the field test study is conducted at a vacant land of construction site at a certain distance far from the high-speed railway, in order to provide direct guidance for the undercrossing construction. Specific location of the test is shown in Fig. 1.

Test Scheme

Working Conditions

According to the design scheme and actual influence of the construction on BeiJing-TianJin Inter-city Railway, tests of three different working conditions are conducted: ① Case 1: test of influence range of construction using single row JGP without heaped load; ② Case 2: test of influence on abutment using JGP with heaped load; ③ Case 3: test of influence on abutment of earth excavation under the bridge of BeiJing-TianJin Inter-city Railway with heaped load.

(a) Planar graph　　(b) Cross-section profile　(c) Longitudinal profile
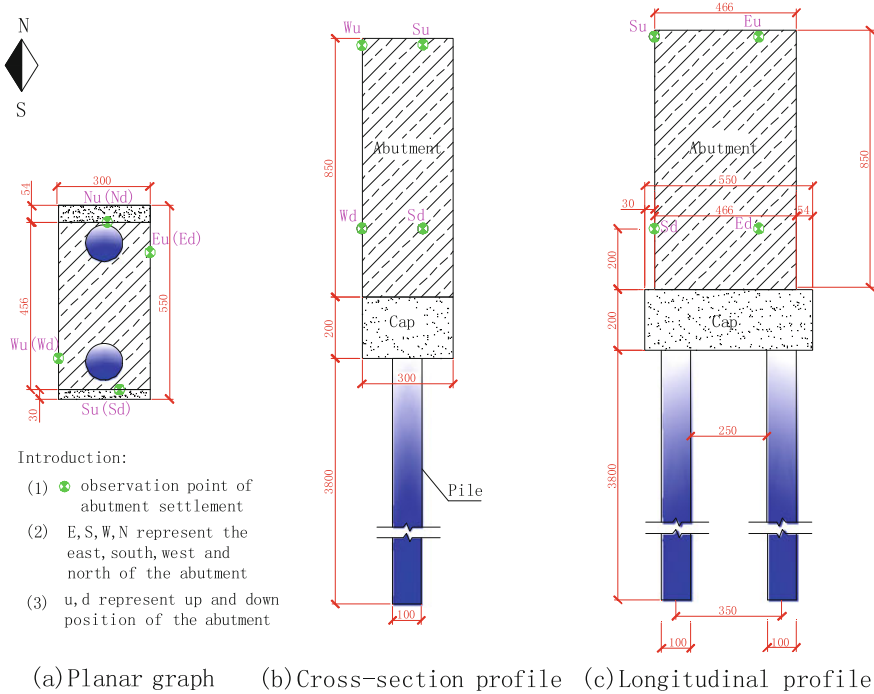
Fig. 2 Structure of field test and layout of measuring points (unit: cm)

Test Contents and Layout of Measuring Points

Abutment, cap and pile foundation for the test are all made of C30 reinforced concrete. Test contents include lateral deformation and vertical settlement of the abutment. The size of each structure and layout of measuring points are shown in Fig. 2. There are 8 displacement measuring points arranged around the abutment in the test, because laws of some measuring points are similar and space of this paper is limited, only a total of 4 measuring points in the south and west will be analyzed in this paper.

Test Results

Case 1

The first case is test of influence range of construction using single row JGP without heaped load. The construction is as follows, at 10 m east of the test abutment, a total of 25 JGP are constructed from east to west in turn, as shown in Fig. 3. And

(a) Planar graph   (b) Elevation graph
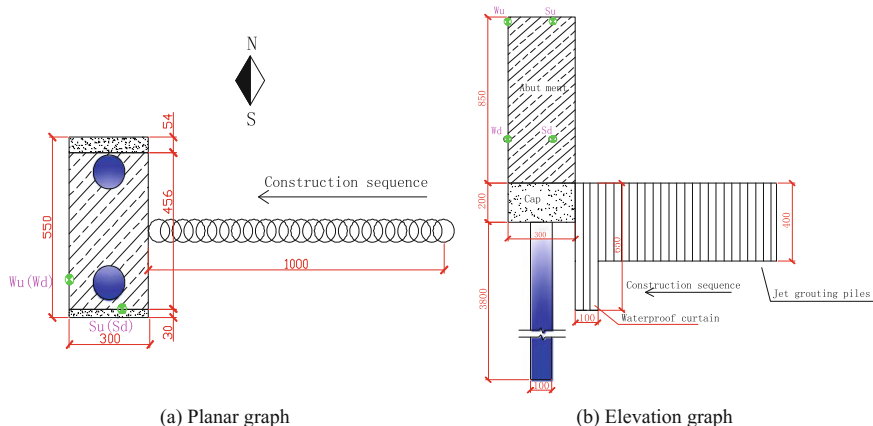
Fig. 3 Sketch of Case 1 (unit: cm)

cement content of JGP is 20%, diameter of the pile is 0.6 m. The JGP of Case 2 and Case 3 are the same with those of Case 1.

Lateral Deformation

Lateral deformations in Case 1 are shown in Figs. 4 and 5.

As can be seen in the figures, after the construction of JGP, lateral deformations of measuring points Wu and Wd in the abutment are respectively 1.9, 1.4 mm westward, and 1.2, 1.0 mm southward. This shows that the construction of single row JGP has influence on deformation of the abutment, and when the construction is very close to the abutment, the influence grows exponentially. It also can be seen that lateral deformations occur not only in the direction of the construction, but also in the direction perpendicular to the construction, but the former is greater than the latter. In addition, the construction of last 7 piles has an obvious influence on the deformation of the direction of the construction, and the construction of last 5 piles has an obvious influence on the deformations on the direction perpendicular to the construction.

Fig. 4 Westward lateral deformation curves
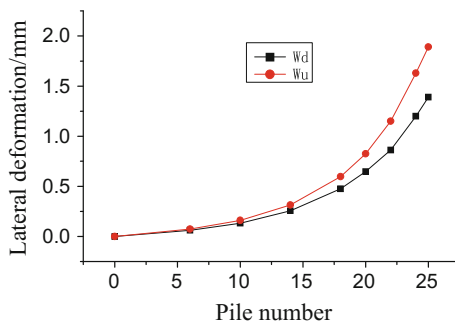
Fig. 5 Southward lateral deformation curves
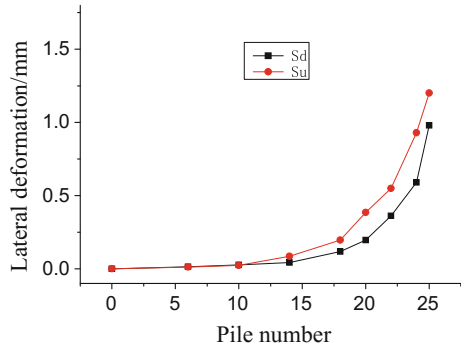
It can be seen from the test results that the construction of single row JGP has a little influence on the structure generally. After the construction of JGP, the maximum value of abutment deformation is 1.9 mm, which is far less than 20 mm allowed according to the code (lateral deformation should be less than $5\sqrt{L}$ according to the code [3]. L is length of bridge span, so it is 20 mm according to calculation in this case). So the construction under Case 1 is safe for the structure.

Vertical Settlement

Vertical settlements in Case 1 are shown in Figs. 6 and 7.

As can be seen in the above figures, after the construction of JGP, settlement of measuring point *Wu* is 0.5 mm, and settlement of measuring point *Su* is 0.4 mm. And there are some fluctuations in the curves. This shows that the construction of single row JGP has little influence on settlement of pile foundation of the bridge, and the settlement values are far less than 20 mm allowed according to the code.

Fig. 6 Settlement curve of measuring point *Wu*

Fig. 7 Settlement curve of measuring point *Su*

(a) Planar graph   (b) Elevation graph
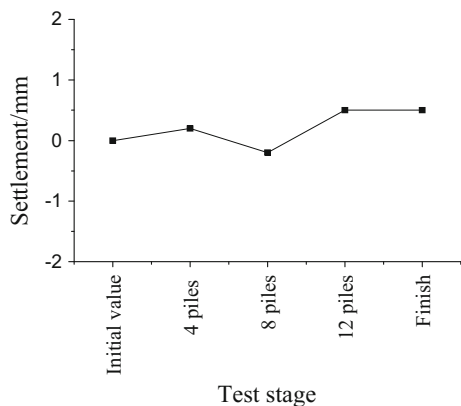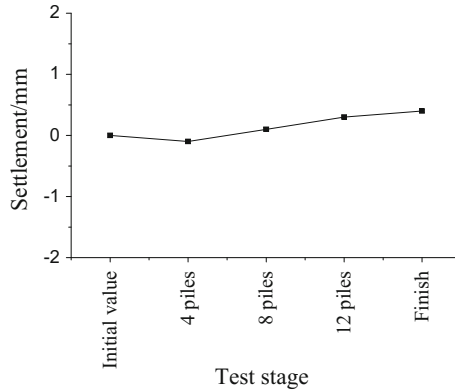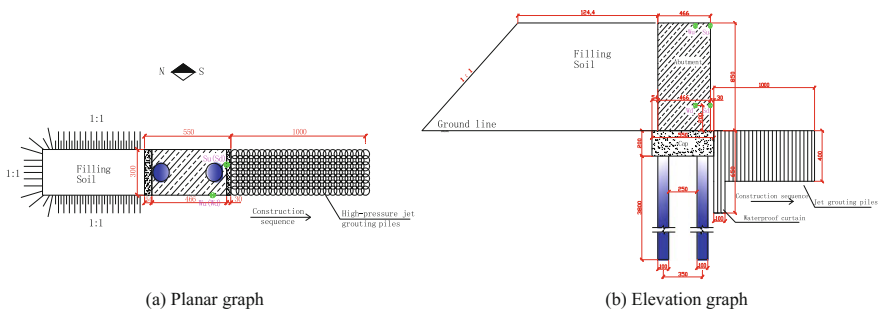
Fig. 8 Sketch of Case 2 (unit: cm)

Case 2

The Case 2 is test of influence on abutment using JGP with heaped load. There are two stages in Case 2. The first stage is filling soil in the north of the bridge, the height of the soil is 8.5 m, and it is as high as the top of the abutment. The second stage is, after filling the soil, 25 rows of JGP are constructed from north to south in turn, and there are 7 piles in a row, as shown in Fig. 8.

Filling Soil

(1) **Lateral deformation**

Lateral deformations of the abutment structures in the first stage of Case 2 are shown in Figs. 9 and 10.

As can be seen in the figures, after filling the soil, lateral deformation increments of measuring points *Wu* and *Wd* in the abutment are respectively 4.3, 3.4 mm

Fig. 9 Westward lateral
deformation curves
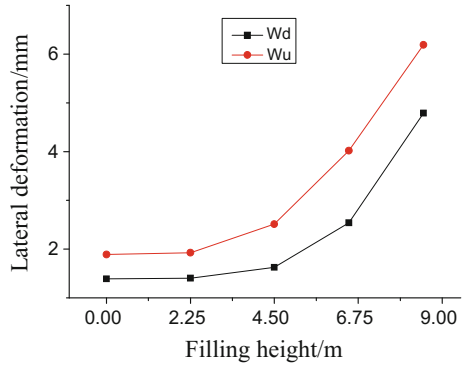
Fig. 10 Southward lateral
deformation curves
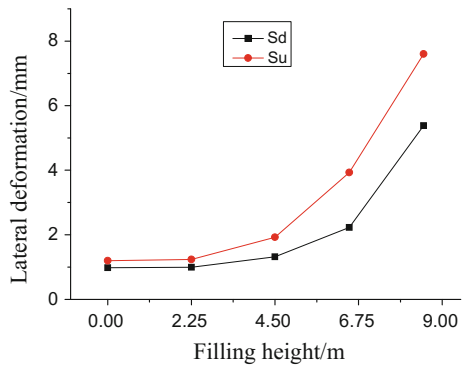
westward, at a total of 6.2 and 4.8 mm; lateral deformation increments of measuring points Su, Sd in the abutment are respectively 6.4, 4.4 mm southward, at a total of 7.6 and 5.4 mm. It can be seen from the curves and test values that the height of the soil has an obvious influence on the abutment structure, and higher of the soil, greater the influence of height.

As can be seen from the test data, the construction of filling soil has an obvious influence on lateral deformation of the abutment, after filling all the soil, the maximum value of lateral deformation of abutment is 7.6 mm, which is less than 20 mm allowed according to the code, so the structure is safe.

(2) **Vertical settlement**

Vertical settlements of the abutment structures in the first stage of Case 2 are shown in Figs. 11 and 12.

As can be seen in the figures, after filling the soil, vertical settlement increment of measuring point Wu is 2.3 mm, at a total of 2.8 mm; settlement increment of measuring point Su is 2.7 mm, at a total of 3.1 mm. Comparing the test results of Case 2 with those of Case 1, it can be seen that the construction of filling soil under Case 2 has more influence on vertical settlement of the abutment. But the settlement is less than 20 mm allowed according to the code, the structure is safe.

Fig. 11 Settlement curve of measuring point *Wu*
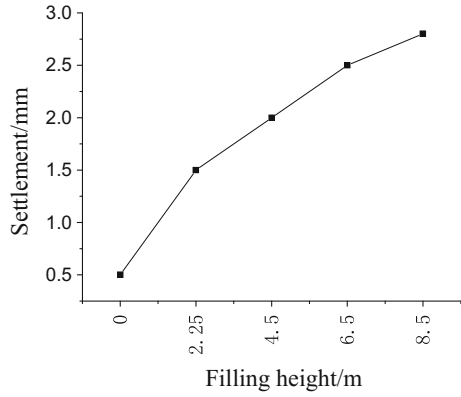
Fig. 12 Settlement curve of measuring point *Su*
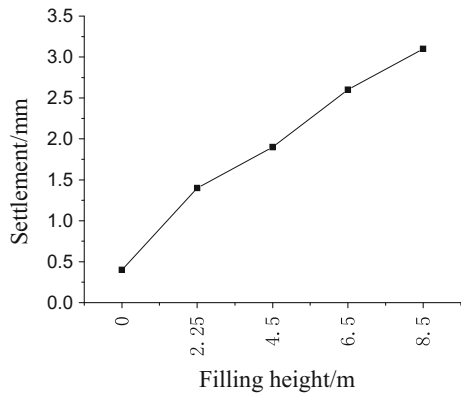
Construction of JGP

(1) **Lateral deformation**

Lateral deformations of the abutment structures in the second stage of Case 2 are shown in Figs. 13 and 14.

As can be seen in the figures, after the construction of JGP, lateral deformation decrements of measuring points Wu and Wd are respectively 2.9 and 2.6 mm, at a total of 3.3 and 2.2 mm; lateral deformation decrements of measuring points Su, Sd are respectively 4.0 and 3.2 mm, at a total of 3.6 and 2.2 mm, and the variation laws are similar. As can be seen from the curves, the compacting effect of the construction of JGP in the south reduces lateral deformation of the abutment structure. Meanwhile, because the piles are constructed from near to far, the change of lateral deformation slows down with the increase of pile number.

As can be seen from the test data, the maximum variation value of lateral deformation is 4.0 mm, and after the sixth row of piles are constructed, the

Fig. 13 Westward lateral deformation curves
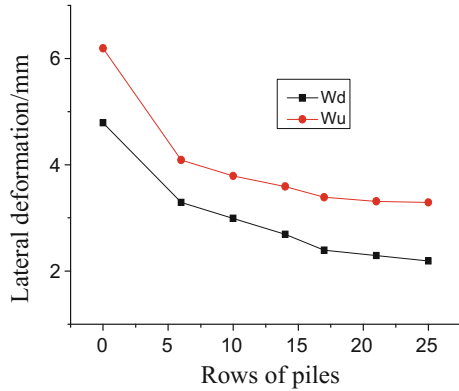
Fig. 14 Southward lateral deformation curves
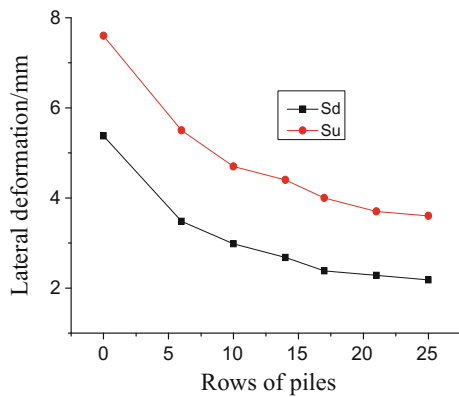
influence of subsequent construction on deformation of the abutment decreases. In general, because of the compacting effect of the JGP construction under Case 2, lateral deformations of the abutment have some decrease, so the structure is safe.

(2) **Vertical settlement**

Vertical settlements of the abutment structures in the second stage of Case 2 are shown in Figs. 15 and 16.

As can be seen in the figures, after the construction of JGP, vertical settlement decrement of measuring point *Wu* is 1.0 mm, at a total of 1.8 mm; vertical settlement decrement of measuring point *Su* is 0.9 mm, at a total of 2.2 mm. As can be seen from the curves, the settlement decreases slowly. This is because of the compacting effect of JGP in the second stage, so the settlement of abutment has some decrease. As can be seen from the test data, the settlement values are far less than 20 mm allowed according to the code.

Fig. 15 Settlement curve of
point *Wu*
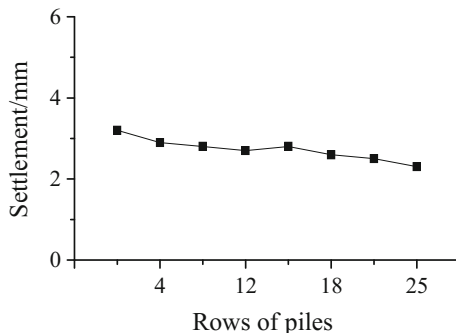
Fig. 16 Settlement curve of
point *Su*
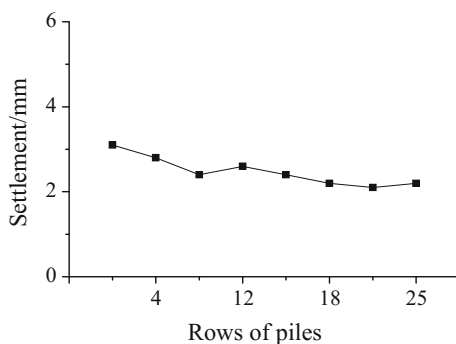
Case 3

The Case 3 is test of influence on abutment of earth excavation under the bridge of BeiJing-TianJin Inter-city Railway with heaped load. According to the design requirements, reinforced soil in the south of the test abutment were excavated, the width is 1.5 m and depth is 3.0 m, as shown in Fig. 17.

Lateral Deformation

Lateral deformation curves of the test are shown in Figs. 18 and 19.

As can be seen in the figures, after the construction of JGP, lateral deformation increments of measuring points Wu and Wd are respectively 0.76 and 1.2 mm, at a total of 4.06 and 3.4 mm; lateral deformation increments of measuring points Su, Sd are respectively 1.7 and 1.4 mm, at a total of 5.3 and 3.6 mm. This shows that excavation construction has some influence on the structure.

As can be seen from the test data of Case 3, after excavation construction, the maximum lateral deformation of abutment is 5.3 mm. In general, lateral deformations of the abutment are far less than 20 mm allowed according to the code, so the structure is safe.

(a) Planar graph   (b) Elevation graph

Fig. 17 Sketch of Case 3

Fig. 18 Westward lateral deformation curves

Fig. 19 Southward lateral deformation curves

Vertical Settlement

Vertical settlement curves of the test are shown in Figs. 20 and 21.

As can be seen in the figures, after the construction of JGP, the variation value of vertical settlement is very small, so the structure is safe. This shows that shallow

Fig. 20 Settlement curve of point *Wu*
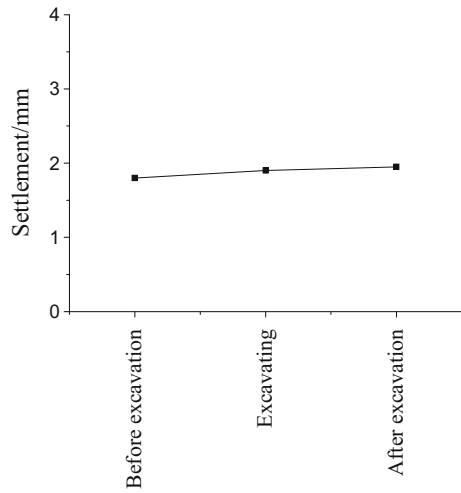
Fig. 21 Settlement curve of point *Su*
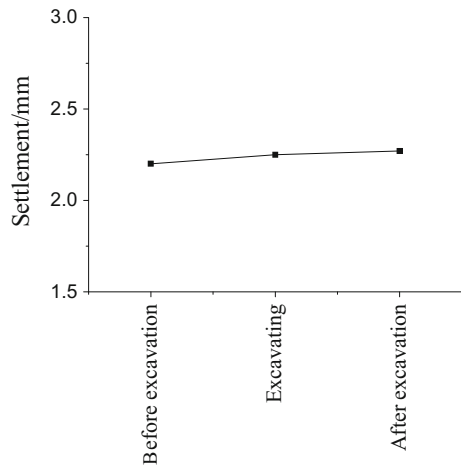
excavation (≤ 3 m) near existing pile foundation of bridge has a little influence on deformation of the bridge. Generally speaking, it won't affect the safety of the structure.

Conclusions and Suggestions

(1) The construction under three Cases all has some influence on lateral deformation and vertical settlement of the structure, but generally the deformation values are very small, so the structure is safe. This shows that construction

using JGP or near the high-speed railway has some influence on train operation, but it is safe and controllable.

(2) In comparison, the Case 2 of filling soil and multi rows JGP construction has greater influence than the Case 1 and the Case 3. From comparison of test data, it can be seen that lateral deformation is more sensitive than vertical settlement, and its values are greater. It is suggested that lateral deformation should be regarded as control index and be paid more attention when undercrossing construction or adjacent construction is conducted.

(3) For construction of JGP from far to near, closer to the abutment, greater the influence, and the influence grows exponentially. For construction from near to far, after the sixth row of piles are constructed, the influence decreases.

References

1. Code for design of high speed railway (TB 10621-2009) [S]. China railway publishing house, 2009.12.
2. Guan Baoshu. Underground engineering in 21 century. Journal of academic trends, 1996.3: 9–15.
3. Fundamental code for design on railway bridge and culvert (TB 10002.1-2005) [S]. China railway publishing house, 2005.8.

Field Test and Analysis on Subway Train Induced Vibration

Hongming Liu, Jing Hu and Xuecheng Bian

Introduction

Long-term vibration induced by subway train vibration can affect not only the structure of subway tunnel, but also the soil and superstructure around it. So it really necessary to understand the regularity of vibration's propagating and damping properties. In the last few decades, many researchers all around the world have launched extensive and profound research on vibration induced by subway train.

Pan Changshi and Li Dewu conducted a field measurement and a corresponding numerical simulation on Beijing subway tunnel in 1990 and discussed the influence of train vibration to the environment [1]. Bian Xuecheng developed a method of combining 2.5D finite element with boundary element, through which he analyzed the vibration in subgrade around tunnel [2, 3]. On the basis of field measurement, Zhang yu'e and Bai Baohong obtained an expression of track vibration acceleration induced subway train's operation, deduced subway train's vibration load which laid a foundation of analyzing train vibration load induced dynamic response of substructure [4]. Sun Xiaojing combined in situ measurement numerical simulation, laboratory test and theoretical analysis to present a comprehensive research of the vibration-induced influence on surroundings [5, 6]. Many scholars abroad have also done a lot of research on this. Kurzweil and Lang proposed a simplified prediction formula of vibration level changing with distance [7, 8]. Uger predicted the

H. Liu (✉) · J. Hu · X. Bian
Department of Civil Engineering, Zhejiang University, Hangzhou, China
e-mail: 11412020@zju.edu.cn

J. Hu
e-mail: 11312009@zju.edu.cn

X. Bian
e-mail: bianxc@zju.edu.cn

vibration response induced by subway operation through determining the correction factor of different trains, tracks and tunnels [9].

In this paper, a field measurement of shield tunnel vibration induced by subway trains is conducted at Ningbo Metro Line 2. Subway train runs through the texting section at fixed speeds of 20, 30 and 40 km/h every other 10 min. At the same time, vibration measurements are undertaken till the vibration is small enough.

Field Text and Data Processing

This text is undertaken in Ningbo Metro Line 2 before its commercial operation. As Ningbo is a city located in the southeast coast of China, the soil Ningbo Metro Line 2 crosses is mostly silt. Monolithic roadbed track is adopted in Ningbo Metro Line 2 which has good stability, strong integrity and long-term durability. The detailed structure is presented in Fig. 1. The width of track slab is 2.8 m, and track gauge is 1435 mm.

The car running in this test is B_2 type car with 6 carriages. The size of the car is shown in Fig. 2.

A section has been selected between Qiuga Station and South Donghuan Road Station to install sensors according to the text conduction in the tunnel. Specific sensor-installing plan is show in Fig. 3

The sensors fixed on the track and lining are velocity sensor named VSE-15D6 from Japan, and the data collection system is ECON AVANT System (see Fig. 4). The detailed parameter of the sensor and the data collection system is present at Table 1.
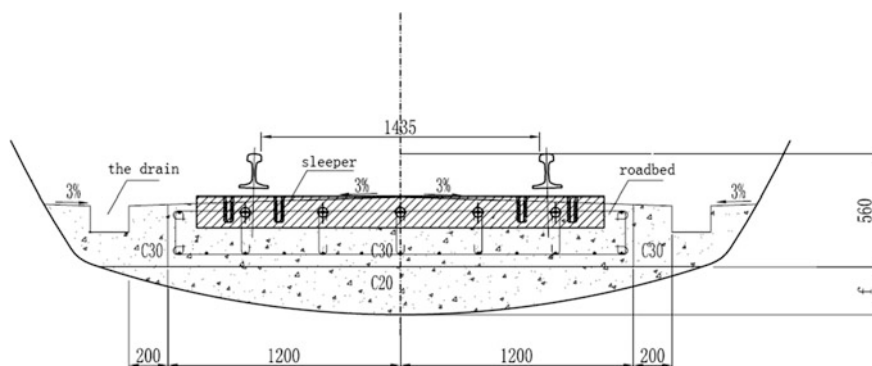
Fig. 1 Structure of monolithic roadbed track

(a) Subway train

(b) One carriage of train
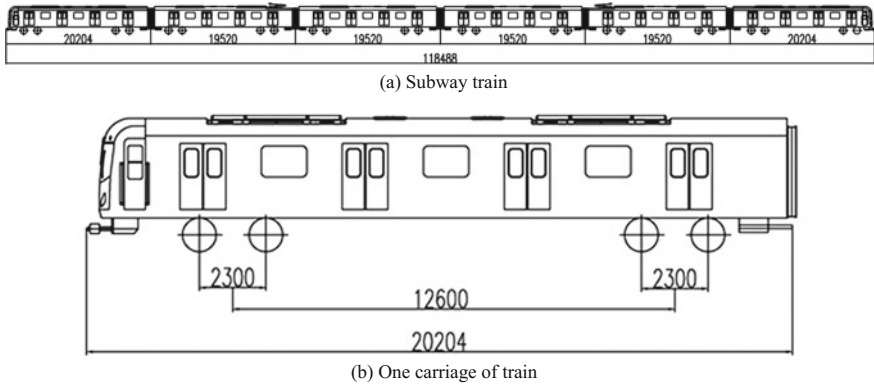
Fig. 2 The size of running car

4 velocity sensors are placed at the surface of track slab on two sides of the rail and one is placed on the tunnel lining to measure the velocity of subway tunnel. Thus the time-velocity curve can be obtained from the real-time measurement. The time-velocity curve can reflect the influence of velocity on the track slab at different spots.

V = 40 km/h
Figure 5 shows the time-velocity curve for different texting spots at train speed of 40 km/h. As the train coming close to the measurement section, the track slab vibrates more and more severe. When the train runs across the section, there is a sudden growth of vibration velocity. And when train run away from the measurement section, track slab's vibration goes down suddenly. Combined with the time-velocity curves on three different spot, it can be seen that spot 2 has the most severe vibration which has reached a vertical velocity of 10 mm/s, comparing with 5 mm/s on spot 1 and 0.0005 mm/s on spot 4. From the time-velocity curves it can be concluded that the vibration outside the rail is larger than the inside. The vibration degraded to a much lower level when it propagates to side lining of tunnel.

V = 30 km/h
Figure 6 shows the time-velocity curve for different texting spots at train speed of 30 km/h. Same with the first train load, spot 2 responses most severely on which the vertical vibration velocity reached to 6.8 mm/s, comparing with 3.5 mm/s on spot 1 and 0.0005 mm/s on spot 4. However, the peak value of vibration velocity is smaller compared with 10 mm/s on the same spot at train speed of 40 km/h. It not hard to understand since the higher train speed is, the more severe the contact between the train and track will be.
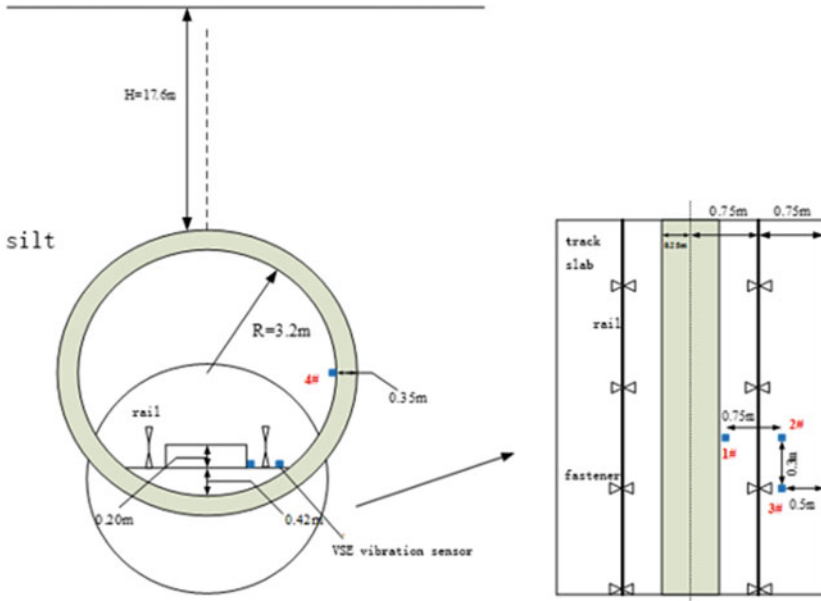
(a) Spots where sensors installed
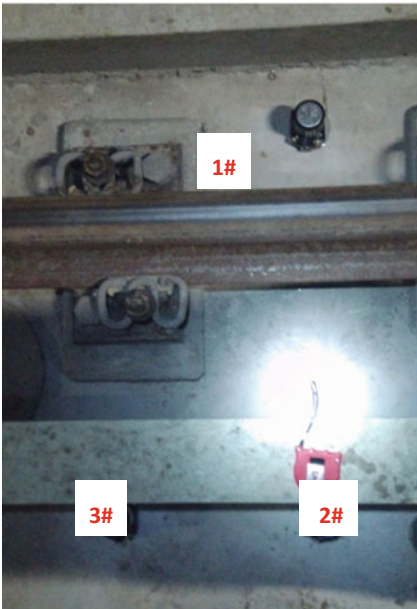
(b) Sensors on track slab
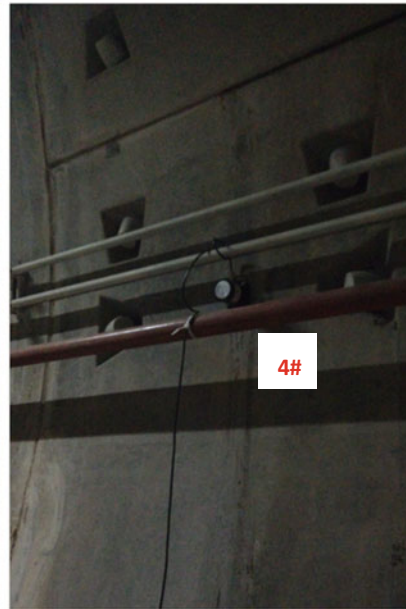
(c) Sensor on tunnel lining

Fig. 3 The installation of vibration sensors

(a) Velocity sensor;   (b) Data collection system
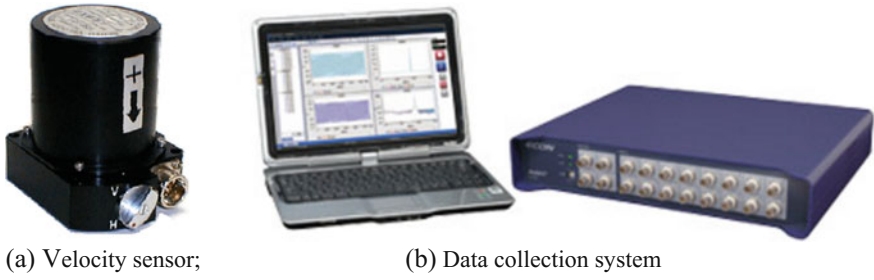
Fig. 4 Text facilities

Table 1 Basic parameters of velocity sensor and data collection system

	Quantities	Magnitude	Unit
Vibration sensor	Output(high)	1000	V/m/s
	Output(low)	100	V/m/s
	Output(tilt)	730	mV/degree
	Frequency range	0.1–70	Hz
	Max. measuring range	±0.1	m/s
Data collection system	Input tunnel	16	
	Output tunnel	4	
	Sampling frequency	204.8	kHz
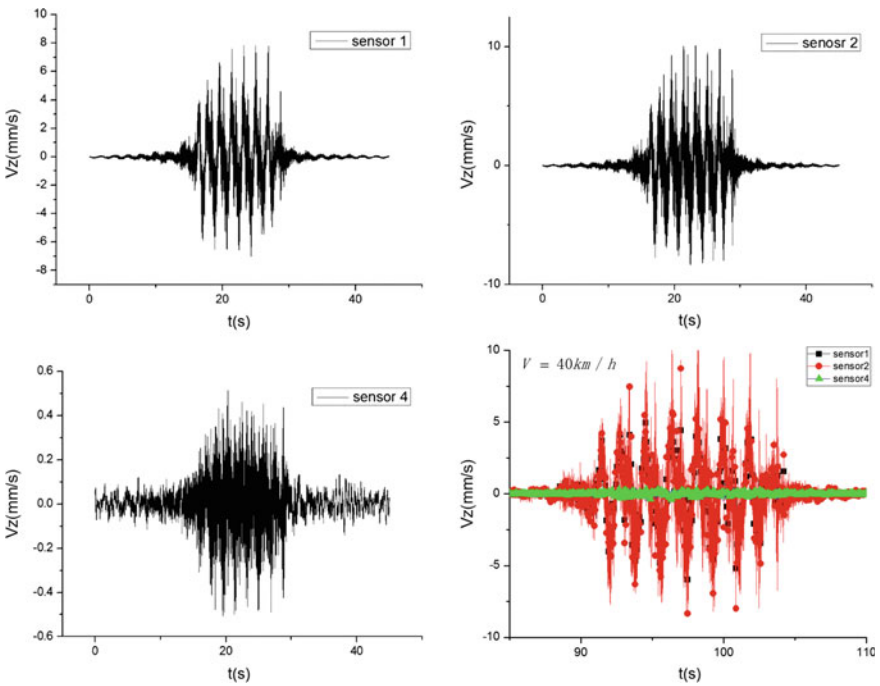
Fig. 5 Vibration response of different spots at 40 km/h
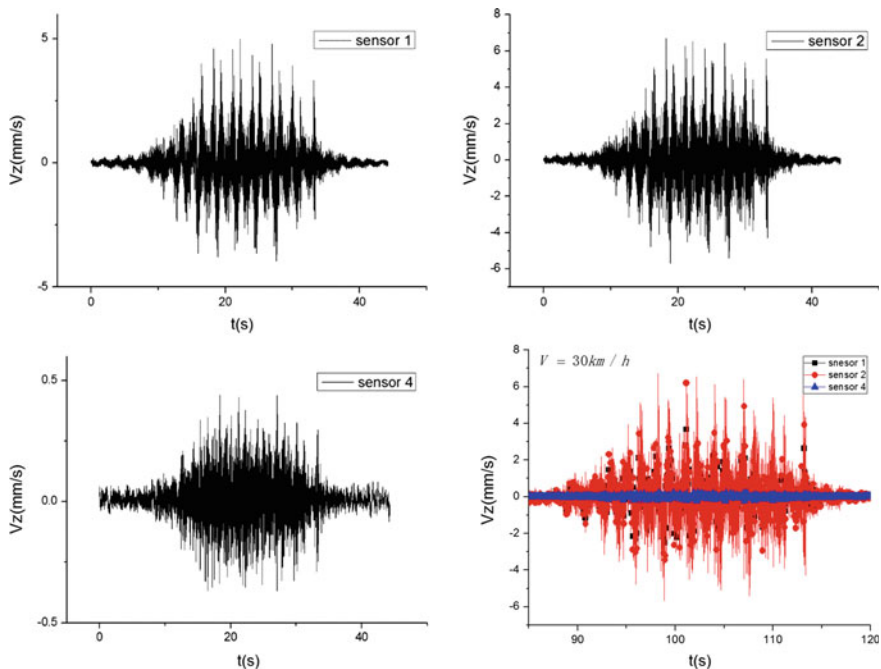
Fig. 6 Vibration response of different spots at 30 km/h

V = 20 km/h

Figure 7 shows the time-velocity curve for different texting spots at train speed of 20 km/h. The vibration induced by the moving train load is much smaller than that at former two train speeds. The peak value of vertical vibration velocity is only 4.5 mm/s on spot 2, and the response on spot 4 seems to have little regularity compared with that at train speeds of 40 and 30 km/h.

Figure 8 show the peak values of different sensors at three different speeds. It's obvious to see that track vibration grows up with the train speed increases. Spot 2 has the greatest vertical vibration velocity which is 0.25 m away from rail. On spot 4 the vibration velocity is always close to zero at three different speed.
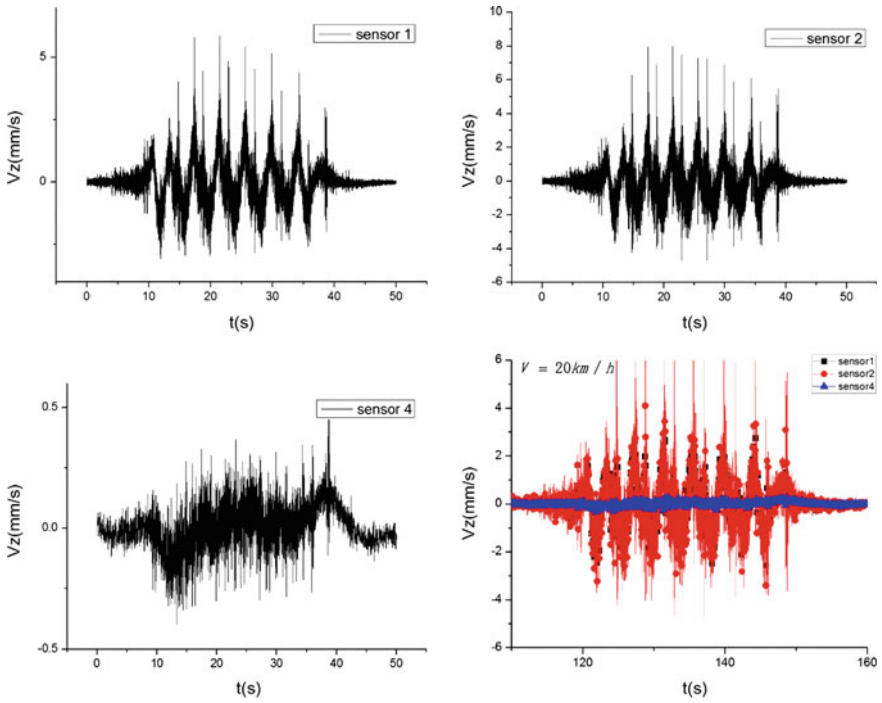
Fig. 7 Vibration response of different spots at 20 km/h

Fig. 8 Peak value of different sensors at three different speeds
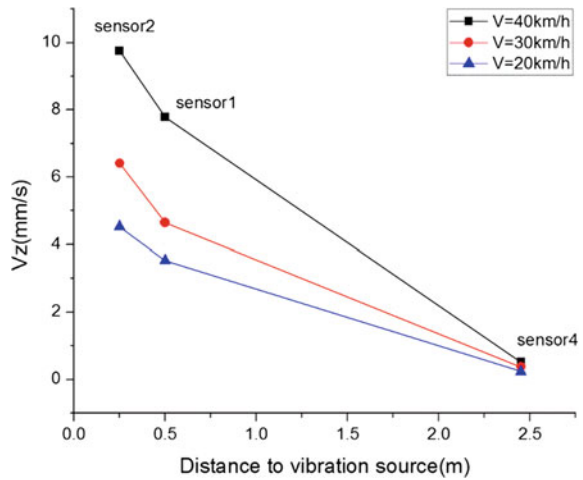
Conclusions

Train speed has a great influence on the intensity of track slab vibration. When subway train speeds up, vertical vibration of track slab become severe subsequently. It's mainly because that the growing train speed has aggravated the dynamic interaction between train wheel and rail.

Dynamic response induced by running car is mainly occurred on track slab. From the vibration data of spot 4, it's easy to see that vibration has degraded to a much lower level compared to that of track slab.

References

1. Pan, C.S., Li, D.W. (1995). A discussion of Beijing subway train induced impact on environment. Journal of Vibration and Shock, 14(4): 29–34.
2. Bian, X.C. (2005). Dynamic analysis of ground and tunnel responses due to high-speed train moving loads. [D]. Hangzhou: Zhejiang University.
3. Bian, X.C., Chen, Y.M. (2016). Ground vibration generated by train moving loadings using 2.5D Finite Element, Method. Chinese Journal of Rock Mechanics and Engineering, 25(11): 2335–2342.
4. Zhang. Y.E., Bai, B.H. (2000). Simulating of subway train vibration induced load on tunnel structure. Journal of Vibration and Shock, 19(3): 68–76.
5. Sun, X.J. (2008). Prediction of environment vibrations induced by metro trains and mitigation measures analysis. [D]. Beijing: Beijing Jiaotong University.
6. Yang, Y.B., Hung, H.H., Chang, D.W. (2003). Train-induced wave propagation in multi–layered soils using finite/infinite element simulation. Soil Dynamic Earthquake Engineering, 23 (4): 263–278.
7. Kurzweil, G. (1979). Ground borne Noise and Vibration from Underground Rail System. Journal of Sound and Vibration, 66(3): 363–370.
8. Lang, J. (1971). Result of measurements on the control of structure-borne noise from subways. Seventh International Congress on Acoustics. Budapest: 421–424.
9. Urgar, E. (1975). Vibrations produced in buildings by passage of subway trains: Parameter estimation for preliminary design. Inter-noise: 491–498.

Discrete Element Simulation Study of Contact Pressure Distribution Between Sleeper and Ballasts

Huahan Chen and Xuecheng Bian

Introduction

With the rapid development of economics in China, high-speed railway plays an increasingly important role in public transport. The larger loads and the stronger demand for riding comfort require more rigorous design criteria which bases on a better understanding of the track structure behavior, especially the behavior of sleepers, since sleepers play a crucial part in transmitting the rail seat loads to the ballast layer. Although there have been some theoretical and experimental researches into the distribution of contact pressure underneath sleeper, it is hard to predict the exact distribution under specific situations, for both sleeper's condition and ballasts' condition have an effect on the distribution. It is more efficient and more economical to develop a numerical model to analyze the distribution and its variation with different parameters.

Since railway ballast layer under sleepers consists of large particles and large void, it is hard to treat it as a homogeneous continuum. The Discrete Element Method (DEM) proposed by Cundall [1, 2] in 1971 is a numerical method for describing the mechanical behavior of a large number of particles. This method is suited for studying railway ballast due to its discrete structure. However, all of the elements in DEM including particle and wall are perfectly rigid. Thus, it is difficult to represent deformable sleepers in a discrete element simulation. In the model described later, a new bonded contact model based on the Timoshenko beam theory which considers axial, bending and shear behavior of the bond is introduced to bond a number of particles forming a deformable sleeper.

H. Chen (✉) · X. Bian
Department of Civil Engineering, Zhejiang University, Hangzhou 310058, China
e-mail: chenhuahan@zju.edu.cn

X. Bian
e-mail: bianxc@zju.edu.cn

Numerical Simulation

EDEM is a discrete element software that has the ability to simulate and analyze the behavior of bulk materials quickly and accurately. In EDEM, forces and moments, which are calculated from mutual displacement and rotation of individual particles according to a certain contact model, are used to compute the accelerations of each particle on the basis of Newton's Second Law. Then the velocities and displacements can be given by integrating the accelerations and the cycle restarts.

A contact model in EDEM describes how elements behave when they come into contact with each other. Using the EDEM API, custom contact models can be implemented as a User Defined Library. In order to represent flexible sleepers, a contact model [3, 4] called Timoshenko Beam Bond Model (TBBM) has been introduced in EDEM. The model has been shown to be suitable for modeling the behavior of cemented granular materials [3, 4]. In the TBBM cementitious material are represented by an assembly of particles which may interact at either non-bonded or bonded contacts. At a non-bonded contact the model calculates contact forces according to the well-used Hertz-Mindlin (no slip) contact law [5]. At a bonded contact a beam element is assumed to rigidly connect the centers of the two particles, so that each end of the beam shares the same degrees of freedom as the particle. The behavior of the beam bond follows the Timoshenko beam theory so that the bond can resist forces, bending and twisting moments.

DEM Model of Track Bed

The general layout of the model is shown in Fig. 1a. A sleeper is placed on the top of a ballast layer. The thickness of the ballast layer under the sleeper is 335 mm and the dimension in the train moving direction is only set as 0.4 m which is slightly larger than the width of the sleeper in order to save the computing time. Figure 1b gives information about the size of the sleeper in the model. For the convenience of choosing the bond's parameters and the computational efficiency, the height of the

(a) General size   (b) Size of the sleeper
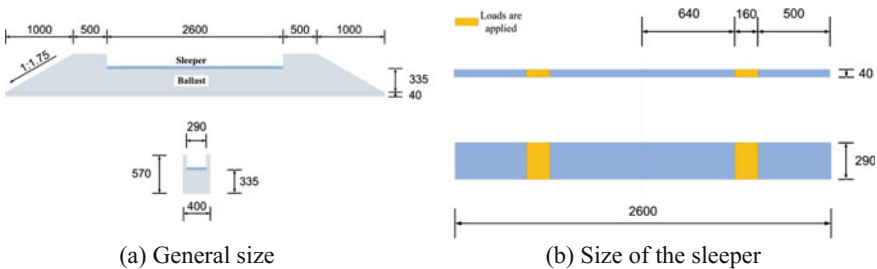
Fig. 1 Layout and size of the model

model sleeper is chosen to be 40 mm so that it only needs a layer of bonded balls to form the sleeper. The two yellow areas in Fig. 1b representing the positions of rail seats are where loads are applied.

Figures 2 and 3 show the 3D images of the EDEM model. The sleeper is formed by bonding spheres with the size of 40 mm in a plane according to the size shown in Fig. 1b. Only adjacent particles are bonded and the distance between adjacent particles is small enough to ensure that even the tiniest ballast underneath cannot pass through. The bond parameters of central part of the sleeper are different from the parameters of the other parts to simulate the rigidity difference existing in actual sleeper. The Young's Modulus of the bonds within the gray area in Fig. 3 is chosen to be 45,000 MPa, while the Young's Modulus of the other bonds is 90,000 MPa which is much higher. The values of the Young's modulus are chosen to make the model sleeper's rigidity close to the reality.

A total of 13,300 spheres with size distribution are generated to simulate the ballast layer. To roughly catch the size distribution used in practice, the particles with the size of 33, 44 and 55 mm are assigned with the percentage of 20, 60 and 20% of total ballast particles mass respectively. The ballast layer can be compacted by creating a plane on the top of the ballasts and pushing downward until specific packing density is achieved and every particle becomes stable.

As shown in Figs. 2 and 4, under the ballast layer, there are a layer of relatively soft spheres with the size of 40 mm in grid which can only allow every sphere to move upward or downward. Thus, the interlocking from the sub-ballast layer can be simulate by this boundary.

After sample preparation, vertical loads are applied on the sleeper by the means of setting body force to act on specific particles which are within the yellow areas in
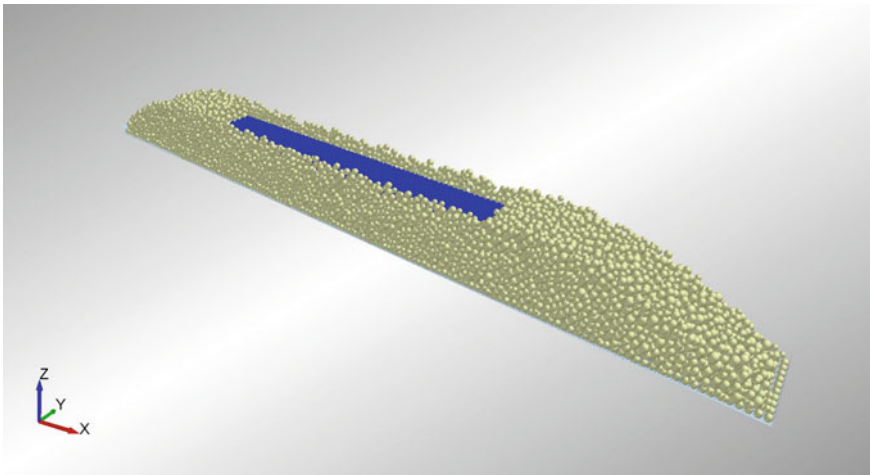
Fig. 2 Image of whole model
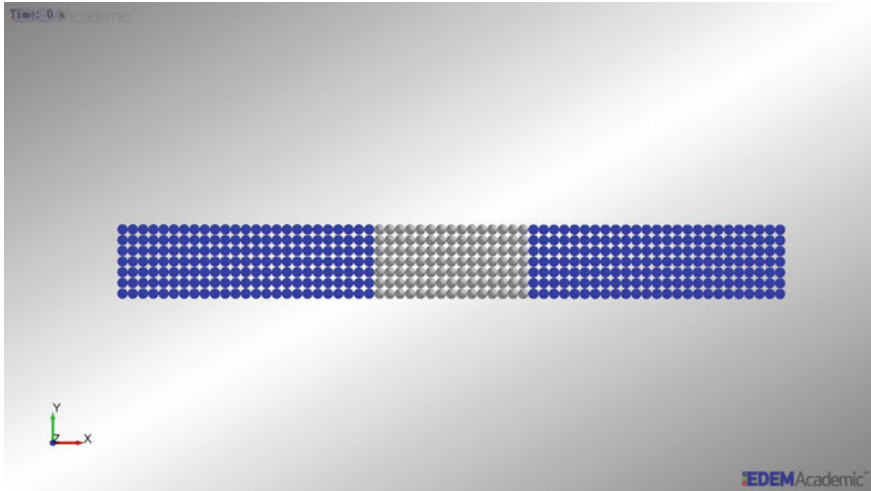
Fig. 3 Image of the sleeper. *The gray area* bonds of low Young's Modulus; *The blue areas* bonds of high Young's Modulus
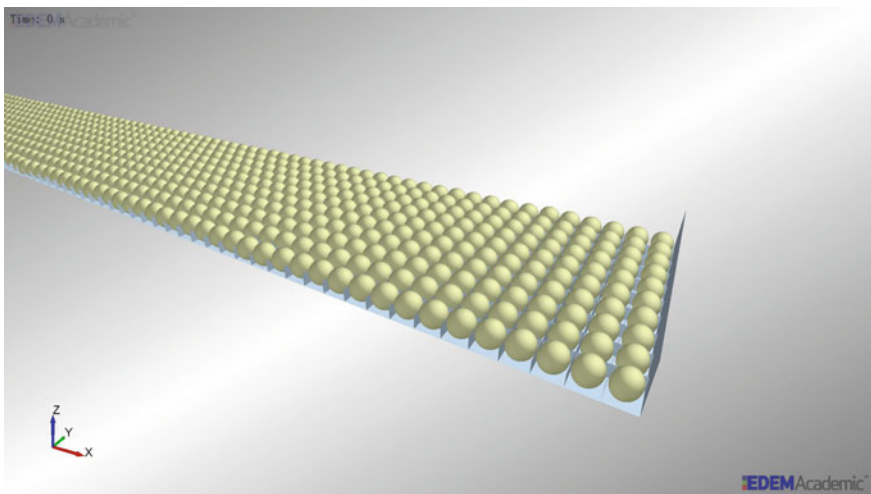
Fig. 4 Image of model bottom

Fig. 1b. During the first 0.05 s, the total force applied on the sleeper increases linearly from 0 to 72 kN. The force then remains unchanged until the simulation finishes.

The parameters for the particles, the contacts and the sleeper bonds are summarized in Tables 1, 2 and 3 respectively.

Table 1 Particle parameters

	Poisson's ratio	Density (kg/m^3)	Young's modulus (MPa)
Ballast particles	0.2	2600	4000
Sleeper particles	0.2	23,000	3600
Bottom particles	0.2	2000	85

Note The density of sleeper particles in the model is calculated from a real sleeper's mass, which makes the thin model sleeper have the same total mass with a real one

Table 2 Contact parameters

	Coefficient of restitution	Coefficient of static friction	Coefficient of rolling friction
Ballast particle-ballast particle	0.2	0.6	0.25
Ballast particle-sleeper particle	0.2	0.6	0.01
Ballast particle-bottom particle	0.2	0.6	0.25

Table 3 Bond parameters

	Poisson's ratio	Young's modulus (MPa)
Central part	0.2	90,000
The other parts	0.2	45,000

Note The Young's modulus is chosen to make the model sleeper's rigidity close to the reality

Results

After every particle is stabilized, the simulation can be stopped. Then the simulation data can be exported for analysis. Figure 5 shows the simulation results for the measured contact pressure between the sleeper and ballast layer along the sleeper length. In the graph, every node represents average pressure of an area on the bottom surface of the sleeper. For the two nodes at both ends, the area covers the length of 400 mm of the sleeper. For the other nodes, the area covers the length of 360 mm. It is clear that the pressure distribution is not uniform under this circumstance. The distribution doesn't have perfect symmetry about the center line of the sleeper. This is thought to be because the compaction of the ballasts under the sleeper is not even enough. However, the two half of the line graph still follow the same trend. The pressure increases from the edge of the sleeper and reaches its maximum value under the areas where force is applied. It then decreases until it gets to a minimum value at the center of the sleeper. This pressure distribution is compatible with the conclusions of an experimental research [6] in which the results show that the pressure
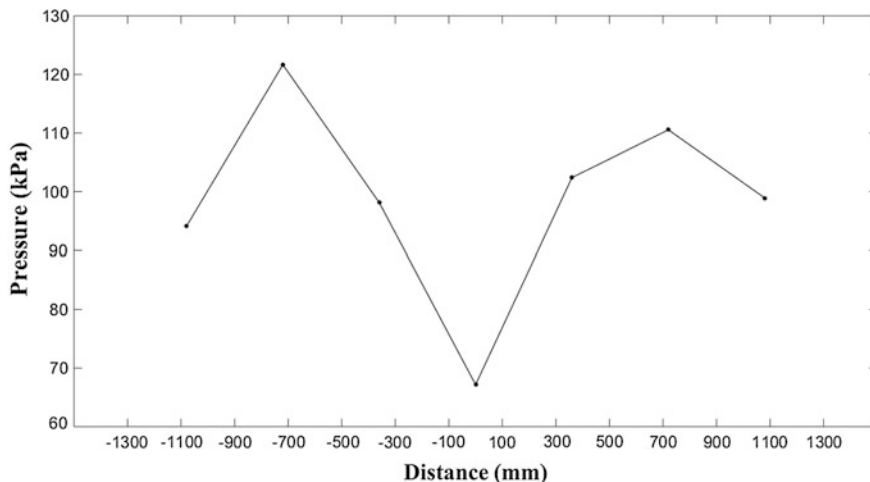
Fig. 5 Contact pressure distribution between the sleeper and the ballasts

distribution between the sleeper and the ballasts follow a parabolic shape, having a maximum value at the rail positions and a symmetrical pattern.

Conclusions

The discrete element method for measuring contact pressure between a sleeper and ballasts under static loads is introduced. A model of track bed with single sleeper and ballast layer is established. The results of it show that the contact pressure distribution between the sleeper and the ballasts follows a double-peak pattern where the maximal pressure occurs below each rail seat. This pressure distribution is compatible with the results of an experimental research in railway sleeper [6]. Although the model still needs to be elaborated and calibrated further, this work adds to the understanding of the behavior of sleepers used in service.

References

1. Cundall, P.A. (1971). A Computer Model for Simulating Progressive, Large-Scale Movements in Block Rock Systems. Symposium of International Society of Rock Mechanics (Vol. 1(ii-b), pp. 11–8).
2. Cundall, P. A., & Strack, O. D. L. (1979). A discrete numerical model for granular assemblies. Geotechnique (Vol. 29, pp. 47–65).

3. Brown, N., Chen, J. F., & Ooi, J. (2014). A bond model for dem simulation of cementitious materials and deformable structures. Granular Matter, 16(3), 299–311.
4. Brown, & John, N. (2013). Discrete element modelling of cementitious materials. University of Edinburgh.
5. Renzo, A. D., & Maio, F. P. D. (2004). Comparison of contact-force models for the simulation of collisions in dem-based granular flow codes. Chemical Engineering Science, 59(3), 525–541.
6. Sadeghi, J. M. (2008). Experimental evaluation of accuracy of current practices in analysis and design of railway track sleepers. Canadian Journal of Civil Engineering, 35(9), 881–893.

Seismic Response Analysis of Cylindrical Hollow Pier Based on Morison Equation

Huaxi Lu and Zhenwei Zhou

Introduction

With the development of transportation, numerous bridges have been built in recent years all over the world especially in China. These bridges are always under threat of earthquakes and hydrodynamic pressures when bridges are seated in the deep area of river and sea. When subjected to earthquake loads, the interaction between the bridge pier and the surrounding water induces hydrodynamic loads while affecting the natural frequencies and dynamic responses of the piers. Thus, the estimation of hydrodynamic force on deep-water bridge piers has received considerable attention from scholars and designers.

The Morison equation [1] assumed that the characteristics of the cylinder had no significant effect on wave motion, and considered that the wave force was made up of two components, named as: a drag force and an inertia force. This method has been widely used to estimate the wave force acting on offshore structures, the catenary anchor leg mooring system, submerged floating tunnels, bridge piers and so on [2–5]. It has been widely accepted that Morison equation is a considerable appropriate approximate method to evaluate the effect of hydrodynamic pressure on piers. A method for analyzing the effect of Fluid-structure Interaction on deep water bridge is proposed based on the Airy wave theory [6]. Literature [7, 8] studied the effect of hydrodynamic force on cable-stayed bridge based on Morison equation and presented a simple calculation method of hydrodynamic force for elevated pile caps.

H. Lu · Z. Zhou (✉)
Department of Civil Engineering and Architecture,
East China Jiaotong University, Nanchang 330013, China
e-mail: 7643674717@qq.com

H. Lu
e-mail: 782226042@qq.com

The current researches showing that the main methods to study the hydrodynamic pressure is Morison equation method, radiation wave method and fluid element method, the scope of the study has been extended from the cylindrical bridge pier to the different section of the bridge piers, from solid piers to the hollow piers.

Based on the Morison equation considering the dynamic water pressure, in the numerical calculation of bridge piers, it usually needs to make numerous simplifications. The bridge pier is simplified as a series of mass points, and the upper structure is simplified as the bar element model, leading to the narrow the Morison equation application range. In this paper, the bridge pier is built as a 3D solid element model, and the additional mass is applied to the nodes which are the most peripheral of the model. The seismic response of cylindrical solid pier in deep water are analyzed by three kinds of different methods which are the proposed method, relevant literatures method and fluid unit method, And the calculation results of the three methods are compared. Furthermore, the seismic response of cylindrical hollow bridge piers considering the dynamic water pressure is analyzed by proposed method, the natural frequency of bridge pier and internal force of the piers bottom are extracted to compare with the calculation results of the fluid element method. The results show that this proposed method is suitable for the analysis of outer water on seismic response of circular bridge hollow pier, and it has a high calculation precision.

The Morison Equation

Morison is applied on the premise that structure is to small too neglect the influence on water body, that is, the structure has no effect on the movement of the water body. When the Morison equation is used to analyze the effect of earthquake hydrodynamic pressure on the deep-water pier, the hydrodynamic pressure should be translated into the additional mass, and the seismic response of bridge pier structure is calculated by the finite element method. Based on the modified Morison equation, the nonlinear terms into linearity in proposed method

$$F = -M_W(\ddot{x} + \ddot{x}_g) - C_W(\dot{x} + \dot{x}_g) \tag{1}$$

where: defined $M_W = (C_M - 1)\rho \frac{\pi D^2}{4}$ as additional mass of hydrodynamic, defined $C_W = -\frac{1}{2}C_D\rho D\sigma_{x+x_g}\sqrt{\frac{8}{\pi}}$ as additional damping of hydrodynamic, $\dot{x}, \dot{x}_g$ are respectively as relative velocity and ground motion velocity of structure, the $\ddot{x}$ and $\ddot{x}_g$ are defined as the relative acceleration and ground motion acceleration respectively.

The dynamic response of the structure caused by hydrodynamic resistance is small, and which the maximum influence is not more than 2% [9]. So that the

influence of the C_W can be ignored, at this point, the dynamic equilibrium equation of the whole system under earthquake action is expressed as

$$[M + M_W]\ddot{x} + C\dot{x} + Kx = -[M + M_W]\ddot{x}_g \tag{2}$$

Therefore, the hydrodynamic pressure of the bridge pier can be converted to additional mass, and the additional mass applied to the bridge pier structure to complete the simulation of hydrodynamic pressure.

Literature [10] presented a method is used to calculate the earthquake hydro-dynamic pressure by Morison method since the foundation is assumed as rigid. The circular bridge pier is simplified as beam element which including number of N units, and the upper structure is simplified as lumped mass element. It is assumed that the relative velocity of two adjacent elements between water and structure are immovability, and each node is subjected to half of the force of the unit, the equivalent mass of the water at the node is expressed as

$$M_{iW} = \sum (C_M - 1)\rho V l_{ij} \tag{3}$$

where: nodes of i and j are adjacent, and l_{ij} is a half of the effective length of ij element.

In proposed method, the additional mass is calculated by the formula of Morison equation and it is applied on the outside-wall of the finite element model of the bridge pier, which of the cylindrical bridge pier is simulated by Solid65 element in numerical tests, at this point, the equivalent mass of water at any node in the model is expressed as

$$M_{iW} = (C_M - 1)\rho h \frac{\pi D^2}{4} / n \tag{4}$$

In the formula, h is the water depth of bridge pier, and n is the total number of the outside-wall nodes of the model.

Seismic Response Analysis of Circular Bridge Piers

The Establishment of Calculation Models

In organization.10, bridge piers are established by beam188 element which is divided into N units, and mass unit are established by mass21 unit. Bridge pier is established by Solid45 unit and quality unit is still modeled by mass21 in proposed method. While the water body of the fluid element method is simulated by Fluid30 and Fluid130 units. Concrete density of pier is $\rho_1 = 2400$ kg/m^3, elastic modulus is $E = 3.0 \times 10^{10}$ Pa, Poisson ratio is $\upsilon = 0.2$, the damping is Rayleigh damping

(a) The model based on proposed method

(b) The model based on fluid unit method
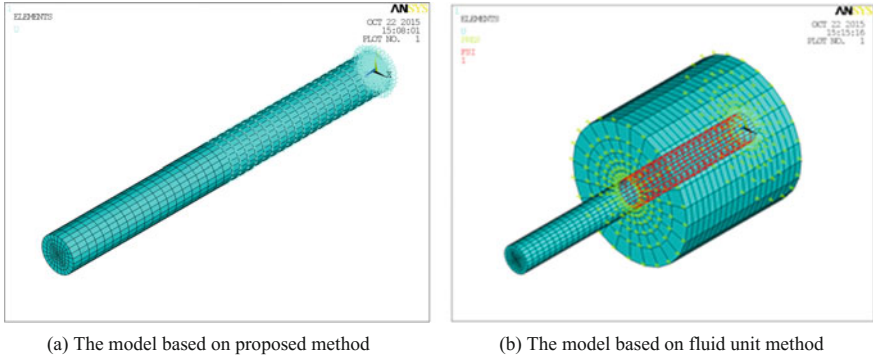
Fig. 1 Three-dimensional finite element models of bridge pier

which it is 0.05, the density of water is $\rho_2 = 1000$ kg/m^3, sound speed in water is $v = 1460$ m/s, bridge pier height is h = 40 m, radius is r = 2 m, finite element model of cylindrical pier based on proposed method and fluid element method are shown in Fig. 1.

Seismic Wave Selection

Along the horizontal direction of the Tianjin seismic wave is selected, peak acceleration time interval, seismic duration are respectively as 104.18 cm/s^2, 0.01 s, 19.20 s, and predominant frequency is 0.962 Hz, the Fourier spectrum of Tianjin wave is shown in Fig. 2.

Fig. 2 The Fourier spectrum of Tianjin wave
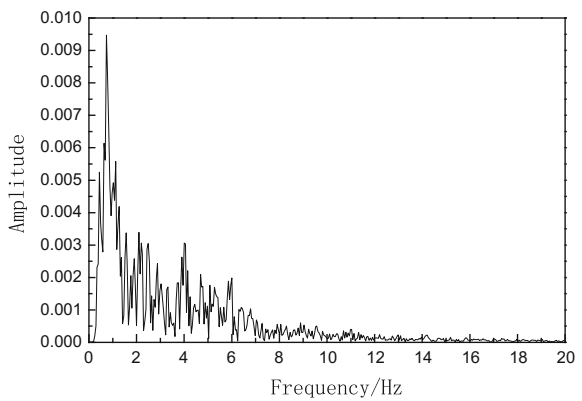
Seismic Response Analysis

In order to research the influence of hydrodynamic pressure on the seismic responses of deep-water pier and to verify the calculation accuracy of the proposed method, the peak value of shear, bending moment and pier top displacement are extracted by three methods. As the accuracy of fluid element method is the highest, it will be used as a comparative reference.

While the bridge pier in the case of different water depth, Fig. 3 show the peak values of internal force response and pier top displacement at the different water deep of pier by the above three methods respectively. The results show that the calculation results of the three methods are very close when the water depth is less than 15 m; compared with the calculation results of organization.10 method, the calculation results of this proposed method are much closer to the calculation results of the fluid element method; the maximum error of he peak value of shear, bending moment and pier top displacement during these two methods are respectively as 5.4, 4, 4.5%.

From the above analysis results can be drawn: the seismic response of bridge piers can be influenced by the existence of water, the calculation results of seismic

(a) The peak shear of pier bottom   (b) The peak bending moment of pier bottom

(c) The peak displacement of pier top
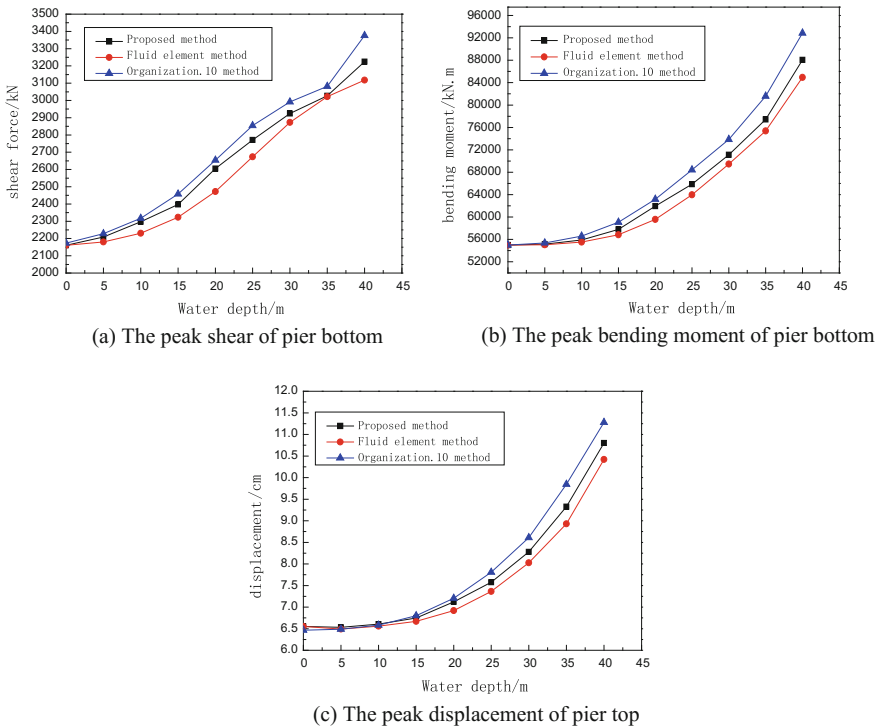
Fig. 3 The peak seismic response of cylindrical pier

response of bridge piers with the above three kinds of numerical methods are completely consistent, and the deviation is small; compared with the calculation results of fluid element method, the influence of hydrodynamic pressure on seismic response of bridge piers is overestimated by based on Morison equation; the calculation results of this proposed method are more close to the calculation results of fluid element method, and the calculation accuracy is higher than organization.10 method.

Seismic Response Analysis of Circular Hollow Piers

Due to Morison equation can only be used for solving the additional mass emerged from outland water, so this section only discuss the hollow pier which it is only considering the influence of outer water. This research of seismic response of hollow bridge piers in deep water is studied by proposed method, and the calculation results of the fluid element method are still used as a reference to discuss the rationality of this proposed method. The model of circular hollow pier with its height of 40 m, and the inner and outer diameter are 2 and 0.8 m respectively.

Analysis of Natural Vibration Characteristics

Due to circular hollow pier, the first and second frequencies are equal, and the vibration mode is the same and orthogonal. Thus, the first and third natural frequencies of circular hollow pier with different water depth are compared by this proposed method and fluid element method, to verify the rationality and validity of this proposed method. The calculation results are shown in Table 1.

The simulation results show the natural frequency of the cylindrical hollow bridge piers is gradually smaller with the increase of water depth, and the natural

Table 1 The natural frequency comparison of hollow piers

Water depth (m)	First modal (Hz)		Second order (Hz)	
	Proposed method	Fluid unit method	Proposed method	Fluid unit method
0	1.3174	1.3174	7.9247	7.9247
5	1.3173	1.3174	7.9180	7.9227
10	1.3166	1.3170	7.8214	7.8746
15	1.3124	1.3147	7.5286	7.6697
20	1.2966	1.3059	7.1633	7.3107
25	1.2716	1.2848	6.9433	7.0034
30	1.2235	1.2452	6.9024	6.9222
35	1.1522	1.1847	6.8305	6.8919
40	1.1073	1.1089	6.4630	6.7031

frequencies calculated by these two methods are very close, the results calculated by this method are slightly faster while compared with fluid element method, but the maximum error is no more than 3.6%. It is shows that the proposed method can be used to research the effect of hydrodynamic pressure on seismic response of cylindrical hollow piers in deep water.

Seismic Response Analysis

Figure 4 show the peak values of internal force response and pier top displacement at the different water deep of hollow pier by the above two methods respectively, it can be found that the increase of the peak values of shear, bending moment and pier top displacement are completely consistent under the same conditions, and the calculation results of this proposed method are slightly larger than that of the fluid element method. The calculation results of the two methods are very close, the maximum error of the peak values of shear, bending moment and pier top displacement are 5.6, 5.6 and 5.3% by the above two methods respectively.

(a) The peak shear of pier bottom

(b) The peak bending moment of pier bottom

(c) The peak displacement of pier top
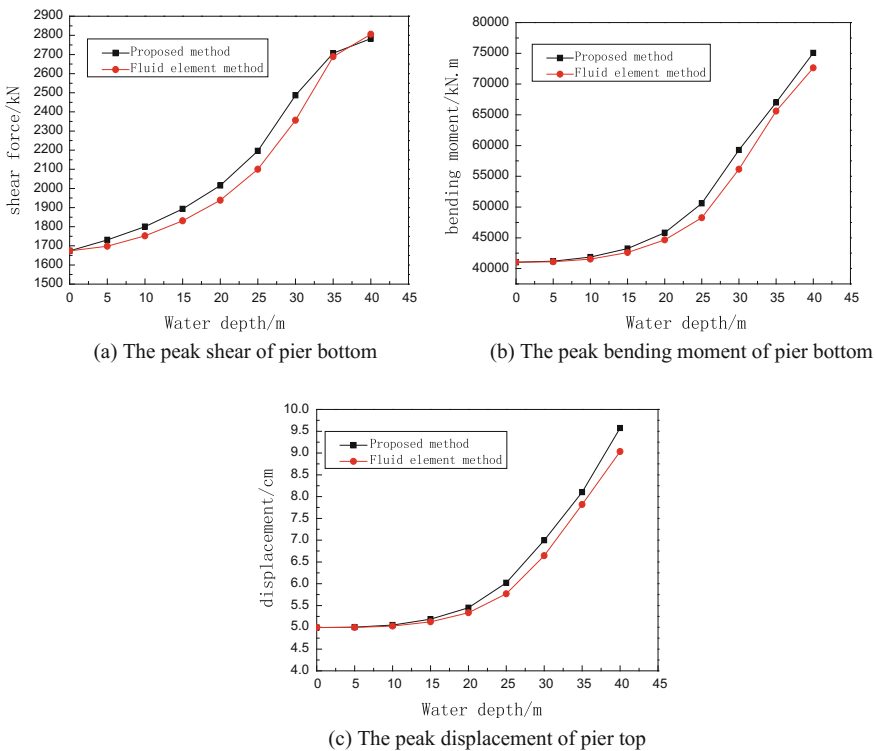
Fig. 4 The peak seismic response of circular hollow pier

The results show that the proposed method can be used in solver the effect of the outer water on the seismic response of hollow pier, and its accuracy is kept in good rank. While the "added mass" of this method is based on the solution of the Morison equation, the influence will overestimate the impact of hydrodynamic pressure on the seismic response of hollow bridge pier in deep water by compared with the fluid unit method while the pier radius is too large.

Conclusion

The proposed method based on the Morison equation, which transformed the hydrodynamic pressure into additional mass to simulate the influence of hydrodynamic pressure effect on seismic response analysis of deep water pier, and compared with the results of different methods. Examples include deep water cylindrical piers and cylindrical hollow piers, the peak values of shear, moment and pier top displacement at the different water deep of pier are extracted for comparative analysis, obtained the following conclusions.

Three numerical methods has taken to analysis the effect of hydrodynamic pressure on seismic response of bridge piers, results shows that the effect is very significant, in the seismic design of bridge piers, the influence of water body should be considered. Compared with the calculation results of the relevant literature method, this proposed method is more close to the calculation results of the fluid element method, with high calculation precision.

The effect of hydrodynamic pressure on seismic response of circular hollow pier has analyzed by the proposed method and fluid element method, the calculation error of two methods of the natural frequency and dynamic response are very small, the feasibility and correctness of the inversion method can used to analyze the seismic response of hollow pier for outer water has verified.

The effect of hydrodynamic pressure on bridge pier is simulated by applying the "additional mass" in this proposed method, which will be overestimated the effects while the pier diameter is too large for both circular solid and hollow piers.

References

1. Morison, J.R., O'Brien, M.P., Johnson, J.W., Schaff, S.A., 1950. Forces exerted by surface waves on piles. Pet. Trans., AIME 1950, 189.
2. Sarpkaya, T., 1986. Force on a circular cylinder in viscous oscillatory flow at low Keulegan–Carpenter numbers. J. Fluid Mech. 165, 61–71.

3. Sagrilo, L.V.S., Siqueira, M.Q., Ellwanger, G.B., et al., 2002. A coupled approach for dynamic analysis of CALM systems. Appl. Ocean Res. 24, 47–58.
4. Hiroshi, K., 2010. Evaluation of wave force acting on submerged floating tunnels. ISAB-2010, Procedia Eng. 4, 99–105.
5. Lei, F., Yang, J.X., Liu, H. (2011). Dynamic response analysis of deepwater pier with fluid–solid interaction. Adv. Mater. Res. 168–170, pp 161–166. (in Chinese).
6. Liu, C.G., Qi, N. (2009). Seismic response analysis of piers in deep water considering Fluid-Structure Interaction. Journal of Disaster Prevention and Mitigation Engineering, 2009, 29(4): 433–437. (in Chinese).
7. Li, Y., Song, B. (2010). Study of the effect of hydrodynamic force on cable-stayed bridges under earthquake. China Civil Engineering Journal, 2010 (12): 94–99. (in Chinese).
8. Song, B., Li, Y. (2011). Simplified calculation method of hydrodynamic force for elevated pile caps. Journal of University of Science and Technology Beijing, 2011, 33(4): 509–514. (in Chinese).
9. Yuan, Y.C., Lai, W., Wang, J.J., Hu, S.D., The effect of hydrodynamic damping on seismic response of bridge piles. World Earthquake Engineering, 2005, 21(4): 88–94. (in Chinese).
10. Gao, X.K., Zhu, X., Hydrodynamic effect on seismic response of bridge pier in deep water. Journal of Beijing Jiaotong University, 2006, 30(1): 55–58. (in Chinese).

Experimental Study on Vibration Decay Rate Characteristics and Improvement for Beijing Metro

Jialiang Chen, Weining Liu and Weifeng Liu

Introduction

Urban rail transit has achieved remarkable development in China recently. It provides great convenience for the public and promotes urban development. However, environmental vibrations and noise problems induced by metro operation have been paid much attention [3]. These concerns are mostly relative to wheel/rail interaction. Thus, research on the interaction between the wheels of metro vehicles and the rails of track during operation appears especially important. The DR express the dynamic behavior directly which can be measured for an estimation of the dynamic behavior of a track [1].

Beijing metro network is intensive now with vary track forms, to satisfy different vibration or noise abatement demands. Five or more track forms are included in one Beijing metro line, such as Line 6 and Line 10. Meanwhile, an estimation of vibration propagation properties for those different track forms along rails is absent. Field measurements for decay rates of different track forms of Beijing metro are carried out, including standard track with DTVI2 fasteners, Egg fastening system track un/installed with rail dampers, and ladder track.

J. Chen (✉) · W. Liu · W. Liu
Department of Civil Engineering, Beijing Jiaotong University, Beijing 100044, China
e-mail: jialiang_chen@sina.cn

W. Liu
e-mail: wnliu@bjtu.edu.cn

W. Liu
e-mail: wfliu@bjtu.edu.cn

Decay Rates

The definition of decay rate is that: vibration amplitude decay rate of the vertical or transverse bending waves of the rail as a function of the distance along the rail. It is represented by a one-third octave band spectrum of the values of the decay rate, expressed in decibels per meter (dB/m) representing the attenuation as a function of the distance.

Calculation

If $A(x)$ corresponds to the amplitude of an FRF in a one-third octave band at a point on the rail head at a distance of x, the power radiated by the rail is proportional to the FRF of the excitation of the wheel/rail contact

$$\int_0^\infty |A(x)|^2 \mathrm{d}x \tag{1}$$

Assuming that the vertical and lateral waves in the rail decrease as a function of the distance along the rail, then

$$A(x) \approx A(0)e^{-\beta x} \tag{2}$$

β can be converted into a decay rate expressed in dB/m, *DR*, such that
$$DR = 20\log_{10}(e^\beta) = 8686\beta \tag{3}$$

Then, $\int_0^\infty |A(x)|^2 \mathrm{d}x$ is expressed simply as a function of the decay rate of the vertical and lateral wave by the equation:

$$\int_0^\infty |A(x)|^2 \mathrm{d}x = |A(x=0)|^2 \int_0^\infty e^{-2\beta x}\mathrm{d}x = |A(x=0)|^2 \frac{1}{2\beta} \tag{4}$$

In principle, the decay rates can be estimated as a slope of the amplitude response curve in dB as a function of the distance x. In practice, however, because of the simplifying assumption of a rail response, expressed as the superposition of a vertical bending wave and a transverse bending wave, the actual change in amplitude as a function of the distance differs by a simply exponential decrease. In these conditions, it is preferable to evaluate the decay rate based on a direct estimation of the accumulated response:

$$\int_{0}^{\infty} \frac{|A(x)|^2}{|A(x_0 = 0)|^2} dx = \frac{1}{2\beta} \approx \sum_{n=0}^{n_{max}} \frac{|A(x_n)|^2}{|A(x_0)|^2} \Delta x_n \tag{5}$$

The decay rate in each one-third octave band may then be estimated with the formula:

$$DR \approx \frac{4.343}{\sum_{n=0}^{n_{max}} \frac{|A(x_n)|^2}{|A(x_0)|^2} \Delta x_n} \tag{6}$$

where x_n is one set of points at which the response is sampled and n_{max} is linked to the point at distance x_{max} which is the maximum measuring distance, and where the summation is carried out at the response measurement points with Δx_n corresponding to the interval between the points situated at half-distance between the measuring positions on either side of the excitation position. The last distance interval Δx_{max}, at position max x, shall be taken as symmetrical to position x_{max}. The interval linked to $A(x_0 = 0)$ shall be regarded from position $x = 0$ to midway between this point and the adjacent point, as the integral expression implicitly assumes.

Measurement Process

The test section of the measurement should be selected cautiously, that the constitution of the track shall be constant over the whole test section for all the parameters that could affect the decay rates, and any rail expansion joints can not exist in the selected section.

Position of the accelerometers should meet the requirements of the specification as well, and be settled at the position x_0 for practical consideration. The vertical accelerometers may either be on the center position of rail head or rail bottom, and the transverse accelerometers may either be on the transverse position of rail head one side or the other (As shown in Fig. 1).

The specification also rules the positions of excitation force. The excitation force is actualized by hammer impact. Vertical and transverse forces should be loaded on the positions of cross-section of the rail as Fig. 1. On the direction along rail, loading positions of vertical and transverse forces are specified as Fig. 2.

A force pulse is applied to the rail head in the vertical and transverse directions with an instrumented hammer fitted with a tip of adequate rigidity to ensure a good quality measurement of the force and the response in a frequency range of interest.
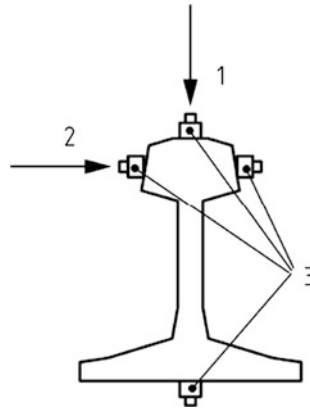
Fig. 1 Position of the accelerometers on the cross-section of the rail (*1* vertical force; *2* transverse force; *3* accelerometers)
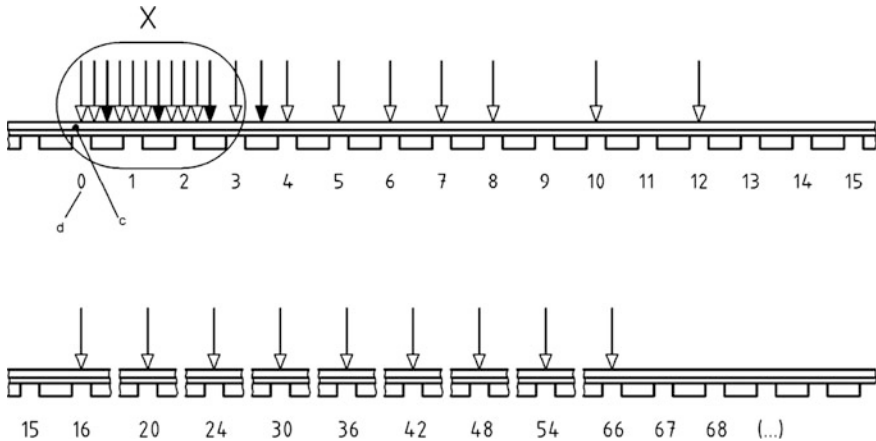
Fig. 2 Positions of hammer impact

And high precision data acquisition system is needed, including data acquisition instrument and acceleration sensor mainly. Major equipment for data acquisition are listed in Table 1.

In the process of measurement, the position of each exciting point is identified accurately on rail head. Each position is hammered three times to ensure the reliability of data. Field test is shown as Fig. 3.

The typical excitation force and the spectrum in the measurement of *DR* are shown as Fig. 4. Three hammering signal should be kept stable, and attenuation of high frequency should be kept to a certain extent. Coherence coefficient of out/input transfer function should be kept beyond 0.8 (as Fig. 5), to guarantee the accuracy of data results [4].

Table 1 Major equipment for data acquisition

No.	Information	Picture
1	INV3018C-type 24-bit high-precision data acquisition instrument	
2	LC-series acceleration sensor	
3	Instrumented impact hammer (DYNAPULSE 5800B4)	
4	Computer	

Fig. 3 Field data acquisition (the portrait rights have been granted)

Analysis of Measured Results

Field measurements for decay rates of different track forms of Beijing metro are carried out. The tracks include: standard track with DTVI$_2$ fasteners un/installed with rail dampers, Egg fastening system track un/installed with rail dampers, and ladder track. These test sections are selected in three metro lines (including L 6, L 10 and L Yizhuang), certain model and representativeness are fully considered.

(N) [1:锤击力] 全程波形图

(N) [1:锤击力] 单峰值谱 光标:A:5.13617

Fig. 4 Typical excitation force and the spectrum

(g/N) [1 & 2] 幅值 光标: Nc=3201,f=5000Hz,H=0.00257

(°) [1 & 2] 相位 光标: Nc=3201,f=5000Hz,Ph=58.0308

[1 & 2] 相干 光标: Nc=3201,f=5000Hz,Co=0.93917
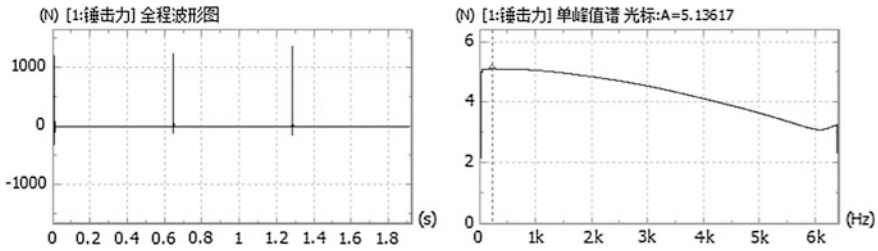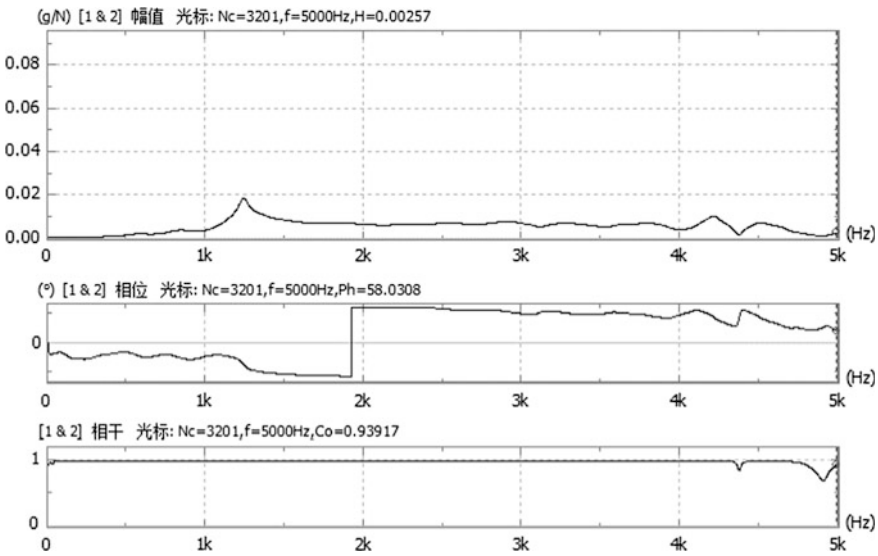
Fig. 5 Typical transfer function

The whole results are compared with the limit of track decay rates (TRD-limit) suggested in *TSI-NOI* (short for 'the technical specifications of interoperability relating to the subsystem 'rolling stock—noise' of the trans-European conventional rail system'). The results of *DR* measurements are as follows.

Standard Track with DTVI2 Fasteners Un/Installed with Rail Dampers

The test section of Standard track with $DTVI_2$ fasteners un/installed with rail dampers is selected in a straight line segment. The vehicle is passing at uniform speed of 90 km/h.

As shown in Figs. 6 and 7, the vertical *DR* of the standard track with DTVI$_2$ fasteners measured is lower than 1 dB/m on the band of 200–4000 Hz; the transverse *DR* is lower than 1 dB/m almost at whole frequencies. The vibration of this system can not be decayed regularly in both directions.

Installing with rail dampers, the vertical *DR* of the standard track with DTVI$_2$ fasteners is raised exponentially at frequencies larger than 200 Hz, the transverse *DR* is raised at whole frequencies concerned. However, vertical *DR* is reduced on the band of 80–160 Hz comparing with uninstalling condition.
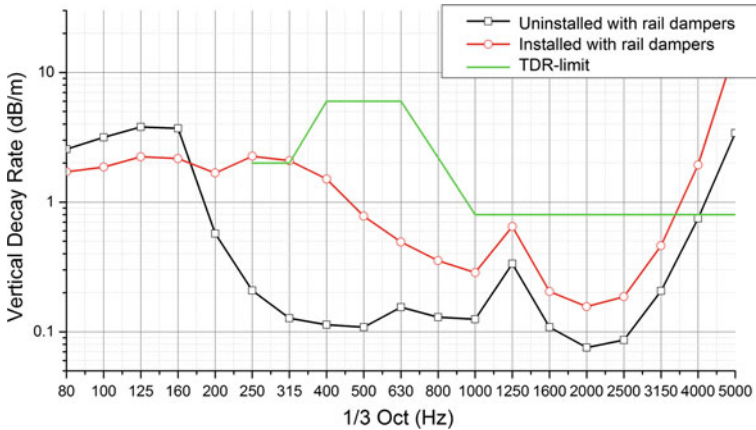
Fig. 6 Vertical decay rate of the standard track with DTVI2 fasteners un/installed with rail dampers
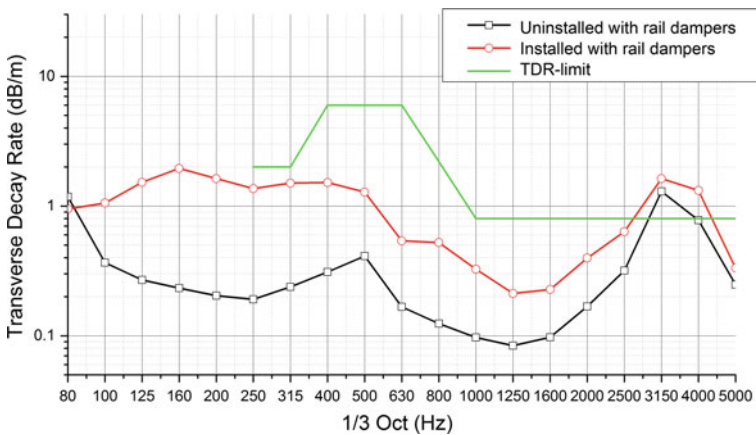
Fig. 7 Transverse decay rate of the standard track with DTVI2 fasteners un/installed with rail dampers

Although the TDR-limits of TSI-NOI is for pass-by noise test, they provide an angle to estimate the dynamic condition of track. From the figures, the vertical and transverse *DR* are both hard to meet the requirements. In other words, the vibration propagation characteristics of the standard track with DTVI$_2$ fasteners measured are not good.

Egg Fastening System Track Un/Installed with Rail Dampers

The test section of the Egg fastening system track un/installed with rail dampers is selected in a curve segment (radius = 600 m). The vehicle is passing at uniform speed of 60–70 km/h.

As shown in Figs. 8 and 9, the vertical *DR* of the Egg fastening system track measured is lower than 1 dB/m except at 800 Hz, even lower than 0.1 dB/m at the
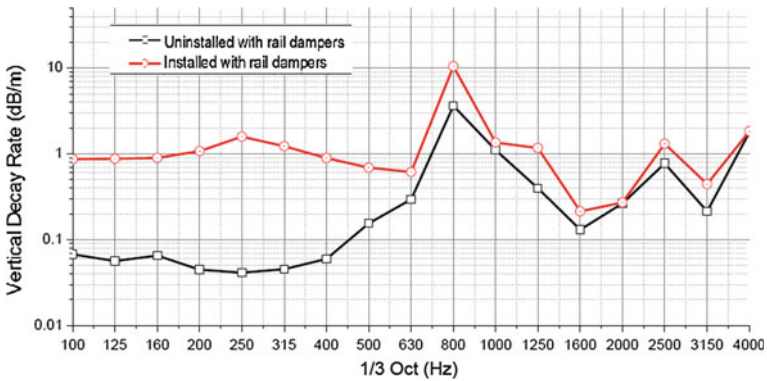
Fig. 8 Vertical decay rate of the egg fastening system track un/installed with rail dampers
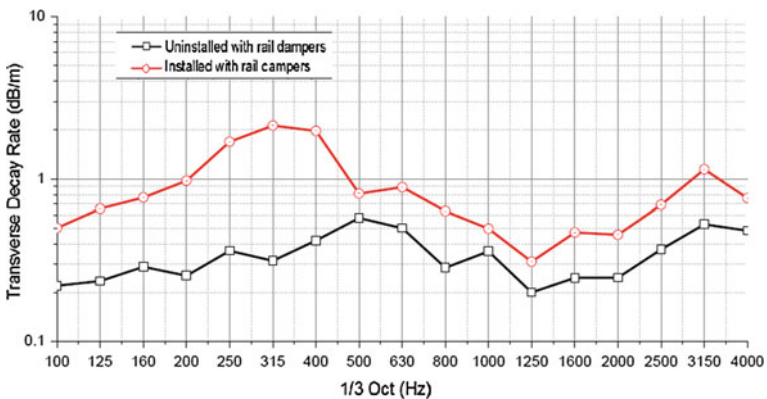
Fig. 9 Transverse decay rate of the egg fastening system track un/installed with rail dampers

frequencies under 400 Hz; the transverse *DR* is lower than 1 dB/m almost at whole frequencies, but all higher than 0.2 dB/m and the curve shows the stability. The wheel and rail anti/resonance at the frequencies of 100–400 Hz is regarded as the reason to abnormal rail corrugation and noise problems [5, 6]. However, the track system vibration can not be decayed effectively on the band. This may explore a way to solve the problems.

Installing with rail dampers, the vertical and transverse *DR* of the Egg fastening system track are both raised exponentially at frequencies of 100–500 Hz. The contact between rail and wheel is effectively improved.

Ladder Track

The test section of the ladder track is selected in a straight line segment. The vehicle is passing at uniform speed of 70–80 km/h.

As shown in Figs. 10 and 11, the vertical *DR* of the ladder track measured is lower than 1 dB/m at whole frequencies, but higher than 0.1 dB/m, and peak amplitude appears at 400 and 4000 Hz; the transverse *DR* is lower than 1 dB/m almost at whole frequencies except at 315 Hz with peak amplitude of 2 dB/m, and higher than 0.1 dB/m. The vertical and transverse *DR* are both hard to meet the requirements of TRD-limit.
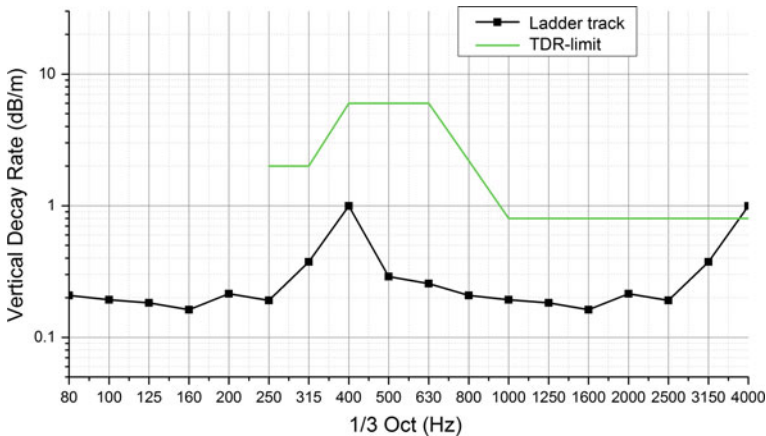
Fig. 10 Vertical decay rate of the ladder track
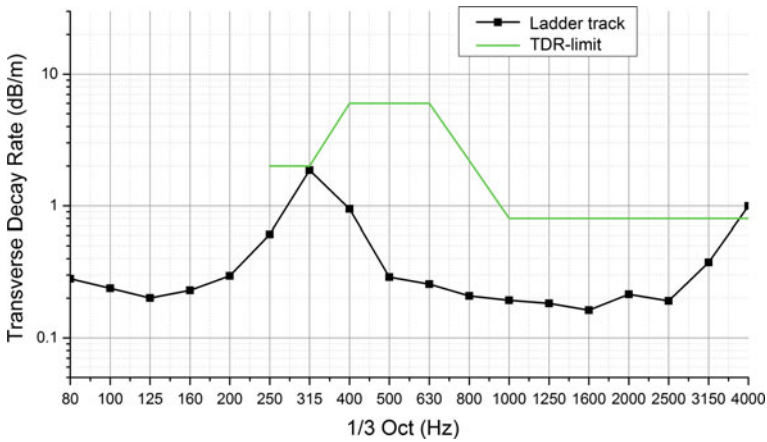
Fig. 11 Transverse decay rate of the ladder track

Conclusions

DR field measurements of different track structure forms are carried out to vibration propagation behaviors of tracks for Beijing metro. Including standard track with $DTVI_2$ fasteners un/installed with rail dampers, Egg fastening system track un/installed with rail dampers, and ladder track. Measurement results analyzed before come the following conclusions.

Installing with rail dampers can improve the *DR* characteristics for tracks in some frequency bands. The vertical and transverse *DR* are both improved at most frequencies, but vertical *DR* is reduced on the band of 80–160 Hz comparing with uninstalling condition. The vertical and transverse *DR* of the Egg fastening system track are both raised at different levels.

Some bad wheel/rail contact may be induced by the deficiencies of *DR* characteristics at some frequencies of tracks. The deficiencies of *DR* of Egg fastening system track at frequencies of 100–500 Hz should be improved to solve problems.

Comparing with lower limits of TSI-NOI may conduct the optimization of track structure. Those Beijing metro track forms analyzed above may be improved regarding the lower limits as target, to improve the contact between wheel and rail.

References

1. B. S. Institution. BS EN 15461:2008+A1:2010 Railway Applications- Noise Emission – Characterization of the Dynamic Properties of Track Selections for Pass by Noise Measurements [S]. BSI, 2010.
2. Concerning Technical Specifications of Interoperability relating to the Subsystem 'rolling stock–noise' of the trans-European conventional rail system [J]. Official Journal of the European Union, 2011, L99/1–39.

3. He Xia, Yanmei Cao. Problem of railway traffic induced vibrations of environments [J]. Journal of Railway Science and Engineering., 2004, 1(1):44–51.
4. D. J. Thompson, N. Vincent. Track Dynamic Behaviour at High Frequencies. Part 1: Theoretical Models and Laboratory Measurement [J]. Vehicle System Dynamics: International Journal of Vehicle Mechanics and Mobility, 1995(S24): 86–99.
5. Hougui Zhang, Weining Liu, etc. Study on the cause and treatment of rail corrugation for Beijing metro [J]. Wear, 2014, Vol. 317 (1–2).
6. Weifeng Liu, Weining Liu, etc. A Test Study on Treating Rail Corrugation for Egg Fastener in Beijing Metro [J]. Journal of Mechanical Engineering, 2015, 51(21):73–79.

Numerical Analysis of Dynamic Stress Response to Moving Load Using Infinite Element and Visco-elastic Boundary

Jiangu Qian, Jingliang Zhang and Zhiguo Lin

Introduction

The velocity of moving loads has a remarkable impact on dynamic stresses in an infinite half-space, causing big differences between dynamic stresses and static stresses. It's therefore important to predict dynamic stresses in the ground precisely and efficiently, which can be useful in bearing capacity analysis, shakedown analysis, etc. Analytical solutions [1, 2] are still widely used today as benchmarks because of their accuracy, which are limited to solve simple problems in terms of load type and soil geometry. The development of computer technology and numerical methods provide alternative ways to predict dynamic stresses, which must be able to model the infinite half-space effectively. The boundary element method (BEM) is an efficient numerical method, but the difficulty in finding the correct solution for each case limits its use to linear formulations and simple geometries. The finite element method (FEM) can tackle problems with complex soil geometries and constitutive models, making it widely used in numerical analysis and engineering [3], especially with the help of commercial finite element software, such as ABAQUS [4–6]. The key problem is to choose proper boundary conditions, which can minimize the influence of the reflection of the waves at the boundary. Among them, several local boundaries are widely used such as the viscous boundary [7], the visco-elastic boundary (VEB) [8, 9], the Sommerfeld

J. Qian (✉) · J. Zhang · Z. Lin
Department of Geotechnical Engineering, Tongji University, Shanghai 200092, China
e-mail: qianjiangu@tongji.edu.cn

J. Zhang
e-mail: jingliangzhang@outlook.com

Z. Lin
e-mail: linzhiguo1990@163.com

boundary [10], the Clayton-Engquist boundary [11], the infinite element boundary (IEB) [5, 6]. Previous work was mainly devoted to ground vibrations or fixed vibration source, but few was concerned with dynamic stress response considering velocity effects of moving loads.

This paper chooses the most widely used artificial boundaries, the IEB and the VEB, to analyze the impact of the velocity of the moving loads on dynamic stresses. Two similar models are developed in the commercial finite element software ABAQUS, which both have the same finite element interior domain and have different boundary conditions. The calculated dynamic stresses under moving loads of different velocities are then compared with analytical solutions to validate these methods.

Concepts of IEB and VEB

To minimize the reflection of the waves, it's crucial to select a suitable boundary to predict the dynamic stresses subjected to moving loads, including the geometric shape and the material properties, which will be briefly introduced in this section.

The Concept of the IEB

The infinite element formulation includes the mapping of the element from finite to infinite domain and the decay functions together with the finite element shape function [5]. The commercial finite element software ABAQUS adopts infinite elements which satisfy the above needs to simulate an infinite domain, so Boussineq's solution can be achieved in static analysis. To attenuate the reflection of the incident waves, ABAQUS adds viscous boundaries between finite and infinite elements automatically in dynamic analysis, which can be expressed as follows:

$$\sigma = a\rho c_p v_n \tag{1}$$

$$\tau = b\rho c_s v_t \tag{2}$$

where σ and τ are the normal and shear stress; a and b are dimensionless parameters; ρ is the medium density; c_p and c_s are longitudinal wave velocity and shear wave velocity; v_n and v_t are the normal and shear velocities of the boundary.

According to Kouroussis et al. [6], when $a = b = 1$, the maximum of absorption of longitudinal and shear waves can be obtained, which is also adopted in ABAQUS. Cooperated with the viscous boundary, the IEB provides an effective way to predict dynamic stresses in an infinite half-space, and no additional parameters need to be selected in ABAQUS.

Fig. 1 The propagation
modes of stress waves
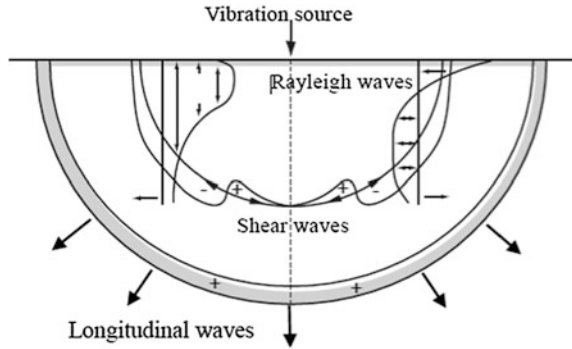
Considering the propagation modes of longitudinal waves (*P*-waves) and shear
waves (*S*-waves), Fig. 1, Kouroussis [5, 6] finds that the incident angel plays an
important role in energy absorption and suggests a half-sphere as an effective
boundary, which absorb most waves and can be meshed simply without affecting
the interior finite element model.

The Material Properties of the VEB

Liu et al. [9] derive three-dimensional visco-elastic artificial boundary equations
along normal and tangent directions based on three-dimensional wave motion
equations, which can simulate an infinite domain by using suitable spring and
damping at the boundary. Gu et al. [12] deduce the stiffness and damping matrixes
based on the viscous-spring artificial boundary theory, and give a convenient way to
calculate the material elastic properties as follows:

$$G' = \alpha_T h \frac{G}{R} \tag{3}$$

$$E' = \alpha_N h \frac{G}{R} \cdot \frac{(1+v')(1-2v')}{(1-v')} \tag{4}$$

$$v' = \frac{\alpha - 2}{2(\alpha - 1)} \tag{5}$$

where G', E', v', are equivalent shear modulus, equivalent elastic modulus and
equivalent Poisson's ratio of the VEB; h is the thickness of the equivalent element;
R is the distance between the vibration source and the boundary; G is shear
modulus; α_N, α_T are both coefficients of this artificial boundary; and $\alpha = \alpha_N/\alpha_T$.

α_N, α_T are suggested to choose as 0.67 and 1.33 respectively in [12], and take v'
as 0, which cannot be negative.

Equivalent damping ratio can be calculated as follows:

$$\eta' = \frac{\rho R}{3G}\left(2\frac{c_s}{\alpha_T} + \frac{c_p}{\alpha_N}\right) \tag{6}$$

Model Description

The two models are developed using the commercial finite element software ABAQUS. The interior ground using the finite element method is modelled as a lengthened half-sphere (Fig. 2), which enables the dynamic stress in the soil to stabilize after the loads move a certain distance. The total length of the model is 25 m, and the interior domain is 15 m in length. The height of the model and the interior domain is 10 and 5 m respectively. The front face represents a plane of symmetry, so the horizontal movement is restrained. The upper face is a free boundary and all movements on the spherical boundary are restrained. The visco-elastic artificial boundary can be achieved with the IEB changed into visco-elastic material (0.01 m in thickness), which is omitted here for succinctness.

The IEB is discretized by 8-noded infinite element (CIN3D8), while the interior domain and the VEB are discretized by 8-noded, reduced-integrated, hex elements (C3D8R). The total element number is 1002627 in order to get better results.

The interior elastic domain can be described using the elastic modulus and the Poisson's ration, which are chosen as $E = 30$ MPa and $v = 0.25$ respectively. No additional coefficients need to be selected for the IEB. Material properties of the VEB are calculated with Eqs. (3-6), and the calculated equivalent elastic modulus
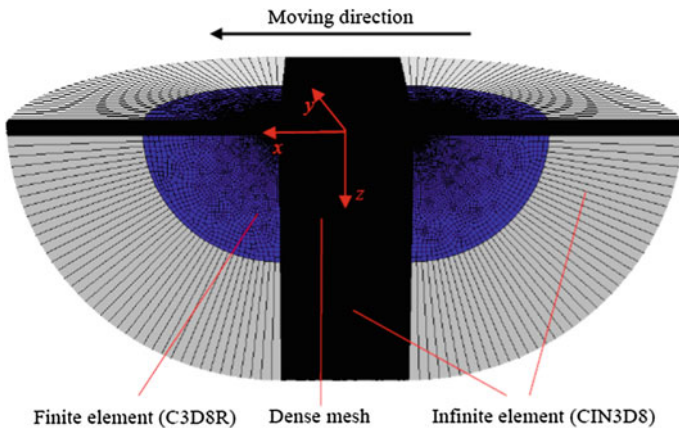
Fig. 2 Finite element model with infinite element boundary

$E' = 29236.4$Pa, equivalent Poisson's ratio $v' = 0$, and equivalent damping ratio $\eta' = 0.098878$. The density of all material is chosen as $\rho = 2000$ kg/m^3.

A user-subroutine VDLOAD was programmed to model moving loads, and in this paper, this $p = 10$ kPa uniform load is distributed normally in a 0.2 m × 0.2 m area moving from one end of this model to the other.

Results and Discussion

To show the impact of the velocity on dynamic stresses, the maximum dynamic stresses under different velocities calculated using the IEB are illustrated in Fig. 3, where the stresses and velocities are normalized by the uniform load p and the shear wave velocity c_s respectively. It's important to notice that Fig. 3 concentrates on the maximum value of the stresses, which may not occur in the same position. The results show that the velocity of the moving load has a huge effect on maximum dynamic stresses, which increase slowly with an increasing velocity at first, then increase remarkably when the velocity is closer to the Rayleigh wave speed. Keep in mind, stress is assumed positive in compression in this paper.

As shown in Eqs. (3-6), material properties of the VEB depends on the distance between the vibration source and the boundary, which keeps changing as the load moves. It's then hard to find the correct coefficients which can be updated with the change of the distance, making the results worse than those calculated using an IEB. Figure 4 shows the normal dynamic stresses in three directions versus the velocity, which are normalized by the uniform load p and the shear wave velocity c_s respectively, compared with analytical solutions [1] at different depth z (which is normalized by a, the length of the sides of the utilized uniform load). It's shown that when the velocity of the moving loads is low (less than 70% of the Rayleigh wave speed), dynamic stresses using both boundaries match analytical solutions well. When the velocity of the moving loads increases, especially when it's near the Rayleigh wave speed, the numerical results increasingly deviate from the analytical results, more obvious at shallower depth. The figure also shows that IEB results

Fig. 3 Maximum dynamic stress versus velocity
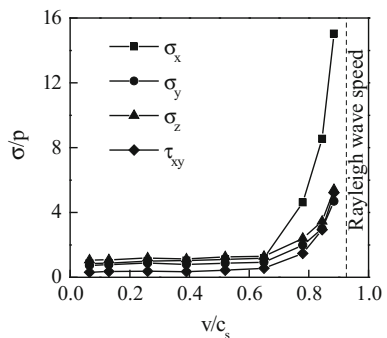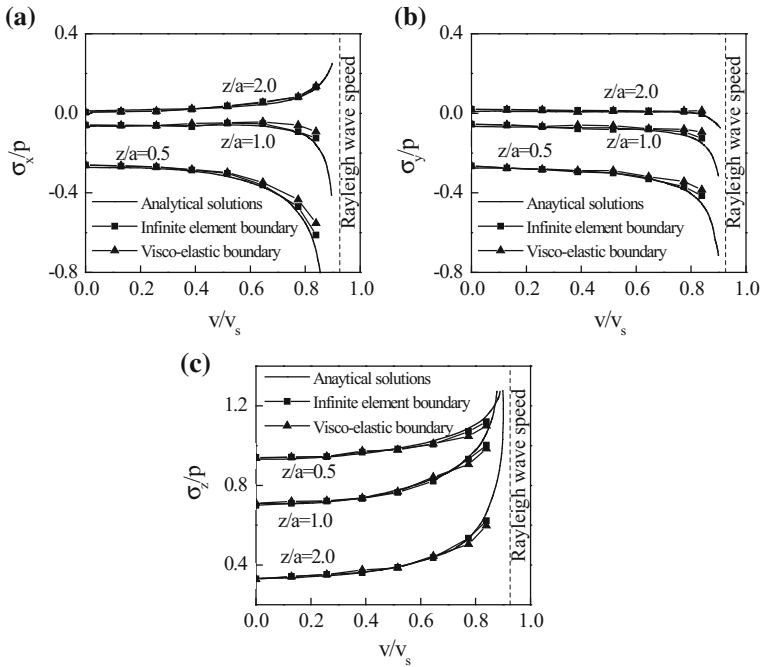
Fig. 4 Comparison of dynamic stresses versus velocity with analytical results: **a** variation of σ_z with velocity; **b** variation of σ_y with velocity; **c** variation of σ_z with velocity

provide better predictions than VEB. It is due to the fact that the coefficients of IEB are comparably simple and independent upon the distance between the vibration source and the boundary. Considering that traffic velocities are usually less than 250 km/h (approximately 70 m/s) and the modulus of pavement material is relatively high, the numerical model used in this paper can be used in other analyses of traffic loads.

Conclusions

The finite element method, cooperated with two artificial boundary conditions (i.e. IEB and VEB here) has been used to model dynamic stress response to moving loads. The numerical results show that the velocity of the moving loads has a huge impact on predictions. In principle, maximum dynamic stresses increase gradually with the velocity at first and grow rapidly when the velocity is closer to the Rayleigh wave speed. This paper also compares the effect of two different boundary conditions (IEB and VEB). It's found that both boundaries provide reasonable predictions of dynamic stresses when the velocity of the load is low (less than 70%

of the Rayleigh wave speed), consistent with analytical results. When the velocity is relatively high (over 70% of the Rayleigh wave speed), the numerical results increasingly deviate from analytical results with an increase of the velocity. In addition, IEB provides closer results to analytical solutions than VEB. It's mainly because the material properties of VEB largely depends on the distance between the vibration source and the boundary.

References

1. Eason, G. (1965). The stresses produced in a semi-infinite solid by a moving surface force. International Journal of Engineering Science, 2(6): 581–609.
2. Cai, Y.Q., Sun, H.L., Xu, C.J. (2007). Effect of rail rigidity on track-ground vibration due to a high-speed train. Chinese Journal of Geotechnical Engineering, 29(12): 1787–1793. (in Chinese).
3. Bian, X.C., Hu, T., Chen, Y.M. (2008). Stress path in soil element of ground under moving traffic loads. China Civil Engineering Journal, 41(11): 86–92. (in Chinese).
4. Connolly, D., Giannopoulos, A., Forde, M.C. (2013). Numerical modelling of ground borne vibrations from high speed rail lines on embankments. Soil Dynamics and Earthquake Engineering, 46: 13–19.
5. Kouroussis, G., Verlinden, O., Conti, C. (2009). Ground propagation of vibrations from railway vehicles using a finite/infinite-element model of the soil[J]. Proceedings of the Institution of Mechanical Engineers, Part F: Journal of Rail and Rapid Transit, 223(4): 405–413.
6. Kouroussis, G., Van, P.L., Conti, C., et al. (2014). Using three-dimensional finite element analysis in time domain to model railway-induced ground vibrations. Advances in Engineering Software, 70: 63–76.
7. Lysmer, J., Kuhlemeyer, R.L. (1969). Finite dynamic model for infinite media. Journal of the Engineering Mechanics Division, 95(4): 859–878.
8. Deeks, A.J., Randolph, M.F. (1994). Axisymmetric time-domain transmitting boundaries. Journal of Engineering Mechanics, 120(1): 25–42.
9. Liu, J.B., Wang, Z.Y., Du, X.L., et al. (2005). Three-dimensional visco-elastic artificial boundaries in time domain for wave motion problems. Engineering Mechanics, 22(6): 46–51. (in Chinese).
10. Sommerfeld, A. (1964). Optics: Volume IV of lectures on theoretical physics.
11. Clayton, R.W., Engquist, B. (1980). Absorbing boundary conditions for wave-equation migration. Geophysics, 45(5): 895–904.
12. Gu, Y., Liu, J.B., Du, Y.X. (2007). 3D consistent viscous-spring artificial boundary and viscous-spring boundary element. Engineering Mechanics, 24(12): 31–37. (in Chinese).

DEM Modeling of Vane Shear Test in Cohesive Solids

Jiawei Xu and Xuecheng Bian

Introduction

The Discrete Element Method (DEM) is a powerful numerical methodology developed and applied for analyzing rock mechanics by Cundall and Starck [1]. In the DEM model, materials are represented by particles and contact force between particles are calculated by means of contact model, the velocity and position are computed by Newton laws of motion [2]. In the last few decades, the discrete element methods (DEM) has been used in soil mechanics, e.g. Jiang Mingjing's work in dense and loose granulates [3]. This numerical method has been successfully applied in exploring the interaction mechanism.

The vane shear test (VST) is used for calculating the undrained shear strength of cohesive soil [4], this paper is aimed to build a numerical model based on the EDEM software to see if the result of simulation is subjected to the laboratory test. Appling a suitable cohesive model is the challenge to simulate the VST, the literature choose the JKR model to reproduce the contact between cohesive soil particles. And verify if it is reasonable to be applied in homogeneous visco-elastic soil.

EDEM software allows any property to be associated with particles contacts, geometry elements and globally within a model [5]. Between particle and particle, we can choose the contact model it owned or add the new model to the software. Apart form other DEM software, EDEM provides a geometry which can be endowed with parameters such as young's modulus and geometry can be set as a rigid body. In this paper, the vane blade is simulated by the geometry which was endowed parameters as the same as the vane blade in the suit test.

J. Xu (✉) · X. Bian
Department of Civil Engineering, Zhejiang University, Hangzhou 310058, China
e-mail: xujiawei@zju.edu.cn

X. Bian
e-mail: bianxc@zju.edu.cn

Numerical Model

As we know, a small soil specimen of about 1 cm^3 contain more than 10^{-9} micro-sized soil particles and 1 s of simulation time will need several years on a workstation. And the soil particles is roughness and asperities. Reproducing it in the EDEM is complex, so we use the mesoscopic scale approach for this model. Each particle is a representation at an intermediate length scale between the actual size and the bulk size [2]. This approach can reduce the simulation time in the current source. And the contact model in the following section simulates the cohesive force between soil particles.

Contact Model

EDEM provides some contact models, this paper choose Hertz-Mindling with JKR cohesive model, in this model, normal elastic contact force based on the theory proposed by Johnson et al. [6]. The JKR normal elastic contact force depends on the overlap δ and surface energy γ:

$$F_{jkr} = -4\sqrt{\pi\gamma E^*}\alpha^{3/2} + \frac{4E^*}{3R^*}\alpha^3$$
$$\delta = \frac{\alpha^2}{R^*} - \sqrt{4\pi\gamma\alpha/E^*}$$

E* is equivalent young's modulus, R^* is equivalent radius.

The JKR model provide the cohesive force even the particles doesn't contact directly, when the distance of particles less than δ_c and the particles doesn't contact, the cohesive force reach the maximum, we called the force pull-out force, the formal is:

$$F_{\text{pullout}} = -\frac{3}{2}\pi\gamma R^*$$

In EDEM, defining the parameter γ to calculate the cohesive force between soil particle.

VST Model

In EDEM, generating a rectangular block filled with particles to simulate soil bulk. The soil domain considered herein has a length of 22 mm, width of 22 mm and height of 30 mm. Before generating soil particles, set the vane blade inside the soil domain, the center of the blade is as the same as the soil domain, the coordinate is (0,0,0). The vane blade herein has a thickness of 0.05 mm, height of 20 mm, diameter of 10 mm. Figure 1 shows the soil domain and the vane blade in

simulation. Set the soil domain as a particle factory to generate soil particles. The diameter of particle is 1 mm, and the number of particles is 15,000. Figure 2 shows the soil bulk in the simulation.

Set the soil domain as a particle factory to generate soil particles. The diameter of particle is 1 mm, and the number of particles is 15,000. Table 1 shows the parameters of three different soil sample. In order to replicate the suit test, set the velocity of the bottom as zero ($V_x = V_y = V_z = 0$), set the velocity of the outer surface of the soil domain as zero ($V_x = V_y = V_z = 0$).
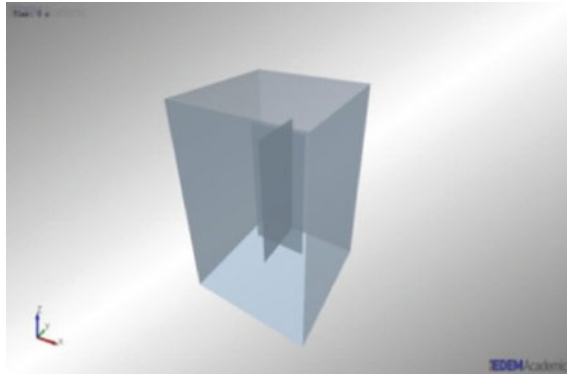
Fig. 1 soil domain and the vane blade numerical model

Fig. 2 soil bulk consist of particles in numerical model

Table 1 Soil properties for vane shear test

Soil particle type	Density (kg/m^3)	Young's modulus (MPa)	Poisson's ratio	Surface energy (J/m^2)
1	3272	4.0	0.49	5
2	3272	4.0	0.49	10
3	3272	4.0	0.49	15

Table 2 Vane characteristics and properties

Blade height (mm)	Blade thickness (mm)	Blade width (mm)	Young's modulus (GPa)	Poisson's ratio	Density (kg/m^3)
20	0.05	10	200	0.3	7750

Table 3 simulation parameters

Parameter	Value
Number of particles	15,000
Particle static friction	0.3
Particle rolling friction	0.1
Coefficient of restitution	0.2

The Simulation of Vane Shear Test

Three vane rotation speeds has been set for vane blade, these are 6, 8 and 10°/s for comparison purpose. The gravity of the system is 9.8 m/s^2 in—z direction. The time of movement is 4 s. Table 2 gives the vane properties used herein. Table 3 gives the simulation parameters.

Results and Discussion

Figure 3 shows the different rotation speed when surface energy is 15 J/m^2. As we can see, the torque of these three different is nearly the same. They have the same peak torque and the same trend to reach the peak value. A little fluctuation due to the discrete nature. The results can prove the independence of numerical model on different rotation speed.

Fig. 3 Numerical result for three different rotation speed
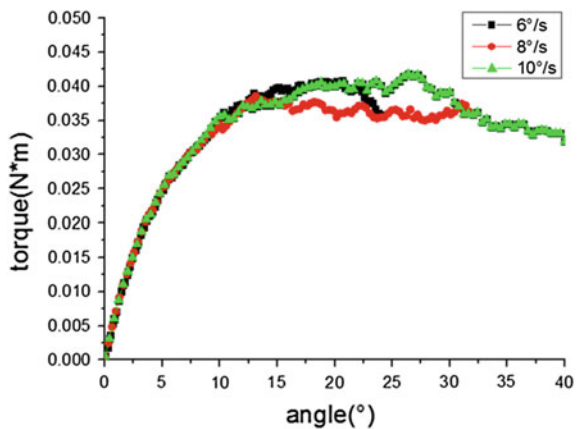
Change the cohesive of the system by input different surface energy to represent the different soil sample which has different shear strength, these are 5, 10, 15 J/m². Set the rotation speed as 360°/s to reduce the simulation time. Figure 4 shows the torque of the vane changes with the rotation angle. With the rotation of the vane blade, the torque of the vane will reach a peak value, and then, with the vane continue shearing the soil sample, the torque will decrease. And the higher the cohesive force is, the higher the peak value is. That represents the soil sample has the higher shear strength if the cohesive force is higher. Compare with the laboratory test from the research done by Gupta and Chakraborty [5]. The numerical results has the same trend with laboratory test. Figure 5 shows the laboratory, and the cohesive force of soil sample 3 is larger than soil sample 2, and the cohesive force of soil sample 2 is larger than soil sample 1. The result of the laboratory test also represents that the higher the cohesive force is, the larger the shear strength the soil has.

Fig. 4 Numerical result for three different soil
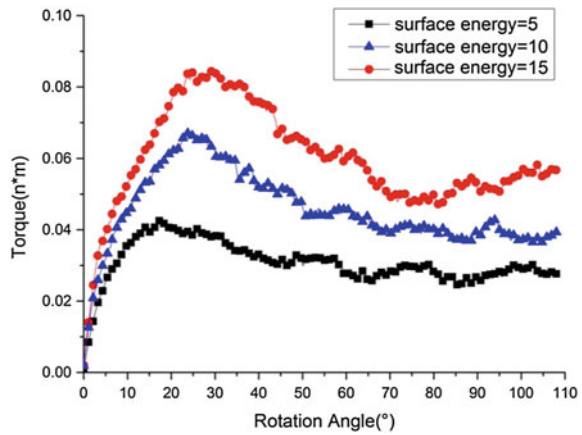
Fig. 5 Laboratory result from Gupta et al. [7]
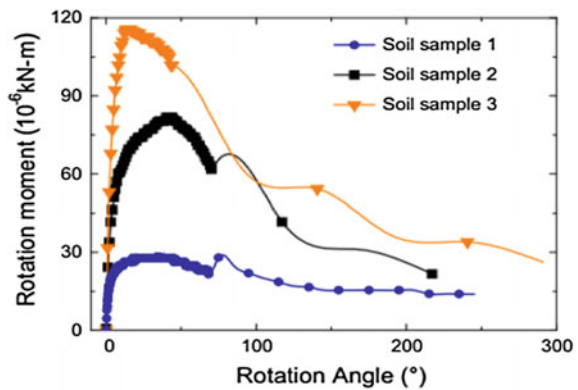
Conclusions

We have presented a DEM model of mechanical behaviors of cohesive soil during the van shear test using the Hertz-Mindling with JKR cohesive model. The results show that the vane shear test in cohesive soil specimens is qualitatively reproduced in the simulation. Comparing with the laboratory test, the numerical model explains the response of the cohesive soil is subject to the vane shear test. In the simulation, the contact model between particles is Hertz-Mindling with JKR cohesive model, and the result shows this contact model for cohesive soil is reasonable.

The current study can be a foundation which has built the cohesive soil in EDEM, in the future, the contact model can be improved and EDEM can be a powerful software to simulate the soil particles.

References

1. P. Cundall, O. Starck. (1979). A discrete numerical method for granular assemblies, Geotechnique, 29 (1), 45–47.
2. Alvaro Janda, Jin Y. Ooi. (2016). DEM modeling of cone penetration and unconfined compression in cohesive solids, powder Technology, 293: 60–68.
3. JIANG Mingjing, HU Hai-jun (2010). Numerical simulation of triaxial shear test of dense and loose granulates under constant suction by discrete element method. Journal of Central South University: Science and Technology, 41(6):2350–2359.
4. Bjerrum L, Embankments on soft ground. (1972). In: Proceedings of ASCE conference on performance of earth-supported structures, Purdue University, vol 2, pp 1–54.
5. EDEM user guide, Version 2.7.6. 6–14.
6. K. L. Johnson, K. Kendall and A. D. Roberts. (1971). Surface energy and the contact of elastic solids. Proc. R. Soc. Lond. A. 324, 301–313.
7. T. Gupta, T. Chakraborty, K. Abdel-Rahman, M. Achmus. (2016). Large deformation finite element analysis of vane shear tests. Geotechnical and Geological Engineering, pp 1–8.

Dynamic Stresses in Embankment and Ground Caused by HST with the Considering of Track Irregularity

Jing Hu, Xiang Duan, Xuecheng Bian and Jianqun Jiang

Introduction

Modern high-speed trains generate strong impact to railway structure and underlying foundation. In railway engineering practices, excessive dynamic stress expedite the degradation of track structure and cause unexpected permanent deformation in embankment. Dynamic responses of foundation induced by train's moving loads have received increasingly attention in last several decades. At earlier time, researches simplified the track structure and foundation as a half space to investigate dynamic response of a solid medium subjected to moving loads [1–3]. To study the track-foundation dynamic interaction under train's moving loads, some elaborated analytical models have been reported. Sheng et al. [4] theoretically studied the propagation of vibration generated by a harmonic or a constant load moving along a beam resting on the layered half-space. Takemiya and Bian [5] proposed a discrete supported beam on the layered foundation to investigate the effect of sleepers in track-foundation interaction. But, most existing track-foundation model are simplified track structure as a beam resting on homogeneous foundation. Recent years, track-embankment-foundation coupled model which is closer to the real railway had been proposed. With the finite element method, the irregularity of geometry and material of foundation, including the track

J. Hu (✉) · X. Duan · X. Bian · J. Jiang
Department of Civil Engineering, Zhejiang University, Hangzhou 310058, China
e-mail: 11312009@zju.edu.cn

X. Duan
e-mail: bianxc@zju.edu.cn

X. Bian
e-mail: 3100101601@zju.edu.cn

J. Jiang
e-mail: jianqun@zju.edu.cn

structure and embankment, can be dealt without difficulties [6–10]. However, 2D FEM models are limited in scope due to the plane strain/stress assumption, and can't simulate the true train load, 3D models are still time-consuming. By taking the advantage of invariance of the geometry and material in track direction, Yang and Hung [11] proposed the 2.5D finite/infinite-element approach for modeling the viscoelastic bodies subjected to moving loads.

In addition to the above analytical and numerical methods, the dynamic response of ballast tracks are mostly measured by field test in early time. In 1997, Swedish Rail Administration (SRA) started running the X-2000 passenger HST along the West Coast Line between Göteborg and Malmö [12]. Kouroussis [13] collected vibration results in Belgium on the Brussels to Paris high speed line under Thalys HST. In China, a large scale field test had been made at "Qin-Shen" high speed railway in 2002–2003 [14]. Lately, different full-scale models had also been built to simulation the dynamic response during under the train loads [15, 16].

Most numerical methods had used test data to verify their calculation models [7, 9, 10]. However, it's very common to find that the numerical results always exist some difference with test data. In addition to the influence of the simplified model itself, the main reason caused the difference is the existence of track irregularity in real railway. Thus, in this paper, a 2.5D finite element track-embankment-foundation model is established based on the field test at "Qin-Shen" high speed railway to explore the effect of track irregularity on dynamic response. Comparing to the existing computation models, more detail on track structure like sub-ballast, filling materials, embankment and track irregularity are taken into account. The field test results of ballast railways collected from predecessor's research are summarized and normalized to compare with the 2.5D results of ballast railway. Effect of track irregularity on dynamic stress have been mainly discussed. Numerical results have presented the relationship between dynamic stress and train speed inside embankment under different grades of track irregularity PSD of U.S. railways. A preliminary division of the irregularity of track running state have been made and the tendency of dynamic stress development with track irregularity has been analyzed. At the last part, a discussion about the attenuation law of dynamic stress under different grades track irregularities along depth has been presented.

Numerical Modelling of Railway Track-Embankment-Foundation System

2.5D Modelling of "Pioneer" HST Railway in China

In 2001–2002, Nie [14] implemented the field test on China's first high speed railway—"Qin-Shen" high speed railway, six months before the railway put into operation. This test site located at the section of the embankment. The ballast bed is formed by crushed stone of class I, the surface layer of the embankment is fill by

graded crushed stone and the bottom layer is made up of grain material. As for the geological conditions of ground soil, surface layer is winded granite, which is about 4.5 m, second layer is moderately weathered granite, about 15.5 m, under the second layer a homogeneous soil stratum of 20 m height. Track structure and geometry parameters are showed in Tables 1 and 2, respectively. In this paper, the ballast and sub-ballast layers are modeled as viscoelastic layers with consider the actual elasticity modulus, geometry size and mass per unit length.

To observe the dynamic stress of the embankment, the soil pressure sensors are buried in the embankment as Fig. 1 has showed.

The test "Pioneer" train includes 6 coaches, the length of a coach is 23 m and the axle load P is 145 kN. Figure 2 shows the actual measured PSD of rail vertical irregularity of "Qin-Shen" high speed railway along the test section [14].

Table 1 Rail-track properties of this test

Mass of rail beam per unit length of track	120 kg/m
Bending stiffness of rail beam	1.324e7 Nm^2
Mass of sleeper per unit length of track	490 kg/m
Rail pad stiffness	8.3e8 N/m^2
Contact width of railway and foundation	2.6 m

Table 2 Physical parameters for embankment and ground of "Qin-Shen" railway

	Thickness (m)	Density (kg/m^3)	Vs (m/s)	Poisson's ratio
Ballast	0.35	2000	200	0.25
Sub-ballast	0.4	1950	190	0.3
Filling materials	2.6	1800	150	0.3
Soil Layer 1	4.5	1600	90	0.35
Soil Layer 2	15.5	1800	100	0.35
Soil Layer 3	20	1850	120	0.35
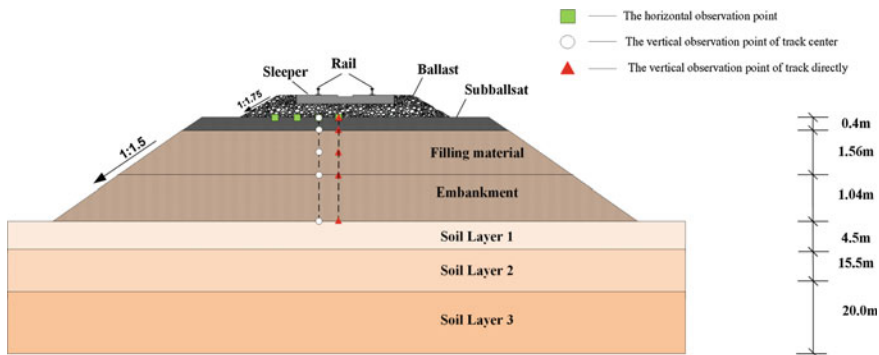
Fig. 1 Track geometry and decorate of test sensors
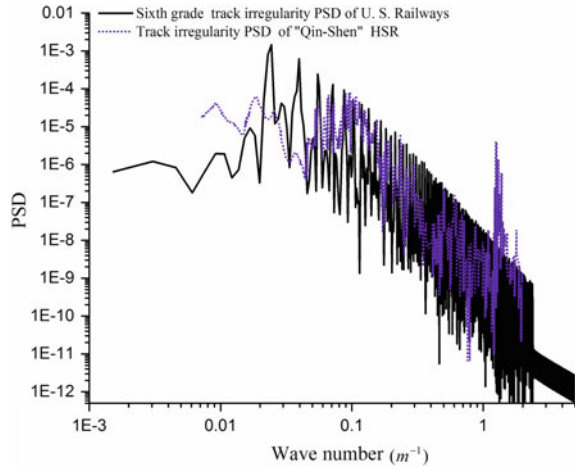
Sixth grade track irregularity PSD of U.S. railways is also been plot here to describe the irregularity of "Qin-Shen" railway. It was in a good condition and approximately in the Sixth grade track irregularity PSD of U.S. railways.

Validation of 2.5D Modelling of "Pioneer" HST Railway in China

To validate the 2.5D modelling of the "Pioneer" HST railway established above, the time-history of dynamic stresses at the surface of sub-ballast layer during the passage of train at two different speeds of 160, and 250 km/h are calculated. Figure 3 shows the validation between calculated dynamic stresses and field data under train speed 160 and 250 km/h.
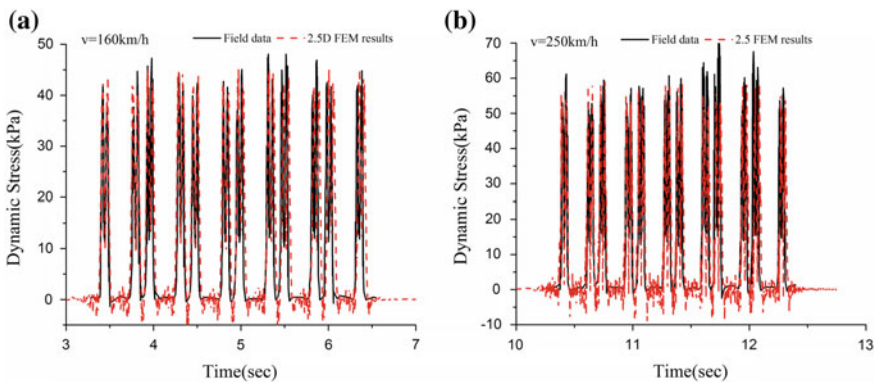
Fig. 3 Validation of 2.5D finite ballast track model

For all train speeds, it is clearly shown in Fig. 3 that the numerical results of 2.5D finite ballast track model have a good match with field data, which proved the accuracy of the 2.5D finite ballast track model. The curve with obvious periodicity reflect the dynamic stress distributions when the train pass through. The sub-ballast surface dynamic stresses grow with the train speed: when train speed is 160 km/h, the maximum stress intensity is 45 kPa, while train speed is 250 km/h, the maximum value increases to 59 kPa.

Numerical Results Under Different Greades of Track Irregularity PSD of U.S. Railways

Track irregularity is mainly caused by two aspects: the irregularity of wheel or rail surface; differential deformation of underlying ballast layer. Two categories of wavelength were identified by Selig and Waters [17] for a passenger train running at 200 km/h: larger than 5 m caused mainly by the shape of the ballast layer; and less than 2 m caused mainly by the shape of the rail. Previous investigations have focused mainly on single wavelength harmonic track irregularity, however, the real track irregularity is very complex with combinations of many different wavelength wave. Based on tremendous amount of measured data, Technical Center of Association of American Railroads had proposed the track irregularity PSD of U.S. railways with six grades totally. In this section, the track irregularity PSD of U.S. railways have been adopted to the ballast track model, the effects of real track irregularity on dynamic stress in the embankment and ground are investigated using the 2.5D dynamic finite-element model mentioned above.

Track irregularity PSD of U.S. railways from first to six grade are plotted in Fig. 4, totally 6 different grades of track irregularity are adopted to this model,

Fig. 4 Different grades track irregularity PSD of U.S. railways
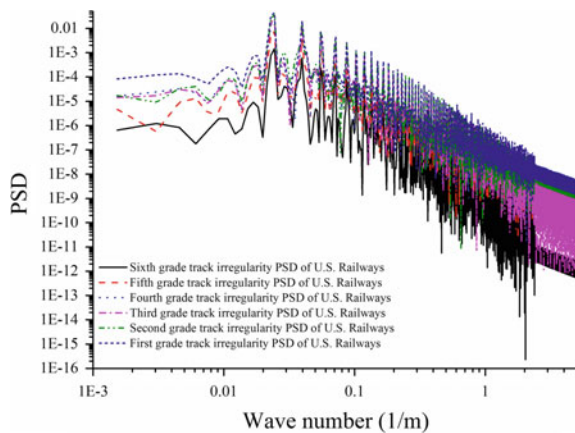
with smooth track results as a reference. Based on trigonometric series method, totally 200 cosine distribution are used to fit the spatial distribution of the PSD.

Division of the Track Irregularity on the Field Test Data

Based on the "Qin-Shen" ballast track model established above, the dynamic stresses at the surface sub-ballast under 6 different grades of track irregularity PSD of U.S. railways have been calculated. The field test results of ballast tracks around the world are summarized in Fig. 5, after the normalization of axle loads. China academy of railway science had proposed an empirical formula to calculate dynamic stress at surface embankment:

$$\sigma_d = \sigma_p (1 + \alpha \cdot V) \qquad (1)$$

where σ_d is the dynamic stress at the surface embankment; σ_p is the dynamic stress at the surface embankment under the condition of quasi static; α characterize the effect of the train speed to dynamic stress in embankment. For a high speed railway, the critical value of α was 0.003, its dynamic stresses of empirical formula is also in Fig. 5.

Figure 5 shows that the dynamic stresses at surface sub-ballast are mainly distributed in the range of 40–60 kPa, for some diseased railways or poor lines it may reach 72 kPa even at a very low train speed. At low speed stage, the dynamic stresses under different grades track irregularities are very close, with the increasing of the train speed, the difference become significant. More details are presented in Fig. 6.
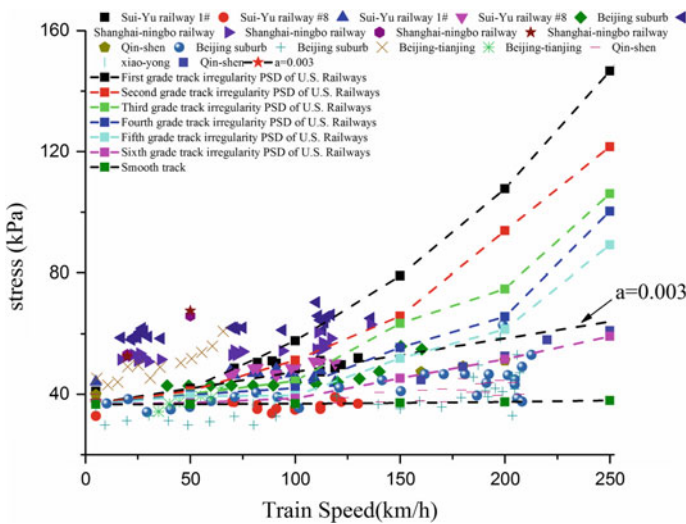
Fig. 5 Dynamic stresses with the train speed
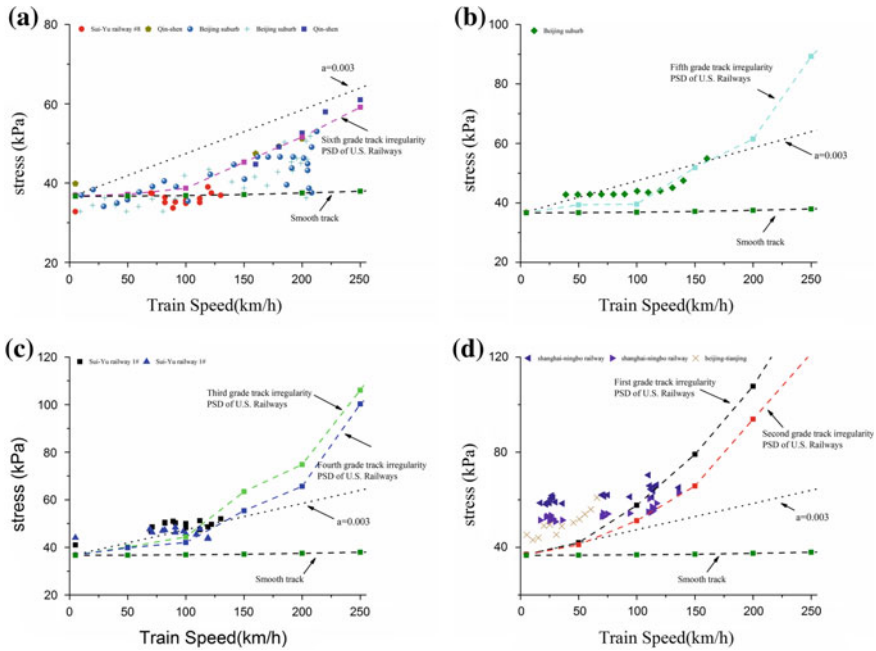
Fig. 6 Division of the track irregularity on the field test data

For the railway lines built after 2000 year, showed in Fig. 6a, b, the maximum dynamic stresses at surface sub-ballast were less than 50 kPa when the train ran at 200 km/h. The dynamic stresses of these railway lines were between the values of smooth track and sixth grade track irregularity, which means the track irregularity were small, these lines were in a very good condition. For another Beijing suburb line, its dynamic stresses were close to the value of the fifth grade track irregularity. The dynamic stresses of empirical formula is between sixth and fifth grades. However, it's very important to notice that, these field test mentioned in Fig. 6a, b were made before the operations, which means the track irregularity of a new built railway is very small, even less than sixth grade track irregularity PSD of U.S. railways and the empirical formula is suitable for this situation.

As for Sui-Yu railway lines presented in Fig. 6c, the dynamic stresses were close to the value of fourth and third grades track irregularity. The diseased line Shanghai-Ningbo railway plotted in Fig. 6d was almost in a state of first grade track irregularity. Beijing-Tianjin railway line was built in 1970, after a longtime operation, track irregularity of this line was in an extremely serious condition that larger than first grade track irregularity PSD of U.S. railways.

Fig. 7 Stress development
with track irregularity
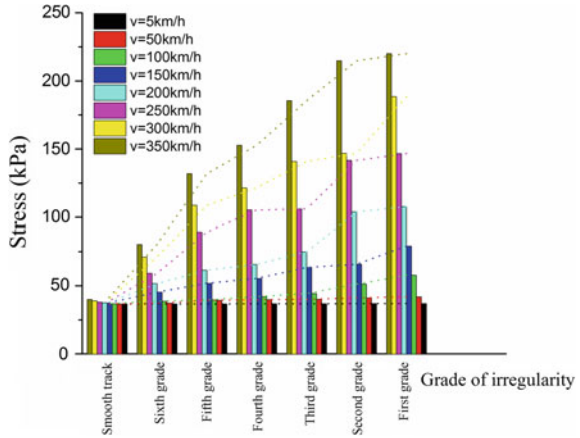
Stresses Along with the Development of Track Irregularity

Figure 7 plots the development of maximum dynamic stresses at surface sub-ballast with track irregularity. For certain grade track irregularity, the dynamic stresses grow with the train running speed. As for the certain low train speed (≤ 100 km/h), the amplification of dynamic stress caused by track irregularity is limited, even at the first grade track irregularity, the maximum stresses increase from 38 to 50 kPa compared with smooth track, growth of 31%, when train running at 100 km/h. With the increasing of train speed, the amplification effect appears more significant, at train speed 150 km/h, the growth of maximum dynamic stress become 89%. At high speed stage, the maximum dynamic stresses show multiple increase. For the first grade track irregularity, the growth at 200 km/h is 150, 258% for 250 km/h, 350% for 300 km/h and 449% for 350 km/h. The increase of dynamic stress can be very considerable, which is bad for the stability of track structure and embankment.

The Attenuation Law of Dynamic Stress Within Ballast Track Embankment and Ground

Figure 8 is about the attenuation law of dynamic stress within ballast track embankment and ground. A quasi static train caused almost no distributed difference between irregular and smooth track. However, for the train speed at 250 km/h, track irregularity caused much larger dynamic stresses in the embankment than smooth track even it decay very rapidly along the depth. At the surface ground, the dynamic stress of smooth track is 5 kPa but 20 kPa for first grade track irregularity. It can be concluded that the irregularity of track cause a deeper transmission and
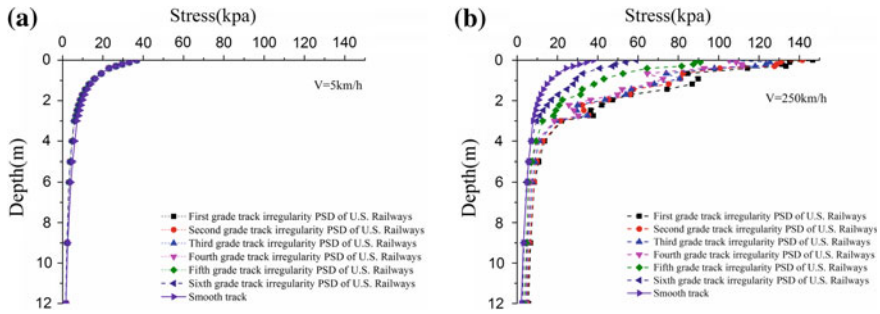
Fig. 8 The attenuation law of dynamic stress within ballast track embankment and ground

wider influence range of dynamic stress. Such a high dynamic stresses will cause larger deformation in embankment and track structure which aggravate track irregularity in turn.

Conclusions

Train moving load induced dynamic stress in embankment and ground is essential to design of high-speed railway, and is frequently used in determining soil treatment depth and methodologies. In this paper, a high efficient 2.5D track-embankment-foundation analysis method has been proposed to investigate the dynamic stress in embankment and ground during train's passages. The results of this paper can be summarized as follows:

1. The high-efficient 2.5D finite ballast track model proposed in this paper have a good match with field data, which proved the accuracy of this model.
2. The field test results show that the dynamic stresses at surface sub-ballast are mainly distributed in the range of 40–60 kPa, for some diseased railway lines it may reach 72 kPa even at a very low train speed.
3. Track irregularity of a new built railway is very small and it's less than six grade track irregularity PSD of U.S. railways. And the empirical formula proposed by China academy of railway science is suitable for new built lines.
4. At low train speed stage (≤ 100 km/h), the amplification of dynamic stress caused by track irregularity is limited, but at high train speed stage, the dynamic stresses show multiple increase. With the increasing of operation time, track irregularity will gradually develop. The increase of dynamic stress can be very considerable, which is bad for the stability of track structure and embankment.
5. The irregularity of rail will cause deeper transmission and wider influence range of dynamic stress. Large dynamic stresses will cause large deformation in embankment and track structure which aggravate track irregularity in turn.

References

1. Andersen Lars, Cjc Jones. (2006). Coupled boundary and finite element analysis of vibration from railway tunnels—a comparison of two-and three-dimensional models [J]. Journal of Sound and Vibration, 293(3):611–625.
2. De Barros Fcp, Je Luco. (1995). Stresses and displacements in a layered half-space for a moving line load [J]. Applied Mathematics and Computation, 67(1):103–134.
3. Eason Gt. (1965). The stresses produced in a semi-infinite solid by a moving surface force [J]. International Journal of Engineering Science, 2(6):581–609.
4. Sheng X., C. J. C. Jones, M. Petyt. (1999). Ground vibration generated by a load moving along a railway track [J]. Journal of Sound and Vibration, 228(1):129–156.
5. Takemiya H., X. C. Bian. (2005). Substructure simulation of inhomogeneous track and layered ground dynamic interaction under train passage [J]. Journal of Engineering Mechanics-Asce, 131(7):699–711.
6. Balendra T, Kh Chua, Kw Lo, Sl Lee. (1989). Steady-state vibration of subway-soil-building system [J]. Journal of Engineering Mechanics, 115(1):145–162.
7. Connolly D, A Giannopoulos, Mc Forde. (2013). Numerical modelling of ground borne vibrations from high speed rail lines on embankments [J]. Soil Dynamics and Earthquake Engineering, 46:13–19.
8. Hall Lars. (2003). Simulations and analyses of train-induced ground vibrations in finite element models [J]. Soil Dynamics and Earthquake Engineering, 23(5):403–413.
9. Sayeed Md Abu, Mohamed A Shahin. (2016). Three-dimensional numerical modelling of ballasted railway track foundations for high-speed trains with special reference to critical speed [J]. Transportation Geotechnics, 6:55–65.
10. Yang La, W Powrie, Ja Priest. (2009). Dynamic stress analysis of a ballasted railway track bed during train passage [J]. Journal of Geotechnical and Geoenvironmental Engineering, 135 (5):680–689.
11. Yang Y. B., H. H. Hung. (2001). A 2.5D finite/infinite element approach for modelling visco-elastic bodies subjected to moving loads [J]. International Journal for Numerical Methods in Engineering, 51(11):1317–1336.
12. Madshus C, Am Kaynia. (1999). Dynamic ground interaction: a critical issue for high speed train lines on soft soil [C]. Twelfth European Conference on Soil Mechanics & Geotechnical Engineering, 1829.
13. Kouroussis Georges, Olivier Verlinden, Calogero Conti. (2011). Free field vibrations caused by high-speed lines: measurement and time domain simulation [J]. Soil Dynamics and Earthquake Engineering, 31(4):692–707.
14. Zhihong Nie. Study on vertical dynamic response of the track/subgrade in high-speed railway [D]. Central south university, 2005, PHD.
15. Bian Xuecheng, Hongguang Jiang, Chong Cheng, Yunmin Chen, Renpeng Chen, Jianqun Jiang. (2014). Full-scale model testing on a ballastless high-speed railway under simulated train moving loads [J]. Soil Dynamics and Earthquake Engineering, 66:368–384.
16. Chen Xiaobin, Jiasheng Zhang, Xuan Wang. (2015). Full-scale field testing on a highway composite pavement dynamic responses [J]. Transportation Geotechnics, 4:13–27.
17. Selig Ernest Theodore, John M Waters. Track geotechnology and substructure management [M]. Thomas Telford. 1994.

Soft Soil Performances Under Combined Static and Cyclic Loading

Jing Ni, Xueyu Geng, Yi Wei and Yin Zhu

Introduction

Coastal areas are plenty of soft clays, on which there are static infrastructure loads as well as cyclic loads including traffic loads, wave loads, earthquake loads, etc. Recent research results indicate that the cyclic degradation of soft clays is closely related to the initial static shear stress apart from cyclic stress ratio, loading frequency, overconsolidated ratio, etc. In real situation, the excess pore pressure caused by the initial static shear stress can be either drained, partially drained or undrained, before the application of cyclic loads.

The application of a drained initial static stress, also referred to as anisotropic consolidation, is to simulate the condition where enough time has elapsed after the embankment has been constructed and before cyclic loading has been applied, so that excess pore pressures have dissipated and the soft soil subgrade has gained sufficient strength. Researchers pointed out that the total shear strength might be proportional to the drained initial static shear stress [1–3].

J. Ni · Y. Wei · Y. Zhu
Department of Civil Engineering, University of Shanghai
for Science and Technology, Shanghai 200093, China
e-mail: wendy_1943@163.com

Y. Wei
e-mail: cynthia_1128@163.com

Y. Zhu
e-mail: 35zhuying@sina.com

X. Geng (✉)
School of Engineering, University of Warwick, Coventry CV4 7AL, UK
e-mail: Xueyu.Geng@warwick.ac.uk

However, the application of an undrained initial static stress is to dissociate the effect of the initial static shear stress from the drainage that occurs during the application of a drained static shear stress. For an existing highway or an existing dam to be broadened, there may not be enough time for the dissipation of the excess pore pressures induced by the embankment before the application of traffic loads and wave loads, and therefore the excess pore pressures induced by the initial static shear stress can be considered undrained.

The excess pore pressures and the axial stains induced by the initial static shear stress can be either included or excluded in the experimental analysis. Huang et al. [4] conducted cyclic triaxial tests on reconstituted Shanghai clays and found that a relatively large cyclic stress induces larger cyclic excess pore pressures and cyclic axial strains for a given value of combined static and cyclic stresses. The test results [5] from a series of direct, simple, cyclic shear tests conducted on intact sensitive clay from the St. Lawrence valley indicated that for an undrained initial shear stress of 0.3–0.8 times the undrained shear strength, the total shear strength was increased by 30% if 12 cycles are considered as the number of cycles to failure.

In this paper, a series of tests on reconstituted Shanghai clay are conducted. Combined static and cyclic stresses with respect to different ratios are applied in sequence. Excess pore pressures and axial strains induced by static and cyclic stresses were recorded respectively and analyzed. A cyclic model is modified to incorporate the effect of initial static shear stress and is verified by the experimental results. Parametric analyses are also carried out to investigate the sensitivity of static stress and cyclic stress to the performances of soft clays.

Experimental Investigation

Sample Preparation

Reconstituted specimens made of Shanghai clay with a height of 80 mm and a diameter of 39.1 mm are tested under combined static and cyclic shear stresses. The main physical parameters of Shanghai clay are as follows: specific gravity $G_s = 2.75$, plastic limit $w_p = 23.6\%$, and liquid limit $w_L = 47.2\%$. Before the application of static and cyclic stresses, the specimens were consolidated under a confining pressure of 115 kPa and $k_0 = \sigma_{c1}/\sigma_{c3} = 0.7$ to simulate the in-situ state.

Experimental Scheme

An initial static shear stress q_s was first applied at an undrained condition until a designated value was obtained. The excess pore pressures and axial strains at the end were recorded. Then a cyclic stress q_{cyc} with 10,000 cycles was imposed on the

specimen. In order to investigate the sensitivity of static stress and cyclic stress to the excess pore pressures and axial strains of soft clays, a test method is designed as shown in Table 1. The static stress ratio η_s and cyclic stress ratio η_d are defined as ratios of static stress q_s and cyclic stress q_{cyc} to the mean effective stress after consolidation p'_{c0} respectively, where $p'_{c0} = (\sigma'_{c1} + 2\sigma'_{c3})/3$.

Test Results

The variation of total excess pore pressures and total axial strains at $N = 10000$ where the excess pore pressures and axial strains caused by the initial static shear stress are included are shown in Fig. 1. Both u/p'_{c0} and ε_a increase when either static stress ratio or cyclic stress ratio increases. Generally, higher values of total excess pore pressures and total axial strains can be expected for a higher value of η_c. Furthermore, the ratios of $\Delta u/p'_{c0}$ to $\Delta\eta_d$ and $\Delta\varepsilon_a$ to $\Delta\eta_d$ increase as η_d increases, indicating that the soil structure softens obviously at a higher stress level.

Table 1 Test scheme

Specimens	$\eta_c = \eta_s + \eta_d$	η_s	η_d	f (Hz)
U_{01}, U_{02}, U_{03}, U_{04}	0.20	0.14, 0.10, 0.07	0.07, 0.10, 0.14	2
U_{05}, U_{06}, U_{07}	0.27	0.17, 0.14, 0.10, 0.07	0.10, 0.14, 0.17, 0.20	2
U_{08}, U_{09}, U_{10}, U_{11}	0.34	0.14, 0.10, 0.07	0.17, 0.20, 0.24, 0.24	2

(a) Total excess pore pressures (b) Total axial strains
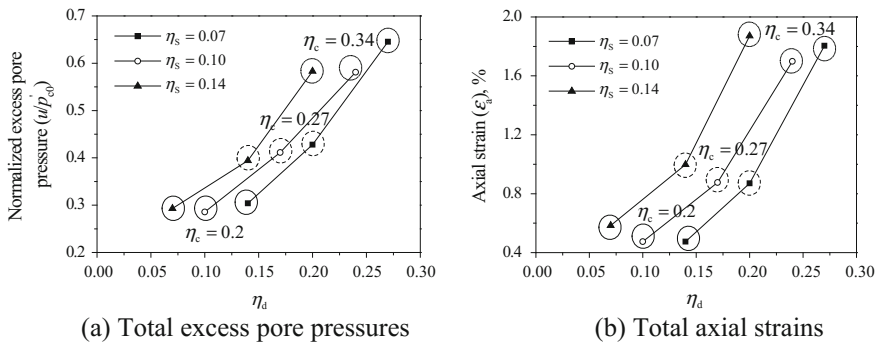
Fig. 1 Total excess pore pressures and total axial strains at $N = 10000$

Modified Cyclic Model

A soil model to predict the behavior of soft clays under undrained cyclic triaxial loading was presented by Ni et al. [6], in which only two additional parameters that characterize the yield surface for elastic unloading are used together with the traditional parameters associated with the modified Cam-clay constitutive model. In this paper, a modified model is proposed to incorporate the initial static shear stress. The stress path during loading is given in Fig. 2 and the framework of the model and computational procedure refer to Ni et al. [6].

The details of the relevant soil properties, initial states, and cyclic degradation parameters for simulation are given in Table 2. The model predictions are generally found to be in agreement with the measured cyclic excess pore pressures and cyclic axial strains as shown in Fig. 3.

Parametric analyses are also conducted to investigate the effect of static stress ratio η_s, cyclic stress ratio η_d, cyclic degradation parameters ξ_1 and ξ_2 on the development of excess pore pressures and axial strains. The parameters for the undrained model analysis are listed in Table 3.

Figure 4 shows the effect of static stress ratios on the development of cyclic excess pore pressures and cyclic axial strains. u_p and ε_{ap} are the excess pore pressure and axial strain respectively corresponding to the maximum deviator stress, while u_b and ε_{ab} are corresponding to the minimum deviator stress. It can be seen in Fig. 4a that even a smaller value of η_d can induce a larger excess pore pressure given a higher value of combined stress ratio, e.g., the excess pore pressure
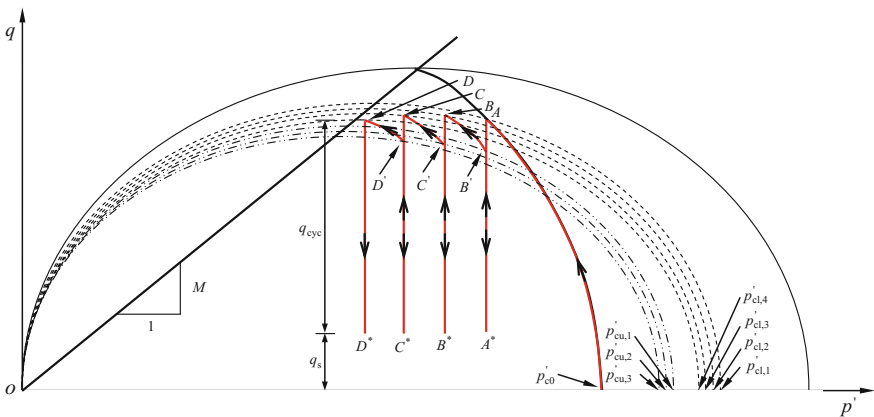
Fig. 2 Stress path for combined static stress and cyclic stress

Table 2 Parameters for cyclic loading

λ	κ	M	P'_{c0} (kPa)	P'_0 (kPa)	q (kPa)	e_0	ξ_1	ξ_2
0.143	0.015	1.65	131	131	49	1.12	2.7	400
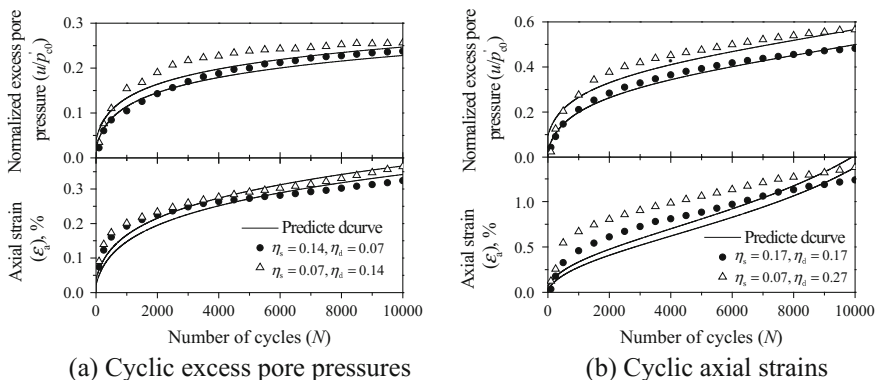
Fig. 3 Accumulation of cyclic excess pore pressures and cyclic axial strains

Table 3 Parameters for undrained model analysis

λ	κ	M	P'_{c0} (kPa)	P'_0 (kPa)	e_0	G
0.25	0.05	1.2	30	30	0.6	$200 S_{u0}$[a]

[a] $S_{u0} = P'_{c0}(M/4)\left(2P'_0/P'_{c0}\right)^{\kappa/\lambda}$
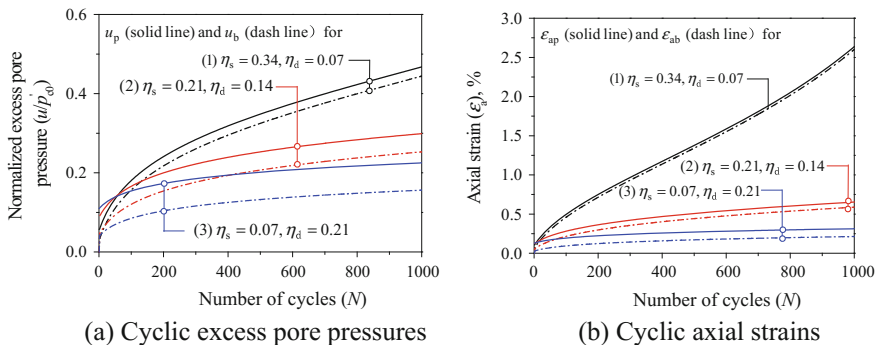
Fig. 4 Soil performance under various combined stress ratios ($\xi_1 = 1.5$ and $\xi_2 = 50$)

curve for $\eta_d = 0.07$ ($\eta_c = 0.41$) is obviously higher than those for $\eta_d = 0.14$ ($\eta_c = 0.35$) and $\eta_d = 0.21$ ($\eta_c = 0.28$). Figure 4b shows that the cyclic axial strains for $\eta_d = 0.14$ and $\eta_d = 0.21$ after 1000 loading cycles are 0.2 and 0.5% respectively, while the cyclic axial strain for $\eta_d = 0.07$ increases substantially and reaches 2.5% at $N = 1000$, indicating the failure of the soil.

Figure 5 shows the variation of total excess pore pressures and total axial strains with different proportions of static stress and cyclic stress for a fixed combined value. At the initial stage of cyclic loading, the highest total excess pore pressure u_b

(a) Total excess pore pressures   (b) Total axial strains
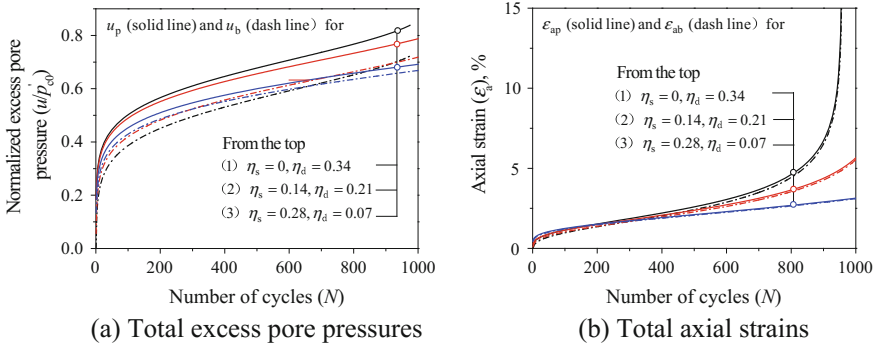
Fig. 5 Soil performance under a fixed combined stress ratio ($\xi_1 = 1.6$ and $\xi_2 = 0$)

is observed for the smallest cyclic stress ratio $\eta_d = 0.07$. However, u_b for $\eta_d = 0.34$ exceeds that for $\eta_d = 0.07$ after certain loading cycles and shows an accelerated generation rate, indicating the failure of the soil. Figure 5b indicates that the total axial strain for ε_{ab} $\eta_d = 0.34$ is smaller compared with those for $\eta_d = 0.07$ and $\eta_d = 0.21$ at the beginning of the cyclic loading, increases rapidly afterward, and exceeds the other two curves, reaching 10% at $N = 950$.

Conclusions

In this paper, reconstituted clay specimens are tested under combined static and cyclic stresses at undrained condition. A modified cyclic model is proposed to capture the soil behavior under the influence of initial static shear stress and is verified by the measured data. Parametric analyses are also carried out, and the following conclusions could be drawn: (1) For a given combined stress ratio, the cyclic excess pore pressures and cyclic axial strains increases with the increasing cyclic stress ratio. (2) Higher cyclic excess pore pressures and cyclic axial strains can be expected even for a lower cyclic stress ratio given a higher combined stress ratio. (3) Smaller values of ξ_1 and ξ_2 will induce larger shrinkage of yield surface during elastic unloading stage, and therefore more cyclic excess pore pressures and cyclic axial strains will develop, and as a result, larger total excess pore pressures and total axial strain could be observed for a higher cyclic stress ratio given the same combined stress ratio.

References

1. Seed, H.B., Chan, C.K. (1966). Clay Strength under Earthquake Loading Conditions. Proc. Amer. Soc. Civil Eng., 1966, 92(SM2), 53–78.
2. Yasuhara, K., Yamanouchi, T., Hirao, K. (1982). Cyclic strength and deformation of normally consolidated clay. Soils and Foundations, 22: 77–91.
3. Hyodo, M., Yamamoto, Y., Sugiyama, M. (1994). Undrained cyclic shear behaviour of normally consolidated clay subjected to initial static shear stress. Soils and Foundations, 34(4): 1–11.
4. Huang, M.S., Li, J.J., Li, X.Z. (2006). Cumulative deformation behaviour of soft clay in cyclic undrained tests. Chinese Journal of Geotechnical Engineering, 28(7): 891–895 (in Chinese).
5. Lefebvre, G., Pfendler, P. (1996). Strain rate and preshear effects in cyclic resistance of soft clay. J. Geotech. Engrg., 122(1): 21–26.
6. Ni, J., Indraratna, B., Geng, X.Y., Carter, J.P., Chen, Y.L. (2015). Model of soft soils under cyclic loading. International Journal of Geomechanics, 2015, 15(4), 04014067 (10 pp.), DOI: 10.1061/(ASCE)GM.1943-5622.0000411.

Micro-vibration Measurement and Analysis of High-Tech Electronics Workshop in Guangzhou

Juan Chen, Guangyun Gao, Jian Song and Wei Zhang

Introduction

Environmental vibration is always present there is no such thing as a vibration-'free' environment. However, its effect on structures seems not as disastrous as many other geological phenomenon such as differential settlement and liquefaction. But when it comes to high-tech electronics workshop, environmental vibration, especially micro-vibration, is much more than an annoyance. Many processes involved in advanced technology applications are highly sensitive to vibrations. Vibrations would cause serious error or damage to high-tech electronics that produced in unqualified conditions. As a result, increasingly strict limits on ground and floor vibration are required for high-tech electronics workshops to ensure the normal operation of modern high-tech equipment [1–3].

J. Chen · G. Gao
Department of Civil Engineering, Tongji University, Shanghai
200092, China
e-mail: 2014chenjuan@tongji.edu.cn

J. Chen · G. Gao (✉)
Key Laboratory of Geotechnical and Underground Engineering of Ministry
of Education, Tongji University, Shanghai 200092, China
e-mail: gaoguangyun@263.net

J. Song
College of Civil and Transportation Engineering, Hohai University,
Nanjing 210098, China
e-mail: jiansonghh@163.com

W. Zhang
China JK Institute of Engineering Investigation and Design, Co. Ltd.,
Xian 710043, China
e-mail: zhangwei@jk.com.cn

Owing to the fact that, micro-vibration is a microscopic movement that has minor magnitude, and is influenced by various factors; it could hardly be depicted with analytical or empirical equations to guide the practice. The newly enacted Chinese Technical Code for Anti-microvibration Engineering of Electronics Industry (GB51076-2015) suggests a four-stage micro-vibration measurement in the construction of an electronics workshop to ensure its smooth functioning [4]. The four-stage measurements includes: (1) free field vibration test before the construction of the building, (2) floor vibration test after the construction of the building and before the installation of any production equipment, (3) floor vibration test after the fabrication of the air-conditioner and other power plants, (4) floor vibration after the installation of the high-tech equipment. In practice, measurements in the last 2–4 stages are generally compacted into 1, referred to as floor vibration test, occasionally conducted during the installation of all facilities.

Our research group has been working on micro-vibration measurement and analysis since the early 21th century. Both free field and floor vibration measurements have been performed successively for electronic workshops projects over China, such as in Guangzhou [5, 6], Yantai [7–10], Suzhou [11, 12], Kunshan and Shenyang City. The tested data is analyzed in both time and frequency domains to reveal the characteristics of free field and floor vibration. In the frequency domain analysis, the one third octave band method is adopted. The rms (root-mean-square) value of vibration velocity (acceleration/displacement) on the one-third octave band spectral is the direct metric to be compared with the vibration criterion, so as to judge whether the tested vibration meets the vibration standards. The vibration standards utilized in our measurement is the Chinese code or tool-specific criterion provided by the producer of the vibration sensitive equipment, which is more strict. In recent years, the criterion used has a tendency of unification, the so called VC (vibration criterion) curves is becoming predominant. The newly released Chinese code is in consistence with this criterion as well. The VC curves were developed by Gordon and his colleagues in the early 80s [13–15]. It has great advantage to use such unified and generic criterion rather than specific criterion applicable to particular items of equipment.

Apart from the in situ measurements, numerical simulation is utilized as an auxiliary approach. The numerical simulation is performed at the end of the first stage measurement. Typical time-history selected from the free field measurement is exerted on the established numerical model as the external stimulation. The simulated results of different cases could provide good reference to the structure design of the electronics warehouse. Simulation of the reconstruction projects (to reconstruct parts of non-micro-vibration zone of the workshop into micro-vibration zone for expanding the production line) in Guangzhou indicates that increased pillar dimension could effectively reduce the micro-vibration amplitude [5]. Simulation of the project in Yantai indicates that, increment of pillar dimension could increase the natural frequency of the structure, while establishment of ring beam hardly have any effect on the natural frequency of the structure [9]. In addition, the difference between the predicted vibration through numerical simulation and the measured floor vibration is compared [12].

Though various research has been conducted as is mentioned in the preceding review, the focus of the previous research majorly lies on the vibration characteristics of the specific project; and pitifully the one-third octave band spectral methodology, which is the fundamental of the data processing, is not clearly described in any of these papers. In addition, the acquisition system (testing instrument), the applicable standards and the signal processing method for micro-vibration have been improved these years. In view of this, this paper gives a comprehensive introduction of the issues involved in processing of vibration data, especially the methodology of the one-third octave band spectral, reports the newly conducted floor vibration test of the electronic workshop in Guangzhou, and analyzed the tests results from a new perspective to reveal the vibration characteristics during the vibration mitigation process. This work would provide reference for the design and construction of similar advanced high-tech electronic workshops.

Micro-vibration Measurement

Project Overview

The micro-vibration measurement is carried out for a smart display company in Huizhou, Guanguzhou City at the end of 2015 to determine whether vibration of the floor pedestal, where the high-tech equipment would be installed on, could meet the anti-micro-vibration standard. It is the second stage floor vibration measurement as is defined in the Chinese code, performed at the time when the construction of the main structure were completed, and the ventilating fans and other power facilities set up. And the vibration-sensitive production equipment were not installed yet. The measurement results could provide basis for the warehouse commissioning and the compilation of the future anti-vibration management regulations.

According to the proprietor's requirements, a total number of 140 measuring points are set on the center of the equipment bases before installation, as is schematically depicted in Fig. 1. The vibration criterion to be catered is the VC curves, including VC-A, VC-B and VC-C, as is shown in Fig. 2 and Table 1. The vibration control requirements elevated step by step from VC-A to VC-C. Equipment bases with higher vibration control standards has specified laying method, that is, VC-A bases with normal floor board, VC-B bases with thicken steel plate, and VC-C bases using cast-in-place concrete. Among all the 140 measuring points, 1 is for VC-A base, 124 for VC-B bases, and 15 points for VC-C bases. In each type of the bases, one point that is representative of this type's vibration characteristics is selected and marked in Fig. 1; and these three points are the only points to be analyzed in this paper.
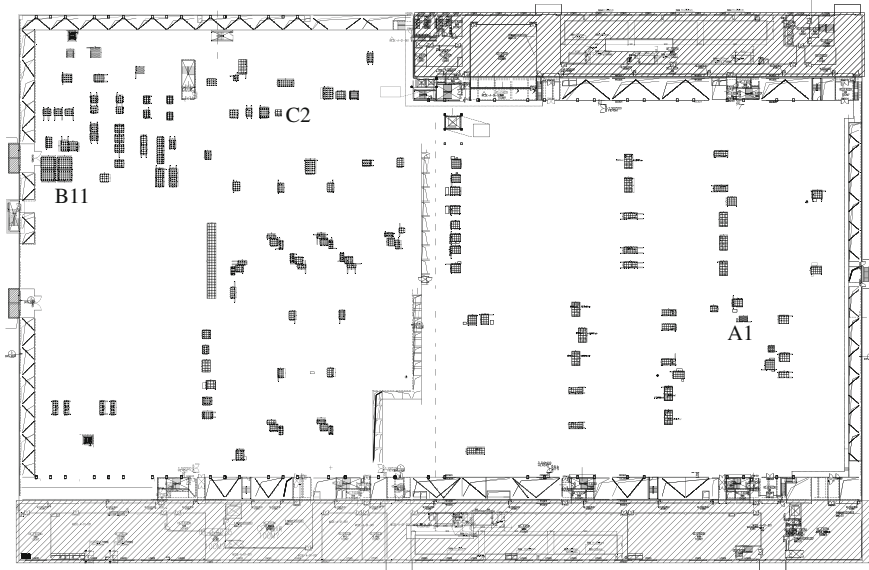
Fig. 1 Schematic layout of the testing points
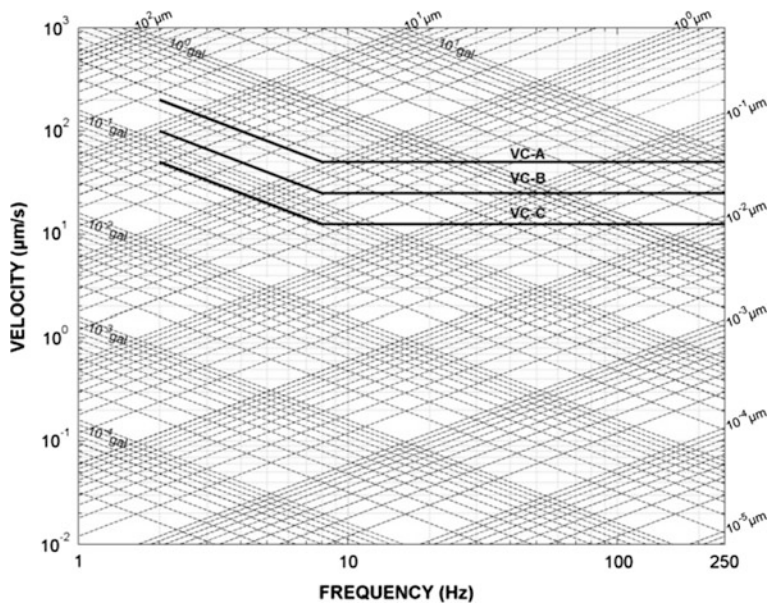
Fig. 2 The employed vibration criterion VC curves

Table 1 Vibration criterion for vibration sensitive areas of a plant

Criterion	Frequency range (Hz)	Horizontal	Vertical
VC-A	2–8	< 0.25 gal	< 0.25 gal
	8–250	< 50 μm/s	< 50 μm/s
VC-B	2–8	< 0.13 gal	< 0.13 gal
	8–250	< 25 μm/s	< 25 μm/s
VC-C	2–8	< 0.06 gal	< 0.06 gal
	8– 250	< 12.5 μm/s	< 12.5 μm/s

Note 1 gal = 1.0×10^{-2} m/s^2

Measuring Equipment and Testing Procedures

The measuring instrument is named TROMINO, made in Italy. TROMINO is a portable ultra-compact and ultra-lightweight acquisition system for seismic noise and vibrations. It has the signal acquisition system (sensors), data storage system and power supply system compacted in a portable box, as is shown in Fig. 3. The miniature (10 × 14 × 8 cm) and lightweight (1.1 kg), the ultra-low energy consumption and the total absence of external cables make TROMINO an almost pocketable instrument and privileged than other instrument with the same goal.

TROMINO is powered by 2 internal alkaline 1.5 V AA batteries, and the consumption of 75 mW (GPS inactive) ensures 100 h continuous measurement. The minimum capacity of the memory cards is 1 Gb but limits could be broke through with the memory card technology developing. TROMINO is equipped with two triplets of orthogonal sensors: velocimeters and accelerometers. And different sensitivity levels can be set for the velocimeters, that is, the low gain channel and the high gain channel. The saturation level of the low gain channels is ±45.6 mm/s, and that for high gain channels is ±1.2 mm/s. Use the high gain channels to record

(a) Appearance   **(b) Operation state**

Fig. 3 TROMINO

microtremor, and the low gain channels for very noise sites. The scale of the three orthogonal digital accelerometer is ±5 g. The detectable frequency range is 0–360 Hz. All these instrument parameters make TROMINO a qualified tool in micro-vibration measurement of high-tech buildings.

To start the measuring, the black arrow on the upper left side of the box indicating north should firstly be orientated the actual north direction. Then mount the long/short spikes on the bottom of TRONIMO depending on hardness of the objects detected, and leveling it until the bubble touches the edge of the circle in Fig. 3a. Operate the soft keys on the interface of the instrument according the user's manual to set sampling parameters, acquire data and save data. Data acquired are exported in txt format through GRILLA, the mating software of TRONIMO. In this measurement, the sampling rate is set as 512 Hz, and the acquisition length is 6 min for each measuring point.

Vibration Data Processing

Vibration displacement, velocity or acceleration can be stated in either time or frequency domain. For the time domain analysis, the acceleration is chosen to be analyzed since it is more difficult to control in micro-vibration. For the frequency domain analysis, it is proved that no one metric is inherently better than another for representing spectral data. We choose to analyze the FFT(Fast Fourier Transform) spectral of acceleration in conjunction with the one-third octave band spectral in a tri-axial paper, where the rms values of all the three metrics could be read from it. The reasons for selection of this kind of frequency domain analysis is as follows.

Floor vibrations in virtually any operational advanced-technology building will be a similar complex mixture of random and almost-periodic tonal signals [16]. The source of the random signals including the low frequency airborne vibration, the medium-high frequency surrounding traffic induced vibration and the impact loading induced by people walking; The most common sources of periodic vibrations are adjacent constant-speed rotating equipment. Random vibrations are best characterized by one-third octave band rms values, so is the random and periodic mixed vibrations. However, the one third octave band methodology dose not, in any way, displace the value of high-resolution narrowband spectrum (e.g. the FFT spectral) analysis for diagnostic studies [13]. Such analysis are essential to the process of quantifying resonance phenomena and identifying sources of vibration. As a result, the frequency domain analysis includes FFT spectral analysis of acceleration and the one-third octave band spectral analysis.

Time-History of Accleration

The time history is plotted directly using the acquired acceleration data, which could be represented as $\mathbf{x}(n)$ or $\mathbf{x}(n\Delta)$, as a discrete of the virtual continuous signal $\mathbf{x}(t)$, where Δ is the sampling interval. From the time-history, the peak amplitude could be determined.

FFT Spectral of Acceleration

The FFT spectral is obtained through the Fast Fourier Transform of the discrete time history. It is a fast implementation of the discrete Fourier Transform (DFT), which is a discrete form of the exact Fourier Transform (FT). The formulation of this process could be reflected by Eqs. (1–3b), that could be found in any signal processing textbooks [17]. We listed them here for convenience of next part's formulation of rms values.

$$\mathbf{X}(f) = \int_{-\infty}^{+\infty} \mathbf{x}(t)\,e^{-i2\pi ft}\,\mathrm{d}t, \ \ \text{and} \ \ \mathbf{x}(t) = \int_{-\infty}^{+\infty} \mathbf{X}(f)\,e^{i2\pi ft}\mathrm{d}f \tag{1}$$

$$\mathbf{X}_{\Delta}(f) = \Delta \sum_{n=-\infty}^{+\infty} \mathbf{x}(n\Delta)\,e^{-i2\pi fn\Delta}, \ \ \text{and} \ \ \mathbf{x}(t) = \int_{-1/2\Delta}^{+1/2\Delta} \mathbf{X}_{\Delta}(f)e^{i2\pi ft}\,\mathrm{d}f \tag{2a}$$

$$\mathbf{X}_{\Delta}(f_m) = \Delta \sum_{n=0}^{N-1} x(n\Delta)\,e^{-imn\frac{2\pi}{N}}, \ \ \text{and} \ \ \mathbf{x}(t) = \frac{1}{N\Delta}\sum_{m=0}^{N-1} X_{\Delta}(f_m)e^{imn\frac{2\pi}{N}} \tag{2b}$$

$$\mathbf{X}(f) = \sum_{n=-\infty}^{+\infty} \mathbf{x}(n\Delta)\,e^{-i2\pi fn\Delta}, \ \ \text{and} \ \ \mathbf{x}(t) = \Delta \int_{-1/2\Delta}^{+1/2\Delta} \mathbf{X}(f)\,e^{i2\pi ft}\,\mathrm{d}f \tag{3a}$$

$$\mathbf{X}(f_m) = \sum_{n=0}^{N-1} x(n\Delta)\,e^{-imn\frac{2\pi}{N}}, \ \ \text{and} \ \ \mathbf{x}(n\Delta) = \frac{1}{N}\sum_{m=0}^{N-1} X(f_m)\,e^{imn\frac{2\pi}{N}} \tag{3b}$$

Equation (1) shows the exact form of the FT. Substitute the $t = n\Delta$ into Eq. (1), the DTFT [discrete time Fourier transform, Eq. (2a)] is obtained. It is noted that, the frequency f in Eq. (2a) is still in continuity. Substitute $f_m = m/N\Delta$ into Eq. (2a), we got the DFT [discrete Fourier transform, Eq. (2b)], and FFT has the same formulation but a speeded algorithm. For simplicity, the DFT or FFT is actually defined as Eq. (3b), neglecting the Δ in Eqs. (2a, 2b); and this is exactly the intrinsic

definition of FFT in most commercial softwares with this function including MATLAB. Owing to this definition, there is a gap of $N/2$ between the magnitude of the FFT spectral and the actual amplitude with definite physical meaning, that is, $\mathbf{A}_n = \mathbf{X}_n/(N/2)$, where $\mathbf{X}_n$ is the calculated magnitude of the FFT spectral, and $\mathbf{A}_n$ the actual amplitude.

From the FFT spectral, the dominant frequency could be identified, so as to provide reference for prediction of the resonance frequency that must be avoided in the design process.

One-Third Octave Band Spectral

The one-third octave band spectral is the final form of the measured metrics to be compared with the VC curves. It reveals the features of the vibration from the perspective of energy. As is seen in Fig. 2, the VC curves is essentially a velocity based criterion. This is because that, it has been found in various studies that while different items of equipment may exhibit maximum sensitivity at different frequencies, often these points of maximum sensitivity lie on a curve of constant velocity. Apart from compulsive requirements from the VC curves, this form of vibration signal presentation has its own specific advantages as well. On the basis of the traditional one-third octave band spectral, a 'tri-axial paper' is added to finally obtain the so called one-third octave band spectral monograph. As a matter of fact, the one-third octave band, the rms values, and the tri-axial paper are equivalents of a common system in which the VC curves is compared with.

There are generally three elements in a typical one-third octave band spectral, e.g. the horizontal axis, the vertical axis and the tri-axial paper. The one-third octave band spectral is a log-log plot. Since the magnitude of the vibration varied greatly, to present vibration data in logarithmic can help data show more easily over as many orders of magnitude as necessary, without losing the significance of the low frequency vibration.

(1) **The horizontal axis**

The horizontal axis of the one-third octave band spectral is the frequency. But the bandwidth of the frequency is not linear but proportional. The bandwidth of the octave band spectral is 23% of the center frequency. The center frequency of each bandwidth is $f_c = 2^{1/3(i-1)}$, $i = 1, 2, 3\ldots n$, and there is the following relationship between the upper and lower bound of the bandwidth.

$$\frac{f_u}{f_l} = 2^{1/3}, \quad \frac{f_c}{f_l} = \frac{f_u}{f_c} = 2^{1/3} \tag{4}$$

where, f_l, f_c and f_u is the lower bound, center and upper bound of the bandwidth.

Table 2 Bandwidth division of one-third octave band spectral

Center frequency (Hz)	Lower bound (Hz)	Upper bound (Hz)
1	0.89	1.12
1.25	1.12	1.41
1.6	1.41	1.78
2	1.78	2.24
2.5	2.24	2.82
3.15	2.82	3.55
4	3.55	4.47
5	4.47	5.62
6.3	5.62	7.08
8	7.08	8.91
10	8.91	11.2
12.5	11.2	14.1
16	14.1	17.8
20	17.8	22.4
25	22.4	28.2
31.5	28.2	35.5
40	35.5	44.7
50	44.7	56.2
63	56.2	70.8
80	70.8	89.1

The calculated center, upper and lower bound of the bandwidth of a one-third octave band spectral is shown in Table 2. From the table, a regulation that would be meaningful in programming is drawn. That is, the center frequency doubles every three values.

(2) **The vertical axis**

The vertical axis of the one-third octave band spectral is the rms value of velocity. If we use the $\mathbf{x}(t)$ to symbol the acquired velocity signal, the rms value is defined as,

$$RMS = \sqrt{\frac{1}{T}\int_0^T \mathbf{x}^2(t)\mathrm{d}t} \qquad (5a)$$

where, T is the sampling interval.

The discrete form of Eq. (5a) is,

$$RMS = \sqrt{\frac{1}{N}\sum_{n=0}^{N-1}\mathbf{x}^2(n)} \tag{5b}$$

The rms value could be calculated through FFT spectral value $\mathbf{X}(m)$, when substituting the discrete Parseval Equation into Eq. (5b). The Parseval Equation in the exact form is,

$$\int_{-\infty}^{+\infty}|\mathbf{x}(t)|^2\,\mathrm{d}t = \int_{-\infty}^{+\infty}|\mathbf{x}(f)|^2\mathrm{d}f \tag{6a}$$

Discrete Eq. (6a), considering the neglecting of Δ in Eq. (3b), we get,

$$\sum_{n=0}^{N-1}|\mathbf{x}(n)|^2 = \frac{1}{N}\sum_{m=0}^{N-1}|\mathbf{X}(m)|^2 \tag{6b}$$

Substituting Eq. (6b) into Eq. (5b), we obtain the expression of rms value to be calculated in frequency domain.

$$RMS = \sqrt{\frac{1}{N}\sum_{m=0}^{N-1}\mathbf{X}^2(m)} \tag{7}$$

Equations (5b) and (7) constitute the two methods to determine the rms values, e.g. parallel filtering or a synthesis based on FFT analysis. The core MATLAB codes of both of the two methods are listed in Appendix "MATLAB Codes for rms Calculation".

(3) The tri-axial paper

Figure 2 showing the VC curves employs the tri-axial paper. From the figure, it is noted that, apart from the vertical axis indicating velocity, there are another two inclined axes marked with axis label as 'gal' and 'μm/s'. These two axes are the another two axis in the tri-axial paper.

In the frequency domain, there exists the following relationship between the acceleration, velocity and displacement.

$$S = \frac{V}{2\,\pi f} \tag{8a}$$

$$A = 2\pi f \cdot V \tag{8b}$$

Take log of the both sides of the two equations, we get,

$$\lg S = \lg(V/2\pi) - \lg(f) \tag{9a}$$

$$\lg A = \lg(2\pi V) + \lg(f) \tag{9b}$$

As a result, on a log-log plot of velocity as a function of frequency, constant displacement can be shown as a line inclined upward to the right. Likewise, acceleration can be shown as a line inclined upward to the left. This is the implied evidence of the rationality of tri-axial paper. Thus, one can read all the three metrics from a single graph.

Results Analysis

According to the data processing methods systematically introduced in the preceding part, the acceleration time-history, FFT spectral and the one-third octave band spectral of the three selected measuring points A1, B11 and C2 on three different directions are plotted in Figs. 4, 5 and 6 respectively.

Figure 4a shows the acceleration time-history of A1 point on North-south (NS), East-west (EW) and vertical directions. The time-history shows no sign of obvious periodicity. This re-confirms that, floor micro-vibrations of high-tech buildings are attributed from complicated types of vibration sources. The peak accelerations on the three directions are 16.683, 12.262 and 25.345 gal, respectively. The vibration of the vertical direction is generally larger than that of horizontal directions. Figure 4b is the FFT spectral of A1 point on three directions. The dominant frequencies of the horizontal directions are 70.41 and 105.43 Hz; and that of the vertical direction is 91.94 Hz, and several other higher frequencies.

In Fig. 4c, the one-third octave band rms values on the vertical direction is generally bigger than that on the horizontal directions, except at the center frequencies around 100 Hz. Besides, at the same frequencies, the one-third octave spectral slightly exceeded the VC-A curve in the EW and vertical directions; and there is not enough safety reserves of the vibration in the NS direction. Taking into account the fact that certain types of equipment are often supplied by the manufacturer with built-in vibration isolation, equipment installed on A1 base possibly operates smoothly. However, for sake of safety, it is still recommended to reinforce the A1 base.

Figure 5 presents the corresponding three figures of testing point B11. From these figures, similar variation laws with that of A1 point is observed. But the specific magnitude differs. The peak accelerations of B11 point are 4.86 gal (NS direction), 3.36 gal (EW direction) and 6.36 gal (vertical direction), which is much lower than that of A1 point. The dominant frequencies on the horizontal directions are 0.0028 and 66.51 Hz; and that of vertical direction is 0.0028 Hz. Clearly, the high dominant frequency bigger than 100 Hz disappeared, and a new dominant low

Fig. 4 Testing results of A1 point
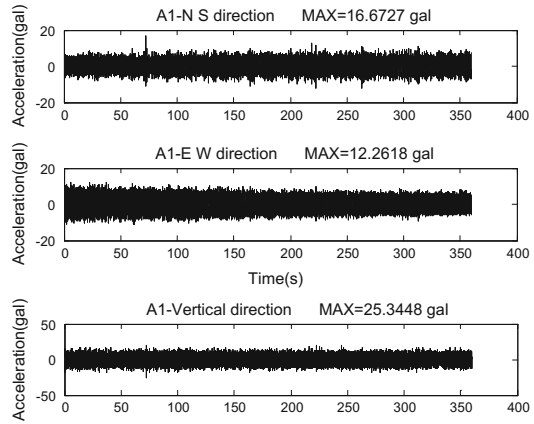
(a) **Acceleration time-history of A1 point**
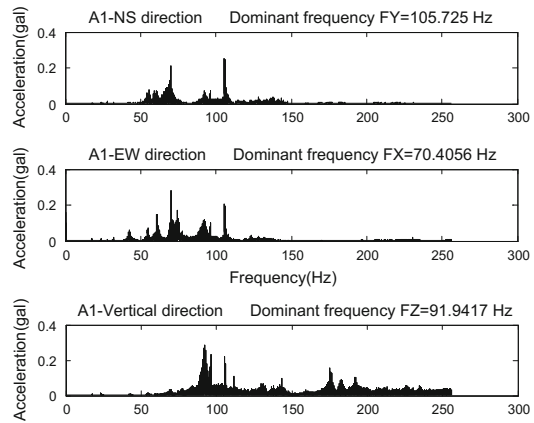
(b) **Acceleration FFT spectral of A1 point**
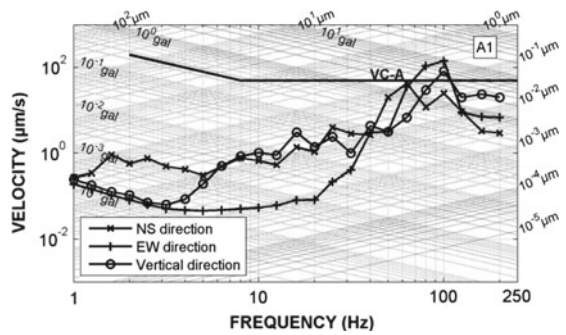
(c) **One-third octave band spectral of A1 point**

Fig. 5 Testing results of B11 point
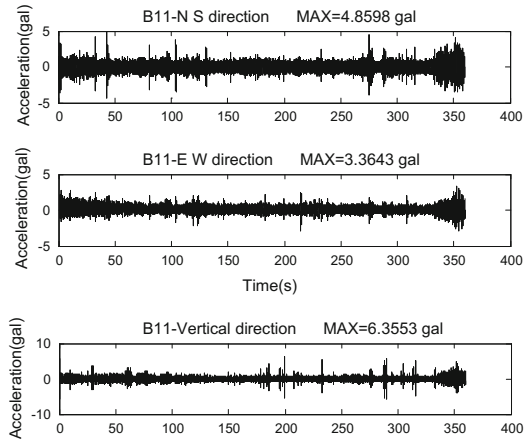
(a) Acceleration time-history of B11 point
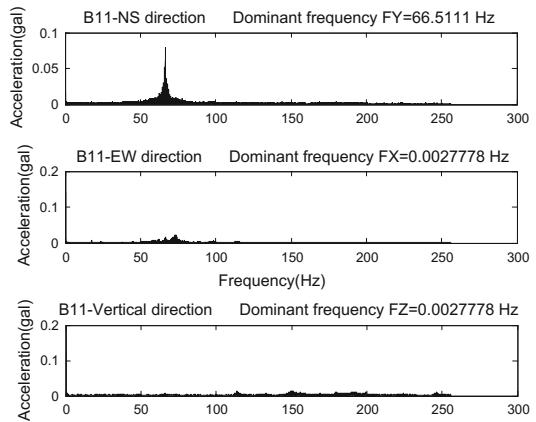
(b) Acceleration FFT spectral of B11 point
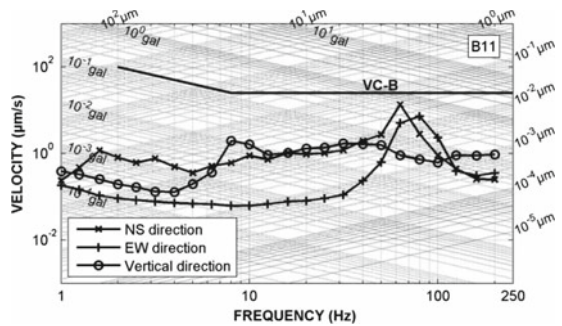
(c) One-third octave band spectral of B11 point

Fig. 6 Testing results of C2 point
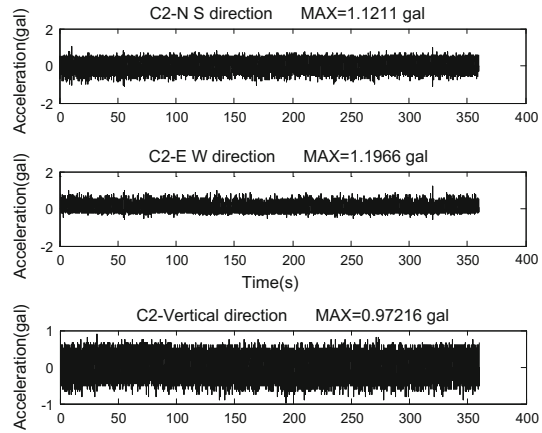
(a) Acceleration time-history of C2 point
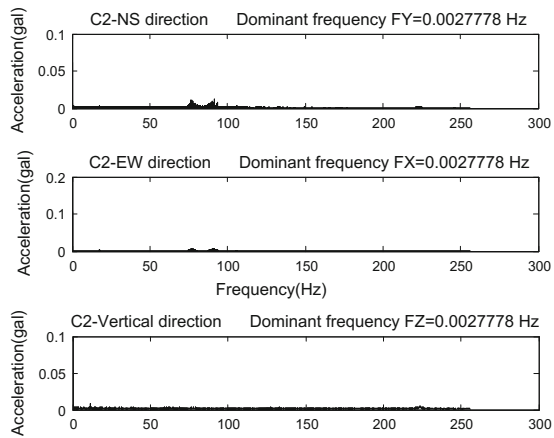
(b) Acceleration FFT spectral of C2 point
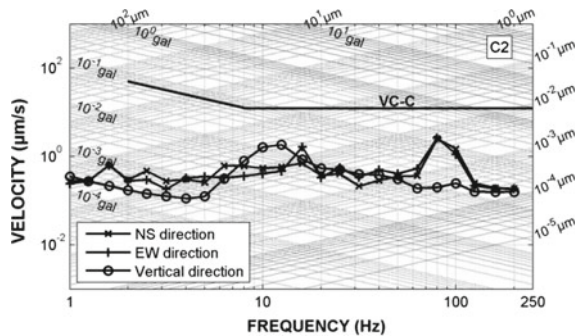
(c) One-third octave band spectral of C2 point

frequency aroused, compared with A1 point. The one-third octave band spectral on the three directions all lies below the VC-B curve, which indicates that B11 base is qualified for the specified vibration criterion.

Testing results of C2 point is shown in Fig. 6. In the time history of Fig. 6a, the acceleration magnitude is similar, and the peak acceleration in the horizontal directions (1.12 gal and 1.20 gal) is slightly larger than that in the vertical direction (0.97 gal). The dominant frequency is consistent in all the three directions, that is 0.0028 Hz. All of the medium and high dominant frequencies disappeared, and only the rather low dominant frequency reserved. The one-third octave band spectral of the three directions lies far below the assigned VC-C curves, with high safety stock. Compared with the one-third octave band spectrum of A1 and B11 points, the gap between the rms values on three direction narrowed. The one-third octave band spectral are almost the same in the three directions, except at the frequency of 80 Hz, where the spectral value on the horizontal directions exceeds that of the horizontal direction.

All in all, with the enhancement of the anti-vibration techniques, the acceleration amplitude decreases, the medium and high dominant frequencies disappears, while the low frequency dominants all the three directions; and the one-third octave band spectral become roughly the same in both the horizontal and vertical directions.

Conclusions

According to the formulation of data processing related equations and analysis of floor vibration for high-tech electronics warehouse, following conclusions can be drawn.

(1) The actual amplitude of the FFT spectral should be the product of the magnitude defined by Eq. (2a, 2b) and the factor $N/2$.
(2) One-third octave band spectral has privileges in presenting micro-vibrations in high-tech buildings, and should be employed in conjunction with the FFT analysis to fully reveal the vibration characteristics in frequency domain.
(3) The gap between the vertical and horizontal vibrations greatly narrowed both in time-history and one-third octave band spectral, when the anti-vibration techniques strengthened.
(4) When the anti-vibration techniques enhanced, medium and high dominant frequencies disappeared, while low frequency took the dominant role in all of the three directions.
(5) There is an abrupt rise of the one-third octave band spectral in horizontal direction at the frequency of 70–100 Hz, which may result from traffic disturbance. It is suggested that, A1 point should be re-enhanced to meet the assigned VC-A curve.

Appendix 1: MATLAB Codes for rms Calculation

Core Codes for rms Calculation in Frequency Domain Using Eq. (7)

```
f=[1.00 1.25 1.60 2.00 2.50 3.15 4.00 5.00 6.30 8.00];
fc=[f,10*f,100*f,1000*f,10000*f];         % set the value of the center fre-
quency
oc6=2^(1/6);
a=fft(x,nfft);                              % FFT on signal x
for j=1:nc
  fl=fc(j)/oc6;                        % lower bound
  fu=fc(j)*oc6;                          % upper bound
  nl=round(fl*nfft/sf+1);                 % position of the lower bound
  nu=round(fu*nfft/sf+1);                  % position of the upper bound
  if fu>sf/2
    m=j-1; break;             % the loop ended when the upper bound reaches
  end                          % half the sampling rate/cut-off frequency
  yc(j)=norm(abs(a(nl:nu)))*sqrt(2)/n;   % Eq. (7)
end
```

Core Codes for rms Calculation in Time Domain Using Eq. (5b)

```
f=[1.00 1.25 1.60 2.00 2.50 3.15 4.00 5.00 6.30 8.00];
fc=[f,10*f,100*f,1000*f,10000*f];
oc6=2^(1/6);
a=fft(x,nfft);
for j=1:nc
  fl=fc(j)/oc6;
  fu=fc(j)*oc6;
  nl=round(fl*nfft/sf+1);
  nu=round(fu*nfft/sf+1);
  if fu>sf/2
    m=j-1; break;
  end
```

```
  b=zeros(1,nfft);
  b(nl:nu)=a(nl:nu);
                          b(nfft-nu+2:nfft-nl+2)=a(nfft-nu+2:nfft-nl
+2);  % Filtering of desired bandwidth
                                                    c=ifft(b,
nfft);                              % inverse FFT on the filtered signal
  yc(j)=norm(real(c(1:n)))/sqrt(nfft);          % Eq.(5b)
end
```

References

1. Cheng, K. J., Lee, S. L., Yang, J. Y. (2012). The simulation of ambient vibration signal of high-tech factory buildings ground base. Applied Mechanics and Materials, 170–173: 3672-3677.
2. Jaswal, H. (2007). Analysis of micro-vibration in buildings, technical report. Proceedings of 2007 Earthquake Engineering Symposium for Young Researchers, Seattle, vol9, pp 1–12.
3. Nishiyama, K., Taoda, K., Dyke, S.J. (1997). Temporary threshold shift of vibratory sensation induced by hand-arm vibration composed of four one-third octave band vibrations. Journal of Sound and Vibration, 200(5): 631–642.
4. GB 5107-2015. Technical code for anti-vibration engineering of electronics industry. China Planning Press, Beijing (in Chinese).
5. Gao, G.Y., He, Z.K., Feng, S.J. (2008). Analysis of ground random vibration response of clear workshop in medium-weathered granite area. Journal of Engineering Geology, 16(Suppl.): 477–482 (in Chinese).
6. Gao, G.Y., Li, N., Xiong, H., Fang, C.P. (2008). Micro-vibration measurement of electronics workshop. Journal of Disaster Prevention and Mitigation Engineering, 2008 (Suppl.): 94–100 (in Chinese).
7. Gao, G.Y., Zhang, B., Li, N., Li J. (2010). Micro-vibration test and analysis for high-tech electronic industrial workshop. Proceedings of the 11th national geo-mechanics and engineering conference, Wuhan, pp. 303–306 (in Chinese).
8. Gao, G.Y., Song, J., Chen, Q.S., Zhang, B., Li, N. (2011). Field measurement and analysis of micro-vibration for high-tech electronics workshop. Advances in Environmental Vibration, Fifth International Symposium on Environmental Vibration, Chengdu, pp. 173–178.
9. Gao, G.Y., Zhang, B., Li, N. (2011). Micro-vibration test and numerical analysis of electronics industrial workshop. Site Investigation Science and Technology Site Investigation Science and Technology, (3): 51–55(in Chinese).
10. Gao, G.Y., Li, J., Zhang, B., Chai, J.L. (2012). Test and analysis of environmental vibration for electronic industrial workshop. Journal of Guilin University of Technology, 32(3): 381–385 (in Chinese).
11. Jiang, Z., Gao, G.Y., Song, J., Zeng, L., Feng, S.J. (2013). Vibration test and analysis of a high-tech electronics plant in Suzhou. Advances in Environmental Vibration, Sixth International Symposium on Environmental Vibration: Prediction, Monitoring, Mitigation and Evaluation, Shanghai, pp. 254–259
12. Gao, G.Y., Nie, C.X., Li, S.Y. (2016). Test and finite element analysis of micro-vibration of electronic warehouse. Journal of Heifei University of Technology, 39(4): 518–522 (in Chinese).

13. Gordon, C. G. (1992). Generic criteria for vibration-sensitive equipment. Proceedings of SPIE - The International Society for Optical Engineering, San Mateo, vol.1619, pp. 71–85.
14. Gordon, C. G. (1999). Generic vibration criteria for vibration-sensitive equipment. Proceedings of SPIE - The International Society for Optical Engineering, San Mateo, vol.3786, pp. 22–33.
15. Romdhane, L. (1999). Design and analysis of a hybrid serial-parallel manipulator. Mechanism and Machine Theory, 34(7): 1037–1055.
16. Amick, H. (1997). On Generic Vibration Criteria for Advanced Technology Facilities. Journal of the IES, 40(5): 35–44.
17. Richard, G.L. (2012). Understanding digital signal processing. Publishing House of Electronics Industry, Beijing.

Theoretical Solutions for Static and Dynamic Shakedown of Cohesive-Frictional Materials Under Moving Loads

Juan Wang, Shu Liu and Xiaojun Tang

Introduction

When an elastic–plastic structure is subjected to a cyclic load and the load level is higher than a yield limit but lower than a 'shakedown limit', the structure may adapt itself to the cyclic loads and respond purely elastically to the following load cycles, leading to no further exhibition of plastic strain. This phenomenon is called 'shakedown' [1]. In the application of transportation engineering, the shakedown phenomenon is recognized as that the plastic deformation of pavements or railways ceases to increase after a number of load passes. Otherwise, if the plastic deformation accumulates at each load application, excessive rutting or settlement will eventually occur. Therefore, the shakedown theory can be used to predict the long-term bearing capacity of a pavement or a railway.

The determination of the shakedown limit is the key task in the application of the shakedown theory. The shakedown limit can be determined by using either numerical elastic-plastic analyses [2] or the lower-bound and upper-bound shakedown theorems [3, 4]. The usage of the classical shakedown theorems allows a

J. Wang (✉) · S. Liu
Ningbo Nottingham New Materials Institute, The University of Nottingham,
Ningbo 315100, China
e-mail: juan.wang@nottingham.edu

S. Liu
e-mail: shu.liu@nottingham.edu.cn

J. Wang · S. Liu
State Key Laboratory for GeoMechanics and Deep Underground Engineering,
China University of Mining and Technology, Xuzhou 221116, China

X. Tang
Ningbo Nottingham International Academy for the Marine Economy
and Technology, The University of Nottingham, Ningbo 315100, China
e-mail: zx17874@nottingham.edu.cn

direct calculation of the shakedown limit by searching for the critical point or failure mechanisms of the structure, and therefore it draws much attention in the recent decades. Its corresponding analysis method is called 'shakedown analysis'. In the field of transportation engineering, shakedown analyses have been conducted by a number of researchers [5–16] for both plane strain and three-dimensional problems. Despite of those valuable work, the effect of the dynamic response of the material to the moving load on the shakedown limit was not well quantified, while recent practices demonstrate a great impact of the dynamic load on the real capacity of the foundations. In this paper, theoretical shakedown solutions considering the dynamic effect will be examined in detail as well as the static solutions for a plane strain cohesive-frictional half-space under a moving surface load.

Shakedown Analysis

A two-dimensional (2D) plane strain problem is considered under the simplifying assumption that the load is applied by an infinitely long roller, as shown in Fig. 1, where $2a$ is the contact width, P is the total normal loads per unit length applied in the vertical direction due to wheel rolling and Q is the total shear loads per unit length applied in the travel direction due to sliding. The normal and shear load distribution p and q on the contact area between the wheel and the pavement surface are described as follows:

$$p = \frac{2P}{\pi a^2}\left(a^2 - x^2\right)^{1/2},$$
$$q = \frac{2Q}{\pi a^2}\left(a^2 - x^2\right)^{1/2}.$$
$$(-a \leq x \leq a)$$

(1)
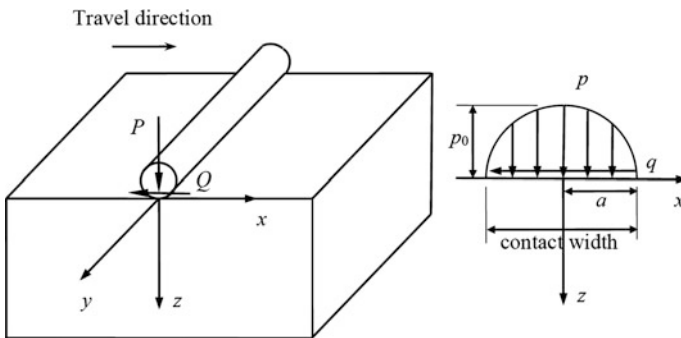
Fig. 1 An idealized plane strain problem

This load distribution is normally regarded as the 2D Hertz load distribution [17] and its maximum compressive pressure is $p_0 = 2P/\pi a$ occurring at the load centre ($x = z = 0$). Due to the relation between sliding and rolling, the normal and shear loads are correlated by the frictional coefficient μ as:

$$Q = \mu P. \tag{2}$$

This frictional coefficient is determined by the materials and the physical conditions of the interface.

Melan [3] first presented the lower-bound shakedown theorem: If a self-equilibrated residual stress field σ^r can be found, which when combined with the load-induced elastic stress fields σ^e satisfies the yield condition $f \leq 0$ everywhere, shakedown will occur. Ceradni [18] further enunciated and proved the dynamic lower-bound shakedown theorem for elastic perfectly plastic bodies. The difference between the dynamic and static shakedown theorems is that the dynamic theorem requires the elastic stress fields to be calculated using the dynamic equilibrium equations. The dynamic lower-bound shakedown theorem can be reduced to Melan's theorem if inertia and damping forces are neglected.

According to the static and dynamic shakedown theorems, the establishment of a residual stress field is essential for the calculation of shakedown limit. Residual stress is such that can remain in the half-space after the load applications as a result of plastic deformation. For the problem considered here that the plane strain half-space retains a flat surface after a number of load passes, every cross-section perpendicular to the travel direction experienced the same load history and therefore the residual stress field is only dependent on the depth z. When the equilibrium and boundary conditions are applied, it is not difficult to find that the normal residual stress σ^r_{zz} and the shear residual stress σ^r_{xz} cannot exist. As a result, the existing residual stresses in the 2D half-space are only σ^r_{xx} and σ^r_{yy}, as functions of depth z. This has also been numerically verified by the finite element analyses of Wang and Yu [2].

The total stresses for a general point in the half-space can be defined as the sum of the elastic stresses and the residual stresses. If the total applied load is denoted by λp_0 (λ is a dimensionless scale parameter, p_0 is conveniently set as unit pressure), then all the induced elastic stresses are also proportional to λ. On the x-z plane in the 2D model, the total stresses can be expressed as follows:

$$\begin{aligned}
\sigma_{xx} &= \lambda \sigma^e_{xx} + \sigma^r_{xx}, \\
\sigma_{zz} &= \lambda \sigma^e_{zz}, \\
\sigma_{xz} &= \lambda \sigma^e_{xz}.
\end{aligned} \tag{3}$$

Assuming the soil material obeys the Mohr-Coulomb yield criterion, the static and dynamic lower-bound shakedown theorems then requires that the total stress state of any point in the half-space has to lie within the Mohr-Coulomb yield

surface. Since σ_{yy}^r can be chosen such that σ_{yy} is an intermediate principle stress, the above requirement leads to the following expression:

$$f = \left(\sigma_{xx}^r + M\right)^2 + N \le 0, \tag{4}$$

with

$$M = \lambda\sigma_{xx}^e - \lambda\sigma_{zz}^e + 2\tan\phi\left(c - \lambda\sigma_{zz}^e\tan\phi\right),$$
$$N = 4\left(1 + \tan^2\phi\right)\left[\left(\lambda\sigma_{xz}^e\right)^2 - \left(c - \lambda\sigma_{zz}^e\tan\phi\right)^2\right].$$

where ϕ is friction angle and c is cohesion.

Furthermore, the residual stress σ_{xx}^r at any point i in the half-space must be between two roots of $f = 0$. For the system to be independent of the travel direction x, the possible residual stress σ_{xx}^r at any depth z is unique and has to lie between two critical residual stresses according to Yu and Wang [12]:

$$\max_x\left(-M_i - \sqrt{-N_i}\right) \le \sigma_{xx}^r \le \min_x\left(-M_i + \sqrt{-N_i}\right). \tag{5}$$

By substituting either of the critical residual stresses into Eq. (4), the shakedown condition of the current problem can be written as:

maximise λ,

$$\text{subject to} \begin{cases} f\left(\sigma_{xx}^r(\lambda\sigma^e), \lambda\sigma^e\right) \le 0 \\ \sigma_{xx}^r(\lambda\sigma^e) = \min_{z=j}\left(-M_i + \sqrt{-N_i}\right) \text{ or } \sigma_{xx}^r(\lambda\sigma^e) = \max_{z=j}\left(-M_i - \sqrt{-N_i}\right) \end{cases}.$$
$$\tag{6}$$

The above mathematical formulation can be solved by using a procedure suggested in Yu and Wang [12] thus will not be repeated here. Finally, the maximum admissible load parameter gives the shakedown limit of the half-space $\lambda_{sd}p_0$. The shakedown limit is usually represented as a dimensionless factor $\lambda p_0/c$, known as 'normalized shakedown limit' in the following sections.

Elastic Stress Fields

In order to implement the shakedown analysis, the elastic stress fields are required to be solved first. If the compressive stresses are treated as negative, the analytical solutions for elastic stresses due to the normal load P are given as examples for static and dynamic situations respectively. Solutions for the elastic stress fields induced by the surface traction Q can also be found in literatures.

Static Elastic Stress Fields

The static elastic stress fields for the case of a 2D Hertz load distribution can be found in Johnson [17]:

$$\sigma_{xx}^e = -\frac{2P}{\pi a^2}\left\{ m\left(1 + \frac{z^2 + n^2}{m^2 + n^2}\right) - 2z \right\} \tag{7}$$

$$\sigma_{zz}^e = -\frac{2P}{\pi a^2} m\left(1 - \frac{z^2 + n^2}{m^2 + n^2}\right) \tag{8}$$

$$\sigma_{xz}^e = \frac{2P}{\pi a^2} n \frac{m^2 - z^2}{m^2 + n^2} \tag{9}$$

with

$$m^2 = \frac{1}{2}\left\{ \sqrt{(a^2 - x^2 + z^2)^2 + 4x^2 z^2} + (a^2 - x^2 + z^2) \right\},$$

$$n^2 = \frac{1}{2}\left\{ \sqrt{(a^2 - x^2 + z^2)^2 + 4x^2 z^2} - (a^2 - x^2 + z^2) \right\},$$

in which the signs of m and n are the same as the signs of z and x respectively.

Dynamic Elastic Stress Fields

The stresses induced in an elastic 2D half-space by a concentrated line load moving at a constant speed V were provided by Cole and Huth [19]. Here only the solutions for subsonic cases are listed.

$$\sigma_{xx}^e = -\frac{P}{\pi}\left[-k_1(M_T^2 - 2M_L^2 + 2)\frac{\sin\theta_L}{r_L} + 2k_2\beta_T\frac{\sin\theta_T}{r_T} \right] \tag{10}$$

$$\sigma_{zz}^e = -\frac{P}{\pi}\left[k_1(2 - M_T^2)\frac{\sin\theta_L}{r_L} - 2k_2\beta_T\frac{\sin\theta_T}{r_T} \right] \tag{11}$$

$$\sigma_{xz}^e = -\frac{P}{\pi}\left[2k_2\beta_L\left(\frac{\cos\theta_L}{r_L} - \frac{\cos\theta_T}{r_T}\right) \right] \tag{12}$$

with

$$k_1 = \frac{2 - M_T^2}{(2 - M_T^2)^2 - 4\beta_L\beta_T}, \ k_2 = \frac{2\beta_L}{(2 - M_T^2)^2 - 4\beta_L\beta_T},$$

$$\beta_L = (1 - M_L^2)^{1/2}, \ \beta_T = (1 - M_T^2)^{1/2}, \xi_L = x + i\beta_L z = r_L e^{i\theta_L}, \ \xi_T = x + i\beta_T z = r_L e^{i\theta_T},$$

$$M_L = \frac{V}{C_L}, \ M_T = \frac{V}{C_T}, \ C_L = (\frac{\lambda + 2\mu}{\rho})^{1/2}, \ C_T = (\frac{\mu}{\rho})^{1/2}, \ \mu = \frac{E}{1 + \upsilon}, \ \lambda = \frac{\upsilon E}{(1 + \upsilon)(1 - 2\upsilon)},$$

where C_L and C_T are compressional and shear wave velocity respectively; E is Young's Modulus; υ is Poisson's ratio and ρ is density of the material.

The induced elastic stress field for a Hertz load distribution can be obtained by superposition of these concentrated load solutions. Solutions for the present study were validated through comparisons with plots in Cole and Huth [19] and results of finite element simulations.

Static Shakedown Limits

The normalized shakedown limits are dependent on the soil friction angle and surface frictional coefficient.

Figure 2 demonstrates the variation of the shakedown limit with the frictional coefficients μ for cohesive materials. The normalised shakedown limit decreases markedly with increasing frictional coefficient. Further investigation shows that the critical point moves towards the surface with the rise of the frictional coefficient. When $0.3 < \mu < 0.4$, the failure mode changes from subsurface failure (i.e. critical point lies below the surface) to surface failure (i.e. critical point lies on the surface). The present shakedown solutions are in agreement with the numerical shakedown solutions of Shiau [7] in which the Hertz load distribution was adopted. Moreover, the present results are between Sharp and Booker's [20] lower-bounds and Li and Yu's [1] upper-bounds in which the trapezoidal load distribution was applied. Li and Yu [10] only presented the shakedown limits for the frictional coefficient from 0 to 0.5.

The theoretical lower-bound shakedown limits are presented in Table 1 in detail. As can be seen, the shakedown limit increases with rising friction angle but decreases with increasing frictiodnal coefficient. In addition, the present lower-bound shakedown limits agree well with those in Krabbenhøft et al. [11]. When the normalized shakedown limit is multiplied by the corresponding frictional coefficient, the shakedown limit in terms of surface traction is obtained, as shown in Fig. 3. It is interesting to notice that the results do change with increasing frictional coefficient once the critical point lies on the surface of the half-space. This implies the 2D lower-bound shakedown limit is not affected by the normal pressure when surface failure occurs.
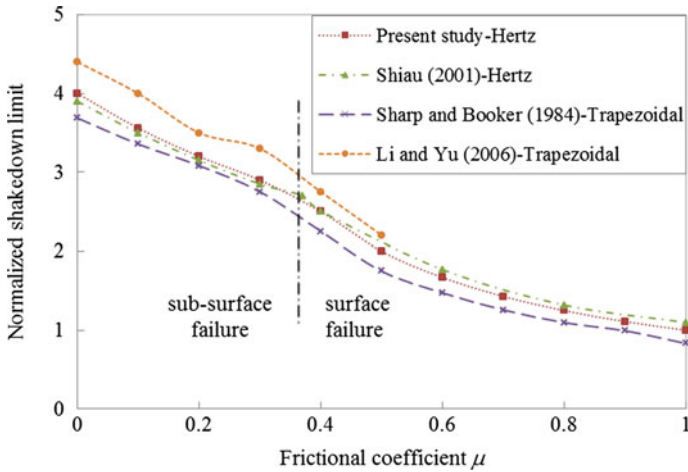
Fig. 2 Comparison with literatures

Table 1 Normalized shakedown limits for various frictional coefficients and friction angles

μ	$\phi = 0°$	5°	10°	15°	20°	25°	30°	35°	40°	45°
0.0	4.00	4.66	5.45	6.40	7.56	9.00	10.82	13.16	16.25	20.39
0.1	3.56	4.11	4.76	5.53	6.46	7.59	8.98	10.72	12.95	14.24
0.2	3.20	3.67	4.21	4.85	5.34	5.54	5.79	6.13	6.55	7.09
0.3	2.90	3.30	3.38	3.46	3.56	3.69	3.86	4.08	4.37	4.73
0.4	2.50	2.51	2.54	2.59	2.67	2.76	2.89	3.05	3.27	3.54
0.5	2.00	2.01	2.03	2.07	2.13	2.21	2.31	2.44	2.62	2.83
0.6	1.67	1.67	1.69	1.73	1.77	1.84	1.93	2.03	2.18	2.36
0.7	1.43	1.43	1.45	1.48	1.52	1.58	1.65	1.74	1.87	2.02
0.8	1.25	1.25	1.27	1.30	1.33	1.38	1.44	1.53	1.63	1.77
0.9	1.11	1.12	1.13	1.15	1.18	1.23	1.28	1.36	1.45	1.57
1.0	1.00	1.00	1.02	1.04	1.06	1.10	1.16	1.22	1.31	1.42

Dynamic Shakedown Limits

In this study, the material is assumed to have a stiffness modulus of 20 MPa, a Poisson's ratio of 0.2 and a density of 1800 kg/m³. This gives a Raleigh velocity of 62 m/s. Figure 4 and Table 2 demonstrate the decrease of the dynamic shakedown limit with increasing load moving speed towards the Rayleigh velocity. Figure 5 further exhibits the reductions of the shakedown limits from the static solutions in percentage. When the load moving speed is 1 m/s, the maximum difference between the static and dynamic shakedown limits is less than 1%. This value however is as high as 99% when the speed reaches 60 m/s. That is to say, the half-space can barely resist any moving load in long-term when the load moving
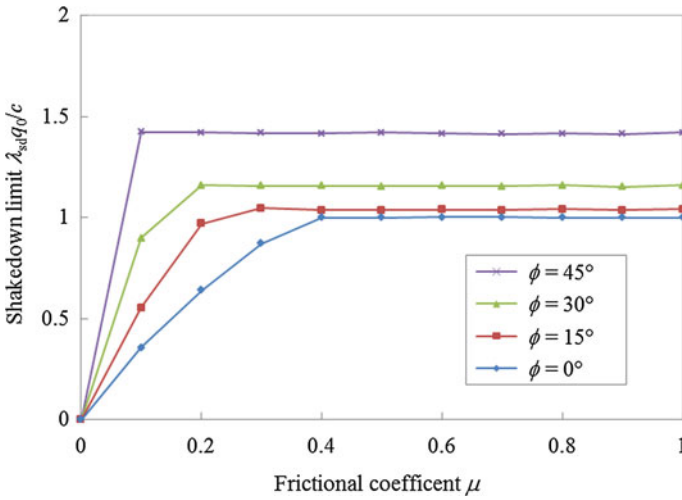
Fig. 3 Effect of surface traction on shakedown limit

speed approaches the wave propagation speed in the semi-infinite medium. A similar finding has also been identified numerically by Wang and Qian [15] when finite element simulations were used to obtain dynamic elastic stress fields for a three-dimensional pavement problem. When the load is travelling at a specified speed, the reduction of the shakedown limit from the static solution is more pronounced when the friction angle is relatively high. The theoretical solutions obtained in the present study can be used to benchmark numerical shakedown results.
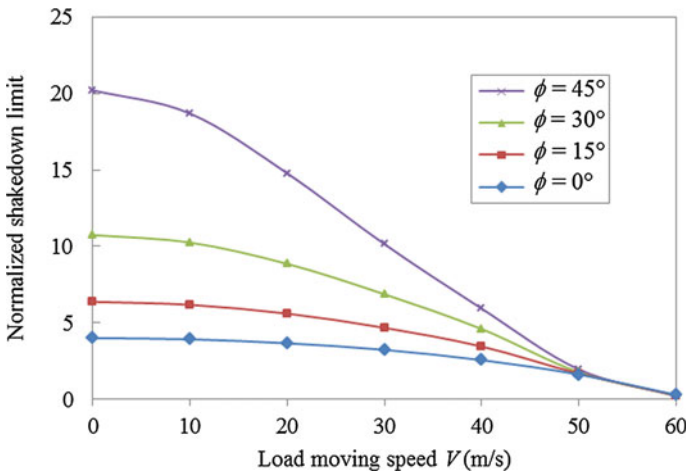
Fig. 4 Effect of surface traction on dynamic shakedown limit

Table 2 Normalized shakedown limits for various load moving speeds and friction angles

V (m/s)	$\phi = 0°$	5°	10°	15°	20°	25°	30°	35°	40°	45°
1	4.01	4.65	5.43	6.37	7.52	8.96	10.74	13.07	16.09	20.20
10	3.93	4.55	5.29	6.18	7.27	8.6	10.25	12.35	15.08	18.68
20	3.67	4.22	4.85	5.61	6.51	7.58	8.86	10.44	12.37	14.77
30	3.24	3.65	4.13	4.68	5.32	6.04	6.87	7.80	8.90	10.14
40	2.57	2.84	3.14	3.46	3.81	4.19	4.60	5.03	5.47	5.93
50	1.63	1.67	1.68	1.69	1.71	1.74	1.78	1.84	1.90	1.96
60	0.30	0.29	0.28	0.27	0.26	0.26	0.25	0.24	0.23	0.22
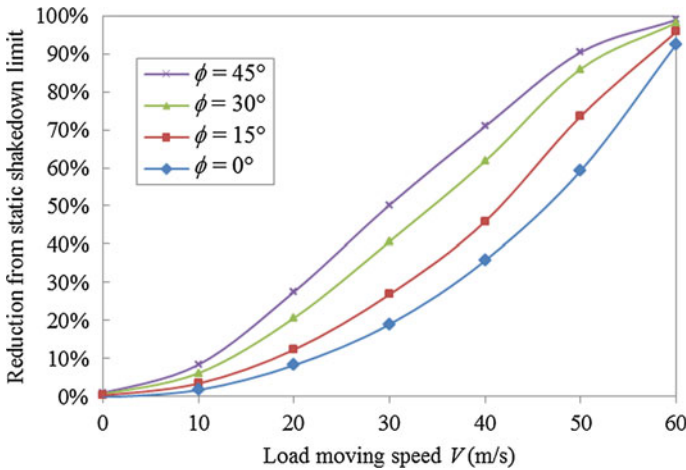
Fig. 5 Reduction of shakedown limit compared to the static solution

Conclusions

Theoretical solutions for static and dynamic shakedown of a Mohr-Coulomb plane strain half-space under a moving load are presented in this paper. Key findings are summarised as follows:

1. The increasing friction angle can significant raise the static and dynamic shakedown limits.
2. The use of the surface traction reduces the shakedown limit. When the traction is limited, the shakedown limit is dependent on both normal pressure and tangential shear and the critical point lies within the half-space. When the traction is relatively high, the shakedown limit is only controlled by the horizontal force, and the failure mode is changed to surface failure.
3. When the dynamic response of the half-space to the moving load is considered, the shakedown limit (or long-term bearing capacity) is decreased with the rise of the load travelling speed. The reduction in percentage is also affect by the

friction angle of the material. The higher the friction angle, the larger the reduction. The long-term bearing capacity of the half-space will be nearly zero if the load moving speed approaches the wave velocity.

Although the theoretical solutions presented in this paper are for a single layered medium, the shakedown condition developed in this paper is also applicable to multi-layered systems. For the case of a multi-layered medium, the static or dynamic elastic stress fields need to be solved numerically. And the theoretical results in the present paper can be used as benchmark data.

References

1. Yu, H.S. (2006). Plasticity and Geotechnics. Springer.
2. Wang, J., Yu, H.S. (2013). Residual stresses and shakedown in cohesive-frictional half-space under moving surface loads. Geomechanics and Geoengineering, 8(1): 1–14.
3. Melan, E. (1938). Der spannungsgudstand eines henky-mises schen kontinuums bei verlandicher belastung. Sitzungberichte der Ak Wissenschaften Wie, 147: 73.
4. Koiter, W.T. (1960). General theorems for elastic-plastic solids. In Progress in Solid Mechanics, edited by R. Hill. eds I. N. Sneddon. North-Holland, Amsterdam.
5. Sharp, R.W., Booker, J.R. (1984). Shakedown of pavements under moving surface loads. Journal of Transportation Engineering, ASCE, 110: 1–14.
6. Yu, H.S., Hossain, M.Z. (1998). Lower bound shakedown analysis of layered pavements using discontinuous stress fields. Computer Methods in Applied Mechanics and Engineering, 167(3–4): 209-222.
7. Shiau, S.H. (2001). Numerical methods for shakedown analysis of pavements under moving surface loads, Ph.D. Thesis, The University of Newcastle, Australia.
8. Boulbibane, M., Ponter, A.R.S. (2005b). Linear matching method for limit load problems using the Drucker-Prager yield condition. Géotechnique, 55: 731–739.
9. Yu, H.S. (2005). Three-dimensional analytical solutions for shakedown of cohesive-frictional materials under moving surface loads. Proceedings of the Royal Society A: Mathematical, Physical and Engineering Science, 461(2059): 1951–1964.
10. Li, H.X., Yu, H.S. (2006). A nonlinear programming approach to kinematic shakedown analysis of frictional materials. International Journal of Solids and Structures, 43(21): 6594–6614.
11. Krabbenhøft, K., Lyamin, A.V., Sloan, S.W. (2007). Shakedown of a cohesive-frictional half-space subjected to rolling and sliding contact. International Journal of Solids and Structures, 44 (11–12): 3998-4008.
12. Yu, H.S., Wang, J. (2012). Three-dimensional shakedown solutions for cohesive-frictional materials under moving surface loads. International Journal of Solids and Structures, 49(26): 3797–3807.
13. Wang, J., Yu, H.S. (2013). Shakedown analysis for design of flexible pavements under moving loads. Road Materials and Pavement Design, 14(3): 703–722.
14. Wang, J., Yu, H.S. (2014). Three-dimensional shakedown solutions for anisotropic cohesive-frictional materials under moving surface loads. International Journal for Numerical and Analytical Methods in Geomechanics, 38(4): 331–348.

15. Wang, Y.G., Qian J.G. (2016). Dynamic shakedown lower-bound analysis of three-dimensional half-space under moving load. Rock and Soil Mechanics, 37(1): 570–576.
16. Liu, S., Wang, J., Yu, H.S., Wanatowski, D. (2016). Shakedown solutions for pavements with materials following associated and non-associated plastic flow rules. Computers and Geotechnics, 78: 218–266.
17. Johnson, K.L. (1985). Contact Mechanics. Cambridge University Press.
18. Ceradni, G. (1980). Dynamic shakedown in elastic-plasticity bodies. Journal of Engineering Mechanics Division, 106: 481–499.
19. Cole, J., Huth, J. (1958). Stresses produced in a half plane by moving loads. Journal of Applied Mechanics, 25: 433–436.
20. Sharp, R.W., Booker, J.R. (1984). Shakedown of pavements under moving surface loads. Journal of Transportation Engineering, ASCE, 110: 1–14.

Influences of Subgrade Bed Structure on Dynamic Responses of Railway Subgrade Under Train Loading: Field Testing Case Study

Junhua Xiao, Chengyu Liu, Ye Shengyu and Binglong Wang

Introduction

Safe and comfortable operations of high-speed railway significantly raise the demands of railway subgrade with long-term stability under cyclic train loading. Although countries independently constructing high-speed railway, such as Japan, France, Germany, and China, have spent a long time in the research of railway subgrade, significant differences in the design of subgrade exist among countries [1–5]. So it is necessary to have a thorough knowledge of the mechanical behavior of railway subgrade under long-term cyclic train loading, and thus to make the optimization design.

Especially, the upper part of railway subgrade, which is the most susceptible part to train cyclic loading and environmental variations, should be strengthened in railway subgrade design, to provide a solid foundation for track with enough strength, high stiffness and long-term stability. However, the strengthening methods in countries are different [1–5]. Therefore, it is meaningful to study the behaviors of different upper part of subgrade structures under train loading, and to make an optimized design in the future. Designations for the upper part of subgrade structure vary amongst countries, for simplicity, this paper addresses it as

J. Xiao (✉) · C. Liu · Y. Shengyu · B. Wang
Key Laboratory of Road and Traffic Engineering of the Ministry
of Education, Tongji University, Shanghai, China
e-mail: jhxiao@tongji.edu.cn

C. Liu
e-mail: wer5lcy@tongji.edu.cn

Y. Shengyu
e-mail: yeshengyu_tj@163.com

B. Wang
e-mail: wangbl8@163.com

SUBGRADE BED in accordance to Chinese *Code for Design of High Speed Railway* (TB10621-2014) [3].

In this paper, in order to investigate the influences of subgrade bed structure on dynamic responses of railway subgrade under train loading, four sections of railway subgrades with different thickness and stiffness of subgrade bed were built on the same construction. Then, in situ large number cyclic loading test on subgrade surface was conducted to simulate long-term effect of train loading, and consequently, subgrade dynamic responses, such as dynamic stress, elastic deformation, dynamic stiffness, and accumulative plastic deformation were measured and analyzed. The study should be valuable for deepening the understanding of subgrade dynamic behavior under train loading, as well as for the decision of subgrade design parameters in the future.

Design of Field Testing

Subgrade Parameters

Four different subgrade sections marked as A, B, C, and D were built for cyclic loading tests. For each subgrade, the cross section was trapezoidal, as shown in Fig. 1. The width of the subgrade surface was 13.8 m; the slope rate was 1:1.5; the height was 4.5 m, of which the thickness of subgrade bed (including the surface layer and the bottom layer) was 3.0 m and the rest of 1.5 m was embankment fill.

The surface layer of subgrade bed was made of well-graded gravels [2, 3], with the thickness of 0.7, 0.5, 0.65, and 0.9 m for sections A, B, C, and D, respectively, and the top of the surface layer of C was covered by a 0.05 m layer of bituminous concrete [2, 3, 5]. The bottom layers of subgrade bed of A and B were filled with weathered granite; but for C and D, Xiashu clay was used. Below subgrade bed, the embankments were filled with Xiashu clay. The relative compactions of the filling materials for the bottom layer of subgrade bed and embankment were 95 and 90%, respectively [2, 3]. The natural subsoil below the subgrade was improved by vacuum Preloading with prefabricated vertical drain method. The cyclic loading test was carried out after subgrade settlement caused by self-weight finished. The specified design of the tested subgrade is shown in Table 1.
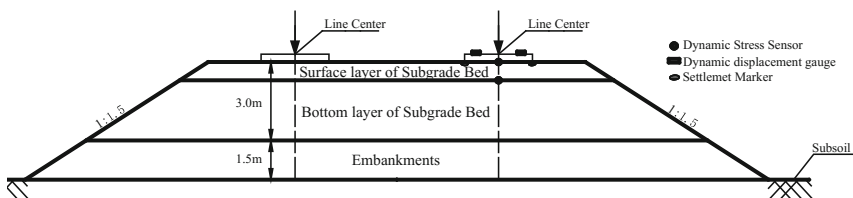
Fig. 1 Subgrade cross section and sensors layout

Table 1 Design of subgrade structures

Section	Range	Length (m)	Thickness of the surface layer of subgrade bed (m)	Thickness of the bottom layer of subgrade bed (m)	Filling material of the bottom layer of subgrade bed	Notes
A	k0 + 40–k0 + 45	5	0.7	2.3	Weathered granite	
B	k0 + 45–k0 + 50	5	0.5	2.5	Weathered granite	
C	k0 + 50–k0 + 55	5	0.65	2.3	Xiashu Clay	With additional 0.05 m layer of bituminous concrete on the top
D	k0 + 55–k0 + 60	5	0.9	2.1	Xiashu Clay	

In regard to the properties of the two filling materials of weathered granite and Xiashu clay, the former had the main mineral compositions of quartz and feldspar, with a coefficient of curvature of 1.08, a coefficient of nonuniformity of 14.71, a dry density of 2.15 kg/m^3, and an optimum moisture content of 7.2%. For the latter, all particles passed No. 200 (0.075 mm) U.S. standard sieve; the soil had a liquid limit of approximately 38.4, a plasticity index of approximately 21.2, a dry density of 1.80 kg/m^3, and an optimum moisture content of 15.9%. Additionally, the average unconfined compressive strength and compression modulus of undisturbed Xiashu clay sample were 776 kPa and 47.28 MPa, respectively.

Loading Apparatus and Measurement System

The dynamic stress pulse on subgrade surface induced by moving train can be simulated by haversine pulse, and two adjacent axles under the same bogie generate approximately a single stress pulse [6]. According to the railway grade in this case study, the possible maximum dynamic stress on subgrade surface would be exerted by a passenger-train with the axle load of 16t running at 200 km/h. The stress amplitude was calculated as approximately 67 kPa using the formula $\sigma = 2.6P (1 + \alpha v)$ [6], where P was the static axle load, α was a velocity factor which was 0.003, and v was train speed. Additionally, loading frequency of the stress pulse ranged from 3 to 14 Hz determined by the distance of two bogies, vehicle length and train speed [6].

As shown in Fig. 2, the in situ excitation system was a vibrator seated on a concrete foundation on subgrade surface. The concrete foundation, which was 11.5t

Fig. 2 In-situ excitation system on subgrade surface

Fig. 3 The NI-DAQ data acquisition system
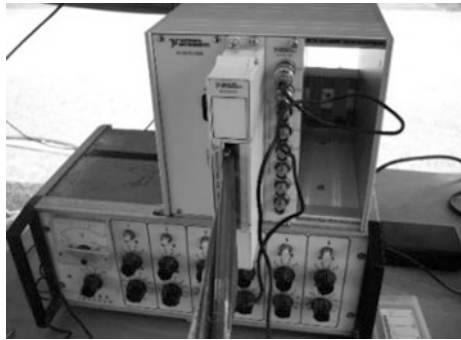
in weight and acted as a counter weight in tests, was 2.6 m in length, 1.2 m in width, and 1.5 m in height. The vibrator generated cyclic loading by rotating a centrifugal mass block. Self-weight of the vibrator was 4t, and the excitation forces could be set from 0 to 300 kN with a maximum frequency of 30 Hz. In the tests, the frequency of cyclic loading was selected as 10–13 Hz.

All dynamic data were collected via the NI-DAQ system developed by National Instruments, as shown in Fig. 3. The dynamic stress was measured by double-oil-cylinders strain-gauge type transducer pressure cells, as shown in Fig. 4a. Elastic dynamic displacement and acceleration were measured by Type 891-2 vibrometer shown in Fig. 4b, which were developed by *Institute of Engineering Mechanics, China Earthquake Administration*, whose accuracies were 2×10^{-8} m in deformation and 1×10^{-5} m/s^2 in acceleration. Cumulative deformation was measured using a Type S$_1$ level gauge and markers on the sub-grade, whose accuracy was 0.01 mm.

The sensors layout in subgrade is depicted in Fig. 1. The dynamic elastic deformation sensors were directly set on the top of concrete foundation as the concrete foundation always kept close contact with subgrade surface during tests. The data of subgrade dynamic stress, dynamic elastic deformation and accumulative plastic deformation were collected every 100,000 times of load cycles.

(a) Pressure Cell   (b) Type 891-2 vibrometer
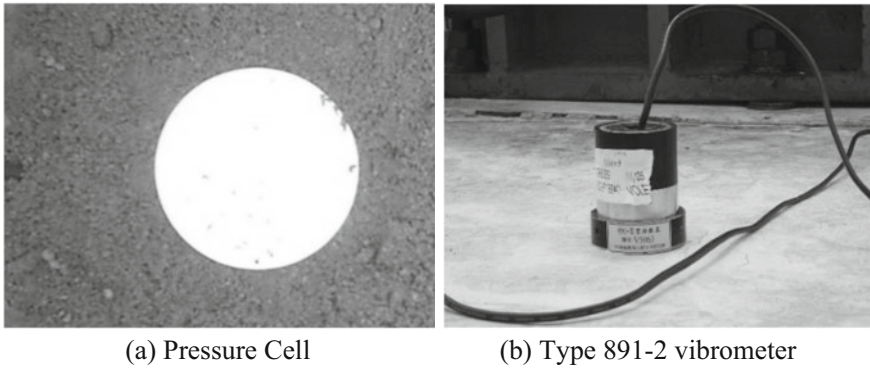
Fig. 4 Sensors used in the experiment

Tests Results and Analysis

Attenuation of Dynamic Stress in Subgrade

The dynamic stress applied on subgrade by moving train is one of the major factors affecting subgrade stability and permanent deformation. To ensure long-term stability of subgrade, subgrade dynamic stress should not exceed the dynamic strength of filling materials, and the surface layer of subgrade bed should significantly attenuate the dynamic stress on subgrade surface in order to reduce the dynamic stress transmitted to underlying weak subgrade soil [3]. Figure 5 shows the typical dynamic stress waveform in different subgrade depth for section A under cyclic loading, it can be seen that the peak dynamic stress on subgrade surface during tests was approximately equal to the set value of 67 kPa.

Table 2 shows the average attenuation coefficients of dynamic stress for the surface layer of subgrade bed (i.e. the ratio of dynamic stress on the bottom of the surface layer of subgrade bed and on subgrade surface) for 4 different sections.

It can be seen from Table 2, the average attenuation coefficient of dynamic stress for the surface layer of subgrade bed ranged from 0.341 to 0.492. The attenuation coefficient was influenced by both the thickness and the stiffness of the surface layer of subgrade bed. Comparing section A with section B, the surface layer of subgrade bed of section A was 0.2 m thicker than section B, and consequently section A attenuated an additional 10% of dynamic stress more than section B. This represents that a thicker surface layer of subgrade bed increased the attenuation effect of dynamic stress. Similarly, section C, with a 0.05 m layer of bituminous concrete on the top of subgrade while with a thinner surface layer of subgrade bed than section D, nearly matched section D in dynamic stress attenuation. This indicates that the attenuation effect also increased with increasing in subgrade bed stiffness, and the 0.05 m layer of bituminous concrete played a conspicuous role in dynamic stress attenuation in fielding tests.
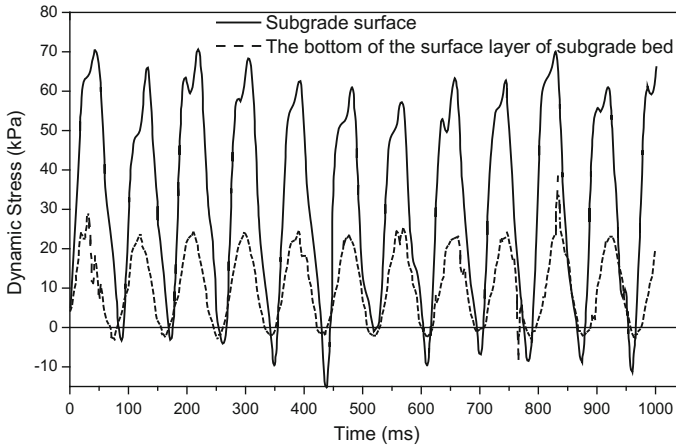
Fig. 5 Typical dynamic stress waveform in different subgrade depth

Table 2 Average attenuation coefficient of subgrade dynamic stress

A	B	C	D	Notes
0.393	0.492	0.352	0.341	The attenuation coefficient of dynamic stress for a 0.05 m layer of bituminous concrete was 0.85

Subgrade Elastic Deformation and Dynamic Stiffness Under Cyclic Loading

The value of subgrade elastic deformation directly affects the stabilities of subgrade and track bed, and subgrade elastic deformation reflects in track deformation, which affects running safely and comfortably of high-speed train. In addition, when subgrade reached a steady forced vibration state under cyclic loading, its dynamic stiffness can be directly obtained from the dynamic stress and elastic deformation if neglect the influence of damping.

Table 3 shows the elastic deformation on subgrade surface and subgrade dynamic stiffness for different sections in tests.

It can be seen from Table 3, for all sections in tests, the elastic deformations on subgrade surface ranged from 0.32 to 0.43 mm, which were much smaller than the generally accepted upper limit of subgrade elastic deformation for high-speed railway, i.e. 1 mm [3]; and dynamic stiffness of subgrade ranged from 148.5 to

Table 3 Subgrade elastic deformation and dynamic stiffness

	A	B	C	D
Elastic deformation on subgrade surface (mm)	0.320	0.412	0.370	0.430
Subgrade dynamic stiffness (MPa/m)	201.4	151.4	170.1	148.5

201.4 MPa/m. In this testing, section A achieved the smallest elastic deformation and the largest dynamic stiffness. Though the thickness or stiffness of the surface layers of subgrade bed of sections C and D were larger than A, the dynamic stiffness of the two sections were smaller than A, because the bottom layers of subgrade bed of sections C and D were filled by weaker material (i.e. Xiashu Clay). Consequently, subgrade dynamic stiffness of sections C and D were approximately the same as section B, while section B had the thinnest surface layer of subgrade bed but had a stiffer bottom layer of subgrade bed (i.e. weathered granite). These results indicate that an optimized subgrade dynamic stiffness requires comprehensive matching of the thickness and stiffness of the layer structure of subgrade. Additionally, a higher dynamic stiffness of section C than section D shows that the 0.05 m layer of bituminous concrete covered on subgrade surface significantly increased subgrade dynamic stiffness.

Subgrade Accumulative Plastic Deformation

The development of accumulative plastic deformation (the average values of the left and right sensors) on subgrade surface with load cycles is shown in Fig. 6. It can be seen from Fig. 6 that, the accumulative plastic deformation developed fast in the initial stage of load cycles, and it became stable gradually. The accumulative plastic deformation became stable after 1.8, 1.8, 1.0 and 2.5 million load cycles for sections A, B, C, and D, respectively.

Table 4 lists the accumulative deformations on subgrade surface observed for 4 sections. On the whole, the ultimate accumulative deformations were smaller than
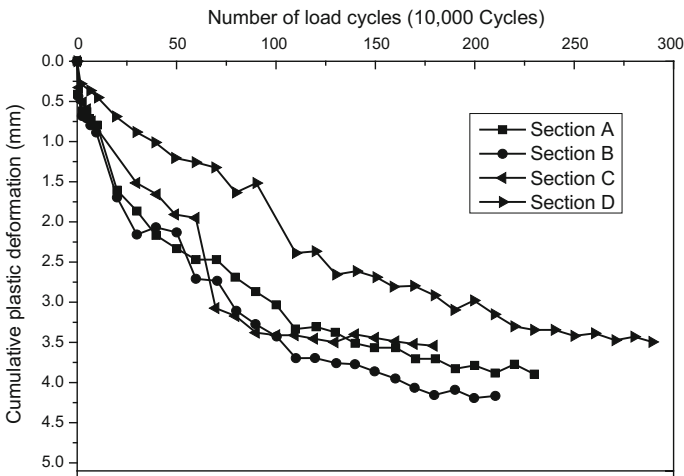
Fig. 6 Subgrade accumulative plastic deformation during cyclic loading tests

Table 4 Accumulative deformation on subgrade surface

Section	A	B	C	D
Accumulative deformation (mm)	3.7	4.2	3.4	3.5

5 mm, meeting the requirement that subgrade permanent deformation due to train traffic load should not exceed 5 mm [1]. Additionally, the accumulative deformations of different subgrade bed structures differed slightly, representing the appropriate abilities of resistance to permanent deformation for both weathered granite and Xiashu clay as the filling materials for the bottom layer of subgrade bed. Comparing Table 2 with Table 4, it indicates that the accumulative plastic deformation had relationship with the attenuation effect of dynamic stress in subgrade. The more the attenuation of dynamic stress in subgrade, the smaller the accumulative deformation of subgrade.

Conclusions

In situ cyclic train loading simulation tests on railway subgrade were conducted towards four different subgrade bed structures to explore the influences of the thickness and stiffness of subgrade bed on dynamic responses of railway subgrade. The following conclusions were concluded.

(1) Section A achieved the smallest subgrade elastic deformation and the largest dynamic stiffness, indicating an optimized subgrade dynamic stiffness requires comprehensive matching of both the thickness and stiffness of the layer structure of subgrade.
(2) Both weathered granite and Xiashu clay had appropriate abilities of resistance to permanent deformation as the filling materials of the bottom layer of subgrade bed, but subgrade dynamic stiffness and elastic deformation were significantly affected by the stiffness of the bottom layer of subgrade bed.
(3) The increase of the thickness or stiffness of the surface layer of subgrade bed promoted the attenuation of dynamic stress in subgrade. The more the attenuation of dynamic stress in subgrade, the smaller the accumulative deformation of subgrade.
(4) A 0.05 m layer of bituminous concrete on subgrade top significantly increased subgrade dynamic stiffness.

References

1. German Railway Standard (GRS) (2008). Erdbauwerke planen, bauen und instand halten. Richtlinie 836, DB Netz AG.
2. Ministry of Railways of PRC (MORPRC). (2005). Interim design provisions for newly-built passenger railway line at speed of 200 to 250 km/h. China Railway Publishing House, Beijing, China.
3. National Railway Administration of PRC (NRAPRC). (2014). Code for Design of High speed Railway (English Edition) (TB 10621-2014). China Railway Publishing House, Beijing, China.
4. UIC. (1994). Earthworks and Track-Bed Layers for Railway Lines (UIC Code 719 R). International Union of Railways, Paris, France.
5. WJRC. (2002). Construction and maintenance standards for Shinkansen track. West Japan Railway Company, Osaka, Japan.
6. Liu, J.K., and Xiao, J.H. (2010). Experimental study on the stability of silt railroad subgrade with increasing train speed. Journal of Geotechnical and Geoenvironmental Engineering, 136 (6), 833–841.

A Study on Unsaturated Dynamic Constitutive Model Under Cyclic Loading for Western Sichuan Talus Mixed Soil

Kai Cui and Yongkui Li

Introduction

The subgrade settlement of expressway, railway, and city subway in the operation process has become a hot issue for geotechnical engineering in recent years. By observing the settlement in a later period, it was found that different degrees of settlement and deformation occur for subgrade under the function of long-term traffic load in the operation of many engineering works [1–4]. The settlement and deformation of the engineering subgrade in the Western Sichuan area mainly occur in the soil subgrade mixed with sand gravel and clay particles. The geologic origin classification states that it belongs to talus mixed soil formed out of collapse and landslide. The settlement and deformation of the subgrade are mainly caused by the long-term traffic load during operation. Meanwhile, the common practice for the traffic load simulation is the equivalent substitution with cyclic loading. Therefore, the core of the subgrade settlement and deformation during the operation is converted into a description of the soil accumulative deformation under cyclic loading.

The fundamental difference between talus mixed soil in Western Sichuan area and the current accumulative deformation research object (sandy soil or soft clay) is that the talus mixed soil in Western Sichuan area has the following two major features: (1) the talus mixed soil in the operation is usually in unsaturated state [5]; and (2) the content of fine particle has significant impact on the dynamic deformation characteristics of soil [6, 7].

Vaid and Eliadorani [8], Leong et al. [9], Chu et al. [10] and Karam et al. [11] have proven that the saturation of the coarse granular soil, especially sandy soil, and loosen silt is less than 100% (i.e., unsaturated state) when they are unstable under cyclic loading. Therefore, studying the dynamic characteristics of soil in the

K. Cui (✉) · Y. Li
Department of Civil Engineering, Southwest Jiaotong University,
Chengdu 610031, China
e-mail: cuikai@swjtu.cn

unsaturated state under the cyclic loading is very necessary. Through more than twenty years of development, the elastic–plastic constitutive description has increasingly matured and formed two huge kinds of unsaturated elastic–plastic constitutive models based on independent bivariate [12] and related bivariate [13] theories. However, the abovementioned researches seldom involve a dynamic characteristics research of soil. Moreover, the few research achievements involved in the unsaturated soil constitutive model is only applicable to sandy or silty soil.

This paper takes the Western Sichuan talus mixed soil as the research object, considers two basic features (i.e., unsaturated state and fine particle content difference) and explores the dynamic constitutive description of soil accumulative deformation under cyclic loading to establish an unsaturated mixed soil dynamic constitutive model. This model is then used to analyze the traffic load dynamic reaction considering the accumulative deformation and provide a reliable theoretical basis and analytic method for the dynamic stability analysis and disaster prevention and control of such a mixed soil structure. The model has an extremely important theoretical and engineering practical value in the safe operation of structures, such as various mixed soil high embankment, expressway, and railway bed, in the Western Sichuan area and the whole southwest area.

Modelling and Method

Physical Property Test

This study selected two kinds of typical talus mixed soils in the Western Sichuan area as the research object the related physical index was also measured. Soil #1 $C_u = 32.69$, $C_c = 1.02$ and Soil #2 $C_u = 37.50$, $C_c = 2.13$.

According to the characteristics of the talus mixed soil found in the literature [14], the characteristics of soils #1 and #2 are as follows:

- They are dominated by coarse particles (the particle size is bigger than 0.075 mm). The content is above 84.5%. The mechanical property of the mixed soil is mainly decided by the coarse particle grain skeleton.
- The fine particle content in the clay mineral is high, and the clay mineral and carbonate easily form cement among the particles. The higher the fine particle content, the richer the cement and the more obvious the cementation. The fine particle content may affect the mechanical property of the mixed soil.

The water soil characteristic test adopted the Van Genuchten model fitting test curve Eq. (1) by controlling the suction using a pottery soil plate. Figure 1 shows the soil water characteristic curve.
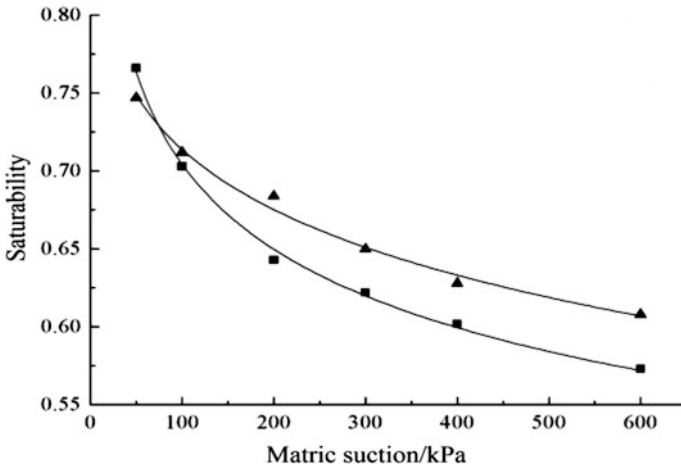
Fig. 1 Soil-water characteristic curve (square for Soil #1 and triangle for Soil #2)

$$S_r(s) = \left(\frac{1}{1 + (\beta_{S_r} s)^n} \right)^m \tag{1}$$

Dynamic Constitutive Model of Mixed Soil Under Cyclic Loading

The research on dynamic property of talus mixed soil under traffic load can be translated into a description of the mixed soil unsaturated dynamic constitutive model under cyclic loading that can reflect an accumulative deformation. The mixed soil unsaturated dynamic model herein is abbreviated as the HHT model.

Literature [12, 15] indicated that the strength and rigidity of the soil increases with the suction increase when the soil is in an unsaturated state. The present study applied the loading–collapse (LC) yield surface curve in the BBM [12] model and utilised the soil water characteristic curve (SWCC) to deduce the coupling function between the suction and the reaction.

Description of the Mechanical Behavior in the Unsaturated State

The SWCC theory proposed by Van Genuchten [16] was used as follows according to the LC yield curve Eq. (2) proposed by Alonso et al. [12] to study and take the (p, s) surface as the LC yield surface:

Fig. 2 Three-dimensional
view of the yield surfaces in
the (p, q, s) stress space
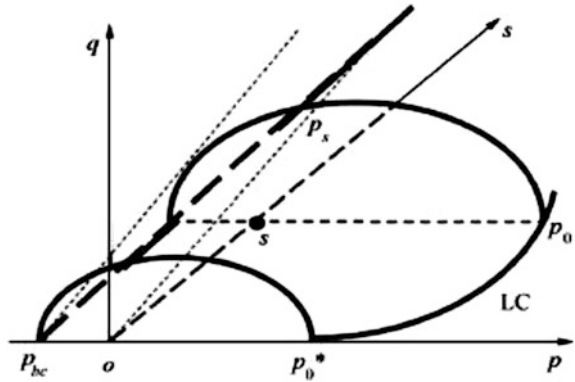
$$\frac{p_0(s)}{p^c} = \left(\frac{p_0^*}{p^c}\right)^{\frac{\lambda(0)-\kappa_m}{\lambda(s)-\kappa_m}} \tag{2}$$

where, p_0^* denotes the induration parameter representing the pre-consolidation
pressure in the saturation condition; $p_0(s)$ is the pre-consolidation pressure in the
unsaturation condition; p^c represents the reference stress; $\lambda(s)$ is the compression
index of the unsaturated soil; and κ_m is the resilience index.

$$\lambda(s) = \lambda(0)[(1 - r_s)\exp(-\beta_s s) + r_s] \tag{3}$$

where, r_s is the constant related to the maximum soil rigidity; β_s represents the
control of the change rate of the soil rigidity with the change of the suction; and
$\lambda(0)$ denotes the compression index of the saturated soil.

Figure 2 shows that one can establish an interaction model between the external
force and the suction in a 3D stress space (p, q, s). Herein, p_s is the incoming
variable describing the change of soil cohesion. The tensile strength of the soil
affected by the suction is expressed as follows:

$$p_s = k_s \cdot s \tag{4}$$

where, k_s is the tensile strength influence coefficient.

Mechanical Behavior Description of the Fine Particle Effect

Based on the view of Literature [17, 18], according to the microcosmic soil
mechanics theory, the fine particle effect is mainly reflected in two following
aspects:
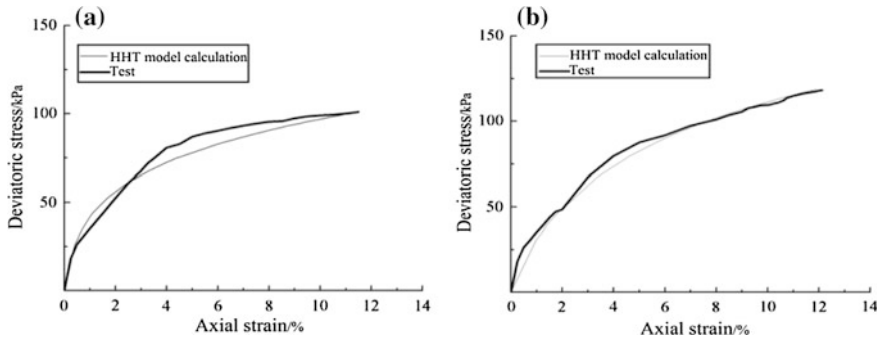
Fig. 3 a Soil #1 and **b** Soil #2 static triaxial test results and model calculations

- It causes a soil void ratio change, and the actual void ratio is not anymore equal to the apparent void ratio (i.e., the apparent void ratio for the mixed soil is determined by the coarse grain skeleton). The higher the fine particle content, the bigger the difference.
- It may cause the contact density of the coarse grain to change. The coarse grain may obtain a tensile strength increment because of the fine particle intervention. The bigger the amount of intervention, the bigger the tensile strength increment. The fine particle intervention will reduce the pairs among the coarse grains and decline the frictional strength.

The void ratio in the model is revised to the actual void ratio e_0 based on the abovementioned two points and the model established in the first step. The tensile strength increment caused by the fine particle intervention in the stress variable is then reflected and considered together with the increment caused by the unsaturation, which is reflected in tensile strength influence coefficient, k_s. This study realizes the description of the fine particle in the HHR model through the two aspects. Accordingly, p_{bc} in Fig. 3 denotes the external tensile strength of soil caused by cementation formed by the clay mineral and carbonate of the fine particles in the coarse grains. Its influence in k_s is considered as an aspect of the fine particle effect. The influence of the fine particle content on the normal solidification and resilience curve slopes is also considered to complete the construction of the talus mixed soil unsaturated hybrid constitutive model.

Elastic-Plastic Constitutive Model Based on Boundary Surface Theory

This study adopted critical state theory and considered the abovementioned unsaturation state and fine particle effect in the current boundary surface model frame to establish the HHT constitutive model that can describe the accumulative deformation behavior of the unsaturated soil in the Western Sichuan Area under cyclic loading.

Stress Variable Selection

In this chapter, the stress variable $\left(\boldsymbol{\sigma} = (p,q)^T\right)$, suction ($s$) and induration parameter (p_0) were defined as the stress state variables of the model by considering the soil's self-structure.

Boundary Surface Equation Based on the MCCM Model

The revised Cambridge model (MCCM) can reflect the major deformation characteristics of remodeling the normal consolidation or over consolidation clay well. The model has a simple form, a few model parameters and a simple parameter determination. Therefore, it is one of the few recognized models used to describe the soil constitutive model. The study adopts the boundary surface equation as follows by combining with the unsaturation of the talus mixed soil:

$$F(\boldsymbol{\sigma}, s, p_0^*) = q^2 - M_f^2(p + p_s)(p_0 - p) \tag{5}$$

where, M_f is the slope of the critical condition line; and p_0^* is the induration parameter representing the pre-consolidation pressure.

Related Mobility Law

This study adopts the following related flow rule to simplify the HHT model:

$$\begin{cases} d\boldsymbol{\varepsilon}^p = \mathbf{n}_{gL/U} \cdot \dfrac{\mathbf{n}_f^T d\boldsymbol{\sigma}}{H_{L/U}} \\ \mathbf{n}_{gL/U} = \mathbf{n}_f \end{cases} \tag{6}$$

where, $\mathbf{n}_{gL/U}$ is the unit normal vector on the plastic power surface; $\mathbf{n}_f$ is the unit normal vector on the boundary surface; and $H_{L/U}$ is the loading and unloading plastic modulus.

One can deduce and obtain the unit normal vector, $\mathbf{n}_f$, on the boundary surface as follows according to Eq. (5):

$$\mathbf{n}_f = \frac{1}{\left[\left(\frac{\partial F}{\partial \boldsymbol{\sigma}}\right)^T \left(\frac{\partial F}{\partial \boldsymbol{\sigma}}\right)\right]^{1/2}} \left(\frac{\partial F}{\partial \boldsymbol{\sigma}}\right)^T \tag{7}$$

Induration Law

$$\frac{dp_0^*}{p_0^*} = \frac{1+e_m}{\lambda(0) - \kappa_m} d\varepsilon_{vm}^p \tag{8}$$

Plastic Loading Modulus on the Boundary Surface

The consistency condition indicates that the following equation exists:

$$dF = \left(\frac{\partial F}{\partial \boldsymbol{\sigma}}\right)^T d\boldsymbol{\sigma} + \frac{\partial F}{\partial p_0^*} dp_0^* + \frac{\partial F}{\partial s} ds = 0 \tag{9}$$

Meanwhile, the following equation is obtained by substituting Eq. (8) into Eq. (9) and organizing them:

$$\frac{\partial F}{\partial p} \cdot dp + \frac{\partial F}{\partial q} \cdot dq + \frac{\partial F}{\partial s} ds + \frac{\partial F}{\partial p_0^*} p_0^* \frac{1+e_m}{\lambda(0) - \kappa_m} d\varepsilon_{vm}^p = 0 \tag{10}$$

One can then compute the plastic loading modulus, $H_{L/U}^{BS}$, on the boundary surface as follows by utilizing Eq. (6):

$$H_{L/U}^{BS} = -\frac{A \cdot B}{C} \tag{11}$$

Herein,

$$A = \frac{\frac{\partial F}{\partial p} \cdot dp + \frac{\partial F}{\partial q} \cdot dq}{\sqrt{\left(\frac{\partial F}{\partial p}\right)^2 + \left(\frac{\partial F}{\partial q}\right)^2} \sqrt{\left(\frac{\partial G}{\partial p}\right)^2 + \left(\frac{\partial G}{\partial q}\right)^2}} \tag{12}$$

$$B = \frac{\partial G}{\partial p} \cdot \frac{\partial F}{\partial p_0^*} p_0^* \frac{1+e_m}{\lambda(0) - \kappa_m} \tag{13}$$

$$C = \frac{\partial F}{\partial p} \cdot dp + \frac{\partial F}{\partial q} \cdot dq + \frac{\partial F}{\partial s} ds \tag{14}$$

Each differential expression of the plastic loading modulus, $H_{L/U}$, is computed as follows by combining with the soil unsaturation and utilizing Eq. (5):

$$\frac{\partial G}{\partial p} = \frac{\partial F}{\partial p} = M_f^2(2p + p_s - p_0) \tag{15}$$

$$\frac{\partial G}{\partial q} = \frac{\partial F}{\partial q} = 2q \tag{16}$$

$$\frac{\partial F}{\partial p_0^*} = \frac{\partial F}{\partial p_0}\frac{\partial p_0}{\partial p_0^*} = -M_f^2(p+p_s) \cdot \frac{\lambda(0)-\kappa_m}{\lambda(s)-\kappa_m}\left(\frac{p_0^*}{p^c}\right)^{\frac{\lambda(0)-\lambda(s)}{\lambda(s)-\kappa_m}} \tag{17}$$

$$\frac{\partial F}{\partial s} = \frac{\partial F}{\partial p_s}\frac{\partial p_s}{\partial s} + \frac{\partial F}{\partial p_0}\frac{\partial p_0}{\partial s} = k_s M_f^2(p-p_0) - M_f^2(p+p_s)\frac{\partial p_0}{\partial s} \tag{18}$$

Mapping Laws Based on the Mobile Mapping Center

The strain stress hysteresis that occurs in the soil unloading–reloading procedure is called the "hysteresis loop phenomenon". Huang et al. [19] amended the radius mapping criterion in traditional boundary surface theory to simulate such a soil phenomenon [20]. The present study adopted such a kind of simulation method.

The mapping criterion is as follows:

$$H_{L/U} = H_{L/U}^{BS}\left(\frac{\delta_0}{\delta}\right)^{r_{L/U0}} \tag{19}$$

where, r_{L0} and r_{U0} are the initial loading and unloading mapping indices of the equivalent remodeling soil; δ_0 is the distance from the mapping point to the mapping center; and δ is the distance from the stress point to the mapping center.

$$\delta_0 = \sqrt{(p_1-p_{OL/U})^2 + (q_1-q_{OL/U})^2} \tag{20}$$

$$\delta = \sqrt{(p-p_{OL/U})^2 + (q-q_{OL/U})^2} \tag{21}$$

The computation process of the mapping point on the boundary surface is obtained as follows according to the loading direction difference:

• Forward loading process

The origin of the coordinates, O_s, in the stress space, $p_s - q_s$, is taken as the mapping center, P_{OL}, at the time of forward loading. Thus, the following equation is obtained according to the definition of the traditional radial direction criterion:

$$\eta_s = \frac{q}{p+p_s} = \frac{q_1}{p_1+p_s} \tag{22}$$

One can adopt the yield surface equation shown in Eq. (23) to facilitate the computation:

$$\frac{p+p_s}{p_0+p_s} - \frac{M_f^2}{M_f^2+\eta_s} = 0 \tag{23}$$

Subsequently, η_s is computed according to the current stress point. One can then compute the mapping point, $P_{L1}(p_{L1}, q_{L1})$, on the boundary surface as follows by substituting Eq. (22) into Eq. (23):

$$\begin{cases} p_{L1} = (p_0+p_s) \cdot \frac{M_f^2}{M_f^2+\eta_s} \\ q_{L1} = (p_{L1}+p_s) \cdot \eta_s \end{cases} \tag{24}$$

- Reverse loading process

The initial stress point, P_{OU}, of unloading is taken as the mapping center at the time of reverse loading. Therefore, the traditional radial criterion is not any more applicable. However, the stress path of the test is usually selected, such that the gradient, k, of reverse loading can be computed as follows according to the stress path:

$$k = \frac{\Delta q_U}{\Delta p_U} \tag{25}$$

where, Δ is the stress increment in each computational step.

Consequently, the following relation between the current stress point, P (p, q), and the mapping point, $P_{U1}(p_{U1}, q_{U1})$, on the boundary surface is obtained as follows:

$$\frac{q - q_{U1}}{p - p_{U1}} = k \tag{26}$$

One can then compute the deviatoric stress, q_{U1}, as follows:

$$q_{U1} = q - k(p - p_{U1}) \tag{27}$$

Equations (27) and (5) can now be combined as a simultaneous equation set. One can then compute the mapping point, $P_{U1}(p_{U1}, q_{U1})$, on the boundary surface as follows:

$$\begin{cases} p_{U1} = \frac{-b-\sqrt{b^2-4ac}}{2a} \\ q_{U1} = q - k(p - p_{U1}) \end{cases} \tag{28}$$

where, $a = \left(k^2 + M_f^2\right), b = \left[2k(q-kp) + M_f^2(p_s - p_0)\right]$, and $c = \left[(q-kp)^2 - M_f^2 p_s p_0\right]$

Loading Criterion and Plastic Deformation

This study considered the loading process as reverse loading. Hence, the stress increment vector, $d\sigma$, and the yield surface normal vector, n_f, during the loading and unloading processes shall meet the following formulae:

$$\begin{cases} \frac{n_f^T d\sigma}{H_L} > 0, & Positive/negative\ loading \\ \frac{n_f^T d\sigma}{H_L} = 0, & Neutral\ loading \end{cases} \quad (29)$$

Based on the boundary surface equation Eq. (5), one can compute the plastic modulus equation Eq. (19) of the stress point during the loading and unloading procedure by combining the induration criterion equation Eq. (11) and the mapping criterion of the mobile mapping center. Moreover, one can now finally use the associated flow criterion equation Eq. (6) to obtain the plastic strain increment, $d\varepsilon^p$.

Determination of the HHT Model Parameters

A total of 16 parameters are used in the HHT model. Accordingly, e_0 can be obtained after revising the measured apparent void ratio via a physical nature test [21], p^c, p_0^*, $\lambda(0)$, κ_m, r_s and β_s can be acquired through an isotropy water drainage compression test using different suctions (different water contents). M_f and k_s can be determined through static triaxial shear test and isotropy water drainage compression tests. s_0 can be got through a suction measurement. β_{Sr}, n and m can be determined by fitting the soil water characteristic curve. u_m (Poisson's ratio) can be valued as 0.45 according to the experience. r_{L0} and r_{U0}, which are the parameters imported from the interpolation function of the mixed soil plastic loading and unloading modulus, can be determined by fitting the loading and unloading curves.

Table 1 shows a summary of the soil sample parameters for the HHT model.

Table 1 Parameter value table

(a)

No.	e_0	λ_0	κ_m	u_m	k_s	M_f	r_{L0}	r_{U0}
Soil #1	0.714	0.058	0.012	0.45	0.655	1.016	0.008	0.1
Soil #2	0.903	0.135	0.035	0.45	0.787	1.245	0.008	0.1

(b)

No.	s_0 (kPa)	p^c (kPa)	p_0^* (kPa)	r	β_s	n	m	β_{Sr}
Soil #1	50	8	75	0.512	0.007	5.4	0.022	0.205
Soil #2	50	43.1	90	0.563	0.013	0.227	5.754	0.004

Model Results, Discussions and Verification

This study applied the constructed HHT model to forecast the deviatoric stress under static and cyclic loading. The applicability of the HHT model to the talus mixed soil was judged by forecasting the curve result and the comparison between the static and dynamic triaxial experimental results.

The corresponding parameter was then substituted into the model, and the result was compared with that of the constant water content shear test (Fig. 3) and the constant water content cyclic shear test (Fig. 4). The specimen size in the dynamic triaxial cyclic loading test was $\Phi 300$ mm $\times$ 600 mm. The deviatoric stress and the solidification confining pressure imposed on the half sine were 25 kPa. The load amplitudes of soils #1 and #2 were 15 and 22 kPa, respectively. The cyclic loading frequency was 0.05 Hz, while the cycle index was 100 times.

Figure 3 shows a comparison of the deviatoric stress and the axial strain curve of soils #1 and #2 under the constant water content situation. The suction, s, was about 50 kPa.

The comparison between the test and the computational result of the HHT model showed that the test curves of soils #1 and #2 and the computational result of the model had better consistency.

Figure 4 presents a comparison of the deviatoric stress and the axial strain curve of soils #1 and #2 under the constant water content cyclic loading. The suction, s, was about 50 kPa.

The comparison between the test and the computational result of the HHT model showed that the cyclic shear test curves of soils #1 and #2 conformed better to the computational result of the model.

The combination of Figs. 3 and 4 illustrated that the computation result of the HHT model was identical to the test result, indicating that the model can simulate the mechanical property of the unsaturated talus mixed soil under cyclic loading.
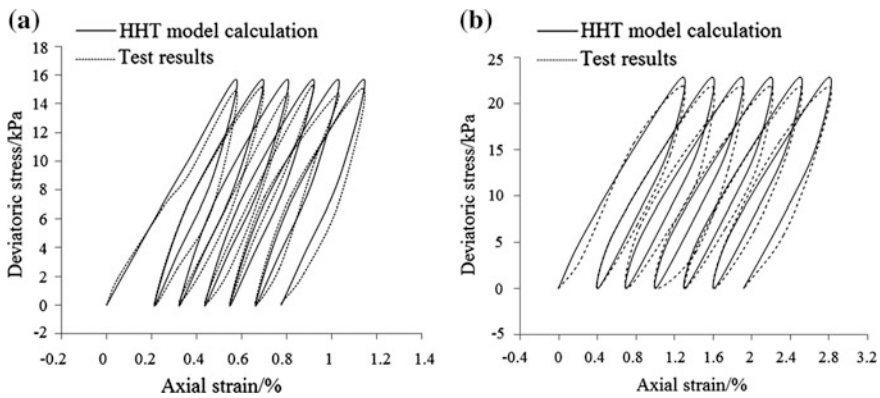
Fig. 4 a Soil #1 and b Soil #2 dynamic triaxial test results and model calculations

Conclusions

The saturated mixed soil in the Western Sichuan area had two major features, namely, unsaturation and fine particle content difference. This study combined the effect of the two major features based on current boundary surface theory to obtain an unsaturated mixed soil HHT dynamic constitutive model of accumulative deformation under traffic cyclic load. Accordingly, the model parameters can be obtained through common test result or fitting. This study also verified the applicability of the model using the static and dynamic triaxial test results. The comparative analysis showed that the model was able to reflect the mechanical property of the unsaturated mixed soil under static load, especially cyclic loading. Furthermore, the model was able to reflect the hysteresis characteristics of the soil in the loading and unloading processes.

References

1. Tarumi, N., Sunaga, M. (1988). Behaviors of low embankments on soft grounds during train passage, Proc JSCF, vol. 400, pp. 1–11.
2. Miura, N., Fujikawa, K., Sakai, A. (1995). Field measurement of settlement in Saga airport highway subjected to traffic load. Soil Mechanics and Foundation Engineering, 43(6): 49–51.
3. Ling, J.M., Wang, W., Wu, H.B. (2002). On residual deformation of saturated clay subgrade under vehicle load. Journal of Tongji University(Natural Science), 30(11): 1315–1320.
4. Ye, Y.D., Zhe, H.H., Wang, R.L. (2007). Analysis on the current status of metro operating tunnel damage in soft ground and its causes. Chinese Journal of Underground Space and Engineering, 3(1): 157–160, 166.
5. Yin, Y.P. (2009). Features of landslides triggered by the Wenchuan earthquake. Journal of Engineering Geology, (01): 29–38.
6. Ding, Z.Y., Feng, T.G., Zhou, J., Li, H. (2013). Experimental study of influence of fine particle content on dynamic properties of saturated silty soil. Yellow River, 35(3): 138–140.
7. Zheng, Q. (2014). Experimental study on the influence of percent fines on the dynamic properties of silt [Master Thesis D]. Hangzhou: Zhejiang University of Technology.
8. Vaid, Y.P., Eliadorani, A. (1998). Instability and liquefaction of granular soils under undrained and partially drained states. Canadian Geotechnical Journal, 35: 1053–1062.
9. Leong, W.K., Chu, J., The, C.I. (2000). Liquefaction and instability of a granular fill material. Geotechnical Testing Journal, 23(2): 178–192.
10. Chu, J., Leroueil, S., Leong, W.K. (2003). Unstable behavior of sand and its implication for slope instability. Canadian Geotechnical Journal, 40: 873–885.
11. Karam, J.P., Cui, Y.J., Tang, A.M., Terpereau, J.M., Marchadier, G. (2009). Experimental study on the cyclic resistance of a natural loess from northern France. Soils and Foundations, 49(3): 421–429.
12. Alonso, E.E., Gens, A., Josa, A. (1990). A constitutive model for partially saturated soils[J]. Geotechnique, 40(3): 405–430.
13. Wheeler, S.J., Sharma, R.S., Buisson, M.S.R. (2003). Coupling of hydraulic hysteresis and stress-strain behavior in unsaturated soils. Geotechnique, 53(1): 41–54.

14. Zhou, Q. (2012). Experimental study of unsaturated strength characteristics for Chuanxi talus mixed soil [Master Thesis D]. Chengdu: Southwest Jiaotong University.
15. Wheeler, S.J., Sivakumar, V. (1995). An elasto-plastic critical state framework for unsaturated soil. Geotechnique, 45(1): 35–53.
16. Van, Genuchten, M.TH. (1980). A closed-form equation for predicting the hydraulic conductivity of unsaturated soils. Soil Science Society Of America Journal, 44: 892–898.
17. Lambe, T.W., Whitman, R.V. (1969). Soil mechanics. Wiley, New York.
18. Mitchell, J.K. (1976). Fundamentals of soil behaviour. Wiley, New York.
19. Huang, M.S., Yang, C., Cui, Y.J. (2009). Elasto-plastic bounding surface model for unsaturated soils under cyclic loading. Chinese Journal of Geotechnical Engineering, 31 (6): 817–823.
20. Dafalias, Y.F., Herrmann, L.R. (1982). Bounding surface formulation of soil plasticity. Soil Mechanics Transient and Cyclic Loads. John Wiley & Sons Ltd, New York, pp. 253–282.
21. Kuerbis, R.H. (1989). The effect of gradation and fines content in the undrained loading response of sand. Master of Applied Science dissertation, University of British Columbia, Vancouver, Canada.

Study on Mitigation Measures to the Vibration of Vehicle-Track System

Li Zhou, Yanyun Luo, Yan Liu and Qiutong Li

Introduction

Recently concerns about environmental problems induced by urban viaduct rail transit, especially vibration and noise, have increased substantially. More and more researchers and businesses devote into control and administration of noise and vibration pollution directly affected by elevated lines. Currently measures in control of viaduct vibration are mainly by improving and optimizing the rail structure with low elastic stiffness to achieve, but rarely considered the impact of the wheel-rail vibration and noise. The vibration acceleration of foundation under rail can be reduced by low stiffness of rail system and therefore its work performance can meet the requirement of environment. However, it might lead to enlarge dynamic response of railway vehicles [1]. As mentioned above, most energy produced by dynamic interaction between wheels and rail would be left around wheels and rail instead of propagating to tunnel or bridge. Previous experimental results indicated that vibration acceleration of bogie increased by 0.6–0.8 dB along with the decrease of fastener stiffness by 10 kN/mm [2]. Xu and Li [3] constructed a vehicle-track-subgrade model and analyzed the effect of fastener stiffness from 20 to 80 kN/mm. The results of numerical simulation showed that by increasing fastener

L. Zhou · Y. Luo · Y. Liu (✉) · Q. Li
Institute of Rail Transit, Tongji University, Shanghai 200000, China
e-mail: liuyans.851010@hotmial.com

L. Zhou
e-mail: zhouli201007@163.com

Y. Luo
e-mail: yyluo15@163.com

Q. Li
e-mail: lqt910818@163.com

stiffness, wheels and bogie acceleration would be dropped by 40.1 and 28.4%, respectively. Wang and Xu [4] found enhancing fastener stiffness could result in the acceleration of rail and wheels rising, especially for high frequency range.

Noise pollution induced by viaduct vibration during urban rail transit operation has become one of the prominent problems in the field of urban transportation nowadays. In order to reduce structural noise of viaduct, measures to control the dynamic response of bridge structure should be taken firstly. Based on the previous research, conventional method by lowering stiffness of track structure referred before is not applicable to this situation. However, dynamic vibration absorber which is also called tuned mass damp (TMD) has been widely used to control and reduce the excessive vibration of the bridge structure under external excitation. Zhang [5] has proved that Multiple-TMDs (MTMD) was good enough to be adopted in bridge vibration reduction by numerical analysis. Shen [6] proposed that MTMD is a powerful and applicable solution to reduce vibration of both bridge and vehicles.

This paper presents a numerical model to simulate dynamic response of all the parts in urban viaduct rail transit, including vehicle, rail system and viaduct. Aimed at evaluating the effect of track structure stiffness to dynamic response of each component in vehicle-track-bridge system, 3-Dimension wheel-track-bridge coupling system [7] is modeled by ABAQUS software. Track irregularity is an important excitation source which can cause vibration of wheel-track system. As a consequence, this article utilize the sixth grade track irregularity power spectral density of U.S as the excitation to simulation analysis of vibrating process. The simulation results are obtained to verify the accuracy of previous theoretical studies, also to provide a simulation basic platform for dynamic vibration absorber. Furthermore, in order to reduce vibration of foundation under rail while not increase vibration of rail vehicles, a new method is proposed by using dynamic vibration absorber. 2-Dimension simplified model of rail-absorber will be established to validate if this way can reduce vibration of the whole coupling system. Performance evaluation and parameter optimization of dynamic vibration absorber are also discussed. Mass and stiffness which are the most important parameters will be considered at the end of this article.

Numerical Analysis of Wheel-Track-Bridge System

Numerical Model of Wheel-Track-Bridge System

The model of wheel-track-bridge was built by ABAQUS software. The span of girder is 30 m while the width is 9.6 m, shown in Fig. 1. Density of the concrete is 2.5×10^3 kg/m^3, elastic modulus 3.45×10^{10} N/m^2, Poisson ratio 0.17. Parameters of rail section are based on the type of 60 kN/m U71Mn(k), elastic modulus 2.059E + 11 kN/mm, density 7830 kg/m^3 and Poisson ratio 0.3. The fastening systems are simulated as spring-damper elements, of which stiffness is

Fig. 1 Box girder cross section (unit: mm)
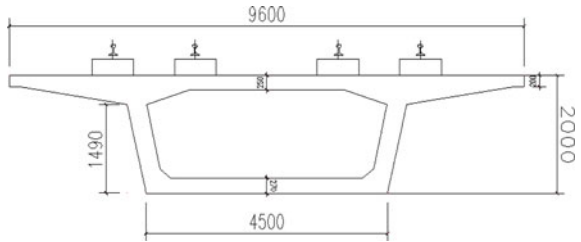
30 kN/mm and damper 10,000 N/(m/s). Rubber bearings of viaduct are also simulated by spring-damper elements with stiffness 1.26E + 9 kN/mm and damper 204,000 N/(m/s).

In the model, wheels of vehicles are simplified as discs with elastic modulus 2.059E + 11 kN/mm and density 7830 kg/m³. The normal interaction between wheel and rail conforms to the Hertz nonlinear elastic contact theory, illustrated in Fig. 2 and the expression is shown as follow,

$$P_n = \left(\frac{1}{G}\Delta Z\right)^{3/2} \tag{1}$$

where P_n is the wheel/rail normal force, ΔZ is elastic displacement of wheel/rail at the contact point, $G = 3.86 \times R^{-0.115} \times 10^{-8}$ m/N²/³ for Worn Profile Wheel, and R the wheel radius, which equals 420 mm. By the support of built-in model in
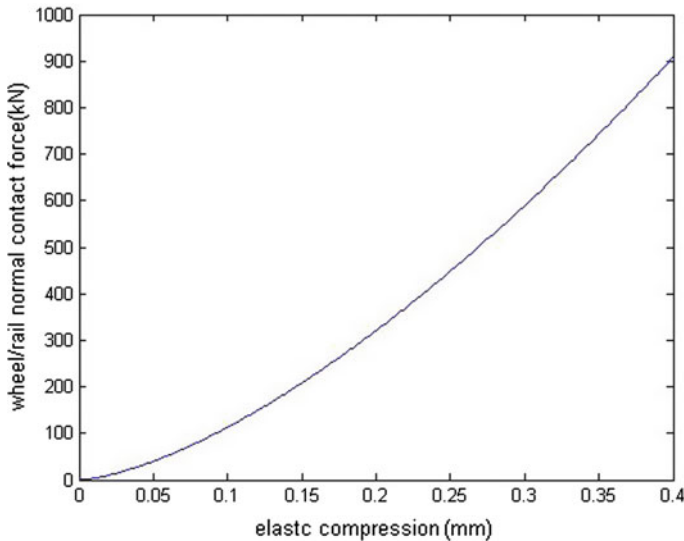
Fig. 2 Wheel/rail contact force and deformation curve

ABAQUS, the wheel/rail normal interaction is defined as soft contact based on the data [8] shown in Fig. 2.

Besides, wheel rail tangential contact characteristic is based on formula (2).

$$F = \mu P_n \tag{2}$$

where F is the tangential force between wheel and rail. μ friction coefficient, equals 0.25, and P_n the wheel/rail normal force. The wheel-track-bridge coupling system model is shown in Fig. 3.

This dynamic response of wheel-track-bridge system is excited by utilizing the sixth grade track irregularity power spectral density of U.S, and the track irregularity power spectrum density function showed as follows:

$$S_v(\omega) = \frac{kA_v\omega_c^2}{(\omega^2 + \omega_c^2)\omega^2} \tag{3}$$

where ω is spatial frequency, ω_c cut-off frequency, A_v roughness coefficient and related to line level, k usually equals 0.25.

As shown in Fig. 4, it can be seen that there are two dominant frequencies of vibration acceleration of top plate of bridge, the higher is at about 30–50 Hz and the other one is around 175–200 Hz. The simulation time is 0.25 s and sampling interval is 0.002 s, thus the sampling resolution can only reach to 4 Hz. That is why the vibration acceleration spectrum is a little rough.
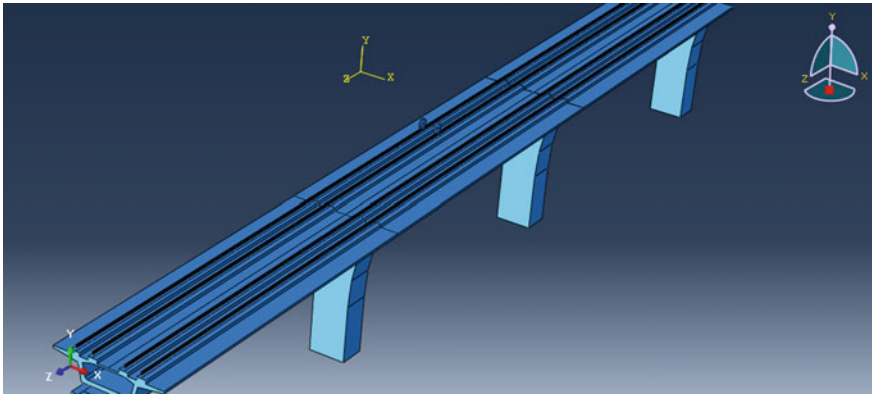
Fig. 3 The model of wheel-track-bridge system
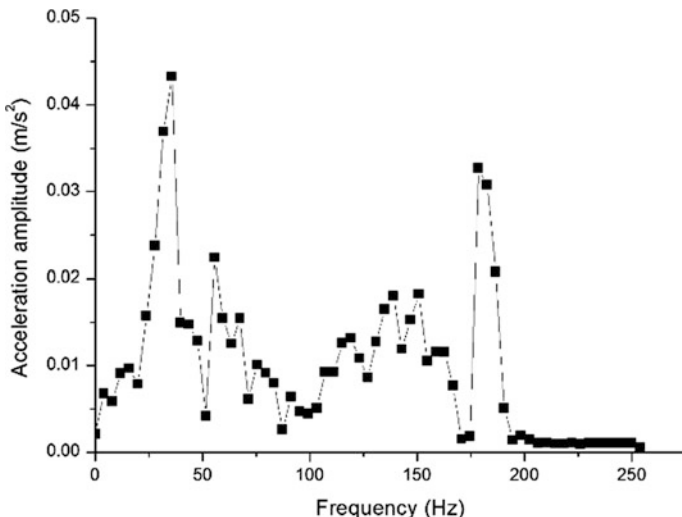
Fig. 4 Vibration acceleration spectrum of top plate of bridge

Numerical Analysis on Dynamic Response of Wheel-Track-Bridge Coupling System with Respect to Stiffness of Fastener

In order to study the effect of fastener stiffness on dynamic response of wheel-track-bridge system, the range of stiffness will be set from 30 to 50 kN/mm according to the field test. From the simulating results as shown in Fig. 5, it can be concluded that the vibration of bridge will be improved with the decrease the fastener stiffness, especially from 125 to 200 Hz.

However, the vibration acceleration of rail and wheels changes in the opposite trend simultaneously, as shown in Table 1. It can be found there is a negative correlation between the stiffness of fastener and vibration acceleration of rail and wheels. As stiffness of fastener increases, the maximum vibration acceleration amplitude of rail and wheels decrease from 2.140 to 2.115 m/s^2 and from 5.513 to 5.500 m/s^2, respectively. Finally, the estimation results of simulation data verify the validity of previous conclusion that it is very likely to enlarge the vibration of rail vehicles by lowering fastener stiffness, and thus that reducing the stiffness of fastener may not apply to control vibration and noise pollution directly affected by elevated lines.
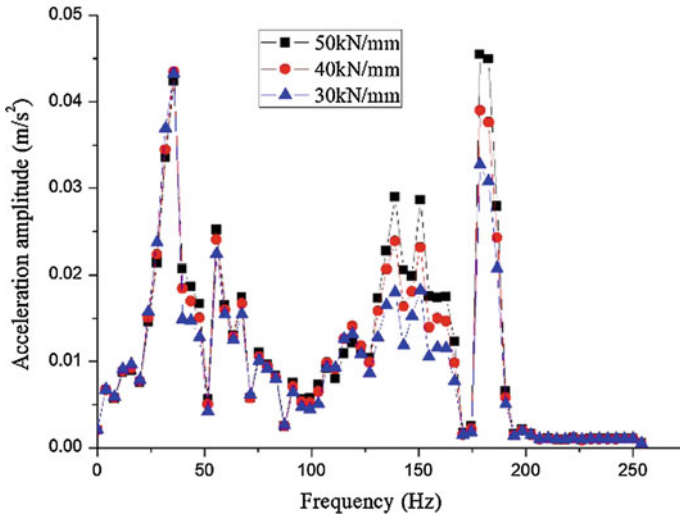
Fig. 5 Vibration acceleration spectrum of bridge with different fastener stiffness

Table 1 Maximum vibration acceleration amplitude of rail and wheels with different fastener stiffness

Wheel-track-bridge system	Stiffness of fastener (kN/mm)		
	30	40	50
Maximum of wheel acceleration amplitude (m/s^2)	2.140	2.129	2.115
Maximum of rail acceleration amplitude (m/s^2)	5.513	5.508	5.500

Dynamic Vibration Absorber

Dynamic vibration absorber is a tuned spring-mass system which reduces or eliminates the vibration of a harmonically excited system in the field of civil engineering, for the first time studied to reduce vibration of foundation under rail while not increase vibration of rail vehicles. A simplified two dimensional numerical model without damping is shown in Fig. 6 in order to show how the dynamic vibration absorber works.

As shown in Fig. 6, the foundation under rail and box girder are simplified as a rigid block (block G for short). The absorber and block G are connected with a spring, of which stiffness is K2. K1 represents the fastener stiffness and K3 bridge bearing stiffness. Bridge piers are fixed to the ground. Assuming that the mass of rail, absorber and block G are 60, 200 and 3000 kg, respectively. While K1, K3 are equal to 30 and 42 kN/mm, respectively. K2 is a variable.

Supposing that the rail is applied by sinusoidal wave load at 40 Hz, the kinetic equations of this 2-D model can be represented as follow,

Fig. 6 Simplified two dimensional model of dynamic vibration absorber
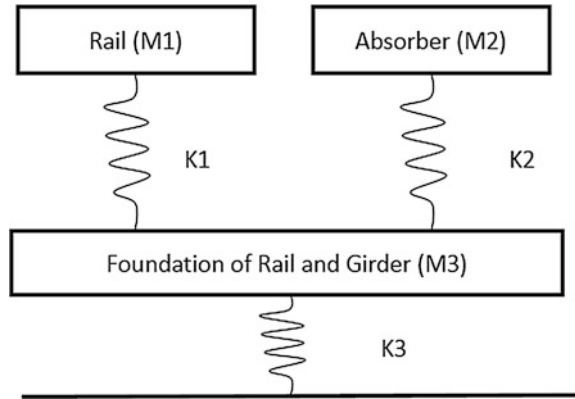
$$M_1 \times \ddot{Y}_1 + K_1 \times (Y_1 - Y_3) = F$$
$$M_2 \times \ddot{Y}_2 + K_2 \times (Y_2 - Y_3) = 0 \tag{4}$$
$$M_3 \times \ddot{Y}_3 + K_1 \times (Y_3 - Y_1) + K_2 \times (Y_3 - Y_2) + K_1 \times Y_3 = 0$$

where M_1 the mass of rail, M_2 the mass of dynamic vibration absorber, M_3 the mass of block G, Y_1 the displacement of rail, Y_2 the displacement of dynamic vibration absorber; Y_3 the displacement of block G.

Based on Mode Superposition Method [9], the relationship between displacement amplitude and stiffness K2 of dynamic vibration absorber can be obtained by MATLAB, as shown in Figs. 7 and 8.

As is shown in Fig. 7, the black curve represents vibration displacement amplitude of block G without absorber while the red one represents the change trend of displacement amplitude of block G with stiffness K2 of vibration absorber. When the absorber stiffness equals 0.3 kN/mm, the displacement amplitude of block G falls to 0.00192 m (by 12.7% compared to the initial one). With the increase of absorber stiffness, dynamic response of block G drops further. If the absorber stiffness exceeds 0.32 kN/mm, block G begins to vibrate in the opposite phase. As the absorber stiffness approaches infinity, the displacement amplitude of block G tends to be 0.0022 m. All of these lead to the conclusion that the optimal stiffness of absorber seems to be 0.32 kN/mm. However the absorber is much easier to resonate with this stiffness. Therefore, it needs to consider on the vibration absorption effects and the safe conditions to avoid resonance in the absorber design.

Figure 8 demonstrates that the vibration absorber can also mitigate the dynamic response of rail. The displacement amplitude of rail drops from 0.0046 to 0.00267 m when absorber stiffness increases from 0.3 to 0.32 kN/mm. With the results gained from Fig. 7, it can be concluded that the absorber can improve vibration of the whole system.
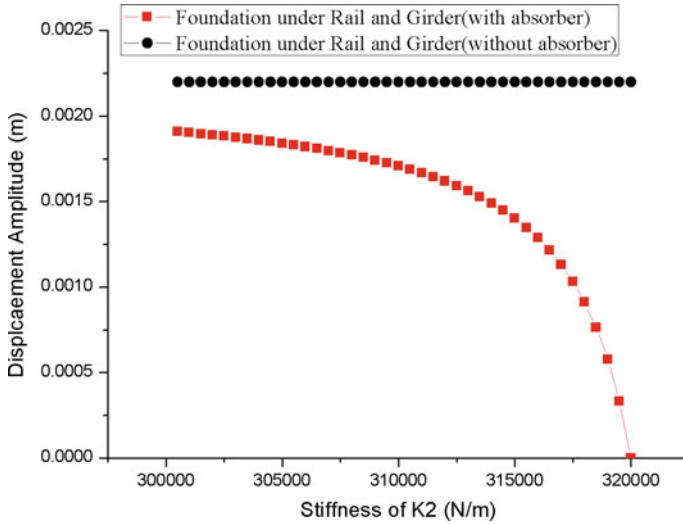
Fig. 7 Comparison of foundation under rail and girder vibration displacement amplitude with and without vibration absorber (mass is 200 kg)
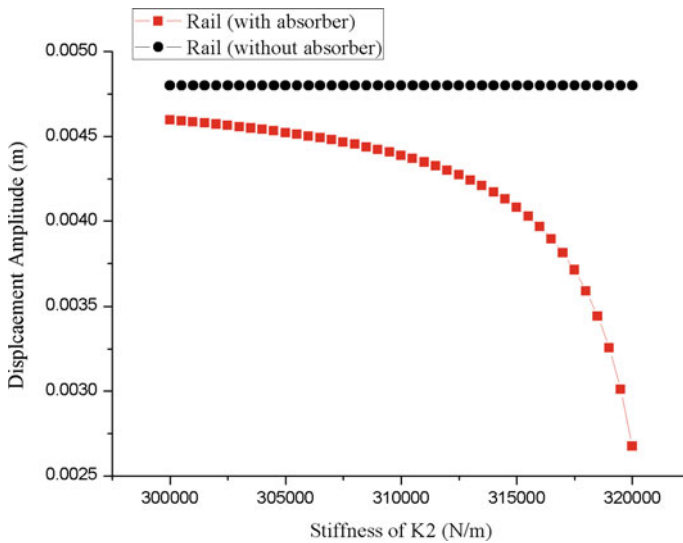
Fig. 8 Comparison of rail vibration displacement amplitude with and without vibration absorber (mass is 200 kg)

As illustrated in Figs. 8 and 9, the optimal stiffness changes with mass of absorber. When the stiffness equals 0.62 kN/mm (0.02 kN/mm smaller than optimal stiffness), the block G displacement amplitude decreases by 35.9%, from
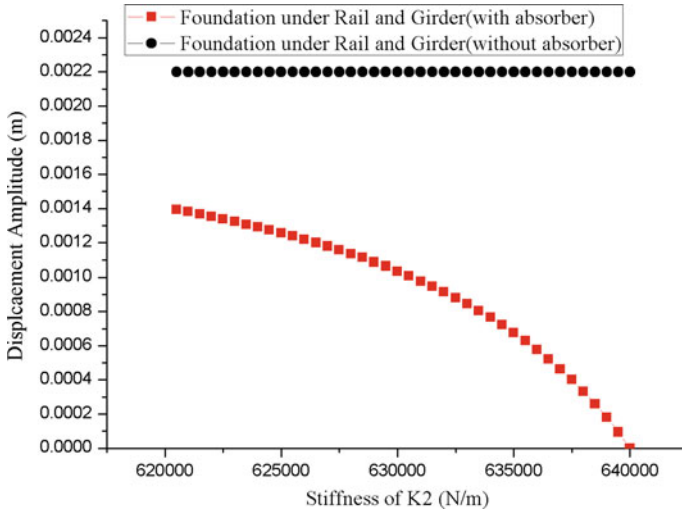
Fig. 9 Comparison of foundation under rail and girder vibration displacement amplitude with and without vibration absorber (mass is 400 kg)

0.0022 to 0.00141 m. When the mass of absorber is 200 kg, the block G displacement amplitude decreases by 12.7% as stated above. So it is indicated that higher mass of dynamic vibration absorber can enhance the damping effects of absorber.

Conclusions

On the basis of the numerical model simulation in this article, it is proved that low fastener stiffness will reduce the vibration of bridge while enlarge the vibration of rail and wheel. Thus that the vibration reduction of elevated lines should be based on the whole system.

Dynamic vibration absorber can effectively control the vibration of bridge and track affected by elevated lines, but the range of its work frequency band is very narrow. If the frequency deviates from its optimum operating condition, the effect of dynamic vibration absorber will be reduced or even become the biggest threat to the whole system. In conclusion, it is necessary to optimize the design of dynamic vibration absorber for a particular track structure in the future. Furthermore, mass and stiffness are key parameters on the efficiency of inducing vibration.

References

1. Xiaoyan Lei. High Speed Railway Track Dynamics: Model, Algorithm and Application. Beijing: China Science Press, 2015:274–276.
2. Tongtong. Study on the influence of fastener stiffness on the dynamic performance of vehicle track system. Journal of ShanXi Architecture, 2015, 41(5):118–120.
3. Hao Xu, Peigang Li. Analysis of the influence of element slab track fastener stiffness mutation on driving safety. Journal of China Safety Science, 2012, 22(3):134–138.
4. Ping Wang, Jinhui Xu. The influence of track stiffness on the frequency response of vehicle track system. Journal of Railway Engineering Society, 2014, 9:46–52.
5. Xun Zhang. Study on the prediction and control of structure-borne noise of rail transit bridges [D]. Cheng Du: Southwest Jiaotong University, 2012:113–126.
6. Huoming Shen. Vibration theory and nonlinear analysis in bridge subjected to moving load [D]. Cheng Du: Southwest Jiaotong University, 2005:30–43.
7. Wanming Zhai. Vehicle-Track Coupled Dynamics. Beijing: China Science Press, 2015: 11–89.
8. Kun Yang. Safety Research on Running Response of Vehicle-Track-Viaduct Simple Beam Subjected to Earthquake Loading [D]. Beijing: Beijing Jiaotong University, 2010:38–44.
9. R. W. Clough, J. Penzien. Dynamics of Structures. McGraw-Hill, New York, 1975:161–181.

Experimental Study on Vibration Reduction Effect of New Anti-vibration Bearing

Liangming Sun, Weiping Xie and Xu Liang

Introduction

For the elevated urban rail transit, the train-induced vibrations often bring some continuous annoyances to residents alongside railway lines or malfunction to the vibration-sensitive equipment housed in the nearby buildings [1]. Especially in the sensitive districts for the vibration, the vibration control measures must be taken to mitigate the train-induced vibrations. At present, there are a lot of countermeasures such as elastic rail fastening, spring-steel floating slab track, in-filled trench, WIB and so on [2–4]. Most of them are limited by some factors such as damping effect, cost, construction difficulty, site and so on. As far as we know, the bearing is an important part of the bridge to connect both superstructure and substructure. From the principle of vibration reduction, it is effective to control vibration transmission by itself. However, existing bridge bearings except elastic bearing pad (EBP) have not been considered as an anti-vibration bearing to reduce train-induced vibrations. The EBP was firstly adopted to reduce vertical train-induced vibrations in Taiwan High-speed Railway to protect from the vibration a high-tech industrial area [5]. But it must be assorted with the shear key to support the superstructure of bridge. Therefore, in order to optimize damping effect and arrangement of bridge bearing,

L. Sun · W. Xie (✉)
School of Civil Engineering & Architecture, Wuhan University of Technology,
Wuhan 430070, China
e-mail: wpxie@sina.com

L. Sun
e-mail: sunliangming@126.com

X. Liang
Wuhan Hirun Engineering Equipment Co., Ltd., Wuhan 430084, China
e-mail: 434647564@qq.com

a new anti-vibration bearing is proposed by using the sloping high-damping rubber block to isolate the vibration [6]. Mechanical property test has carried out to verify the basic requirement of the bearing. In this paper, the scale model test is performed to investigate the vibration reduction effect of the new anti-vibration bearing.

Design of the New Anti-vibration Bearing

From the attenuation mechanism of rubber bearing [7], the principle of vibration reduction is to increase the frequency ratio as much as possible and to decrease natural frequency of the vibration system, meanwhile to provide proper damping for the bearing to avoid the resonance. And then, the anti-vibration bearing is expressed as the linear behavior in the condition of train loads, so the vertical stiffness of the anti-vibration bearing can be estimated from the load-deformation curve obtained by the mechanical property test. If the damping of the anti-vibration bearing is ignored, its natural frequency f(Hz) can be calculated according to the deflection D(m) of bridge structure under static load in Eq. (1). It is indicated that the natural frequency of the anti-vibration bearing can be decreased with the increase of the deflection of the bridge, but the deflection should not exceed 3–4 mm, or it would impact the comfort and safety of running train. Therefore, through applying the characteristics of lower stiffness and higher damping for rubber material, a new anti-vibration bearing with four sloping high-damping rubber blocks is proposed to reduce the vibrations as shown in Fig. 1. It includes two types: movable type and fixed type. They are useful to support unidirectional and bidirectional horizontal loads, respectively. Their key design parameters are shown in Table 1.

$$f = \frac{\sqrt{g}}{2\pi\sqrt{D}} \approx \frac{1}{2\sqrt{D}} \qquad (1)$$

where g is the gravitational acceleration.

Fig. 1 Movable and fixed types of new anti-vibration bearing

Table 1 Key design parameters of the new anti-vibration bearing

Parameters	Unit	Value	
		Movable type	Fixed type
Vertical stiffness	kN/mm	372	372
Longitudinal stiffness	kN/mm	6.62	263.5
Transversal stiffness	kN/mm	372	263.5
Damping ratio		10%	10%
Natural frequency	Hz	8	8
Vertical bearing capacity	kN	3500	3500
Horizontal bearing capacity	kN	700	700
Longitudinal deformation	mm	±50	±0
Transversal deformation	mm	±0	±0
Rotation angle	rad	0.02	0.02
Applicable temperature	˚C	−25∼60	−25∼60

Damping Effect Test of the New Anti-vibration Bearing

Test Scheme of Scale Model Test

In this paper, a scale model test is carried out to verify the vibration reduction effect of the new anti-vibration bearing in Earthquake Engineering Center of Guangzhou University. The scale models of a new anti-vibration bearing and a steel bearing are shown in Fig. 2. Their similarity relations between model and prototype are shown in Table 2. The similarity ratio is set as 1/5.5. The test scheme of scale model test is shown in Fig. 3. Four scale models of bridge bearings are placed in the four corners of the square ground. Every two bearings are placed by T-type relations. Additional weight composed by the concrete and steel slab is 17.16 t for the normal operation

Fig. 2 Scale models of new anti-vibration bearing and steel bearing

Table 2 Similarity relation between model and prototype

Similarity factor	Symbol	Formula	Value (model/prototype)
Size	S_l	$S_l = l_M / l_P$	0.182
Elastic modulus	S_E	$S_E = E_M / E_P$	1.000
Acceleration	S_a	$S_a = S_E S_l^2 / S_m$	1.002
Mass	S_m	$S_m = m_M / m_P$	0.033
Time	S_t	$S_t = (S_l / S_a)^{0.5}$	0.426
Frequency	S_f	$S_f = 1 / S_t$	2.347
Displacement	S_u	$S_u = S_l$	0.182
Stress	S_σ	$S_\sigma = S_E$	1.000
Strain	S_ε	$S_\varepsilon = 1$	1.000
Force	S_F	$S_F = S_E S_l^2$	0.033

of bearing (260 t). Dynamic loads are excited by an electromagnetic vibrator which is placed at the center of slab. Sweep frequency is 5–230 Hz. Four accelerometers are adopted to gather vertical acceleration responses as shown in Fig. 3. Accelerometer 1 is located at the lower plate of bridge bearing. Accelerometers 2 and 3 are located on the concrete slab. Accelerometer 4 is located on the vibrator.

Fig. 3 Test scheme of scale model test

Test Results and Analysis

Focused on the vertical vibration acceleration of the bearings excited by the vibrator, the time histories and Fourier spectra of the new anti-vibration bearing at the upper and lower plates are shown in Fig. 4. It is indicated that acceleration amplitudes of the upper and lower plates are 0.11 and 0.00483 m/s^2, respectively. The main frequency components are around 20 Hz and 50–60 Hz.

Based on the national standards GB10071-88 [8], the vibration level is described as:

(1) Vibration acceleration level

$$VAL = 20\lg\frac{a_{RMS}}{a_0} \tag{2}$$

where $a_0 = 10^{-6}$ m/s^2 is a reference vibration acceleration, a_{RMS} is the vibration acceleration RMS.

(2) Z vibration level

According to ISO2631/1-1985, the vibration acceleration level corrected by Z-weighted factor of the whole body vibration is noted as VL_Z.

Then 1/3 octave band analysis is carried out to discuss the vertical Z vibration level in the range of 1–80 Hz. For the steel bearing, the average VL_Z of upper and lower plates are 67.67 and 59.50 dB, respectively. The whole insertion loss
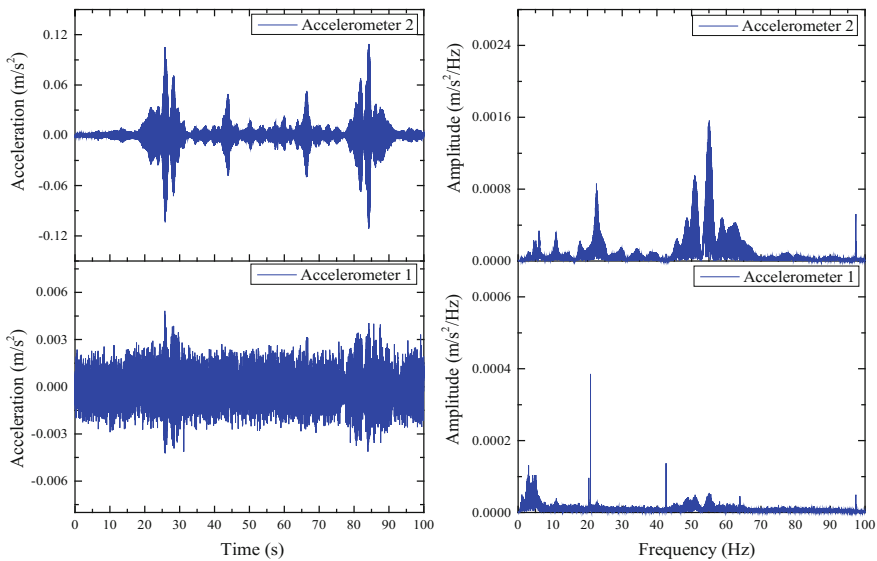
Fig. 4 Vertical acceleration time histories and Fourier spectra of new anti-vibration bearing
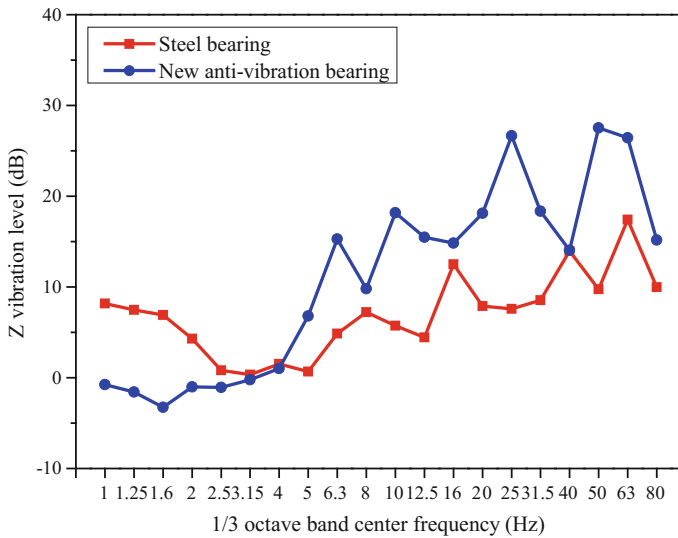
Fig. 5 Comparison of the insertion loss for steel bearing and new anti-vibration bearing

between the upper and lower plates is 8.17 dB. For the new anti-vibration bearing, the average VL_Z of upper and lower plates are 70.29 and 56.80 dB, respectively. The whole insertion loss between the upper and lower plates is 13.49 dB. It is shown that the whole insertion loss of new anti-vibration bearing is 5.32 dB larger than that of steel bearing.

The insertion loss of steel bearing and new anti-vibration bearing are compared in the frequency domain of 1–80 Hz as shown in Fig. 5. The results show that the both the steel bearing and new anti-vibration bearing can cause the insertion loss of most frequency components. It is indicated that they have a certain vibration reduction effect in the vertical direction. But the vibration responses of the new anti-vibration bearing are amplified below 1/3 octave band center frequency 4 Hz, that is because the bearing as the flexible structure can isolate some vibration energy.

Conclusions

A new anti-vibration bearing is proposed by using the sloping high-damping rubber block to mitigate train-induced vibrations and then improve vibration environment around the elevated urban rail transit. Its vibration reduction effect is verified by the scale model test. It is shown that vibration amplitudes of new anti-vibration bearing at the upper and lower plates are smaller than those of steel bearing while the electromagnetic vibrator is working on the test model. The whole insertion loss of anti-vibration bearing is 13.49 dB, which is 5.32 dB larger than that of steel bearing.

For most frequency components, the new anti-vibration bearing can reduce more vibrations than the steel bearing in the vertical direction. Therefore, this kind of bearing is effective to isolate the vertical vibration.

References

1. Xia, H. (2010). Traffic induced environmental vibrations and controls. Science Press, Beijing, China.
2. Remington, P.J. Webb, J. (1996). Wheel/rail noise reduction through profile modification. Journal of Sound and Vibration, 193(1): 335–348.
3. Hui, C.K. Ng, C.F. (2009). The effects of floating slab bending resonances on the vibration isolation of rail viaduct. Applied Acoustics, 70(6): 830–844.
4. Takemiya, H. Fujiwara, A. (1994). Wave propagation/impediment in a stratum and wave impeding block (WIB) measured for SSI response reduction. Soil Dynamics and Earthquake Engineering, 13(1): 49–61.
5. Marioni, Chen, L. Hu, J.T. (2011). Application of EBP on Taiwan High-speed Railway. Earthquake Resistant Engineering and Retrofitting, 33(2):63–66.
6. Sun, L.M. Xie, W.P. Liang, X. (2016). Experimental study of mechanical property of new anti-vibration bearing reduced train-induced vibration. 4th International Conference on Railway Engineering (ICRE2016), China Railway Publishing House, Beijing, China, pp. 196–200.
7. Clough, R. Penzien, J. (2006). Structural dynamics. Translated by WANG G Y, etc. Higher Education Press, Beijing, China.
8. GB 10071-88. (1988). Measurement method of environmental vibration of urban area. National Environmental Protection Agency.

Study on Evaluation Index of Environmental Vibration Induced by Urban Transit

Linlin Du, Weining Liu, Weifeng Liu and Meng Ma

Introduction

With the rapid development of rail transit system, rail lines are inevitably go through residential areas and affect normal life of residents around lines [1]. Current standards for evaluating rail transit environmental vibration are "GB10070-88 Standard of Environmental Vibration in Urban Area" [2] and "JGJ/T170-2009 Standard for Limit and Measuring Method of Building Vibration and Secondary Noise Caused by Urban Rail Transit" [3]. The evaluating index are the maximum vibration level of Z direction (VLzmax) and maximum vibration level in dividing frequency of Z direction (VLmax).

The current standards don't give overlapping coefficient about two adjacent waveforms specifically when calculating VLzmax and VLmax. Frequency weighting curve recommended by ISO 2631-1:1985 is adopted when calculating VLzmax according to GB10070-8. This version of frequency weighting curve considering the "fatigue-decreased proficiency limit" caused by vibration is outdate and should be advised. Furthermore, specific calculation method is not given for VLmax in JGJ/T170-2009. Different algorithm for calculating VLmax such as linear averaging method, peak hold method have important effect on the result.

L. Du (✉) · W. Liu · W. Liu · M. Ma
School of Civil Engineering, Beijing Jiaotong University, Beijing 100044, China
e-mail: 14115285@bjtu.edu.cn

W. Liu
e-mail: wnliu@bjtu.edu.cn

W. Liu
e-mail: wfliu@bjtu.edu.cn

M. Ma
e-mail: mameng@bjtu.edu.cn

In order to provide guidance for the accurate calculation of evaluating index of environmental vibration, several items are researched. Firstly, a reasonable overlapping coefficient is obtained according to the research of overlapping coefficient of VLzmax and VLmax. Then, a comparative study of different frequency weighting curve versions on VLzmax is conducted and a reasonable frequency weighting curve is recommended. Finally, calculating method for VLmax is recommended according to the results of VLmax in different methods.

Evaluation Index of Environmental Vibration in Urban Areas

Measurement and Evaluation Method for VLzmax

Standards of GB10070-88 and GB10071-88 point out that vibration level in vertical Z direction should be measured for evaluating environment vibration in urban area. Time weighting value is 1 s and range of frequency weighting is 1–80 Hz [4]. Frequency weighting factor can be seen in GB10070-88 [5]. Measuring point is located outdoors on vibration sensitive place within 0.5 m out of all kinds of buildings, if necessary the measuring point can be located on the floor of building. Calculating VLzmax in the measuring point during the train passing each time and each point should monitor 20 trains continuously. Take the arithmetic average of the 20 VLzmax values as evaluating result and then comparing with the limit value given in GB10070-88 to evaluate environmental vibration level.

Measurement and Evaluation Method for VLmax

Standard of GB10070-88 mainly evaluating environmental vibration caused by urban rail transportation routes and railway lines. Rail transit system is different from it because of line distribution area, track form and operating conditions. Therefore, VLmax is recommended in JGJ/T170-2009 as the evaluating index of rail transit environmental vibration. 1/3 octave of vertical acceleration is obtained within 4–200 Hz. Maximum acceleration level in the frequency center of 1/3 octave band can be obtained after correcting by frequency weighting factor, which is VLmax. Frequency weighting factors and evaluation criteria values of environmental vibration can be seen in JGJ/T170-2009 [6, 7]. Measuring point can be placed on first floor of building and it can also be placed on base of building outside the wall within 0.5 m. Calculating VLmax during the train passing by for each time and take arithmetic average of VLmax values as vibration evaluation result.

Calculating Methods of VLzmax and VLmax

Calculating of VLzmax

According to standard GB10070-88 the time weighting value is 1 s and the sampling time signal can be divided into pieces of waveform for analyzing. 1/3 octave analyzed for each piece of waveform is conducted and obtains vibration level corresponding with each center of frequency bands, as shown in Table 1. Vibration level in Z direction corresponding with this piece of waveform is calculated according to Eq. (1). Finally, we can get vibration level in Z direction changes with time.

$$VL_z = 10\log\left(\sum 10^{(VL_i + \alpha_i)/10}\right) \tag{1}$$

where VLz (dB) represents vibration level of frequency weighted in Z direction. VL_i represents acceleration level corresponding with each center of 1/3 octave frequency bands. α_i represents weighting factor of each center of 1/3 octave frequency bands, the specific values can be seen in GB10070-88.

Environmental vibration is a stochastic process. Data obtained by the data acquisition device are discrete data. Sampling data with length of 1 s is calculated for vibration evaluate index. In order to make the result of discrete data truly reflect continuous vibration process, the overlap rate should set on the two adjacent waveform, i.e. overlapping coefficient L. Given the overlap between two adjacent waveforms, total number of waveforms for calculating is obtained as follows:

Table 1 Diagrammatic sketch of calculating vibration level for each waveform

	t_1	t_2	t_3	…	t_k	t_{k+1}	…	t_{n-1}	t_n
f_1	VL_{11}	VL_{12}	VL_{13}	…	VL_{1k}	$VL_{1(k+1)}$	…	$VL_{1(n-1)}$	VL_{1n}
f_2	VL_{21}	VL_{22}	VL_{23}	…	VL_{2k}	$VL_{2(k+1)}$	…	$VL_{2(n-1)}$	VL_{2n}
f_3	VL_{31}	VL_{32}	VL_{33}	…	VL_{3k}	$VL_{3(k+1)}$	…	$VL_{3(n-1)}$	VL_{3n}
⋮	⋮	⋮	⋮	⋱	⋮	⋮	⋱	⋮	⋮
f_i	VL_{i1}	VL_{i2}	VL_{i3}	…	VL_{ik}	$VL_{i(k+1)}$	…	$VL_{i(n-1)}$	VL_{in}
f_{i+1}	$VL_{(i+1)1}$	$VL_{(i+1)2}$	$VL_{(i+1)3}$	…	$VL_{(i+1)k}$	$VL_{(i+1)(k+1)}$	…	$VL_{(i+1)(n-1)}$	$VL_{(i+1)n}$
⋮	⋮	⋮	⋮	⋱	⋮	⋮	⋱	⋮	⋮
f_{m-1}	$VL_{(m-1)1}$	$VL_{(m-1)2}$	$VL_{(m-1)3}$	…	$VL_{(m-1)k}$	$VL_{(m-1)(k+1)}$	…	$VL_{(m-1)(n-1)}$	$VL_{(m-1)n}$
f_m	VL_{m1}	VL_{m2}	VL_{m3}	…	VL_{mk}	$VL_{m(k+1)}$	…	$VL_{(m-1)(n-1)}$	$VL_{(m-1)n}$

$$n = \frac{N - F_s}{(1 - l) \cdot F_s} + 1 \tag{2}$$

where N is the sampling points, F_s is the sampling frequency.

Calculating of VLmax

VLmax is recommended by JGJ/T170-2009 as the environmental vibration evaluate index [8]. However, the specific calculating method is not given which will affect the vibration evaluation results. Methods to calculate VLmax are linear averaging method and peak hold method, calculation process for these methods are shown below.

Linear averaging method calculating RMS value of acceleration in 1/3 octave frequency bands of each waveform, similarly like the one shown in Table 1. And then calculating linear average value of the acceleration RMS value in 1/3 octave frequency bands based on Eq. (3). Calculating the frequency weighted vibration level of each 1/3 octave frequency bands and getting the maximum value as the VLmax, as shown in Eq. (4).

$$a_{rmsi} = \frac{1}{n} \sum_{k=1}^{k=n} a_{rmsik}, i \in (1, 2, \cdots, m) \tag{3}$$

$$\mathrm{VL}_{\max} = \max_{i=1 \to m} \left(20 \log \frac{a_{rmsi}}{a_0} + \alpha_i \right) \tag{4}$$

where a_{rmsi} is the average of acceleration RMS value corresponding with center frequency f_i of 1/3 octave band. a_{rmsik} is acceleration RMS value corresponding with center frequency f_i of 1/3 octave band for the kth waveform. i is number of center frequency of 1/3 octave band. n is the total number of waveforms for calculating. a_0 is the reference vibration acceleration, which value is 10^{-6}m/s^2. α_i is the vertical weighting factor of each center frequency in 1/3 octave band, specific data can be seen in JGJ/T170-2009.

Peak hold method calculating vibration level of acceleration in 1/3 octave frequency bands of each waveform, as shown in Table 1. The maximum vibration level of each frequency bands in 1/3 octave can be obtained by Eq. (5) and VLmax can be obtained according to Eq. (6).

$$\mathrm{VL}_{i\max} = \max_{k=1 \to n} (\mathrm{VL}_{ik} + \alpha_i), i \in (1, 2, \cdots, m) \tag{5}$$

$$\mathrm{VL}_{\max} = \max_{i=1 \to m} \mathrm{VL}_{i\max} \tag{6}$$

where VL_{ik} represents vibration level of acceleration corresponding with center frequency f_i of 1/3 octave band for the kth waveform (dB). VL_{imax} is the maximum vibration level corresponding with center frequency f_i of 1/3 octave band.

Calculating and Analyzing of VLzmax and VLmax

Vibration acceleration time history shown in Fig. 1 is the vertical acceleration at the corner out of a building, which is selected to calculate vibration evaluating index.

Calculating and Analyzing of VLzmax

Relationships between VLz with time is shown in Fig. 2. As it can be seen that vibration strength is changing with time, VLzmax is reaching up to 63.96 dB.

In order to research influence of overlapping coefficient on calculating accuracy and efficiency of vibration level, overlapping coefficients of 0, 1/2, 3/4, 7/8 are selected to calculate VLzmax. As shown in Fig. 3, overlapping coefficient have influence on the results of VLzmax and the calculating results are stable when overlapping coefficient is over 3/4.

Influence of Frequency Weighting Curve on VLzmax

Frequency weighting curve used in GB10070-88 is the one recommended by ISO2631-1:1985, which is based on "fatigue-decreased proficiency" curve due to vibration exposure. "Fatigue-decreased proficiency" curve means the limit vibration

Fig. 1 Vertical vibration acceleration of ground outside the buildings
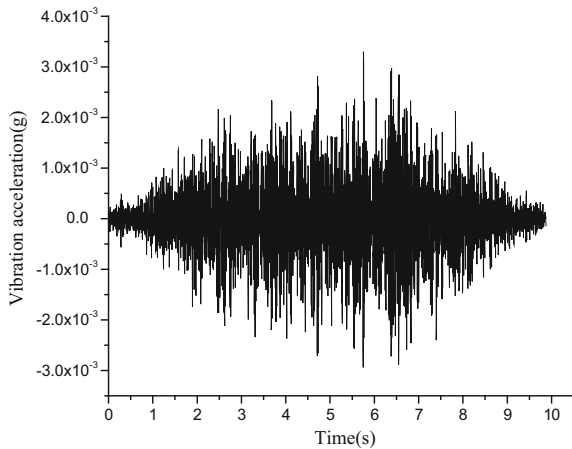
Fig. 2 Changing process
with time of VLz
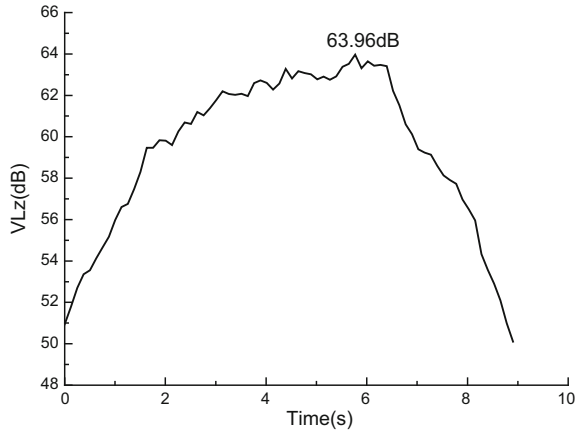
Fig. 3 Changing process
with overlapping coefficient
of VLz
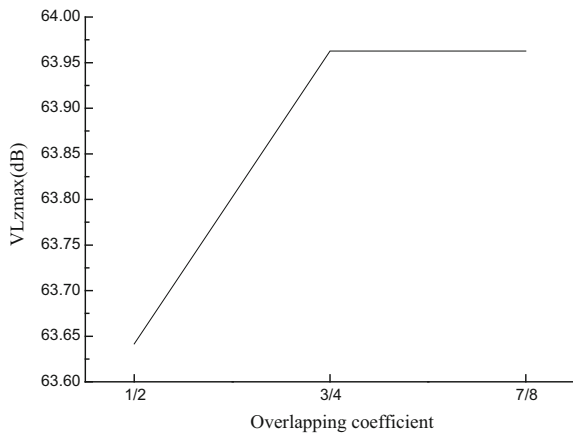
value resulting in worker fatigue or proficiency decreased under certain times. This
curve is firstly used to evaluate impact of vibration on human body in Japan.
However, "fatigue-decreased proficiency limit" is a concept proposed for industrial
workers exposed to vibration, it can't fully reflect influence of environmental
vibration on human body. For the evaluation of environmental vibration in urban
areas caused by rail transport, the main research object is the staff in buildings. Lots
of people is seated and keep sitting posture for a long time. Health, perception and
comfort of these people should be considered first. Few people keep standing or
prone position for a long time, which concern perception and comfort. Therefore, a
new frequency weighting curve is proposed by the International Organization for
Standardization in ISO2631-1:1997, which considering the effects of vibration on
health, comfort and perception. The new version of frequency weighting curve
make it easy to evaluating environmental vibration.

The two versions of frequency weighting curves are shown in Fig. 4. As it can be seen that, a significant difference of frequency weighting factor is observed in 1–4 Hz and 8–80 Hz. Influence of different frequency weighting factors on results of VLz is analyzed.

Figure 5 shows results of VLz with different frequency weighting curves. As it can be seen that the results have the same trend with time, which reflecting vibration level changes process over time as the train passing by. Frequency weighting factors have a significant impact on the calculation of vibration level. Calculating results based on frequency weighting curve of ISO2631-1:1997 is greater than ISO2631-1:1985 of 3.3∼3.6 dB.

Fig. 4 Comparing of frequency weighting curves
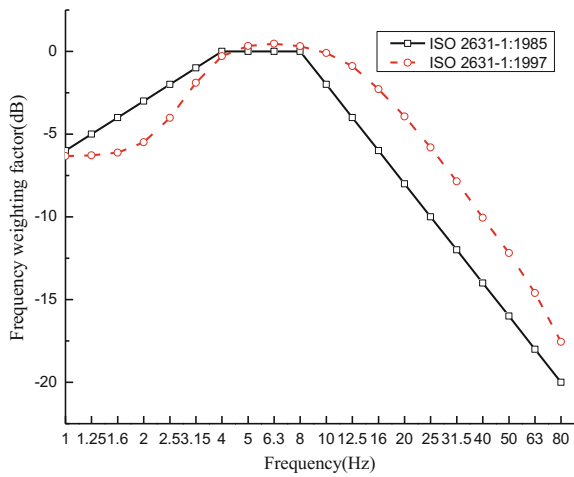
Fig. 5 Influence of frequency weighting curves on the calculating result of *VLz*
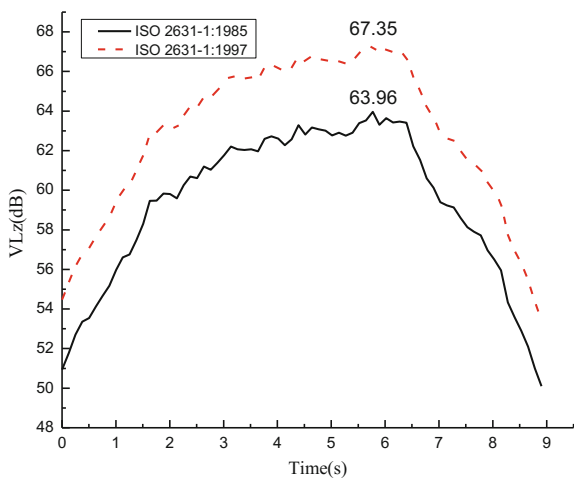
In order to accurately reflect impact of environmental vibration induced by rail transit on human health, comfort and perception. Frequency weighting curve of ISO2631-1:1997 is recommended to GB10070-88.

Calculating and Analyzing of VLmax

According to Sect. 2 of this article, the effect of overlapping coefficient on VLmax result is calculated by programming. Wherein the time length of waveform is 1 s and the calculating frequency range is 4–200 Hz. The results with different overlapping coefficients 0, 1/2, 3/4, 7/8 is calculated respectively, use peak hold as an example. Calculating results is shown in Fig. 6. As it can be seen from Fig. 6 that overlapping coefficient has a certain effect on calculating result of peak hold method and has a small influence on results of linear average method. When overlapping factor over 3/4, influence of overlapping factor is small. Therefore, take overlapping coefficient as 3/4 to calculate VLmax is reasonable.

Influence of different calculating methods on the results of VLmax, such as linear averaging method and peak hold method are researched in the next. Calculating results is shown in Fig. 7 as overlapping factor is 3/4. Figure 7 shows that significant differences are between different calculating methods. VLmax result calculated by peak hold method is bigger than linear averaging method of 5.6 dB.

According to the calculating results, peak hold method represent the worst case. In order to achieve a quiet rail transit system and ensure the reliability of evaluation results, peak hold method is recommended as the VLmax calculating method to evaluate environmental vibration.

Fig. 6 Influence of overlapping coefficient on results of peak hold method
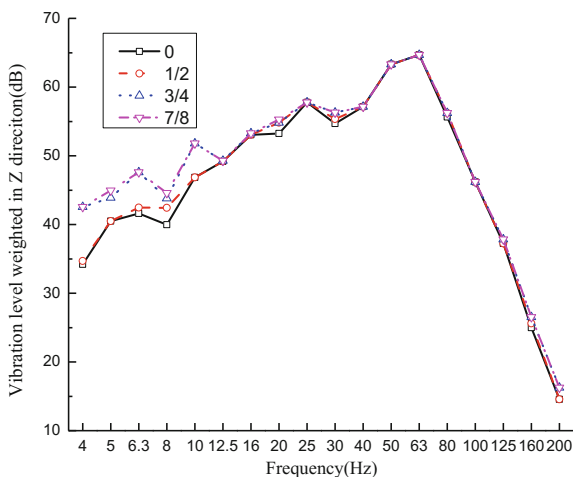
Fig. 7 Comparing of Z-weighted vibration level of different calculating methods
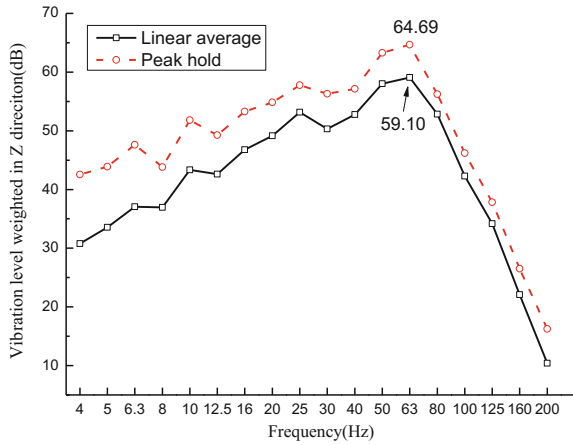
Conclusions

(1) Overlapping coefficient has a certain influence on the calculating results of VLzmax and VLmax. As the overlapping coefficient is 3/4, the result of VLzmax is reliable. For the calculating of vibration evaluation index, overlapping coefficient should over 3/4.

(2) Frequency weighting curve in ISO 2631-1:1997 considering the effect of rail transit vibration on human health, comfort and perception, which is recommended for the amendments on the GB10070-88 Standard of environmental vibration in urban area.

(3) Calculating methods of linear averaging, peak hold have significant influence on the VLmax result, which could affect the evaluating result. In order to ensure the reliability of evaluation results, peak hold method should be adopted as the calculating method.

References

1. Yuan Yang. Study on the artificial single-point pulse excitations method for metro train-induced environmental vibration prediction [D]. Beijing, Beijing Jiaotong University, 2014.
2. National Environmental Protection Agency. GB10070-88 Standard of environmental vibration in urban area[S]. Beijing: Press of China Standards, 1989.

3. Ministry of Housing and Urban-Rural Development of the People's Republic of China. JGJ/T170-2009 Standard for limit and measuring method of building vibration and secondary noise caused by urban rail transit[S]. Beijing: China Architecture and Building Press, 2009.
4. Wu Yongfang. Investigation into the evaluation method for vibration damping effect of track systems [J]. China Railway Science, 2013, 34(3):1–6.
5. National Environmental Protection Agency. GB10071-88 Measurement method of environmental vibration of urban area[S]. Beijing: Press of China Standards, 1989.
6. International Organization for Standardization. ISO2631-1:1997 Mechanical vibration and shock–Evaluation of human exposure to whole-body vibration-Part 1: General requirements [S]. Geneva: International Organization for Standardization.
7. International Organization for Standardization.ISO2631-2:2003 Mechanical vibration and shock –Evaluation of human exposure to whole-body vibration-Part2: Vibration in buildings (1 Hz∼80 Hz) [S]. Geneva: International Organization for Standardization.
8. Liu Weining, Ma Meng. Prediction, evaluation and control of environmental vibration induced by metro rail transit [M]. Beijing: Science Press, 2014.

Bridge Structure-Borne Noise of Concrete Trough-Girder Beam and Its Influence Factors

Linya Liu, Feng Zeng, J.D. Yau and Quanmin Liu

Introduction

Developing urban rail transit is one of the most effective ways to solve urban traffic congestion [1]. But the vibration and noise of the elevated structure has become an important factor restricting the development of urban rail transit [2]. Therefore, it is urgent to investigate the influence parameters of radiation noise on rail transit viaduct structure, to optimize the design of bridge structure and to promote the development of the transportation industry.

Under the load of moving trains, the rail transit trough-girder beam induced vibration and then, radiated noise to the surrounding environment. Among them, the noise of 0–100 Hz frequency band belongs to low frequency noise [3–8]. However, the low frequency noise has strong diffraction capability, slow attenuation characteristics, and the band noise has a long-term harm to the human body. So, it is necessary to research rail transit trough-girder beam bridge structure [9].

There are many factors that affect the radiation noise of the rail transit trough-girder beam structure, such as bridge structure, structural parameters, structural stiffness and so on. However, in engineering practice, the special

L. Liu (✉) · F. Zeng · Q. Liu
Railway Noise and Vibration Environment Engineering Research Center
of the Ministry of Education, East China Jiaotong University,
Nanchang 330013, China
e-mail: 316058254@qq.com

F. Zeng
e-mail: zengfengaaaa@163.com

Q. Liu
e-mail: 547784486@qq.com

J.D. Yau
Department of Civil Engineering, Tamkang University, Taiwan 25137, China
e-mail: 3109380441@qq.com

characteristic that trough-girder web on both side has the function of blocking the wheel/rail noise, at the same time, it makes the use of sound barrier greatly reduce [10]. But, the influence of web structure height on the integrated radiation field is rare.

In this paper, we take a proposed simple supported trough-girder beam as the research object firstly. Then, based on the combination of SIMPACK and ANSYS simulation method, we can obtain the vibration response of the trough-girder beam under the load of moving trains, and make it as a boundary condition. The indirect boundary element method is applied to analyze structure-noise. Finally, the sound pressures from trough-girder beam is calculated and compared with the measured pressures. Besides, a spatial propagation analysis of the trough-girder beam structure-noise along the cross horizontal axis of the track and the influence of trough-girder beam web height are also conducted to investigate with the hybrid FEM-IBEM method.

Vibration Sound Radiation Calculation Model

Finite Element Model of Trough-Girder Beam

A rail transit trough-girder beam model is established in this paper by finite element method. And, in the analysis model, all the materials are in linear elastic stage. The rail is considered as a Euler beam, and we use the beam element to simulate it; solid element is adopted to simulate the trough-girder beam body, track plate and CA mortar layer. In order to avoid the emergence of ill condition grid, we use the swept volume method to divide it into hexahedron element size. The fastening system of rail and rail plate is connected with a discrete spring damper unit with a spacing of 0.625 m. Main material parameters are shown in Table 1.

We select trough-girder beam section with a rail transit simply supported beam in the paper. The web is the asymmetrical structure, one side of the beam body is a circular arc structure, and the other side adopts the fold straight line structure. The finite element model is shown in Fig. 1. After several debugging, the parameters can meet the requirement of the GB50157-2013 Code for design of metro.

Table 1 Main parameters of trough-girder finite element model

Parameters	Elastic modulus/Mpa	Poisson ratio	Density/kg/m^3
Bridge	3.45 × 10^4	0.2	2.6 × 10^3
Steel rails	2.10 × 10^5	0.3	7.83 × 10^3
Track slab	3.9 × 10^4	0.15	2.5 × 10^3
Cement asphalt mortar	3.6 × 10^3	0.2	1.3 × 10^3

Fig. 1 Finite element model
of trough-girder beam
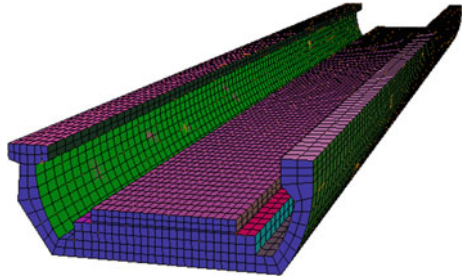
Boundary Element Model of Trough-Girder Beam

Based on the conservation principle of fluid medium and some basic assumptions about the acoustic wave, we can know that the expression of Helmholtz equation for acoustic radiation of trough-girder beam is as follows:

$$\left(\nabla^2 + k^2\right)p = 0$$

where, ∇^2 is Laplacian Operator; $k = \omega/c$ is Acoustic wave number; c is Sound velocity in air; ω is circular frequency; p is sound pressure.

Coincident points have the same boundary conditions on the boundary of the sound field and the solid structure. Therefore, the sound pressure on the acoustic boundary can be calculated by means of the displacement response on the solid boundary, and then, the sound pressure at any point in the whole sound field can be obtained. Compared with the test data, the hybrid FEM-IBEM coupled method for solving large-scale complex structure vibration noise level has higher accuracy.

On the basis of FEM-IBEM coupled acoustic theory, the boundary element model of trough-girder beam is established. In the boundary element model, we consider the maximum length of structure unit is less than the calculated frequency of the shortest wavelength. That is, the maximum length of structure unit should meet the following expression:

$$L \leq \frac{c}{6f} = \frac{340}{6 * 100} = 0.567$$

where, c is set as 340 m/s; Considering the trough-girder beam structure is special, A approach of indirect boundary element method are applied to the noise analysis of trough-girder beam. Bridge boundary element mesh maximum element size is 0.3125, trough-girder beam boundary element mesh and far field grid as shown in Fig. 2.

Fig. 2 Boundary element
model of trough-girder beam
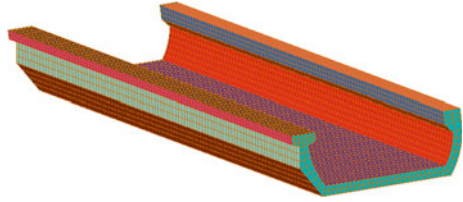
Vehicle Bridge Coupling Model

To avoid the disadvantages of large amount of cross iteration computation caused by using the analytic method of vehicle bridge coupling vibration, we establish the spatial vehicle bridge coupling dynamic analysis refined model that is based on the theory of multi-body dynamics theory in this paper. The model of subway train is refer to the structural parameters and dynamic parameters of the actual subway B type train, which is built by SIMPACK with some simplification. Among them, each section of the subway train dynamics analysis model can be considered to be composed of some rigid bodies, such as a vehicle body, two bogie, four wheel set and so on. 42 degrees of freedom are considered in each of the vehicle. The wheel set and the bogie are connected with the primary spring, the bogie and the vehicle body are connected by secondary springs. The track irregularity is the six order level irregularity spectrum of the United States. Train basic parameters as shown in Table 2.

The finite element model of trough-girder beam is introduced into the multi-body dynamics software SIMPACK as a flexible body. At the same time, the results of modal analysis and substructure analysis are introduced. By using the flexible track module in SIMPACK, the train model and bridge model are solved together. The train model and the finite element model of trough-girder beam are respectively used as two systems. The exchange between the bridge coupling model through the wheel/rail contact points to realize the exchange of displacement, velocity, force. In order to control the calculation results does not exceed the error precision of the system iterative control requirements, the control accuracy is 10^{-4} in this paper Fig. 3.

Table 2 Main parameters of vehicle

Motorcycle type	Mass of car body/kg	Mass of bogie/kg	Mass of wheel-set/kg	Distance between bogie centers/m	Wheelbase/m
The subway car B	39,540	3520	1539	12.6	2.2

Fig. 3 Vehicle bridge coupling model

Structural Vibration Response and Radiated Noise

In this paper, the subway vehicle is loaded with 6 sections, and the calculation speed is 80 km/h. The actual operation process of the train is simplified as s series of force loads with time moving. Besides, the dynamic response of trough-girder beam is analyzed by means of nodal loading. Each of train is accordance with the subway vehicle wheel, the left and right symmetrical distribution of a total of 8 force load, loading time step is 0.0045 s.

In order to further study the radiation noise sound field distribution of trough-girder structure, five point numbers along the horizontal direction of route center line are chosen to analyzed. Point number 1 to Point number 5 are located in the bridge cross section at the 2 m distance from the ground, and far from perpendicular to the route center line 0, 5, 10, 20 and 25 m respectively. Acoustic field distribution map showed in Fig. 4.

By applying vehicle bridge coupling model, wheel/rail exciting force is calculated in this paper, and loaded into track-bridge finite element model, analyzes the transient dynamic response of trough girder beam, which is taken as the boundary condition. A hybrid FEM-IBEM (finite element method and indirect boundary element method) is applied to the structure-noise analysis of trough-girder beam.

From Fig. 5 trough-girder beam Acoustic field 1/3 octave center frequency, we can be found that, the dominant frequency band of the rail transit trough-girder beam structure-noise is range from 20.0 to 80.0 Hz, and the peak appears in 63.0 Hz. The research results are in good agreement with the peak frequency band of the trough-girder beam structure-noise mentioned in the article [7], it can be
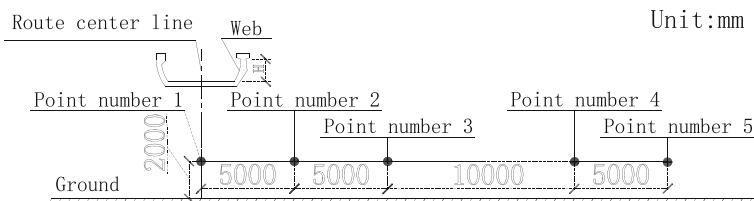
Fig. 4 Acoustic field distribution map

Fig. 5 Acoustic field 1/3
octave center frequency
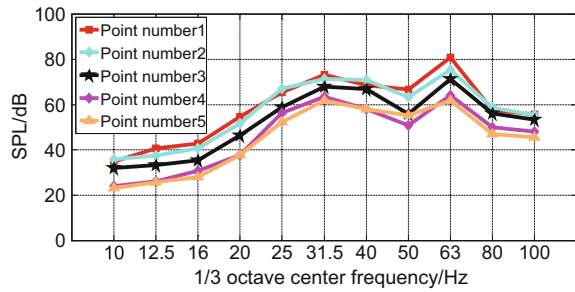
known that the hybrid FEM-IBEM method is suitable for the analysis of
trough-girder beam structure-noise. As Fig. 5 shows that from acoustics field point
number 1 to point number 5, each band sound pressure level decreases with the
increase of distance from route center line. At low frequency ranges from 20.0 to
80.0 Hz, the change of sound pressure value is smaller and smaller with the
increase of the same distance, so it is urgent to study the bridge structure-noise
reduction.

Parameter Analysis

For investigating the influence of structural parameters of trough-girder beam
structure-noise, we take a span of 30 m trough-girder beam web height 1.2 m as the
standard model. Through changing trough-girder beam web height, we consider
four conditions of web height 1.2, 1.4, 1.6 and 1.8 m in this paper. Among them,
the change of trough-girder beam web height is satisfied with the research of
Handbook of concrete structures [11].

Because the frequency range of human hearing and trough-girder beam
structure-noise dominant frequency mainly are below 100.0 Hz, it can be known
that the linear sound pressure level of the sound field range from 10.0 to 100.0 Hz is
chosen to analyze the bridge structure-noise of different trough-girder beam web
height. Figure 6 shows the different acoustic field linear maximum sound pressure
level in 10.0 ~ 100.0 Hz band.

Fig. 6 The maximum point
linear SPL
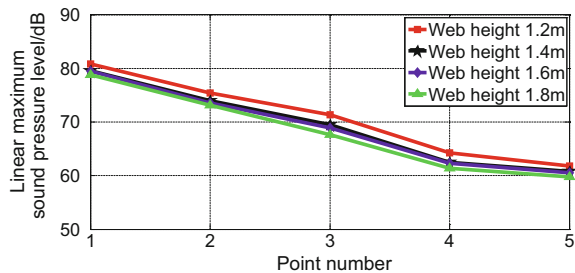
Fig. 7 The total sound
pressure of sound pressure
maximum level
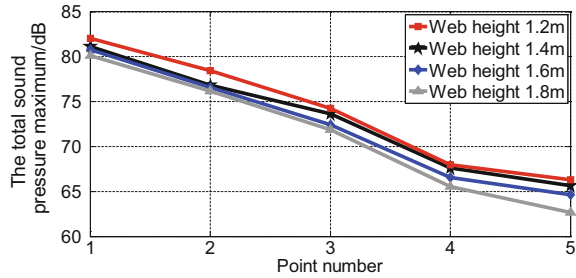
As is shown in Fig. 6, from point number 1 to point number 2, with the increase of trough-girder beam web height, bridge structure radiation noise reduction is not significant. In the distance of route center line 10.0, 20.0 and 25.0 m, that is ranges from point number 3 to point number 5, the linear maximum sound pressure level decreased obviously. It is found that the increase of trough-girder beam web height has a certain effect on the bridge structure-borne noise. It is due to the change of trough-girder beam web height, which has significant influence on bridge structure radiated noise angle. But, in the distance of route center line 20.0, 25.0 m at point number 4, point number 5, the trough-girder beam web height range from 1.40 to 1.60 m, bridge structure-noise reduces not significant, it is seen that the structure-noise of trough-girder beam should be controlled properly by changing trough-girder beam web height.

From the Fig. 5 we can see that, trough-girder beam structure-noise radiation characteristics are complicated, the influence of the structure noise radiation induced by the height of the web plate is not the same in all frequency bands. Therefore, based on the analysis of each point in 1/3 octave band center frequency maximum linear sound pressure level, we use cumulative superposition principle of sound pressure level to calculate each point the overall linear sound pressure level in the frequency range from 10.0 to 100.0 Hz.

From the Fig. 7 we can see that, in the bottom of the trough-girder beam body near sound field (less than 5 m), web height increased on trough-girder beam has little influence on the bridge structure-noise. But, the increase of the trough-girder beam web has obvious effect on the bridge structure-noise in the far sound field of far from the route center line 10∼25 m, especially, the total sound pressure of sound pressure maximum level is reduced by about 4 dB in the distance far from route center line 25 m. This shows that the increase of trough-girder beam web height can reduce structure-noise obviously in the far sound field.

Conclusions

The main conclusions were as follows:

(1) The combination of SIMPACK and ANSYS coupled simulation and hybrid FEM-IBEM method were applied to the structure-borne noise of 30 m simply-supported concrete trough-girder beam bridge. This paper confirm the hybrid FEM-IBEM method is suitable for the analysis of trough-girder beam structure-noise.

(2) When the train passes through the bridge at the speed of 80.0 km/h, the trough-girder beam structure-borne noise is low frequency, range mainly from 20.0 to 80.0 Hz, while the peak frequency appears in 63.0 Hz.

(3) The structure-borne noise decreases with the increase of web height, and the influences of the far sound field is the more obvious.

References

1. Jiahua Liu, Songliang Lian. Vibration and Noise of the Urban Rail Transit[J]. Journal of Traffic and Transportation Engineering, 2002(1):29–33.
2. Fei Gao, He Xia, Ning An. Analysis and Experimental Study on the Radiation Noise of the Elevated Structures of Beijing Metro Line 5[J]. China Railway Science, 2010(5):134–139.
3. Linya Liu, Daiyan Xu. Structural Noise radiation Characteristics of Box Beams with Web holes[J]. Journal of Vibration and Shock,2016, 35(15):204–210.
4. W Ngai K, F Ng C. Structure-noise and Vibration of Concrete Box Structure and Rail Viaduct [J]. Journal of Sound and Vibration,2002, 255(2):281–297.
5. O.G.Bewes. The calculation of noise from railway bridges and viaducts. Eng D thesis, University of Southampton, 2005.
6. Xun Zhang, Xiaozhen Li, Dejun Liu. Sound Radiation Characteristics of 32 m Simply Supported Concrete Box Girder Applied in High-speed Railway[J]. Journal of the China Railway Society, 2012, 34(7):96–102.
7. Jianglong Han, Dingjun Wu, Qi Li. Influence of Deck Thickness and Stiffeners on Structure-borne Noise of the Trough Beams[J]. Journal of Vibration Engineering, 2012, 25 (5):589–594.
8. Linya Liu, Qichuan Fu, Wenjie Shao, Jiyang Li. Application of Panel Acoustic Contribution Theory in Study of Noise From Simply-supported Box Girder in High Speed Rail Way[J]. Journal of Railway Science and Engineering, 2015(8), 12(4):743–748.
9. He Zhang, Xu Xie, M Yamashita. Analysis on Low-frequency Noise Included by Vehicle-bridge Coupling Vibration[J]. Journal of Vibration Engineering, 2010, 23(5): 514–522.
10. Junwang Ma. Environment and Landscape Adaptability of Elevated Urban Rail Transit Line [J]. Urban Rapid Rail Transit, 2015, 28(6):132–137.
11. Wendong Wang. Handbook of concrete structures (Fourth Edition) [M]. Beijing: China Architecture Building Press, 2012.

Measurement and Evaluation of Freight Train-Induced Ground Vibrations

Meng Ma, Wenbin Wang and Xiaojing Sun

Introduction

In recent years, the challenges have risen for research of railway vibration and its influences on the environment. For understanding of the characteristics of ground vibration and calibration the numerical tools, physical experiments were believed the first means researchers used to evaluate the effect of moving rail vehicles and improve the prediction veracity [1]. By means of field measurement, the response of ground vibrations and existing structures can be obtained directly. A great deal of experimental research has been done on the environmental vibration induced by trains, especially metro trains and high-speed trains which causes more significant vibration problem [2–6].

Compared with the passenger trains and high-speed trains, research on the freight train-induced vibration is rare. Nevertheless, with the substantial increase in transportation of goods on railway, the problem of ground-borne vibration induced by freight trains has received increasing interest in the recent years. The research by Woodcock et al. [7] shows that there is a significant difference between annoyance response for passenger and freight railway traffic in residential environments. Smith et al. [8] analysed the freight train-induced vibration and low frequency noise on subjective sleep quality, subjective sleep disturbance and heart rate. The in situ

M. Ma (✉) · X. Sun
School of Civil Engineering, Beijing Jiaotong University, Beijing 100044, China
e-mail: mameng@bjtu.edu.cn

X. Sun
e-mail: xjsun1@bjtu.edu.cn

W. Wang
Urban Rail Transit Center, China Academy of Railway Sciences,
Beijing 100081, China
e-mail: 10693511@qq.com

measurement on both passenger and freight train-induced ground vibration in Belgium and Poland indicates that, below 20 Hz vibration levels of freight trains are in average 15 dB higher than vibration levels of passenger trains [9]. From the state of the art one can find that, the vibration measurement for freight trains is rare. In addition, the freight train causes more annoyance on human being due to its heavy axle loads and long pass-by time.

In order to learn the vibration characteristic of freight train-induced vibrations and evaluate its vibration impact on human being, in this paper, an in situ experiment was carried out in the suburb of Beijing. The vibrations induced by both freight trains and passenger trains were considered. Then, a new vibration descriptor was presented to describe the received vibration energy from the passage of trains at sensitive locations.

Experiment Outline

The in situ experiment was carried out in the suburb of Beijing, between Beijing Railway Station and Tongzhou West Station (Fig. 1). The test section was at two curve railway lines with regular ballasted tracks. Each railway line was mixed used for both freight and passenger trains. On the section of Track 1, the passage train speed was 40 km/h, while on the section of Track 2, the passage train speed varied between 10 and 20 km/h.
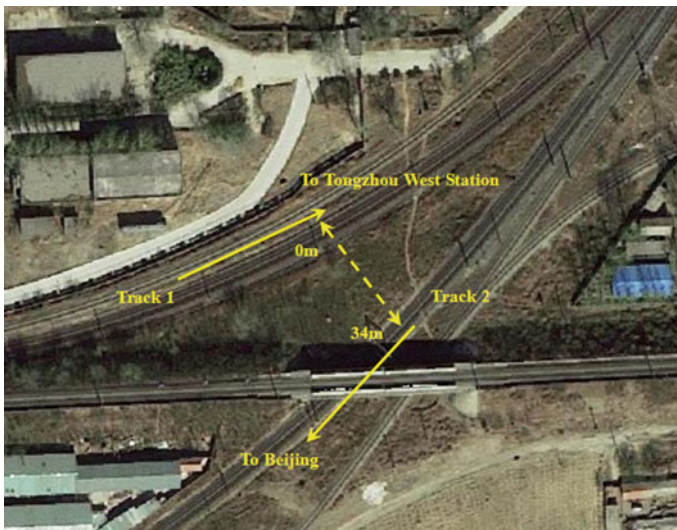
Fig. 1 The test location
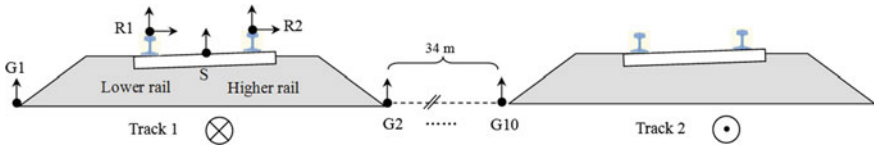
Fig. 2 Layout of experimental site and arrangement of sensors

The sensors were arranged on the rails (R1 and R2), the sleeper (S) of the Track 1, and on the ground. As shown in Fig. 2, G1 was arranged at the ballast slope on the north side of Track 1, while G2–G10 was arranged between the two test tracks where were 5, 10, 15.3, 20, 25, 27.5, 29 and 34 m away from the ballast slope of Track 2, respectively.

The instruments used in the test included two 24 bit AD inverter INV 3018C Data Acquisition and Signal Processing Systems and Lance AS0123T/AS0105/AS0115 acceleration sensors. All instruments and sensors were calibrated before the measurements.

Vibration Responses on the Track

Figure 3 shows the typical time history of track vibrations in the vertical direction induced by passenger and freight trains. On the rails, an obviously vibration impact by the wheel-rail contact can be observed. On the sleepers, the responses induced by passenger trains were more regular than those induced by freight trains. On the toe of the slope, the peak values in time histories were induced by the locomotive or vehicle with maximum axle loads. In addition, the vibration energy attenuates a lot through the ballast. Finally, it was obvious that the vibration duration induced by freight trains was longer than that by passenger trains.

Figure 4 shows the typical frequency spectra of vertical acceleration on the rails. Below 10 Hz, the vibrations are mainly caused by quasi-static train loads. Then, due to the larger axle load of freight train, it induces obviously larger low-frequency vibration contents than the passenger train. A peak value around 18 Hz can be found in both Fig. 4a, b. It is the passing frequency rail support space (0.6 m) under the train speed of 39 km/h. Nevertheless, the amplitude at 18 Hz in Fig. 4a is obviously larger than that in Fig. 4b. That is, the amplitude of the passing frequency also depends on the values of axle loads. In addition, the high vibration level between 100 and 2000 Hz can be observed, which depends on the rail unevenness. In the frequency range above, the response on the high rail are larger than that on the low rail.
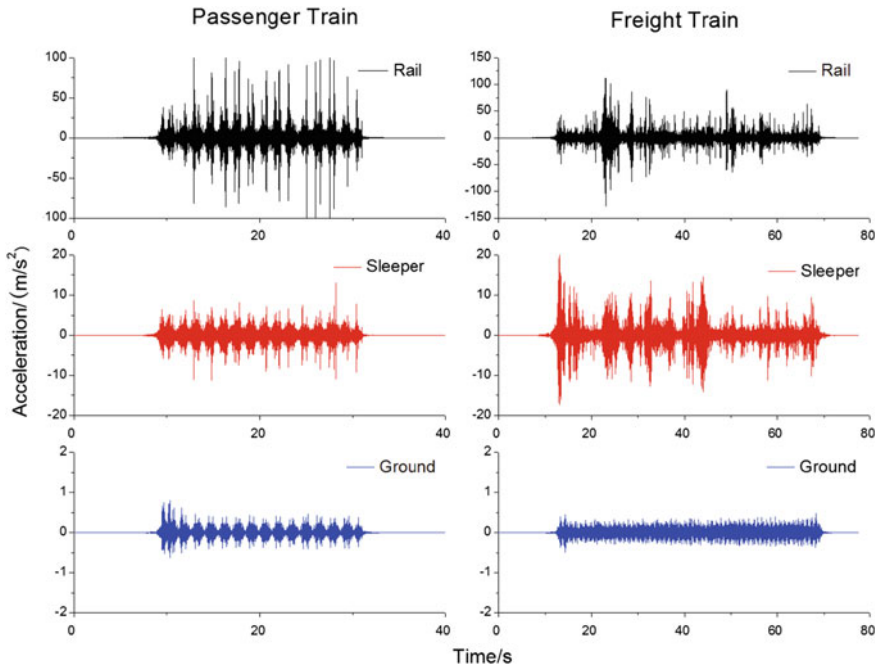
Fig. 3 Typical time history of track vibrations
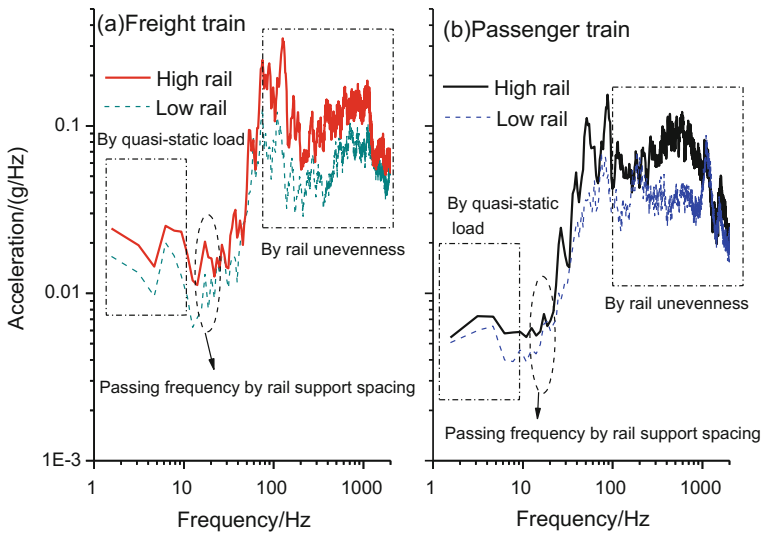
Fig. 4 Typical frequency spectra of vertical acceleration on the rails

Evaluation the Ground Vibration

Evaluation the Ground Vibration by Maximum Z-Vibration Level

According to the *Standard of Environmental Vibration in Urban Area* [10], the train-induced environmental vibration should be described and evaluated by Maximum Z-vibration Level, or $VL_{z,\max}$, which was defined as:

$$VL_{z,\max} = \max_t[VL_z(t)] \tag{1}$$

where $VL_z(t)$ is the vertical acceleration level, which can be expressed as

$$VL_z(t) = 20\log_{10}\frac{a_{w,\tau}(t)}{a_0} = 20\log_{10}\frac{\left[\frac{1}{\tau}\int_{t-\tau}^{t}a_w^2(\xi)\mathrm{d}\xi\right]^{\frac{1}{2}}}{a_0} \tag{2}$$

where a_0 is the reference acceleration, defined as 10^{-6} m/s^2, $a_{w,\tau}(t)$ is the running root-mean square (r.m.s.) weighted acceleration, and $a_w(\xi)$ is the frequency-weighed instantaneous vibration acceleration at time ξ.

Figure 5 shows two vertical acceleration levels as the function of time for the two types of trains. The maximum Z-vibration Levels are 87.2 and 85.9 dB for passenger and freight trains, respectively. It is clear that $VL_{z,\max}$ could not reflect the real vibration impact on human being, because $VL_{z,\max}$ mainly depends on the maximum axle load while the effect of vibration duration is not taken into account.

Figure 6 shows the $VL_{z,\max}$ attenuates with the distance. Also, it is difficult to distinguish the ground vibration by using the descriptor $VL_{z,\max}$. Accordingly, a new vibration descriptor is needed to evaluate the freight train-induced ground vibrations, which induces longer vibration duration.

Fig. 5 Z-vibration level for two types of trains
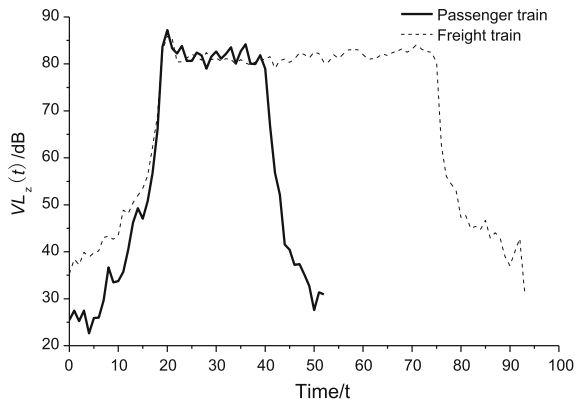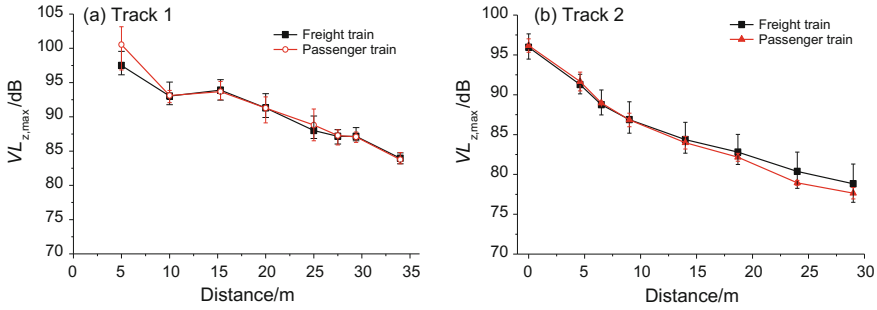
Fig. 6 $VL_{z,max}$ changes with the distance

Evaluation the Ground Vibration by Vibration Exposure Level

To evaluate the ground vibration impact induced by one pass-by train, the concept of vibration exposure level (VEL) is proposed. Similar to sound exposure level, VEL is defined as:

$$VEL = 10 \log_{10} \int_{t_1}^{t_2} \frac{a_w^2(t)}{a_0^2} \, dt = 10 \log_{10} \frac{A}{a_0^2} \tag{3}$$

where $a_w(t)$ is the running r.m.s. weighted acceleration, a_0 is the reference acceleration, defined as 10^{-6} m/s^2. A is the area under the function of $a_w^2(t)$ between the time t_1 and t_2, shown in Fig. 7. The value of A stands the vibration energy affecting on receiver, which is induced by one pass-by train. Then VEL can be also considered as another form of the vibration energy. With VEL, three important factors of vibration impact to human being are taken into account—amplitude, frequency and duration.

Fig. 7 Areas under the function of $a_w^2(t)$
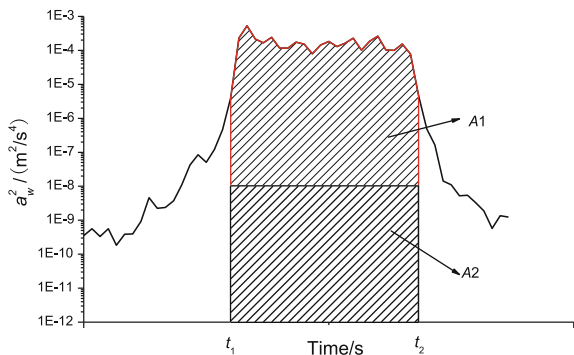
In Fig. 7, the area A can be divided into two parts: $A1$ and $A2$. Now, VEL can also divided into two parts:

$$VEL = eVEL + VEL_0 \qquad (3)$$

Suppose there is an threshold value of annoyance for human being, VEL_0 is the vibration exposure level which below the threshold. Then as the part above the threshold, effective Vibration Exposure Level ($eVEL$) is defined as:

$$VEL_0 = 10\lg\frac{a_{w\Sigma}^2 \Delta T}{a_0^2} \qquad (3)$$

where $a_{w\Sigma}$ is an uncertain reference weighted acceleration, ΔT is the duration during which human being can be annoyed under the vibration acceleration of $a_{w\Sigma}$. The combined effect by the two factors $a_{w\Sigma}^2 \Delta T$ is the area of $A2$. When ΔT is comparable to the pass-by time of a train, $a_{w\Sigma}$ is relative large if ΔT is relative small. Accordingly, $eVEL$ can be expressed as:

$$eVEL = VEL - VEL_0 = 10\lg\int_{t_1}^{t_2}\frac{a_w^2(t)}{a_0^2}dt - 10\lg\frac{a_{w\Sigma}^2 \Delta T}{a_0^2} = 10\lg\frac{\int_{t_1}^{t_2} a_w^2(t)dt}{\left[a_{w\Sigma}\Delta T^{1/2}\right]^2} \qquad (3)$$

where $a_{w\Sigma}\Delta T^{1/2}$ can be regarded as an annoyance threshold to human being, which is contributed by weighted acceleration and time. This threshold has the same dimension as the motion sickness dose value (MSDVz) defined in ISO 2631-1 [11]. MSDVz is directly relative to motion sickness, while $a_{w\Sigma}\Delta T^{1/2}$ is directly relative to annoyance. Therefore, by using VEL or $eVEL$, it is better to evaluate the human comfortable under the environmental vibration induced by trains with longer duration.
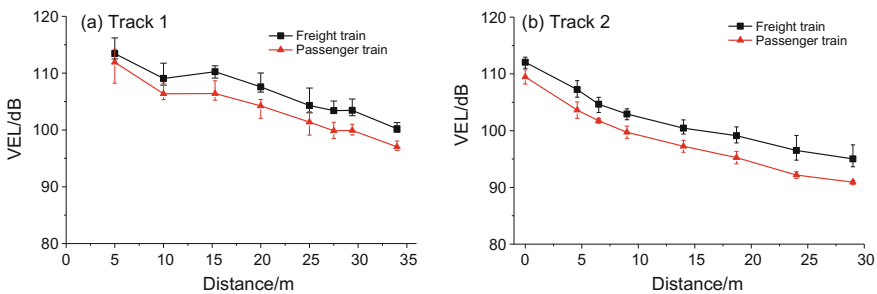
Fig. 8 VEL changes with the distance

Figure 8 shows the *VEL* attenuates with the distance. Compared with Fig. 6, by using the descriptor *VEL*, it is reasonable to distinguish the ground vibration induced by freight and passenger trains.

Conclusions

In this study, an in situ measurement of track and ground vibration was performed. The freight and passenger train-induced vibrations were compared and evaluated. The following conclusions can be drawn:

(a) Compared to normal passenger trains, the freight train induces obviously larger vibrations on the track and near field, especially in the low frequency range below 10 Hz.
(b) The pass-by time of freight train is much longer, which may induce larger annoyance to residents nearby. However, by using the maximum Z-vibration level, it is difficult to distinguish this type of annoyance in near field.
(c) As a new vibration descriptor, vibration exposure level was proposed and defined in detail in this paper. By using *VEL* or *eVEL*, it is better to consider the negative duration and to evaluate the ground vibrations by freight trains.

References

1. Kouroussis, G., Connolly, D. P., Verlinden, O. (2014). Railway-induced ground vibrations – a review of vehicle effects. International Journal of Rail Transportation, 2(2), 69–110.
2. Xia, H., Zhang, N., Cao, Y. M. (2005). Experimental study of train-induced vibrations of environments and buildings. Journal of Sound and Vibration, 280(3), 1017–1029.
3. Ju, S. H., Lin, H. T., Chen, T. K. (2007). Studying characteristics of train-induced ground vibrations adjacent to an elevated railway by field experiments. Journal of Geotechnical and Geoenvironmental Engineering, 133 (10), 1302–1307.
4. Connolly, D. P., Kouroussis, G., Woodward, P. K., Costa, P. A., Verlinden, O., Forde, M. C. (2014). Field testing and analysis of high speed rail vibrations. Soil Dynamics and Earthquake Engineering, 67, 102–118
5. Connolly, D. P., Costa, P. A., Kouroussis, G., Galvin, P., Woodward, P. K., Laghrouche, O. (2015). Large scale international testing of railway ground vibrations across Europe. Soil Dynamics and Earthquake Engineering, 71, 1–12.
6. Zhai, W., Wei, K., Song, X., Shao, M. (2015). Experimental investigation into ground vibrations induced by very high speed trains on a non-ballasted track. Soil Dynamics and Earthquake Engineering, 72, 24–36.

7. Woodcock, J.S., Sharp, C., Sica G, Peris, E., Moorhouse, A.T. (2012). Human response to vibration from passenger and freight railway traffic in residential environments, in 19th International Congress on Sound and Vibration, Vilnius, Lithuania.

8. Smith, M. G., Croy, I., Ögren, M., Waye K.P. (2013). On the influence of freight trains on humans: a Laboratory investigation of the impact of nocturnal low frequency vibration and noise on sleep and heart rate. PloS ONE, 8(2).

9. Vanhonacker, P. (2013). Attenuation of ground-borne vibration affecting residents near railway lines, Deliverable 2.2. Leuven, Belgium: Alfa Products and Technologies.

10. Chinese National Standard. (1988). Standard of environmental vibration in urban area, GB 10070-88.

11. International Organization for Standardization. (1997). Mechanical vibration and shock-Evaluation of human exposure to whole-body vibration-Part 1: General requirements, ISO 2631-1.

Dynamic Stress Distribution of Arbitrarily Arranged Deep Cavities Subjected to Incident Plane P Waves by Multiple Scattering Method

Miaomiao Sun, Huajian Fang, Shimin Zhang and Xinjiang Wei

Introduction

Underground space is a result which is bound to follow the society development. It effectively solves the traffic congestion, saves the ground resources, and uses the underground space resources sufficiently. However it is inevitably encountered earthquake, traffic and explosion induced vibrations, which greatly influence structures and surrounding soils, especially at the case of multiple municipal pipelines and metro stations with interchange tunnels. It is necessary to investigate multiple scattering problems of elastic waves by underground deep cavities group to evaluate the stability and safety of those structures.

Multiple scattering theory is utilized in deep cavity and lining problems since elastic scattering theories are established. Pao and Mow [1] initiated single cavity and lining in infinite space under the incident elastic waves with wave function expansion methods, accompanied with dynamic stress concentration problem. Lee and Trifunac [2–5] studied multiple scattering problems of elastic waves at deep

M. Sun (✉) · S. Zhang · X. Wei
Department of Civil Engineering, Zhejiang University City College,
Hangzhou 310015, China
e-mail: sunmm@zucc.edu.cn

S. Zhang
e-mail: zhangsm@zucc.edu.cn

X. Wei
e-mail: weixj@zucc.edu.cn

H. Fang
Zhejiang Provincial Key Laboratory of Hydraulics Disaster
Prevention and Mitigation, Zhejiang Institute of Hydraulics and Estuary,
Hangzhou 310020, China
e-mail: 490123734@qq.com

cavity in infinite half-space. Lee and Karl [6, 7] delivered analytical solution of P and SV waves scattering by half-space cavity. Luco and Barros [8] solved scattering problem of single lining with Green function and Bonnell shell theory. Liang and Ji [9] proposed analytical solutions of lining and cavity with incident Rayleigh waves. Wang and Gao [10–12] investigated the influences of deep and shallow circular composite lining in infinite half-space with incident SH and SV waves by wave function expansion method.

It is worthy noted that most of those research works mentioned above are based on single cavity or double cavities, which are not involved with several irregular arranged and different sized parallel cavities. Those analytical solutions can barely meet the requirements of practical engineering, and are just considered single scattering hypothesis which is ignoring the multiple scattering influences. The radius dimensions cannot be neglected with elastic wavelength, which brings about inadmissible errors in engineering application.

Based on multiple scattering theory in vibration isolation with rows of piles [13], it is derived multiple scattering theoretical solutions of elastic wave by several irregularly arranged deep parallel cavities, analyzed Dynamic Stress Concentration Factors (DSCF) with different parameters of cavities.

Problem of Incident P Waves

It's basically similar to tubular piles when it is encountered the multiple scattering problems of deep cavity in total space. Which it is assumed polarization directions of incident waves are parallel to cavities' axis. The analysis model is illustrated in Fig. 1 of Sun's former research work [13, 14]. Deep linings under the incident plane waves are regarded analogous as pipe-piles. If the problem goes to arbitrarily arranged and configuration deep cavities, it refers to the condition when the lining thickness equals 0, or the radius of solid pile equals 0 as well.

When cylinders group is subjected to incident P or SV waves, it is simplified to plane-strain problem, which leads to coupling scattering of P and SV waves. Incident and scattering wave's expressions are

(a) Linearly arranged   (b) Hexagonally arranged
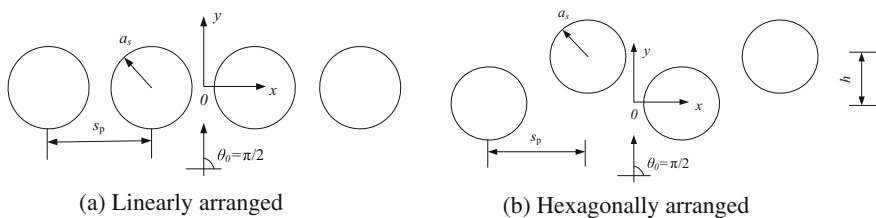
Fig. 1 The preference coordinate system and analysis model of parallel deep cavities ($N = 4$)

$$\phi^{\mathrm{inc}} = e^{i\alpha_s r_{0s}\cos(\theta_0 + \theta_{0s})} \sum_{n=-\infty}^{+\infty} \mathrm{J}_n(\alpha_s r_s) e^{in\varphi_s} \tag{1}$$

$$^s\phi_m^{\mathrm{sc}} = \sum_{n=-\infty}^{+\infty} {}^s A_m \mathrm{H}_n(\alpha_s r_s) e^{in\theta_s} \tag{2}$$

$$^s\psi_m^{\mathrm{sc}} = \sum_{n=-\infty}^{+\infty} i^s B_m \mathrm{H}_n(\beta_s r_s) e^{in\theta_s} \tag{3}$$

where the certain notations' meaning are listed at [13, 14].

It is simplified deep cavities to solid-piles when $b_s = a_s = 0$, which is equivalent to cylindrical cavities, and there is tensile stress-free at the internal surfaces. The boundary conditions are

$$\left[\sigma_{r_s r_s}^{\mathrm{inc}}(r_s, \theta_s) + {}^s\sigma_{r_s r_s}^1(r_s, \theta_s)\right]\Big|_{r_s = a_s} = 0 \tag{4}$$

$$\left[\sigma_{r_s \theta_s}^{\mathrm{inc}}(r_s, \theta_s) + {}^s\sigma_{r_s \theta_s}^1(r_s, \theta_s)\right]\Big|_{r_s = a_s} = 0 \tag{5}$$

$$s = 0, 1, 2 \ldots N, \quad 0 \le \theta_s \le 2\pi$$

where

$$\sigma_{r_s r_s}(r_s, \theta_s) = \frac{2G_s}{r_s}\left[-(r_s\frac{\partial\phi}{\partial r_s} + \frac{\partial^2\phi}{\partial\theta_s^2} + \frac{\beta_s^2 r_s^2}{2}\phi) + (r_s\frac{\partial^2\psi}{\partial r_s \partial\theta_s} - \frac{\partial\psi}{\partial\theta_s})\right] \tag{6}$$

$$\sigma_{r_s \theta_s}(r_s, \theta_s) = \frac{2G_s}{r_s}\left[(r_s\frac{\partial\phi}{\partial r_s \partial\theta_s} - \frac{\partial\phi}{\partial\theta_s}) + (r_s\frac{\partial\psi}{\partial r_s} + \frac{\partial^2\psi}{\partial r_s^2} + \frac{\beta_s^2 r_s^2}{2}\psi)\right] \tag{7}$$

Substitute (1) and (2) to (16), (17) with (4) and (5)
The first scattering coefficients are

$$\sum_{n=-\infty}^{+\infty} \begin{bmatrix} \mathrm{E}_{11}^{(3)}(\alpha_s a_s) & \mathrm{E}_{12}^{(3)}(\beta_s a_s) \\ \mathrm{E}_{41}^{(3)}(\alpha_s a_s) & \mathrm{E}_{42}^{(3)}(\beta_s a_s) \end{bmatrix} \begin{bmatrix} {}^s A_1 \\ {}^s B_1 \end{bmatrix} = -\sum_{n=-\infty}^{+\infty} \begin{bmatrix} \mathrm{E}_{11}^{(1)}(\alpha_s a_s) \\ \mathrm{E}_{41}^{(1)}(\alpha_s a_s) \end{bmatrix} {}^s\theta_\alpha \tag{8}$$

where ${}^s\theta_\alpha = e^{in(\theta_0 + \pi/2) + i\alpha_s r_{0s}\cos(\theta_{0s} + \theta_0)}$, the definition of squiggle letters are listed on [14].

When $m \ge 2$, in order to obtain the mth scattering coefficients, boundary conditions refer to

$$[{}^s\sigma_{r_s r_s}^m (r_s, \theta_s) + \sum_{s'=0, s'\neq s}^{N'} {}'^{s'}\sigma_{r_s r_s}^{m-1}(r_{s'}, \theta_{s'})]\bigg|_{r_s = a_s} = 0 \tag{9}$$

$$[{}^s\sigma_{r_s \theta_s}^m (r_s, \theta_s) + \sum_{s'=0, s'\neq s}^{N'} {}'^{s'}\sigma_{r_s \theta_s}^{m-1}(r_{s'}, \theta_{s'})]\bigg|_{r_s = a_s} = 0 \tag{10}$$

$$s = 0, 1, 2 \dots N, \quad 0 \le \theta_s \le 2\pi, \quad m \ge 2$$

and

$${}^s\sigma_{r_s r_s}^m\big|_{r_s = a_s} = \frac{2G_s}{a_s^2} \sum_{n=-\infty}^{+\infty} [{}^s A_m E_{11}^{(3)}(\alpha_s a_s) + {}^s B_m E_{12}^{(3)}(\beta_s a_s)] e^{in\theta_s} \tag{11}$$

$${}^s\sigma_{r_s \theta_s}^m\big|_{r_s = a_s} = -\frac{2G_s}{a_s^2} \sum_{n=-\infty}^{+\infty} i[{}^s A_m E_{41}^{(3)}(\alpha_s a_s) + {}^s B_m E_{42}^{(3)}(\beta_s a_s)] e^{in\theta_s} \tag{12}$$

With the Graf's addition theorem,
mth scattering coefficients follow the iteration formula as

$$
\begin{bmatrix} E_{11}^{(3)}(\alpha_s a_s) & E_{12}^{(3)}(\beta_s a_s) \\ E_{41}^{(3)}(\alpha_s a_s) & E_{42}^{(3)}(\beta_s a_s) \end{bmatrix} \begin{bmatrix} {}^s A_m \\ {}^s B_m \end{bmatrix}
$$
$$
= -\sum_{s'=0, s'\neq s}^{N'} {}' \sum_{n'=-\infty}^{+\infty} \begin{bmatrix} {}^s H_{n'n}(\alpha_s a_{ss'}) E_{11}^{(1)}(\alpha_s a_{s'}) & {}^s H_{n'n}(\beta_s a_{ss'}) E_{12}^{(1)}(\beta_s a_{s'}) \\ {}^s H_{n'n}(\alpha_s a_{ss'}) E_{41}^{(1)}(\alpha_s a_{s'}) & {}^s H_{n'n}(\beta_s a_{ss'}) E_{42}^{(1)}(\beta_s a_{s'}) \end{bmatrix} \begin{bmatrix} {}^{s'} A_{m-1} \\ {}^{s'} B_{m-1} \end{bmatrix} \tag{13}
$$

Thus,

$${}^s A_m = -\sum_{s'=0, s'\neq s}^{N'} {}' \sum_{n'=-\infty}^{+\infty} \frac{\begin{aligned} &[E_{11}^{(1)}(\alpha_s a_{s'}) - E_{41}^{(1)}(\alpha_s a_{s'}) E_{12}^{(3)}(\beta_s a_s)]{}^s H_{n'n}(\alpha_s a_{ss'}){}^{s'} A_{m-1} \\ &+ [E_{12}^{(1)}(\beta_s a_{s'}) - E_{42}^{(1)}(\beta_s a_{s'}) E_{12}^{(3)}(\beta_s a_s)]{}^s H_{n'n}(\beta_s a_{ss'}){}^{s'} B_{m-1} \end{aligned}}{E_{11}^{(3)}(\alpha_s a_s) E_{42}^{(3)}(\beta_s a_s) - E_{41}^{(3)}(\alpha_s a_s) E_{12}^{(3)}(\beta_s a_s)} \tag{14}$$

$${}^s B_m = \sum_{s'=0, s'\neq s}^{N'} {}' \sum_{n'=-\infty}^{+\infty} \frac{\begin{aligned} &[E_{11}^{(1)}(\alpha_s a_{s'}) - E_{41}^{(1)}(\alpha_s a_{s'}) E_{11}^{(3)}(\alpha_s a_s)]{}^s H_{n'n}(\alpha_s a_{ss'}){}^{s'} A_{m-1} \\ &+ [E_{12}^{(1)}(\beta_s a_{s'}) - E_{42}^{(1)}(\beta_s a_{s'}) E_{11}^{(3)}(\alpha_s a_s)]{}^s H_{n'n}(\beta_s a_{ss'}){}^{s'} B_{m-1} \end{aligned}}{E_{11}^{(3)}(\alpha_s a_s) E_{42}^{(3)}(\beta_s a_s) - E_{41}^{(3)}(\alpha_s a_s) E_{12}^{(3)}(\beta_s a_s)} \tag{15}$$

It is easily noticed that they are the degradation form of tubular pile scattering coefficients only if $b_s \rightarrow a_s$, $G_{\mathrm{p}} \rightarrow 0$ [14].

There is also P-SV waves coupled scattering when it is encountered incident SV waves, so it is confirmed with stress-free boundary conditions. The first scattering coefficients are

$$\sum_{n=-\infty}^{+\infty} \begin{bmatrix} \mathrm{E}_{11}^{(3)}(\alpha_s a_s) & \mathrm{E}_{12}^{(3)}(\beta_s a_s) \\ i\mathrm{E}_{41}^{(3)}(\alpha_s a_s) & i\mathrm{E}_{42}^{(3)}(\beta_s a_s) \end{bmatrix} \begin{bmatrix} {}^s A_1 \\ {}^s B_1 \end{bmatrix} = -\sum_{n=-\infty}^{+\infty} \begin{bmatrix} i\mathrm{E}_{41}^{(1)}(\beta_s a_s) \\ \mathrm{E}_{11}^{(1)}(\beta_s a_s) \end{bmatrix} {}^s\theta_\beta \qquad (16)$$

where ${}^s\theta_\beta = e^{in(\theta_0 + \pi/2) + i\beta_s r_{0s} \cos(\theta_{0s} + \theta_0)}$, the definition of squiggle letters are also listed on [14].

It is obviously noticed that the mth scattering iteration formula composed with both P and SV waves. No matter whether it is subjected to incident P or SV waves, it generates an identical expression showed as (13).

Numerical Analysis

1. Dynamic Stress Concentration Factor (DSCF) of deep cavities

The dynamic respond stress field is determined when scattering coefficients are obtained. The cavities circumferential stress is $\sigma_{\theta_s \theta_s}$, and if $r_s = a_s$,

$$\sigma_{\theta_s \theta_s}^* = \frac{\sigma_{\theta_s \theta_s}}{\sigma_0}\bigg|_{r_s = a_s} \qquad (17)$$

where $\sigma_{\theta_s \theta_s}^*$ is dimensionless Dynamic Stress Concentration Factor (DSCF) of the cavity.

It is known that the circumferential stress of cavity is

$$\left.{}^s\sigma_{\theta_s \theta_s}^m\right|_{r_s = a_s} = \frac{2G_{\mathrm{p}}}{a_s^2} \sum_{n=-\infty}^{+\infty} [{}^s A_m \mathrm{E}_{21}^{(3)}(\alpha_s a_s) + {}^s B_m \mathrm{E}_{22}^{(3)}(\beta_s a_s)]e^{in\theta_s} \qquad (18)$$

The Dynamic Stress Concentration Factor (DSCF) of mth scattering is

$$\sigma_{\theta_s \theta_s}^* = \frac{2 \sum_{n=-\infty}^{+\infty} [{}^s A_m \mathrm{E}_{21}^{(3)}(\alpha_s a_s) + {}^s B_m \mathrm{E}_{22}^{(3)}(\beta_s a_s)]}{\beta_s^2 a_s^2} e^{in\theta_s} \qquad (19)$$

2. Dynamic Stress Concentration Factor (DSCF) of incident P waves

It is chosen 4 circular cavities with identical radius, $r_s = a_s$, separation between cavities is s_{p}, the Poission's ratio v_s of soil is 0.26, incident angle θ_0 of P wave is $\pi/2$, the distance of cavity group rows with hexagonally arranged is h, reference

(a) the 1st cavity (from left)

(b) the 2nd cavity (from left)

(c) the 3rd cavity (from left)

(d) the 4th cavity (from left)

Fig. 2 DSCF of cavity group with the variation of angle (incident P waves, $s_p = 6.0a_s$, $h = 0$, $m = 4$, $N = 4$)

coordinate systems and analysis modals with linear and hexagonal shaped are illustrated as Fig. 1.

Figure 2 is the distribution map of 4 cavities with 4 scattering Dynamic Stress Concentration Factor (DSCF) under incident P waves. s_p is 6 times of cavity radius a_s. Stress is distributed at the two sides of vertical axis, the Dynamic Stress Concentration Factor (DSCF) of the 2nd and 3rd cavities from left are symmetrical with vertical and horizontal axis. The curves of 1st and 4th cavities from left are symmetrical with axis y.

It is observed that stress varies not conspicuous when incident P waves are at a lower frequency ($\alpha_s b_s = 0.2$), shaping like twin ellipses. Scattering coherent relation is not obvious as the maximum value of DSCF is 0.7. $\sigma^*_{\theta_s \theta_s}$ at vertical (90°–270°) axis is almost 0. When incident P waves are at a higher frequency range ($\alpha_s b_s = 1.0$), circumferential stress is radially distributed. The maximum $\sigma^*_{\theta_s \theta_s}$ of all cavities is about 0.3, of whose value of the 1st and 4th cavities from left is no more than 50% of the one with lower incident P waves.

Figure 3 shows the variation of DSCF with angle changing when the separation s_p between cavities is $12.0a_s$. Compared with Fig. 2, it's only revealed the distribution of stress curves of the 2nd and 3rd cavities are symmetrical with 90°–270° axis, meanwhile the curves of the 1st and 4th are asymmetrical, especially under the circumstance of incident P waves with higher frequency ($\alpha_s b_s = 1.0$). It can be observed that the similar DSCF curves with lower frequency incident P waves, which are shaped as symmetrical twin ellipses, are at the maximum $\sigma^*_{\theta_s \theta_s}$ value of

(a) the 1st cavity (from left)

(b) the 2nd cavity (from left)

(c) the 3rd cavity (from left)

(d) the 4th cavity (from left)
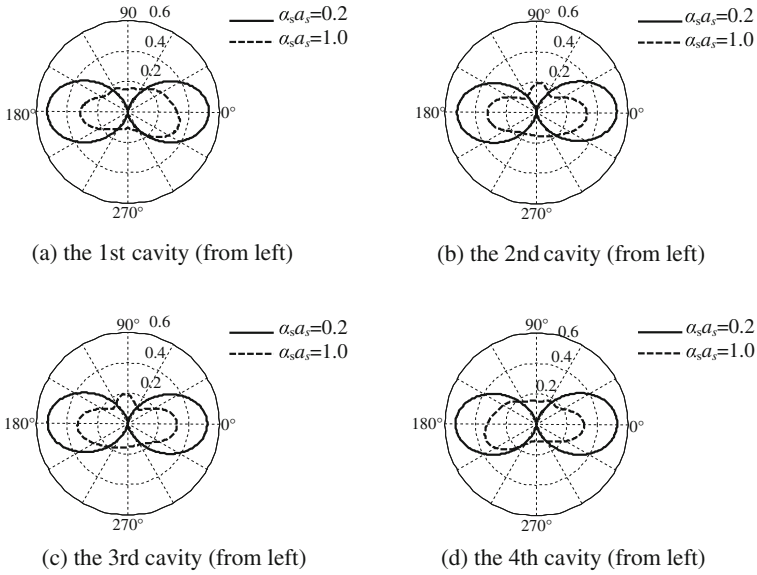
Fig. 3 DSCF of cavity group with the variation of angle (incident P waves, $s_p = 12.0a_s$, $h = 0$, $m = 4$, $N = 4$)

(a) the 1st cavity (from left)

(b) the 2nd cavity (from left)

(c) the 3rd cavity (from left)

(d) the 4th cavity (from left)
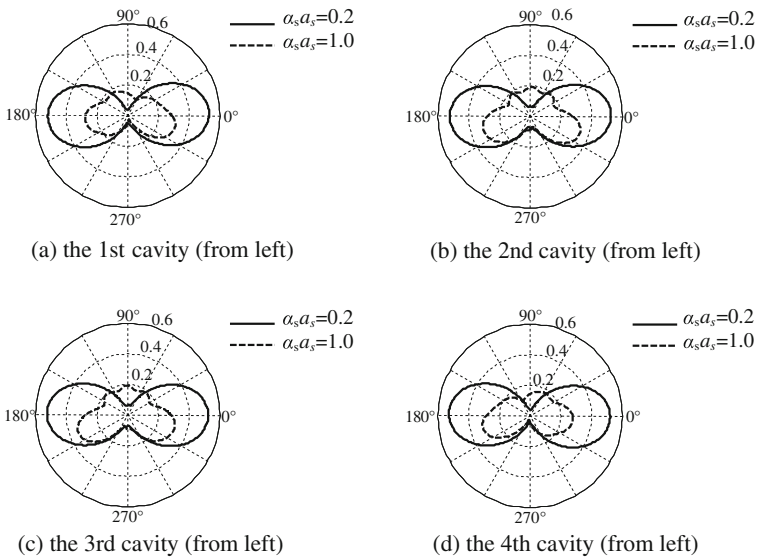
Fig. 4 DSCF of cavity group with the variation of angle (incident P waves, $s_p = 24.0a_s$, $h = 0$, $m = 4$, $N = 4$)

0.55. The DSCF is distributed as the same as it is under the incident waves with lower frequency and with a maximum $\sigma^*_{\theta_s\theta_s}$ value of 0.35.

It is plotted at Fig. 4, no matter lower or higher frequency the incident P waves are performed with, there is barely any difference of DSCF distribution, which gradually presents symmetrical curves with 90°–270° axis. It is illustrated that multiple scattering effectiveness is weaken with the separation between cavities broadened, as the result of scattering waves' coherence is not significant. In other words, the longer the separation between cavities is, the weaker the multiple scattering effect they perform. Therefore the influence of cavities with each other can be neglected finally as cavities become isolated scatterers.

Figure 5 is depicted the variation of DSCF with angle changing as the cavities group hexagonally arranged in Fig. 1b, the separation and distance along horizontal and vertical axis are both equal $6.0a_s$. There is certain imparity of $\sigma^*_{\theta_s\theta_s}$ with longer wavelength or lower frequency incident waves (@@$\alpha_s b_s = 0.2$) in contrast with the linearly arranged parallel cavities in Fig. 1a. DSCF distributions are symmetrical with both vertical axis 90°–270° and horizontal axis 0°–180°, shaping like twin ellipses and differing from the linearly arranged presenting lower eccentricity. The maximum value of DSCF is 0.5, occurring perpendicular to the incident orientation, which is similar to $s_p = 12.0a_s$ with linear displayed. DSCF distributions curves of cavities hexagonally arranged are as closer as cavities linearly arranged. When $s_p = 12.0a_s$ or $24.0a_s$, the DSCF curves are asymmetrical with axis 90°–270°

(a) the 1st cavity (from left)   (b) the 2nd cavity (from left)

(c) the 3rd cavity (from left)   (d) the 4th cavity (from left)

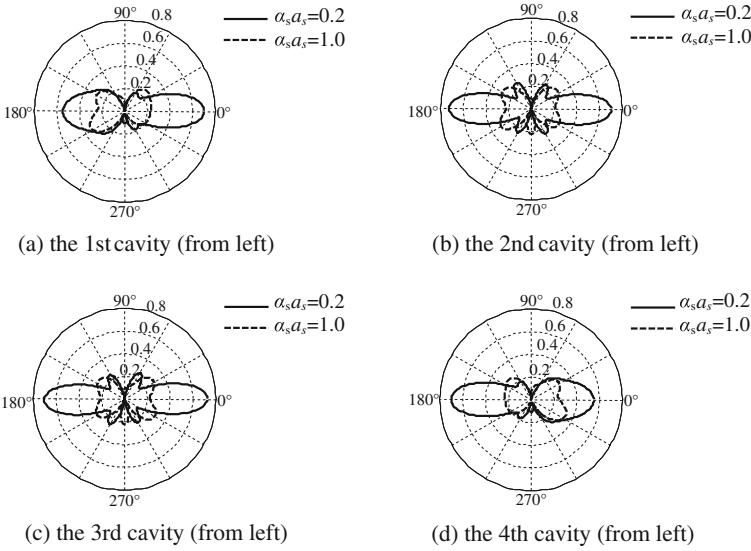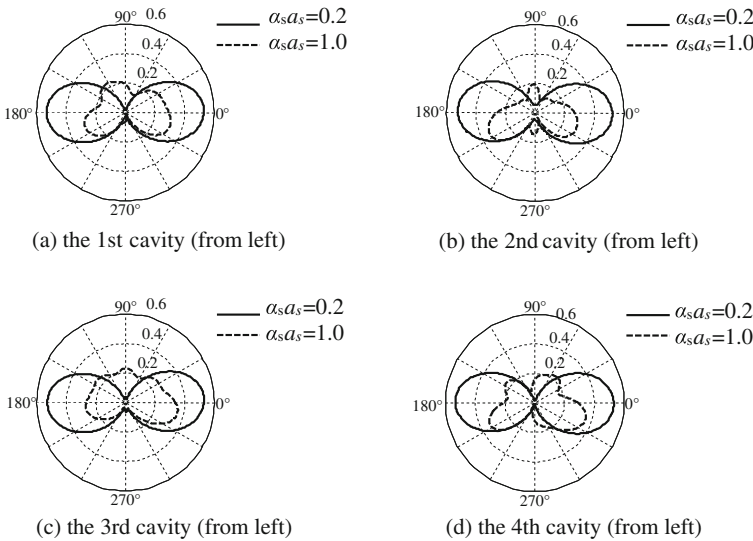**Fig. 5** DSCF of cavity group with the variation of angle (incident P waves, $s_p = 6.0a_s$, $h = 6.0a_s$, $m = 4$, $N = 4$)

because cavities are geometric asymmetrical. It is concluded that no matter what kind of methods for widening separations between cavities, it'll weaken the multiple scattering coherent effect between cavities, and it is led the stress distributions to asymptotically uniform.

Conclusions

It is provided a solution for multiple scattering of elastic waves by several arbitrarily arranged and radius parallel deep cavities in elastic, homogeneous, isotropic media by multiple scattering method. It is established transmitted wave field inside cavities, expanding incident waves to the form of Fourier-Bessel series and solving the first scattering and transmitted complex coefficients by rigid or elastic boundary conditions. Secondly, it is translated the other cavities' coordinate axes into the specific one with Graf's addition theorem, and obtained subsequent scattering and transmitted coefficients by equilibrium equations and boundary conditions as a result. The scattering and transmitted field are determined ultimately, so as the stress field of cavities.

It is researched circumferential DSCF of several deep cavities with the incident P waves. The maximum value of DSCF occurs at horizontal axis, shaping like twin ellipses when incident waves are at lower frequency range. The DSCF of every cavity in linearly arranged is symmetrical with axis 90°–270° when incident waves are at higher frequency range because it is interfered by scattering waves from any other cavities. With the increasing of separations between cavities, the interaction and interference of multiple scattering are weakening, stress distributions are asymptotically uniform and presenting geometric symmetrical. The value of DSCF which the cavities group is arranged as hexagon is approximately the same as the ones arranged as linear shaped meanwhile the separation between cavities is half of the former one.

References

1. Pao Y H, Mow C C. (1973). Diffraction of elastic waves and dynamic stress concentrations [M]. New York, Crane and Russak.
2. Lee V W. and Trifunac, M. D. (1979). Response of tunnels to incident SH waves [J]. Journal of the Engineering Mechanics Division, 105 (4): 643–659.
3. Nasser M, Trifunac M D. (1981). A note on the vibrations of a semi-circular canal excited by plane SH-wave [J]. Bulletin of the Indian Society of Earthquake Technology, 18 (2): 88–100.

4. Lee V W. (1984). Three dimensional diffraction of plane P, SV and SH waves by a hemispherical alluvial valley [J]. Soil Dynamics and Earthquake Engineering, 3 (3):133–144.
5. Lee V W, Cao H. (1989). Diffraction of SV waves by circular cylindrical canyons of various depths [J]. Journal of Engineering Mechanics, 115(9): 2035–2056.
6. Lee V W, Karl J. (1993). Diffraction of SV waves by underground, circular, cylindrical cavities [J]. Soil Dynamic and Earthquake Engineering, 11 (8): 445–456.
7. Lee V W, Karl J. (1993). Diffraction of elastic plane P waves by circular, underground unlined tunnels [J]. European Journal of Earthquake Engineering, 1 (1): 29–36.
8. Luco J E, Barros de F C P. (2001). Seismic response of a cylindrical shell embedded in a layered viscoelastic half-space. I: Formulation [J]. Earthquake Engineering and Structural Dynamics, 23 (5): 553–567.
9. Liang J W, Ji X D. (2006). Amplification of Rayleigh waves due to underground lined cavities [J]. Earthquake Engineering and Engineering Dynamics, 2006, (04): 024–31.
10. Wang S S, Gao B, Shen Y S, et al. (2014). Study on the mechanism of resistance and damping technology of deep soft rock tunnels subjected to incident plane SH waves [J]. China Civil Engineering Journal, 47 (Sup.1): 280–286.
11. Gao B, Wang S S. (2016). Dynamic response study on shallow circular composite-lining tunnels [J]. Journal of Southeast Jiaotong University, 51(4): 599–606.
12. Wang S S, Gao B. (2016). Damping mechanism and shaking table test on mountain tunnel linings with buffer layers [J]. Chinese Journal of Rock Mechanics and Engineering, 35 (3): 592–603.
13. T D Xia, M M Sun, C Chen, et al. (2011). Analysis on multiple scattering by an arbitrary configuration of piles as barriers for vibration isolation [J]. Soil Dynamics and Earthquake Engineering, 31 (3): 535–545.
14. M M Sun, G Q Liang, T D Xia, et al. (2014). Ground vibration isolation of multiple scattering by using rows of tubular piles as barriers [J]. Shock and Vibration, 2014: 1–20.

Earth Pressures of the Buried HDPE Pipe Subjected to Ground Subsidence

Min Zhou, Yanjun Du and Fei Wang

Introduction

The buried High density polyethylene (HDPE) pipe is vulnerable to the ground subsidence due to its relative low stiffness. The failure of buried HDPE pipes could cause the waste of water resources, the worsening of ground subsidence, and destruction of various types of adjacent surface structures [1]. Many empirical and theoretical design methods are proposed for calculation of the earth pressure at the top of the pipes during the installation process [2–4]. Marston investigates the earth pressure acting on buried pipes in trench and embankment conditions and proposes "the Marston Load theory" by using the limit equilibrium method [2]. Spangler assumes the earth pressure at the springline of the pipe is proportional to the horizontal deflection of the pipe [3]. AASHTO LRFD Bridge Design Specification indicates that the earth pressure at the top of the pipes is calculated by the soil prism load multiplied by the Vertical Arching Factor (*VAF*) [4]. However, the load distribution of buried pipes subjected to the ground subsidence receives less attention.

In this study, full-scale model tests are conducted in a custom-made test box. Plates installed at the bottom of the box are moved downward to generate the ground subsidence. 200-mm-diameter and 400-mm-diameter HDPE pipes with a length of 2 m are used in the model tests. Earth pressures at the top, springline and bottom of the pipes are measured during the downward moving of the bottom

M. Zhou (✉) · Y. Du · F. Wang
Jiangsu Key Laboratory of Urban Underground Engineering & Environmental Safety,
Institute of Geotechnical Engineering, Southeast University, Nanjing 210096, China
e-mail: 230139499@seu.edu.cn

Y. Du
e-mail: duyanjun@seu.edu.cn

F. Wang
e-mail: feiwangseu@gmail.com

plates. The effect of magnitude of the ground subsidence on earth pressures of buried HDPE pipes is investigated.

Testing Instrumentation and Measurements

Tested Pipes

Two HDPE double-wall corrugated pipes (labeled as P1 and P2) with inside diameter of 200 and 400 mm are adopted in the model tests, respectively. The pipe stiffness is determined as 215 kPa using parallel plate loading test [5]. The physical parameters of the HDPE pipes are tabulated in Table 1.

Backfilling Material

Yangtze River sand is used as the backfill material, and the uniformity coefficient and curvature coefficient of the sand are 2.86 and 0.94, respectively. Based on the Unified Soil Classification System [6], the sand is classified as poorly graded sand (SP). The specific gravity of the sand is 2.65, and the minimum and maximum densities are 1.43 and 1.74 Mg/m^3, respectively.

Instrumentation

The model tests are conducted in a model box with a dimension of 2 m in width, 2 m in length, and 1.5 m in height, as shown in Fig. 1. The side walls of the model box are made of 15-mm-thick polyethylene plates and reinforced by steel frames. Vaseline is placed on the wall of the model box to minimize the effect of the friction between the side wall and the backfill. The bottom of the box is built with eight movable plates, and each is 0.1 m thick, 0.25 m wide and 2 m long. The details of the model box can be found in [7].

Table 1 Physical properties of the HDPE pipes

Pipe ID	Nominal diameter (mm)	Inner wall thickness (mm)	Laminated wall thickness (mm)	Corrugation depth (mm)	Pitch (mm)	Pipe stiffness (kPa)	Bending stiffness (kNm^2)
P1	200	1.2	1.7	10	30	215	4.16
P2	400	2	2.5	25	50	215	48
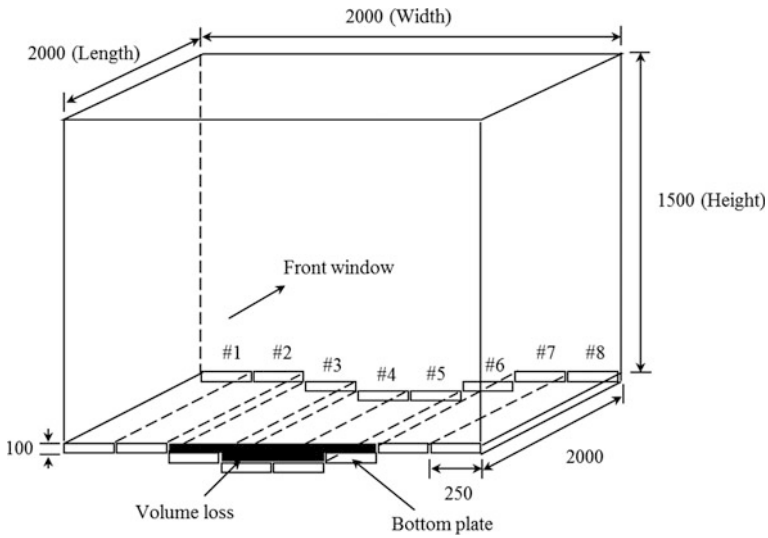
Fig. 1 Schematic diagram of physical model box (unit: mm)

Model Testing Methodology

The P1 and P2 pipes are installed in the model box at a buried depth of 0.85 and 0.9 m from the backfill surface to the centerline of the pipe, respectively. Both ends of HDPE pipes are connected with the walls of the model box by custom-made fixing frames to simulate pipe joints. Three testing profiles 1, 2 and 3 along the longitudinal direction of the pipe are instrumented, as shown in Fig. 2. Earth pressure cells in a range of 0–0.2 MPa are used in the model tests. To ensure the uniformity of backfilling, the sand is backfilled using a sand pluviation device from a height of 0.7 m, and the sand density obtained is determined as 1.46 Mg/m³. A data acquisition system is connected with the earth pressure cells to record earth pressure at a time interval of 2 s automatically. The settlement plates and strain gauges are also instrumented to monitor the vertical displacements and strains of the pipe and the results are not presented considering the paper length.

The middle four bottom plates of the model box (labeled as #3, #4 #5 and #6) are lowered down step by step to simulate the land ground subsidence. Motion Movement pattern of the bottom plates is shown in Fig. 3.
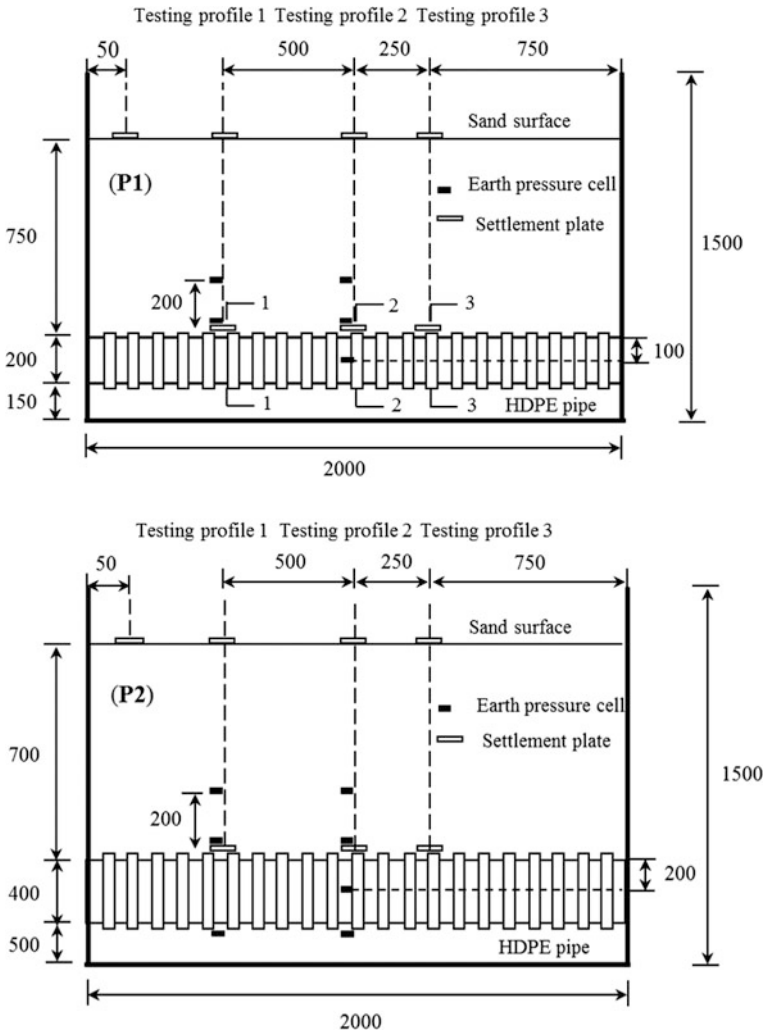
Fig. 2 Schematic diagram of testing instrumentation

Test Results

Figure 4 shows that the earth pressures at the top of P1 and P2 pipes are smaller than the geostatic stress of the backfill when the backfilling is completed, indicating the positive soil arching is triggered at the top of the pipe. The earth pressure at the top of the pipe experiences an overall increase with lowering down the bottom plates. The possible reason is that the existence of the HDPE pipe restrains the soil settlement above the pipe, and negative soil arching is triggered along the cross-sectional direction of the pipe. When the bottom plates #4 and #5 are lowered
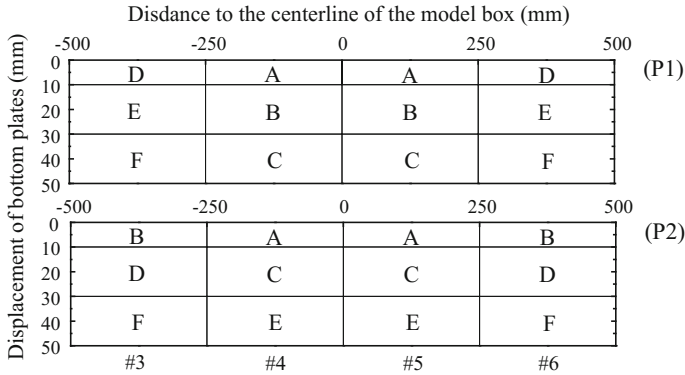
Fig. 3 Motion pattern of the bottom plates of the model box (letters *A–F* represent the lowering sequence of bottom plates)
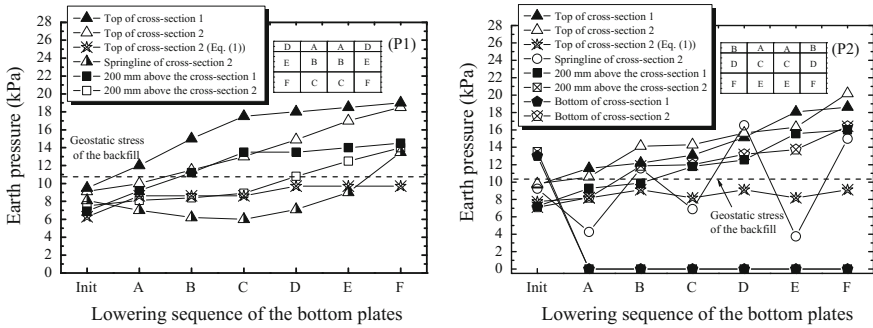
Fig. 4 Variation in earth pressures at the top of the pipes ("Init" represents completion of backfilling)

down, the earth pressures at the top of P1 and P2 pipe for testing profile 1 increase by 19–26%, while those for testing profile 2 increase only by 4–13%. The possible reason is that the positive soil arching is triggered along the longitudinal direction of the pipe at the top of the cross-section 2 when the bottom plates #4 and #5 were lowered down, and it partly counteracted the effect of the negative soil arching triggered along the transverse direction. When the bottom plates #3 and #6 are lowered down, the earth pressures at the top of P1 and P2 pipes for testing profile 1 increase by 2–5%, while those for testing profile 2 increase by 10–33%. The possible reason is that the positive soil arching along the longitudinal direction of the pipe is triggered at the top of the cross-section 1 when the bottom plates #3 and #6 were lowered down. The earth pressures measured at 0.2 m above the P1 and P2 pipes exhibit similar patterns with those at the top of the pipes.

The earth pressure at the top of the pipe can be calculated by the two dimensional soil arching theory [5]:

$$P = B\gamma(1 - e^{\wedge}(-2K\mu h/B))/2K\mu \tag{1}$$

where P is the earth pressure acting on the pipe top (kPa); B is the width of the sliding area of the soil; γ is the unit weight of the soil (kN/m^3); K is the lateral earth pressure coefficient; μ is the internal friction coefficient of the soil; h is the buried depth (m).

It is seen from Fig. 4 that the earth pressures measured at the top of the pipe are 16–90% larger than those calculated by Eq. (1). The reason for this is that the negative soil arching triggered along the cross-sectional direction of the pipe is not considered by Eq. (1).

The earth pressure at the springline of the cross-section 2 of the P1 pipe decreases by 13, 11 and 3% when the bottom plates #4 and #5 are lowered down for the first, second and third times, while it increases by 18, 27 and 50% when bottom plates #3 and #6 for the fourth, fifth and sixth times. For the P2 pipe, the springline pressure decreased 45, 40 and 79% with lowering down the bottom plates #4 and #5 for the first, third and fifth times, while it increased 147, 120 and 300% with lowering down the bottom plates #3 and #6 for the second, fourth and sixth time, respectively. The possible reason is that the soil settlement at the springline area of the cross-section 2 of the pipe is larger than those at its adjacent areas when the bottom plates #4 and #5 were lowered down, which causes positive soil arching at the springline of the cross-section 2; on the contrary, the negative soil arching is triggered when the bottom plates #3 and #6 were lowered down.

The earth pressures measured at the bottom of the cross-section 1 and cross-section 2 of the P2 pipe become 0 kPa when the bottom plates are lowered down for the first time and they remain unchanged with the bottom plates lowered down for the second time to sixth time. It is indicative that the gap formation occurs at the lower half of the pipe-soil interface.

Conclusions

The distribution of earth pressures around the HDPE pipe subjected to the ground subsidence is presented. The earth pressure at the top of the HDPE pipes experiences an overall increase with lowering down the bottom plates of the model box. The two dimensional soil arching theory underestimates the earth pressure at the top of the pipe due to without considering the negative soil arching triggered by the ground subsidence along the transverse direction of the HDPE pipe.

References

1. Xing L.X., Que L.D. The distribution and harm of the land collapses in China. The Chinese Journal of Geological Hazaro and Control, 1997, 8(S): 23–28. (in Chinese).
2. Marston, A (1930). The theory of external loads on closed conduits in the light of the latest experiments. Highway Research Board Proceedings 9: 138–170.
3. Spangler, M.G. (1941). The structural design of flexible pipe culverts. Bulletin 153, Iowa State College Engineering Experimental Station.
4. AASHTO (2012). AASHTO LRFD bridge design specifications (second edition). Sec. 12, Washington, D. C.
5. ASTM. (2011). Standard Test Method for Determination of External Loading Characteristics of Plastic Pipe by Parallel-plate Loading-D2412-11, Annual Book of ASTM Standards, ASTM International, West Conshohocken, Pa.
6. ASTM. (2011). Standard practice for classification of soils for engineering purpose-D2487-11, Annual Book of ASTM Standards, ASTM International, West Conshohocken, Pa.
7. Wang, F., Du, Y.J., and Yang, X.M. (2015). Physical modeling on ground responses to tunneling in sand considering the existence of HDPE pipes. ASTM Geotech. Test. J, 38(1): 85–97.

Semi-analytical Solution for the Dynamic Response of a Cylindrical Structure Embedded in a Homogeneous Half-Space

Mingjuan Zhao, Karel N. van Dalen, João M. Barbosa and Andrei V. Metrikine

Introduction

The study of wave propagation in elastic solids has been of interest in seismology and civil engineering for a long time. Given the fact that more underground facilities (for instance, lifelines and tunnels) need to be designed and constructed with the development of the modern world, it is important to investigate the dynamic response of underground structures to either earthquake excitation or other dynamic loads if applicable. A detailed review of the earthquake response and seismic-resistant design of underground pipeline systems was presented by Ariman and Muleski [1]. The existing methods to solve the wave scattering problem by different types of inclusions embedded in a full space or a half-space were reviewed by Stamos and Beskos [2]. The advantages and disadvantages of each method were discussed in detail.

The studies on three-dimensional wave scattering by inclusions are much less numerous than those on the two-dimensional ones. In this paper, a solution to the problem of the three-dimensional wave scattering by an infinitely long underground structure with a circular cross-section embedded in an elastic half-space is presented.

M. Zhao (✉) · K.N. van Dalen · J.M. Barbosa · A.V. Metrikine
Department of Structural Engineering, Delft University of Technology,
2628 CN Delft, The Netherlands
e-mail: M.Zhao@tudelft.nl

K.N. van Dalen
e-mail: K.N.vanDalen@tudelft.nl

J.M. Barbosa
e-mail: J.M.DeOliveiraBarbosa@tudelft.nl

A.V. Metrikine
e-mail: A.Metrikine@tudelft.nl

Special attention is paid to a comparison of the obtained results with those of the previous works dealing with the same type of underground structures as in this paper. Luco and De Barros [3] investigated the two-dimensional response of a viscoelastic half-space containing a buried infinitely long cylindrical cavity of circular cross-section subjected to harmonic plane SH, P, SV and Rayleigh waves by using an indirect boundary integral method based on two-dimensional Green's functions for a viscoelastic half-space. They also obtained the three-dimensional response of an infinitely long cylindrical shell of circular cross-section embedded in a layered viscoelastic half-space and subjected to harmonic waves impinging at an oblique angle with respect to the longitudinal axis of the shell [4, 5]. The procedure employed in the latter references combines an indirect integral representation for the field in the exterior half-space with a model of the pipeline or tunnel based on the Donnell shell theory. The integral representation for the soil is based on the use of the so-called moving Green's functions for the layered viscoelastic half-space. In the paper [5], the authors validated the accuracy of the proposed method by extensive comparisons with the work by Wong et al. [6] who used the cylindrical eigenfunctions method and the work by Liu et al. [7] who used the boundary integral representation and finite element method for the three-dimensional cases. They also compared their results with those presented by Datta et al. [8] who employed a hybrid technique combining a finite element method with the eigen-function expansion, Balendra et al. [9] who applied the method of wave function expansion and the image technique, Wong [6], and Liu [7] for the two-dimensional cases.

In this paper, a semi-analytical method is proposed to calculate the scattering of elastic waves by an infinitely long cylindrical structure of circular cross-section embedded in an linearly elastic, isotropic and homogeneous half-space. The method can be considered to be a straightforward extension of the method used to solve the two-dimensional scattering problems of P, SV, Rayleigh waves [10] and SH waves [11].

When the scattered waves from the underground structure (tunnel) impinge on the half-space surface, a secondary reflected wave field is generated (the primary reflected wave field is generated directly by the incident plane wave that excites the system). In the spirit of the image technique [12], the latter are sought for in the form of cylindrical waves that are generated by an imaginary source of an a priori unknown intensity placed at the image point that is positioned symmetrically to the centre of the tunnel with respect to the half-space surface. One of the aims of this paper is to evaluate the contributions of the wave field directly scattered by the tunnel and the secondary reflected wave filed on the dynamic response of the system at the half-space surface and at the half-space interface with the tunnel. Different circumferential modes are taken into account in this evaluation and various convergence tests are presented. The hoop stresses and motions at the interface with the tunnel as well as the ground surface motions are also analysed for two- and three-dimensional cases in order to investigate the effects of the dimension and the presence of the tunnel on the system response.

Statement of the Problem

Figure 1 defines the problem to be analysed: an infinitely long cylindrical tunnel with a circular cross-section, whose axis is parallel to the half-space surface, is subjected to plane harmonic body waves of arbitrary propagation direction, which results in a three-dimensional problem. The materials of both the half-space and the tunnel are assumed isotropic and linearly elastic, and characterized by the Lamé parameters λ_i, μ_i and densities ρ_i (the subscripts $i = 1, 2$ refer to the half-space and the tunnel, respectively). The centre of the tunnel (o_1) is at depth h beneath the half-space surface. o_2 is the image point that is positioned symmetrically to the centre of the tunnel with respect to the half-space surface. R_I, R_O and R_C stand for the inner and outer radii of the tunnel, and the centre line of the tunnel, respectively. To aid in the mathematical description of the different waves, six reference systems are represented: the global Cartesian (xyz) and cylindrical $(xr\Theta)$ coordinate systems, the local Cartesian (xy_1z_1) and cylindrical $(xr_1\Theta_1)$ coordinate systems centred at the tunnel, and (xy_2z_2) and $(xr_2\Theta_2)$ originated at the image of the tunnel. Anti-clockwise is defined as the positive direction in the cylindrical coordinate systems.

The time dependence of the incident plane harmonic wave and the response of the system to this wave are assumed to be harmonic and proportional to $e^{-i\omega t}$, where $i = \sqrt{-1}$ is the imaginary unit and ω is the angular frequency of the wave. In what follows, the factor $e^{-i\omega t}$ will be dropped from all the expressions for brevity. The angle between the incident wave direction and the vertical axis z is θ_v (see Fig. 1b, $\theta_v = 0$ for vertical incidence). The horizontal projection of the propagation
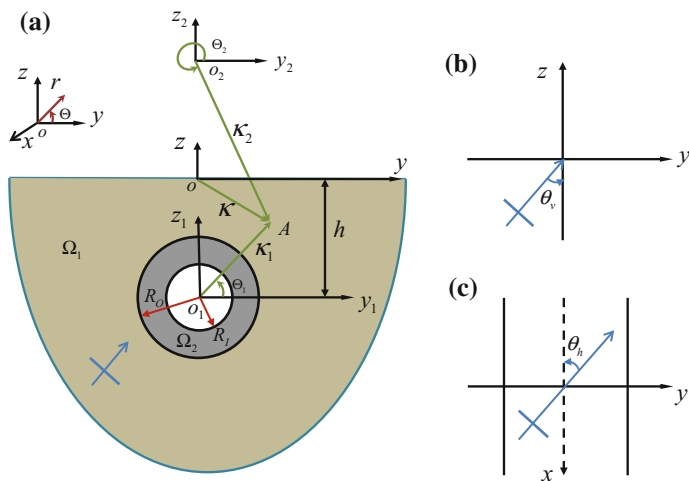
Fig. 1 **a** The cross-section of the model; **b** The vertical incident angle; **c** The horizontal incident angle

direction on *xoy* plane forms an angle θ_h (see Fig. 1c) with the x axis. The regions Ω_1 and Ω_2 refer to the domains of the soil medium and the tunnel, respectively.

Governing Equations

In the absence of the body forces, the equations of motion in the mediums in terms of the displacement vectors $\mathbf{u}_i$ can be written as

$$(\lambda_i + \mu_i)\nabla\nabla\cdot\mathbf{u_i} + \mu_i\nabla^2\mathbf{u_i} = \rho_i\ddot{\mathbf{u}}_i \tag{1}$$

Substituting the Helmholtz decomposition $\mathbf{u}_i = \nabla\phi_i + \nabla \times \boldsymbol{\psi}_i$ into the governing Eq. (1), we obtain two uncoupled scalar and vector potential Helmholtz equations:

$$\nabla^2\phi_i + k_{pi}^2\phi_i = 0 \tag{2}$$

$$\nabla^2\boldsymbol{\Psi}_i + k_{si}^2\boldsymbol{\Psi}_i = 0 \tag{3}$$

where ϕ_i and $\boldsymbol{\Psi}_i$ are the compressional and shear wave potentials, respectively, $k_{pi} = \omega/c_{pi}$ and $k_{si} = \omega/c_{si}$ are the compressional and shear wavenumbers, respectively, and $c_{pi} = \sqrt{(\lambda_i + 2\mu_i)/\rho_i}$ and $c_{si} = \sqrt{\mu_i/\rho_i}$ are the velocities of the compressional and shear waves, respectively.

The vector wave potential $\boldsymbol{\Psi}_i$ is chosen to satisfy the gauge condition $\nabla \cdot \boldsymbol{\Psi}_i = 0$, therefore, only two of the three components of $\boldsymbol{\Psi}_i$ are independent. Correspondingly, Eq. (3) can be reduced to two uncoupled scalar Helmholtz equations [13, 14]

$$\nabla^2\psi_i + k_{si}^2\psi_i = 0 \tag{4}$$

$$\nabla^2\chi_i + k_{si}^2\chi_i = 0 \tag{5}$$

by defining the vector wave potentials $\boldsymbol{\Psi}_i$ as

$$\boldsymbol{\Psi}_{ii} = \boldsymbol{\Psi}_{i1} + \boldsymbol{\Psi}_{i2} \tag{6}$$

$$\boldsymbol{\Psi}_{i1} = \psi_i e_x + \frac{1}{k_{si}^2}\nabla\left(\frac{\partial\psi_i}{\partial x}\right) \tag{7}$$

$$\boldsymbol{\Psi}_{i2} = \frac{1}{k_{si}}\nabla \times (\chi_i e_x) \tag{8}$$

in which e_x is the unit vector along x axis.

The displacement fields are written in terms of the scalar wave potentials ϕ_i, ψ_i and χ_i as

$$u_{xi} = \frac{\partial \phi_i}{\partial x} + \frac{1}{k_{si}}\left(k_{si}^2 \chi_i + \frac{\partial^2 \chi_i}{\partial x^2}\right) \tag{9}$$

$$u_{yi} = \frac{\partial \phi_i}{\partial y} + \frac{\partial \psi_i}{\partial z} + \frac{1}{k_{si}}\frac{\partial^2 \chi_i}{\partial x \partial y} \tag{10}$$

$$u_{zi} = \frac{\partial \phi_i}{\partial z} - \frac{\partial \psi_i}{\partial y} + \frac{1}{k_{si}}\frac{\partial^2 \chi_i}{\partial x \partial z} \tag{11}$$

The stress components can be derived by the Hooke's law [15]. The displacement vector $\mathbf{u}$ and stress tensor $\boldsymbol{\sigma}$, where the subscript i is omitted for brevity, can be further written in the cylindrical coordinate system defined as $y = r \cos\Theta$ and $z = r \sin\Theta$ according to the linear transformation

$$\begin{bmatrix} u_x \\ u_r \\ u_\theta \end{bmatrix} = \begin{bmatrix} 1 & 0 & 0 \\ 0 & \cos\Theta & \sin\Theta \\ 0 & -\sin\Theta & \cos\Theta \end{bmatrix}\begin{bmatrix} u_x \\ u_y \\ u_z \end{bmatrix} \tag{12}$$

$$\begin{bmatrix} \sigma_{xx} & \sigma_{xr} & \sigma_{x\theta} \\ \sigma_{rx} & \sigma_{rr} & \sigma_{r\theta} \\ \sigma_{\theta x} & \sigma_{\theta r} & \sigma_{\theta\theta} \end{bmatrix} = \begin{bmatrix} 1 & 0 & 0 \\ 0 & \cos\Theta & \sin\Theta \\ 0 & -\sin\Theta & \cos\Theta \end{bmatrix}\begin{bmatrix} \sigma_{xx} & \sigma_{xy} & \sigma_{xz} \\ \sigma_{yx} & \sigma_{yy} & \sigma_{yz} \\ \sigma_{zx} & \sigma_{zy} & \sigma_{zz} \end{bmatrix}\begin{bmatrix} 1 & 0 & 0 \\ 0 & \cos\Theta & -\sin\Theta \\ 0 & \sin\Theta & \cos\Theta \end{bmatrix} \tag{13}$$

This transformation is instrumental for description of the cylindrical displacements and stresses at the tunnel surfaces.

Boundary Conditions

The method presented in this paper is general. It can be applied to analyse the dynamic response of the tunnel embedded in a half-space to either external dynamic forces or seismic waves. Considering the problem of vehicles moving either along the half-space surface or through the tunnel, external traction vector are acting either on the half-space surface ($\boldsymbol{\sigma}^{ext1} = [\sigma_{zz}, \sigma_{zy}, \sigma_{zx}]$) or on the inner surface of the tunnel ($\boldsymbol{\sigma}^{ext2} = [\sigma_{rr}, \sigma_{r\theta}, \sigma_{rx}]$). The boundary conditions considering, for generality, both of the above excitations are written as

$$[\sigma_{zz1}, \sigma_{zy1}, \sigma_{zx1}] = \boldsymbol{\sigma}^{ext1}, \quad z = 0 \tag{14}$$

$$[\sigma_{rr2}, \sigma_{r\theta2}, \sigma_{rx2}] = \boldsymbol{\sigma}^{ext2}, \quad r_1 = R_I \tag{15}$$

If only the incident harmonic plane wave excites the system, the external stresses acting on the half-space surface and the inner surface of the tunnel will vanish, resulting in the traction-free boundary conditions at these surfaces.

We assume that the contact condition between the soil medium and the tunnel is perfect. This implies that there is neither partial nor full slip motion at the soil-tunnel interface and there is also no separation at the soil-tunnel interface along normal direction, which results in continuity conditions of all tractions and displacements. The equilibrium of the tractions and compatibility of the displacements at the soil-tunnel interface can be written as

$$\sigma_{rr1} = \sigma_{rr2}, \sigma_{r\theta1} = \sigma_{r\theta2}, \sigma_{rx1} = \sigma_{rx2}, \quad r_1 = R_O \tag{16}$$

$$u_{r1} = u_{r2}, u_{\theta1} = u_{\theta2}, u_{x1} = u_{x2}, \quad r_1 = R_O \tag{17}$$

To demonstrate the merit of the proposed method, in what follows, we consider a harmonic compressional wave as external excitation.

Solutions of the Governing Equations

In this section, the obtained solutions of the governing equations using the method of separation of variables are given in the Cartesian and cylindrical coordinate systems [13]. These solutions are used to construct the complete wave field in the system [15].

The Incident and the Primary Reflected Waves

In the absence of the underground structure in the half-space, the wave field is the sum of the incident (ϕ^i) and the primary reflected wave fields (ϕ^r, ψ^r, χ^r):

$$\phi^i = \phi_0 e^{ik_x x + ik_y y + ik_{pz1} z} \tag{18}$$

$$\phi^r = A\phi_0 e^{ik_x x + ik_y y - ik_{pz1} z} \tag{19}$$

$$\psi^r = B\phi_0 e^{ik_x x + ik_y y - ik_{sz1} z} \tag{20}$$

$$\chi^r = C\phi_0 e^{ik_x x + ik_y y - ik_{sz1} z} \tag{21}$$

with ϕ_0 the amplitude of the incident compressional wave, A, B and C the unknown coefficients of the primary reflected waves ϕ^r, ψ^r and χ^r, respectively, $k_x = -\omega/c_{p1} \sin(\theta_v) \cos(\theta_h)$ and $k_y = \omega/c_{p1} \sin(\theta_v) \sin(\theta_h)$ the wave numbers along x and y axis, respectively, c_{p1} the velocity of the incident wave, $k_{pz1} = \sqrt{k_{p1}^2 - k^2}$ and $k_{sz1} = \sqrt{k_{s1}^2 - k^2}$ the wave numbers of the compressional and shear waves along z axis in the soil medium, respectively, $k^2 = k_x^2 + k_y^2$. The unknown coefficients A, B and C can be determined by satisfying the traction free boundary conditions at the half-space surface.

Wave Fields Generated Due to the Presence of the Tunnel

Due to the presence of the tunnel, the scattered compressional and shear waves are generated at the outer surface of the tunnel; they are denoted as ϕ_{11}^s, ψ_{11}^s, χ_{11}^s, respectively. When these scattered waves impinge on the half-space surface, a secondary reflected wave field is generated. In the spirit of the image technique [12], the generated secondary reflected waves are sought for in the form of cylindrical waves that are generated by an imaginary source of an a priori unknown intensity placed at o_2 (see Fig. 1), and denoted as ϕ_{12}^s, ψ_{12}^s, χ_{12}^s. All these wave potentials satisfy the Helmholtz equations in the two cylindrical coordinate systems shown in Fig. 1 (the origins of these systems are located at o_1 and o_2) and are expressed as [13]

$$\phi_{11}^s = \sum_{n=-\infty}^{\infty} a_n H_n^{(1)}(k_{\alpha 1} r_1) e^{in\Theta_1} e^{ik_x x} \tag{22}$$

$$\psi_{11}^s = \sum_{n=-\infty}^{\infty} b_n H_n^{(1)}(k_{\beta 1} r_1) e^{in\Theta_1} e^{ik_x x} \tag{23}$$

$$\chi_{11}^s = \sum_{n=-\infty}^{\infty} c_n H_n^{(1)}(k_{\beta 1} r_1) e^{in\Theta_1} e^{ik_x x} \tag{24}$$

$$\phi_{12}^s = \sum_{n=-\infty}^{\infty} d_n H_n^{(1)}(k_{\alpha 1} r_2) e^{in\Theta_2} e^{ik_x x} \tag{25}$$

$$\psi_{12}^s = \sum_{n=-\infty}^{\infty} e_n H_n^{(1)}(k_{\beta 1} r_2) e^{in\Theta_2} e^{ik_x x} \tag{26}$$

$$\chi_{12}^s = \sum_{n=-\infty}^{\infty} f_n H_n^{(1)}(k_{\beta1}r_2)e^{in\Theta_2}e^{ik_xx} \qquad (27)$$

where $H_n^{(1)}$ denotes the Hankel function of the first kind and order n, and stands for outgoing (propagating from the tunnel) waves considering the time dependent factor $e^{-i\omega t}$. $k_{a1} = \sqrt{k_{p1}^2 - k_x^2}$ and $k_{\beta1} = \sqrt{k_{s1}^2 - k_x^2}$ are the cylindrical wave numbers of the compressional and shear waves in the soil medium, respectively.

The wave fields in the tunnel also satisfy the Helmholtz equations in the cylindrical coordinate system and are written as

$$\phi_2^s = \sum_{n=-\infty}^{\infty} g_n H_n^{(1)}(k_{\alpha2}r_1)e^{in\Theta_1}e^{ik_xx} + \sum_{n=-\infty}^{\infty} h_n H_n^{(2)}(k_{\alpha2}r_1)e^{in\Theta_1}e^{ik_xx} \qquad (28)$$

$$\psi_2^s = \sum_{n=-\infty}^{\infty} i_n H_n^{(1)}(k_{\beta2}r_1)e^{in\Theta_1}e^{ik_xx} + \sum_{n=-\infty}^{\infty} j_n H_n^{(2)}(k_{\beta2}r_1)e^{in\Theta_1}e^{ik_xx} \qquad (29)$$

$$\chi_2^s = \sum_{n=-\infty}^{\infty} k_n H_n^{(1)}(k_{\beta2}r_1)e^{in\Theta_1}e^{ik_xx} + \sum_{n=-\infty}^{\infty} l_n H_n^{(2)}(k_{\beta2}r_1)e^{in\Theta_1}e^{ik_xx} \qquad (30)$$

where $H_n^{(2)}$ denotes the Hankel function of the second kind and order n, and stands for ingoing (propagating towards the origin of the coordinate system) waves considering the time dependent factor $e^{-i\omega t}$. $k_{a2} = \sqrt{k_{p2}^2 - k_x^2}$ and $k_{\beta2} = \sqrt{k_{s2}^2 - k_x^2}$ are the cylindrical wave numbers of the compressional and shear waves in the tunnel, respectively. According to the phase matching principle, in both the soil medium and the tunnel, the wavenumbers of the compressional and shear waves along x axis are the same as in the incident wave and, accordingly, are equal to k_x. The unknown coefficients in Eqs. (22)–(30) will be determined from the boundary conditions.

Total Wave Fields

The total wave field in the soil medium (ϕ_1, ψ_1 and χ_1) consist of the incident, primary reflected, scattered and secondary reflected wave fields. The total wave field in the tunnel (ϕ_2, ψ_2 and χ_2) are the sum of outgoing and ingoing wave fields.

$$\phi_1 = \phi^i + \phi^r + \phi_{11}^s + \phi_{12}^s \qquad (31)$$

$$\psi_1 = \psi^r + \psi_{11}^s + \psi_{12}^s \qquad (32)$$

$$\chi_1 = \chi^r + \chi_{11}^s + \chi_{12}^s \tag{33}$$

$$\phi_2 = \phi_2^s \tag{34}$$

$$\psi_2 = \psi_2^s \tag{35}$$

$$\chi_2 = \chi_2^s \tag{36}$$

Stresses and Displacements Expressed in Terms of Complex Variables

In this section, we introduce a complex variable $\kappa = y + iz = re^{i\Theta}$ and its conjugate $\bar{\kappa} = y - iz = re^{-i\Theta}$, where y, z and r, Θ are the Cartesian and cylindrical coordinates introduced earlier. Using those, the polar angles Θ_1 and Θ_2 related to the local coordinate systems in Fig. 1a can be written in terms of the complex variable κ related to the global coordinate system as

$$e^{i\Theta_1} = \frac{\kappa_1}{|\kappa_1|} = \frac{\kappa + ih}{|\kappa + ih|} \tag{37}$$

$$e^{i\Theta_2} = \frac{\kappa_2}{|\kappa_2|} = \frac{\kappa - ih}{|\kappa - ih|} \tag{38}$$

The components of the displacements and stresses in Cartesian coordinates xyz can be expressed in terms of the complex variables κ and $\bar{\kappa}$ as

$$u_{xi} = ik_x\phi_i + \frac{k_{\beta i}^2}{k_{si}}\chi_i \tag{39}$$

$$u_{yi} = \left(\frac{\partial\phi_i}{\partial\kappa} + \frac{\partial\phi_i}{\partial\bar{\kappa}}\right) + i\left(\frac{\partial\psi_i}{\partial\kappa} - \frac{\partial\psi_i}{\partial\bar{\kappa}}\right) + \frac{ik_x}{k_{si}}\left(\frac{\partial\chi_i}{\partial\kappa} + \frac{\partial\chi_i}{\partial\bar{\kappa}}\right) \tag{40}$$

$$u_{zi} = i\left(\frac{\partial\phi_i}{\partial\kappa} - \frac{\partial\phi_i}{\partial\bar{\kappa}}\right) - \left(\frac{\partial\psi_i}{\partial\kappa} + \frac{\partial\psi_i}{\partial\bar{\kappa}}\right) + \frac{-k_x}{k_{si}}\left(\frac{\partial\chi_i}{\partial\kappa} - \frac{\partial\chi_i}{\partial\bar{\kappa}}\right) \tag{41}$$

$$\sigma_{xxi} = -(\lambda_i + 2\mu_i)k_x^2\phi_i - \lambda_i k_{\alpha i}^2\phi_i + \frac{2i\mu_i k_x k_{\beta i}^2}{k_{si}}\chi_i \tag{42}$$

$$\sigma_{yyi} = -\lambda_i k_x^2 \phi_i - (\lambda_i + \mu_i) k_{\alpha i}^2 \phi_i + 2\mu_i \left(\frac{\partial^2 \phi_i}{\partial \kappa^2} + \frac{\partial^2 \phi_i}{\partial \bar{\kappa}^2} \right) + 2i\mu_i \left(\frac{\partial^2 \psi_i}{\partial \kappa^2} - \frac{\partial^2 \psi_i}{\partial \bar{\kappa}^2} \right)$$
$$- \frac{i\mu_i k_x k_{\beta i}^2}{k_{si}} \chi_i + \frac{2i\mu_i k_x}{k_{si}} \left(\frac{\partial^2 \chi_i}{\partial \kappa^2} + \frac{\partial^2 \chi_i}{\partial \bar{\kappa}^2} \right)$$

$$(43)$$

$$\sigma_{yxi} = 2i\mu_i k_x \left(\frac{\partial \phi_i}{\partial \kappa} + \frac{\partial \phi_i}{\partial \bar{\kappa}} \right) - \mu_i k_x \left(\frac{\partial \psi_i}{\partial \kappa} - \frac{\partial \psi_i}{\partial \bar{\kappa}} \right)$$
$$+ \frac{\mu_i \left(k_{si}^2 - 2k_x^2 \right)}{k_{si}} \left(\frac{\partial \chi_i}{\partial \kappa} + \frac{\partial \chi_i}{\partial \bar{\kappa}} \right)$$

$$(44)$$

$$\sigma_{zzi} = -\lambda_i k_x^2 \phi_i - (\lambda_i + \mu_i) k_{\alpha i}^2 \phi_i - 2\mu_i \left(\frac{\partial^2 \phi_i}{\partial \kappa^2} + \frac{\partial^2 \phi_i}{\partial \bar{\kappa}^2} \right) - 2i\mu_i \left(\frac{\partial^2 \psi_i}{\partial \kappa^2} - \frac{\partial^2 \psi_i}{\partial \bar{\kappa}^2} \right)$$
$$- \frac{i\mu_i k_x k_{\beta i}^2}{k_{si}} \chi_i - \frac{2i\mu_i k_x}{k_{si}} \left(\frac{\partial^2 \chi_i}{\partial \kappa^2} + \frac{\partial^2 \chi_i}{\partial \bar{\kappa}^2} \right)$$

$$(45)$$

$$\sigma_{zyi} = 2i\mu_i \left(\frac{\partial^2 \phi_i}{\partial \kappa^2} - \frac{\partial^2 \phi_i}{\partial \bar{\kappa}^2} \right) - 2\mu_i \left(\frac{\partial^2 \psi_i}{\partial \kappa^2} + \frac{\partial^2 \psi_i}{\partial \bar{\kappa}^2} \right) - \frac{2\mu_i k_x}{k_{si}} \left(\frac{\partial^2 \chi_i}{\partial \kappa^2} - \frac{\partial^2 \chi_i}{\partial \bar{\kappa}^2} \right) \quad (46)$$

$$\sigma_{zxi} = -2\mu_i k_x \left(\frac{\partial \phi_i}{\partial \kappa} - \frac{\partial \phi_i}{\partial \bar{\kappa}} \right) - i\mu_i k_x \left(\frac{\partial \psi_i}{\partial \kappa} + \frac{\partial \psi_i}{\partial \bar{\kappa}} \right)$$
$$+ \frac{i\mu_i \left(k_{si}^2 - 2k_x^2 \right)}{k_{si}} \left(\frac{\partial \chi_i}{\partial \kappa} - \frac{\partial \chi_i}{\partial \bar{\kappa}} \right)$$

$$(47)$$

By applying the transformation relations between the Cartesian and cylindrical coordinate systems (Eqs. 12–13), the expressions for the displacements and stresses in the cylindrical coordinate system $xr\Theta$ can be written in terms of the variables κ and $\bar{\kappa}$ as

$$u_{ri} = \left(e^{i\Theta} \frac{\partial \phi_i}{\partial \kappa} + e^{-i\Theta} \frac{\partial \phi_i}{\partial \bar{\kappa}} \right) + i \left(e^{i\Theta} \frac{\partial \psi_i}{\partial \kappa} - e^{-i\Theta} \frac{\partial \psi_i}{\partial \bar{\kappa}} \right)$$
$$+ \frac{ik_x}{k_{si}} \left(e^{i\Theta} \frac{\partial \chi_i}{\partial \kappa} + e^{-i\Theta} \frac{\partial \chi_i}{\partial \bar{\kappa}} \right)$$

$$(48)$$

$$u_{\theta i} = i \left(e^{i\Theta} \frac{\partial \phi_i}{\partial \kappa} - e^{-i\Theta} \frac{\partial \phi_i}{\partial \bar{\kappa}} \right) - \left(e^{i\Theta} \frac{\partial \psi_i}{\partial \kappa} + e^{-i\Theta} \frac{\partial \psi_i}{\partial \bar{\kappa}} \right)$$
$$+ \frac{-k_x}{k_{si}} \left(e^{i\Theta} \frac{\partial \chi_i}{\partial \kappa} - e^{-i\Theta} \frac{\partial \chi_i}{\partial \bar{\kappa}} \right)$$

$$(49)$$

$$u_{xi} = ik_x \phi_i + \frac{k_{\beta i}^2}{k_{si}} \chi_i$$

$$(50)$$

$$\sigma_{rri} = -\lambda_i k_x^2 \phi_i - (\lambda_i + \mu_i) k_{\alpha i}^2 \phi_i + 2\mu_i \left(e^{2i\Theta} \frac{\partial^2 \phi_i}{\partial \kappa^2} + e^{-2i\Theta} \frac{\partial^2 \phi_i}{\partial \bar{\kappa}^2} \right) - \frac{i\mu_i k_x k_{\beta i}^2}{k_{si}} \chi_i$$

$$+ 2i\mu_i \left(e^{2i\Theta} \frac{\partial^2 \psi_i}{\partial \kappa^2} - e^{-2i\Theta} \frac{\partial^2 \psi_i}{\partial \bar{\kappa}^2} \right) + \frac{2i\mu_i k_x}{k_{si}} \left(e^{2i\Theta} \frac{\partial^2 \chi_i}{\partial \kappa^2} + e^{-2i\Theta} \frac{\partial^2 \chi_i}{\partial \bar{\kappa}^2} \right)$$

$$(51)$$

$$\sigma_{r\theta i} = 2i\mu_i \left(e^{2i\Theta} \frac{\partial^2 \phi_i}{\partial \kappa^2} - e^{-2i\Theta} \frac{\partial^2 \phi_i}{\partial \bar{\kappa}^2} \right) - 2\mu_i \left(e^{2i\Theta} \frac{\partial^2 \psi_i}{\partial \kappa^2} + e^{-2i\Theta} \frac{\partial^2 \psi_i}{\partial \bar{\kappa}^2} \right)$$

$$- \frac{2\mu_i k_x}{k_{si}} \left(e^{2i\Theta} \frac{\partial^2 \chi_i}{\partial \kappa^2} - e^{-2i\Theta} \frac{\partial^2 \chi_i}{\partial \bar{\kappa}^2} \right)$$

$$(52)$$

$$\sigma_{rxi} = 2i\mu_i k_x \left(e^{i\Theta} \frac{\partial \phi_i}{\partial \kappa} + e^{-i\Theta} \frac{\partial \phi_i}{\partial \bar{\kappa}} \right) - \mu_i k_x \left(e^{i\Theta} \frac{\partial \psi_i}{\partial \kappa} - e^{-i\Theta} \frac{\partial \psi_i}{\partial \bar{\kappa}} \right)$$

$$+ \frac{\mu_i \left(k_{si}^2 - 2k_x^2 \right)}{k_{si}} \left(e^{i\Theta} \frac{\partial \chi_i}{\partial \kappa} + e^{-i\Theta} \frac{\partial \chi_i}{\partial \bar{\kappa}} \right)$$

$$(53)$$

$$\sigma_{\theta\theta i} = -\lambda_i k_x^2 \phi_i - (\lambda_i + \mu_i) k_{\alpha i}^2 \phi_i - 2\mu_i \left(e^{2i\Theta} \frac{\partial^2 \phi_i}{\partial \kappa^2} + e^{-2i\Theta} \frac{\partial^2 \phi_i}{\partial \bar{\kappa}^2} \right) - \frac{i\mu_i k_x k_{\beta i}^2}{k_{si}} \chi_i$$

$$- 2i\mu_i \left(e^{2i\Theta} \frac{\partial^2 \psi_i}{\partial \kappa^2} - e^{-2i\Theta} \frac{\partial^2 \psi_i}{\partial \bar{\kappa}^2} \right) - \frac{2i\mu_i k_x}{k_{si}} \left(e^{2i\Theta} \frac{\partial^2 \chi_i}{\partial \kappa^2} + e^{-2i\Theta} \frac{\partial^2 \chi_i}{\partial \bar{\kappa}^2} \right)$$

$$(54)$$

$$\sigma_{\theta x i} = -2\mu_i k_x \left(e^{i\Theta} \frac{\partial \phi_i}{\partial \kappa} - e^{-i\Theta} \frac{\partial \phi_i}{\partial \bar{\kappa}} \right) - i\mu_i k_x \left(e^{i\Theta} \frac{\partial \psi_i}{\partial \kappa} + e^{-i\Theta} \frac{\partial \psi_i}{\partial \bar{\kappa}} \right)$$

$$+ \frac{i\mu_i \left(k_{si}^2 - 2k_x^2 \right)}{k_{si}} \left(e^{i\Theta} \frac{\partial \chi_i}{\partial \kappa} - e^{-i\Theta} \frac{\partial \chi_i}{\partial \bar{\kappa}} \right)$$

$$(55)$$

Conformal Mapping

The problem under consideration is complicated by the fact that the half-space and the tunnel surfaces possess different symmetries. In order to circumvent this difficulty, the physical domain is mapped onto an auxiliary domain represented by a complex variable $\zeta = \xi + i\eta = \rho e^{i\theta}$ and its conjugate $\bar{\zeta} = \xi - i\eta = \rho e^{-i\theta}$. We search for two mapping functions to map the two regions Ω_1 and Ω_2 in the physical domain (as shown in Fig. 1) onto regions Γ_1 and Γ_2 in the image domain (as shown in Fig. 2), respectively, and make the two regions in the image domain possess the same symmetry and be concentric.

The transformation of the region Ω_1 in the physical domain into the region Γ_1 in the image domain is accomplished by the mapping function [16]

Fig. 2 Image domain
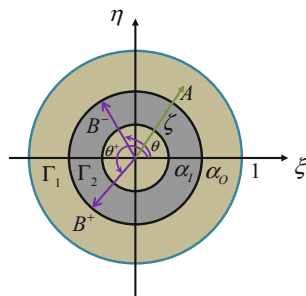
$$\kappa_1 = w_1(\zeta) = -iT\frac{1+\zeta}{1-\zeta} \tag{56}$$

where $T = h(1 - \alpha_O^2)/(1 + \alpha_O^2)$, $\alpha_O = h/R_O - \sqrt{(h/R_O)^2 - 1}$. The half-space surface and the outer surface of the tunnel in the physical domain correspond to the circles $|\zeta| = 1$ and $|\zeta| = \alpha_O$ in the image domain, respectively.

The second mapping function determines a transformation of the region Ω_2 into the region Γ_2:

$$\kappa_2 = w_2(\zeta) = -ih + \frac{R_O}{\alpha_O}\zeta \tag{57}$$

The outer and inner surfaces of the tunnel in the physical domain correspond to the circles $|\zeta| = \alpha_O$ and $|\zeta| = \alpha_I = R_I\alpha_O/R_O$ in the image domain, respectively.

The relation between the angle Θ in the physical domain and the polar angle θ in the image domain is written as [17]

$$\exp(i\Theta) = \frac{\zeta}{\rho}\frac{w'(\zeta)}{|w'(\zeta)|} \tag{58}$$

It can be shown that the mapping functions $w_1(\zeta)$ and $w_2(\zeta)$ are analytic and their derivatives $w_1'(\zeta)$ and $w_2'(\zeta)$ are not zero in the regions Γ_1 and Γ_2, which ensures the transformation be conformal, reversible and single-valued in each domain.

Using conformal mapping functions $w_1(\zeta)$ and $w_2(\zeta)$, a point B at the outer surface of the tunnel in the physical domain (see Fig. 1) is mapped to two different points B^+ and B^- in the image domain (as shown in Fig. 2), respectively. When we apply the continuity conditions at the soil-tunnel interface, we have to consider this discontinuous relation at $|\zeta| = \alpha_O$ in the image domain. Let θ^+ and θ denote the angles between the vectors $\overrightarrow{OB^+}$ and $\overrightarrow{OB^-}$, and the horizontal axis in the image plane, respectively. The relation between these two angles is given as

$$\theta^+(\theta) = \arg\left[\frac{iR_O e^{i\theta} + h - T}{iR_O e^{i\theta} + h + T}\right] \tag{59}$$

Derivation of the Unknown Coefficients Using Boundary Conditions

The traction-free boundary conditions at the half-space surface and at the inner surface of the tunnel, and the continuity conditions of the tractions and displacements at the soil-tunnel interface lead to a linear system of equations in terms of the unknown coefficients.

Based on the relation between the complex variables κ and ζ defined by the conformal mapping functions (Eqs. 56–57), the wave potentials and the expressions for the displacements and stresses can be derived in terms of the complex variables ζ and $\bar{\zeta}$. The expressions are not given in this paper for brevity, they are similar to those presented in the papers on the two-dimensional problems [10, 11]. The derivatives of the cylindrical wave potentials with respect to the complex variables are given by Liu et al. in [18]. Substituting Eqs. (31)–(36) into Eqs. (45)–(53) and taking into account the formulated boundary conditions (14)–(17) we obtain a set of algebraic equations in terms of the complex variables κ and $\bar{\kappa}$. Finally, using the mapping functions (Eqs. 56–57), a set of algebraic equations in terms of the complex variables ζ and $\bar{\zeta}$ can be formulated as

$$\sum_{i=1}^{12} \sum_{n=-\infty}^{\infty} K_n^{(ij)} X_n^{(i)} = R^{(j)}, \quad (j = 1, \ldots, 12) \tag{60}$$

where $X_n^{(1)} = a_n$, $X_n^{(2)} = b_n$, $X_n^{(3)} = c_n$, $X_n^{(4)} = d_n$, $X_n^{(5)} = e_n$, $X_n^{(6)} = f_n$, $X_n^{(7)} = g_n$, $X_n^{(8)} = h_n$, $X_n^{(9)} = i_n$, $X_n^{(10)} = j_n$, $X_n^{(11)} = k_n$, $X_n^{(12)} = l_n$; each i and j correspond to an unknown coefficient and a boundary condition, respectively. $j = 1, 2, 3$ refer to the traction-free boundary conditions at the half-space surface, $j = 4, 5, 6$ refer to the traction-free boundary conditions at the inner surface of the tunnel, $j = 7, 8, 9$ and $j = 10, 11, 12$ refer to the traction and displacement continuity conditions at the soil-tunnel interface, respectively. $K_n^{(ij)}$ and $R^{(j)}$ are functions of the complex variables ζ and $\bar{\zeta}$; they are not given in this paper for brevity. For the set of algebraic equations $(j = 7 - 12)$ formulated based on the continuity conditions, all the tractions and displacements related to soil medium, namely, σ_{rr1}, $\sigma_{r\theta1}$, σ_{rx1}, u_{r1}, $u_{\theta1}$ and u_{x1}, are functions of θ^+ while those related to the tunnel are all functions of θ.

It is obvious that $K_n^{(ij)}$ and $R^{(j)}$ are functions of θ in the image domain. Multiplying both sides of Eq. (60) by a weighting function $\exp(-is\theta)$ and integrating over the interval $[0, 2\pi]$, we obtain:

$$\sum_{i=1}^{12} \sum_{n=-\infty}^{\infty} K_n^{(ijs)} X_n^{(i)} = R^{(js)}, \quad (j = 1, \ldots, 12; \; s = 0, \pm 1, \pm 2, \ldots) \qquad (61)$$

where $K_n^{(ijs)} = \int_0^{2\pi} K_n^{(ij)} \exp(-is\theta) d\theta/(2\pi)$ and $R_n^{(js)} = \int_0^{2\pi} R_n^{(j)} \exp(-is\theta) d\theta/(2\pi)$.

To compute the unknown coefficients, the summation over circumferential modes is truncated. When we use the same modes N for both the waves scattered by the tunnel and the secondary reflected waves, we use the weighting function:

$$\exp(-is\theta), \quad (j = 1, \ldots, 12; \; s = 0, \pm 1, \pm 2, \ldots, \pm N) \qquad (62)$$

When we use N modes for the directly scattered waves by the tunnel and M modes for the secondary reflected waves, in order to formulate a square matrix, Eq. (60) are multiplied by different weighting functions, according to

$$\begin{aligned} \exp(-is_I\theta), \quad (j = 1, \ldots, 3; \; s_I = 0, \pm 1, \pm 2, \ldots, \pm M) \\ \exp(-is\theta), \quad (j = 4, \ldots, 12; \; s = 0, \pm 1, \pm 2, \ldots, \pm N) \end{aligned} \qquad (63)$$

Convergence Tests, Validations and Numerical Analysis

In this paper, a stiff soil medium and a concrete tunnel are considered. The stiff soil medium has a modulus of elasticity $E_1 = 7.567 \cdot 10^9$ N/m^2, Poisson's ratio $v_1 = 0.333$ and mass density $\rho_1 = 2.664 \cdot 10^3$ kg/m^3, while for the concrete tunnel $E_2 = 1.6 \cdot 10^{10}$ N/m^2, $v_2 = 0.2$ and $\rho_2 = 2.24 \cdot 10^3$ kg/m^3. A dimensionless frequency is defined as $\varpi = \omega R_O/\pi c_{s1}$. The normalized displacement vector and the stress tensor are given by $\mathbf{U} = \mathbf{u}/u_0$ and $\boldsymbol{\Sigma} = \boldsymbol{\sigma}/(\omega \rho_1 c_{s1} u_0)$, where u_0 denotes the displacement amplitude of the incident wave.

When the incident harmonic wave propagates in the direction perpendicular to the axis of the tunnel, the problem reduces to a two-dimensional one. Figure 3 depicts various convergence tests for a two-dimensional wave scattering problem of a half-space with a cavity (limiting case of the half-space with just a cylindrical cavity of the same radius as the outer radius of the tunnel) under a relatively high excitation frequency of $\varpi = 0.5$ ($f = 51$ Hz). Figure 3a–c show that, considering $N = 6$ for the directly scattered waves by the cavity, 3 and 9 modes for the second reflected waves are needed to get the hoop stress ($\Sigma_{\theta\theta}$) at the cavity surface and the ground surface motions (U_y, U_z) to converge, respectively. Figure 3d–f show that, considering $M = 9$ for the secondary reflected waves, 5 and 2 modes for the waves directly scattered by the cavity are needed to get the hoop stress and the ground surface motions to converge, respectively. Therefore, 5 modes for the directly scattered waves by the cavity and 9 modes for the secondary reflected waves are enough to represent the wave fields in the half-space due to presence of the cavity under the high-frequency excitation of $\varpi = 0.5$.
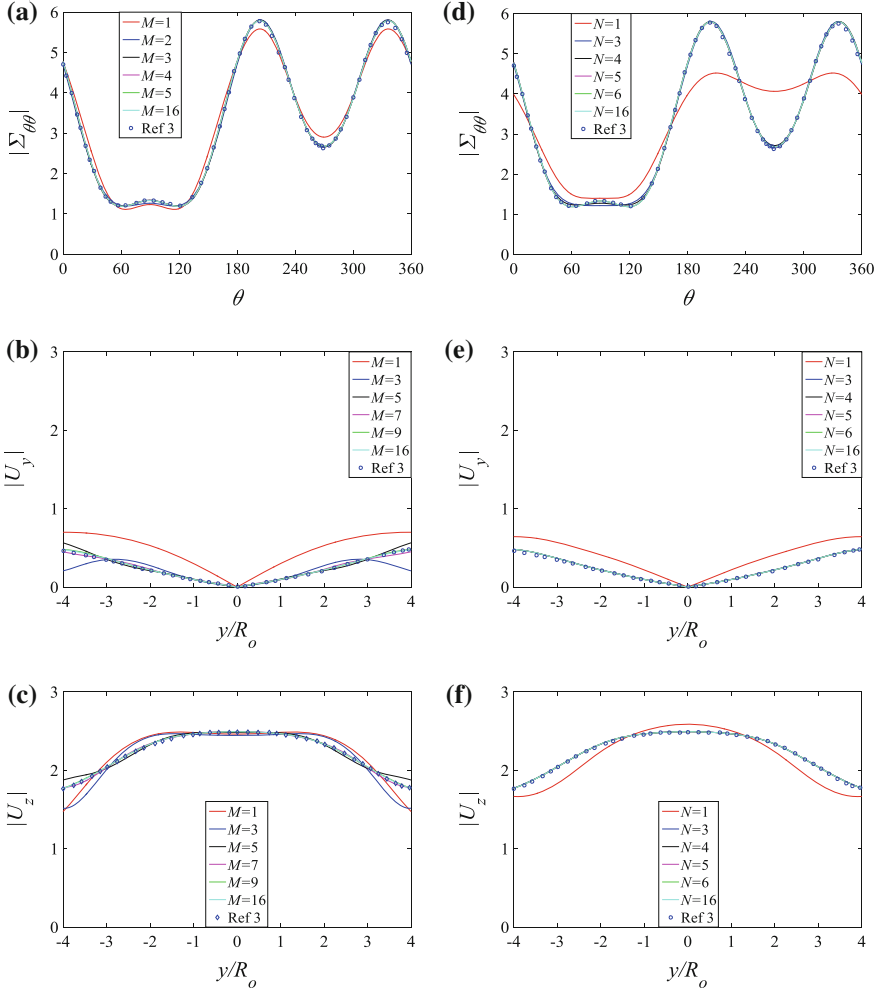
Fig. 3 Two-dimensional case convergence tests and validations: **a–c** Modes M for the secondary reflected waves with $N = 6$; **d–f** Modes N for the directly scattered waves by the cavity with $M = 9$; (**a**), (**d**) Normalized hoop stress at $r = R_o$; (**b**), (**e**) Normalized horizontal displacement at $z = 0$; (**c**), (**f**) Normalized vertical displacement at $z = 0$; $\theta_v = 0$, $\theta_h = 90$, $h/R_o = 5$, $\varpi = 0.5$

Figure 4 depicts various convergence tests of a three-dimensional wave scattering problem of a tunnel embedded in the half-space under a low-frequency excitation of $\varpi = 0.105$ ($f = 10.8$ Hz). Figure 4a–c show that for the secondary reflected waves with $N = 3$, 3 modes are needed to get convergence for the hoop stress and the motion at the tunnel surface, as well as for the ground surface motion.
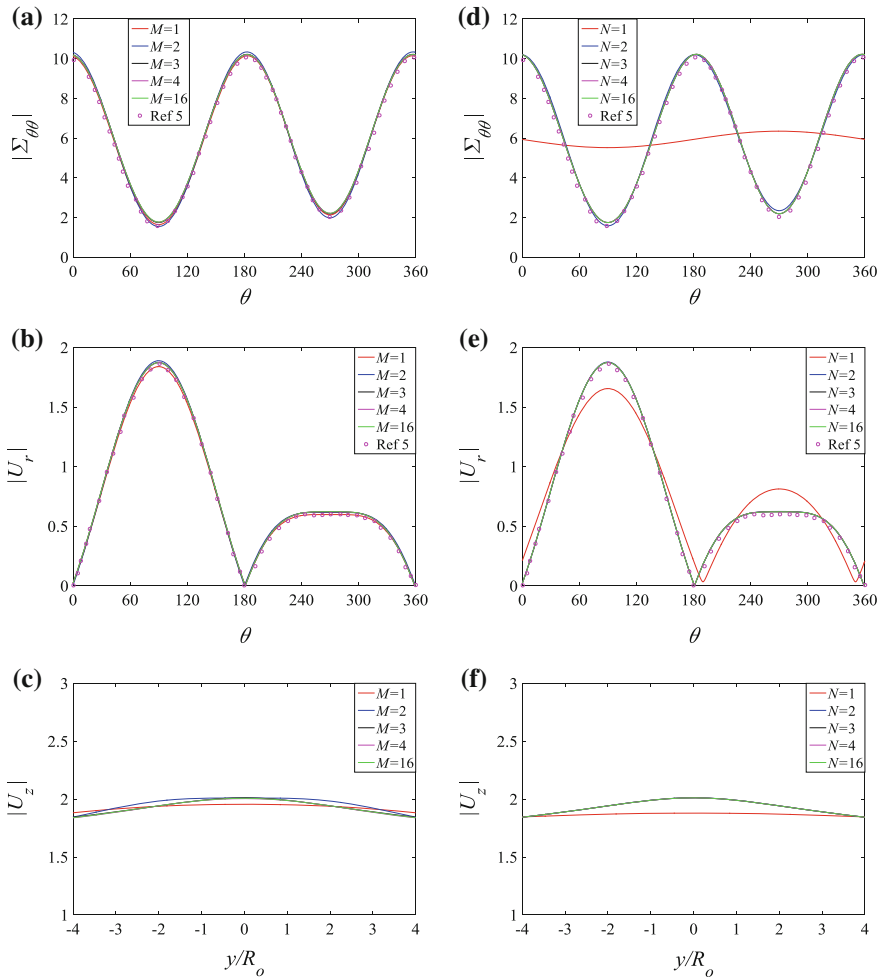
Fig. 4 Three-dimensional case convergence tests and validations: **a–c** Modes M for the secondary reflected waves with $N = 3$; **d–e** Modes N for the directly scattered waves by the cavity with $M = 3$; (**a**), (**d**) Normalized hoop stress at $r = R_C$; (**b**), (**e**) Normalized radial displacement at $r = R_O$; (**c**), (**f**) Normalized vertical displacement at $z = 0$; $\theta_v = 30$, $\theta_h = 0$, $h = 5R_i = 4.545R_o$, $\varpi = 0.105$

Figure 4d–f show that for the waves directly scattered by the tunnel with $M = 3$, 3 modes are needed to get convergence for the hoop stress, while 2 modes are needed to get the convergence for the motions at both the tunnel and half-space surfaces. Therefore, 3 modes for both the directly scattered waves and the secondary reflected waves are sufficient to accurately represent the wave fields in the system under the low-frequency excitation of $\varpi = 0.105$.

As shown in Figs. 3 and 4, the results are in good agreement with those pre-
sented by Luco and De Barros [3] for the two-dimensional case and by De Barros
and Luco [4, 5] for the three-dimensional case, which confirms the accuracy of the
proposed method. There are some benefits of using different numbers of circum-
ferential modes for the waves directly scattered by the tunnel and for the secondary
reflected waves compared with the case of using the same number of modes for
both waves as done in [10, 11]. The size and condition number of the coefficient
matrix in Eq. (61) become smaller and the computational time is reduced. It is also
helpful to understand that under low-frequency excitation only a few modes are
needed to model the cylindrical waves fields due to presence of the tunnel, while
under high-frequency excitation we need more modes to model the secondary
reflected waves. In addition, the waves directly scattered by the tunnel affect the
satisfaction of the boundary conditions and responses at the tunnel surfaces and
barely affect those at the half-space surface. Correspondingly, the secondary
reflected waves contribute to the satisfaction of the boundary conditions and
responses at the half-space surface and barely contribute to those at the tunnel
surfaces. The reason for this phenomenon is the geometrical attenuation of the
cylindrical waves. Obviously, the wave potentials have stronger contributions in the
near field compared with the far field.

Figure 5a shows the hoop stresses at the soil-tunnel interface from the soil side
$(r = R_O)$ for the two- and three-dimensional cases with cavity and tunnel.
Figure 5b shows the hoop stresses on the centreline of the tunnel $(r = R_C)$ for the
two- and three-dimensional cases with tunnel. It is observed that the distributions of
the hoop stress in each case are similar, though the magnitudes are quite different.
Additionally, the hoop stresses in the two-dimensional cases are larger than those in
the three-dimensional cases, and the hoop stresses in the cavity cases are larger than
those in the tunnel cases. Furthermore, the hoop stress in the three-dimensional
cavity case is greater than that in the two-dimensional tunnel case. The hoop stress
at the soil-tunnel interface from the soil side is reduced mainly due to the fact that
the waves also propagate in the longitudinal direction of the structure and also due
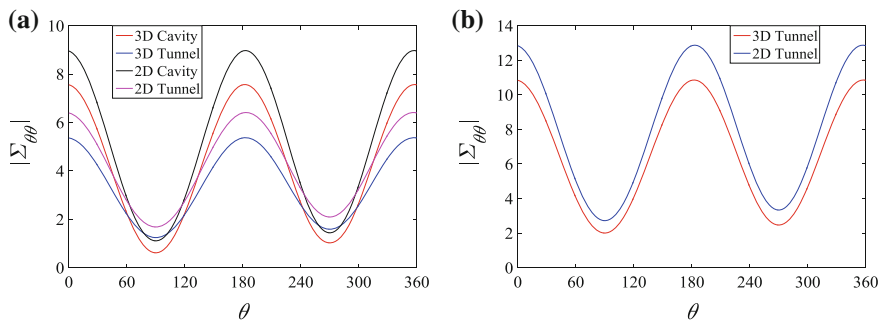
Fig. 5 **a** Normalized hoop stress at $r = R_O$; **b** Normalized hoop stress at $r = R_C$; $N = M = 4$,
$h = 5R_O$, $\varpi = 0.105$, 2D case $(\theta_v = 0, \theta_h = 90)$, 3D case $(\theta_v = 30, \theta_v = 30)$
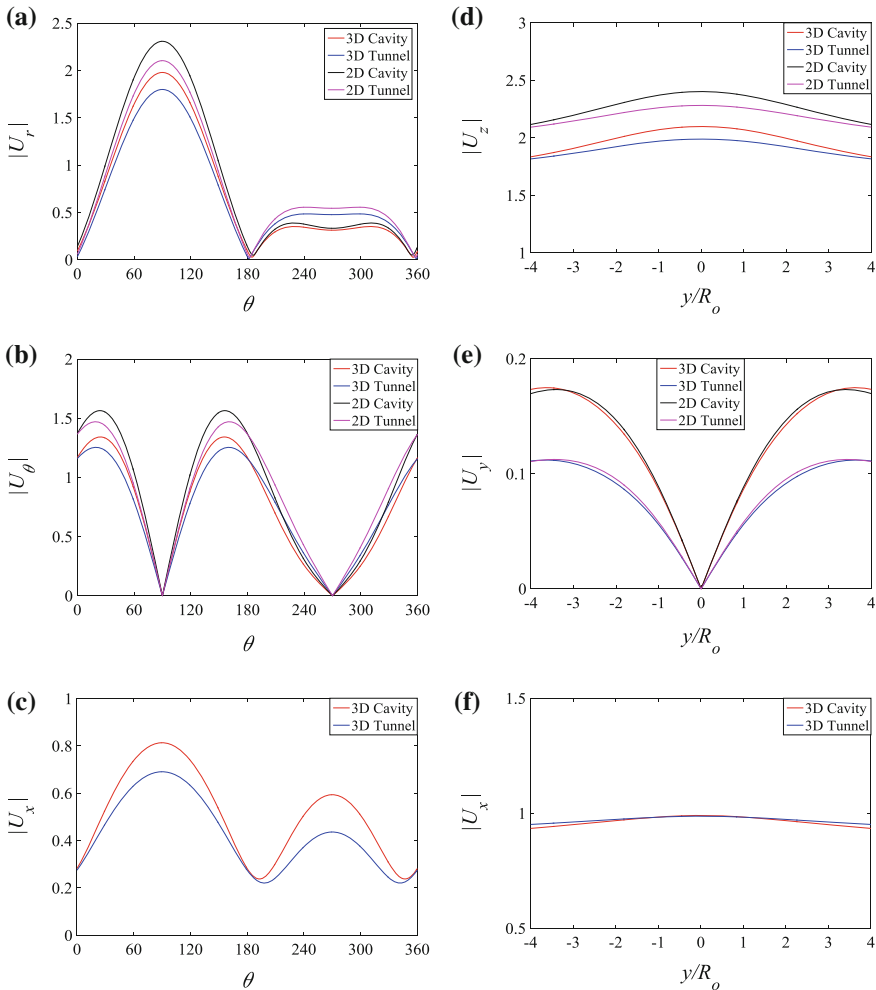
Fig. 6 **a–c** Normalized displacements at $r = R_O$; **d–f** Normalized displacements at $z = 0$; $N = M = 4$, $h = 5R_O$, $\varpi = 0.105$, 2D case $(\theta_v = 0, \theta_h = 90)$, 3D case $(\theta_v = 30, \theta_h = 0)$

to the presence of the scattered waves in the tunnel, both taking away energy. For the two- and three-dimensional cases, we observe that the hoop stress on the centre line of the tunnel are larger than that at the soil-tunnel interface from the soil side.

Figure 6a–c and d–f show the motions at $r = R_O$ and $z = 0$ for all cases. We observe the same trend for the normal and tangential displacements at $r = R_O$ and vertical displacements at $z = 0$ as for the hoop stress, but the motions in the two-dimensional tunnel case are greater than those in the three-dimensional cavity case. The horizontal displacements at $z = 0$ are smaller compared with the vertical

and x axial displacements. That is because the horizontal motions are barely excited under nearly vertically incident wave.

Conclusions

A semi-analytical method was presented for the theoretical analysis of two- and three-dimensional seismic responses of a tunnel embedded in an elastic half-space. The complex variable theory, conformal mapping and the spirit of the image technique were applied to solve the problem. The results obtained using the proposed method for both the two- and three-dimensional cases are in good agreement with those obtained by the other methods, which confirms the accuracy of the proposed method. This paper also evaluates the contribution of the wave field directly scattered by the tunnel and the secondary reflected wave field on the satisfaction of the boundary conditions at the half-space surface and at the soil-tunnel interface. It was shown that the waves directly scattered by the tunnel affect the satisfaction of the boundary conditions and responses at the soil-tunnel interface and barely affect those at the half-space surface. Correspondingly, the secondary reflected waves contribute to the satisfaction of the boundary conditions and responses at the half-space surface and barely contribute to those at the soil-tunnel interface. The investigation of the effects of the dimension and the presence of the tunnel on the system response showed that the additional dimension and the presence of the tunnel reduce the hoop stress at the interface form the soil side. If the design of the underground structure is based on a simple two-dimensional cavity model, it would be a conservative design according to our analysis.

The advantages of the proposed method are as follows. First, it is a semi-analytical solution of the problem which reveals that the directly scattered waves and the secondary reflected waves contribute to the system response differently. Secondly, the traction-free boundary conditions are in principle satisfied at the entire half-space surface without truncating at a certain distance from the tunnel. Thirdly, when compared with numerical methods, the computational time is significantly reduced. Furthermore, the solution in the half-space can be combined with a finite-element representation for embedded structures that are complex in shape.

The disadvantage of the proposed method is that the matrix used to determine the unknown coefficients of the cylindrical waves becomes ill-conditioned when we consider very high-frequency excitation, very large shear modulus ratio of the tunnel to the medium and very small depth ratio of the embedded depth to the radius of the tunnel. Correspondingly, the far-field boundary conditions at the half-space surface cannot be satisfied exactly due to some numerical issues, even though the boundary conditions are supposed to be satisfied exactly. Other techniques or a hybrid method will be investigated in the future to overcome this problem.

References

1. Ariman, J., Muleski, G. E. (1981). A review of the response of buried pipelines under seismic excitations, Earthquake Engineering and Structure Dynamics, 9: 133–151.
2. Stamos, A. A., Beskos, D. E. (1995). Dynamic analysis of large 3-D underground structures by the BEM, Earthquake Engineering and Structural Dynamics, 24: 917–934.
3. Luco J. E., De Barros F. C. P. (1994). Dynamic displacements and stresses in the vicinity of a cylindrical cavity embedded in a half-space, Earthquake Engineering and Structural Dynamics, 23: 321–340.
4. Luco, J. E., De Barros, F. C. P. (1994). Seismic response of a cylindrical shell embedded in a layered viscoelastic half-space. I: Formulation, Earthquake Engineering and Structural Dynamics, 23: 553–567.
5. De Barros, F. C. P., Luco, J. E. (1994). Seismic response of a cylindrical shell embedded in a layered viscoelastic half-space. II: Validation and numerical results. Earthquake Engineering and Structural Dynamics, 23: 569–580.
6. Wong, K. C., Datta, S. K., Shah, A. H. (1986). Three-dimensional motion of buried pipeline. II: Numerical results, Journal of Engineering Mechanics, 112: 1338–1345.
7. Liu, S. W., Datta, S. K., Khair, K. R. (1991). Three dimensional dynamics of pipelines buried in backfilled trenches due to oblique incidence of body wave, Soil Dynamics and Earthquake Engineering, 10: 182–191.
8. Datta S. K., Shah A. H., Wong K. C. (1984). Dynamic stresses and displacements in buried pipe, Journal of Engineering Mechanics, 110 (10): 1451–4166.
9. Balendra T., Thambiratnam D. P., Koh C. G., Lee S. -L. (1984). Dynamic response of twin circular tunnels due to incident SH-waves, Earthquake Engineering and Structural Dynamics, 12: 181–201.
10. Liu, Q., Zhao, M., Wang, L. (2013). Scattering of plane P, SV or Rayleigh waves by a shallow lined tunnel in an elastic half space, Soil Dynamics and Earthquake Engineering, 49: 52–63.
11. Liu, Q., Zhao, M., Zhang, C. (2014). Antiplane scattering of SH waves by a circular cavity in an exponentially graded half space, International Journal of Engineering Science, 78: 61–72.
12. Gregory R. D. (1967). An expansion theorem applicable to problems of wave propagation in an elastic half-space containing a cavity, Mathematical Proceedings of the Cambridge Philosophical Society, 63 (4): 1341–1367.
13. Kausel E. (2006). Fundamental Solution in Elastodynamics: A Compendium, Cambridge University Press, UK.
14. Aki K., Richards P. (2002). Quantitative Seismology, University Science Books, Sausalito, California.
15. Graff, K. F. (1975). Wave Motion in Elastic Solids, Courier Corporation.
16. Verruijt A. (1998). Deformations of an elastic half plane with a circular cavity, International Journal of Solids and Structures, 35: 2795–2804.
17. Muskhelishvili NI. (1966). Some Basic Problems of the Mathematical Theory of Elasticity, Cambridge University Press.
18. Liu D. K., Gai B., Tao G. (1982). Application of the method of complex functions to dynamic stress concentrations, Wave Motion, 4: 293–304.

Evaluation of Environmental Vibration in the Surrounding Building Caused by the Punching Machine

Pengfei Zuo, Liangming Sun and Weiping Xie

Introduction

The punching machine is widely used in machinery manufacturing and metal processing industry, such as punching machine tool, punching and shearing machine etc. In the process of operation, a large part of the impact energy will be transformed into elastic wave which propagates in the soil, and it will cause ground vibration. When the vibration exceeds a certain limit [1], it adversely affects the surrounding environment. Especially the floor stiffness of the near building is relatively small. Strong ground vibration will interfere with the normal work of the staff in surrounding buildings, causing vibration comfort problem [2]. In recent years, the adverse environmental problem caused by punching machine has caused the attention of the engineering and relevant departments. The problem how to accurately define the safety distance of the impact to the surrounding has to be solved. Therefore, we should control the punching production in the safe distance or take the corresponding vibration reduction measures.

Over the years, the domestic and foreign scholars carry out relevant research about the vibration caused by punching production and dynamic compaction. For example, Shang et al. [3] study the damage to nearby buildings and put forward the

P. Zuo · L. Sun · W. Xie (✉)
School of Civil Engineering and Architecture,
Wuhan University of Technology, Wuhan 430070, China
e-mail: wpxie@sina.com

P. Zuo
e-mail: 17239634@qq.com

L. Sun
e-mail: sunliangming@126.com

corresponding measures of vibration reduction; Meng et al. [4] carry out the model test of impact vibration on the surrounding environment; Hwang et al. [5] analyses that isolation ditch has influence on the attenuating amplitude of impact vibration with distance. Although the above scholars have made remarkable achievements in the influence of vibration on the surrounding, the vibration law for the punching production and mitigation measures, but their quantitative evaluation and research on the surrounding is not much. With the improvement of our life, legal and safety consciousness strengthen constantly, and vibration problem has been controversial. Therefore, this problem has become an important reason for the civil disputes caused by punching production. Since the punching machine in Dongfeng Die & Punching Technology Co., Ltd. (D.D.T.C.) lead to obvious vibration of a light steel structure workshop of other company, the vibration evaluation is carried out to investigate the vibration comfort of surrounding buildings.

Test Profile

The punching machine (Fig. 1) of the D.D.T.C. is mainly used for the automatic production of medium-sized punching part, and the nominal force of the sliding block reaches 31,000 kN. It is not directly placed on the ground floor, but the use of

Fig. 1 The punching machine

Table 1 Limit value of vertical vibration of environment vibration (dB) [7]

Vibration environment function category		Limit value of vertical vibration	
		Day	Night
0		65	65
1		70	65
2		75	70
3		75	70
4	4a	75	70
	4b	80	80

Note the 3 kinds of function areas refers to industrial production, warehousing and logistics as the main function, need to prevent industrial vibration sources
Day: 06:00–22:00; night: 22:00–06:00

a separate pile foundation. A three-floor of light steel structure building is about 75 m far from the punching machine. There are many staffs in the workshop, and the operation is mainly in a sitting position which is more sensitive to vibration compared to the standing posture [6], so it requires a higher degree of comfort. Therefore, it is necessary to study the dynamic response caused by the operation of punching machine and evaluate the comfort status.

Two sets of equipment is mainly used in field test, a Danish B&K 3050-B-060 civil engineering vibration and noise test system, a set of SPC-51 vibration data collection instrument produced by Tokyo Sokushin. Comfort evaluation performs the relevant provisions of GB50894-2013 [7]. The threshold values are shown in Table 1. Environmental vibration monitoring performs the relevant provisions including GB10070-1988 [8] and GB10071-1988 [9].

Test Scheme

Vibration Source Intensity Test of Punching Machine

The layout diagram of measure point for the vibration source intensity test of punching machine is shown in Fig. 2. Measure point 1# is located in the pillar on the basis of punching machine. Three sensors are arranged to test the acceleration responses for three directions. The site measure point is shown in Fig. 3.

Fig. 2 The layout diagram of measure point for the vibration source
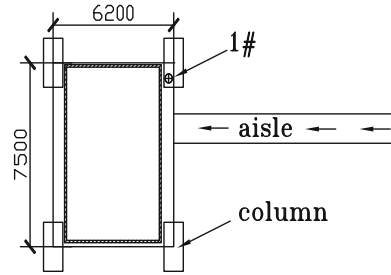
Fig. 3 The site measure point of vibration source in the scene

Arrangement of Measuring Points in Evaluation of Vibration Comfort

The layout diagram of measure points for the surround building near the window for vibration comfort evaluation is shown in Fig. 4. Four sensors were arranged to test vertical acceleration responses. Measure point 1# is located within 0.5 m on the ground outside the window of workshop which is the shortest straight-line distance away from punching machine. Measure points 2# and 3# are located in the second floor of working area and the floor near the window of toilet. Measure point 4# is located at the third floor near the window. Measure points 2#, 3# and 4# are vibration-sensitive positions reflected by the staffs and also are the nearest distance from the punching machine. The site measure points are shown in Fig. 5.

According to above test results, the vibration response of the third floor of the light steel structure is relatively large, so the vibration response at the hallway is collected on third and first floors to compare and analyze. The layout diagram of measure point of vibration comfort evaluation at the center of third floor is shown in Fig. 6. The measure point of the first floor is the same as those of the third floor. The site measure point is shown in Fig. 7.
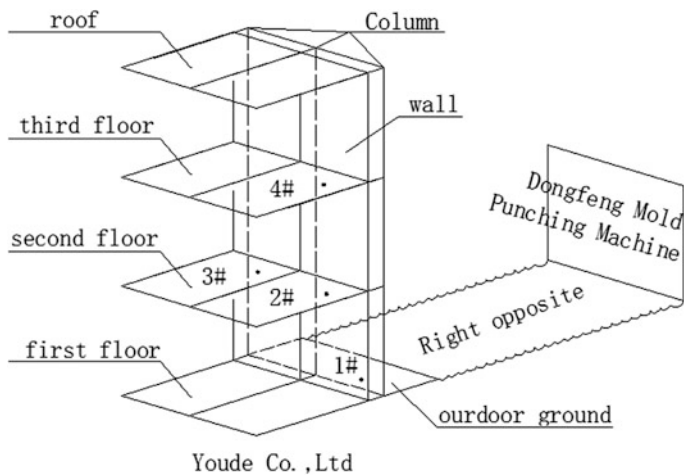
Fig. 4 The layout diagram of measure points for the surrounding building

Fig. 5 The site measure point of surrounding building in the scene

Fig. 6 The layout diagram of measure point at the central floor
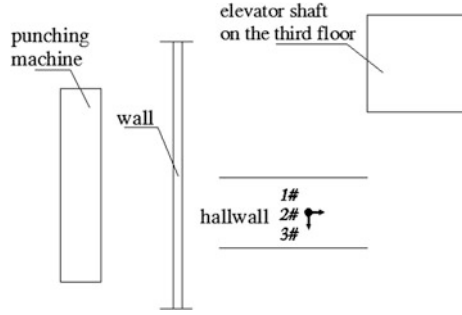
Fig. 7 The site measure point at the central floor in the scene

Result Analysis

Vibration Intensity of Punching Machine

Measure point 1# collected multiple sets of data. The typical vertical acceleration time history and Fourier spectrum are shown in Fig. 8. It is indicated that the maximum value is 18.41 gal for the vibration intensity of punching machine. The vertical peak on the base column is larger than that on the ground because the vibration caused by the punching machine passed to the foundation through four pillars, and the ground of the foundation and the pillars are separate.

Vibration Comfort Evaluation

The VL_Z of the surrounding building near the window is listed in Table 2. It is indicated that the vibration responses of building increase with the increase of the floor. The vibration response of third floor is the largest. Its VL_Z is 76.12 dB which
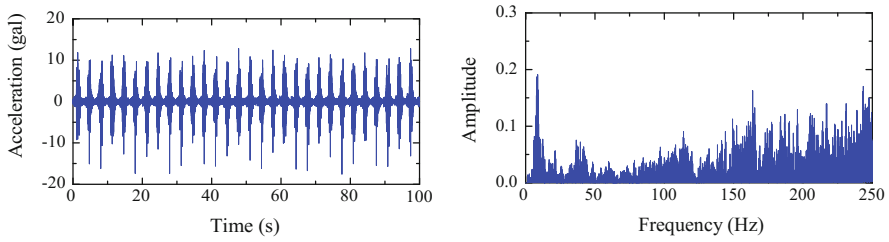
Fig. 8 Typical vertical acceleration time history and Fourier spectrum

Table 2 VL$_Z$ of the surrounding building near the window (dB)

Test group		1	2	3	4	5	Threshold	Max. value
Outdoor ground		70.25	70.00	70.55	70.12	70.10	75	70.55
Second floor	Windows	75.17	75.14	75.48	75.14	75.12	75	75.48
	Toilet	73.24	73.29	73.69	73.31	73.30	75	73.69
Third floor		75.90	76.12	76.08	75.66	75.70	75	76.12
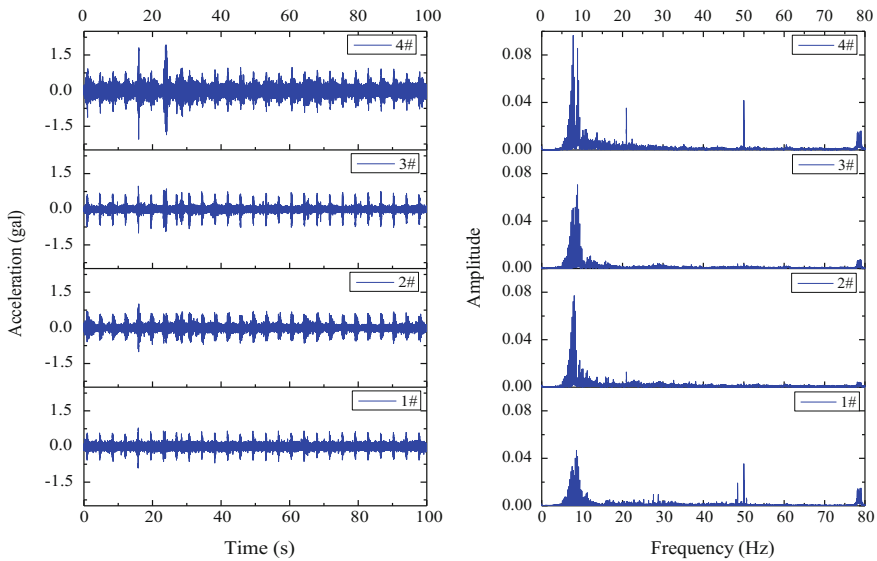
Fig. 9 Typical vertical acceleration time history and Fourier spectrum

exceeds the threshold of 75 dB in GB50894-2013. Their typical vertical accelera-
tion time history and Fourier spectrum are shown in Fig. 9. It is shown that the
frequency components of vibration responses for the workshop structure are mainly
focused on 6–12 Hz.

Table 3 VL$_Z$ of the central floor for surrounding building (dB)

Test group	1	2	3	4	5	Threshold	Max. value
First floor	70.47	70.39	70.17	70.45	70.40	75	70.47
Third floor	84.39	82.88	83.39	82.87	83.32	75	84.39

The VL$_Z$ of the central floor for the first and third floors is shown in Table 3. It is shown that the vibration response on the third floor is significantly larger than that on the first floor. Because the measure point is located at the center of the third floor which of the span is larger, it will cause the resonance response of the structure. The VL$_Z$ is 84.39 dB, exceeding the threshold of 75 dB in GB 50894-2013. The difference in the specification is that the main evaluation index adopts the VL$_Z$ of the first floor in the building which does not exceed the threshold, but the VL$_Z$ of the third floor exceeds seriously the threshold and causes comfort problem. The frequency components of the vibration response of the central floor are also focused on 6–12 Hz and the maximum vibration amplitude is at 7.85 Hz.

Conclusion

The environmental vibration evaluation in the surrounding building caused by the punching machine is carried out by field test. Test results show that the VL$_Z$ at the outdoor 0.5 m of a three-story lightweight steel construction which is 75 m from the punch machine is 70.55 dB. The VL$_Z$ of the first indoor ground is 70.47 dB, that of the second floor is 75.48 dB, and the third floor is 84.39 dB. The VL$_Z$ of outdoor and first indoor ground do not exceed the threshold, while the VL$_Z$ of the second and third floors exceed the threshold. It may cause the uncomfortable problem for the staffs in the light steel structure building due to the operation punching machine. Therefore, it is necessary to take measure to reduce the vibration to meet the requirement of environmental vibration.

References

1. Sun, P.M., Chen, S.Q. (2012). Research and development of the disc spring buffer of the punching machine. Mechanical & Electrical Engineering Technology, 41(8):107–109.
2. Sun, P.M., Gong, S.C. (2012). The vibration buffering and the design of buffer of the punching machine. Mechanical Research & Application, (2):108–109.
3. Shang, J.L., Xu, F., Wang, S.G. (2006). The vibration damage to the adjacent buildings during construction. College of Disaster Prevention Techniques, 36(s1):22–23.
4. Meng, Q.J., Qiao, J.S., Wang, L. (2011). Model test study on transfer law of dynamic stress produced by dynamic compaction. Systems Engineering Procedia, (1): 74–79.
5. Hwang, J.H., Tu, T.Y. (2005). Ground vibration due to dynamic compaction. Soil Dynamics and Earthquake Engineering, 26 (5): 337–346.

6. Song, Z,G. (2003). A new annoyance-based vibration comfort design theory on engineering structures. Zhejiang: Zhejiang University.
7. GB50894-2013. (2013). Mechanical industry environmental protection design specification. Beijing.
8. GB10070-1988. (1988). Urban regional environmental vibration standard. Beijing.
9. GB10071-1988. (1988). Urban regional environmental vibration measuring method. Beijing.

Dynamic Behavior of Vehicle-Slab Track in the Condition of Subgrade and Culvert Transition Settlement

Xiaopei Cai, Yongwang Kai, Chuangchuang Ren, Liangwu Guo and Qian Miao

Introduction

In high speed railway lines, there exists big difference between culvert and subgrade stiffness. In order to enhance the safety and stability of the train, it is necessary to establish transition structure between the subgrade and culvert, making stiffness change uniformly and stably. However, due to the complex filling materials of the subgrade and culvert transition section, it is common phenomenon for transition area to be affected by rain, freeze and other adverse natural conditions, resulting in reduction of safety and stability of the train. Therefore, the domestic and foreign scholars put a lot of work in the subgrade and culvert transition section for dynamic characteristics analysis and maintenance measurements, putting forward many innovative theories and methods.

The settlement of the subgrade and culvert transition area will cause the serious wheel rail impact, which will aggravate the deterioration of the track structure, and reduce the safety and stability of the train. Japan [1] researched settlement problems of subgrade and culvert transition section. German [2] studied the stiffness variation

X. Cai (✉) · C. Ren · L. Guo · Q. Miao
School of Civil Engineering, Beijing Jiaotong University, Beijing 100044, China
e-mail: xpcai@bjtu.edu.cn

C. Ren
e-mail: 14121181@bjtu.edu.cn

L. Guo
e-mail: 1040525703@qq.com

Q. Miao
e-mail: 405311036@qq.com

Y. Kai
Zhejiang Institute of Communications, Hangzhou, Zhejiang 311112, China
e-mail: Kaiboyang@163.com

of transition section influence on the wheel rail impact. America [3] researched optimization problem of the subgrade and culvert transition structure form. Momoya [4] through the finite element calculation and field test, studied the development mechanism of subgrade settlement under train load. A further study on the optimization problem of the subgrade and culvert transition section structure was made by Da and Shen et al. [5]. Tian [6] made a study on the dynamic response and the influence scope of the subgrade and culvert transition of high speed railway. The subgrade and culvert transition section of the dynamic performance test was made by Yang et al. [7]. Overall, on the part of the settlement deformation in subgrade and culvert transition section, the existing researches mostly focus on the optimization of the transition structure and prevention measures. Fewer researches are made on the vehicle-track dynamics behavior effected by the settlement deformation of transition area. Study on the dynamic characteristics of the vehicle-track structure is incomplete.

Based on the dynamic theory of the vehicle-track coupling system [8, 9], the dynamic model of the vehicle-track-subgrade interaction system was developed. The dynamic behaviors of the vehicle, the track in uneven settlement were calculated and the wheel rail interaction relationship and the vibration characteristics were researched.

Dynamic Model of Vehicle-Slab Track-Subgrade and Culvert Transition Section

Vehicle Model

The vehicle of CRH3 is used in the model which is composed of the car body, bogie and wheel set. Car body, bogie and wheel set are considered the lateral, floating, rolling, yawing, and nodding directions, the whole system of vehicle total of 35 degrees of freedom. Primary suspension between the wheelset and the bogie and the secondary suspension between the car body and the bogie are simulated by spring-damper element. The vehicle model is shown in Fig. 1.

Infrastructure Model Under Rail

The track structure adopts the type of CRTSIII slab track, with the track length of 120 m, whose fasteners are simulated with spring-damping element. The rail is of CHN60 type, whose elastic modulus is 2.1×10^{11} Pa. The vertical stiffness of the fastener is 35 kN/mm, and the slab size is 5.6 m $\times$ 2.5 m $\times$ 0.21 m. The rebar are reserved in the track structure, connected with self-consolidating concrete. The base is bonding with the self-consolidating concrete, and the position of the concrete

(a) Calculation model of the vehicle   (b) Finite element model of the vehicle
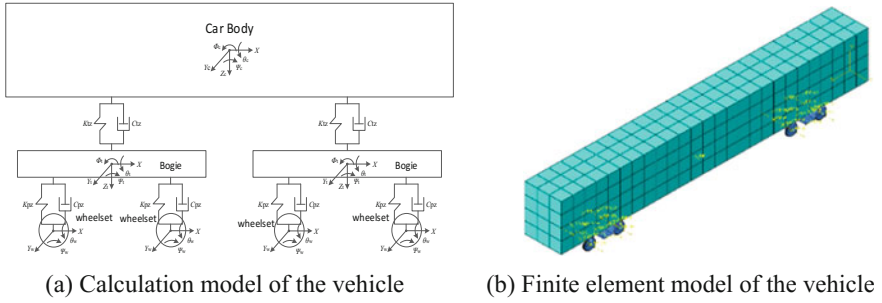
Fig. 1 Vehicle model

Fig. 2 Full model of CRTSIII slab track
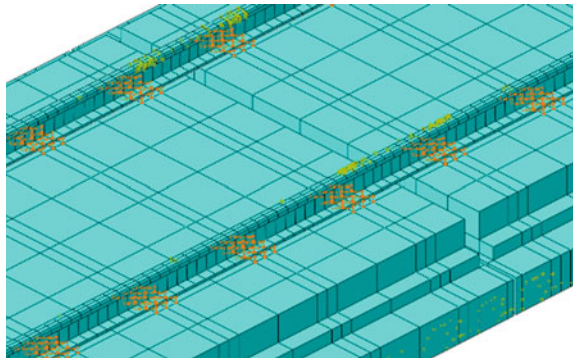
Fig. 3 Subgrade and culvert transition section
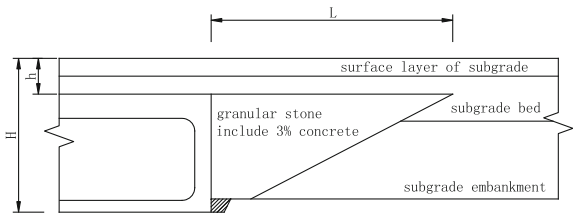
boss is provided with a groove, whose inner side is filled with elastic cushion. The finite element model of the track structure is shown in Fig. 2.

The diameter of culvert is 5 m, which accords with the design code of railway culvert. The elastic modulus of the culvert is 3.25×10^{10} N/m^2, with Poisson ratio of 0.15, and the density of 2550 kg/m^3. In engineering practice, adhesive strength between the base and subgrade surface is relatively low, so the Hard Contact model is adopted in the model. The subgrade, culvert and transition section are simulated by the C3D8R solid element, and the structure of the transition section of the culvert is shown in Fig. 3.

Wheel Rail Contact Model

The wheel rail contact model is the link between the vehicle model and track model, which includes the wheel rail normal contact and the wheel rail tangent contact. The wheel rail contact is determined by defining contact relationship of the master surface and slave surface in ABAQUS software. The master surface is the rigid wheel tread and slave surface is flexible rail profile. Hertz contact function is defined in vertically, and column friction function in tangent direction is defined between the master and slave surfaces, as is shown in Fig. 4.

Hertz nonlinear elastic contact theory is adopted in the wheel rail normal contact theory, and the vertical force is determined by the elastic compression of the contact surface between the vehicle and the rail, as is shown:

$$p(t) = \left[\frac{1}{G} \delta Z(t) \right]^{\frac{3}{2}} \tag{1}$$

where G is the wheel-rail contact coefficient and $\delta Z(t)$ is the normal elastic compression deformation at the wheel-rail contact point.

Fig. 4 Wheel-rail contact model
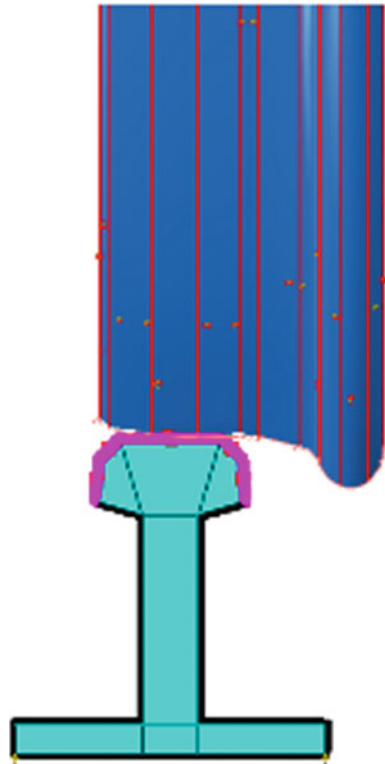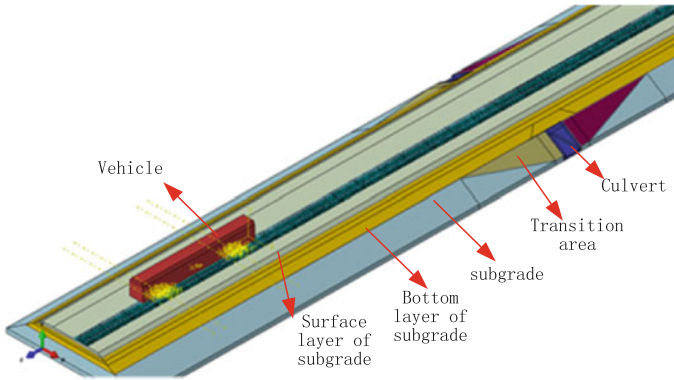
Fig. 5 Dynamic model of vehicle-track-subgrade and culvert transition area

The wheel rail tangential direct uses column friction model. The tangential action is the product of vertical pressure and friction coefficient of wheel rail surface.

$$F = \mu \times P(t) \tag{2}$$

Dynamic coefficient of friction is in the range of 0.25–0.35.

In this paper, the dynamic model of the vehicle-track-subgrade and culvert transition is shown in Fig. 5.

Dynamic Characteristic Analysis of Cosine Settlement

The common length of subgrade and culvert transition section is 20 m. In this part, the integral settlement occurred in transition section. And the dynamic characteristic of track structure and wheel-rail force was studied. The type of cosine settlement is shown in Fig. 6.
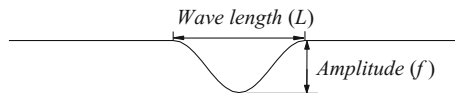
Fig. 6 The cosine settlement of subgrade and culvert transition section

The Wheel-Rail Dynamic Characteristic for Cosine Settlement in Transition Section

It is common for cosine type settlement in subgrade and culvert transition section. The wheel-rail dynamic characteristic is influenced by different lengths and amplitudes of the cosine wave. The length of transition section is 20 m, so the different amplitude of cosine wave was studied. Typical wheel-rail force curve is shown in Figs. 7 and 8. The peak value of curve is shown in Table 1.

As is shown in Figs. 7, 8 and Table 1, in the transition section area, the bigger the amplitude value of cosine settlement is, the bigger wheel-rail compact force is. When the amplitude of cosine settlement is 5 mm, the vertical wheel-rail force is 106.67 kN, and lateral wheel-rail force is 17.2 kN, with the wheel-rail load reduction of 0.237 and the derailment coefficient of 0.178. When the amplitude of cosine settlement is 20 mm, the vertical wheel-rail force is 162.86 kN and lateral wheel-rail force is 20.29 kN, with wheel-rail load reduction of 0.635 and derailment coefficient of 0.191. The amplitude of settlement increase from 5 mm to 20 mm,

Fig. 7 Vertical wheel-rail force
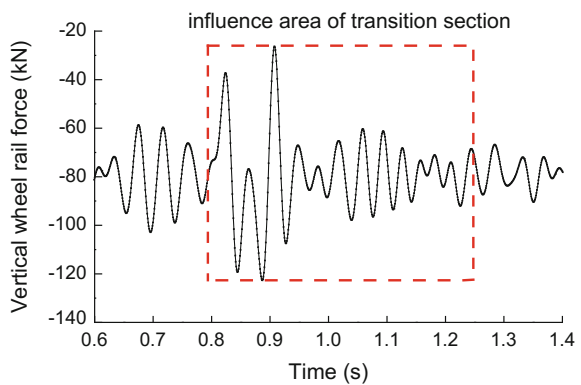
Fig. 8 Lateral wheel-rail force
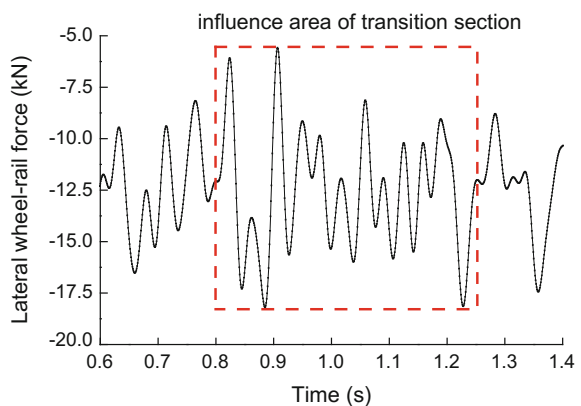
Table 1 Dynamic index of wheel-rail interaction in different amplitude values of cosine wave

Settlement condition (mm/m)	5/20	10/20	15/20	20/20
Vertical wheel-rail force (kN)	106.67	122.68	140.92	162.86
Lateral wheel-rail force (kN)	17.26	18.19	19.20	20.29
Rate of wheel-rail load reduction	0.237	0.364	0.481	0.635
Derailment coefficient	0.178	0.182	0.187	0.191

vertical wheel-rail force increases by 52.7% and lateral wheel-rail force increases by 17.55%. Wheel-rail load reduction increases by 167.9% and derailment coefficient increases by 7.3%. With the settlement amplitude increasing, the vertical wheel-rail force, lateral wheel-rail force, wheel rail load reduction and derailment coefficient are increasing and the safety and stability of train reduce obviously. So the amplitude value of settlement do obvious influence on wheel rail interaction relationship.

The Vibration Characteristic of Track Structure for Cosine Settlement in Transition Section

The cosine settlement intensify the vibration of track structure. The typical acceleration time history curve of rail, slab and surface layer of subgrade and tendency curve of vibration acceleration for different structure in settlement are shown in Figs. 9, 10 and Table 2.

It can be concluded from Figs. 9, 10 and Table 2 that the acceleration vibration from rail to surface layer of subgrade decreases gradually. And with the amplitude of settlement increases gradually, the vibration acceleration of track structure increases obviously. In the process of amplitude increasing from 5 to 20 mm, the rail vibration acceleration increases by 11.44% and the slab vibration acceleration

Fig. 9 Vibration acceleration time history curve of cosine settlement
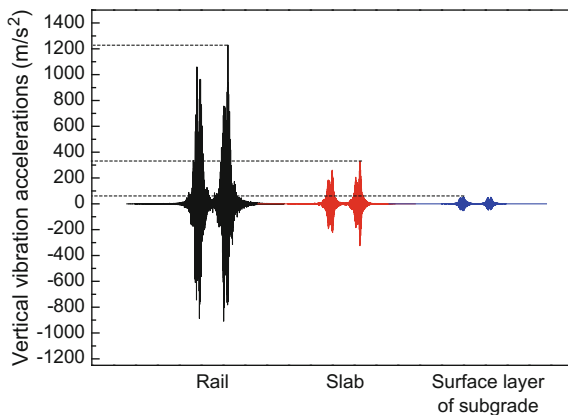
Fig. 10 Tendency curve of vibration acceleration for different structure in different settlement amplitude
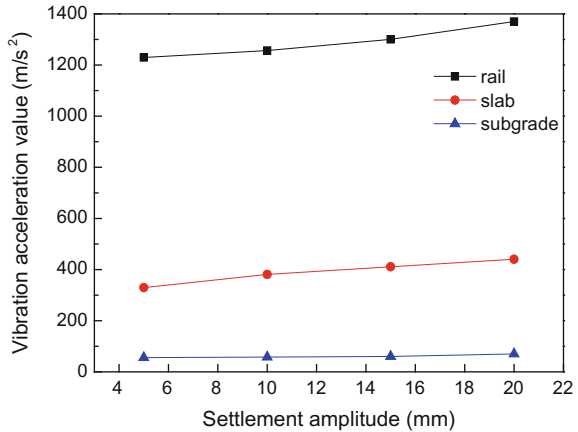
Table 2 Vibration acceleration of track structure in different settlement amplitudes (m/s^2)

Settlement condition	5/20	10/20	15/20	20/20
Rail	1229.56	1256.62	1300.34	1370.24
Slab	329.47	380.93	410.86	440.37
Surfaces layer of subgrade	55.72	57.76	60.22	69.88

increases by 33.7% and the surface layer of subgrade increases by 25.5%. It is obvious that cosine settlement has obvious influence on the track structure, so it is important to control the settlement amplitude value in subgrade and culvert transition area.

Dynamic Characteristics Analysis of Bending Angle Settlement Deformation

Bending angle settlement is a main deformation form in the subgrade and culvert transition section area. Due to the sudden changing stiffness of the transition section, the settlement of subgrade will suddenly occur in the process of train operation, and bending angle between the subgrade and the culvert structure will be formed. The bending angle settlement deformation has great influence on the safety and stability of the train, increasing the risk of train jumping and derailment. The settlement type is shown in Fig. 11.

Fig. 11 The bending angle settlement of subgrade and culvert transition section
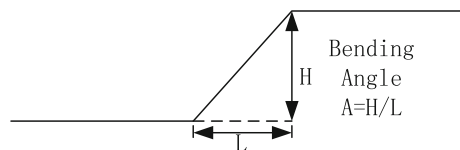
The Wheel-Rail Dynamic Characteristic for Bending Angle Settlement in Transition Section

The bending angle of subgrade and culvert transition section has great influence on the wheel-rail impact force. Serious bending angle settlement will increase the risk of derailment. So it is necessary to study the different values of angle settlement impact on train. The impact of bending angle changing rates on the train is analyzed through the calculation of settlement amount of 5 and 10‰. Typical wheel-rail force curve is shown in Figs. 12 and 13, and the dynamics index of different bending angle changing rates are shown in Table 3.

From Figs. 12, 13 and Table 3, it can be seen that with the increase of the bending angle changing rates, the wheel-rail vertical force, lateral force, wheel load reduction ratio and derailment coefficient increase significantly. Bending angel changing rates increasing from 5 to 10‰, wheel-rail vertical force increases by 4.1% and the wheel-rail lateral force increases by 6.7%, with reduction rates of

Fig. 12 Vertical wheel-rail force
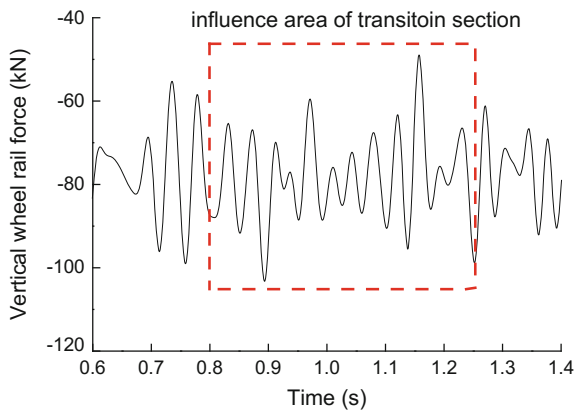
Fig. 13 Lateral wheel-rail force
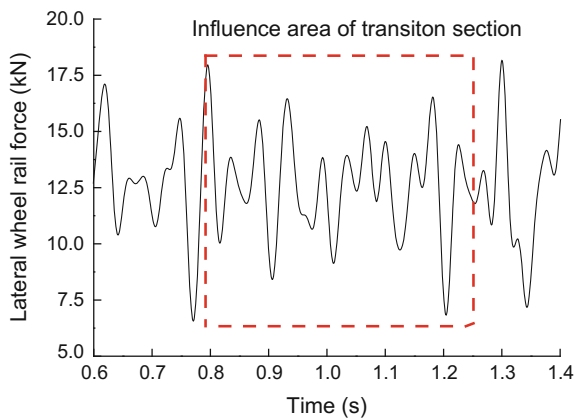
Table 3 Dynamic index of wheel-rail interaction in different value of bending angle settlement

Bending angle	5‰	10‰
Vertical wheel-rail force (kN)	99.16	103.23
Lateral wheel-rail force (kN)	17.02	18.16
Rates of wheel-rail load reduction	0.234	0.338
Derailment coefficient	0.176	0.179

wheel load increasing by 44.4% and the derailment coefficient increasing by 1.7%. With the increase of the bending angle changing rates, the safety and the stability of the vehicle is gradually reduced, and the bending angle changing rates settlement have a great influence on the train.

The Vibration Characteristic of Track Structure for Bending Angle Settlement in Transition Section

The bending angle changing rates of 5 and 10‰ of the subgrade and culvert transition section is studied. The typical vibration acceleration curve of rail and track structure are as shown in Fig. 14, and the peak value of the track vibration acceleration is shown in Fig. 15 and Table 4.

From the Figs. 14, 15 and Table 4, it can be seen that the vibration acceleration of the track structure is gradually increasing with the increase of the bending angle. In the process of the bending angle increasing from 5 to 10‰, rail vibration acceleration increases by 12.2%, and the vibration acceleration of track slab increases by 8.4%, with the vibration acceleration of subgrade surface layer increasing by 13.1%. In addition, the vibration response of the track structure under bending angle settlement is obviously higher than that of the cosine type. Compared with the cosine settlement, the bending angle settlement has greater influence on the dynamics of structure. Therefore, for the track maintenance period, the bending angle of transition section should be strictly controlled.

Fig. 14 Vibration acceleration time history curve of bending angle settlement track structure
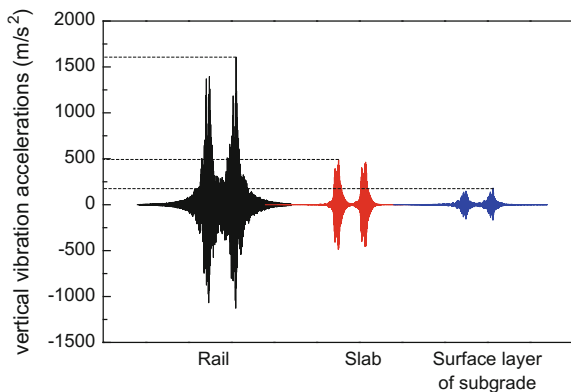
Fig. 15 Tendency curve of different structure in different bending angle value
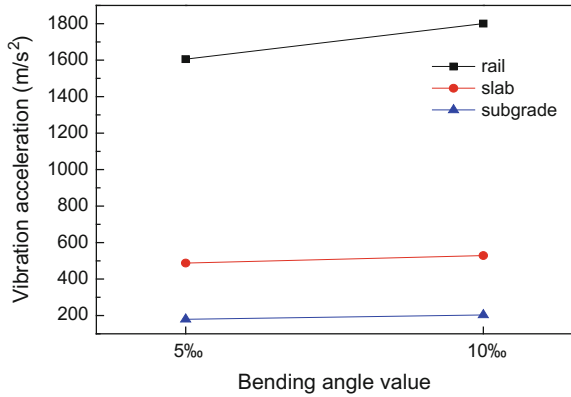
Table 4 Vibration acceleration of the track structure in different bending angle settlement (m/s^2)

Bending angle	5‰	10‰
Rail	1605.4	1800.7
Slab	487.9	528.9
Surface layer of subgrade	179.5	203.1

Conclusion

Based on the vehicle track dynamic theory, the vehicle-slab track-subgrade and culvert transition section model was established, and the influence of vehicle-track dynamic characteristic in different settlement forms and amplitudes was studied. The researches show that:

(1) When the cosine and bending angle settlement occurred in the transition of subgrade and culvert section, with the increasing of the settlement amplitude, the vehicle track interaction dynamic response is more intensified. And the maximum response occurred in transition section and culvert section

(2) For the cosine settlement, the bigger settlement amplitude is, the bigger wheel rail impact force is. The value of wheel rail load reduction and derailment coefficient increase with the settlement amplitude increasing. So it is important to control the settlement value in order to reduce the track irregularity.

(3) For the bending angle settlement, with the increase of bending angle, the wheel-rail impact force increases obviously. Bending angle settlement has obvious influence on derailment coefficient. Compared with the cosine settlement, the bending angle settlement is more intensified in dynamic response of track structure.

References

1. Sunage, M., Sekine, E. (1990). Vibration Behavior of Roadbed on Soft Ground under Train load. Quartly Report of RTRI, 31(1), pp. 29–35.
2. Gunther, L., Lothar, M. (1990). Elastisches Verformungs Verhalten Des Eisenbahnoberbaus. Eisenbahnigenieur, 41(3), pp. 111–119.
3. Read, D., Li, D. Q. (2006). Design of Track Transition. Transportation Research Board, Washington D C.
4. Momoya, Y., Sekine, E., Tatsuoka, F. (2008). Deformation Characteristic of Railway Roadbed and Subgrade under Moving-Wheel Load. Soil and Foundation, 45(4), pp. 99–118.
5. Da, Z.H., Shen, Y.P., Wang, Y.C. (2016). Optimization Design of Road-culvert Transition Section of CRTSII. Journal of engineering society, 4, pp. 54–59.
6. Tian, Y.H., Chen, M., Shen, Y.P. (2014). Study on Dynamic Response and Scope of the Transition between Culvert and Subgrade in Beijing-Shanghai High-speed railway. Journal of China Railway Society, 36(11), pp. 86–91.
7. Chen, G.Y., Yang, G.L., Wei, L.M. (2010). An Experimental Study of Dynamic Characteristic of Road-Culvert Transition in Passenger Dedicated Railway. Journal of Railway Science and Engineering, 7(1), pp. 47–51.
8. Zhai, W.M. (2007). Vehicle-Track Dynamic. Science press, Beijing.
9. Liu, X.Y., Wang, P. (2010). Vehicle-Track-Subgrade Dynamic System. Southwest Jiaotong University Press, Chengdu.

Preliminary Analysis of the Interaction Between Tunnel and Soil by the 2.5D FEM-BEM Method

Qingsong Feng, Shiyue Liu and Xiaoyan Lei

Introduction

The problem of ground-borne vibration has caught the attention of researchers during the past decades. To better understand the transmission of vibration from underground railways, different simulations have been exploit.

A 2.5D model was reported to investigate the vibration of tunnel systems. In this model, an artificial boundary was introduced for the application of the element technology. The wave number finite element method was first proposed by Gavric in the study of how to calculate the dispersion curves of free steel rails [1, 2]. Using this method, the frequency dispersion characteristics of the plate system is calculated in [3]. The wave number boundary element method is well applied in the earthquake engineering [4, 5]. In the paper [6, 7], the ground vibration problems that generated by the train has been investigated by using the finite element method and the boundary element method. In the derivation of the wave number boundary element method, it is needed to know the Green's function of the 2.5 dimensional infinite homogeneous elastic body, which has been given in [8].

In this paper, the coupled model of tunnel-soil system were established, the tunnel is simulated by finite element, soil is simulated by boundary element. The current tunnel model is validated numerically by means of the exact solution for an

Q. Feng (✉) · S. Liu · X. Lei
Engineering Research Center of Railway Environment Vibration and Noise,
Ministry of Education, East China Jiaotong University,
Nanchang, Jiangxi 330013, China
e-mail: fqshdjtdx@aliyun.com

S. Liu
e-mail: 670281324@qq.com

X. Lei
e-mail: xiaoyanlei2013@163.com

411

analysis model whereas the soil-tunnel model is validated against a previous boundary model. In addition, the responses of the soil and tunnel are investigate by this model.

Model and Parameters

Numerical Model

For a column inclusion improved soft subsoil, the improvement area ratio used to the tunnel-soil system can be seen as a system composed of two elastic sub-domains, within which the frequency domain wave equation

$$(\lambda + 2\mu)\nabla\nabla \cdot u - \mu\nabla \times \nabla + \omega^2 \rho u = 0 \tag{1}$$

must be satisfied; in this equation, u is the displacement vector, λ and μ are the Lamé's constants and ρ is the mass density of the elastic medium.

Consider a system which a solid inside, with a constant geometry along infinite distance at x-axis, is embedded in a elastic medium, and subjected to a harmonic unit point source with an frequency f. Since the system' geometry does not change along x-direction, it can be apply a Fourier transformation along x-axis and change the 3D displacement field as a continuous integral of 2D solution, as

$$u^{3D} = \int_{-\infty}^{+\infty} u^{2D}(\beta)e^{-i\beta(x-x_0)}d\beta \tag{2}$$

discrete form can be written as

$$u^{3D} = \sum_{-\infty}^{+\infty} u^{2D}(\beta)e^{-i\beta(x-x_0)}\Delta\beta e^{-i\beta(x-x_0)} \tag{3}$$

where the β is the axial wave-number.

The 2.5D finite elements method is based on the assume that the elastic body have infinite length along x direction and cross-section have similar geometry and material properties. With the 3D solution make use of Fourier transformation at x direction, equation form

$$\left[K_{s2}(-i\kappa)^2 + K_{s1}(-i\kappa) + K_{s0} - \omega^2 M_s\right]\tilde{u}_{fe}(\kappa) = \widetilde{F}_{fe}(\kappa) \tag{4}$$

where K_{s0}, K_{s1}, K_{s2} is the stiffness matrix, M_s is the mass matrix, $\tilde{u}_{fe}(\kappa)$ is the displacement vector, $\widetilde{F}_{fe}(\kappa)$ is the nodal force vector, κ is wave-number. For each

wave-number equation only related to y, z coordinate. In this way, the 3 dimensional elastic body element can be represented by a 2 dimensional plane element.

Three node element which shape function is the two degree polynomial are used in the boundary element.

The basic equation of the boundary element is

$$H\tilde{u}_{be}(\kappa) - G\tilde{p}_{be}(\kappa) = \tilde{p}_{in}(\kappa) \tag{5}$$

where $\tilde{u}_{be}(\kappa)$ is the displacement vector, $\tilde{p}_{be}(\kappa)$ is the surface force vector. $\tilde{p}_{in}(\kappa)$ is the surface which at surface. H, G is the coefficient matrix.

When the elastic body is mixed with finite element and boundary element, the finite element equation must be coupled with the boundary element equation at the common interface. In order to facilitate the modeling and solving, the finite element method is consistent with the boundary element coupling interface. The displacement of the finite element nodal point on the coupling interface is equal to the displacement of the boundary element,

$$C_2\tilde{u}_{feII}(\kappa) = I_2\tilde{u}_{beII}(\kappa) \tag{6}$$

where C_2, I_2 is unit matrix.

Considering the coupling of finite element and boundary element, the global equation of the system structure can be expressed as,

$$\begin{bmatrix} -G & H & [0] \\ -C_1 & [0] & D \\ C_B & C_A & [0] \\ [0] & I_2 & -C_2 \end{bmatrix} \begin{bmatrix} \tilde{p}_{be}(\kappa) \\ \tilde{u}_{be}(\kappa) \\ \tilde{u}_{fe}(\kappa) \end{bmatrix} = \begin{bmatrix} \tilde{p}_{in}(\kappa) \\ \tilde{F}_{fe}(\kappa) \\ C_C \\ [0] \end{bmatrix} \tag{7}$$

each node of the boundary element has three displacement components and three surface force components. At the common interface, the position of finite element nodes are the same as the nodes of boundary element, and each finite element node also has three displacement components. In this way, the number of the boundary condition in boundary element is just equal to the order number of nodal surface force. Solving linear equations (6) for each wave-number we can get the displacement and stress components of the nodes of the boundary element and the displacement components of the nodes of the finite element.

In this paper, both full space model and half model are established. The full space can be seen as a hollow cylinder with internal radius R1 and internal R2 which modeled by FES embedded in full space, as shown in Fig. 1.

The half space model can be regarded as a hollow cylinder with internal radius R1 and external R2 which simulated by FES embedded in half space, as well as the full space model, the soil simulated by BES, as shown in Fig. 2.
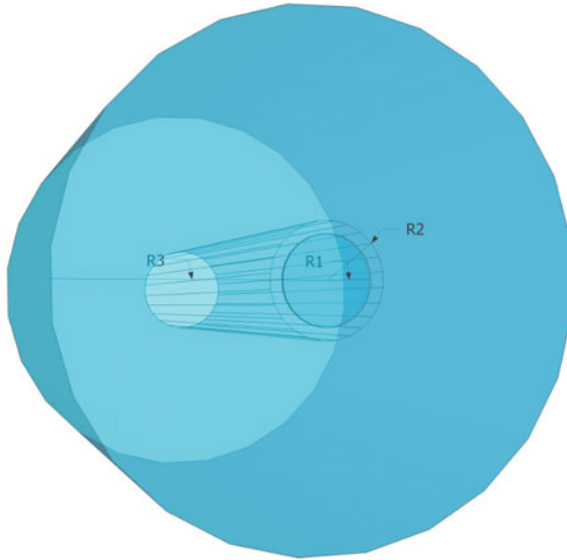
Fig. 1 The full space tunnel-soil model
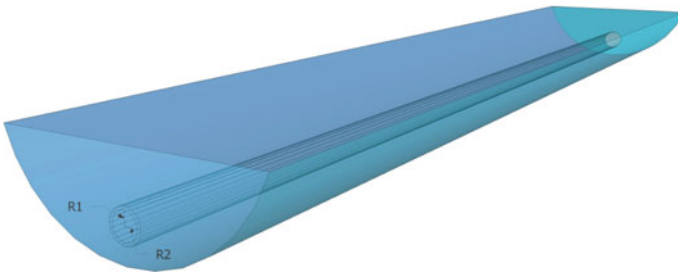
Fig. 2 The half space tunnel-soil model

Model Parameters

There is parameter of the full space tunnel-soil model validation, see Table 1.

In the case of the tunnel-soil model, the FFT is used to transform wave-number to displacement. In the performance of the FFT, 2048 sample are used with a spacing of $\beta = 0.0025 \times 2\pi$.

There is parameter of the full space tunnel-soil model for analysis of tunnel response, see Table 2.

Table 1 The parameters for the tunnel-soil model validation

Young's modulus ($\times 10^6$ Nm^{-2})	Poisson's ratio	Density (kg/m^3)	Loss factor	P-wave speed (m/s)	S-wave speed (m/s)
1770	0.4	1700	0.15	1500	610

Table 2 The parameters for the tunnel-soil analysis

Parameter	Symbol	Value
Tunnel		
Density	ρ	2500 kg/m^3
Young's modulus	E	30×10^9 Nm^{-2}
Poisson's ratio	v	0.15
Damping loss factor	η	0.01
Soil		
Density	ρ_s	1700 kg/m^3
Young's modulus	E_S	17.1×108 Nm^{-2}
Poisson's ratio	v_s	0.4
Damping loss factor	η_s	015
Shear wave speed	C_S	1500 m/s
Pressure wave speed	C_p	610 m/s

Model Validation

The solution was compared by exact solution for an undamped homogeneous subject to constant moving point load. The direction of the tunnel is parallel to the x-axis. Assumed R1 very small (0.05 m). Then we can use the full space tunnel model simulate a solid cylinder which calculated by the exact solution. The result of such calculation shown in Figs. 3 and 4 which load speed at 500 m/s.

The calculation well confirm model proposed in this paper.

Fig. 3 Longitudinal displacements along the straight line (y = 0 m, z = 5 m) due to unit vertical constant load moving along the x-axis at 500 m/s. *Continuous line* by the FEM-BEM tunnel-soil model; *dash dotted line* by the exact solution for a point moving load
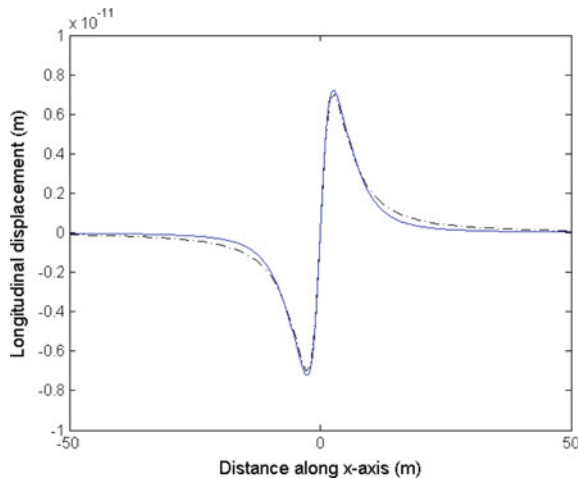
Fig. 4 Vertical displacements along the straight line (y = 0 m, z = 5 m) due to a unit vertical constant load Moving along the x-axis at 500 m/s. *Continuous line* by the FEM-BEM tunnel-soil model; *dash dotted line* by the exact solution for a point moving load
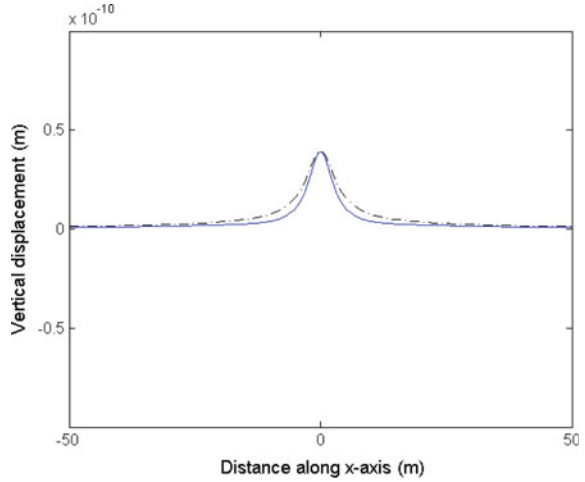
Analysis the Tunnel-Soil Response

Tunnel Embedded in Full Space

We chose four points: A(4,0), B(0,4), C(0,4.5) and D(0,5) to analysis the response of the tunnel-soil coupled system. And Fig. 4 shows the Meshing of the model. Tunnel wall is simulated by 8 nodes FES and soil is simulated by 3 nodes BES, FES and BES meshing can be seen in Fig. 5.

Fig. 5 FEM and BEM mesh
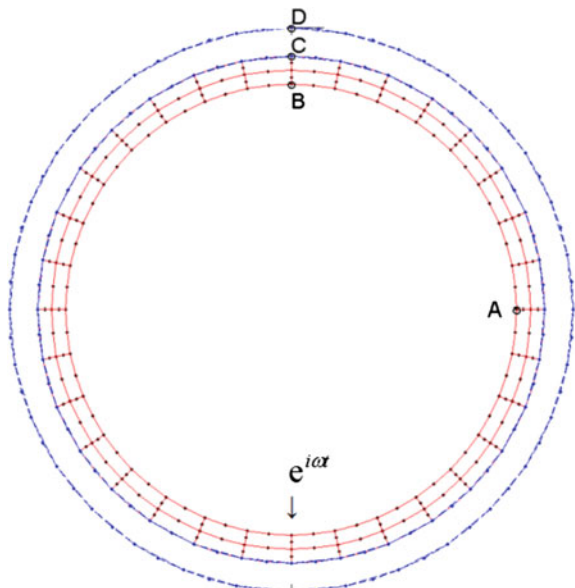
The unit point harmonic load in (0, −4) position, respectively, using the 10, 30, 60, 100 Hz input frequency. We obtained the A, B, C, D four points response under different frequency, as shown in Figs. 7, 8, 9 and 10.

Tunnel Embedded in Half-Space

In spite of the theoretical interest in the full-space, it is obvious that it truly is not close to real problem, since practical cases usually comprise a bounded surface. In order to assess the capability of the response of tunnel under more realistic physical configurations, a half space model is now presented. We select the shallow tunnel for example, see Fig. 8. In this case we also chose four points: A(4,0), B(0,4), C(0,4.5) and D(0,5) to analysis the response of the tunnel-soil coupled system. And Fig. 6 shows the Meshing of the model. The points' location show in Fig. 5.

Fig. 6 Half space model tunnel mesh
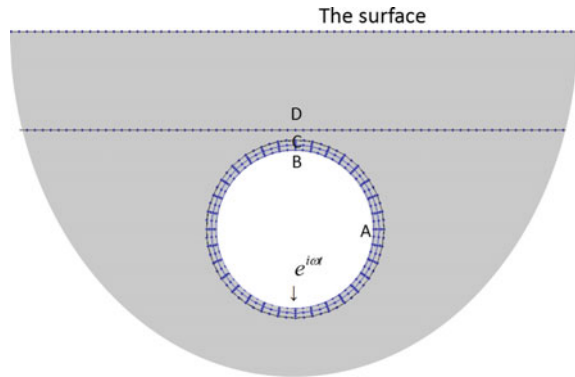
Fig. 7 Displacement along the x-axis due to a vertical load 10 Hz in full space
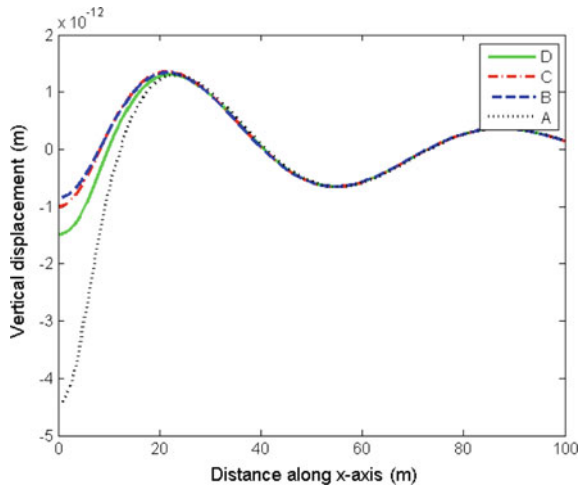
Fig. 8 Displacement along
the x-axis due to a vertical
load 30 Hz in full space
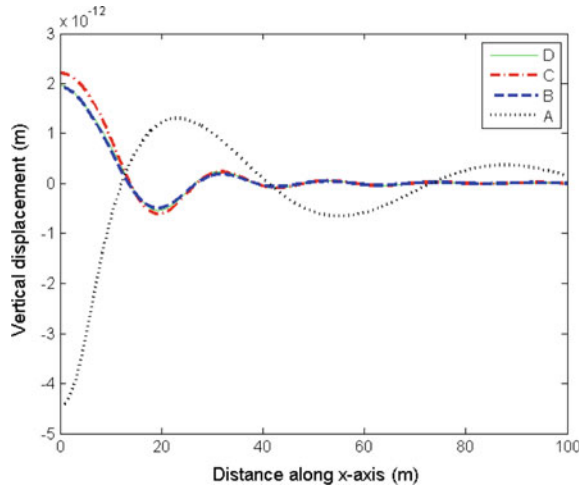
Fig. 9 Displacement along
the x-axis due to a vertical
load 60 Hz in full space
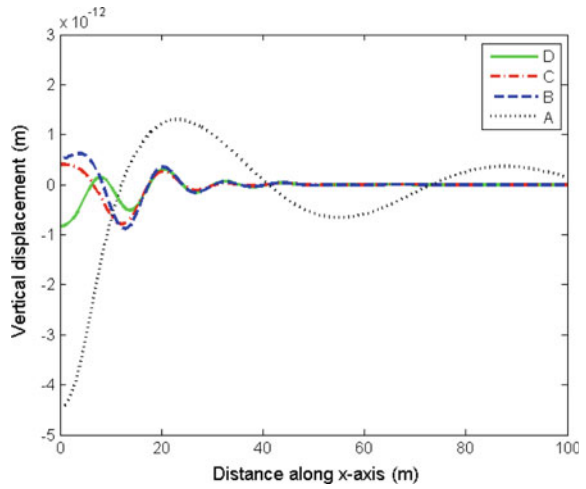
The unit point harmonic load in (0, −4) position, respectively, using the 10, 30, 60, 100 Hz input frequency. We obtained the A, B, C, D four points response under different frequency, as shown in Figs. 11, 12, 13 and 14.

Fig. 10 Displacement along the x-axis due to a vertical load 100 Hz in full space
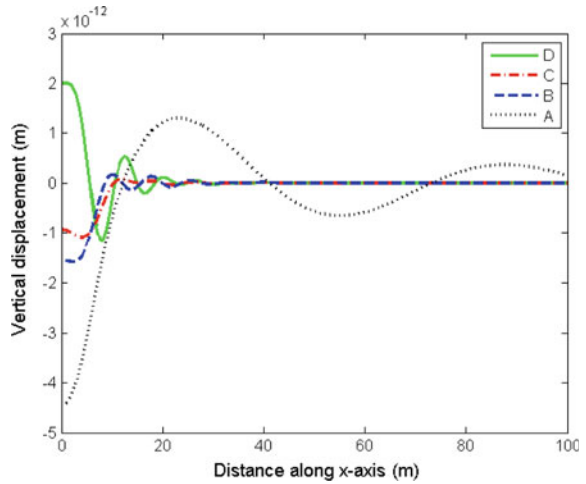
Fig. 11 Displacement along the x-axis due to a vertical load 10 Hz in half space
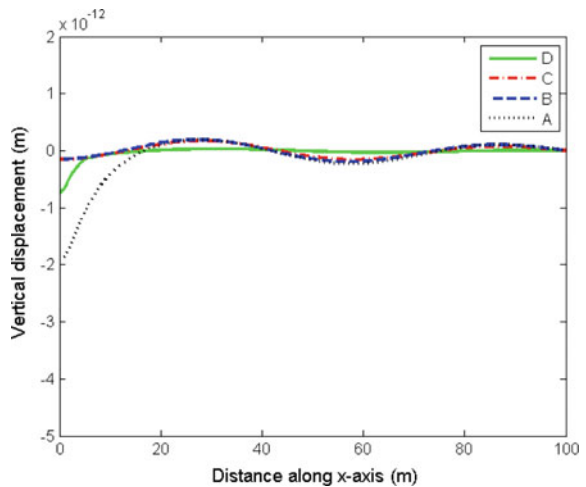
Discussion

(1) Whether in the full space or the half space, the attenuation of displacement along the x-axis at the lateral of the tunnel wall is much slower than that the top of the tunnel points. At the same time, the response in the lateral tunnel wall is always large than in the top tunnel wall.

(2) As shown in 4 different input frequencies, the displacement attenuation along x-axis in the half space is faster than that in the full space.

Fig. 12 Displacement along the x-axis due to a vertical load 30 Hz in half space
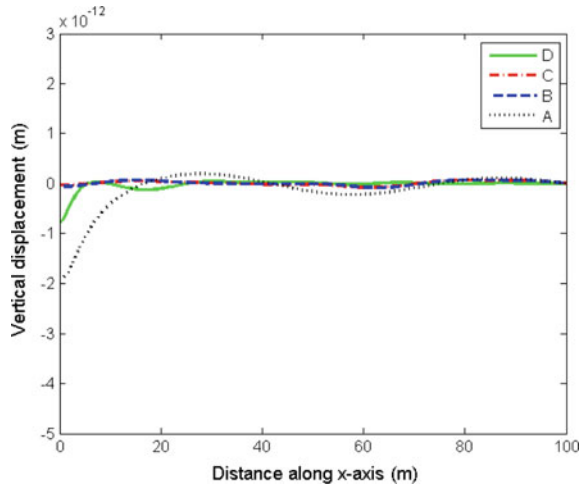
Fig. 13 Displacement along the x-axis due to a vertical load 60 Hz in fhalf space
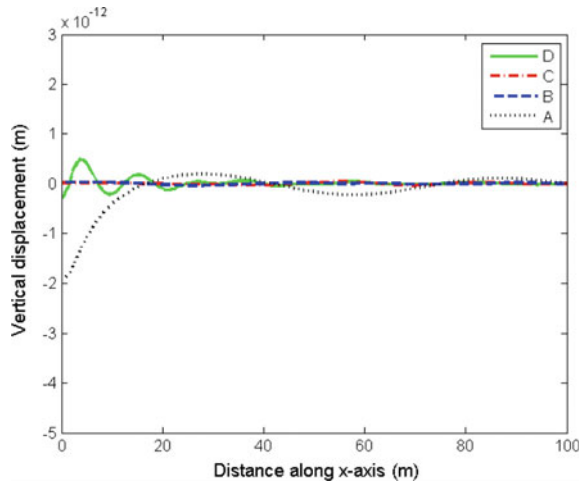
(3) The displacement response of half space tunnel is smaller than that tunnel embedded in the full space. A, D points' displacement in half space almost half of that in full space.

Fig. 14 Displacement along
the x-axis due to a vertical
load 100 Hz in half space
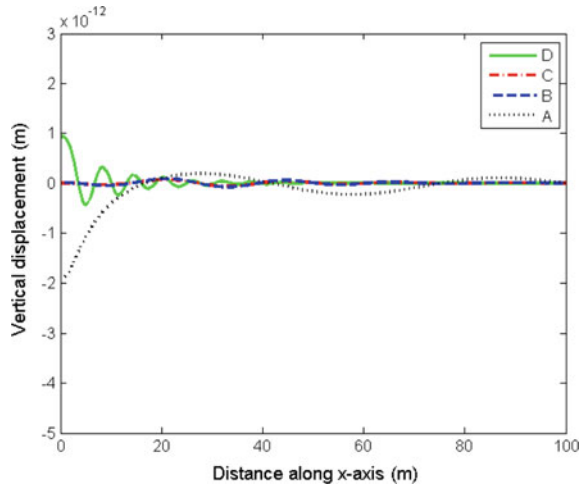
Conclusions and Future Work

This paper has established both a full space and half space finite element-boundary element model for calculate tunnel-soil coupled response. The method is based on the coupling between finite element and boundary element, both methods formulated in the 2.5D version of model. The paper has first presented the results of the dynamic interaction between a tunnel and soil and compared them against the exact solution. And the results are well confirmed. The paper has also presented the dynamic interaction between tunnel and soil both in full space and half space. The displacement response comparison between tunnel embedded in full space and half space. It is reveal that the displacement attenuation along x-axis in the half space is faster than that in the full space and the displacement response of half space tunnel is smaller than that tunnel embedded in the full space.

In general, the present results have highlighted ability of this method in predicting tunnel and soil interaction. Next step we will take more comprehensive research where the surface soil's response will be consider and more different buried depth of tunnel will take into our count.

References

1. Peplow A T, Jones C J C, Petyt M. Surface vibration propagation over a layered elastic half-space with an inclusion. Applied Acoustics, 1999, 56:283–296.
2. Gavric L. Computation of propagative waves in free rail using a finite element technique. Journal of Sound and Vibration, 1995, 185:531–543.
3. Gavric L. Finite element computation of dispersion properties of thin-walled wave guides. Journal of Sound and Vibration, 1994, 173:113–124.
4. Shah A H, Zhuang W, Popplewell N and Rogers J B C. Guided waves in thin-walled structural members. Transaction of ASME. Journal of Vibration and Acoustics, 2001, 123:376–382.
5. Kim J and Papageorigiou A S. Discrete wave number boundary element method for study of the 3-D response of 2-D scatters. Earthquake Engng. Struct. Dyn., 1998,27:619–638. Sheng X, Jones C J C, Thompson D J.A theoretical model for ground vibration from trains generated by vertical track irregularities [J]. Journal of Sound and Vibration, 2004, 272:93-7-965.
6. Sheng X, Jones, C J C and Thompson DJ. Modelling ground vibration from railways using wavenumber finite and boundary-element method. Proceedings of the Royal Society A, 2005, 461:2043–2070.
7. G. Degraden, D. Clouteau, R. Othman, et al. A numerical mode for ground-borne vibrations from underground railway traffic based on a periodic finite element-boundary element formulation, Journal of Sound and Vibration, 2006, 293:645–666.
8. S. Gupta. G. Degrande, G. Lombaert. Experimental validation of a numerical mode for subway induced vibrations, Journal of Sound and Vibration, 2009, 321:786–812.

DEM Simulation of Simplified Railway Embankment Under the Effect of Train-Induced Dynamic Load

Qiusheng Gu, Xuecheng Bian and John P. Morrissey

List of symbols

L_b Length of bond (m)
r_b Radius of bond (m)
L Length of the beam (m)
E Young's modulus (Pa)
W Moving load (N)
v Velocity of the moving load (m/s)
n Number of the particles
r Radius of the beam (m)
r_p Radius of particles (m)
E_b Young's modulus of bond (Pa)
G Shear modulus (Pa)
μ Coefficient of friction
ρ Density of beam (kg/m^3)
ρ_b Density of particles (kg/m^3)
d Diameter of the particles (m)
H Height of the embankment model (m)

Q. Gu (✉) · X. Bian · J.P. Morrissey
Department of Civil Engineering, Zhejiang University, Hangzhou 310058, China
e-mail: qiushengzxc@zju.edu.cn

X. Bian
e-mail: bianxc@zju.edu.cn

J.P. Morrissey
e-mail: J.Morrissey@ed.ac.uk

Q. Gu · X. Bian · J.P. Morrissey
School of Engineering, Institute for Infrastructure and Environment,
The University of Edinburgh, The King's Buildings,
Edinburgh EH9 3JL, Scotland, UK

Introduction

The Discrete Element Method (DEM) was proposed by Cundall [1] for the study of
rock mechanics and then applied to granular materials [2]. DEM is suitable for
studying cemented granular materials (e.g. rocks and concrete) due to their naturally
discrete inhomogeneous structure. The ability for the DEM to model cemented
granular materials depends largely on the implementation of the inter-particle
bonded contact model. Several typical bonded contact models have been devel-
oped. The spring model just connects the centres of interacting particles and resists
the relative displacement of bonded particles in compression and tension. Potyondy
and Cundall [3] improved the spring model into the parallel bond model that able to
transmit moments besides normal and shear forces. The beam model connects the
centres of particles in a bonded contact e.g. [4–7] according to the Euler-Bernoulli
or Timoshenko beam theory, resists tensile force, bending and twisting moments.
Brown et al. [8] presented a bond model for DEM simulation of cementitious
materials and deformable structures; the bond behavior is based on the Timoshenko
beam theory which is suited to describing the behavior of short beams [9]. The
bonds are assumed to have no mass, virtual and rigidly connect the two particles
(Fig. 1) in contact in the DEM model—all mass is appropriately assigned to the
particles. Bonds are subjected to internal forces caused by relative displacements
and rotations of the particles they connect. In the following sections, the bonded
contact model is verified by comparing the predictions with analytic solution, and
then used to model a simplified railway embankment under the effects of moving
load.

When it comes to the railroad ballast, DEM has many advantages to model the
deformation and stability of embankment compared with other numerical
techniques.

Fig. 1 TBBM between
ParticleA and *ParticleB*
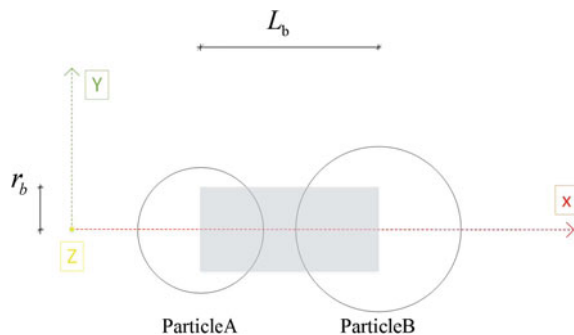
Model Verification

The verification of a numerical model is a significant procedure to ensure that the mathematical model in the program work as desired. Brown et al. [8] verified the static loading and free vibration of a simply supported beam, and then used to simulate an unconfined compression test of a concrete cylinder sample. The dynamic response of a simply supported beam under the effects of moving load is studied in the following sections. The results are compared with the analytic solution to ensure the TBBM work as desired under the moving load. Then TBBM are applied to a simplified railway embankment under the effect of train-induced dynamic load.

Moving Loading of a Simply Supported Beam

The simply supported beam (Fig. 2) is made for bonding 51 particles with 50 bonds in a line. The extreme left-hand particle is fixed against all translational displacement, the extreme right hand particle is fixed against vertical translational displacements, and both particles can rotate freely in plane.

Lee [10] presented the response of a Timoshenko beam to a constant moving force based on the beam theory with corrections for the shear deformation and rotatory inertia. The simply supported beam based on EDEM is made according to the Timoshenko beam H.P. Lee built. The deflection in the Y-direction under the moving load, w evaluated at $x = s$ while s is the distance force moved, is normalized by the static deflection w_{st}, defined by Eq. (1) at $x = L/2$ when the load W is applied at the same point. The normalized deflection under the moving load is denoted by $\overline{U}$, defined by Eq. (2). The model is simulated and the results of constant moving load with different velocity are compared with the analytic solution (Figs. 3, 4, 5).
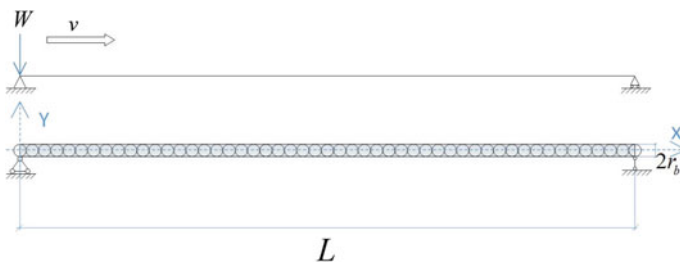
Fig. 2 A simply supported beam of length L made from connecting particles with bonds of length L_b
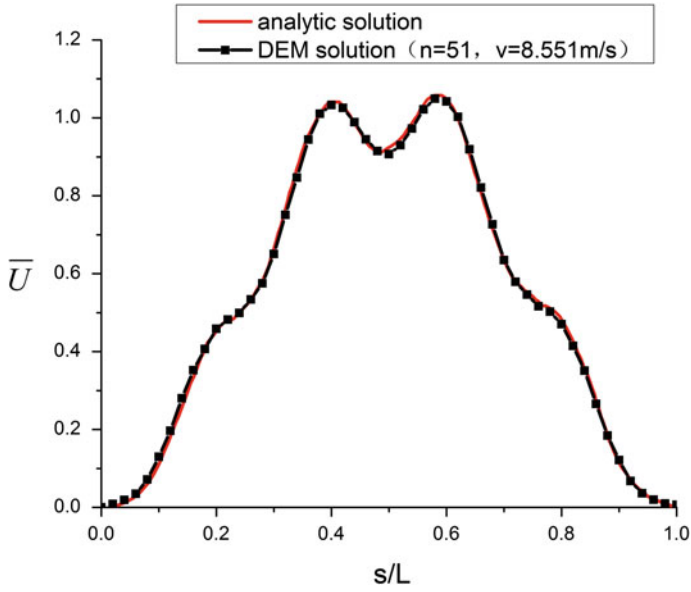
Fig. 3 The normalized deflection under the moving load at v = 8.551 m/s
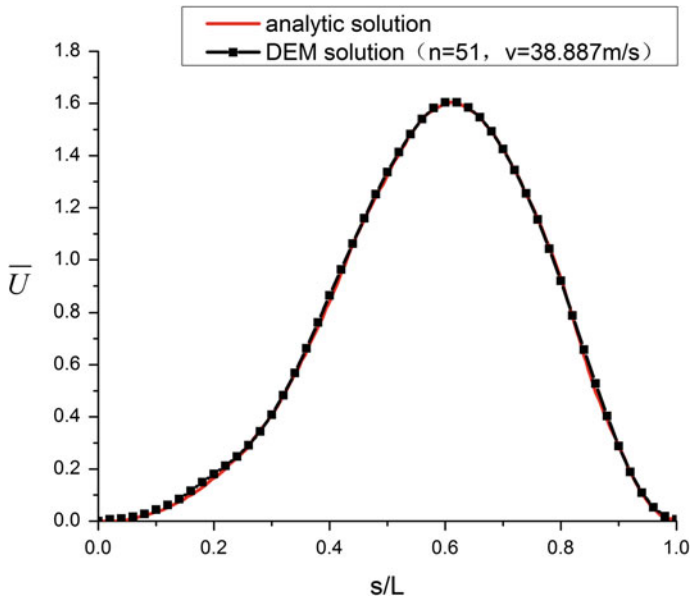
Fig. 4 The normalized deflection under the moving load at v = 38.887 m/s
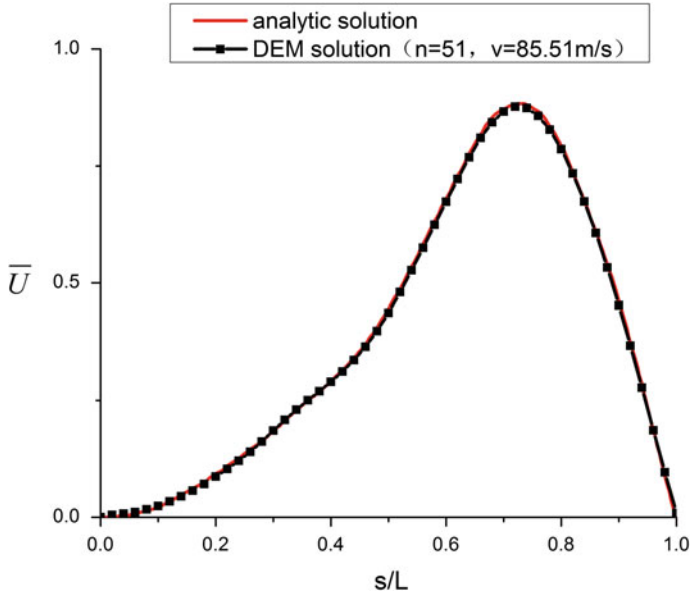
Fig. 5 The normalized deflection under the moving load at v = 85.51 m/s

The parameters adopted for the simply supported beam are recalculated from analytic solution and shown in Table 1. The particles are the points of adding force and represent mass of the beam equally during the simulation.

$$w_{st} = \frac{WL^3}{48EI} \tag{1}$$

Table 1 Parameters adopted for the simply supported beam

	Analytic solution	DEM model
L	1 m	1 m
n		51
L_b		0.02 m
r	9.5493 m	9.5493 m
r_b		9.5493 m
r_p		9.5493 m
E	2.07e11 N/m²	
E_b		2.07e11 N/m²
G	7.76e10 N/m²	
μ		0.3338
ρ	7700 kg/m³	
ρ_p		12,095.13 kg/m³
W	4.3235 N	4.3235 N

$$\overline{U} = \frac{w(x = s)}{w_{st}} \tag{2}$$

The DEM predicted results of the simply supported beam match well with the analytic solution (Figs. 3, 4, 5). It indicates that the TBBM follow the Timoshenko theory under the effects of constant moving load. The results show that the TBBM can be applied to model the performance of Timoshenko beam under the moving load.

Application to Railway Embankment

It's ideally suited to use DEM to model the railroad ballast layer considering the naturally discrete inhomogeneous structure. To make a compromise between computational time and accuracy, the railway embankment is simplified into an equal-sized model (Figs. 6, 7), only one track and the ballast layer are considered. The track and sleepers are formed by particles connected with TBBM.
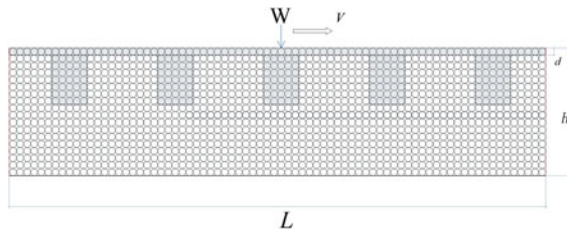
Fig. 6 Simplified railway embankment of equal-sized particles
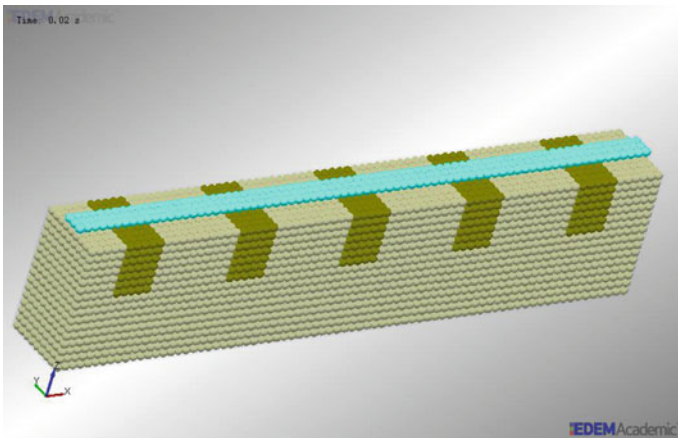
Fig. 7 Simplified railway embankment of equal-sized particles in EDEM

The parameters of the equal-sized model are shown below (Tables 2, 3, 4), W is 20,000 N, d is 40 mm, H is 680 mm. The constant moving load W moves from the extreme left-hand to the extreme right-hand particle of the track. The extreme left-hand particle is fixed against all translational displacement, the extreme right hand particle is fixed against vertical translational displacements, and both particles can rotate freely in plane. The boundary condition of the simplified model is all fixed boundary and the track can be treated as simply supported beam. The track and sleepers are bonded together to model the effects of fasteners.

Though the model is quite simple, the displacement of sleepers and mid-span of the track (Figs. 8, 9) can show the influence of moving load. The results indicate that the TBBM can model the railway track as except.

Table 2 Particle parameters

	Poisson's ratio	Density (kg/m^3)	Young's modulus (MPa)
Track particles	0.3	2487	182,000
Ballast particles	0.25	2600	2500
Sleeper particles	0.25	2500	2500

Table 3 Contact parameters

	Coefficient of restitution	Coefficient of static friction	Coefficient of rolling friction
Ballast-ballast	0.2	0.6	0.25
Ballast-sleeper	0.2	0.6	0.25
Ballast-track	0.2	0.6	0.25

Table 4 Bond parameters

Global damping coefficient	Poisson's ratio	Young's modulus (MPa)
0.95	0.3	11,000
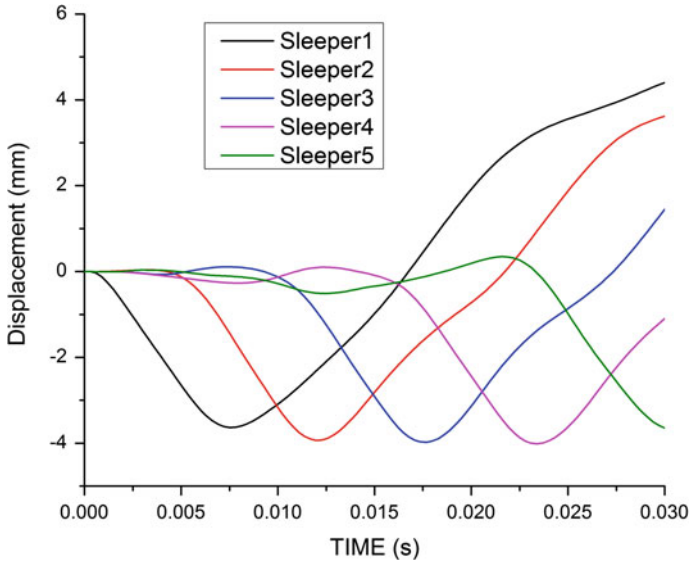
Fig. 8 Displacement of sleepers
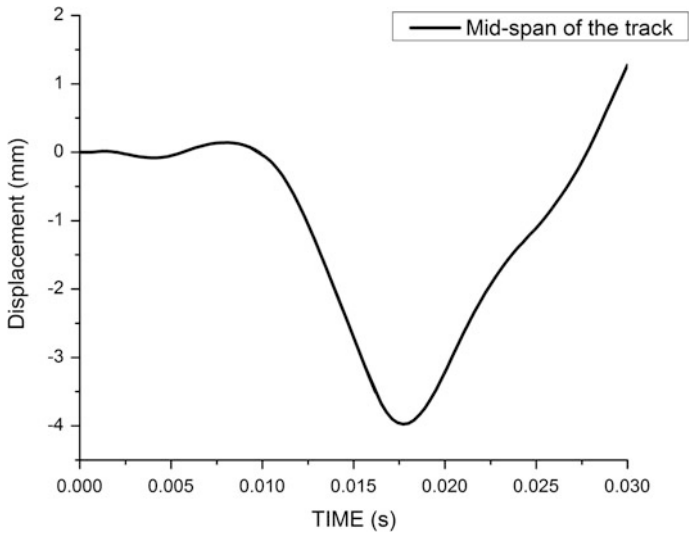
Fig. 9 Displacement of the mid-span of the track

Conclusions

The DEM predicted results of the simply supported beam under the moving load match well with the analytic solution. It indicates that the TBBM follow the Timoshenko theory under the effects of constant moving load and can be applied to model the performance of Timoshenko beam under the moving load. The displacement of the sleepers and track mid-span show that the TBBM can model the track as a Timoshenko beam as expect. The results show the feasibility of modeling train-induced dynamic load through adding moving load to railway track made up with the bonded particles. As the simplified embankment model is too simple, the results can't be compared with the field tests yet and many influencing factors need to be taken into consideration.

References

1. Cundall, P.A.(1971). A Computer Model for Simulating Progressive, Large-Scale Movements in Block Rock Systems. Symposium of International Society of Rock Mechanics (Vol.1(ii-b), pp. 11–8).
2. Cundall, P. A., & Strack, O. D. L. (1979). A discrete numerical model for granular assemblies. Geotechnique (Vol.29, pp. 47–65).
3. Potyondy, D. O., & Cundall, P. A. (2004). A bonded-particle model for rock. International Journal of Rock Mechanics and Mining Sciences, 41(8), 1329–1364. doi:10.1016/j.ijrmms.2004.09.011.
4. Schneider, B., Bischoff, M., & Ramm, E. (2010). Modeling of material failure by the discrete element method.Pamm,10(1),685–688.
5. André, D., Iordanoff, I., Charles, J., & Néauport, J. (2012). Discrete element method to simulate continuous material by using the cohesive beam model. Computer Methods in Applied Mechanics and Engineering, 213–216, 113–125.
6. Carmona, H. A., Wittel, F. K., Kun, F., & Herrmann, H. J. (2008).Fragmentation processes in impact of spheres. Physical Review E - Statistical, Nonlinear, and Soft Matter Physics, 77(5), 051302.
7. D'Addetta, G. A., Kun, F., & Ramm, E. (2002). On the application of a discrete model to the fracture process of cohesive granular materials. Granular Matter, 4(2), 77–90.
8. Brown Nicholas J., Jian-Fei Chen, Jin Y. Ooi. (2014). A bond model for DEM simulation of cementitious materials and deformable structures [J]. Granular Matter, 16(3):299–311.
9. Przemieniecki, J.S. (1968).Theory of Matrix Structural Analysis. McGraw-Hill, New York.
10. Lee, H. P. (1996). The Dynamic Response of A Timoshenko Beam Subjected to A Moving Mass. Journal of Sound and Vibration, 198(2), 249–256.

Vibration Isolation of In-filled Trench in Layered Ground Under High-Speed Train Load with Track Irregularity

Qiwei Zhang, Guangyun Gao and Jian Song

Introduction

In recent years, the rapid development of China's high-speed trains has brought not only great convenience, but also disturbances to the buildings, precision instruments and daily life of residents along the track. In order to alleviate the effects of these vibrations, some vibration isolation measures should be taken. The most common vibration isolation measures in transportation include three types: open trench, in-filled trench and row piles. Performance of open trench is limited to groundwater and stability of soil, and it cannot reach the ideal vibration isolation effect when the Rayleigh wave length is large since the desirable depth could hardly be attained. In-filled trench has been widely used in engineering practice, because it can be easily set up in a larger depth. Train induced vibration is transmitted in the ground in the form of stress waves. When confronted with obstacles, transmission, diffraction and reflection of the stress wave will occur. In addition, the energy carried by stress wave will have a larger degree of dissipation because of the damping effects in the foundation.

Q. Zhang (✉) · G. Gao
Department of Civil Engineering, Tongji University, Shanghai 200092, China
e-mail: langmansanguo@163.com

G. Gao
e-mail: gaoguangyun@263.net

Q. Zhang · G. Gao
Key Laboratory of Geotechnical and Underground Engineering
of Ministry of Education, Tongji University, Shanghai 200092, China

J. Song
College of Civil and Transportation Engineering,
Hohai University, Nanjing 210098, China
e-mail: jiansonghh@163.com

Because of the complexity of the in-filled trench isolation, tests were widely used to analyze the effect of in-filled trench isolation in the early stage. With the development of the theory and computer technology, the research of in-filled trench isolation has been greatly promoted. Analytical method is generally difficult to get a closed solution, so the numerical method is usually used to study the effect of in-filled trench isolation. Saikia [1] dealt with a 2D finite element study in PLAXIS 2D to analyze the vibration isolation effect of in-filled trench. Effects of the geometry and in-filled material on reducing vertical and horizontal components of surface displacements are investigated. Chang and Sheng [2] used the BEM to analyze the horizontal amplitude screening effects of an in-filled trench, considered the effects of the foundational embedment, shear wave velocity ratio of the in-filled material to the surrounding soil and the filling material.

2.5D FEM has been used to analyze the dynamic response of the foundation under dynamic loading in recent years. 2.5D FEM is used to transform the 3D finite element model into a 2D finite element model, which greatly reduces the amount of calculation of the numerical model. Gao et al. [3] developed the 2.5D FEM theory of saturated soil based on the Biot theory, and the vibration and vibration isolation of saturated soil foundation are analyzed. Bian et al. [4] presented a dynamic analysis model comprising track, embankment and layered ground based on the 2.5D finite elements combining with thin-layer elements to predict vibrations generated by train moving loads. Huang et al. [5] considered the influence of railway irregularity and analyzed the soil vibrations caused by subway trains based on the 2.5D FEM.

Generally, the vibration isolation effect of in-filled trench depends on the frequency range of vibration, the dynamic foundation is usually a single-frequency vibration source, and a good vibration isolation effect can be more easily achieved. However, the frequency range of the ground vibration caused by train dynamic load is relatively wide, which depends on the speed of the train running, and there are few researches on in-filled trench isolation under the train load so far. Due to the good effectiveness of vibration isolation of the in-filled trench, it is of vital importance to study the vibration isolation performance of in-filled trench under the train load. In this paper, a train-track-foundation-trench model is developed by FEM, including the track irregularity effects. The vibration isolation effects of in-filled trench under track irregularity are investigated. The results can provide basis in engineering application of the in-filled trench to train-induced vibrations.

Analysis Model

Based on the 2.5D FEM from Ref. [3] to analyze the subgrade and in-filled trench. The train load including the track irregularity is deduced by simplifying the track as an Euler-Bernoulli beam resting on a visco-elastic layered subgrade [6]. The finite element calculation model of the in-filled trench is shown in Fig. 1.

Fig. 1 2.5D FEM model
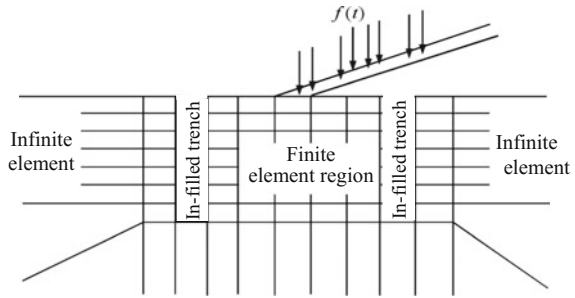
Fig. 2 Time history curve of vertical vibration velocity
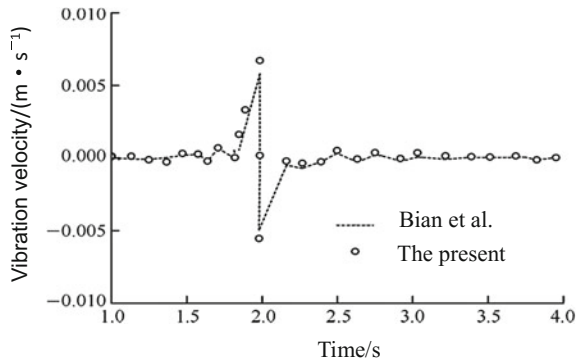
The calculation results are compared with the results from Bian et al. [7]. Figure 2 shows the comparison between the established method and the method of Ref. [7], the two results are in good agreement. Due to considering the track bending displacement's contribution to the displacement of the wheel in the process of deducing the train load, the results are slightly different from Ref. [7].

In-filled Trench Isolation Analysis

In order to analyze the vibration isolation effectiveness of in-filled trench in the layered elastic foundation, in-filled trenches are symmetrically arranged on both sides of the track center. Then the parameters of in-filled trench are analyzed in detail, the parameters here include the width w and depth h of the in-filled trench (Table 1). shows the soil parameters in the model. By using the Rayleigh wave length $(L_R \approx 4.5 \text{ m})$ of the top-layer soil to normalize the size parameters of in-filled trench, the normalized parameters are $w^* = w/L_R, h^* = h/L_R$.

The track is simplified as an Euler beam resting on the layered ground, the width is 3 m. CRH3 is used as the train model which consists of 8 cars, including 4 motor-cars and 4 trailers, and the MTM + T + T + MTM is the organization form. The total length of the train is 200 m, the length of the head car is 25.675 m, and

Table 1 Calculation parameters of layered ground

Soil layer number	Thickness (m)	Shear wave velocity (m s^{-1})	Density (kg m^{-3})	Poisson's ratio	Damping ratio
1	2	95	1500	0.35	0.05
2	2	150	1700	0.30	0.05
3	26	280	1800	0.25	0.05

the length of the intermediate vehicle is 24.775 m. There are 32 wheels, the bogie pivot pitch is 17.375 m, and the fixed axle spacing is 2.5 m. The axle load is 17,000 kg, and the mass of vehicle body, bogie and wheels are 40,000, 3200, and 2400 kg, respectively. The stiffness and damping of the primary and secondary spring are 2.08×10^6 N m^{-1} and 1.0×10^5 N s m^{-1}, 0.8×10^6 N m^{-1} and 1.2×10^5 N s m^{-1}, respectively. The train speeds considered are 300 and 350 km/h, which represents the normal and high speed.

When analyzing the effects of one parameter of the model, the other parameters are constants. The attenuation coefficient proposed by Woods are used to evaluate the ground vibration isolation effectiveness [8].

$$A_R = \frac{the\ surface\ displacement\ amplitude\ with\ WIB}{the\ surface\ displacement\ amplitude\ without\ WIB} \tag{1}$$

The Influence of the Width w* of the in-Filled Trench

To analyze the influence of the width of the in-filled trench on vibration isolation effectiveness, the depth of the in-filled trench is fixed as 2.0000, and the filling material is concrete. The width of the in-filled trench is 0.2222, 0.4444, 0.6667, 1.3333 and 2.0000, respectively. The vibration isolation effects of in-filled trenches with different widths in layered ground measured at different distances from the center of track are shown in Fig. 3.
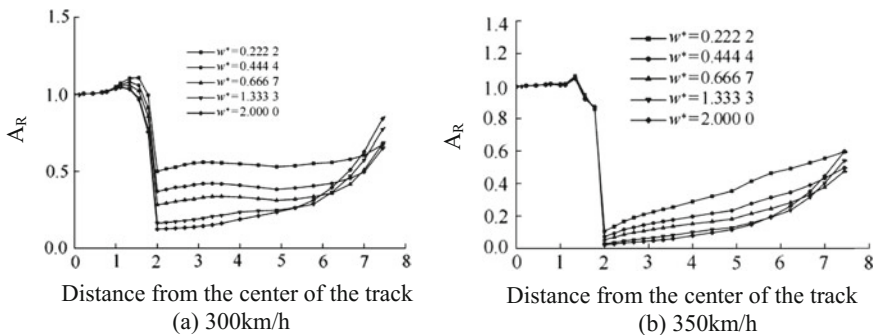
Fig. 3 Influence of in-filled trench width on screening under different train speeds

It can be seen that the in-filled trench can effectively reduce the ground vibration. A wider in-filled trench leads to a better vibration isolation performance. With the increase of the train running speed, the range of the vibration isolation area increases and the vibration isolation effect promoted as well. When the train runs at a low speed, the stress wave will have a certain degree of attenuation due to the damping effect of soil, and when the train runs at a high speed, a longer wavelength of Rayleigh wave will be produced in the soil surface, and carry large amounts of energy in the dissemination process. Due to the slow attenuation of Rayleigh wave in the soil surface, the damping effect of soil is not obvious. Therefore, the higher train speed and the wider isolation trench are, the better effect of vibration isolation will be.

The Influence of the Depth h* of the In-filled Trench

Taking constant width value as $w^* = 0.1111$, and the filling material concrete, the depth h^* of the in-filled trench is set as 0.1111, 0.2222, 0.6667, 1.3333, 2.0000, respectively. The isolation effect of in-filled trench under different train speeds are shown in Fig. 4. From Fig. 4, it is observed that in-filled trench exhibit better vibration mitigation performance under higher train speed. Under the two speeds, vibrations both increased before reaching the trench due to the reflection of stress wave. The deeper in-filled trench is the more difficult for stress wave to bypass the trench, the reflection phenomenon is more obvious, and the vibration displacement of soil before trench is greater. Setting in-filled trench can effectively inhibit stress wave diffraction, and there is a good vibration isolation effect in the area behind the trench. The vibration isolation effect and the vibration isolation range can be improved by appropriately increasing the depth of the in-filled trench. Moreover, the in-filled trench will cause vibration amplification in the front of the trench, the
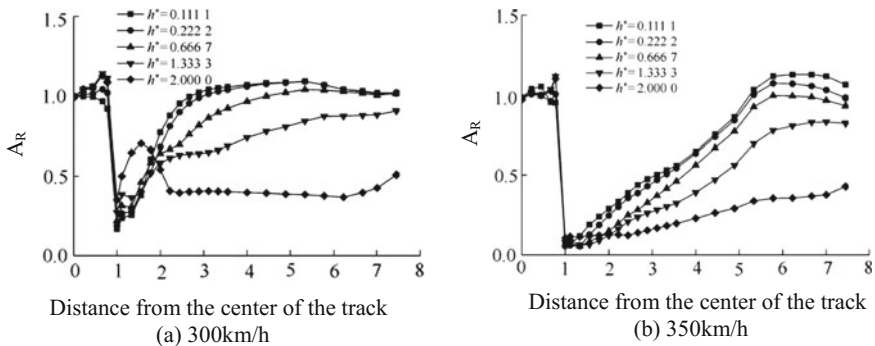
Fig. 4 Influence of in-filled trench depth on screening under different train speeds

deeper trench is, and the more obvious vibration amplification effect will be. Therefore, the influence on the construction before the trench should be considered when setting the in-filled trench.

Conclusions

In this paper, dynamic train load considering the track irregularity was deduced. Based on the 2.5D FEM, the vibration isolation effect of in-filled trench under track irregularity is analyzed. The results show that the screening effectiveness of in-filled trench is better when the train runs at a high speed than that at a low speed. Increasing the depth and width of the in-filled trench can improve the screening effectiveness. Moreover, the in-filled trench causes vibration amplifications in the front of the trench, and the deeper the trench is, the more significant vibration amplification effect will be. Therefore, the influence on the buildings that in front of the trench should be considered when setting the in-filled trench.

References

1. Saikia, A. (2016). Numerical investigation on vibration isolation by softer in-filled trench barriers. Journal of Geo-Engineering Sciences, 6 (3): 31–42.
2. Chang, C.H., Sheng, H.N. (2013). The horizontal amplitude screening effects of a rectangular strip in-filled trench. Journal of the Chinese Institute of Engineers, 36(7):932–9.
3. Gao, GY., He, J.F., Li, N., Yang, C.W. (2011). Analysis of isolating ground Vibration induced by trains running on saturated ground. Journal of Rock and Soil Mechanics, 32(7):2191–2198 (in Chinese).
4. Bian, X.C., Cheng, C., Jiang, J.Q., Chen, R.P., Chen, Y.M. (2014). Numericalanalysis of soil vibrations due to trains moving at critical speed. Journal of Acta Geotechnica, 11(2):281–294.
5. Huang, H.H., Chen, G.H., Yang, Y.B. (2013). Effect of railway roughness on soil vibrations due to moving trains by 2.5D finite/infinite element approach. Journal of Engineering Structures, 57(1):254–266.
6. Chen, G.Q. (2015). Ground vibration analysis induced by high-speed train based on in-situ data. Chinese Journal of Rock Mechanics and Engineering, 34(3):601–611 (in Chinese).
7. Bian, X.C., Chao, C., Jin, W.F. (2011). A 2.5D finite element approach for predicting ground vibrations generated by vertical track irregularities. Journal of Zhejiang University:Applied Physics and Engineering, 12(12):885–894.
8. Woods, R.D. Screening of surface waves in soils. Journal of Soil Mechanics Foundation Engineering Div., ASCE, 1968, 94 (4):951–79.

Computation Model for Structure-Borne Noise from Railway Bridge with CLD

Quanmin Liu, Xiaozhen Li and Xun Zhang

Introduction

The wayside sound pressure level induced by running trains from steel or composite bridge is frequently higher about 5–20 dB than that from plain track [1]. One of the reasons causing this phenomenon is the addition of a new source, i.e. structure-borne noise emitting from bridge. If the sound pressure level around the railway bridge is needed to be reduced, the structure-borne noise radiated by steel beams must be suppressed. Kerwin [2] firstly presented a constrained layer damping (CLD) configuration where a constrained layer with high Young's modulus is adhered to the surface of the damping layer, so that the shear deformation occurs in the damping core. CLD is very effective to reduce vibration and noise of thin-walled structure with the flexural vibration. Treatment of additional damping can be implemented either in the construction process of structure, or after the structure construction is completed. CLD with high damping over a wide frequency range is suitable for reducing vibration and noise from railway steel-concrete composite bridge.

Q. Liu (✉)
Engineering Research Center of Railway Environmental Vibration
and Noise of the Ministry of Education, East China Jiaotong University,
Nanchang 330013, China
e-mail: qmlau007@126.com

X. Li · X. Zhang
Department of Bridge Engineering, Southwest Jiaotong University,
Chengdu 610031, China
e-mail: xzhli@swjtu.edu.cn

X. Zhang
e-mail: zhxunxun@126.com

CLD is widely used to control vibration and noise in automobiles, satellites, ships, railway rails and train wheels [3, 4]. Hanel and Seeger [5] carried out full-scale structure-borne sound damping tests on two steel box girder railway bridges using three-layer sandwich plates as the sound-damping material and found that the average sound pressure levels from bridge I and bridge II were reduced by 13 dB and 18 dB. Wilson and Kirschner [6] reported that CLD can reduce the vibration level of web and bottom slab by 9–12 dB above 50 Hz, and reduce low-frequency noise by 6–9 dB in field test. Koller et al. [7] found that CLD on the bridge web reduced the overall noise by 0–1.5 dB.

Currently there is just a small amount of literatures all over the world reporting the experimental studies using CLD to suppress vibration and noise from bridges, and it is short of theoretical methods and cases applying CLD for vibration and noise control of bridge structures. Moreover theoretical analysis of CLD is concentrated on simple and regular structures, such as beams with uniform section, plates, shells and so on. Vibration and noise from small structure with CLD could be directly derived by using the analytical method or finite element method, but for the actual bridge structure which is complicated and large-scale, it is not available to employ traditional methods to carry out theoretical analysis on CLD bridge. Existed theoretical studies of vibration and noise from CLD structure are mainly concerning on the first several modal loss factors of structure, which is not enough to analyze the change of structure-borne vibration and noise. Therefore, the establishment of theoretical method on applying CLD to reduce vibration and noise of railway bridge is very urgent. A theoretical method to analyze vibration and noise from railway composite bridge with CLD is proposed. Then a case study applying CLD to reduce vibration and noise from a (32 + 40 + 32) m steel-concrete composite bridge is conducted in this paper.

Establishment of Computation Model

Combining train-track-bridge coupled vibration, modal strain energy (MSE) with statistical energy analysis (SEA), a prediction method on the bridge structure-borne noise induced by running train is proposed. There is no precedent using the SEA method to study CLD structure, and this article attempts to employ SEA for the vibration and noise analysis of railway steel-concrete composite bridge with CLD.

It is assumed that only damping loss factor of subsystem with CLD is changed. Firstly, the vibration energy of bridge deck is obtained by train-track-bridge coupled vibration calculation. Secondly, power balance equations of bridge subsystems in SEA are listed, substituting the vibrational energy of the bridge deck and the damping loss factor of CLD subsystem determined by MSE method into the equations, so the transmit results of vibratory energy among various bridge subsystems are obtained by solving the power balance equations. Finally, the structure-borne noise from the bridge is achieved according to the obtained vibratory energy of bridge subsystems and vibro-acoustic theory. The effect of CLD

is simulated by the change of damping loss factors in SEA and frequency dependent loss factor and shear modulus of viscoelastic material in damping layer are adopted when the vibration and noise of CLD bridge is calculated.

In fact, not only the structural damping is increased, but also the acoustic radiation efficiency of the structure is altered after CLD is installed on the surface of the structure. Research in literature [8] presents that CLD is capable of increasing the radiation efficiency of the structure, but the increment of radiation efficiency is quite little. When vibration and noise reducing effect of CLD is analyzed using SEA, the alternation of CLD on radiation efficiency is omitted in this paper. CLD has the effects of add-on damping and acoustic insulation to reduce vibration and noise, but the former is predominant, so only its damping effect is taken into account in this paper. CLD is capable of changing the local vibration and the sound radiation from steel plates of bridge, while the mass and stiffness of CLD are quite small compared with those of bridge itself. The influence of CLD on the natural frequency of bridge can be ignored. Because the large stiffness of the bridge structure and the small density of the air medium, the interaction between the structure and the sound is weak and the coupling effect between the structure and the air can be neglected.

Train-Track-Bridge Coupled Vibration

The train model is established based on the multi-body system dynamics. The ballast track composed of rail, fastener, rail pad, sleeper and ballast is modeled as discretely supported three-layer system considering the degrees of the rail, the sleeper and the ballast. The dynamic bridge model is established by employing FEM. The damping of the bridge is assumed to be Rayleigh damping. The damping ratio of the bridge is assigned as constant 0.01 in train-track-bridge coupled vibration calculation.

The track irregularity is considered as the source of self-excitation. The train subsystem, the track subsystem and the bridge subsystem are coupled by the wheel/rail and the track/bridge interactions. In this paper, the track/bridge interaction is discretised into a series of point-to-point interactions which are connected with linear spring and damping element at each contact point. The integration time step is 0.0001 s. The details of train-track-bridge coupled vibration calculation are found in [9].

MSE Method

According to the MSE theory, it is thought that the ratio between modal loss factor and viscoelastic damping material loss factor can be approximated by the ratio

between the strain energy of viscoelastic core and the total elastic strain energy of the entire structure under a certain modal.

$$\eta = \eta_v \frac{\boldsymbol{\Phi}_R^T \mathcal{K}_{vR} \boldsymbol{\Phi}_R}{\boldsymbol{\Phi}_R^T (\mathcal{K}_e + \mathcal{K}_{vR}) \boldsymbol{\Phi}_R} \tag{1}$$

where η denotes the modal loss factor, η_v denotes the material loss factor, $\boldsymbol{\Phi}_R$ denotes the real part of the complex mode shape, $\boldsymbol{K}_e$ denotes the stiffness matrix of base plate and constrained sheet and $\boldsymbol{K}_{vR}$ denotes the real part of the damping layer's stiffness matrix. The MSE theory is an approximate method omitting the influence of viscoelastic damping material hysteresis on the structural vibration mode, and it is thought that the modal of the damping system can be approximated by the real modal of the corresponding non-damping system.

SEA Method

By applying SEA to predict the average vibration in various frequency bands generated by a complex structure, the bridge should be divided into structural subsystems according to similar natural modal groups and boundary condition. If the structure has enough modal number in the analysis frequency bands, equipartition of energy among modes within a subsystem is assumed reasonably. Additionally, it is assumed that the energy is uniformly distributed within each subsystem. The power balance equations are derived by making out the relationship among storage energy, dissipated energy and the transmitting energy between subsystems [10]. Assuming that a linear system consisting of n coupled subsystems is conservative, the power balance equations are expressed as

$$\omega \begin{pmatrix} \eta_1 + \sum_{i \neq 1} \eta_{1i} & \cdots & -\eta_{k1} & \cdots & -\eta_{n1} \\ \vdots & \ddots & \vdots & \ddots & \vdots \\ -\eta_{1k} & \cdots & \eta_k + \sum_{i \neq k} \eta_{ki} & \cdots & -\eta_{nk} \\ \vdots & \vdots & \vdots & \ddots & \vdots \\ -\eta_{1n} & \cdots & -\eta_{kn} & \cdots & \eta_n + \sum_{i \neq n} \eta_{ni} \end{pmatrix} \begin{pmatrix} E_1 \\ \vdots \\ E_k \\ \vdots \\ E_n \end{pmatrix} = \begin{pmatrix} P_1 \\ \vdots \\ P_k \\ \vdots \\ P_n \end{pmatrix} \tag{2}$$

where ω is the center frequency of the band, η_i represents the damping loss factor of subsystem i, η_{ij} denotes the coupling loss factor from subsystem i to j, P_i is the input power of subsystem i, E_i is the vibratory energy of subsystem i. The first k subsystems are the bridge deck and their vibratory energies E_1, E_2, ..., E_k are derived from the train–track–bridge coupled analysis.

For the last n–k subsystems which do not contact with the track, their outer input power of P_{k+1}, P_{k+2}, …, P_n is 0 and their vibratory energies E_i are derived by solving Eq. (2) which is n-dimensional linear algebraic equations with n unknown variables, and then the mean–square velocity $\langle v^2 \rangle$ of each subsystem is obtained.

Computation Method for Radiated Noise

In order to calculate the noise emission, each subsystem of a composite bridge can be considered as a rectangular sound board of $a \times b$ ($a < b$). The radiated sound power of plate subsystem i with mean–square velocity $\langle v_i^2 \rangle$ can be expressed as

$$W_i = \rho_0 c_0 \sigma_i S_i \langle v_i^2 \rangle \tag{3}$$

where ρ_0 and c_0 denote the air density and the sound speed in air respectively, σ_i and S_i are the radiation efficiency and area of plate subsystem i respectively. Radiation efficiency for a flat plate is determined by [11].

According to the simplified method above, subsystems of the bridge will be treated as a series of simple sound sources considering the distance from subsystems to the field point P. Superposition principle is applied to the sound radiated by the multiple subsystems (i.e. sound sources). Neglecting the influence of directivity. The overall sound pressure at field point P can be expressed as

$$\langle p^2 \rangle = \rho_0 c_0 \sum_i \frac{W_i}{A_i} G_i \tag{4}$$

where A denotes the cross-sectional area through which the energy radiated by the subsystem is assumed to flow, G_i is the influence coefficient due to ground reflection. There is usually hard pavement under the railway viaduct in urban area, and thus the ground reflection effect should be considered. According to the conclusions reported in [12], G_i is set as a constant value 2 and it is applied in our study.

The Computation Results

The measured track irregularities with wavelength of 1–50 m are employed in this paper. At the same time, the vertical track irregularities with short wavelength of 0.01–1 m should also be taken into account. Sato's roughness spectrum [13] which presented combined wheel/rail surface roughness is adopted here. The excitation frequency is 1.1–5555.6 Hz at the train speed of 200 km/h, which covers the dominant frequency range of bridge-borne noise.

The computed running speed of the train is 200 km/h and the 16-vehicle formation is 2(M + M + M + T + M + M + T + T) (M means motor car and T means Trailer). In the numerical simulation, the train runs on the track close to the field point. The bridge deck response obtained from train–track–bridge coupled vibration analysis is converted to frequency domain using FFT.

The shear modulus and the loss factor of viscoelastic damping material are the main indicators evaluating energy dissipation characteristics. Figure 1 shows the storage shear modulus and the material loss factor curves of the viscoelastic damping material versus frequency at 20 °C.

Owing to the steel plate itself damping is too weak, the steel structure subjected to dynamic loads is prone to generate excessive vibration and noise. The initial damping loss factor of 24 mm thick steel plate is set as 0.001. The damping loss factor of steel plate is increased to 0.006–0.03 by installing CLD, so it is concluded that CLD is able to increase the damping loss factor of the bridge steel web obviously. It is the significant increase of the damping loss factor leading to the obvious increase of the dissipation energy. Thus the reduction effect of vibration and noise is achieved when the steel web of bridge is vibrating.

The comparison of vibration before and after installing CLD is displayed in Fig. 2 indicating that the structure vibration has a decreasing trend with the frequency increasing. After CLD is attached, the vibration of the structure is significantly reduced. The vibration velocity levels of stringer web and bottom flange are reduced by 10.5 and 6.1 dB respectively, indicating that CLD can reduce the vibration of the bridge with thin-walled steel plate effectively. CLD can achieve an effective reduction of vibration and noise in broad frequency band, and has a good application prospect in the suppression of bridge structure-borne noise.

Field point M is 30 m to the track centerline in horizontal direction and 1.5 m to the ground in vertical direction. Figure 3 shows the comparison of noise at M in the frequency domain before and after the bridge is attached by CLD. It can be found that structure-borne noise over the entire frequency band has been reduced and the sound pressure level is reduced by 4.3 dB(A) after the bridge is attached by CLD,

Fig. 1 Physical properties of viscoelastic material at 20 °C
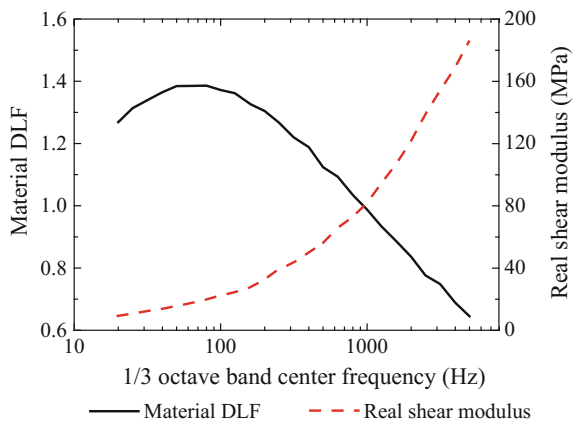
Fig. 2 The comparison of web's vibration velocity level
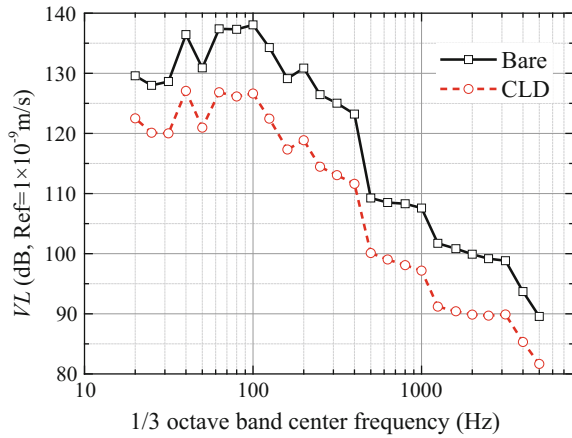
Fig. 3 The comparison of sound pressure level at field point M
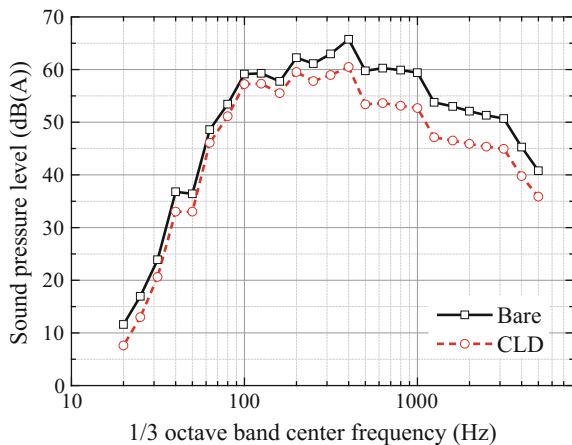
indicating that the treatment with CLD is a very effective measure for reducing the noise from railway composite bridges. Another conclusion can be seen from the figure that CLD is more effective to suppress the high-frequency noise.

Conclusions

In this paper, a prediction method on applying CLD to suppress train-induced vibration and noise from railway steel-concrete composite bridge was proposed. Then a numerical simulation of applying CLD to suppress vibration and noise from a (32 + 40 + 32) m railway composite bridge were carried out. The simulation results are concluded as below.

(1) The vibration and the structure-borne noise have been significantly reduced in the whole frequency band after a (32 + 40 + 32) m steel-concrete composite bridge is attached by CLD.

(2) After the bridge is treated by CLD, vibration velocity levels of steel beam's web and bottom flange achieve the reduction of 10.5 and 6.1 dB, indicating that CLD is capable of reducing vibration and noise from the bridge obviously.

(3) The sound pressure level at field points M is reduced by 4.3 dB(A), so it is concluded that the noise under the side of the bridge is reduced more than that above the side of the bridge.

References

1. Janssens M.H.A. Thompson D.J. (1996). A Calculation Model for the Noise from Steel Railway Bridges. Journal of Sound and Vibration, 193(1): 295–305.
2. Kerwin E.M. (1959). Damping of flexural waves by a constrained viscoelastic layer [J]. Journal of the Acoustical Society of America, 31(7): 952–962.
3. Jones C.J.C. Thompson D.J. (2000). Rolling noise generated by railway wheels with visco-elastic layers. Journal of Sound and Vibration, 231(3): 779–790.
4. He B., Xiao X.B., JIN X.S. Fang J.Y. (2011). Vibro-acoustic Radiation Characteristics Analysis of Railway Vehicle Wheel with Damping Ridges Based on Modal Strain Energy. Chinese Journal of Mechanical Engineering, 24(6): 1056–1067.
5. Hanel J.J. Seeger T. (1978). Full-scale sound damping tests on two steel box girder railway bridges. TRIS, 47(12): 353–361.
6. Wilson G.P. Kirschner F. (2008). Reduction of Noise from Composite/Steel Concrete Aerial Structures by Damping Steel Plates. The Journal of the Acoustical Society of America, 123 (5): 2857–2862.
7. Koller G., Kalivoda M., Jaksch M., Muncke M., Oguchi T. Matsuda Y. (2012). Railway Noise Reduction Technology Using a Damping Material. Noise and Vibration Mitigation for Rail Transportation Systems: 159–166.
8. Foin O., Nicolas J. Atalla N. (1999). An efficient tool for predicting the structural acoustic and vibration response of sandwich plates in light or heavy fluid [J]. Applied Acoustics, 57(3): 213–242.
9. Li, X., Liu, X., Liu, D., Zhang, X. (2013). Influences of Soil-Structure Interaction on Coupled Vibration of Train-Bridge System: Theoretical and Experimental Study. Advances in Structural Engineering, 16(8): 1355–1364.
10. Ver, I. L., Beranek, L. L. (2006). Noise and Vibration Control Engineering: Principles and Applications, John Wiley & Sons, Inc., New Jersey.
11. Thompson D.J. 2009. Railway Noise and Vibration -Mechanisms, Modeling and Means of Control. Elsevier Ltd, Oxford.
12. Remington, P. J., Wittig, L. E. (1985). Prediction of the Effectiveness of Noise Control Treatments in Urban Rail Elevated Structures. The Journal of the Acoustical Society of America, 78(6): 2017–2033.
13. Sato, Y. (1977). Study on high-frequency vibration in track operation with high-speed trains. Japanese National Railways.

Comparison of Crane Induced Vibration on Steel Structural Levels in High-Tech Factories Using FEA and Experiments

S.H. Ju, H.H. Kuo and S.W. Yu

Introduction

The equipment in high-tech factories needs to meet very strict micro-vibration criteria, while moving cranes transporting the high-tech product on factory floors are the major source of vibration, but not many researchers focused on this topic. Guo et al. used a hybrid control platform to mitigate the vertical micro-vibration of sensitive equipment installed in high-tech building subjected to vehicle-induced ground motion [1]. Lin et al. proposed a micro vibration mitigation system using viscous dampers for high-tech buildings, and the results showed that the vibration could be effectively captured by the viscous damper and converted to lower frequency-content tremors [2]. Lee et al. explored the vertical floor micro-vibration induced by automated guided vehicles. They reported that the energy-dissipation device is effective in vibration suppression [3]. Wang et al. investigated the seismic behavior of the automation stocker system, and found that the speed type viscous dampers can reduce the acceleration and displacement response of the stocker, and avoid cassette sliding and collision [4]. Lee et al. proposed a simplified sub-structural model to explore the floor micro-vibration induced by automated guided vehicles, and reported that energy dissipation devices can be effective in vibration-mitigation [5].

In this study, the experiment in the clean room of the high-tech factory was performed to measure the vibration induced by the moving crane, and finite element

S.H. Ju (✉) · H.H. Kuo · S.W. Yu
Department of Civil Engineering, National Cheng-Kung University,
Tainan City, Taiwan
e-mail: juju@mail.ncku.edu.tw

H.H. Kuo
e-mail: QQDe1012@hotmail.com

S.W. Yu
e-mail: sam870161@gmail.com

447

results are then compared with those experimental results to study the accuracy of the numerical model.

Finite Element Model of High-Tech Factories with Moving Cranes

This study analyzed a three-story factory for photovoltaic panels, where the first story is the RC structure with dense columns and the other two are the steel structure with long-span truss frames. Figure 1 shows two typical frames in the X and Y directions, where the RC columns spans in the X and Y directions are 6 and 5.2 m, respectively, and those of steel columns are 12 and 32 m, respectively. The RC waffle slab has the depths of 0.625, 0.55, and 0.45 m for the first to third floors, respectively.

The moving crane shown in Fig. 2 contains four wheels, a loading frame, and a product support. It was modeled as the combination of four moving wheel elements with lumped mass for wheels, four three-direction spring-damper elements for the loading frame, and a lumped mass for the product support. The crane moves on the railway system with a distance of 46 m, while the crane velocity is shown in Fig. 2. The finite element models for the above elements are similar to those in the literature [6], and they are briefly explained in this section. For the moving wheel element, the three-node element stiffness for the nodal displacements $(d1, \theta_1, d2, d3, \theta_3)$, is as follows:
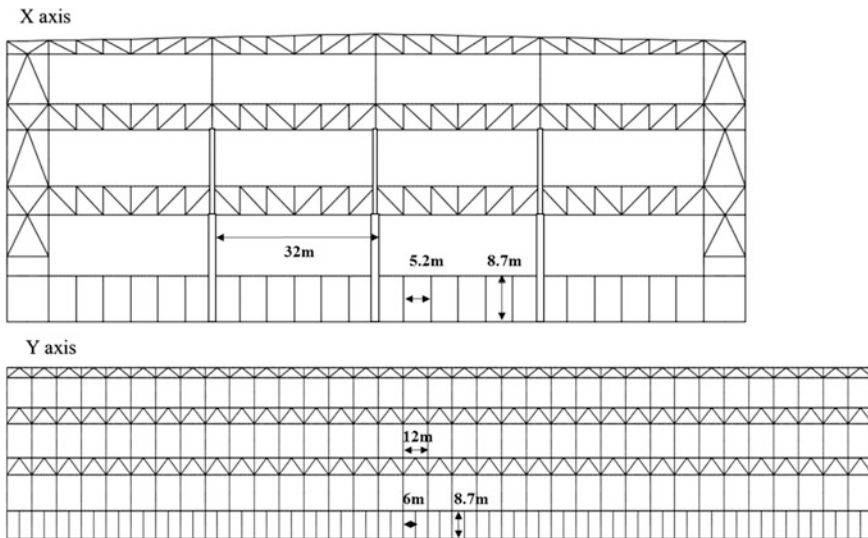
Fig. 1 Two typical frames of the high-tech factory in the X and Y directions
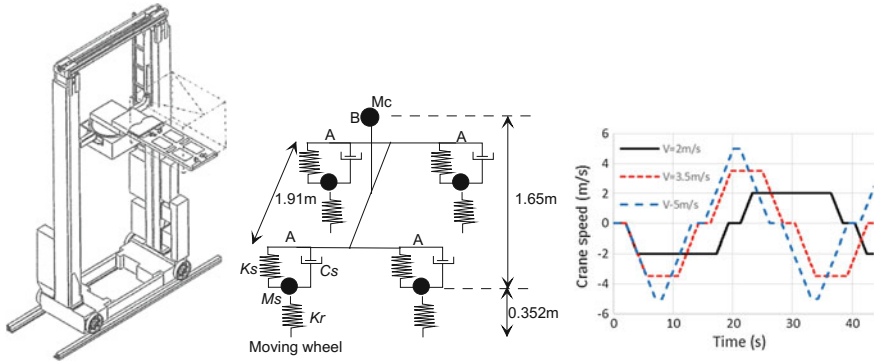
Fig. 2 Dimensions, speed, and finite element model of the moving crane used in this study (Mc = 2t, Ms = 0.9 t, Kr = 0.44E5 kN/m, Ks = 1.2E5 kN/m, Cs = 1 kN-s/m)

$$S = T^T \begin{bmatrix} k_r & -k_r \\ -k_r & k_r \end{bmatrix} T, \quad T = \begin{bmatrix} 0 & 0 & 1 & 0 & 0 \\ N_1 & N_2 & 0 & N_3 & N_4 \end{bmatrix} \tag{1}$$

where d1, θ_1, d3 and θ_3 are the translations and rotations at target nodes 1 and 3, d2 is the translation of the wheel node, Ni = the cubic Hermitian interpolation functions, and kr is the stiffness between the rail and wheel. The internal forces of the wheel elements are:

$$\begin{aligned} [f_1 \quad m_1 \quad f_2 \quad f_3 \quad m_3]^T &= \mathbf{S}[d_1 \quad \theta_1 \quad d_2 \quad d_3 \quad \theta_3]^T \\ &- [N_1 \quad N_2 \quad -1 \quad N_3 \quad N_4]k_r r_v(X) \end{aligned} \tag{2}$$

where (f1, m1, f2, f3, m3) are internal forces and moments at nodes 1, 2 and 3, and the nodal forces should exclude the terms of rail irregularities $r_v(X)$, which are modeled using the reference [7]. The rail irregularity has an amplitude of 1.5 mm per 10 m of the rail in the vertical and transverse directions of the rail, and the irregularity parameters are shown in Table 1 for both directions. For a spring or damper connected to two master nodes, the stiffness or damping matrix is:

$$S = sBB^T \tag{3}$$

where s is the spring constant for the stiffness matrix **S**, or the damping constant for damping matrix **S**, and **B** is a vector generated from the coordinate difference between the master and spring-damper nodes.

Table 1 Rail irregularity parameters used in the numerical analyses

A_r (m^2 rad/m)	ω_1 (rad/m)	ω_2 (rad/m)	ω_l (rad/m)	ω_u (rad/m)	N
A_{r0} = 0.6E−7	0.0	2.1	0.08	150	2000
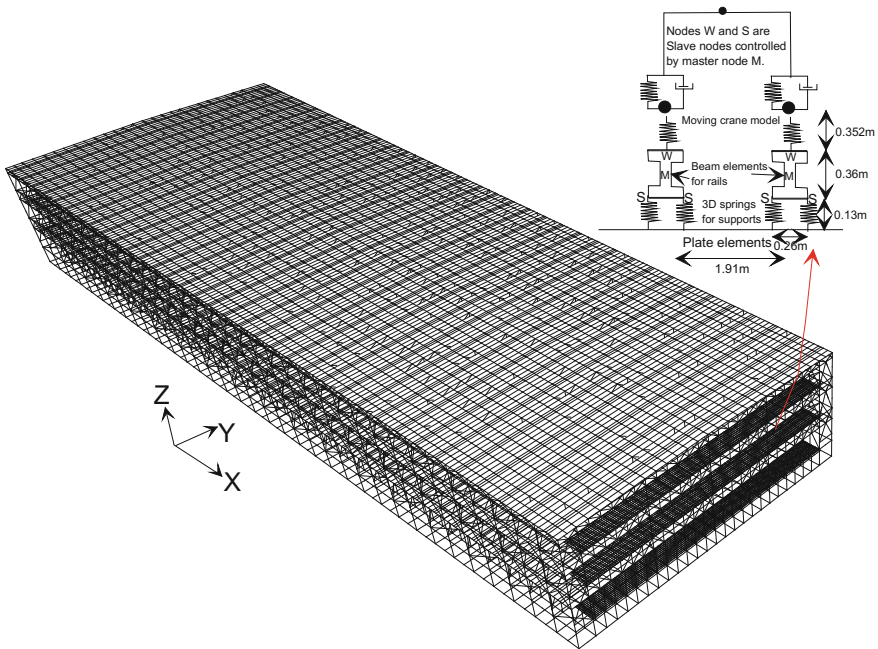
Fig. 3 Finite element model including the high-tech factory, rails, crane, and slabs

Figure 3 shows the finite element mesh, including the high-tech factory, rail system, crane, and waffle slabs, where the total number of degrees of freedom is 1,605,894. The beams, columns, and trusses are modeled using the 2-node 3D beam element with the shear deformation effect, and the end released function is used to simulate the truss member. The waffle slab is simulated using the 2-node 3D beam element, with a width of 0.4-m and a 0.18-m rigid zone at both ends of the element. The slabs at the bottom levels of the trusses on the second and third stories are modeled using 4-node plate elements. The rail system, located at the 2nd floor, contains two steel rails, which are modeled using 2-node 3D beam elements, and the spring-damper element with the stiffness of 4.8E5 kN/m and the damping of 10 kN-s/m is used to simulate the support between rails and slabs, where the interval of the supports is 1.3 m. Then, the crane model can move on the rail system connected to the high-tech structure. The average acceleration Newmark method, and the consistent mass scheme are used to solve this problem, where the time step length is 0.005 s, with 10,000 time steps being simulated.

Comparisons Using Finite Element and Experimental Results

The vibration standard of the one-third octave band in high-tech factories is used in this paper [8]. First, the particle velocities at a certain location in the analyzed high-tech building were obtained from the finite element analysis or experiment. We selected the time period equal to 8 s, and shifted 1 s to select another 8 s until the last time period was less than 8 s. Computer software was then used to find the maximum 1/3 octave band results for all the time periods.

The experimental station is located at 4.5 m from the rail centerline, and three velocity sensors were set up to measure the X, Y, and Z vibration velocities with a sample rate of 512 Hz. A crane moved the distance of 46 m at the steel structural level with the speed of 2 or 3 m/s (120 or 180 m/min). Computer software picked up the 40-s data for the crane passing over this region to find the one-third octave band vibration due to the field experiment. Since finite element analysis only contains the moving crane loading without the ambient vibration effect, the 600-s ambient vibration data were also obtained before the experiment to calculate the power spectrum density function, which were then added into Eq. (3) of the finite element result to find the vibration dB. The experimental and finite element results of the vertical vibration are shown in Fig. 4 for the 4.5-m station. The figure indicates that the comparisons between the experimental and finite element results are acceptably accurate. The major difference is that the vibration in the finite element results near 8 Hz is overestimated, and this may be because the rail irregularity data used in Table 1 is not accurate enough. It is noted that the rail irregularities with random angles are not exact but statistical.

Figure 5 shows the particle velocity vibration dB changing with the distance from the rail centerline. This figure indicates that the trend of the vibration decreases with the increase of the distance from the centerline, and the vibration slightly oscillates with the steel truss locations. The vibration is the relatively largest and smallest at the steel truss location and slab center, respectively, but the
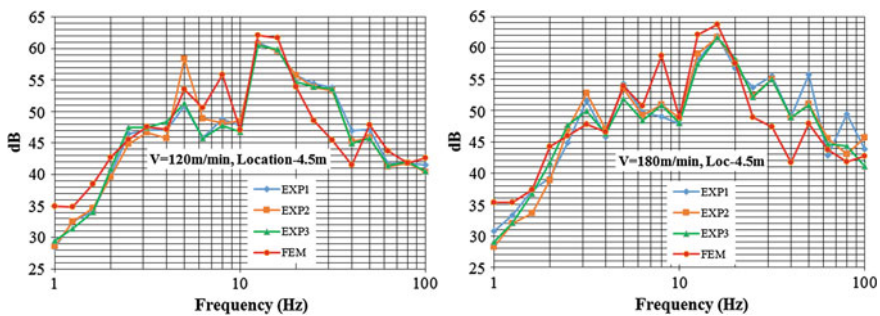
Fig. 4 18 Velocity vibration dB induced by moving crane at the location of 4.5 m from the rail centerline (crane speed = 120 and 180 m/min)

Fig. 5 Particle velocity vibration total dB changing with the distance from the rail centerline
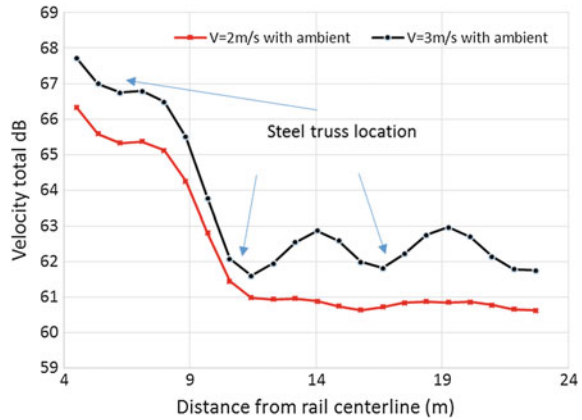
difference of about one dB, as shown in Fig. 5, is considerably small. This means that the stiffness of the long-span steel truss is not enough to largely decrease the crane induced vibration.

Conclusion

This study developed a finite element model to simulate the crane induced vibration of the waffle slabs on the steel structural level of high-tech factories, in which the model contains 3D beam elements to simulate the high-tech structure and rails, spring-damper elements to simulate pads and supports between rails and slab, and moving wheel elements with the lumped mass to simulate the crane. Moreover, rail irregularities are included in the finite element analysis. The finite element results were validated using the experimental measurements, and found to be in good agreement. Therefore, the parametric studies can be performed using this correct finite element model to investigate the vibration behavior in the high-tech factory due to the moving crane, and moreover, the reduction of crane induced vibration can be also achieved.

References

1. Guo, A.X., Xu, Y.L., and Li, H. (2004). Hybrid control of micro-vibration for high technology facilities. Earthquake Engineering and Engineering Vibration, 24(1): 1000–1301.
2. Lin, T.K., Chen, C.C., and Chang, K.C. (2009). Mitigation of micro vibration by viscous dampers. Earthquake Engineering and Engineering Vibration, 8(4): 569–582.
3. Lee, C.L., Wang, Y.P., and Su, R.K.L. (2012). A study on AGV-induced floor micro-vibration in TFT-LCD high-technology fabs. Structural Control and Health Monitoring, 19(3): 451–471.

4. Wang, J.C., Hwang, J.S., and Lin, W.J. (2013). Shockproof Experimental Study of Automated Stocker System in the High-Tech Factory. Open Journal of Earthquake Research, 2: 47–59.
5. Lee, C.L., Wang, Y.P., and Su, R.K.L. (2013). Assessment of vibrations induced in factories by automated guided vehicles. Proceedings of the Institution of Civil Engineers-Structures and Buildings, 166(4): 82–196.
6. Ju, S.H. (2012). Nonlinear analysis of high-speed trains moving on bridges during earthquakes. Journal of Nonlinear Dynamics, 69: 173–183.
7. Au, F.T.K., Wang, J.J., Cheung, Y.K. (2002). Impact study of cable-stayed railway bridges with random rail irregularities. Engineering Structures, 24(5): 529–541.
8. Gordon, C.G. (1991). Generic criteria for vibration sensitive equipment. Optics and Metrology, 1619: 71–75.

The Analysis of Unsaturated Ground Vibration Induced by Train Loading by 2.5D FEM

Shaoyi Li

Introduction

The ground vibration caused by high speed train can endanger the safety of vicinity structures or interfere the operation of precision devices. Ways of controlling environmental vibration induced by rail line attract considerable attentions from engineers and researchers. In China and around the world many research papers focus on ground vibration on saturated subgrade. Methods such as analytic method, semi-analytic method and FEM numerical method are used to investigate the ground vibration on both elastic and saturated ground and the propagation and isolation of ground vibration. Furthermore, some researchers take transversely isotropic characteristics of saturated soil into consideration.

Huangyi et al. [1], Jinbo [2] solved the Biot dynamic equations for two phases porous medium by integral transform to study the dynamic responses of beams and saturated half space under high speed train loading. Cao and Bostran [3] used semi-analytic numerical method to study the influence of train speed on saturated ground vibration. Cai yuanqiang et al. [4], Cao zhigang et al. [5, 6] used semi-analytic method to study vibration of the whole rail system that combined by train, track and saturated ground. Cai yuanqiang et al. [7, 8] used Fourier transform to solve the fundamental dynamic equations of saturated soil to study the influence of track stiffness on saturated ground vibration. Sun honglei et al. [9] used analytic method to study the dynamic responses of track and layered subgrade.

Gao guangyun et al. [10] used thin layer method (TLM) to solve Biot equations to study ground vibration on layered saturated subgrade under train loading. Gao et al. [11–13] used 2.5D FEM to investigate dynamic response of layered saturated subgrade under moving loading. Yuan wan et al. [14] used 2.5D FEM to study

S. Li (✉)
Department of Engineering Institute, Shanghai Construction
No.1 (Group) Co., Ltd., Shanghai, China
e-mail: greatlsy@163.com

455

vibration isolation of empty trench in homogeneous saturated subgrade, layered saturated subgrade and elastic superstratum over saturated subgrade.

Li liang et al. [15, 16] used explicit FEM in time domain to study the wave propagation in transversely isotropic saturated ground. Zhu yanzhi et al. [17], Ye junneng [18], Li jia et al. [19], Sun hong-lei et al. [20], Cai yuanqiang et al. [21] used Biot wave equation and transversely isotropic constitutive relation to study the dynamic response of layered ground.

Despite of the abundant papers on fully saturated ground vibration, the researches on the propagation and mitigation of vibration wave in unsaturated soil is developing. Rihcart et al. [22] used experiments to study influence of air on wave propagation in unsaturated soil, and found differences between unsaturated soil and saturated one.

Yang jun et al. [23–26] investigated the transmission and reflection of wave in unsaturated layered soil, and discussed the influence of saturation on wave propagation. Vardoulkais and Beskos [27] deduced wave equations for unsaturated porous medium by three phase model. Lo [28–30] built wave equations for unsaturated porous medium with a soil-water characteristic curve (SWCC) described by VG model. Huang yi et al. [31, 32] investigated the constitutive relation equations and the dynamic equations for unsaturated porous medium. Li baozhong and Cai yuanqiang [33] studied the propagation of elastic wave in transversely isotropic unsaturated soil and discussed the influence of soil saturation. Xu changjie and Shi yanyong [34] studied the wave propagation in unsaturated soil. Yang [35] investigated the saturation of soil, the angle and frequency of input SV wave and found the saturation of soil can notably alter the ratio of ground vibration at horizontal and vertical direction. Ravichandran and Krishnapillai [36] used simplified finite element method to investigate the matric suction and deformation suction for silt and clay under static and dynamic condition. Ye and Jeng [37] used unsaturated numerical model to discuss the dynamic response of coastal embankment under seismic loading. Xu mingjiang and Wei demin [38] used Bishop effective stress equation and VG model to build dynamic governor equations for unsaturated soil and discussed the dynamic responses of half space under surface harmonic loading.

There are two numerical models of unsaturated porous medium used in the above papers. The first is two phases model derives from Biot theory and adopts modified compression modulus of water. The second one is three phases model which takes the movement of air, water and solid respectively into consideration. The distinctions of the two kinds of numerical models for unsaturated medium are seldom reported and requires detailed investigation to clarify the characteristics and applicability for each model. This paper uses 2.5D FEM to build numerical model of unsaturated subgrade by the two kinds of models to discuss their differences on simulating ground vibration and to investigate the ground vibration of unsaturated ground. Finally the unsaturated ground vibration on layered subgrade is studied.

Numerical Model

2.5D Finite Element Method

The properties and distribution of track and subgrade are assumed to be continuous and uniform at the direction of moving train in 2.5D FE model. So the wave number expansion can be used at train moving direction to transform the three dimension problem into two dimension. In addition, by applying Fourier transform to the model, the ground vibration problem can be expressed in frequency domain and solved by 2.5D FEM.

The displacement of node in 3D numerical model is assumed as $u(x, y, z, t)$. By applying wave number expansion and Fourier transform, the node displacement in finite element model in wave number and frequency domain can be given as:

$$\tilde{\bar{u}}(\xi_x, y, z, \omega) = \int\limits_{-\infty}^{+\infty} \int\limits_{-\infty}^{+\infty} u(x, y, z, t) e^{i\xi_x x} e^{-i\omega t} dx dt \tag{1}$$

where $\tilde{\bar{u}}(\xi_x, y, z, \omega)$ is the node displacement in frequency and wave number domain, ξ_x is the wave number at train moving direction, ω is the circular frequency.

By Eq. (1), the train-subgrade 3D FE model can be converted into 2D FE model. Then the displacement of 2D FE element node can be solved by FEM and be transformed to time domain by double Fourier transform as:

$$u(x, y, z, t) = \frac{1}{4\pi^2} \int\limits_{-\infty}^{+\infty} \int\limits_{-\infty}^{+\infty} \tilde{\bar{u}}(\xi_x, y, z, \omega) e^{-i\xi_x x} e^{i\omega t} d\xi_x d\omega \tag{2}$$

To take damping coefficient of soil into consideration, the Lame constant in imaginary form is used in 2.5D FEM, the Lame constant can be written [39] as:

$$\bar{\lambda} = (1 + 2i\eta_s)\lambda, \quad \bar{\mu} = (1 + 2i\eta_s)\mu \tag{3}$$

where $\bar{\lambda}$, $\bar{\mu}$ are Lame constants with damping coefficient, η_s is damping coefficient of soil.

Two Phases Unsaturated Model

Deriving from Biot theory of saturated porous medium, the two phases model for unsaturated porous medium can be deduced by introducing modified compression modulus of water which affected by the saturation of soil. The two phases model

scatters air among the water in the form of bubble and simplifies the air and water as mixed fluid.

The displacement of solid skeleton and mixed fluid at i direction can be indicated by vector u_i and w_i, So the relative displacement of mixed fluid to solid skeleton at i direction is $W_i = n(w_i - u_i)$. The equation of motion for porous medium can be given as [11]:

$$\sigma_{ij,j} + F_i = (1 - n)\rho_g \ddot{u}_i + n(S_r\rho_w + S_a\rho_a)\ddot{w}_i = \rho\ddot{u}_i + \rho_f \ddot{W}_i \tag{4}$$

where $\rho = (1 - n)\rho_g + nS_r\rho_w + nS_a\rho_a$, $\rho_f = S_r\rho_w + S_a\rho_a$, ρ_g is density of soil grain, ρ_w is density of water, ρ_a is density of air, ρ_f is density of mixed fluid, n is porosity, S_r is saturation for water, S_a is saturation for air.

Applying Darcy law, the velocity of mixed fluid in porous medium can be given as:

$$-p_{,i} = \rho_f \ddot{u} + \frac{\rho_f}{n}\ddot{W}_i + \frac{\rho_f g}{k_d}\dot{W}_i \tag{5}$$

where k_d is permeability coefficient of mixed fluid.

Applying effective stress principle and the pressure of mixed fluid, the stress-strain relationship for elastic porous medium can be given as:

$$\sigma_{ij} = 2\bar{\mu}\varepsilon_{ij} + \bar{\lambda}\delta_{ij}\varepsilon_{kk} - \delta_{ij}\alpha p_f \tag{6}$$

where ε_{ij} is strain vector, δ_{ij} is Kronecker sign, p_f is pressure of mixed fluid, α is Biot coefficient and $\alpha = 1 - K_{sk}/K_g$, K_{sk} is compression modulus of soil skeleton and K_g is compression modulus of soil grain.

The compression properties of mixed fluid can be given as:

$$-d\varepsilon_f = \frac{d\rho_f}{\rho_f} = \frac{dp_f}{K_f} \tag{7}$$

where K_f is compression modulus of mixed fluid. Researches show that when air uniformly distributes in the pore water as tiny bubbles and moving along with the water, the air and water can be treated as mixed fluid and the compression modulus of mixed fluid can be described as function of the saturation of soil which can be given as [24]:

$$K_f = \frac{1}{\frac{1}{K_w} + \frac{1 - S_r}{p_a}} \tag{8}$$

where K_w is compression modulus of water, P_a is standard atmospheric pressure and equals to 100 kPa.

The continuous equation for porous medium can be given as:

$$-\frac{n}{K_f}\dot{p} = \dot{W}_{i,i} + \dot{u}_{i,i} \tag{9}$$

To use 2.5D FEM of solving wave equations of unsaturated porous medium, Fourier transform is applied to Eq. (5) to obtain the average displacement of mixed fluid which is:

$$W_i = F(\omega^2 \rho_f \tilde{u}_i - \tilde{p}_{,i}) \tag{10}$$

where $F = nk_d/(i\omega\rho_f gn - \omega^2 k_d \rho_f)$, g is gravity acceleration, '$\sim$' is the component in frequency domain.

Applying Fourier transform to Eq. (9), the continuous equation of porous medium in frequency domain can be obtained. Eliminating the relative fluid displacement by Eq. (10), the continuous equation expressed by skeleton displacement and mixed fluid pressure can be written as:

$$-FK_f \tilde{p}_{f,ii} + (\omega^2 \rho_f FK_f + K_f)\tilde{u}_{i,i} + n\tilde{p}_f = 0 \tag{11}$$

Applying compatibility equation, effective stress principle and Fourier transform to Eq. (4), and eliminating the relative displacement of mixed fluid by Eq. (10), the equation of motion for porous medium in frequency domain can be obtained as:

$$\bar{\mu}\tilde{u}_{i,jj} + (\bar{\lambda} + \bar{\mu})\tilde{u}_{i,jj} - \alpha_{ij}\tilde{p}_{f,i} + \omega^2 \rho\tilde{u}_i + \omega^2 \rho_f F(\omega^2 \rho_f \tilde{u}_i - \tilde{p}_{f,i}) = 0 \tag{12}$$

Equations (11) and (12) are the governor equations for unsaturated medium in 2.5D FEM. Solving Eqs. (11) and (12) by finite element method, the displacement and pore pressure can be obtained.

Three Phases Unsaturated Model

The governor equations for unsaturated porous medium is built based on three phases assumption. The unsaturated porous medium is assumed to be combined by solid, water and air, and those components are continuous. The mass conservative equations and momentum conservative equations of solid, water and air are used to deduce the governor equations which requires those following assumptions:

(1) The solid, water and air is continuously and uniformly distributed in unsaturated porous medium and the dimension of each components meet the continuous assumption.
(2) The permeability of water and air meet the Darcy law.

(3) The density of soil grain is determined by pore pressure and volume defor-
   mation, and the density of water and air is function of water and air pressure.

In the region Ω, the mass conservative equations for those three phase can be
given as [40]:

$$\frac{d^{\alpha_m}}{dt} \int_{\Omega} \rho_{\alpha_m} n^{\alpha_m} d\Omega = 0 \Leftrightarrow \frac{d^{\alpha_m}}{dt} \left(\rho_{\alpha_m} n^{\alpha_m} \right) + \rho_{\alpha_m} n^{\alpha_m} \nabla \cdot \mathbf{v}^{\alpha_m} = 0 \qquad (13)$$

where $\alpha_m = s, w, a$ indicate solid phase, fluid phase and air phase respectively, n^{α_m}
is volume ratio of each component which $n^s + n^w + n^a = 1$, ρ_{α_m} is the density of
each component, $\mathbf{v}^{\alpha_m}$ is the velocity of each phase, ∇ is Laplacian operator.

The mass conservative equation for solid can be written as:

$$\frac{\partial}{\partial t} (\rho_s (1 - n)) + \rho_s (1 - n) \nabla \cdot \dot{u} = 0 \qquad (14)$$

where ρ_s is soil grain density, n is porosity, u is displacement of solid grain.

The relationship of grain density and pore pressure can be written as:

$$\frac{1}{\rho_s} \frac{\partial p_c}{\partial t} = \frac{\alpha - n}{K_g} \frac{\partial p_c}{\partial t} - (1 - \alpha) \frac{\partial \varepsilon_s}{\partial t} \qquad (15)$$

where K_g is compression modulus of grain, ε_v is volume deformation, p_c is pore
pressure which $p_c = S_r p^w + (1 - S_r) p^a$, p^w, p^a are pore water pressure and pore air
pressure, S_r is saturation. Substituting Eq. (15) into Eq. (14):

$$\frac{\partial n}{\partial t} = \frac{\alpha - n}{K_g} \frac{\partial (S_r p^w + (1 - S_r) p^a)}{\partial t} + (\alpha - n) \nabla \cdot \dot{u} \qquad (16)$$

The mass conservative equation for water is:

$$\frac{\partial}{\partial t} (\rho_w n S_r) + \rho_w n S_r \nabla \cdot \dot{u}^w = 0 \qquad (17)$$

where ρ_w is water density, u^w is displacement of water. Unfolding Eq. (17), there is:

$$S_r \rho_w \frac{\partial n}{\partial t} + n S_r \frac{\partial \rho_w}{\partial t} + n \rho_w \frac{\partial S_r}{\partial t} + \rho_w n S_r \nabla \cdot \dot{u}^w = 0 \qquad (18)$$

The relationship of water density and pore water pressure can be given as:

$$\frac{d\rho_w}{\rho_w} = \frac{dp^w}{K_w} \qquad (19)$$

where K_w is compression modulus of water. Substituting Eqs. (19) and (16) into Eq. (18):

$$S_r \rho_w \left[\frac{\alpha - n}{K_g} \frac{\partial(S_r p^w + (1 - S_r)p^a)}{\partial t} + (\alpha - n)\nabla \cdot \dot{u} \right]$$
$$+ nS_r \frac{\rho_w}{K_w} \frac{\partial p^w}{\partial t} + n\rho_w \frac{\partial S_r}{\partial t} + \rho_w nS_r \nabla \cdot \dot{u}^w = 0$$
(20)

Equation (20) can be rewritten as:

$$S_r(\alpha - n)\nabla \cdot \dot{u} + nS_r \nabla \cdot \dot{u}^w + \left[\frac{S_r^2(\alpha - n)}{K_g} + \frac{nS_r}{K_w} \right] \frac{\partial p^w}{\partial t} + \frac{S_r(1 - S_r)(\alpha - n)}{K_g} \frac{\partial p^a}{\partial t}$$
$$+ \left(n - \frac{\alpha - n}{K_g} S_r s \right) \frac{\partial S_r}{\partial t} = 0$$
(21)

where s is suction of soil which $s = p^a - p^w$, the relationship of saturation S_r and suction s can be described by soil water characteristics curve (SWCC) which is:

$$S_r = S_r(s) = S_r(p^a - p^w)$$
(22)

Differentiating Eq. (22) by time, there is:

$$\frac{dS_r}{dt} = \frac{dS_r}{ds} \frac{ds}{dt} = \frac{dS_r}{ds} \left(\frac{dp^a}{dt} - \frac{dp^w}{dt} \right)$$
(23)

Substituting Eq. (23) into Eq. (21), there is:

$$A_{11}\dot{p}^w + A_{12}\dot{p}^a + A_{13}\nabla\dot{u} + A_{14}\nabla\dot{u}^w = 0$$
(24)

where $A_{11} \sim A_{14}$ are:

$$A_{11} = \frac{(\alpha - n)S_r^2}{K_g} + \frac{nS_r}{K_w} - A_{ss}\left(n - \frac{(\alpha - n)S_r s}{K_g}\right), A_{12} = \frac{(\alpha - n)S_r(1 - S_r)}{K_g}$$
$$+ A_{ss}\left(n - \frac{(\alpha - n)S_r s}{K_g}\right)$$

$A_{13} = S_r(\alpha - n)$, $A_{14} = nS_r$, which A_{ss} is the derivative of saturation to suction and $A_{ss} = \frac{\partial S_r}{\partial s}$.

The mass conservative equation of air is:

$$\frac{\partial(n(1-S_r)\rho_a)}{\partial t} + n(1-S_r)\rho_a\nabla\cdot\dot{u}^a = 0 \tag{25}$$

where ρ_a is density of air, u^a is displacement of air. Unfolding Eq. (25) there is:

$$(1-S_r)\rho_a\frac{\partial n}{\partial t} + n(1-S_r)\frac{\partial\rho_a}{\partial t} - n\rho_a\frac{\partial S_r}{\partial t} + n(1-S_r)\rho_a\nabla\cdot\dot{u}^a = 0 \tag{26}$$

The relationship of air compression and air pressure is:

$$\frac{d\rho_a}{\rho_a} = \frac{dp^a}{p^a} \tag{27}$$

Substituting Eqs. (16) and (27) into Eq. (26), there is:

$$\begin{aligned}
(1-S_r)\rho_a&\left[\frac{\alpha-n}{K_g}\frac{\partial(S_rp^w+(1-S_r)p^a)}{\partial t} + (\alpha-n)\nabla\cdot\dot{u}\right] \\
&+ n(1-S_r)\frac{\rho_a}{p^a}\frac{\partial p^a}{\partial t} - n\rho_a\frac{\partial S_r}{\partial t} + \rho_an(1-S_r)\nabla\cdot\dot{u}^a = 0
\end{aligned} \tag{28}$$

Equation (28) can be rewritten as:

$$\begin{aligned}
(1-S_r)(\alpha-n)\nabla\cdot\dot{u} &+ n(1-S_r)\nabla\cdot\dot{u}^a + \left[\frac{(1-S_r)^2(\alpha-n)}{K_g} + \frac{n(1-S_r)}{p^a}\right]\frac{\partial p^a}{\partial t} \\
&+ \frac{S_r(1-S_r)(\alpha-n)}{K_g}\frac{\partial p^w}{\partial t} - \left(n+\frac{\alpha-n}{K_g}(1-S_r)s\right)\frac{\partial S_r}{\partial t} = 0
\end{aligned} \tag{29}$$

Substituting Eq. (23) into Eq. (29) there is:

$$A_{21}\dot{p}^w + A_{22}\dot{p}^a + A_{23}\nabla\dot{u} + A_{24}\nabla\dot{u}^a = 0 \tag{30}$$

where parameters $A_{21}\sim A_{24}$ are:

$$A_{21} = \frac{(\alpha-n)S_r(1-S_r)}{K_g} + A_{ss}(n+\frac{(\alpha-n)(1-S_r)s}{K_g}),$$

$$A_{22} = \frac{(\alpha-n)(1-S_r)^2}{K_g} + \frac{n(1-S_r)}{p^a} - A_{ss}(n+\frac{(\alpha-n)(1-S_r)s}{K_g}), A_{23}$$
$$= (1-S_r)(\alpha-n),$$

$$A_{24} = n(1 - S_r).$$

As Darcy law suggests, the movement equations for pore water and air are:

$$nS_r(\dot{u}_i^w - \dot{u}_i) = -\frac{k_w}{\rho_w g}(p_{,i}^w + \rho_w \ddot{u}_i^w) \tag{31}$$

$$n(1 - S_r)(\dot{u}_i^a - \dot{u}_i) = -\frac{k_a}{\rho_a g}(p_{,i}^a + \rho_a \ddot{u}_i^a) \tag{32}$$

Applying Fourier transform to Eqs. (31) and (32), the equation for the average displacement of pore water and pore air are:

$$\tilde{u}_i^w = (F_w \tilde{u}_i - \tilde{p}_{,i}^w)/(F_w - \rho_w \omega^2) \tag{33}$$

$$\tilde{u}_i^a = (F_a \tilde{u}_i - \tilde{p}_{,i}^a)/(F_a - \rho_a \omega^2) \tag{34}$$

where $F_w = nS_r \rho_w g \omega i / k_w$, $F_a = n(1 - S_r)\rho_a g \omega i / k_a$.

Applying Fourier transform to Eqs. (24) and (30), eliminating displacement of pore water and air by Eqs. (33) and (34), the mass conservative equations for water and air can be written as:

$$\left(A_{13} + \frac{A_{14}F_w}{F_w - \rho_w \omega^2}\right)\tilde{u}_{i,i} - \frac{A_{14}}{F_w - \rho_w \omega^2}\tilde{p}_{,ii}^w + A_{11}\tilde{p}^w + A_{12}\tilde{p}^a = 0 \tag{35}$$

$$\left(A_{23} + \frac{A_{24}F_a}{F_a - \rho_a \omega^2}\right)\tilde{u}_{i,i} - \frac{A_{24}}{F_a - \rho_a \omega^2}\tilde{p}_{,ii}^a + A_{21}\tilde{p}^w + A_{22}\tilde{p}^a = 0 \tag{36}$$

The momentum conservative equation of unsaturated porous medium is:

$$\sigma_{ij,j} + F_i = \bar{\rho}_s \ddot{u}_i + \bar{\rho}_w \ddot{u}_i^w + \bar{\rho}_a \ddot{u}_i^a \tag{37}$$

where σ_{ij} and F_i are stress vector and body force vector, $\bar{\rho}_s, \bar{\rho}_w, \bar{\rho}_a$ are the relative density of solid, water and air, which $\bar{\rho}_s = (1 - n)\rho_s$, $\bar{\rho}_w = nS_r \rho_w$, $\bar{\rho}_a = n(1 - S_r)\rho_a$.

Applying effective stress principal for unsaturated porous medium, the elastic constitutive relationship can be given as:

$$\sigma_{ij} = 2\mu\varepsilon_{ij} + \lambda\delta_{ij}\varepsilon_{kk} - \delta_{ij}\alpha p_c \tag{38}$$

where ε_{ij} is strain vector of soil, p_c is pore pressure, which $p_c = S_r p^w + (1 - S_r)p^a$, p^w, p^a are the pore pressure of water and air, S_r is saturation of soil.

Applying Fourier transform to Eq. (37), eliminating displacement item by Eqs. (33) and (34), eliminating stress component by Eq. (38), the momentum conservative equation can be rewritten as:

$$\bar{\mu}\tilde{u}_{i,jj}+(\bar{\lambda}+\bar{\mu})\tilde{u}_{i,ji}-S_r\tilde{p}^w_{,i}-(1-S_r)\tilde{p}^a_{,i}+\omega^2\left[(1-n)\rho_s+\frac{nS_r\rho_wF_w}{F_w-\rho_w\omega^2}+\frac{n(1-S_r)\rho_aF_a}{F_a-\rho_a\omega^2}\right]\tilde{u}_i$$
$$-\frac{\omega^2nS_r\rho_w}{F_w-\rho_w\omega^2}\tilde{p}^w_{,i}-\frac{\omega^2n(1-S_r)\rho_a}{F_a-\rho_a\omega^2}\tilde{p}^a_{,i}=0$$

$$(39)$$

Combining Eqs. (24), (30) and (39), the governor equations for unsaturated porous medium in frequency domain can be obtained.

Train Loading Model

Moving at x direction in the numerical model, the train loading can be written as [39]:

$$P(x,y,z,t) = \sum_{n=1}^{N}\left[P_{n1}\delta(x-V_ct+\sum_{i=0}^{n-1}L_i)+P_{n1}\delta(x-V_ct+\sum_{i=0}^{n-1}L_i+a_n)\right.$$
$$\left.+P_{n2}\delta(x-V_ct+\sum_{i=0}^{n-1}L_i+a_n+b_n)+P_{n2}\delta(x-V_ct+\sum_{i=0}^{n-1}L_i+2a_n+b_n)\right]$$

$$(40)$$

where V_c is train speed, P_{n1} and P_{n2} is front and rear axle weight, L_0 is the distance between the head and the front axle of the first carriage, L_i is the distance of axle between the vicinity carriage, a_n is the distance between the front axles in a carriage and b_n is the distance between the front and rear axles in a carriage, N is the number of carriages.

Applying Fourier transform and wave number expansion to Eq. (40), the train loading in frequency and wave number domain can be written as [39]:

$$\tilde{\tilde{p}}(\xi_x,y,z,\omega) = \frac{2\pi}{V_c}\delta\left(\xi_x-\frac{\omega-\omega_0}{V_c}\right)\chi(\xi_x) \tag{41}$$

where

$$\chi(\xi_x) = \sum_{n=1}^{N-1}\left[P_{n1}\left(1+e^{-ia\xi_x}\right)+P_{n2}\left(e^{-i(a_n+b_n)\xi_x}+e^{-i(2a_n+b_n)\xi_x}\right)\right]e^{-i\sum_{k=0}^{N-1}L_k\xi_x}.$$

Track Model

Euler beam is used to model the track. A moving axle loading can be written as $p_0\delta(x-ct)$, where p_0 is dynamic loading of axle, $\delta(x)$ is Dirac function. Using the

dynamic equation for Euler beam, the equation of track under axle loading can be written as [39]:

$$EI\frac{\partial^4 u_r}{\partial x^4} + m\frac{\partial^2 u_r}{\partial t^2} = f_{IT}(x,t) + p_0\delta(x - ct) \tag{42}$$

where u_r is the displacement of track, EI is the bending stiffness of track, m is the united mass of track and sleepers, $f_{IT}(x,t)$ is the reaction force under the track.

Applying Fourier transform to Eq. (42), the dynamic equation for track in frequency and wave number domain can be written as:

$$(EI\xi_x^4 - m\omega^4)u_r^{xt} = f_{IT}^{xt}(\xi_x, \omega) + p_0^{xt}(\xi_x, \omega) \tag{43}$$

Verification and Discussions

Verification

The in-situ test of X2000 high speed train provides detailed data for the study of ground vibration induced by train loading. The vibration displacement at center of the track of X2000 is used to verify the 2.5D FEM in this paper. The properties of layered subgrade, parameters and dimension of train loading are shown in Tables 1 and 2. The FE numerical model is shown in Fig. 1. The comparison of in-situ test data and numerical simulated results are shown in Fig. 2. Figure 3 suggests the numerical results match the field test data and the 2.5D FEM can simulate the ground vibration.

Table 1 Properties of subgrade [39]

Layered subgrade	Thickness (m)	Density (kg/m³)	Shear velocity (m/s)	Poison ratio
Refilled covering	1.0	1500	72	0.39
Silt	3.0	1260	41	0.35
Clay	4.5	1475	65	0.41
Clay	15.0	1475	87	0.33

Table 2 Distribution and axle loading of train [39]

Carriage number	P_1 (kN)	P_2 (kN)	a (m)	b (m)	L (m)
1	160.5	117.5	2.9	11.6	0.0
2	122.5	122.5	2.9	14.8	22.2
3	122.5	122.5	2.9	14.8	24.4
4	122.5	122.5	2.9	14.8	24.4
5	180.0	181.5	2.9	6.6	24.4
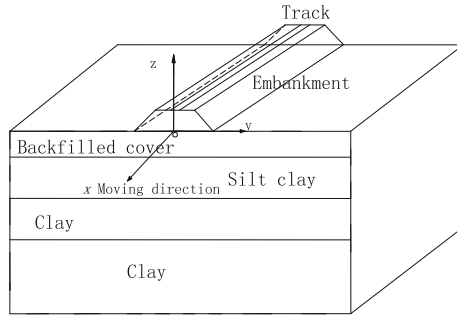
Fig. 1 Model of the subgrade
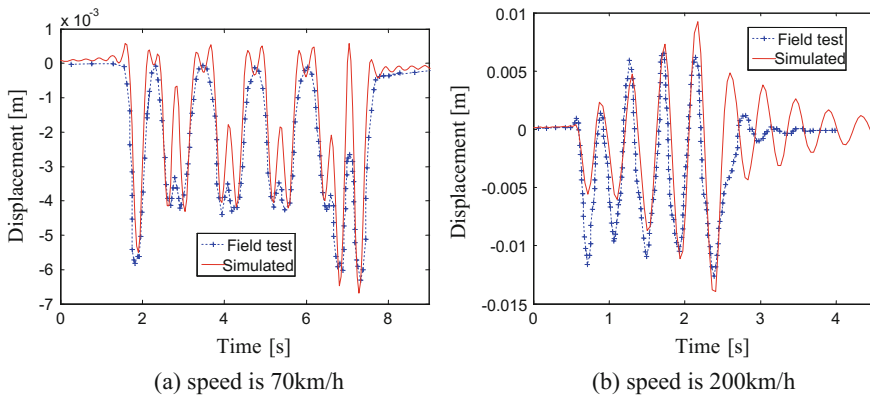
Fig. 2 Verification of 2.5D FEM

Comparison of Two Unsaturated Models

The two unsaturated numerical models are used to investigate the unsaturated ground vibration induced by train loading and to compare the difference between the two models. For the two phases model the parameters are as follow: the permeability coefficient is $k_d=1.0 \times 10^{-6}$ m/s and the compression modulus of water is $K_w=1.5 \times 10^9$ N/m^2. For the three phases numerical model, the VG model is used to simulated the SWCC, which is [38]:

$$S_e = \left[1 + (\alpha_1 s)^k\right]^{-m} \tag{44}$$

where $\alpha_1 = 1 \times 10^{-5}$, $k = 4$, $m = 1 - 1/k$, $S_e = (S_r - S_{wo})/(1 - S_{wo})$, which S_{wo} is irreducible saturation and $S_{wo} = 0.05$, s is the suction of soil.

Fig. 3 Vibration displacement at track center in time domain
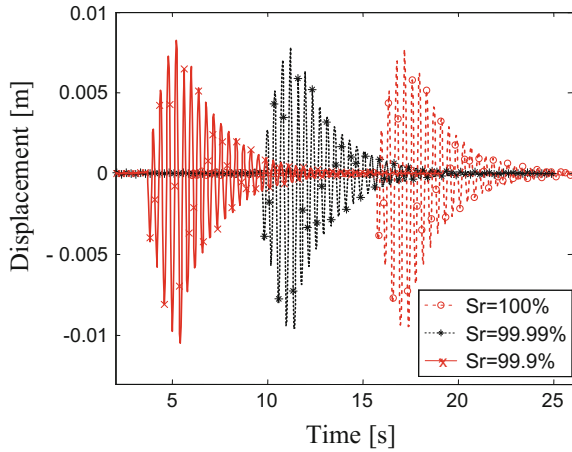
The permeability coefficients of water and air follow the model of Mualem [38], which is:

$$k_w = \frac{\rho_w g \kappa}{\eta_w} \sqrt{S_r}\{1 - [1 - (S_e)^{\frac{1}{m}}]^m\}^2 \tag{45a}$$

$$k_g = \frac{\rho_g g \kappa}{\eta_g} \sqrt{1 - S_r}[1 - (S_e)^{\frac{1}{m}}]^{2m} \tag{45b}$$

where $\eta_w \cdot \eta_g$ are the viscosity coefficient of water and air which $\eta_w = 1.0\,\mathrm{mPa\,s}, \eta_g = 0.015\,\mathrm{mPa\,s}$, κ is the permeability of soil, and $\kappa = 1.0\,\mu m^2$.

In the 2.5D FE model, the layered subgrade is the same as Fig. 1. Track system including track, sleepers and embankment is simulated by Euler beam [40], whose united bending stiffness is $EI=1.4 \times 10^5\,\mathrm{kNm^2}$, and the united mass per unit is $m=1.08 \times 10^4$ kg/m. The following paragraphs compares the results of the two kinds of unsaturated numerical models for different saturation as train speed is 200 km/h.

(1) Two phases model

Figure 3 shows the ground vibration displacement at the center of track simulated by two phases model when the saturation is 100, 99.99 and 99.9%. As figure (a) shows, the peak ground displacement of saturated soil is 9 mm. When the train speed approaches the shear velocity of soil [39], the ground vibration amplitude is amplified. The shear velocity of subgrade is around 200 km/h, so the vibration amplitude for both elastic (Fig. 2b) and saturated (Fig. 3) model is high. While the saturated result is smaller than the elastic one. The pore water bears part of train loading leading to a smaller quota of loading on the soil skeleton and to a smaller ground vibration. When the saturation deceases to 99.9%, the peak amplitude of ground vibration is higher than 9 mm. The vibration amplitude of unsaturated soil

Fig. 4 Vibration acceleration at track center in frequency domain
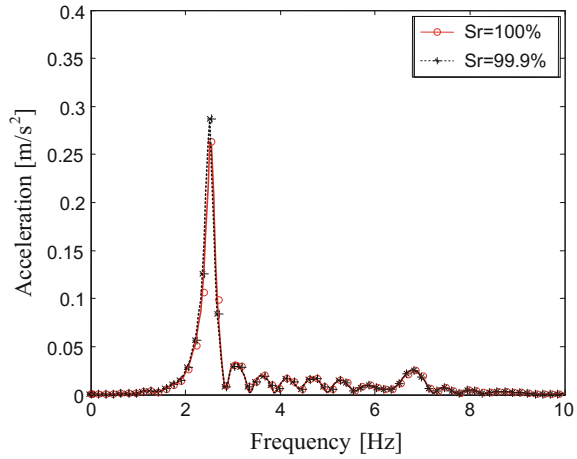
Fig. 5 Pore water pressure at 0.5 m depth under the track
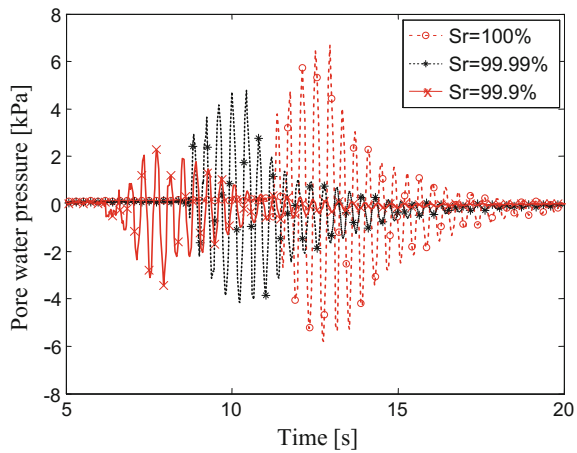
is higher than saturated soil in two phases numerical model, which is partially because of water compression modulus in unsaturated soil is reduced, leading to lower bearing capacity of pore water and higher loading on soil skeleton.

Figure 4 shows the vibration acceleration amplitude at track center in frequency domain as saturation is 100 and 99.9%. The dominant frequency for both cases are 2.5 Hz, which induced by the length of carriage as 22.2 m (200 km/h/3.6/2.5 Hz = 22.2 m). The peak acceleration amplitude of unsaturated ground is slightly higher than that of saturated one, suggesting the decreasing of saturation increases vibration acceleration. While the high frequency part of frequency spectrum is alike for different saturation rate, indicating saturation rate cast little influence on vibration frequency in two phases numerical model.

Figure 5 shows the pore water pressure at 0.5 m depth under the track center when saturation is 100, 99.99 and 99.9%. The peak pore water pressure decreases

as the saturation decreasing, which peaks at 6.5, 4.7 and 3.4 kPa respectively. This results suggest the ground vibration and pore water pressure is affected by saturation of soil. In two phases model the slightly decreasing of saturation reduces the compression modulus of water and alters share quota between water and soil skeleton leading to a notable decreasing of water pressure.

(2) **Three phases model**

Figure 6 shows the vibration displacement at track center using the three phases numerical model when the saturation rate is 100, 99 and 90%. As the saturation decreases from 100 to 90%, the peak vibration displacement reduces from 9.4 to 6.2 mm. In three phases model as the saturation decreasing, the resonance of ground vibration and train loading disappears and the ground vibration displacement is reduced. The presents of air significantly weaken the resonance of ground vibration in three phases model when the train speed approaches ground shear velocity, which is not observed in the results of two phases model.

Figure 7 shows the acceleration of ground vibration at the center of the track in frequency domain as the saturation is 100 and 90%. The dominant frequency of unsaturated ground is 16 Hz which is much higher than that of saturated one as 2.5 Hz. In three phase model, the pore air is simulated as a component that interacting with the solid and water phase and the influences of pore air on wave propagation can be simulated. The vibration wave in unsaturated medium reflects and scatters at the interface of pore air and water, which may leading to a alteration of vibration energy distribution and higher dominant frequency. And as the paper [41] suggests the changing of saturation may leading to alteration of the modulus and damping of soil, which also changes the dominant frequency of ground vibration.

Figure 8 shows the pore water pressure at 0.5 m depth beneath the track center when the saturation is 99 and 90% respectively. As the saturation is 99%, the peak

Fig. 6 Vibration displacement at track center in time domain
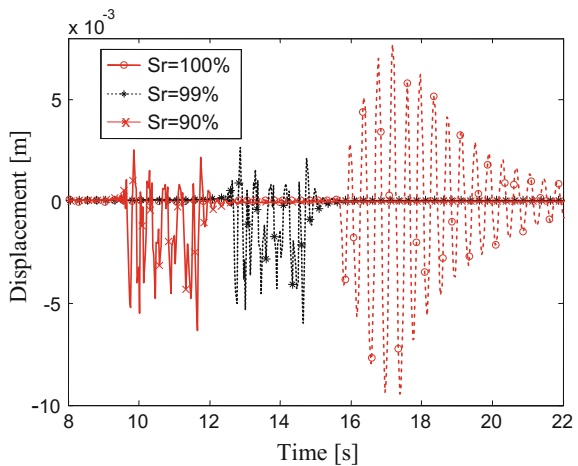
Fig. 7 Vibration acceleration at track center in frequency domain
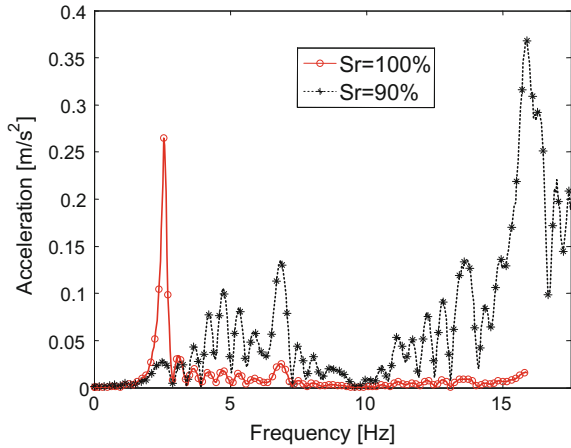
Fig. 8 Pore water pressure at 0.5 m depth under the track
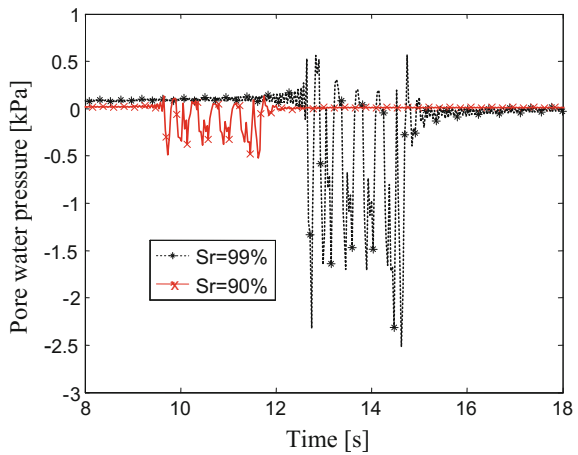
pore water pressure is 2.5 kPa and higher than that of 90% saturation which maximum at 0.5 kPa. The pore water pressure in three phase model is reduced as the saturation decreasing, which is the same as that in the two phases model. While the present of air, which interfere the resonance of ground vibration in three phases model, vastly reduces the suction of pore water pressure comparing with Fig. 5.

Simulating vibration of unsaturated porous medium by numerical models, the results of the two kinds of numerical model is different which is mainly contribute to different model of pore air. Firstly, when the train speed reaches subgrade shear velocity, the three phases numerical model predicts a sharply reduction of ground vibration as saturation decreasing, which is not observed in the two phases model. In the two phase model, decreasing of saturation reduces water compression modulus and increases ground vibration. Secondly, the transmitting and reflecting of vibration wave at the interface of air and water in three phases model lead to a

higher dominant frequency for ground vibration, which is neglected in two phases model. Despite of the ground vibration, the pore water pressure is reduced as the decreasing of saturation, that is agreed by the two kinds of unsaturated models.

Layered Subgrade

Properties and Dimensions

This subsection analyzes the influence of layered unsaturated subgrade on ground vibration by the three phases unsaturated numerical model. The parameters of train loading and dimensions of carriage is shown in Tables 1 and 2. The mass and stiffness of embankment is the same as paper [39] and the train speed is 200 km/h. The subgrade is 19 m in depth, and 4 different cases of subgrade are investigated. (1) homogeneous soft subgrade, (2) homogeneous hard subgrade, (3) 3 m soft superstratum over hard subgrade, (4) 3 m hard superstratum over soft subgrade, as shown in Fig. 9. The properties of soft and hard soil are shown in Table 3.
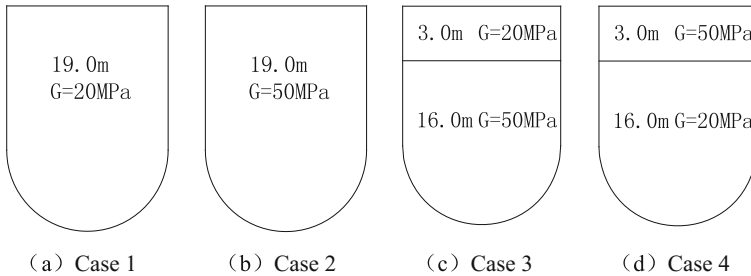
Fig. 9 Dimension of 4 different subgrades

Table 3 Properties of soil

Layers	Shear modulus (MPa)	ρ (kg/m³)	Poison ratio	Damping	V_p (m/s)	V_s (m/s)
Soft layer	20	1700	0.4	0.05	266	108
Hard layer	50	1800	0.3	0.05	312	167

Ground Vibration Analysis

Figure 10 shows the ground vibration acceleration at the center of the track in frequency domain when the saturation is 100 and 90% for 4 different cases. Figure (a) is homogeneous soft subgrade and when the saturation is 100% the dominant frequency is 6.5–9.0 Hz, and the peak acceleration is 0.078 m/s^2; when the saturation is 90%, the dominant frequency is 16–25 Hz, with a peak acceleration of 0.16 m/s^2. The high frequency vibration increases as saturation decreasing. In figure (b) the dominant vibration frequency of hard subgrade is 13–18.5 Hz, and peak vibration acceleration is 0.23 m/s^2; when saturated decreases to 90%, the dominant vibration frequency is 16–25 Hz with vibration acceleration peak at 0.068 m/s^2. As the modulus of subgrade increasing, the peak amplitude in frequency spectrum of saturated model is increased and the peak amplitude of unsaturated model is reduced. In figure (c) and (d), the frequency curve of case 3 is alike that of case 1, and the frequency curve of case 4 is alike that of case 2. So the

(a) case 1

(b) case 2

(c) case 3

(d) case 4
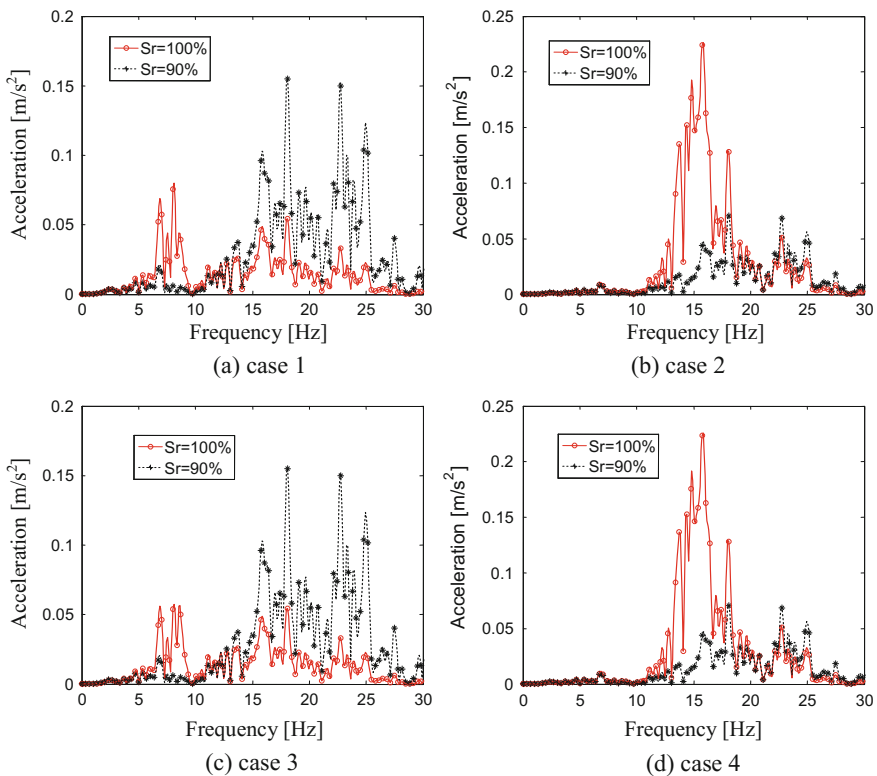
Fig. 10 The vibration acceleration at track center in frequency domain

ground vibration under the track is mainly controlled by the properties of surface layer and the subjacent layer cast little influences.

Figure 11 is the vibration acceleration in frequency domain at 8 m from the track when the saturation is 100 and 90%. In figure (a), the dominant vibration frequency is 2.3 Hz for two different saturation with a higher amplitude of dominant frequency for saturated one. And the frequency spectrum amplitude at 5–8 Hz of saturated subgrade is higher than that of unsaturated subgrade. In figure (b) the dominant vibration frequency is 2.3 Hz respectively with a higher amplitude at dominant frequency for unsaturated one, while the frequency spectrum amplitude between 5 and 8 Hz is the same for both saturation. In figure (c), the vibration frequency spectrum between 1 and 4 Hz of case 3 is alike that of homogeneous hard subgrade (case 2) and the frequency spectrum between 5 and 8 Hz is alike that of homogeneous soft subgrade (case 1). In figure (d), the low frequency section between 1 and 4 Hz is alike that of case 1 and high frequency section between 5 and 8 Hz is alike that of case 2. It can be concluded that the superstratum of layered subgrade affects the high frequency ground vibration far from the track and the subjacent layer controls the low frequency vibration.
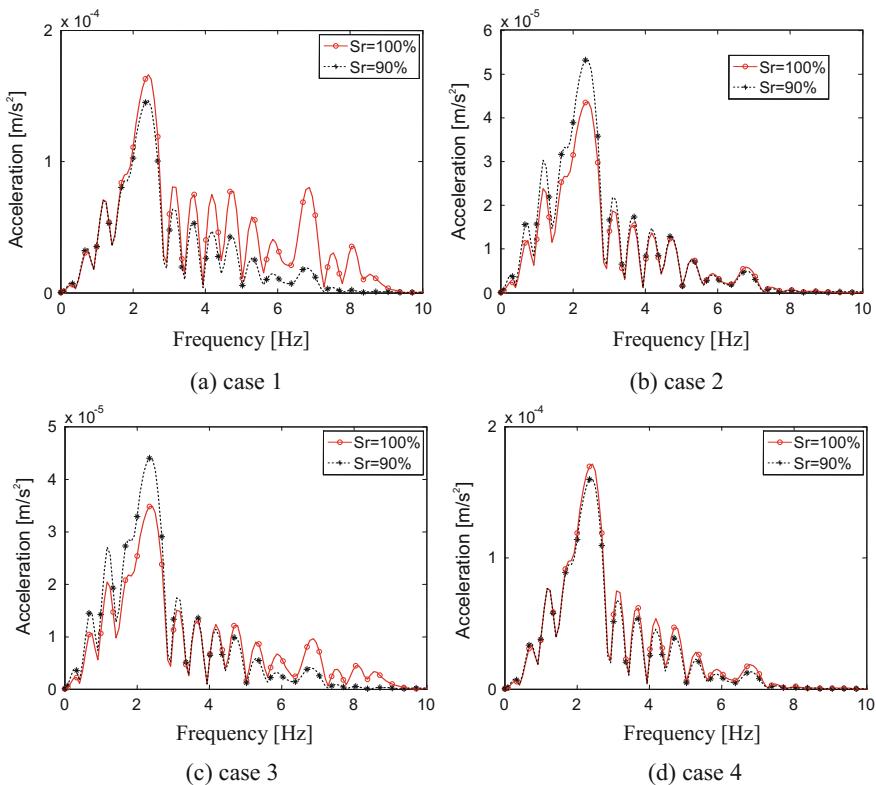
Fig. 11 The vibration acceleration at 8 m from track in frequency domain

Conclusions

Two different kinds of numerical models of unsaturated porous medium is studied by 2.5D FEM. The amplitude of ground vibration displacement, dominant frequency of vibration acceleration and peak pore water pressure for those two unsaturated models are compared and the causes for the contradiction results of the two models are analyzed. Then the ground vibration for 4 kinds of subgrade is compared to study the influence of layers on vibration frequency spectrum. The following conclusions can be drew:

(1) The three phases model takes interaction of air, water and solid into consideration, while the two phases model only value the pore air by modified compression modulus of water. So in three phases model the pore air of unsaturated subgrade can interfere the resonance of ground vibration and train loading and reduce ground vibration largely, while the two phases model just reduces the water modulus and increases the loading of skeleton and ground vibration amplitude.

(2) The dominant vibration frequency for two unsaturated models is different. In three phase model, dominant vibration frequency is higher than that of two phases model, as a result of reflecting and scattering of vibration wave at the interface of air, water and solid.

(3) The pore water pressures are observed reduced as saturation decreasing for both of those two models.

(4) In layered subgrade, the ground vibration at the track center is mainly controlled by superstratum. While for the ground vibration far away from the track, the high frequency ground vibration is mainly affected by the superstratum and the low frequency vibration is controlled by the subjacent layer.

References

1. Huang yi, Zhang yuhong. (2000). Three dimensional non-axisymmetric Lamb problem of saturated soil, Science in China: (Series E), 30(4): 375–384.
2. Jin bo. (2004). Dynamic responses of a poroelastic half space generated by high speed load, Chinese Quarterly of Mechanics, 25(2): 168–174.
3. Cao Z, Boström A. (2013). Dynamic response of a poroelastic half-space to accelerating or decelerating trains. Journal of Sound and Vibration, 332(11): 2777–2794.
4. Cai yuan-qiang, Wang yu, Cao zhi-gang, Xu chang-jie. (2012). Study of ground vibration from trains caused by track irregularities. Rock and Soil Mechanics, 33(2): 327–335.
5. Cao zhi-gang, Cai yuan-qiang, Sun Hong-lei, Zeng chen. (2010). Ground vibration caused by axle load and dynamic wheel-rail force of a moving train. Chinese Journal of Geotechnical Engineering, 32(5): 681–687.
6. Cao zhi-gang, Cai yuan-qiang, Sun hong-lei, Xu chang-jie. (2011). An analytical solution to train-induced ground vibration. Engineering Mechanics, 28(10): 250–256.

7. Cai yuan-qiang, Sun hong-lei, Xu chang-jie. (2008). Effect of rail rigidity on track-ground vibration due to a high-speed train. Chinese Journal of Geotechnical Engineering, 29(12): 1787–1793.

8. Cai yuan-qiang, Wang yu, Cao zhi-gang. (2011). Dynamic analysis of a slab track on the poroelastic soil subjected to moving load. Journal of Vibration Engineering, 24(001): 48–54.

9. Sun hong-lei, Cai yuan-qiang, Chen cheng-zhen. (2009). Dynamic response of railways on layered half-space subjected to moving train load. Chinese Journal of Geotechnical Engineering, 31(6): 922–928.

10. Gao guangyun, Zhao hong, Zhang bo, He junfeng. (2013). Analysis of ground vibration induced by trains on saturated layered ground. Journal of Tongji University (Natural Science), 41(12): 1805–1811.

11. Gao G Y, Chen Q S, He J F, Liu F. (2012). Investigation of ground vibration due to trains moving on saturated multi-layered ground by 2.5 D finite element method. Soil Dynamics and Earthquake Engineering, 40: 87–98.

12. Gao guang-yun, Li ning, He jun-feng, Gao meng. (2011). Analysis of ground vibration generated by train moving loads on saturated soil. Journal of Vibration and Shock, 30(6): 86–92.

13. Gao guang-yun, He jun-feng, Yang cheng-bin, Zhao yuan-yi. (2011). Ground vibration induced by trains moving on saturated ground using 2.5D FEM. Chinese Journal of Geotechnical Engineering, 33(2): 234–241.

14. Yuan wan, Cai yuan-qiang, Shi li, Cao zhi-gang. (2013). Study of vibration-isolation efficiency of open trench in saturated ground by 2.5D finite element method. Rock and Soil Mechanics, 7:2111–2118.

15. Li liang, Zhai wei, Du xiu-li. (2012). Time-domain explicit finite element method for wave propagation of transversely isotropic fluid-saturated porous media. Chinese Journal of Geotechnical Engineering, 34(3): 464–470.

16. Li liang, Du Xiu-li, Zhai wei. (2013). Wave propagation in transversely isotropic elasto-plastic fluid-saturated porous media. Journal of Hydraulic Engineering, 44(3): 312–318.

17. Zhu yan-zhi, Li dong-xia, Fang zhi. (2005). Three dimensional 3-D viscoelastic dynamic analysis of transversely isotropic fluid-saturated poroelastic soil in time domain. Rock and Soil Mechanics, 10: 36–43.

18. Ye jun-neng. (2010). Dynamic response of track system-layered transversely isotropic saturated subgrade to train loads. Rock and Soil Mechanics, 5: 1597–1603+1614.

19. Li jia, Gao guangyun, Zhao hong. (2013). Study of ground vibration induced by train load in transversely isotropic soil using 2.5D finite element method. Chinese Journal of Rock Mechanics and Engineering, 32(1): 78–87.

20. Sun hong-lei, Cai yuan-qiang, Xu chang-jie. (2006). Response of transversely isotropic poroelastic half-space to moving load. Journal of Zhejiang University (Engineering Science), 40(8): 1382–1387.

21. Cai Yuan-qiang, Zhao guo-xing, Zheng zao-feng, Xu chang-jie. (2006). Vertical vibration analysis of transversely isotropic saturated soils with elastic superstratum. Journal of Zhejiang University (Engineering Science), 40(2): 267–271.

22. Richart F E, Hall J R, Woods R D. (1970). Vibrations of soils and foundations. Prentice-Hall, Inc.

23. Yang J, Sato T. (2000). Interpretation of seismic vertical amplification observed at an array site. Bulletin of the Seismological Society of America, 90(2): 275–285.

24. Yang J, Sato T. (2000). Influence of water saturation on horizontal and vertical motion at a porous soil interface induced by incident SV wave. Soil Dynamics and Earthquake Engineering, 19(5): 339–346.

25. Yang J. (2001). A note on Rayleigh wave velocity in saturated soils with compressible constituents. Canadian geotechnical journal, 38(6): 1360–1365.

26. Yang J. (2002). Saturation effects of soils on ground motion at free surface due to incident SV waves. Journal of Engineering Mechanics, 128(12): 1295–1303.

27. Vardoulakis I, Beskos D E. (1986). Dynamic behavior of nearly saturated porous media. Mechanics of Materials, 5(1): 87–108.
28. Lo W C. (2006). Decoupling of the coupled poroelastic equations for quasistatic flow in deformable porous media containing two immiscible fluids. Advances in Water Resources, 29 (12): 1893–1900.
29. Lo W C, Sposito G, Majer E. (2007). Low-frequency dilatational wave propagation through unsaturated porous media containing two immiscible fluids. Transport in Porous Media, 68 (1): 91–105.
30. Lo W C, Sposito G, Majer E. (2009). Analytical decoupling of poroelasticity equations for acoustic-wave propagation and attenuation in a porous medium containing two immiscible fluids. Journal of Engineering Mathematics, 64(2): 219–235.
31. Huang yi, Zhang yin-ke. (2003). Constitutive relation of unsaturated soil by use of the mixture theory-nonlinear constitutive equations and field equations. Applied Mathematics and Mechanics, 2: 111–123.
32. Huang yi, Zhang yin-ke. (2003). Constitutive relation of unsaturated soil by use of the mixture theory-linear constitutive equations and field equations. Applied Mathematics and Mechanics, 2:124–137.
33. Li bao-zhong, Cai yuan-qiang. (2003). Influence of water saturation on elastic wave propagation in transversely isotropic quasi-saturated porous media. Journal of Hydraulic Engineering, 9: 94–100.
34. Xu chang-jie, Shi yan-yong. (2004). Characteristics of wave propagation in unsaturated soils. Rock and Soil Mechanics, 25(3): 354–358.
35. Yang J. Saturation effects on horizontal and vertical motions in a layered soil–bedrock system due to inclined SV waves. Soil Dynamics and Earthquake Engineering, 2001, Vol. 21(6): 527–536.
36. Ravichandran N, Krishnapillai S H. (2012). Effect of deformation-induced suction in the behavior of unsaturated fine-grained soils using simplified finite-element model. International Journal of Geomechanics, 13(5): 483–495.
37. Ye J H, Jeng D S. (2013). Three-dimensional dynamic transient response of a poro-elastic unsaturated seabed and a rubble mound breakwater due to seismic loading. Soil Dynamics and Earthquake Engineering, 44: 14–26.
38. Xu ming-jiang, Wei de-min. (2011). 3D non-axisymmetrical dynamic response of unsaturated soils. Engineering Mechanics, 3: 78–85.
39. Bian xuecheng, Chen yunmin. (2006). Ground vibration generated by train moving loadings using 2.5D finite element method. Chinese Journal of Rock Mechanics and Engineering, 25 (11): 2335–2342.
40. Zhang yinke. (2001). The mixture theory of unsaturated soil and its applications. Xi'an Jiaotong University, (Doctoral Dissertation).
41. Sun de-an, Wu bo. (2012). Study on dynamic modulus and damping ratio of unsaturated silt. Journal of Hydraulic Engineering, 9:1108–1113.

Study of Infiltration into Partially Saturated Clay Soil Railway Embankment

Taifeng Li, Qianli Zhang, Degou Cai, Jianping Yao and Feng Chen

Introduction

The infiltration of rainfall into partially saturated clay soil could change the distribution of pore-water pressure significantly, which could influence the soil shear strength and the stability of clay railway embankment. The process of rainfall infiltration have been previously studied by many researchers (Lumb [7]; Leach and Herbert [6]; Anderson and Pope [1]; Lam et al [5]). However, it is difficult to predict the distribution of pore-water pressure in the partially saturated clay soil accurately, since the complex ground conditions.

Vadose/W, a commercial FEA software can simulate the whole process of rainfall infiltration into partially saturated clay soil and estimate the distribution of pore-water pressure in the vadose zone [4]. The aim of this paper is to model and analyze the process of rainfall infiltration with different flow boundary condition. The influences on the infiltration caused by variable rainfall and soil water properties will be investigated, in order to find the relationship between them.

T. Li (✉)
China Academy of Railway Sciences, Beijing 100081, China
e-mail: typhoon_li@qq.com

Q. Zhang · D. Cai · J. Yao · F. Chen
China Academy of Railway Sciences Railway Engineering
Research Institute, Beijing 100081, China
e-mail: tkyzql@139.com

D. Cai
e-mail: caidegou@126.com

J. Yao
e-mail: yjppaul@163.com

F. Chen
e-mail: chenfeng7@163.com

Numerical Modelling and Parameter Selection

Based on the research from Briggs et al. [2, 3] and some currently existing field data, the transient rainfall infiltration model will be made in this paper, the research will focus on the analysis of rainfall infiltration into partially saturated clay soil in the winter period.

Time Duration and Time Segment

Both short-term and long-term analysis will be considered in this paper with comparison and discussion between them. For long-term analysis each time segment has been set as 6 days with overall 30 time steps for the winter period. For short term analysis, the time duration has been set as 30 days, each time segment is 1 day with 30 time steps.

Material Properties

There are four types of clay soil material with different saturated hydraulic conductivity will be used in the FEA model. Table 1 shows the properties of all clay soil materials which will be used in this paper, based on investigation of currently existing field records. Also, each clay soil material was assumed isotropic.

One-Dimensional Soil Column Model in Vadose/W

The one-dimensional FEA model will be used in this paper, since both efficiency and workability consideration [2]. Each column is 9 m deep and 1 m width, and divided into three layers, each layer will have its own value of saturated permeability. The water table was assumed to be located at 7 m deep from the ground surface, and the pore-water pressure was set as initially hydrostatic. The material at the both left and right boundary of single soil column model has been set as impermeable. The water flow at the ground surface has been ignored in this paper.

Table 1 Summary of soil properties used in FEA model (after Briggs et al. [2])

Soil type	k_{sat} (m/s)	a^c	θ_s	θ_t	m	n
Surface clay fill (A, B and C)	5×10^{-7}	30.3	0.47	0.1	0.13	1.15
Clay fill (A and B)	5×10^{-8}	30.3	0.47	0.1	0.13	1.15
Clay fill (C)	5×10^{-9}	30.3	0.47	0.1	0.13	1.15

At the top of column model, the rainfall intensity will be represented as different amount of rainfall flux, which adds to the ground surface vertically downwards. The temperature has been set as constant 10 °C in the whole winter period.

Discussion and Analysis of Results

Influence of Saturated Permeability of Soil

The rainfall intensity in both short-term and long-term analysis has been assumed as constant 1.7 mm/day (1.97×10^{-8} m/s). Table 2 shows the detailed information of the FEA models which will be used in this section

Short-Term Analysis

Figures 1, 2, 3, and 4 illustrate that the value of pore-water pressure for the clay soil material with relatively higher permeability is less than it in the lower permeability clay soil material in the same time period. Figure 1 shows that the value of pore-water pressure will increase slightly as a result of a period of persistent rainfall. In other word, the negative value of pore-water pressure could improve the value of totally effective stress of soil, which is very useful for maintaining the stability of clay railway embankment. Figures 3 and 4 illustrated that the clay soil material which located in the ground surface has become fully saturated without any matric suction of soil, since the value of pore-water pressure has reached zero point.

Long-Term Analysis

Figures 5, 6, 7, and 8 show the long-term analysis of rainfall infiltration, the time duration has been set as 180 days in this case. By compare Figs. 1 and 5, it shows that the rainwater in the long-term analysis can infiltrate into the unsaturated clay soil more deeply than it in the short-term analysis. From the comparison between

Table 2 The list of FEA model with different saturated permeability of soil

Short-term analysis (30 days)			Long-term analysis (180 days)		
Model number	Rainfall intensity (mm/day)	Saturated permeability (m/s)	Model number	Rainfall intensity (mm/day)	Saturated permeability (m/s)
1.0.1	1.7	5×10^{-7}	2.0.1	1.7	5×10^{-7}
1.0.2	1.7	5×10^{-8}	2.0.2	1.7	5×10^{-8}
1.0.3	1.7	5×10^{-9}	2.0.3	1.7	5×10^{-9}
1.0.4	1.7	5×10^{-10}	2.0.4	1.7	5×10^{-10}
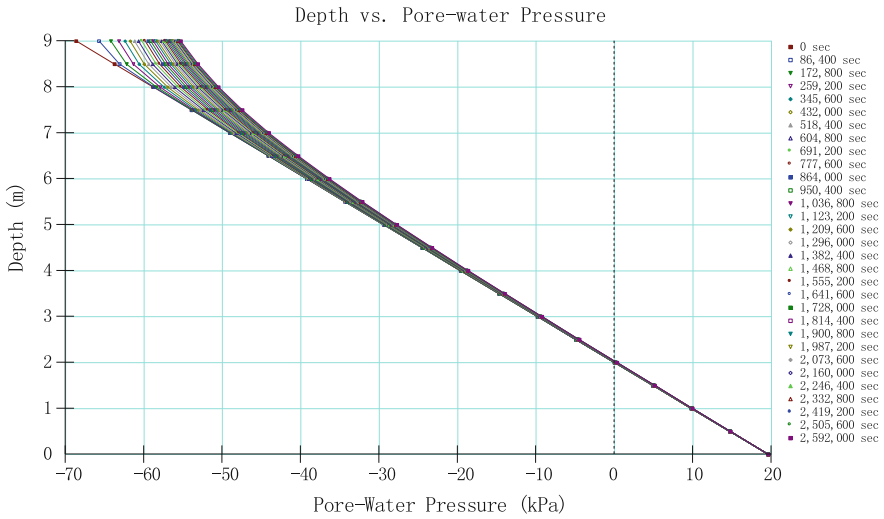
Fig. 1 Short-term analysis model 1.0.1
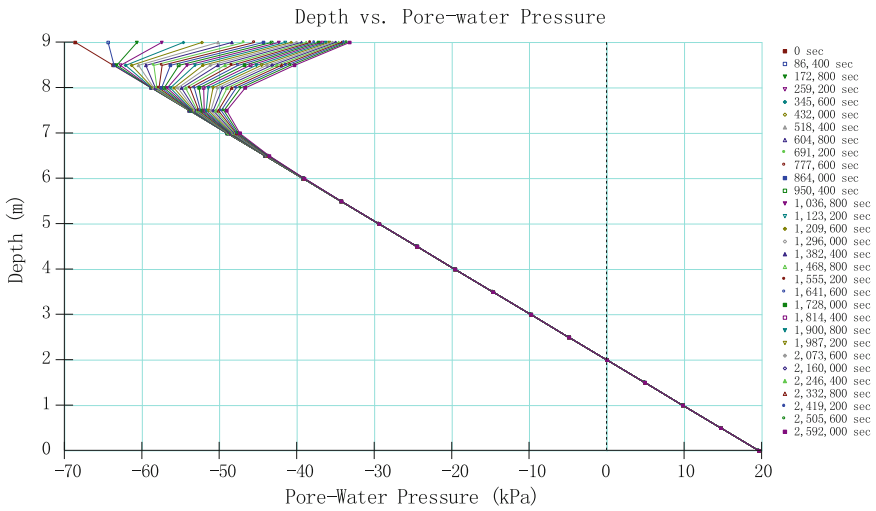
Fig. 2 Short-term analysis model 1.0.2

Figs. 2 and 6, it shows that the pore-water pressure in the long-term analysis increased significantly than it in the short-term analysis. Nearly half depth of the clay railway embankment has been influenced by the rainfall infiltration, the slope become more instable under longer period of continuous rainfall. The significant risks come from the using of clay soil material when the permeability is lower than 5×10^{-9} m/s, which could be recognized by compare Figs. 3 and 7.
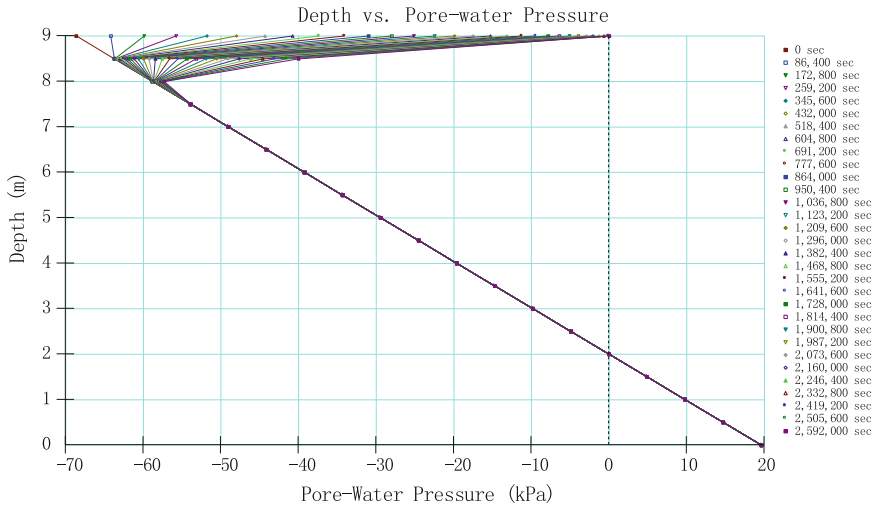
Fig. 3 Short-term analysis model 1.0.3
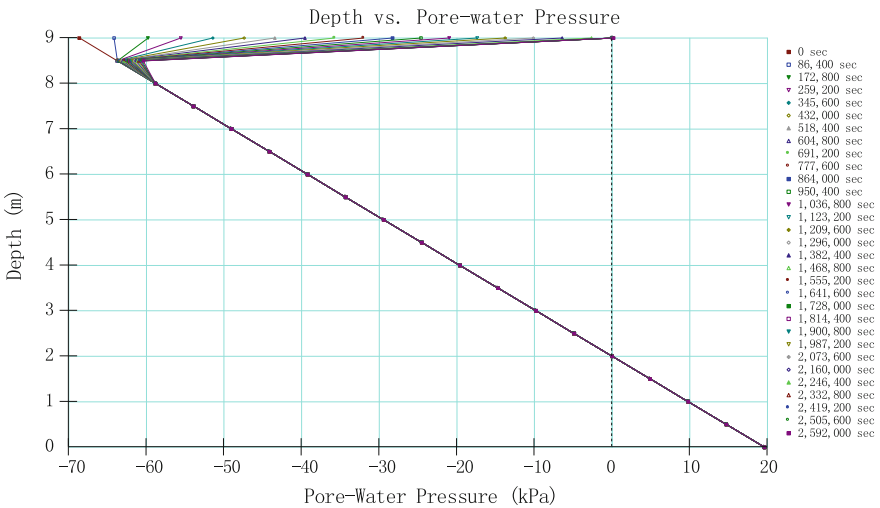
Fig. 4 Short-term analysis model 1.0.4

Influence of Soil Stratum Structure

For the construction of railway embankment foundation, some in-situ materials with relatively lower saturated permeability (5×10^{-9} m/s) will be used, in order to carry the main gravity load from above structures. Table 3 shows the detailed information of FEA models which will be used in this section.
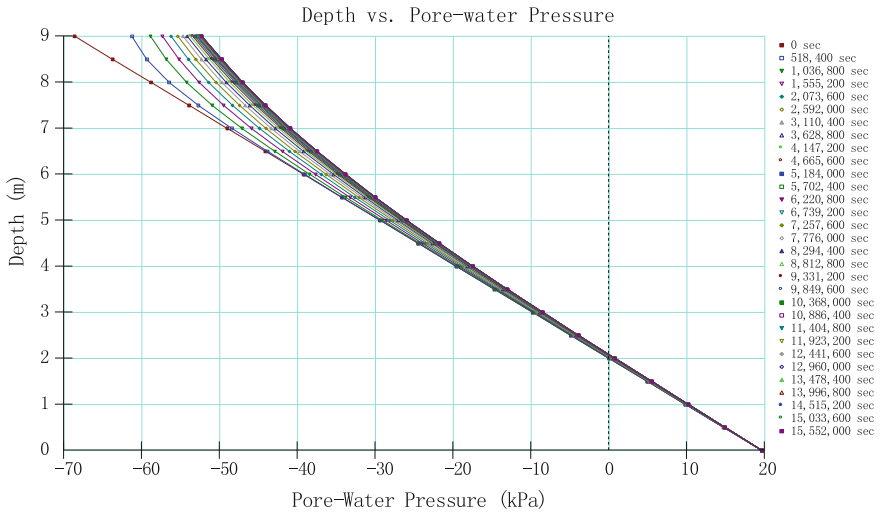
Fig. 5 Long-term analysis model 2.0.1
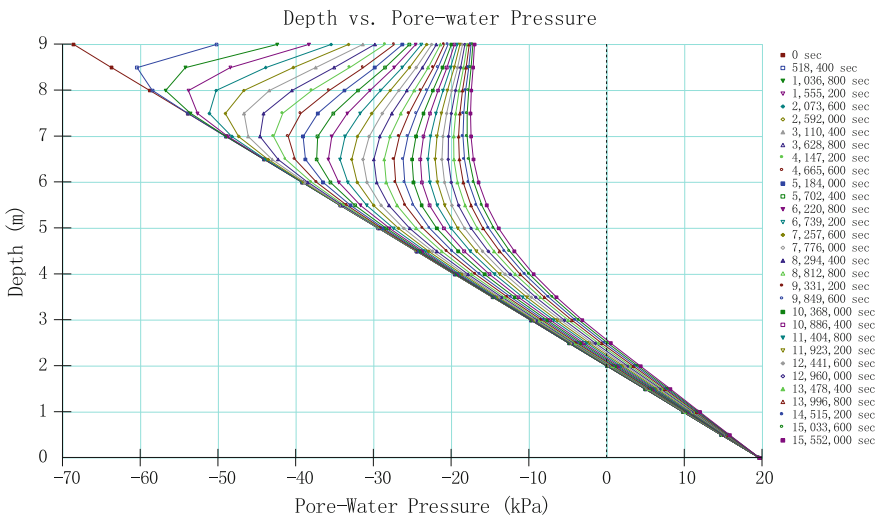
Fig. 6 Long-term analysis model 2.0.2

Short-Term Analysis

Figures 9, 10, 11, and 12 show the distribution of pore-water pressure under different combination of clay soil material with different saturated permeability. By compare Figs. 9, 10 and 11 it shows that the value of pore-water pressure at the ground surface has been reduced significantly by using soil material with relatively higher permeability, also the serious surface ponding problem has been improved obviously.
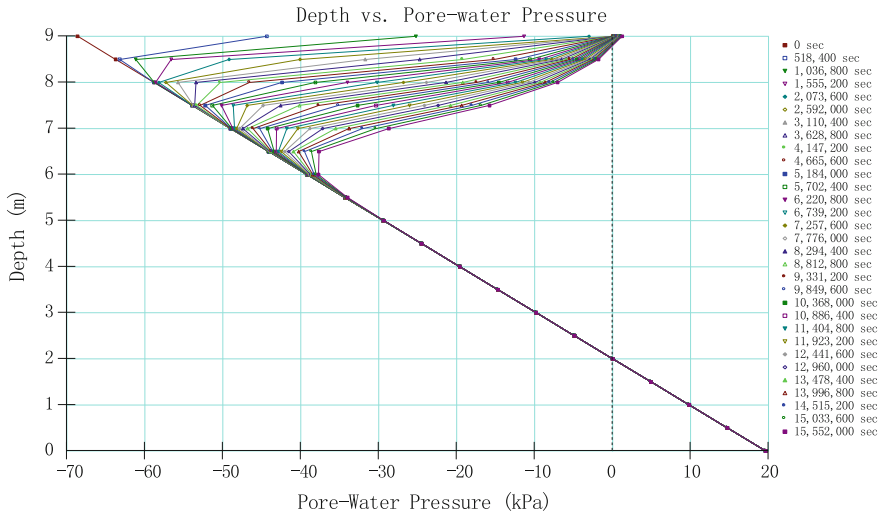
Fig. 7 Long-term analysis model 2.0.3
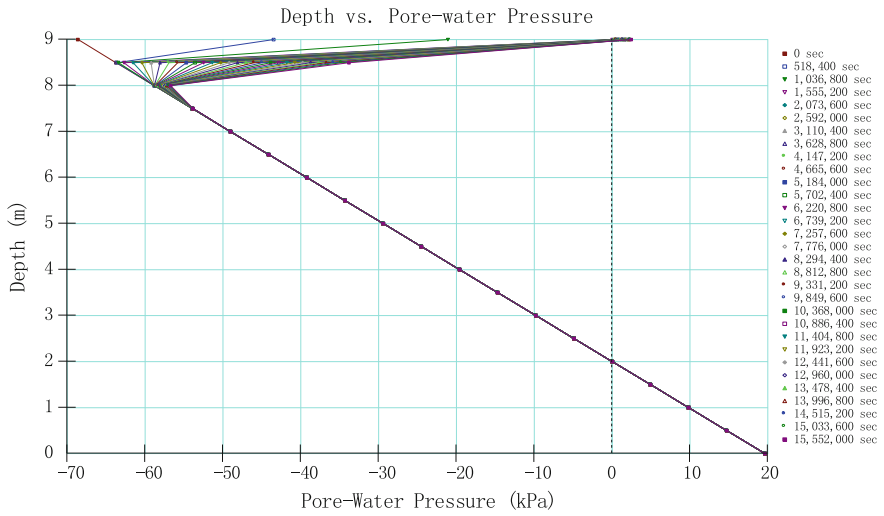
Fig. 8 Long-term analysis model 2.0.4

Table 3 The list of FEA model with different combination saturated permeability of soil

Short-term analysis (30 days)		Long-term analysis (180 days)		Saturated permeability
Model number	Rainfall intensity (mm/day)	Model number	Rainfall intensity (mm/day)	
1.1.1	1.7	2.1.1	1.7	Surface layer 5×10^{-9} m/s Second layer 5×10^{-9} m/s Third layer 5×10^{-9} m/s
1.1.2	1.7	2.1.2	1.7	Surface layer 5×10^{-8} m/s Second layer 5×10^{-8} m/s Third layer 5×10^{-9} m/s
1.1.3	1.7	2.1.3	1.7	Surface layer 5×10^{-7} m/s Second layer 5×10^{-7} m/s Third layer 5×10^{-9} m/s
1.1.4	1.7	2.1.4	1.7	Surface layer 5×10^{-7} m/s Second layer 5×10^{-8} m/s Third layer 5×10^{-9} m/s
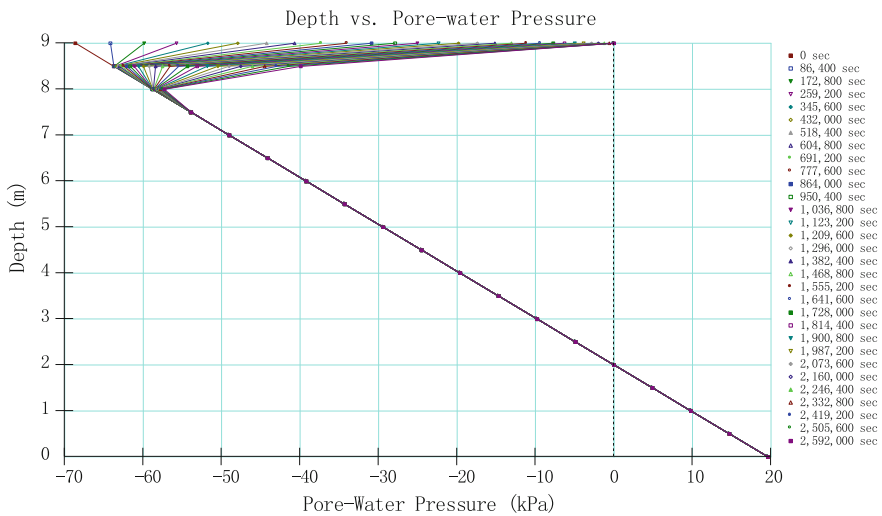
Fig. 9 Short-term analysis model 1.1.1

Long-Term Analysis

Figures 13, 14, 15, and 16 show the long-term analysis of rainfall infiltration influence by the stratum structure. The influence depth increased to 3 m in long-term analysis (Fig. 13) compared with 1 m in short-term analysis (Fig. 9). By compare between Figs. 14 and 13, the improvement on distribution of pore-water pressure could be recognized significantly, since the clay soil material with

relatively higher saturated permeability (5×10^{-8} m/s) has been used in both surface layer and second layer.

Influence of Rainfall Intensity, Duration and Patterns

As mentioned before, the best solution of clay railway embankment is formed with three layers (saturated permeability 5×10^{-7} m/s in surface layer, 5×10^{-8} m/s in second layer and 5×10^{-9} m/s in third layer) as shown in Fig. 5, the same single clay soil column model will be used in this section, detailed information was shown in Table 4.

Short-Term Analysis

By compare Figs. 17 and 18, it illustrates that the higher rainfall intensity could increase the value of pore-water pressure at the ground surface, which can also reduce the matric suction and lower the stability of clay railway embankment.

Figures 19 and 20 show the influence of rapid daily rainfall, which could also lower the stability of railway embankment in some level. The rainfall intensity in Fig. 19 is 51 mm/day (5.9×10^{-7} m/s), which is slightly greater than the saturated permeability of surface layer (5×10^{-7} m/s). Figure 20 shows the influence of

Fig. 10 Short-term analysis model 1.1.2

Depth vs. Pore-water Pressure

Fig. 11 Short-term analysis model 1.1.3

Depth vs. Pore-water Pressure
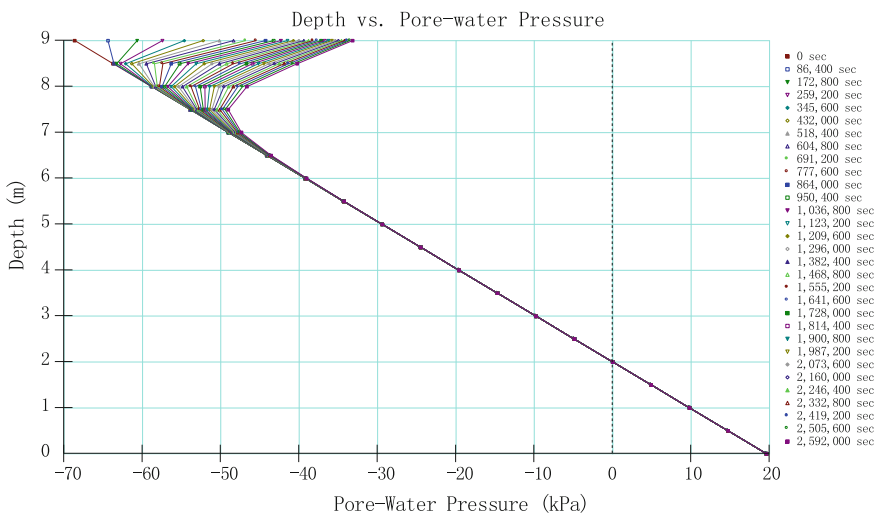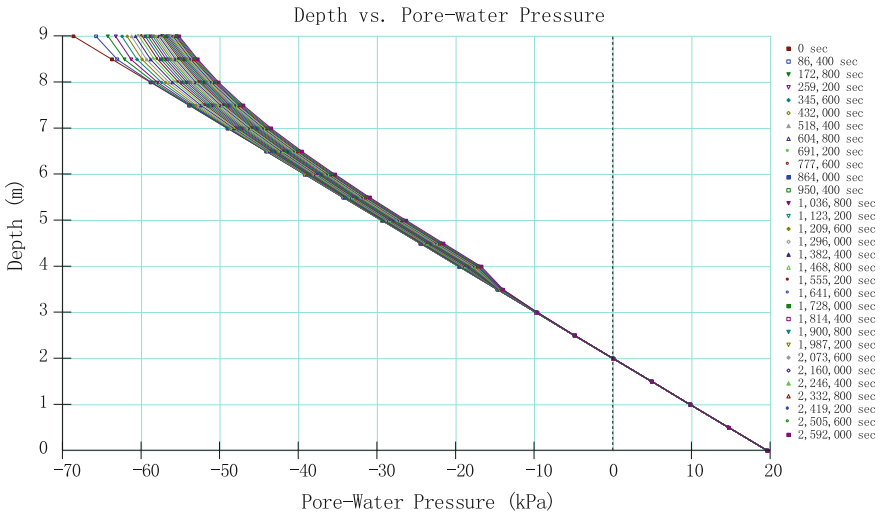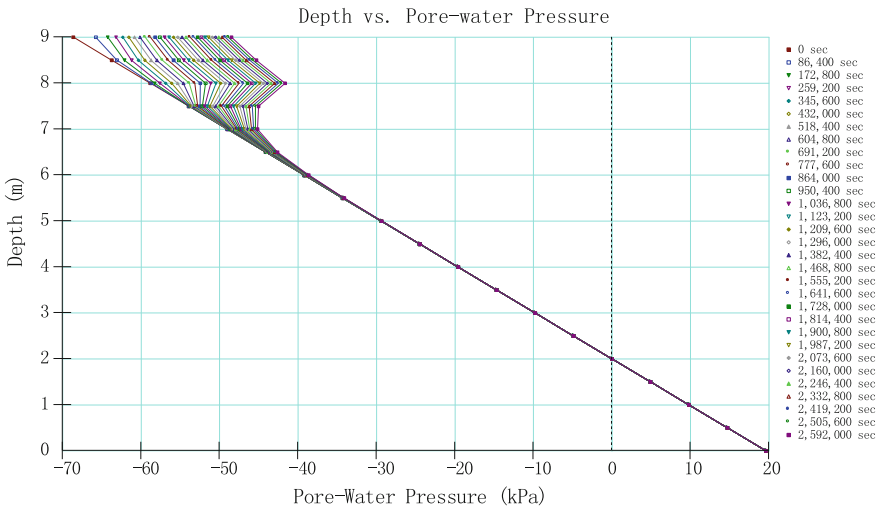
Fig. 12 Short-term analysis model 1.1.4

extreme rapid daily rainfall, the rainfall intensity is 238.5 mm/day (2.76×10^{-6} m/s), which is greater than the saturated permeability of surface layer.

Figures 21 and 22 show the influence of rainfall event in four selected days. The rainfall intensity in Fig. 21 is 12.75 mm/day (1.47×10^{-7} m/s), which is less than the saturated permeability of the surface layer (5×10^{-7} m/s), the rainwater can infiltrate into unsaturated clay soil easily. However, the rainfall intensity in Fig. 22
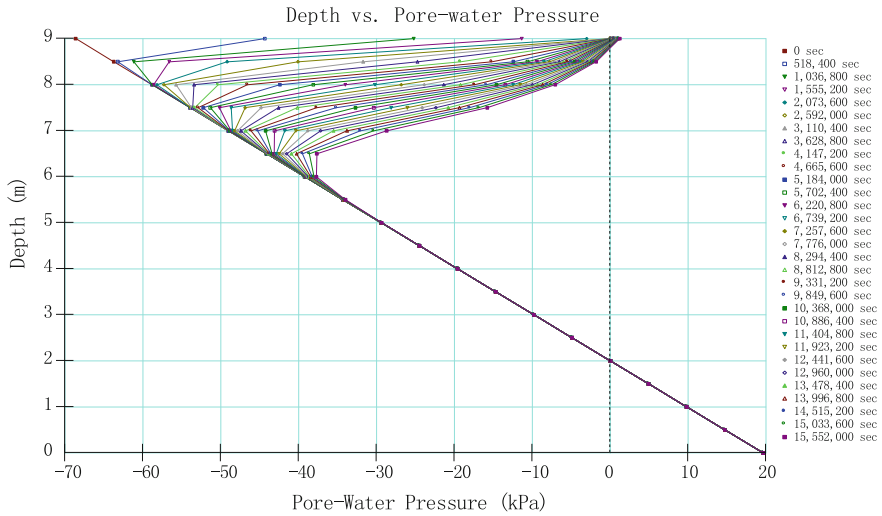
Fig. 13 Long-term analysis model 2.1.1
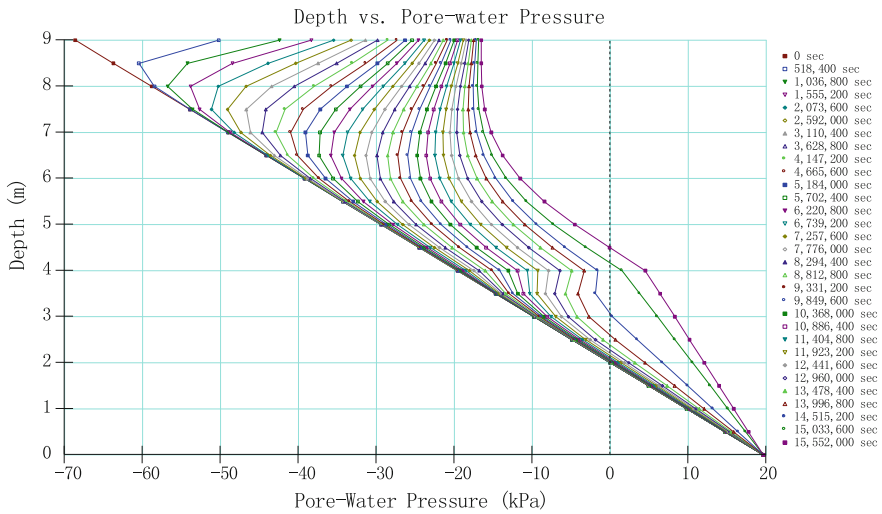
Fig. 14 Long-term analysis model 2.1.2

is 58.95 mm/day (6.82 × 10^{-7} m/s), the surface layer will become saturated and rainwater will be ponded in the interface between the surface layer and the second layer of clay railway embankment. Since the amount of maximum daily rainfall intensity (Fig. 22) is less than it in the extremely rapid daily rainfall (Fig. 20), the results are slightly better in both short-term and long-term analysis.
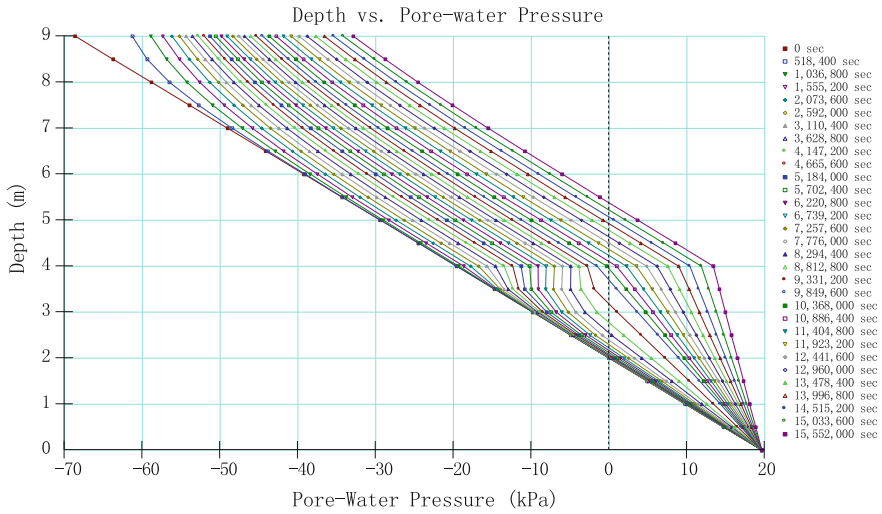
Fig. 15 Long-term analysis model 2.1.3
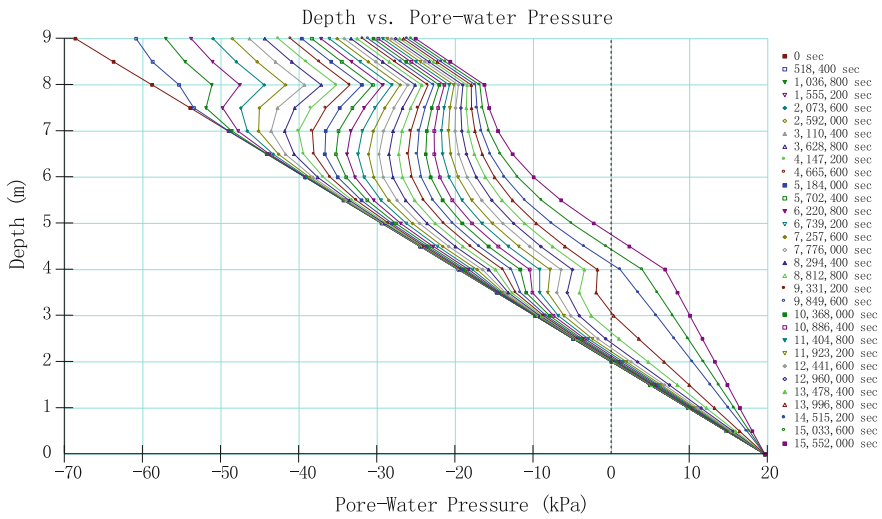
Fig. 16 Long-term analysis model 2.1.4

Long-Term Analysis

The longer rainfall period could give large total amount of rainfall and increase the infiltrated depth than it in the short-term analysis, which could be seen from Figs. 17 and 23. Hence, the stability of whole railway embankment could be significantly influenced by the antecedent rainfall especially for the long duration

Table 4 The list of FEA model with different rainfall intensity, duration and patterns

Short-term analysis (30 days)		Long-term analysis (180 days)	
Model No.	Rainfall intensity	Model No.	Rainfall intensity
1.2.1	Average daily rainfall 1.7 mm/day	2.2.1	Average daily rainfall 1.7 mm/day
1.2.2	Average daily rainfall 7.86 mm/day	2.2.2	7.86 mm/day in the last month
1.2.3	51 mm in the first day of month	2.2.3	51 mm in the first day of each month
1.2.4	235.8 mm in the first day of month	2.2.4	235.8 mm in the first day of last month
1.2.5	12.75 mm in four selected days		
1.2.6	58.95 mm in four selected days		
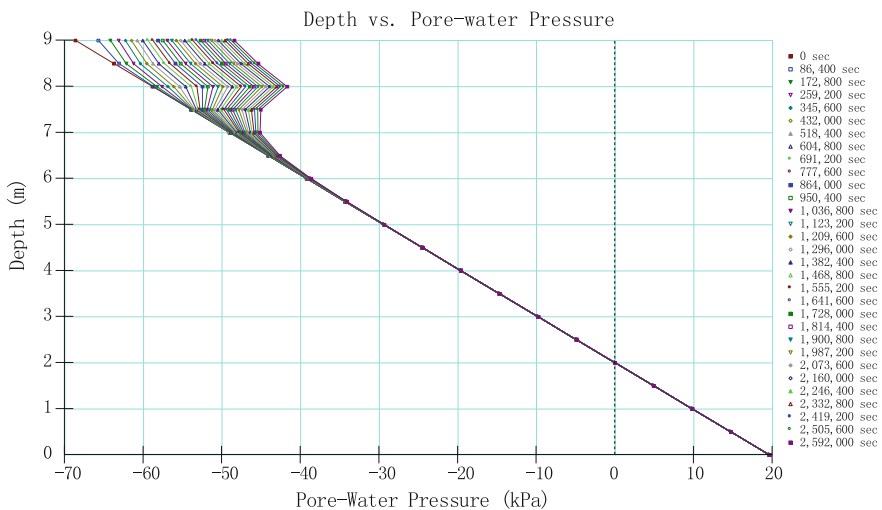
Fig. 17 Short-term analysis model 1.2.1

sustained rainfall with high intensity. Figures 23 and 24 illustrate the influence of continuous rainfall in the long-term analysis. Figure 24 shows that the clay soil material in both surface layer and the second layer has become fully saturated. The head difference is caused by the different saturated permeability of soil between the second layer and the third layer. Also the value of pore-water pressure is constantly 20 kPa in the end, since the water head has been set up as 2 m at the bottom of the single soil column model.
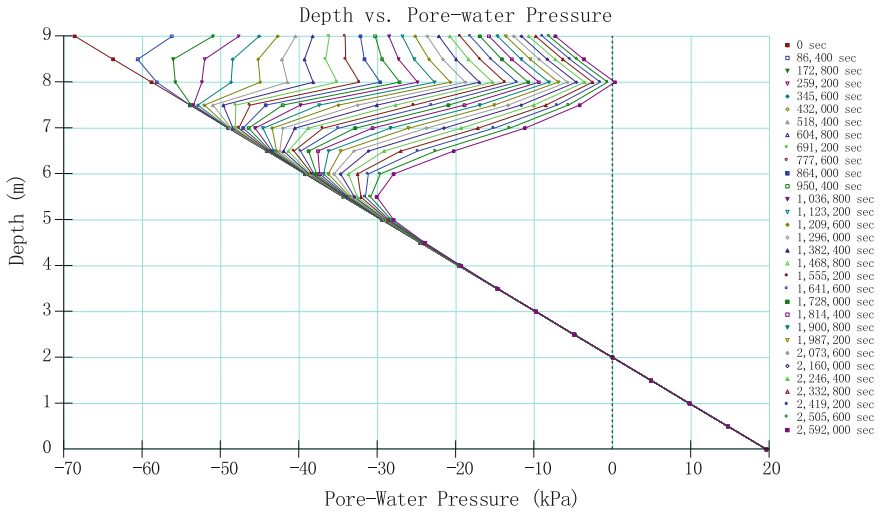
Fig. 18 Short-term analysis model 1.2.2
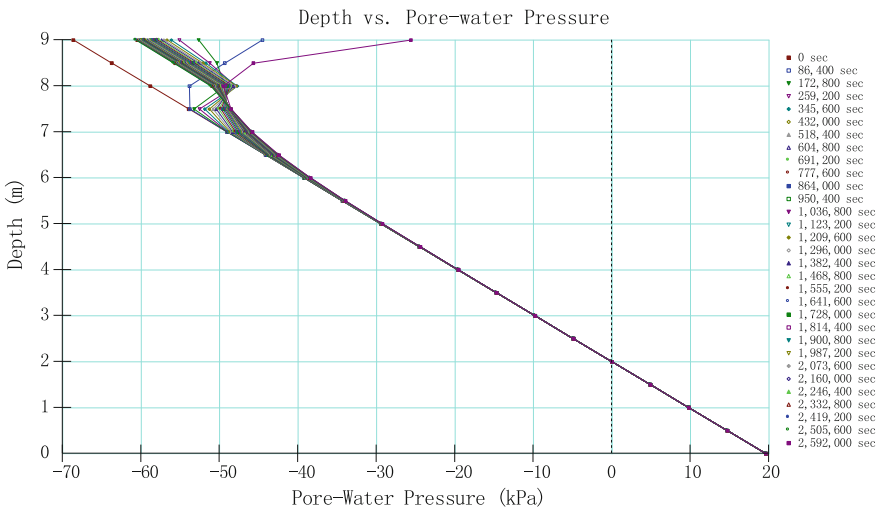
Fig. 19 Short-term analysis model 1.2.3

Figures 25 and 26 show the influence of dis-continuously rapid daily rainfall in the long-term analysis. The fluctuations in the value of ground surface pore-water pressure could be recognized in both Figs. 25 and 26, which caused by the non-continuous rainfall event. By compare Figs. 25 and 26, it illustrates that the
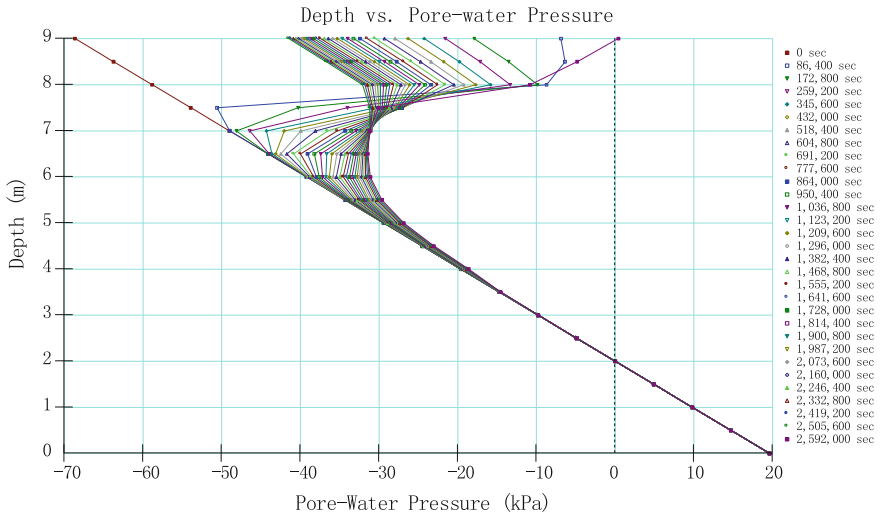
Fig. 20 Short-term analysis model 1.2.4
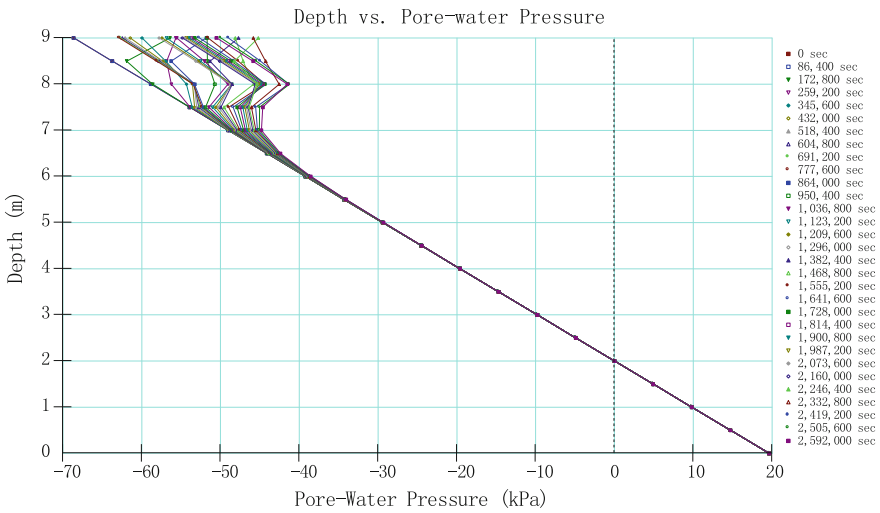
Fig. 21 Short-term analysis model 1.2.5

large amount of rainfall in the later period of rainfall duration could influence the stability of clay railway embankment dramatically, since both surface layer and second layer have become fully saturated in this situation.
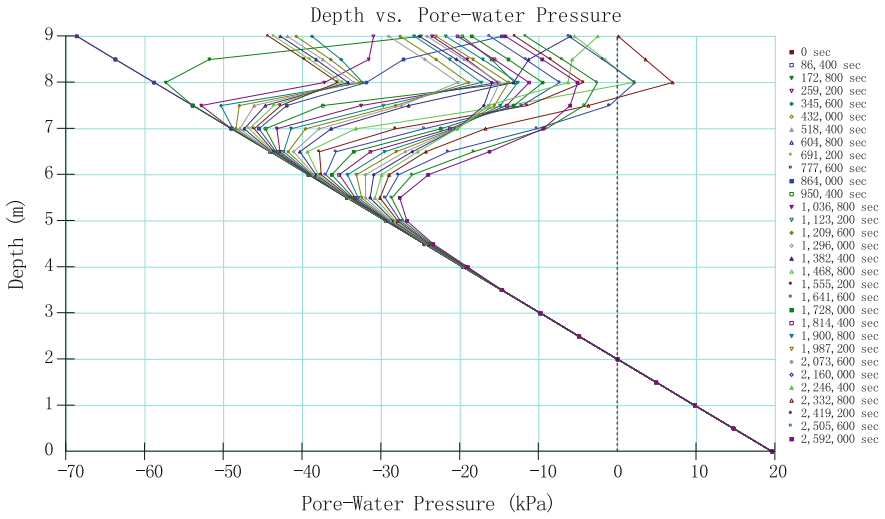
Fig. 22 Short-term analysis model 1.2.6
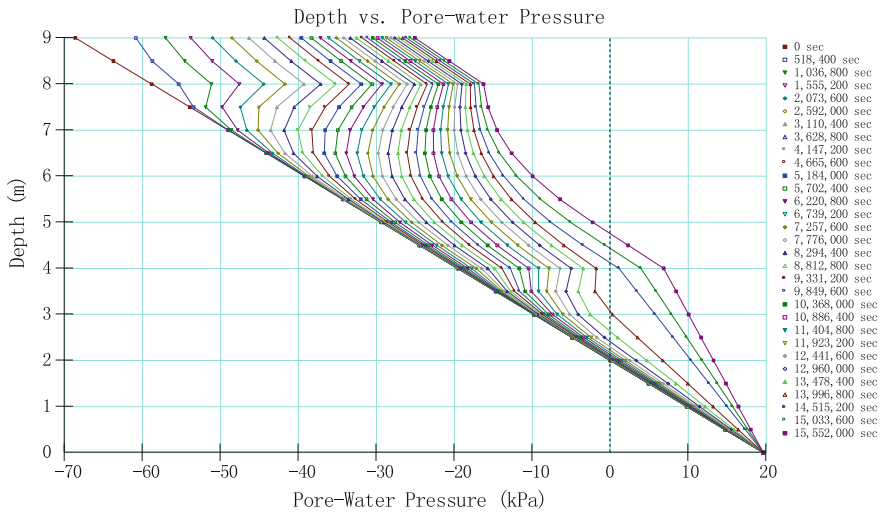
Fig. 23 Long-term analysis model 2.2.1
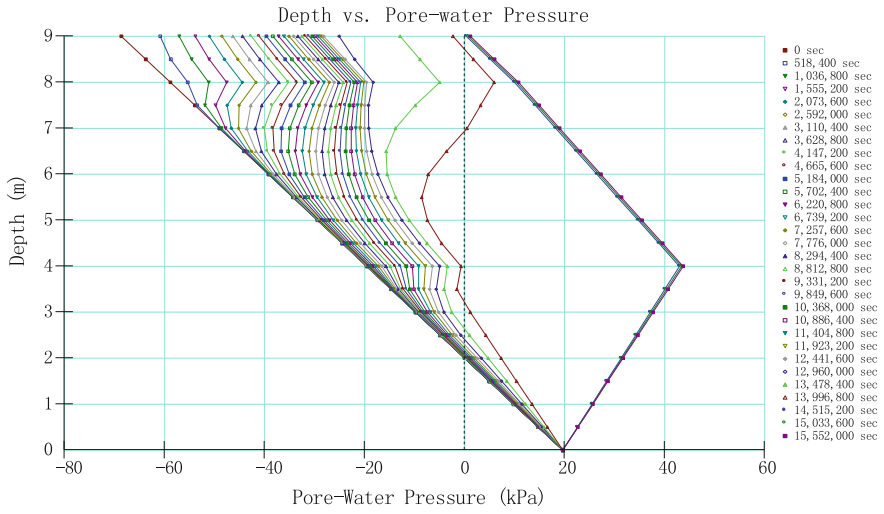
Fig. 24 Long-term analysis model 2.2.2
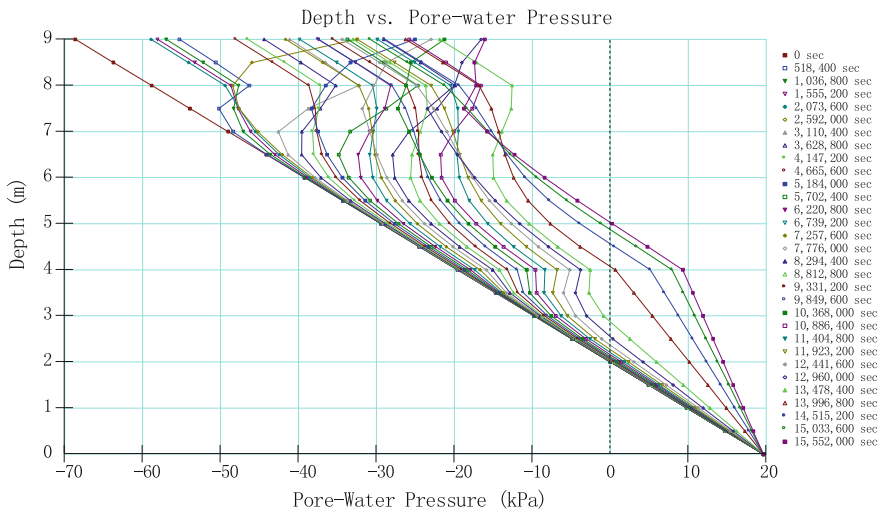
Fig. 25 Long-term analysis model 2.2.3
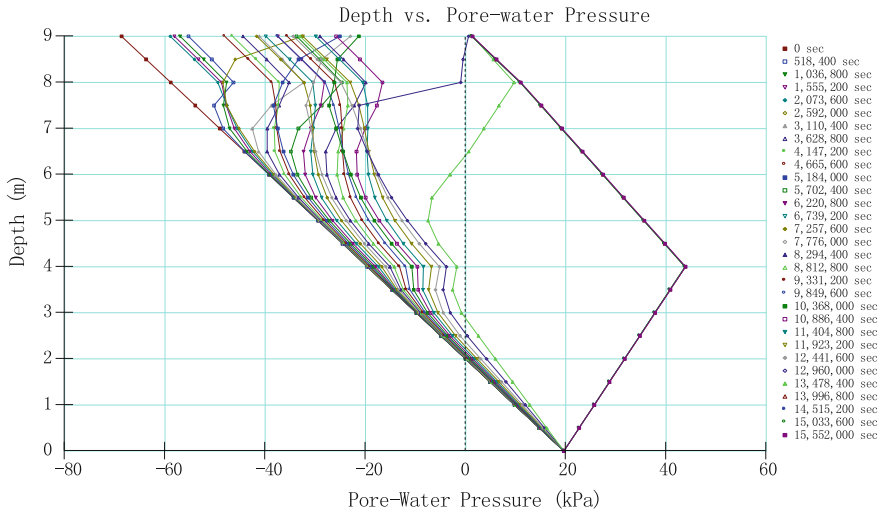
Fig. 26 Long-term analysis model 2.2.4

Conclusions

(1) The saturated permeability of surface filling material should be greater than the average daily rainfall intensity and the maximum value of rapid daily rainfall intensity, in order to avoid water ponding at the ground surface and remain the stability and workability of clay railway embankment.

(2) The using of surface layer with relatively high permeable clay soil material is essential for the construction of clay railway embankment, the depth of high permeable layer (surface layer) should be controlled in a reasonable level.

(3) The arrangement of soil stratum structure is very important for the construction of clay railway embankment. The depth of each layer and the selection of different saturated permeability of clay soil material are based on the local rainfall distribution and the designed value of gravity load above it.

(4) The rainfall intensity, rainfall duration and rainfall patterns should also be considered for the construction of clay railway embankment. The rapid daily rainfall could enlarge the value of surface pore-water pressure and reduce the matric suction significantly, which could reduce the stability of surface part of clay railway embankment.

References

1. Anderson, M. G. & Pope, R. G. (1984). The incorporation of soil water physics models into geotechnical studies of landslide behaviour. Proc. 4th, Int. Sym. On Landslides, Vol. 4, pp. 349–353.
2. Briggs, K., Smethurst, J. A., Powrie, W. & O'Brien, A. S. (2011). Wet winter pore pressures in railway embankments. Proceedings of the Institution of Civil Engineers – Geotechnical Engineering.
3. Smethurst, J. A., Briggs, K. M., Powrie, W., Ridley, A. & Butcher, D. J. E. (2013). Mechanical and hydrological impacts of tree removal on a clay fill railway embankment.
4. Geo-Slope. (2013). User's guide for Vadose/W, Geo-Slope International, Canada.
5. Lam, L., Fredlund, D. G. & Barbour, S. L. (1987). Transient seepage model for saturated-unsaturated soil systems: a geotechnical engineering approach. Can. Geotech. J., 24, 565–580.
6. Leach, B. & Herbert, R. (1982). The genesis of a numerical model for the study of the hydrology of a steep hillside in Hong Kong. Quart. J. Eng. Geol., 15, 243–259.
7. Lumb, P. B. (1962). Effects of rain storms on slope stability. Symposium on Hong Kong Soils', Hong Kong, 73–87.

Experimental and Numerical Study on Structural Vibration Response of Buildings Along the Subway Tunnel

Tianqi Zhang, Yanyun Luo, Yan Liu, Qiutong Li and Jingzhi Liu

Introduction

With the rapid development of urban rail transit, its vibration and noise pollution are gradually concerned by more and more people. Although the vibration generated by urban transit operation is not large enough to destroy building structures along the lines, the vibration may cause the local vibration of structures, such as doors, windows, etc. This kind of vibration will induce the secondary structure noise which shows low-frequency characteristics. This kind of noise has serious impact on people's hearing first and mentality later, even make people suffer from insomnia, etc. [1]. In order to eliminate the effect, it is necessary to study the vibration of buildings along the subway line induced by operating metro. For convenience, the vibration of building structures along metro line caused by subway operation is called "the vibration" in the sections below.

There are number of results concerning "the vibration" at present. Japanese railway technical research institute studied the vibration arising from Shinkansen high-speed trains and its influence on environment [2]. In the U.S.A., Kurzweil and others studied on propagation path and attenuation characteristics of vibration wave

T. Zhang (✉) · Y. Luo · Y. Liu · Q. Li · J. Liu
Institute of Rail Transit, Tongji University, Shanghai 201804, China
e-mail: ztqljs1994@163.com

Y. Luo
e-mail: yyluo15@163.com

Y. Liu
e-mail: liuyans.851010@hotmial.com

Q. Li
e-mail: lqt910818@163.com

J. Liu
e-mail: 1123885247@qq.com

caused by the subway train operation [3, 4]. Volberg in Spain conducted a series of tests to analyze propagation rule and attenuation characteristics of ground vibration caused by train under different soil conditions [5]. Xia He et al. established a train-foundation-soil-structures system by using 2-D dynamic model analysis. The propagation laws of vibration in soil and their effects on surrounding buildings of different heights at different sites are studied under the action of trains in tunnel underground at different depth. Numerical results indicated that the dynamic response of low-rise buildings affected by metro operation is larger than that of high-rise, and the negative correlation between depth of tunnel and vibration of buildings was obtained [6]. In addition, F. Wang et al. found that soil property is a significant factor influencing propagation of vibration, and specifically the vibration amplitude tended to decrease with the increase of soil hardness. Besides that, vertical vibration of bottom of high building is much more obvious while horizontal vibration of higher floors in building is more evident [7]. However, it is still insufficient in numerical models and theoretical research. Firstly, previous numerical models of vibration propagation through tunnel-soil-building are mostly based on two-dimensional models, which cannot really reflect propagation rule of vibration. In addition, the existing research is mostly aimed at the vibration of high-rise buildings along the subway line. Due to the different structures and foundation depths between high-rise and low-rise, the propagation law of vibration of low-rise buildings is not like that of high-rise.

Based on the previous research, study on vibration effects of subway to surrounding buildings is a significant aspect in research of urban rail transit. However, there are a number of problems to be solved. Research technology of 2-D dynamical finite element model to solve vibration of soil is quiet mature and widely used. However, 3-D dynamical FEM model should be explored to calculate vibration problems of building due to the problematic assumption that building cannot be assumed as a surface during the train operation.

In this article, a series of field measurements were performed to study the damping effects of fastening system to the buildings and circumstance around subway lines. Limited by time and experiment condition, the experiment of this research is narrowed down to the stiffness of fastening system. In order to explore influences of varies of factors on vibration of vicinity buildings around the subway lines, a Tunnel-Soil-Building 3-Dimension finite dynamic elements model by ANSYS software is established. Reaction force between rail fastener and rail bed calculated by SIMPACK has been introduced into the FEM model as vibration source. Vibration response of tunnel, ground and building above subway can be obtained from the ANSYS results. Through comparison between the calculated and experimental results measured by a series of tests, the validity of present model is verified. The influences of train speed and of fastening stiffness are obtained by numerical models.

Performed Measurements

Experimental data from inside of buildings was examined on account of the noise and vibration complaints by urban inhabitants who live in residential dwelling near subway lines. This line was buried nearly 13.5 m depth and tunnel's radius is 6.2 m. Aiming at figuring out the relationship between fastener stiffness and vibration of surrounding buildings, two kinds of fasteners (the stiffness of fastener I is 30 MN/m and the stiffness of fastener II is 20 MN/m) were chosen as the tested fastening system to compare the damping effects. The investigated dwelling was a three-story brick masonry building located almost 24 m away from the ground above the tested tunnel centerline.

In the experiment, measured point ▫ – ▫ are applied to investigate the vibration propagation from wheel-rail interaction to tunnel wall through track bed, with accelerometers recording signals of vertical acceleration shown in Fig. 1. The exact locations of measured points in tunnel are set according to GBT 198460-2005 & HJ 453-2008.

All the accelerometers are settled on each floor of tested building (Fig. 2) where all doors and windows are closed for reducing influence of other noises from
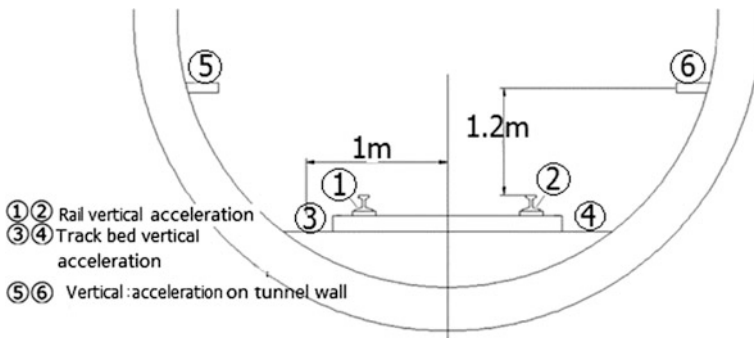
Fig. 1 Measured points in tunnel
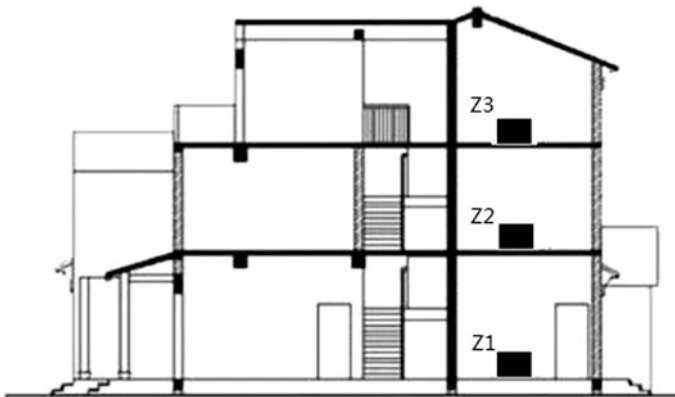
Fig. 2 Measured points in tested building around subway lines

environment, recording signals of vertical acceleration transmitted from both surface traffic and underground. The number of tested train is no less than ten and all the instruments must be integrated into a synchronous acquisition system so as to ensure the reliability of this experiment.

The tested vibration accelerations of the floors in the room of building are transmitted from both surface traffic and underground.

Measurement Analysis

Analysis in Tunnel

Spectrum analysis on vertical acceleration signals of tunnel walls in tested tunnels with different fasteners is conducted to reveal the damping effects of fasteners to tunnel walls. By analyzing test results of vertical vibration on tunnel wall with different fasteners in the tunnel, it can be found that compared with fastener I (the stiffness is 30 kN/m), the linear weighted vibration acceleration level of fastener II (the stiffness is 20 kN/m) within 1–80 Hz is reduced by 3.53 dB, while that within 4–200 Hz is reduced by 3.13 dB, as illustrated in Table 1. Similarly Z-weighted vibration acceleration level of tunnel wall is analyzed as well. The vibration acceleration level of fastener I within 1–80 Hz is 3.04 dB higher than that of fastener II, while that within 4–200 Hz is 2.98 dB higher shown in Table 2.

By analyzing the 1/3 octave shown in Figs. 3 and 4, it can be found that the vibration acceleration level of tunnel walls with two kinds of fasteners in tunnel are almost the same below the frequency of 31.5 Hz, while the vibration acceleration level of tunnel wall with fastener II in tunnel is less than that with fastener I above 31.5 Hz. It can be indicated that lowering stiffness fastener can reduce the vibration of tunnel wall to a certain extent.

Analysis in Surrounding Building

The 1/3 octave of vertical vibration acceleration on each floor of three-story building with fastener I and fastener II in tunnel are shown in Fig. 5. Due to "the vibration" mainly concentrated on low-frequency, only the range of 1–80 Hz of the vibration acceleration are presented here. It can been seen from Fig. 5 that at the range of 1–8 Hz, the vibration acceleration of each floor is almost the same. From

Table 1 Comparison of vertical vibration acceleration level on the tunnel walls (linear weighted, dB)		1–80 Hz	4–200 Hz
	Fastener I	96.07	98.48
	Fastener II	92.54	95.25
	Difference value	3.53	3.13

Table 2 Comparison of vertical vibration acceleration level on the tunnel walls (Z-weighted, dB)

	1–80 Hz	4–200 Hz
Fastener I	82.29	82.41
Fastener II	79.26	79.44
Difference value	3.04	2.98
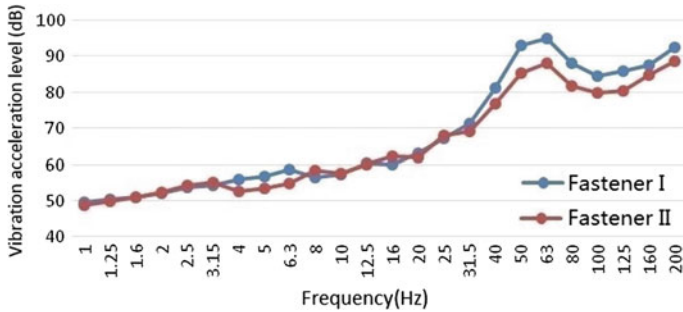
Fig. 3 Comparison of one-third octave on vertical vibration acceleration on one side tunnel wall (linear weighted)
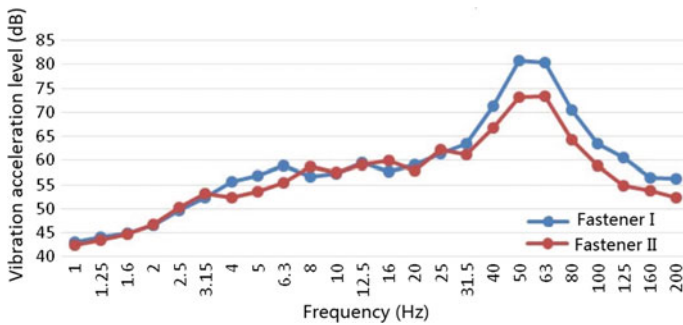
Fig. 4 Comparison of one-third octave on vertical vibration acceleration on one side tunnel wall (Z-weighted)

10 to 25 Hz, the vibration on the first floor is the largest among the three floors. And the vibration in the third floor is larger than that on the second floor basically. From 31.5 to 80 Hz, the vibration in the third floor is the largest. It is implied that the vibration changes with the floor in the low-rise building is different from the rule of vibration change in the high-rise building that the vibration will increase with the floor rising [8]. Therefore the rule of vibration change with the floor is related to the structure of building.

Based on the above analysis of measurement, lowering stiffness fastener can reduce vibration of tunnel wall to some extent, by maximum 4 dB reduction analyzed in 1/3 octave spectrum. Likewise, the indoor vibration acceleration of tested building can be decreased 3 dB by utilizing lower stiffness fastener. However, the

Fig. 5 The 1/3 octave of vertical vibration acceleration on each floor of three-story building (fastener I)
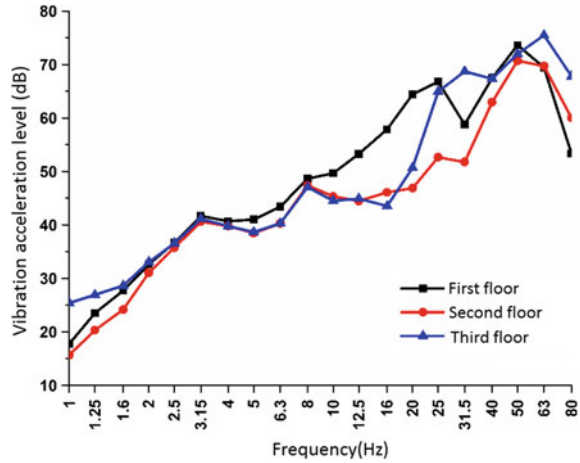
change of vibration acceleration on each floor in building along with the increase of floor numbers is not obvious. Besides that, the vibration acceleration attenuates along with propagation from tunnel to building.

Coupling Dynamic FEM Models

Vehicle-Track Coupling Dynamic Model

Based on the theory of vehicle track coupling dynamics [9], the rigid wheel rail dynamic coupling model is established in three dimension space by using ANSYS. The rail model is the type of 60 km/m while track slab is simulated by solid element (unit type is SOLID185), as shown in Fig. 6.
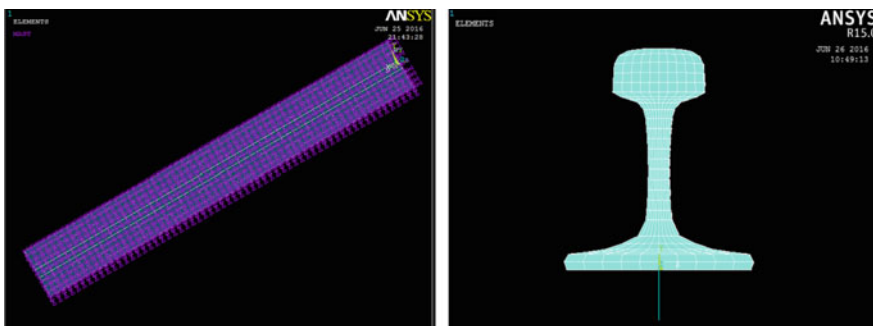
Fig. 6 Rail and track panels finite element model

Based on multi-body system dynamics method and SIMPACK software platform, a rigid-flexible coupling multi-body model is built for vehicle dynamics simulation. As a complex multi-body system, vehicle model can be divided into three elastic bodies: car body, bogies and wheelsets. Among them, car body and bogies are connected by secondary suspension system while bogies and wheelsets are connected by primary suspension system. In the tread contact relationship between wheel and rail, the type of wheel tread is European wheel S1002 while that of rail tread is UIC 60 rail. The normal interaction force between wheel and rail are presented by using Hertz contact theory, while tangential contact forces are based on Kalker creep theory. Calculation by SIMPACK has been carried out in order to obtain reaction force between rail fastener and rail bed, which will be introduced into the tunnel-soil-structure system FEM model as vibration source.

Tunnel-Soil-Building Finite Element Model

The vibration induced by metro train is a kind of linear vibration, which causes vibration of tunnel structure. Thus tunnel structure is not only a source of vibration, but also an important part in propagation of vibration [10]. The vibration when metro train running is transmitted in the form of mechanical waves to the adjacent buildings through the way of wheel-track-soil-tunnel structure. The tunnel model and the soil material parameters are shown in Fig. 7 and Table 3 respectively.

Dynamic FEM model of surrounding building is established on the basis of experimental data measured from residential building mentioned above. The FEM

Fig. 7 Tunnel model
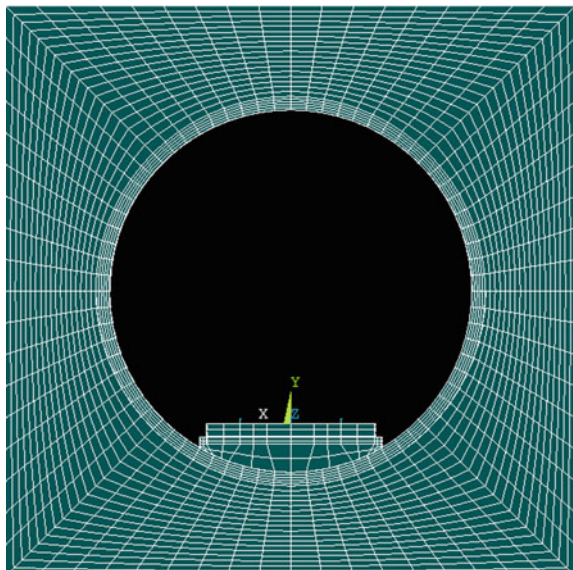
Table 3 The soil material parameters

No	Type	Thickness (m)	Modulus of elasticity (Mpa)	Poisson's ratio	Density (kg/m^3)	Wave velocity (m/s)
1	The soft soil	2.5	60	0.3	1840	110
2	The soft soil	8	160	0.3	1840	180
3	In hard soil	10	380	0.37	1730	240
4	Sandy soil	18	420	0.39	1940	280

Fig. 8 Building structure model
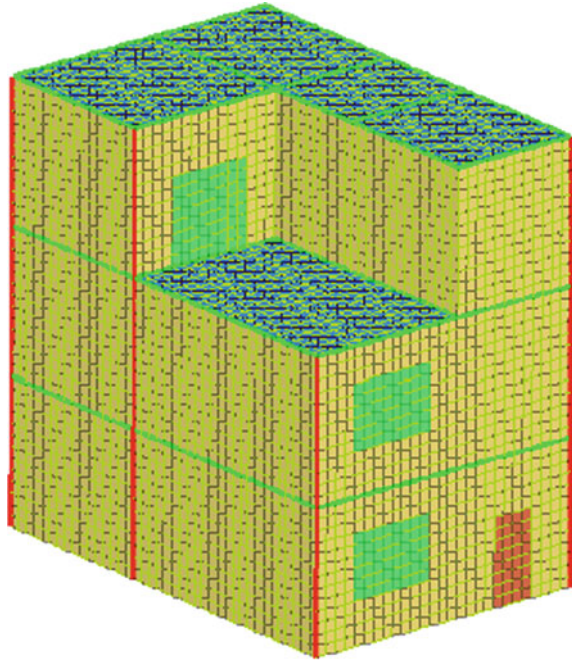
model of building is a three-story reinforced concrete structure with the height of 3-meter on each floor, as shown in Fig. 8. Adopting BEAM188 unit and SHELL 181 unit to simulate beam, column and floor, respectively. The first floor of the structure is rigid fixed on the ground at the bottom of the column. Floors are simulated by C30 concrete with elastic modulus of 3.3e4 MPa, the density of 2500 kg/m^3 and Poisson's ratio of 0.2. The other components are modeled by C40 concrete. The elastic modulus is 3.25e4 MPa, the density is 2700 kg/m^3, and Poisson's ratio is 0.2.

Model Validation

Comparison of vertical vibration spectrum of three floors simulated by FEM models and analyzed by test is shown in Fig. 9. It can be seen that the value of simulation results on the first floor are greater than measured results below 10 Hz, while the simulation results are very similar with experimental results above the frequency of 10 Hz. Then the results of both numerical simulation and experiments reaches the peak at 53 Hz. On the second and third floor, similarly, the measured results are greater than the simulation results below 8 Hz while they are similar above 8 Hz. Simplification of complicated experimental environments such as neglecting effects of ground transportation and other vibration source and utilizing the rigid connection between soil and buildings may lead to the difference between these two results. Nevertheless, in view of the above mentioned facts, the validity of the numerical simulation method is good by comparing simulation results and experimental results.
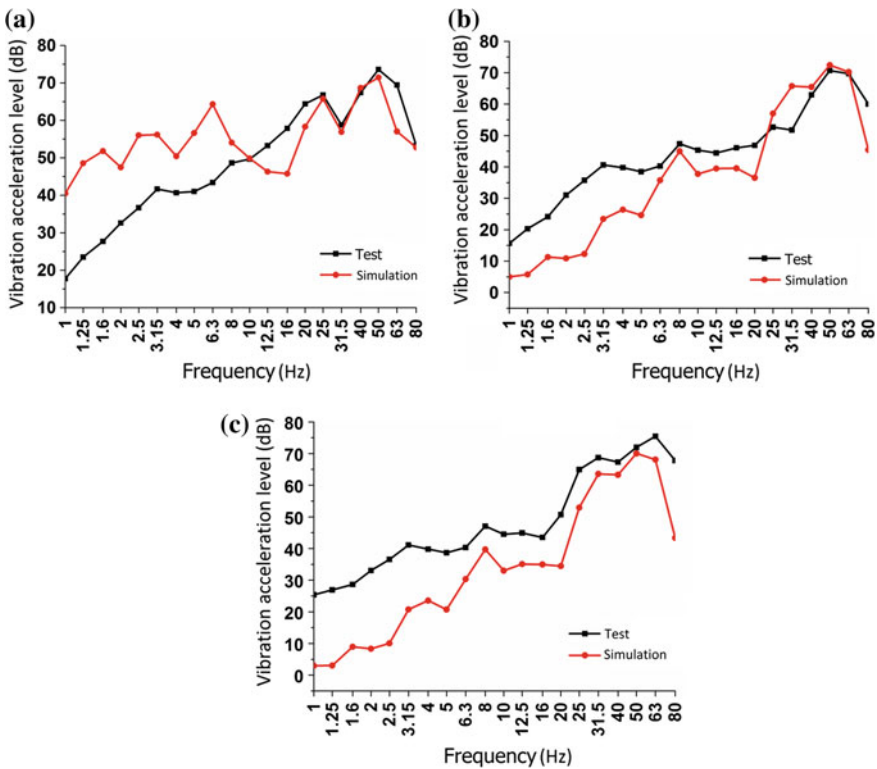
Fig. 9 Vertical vibration on each floor of surrounding buildings. **a** The first floor; **b** the second floor; **c** the third floor

Influence of Train Speed and of Fastening Stiffness

Effect of Fastener Stiffness to Structural Vibration of Surrounding Buildings

Experiments in the present paper show that relatively low stiffness of two fasteners can reduce the vibration response of nearby buildings caused by operation vehicles. In order to validate this conclusion, simulating the vibration responses of building structures with different fastener stiffness from 10 to 30 MN/m, with the interval of 10 MN/m. Analyzing the relationship between vibration acceleration level of each floor and fastener stiffness shown in Fig. 10, it is estimated that a 10 MN/m of fastener stiffness reduction can reduce vertical vibration of each floor by around 2–3 dB on average. Therefore, lowering stiffness fastener can weaken the vibration of buildings around subway lines.

Effect of Train Speed to Structural Vibration of Surrounding Buildings

It is considered that train speed has a great impact on the vibration of track system. Along the way of vibration propagation from rail to surrounding buildings, it can be deduced that with the increase of train speed, vibration of building structure can be reduced. According to this, the numerical simulation of tunnel-soil-building finite element model by different train speeds from 60 to 100 km/h with the interval of 10 km/h has been calculated. It can be seen from Fig. 11 that with train speed increasing, vertical vibration acceleration values on each floor increase gradually. It can also be analyzed that the vertical vibration in the first floor is the largest. And vertical vibration acceleration values of the second floor is a little bit lower than that of the third floor.

Fig. 10 The relationship between vibration of each floor and fastener stiffness
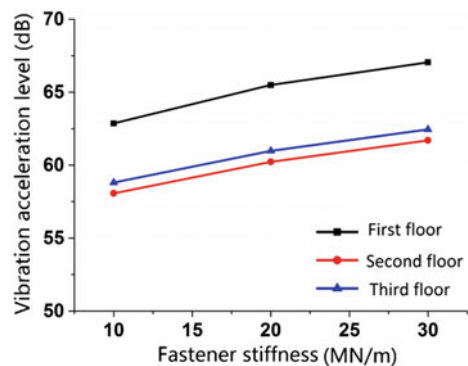
Fig. 11 The relationship between vibration of each floor and train speed
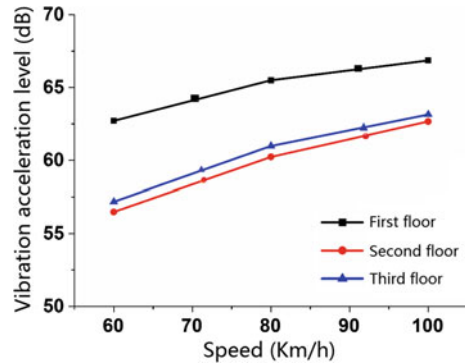
Conclusions

Measurement data are presented in this paper and tunnel-soil-building FEM model are analyzed to study on the vibration response of building along the subway lines induced by running vehicles. By comparison, the result of 3-D finite element model has shown a great agreement with the field test. Some conclusions can be obtained from this paper above,

- Lowering stiffness fasteners can reduce the vibration of building to a certain extent. The maximum insertion loss can be achieved to 2 dB by a 10 km/m reduction of fastener stiffness.
- The vertical vibration of low-rise buildings along the tunnel floor is not very obvious with the change of floor.
- In the case of other conditions unchanged, with the increase of train speed, the vibration of building have a slight increase. And the vibration of the first floor is the largest, with the third floor is slightly larger than the second floor.
- In the case of other conditions unchanged, with the decrease of fastener stiffness, the vibration of the building have a slight decrease, but the amplitude is not obvious.

References

1. Gu Xiao An, Tian Chun Zhi. Metro vibration noise prediction in buildings secondary structure [J]. Railway saving and environmental protection and health and safety, 2000(1):65–67.
2. Fujikake T. A Prediction Method for the Propagation of Ground Vibration from Railway Trains [J]. Journal of Sound and Vibration. 1986, 111 (2): 289–297.

3. L. G K. Ground-borne noise and vibration from underground rail systems [J]. Journal of sound and vibration. 1979, 66(3): 363–370.
4. Wilson, G.P., H.J. Saurenman, J.T. Nelson. Control of ground-borne noise and vibration [J]. Journal of sound and vibration. 1983, 87(2): 339–350.
5. Volberg G. Propagation of ground vibrations near railway tracks [J]. Journal of sound and vibration. 1983, 87(2): 371–376.
6. Wang Feng Chao, Xia He, Zhang Hong Ru Metro Train Vibration on Surrounding Buildings [J]. Beijing Jiaotong University, 1999, 23(5):45–48.
7. Wang Feng Chao, Xia He, The impact on the environment and building train vibration analysis [J] Beijing Jiaotong University: Natural Science, 1999, 23(4):13–17.
8. Sheng Tao, Zhang Shan Li, Shan Jia Zheng, subway and other transfer of vibration and impact of the building measurement and analysis of [J] Tongji University: Natural Science Edition, 2015, 43 (1): 54–59.
9. Zhai Wanming. Vehicle-Track Coupling Dynamics (Forth Edition) [M]. Beijing: Science Press, 2015.
10. Hu Zongyun. The foundation settlement caused by the subway train vibration[D]. Beijing Jiaotong university, 2006.

Evaluation of Liquefaction Potential of Saturated Sands Based on Resistivity Piezocone Penetration Testing—A Case Study

Wei Duan, Guojun Cai, Haifeng Zou and Songyu Liu

Introduction

Liquefaction of saturated cohesionless soils often causes damage to infrastructure such as buildings, and bridges. Therefore, it is essential to evaluated properly the potential of liquefaction occurrence. Due to the difficulties in obtaining high quality undisturbed samples in laboratory testing, the advanced piezocone penetration test (CPTU) has been widely used in geotechnical site characterization due to its high accuracy and repeatability. Numerous CPTU-based approaches to assessing the liquefaction potential of saturated soils have been proposed in the past decades [1]. However, none of the CPTU-based approaches has been accepted as the most effective one. Thus it is of interest to develop a new method for evaluation of soil liquefaction.

The most widely used simplified procedure for evaluating soil liquefaction potential was originally proposed by Seed and Peacock [2] using the blow counts from the SPT. Subsequently, in NCEER seminar [3], the simplified method is applied CPT/CPTU Testing Technology. The CPTU-based simplified deterministic method can be described: the ratio of cyclic stress ratio (CSR) over cyclic resistance ratio (CRR), the soil is determined as liquefiable.

W. Duan · G. Cai (✉) · H. Zou · S. Liu
Institute of Geotechnical Engineering, Southeast University,
Jiangsu, Nanjing 210096, China
e-mail: focuscai@163.com

W. Duan
e-mail: zbdxdw@163.com

H. Zou
e-mail: zhf0728@gmail.com

S. Liu
e-mail: liusy@seu.edu.cn

509

It has been recognized that the liquefaction characteristics of sands are influenced not only by the relative density of deposit, but also by factors including the structural orientation of the particles, gradation of sands, and in situ stress conditions. Resistivity is one of the fundamental parameters of soil, which is highly related to the other soil parameters such as porosity, saturation, shape and size, gradation, and grain orientation. Archie [4] demonstrated that the electrical resistivity model provides a non-destructive method to predict the liquefaction resistance. Therefore, it is supposed that the resistivity may contribute to assessing the liquefaction resistance of soil. Behavior of soils is highly dependent on both density and stress level. The state parameter is widely accepted to represent the soil behavior encompassing both density and stress effects, which is proposed By Been and Jefferies [5] ,the state parameter (Ψ) can be used for effective evaluation of liquefaction potential of saturated soils [6]. Huang et al. [7] Studied liquefaction based on the state parameters and get the relationship between the State parameters and CRR. There are some Scholars proposed typical and reliable situ testing methods for calculating the state parameters [8–10].

In this research the feasibility of evaluating liquefaction potential based on RCPTU data is investigated. First, the correlation between liquefaction potential and RCPTU data is conducted by regression analysis. Finally validation the correctness of the RCPTU method with the standard penetration test (SPT).

Experimental Investigation

Site Description

The testing site is located in Suqian-Xinyi expressway in Jiangsu province. The testing section is in an active seismic zone with a design magnitude (M_w) of 8. The soils in the testing section are mainly partially unconsolidated Quaternary sediments. The ground water table (GWT) is around 3.8 m below the ground surface. The surface layer of the field is the near future artificial mixed soil and the cultivated land, which are silt and silt. The main physical and mechanical indexes of the test site soil are shown in Table 1.

Table 1 Main physic-mechanical index of site soil

Layer	Soil type	Thickness (m)	Specific gravity (Gs)	Clay content (%)	Moisture content (%)	ω_L (%)	I_P	SPT-N63.5 value
1	Plain fill	1.5	2.71	14.9	22.4	26.2	8.8	9
2	Silt	3.8	2.70	3.7	24.1	28.1	5.8	4
3	Silty sand	9.4	2.69	5.4	33.6	28.7	5.7	10
4	Silt	Not exposed	2.68	5.6	23.6	31.6	11.3	24

Testing Results

A representative RCPTU test result is given in Fig. 1. As shown, the cone tip resistance is generally small in silt and silty sand. Aggregation and dissipation of excess pore water pressure are not observed in the CPTU profiles, indicating that the soils are in a relatively loose state and there is the possibility of liquefaction.

Resistivity Index of Liquefaction Assessment

Relation Between ρ, Ic and CRR (Directly Calculate Method)

Previous analysis demonstrated that the CRR tend to increase with the resistivity of soil, but decreases with I_c [11] Hence, a correlation between CRR and the derived variable, $(\rho/\rho_w)^n/(I_c)^m$, is analyzed. Using the multivariate regression analysis the coefficients (n and m) were determined as $n \approx 0.8$ and $m = 4.2$. The fitted curve along with the scatter plot for the correlation between CRR and $(\rho/\rho_w)^n/(I_c)^m$ is shown in Fig. 2. The following expression can be obtained according to Fig. 2:

$$\text{CRR} = 0.08 + 0.02 \exp[10.350 \times (\rho/\rho_w)^{0.8}/(I_c)^{4.2}] \tag{1}$$

The scope of application of Eq. (1) is $1.8 < I_c < 2.5$ with normally consolidated cohesionless soils.

As shown in Fig. 2, the CRR tends to increase with the resistivity of soil, but decrease with I_c. Based on the analysis of soil behavior type index, for clean sand ($I_c < 1.8$), its grain size and strength will both increase as I_c decreases. Therefore,
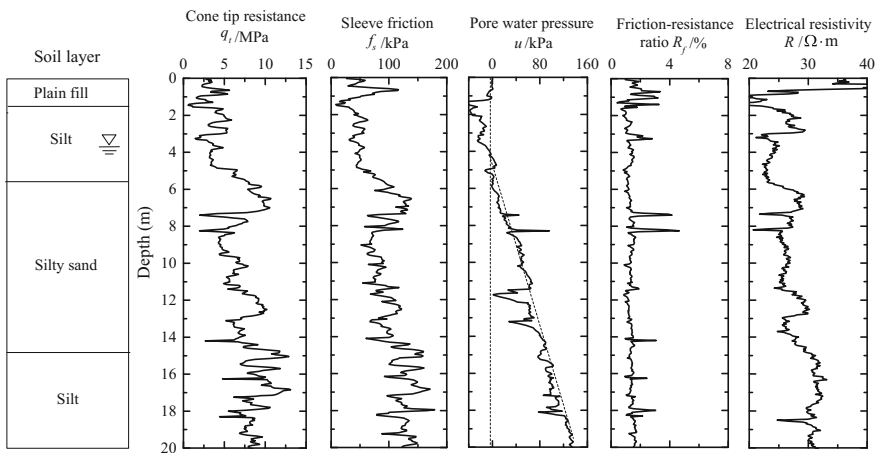
Fig. 1 Typical results of resistivity piezocone tests

Fig. 2 Relationship among
CRR, ρ and I_c

$$CRR = 0.08 + 0.020 * \exp[10.350 * (\rho/\rho_w)^{0.8}/(I_c)^{4.2}]$$

$$n = 138 \ R^2 = 0.90$$
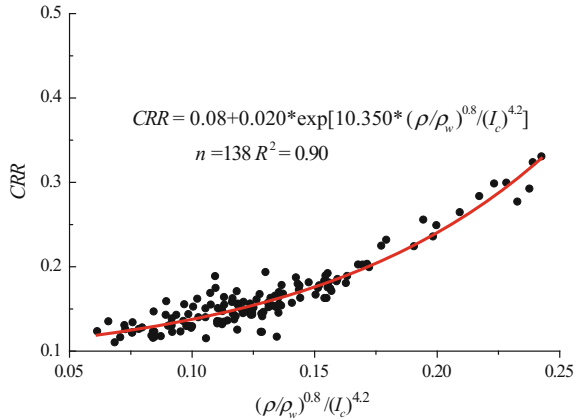
the liquefaction resistance of clean sand would be larger than that of mixed cohesionless deposit.

Based on above analysis, it is inferred that electrical resistivity mainly reflects the impact of the in-suit state characteristics of soil including void ratio and relative density on the liquefaction resistance (CRR). Therefore, the combination of electrical resistivity (ρ) and soil behavior type index I_c can be used to predict the cyclic resistance ratio (CRR) with more accuracy.

Relation Between ψ and CRR (Indirectly Calculate Method)

Figure 3 is the relationship between CRR and ψ that is calculated by the method of resistivity state parameter prediction [12].

From the above we can know the relationship between the two is better and Liquefaction discrimination can be carried out by means of state parameters.

Validation of the Proposed Method (Directly Calculate Method)

In this section the CRR values estimated from the proposed resistivity-based model and those obtained from Robertson [13] modified method are compared to those obtained using the standard penetration test (SPT) data. The estimates of CRR for two adjacent RCPTU test bores and SPT are shown in Fig. 4, which indicates that the CRR values estimated from the resistivity-based method in this research are consistent with those obtained from Robertson [13] modified method. Besides, similar evaluation of liquefaction potential is achieved and confirmed for the SPT-based approach and the resistivity-based method developed in this study. The

Fig. 3 Relation between ψ and CRR

$$CRR=0.04exp(-\psi/0.14)+0.07$$
$$R^2=0.84$$
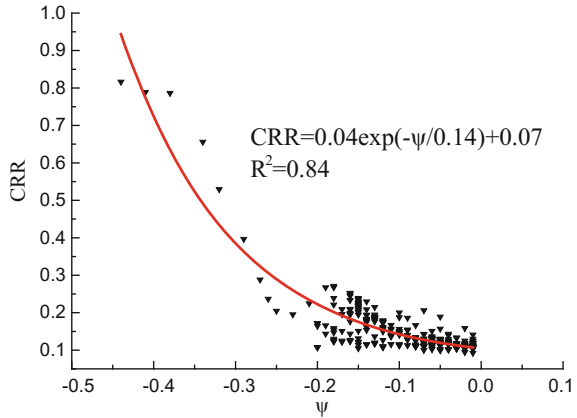
Fig. 4 Representative results of model validation
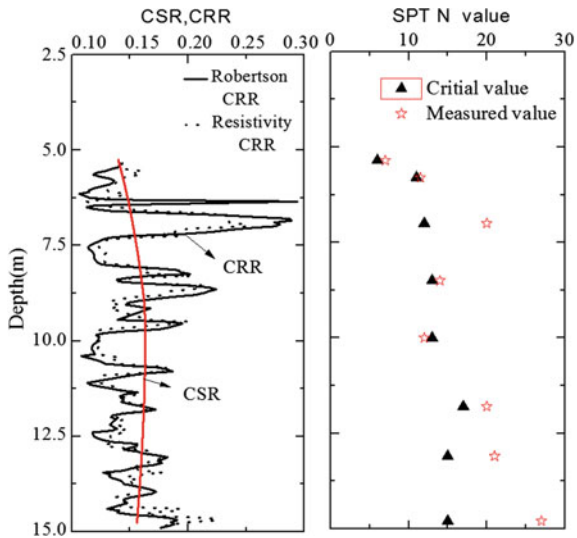
main difference between the estimates of SPT-based method and those of resistivity-based method occurred when $I_c > 2.5$, in this research the data of $I_c > 2.5$ are insufficient for developing a correlation between the CRR and electrical resistivity, which still requires further research.

Conclusions

The method for cyclic resistance ratio (CRR) using ρ and I_c is developed and the estimates of CRR are consistent with those from Robertson [13] modified method. The correlation for predicting cyclic resistance ratio (CRR) using the state

parameter (ψ) is presented. The resistivity-based method provides a novel and more convenient way to estimate the CRR for evaluation of liquefaction potential of saturated soils.

References

1. Cai, G.J., Liu, S.Y., Anand, J.P. (2012). Liquefaction assessments using seismic piezocone penetration (SCPTU) test investigations in Tangshan region in China, Soil Dynamics and Earthquake Engineering, 41: 141–150.
2. Seed, H.B., Peacock, W.H. (1971). Test procedures for measuring soil liquefaction characteristics, Journal of the Soil Mechanics and Foundations Division, ASCE, 97(SM8): 1099–1119.
3. Youd, T. L., & Idriss, I.M. (2001). Liquefaction resistance of soils: summary report from the 1996 NCEER and 1998 NCEER/NSF workshops on evaluation of liquefaction resistance of soils. Journal of Geotechnical & Geoenvironmental Engineering, 127(4), 817–833.
4. Archie, G. (1942). The electrical resistivity log as an aid in determining some reservoir characteristics, Trans, American Institute of Mining Metallurgical and Petroleum Engineers, 146: 54–61.
5. Been, K., Jefferies, M.G. (1985). A state parameter for sands[J]. Geotechnique, London, 35 (2): 99–112.
6. Jefferies, M. G., Been K. (2006). Soil liquefaction: a critical state approach. CRC Press, Taylor & Francis.
7. Huang, A.B., Bunting, R.D., Carney, T.C., (1991). Piezoblade tests in a clay calibration chamber[J]. Calibration Chamber Testing, 1991: 161–173.
8. Plewes, H.D., Davies, M.P., Jefferies, M.G. (2009). CPT based screening procedure for evaluating liquefaction susceptibility[C]. In Proceedings of the 45th Canadian Geotechnical Conference: 41–49.
9. Been, K., Jefferies, M.G., Crooks, J H. A., et al. (2009). The cone penetration test in sands: Part II, general inference of state[J]. Geotechnique, 37(3): 285–299.
10. Roberston, P.K. (2010). Estimating in-situ state parameter and friction angle in sandy soils from CPT[C]. Proceedings of the 2nd International Symposium on Cone Penetration Testing, CPT. 10: 2–43.
11. Zou, H.F., Liu, S.Y., Cai, G.J., Du, G.Y. (2013) . Evaluation of liquefaction potential of saturated sands based on piezocone penetration tests on resistivity, Chinese Journal of Geotechnical Engineering, 35(7):1280–1288.
12. Chu, Y., Cai, G.J., Liu, S.Y. (2014). Study on liquefaction evaluation method based on CPTU in-situ state parameter[J]. Journal of Earthquake Engineering, 36(4):905–910.
13. Robertson, P.K. (2009). "Interpretation of cone penetration tests - a unified approach," Canadian Geotechnical Journal, 46(11): 1337–1355.

Research on Computational Model of Large-Span Flexible Structures for Serviceability Assessment

Wei He and Weiping Xie

Introduction

Large-span flexible structures have achieved great development in China in recent years due to its flexibility in structural function and attractive appearance. The vibration serviceability of the low frequency, low damping structures is of great concern in engineering for better performance in service conditions. Intensive studies have been made on the vibration problem of flexible footbridges [1–3], large-span floors [4–6] and high-rise buildings since the Millennium Bridge accident on its open day in 2000 [7], and some beneficial results have been achieved. Compared with the extensive investigation on dynamic calculation method and vibration mitigation countermeasures of structures under human excitation [1–6], the simplification method for a computational model of the structure for vibration serviceability is rarely concerned, although some experimental results have demonstrated that the calculation model for serviceability may differ [8].

In this paper, we put a special concern on the computational model of large-span flexible structures for vibration serviceability based on experimental results of two large-span railway stations at different construction stages. The differences between the model for serviceability and the model for safety are emphasized and the main influential factors of the computational model of flexible structure for vibration serviceability are presented. Furthermore, the damping for serviceability is discussed based on laboratory test of a cantilever beam.

W. He
Department of Engineering Structure and Mechanics, Wuhan University
of Technology, Wuhan 430070, China
e-mail: heweismile@126.com

W. Xie (✉)
Department of Civil Engineering, Wuhan University of Technology,
Wuhan 430070, China
e-mail: wpxie@sina.com

Modal Test of Two Full-Scale Large-Span Railway Stations

In this section, the modal tests of 2 full-scale large-span railway stations, i.e. East Zhengzhou Railway Station and South Changsha Railway Station at different construction stages are carried out and the modal properties results are presented.

East Zhengzhou Railway Station

East Zhengzhou Railway Station (EZRS, Fig. 1) is one of the largest high-speed railway stations in the word, with its length over 490 m and width 239.8 m. It's the typical representative of China's 3rd generation high-speed railway stations, in which a novel structure type, called train-bridge-structure system, is employed. The details of the EZRS can be found in Ref. [9].

Modal tests of 8 typical floor areas of the large-span floors of EZRS are conducted at two different construction stages—before (stage 1) and after decoration (stage 2). For stage 1, only the main body of the whole structure is completed, while for stage 2, the whole structure is decorated and furnished for normal use. Both the impact method and ambient vibration method are employed during the modal tests. The experimental results of the modal properties are presented in Fig. 2.

It is clear that both the fundamental frequency and damping ratio of the test floors change before and after decoration. As described in Fig. 2a, the frequency of the floor generally decrease after decoration except for floor No. 2, which means the contribution of stiffness provided by floor decoration and non-structural in-filled walls plays a greater role than the mass. While the damping ratio generally increases after decoration as the non-structural components adds damping to the whole structure through connections and joints. As can be seen in Fig. 2b, the damping varies from 0.8 to 1.2% after decoration, which are much smaller than the values we commonly adopted in dynamic analysis for seismic or strong wind excitation.

(a) before decoration   (b) after decoration

Fig. 1 East Zhengzhou Railway Station
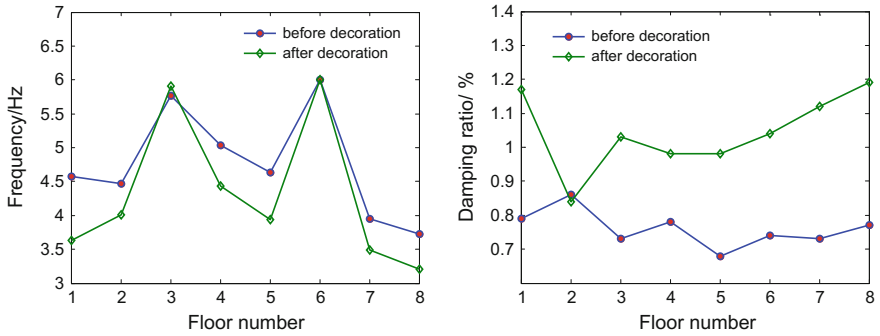
Fig. 2 Modal properties of floors obtained before and after decoration

South Changsha Railway Station

South Changsha Railway Station (SCRS, Fig. 3) is among the largest high-speed railway stations in China, with its gross floor area over 149,000 m^2. The details of the SCRS can be found in Ref. [10]. The floor of SCRS, which employs steel truss-concrete composite floor, is so flexible that its maximum depth-span ratio can reach 1/20 (H/L = 2.45 m/49 m).

Modal tests of 2 typical areas (with its depth-span ratio 1/20) of the large-span floors of SCRS at two different construction stages—before (stage 1) and after decoration (stage 2) are conducted. For stage 1, only the main body of the whole structure is completed, while for stage 2, the whole structure is decorated and furnished for normal use. Both the impact method and ambient vibration method are employed during the modal tests. The experimental results of the modal properties are presented in Table 1.

Fig. 3 South Changsha Railway Station

Table 1 Measured natural frequencies of the floors before and after decoration

Floor number	1st order natural frequency (Hz)		2nd order natural frequency (Hz)	
	Before decoration	After decoration	Before decoration	After decoration
1	3.59	3.33	3.88	3.60
2	3.02	/	3.27	/

Note "/"refers to not measured

Fig. 4 FE model of the floor 1
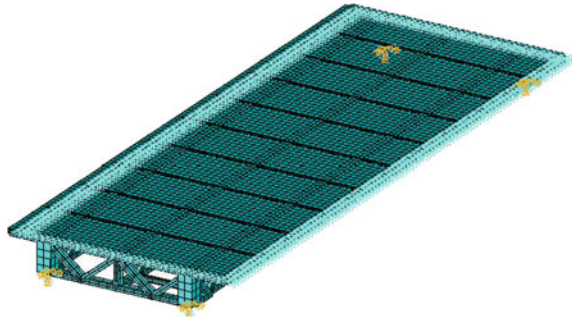
It can be seen from Table 1 that the vertical vibration frequencies of the 2 test floors have a slightly decrease after decoration with a 120 mm thick pavement on the floor. To simulate the influence of floor decoration, the FEM of Floor 1 was developed, as shown in Fig. 4. As we know, in normal service condition, the structure with small vibration amplitude is usually in linear elastic stage. So we can treat the pavement on the floor as additional elastic slab rather than additional mass. The specific simulation method can be found in Ref. [11]. Table 2 gives the results of FE simulation, which agree quite well with the obtained experimental results.

Main Factors Contributing to Dynamic Properties of Structures for Serviceability

As presented above, non-structural elements (i.e. decoration, floor pavement, ceiling, non-structural in-filled walls, hand rails), temperature joints, et al., may contribute to dynamic properties of the main structure in normal in-service conditions. Sometimes the structure may behave totally different due to the great changes in dynamic properties, especially for large-span flexible structures. Here we list some of the probably main factors that would contribute to the dynamic characteristics of structures based on experimental results of a variety of railway stations, stadiums and footbridges we conducted [9, 11].

Table 2 Comparison of measured and simulated results of floor 1

Construction stage	1st order natural frequency (Hz)		2nd order natural frequency (Hz)	
	Measured results	Simulated results	Measured results	Simulated results
W/O pavement	3.59	3.65	3.88	4.02
With pavement	3.33	3.35	3.60	3.76

Non-structural Elements

Non-structural elements (NSE), such as in-filled walls and partitions, are usually treated as secondary or less important elements which do not contribute to the load capacity and stiffness of the structure. The contribution of stiffness of NSE is usually ignored or partially considered in traditional computational modeling for seismic or strong wind excitation analysis, due to their comparatively weak connection with the main structure. That would be true for big amplitude vibration such as seismic or strong wind excitation, whereas, for serviceability evaluation, that would not the case. Xie et al. [9, 11] firstly reported the role of NSE in structural behavior and proposed the modeling method for NSE. As they reported, for floor structures, the contribution of pavement or decoration can be treated as elastic slab based on principles of equivalence of stiffness and mass.

Joints/Connections and Boundary Conditions

As mentioned above, serviceability assessment, characterized with low amplitude vibration and in-service conditions, is usually in linear elastic stage. Therefore, weak joints and connections (i.e. temperature joints, pin connections, et al.) which are traditionally treated as free or pin boundaries should be considered as rigid or semi-rigid for serviceability modeling. However, the method of modeling this effect and the proper values of stiffness of the joints still need more investigation.

Additional Mass

Additional mass refers to those live loads that are considered for loading capacity or deformation analysis in structure design to assure its safety. In seismic excitation analysis, the effect load of gravity is taken as the summation of structural gravity and 50% of the live load. To this extent, the additional masses are basically a ultimate load case. However, a lower value of the live load may be more reasonable for serviceability, based on the in-service condition fact. On one hand, less people participate in structure in normal use condition compared with the capacity design

value, on the other hand, the presence of human-structure interaction may change dynamic properties of the structure with an obvious increase in structural damping, which leads to a lower amplitude of vibration.

Damping

As an fundamental part of structure property, damping plays an important role in structure analysis. Due to its complexity, field measurement method is usually employed in practice to obtain structure damping. Huang et al. [12] reported the common values of damping for steel and concrete infrastructures, the results vary from 0.01 to 0.08. It should be noted that the results were obtained based on strong impact excitation, as damping is amplitude-dependent [13], those value may underestimate the response of the structure under dynamic excitation. The obtain damping ratios of EZRS by Xie et al. [9] range from 0.68 to 0.86% before decoration and the values slightly increase after decoration, ranging from 0.84 to 1.19%.

To explore the damping characteristics in the linear elasticity stage, a relatively uniform and simple steel cantilever beam element is adopted as the test object. The free vibration test of the cantilever beam is carried out to investigate the variation of the damping ratio. Details of the spices and experimental conditions are presented in Ref. [14]. Figure 5 gives the schematic plan of the cantilever and layout of the sensors.

The experiment was conducted in conditions of different initial vibration amplitudes to identify the damping ratio of the cantilever beam through the free vibration attenuation method. The purpose is to investigate the variation of damping ratio of the structural element in the free vibration and analyze the relationship between the vibration amplitude and the damping ratio of the cantilever beam in the range of linear elasticity. The damping ratios of different vibration amplitudes were obtained and illustrated in Fig. 6.

As shown in Fig. 6, the damping ratio of the cantilever beam of free vibration increases linearly with the increase of vibration amplitude in the range of linear elasticity and can be expressed as follows:

$$\xi = 0.000894^* \varepsilon + 1.682 \tag{1}$$

where ξ refers to damping ratio, with its unit 0.001 and ε refers to strain, with its unit $\mu\varepsilon$.

Fig. 5 The sensor placement of the cantilever beam (Unit: mm)
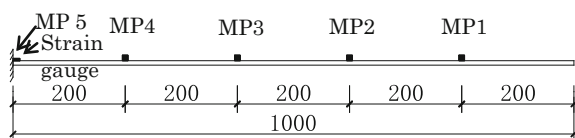
Fig. 6 Fitting result of strain and damping ratio of the cantilever beam
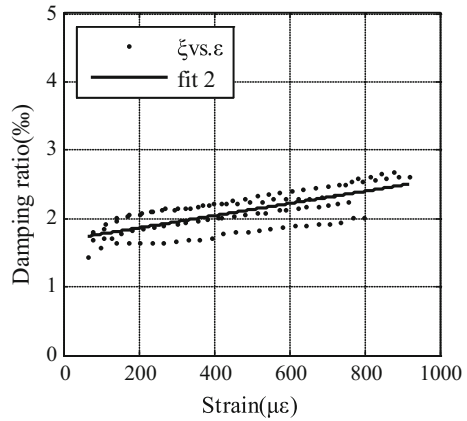
Conclusions

The differences between the model for serviceability and the model for safety are clarified and the main influential factors that a computational model for vibration serviceability should consider are presented. The results show that contributions of non-structural elements, additional mass, boundary conditions and damping should be thoroughly considered for serviceability modeling.

References

1. Živanovic S., Pavic A., Reynolds P. (2005). Vibration serviceability of footbridges under human-induced excitation: a literature review. Journal of Sound and Vibration, 279:1–74.
2. Rolando Salgado, Jorge M. Branco, Paulo J.S. Cruz, Gustavo Ayala. (2014). Serviceability assessment of the Góis footbridge using vibration monitoring. Case Studies in Nondestructive Testing and Evaluation, 2: 71–76.
3. Caetano E., Cunha A., Magalhães F., Moutinho C. (2010). Studies for controlling human-induced vibration of the Pedro e Inês footbridge, Portugal. Part 1: assessment of dynamic behavior. Engineering Structures, 32:1069–81.
4. Xuhong Zhou, Liang Cao, Y. Frank Chen, Jiepeng Liu, Jiang Li. (2016). Experimental and analytical studies on the vibration serviceability of pre-stressed cable RC truss floor systems. Journal of Sound and Vibration, 361:130–147.
5. Rijal R., Samali B., Shrestha R., Crews K. (2015). Experiment and analytical study on dynamic performance of timber-concrete beams. Construction and Building Materials, 75:46–53.
6. Chen J., Xu R.T., Zhang M.S. (2014). Acceleration response spectrum for predicting floor vibration due to occupant walking. Journal of Sound and Vibration, 333:3564–3579.

7. Dallard P., Fitzpatrick T., Flint A., Low A., Smith R.R., Willford M., Roche M. (2001). London millennium bridge: pedestrian-induced lateral vibration. Journal of Bridge Engineering, ASCE, 6:412–417.
8. Reynolds P, Pavic A. (2003). Effects of false floors on vibration serviceability of building floors. I: modal properties. Journal of Performance of Constructed Facilities, ASCE, 17 (2):75–86.
9. He W., Xie W.P. (2014). Study on Sophisticated Calculation Model of Large-span Railway Station Structures. China Civil Engineering Journal, 47(1):13–23. (in Chinese).
10. Zhou D.L., Li A.Q., Zhou C.Y., et al. (2011). Analysis and test on the comfort of the large-span waiting hall floor in South Changsha Railway Station. Building Structure, 41 (1):1175–1198. (in Chinese).
11. Xie W.P., Ma Z.X., He W. (2012). Study on the relationship of natural frequency and vibration serviceability of large-span floor structures. Journal of Wuhan University of Technology, 34(4):96–101. (in Chinese).
12. Huang Z.M., Bai S.L., Lai M. (1998). An investigation of damping in earthquake response time history analysis of structures. China Civil Engineering Journal, 31(2): 75–79. (in Chinese).
13. Li Q S, Yang K, Wong C K, et al. (2003). The effect of amplitude-dependent damping on wind-induced vibrations of a super tall building. Journal of Wind Engineering and Industrial Aerodynamics, 91(9):1175–1198.
14. Xie W.P., Guo M., Sun L.M. Experimental study on damping characteristics of the steel cantilever beam element in the linear elastic range. Journal of Vibration Engineering (in Chinese, accepted).

Quantify the Size and Shape of Aggregate Particles Based on the Double Mirror Method

Wei Li, Huahan Chen, Zhangbo Wan and Xuecheng Bian

Introduction

Coarse aggregates are widely used in constructing railway ballast and subballast layers. The particle size and shape are two key factors that significantly influence the load response and performance of ballast aggregates [1, 2]. Shinohara et al. [3] performed triaxial tests on fine powders with different grain shapes and found that the internal friction angle increased due to the interlocking effect of angular particles. The pavement performances of hot-mix asphalt samples with four different particle shapes, i.e. cubical, rod, disk, and blade, were investigated in the wheel-tracking test by Chen et al. [4], the best rutting resistance was observed when using the cubical aggregate, and void contents as well as particle breakages increased remarkably in the case of flaky and/or elongated aggregate. Tutumluer et al. [5] tested six different aggregate samples classified by angularity index and surface index in the triaxial tests to investigate particle shape effects on the strength and permanent deformation, the strength and stability were greatly improved as the angularity index was high, whereas the dilation effects were mitigated as the surface index increased. Overall, quantifying the particle shape properties accurately plays a vital role in investigating and predicting the mechanical performances of coarse aggregates.

W. Li (✉) · H. Chen · Z. Wan · X. Bian
Department of Civil Engineering, Zhejiang University, Hangzhou 310058, China
e-mail: zjulw222@zju.edu.cn

H. Chen
e-mail: 249867185@qq.com

Z. Wan
e-mail: 452562194@qq.com

X. Bian
e-mail: bianxc@zju.edu.cn

However, traditional manual measuring methods, such as the particle size distribution curves, cannot describe the particle morphological properties comprehensively. With the aid of imaging technology, digital image analysis method serves as an efficient and precise tool in quantifying particle shape properties [6, 7]. Fernlund [8] took two images of a group of particles in lying and standing positions to compute three axial dimensions of each particle, thus the particle flakiness index and shape index were determined, but these two positions were determined manually, plus the details of a particle's morphology were limited by considering only two views. 3D scanning technique was utilized in reconstructing a 3D image of a particle, then the particle size and shape properties were evaluated [9–11]. The 3D scanning technology could produce high-precision results, but more time were needed in order to acquire a high resolution 3D image, in addition the scanning equipment was usually expansive and needed complex operations. Tutumluer et al. [12, 13] established a very innovative equipment named UIAIA which could capture three 2D images of a particle in three orthogonal directions, and also a series of imaging processing algorithms were developed to quantify the aggregate morphological properties, such as angularity index and surface texture index, but the three corresponding cameras should be installed accurately to insure they were equidistant from the object particle in three orthogonal directions.

In order to reduce complexity of the specialist imaging setup such as multi-camera or 3D scanning equipment, Forbes et al. [14] firstly proposed a two mirror setup which can create five views of an object from five view orientations. Based on the double mirror method, this study develops a new aggregate image analyzer to obtain five silhouettes of an aggregate particle, then the particle size and shape properties were quantified by characteristic dimensions, volume, sphericity, convexity, roundness, flat and elongation ratio and angularity index. Two different aggregates were tested in the laboratory to validate the proposed image analysis method. Additionally, the interrelationships of various particle shape properties, i.e. sphericity, convexity, roundness, flat and elongation ratio and angularity index, are investigated.

Image Acquisition and Processing System Based on Double Mirror Method

The established aggregate acquisition setup (Fig. 1) consists of two planar mirrors, a CCD camera with resolution of 1600×1200 pixels and a plastic light-passing platform which is mounted in a LED backlight box. The angle between two mirrors and the position of the camera are adjustable. The camera is connected to the computer with a network wire, thus the captured image of an aggregate particle is directly stored in the computer, and the subsequent procedures, i.e. image segmentation and processing as well as data representation, will be finished.
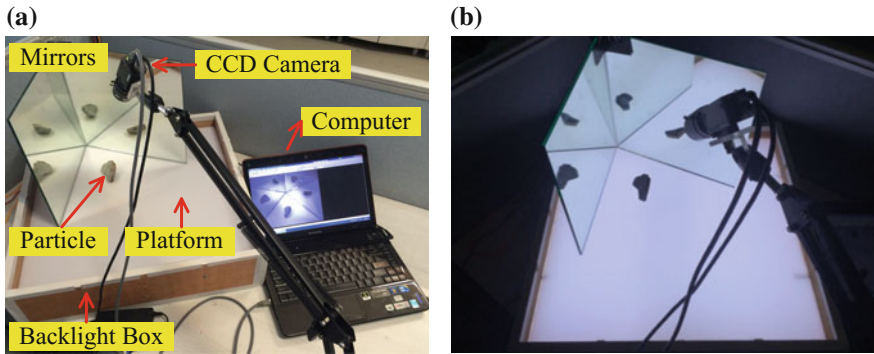
Fig. 1 Aggregate image acquisition setup based on double mirror method
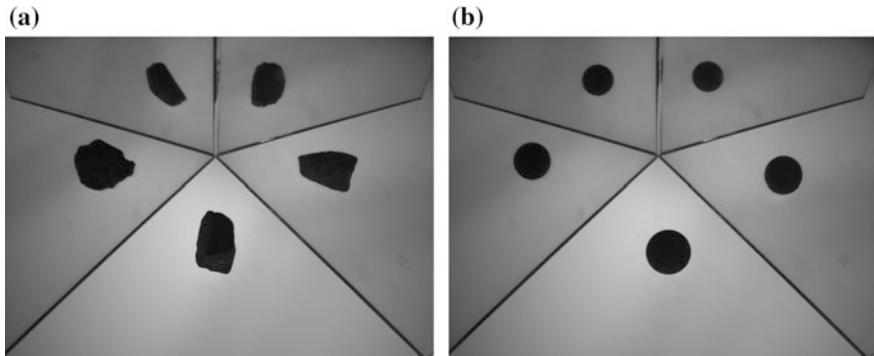
Fig. 2 Images of a ballast particle and a 40 mm-diameter calibrated ball

Based on the double mirror method [14], two planar mirrors with an intersection angle of 72° are used to create five views of an object including a view directly onto the object, two reflections and two reflections of the reflections. Figure 2 shows the captured images of a ballast particle and a 40 mm-diameter calibrated ball, and both of them are located on the symmetric axis of two planar mirrors.

After obtaining the image of an object particle, each view of the object is cut from the original image, and then is processed with the aid of imaging techniques. Figure 3 depicts the flow chart of image processing procedures to convert the original image into a binary image. Firstly the contrast is increased to make the object more distinguishable from the background, then noise is removed by median filter. Subsequently, a black and white image is produced by threshold segmentation. Considering some cases where there are holes in the projection, the holes are filled by pixels with gray scale equal to "255" (white). Then operations of clearing border, dilation and erosion are performed on the image sequentially to clear the white pixels out of the projections as well as remove the irregularities of projection
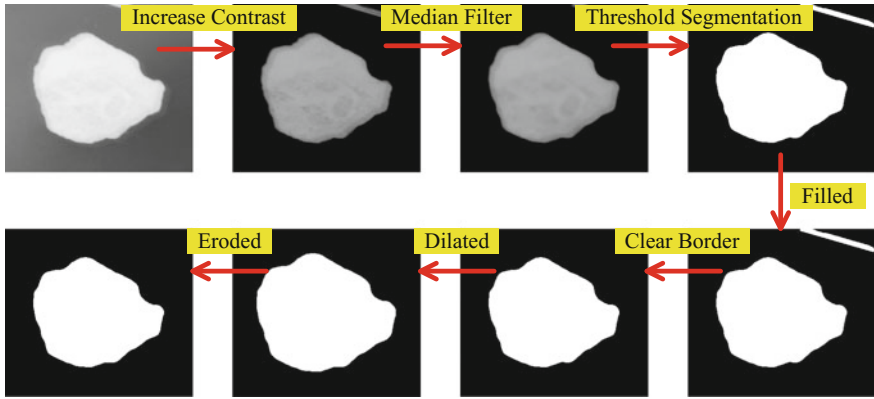
Fig. 3 Image segmentation process of one of a ballast particle's views

border, such as the sharp points. Each view of the object particle is processed by the same procedures and five silhouettes of the object particle are obtained finally.

In order to test the potential applicability of the image analysis technique based on double mirror method, two samples were studied: one is the fresh railway ballast of andesite material and the other is the recycled highway subbase coarse aggregate of granulite material. Two aggregate samples were manually sieved using square sieves, 9.5, 16, 22.4, 26.5, 31.5, 35.5, 40, 45, 50, 56, 63, 75, 80, 90 and 100 mm size. The gradation curves of two samples are presented in Fig. 4.
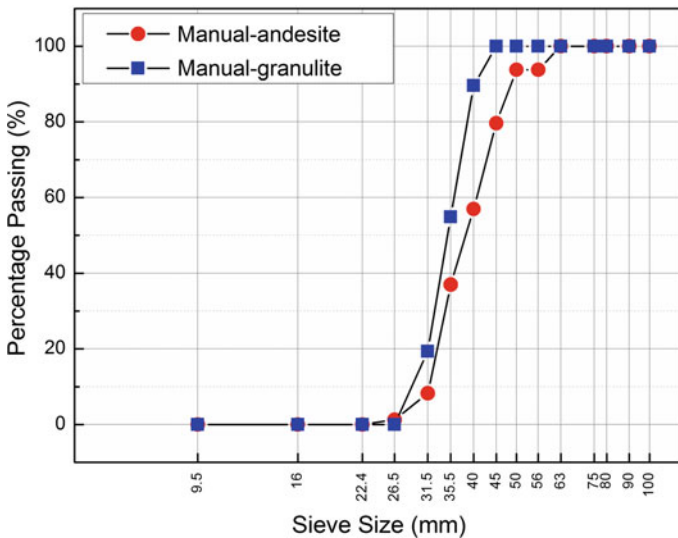
Fig. 4 The gradation curves of two tested aggregate samples

Particle Size and Volume Measurements

The outlines of five views are extracted from five corresponding silhouettes (S, S1, S2, S3, S4) as shown in Fig. 5. Imaging technique works with Ferret diameters [15], determined by the length between two tangential lines on opposite sides of one outline. The longest Ferret diameter is defined as the length, *dmaxi*, and the shortest Ferret diameter is defined as the width, *dmini*. *Dlongest*, *Dshortest* and *Dimin* are defined as the maximum diameter, the minimum diameter and the intermediate diameter of the object particle. *Dlongest* is the maximum value of five views' lengths, *Dshortest* is the minimum value of five views' widths and *Dimin* is the maximum value of five views' width. Besides, *Dimax* is defined as the minimum value of five views' lengths.

The scatter plots of particles' characteristic diameters, i.e. *Dlongest*, *Dshortest* and *Dimin*, are shown in Fig. 6. A good linear correlation between the manual measurement results and the image analysis output can be observed, indicating the image analysis procedure based on double mirror method can predict the particle size well.

The F&E ratio of a particle is defined as the ratio of *Dlongest* to *Dshortest*. Figure 7 shows the scatter points of manual value and image analysis results of F&E ratio, and the R value for granulite and andesite is 0.92126 and 0.89036 respectively, which means the goodness of fitting is good. The image analysis technique based on double mirror method overestimates the shortest diameter of a particle if the minimum cross section is not included in the five silhouettes of the object, thus the F&E ratio of some particles from image analysis is smaller than the manual measurement especially when the value is high.
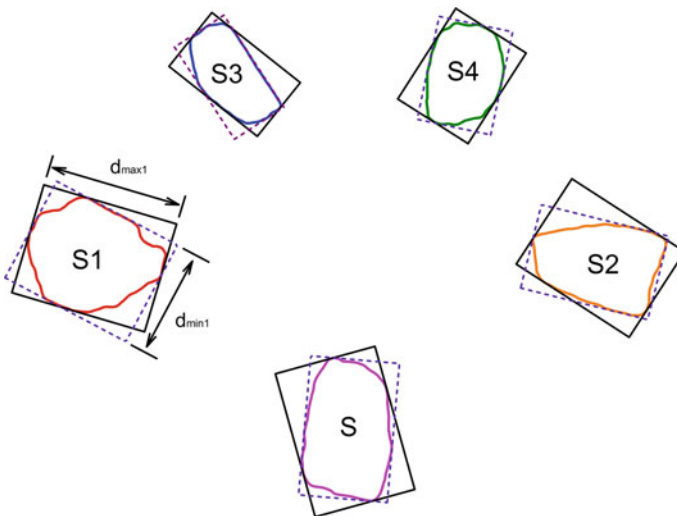
Fig. 5 Particle size measurement on Ferret boxes of particle's five views
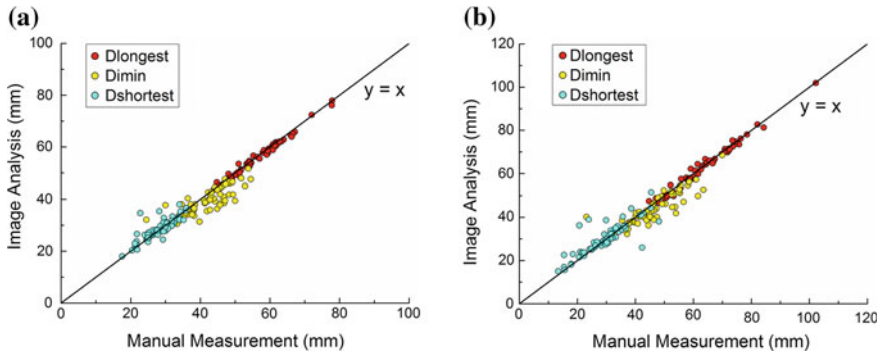
Fig. 6 Particle characteristic dimension measured by manual measurement and image analysis: **a** Granulite; **b** Andesite
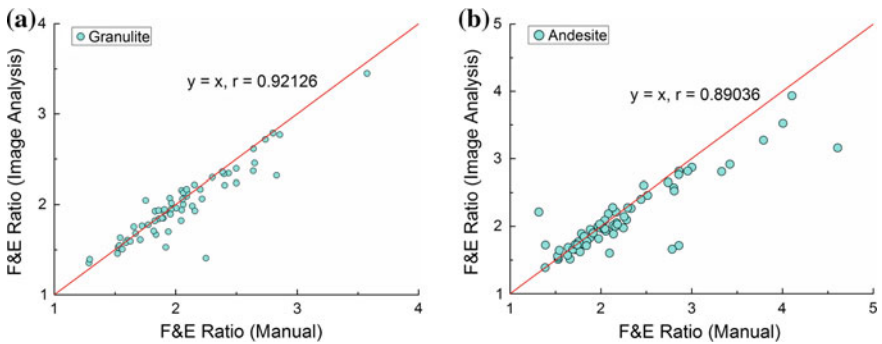
Fig. 7 Particle F&E ratio measured by manual measurement and image analysis

The estimated volume based on the geometric mean is computed as follows:

$$V = c \cdot \exp\left(3/2n \sum_{i=1}^{n} \ln A_i\right) \tag{1}$$

where c is an empirically determined constant; A_i is the projection area of a particle. The mass is then estimated by multiplying V by the aggregate density.

Figure 8 shows the plots of manual measured particle mass versus estimated volume for andesite and granulite aggregates. The plots show a good linear relationship between mass and estimated volume.

After determining the characteristic diameters and the volume of aggregate particles based on image analysis, Fig. 9 compares the distributions of *Dimax*, *Dimin*, *Dshortest* and *Dlongest* of granulite and andesite with sieve analysis. The data presented in Fig. 9 indicates that each gradation curve determined by *Dimax*, *Dimin*, *Dshortest* and *Dlongest* is almost parallel to the sieve data, and no definite
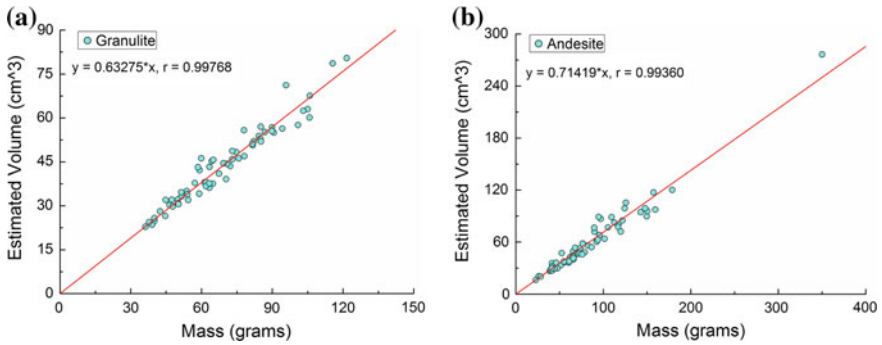
Fig. 8 Particle estimated volume by image analysis against manual measured particle mass
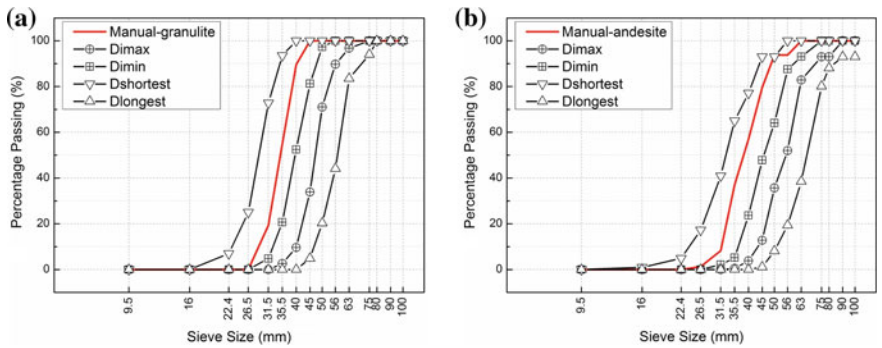
Fig. 9 Particle size distributions of two aggregate samples measured by manual sieving and image analysis

conclusion can be made about which size measure correlates best with the sieve data.

Particle Shape Indices Calculation

Four indexes are chosen to characterize the particle shape, including sphericity, roundness, convexity and angularity, which could be calculated with the following equations.

Roundness is a widely used measurement of particle shape in two dimensions. It is expressed in the following equation:
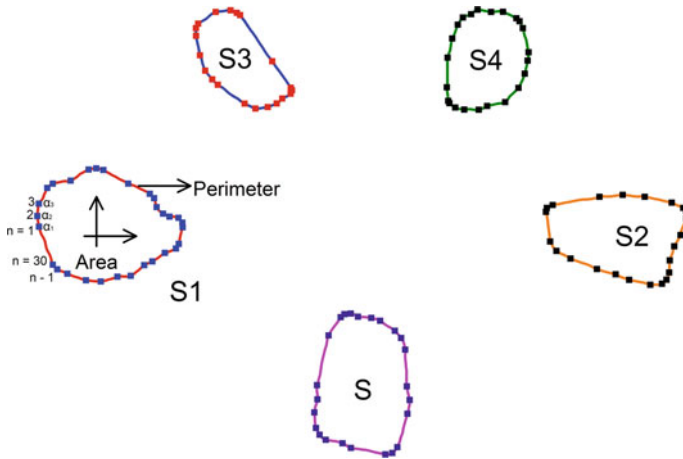
Fig. 10 Illustration of the n-sided polygons approximating the outlines of the particle's five views

$$Roundness = \frac{1}{4\pi} \cdot \sum_{i=1}^{5} P_i^2 / \sum_{i=1}^{5} A_i \qquad (2)$$

where Pi is the perimeter of each silhouette in Fig. 10; Ai is the area of each silhouette in Fig. 10. Roundness is equal to 1.0 when the particle's outline is a circle, otherwise it is larger than 1.0.

Sphericity is defined based on a particle's three characteristic diameters and it is a quantitative description of the proximity of the sphere.

$$Sphericity = \sqrt[3]{d_s \times d_i / d_l^2} \qquad (3)$$

where ds, di and dl are the shortest diameter, the intermediate diameter and the longest diameter of an aggregate particle respectively.

Convexity is evaluated from the two dimensional projection of the particle as shown in Fig. 10. The convexity of a three dimensional particle is determined by taking area-weighted average of five views' convexity values.

$$Convexity = \frac{A}{A+B} \qquad (4)$$

where A is the area of the particle's projection; B is the area of minimum convex boundary circumscribing the particle.

Angularity index describes the irregularity of the particle's shape and is calculated as the changes in the slope of the particle outline [12]. As shown in Fig. 10, the particle's outline is approximated by an n-sided polygon. The subtended angle at each vertex of the polygon is measured and the frequency distributions of the

changes in the vertex angles are grouped in $10°$ intervals. The magnitude and number of occurrences of the subtended angles is related to the angularity of the particle:

$$\text{Angularity} = \sum_{e=0}^{170} e * P(e) \tag{5}$$

where e is the starting angle value for each $10°$ class interval and P(e) is the probability of change in the vertex angle and has a value in the range e–e + 10. Finally, the angularity index is obtained by taking area-weighted average of five silhouettes' angularity.

$$\text{AI} = \frac{\sum_{i=1}^{n} \text{Area(i)} * \text{Angularity(i)}}{\sum_{i=1}^{n} \text{Area(i)}} \tag{6}$$

Figure 11 presents the probability distribution histograms of sphericity, angularity index, convexity and roundness of andesite and granulite aggregates. More granulite particles locate in higher sphericity band, i.e. 0.8–0.9, and lower roundness band, i.e. 1.1–1.3, by analyzing Fig. 11a and d, indicating that the granulite
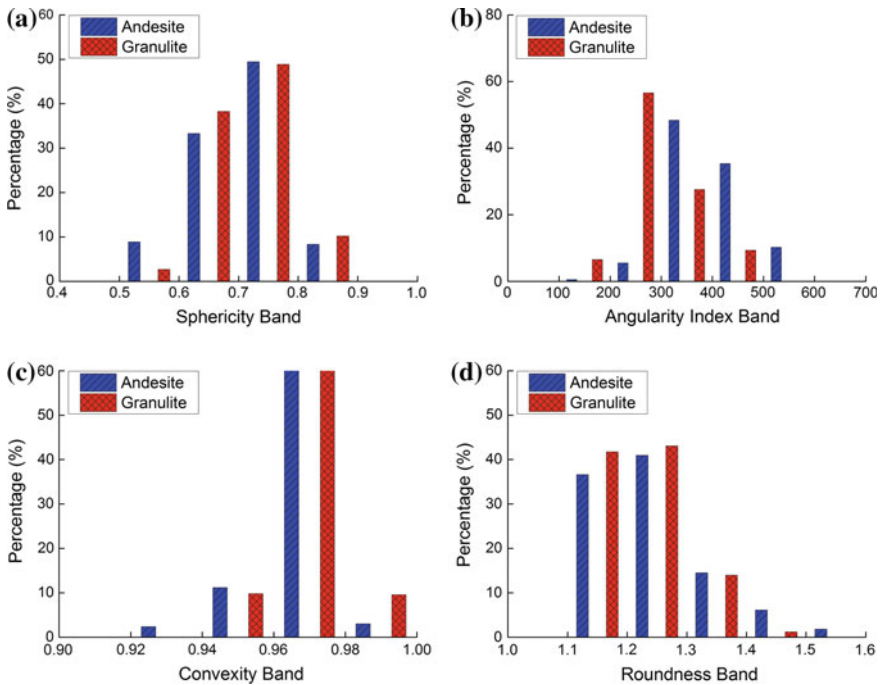
Fig. 11 Comparison of two aggregates shape properties quantified by sphericity, angularity index, convexity and roundness

particles are much rounder than andesite particles. From Fig. 11b and c, a larger proportion of andesite particles locate in higher angularity index band, i.e. 300–600, and lower convexity band, i.e. 0.92–0.96, which means the andesite particles have more irregular shape. The shape indices from the image analysis based on double mirror method have the capacity to distinguish the fresh ballast, i.e. andesite aggregate from the recycled subbase aggregate, i.e. granulite aggregate.

Analyzing the Interrelationships of Particle Shape Properties

The particle shape indexes, i.e. F&E ratio, roundness, convexity and angularity are plotted against the sphericity in Fig. 12. It can be found that F&E ratio and roundness have a strong correlation with the sphericity. To show the overall trend of the correlation, best-fitted lines are drawn on the figures along with data points. On the other hand, the correlation between convexity, angularity and sphericity is much weaker.
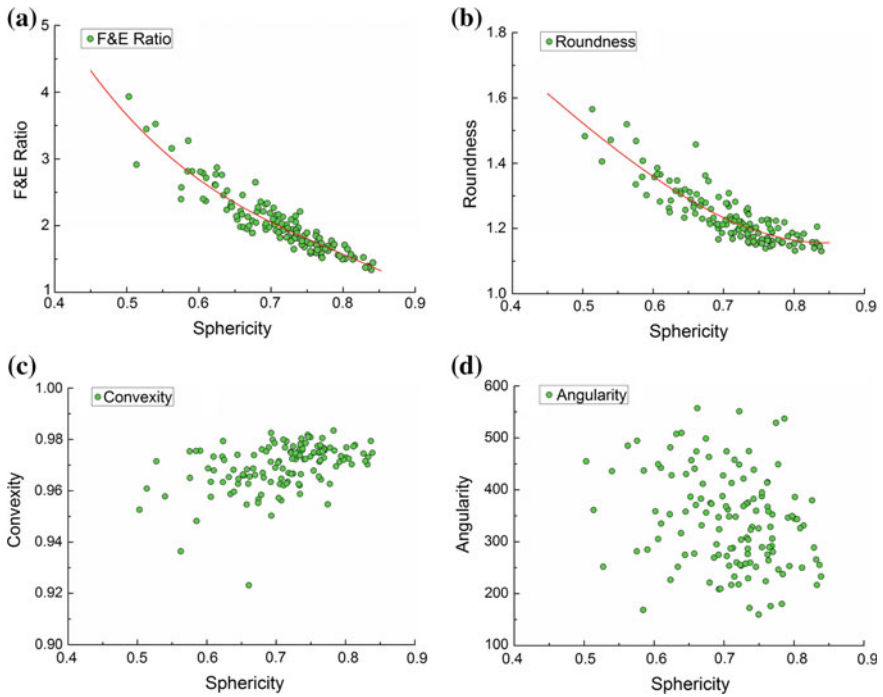
Fig. 12 Correlation of various shape parameters, i.e. F&E ratio, roundness, convexity and angularity to the sphericity

Conclusions

In this study, an image capture setup based on double mirror method is developed to obtain five silhouettes of the aggregates widely used in railway substructure and highway subbase. The image processing procedures are also introduced to obtain particle size and shape properties, i.e. characteristic diameters, F&E ratio, volume, roundness, convexity, angularity index and sphericity. This method has been tested in two different aggregate samples, i.e. granulite and andesite, in the laboratory:

1. The size, F&E ratio and volume results from the image analysis have a good linear correlation with the manual measurements, validating the capacity of the double mirror method to characterize the particle size properties.
2. The gradation curve determined by *Dimax*, *Dimin*, *Dshortest* and *Dlongest* respectively is almost parallel to the sieve data, and no definite conclusion can be made about which size measure correlates best with the sieve data.
3. The shape indices from the image analysis based on double mirror method have the capacity to distinguish the fresh ballast, i.e. andesite aggregate from the recycled subbase aggregate, i.e. granulite aggregate.
4. F&E ratio and roundness have a strong correlation with the sphericity, whereas the correlation between convexity, angularity and sphericity is much weaker.

References

1. Lu, M., Mcdowell, G. R. (2007). The importance of modelling ballast particle shape in the discrete element method. Granular Matter, 9(1–2): 69–80.
2. Boler, H., Qian, Y., Tutumluer, E. (2014). Influence of Size and Shape Properties of Railroad Ballast on Aggregate Packing Statistical Analysis. Transportation Research Record, (2448): 94–104.
3. Shinohara, K., Oida, M., Golman, B. (2000). Effect of particle shape on angle of internal friction by triaxial compression test. Powder Technology, 107(1–2): 131–136.
4. Chen, Jian-Shiuh, Chang, M. K., Lin, K. Y. (2005). INFLUENCE OF COARSE AGGREGATE SHAPE ON THE STRENGTH OF ASPHALT CONCRETE MIXTURES. Journal of the Eastern Asia Society for Transportation Studies, 6: 1062–1075.
5. Tutumluer, Erol, Pan, Tongyan (2008). Aggregate Morphology Affecting Strength and Permanent Deformation Behavior of Unbound Aggregate Materials. Journal of Materials in Civil Engineering, 20(9): 617–627.
6. Kuo, Chun-Yi, Rollings, Raymond S., Lynch, Larry N. (1998). Morphological Study of Coarse Aggregates Using Image Analysis. Journal of Materials in Civil Engineering, 10(3): 135–142.
7. Kwan, A. K. H., Mora, C. F., Chan, H. C. (1999). Particle shape analysis of coarse aggregate using digital image processing. Cement and Concrete Research, 29(9): 1403–1410.
8. Fernlund, J. M. R. (2005). Image analysis method for determining 3-D shape of coarse aggregate. Cement and Concrete Research, 35(8): 1629–1637.

9. Sun, Y., Indraratna, B., Nimbalkar, S. (2014). Three-dimensional characterisation of particle size and shape for ballast. Geotechnique Letters, 4: 197–202.

10. Alshibli, K. A., Druckrey, A. M., Al-Raoush, R. I., Weiskittel, T., Lavrik, N. V. (2015). Quantifying Morphology of Sands Using 3D Imaging. Journal of Materials in Civil Engineering, 27(10).

11. Erdogan, S. T., Quiroga, P. N., Fowler, D. W., Saleh, H. A., Livingston, R. A., Garboczi, E. J., Ketcham, P. M., Hagedorn, J. G., Satterfield, S. G. (2006). Three-dimensional shape analysis of coarse aggregates: New techniques for and preliminary results on several different coarse aggregates and reference rocks. Cement and Concrete Research, 36(9): 1619–1627.

12. Rao, C., Tutumluer, E., Kim, I. T. (2002). Quantification of coarse aggregate angularity based on image analysis. Transportation Research Record: 117–124.

13. Al-Rousan, T., Masad, E., Tutumluer, E., Pan, T. (2007). Evaluation of image analysis techniques for quantifying aggregate shape characteristics. Construction and Building Materials, 21(5): 978–990.

14. Forbes, K., Nicolls, F., De Jager, G., Voigt, A., *Shape-from-Silhouette with Two Mirrors and an Uncalibrated Camera*, in *9th European Conference on Computer Vision, ECCV 2006*. 2006, Springer Verlag: Graz. p. 165–178.

15. Fernlund, J. M. R. (1998). The effect of particle form on sieve analysis: a test by image analysis. Engineering Geology, 50(1–2): 111–124.

Study on Metro Environmental Vibration Influence and Vibration Isolation Effect of Isolation Trench

Wenbin Wang

Vibration, caused by rail transit wheel-rail interaction, via rail system, tunnels (bridges or foundation), soil medium, ground buildings, propagates from source to structure, further induced the second vibration on buildings. The impact on the environment can last as long as 20 h, making many countries have to face the environmental vibration complaints caused by urban rail transit operation [1, 2]. Nowadays, as multi modal system gradually formed, part of rail lines have to pass through residential area, commercial center, or science park, in the form of ground line, underground line and elevated line. The minimum distance can be just a few meters from the buildings, and some lines may even underneath directly. All these make the effect of vibration and noise become increasingly serious, which rail transit construction unit should respond [3, 4].

For the ground rail transit, set vibration isolation in the propagation may be the common vibration propagation isolation, such as open trench, continuous hollow wall, continuous solid wall and WIB [5–10]. When vibration wave propagates to the vibration isolation, besides transmission and reflection, wave diffraction will happen in both ends and bottom of the vibration isolation. Vibration energy through the isolation is mainly composed of transmission wave and diffraction wave, generally less than the energy of the incident wave. Ground vibration can be reduced in this way. While wave reflection may lead to the ground vibration amplification effect ahead of the isolation [11, 12].

Compare to ground vibration source, there are few research on vibration propagation isolation underground. More than 10 m or dozens of meters tunnel depth makes open trench proves infeasible, continuous pile wall and in-filled trench are also limited [13]. Based on the test results of environmental vibration effect in

W. Wang (✉)
Urban Rail Transit Center, CARS, Beijing 100081, China
e-mail: 13811667172@126.com

Qingdao Jiayuan district, caused by Beijing Metro Daxing Line, 3-d simulation model is established to evaluate vibration isolation performance under different isolation vibration materials.

Engineering Background

Qingdao Jiayuan district is located in the west of Beijing Metro Daxing Line, between Gaomidian North station and Gaomidian South station. These five-story cast-in-site structures, applying reinforced concrete strip foundation in 1.5–2 m depth. The shortest distance is only 12.5 m from Building 10 to Daxing right line (down line) center line, while to left (up line) center line is about 25.5 m. Metro tunnel structure with horseshoe shape composite lining, its soil depth is about 8.0–9.6 m. And the left line adopt type DTVI2 fastenings concrete track bed while the right line adopt ladder track, which laying length is 293 m. Residential district top view as shown in Fig. 1.

Fig. 1 Qingdao Jiayuan district top view

Many vibration complaints from residents were received at the late stage of trial operation. For this situation, conducting simulation investigation of periodic row piles vibration isolation performance by means of filed survey and test is necessary.

Environmental Vibration Influence

Evaluation Standard

Qingdao Jiayuan district, as the function area sides main roads in Daxing district regional planning, its environmental vibration limit is 75 dB in the daytime and 72 dB in the nighttime according to "Standard of environmental vibration in urban area" (GB10070-1988) [14].

Based upon "Measurement Method of Environmental Vibration of Urban Area" (GB100071-1988) [15], plumb vibration acceleration grade should be measured. Setting time weight constant to be 1 s and extracting the maximum value when trains passing through. The average of 20 continuous sets of data, as the evaluation measure, is plumb vibration acceleration grade maximum VLzmax.

Environmental monitoring sites must be set outside the buildings 0.5 m far as "Technical Guidelines for Environmental Impact Assessment of Urban Rail Transit" (HJ453-2008) [16] required.

Test Point Arrangement

For vibration complaints, a series of environmental vibration tests have done in tunnels, ground and buildings to analyze the structure vibration level and vibration energy band distribution. Sensors setting on both lines and tunnel walls in the same mileage, to measure vibration level and spectral distribution. Moreover, the ground half meters in front of buildings should be set for the vibration environmental effect.

Test Result Analysis

The 1/3 octave band and Z vibration level in time domain are exploited to estimate environmental vibration effect caused by metro Daxing line.

Under the speed of 60 km/h, the 1/3 octave band acceleration level inside tunnel is shown in Fig. 2, and on the ground is shown in Fig. 3.

As shown in Fig. 2, compare to DTVI2 fastenings concrete track bed, train on the ladder track induced higher vibration acceleration level, even a differential of 20 dB in the frequency band of 30 Hz. In the frequency band of 3–40 Hz, only

Fig. 2 The 1/3 octave band acceleration level inside tunnel
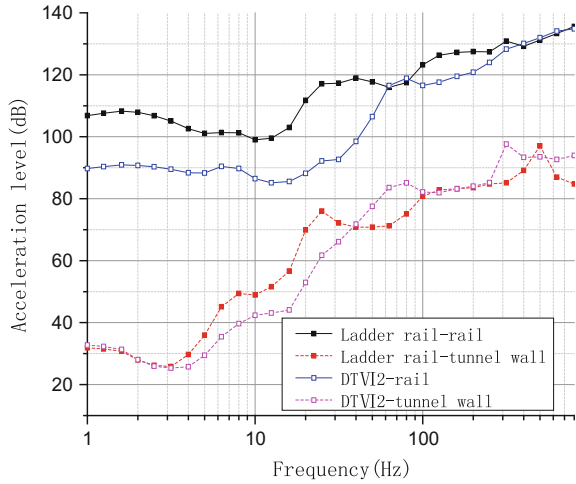
Fig. 3 The 1/3 octave band acceleration level before the building half meter away
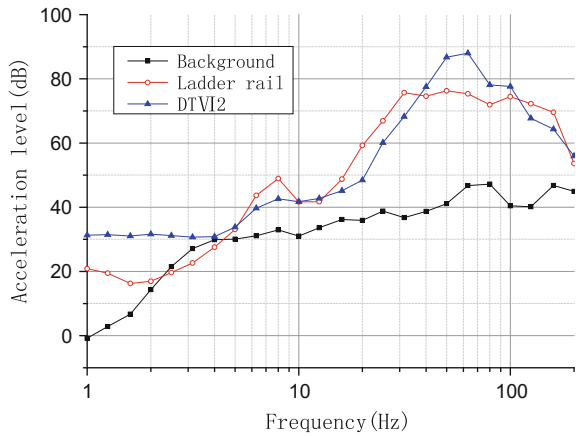
slightly higher than DTVI2 fastenings on tunnel walls, indicates vibration amplification effect caused by DTVI2 fastenings ladder track. The difference can be 15 dB around the frequency band of 25 Hz. While it turned out just the opposite in 40–110 Hz, shows that DTVI2 fastenings ladder track providing with the ability of reducing vibration. The difference can be 13 dB around the frequency band of 60 Hz.

Figure 3 indicates that in the frequency band of 4–200 Hz, trains running makes great contribution to ground vibration, in addition, the vibration acceleration level varies in different frequency bands. The main contribution frequency band of ladder track is about 30 Hz, the same as the vibration source dominant frequency, reached 38 dB. However for DTVI2 fastenings, the main contribution frequency band is about 60 Hz, reached 42 dB. Specifically, the ladder track induced higher vibration

acceleration level than DTVI2 fastenings in the frequency band of 4–35 Hz, reaching 8 dB around 30 Hz. And it becomes lower in 35–200 Hz, with the maximum of 23 dB around 60 Hz.

Results are different in analyzing the 20 sets of the ground test point vibration data caused by trains, with Z vibration level maximum in time domain. Only 6 sets of right line data exceed the limit, with the total average of 70.7 dB, less than 72 dB limit. In contrast, 12 sets of left line data exceed the limit, and the total average is 76.5 dB, exceeding the vibration limit.

Reason Analysis of Overstandard Vibration

Qingdao Jiayuan district vibration issue is building forced vibration caused by train. There is a difference of 6 dB between two lines, that the left line with the exceeding value of 76.5 dB has greater influence than the right, which values 70.7 dB below. And the maximum is almost over 15 dB between trains in good condition and out of condition, shows vehicle state makes significantly influence on ground environmental vibration.

3D Simulation of Vibration Propagation Isolation

3D Simulation Model

The 3D finite element model is established based on the actual relationship with transit network. As shown in Fig. 4, this model with the dimension parameter of 31.5 * 60 * 40 m, setting the maximum size as 1 m for soil layer and tunnel elements. Its soil layer simplified to 4 according to soil distribution and soil layer shear wave velocity. The processed practical measured data can be input as the moving load on rails. The right line test section with 9 m in buried depth contains 5 ladder track, and its center line is 15 m away from building foundation which is 16 m wide. The distance between two center lines is 15 m, and the width of the isolation trench is 1 m.

The parametric analysis is presented for the filled material but not location, width, length and so on in case of the execution conditions. The isolation trench horizontal distance is 4.5 m from the right line tunnel boundary, and 15.6 m in depth, 1 m in thickness, 16 m in width. 5 kinds of materials filled are fly ash, rubber pieces, foam, sandy gravel, aerated concrete and lightweight aggregate concrete.

Fig. 4 3D dynamic simulation model
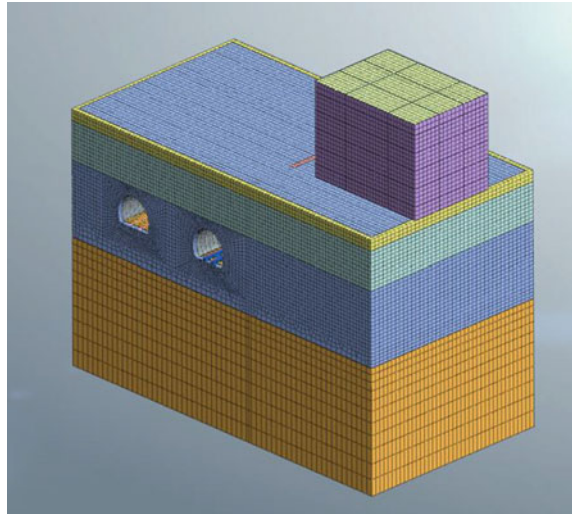
Modeling Parameter

Based on the actual formation parameter and shear wave velocity, the soil layers are simplified to 4. The formation parameter is shown in Table 1.

For tunnel elements, dynamic elastic modulus is 29.0 GPa, dynamic poisson's ration is 0.2, and bulk density is 24 kN/m^3.

Boundary Condition

Viscoelastic artificial boundary, a kind of local artificial boundary, has been widely used in dynamic finite element analysis, with the advantage of no low-frequency drift, semi-infinite medium elastic recovery capacity, good frequency stabilization, and application convenience in finite element software. It can be divided into spring-damper artificial boundary and 3D coherence artificial boundary according

Table 1 Formation parameters of the model

Soil layer	Thickness (m)	Bulk density (kN/m^3)	Dynamic poisson's ration	Dynamic elastic modulus (kPa)	Shear wave velocity (m/s)	Compressive wave velocity (m/s)
1	1.8	18.5	0.37	1.4E5	165	362
2	6.2	19.5	0.35	2.6E5	220	458
3	12	20	0.3	6.0E5	336	629
4	20	21	0.26	7.8E5	380	668

to elements form. In this paper, 3D coherence artificial boundary is chosen, that the solid element is established along boundary normal, with outside nodes fixed.

Filling Materials Parameter

Filling materials are two categories, flexible material and rigid material, according to the shear wave impedance ratio. Flexible material included fly ash, rubber pieces and foam, while the rigid included the others. Physical property indexes such as shown in Table 2.

Vibration Isolation Analysis of Various Isolation Trench Materials

Model Verification

The test point half meter in distance from the building is chosen for the vibration response of the soil layer and the building, in the condition of in no-filling material to prove the model correctly. As shown in Fig. 5, the comparison between the measured result and calculate result in the 1/3 octave band had good similarity, indicates the accuracy of the model.

Table 2 Filling materials dynamic character

Material type	Density (kg/m³)	Elastic modulus (× 10^6 N/m²)	Poisson's ratio	Shear wave velocity (m/s)	Shear wave velocity ratio	Wave impedance ratio
Fly ash	500	25	0.35	136.08	0.5917	0.1509
Rubber pieces	1480	4.5	0.48	32.05	0.1393	0.1052
Foam	80	11.8	0.4	229.5	0.998	0.0407
Aerated concrete	650	1900	0.2	1103.6	4.7983	1.5913
Lightweight aggregate concrete	1800	14,000	0.2	1800.2	7.827	7.1880

(a) Velocity-time test result

(b) Velocity-time calculation result

(c) 1/3 octave band
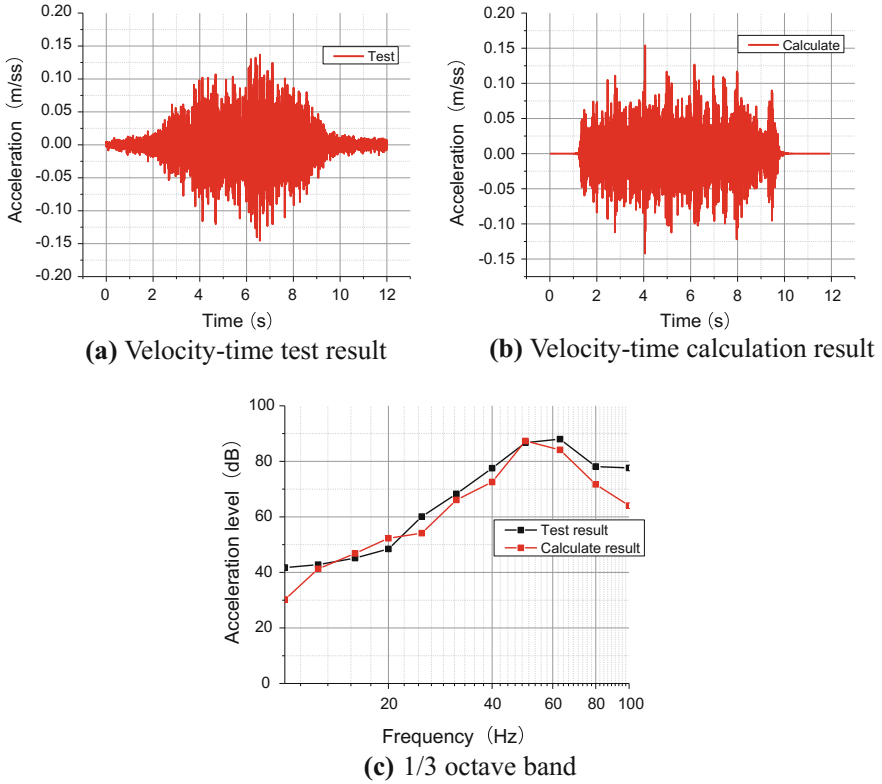
Fig. 5 Comparison of test and calculation result

Floor Vibration Response Analysis

Each floor vibration acceleration spectrum and Z vibration level in the condition of no vibration isolation just as shown in Figs. 6 and 7. It indicates that:

1. The vibration amplification occurs in this band that each floor resonant frequency is about 30 Hz.
2. The Z vibration level decreased first and then increased along with higher floors. The minimum is 77.76 dB in the second floor, and the maximum is 79.15 dB in the sixth floor.

Fig. 6 Vibration acceleration-frequency of each floor
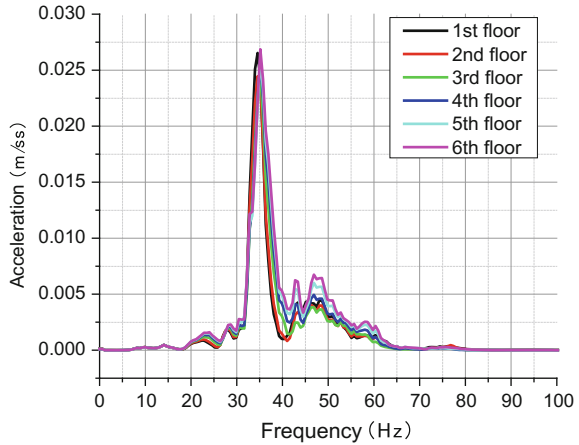
Fig. 7 The Z vibration level of each floor
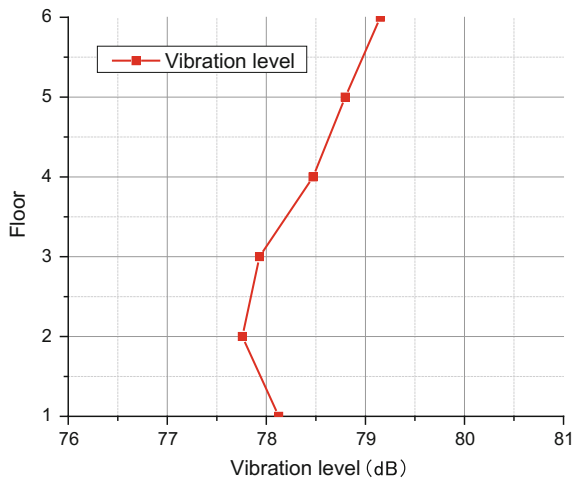
Filling Materials Vibration Effect Analysis

Taking the test point half meter in distance from the buildings as example, Table 3 shows the maximum Z vibration level of each filling materials, and the comparison of the 1/3 octave band and Z vibration level just as shown in Figs. 8 and 9.

From the data above, it indicates that:

1. Isolation trench with different filling materials all have the capacity to induce the vibration effect, with the decrease of 1.5–3.5 dB in the Z vibration level peak value.

Table 3 The Z vibration level of various filling materials

Vibration isolation	Maximum of the Z vibration level (dB)
None	77.52
Fly ash	74.43
Aerated concrete	76.00
Foam	74.47
Lightweight aggregate concrete	75.20
Rubber	73.93

Fig. 8 Vibration acceleration-frequency in the 1/3 octave band of various materials
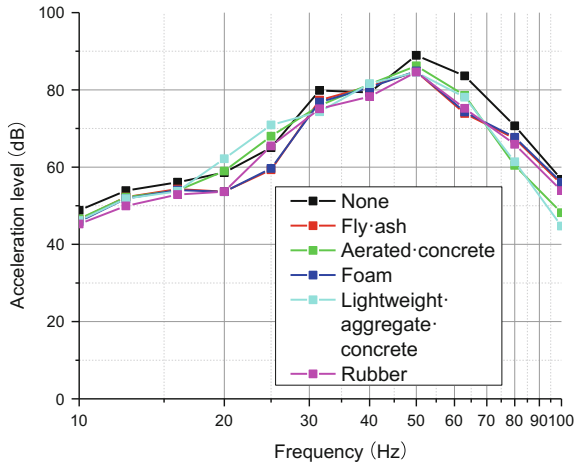
Fig. 9 The Z vibration level of each floor with various materials
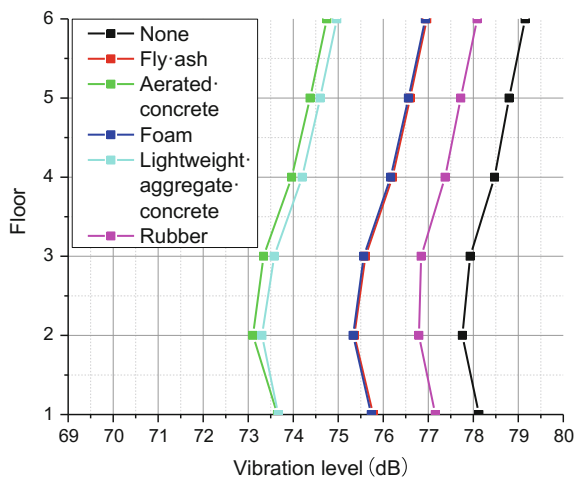
2. The rubber with small stiffness and high elasticity, provides positive effect in the system as a mass-spring vibration isolation structure, which can attenuate the vibration propagation.
3. Each floor Z vibration level all decreased first and then increased in different fillings. And the second floor reached the minimum, the sixth reached the maximum.

Conclusions

1. Compared with DTVI2 fastenings, ladder track can provide vibration isolation effect in the band of 40–110 Hz, and it can reach 13 dB around 60 Hz. The up line played more of a role than the down line in the building vibration caused by rail transit, with the difference of 6 dB, its test point half meter in the distance from the buildings reached 76.5 dB which exceeds the 72 dB limit.
2. Vibration isolation with different filling materials all make good performance in reducing the vibration, by lower the peak of 1.5–3.5 dB in Z vibration level. The rubber with small stiffness and high elasticity, providing positive effect in the system as a mass-spring vibration isolation structure, achieves the best effect.
3. Z vibration level of each floor all decreased first and then increased, indicates the isolation method has little impact on the vibration propagation characteristics of building structures.

References

1. Liu, W.N., Ma, M., Liu W.F., et al. (2016). Research overview of environmental vibration influence induced by urban mass transit in China. Scientia Sinica (Technologica), 2016 (06):547–559. (in Chinese).
2. Xia, H., Zhang, N., Cao, Y.M. (2005). Experimental study of train-induced vibrations of environments and buildings. Journal of Sound and Vibration, 280:1017–1029.
3. Gupta, S., Liu, W.F., Degrande, G., et al. (2008). Prediction of vibrations induced by underground railway traffic in Beijing. Journal of Sound and Vibration, 310(3):608–630.
4. Ma, M., Markine, V.L., Liu, W.N., et al. (2011). Metro train-induced vibrations on historic buildings in Chengdu, China. Journal of Zhejiang University- SCIENCE A., 12(10):782–793.
5. Gao, G.Y.,Yang, X.J., Wang, Y.S., et al. (1997). Theory and Application of Vibration Isolation by Piles in Rows. Journal of Building Structures, 1997(04):58–69. (in Chinese).

6. Gao, G.Y., Li, J., Li, N., et al. (2013). Three-Dimensional Analysis of Far-Field Passive Vibration Isolation for Row of Piles in Layered Foundation. Chinese Journal of Rock Mechanics and Engineering, 2013(S1):2934–2943. (in Chinese).
7. Luo, K., Lei, X.Y. (2010). Numerical Analysis of Railway Vibration Isolation of New Style Trenches. Noise and Vibration Control, 2010(01):67–71. (in Chinese).
8. Luo, K., Lei, X.Y., Liu, Q.J. (2009). Research on the Application of Ground Barrier in Reducing the Vibration Along High-speed Railway. Journal of Railway Engineering Society, 2009(01):1–6. (in Chinese).
9. Shi, Z.F., Cheng, Z.B., Mo, Y.L. (2014). Theoretical and experimental studies of periodic foundation. Earthquake Engineering and Engineering Vibration, 2014(S1):763–768.
10. Huang, J.K. (2014). Application of Periodic Pile Barriers and Wave Barriers to Reduce Vibrations in Civil Engineering. Beijing Jiaotong University. (in Chinese).
11. Li, R.D. (2009). Study on the Metro induced ground vibrations and isolation measures. Beijing Jiaotong University. (in Chinese).
12. Gao, G.Y., Yun, Z.Q., Tan, G.H., et al. (2002). Theoretical Analysis of Unusual Vibration Amplification in Barrier Protected Zone. Chinese Journal of Geotechnical Engineering, 24(5):565–568. (in Chinese).
13. Wang, W.B. (2013). Technology Research and Application of Track Vibration Reduction for Urban Rail Transit. Beijing: China Academy of Railway Sciences. (in Chinese).
14. National Standard of People's Republic of China. (1988). GB10070-88 Standard of environmental vibration in urban area. Beijing: State Bureau of Environmental Protection. (in Chinese).
15. National Standard of People's Republic of China. (1988). GB10071-88 Measurement Method of Environmental Vibration of Urban Area. Beijing: State Bureau of Environmental Protection. (in Chinese).
16. National Environmental Protection Standard of People's Republic of China. (2009). HJ453-2008 Technical Guidelines for Environment Impact Assessment of Urban Rail Transit. Beijing: China Environmental Science Press. (in Chinese).

Effects of One Weak Interlayer on Seismic Response of Municipal Solid Waste Landfill

Wu Gao, Xuecheng Bian and Yunmin Chen

Introduction

Municipal solid waste (MSW) landfills are generally huge structures with the heights varying from 10 m to more than 150 m. Several failures of landfills occurred in the early 20th century under earthquakes have attracted a wide range of domestic and foreign researchers on the seismic response of landfills [1]. Bray et al. [2] carried out one dimensional (1D) seismic wave propagation analysis of landfill under different sites and earthquakes by using SHAKE91 software, and results indicated that the seismic stability of waste fills depends primarily on the dynamic properties and height of the waste fill, and the characteristics of the design bedrock motions (intensity, frequency content and duration). Chouhury and Savoikar [1] conducted 1D equivalent-linear analysis to model the seismic response of MSW landfills subjected to different foundation types, height and stiffness of MSW landfills and seismic base accelerations using the DEEPSOIL software, and the results showed that assumption of constant unit weight and shear wave velocity for landfills underestimates maximum horizontal acceleration, normalized shear stresses and spectral amplification at the top of landfills. Feng and Yang [3] replaced the geosynthetic liner in the MSW landfills with an equivalent soil layer to study the effects of liner interface, landfill height and foundation types on the seismic response of landfills, and it revealed that the propagation of seismic waves is limited

W. Gao (✉) · X. Bian · Y. Chen
Department of Civil Engineering, Zhejiang University, Hangzhou 310058, China
e-mail: gaowu_ed@163.com

X. Bian
e-mail: bianxc@zju.edu.cn

Y. Chen
e-mail: chenyunmin@zju.edu.cn

by the liner interface and some errors might occur without taking the effect of liner interface on the seismic response of landfills.

Weak interlayers often exist in the MSW body of landfill, which displays a layered feature similar to the soil sites. Different from those in the soil sites due to the geological and tectonic processes, the weak interlayers in the MSW body are related to the types of wastes and the landfilling process. On the one hand, urban sewage sludge with a loose structure and a small shear strength is mixed with MSW, and hence weak interlayers with various thicknesses are formed in any depth of the MSW body. On the other hand, soils are used on purpose in some landfills as the temporary covers to prevent the infiltration of rain or slush and control the leakage of landfill gas, and therefore weak layers with certain thicknesses are shaped after they are covered by the subsequent waste.

Numerous studies on the influences of weak interlayers on the seismic response of soil sites under earthquakes demonstrate that the stability and settlement of soil sites are closely connected with the weak interlayers [4–9]. However, there are inadequate researches on the effects of weak interlayers on the seismic response of landfills under earthquakes. In this paper, forty 1D landfill profile models subjected to different ground motion inputs and one weak interlayer with various depths and thicknesses in the MSW body are developed to explore the influences of the depth and thickness of one weak interlayer on the seismic response of landfills.

Modelling Characteristics

Calculation Method and Software

1D equivalent-linear method is firstly proposed by Idriss and Seed [10] and is widely used due to its simplicity and explicit efficiency [11]. In this study, the influences of thickness and depth of one weak interlayer on the dynamic response of landfills subjected to different earthquake motions are studied by performing 1D frequency independent equivalent-linear analysis which is built in the EDT (Elastodynamics Toolbox for MATLAB) software [12, 13]. In addition to that, the direct stuffiness method of EDT is used to obtain the horizontal acceleration and equivalent shear strain, which does not need to divide the MSW body and foundation into many small layers, yet still guarantee the accuracy of calculation and save the modeling time [14].

Landfill and Weak Interlayer Details

In the 1D landfill profile model as shown in Fig. 1, the height of MSW body above the ground is 100 m. Researches [15–19] indicate that the physical and dynamic

properties of MSW are more complex than that of soils, and the variations of unit weight and shear wave velocity of MSW with the buried depth are taken into consideration in the present analysis [1, 19, 20]. An average unit weight of 10.5 kN/m^3 for top 20 m and 12.5 kN/m^3 for the remaining portion is assumed to account for higher compaction and biodegradation of organics in MSW. An average shear wave velocity of 100 m/s for top 20 m and 150 m/s for the remaining portion is assumed to account for higher stiffness of fill in the bottom portion of landfill. In addition to that, the normalized shear modulus reduction and material damping profiles for MSW proposed by Choudhury and Savoikar [20] are used in the 1D equivalent-linear analysis.

Only one weak interlayer is considered in the present analysis. Its thickness varies from 1, 3, 5, 7 and 9 m. And its buried depth which is defined as the distance from the landfill top to the upper interface of weak interlayer varies from 20, 40, 60 and 80 m. Moreover, a shear wave velocity of 100 m/s and a unit weight of 12 kN/m^3 are assumed according to the definition of weak interlayer proposed by Bo et al. [5].

Foundation and Earthquake Details

The layered foundation used in the 1D landfill profile model is illustrated in Fig. 1. Based on the thickness, unit weight and shear wave velocity of each soil layer, the foundation belongs to type III site according to the Chinese code for seismic design of buildings (GB50011-2010). The normalized shear modulus reduction and material damping profiles for sand and soft clay proposed by Seed and Idriss [20] are used. Foundation rock is considered as elastic half space as per requirements of the EDT software [12, 13] and 2% damping are assumed for the bedrock.

Furthermore, Kobe earthquake motion record and Loma Prieta earthquake motion record are used in the present analysis and their acceleration peaks are 0.834 and 0.278 g, respectively [1].

Fig. 1 1D landfill profile model and foundation details

Landfill top

MSW body   100 m

Landfill base

Sand γ = 16 kN/m³, v$_s$ = 200 m/s, 20 m

Sand γ = 17 kN/m³, v$_s$ = 300 m/s, 20 m

Sand γ = 18 kN/m³, v$_s$ = 400 m/s, 20 m

Rock γ = 22 kN/m³, v$_s$ = 2000 m/s
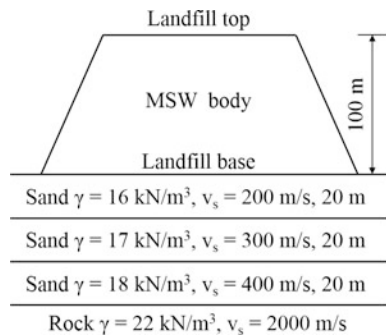
Results and Analysis

Effects of Depth of Weak Interlayer

Figure 2 shows the effects of weak interlayer's depth on the maximum horizontal acceleration (MHA) at the landfill top under Kobe earthquake and Loma Prieta earthquake, respectively. In Fig. 2a and b, MHA is the maximum absolute value of acceleration in the acceleration time history. As shown in the figures, MHA at the landfill top when a weak interlayer exists in the MSW body is much smaller than that when there is no weak interlayer in the MSW body, and the value of 1 m thickness is bigger than that of other thicknesses. In addition to that, when a weak interlayer exists, MHA at the landfill top deceases at the start and then increases with the increase of depth of weak interlayer, and the trend changes in the depths of 40–60 m.

Big deformation happens in the MSW body when there are weak interlayers, and the value of shear strain changes with the variation of weak interlayer's depth. Figure 3a and b are the equivalent shear strain and elevation profiles when a 1 m weak interlayer exists in the MSW body subjected to Kobe earthquake and Loma Prieta earthquake, respectively. In Fig. 3a, the maximum shear strain which is 1.13% happens at the depth of 80 m when subjected to Kobe earthquake, while for Loma Prieta earthquake which is weaker than Kobe earthquake, the maximum shear strain reaches 1.33% at the depth of 60 m as shown in Fig. 3b, and failure may happen under this situation.

MHA changes when weak interlayers exist in the MSW body. Figure 4a and b shows the MHA and elevation profiles when a weak interlayer with the thickness of 9 m exists in the MSW body under Kobe earthquake and Loma Prieta earthquake, respectively. It is clear from the figures that the maximum value of MHA happens at the landfill top when there is no weak interlayer, which shows an apparent free surface amplification effect. However, when there is a weak interlayer,
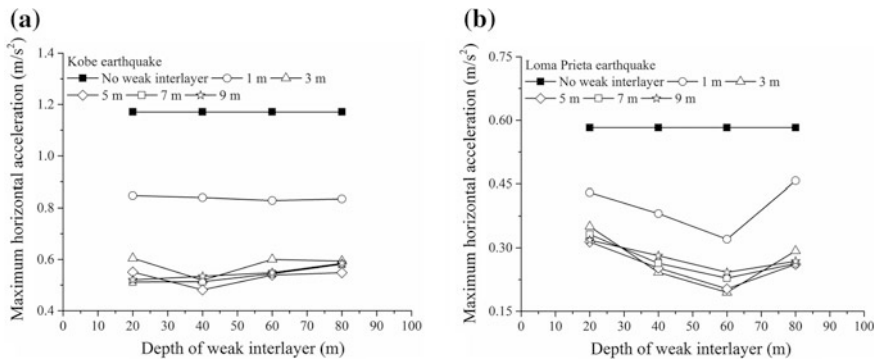
Fig. 2 Effects of depth of weak interlayer on maximum horizontal acceleration at landfill top
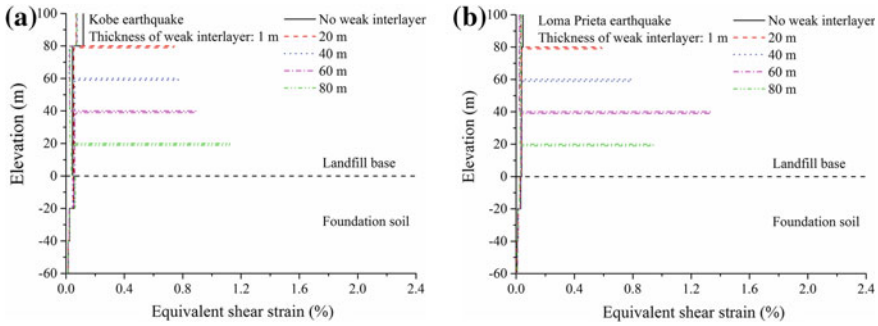
Fig. 3 Effects of depth of weak interlayer on equivalent shear strain of landfill
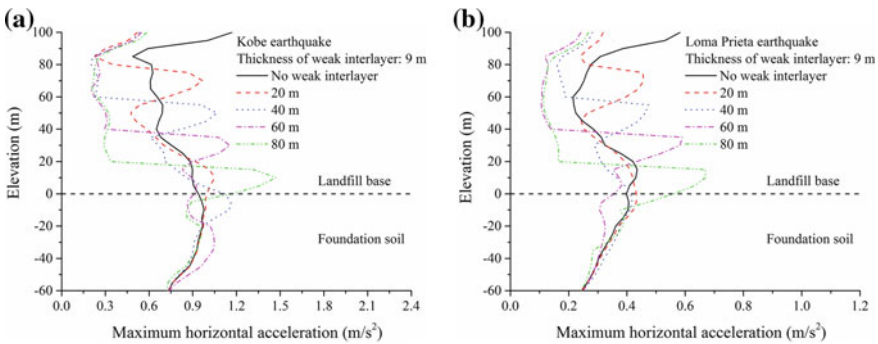
Fig. 4 Effects of depth of weak interlayer on maximum horizontal acceleration with depth of landfill

MHA mutates below the weak interlayer and it increases with the depth. In addition, the maximum value of MHA happens about 10 m below of the weak interlayer.

Effects of Thickness of Weak Interlayer

Figure 5 displays the influences of weak interlayer's thickness on MHA at the landfill top under Kobe earthquake and Loma Prieta earthquake, respectively. From Fig. 5a and b, it can be seen that MHA at the landfill top decreases at the beginning and stabilizes after the thickness of weak interlayer surpasses 5 m.

Thickness of weak interlayer has a noticeable influence on the equivalent shear strain of MSW body. Taking the circumstances when the depths of weak interlayer are 20 and 80 m and under Kobe earthquake as examples, the equivalent shear
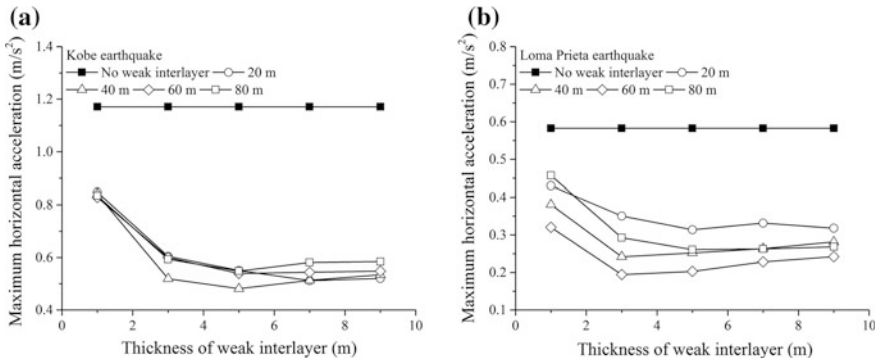
Fig. 5 Effects of thickness of weak interlayer on maximum horizontal acceleration and maximum amplification factor at landfill top
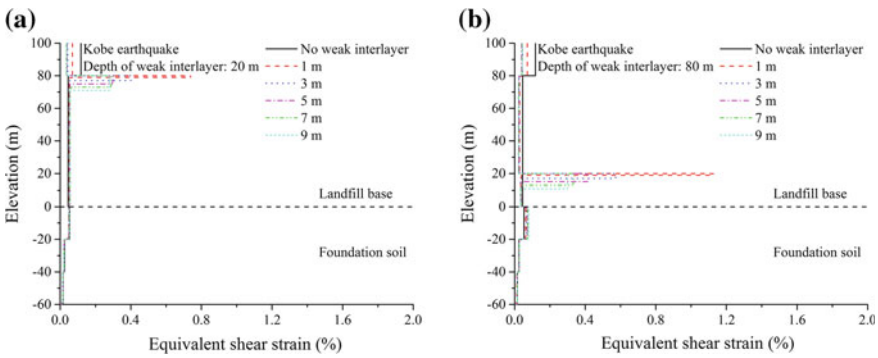
Fig. 6 Effects of thickness of weak interlayer on equivalent shear strain of landfill

strain and elevation profiles are demonstrated in Fig. 6a and b, and the equivalent shear strain at the weak interlayer decreases with the increase of weak interlayer's thickness.

Corresponding to the circumstances in Fig. 6, the MHA and elevation profiles are shown in Fig. 7a and b. After the thickness of weak interlayer reaches a critical thickness, its influence on the MHA declines. As is indicated in the figures, the critical thickness of weak interlayer is 3 m under Kobe earthquake.
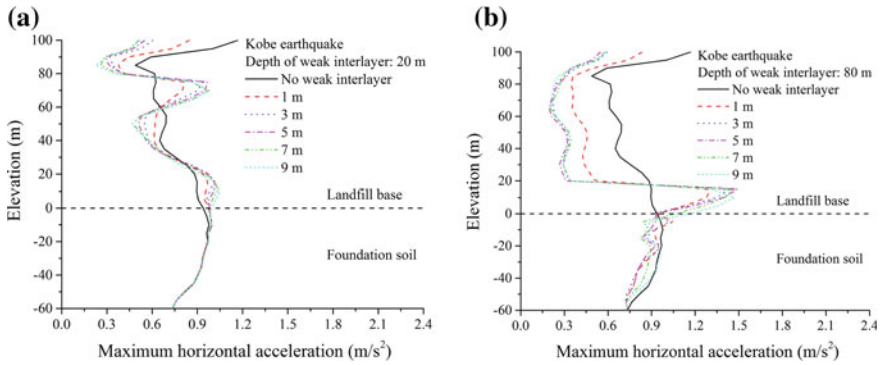
Fig. 7 Effects of thickness of weak interlayer on maximum horizontal acceleration with depth of landfill

Conclusions

Weak interlayers due to the dumping of urban sewage sludge with MSW and the application of soil temporary covers have significant effects on the seismic response of landfills. Using the EDT software to perform 1D frequency independent equivalent-linear analysis, the influences of thickness and depth of one weak interlayer on the dynamic response of landfills subjected to different earthquakes are studied. The conclusions are as followed:

1. Both the maximum horizontal acceleration and the equivalent shear strain mutate when a weak interlayer exists in the MSW body.
2. The maximum value of horizontal acceleration happens about 10 m below of the weak interlayer. And the weak interlayer's influence on the maximum horizontal acceleration of MSW body declines after it reaches a critical thickness.
3. The equivalent shear strain at the weak interlayer decreases with the increase of weak interlayer's thickness, and hence thin weak interlayers in the MSW body should be avoided.

References

1. Choudhury, D., Savoikar, P. (2009). Equivalent-linear seismic analyses of MSW landfills using DEEPSOIL. Engineering Geology, 107(3): 98–108.

2. Bray, J. D., Augello, A. J., Leonards, G. A., Repetto, P. C., Byrne, R. J. (1995). Seismic stability procedures for solid-waste landfills. Journal of geotechnical engineering, 121(2): 139–151.

3. Feng, S. J., Yang, D. Z. (2012). Seismic response of municipal waste landfills with bottom liner interface under different site conditions. Journal of Tongji University: Natural Science, 40(7): 1015–1019. (in Chinese).

4. Chen, G. X., Chen, J. H. (2004). The effect of depth and thickness of soft soil layer on earthquake response for deep soft sites. World Earthquake Engineering, 20(3): 66–73. (in Chinese).

5. Bo. J. S., Li, X. L., Liu, D. D., Liu, H. S. (2003). Effects of soil layer construction on platform value of response spectra. Earthquake Engineering and Engineering Vibration, 23(4): 29–33. (in Chinese).

6. Guidoboni, E., Mariotti, D., Giammarinaro, M. S., Rovelli, A. (2003). Identification of amplified damage zones in Palermo, Sicily (Italy), during the earthquakes of the last three centuries. Bulletin of the Seismological Society of America, 93(4): 1649–1669.

7. Ergin, M., Özalaybey, S., Aktar, M., Yalcin, M. N. (2004). Site amplification at Avcılar, Istanbul. Tectonophysics, 391(1): 335–346.

8. Molhar, S., Cassidy, J. F., Dosso, S. E. (2004). Site response in Victoria, British Columbia, from spectral ratios and 1D modeling. Bulletin of the Seismological Society of America, 94(3): 1109–1124.

9. Satoh, T., Hayakawa, T., Oshima, M., Kawase, H., Matsushima, S., Nagashima, F., Tobita, K. (2014). Site effects on large ground motions at KiK-net Iwase Station IBRH11 during the 2011 Tohoku Earthquake. Bulletin of the Seismological Society of America, 104(2): 653–668.

10. Idriss, I. M., Seed, H. B. (1968). An analysis of ground motions during the 1957 San Francisco earthquake. Bulletin of the Seismological Society of America, 58(6): 2013–2032.

11. Qi, W. H., Bo, J. S. (2007). Summarization on equivalent linear method of seismic responses for soil layers. World Earthquake Engineering, 23(4): 221–226. (in Chinese).

12. Schevenels, M., Francois, S., Degrande, G. (2009). EDT: an ElastoDynamics Toolbox for MATLAB. Computers & Geosciences, 35(8): 1752–1754.

13. Schevenels, M., Francois, S., Degrande, G. (2010). Elastodynamics toolbox for MATLAB, user's guide. Report BWM 2010–11, EDT Version 2.2 Build 20, Faculty of Engineering, Katholieke Unversiteit, Leuven.

14. Kausel, E., Roesset, J. M. (1981). Stiffness matrices for layered soils. Bulletin of the Seismological Society of America, 71(6): 1743–1761.

15. Idriss, I. M., Fiegel, G., Hudson, M. B., Mundy, P. K., Herzig, R. (1995). Seismic response of the operating industries landfill. Earthquake design and performance of solid waste landfills. ASCE, 83–118.

16. Kavazanjian, E., Matasovic, N. (1995). Seismic analysis of solid waste landfills. ASCE, Geotechnical Special Publication, 46(2): 1066–1080.

17. Matasovic, N., Kavazanjian, E. (1998). Cyclic characterization of OII landfill solid waste. Journal of Geotechnical and Geoenvironmental Engineering, 124(3): 197–210.

18. Augello, A. J., Bray, J. D., Abramson, N. A., Seed, R. B. (1998). Dynamic properties of solid waste based on back-analysis of OII landfill. Journal of Geotechnical and Geoenvironmental Engineering, 124(3): 211–222.

19. Feng, S. J., Chen, Y. M., Kong, X. J., Zou, D. G. (2005). Experimental research on dynamic properties of municipal solid waste. Chinese Journal of Geotechnical Engineering, 27(7): 750–754. (in Chinese).

20. Choudhury, D., Savoikar, P. (2009). Simplified method to characterize municipal solid waste properties under seismic conditions. Waste management, 29(2): 924–933.

Applications of Optical Fiber Sensing Technology in Monitoring of Geotechnical Structures

X.W. Ye, T. Liu, Dan-Feng Zhang, Jun Li, Zhi-Feng Liu and Liang Zhang

Introduction

The optical fiber sensing technology has gained significant growth and development due to the advance of laser technology, optical fiber communication technology, modern manufacturing technology, and computer technology. In comparison with the traditional sensors, the optical fiber sensors have some unique advantages, such as small dimension, good resolution and accuracy with low loss, free from electromagnetic interference and corrosion resistance. Therefore, the optical fiber sensing technology has received much attention and is widely employed in the fields of civil engineering, mechanical engineering, and aerospace engineering. In recent years, the optical fiber sensing technology is increasing used to monitor the structural condition and behavior of geotechnical structures.

Usually, the geotechnical structures are too complicated to be accurately understood because of the complexity of geological conditions and the nonlinear characteristics of soil and rock materials. In this connection, the field monitoring will play an essential role in the evaluation of safety state and performance of the geotechnical structures [1]. With the development of laser and instrument technology, the optical fiber sensing technology becomes increasingly mature by overcoming the difficulties in the practical applications. Different types of optical fiber sensors with unique features and advantages are designed and produced for the specific requirements. According to the demodulation principle, the optical fiber sensor can be categorized into different types [2], such as light intensity modulation type sensor, phase modulation type sensor, and wavelength modulation type sensor.

X.W. Ye (✉) · T. Liu
Department of Civil Engineering, Zhejiang University, Hangzhou 310058, China
e-mail: cexwye@zju.edu.cn

D.-F. Zhang · J. Li · Z.-F. Liu · L. Zhang
Guangdong Provincial Academy of Building Research Group Co. Ltd,
Guangzhou 510500, China

In the paper, the sensing principles of three kinds of optical fiber sensors are described, and the applications of optical fiber sensors to geotechnical structures are summarized.

Principles of Optical Fiber Sensing Technology

Generally, a simple optical fiber sensing system consists of a light source, an optical fiber, an optical fiber sensor, a light acceptor, and a modulator element. The optical fiber plays a role in transferring the original light to the optical fiber sensor and then transferring the signal to the light acceptor. The fiber core, cladding layer, and coating layer make up the optical fiber whose constituent is silicon dioxide. The refractive index of the fiber core is higher than the cladding layer's by reason that the fiber core contains a small amount of impurity, germanium for instance. When written into the optical fiber, a beam of white light generates the total reflection at the interface between the fiber core and the cladding layer. The optical fiber sensor bears the function of measurement. The optical fiber sensor can be divided into two categories. One is the functional sensor, and the other is the non-function sensor. The functional sensor is that the sensor is inscribed in the optical fiber leading to the optical fiber has the functions of measurement and transmission. The non-functional sensor only has the function of transmission because that the sensor is an independent element. The transmission principle of the fiber core is shown as Fig. 1. In which, n_1 = refractive index of fiber core, and n_2 = refractive index of cladding layer. The acceptor transfers the received signal to the modulator element in which the signal is modulated and analyzed.

Fig. 1 Transmission principle of fiber core
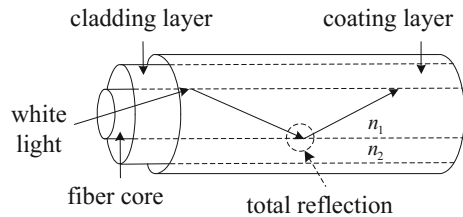
Light Intensity Modulation Type Sensor

The sensing principle is that the measurand (the refractive index of cladding layer, the geometry of optical fiber) will cause the variation of light intensity written into the optical fiber. The distributed optical fiber sensor which is based on the optical time domain reflection technique belongs to the light intensity modulation type sensor. The most obvious advantage is that the distributed optical fiber sensor can realize the distributed measurement along the optical fiber of temperature, strain and other information. The sensing principle [3, 4] of the distributed optical fiber sensor can be illustrated in Fig. 2.

The white light written into the optical fiber will be transferred to the distributed optical fiber sensor which located at the measurement area from one end via the optical fiber. Under the affect of the measurand, there is a backscattered light occurring due to the interaction mechanism between the propagating light pulse and the optical fiber which carrying the temperature and strain state along the optical fiber. Then the backscattered light is transferred to the light acceptor through the optical fiber coupler. The formula shown in Fig. 2 gives a way to analyze the collected backscattered light. The location of the variation of the measurand can be determined by use of the formula.

Phase Modulation Type Sensor

The sensing principle is that the measurand will cause the phase shift of light written into the optical fiber, and the measurand can be measured by demodulating the phase shift utilizing the interferometer. The optical fiber interferometric sensor is based on this kind of sensing principle. The optical fiber interferometric sensor is suitable for the case that the measurement objection with the requirements of high accuracy and large dynamic range. Michelson interferometer [5], Fabry-Perot interferometer [6], and MachZehnder interferometer are the sensors which are the frequently-used sensors belong to the interferometric sensor. The sensing principle [7, 8] of Extrinsic Fabry-Perot interferometer (EFPI) can be described in Fig. 3. In which, the R_1 = the reference reflection, and the R_2 = the sensing reflection.

Fig. 2 Sensing principle of distributed optical fiber sensor

$$Z = \frac{1}{2} \times \frac{ct_i}{n}$$

t_i: time
c: velocity of light
n: refractive index
z: distance
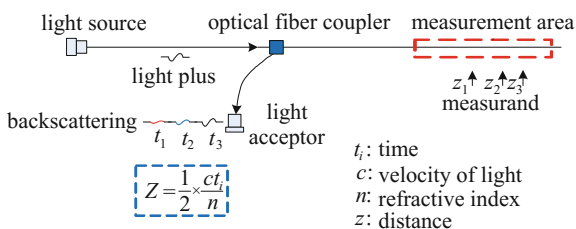
Fig. 3 Sensing principle of
EFPI
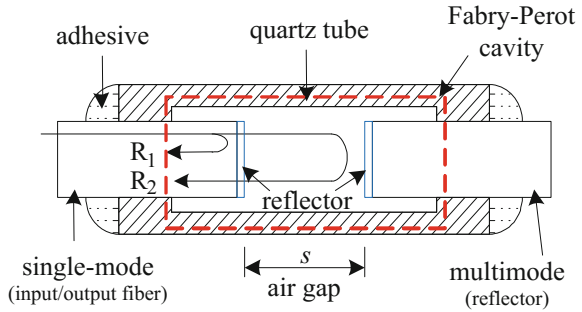
The white light emitted by the light source will be transferred into the Fabry-Perot cavity passing through single-mode and reflector, and 3% of the white light (the reference reflection) will be reflected when via the first reflector. The rest white light whose name is the sensing reflection will be reflected by the next reflector. The reference reflection and the sensing reflection will interfere with each other. The measurand will be determined by demodulating and analyzing the interference.

Wavelength Modulation Type Sensor

The fiber Bragg grating (FBG) sensor belongs to the wavelength modulation type sensor. According to the Bragg's law, the sensing principle of an FBG sensor is that when a white light transmits to the Bragg grating, the light at a particular wavelength is reflected which is related to both the grating period and the effective index of refraction. The Bragg wavelength can be expressed by [9]

$$\lambda_B = 2n_{eff}\Lambda \tag{1}$$

where λ_B = the original wavelength, Λ = the grating period, and n_{eff} = the effective index of refraction.

The measurand (such as temperature and strain) can vary the effective index of refraction and the grating period which leads to the variation of wavelength of the reflected light. The measurand can be distinguished by demodulating the wavelength shift of the reflected white light utilizing the interferometer. The sensing principle [10, 11] of an FBG sensor can be described in Fig. 4.

In a general way, the temperature and strain independently influence the wavelength shift. The shift of wavelength caused by temperature and strain can be calculated by
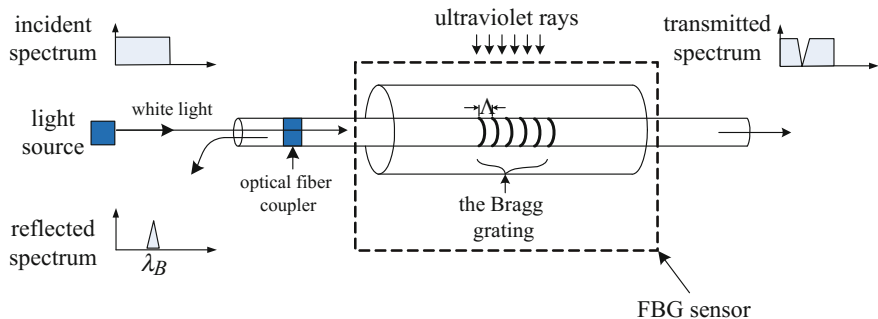
Fig. 4 Sensing principle of FBG sensor

$$\Delta\lambda_B = \lambda_B[(1 - P_e)\Delta\varepsilon + (\alpha + \zeta)\Delta T] \tag{2}$$

where $\Delta\lambda_B$ = the wavelength shift caused by temperature and stress, P_e = the elastic coefficient, α = the coefficient of thermal expansion, ζ = the thermo-optical coefficient, $\Delta\varepsilon$ = the variation of strain, and ΔT = the variation of temperature. The measurand will be determined by demodulating and analyzing the wavelength shift based on the above formula.

Applications of Optical Fiber Sensing Technology

In order to better understand the health condition of the geotechnical structures under various loading and environmental conditions, the analysis of real-structure responding data is imperative. Therefore, the measurement instruments applied into field tests are essential for the responds monitoring of real structures. However, the reliability and effectiveness of the instruments should be proved and verified before applied into field monitoring. The following application examples of optical fiber sensing technology in geotechnical structures demonstrate the reliability and effectiveness of optical fiber sensors.

Slopes

Pei et al. [12] developed a new type of FBG-based in-place inclinometer which considered the deformation of the segment in the calculation. The inclinometer was fabricated and calibrated in the laboratory and used to monitor the deformation of a slope in China. The results showed that the new type of inclinometer was robust and reliable for monitoring the field slope in a harsh environment. Li et al. [13] built a slope model in the laboratory for simulating the slope deformation in the rainy

season. The optical fiber BOTDR sensors were embedded into different positions of the slope, and the FBG sensors were mounted on the surface of the slope at different position. The research showed that the optical fiber BOTDR sensor and the FBG sensor are promising in the slope monitoring field. Ding et al. [14] designed a fiber optic sensing net for slope surface deformation monitoring by embedding the net at a certain depth in slope. Pi et al. [15] installed in situ inclinometer based FBG sensing technology in highway slope for the deformation monitoring, and proposed a new approach for slope stability evaluation.

Foundation Pits

Huang et al. [16] utilized the FBG sensors to monitor the strain curve of reinforced concrete support beam in deep excavation during the excavation process, which proved the FBG sensor is feasible for internal force monitoring of reinforced concrete support beam. Liu et al. [17] proposed a method for on-line monitoring of pit horizontal displacement using BOTDR-based on distributed optical fiber sensor. The successful application of the method in the site test demonstrated the feasibility and effectiveness of the method.

Piles

Kister et al. [18] deployed FBG sensors in reinforced concrete foundation piles for strain and temperature monitoring and structural health condition assessment. Lee et al. [19] used an optical fiber sensor system based on the single path multiplexing technique for the axial load strain monitoring in piles. Weng et al. [20] mounted quasi-distributed fiber Bragg grating (FBG) strain sensors on the surface of pipe piles to monitor the performance of pipe piles.

Dams/Dikes

Notother et al. [21] embedded a distributed sensor system based on Brillouin optical frequency domain analysis into the soil body of river dikes for detection of critical soil displacement, and proposed a method to deal with the issue of local fluctuations of the Brillouin gain attribute to birefringence. Zhu et al. [22] developed rod-type embedded sensors based on FBG sensing technology for the internal deformation monitoring of dam model. The quasi-distributed FBG sensors were axially mounted on the surface of sensor. The researchers utilized the sensors to monitor the deformation of a dam model under overload condition. The results showed that the novel sensor is feasible and effective for the dam deformation monitoring.

Soil Nails

Pei et al. [23] studied the performance of a glass fiber-reinforced polymer (GFRP) bar soil nail in a pullout test in laboratory using FBG sensing technology. Zhu et al. [24] developed an FBG-based monitoring system for the monitoring of average strain of host material as well as localized strain. The system then was used to monitor the strain distributions along soil nails in Hong Kong. The monitoring results showed that the monitoring system was applicable for field soil nail monitoring.

Tunnels

Zhao and Qiu [25] installed FBG sensors on the surface of the tunnel secondary lining to monitor the deformation status of tunnel cross-section. The monitoring data showed that the FBG sensors could relative realistically monitor the strain distributions of tunnel. Mao et al. [26] embedded distributed optical fiber sensors into tunnel secondary lining concrete by air-blowing and vacuum grouting technology, and proposed a method of time series analysis for the tunnel health state assessment.

Conclusions

The sensing principles of the light intensity modulation type sensor, phase modulation type sensor, wavelength modulation type sensor were described. A review of applications of optical fiber sensing technique to geotechnical structures such as the slope, foundation pit, pile, soil nail, and dams/dike was made. The application examples demonstrate that the reliability and effectiveness of the optical fiber sensing technology and indicate that the optical fiber sensors have been used in almost all fields in geotechnical engineering. The optical fiber sensors will have a better application prospect due to the unique advantages and the constant development of manufacture technology and analytical theory.

References

1. Pei, H.F., Teng, J., Yin, J.H., Chen, R. (2014). A review of previous studies on the applications of optical fiber sensors in geotechnical health monitoring. Measurement, 58(3): 207–214.
2. Ding, X.P., Wang, W., Fu, L.C. (2006). Classification and application principles of optical-fibre transducer. Spectroscopy and Spectral Analysis, 26(6): 1176–1178.
3. Guemes, A., Fernandez-Lopez, A., Soller, B. (2010). Optical fiber distributed sensing-physical principles and applications. Structural Health Monitoring, 9(3): 233–245.
4. Zhu, Z.W, Liu, D.Y., Yuan, Q.Y., Liu, B., Liu, J.C. (2011). A novel distributed optic fiber transducer for landslides monitoring. Optics and Lasers in Engineering, 49(7): 1019–1024.
5. Bi, Y.W. (2000). Michelson optical fiber strain sensor. Optics and Precision Engineering, 8 (1): 83–86.
6. Jiang, M.Z., Gerhard, E. (2001). A simple strain sensor using a thin film as a low-finesse fiber-optic Fabry-Perot interferometer. Sensors and Actuators A: Physical, 88(1): 41–46.
7. Kwon, I.B., Choi, M.Y., Moon, H. (2004). Strain measurement using fiber optic total reflected extrinsic Fabry-Perot interferometric sensor with a digital signal processing algorithm. Sensors and Actuators A: Physical, 112(1): 10–17.
8. Akhavan, F., Watkins, S.E., Chandrashekhara, K. (1998). Measurement and analysis of impact-induced strain using extrinsic Fabry-Perot fiber optic sensors. Smart Materials and Structures, 7(6): 745–751.
9. Ye, X.W., Su, Y.H., Han, J.P. (2014). Structural health monitoring of civil infrastructure using optical fiber sensing technology: a comprehensive review. The Scientific World Journal, 2014, ID: 652329.
10. Betz, D.C., Staudigel, L., Trutzel, M. N., Kehlenbach, M. (2003). Structural monitoring using fiber-optic Bragg grating sensors. Acoustics, Speech, and Signal Processing Newsletter, 2(2): 145–152.
11. Moyo, P., Brownjohn, J.M.W., Suresh, R., Tjin, S.C. (2005). Development of fiber Bragg grating sensors for monitoring civil infrastructure. Engineering Structures, 27(12): 1828–1834.
12. Pei, H.F., Yin, J.H., Zhu, H.H., Hong, C.Y., Jin, W., Xu, D.S. (2012). Monitoring of lateral displacements of a slope using a series of special fibre Bragg grating-based in-place inclinometers. Measurement Science and Technology, 23(2), ID: 025007.
13. Li, H.Q., Sun, H.Y., Liu, Y.L., Sun, X.M., Shang, Y.Q. (2008). Application of optical fiber sensing technology to slope model test. Chinese Journal of Rock Mechanics and Engineering, 27(8): 1703–1708.
14. Ding, Y., Shi, B., Cui, H.L., Suo, W.B., Liu, J. (2005). A fiber optic sensing net applied in slope monitoring based on Brillouin scattering. Chinese Journal of Geotechnical Engineering, 27(3): 338–342.
15. Pei, H.F., Yin, J.H., Zhu, H.H., Hong, C.Y., Fan, Y.H. (2010). In-situ monitoring of displacements and stability evaluation of slope based on fiber Bragg grating sensing technology. Chinese Journal of Rock Mechanics and Engineering, 29(8): 1570–1576.
16. Huang, G.L., Zhang, F., Xu, H.Z., Chen, G. (2008). Strain monitoring of interior bracing in deep foundation pit by FBG sensors. Chinese Journal of Geotechnical Engineering, 30: 436–440.
17. Liu, J., Shi, B., Zhang, D., Sui, H.B., Suo, W.B. (2006). Experimental study of foundation pit monitoring using BOTDR-based on distributed optical fiber sensor. Rock and Soil Mechanics, 27(7): 1224–1228.
18. Kister, G., Winter, D., Gebremichael, Y.M., Leighton, J., Badcock, R.A., Tester, P.D., Krishnamurthy, S., Boyle, W.J.O., Grattan, K.T.V., Fernando, G.F. (2007). Methodology and integrity monitoring of foundation concrete piles using Bragg grating optical fibre sensors. Engineering Structures, 29(9): 2048–2055.

19. Lee, W.J., Lee, W.J., Lee, S.B., Salgado, R. (2011). Measurement of pile load transfer using the fiber Bragg grating sensor system. Canadian Geotechnical Journal, 41(6): 1222–1232.
20. Weng, X.L., Chen, J.X., Wang, Y. (2104). Fiber Bragg grating-based performance monitoring of piles fiber in a geotechnical centrifugal model test. Advances in Materials Science and Engineering, 2104, ID: 659276.
21. Notother, N., Wosniok, A., Krebber, K. (2008). A distributed fiber optic sensor system for dike monitoring using Brillouin frequency domain analysis. Proceedings of SPIE, 7003.
22. Zhu, H.H., Yin, J.H., Zhang, L., Dong, J.H., Feng, J.W., Lei, W. (2008). Deformation monitoring of dam model test by optical fiber sensors. Chinese Journal of Rock Mechanics and Engineering, 27(6): 1188–1194.
23. Pei, H.F., Yin, J.H., Zhu, H.H., Hong, C.Y. (2012). Performance monitoring of a glass fiber-reinforced polymer bar soil nail during laboratory pullout test using FBG sensing technology. International Journal of Geomechanics, 13(4): 467–472.
24. Zhu, H.H., Yin, J.H., Jin, W., Zhou, W.H. (2007). Soil nail monitoring using fiber Bragg grating sensors during pullout tests. The Joint 60th Canadian Geotechnical and 8th IAH-CNC Conferences, Ottawa: 821–828.
25. Zhao, X.G., Qiu, H.T. (2007). Application of fiber Bragg grating sensing technology to tunnel monitoring. Chinese Journal of Rock Mechanics and Engineering, 26(3): 587–593.
26. Mao, J.H., He, Y., Jin, W.L. (2011). Life-cycle stress monitoring method for tunnel secondary lining based on distributed optical fiber sensor. China Journal of Highway and Transport, 24 (2): 77–88.

Dynamic Interaction of Vehicle-Track Coupled System Under Different Patterns of Uneven Settlement

Xiang Duan, Jing Hu, Xuecheng Bian and Jianqun Jiang

Introduction

In recent years, high-speed railway has gained rapid development world widely as a fast and energy-saving mass transportation form. In china, the majority of current and planned lines are ballastless track as its high stability, low irregularity and low maintain cost. However, uneven settlement that inevitably occurred in roadbed will arouse drastic vibration and affect the passenger's comfort, operation safety and service life of the track.

A number of researches has been done to investigate the vibration under uneven settlement and propose reasonable limitations. Generally, the uneven settlement are assumed to be a cosine curve with two specified parameters wavelength L and the amplitude H. And both the wavelength and the amplitude affect the dynamic interaction of vehicle-track system significantly. Song [1, 2] established a vertical vehicle-track model and indicated that the wheel-rail interaction showed more sensitive to settlement with short wavelength while the vehicle acceleration were more affected by settlement with long wavelength. And based on simulation, a limitation schedule of subgrade settlement was suggested. based on nonlinear coupled model, Cai [3, 4] suggested that the ratio of amplitude and wavelength (H/L) limitation is 1‰ in terms of control standards of passenger comfort,

X. Duan (✉) · J. Hu · X. Bian · J. Jiang
Department of Civil Engineering, Zhejiang University, Hangzhou 310058, China
e-mail: 3100101601@zju.edu.cn

J. Hu
e-mail: 11312009@zju.edu.cn

X. Bian
e-mail: bianxc@zju.edu.cn

J. Jiang
e-mail: jianqun@zju.edu.cn

(a) Tightly connect at track-subgrade interface   (b) Gapped at track-subgrade interface
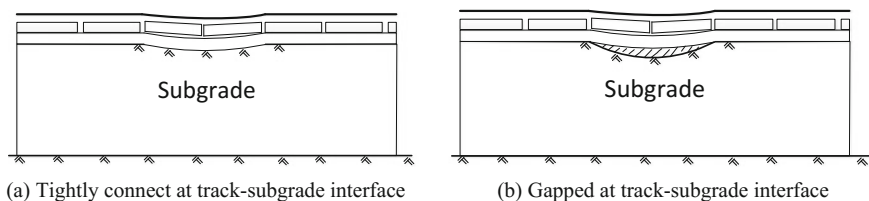
Fig. 1 Two status of track-subgrade interface under the self-graverty

wheel-rail interaction and structural stress. For most of established models, subgrade uneven settlement is usually assumed to occur at the top of subgrade and joint with the track structure tightly [5, 6], thus deformation of subgrade will reflect to the track and affect the vehicle-track interaction directly (as show in Fig. 1a). However, the actual interaction mechanisms in settlement zone are complex. Generally, the gravity caused inflection of track structure fills the settlement zone and makes the track and subgrade contact tightly as show in Fig. 1a. But when wavelength of settlement is short and the gravity caused inflection is small as show in Fig. 1b, the contact between track and subgrade may weaken and even come to be void at the interface, which makes the conventional method unavailable.

To investigate the dynamic interaction of train-track system under sorts of uneven settlements, a vehicle-track coupled model is built based on vehicle-track coupled dynamic theory. In this model, the gravity of track structure is considered and a trail-iterate algorithm in each time step is developed so that the dynamic response can be calculated accurately considering the track-the subgrade complex contact relation due to the uneven settlement. Details of the model and its application on evaluating vibrations under the uneven settlements will be introduced in this paper.

The Vehicle-Track Coupled Model

Model Introduction

The developed vehicle-track coupled model is modeled according to one of the most common ballastless slab track structure in China, which consisting of rail, CRTS I slab, CA mortar, concrete base and subgrade from top to bottom as show in Fig. 2. The proposed model is supposed to investigate the vehicle-track vertical vibration on constant velocity and several assumptions and simplifications are given accordingly. The rail and the concrete base are modeled as simply supported Euler beams; the track slabs are modeled as free-free Euler beams; the support of fasteners and CA mortar is modeled as spring—damping system; the foundation is assumed as Kelvin foundation with the distribution damping. The vehicle is modeled as plane multi—rigid-body system moving at a constant speed and coupled with the track by assuming the linear Hertz contact between wheels and rails. And also the
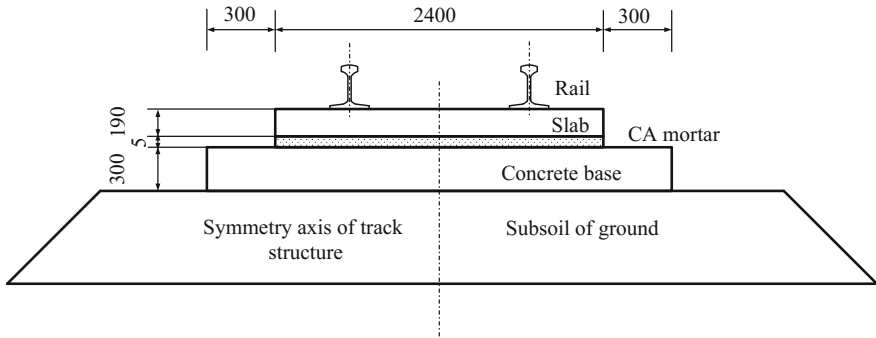
Fig. 2 Schematic section view of ballastless slab track (mm)

gravity of structures and vehicles are induced to consider contact relation between track and subgrade. The diagram of the model is presented in Fig. 3.

Based on the model and vibration theory, the governing differential function of the rails, track slabs and concrete bases were easily obtained as follow:

$$E_r I_r \frac{\partial^4 u_r(x,t)}{\partial^4 x} + \rho_r \frac{\partial^2 u_r(x,t)}{\partial^2 t} = \sum_{i=1}^{n_c} \sum_{j=1}^{4} \delta(x - x_{ij}) R_{ij}(t)$$
$$- \sum_{i=1}^{n_s} \sum_{j=1}^{n_t} \delta(x - x_{tij}) A_{ij}(t) + m_r g \qquad (1)$$

$$E_s I_s \frac{\partial^4 u_{si}(x,t)}{\partial^4 x} + \rho_s \frac{\partial^2 u_{si}(x,t)}{\partial^2 t} + f_{sih}(x,t) = \sum_{j=1}^{n_t} \delta[x - (x_{tij} - x_{si})] A_{ij}(t) + m_s g \quad (2)$$

$$E_h I_h \frac{\partial^4 u_h(x,t)}{\partial^4 x} + \rho_h \frac{\partial^2 u_h(x,t)}{\partial^2 t} + f_g(x,t)$$
$$- \sum_{i=1}^{n_s} \left[H(x - x_{si}) - H(x - x_{s(i+1)}) \right] f_{sih}(x,t)$$
$$= m_h g \qquad (3)$$
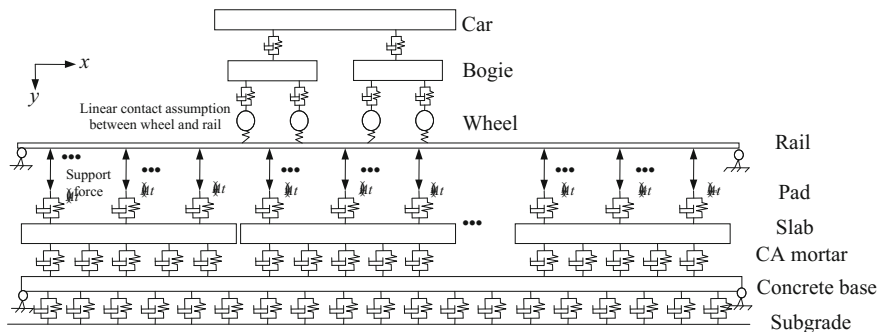
Fig. 3 Simplified vertical vehicle-track model

where E_rI_r, E_sI_s and E_hI_h are the bending stiffness of rails, slabs and concrete bases respectively; ρ_r, ρ_s and ρ_h are the distributed mass of rails, slabs and concrete bases respectively; u_s, u_s and u_s are the displacement responses of rails, slabs and concrete bases respectively and the variate x respects the coordinate along the vehicles' moving direction. $f_{sih}(x,t)$ and $f_g(x,t)$ are distributed force between slabs and concrete bases and underneath the concrete bases. $R_{ij}(t)$ is the wheel-rail contact force; $A_{ij}(t)$ is the support force of the pad to rail. n_s and n_t is the number of slabs and fasteners on one slab respectively is the Dirac-delta function and is the step function.

As mentioned above, $R_{ij}(t), A_{ij}(t), f_{sih}(x,t), f_g(x,t)$ are the wheel-rail contact force, pad force, vertical pressure in CA mortar and subsoil, respectively. The explicit expressions are given as below:

$$R_{ij}(t) = K_{wr}\left[y_{wij}(t) - u_r\left(x_{ij}, t\right)\right] \tag{4}$$

$$A_{ij}(t) = K_{rs}\left[u_r\left(x_{tij}, t\right) - u_{si}\left(x_{tij} - x_{si}, t\right)\right] + C_{rs}\left[\dot{u}_r\left(x_{tij}, t\right) - \dot{u}_{si}\left(x_{tij} - x_{si}, t\right)\right] \tag{5}$$

$$f_{sih}(x,t) = k_{sh}[u_{si}(x,t) - u_h(x + x_{si}, t)] + c_{sh}[\dot{u}_{si}(x,t) - \dot{u}_h(x + x_{si}, t)] \tag{6}$$

$$f_g(x,t) = k_g u_h(x,t) + c_g \dot{u}_h(x,t) \tag{7}$$

where K_{rs}, k_{sh}, k_g and C_{rs}, c_{sh}, c_g are the stiffness and damping of pad, CA mortar and embankment soil, respectively. K_{wr} is the linear stiffness of wheel-rail contact, y_{wij} is the displacement response of the jth wheel on the ith bogie.

To solve the dynamic differential governing functions above, the mode superposition method are adopted and the modes of simply support beams and free-free beams are employed for rails, concrete bases and slabs. Combining governing functions of vehicle and tracks, the differential governing functions of the coupled system can be:

$$[M]_{nz \times nz}^{w}\{\ddot{y}\}_{nz \times 1}^{w} + [C]_{nz \times nz}^{w}\{\dot{y}\}_{nz \times 1}^{w} + [K]_{nz \times nz}^{w}\{y\}_{nz \times 1}^{w} = \{f\}_{nz \times 1}^{w} \tag{8}$$

where nz is the number of DOFs of the whole train-track-ground system. $[M]_{nz \times nz}^{w}, [C]_{nz \times nz}^{w}, [K]_{nz \times nz}^{w}$ are the integral mass, damping and stiffness matrices of the whole system, respectively. $\{f\}_{nz \times 1}^{w}$ is the integral load vector. In this model, the numerical Newmark β method is adopted for solving these equations.

Model Validation

To validate the accuracy of the proposed model, the vibration responses based on coupled model are compared with field test result. Figure 4a shows the comparison of the velocity responses of concrete base measured in Beijing-Tianjin Intercity Passenger Line and simulated based on proposed model, which are both induced by

(a) Comparison of velocity response time-history Curve

(b) Comparison of velocity response in varied speed
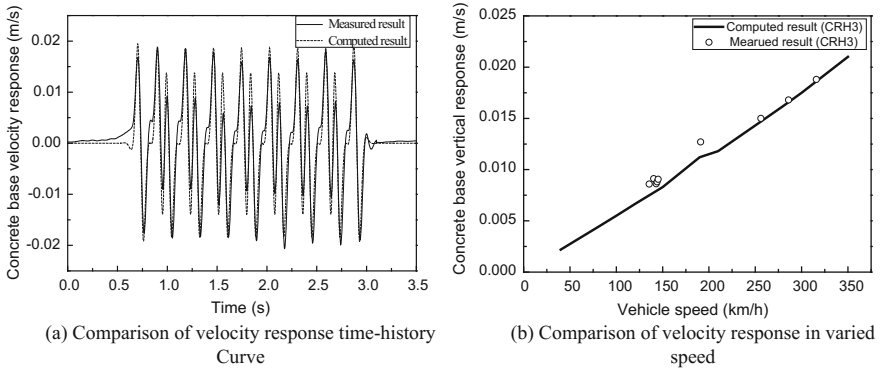
Fig. 4 Comparison of velocity response between measured result and computed result

CRH 3 traveling at a constant speed of 292 km/h. And Fig. 4b shows the peak values of the velocity response on concrete base under different train speed. The time-history curve of simulating velocity response shows well agreement with the field test result. And the growth trend of velocity response at increasing train speeds are also coincidental as shown in Fig. 4b. It's evident that the proposed model can simulate the train induced vibration accurately.

Subgrade Uneven Settlement in Calculation Model

Three Patterns of Uneven Settlement

Different from established model, in this research uneven settlement will be divided into three patterns and modelized respectively according to the contact statues in settlement zone. In the contact pattern, the gravity caused structure deflection fills the settlement zone and the track keeps entire contact with subgrade as shown in Fig. 5a. In the gapped pattern as shown in Fig. 5b, train load induced deflection is smaller than the settlement and the support of subgrade at the settlement zone will be ignored. And in partial contact pattern, the track keeps separation from subgrade at settlement zone in the initial state, and partly contact with the subgrade while the moving trains act on the settlement zone and impact drastic inflection of the track as shown in Fig. 5c.

As the different contact status and action mechanisms, relative simplifications and algorithms are adopt for three settlement patterns respectively. For the contact pattern, deformations at track-subgrade interface are assumed to be continuous so that the conventional algorithms is available and applicable, which is wildly adopted in conventional models. For the gapped pattern, all the reaction force of subgrade are regarded to be zero in calculation. And for partial contact pattern,
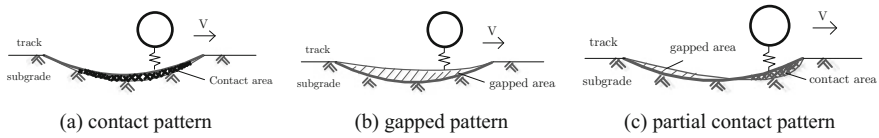
Fig. 5 Contact status of three patterns of settlement in track-subgrade interface

less study and models are put forward so that a new trail-iterate algorithm is proposed and used in this research. More details will be presented in next section.

Trail-Iterate Algorithm in Partial Contact Pattern

In the partial contact pattern, the dynamic vibration response is hard to calculate as both the contact area and contact force are indeterminate in every integral steps. A trail-iterate algorithm is proposed to solve this problem and it works as shown in Fig. 6. In this algorithm, firstly the trial calculation will be done with assuming no contact occurs at settlement zone. With result of this trial computation, the approximate contact area and trail contact force can be determined by comparing the calculated track inflection with settlement curve. Adding the trial contact force into the equation, the related displacement u_i is solve out. According to the u_i, a new trail contact force is given. And by correct the equation, the displacement u_{i+1} is solve out. Only when the difference between u_i and u_{i+1} is less than the control error e, the calculated displacement u is regarded as the final solution and put into next integral step. By the trail-iterate algorithm, the proposed model can simulate the dynamic vibration in partial contact pattern.

Compared with algorithms in the contact pattern and the gapped pattern, in partial contact pattern the trail-iterate algorithm is new-established and lake of verification. The algorithm which correct contact area and contact force in each integral step is also effective in the scope of other two patterns. Thus to verify the

Fig. 6 Flow diagram of trail-iterate algorithm

(a) Comparison of contactforce based on
contact pattern and partial contact pattern

(b) Comparison of contactforce based on
gapped pattern and partial contact pattern
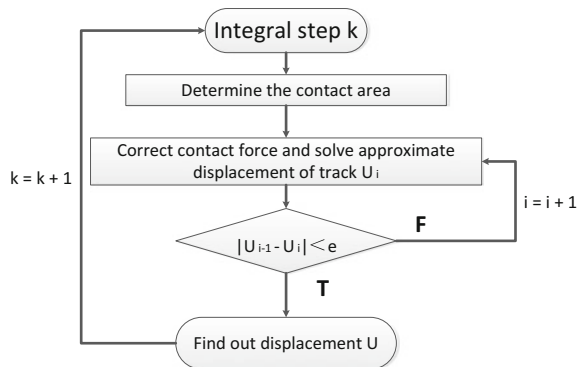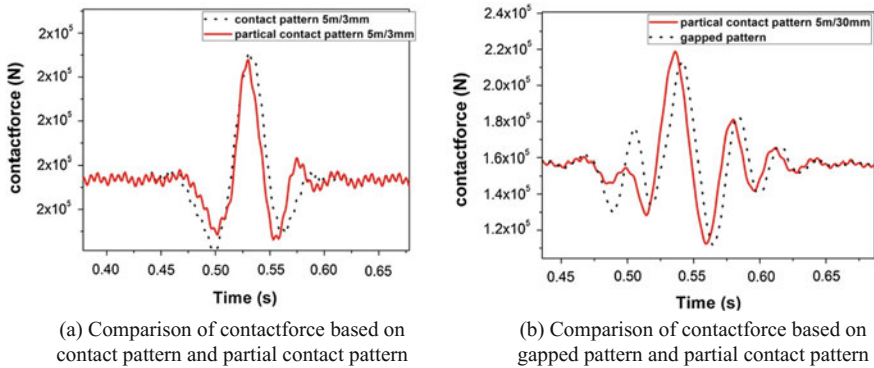
Fig. 7 Comparison of contactforce in partial contact pattern and another two patterns

effectiveness of trail-iterate algorithm, two extreme cases are provided: settlement with 5 m wavelength and 3 mm amplitude and settlement with 5 m wavelength and 30 mm amplitude respectively (here the wavelength 5 m is selected corresponding to the length of slab). In the former case which is tend to be the contact pattern, both the algorithm of contact pattern and partial contact pattern are both employed. Comparison of calculated wheel-rail contact forces are illustrated in Fig. 7a. In the later case which is tend to be the gapped pattern, both the algorithm of gapped pattern and partial contact pattern are employed. Their contact forces are in comparison as show in Fig. 7b. For both Fig. 7a, b, the contact force based on partial contact pattern shows commendable agreement with the result based on other two contact patterns. It's indicated that the new trail-iterate algorithm is effective in calculation of vehicle-track interaction.

As declared above, calculation results in different patterns will tend to be consistent when the settlement is at the junction of two adjacent pattern scopes. Accordingly, the scope boundary of three patterns can be found out by comparing calculation results of a range of cases in three patterns. For example, based on calculation, the scopes will be $0 \sim 7$ mm amplitude for contact pattern, $7 \sim 30$ mm amplitude for partial contact pattern and over 30 mm amplitude for gapped pattern when the wavelength of settlement is 5 m it's indicated that amount of uneven settlements are divided into partial contact pattern and gapped pattern especially when the settlement wavelength is short, which used to be considered to be contact pattern in conventional models.

Vibration Responses at the Settlement Zone

In this section, the responses of wheel-rail contact force and vehicle vertical acceleration in three patterns are introduced in the cases of uneven settlement with wavelength 5 m, amplitude 15 mm and wavelength 5 m, amplitude 35 mm

(a) contactforce under settlement of 5m/15mm

(b) acceleration under settlement of 5m/15mm

(c) contactforce under settlement of 5m/35mm

(d) acceleration under settlement of 5m/35mm
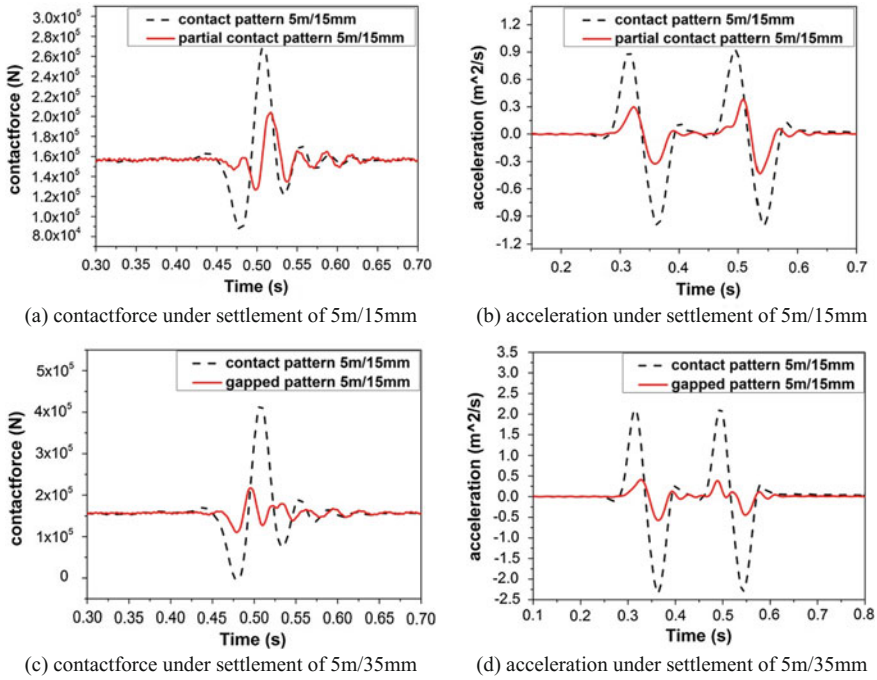
Fig. 8 Dynamic responses in two cases based on three patterns

respectively. For the former case, the settlement is in the scope of partial contact pattern and for the later case, the settlement is in the scope of gapped pattern. In two cases, the dynamic responses are calculated based on appropriate pattern. The dynamic responses based on contact pattern are also adopted as comparison in these two cases as the contact pattern shares the same assumption and simplification with conventional model.

It's obvious that dynamic responses based on contact pattern are greatly exceed the dynamic responses based on their appropriate pattern as shown in Fig. 8, which means that in the scope of partial contact pattern and gapped pattern, the use of conventional models will markedly overrate the dynamic responses aroused by the uneven settlement. The proposed model which divides settlement into three patterns and calculate the response accordingly is indispensable.

Conclusion

High speed moving train load will arouse drastic dynamic response under the affect of uneven settlement. To investigate the dynamic interaction of vehicle-track system, a vertical couple model based on ballastless track is introduced and validated

by the field test. In the proposed model, uneven settlements are divided into three pattern and relative algorithms and assumptions are adopted for each pattern. The results of this paper can be summarized as follows:

1. The vertical vehicle-track coupled model is introduced and well validated by the field test in Beijing-Tianjin Intercity Passenger Line.
2. According to the track-subgrade contact status at the interface, settlement are divided into three patterns. In partial contact pattern, a new-established trail-iterate algorithm is used to correct the contact status in each integral step.
3. In the scope of gapped pattern and partial contact pattern, the dynamic response based on conventional assumption and algorithm will be greatly overrated. The proposed model which divides settlement into three patterns and calculate the response accordingly is indispensable.

References

1. Huanping Song. (2011). Theoretical and field test analysis of high-speed train and slab track coupling interaction [D]. Zhejiang University, Master.
2. Huanping Song, Xuecheng Bian, Jianqun Jiang, Yunmin Chen. (2012). Correlation between subgrade settlement of high-speed railroad and train operation speed [J]. Journal of Vibration and Shock, 31(10):134–140.
3. Chenbiao Cai, Peng Xu. (2010). Dynamic analysis of key design parameters for ballastless track of high-speed railway [J]. Journal of Southwest Jiaotong University, 45(4):493–497.
4. Chenbiao Cai, Wanming Zhai, Yunkai Wang. (2006). Calculation and assessment analysis of the dynamic performance for slab track on Sui-Yu Railway [J]. China Railway Science, 27(4):17–21.
5. Zhang, X., Burrow, M., & Zhou, S. (2016). An investigation of subgrade differential settlement on the dynamic response of the vehicle–track system. Proceedings of the Institution of Mechanical Engineers Part F Journal of Rail & Rapid Transit, 230.
6. Wang, P., Chen, R., Chen, X. P., Wang, P., Chen, R., & Chen, X. P. (2010). Dynamic Assessment of Ballastless Track Stiffness and Settlement in High-Speed Railway. Joint Rail Conference (pp. 203–207).

Experimental Study of Ground Vibrations Induced by HST on an Embankment Section

XiaoLei Zhang, ShiJin Feng, HongXin Chen and Lei Wang

Introduction

Much convenience and high efficiency have been taken to the consumers with the rapid development and wide use of High Speed Railway. However, the vibrations issues caused by the passage of the high speed trains have been arousing many attentions from the government and scholars. The vibration may cause harm to the nearby buildings, breakdown of sensitive equipment and discomfort to people.

The rapid development of the high speed rail network has attracted lots of researchers focusing on the prediction models for high speed train induced vibrations. Hall [1] developed a mathematical numerical model in both the frequency and time domains with finite element method, and analyzed the actual vibration measurements performed at Ledsgaard. Yang et al. [2] studied the transmissibility of soils for vibrations induced by trains at different speeds with a 2.5D finite/infinite element approach, where the train was simplified to a series of moving loads. Kouroussis et al. [3, 4] presented a coupled lumped mass (CLM) model for the vertical dynamical coupling of railway track through the soil. And the dynamic analyses of the CLM model was compared with those of complete track-soil ones. A 3D numerical model which is capable to model the propagation and transmission of ground vibration in the vicinity of high speed railways was presented by

X. Zhang · S. Feng (✉) · H. Chen · L. Wang
Department of Geotechnical Engineering, Tongji University, Shanghai 200092, China
e-mail: fsjgly@tongji.edu.cn

X. Zhang
e-mail: 506720802@qq.com

H. Chen
e-mail: chenhongxin@tongji.edu.cn

L. Wang
e-mail: 1187288987@qq.com

Connolly et al. [5]. And the model was used to investigate the effect of embankment constituent material on ground borne vibration levels.

Although numerical studies are increasingly applied to the practical projects, there are some gaps with the reality, due to the complexity, inhomogeneity and uncertainty of the system [6]. This paper intends to present detailed experimental investigations of HST induced ground vibrations with time-domain, frequency-domain and amplitudes analysis. And the three directional vibrations, which are rare before, provided thoroughly in this paper. The ground vibration measurement was firstly conducted on the Beijing-Shanghai high-speed railway (in China), all along where the CRSII ballast-less track was adopted. Then, field measurement results are analyzed.

Field Experiment of Ground Vibrations

The field experiment was conducted on the Beijing-Shanghai high-speed railway in Fengyang. As shown in Fig. 1, the testing site locates in an embankment section of railway lines. The flat farmland besides the railway provides great convenience to the field test. Thus, the experimental results have high accuracy in the absence of other vibration sources.

Fig. 1 Testing site of ground vibration at the B-S high-speed railway

High Speed Train and Track Structure

The daily operation HSTs, on the Beijing-Shanghai high-speed railway, contain four types, such as, CRH380A/B and CRH380AL/BL. The letter "L" means that the train has 16 cars. Figure 2 shows the geometry of CRH380B train. The length of a typical carriage is 24.2 m, and the spacing of wheels and bogies are 2.5 and 14.9 m, respectively. The repetition of HSR in geometry leads to periodic excitation on the railway structures. These periodicities are then defined as follow:

$$f_{ti} = \frac{v_t}{L_i} \quad i = 1, 2, 3, \ldots \tag{1}$$

where v_t represents the HST's running speed.

As listed in Table 1, L_i denotes the characteristic dimensions of the HST. When v_t is 300 km/h, the corresponding train characteristic frequency (TCF) are also listed in Table 1. The specifications of tested trains can be found in [7]. The geometry and primary dynamic parameters of CRH380A train are similar to those of CRH380B train.

As depicted in Fig. 3, the ballast-less CRTSII slab track and high embankment structure are applied to the railway. The slab track is consist of 60 kg/m rail, rail-pads, track slab, concrete asphalt (CA) mortar and concrete base. Meanwhile, the embankment is composed of surface subgrade, bottom subgrade and subgrade bed. Moreover, the geometrical and physical characteristics are listed in Table 2. Additionally, some supplementary parameters, such as the spatial distribution and geometrical characteristics of each part, are also shown in Fig. 3.
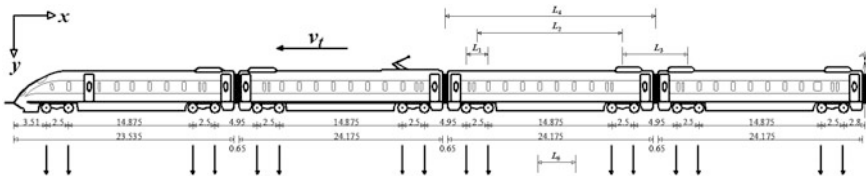
Fig. 2 Geometry of the CRH380B train

Table 1 Characteristic dimensions of the HST and railway structures	Characteristic dimensions (m)	l_1	l_2	l_3	l_4
		2.5	17.5	7.5	25.0
	GCF f_{gi} (Hz)	33.3	4.8	11.1	3.3
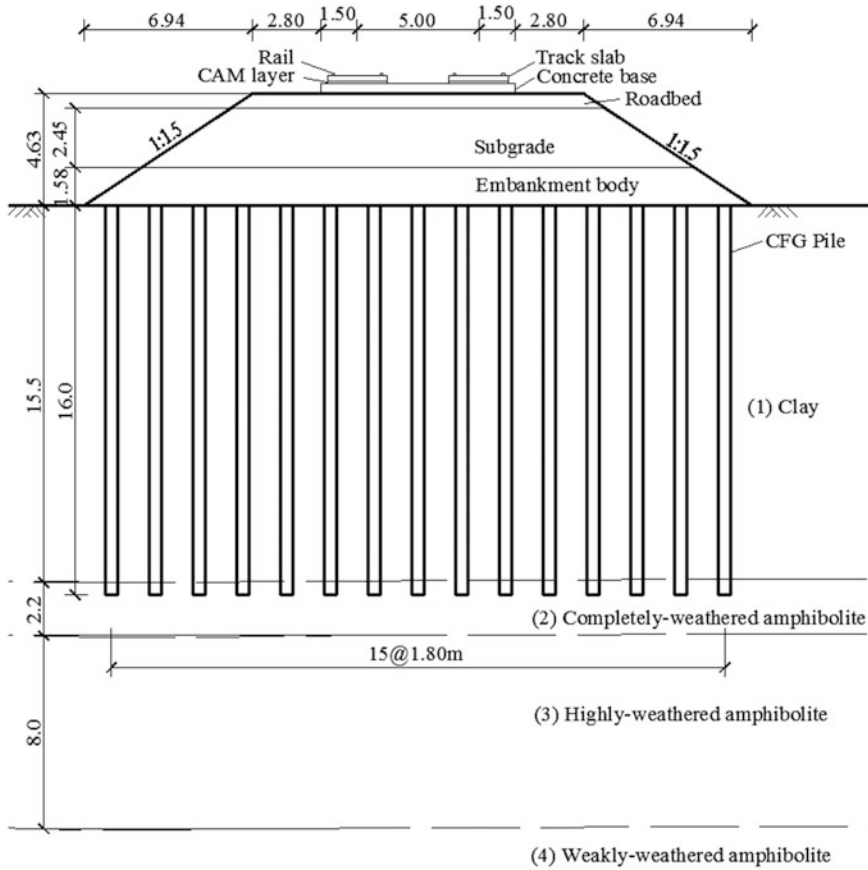
Fig. 3 Cross section of the testing railway (unit: m)

Table 2 Railway infrastructure properties

Name	Thickness (m)	Young's modulus (MPa)	Poisson ratio	Damping ratio	Density (kg/m^3)	Shear wave velocity (m/s)
Roadbed	0.6	150	0.3	0.038	1900	174.3
Subgrade	2.45	110	0.35	0.034	1950	144.5
Embankment body	1.58	50	0.32	0.03	1900	99.8

Underlying Soil Properties

According to geological exploration, the underlying soil of the measuring site is divided into 4 layers. Detailed parameters are listed in Table 3.

Measurement Arrangement

To obtain propagation characteristics of ground vibration, in three direction at the same time, 10 measuring points were arranged in a row at various intervals outside of guardrail. As shown in Fig. 4a, the first test point is located in the outside of embankment guardrail, and the distance to the track center is 16.5 m. To obtain accurate results, the intervals of previous 5 points are 2 m. For the further test points, the intervals range from 4 to 10 m.

Two types of accelerometers are used in this measurement: three-component and one-component types. The accelerometer (Fig. 4b) can be used to test three-component ground vibrations, and its measurement range is 0–5 g, its effective frequency range is 0.1–1000 Hz. The accelerometers of this type is used in the previous 3 measuring points. The accelerometer (Fig. 4c) can only be used to test one-component ground vibration, but in this experiment it was used in triplets

Table 3 Underlying soil properties

Soil layer	Soil type	Thickness (m)	Young's modulus (MPa)	Poisson ratio	Density (kg/m³)
(1)	Qal 3 clay	15.5	47	0.36	2010
(2)	P$_{tlz}$ completely-weathered amphibolite	2.2	85	0.32	2100
(3)	P$_{tlz}$ highly-weathered amphibolite	8	126	0.34	2300
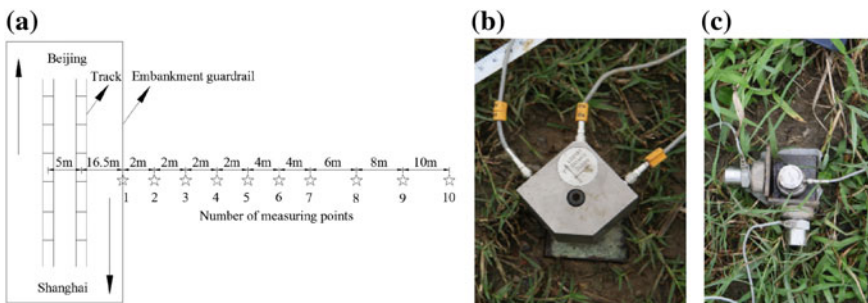
Fig. 4 Test points arrangement and accelerometers: **a** test point arrangement, **b** three-component and **c** one-component accelerometer

to test three-component ground vibrations. Its measurement range is 0–7 g, and the effective frequency range is 0.1–4000 Hz. The accelerometers are used in the latter 7 measuring points.

The adopted vibration signal acquisition instrument is named SIRIUS-HD STGS16 which has 16 channels. Two instruments are used in parallel in this experiment, thus providing 32 channels to collect vibration data. The sampling frequency was set to be 1500 Hz.

Moreover, In order to obtain accurate vibration data, background vibration is collected before a train passed by. As the train passes, the velocity of train is calculated by laser velocity measuring instrument. And the measuring velocity range is 5–500 km/h.

Characteristic of Three Directional Ground Vibrations

The three directional vibrations during the passages of HST have been recorded at the speed of 300 km/h. This passing HST is composed of 16 cars. Except for the passing duration time, the main characteristics of CRH380A/B and CRH380AL/BL are similar, so time domain and frequency domain characteristics of CRH380A/B (composed of 8 cars) will not be listed in the paper.

Time Domain Characteristic of Three Directional Acceleration

For simplicity, only four out of ten measuring points' time history of vertical, transversal and longitudinal ground vibration accelerations from 16.5 m (from the track centerline) to 32.5 m are shown in Fig. 5. As expected, a succession of periodic vibration peak values, induced by wheel-rail interaction, indicate the specific geometry features of the passing train, especially in the field near the track (Fig. 5a–c). And due to the superposition effects of the adjacent bogies, the three directional peak values, from the second to the penultimate, are commonly a little larger than the first and last ones. It is different from the previous references that a significant drop of the three directional vibration in the third measuring point, whose peak value is originally expected to be larger than the following 7 measuring points, is not found (Fig. 5c). As shown in Fig. 5, the vertical vibration peak values are typically largest and the longitudinal vibration peak values are obvious the least within the range of about 28 m, while the transversal vibration peak values are a little weaker than the vertical (Fig. 5a–c). However, the transversal vibration peak values come to the largest outside the range of about 30 m, meanwhile the vertical vibration peak values and longitudinal vibration peak values gradually tend to be at the same grade (Fig. 5d). Moreover, as the compression wave propagates faster
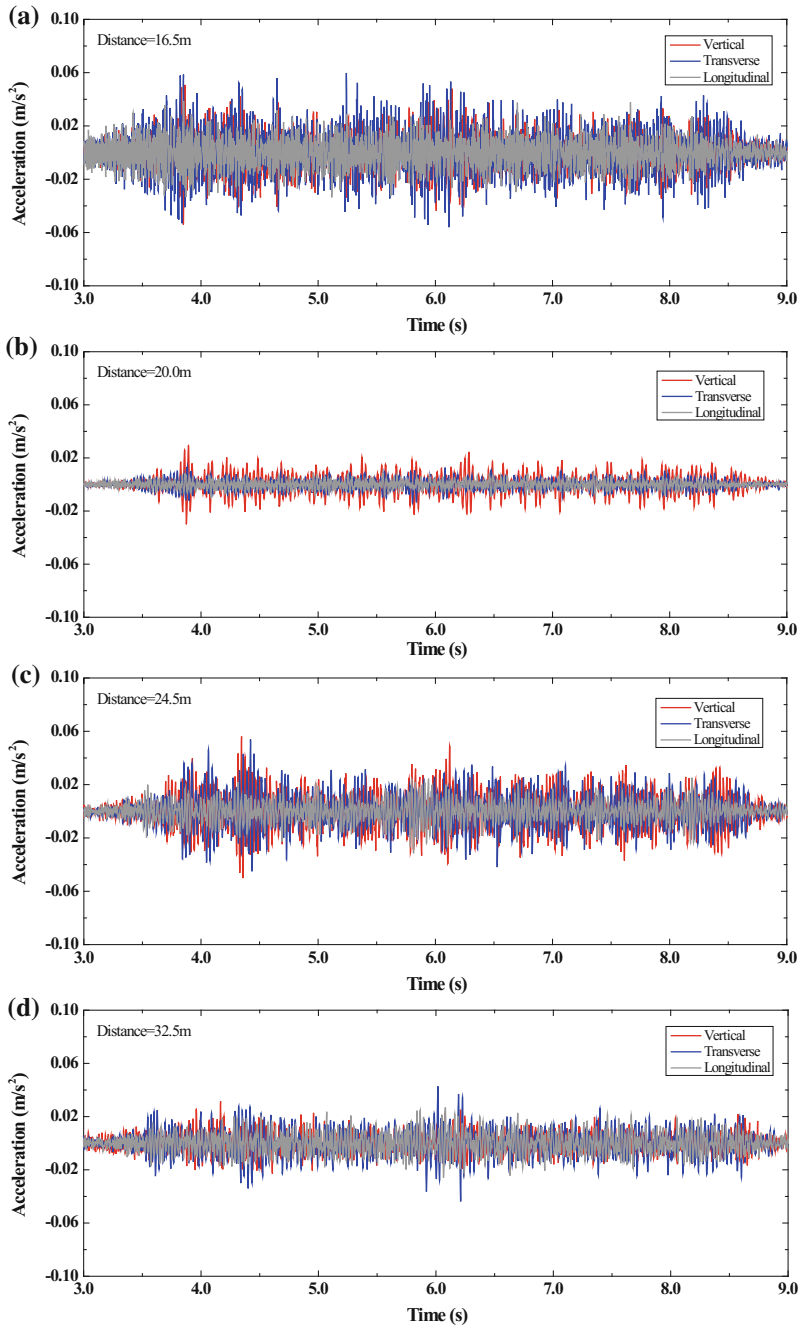
Fig. 5 Time histories of three directional ground vibration accelerations of the measuring points at: **a** 16.5 m, **b** 20.5 m, **c** 24.5 m, **d** 32.5 m

than the shear wave, the first of transversal vibration peak value, which is perpendicular to the high-speed railway line, is generally a little ahead of the first peak values of other two directions.

Frequency Domain Characteristic of Three Directional Acceleration

By the Fourier Transformation, the acceleration amplitude spectra are shown in Fig. 6 corresponding to the time history of ground vibration adopted in previous section (4 measuring points). All the dominant frequencies of the measuring points are then indicated in Fig. 6a, varying from about 3.6 to 135.1 Hz. Except for the peak values of acceleration components, the vertical vibration, transversal vibration and longitudinal vibration have almost the same frequency range at every measuring point. And their remarkable frequency components of ground vibration accelerations are between 20 and 50 Hz. In general, the first dominant frequency is around 33.9 Hz (Fig. 6), close to train characteristic frequency f_{t1} (induced by the distance between adjacent carriages) and 3 times f_{t2} (induced by the wheelbase).
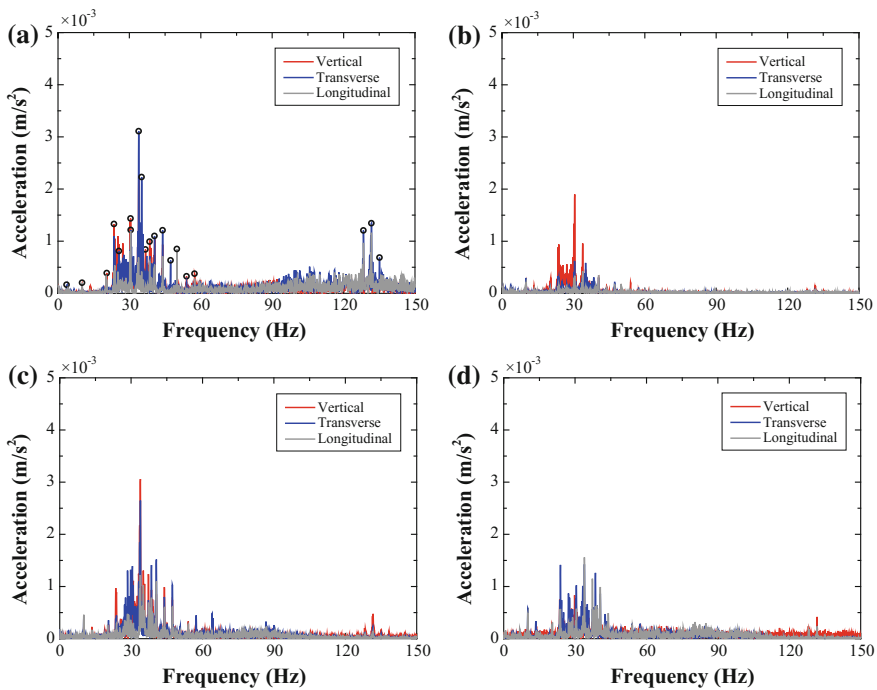
Fig. 6 Frequency spectra of three directional ground vibration accelerations of the measuring points at: **a** 16.5 m, **b** 20.5 m, **c** 24.5 m, **d** 32.5 m

However, when it comes to the first three dominant frequencies, there are a few differences among the three directional vibrations of the measuring points.

Discussions

In this section, results are further analyzed to discuss the application of experimental study in ground vibration evaluation. All the dominant frequencies of the measuring points are indicated in Fig. 6a, varying from about 3.6 to 135.1 Hz. Moreover, a summary of the multiple relationships, between the dominant remaining frequencies and TCFs are indicated in Table 4. Then, it can be indicated that all the dominant frequencies are n times (shown in bold) the train's characteristic frequencies or n times (shown in italics) at least two of the characteristic frequencies, simultaneously. Such as the dominant frequency 36.8 Hz is 1.1 times f_{t1} and is equal to f_{t3} multiply f_{t4} at the same time. It can also be indicated that f_{t1} and f_{t3}, whose columns have more formatted numbers and concentrating to 20–50 Hz, play an important role in the ground vibration. Besides, it is worth mentioning that the noticeable dominant frequencies around 130 Hz, caused by the distance between railpads (0.65 m) at the speed of 300 km/h, are seldom pointed out in the previous literature.

Table 4 The remaining vibration acceleration dominant frequencies of the 4 points

Dominant freqs of the 4 points		Train characteristic freqs f_{ti} (Hz)				
NO.	f_i (Hz)	33.3	4.8	11.1	3.3	128.2
1	3.6	0.1	0.8	0.3	**1.1**	0.0
2	20.5	0.6	4.3	**1.8**	**6.2**	0.2
3	30.5	**0.9**	6.4	2.7	**9.2**	0.2
4	33.9	**1.0**	**7.1**	**3.1**	**10.2**	0.3
5	35.2	**1.1**	7.4	**3.2**	10.6	0.3
6	36.8	**1.1**	7.7	*3.3*	**11.0**	0.3
7	38.5	**1.2**	**8.1**	*3.5*	11.6	0.3
8	40.5	**1.2**	8.5	3.6	**12.2**	0.3
9	43.9	1.3	**9.2**	**4.0**	**13.2**	0.3
10	47.3	1.4	**9.9**	4.3	**14.2**	0.4
11	54.0	1.6	*11.3*	*4.9*	**16.2**	0.4
12	57.4	1.7	**12.1**	5.2	**17.2**	0.4
13	128.4	**3.9**	**27.0**	11.6	38.5	**1.0**
14	131.7	**4.0**	27.7	**11.9**	39.5	**1.0**
15	135.1	**4.1**	28.4	**12.2**	40.5	**1.1**

Conclusions

Field experiment was carried out to investigate the high-speed train induced vibrations of surrounding ground on the Beijing-Shanghai railway. The experiment results would contribute to the study of environment vibration induced by the operating of new built high-speed railway with non-ballast track and CFG pile-supporting embankment. Conclusions are as follows:

(a) The vertical vibration is the largest and the longitudinal is the least in the near field, while the transversal is a little weaker than the vertical.
(b) All the dominant frequencies are n times the train characteristic frequency or n times two of the train characteristic frequencies, simultaneously. The three directional vibrations have almost the same frequency range at the same measuring point.
(c) The first dominant frequency is generally determined by the distance between wheelsets or distance between the bogies at the very train speed.
(d) Amplifying zones of ground vibration accelerations can be found at the distance of 24 m from the track centerline.

References

1. Hall, Lars. (2003). Simulations and analyses of train-induced ground vibrations in finite element models. Soil Dynamics and Earthquake Engineering 23(5): 403–413.
2. Yang, Y. B., H. H. Hung, and D. W. Chang. (2003). Train-induced wave propagation in layered soils using finite/infinite element simulation. Soil Dynamics and Earthquake Engineering 23(4): 263–278.
3. Kouroussis, Georges, et al. (2011). Discrete modelling of vertical track–soil coupling for vehicle–track dynamics. Soil Dynamics and Earthquake Engineering 31(12): 1711–1723.
4. Kouroussis, Georges, and Olivier Verlinden. (2013). Prediction of railway induced ground vibration through multibody and finite element modelling. Mechanical Sciences 4(1): 167–183.
5. Connolly, D., A. Giannopoulos, and M. C. Forde. (2013). Numerical modelling of ground borne vibrations from high speed rail lines on embankments. Soil Dynamics and Earthquake Engineering 46: 13–19.
6. Connolly, D. P., et al. (2014). Field testing and analysis of high speed rail vibrations. Soil Dynamics and Earthquake Engineering 67: 102–118.
7. Wanming Zhai, et al. (2015). Experimental investigation into ground vibrations induced by very high speed trains on a non-ballasted track. Soil Dynamics and Earthquake Engineering 72: 24–36.

Laboratory Measurements of the Dynamic Properties of Shanghai Clay

Xiaoqiang Gu, Lutong Lu, Jun Yang and Xiaofeng Wu

Introduction

The dynamic properties of soil, including shear modulus G and damping ratio D, play important roles in the earthquake ground response analysis and other problems involving dynamic loads. Generally, the dynamic properties of soil are nonlinear in nature and depend on the shear strain amplitude, indicated by the decrease of shear modulus and increase of damping ratio with increasing shear strain. When the shear strain level is less than 0.001%, however, the response of soils is usually assumed to be elastic and the corresponding shear modulus is referred to as the small strain shear modulus G_0 or the maximum shear modulus G_{max}. The small strain shear modulus G_0 (or the shear wave velocity) is also an important parameter in many geotechnical professions, such as soil liquefaction evaluation [1] and deformation calculation in excavation [2].

Shanghai is located at the east coastal area of China and clay is widely distributed in this area. The soil properties of Shanghai clay subjected to static load have been extensively studied in the past [3–5]. Regarding the dynamic properties

X. Gu (✉) · L. Lu · X. Wu
Key Laboratory of Geotechnical and Engineering of the Ministry
of Education, Department of Geotechnical Engineering,
Tongji University, Shanghai 200092, China
e-mail: guxiaoqiang@tongji.edu.cn

L. Lu
e-mail: cixillt@qq.com

X. Wu
e-mail: xiaofengwu@tongji.edu.cn

J. Yang
Department of Civil Engineering, The University
of Hong Kong, Pokfulam, Hong Kong, China
e-mail: junyang@hku.hk

of Shanghai clay, Fei and Wu [6] reported the dynamic properties of the soils at the site of Huangpu River bridge. Li et al. [7] measured the small strain shear modulus of Shanghai clay by bender elements. Nevertheless, it was found that only very limited test data on dynamic properties of Shanghai clay can be found in literature and it has not been investigated systematically in the past, although tremendous engineering projects involving dynamic loads (i.e. Metro lines and tall buildings) have been carried out in Shanghai. Therefore, in this study the dynamic properties of 38 undisturbed clay samples obtained from 9 site investigations in Shanghai were determined by resonant column tests. The main influencing factors of the dynamic properties of the Shanghai clay were determined and empirical equations were established to better predict the dynamic properties of Shanghai clay in practice.

Samples and Test Equipment

38 undisturbed clay samples were collected from 9 sites during site investigations in Shanghai. When the clay was retrieved from the sampler, its basic physical properties, such as density, water content, liquid limit and plastic limit, were determined first. The details of the sample information and soil properties are listed in Table 1. As seen in Table 1, the clay can be further classified as silty clay, clay or mucky clay according to the soil classification system in the Chinese standard GB 50021-2001 [8]. A silty clay means a clay who's plastic index ranges between 10 and 17. If the organic content of a clay is between 5 and 10% and its void ratio is larger than 1.0, the clay can be classified as mucky clay. As seen in Table 1, the plastic index of the tested clay samples are between 10 and 20, while the void ratio of the samples ranges from 0.647 to 1.323. The sampling depth ranges from around 1.2 to 98 m. All the samples are nearly or fully saturated.

The dynamic properties of the clay were measured by resonant column tests. The resonant column is a Stokoe type with top free and bottom fixed configuration. It can accommodate a soil sample 38 mm wide and 76 mm high and the confining pressure is applied by compressed air. During a resonant column test, first a clay sample was trimmed from undisturbed sample and its dimensions were accurately measured. Then the clay sample was consolidated to an isotropic stress which is close to the in situ effective vertical stress. Then an excitation with a certain frequency was applied to the sample by the driving head of the resonant column apparatus and its response was monitored by an accelerometer on the driving arm. By changing the input frequency, the resonant frequency at which the response is maximum can be found and the dynamic shear modulus can be calculated based on dynamic wave propagation theory. Meanwhile, by varying the excitation amplitude (i.e. input voltage), the dynamic shear modulus (i.e. resonant frequency) can be determined at different shear strain levels. Finally, a free vibration at resonant frequency was carried out and the damping ratio can be determined based on the decayed vibration amplitude.

Table 1 Details of tested samples

Bore hole no (site no)	Depth (m)	Soil type	Unit weight (g/cm³)	Water content (%)	Degree of saturation (%)	Void ratio	Liquid limit (%)	Plastic limit (%)	Plasticity index
K1 ~ 21 (1)	33.0–33.2	Silty clay	19.11	27.2	95.6	0.774	32.4	20.1	12.3
K1 ~ 24 (1)	50.8–51.0	Silty clay	19.01	26.3	92.8	0.771	31.9	20.0	11.9
K2 ~ 17 (1)	27.0–27.2	Clay	17.54	43.0	99.1	1.189	41.1	22.4	18.7
K06 ~ 9 (2)	20.8–21.0	Clay	17.44	44.8	99.9	1.229	41.4	22.5	18.9
K06 ~ 11 (2)	26.8–27.0	Clay	17.35	45.9	99.9	1.259	40.8	22.4	18.4
K06 ~ 17 (2)	47.8–48.0	Silty clay	18.42	34.2	98.4	0.949	37.8	21.9	15.9
K09 ~ 10 (2)	18.8–19.0	Clay	17.44	42.3	97.4	1.190	39.9	22.2	17.7
K09 ~ 13 (2)	27.8–28.0	Clay	17.35	43.6	99.7	1.223	40.4	22.3	18.1
K09 ~ 18 (2)	42.8–43.0	Silty clay	18.72	30.6	96.4	0.867	36.2	21.5	14.7
B1 ~ 1 (3)	1.10–1.30	Silty clay	19.89	23.1	96.3	0.655	37.0	21.4	15.6
B1 ~ 3 (3)	26.7–26.9	Silty clay	19.11	27.7	96.0	0.788	37.6	21.5	16.1
B2 ~ 2 (3)	18.6–18.8	Clay	18.03	36.4	96.7	1.031	39.9	22.0	17.9
B2 ~ 7 (3)	97.8–98.0	Silty clay	19.99	22.6	96.3	0.641	37.7	21.1	16.6
K23 ~ 4 (4)	8.8–9.0	Mucky silty clay	17.93	38.0	98.0	1.059	37.9	21.7	16.2
K23 ~ 5 (4)	14.8–15.0	Mucky clay	17.05	47.5	98.4	1.323	42.3	22.6	19.7
K23 ~ 10 (4)	29.8–30.0	Silty clay	19.60	24.1	94.8	0.694	37.2	21.2	16.0
K23 ~ 29 (4)	90.8–91.0	Silty clay	19.89	22.5	94.9	0.647	36.9	21.1	15.8
K2 ~ 1 (5)	5.7–5.9	Mucky silty clay	18.13	37.8	99.9	1.033	37.0	21.4	15.6
K2 ~ 5 (5)	30.0–30.2	Clay	17.25	47.0	99.9	1.289	43.0	22.3	19.7
K2 ~ 7 (5)	44.7–44.9	Silty clay	19.60	24.5	95.7	0.699	36.1	21.0	15.1
K2 ~ 9 (5)	74.7–74.9	Silty clay	19.40	26.4	97.6	0.736	33.2	20.4	12.8
K8 ~ 3 (6)	2.7–2.9	Mucky silty clay	17.84	40.8	100.0	1.104	33.8	20.9	12.9
K8 ~ 9 (6)	11.2–11.4	Mucky silty clay	17.74	41.3	99.7	1.131	38.0	21.8	16.2

(continued)

Table 1 (continued)

Bore hole no (site no)	Depth (m)	Soil type	Unit weight (g/cm³)	Water content (%)	Degree of saturation (%)	Void ratio	Liquid limit (%)	Plastic limit (%)	Plasticity index
K8 ~ 15 (6)	32.3–32.5	Silty clay	18.13	34.2	95.3	0.980	37.0	21.6	15.4
K8 ~ 25 (6)	61.8–62.0	Silty clay	19.11	28.6	97.6	0.800	36.1	21.2	14.9
S45 ~ 1 (7)	1.3–1.5	Silty clay	19.11	26.4	93.6	0.770	37.2	21.3	15.9
S45 ~ 3 (7)	3.8–4.0	Mucky silty clay	17.05	47.8	98.9	1.319	38.2	21.9	16.3
S45 ~ 6 (7)	19.8–20.0	Clay	17.35	45.0	99.0	1.245	41.2	22.0	19.2
S45 ~ 10 (7)	40.8–41.0	Clay	17.44	42.4	97.5	1.192	39.6	21.7	17.9
S45 ~ 11 (7)	53.8–54.0	Silty clay	18.33	31.7	93.8	0.923	36.2	21.3	14.9
S45 ~ 12 (7)	59.8–60.0	Silty clay	18.23	35.3	97.7	0.986	37.1	21.4	15.7
S45 ~ 15 (7)	74.8–75.0	Silty clay	19.21	25.6	93.3	0.749	37.0	21.2	15.8
K03 ~ 1 (8)	3.6–3.8	Mucky silty clay	18.13	38.4	100.0	1.042	38.3	22.4	15.9
K03 ~ 7 (8)	13.6–13.8	Silty clay	18.32	36.3	100.0	0.983	35.5	22.3	13.2
K03 ~ 14 (8)	25.6–25.8	Silty clay	18.42	36.1	100.0	0.976	38.7	22.2	16.5
B2 ~ 4 (9)	21.2–21.4	Silty clay	18.52	33.8	99.3	0.926	33.7	20.4	13.3
B2 ~ 5 (9)	27.4–27.6	Silty clay	19.60	24.4	95.4	0.698	37.8	21.4	16.4
B2 ~ 8 (9)	57.4–57.6	Silty clay	19.31	25.8	94.8	0.743	37.0	21.1	15.9

Results and Discussions

It is well recognized that the small strain stiffness of soil mainly depends on its void ratio e (or density) and the mean effective confining pressure σ'. To quantify their effects, the small strain shear modulus G_0 (in MPa) of the tested clay was fitted by the following equation [9]

$$G_0 = AF(e)\left(\frac{\sigma'}{p_a}\right)^n \tag{1}$$

where A is a constant reflecting soil type, grain properties and fabric, p_a is a reference stress (100 kPa in this study), n is the stress exponent reflecting the effect of confining pressure, and $F(e)$ is a void ratio function reflecting the effect of soil density.

As suggested by Lo Presti et al. [10], a void ratio function $F(e) = e^{-x}$ is used to fit the data and the results were shown in Fig. 1, together with two boundaries of $\pm15\%$ variation. As seen in Fig. 1a, the small strain shear modulus decreases as the void ratio of the soil increases (i.e. soil density decreases) as expected. The exponent x is 1.01, which is generally close to those in Lo Presti et al. [10]. Meanwhile, the void ratio normalized shear modulus increases as the effective confining pressure increases and the stress exponent n is 0.615 which is slightly higher than the commonly used value of 0.5. Furthermore, the difference of the small strain shear modulus between the measurement and the prediction is generally less that 15%. It clearly indicates the stress-dependent and void ratio-dependent characteristics of small strain shear stiffness of Shanghai clay and the following empirical equation may be reasonably used to predict the small stain shear stiffness of Shanghai clay in practice.

$$G_0 = 41.1e^{-1.01}\left(\frac{\sigma'}{p_a}\right)^{0.615} \tag{2}$$

In soil dynamics, the nonlinear and hysteresis behaviors of the soil are described by the shear modulus reduction curve and damping curve. The modulus reduction curve plots the normalized shear modulus G/G_0 against the shear strain amplitude γ, while the damping curve plots the damping ratio D with the shear strain amplitude, as shown in Fig. 2. It is clear that G/G_0 gradually decreases with increasing shear strain amplitude and such reduction is independent of the soil effective stress and void ratio. Vecetic and Dobry [11] showed the modulus reduction of clay mainly depends on the plastic index of the clay. Hence, the test result is consistent with their results, since the plastic index of the Shanghai clay ranges in a narrow band of 10–20. Note that the effective stress will have an apparent effect on the modulus reduction curve of sand. Regarding damping ratio, it increases smoothly first with increasing shear strain and then sharply. It also indicates that the damping ratio curve of Shanghai clay is independent of the soil effective stress and void ratio.
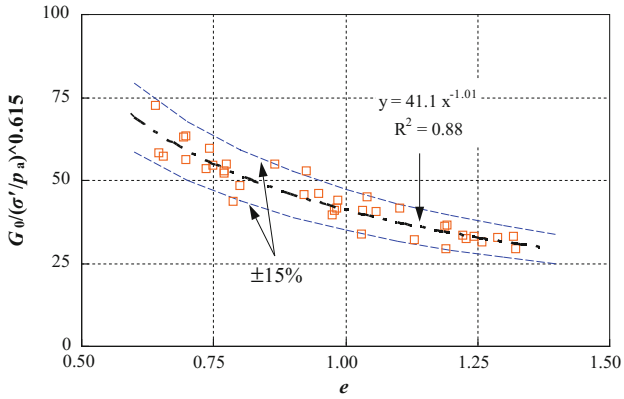
(a) relationship between stress normalized modulus and void ratio
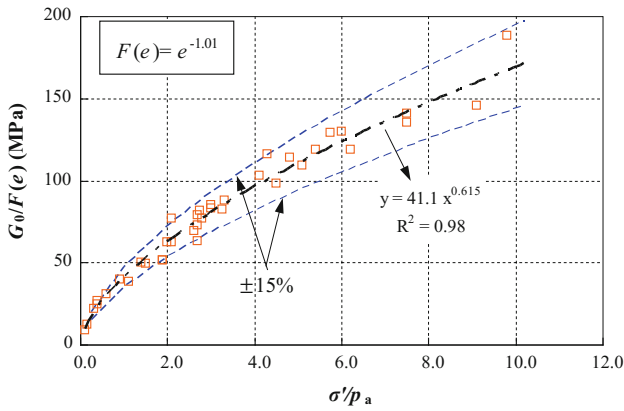
(b) relationship between void ratio normalized modulus and normalized stress

Fig. 1 The small strain shear stiffness of Shanghai clay

For better prediction in practice, the modulus reduction curve and damping curve are fitted by a hyperbolic curve and a quadratic polynomial, respectively. The fitted equations for the modulus reduction curve and damping curves are

$$G/G_0 = 1/(1 + \gamma/\gamma_r)$$
$$\gamma_r = 0.715 \times 10^{-4}$$

(3)

$$D = -7.06 \times 10^6 \gamma^2 + 1.58 \times 10^6 \gamma + 1.02$$

(4)

(a) modulus reduction curve

$$G/G_0 = 1/(1+\gamma/\gamma_r)$$
$$\gamma_r = 0.715 \times 10^{-4}$$

(b) damping curve

$$D = -7.06 \times 10^6 \gamma^2 + 1.58 \times 10^6 \gamma + 1.02$$
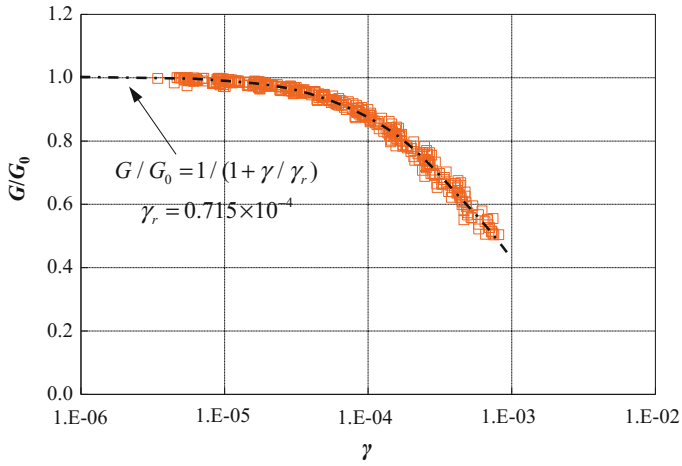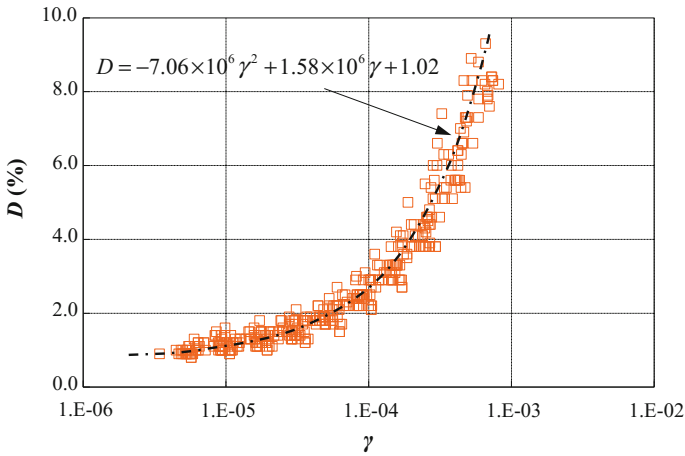
Fig. 2 The modulus reduction curve and damping curve of Shanghai clay

As shown in Fig. 2, the measured shear modulus reduction curve and damping curve successfully predicted by Eqs. (3) and (4), respectively. The shear modulus starts to decrease when the shear strain is larger than 10^{-5} and it decreases to 50% of the small strain shear modulus at a referenced shear strain $\gamma_r = 0.715 \times 10^{-4}$. Meanwhile, the damping ratio D is about 1.0% at very small shear strain levels and it increases to 8% at a shear strain level around 6.0×10^{-4}.

Conclusions

The dynamic properties of undisturbed samples of Shanghai clay have been investigated by laboratory resonant column tests. The results showed that the dynamic small strain shear modulus G_0 of the soil significantly depends on the void ratio and the effective confining pressure. Meanwhile, the shear modulus ratio G/G_0 decreases and the damping ratio increases continuously as the shear strain increases. Meanwhile, the modulus reduction and the damping ratio are generally independent of the void ratio and the effective stress. Empirical equations were provided to predict the small strain shear modulus, the modulus reduction curve and damping ratio of Shanghai clay in practical engineering.

References

1. Andrus, R.D., Stokoe, K.H.II. (2000). Liquefaction resistance of soils from shear-wave velocity. Journal of Geotechnical and Geoenvironmental Engineering, ASCE, 126: 1015–1025.
2. Clayton, C.R.I. (2011). Stiffness at small strain: research and practice. Géotechnique, 61(1): 5–37.
3. Chen, Y.F., Cao, M.B. (1990). The deformation characteristics of soft clay under unloading and reloading in Shanghai. Chinese Journal of Geotechincal Engineering, 1990, 12(2):9–18 (In Chinese).
4. Chen L.-J., Wu, G., Wang, J.H., Hao, J. (2004). Disturbed state concept model for studying on mechanical characteristics of saturated cohesive Soil. Journal of Shanghai Jiaotong University, 38(6):952–955 (In Chinese).
5. Su, W.W., Huang, H.W., Zhang, J. (2012). Risk analysis of the underground passage through rail transit construction scheme. Chinese Journal of Underground Space and Engineering, 8 (A02):1695–1699.
6. Fei, H.C., Wu, Y.W. (1990). Study on dynamic property of Huangpu river bridge site. Proceeding of the Third National Conference on Soil Dynamics of China. Tongji University Press, Shanghai, 303–308.
7. Li, Q., Ng, C.W.W., Liu, G.B. (2012). Determination of small-strain stiffness of Shanghai clay on prismatic soil specimen. Canadian Geotechnical Journal, 49(8): 986–993.
8. Chinese standard GB 50021-2001. Code for investigation of geotechnical engineering (Version 2009).
9. Hardin, B.O. and Richart, F.E. (1963). Elastic wave velocities in granular soils. Journal of Soil mechanics and Foundation Engineering Division, ASCE, 89(SM1): 39–56.
10. Lo Presti, D.C.F., Jamiolkowski, M., Pallara, O., Cavallaro, A., Pedroni, S. (1997). Shear modulus and damping of soils. Géotechnique, 47 (3):603–617.
11. Vucetic, M., Dobry, R. (1991). Effect of Soil Plasticity on Cyclic Response. Journal of Geotechnical Engineering, ASCE, 117(1):89–107.

Research on Seismic Response Calculation Method for Rocking Column

Xin Zhou, Jun Hu and Guobo Wang

Forward

Based on bearing capacity of the current structure seismic design concept is by strengthening structures, make its bearing more than its earthquake fortification intensity, such as the Chinese seismic code specified in: "no collapse under strong earthquake". Under the guidance of the concept, structure seismic design is based on two aspects of the hypothesis: (1) The foundation soil is rigid, namely deformation will not occur; (2) Structure on the bottom of the foundation and foundation soil are fixed together, namely the separation will not occur. In fact, under seismic action, flexibility ability and deformation ability of soil can't be ignored. Once the earthquake effect is larger, relative displacement between the foundation and foundation soil will occur, severe ground motion would progressively swing to the upper structure from the foundation, and even overturn fall. 2500 years' history of the ancient Greek temple's pillars, under horizontal load is easy to collapse, but it can be preserve under strong earthquake region in Greece. Researches have shown that the column at the bottom of the basis of the sliding and uplift are the key factors to survive [1–3]. As long as the earthquake overturning moment is big enough, the uplift of the foundation achieves to a certain degree, the structure is likely to totally collapse.

As a result of the existence of the above speaking, during the 1970s and 1980s, a large number of scholars did theoretical analysis to lift-off phenomenon. Among them, Housner's [4] research work has been recognized as the first explicitly

X. Zhou · J. Hu · G. Wang (✉)
Hubei Key Laboratory of Roadway Bridge and Structure Engineer,
Wuhan University of Technology, 430070 Wuhan, China
e-mail: wgb16790604@126.com

X. Zhou
e-mail: 2580742769@qq.com

J. Hu
e-mail: 2272237606@qq.com

combination of the uplift of the foundation and the earthquake response of the structure. Two main analysis method is put forward in the subsequent researches, one is the "Winkler Foundation Model [5]": the subsoil is simulated as continuous distribution of the spring unit; Another is the contact element method or joint element method [6] based on contact algorithm. But the experimental study is relatively scarce.

Based on rocking structures, this article is going to take an object of this structure, establishing the finite element model, swing by contact element structure, considering the flexibility, the ratio of depth to width and the stiffness of the pillars. Finally, on the basis of the calculation results of to prepare a shaking table test.

Computation Model

Rocking Column Model

Generally speaking, basis of buried depth is advantageous to the aseismic structure, therefore, in this paper, we consider a relatively unfavorable shallow foundation. so, the simplified calculation model of this paper is a single column which is placed on the soil surface, as shown in Fig. 1. In order to correspond to test, the size of soil is 2.5 m × 2.5 m × 0.9 m. The thickness of the square foundation is 10 mm, the width is 5 mm, located in the centre of the soil. The hollow rectangular cross section column is above the foundation. The size of outer section is 0.1 mm × 0.1 mm, the thickness of column wall is 6 mm, the height is 1.0 m, as shown in Fig. 2. To simulate the floor weight, 20 kg weight is put on the top.

Fig. 1 Schematic model

900 mm

2500 mm
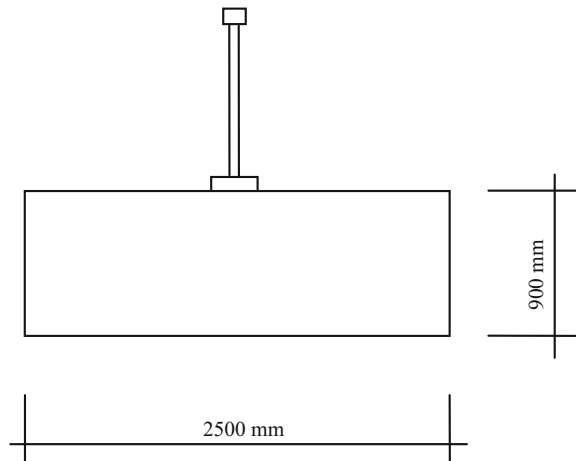
Fig. 2 Schematic diagram of column section

| 6 mm | 88 mm | 6 mm |
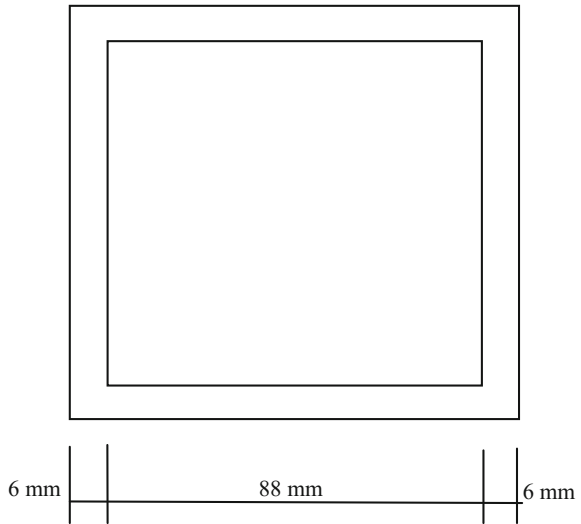
Solid elements are adopted to simulate the soil in the model, shell element to simulate the pole, the quality unit simulation to simulate the concentrated mass of the top of the pillars. The smallest size for grid is 0.5 m.

The density, Young's modulus and Poisson's ratio of steel material are 7850 kg/m^3, 206 GPa and 0.3.

In order to correspond to test, the shear velocity, density and Poisson's ratio are 88 m/s, 1190 kg/m^3 and 0.45. The computation model is shown in Fig. 3.

Fig. 3 Computation model
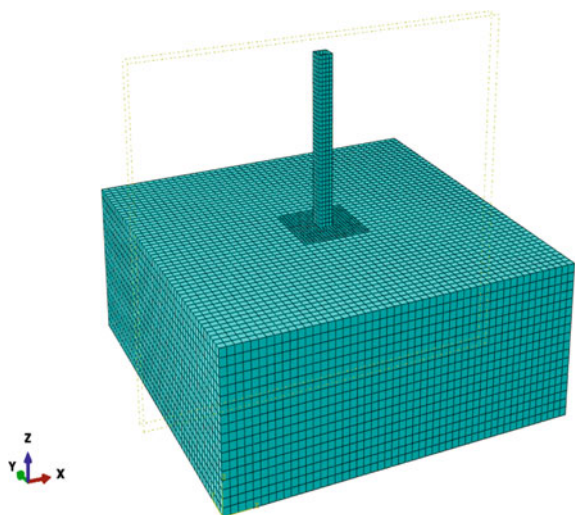
Contact Element

This thesis models and analyzes by using nonlinear finite element analysis software ABAQUS. The surface to surface contact is selected. First, define the surface and the surface of the subordinate, the active surface has bigger stiffness, the slave surface has smaller stiffness; Second, define the contact properties, in this model, contact properties are divided into tangential properties and normal properties. Tangential property is used to define the coefficient of friction, limited the slip between two contact surfaces, this paper does not consider sliding, the friction coefficient should be as large as possible, and take to 10; Normal property is used to set the contact pressure and the relationship of through, this paper is set to hard contact, pressure between two contact surfaces is only allowed, but strain isn't. In the end, define the contact. The active surface and slave surface are linked by "the contact". As shown in Fig. 4, the pink surface is active surface, the red surface is slave surface.

Boundary Conditions

This article only considering the horizontal and unidirectional seismic wave, the mainly deformation of the soil is shear deformation, therefore, constraints of soil around the side is the vertical direction normal direction. For the bottom border, in order to input horizontal cross acceleration in the bottom, vertical direction and horizontal direction are constrained. Normal direction is set free temporarily, it's constrained when the horizontal cross acceleration is added.

Fig. 4 Contact diagram
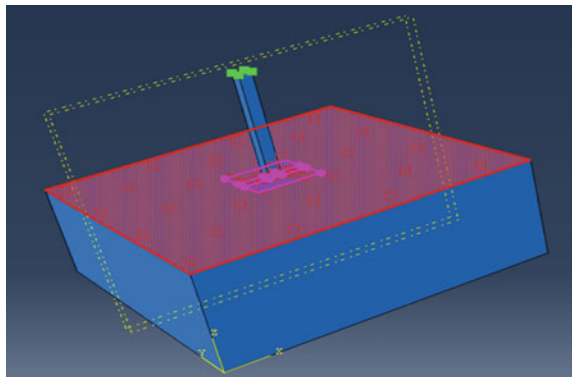
Time Steps and Damping

In order to consider the effects of high frequency as much as possible, time step is 0.001 s in this paper.

In dynamic calculation, the damping must be considered in the material properties. The magnitude of the damping will influence the process of vibration. And the peak stress in the model will be higher. According to the basic theory of structural dynamics, this paper uses the Rayleigh damping.

$$[C] = \alpha[M] + \beta[K] \tag{1}$$

$$\alpha = \frac{2\omega_1\omega_2\xi}{\omega_1 + \omega_2} \tag{2}$$

$$\beta = \frac{2\xi}{\omega_1 + \omega_2} \tag{3}$$

C, M, K refer to damping matrix, mass matrix and stiffness matrix respectively. ξ, $\omega 1$, $\omega 2$ refer to damping ratio and two characteristic frequency respectively. The damping ratio of soil and steel are 0.05 and 0.02. Two characteristic frequency also take the system's first and second order frequency.

The Judgment of Uplift

The compressive stress of the contact surface is used to judge the uplift of the foundation. If the compressive stress is 0, contact separation, the foundation is uplifted.

Seismic Wave

To compare with the experiment, the input seismic waves are SIN wave (Fig. 5) and Wuhan artificial wave (Fig. 6), adjust their amplitude to 0.2 g. In addition, the main frequency of seismic wave is 0–10 Hz, so in this paper, calculation and experimental study were take its frequency of 4 Hz. SIN wave calculation time is 3 s, and Wuhan artificial wave calculation time is 15 s.

Fig. 5 Input seismic wave
(SIN wave)
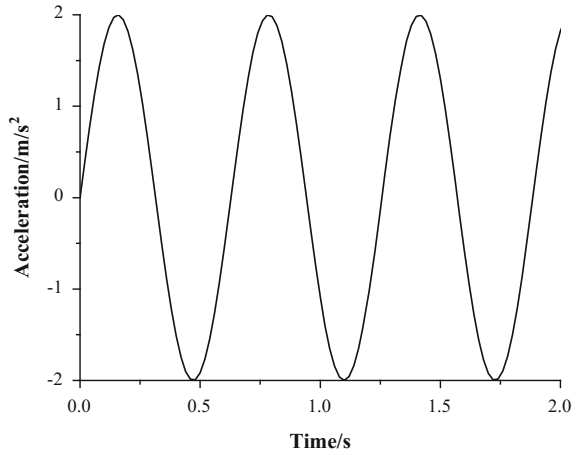
Fig. 6 Input seismic wave
(Wuhan artificial wave)
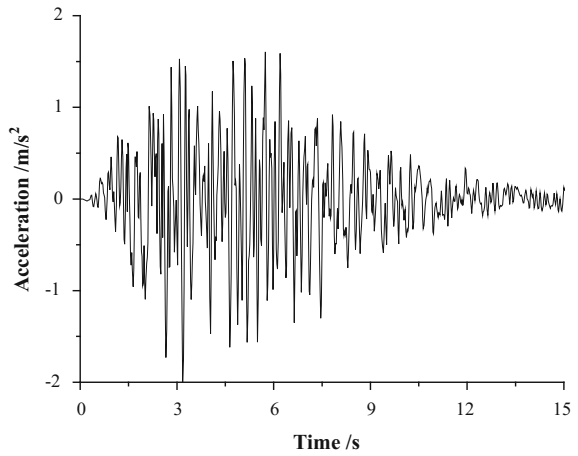
Result and Analysis

Model Analysis

The first order natural frequency of vibration of the structure is 14.383 Hz (Fig. 7).
Selecting the scanning curve of White noisy test, the transfer function is shown in
Fig. 8 after processed. The peak characterization of the transfer function is the
frequency that is possibly existed. In Fig. 8, the first order natural frequency of
vibration is 13.4 Hz, and the calculated results was coincident with the test result.

ODB: tiqupinlv20160518-1.odb   Abaqus/Standard 6.10-1   Wed May 18 1
Step: Step-2
Mode   2: Value =   8166.8   Freq =   14.383   (cycles/time)
Primary Var: U, Magnitude
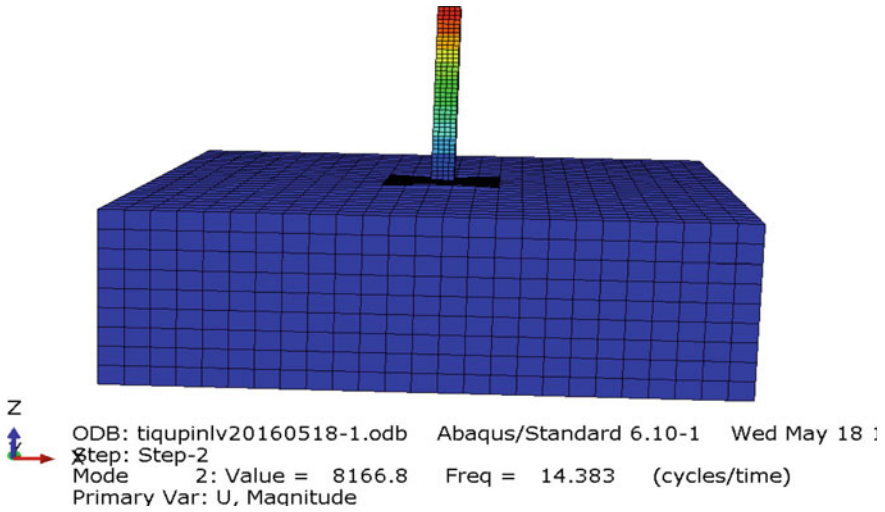
Fig. 7 Natural frequency of the system: calculation result

Fig. 8 Natural frequency of the system: test result
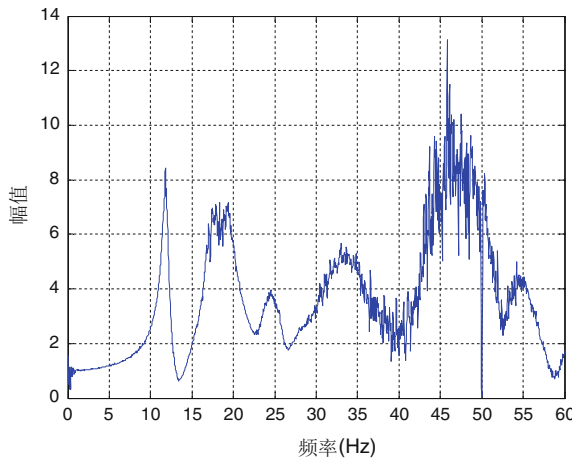
The Horizontal Acceleration of Capital

The horizontal acceleration time history curves under SIN wave and Wuhan artificial wave are shown in Figs. 9 and 10.

Fig. 9 Horizontal acceleration time history curve at column top: SIN wave
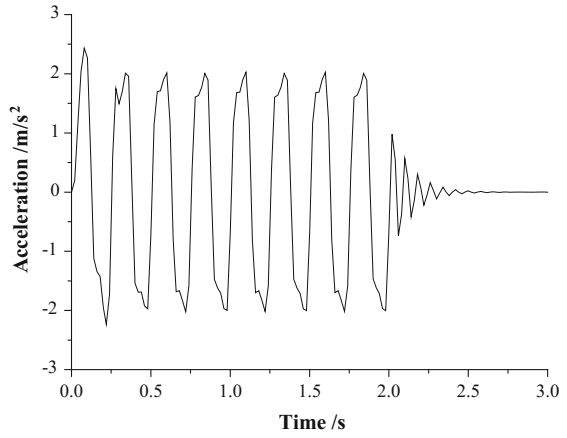
Fig. 10 Horizontal acceleration time history curve at column top: Wuhan artificial wave
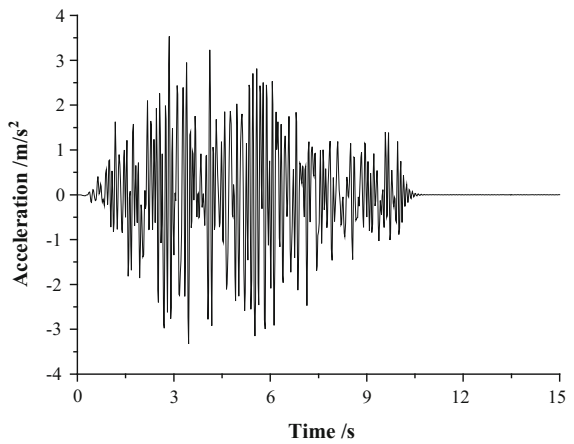
Experimental Research

Based on the above analysis, making the same cross section size of single column model, as shown in Fig. 11.

Fig. 11 Physical column in
the test

Experimental Results

Due to the limited monitoring conditions, some errors are existed in the monitoring
of displacement and earth pressure box, this paper only presents monitoring the
horizontal acceleration response of the top of a pillar (Figs. 12 and 13).

Comparison Between Calculation and Experiment

Because of the complexity of the soil-structure dynamic interaction problems, many
inevitably errors exist in the process of the comparison, but the following results
can be drawn on the whole:

1. The calculated and the measured values of system fundamental frequencies are
   in good agreement, which showed the model can reflect testing dynamic char-
   acteristics of the model;

Fig. 12 Tested horizontal acceleration time history curve: SIN wave
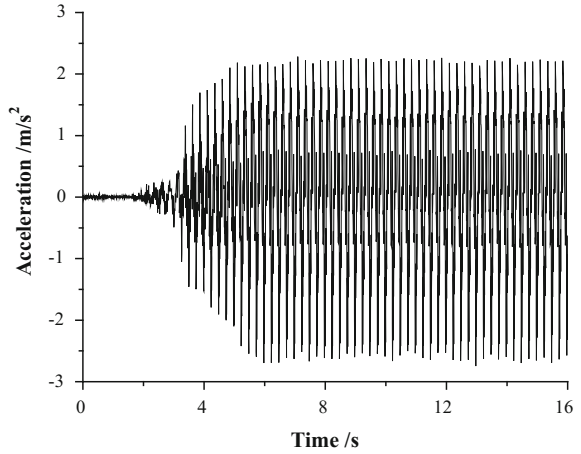
Fig. 13 Tested horizontal acceleration history curve: Wuhan artificial wave
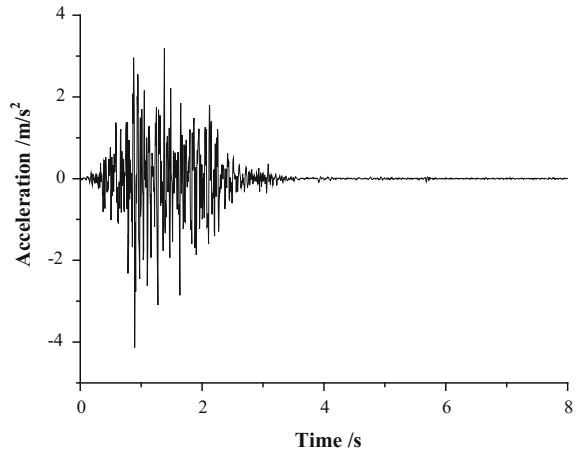
2. The seismic response rules of the calculation values and experimental values are basically coincide, Only the amplitudes have slight differences, which shows that the calculation method and computation model are reasonable.

Considering the complexity of soil-structure interaction and test factors, it can generally think that the calculation method and model are reasonable.

Conclusions

This paper is based on a simplified model, has carried on the detailed calculation of the multiple conditions. And it has analyzed the influence of the uplift of the foundation to swing column, compared the finite element calculation results and test results, the following conclusions can be got:

1. The fundamental frequency of calculated System and the measured values are in good agreement, which shows that this model is reasonable and can be used to the subsequent transient analysis.
2. Although the calculation value of seismic response and experimental value has a slight difference in the amplitude, but the changing rules is basically fit. Considering the complexity of soil-structure interaction and test factors, it can generally think that the calculation method and model are reasonable.

References

1. Makris N. and Vassiliou M. F. Planar rocking response and stability analysis of an array of free-standing columns capped with a freely supported rigid beam [J]. Earthquake Engineering & Structural Dynamics, 2013, 42(3): 431–449.
2. Matthew J. D. and Elias G. D. Dynamically equivalent rocking structures [J]. Earthquake Engineering & Structural Dynamics, 2014, 43(10): 1543–1563.
3. Paolucci R., Figini R. and Petrini L. Introducing dynamic nonlinear soil-foundation-structure interaction effects in displacement-based seismic design [J]. Earthquake Spectrum, 2013, 29(2): 475–496.
4. Housner G. W. The behavior of inverted pendulum structures during earthquake [J]. Bulletin of the Seismological Society of America, 1963, 53(2): 403–447.
5. Yim C. S. and Chopra A. K. Earthquake response of structures with partial uplift on Winkler foundation [J]. Earthquake Engineering and Structural Dynamic, 1984, 12(2): 263–281.
6. Yabushita N., Nakamura N., Suzuki T., et al. Analyses of reactor by 3D nonlinear FEM models considering basement uplift for simultaneous horizontal and vertical ground motions [C]. 19th International Conference on Structural Mechanics in Reactor Technology (SMiRT19), Toronto, 2007, 1–8.

Effect of the Treated Soft Soil Thickness on the Settlement Characteristic of Overlapping Embankment

Yun Dong and Huasheng Sun

Introduction

With the rapid development of economy and transportation, most of the originally built highway has been unable to meet the growing traffic demand. There is an urgent need for reconstruction and extension. In the highway reconstruction and expansion project, to maximize the use of the old, save the project investment, the expansion form along the old one is commonly adopted. However, in this expansion form, especially in soft soil area of the eastern part, the consolidation deformation of embankment and foundation has been completed due to subjected to a long term traffic load. Whereas, for the newly filled embankment, if there is not a good control of its settlement, differential settlement between the new and old embankment may occur, leading to the embankment cracking and pavement damage.

In order to reveal the deformation mechanism of this issue, relevant researches have been investigated by many scholars both at home and abroad. Gao et al. [1] reported that the deformation characteristics of the overlapping embankment is minimum settlement at the center of the old embankment and maximum settlement located at vertical position of the widened embankment section centroid. Fu et al. [2] proposed that there is an abrupt change at the connection between the new and old embankment for the differential settlement of widening highway. Shenyang-Dalian Highway Rebuilding Widening Engineering Embankment Widening Technology Research Group put forward a new control standard that the settlement after construction of the new widening embankment is not larger than

Y. Dong · H. Sun (✉)
Department of Civil Engineering,
Huaiyin Institute of Technology, Huaian 221300, China
e-mail: sunhuadasheng@126.com

Y. Dong
e-mail: dyunhyit@163.com

8 cm. Besides, a number of scholars have conducted research to the reconstruction and extension of highway on the soft soil foundation [3–7]. However, the research mainly focused on the calculation and the prevention of the differential settlement of the overlapping embankment.

However, the effect of the cost in the prevention and treatment of the above differential settlement was not considered. Especially in common highway expansion project, due to limited funds for construction, treatment measures cannot be taken on the soft soil foundation thoroughly, and it is difficult to have complete control over the post-construction settlement of the overlapping embankment. Therefore, in order to make use of the limited construction funds, to fully solve the problem of the deformation of the overlapping embankment in the highway reconstruction and extension project, the main factors that affect the differential settlement should be investigated firstly and the characteristics of the differential settlement of the overlapping embankment should be understood. Based on the above situation, this paper simulates and analyzes the deformation characteristics of the overlapping embankment on the basis of the practice engineering for different soft soil thickness, aiming at providing the basis and reference for the differential settlement control of the overlapping embankment.

Overview of the Support Project

The reconstruction and extension project was based on Da Shan Zi Separation Levee of Jiangsu Provincial Highway S332. Soft soil layer with 12 km was distributed along the route. In the south of Da Shan Zi Separation Levee is Gaoyou Lake, and in its north is Baoying Lake and Jinbao River which is parallel to Da Shan Zi Separation Levee. Thus, due to the limitation of geographical conditions, the most direct reconstruction and expansion programme of the embankment is to widen by filling directly along the original Da Shan Zi Separation Levee proposed at the beginning of the road cross section layout as shown in Fig. 1.

Since the Da Shan Zi Separation Levee has been filled for a long time, and subjected to the long-term traffic load, the consolidation deformation has been
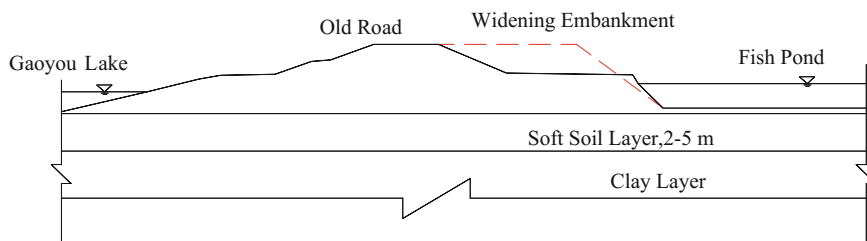
Fig. 1 Sketch of typical section of rely on project

basically completed. The widening embankment is characteristic of distinctive embankment splicing because the platform on the north side is lower about 5 m than Da Shan Zi Separation Levee.

Calculation Model

Dimension of the Model

The finite element model was established as shown in Fig. 2. Based on the results of field survey and route selection, simultaneously considering the influence of boundary effect on the calculation results, the dimension of the model is 125×27 m, where, the height of Da Shan Zi Separation Levee is 7 m, with 3 m thick muddy clay and 17 m clay below it (determined by one section of the field survey). In order to eliminate the effect of the horizontal boundary, the distances between both boundaries in the horizontal direction and the toe of the levee (embankment) are larger than 30 m. The same proportion is adopted in the vertical and horizontal direction of the model.

Considering the influence of the thickness of the soft soil layer on the deformation characteristics of the lap embankment, the calculation model was established for the case the thickness of the soft soil layer is 0–7 m, and the other conditions are exactly the same. The settlement calculation of the overlapping embankment is carried out by the different soft soil thickness, and the influence of the thickness of the soft soil layer on the differential settlement of the overlapped embankment is analyzed.

Calculation Parameters and Working Conditions

After random sampling in the Da Shan Zi Separation Levee, platforms, foundation and embankment fill material, laboratory tests were carried out to obtain the basic model parameters based on field investigation and geological drilling results as shown in Table 1.
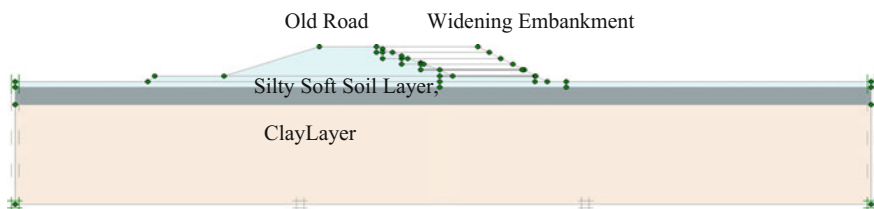
Fig. 2 Finite analysis model

Table 1 Parameters adopted for calculation

Parameters	γ_{unsat}	γ_{sat}	E	ν	C	φ	EA
Units	kN/m^3	kN/m^3	MPa		kPa	°	kN/m
Levee	17.3	18.4	6	0.33	12	19.0	–
Silty clay	17.1	17.9	0.5	0.3	7	10.0	–
Clay	17.7	18.1	8	0.35	15	17.0	–
Embankment	18.5	19.2	8	0.35	41	21.5	–
Geogrid	–	–	–	–	–	–	2E4

Based on the field condition of the support project, calculation and analysis are conducted mainly for the following construction conditions. That is, the soft soil ground was not treated and the steps were excavated and the geogrid was added at the bottom of the embankment according to the routine method. The working conditions are summarized as follows:

1. Calculation and analysis were carried out for the filling of the Da Shan Zi Separation Levee and its consolidation deformation by selecting the investigation section. Filling and deformation of Da Shan Zi Separation Levee during usage were simulated. Besides, comparison and analysis were conducted between the simulation and the measured in order to verify the rationality of the calculation parameter and the reliability of the calculation results.
2. Calculation of the widening embankment filling and consolidation deformation was conducted to analyze the settlement during construction, consolidation deformation, post-construction settlement and the differential settlement of the new and old embankment.
3. Calculation and analysis of instability failure and safety factor of the widening embankment based on strength reduction method [8–10].

The conditions described above were computed under different soft soil thickness in order to explore the effect of the thickness of soft soil on the deformation characteristics of the overlapping embankment, and to take economic and reasonable engineering treatment measures.

Related Description of the Model Calculation

The failure criterion of soil strength and the selection of calculation parameters are briefly described in this paper as follows:

1. Strength failure criterion

In this model, the constitutive model of soil is used as the elastic plastic model and the failure of the soil is subject to the Coulomb failure criterion. The mechanical behavior of the model material was chosen for two kinds of mechanical behavior under the condition of drainage and nondrainage.

2. About the selection of k_0 value

Before the filling of the Da Shan Zi Separation Levee, the ground surface and underground water level are horizontal. Thus, the program with earth pressure at rest can be run to ensure that the stress field within soil is consistent with the actual situation of the soil. About the selection of coefficient of earth pressure at rest, k_0 value, it cannot be determined based on a small number of test results due to the discrete nature of field tests and the limitations of laboratory tests, also taking into account the deficiencies existing in the current standard "Code for design of building foundation". Thus, during the calculation of the model, the k_0 value can be determined by Jaky Equation directly.

3. Influence of groundwater seepage

Taking into account the effect of groundwater seepage on the calculation results, the groundwater flow obeys Darcy's law. Considering that the difference between filed test and indoor test results is large and the field test results can reflect the fracture characteristics of dike, the permeability coefficient of dike are taken as 2×10^{-6} cm/s according to the field test results.

Analyses of the Calculated Results

Calculation and Verification of the Da Shan Zi Separation Levee

Figure 3 shows the overall deformation of embankment during the filling of the Da Shan Zi Separation Levee. The deformation of the old embankment showed significant basin characteristics. In the middle position of the embankment, the settlement is larger, and the vertical settlement is basically the same at the top of the embankment width range. With the distance away from the top of the embankment, the vertical settlement decreases gradually, but obvious heave occur at the foot of the embankment. Meanwhile, the horizontal displacement of the embankment is significant from the middle of the embankment to both sides. The computed
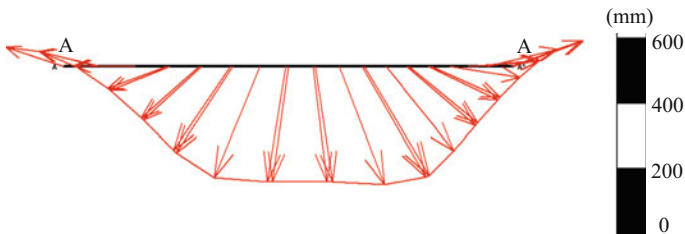
Fig. 3 Total deformation of old embankment

maximum settlement was about 520 mm, and the maximum horizontal displace-
ment was about 373 mm. The results show that the slope and the top of the
embankment have a large number of cut off points, and several inner parts reached
the plastic yield state.

The deformation characteristics and internal fissures investigated by field
excavation from the Da Shan Zi Separation Levee was consistent with literature
[11] record of several collapse showing that the present separation Levee elevations
were generally lower than the design elevation 0.5 m or more. This showed that the
calculation is credible and the parameters are reasonable.

Settlement of the Overlapping Embankment During Construction

Figure 4 shows the settlement of the overlapping embankment for different thick-
ness soft soil. It is noted the cross section for comparison is the horizontal section
where the slope of the widening embankment located. Take the toe of the
embankment horizontal section for contrast and analysis, Fig. 4 shows embankment
splicing of vertical total deformation has three characteristics: one is widened
embankment after, the old embankment will uplift, and the thickness of soft soil
layer is greater, the uplift. Second, the widening embankment, widening will pro-
duce larger settlement, and the old embankment uplift formed significant differ-
ential settlement, easily in new and old subgrade binding site produce crack. Third
is the widening embankment in soft soil area will cause the widening of lateral
slope produces large vertical uplift. Soft soil thickness, slope to the lateral defor-
mation of the greater, indicating that the thickness of soft soil layer on the lap of
embankment slope toe deformation is very significant.

The influence of the thickness of the soft soil layer on the vertical settlement of
the overlapping embankment is shown in Fig. 5. It can be seen from Fig. 5 that
when the thickness of the soft soil layer is much less such as 2 m, the settlement
value increased from 107 to 144 mm. The settlement of the overlap embankment
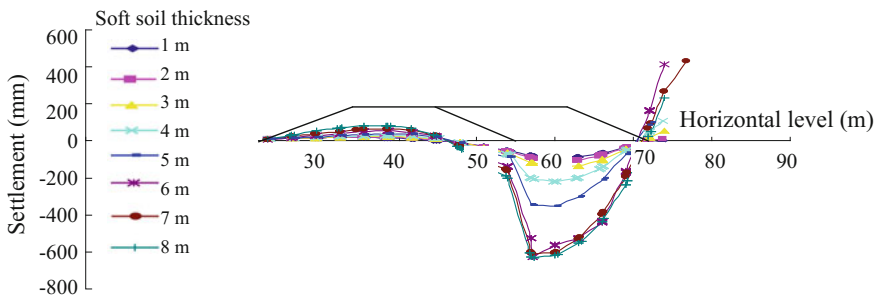
Fig. 4 Settlements of different soft soil thickness

Fig. 5 Relationship between maximum settlement and soft soil thickness
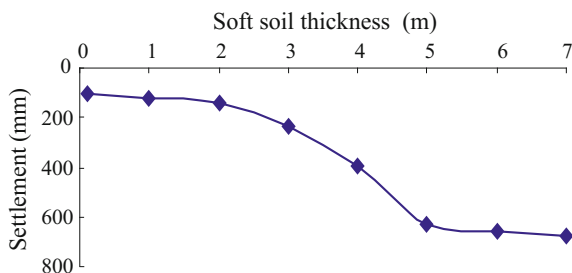
varied a little with the thickness of the soft soil layer. It can be concluded that in this case, the critical value of h_1 is 2 m for the settlement of the embankment is not significantly changed with the thickness of the soft soil. When the soft soil layer thickness increased from h_1 to a certain depth h_2 such as 5 m, the settlement of the overlap embankment increased significantly with the thickness of the soft soil. That is, for the thickness of the soft soil layer is 2–5 m, the settlement of the overlap embankment increased from 144 to 629 mm, and the corresponding soft soil layer was the significant zone for the settlement of the overlap embankment. For the overlap embankment with certain filling depth, and when the thickness of the soft soil layer increased to a certain value, the increment of the soft soil thickness has no significant or only a little influence on the settlement of the overlap embankment. For the case that the thickness of the soft soil layer increased from 5 to 7 m, the settlement of the overlap embankment increased from 629 to 674 mm. The increment rate is much smaller than that of the absolute value.

Comparative Analysis of Differential Settlement

Based on the analyses of differential settlement, it can be seen from Fig. 4 that the differential settlement of the widened embankment has the following trends by comparing the settlement curve for different soft soil overlap embankment.

Firstly, the slope of the straight line between two adjacent points in the figure shows the differential settlement between the two points. It can be seen clearly from the compared figure that not only the overlapping of the slope but also the widened filling zone, the slope changes little for the two adjacent points along the horizontal line of the embankment, i.e., the differential settlement between adjacent two points is not significant. This is consistent with the influence of soft soil layer thickness on the total settlement of the widened embankment.

Secondly, when the thickness of the soft soil layer is greater than the critical thickness of h_1, for the overlap part between the new and old embankment, the slope increases with the increase of the thickness of the soft soil layer, which shows that the differential settlement of the overlap part of the slope increased with the increase of the soft soil layer thickness. It is noted that with the increase of the

thickness of the soft soil layer, the critical depth h_2 did not occur similar to that of the total settlement. It can be explained that the phenomenon is mainly due to that at the overlap part between the new and old embankment, consolidation completed for old embankment but not the new embankment. Thus, the settlement of the overlapping parts increases with the increase of the thickness of the soft soil. However, in contrast to the widening part of the embankment, although the settlement of the overlap part of the slope increases with the increase of the thickness of the soft soil layer, the absolute value of the settlement is much smaller than that of the widening.

Thirdly, it can be seen from the differential settlement of the overlapped part and the widened embankment, settlements of the widened embankment increased significantly for the thickness of the soft soil layer is greater than h_1, and great differential settlement was formed compared with the overlapped part. After the thickness of the soft soil layer is greater than h_2, as shown in Fig. 4, the differential settlement between the overlapped part and the widened one did no longer increase significantly with the increase of the thickness of soft soil layer.

This can be explained that the main reason of this result is that the distribution of settlement is reasonable within the deformation range. The location of the maximum settlement gradually approach to the joint part between the new and old embankment and larger settlement also occurs at the old part of embankment. By calculating and analyzing the height of embankment fill, the critical thickness of h_1 and h_2 can be obtained similarly. This can be deduced that effect of the thickness of soft soil on settlement and differential settlement of overall lap embankment also obeys the law that there are two critical thicknesses of h_1 and h_2 for the overlapping embankment of any filling height.

Analysis on the Characteristics of Long Term Settlement of Overlapping Embankment

The effect of different thickness of soft soil layer on the total settlement of the overlapping embankment is analyzed based on the excess pore water pressure as the control index. Figure 6 shows the time required for the completion of the consolidation of the overlapping embankment for different soft soil thickness from the duration of the consolidation process. It can be seen from the figure that the consolidation time increases largely and lasts longer when there is a soft soil layer. The thickness of soft soil layer is 1, 3, 5, 7 m corresponding to the consolidation time 1531, 1832, 2062 and 2166 days, respectively, with the growth rate of consolidation time 19.6, 12.5, 5.1%, respectively. It can be found that with the increase of the thickness of the soft soil, the growth of the consolidation time decreased significantly.
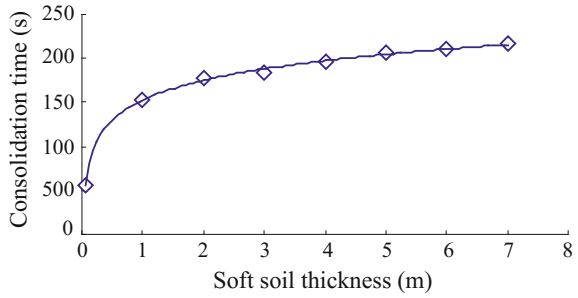
For the convenience of analysis, the thickness of the soft soil 0 m is adjusted as 0.01 m, thus, curves of the consolidation time of the overlapping embankment with the thickness of the soft soil accords with the logarithm curve as follows:

$$t = 325 \ln(d) + 1524 \tag{1}$$

where t is the time required for the consolidation of the overlapping embankment, days; d is the thickness of the soft soil layer, m.

After the consolidation, the variation curves of the settlement of the cross section with the soft soil thickness can be obtained as shown in Fig. 7. It can be seen from Fig. 7 that the long-term settlement of the soft soil layer increases with the increase of the thickness of the soft soil when the thickness of the soft soil layer is less than a certain value which is 5 m in this case. When the thickness of soft soil is over the range, the long-term settlement of the overlapping embankment will no longer be significantly increased. Differential settlement of the overlapping embankment also exhibited similar characteristics with construction period, namely in the certain range of the thickness of soft soil, differential settlement increased rapidly with the thickness of soft soil layer, and when the thickness of soft soil layer is less than a certain range h_1 or is greater than a certain depth h_2, differential settlement of the overlapping embankment with the change of the thickness of soft soil layer is not

Figures on the curve is soft soil thickness
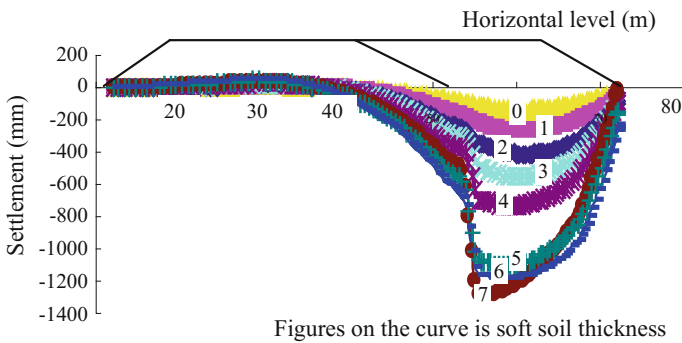
Fig. 7 Relationship between ultimate settlement and soft soil thickness
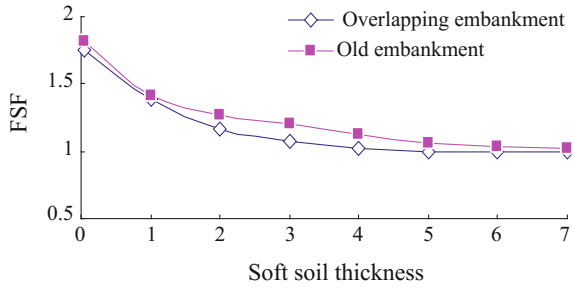
obvious. In addition, from the location of the maximum settlement, with the increase of the thickness of the soft soil, the location of the maximum settlement gradually from the center of the widened embankment to the overlapping embankment between the new and old. When the soft soil layer is greater than a certain thickness of h_2, the maximum settlement location is fixed in the overlapping part of the new and old embankment.

Figure 8 shows the curve between the failure safety factor (FSF) of the widened embankment calculated by using the strength reduction method and the change of soft soil layer. It can be seen from the figure that when the thickness of soft soil layer is small, the safety factor of the old embankment and the overlapping embankment had little difference; when the thickness of soft soil grows in a certain range, the safety factor of the overlapping embankment is smaller than the old embankment; and when the soft soil thickness is greater than a certain value, the safety factor of the old embankment and overlapping embankment both tended to 1. Results of the Safety factor show that the influence of soft soil thickness on the embankment is partitioned.

Differential Settlement Control Analysis of Overlapping Embankment

According to the characteristics of the construction period and the long-term settlement deformation, the settlement control of the overlapping embankment can be considered in the following aspects.

Firstly, the widening part of the filling will cause local uplift in the old road embankment, prone to the formation of larger differential settlement and crack in the overlapping parts. Thus, it is necessary to strengthen the integrity of the embankment.

Secondly, from the viewpoint of the consolidation time, when the thickness of the soft soil layer reaches a certain value, the change of the thickness of the soft soil layer has not cause the large change of consolidation time. Therefore, for soft soil

layer with different thickness the differential settlement can be controlled by preloading for a certain time, pavement structure can be done when the consolidation deformation is basically completed.

Thirdly, from the effect of soft soil layer thickness on settlement deformation of overlapping embankment, the overall settlement deformation, and differential settlement no longer increase either during construction or long-term deformation, when the thickness of soft soil layer is greater than a certain value.

Thus, for certain filling height, the depth of the soft soil foundation treatment should also be corresponding to a certain depth, the depth should be more than h_2 appropriately, and there is no need for deeper treatment.

Conclusions

In order to study the effect of thickness of soft soil layer on settlement deformation of overlapping embankment, finite element model was established based on the project. The rationality of the model and the calculation parameters are verified by comparing the calculated and monitored results.

Through the calculation of the settlement of the overlapping embankment with different thickness of the soft soil layer, the conclusions are obtained as follows.

1. For a certain filling height, the effect of thickness of soft soil layer on settlement deformation of overlapping embankment can be divided into three stages: when the thickness of soft soil layer is less than the $h_1 = 2$ m, overall settlement and differential settlement are smaller; with soft soil layer thickness increased from $h_1 = 2$ m to $h_2 = 5$ m, the overall settlement and differential settlement increased greatly with the thickness of soft soil layer increased. When the thickness of soft soil layer is greater than that of $h_2 = 5$ m, overall settlement and differential settlement do not increase with the thickness of soft soil layer significantly. Thus, for overlapping embankment, the depth of the soft soil foundation treatment should be determined according to the filling height, and there is no need for deeper soft soil treatment.
2. The consolidation time of the overlapping embankment is not linear with the change of the soft soil layer thickness. The increase of the thickness of the soft soil layer causes the consolidation time to become smaller. Thus, when the soft soil layer thickness varies greatly, the differential settlement can be effectively reduced by the natural consolidation or preloading. It should be noted that the conclusions obtained is based on the actual project, further research and demonstration are needed for a wider range application.

References

1. Gao, J.T., Ji, Z.Q. (2009). Settlement characteristics of foundation caused by widening of Expressway Subgrade. Application Technology of Highway Traffic Science and Technology, (4): 95–96.
2. Fu, Z., Wang, X.C., Chen, X.G. (2001). Differential settlement characteristics and influencing factors of widening subgrade. Journal of Traffic and Transportation Engineering, 7(1):54–57.
3. Zhang, D.W., Liu, S.Y. (2006). Numerical Analysis of Interaction Between Old and New Embankment in Widening of Freeway on Soft Ground. China Journal of Highway and Transport, 19(6):7–12.
4. Wang, H., Huang, X.M. (2004). Numerical Analysis of Road Widening on Soft Soil Ground by FEM. Journal of Highway and transportation research and development, 21(8):21–24.
5. Jia, N., Chen, R.P., Chen, Y.M. (2004). Theoretical analysis and measurement for widening project of Hang-Yong Expressway. Chinese Journal of Geotechnical Engineering, 26(4): 755–760.
6. Hu, H.B., Rao, X.B, Chen, Y. (2004). Geotechnical problems caused by new embankment splicing with old one on soft ground and treatment measures. Rock and Soil Mechanics, 25 (sup.2):321–324.
7. Chen, J.F., Yu, S.B. (2011). Centrifugal and Numerical Modeling of a Reinforced Lime-Stabilized Soil Embankment on Soft Clay with Wick Drains. International Journal of Geomechanics, 11(3): 167–173.
8. Wang, J.C., Zhong, J., Cong, L. (2011).Analysis between numerical and field tests of high fill reinforced widening embankment. Chinese Journal of Rock Mechanics and Engineering, 29 (sup.1): 2943–2950.
9. Tang, X.S., Zheng, Y.R., Wu, A.Q. (2014). Stability Analysis of Soil Slope under Seepage by PLAXIS Finite Element Program. Journal of Yangtze River Scientific Research Institute, 23(4):13–17.
10. Chen, J.F., Song, E.X., Xu, M. (2011). Application of strength reduction FEM to stability analysis of high fill slope in Kunming new airport. Rock and Soil Mechanics, 32 (supp.1): 636–642.
11. Water Resources Department of Jiangsu Province. (1985). The report of the investigation of the embankment of the river channel in the lower reaches of Huaihe River. Najing, Water Resources Department of Jiangsu Province.

Structure Noise Test of Rail Transit Box Beam and the Assessment of Environment Impacts

Yan Zhang

Introduction

When trains pass through box beam, structure vibration is therein engendered due to the irregularity of tracks. Vibration energy passes to the lower bridge through track structure. Vibration of panels is elicited and the vibrated panels inspired the air outside to generate radiation noise. The noise is called "structure noise of bridge" [1–3].

Scholars at home and abroad gradually pay attention to research on structure noise of elevated bridges of track traffic in recent years. Nga and Ng [4] analyzed the test result of vibration and radiation noise of box beam structure of elevated bridges through Fast Fourier Methods (FFT). Wilson et al. [5] analyzed noise radiation level after the increase of box beam impedance through vehicle-track-elevated structure math model. Bewes [6] established a calculation model for research on radiation noise of elevated structure through the statistical energy method. XIE Wei-ping and SUN Liang-ming [7] studied sound radiation issues by means of Fourier integral transformation and stationary phase method based on extended homogeneous capacity precision integration method and complex vector virtual boundary spectral method. Traditional A-weighted sound pressure level does a great deal attenuation at low frequency and underestimates the harm of low frequency noise, and new evaluation system for low-frequency structure noise of track traffic has not been established in China.

Taking the 32 m two-lane concrete simply supported box beam as the research object, this paper compares the results of boundary element simulation and the

Y. Zhang (✉)
Department of Civil Engineering and Architecture,
East China Jiaotong University, 330013 Nanchang, China
e-mail: 645031420@qq.com

measured data and, by employing Japan's low frequency noise limit value curve, makes assessment of noise of the rail transit box beam from the perspective of impacts on buildings and on human physical and psychological comfort.

Box Beam Finite Element-Boundary Element Coupling Acoustic Computation Model

Railway Box Beam Finite Element Model

In order to accurately predict box beam vibration of track traffic and radiation of structure noise under the circumstance of loading, this paper establishes a railway box beam three-dimensional finite element model by adopting finite element software. Its cross section is indicated in Fig. 1. The box beam is 32 m long, 2.8 m high and 13 m wide. The thickness of the upright board is 0.34 m and that of the floor is 0.3 m. The pectoral plate is within 0.4–0.47 m thick. The flange plate is 0.2–0.5 m thick. The elasticity modulus is 36.2 Gpa with a density of 2500 kg/m^3. Poisson ratio is 0.2. Damping ratio is 0.03. Support stiffness is set as 3.38×10^9 N/m. Fasteners vertical stiffness is 6×10^9 N/m. Damping is 10^4 N. s/m. Fasteners space is 0.625 m. Impacts from the ground and bridge pier are not considered. Support saddle is simplified as two-sided simple holders. Based on the parameters above, this paper establishes a finite element physical model of box beam, as shown in Fig. 2.

Vibration of box beam is generated from interactions between wheel and rail caused by track irregularity. In order to predict the noise caused by box beam vibration, we need first to simulate interactions between wheel and rail. This paper employs two CRH2 trains to simulate loading. The computation speed is 180 km/h. Germany low disturbance spectrum is treated as the inspiration of irregularity on the surface of wheel and rail. The length of the wave of track irregularity ranges within 5–300 mm. The real operation process is simplified as a concentrated force loading which moves as time passes by. This study simulates the right line unidirectional loading method to analyze radiation characteristics of structure noise of box beam. The step size of loading is 6.4×10^{-4} s. The vibration reaction of surface nodes of box beam structure is reached through transient dynamic analysis.

Fig. 1 Cross section size of box beam
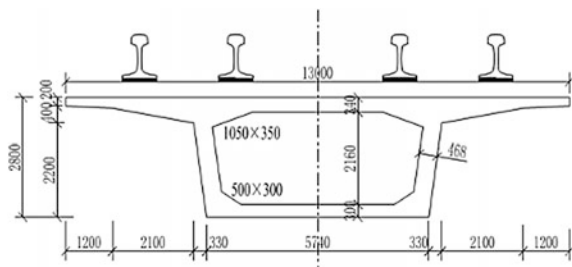
Fig. 2 Finite element model
of box beam
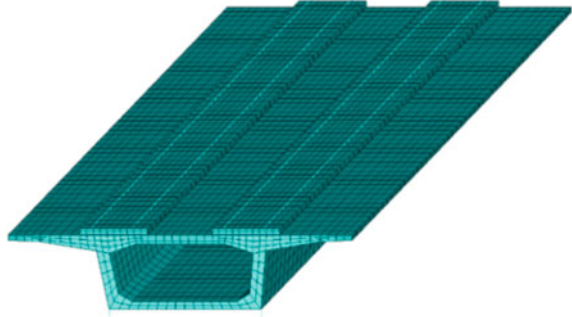
Box Beam Acoustic Boundary Element Model

According to the conservation principle of fluid and basic hypotheses of sound wave, we can know that the equation expression of box beam sound radiation Helmholtz is as follows:

$$(\nabla^2 + k^2)p = 0 \tag{1}$$

In the formula: ∇^2 represents Laplace operator, $k = \omega / c$ acoustic wave number, c the sound speed in the medium of air, ω frequencies and p sound pressure.

That the concurrent points have the same boundary conditions at the coupling boundary of sound field and solid structure makes us know the response result of displacement at the solid boundary. Thus, the sound pressure at the boundary of sound field can be calculated, and so can the sound pressure at any point of this sound field. Compared with testing data through experiments, it is more exact to calculate the vibration noise level of complex structure at large scale based on the finite– boundary element coupling acoustic computation methods [8].

Box beam boundary element model is established based on the theory of finite element—boundary element coupling acoustic calculation. While establishing acoustic boundary element model, we need to consider that the side length of the biggest unit should be shorter than 1/6 of the shortest wave length of the calculation rate, that is, the side length of the biggest unit should meet the following expression:

$$L \leq \frac{c}{6 f_{\max}} \tag{2}$$

In this expression, $c = 340$ m/s, represents the spread speed of sound in the air. This paper employs indirect boundary element method and L, the size of the biggest unit of grid division of box beam boundary element is 0.32 m. From expression (3) we know that the highest calculation rate of this model can reach 177 Hz, which meets the precision requirement of boundary element calculation, within 0–100 Hz. The grid of boundary element of box beam is shown in Fig. 3.

Fig. 3 Acoustic boundary element model of box beam and acoustic calculate grid
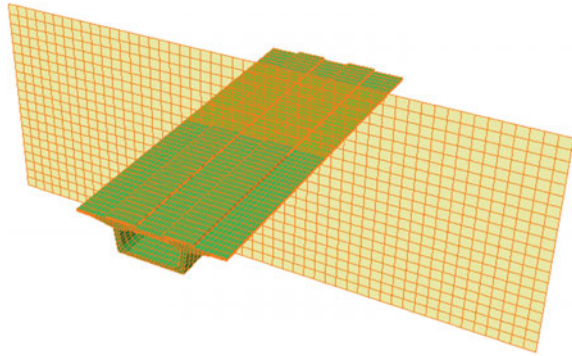
Fig. 4 Sound point distribution in middle span of box beam
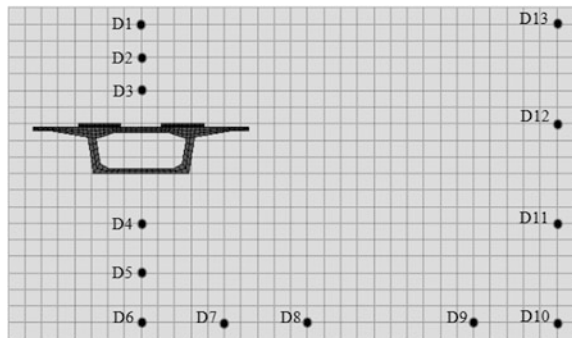
To study the sound distribution regularities of box beam cross section, this research separately picks up 14 field points as marked in Fig. 4 for analysis. Among these points, D1–D3 are just above the bridge span center and their distances to the roof board of box beam are separately 2, 4 and 6 m. D4–D6 are just under the span center and the distances to the floor are 3, 6 and 9 m for each. D7–D9 distribute at the level of 1 m above the floor, perpendicular to rail centerline. Their horizontal distances to rail centerline are separately 5, 10 and 20 m. D10–D13 perpendicularly distribute at 25 m away from cross rail centerline. Their vertical distances to the floor are 1, 7, 13 and 19 m.

Modal Analysis

Knowing the natural vibration frequency of bridge structure has significant meaning to mastering the power performance and dynamic response influenced by external loading. Therefore, modal analysis of bridge structures should be conducted prior to transient dynamic analysis. In modal analysis, Block Lanczos method is employed to extract modes. We can know how the structure will react when the modes are

Table 1 Description of the first ten scales

Modal scale	Natural vibration frequency(Hz)	Mode description	Modal scale	Natural vibration frequency(Hz)	Mode description
1.	5.14	1 Scale vertical bending	6	17.64	Counter symmetry bending
2.	5.80	Girder body rolling over	7	22.39	Bridge deck local vibration
3.	10.86	2 Scale vertical bending	8	24.43	Bridge deck local vibration
4.	13.02	1 Scale reversing	9	26.11	Bridge deck local vibration
5.	14.35	2 Scale reversing	10	26.37	Bridge deck local vibration
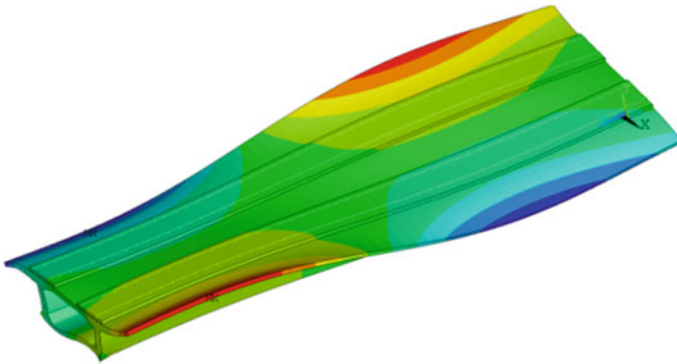
Fig. 5 Vibration type of box beam at the seventh scale

activated, by calculating natural frequency and vibration type through model analysis. The characteristics of the first ten scales of bridge structure are shown in Table 1. The box beam vibration type is featured with board local vibration at the seventh scale, as shown in Fig. 5.

Noise Test

The test is carried out under a Shanghai rail box beam. The box beam has a single box and a single chamber, with a span of 32 m, and a beam of 2.8 m high and 13 m wide. The size of cross section is shown in Fig. 1. Acoustic microphone is located in the cross section, 1.5 m high away from the floor, as indicated in Fig. 6. The
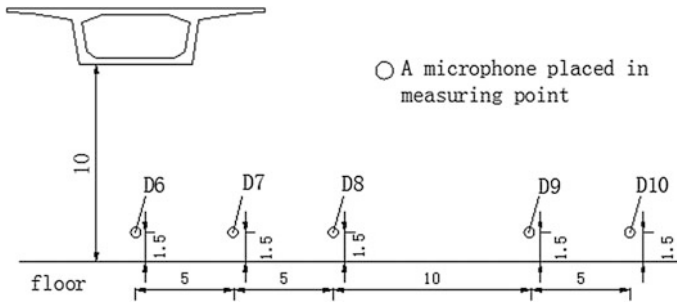
Fig. 6 The distribution of measured points and field points

distances to bridge centerline are separately 0, 5, 10, 20 and 25 m. Just under the box beam, there is hard floor with a width of more than 4 m. The remaining is rather spacious wasteland.

Acceleration reaction of structure vibration of box beam is treated as preliminary input of boundary element in theoretical calculation. This paper employs box beam boundary acoustic computation software called Virtual. Lab to estimate sound pressure reaction. The current A-weighted sound pressure level underestimates the degree of irritation caused by low frequency noise. To estimate the degree irritation caused by bridge noise, German adopts Non-weighted sound pressure level [9]. This paper employs non-weighted linear sound pressure level for analysis. The current test is conducted on vehicles on the right side of the road. The speed is within 179.6–81.5 km/h. When calculating sound pressure, we take 180 km/h.

The measured and calculated sound pressures are shown in Table 2. Points 1 and 2 agree with the measured sound pressures. This is because Points 1 and 2 are close to the beam and the external impacts on them is rather low, while other points are far away, and therefore they are sensitive to external elements. That this paper ignores impacts from the bridge pier and the floor is also a reason of possible inaccuracy. The agreement between measured and calculated values indicates that the finite element—boundary element coupling acoustic computation modal, adopted in this paper, is effective in calculating structure noise of box beam.

Table 2 Linear sound pressure levels of mid-span measured points (dB)

Measure Point	Speed (km/h)			Average value	Calculated value
	179.6	180.2	181.5	180.43	180
D6	85.5	87.7	89.9	87.70	86.01
D7	83.1	86.6	88.6	86.10	84.95
D8	83.7	86.7	88.2	86.20	84.00
D9	76.9	83.3	83.9	81.37	78.46
D10	70.4	80.6	81.2	77.40	75.59

The Assessment of Structure Noise of Rail Transit Box Beam

A-weighted sound pressure level is adopted in rail transit acoustic evaluation index in China [10], but traditional A-weighted sound pressure level does a great deal attenuation at low frequency and underestimates the harm of low frequency noise. Japan's assessment of low frequency noise includes two aspects: panting vibration and physical and psychological comfort. The former refers to noises that might cause vibration in building affiliated staff, like doors and windows. The limit value for reference is given in Fig. 7.

Figure 7 divides sound pressure spectrum curve into four parts: A, B, C, D, according to two reference limit curves. Compares measured 1/3 octave sound pressure level with the limit curve in Fig. 7, and based on Table 3, decides whether the box beam structure noise causes vibration of building affiliated stuff or physical or psychological discomfort in human beings.

Linear sound pressure spectrum curves of box beam span center sites D1–D13 in Fig. 4 are shown in Figs. 8, 9, 10 and 11. As is shown in Fig. 8, no significant change of sound pressure happens in the top of span center of box beam. However,
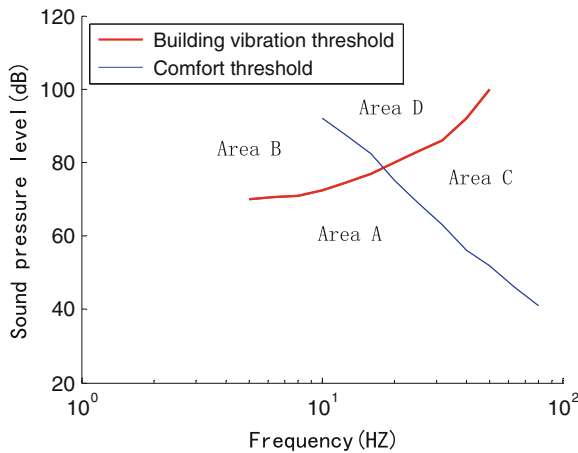
Fig. 7 Japan's low frequency noise reference limit curve

Table 3 Vibration of buildings and discomfort in human body caused by sound pressure

Area	Building vibration	Physical or psychological Discomfort
A	No	No
B	Yes	No
C	No	Yes
D	Yes	Yes

Fig. 8 Sound pressure level of sites D1–D3
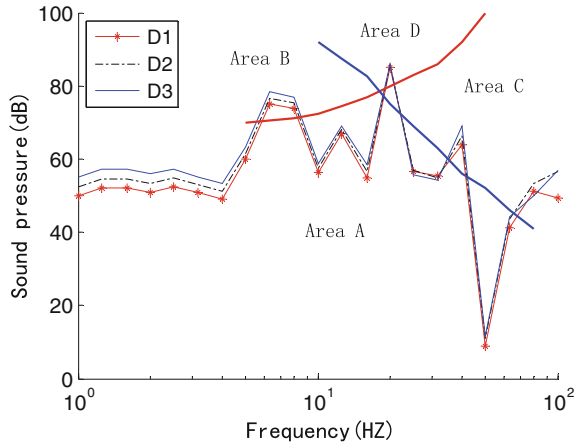
Fig. 9 Sound pressure level of sites D4–D6
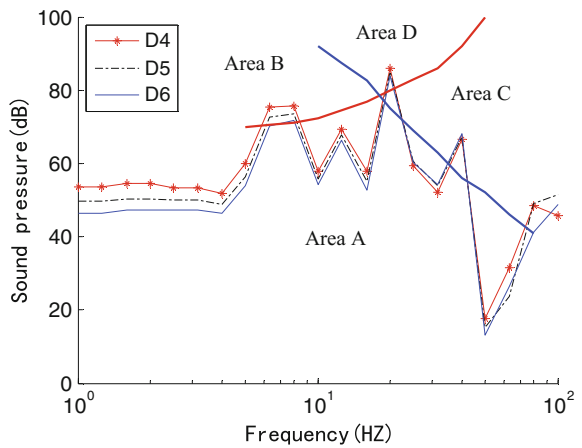
Fig. 10 Sound pressure level of sites D7–D9
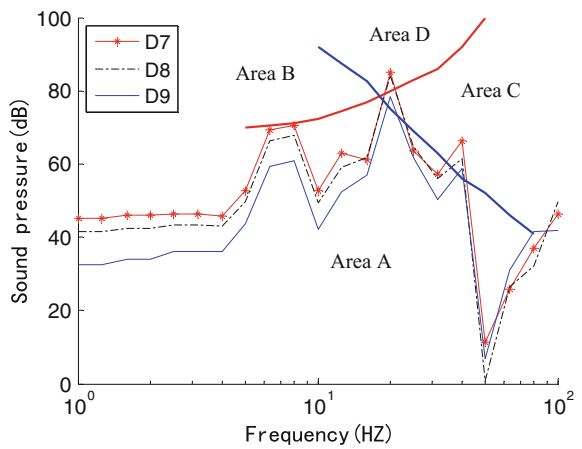
Fig. 11 Sound pressure level
of sites D10–D13
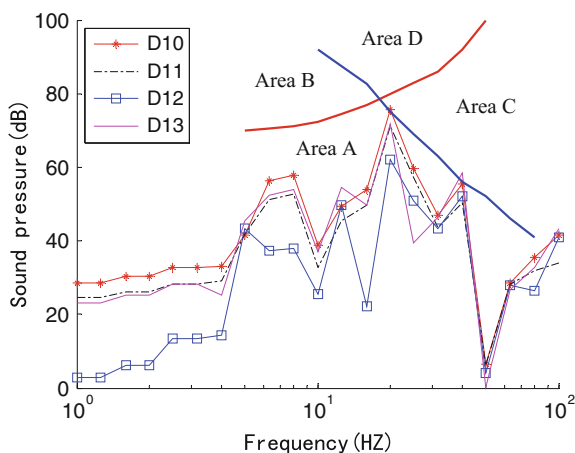
the sound pressure reduces gradually with the increase of the distance to the bridge surface. This suggests that vibration of the bridge board is the main source of structure noise of box beam. It is shown in Fig. 9 that field sound pressures of span center floor of box beam reduce as the distance to the bridge floor increases. As indicated in Fig. 10, field sound pressure, perpendicular to rail centerline, reduces with the distance to rail centerline increasing. Sound pressure attenuation degree also decreases as distance increases, this trend conforms to acoustic laws. From Fig. 11 we know that in the vertical field point, 25 m away from the rail centerline, sound pressure reduces with the increase of height above the ground. D12, at the same height as the bridge board, reduces significantly. It suggests that radiation level of structure noise of box beam has a close relation to vertical vibration of the bridge deck.

Vibration at the peak point of noise frequency is mainly on local vibration of the bridge board (See Fig. 5). Within the width of center frequency of 20 Hz, natural frequency of rail box beam at the seventh scale is 22.99 Hz. Local vibration of structure low scale is easy to be activated, which causes the highest level of radiation of structure noise. From the spectrogram of sound pressure of every field site we know that impacts can be found on both building affiliated stuff and human physical and psychological comfort. When conducting noise-reducing treatments, it will be more effective to start with the noise peak.

Conclusions

A 32 m two-lane concrete simply-supported box beam as the research object, this study compares the calculation result by employing boundary element simulation with measured data, and adopts Japan's low frequency noise limit value curve to estimate impacts on environment. The findings are as follows:

(1) Structure noise of box beam is significant in low frequency below 100 Hz. Radiation level of structure noise of box beam is closely related to vertical vibration of the bridge board. That low order local vibration is activated is an important factor that causes the peak of structure noise of box beam.

(2) By comparing the calculation result with measured data, we know that box beam finite element—boundary element coupling acoustic computation model is accurate and effective in calculation and can be employed in the assessment of impacts of rail noise on the environment.

(3) According to Japan's low frequency noise limit value curve, the noise pressure peak of box beam is located in the most unfavorable district, D. When dealing with noise reducing, it will be more effective to start with the noise peak frequency.

References

1. LI Xiao-zhen, ZHANG Xun, LIU Quan-min, et al.Prediction of Structure-borne Noise of High-speed Railway Bridges in Whole Frequency Band (PartI:heoretical Model[J]. JOURNAL OF THE CHINA RAILWAY SOCIETY,2013,35(1):101–107.
2. LIU Jia-hua, LIAN Song-liang. Vibration and noise of the urban rail transit[J].Journal of Traffic and Trans portation Engineering, 2002,01:29–33.
3. ZHU Yan, CHEN Guang-ye, LIN Chang-ming. Numerical Prediction and Analysis of Radiated Noise from Viaduct of City[J]. Noise and Vibration Control,2005, (3):37–41.
4. Ngai KW, Ng CF. Structure-noise and vibration of Concrete Box Structure and Rail Viaduct [J].Journal of Sound and Vibration, 2002, 255(2):281–297.
5. Wilson, Ihrig & Associates. Viaduct design for minimization of direct and structure-radiated train noise[J]. Journal of Sound and Vibration, 2000, 231(3):883–897.
6. O.G. Bewes, D. J. Thompson, C. J. C. Jones, et al. Calculation of noise from railway bridges and viaducts: Experimental validation of a rapid calculation model [J]. Journal of Sound and Vibration, 2006, 293(4): 933–943.
7. XIE Wei-ping, SUN Liang-ming, et al. Semi-analytical Method of Acoustic Radiation fron Box Beam[J]. Journal of Wuhan University of Technology, 2008. 30(12):165–169.
8. JIAO Ying-hou, KONG Xia, CAI Yun-long, et al. Vibration noise calculation and testing analysis of large vertical planetary transmission gearbox based on FEM and BEM [J]. Journal of Vibration and Shock, 2012, (4):123–127.
9. Schulte-Werning B, Beier M, Degen K G, et al. Research on noise and vibration reduction at DB to improve the environmental friendliness of railway traffic [J]. Journal of Sound & Vibration, 2006, 293(3):1058–1069.
10. GU Xiao-an, XIE Yong-mei, et al. Implementation of Standards to Control Secondary Radiation Noise on Building Caused by Metro Train Operation[J]. Modern Urban Transit, 2012, 04:56–59.

Soil Arching Effect in Piled Embankments Under Moving Shakedown Limit Loads

Yan Zhuang and Kangyu Wang

Introduction

Soil arching is a common phenomenon in piled embankments resting on soft soils, and has long been recognized in the theory of soil mechanics [1]. Consequently, several design methods are proposed for the assessment of soil arching in piled embankment based on various concepts [2–5]. Most research conducted so far has investigated the behavior of soil arching in piled embankment under static loads; knowledge on their dynamic behaviors under transient loads of moving vehicles is rather limited in the literature. Although the soil arching under dynamic loads [6–8], the behavior of dynamic stress transfer in this embankment system under traffic loads is still not well known, and therefore it deserves more research attention.

'Shakedown' is used to refer to a state of structures under repeated loading conditions at which the behavior becomes purely elastic after some initial plastic deformation, and has therefore been a useful tool in the design of a wide range of practical applications such as pavement engineering and railway foundations [9–12]. However, there is a lack of research and knowledge on how the shakedown limit loads are related to the soil arching phenomenon in the piled embankment under cyclic loads.

This paper presents an investigation on the soil arching effect in piled embankment under shakedown limit loads. Firstly, a three-dimensional (3D) finite element (FE) model combined with Melan's lower-bound shakedown theorem is presented. Secondly, the shakedown limit loads were applied onto the surface of

Y. Zhuang (✉) · K. Wang
Key Laboratory of Ministry of Education for Geomechanics
and Embankment Engineering, Geotechnical Research Institute,
Hohai University, 1 Xikang Road, Nanjing 210098, China
e-mail: Joanna_zhuang@163.com

K. Wang
e-mail: kangyu02@163.com

pavement as an external traffic loads to validate whether the piled embankment was in the shakedown status. Finally, the soil arching effect under the moving shakedown limit loads was investigated.

Shakedown Analysis of Piled Embankment

Analytical Shakedown Solutions for Mohr–Coulomb Materials

For Mohr–Coulomb materials, Melan's shakedown theorem requires that the total stress state of any point in the materials has to lie within the Mohr–Coulomb failure surface, which leads to the following expression:

$$f = \left(\sigma_{xx}^r + M\right)^2 + N \leq 0 \tag{1}$$

with

$$M = \lambda\sigma_{xx}^e - \lambda\sigma_{zz}^e + 2\tan\varphi\left(c - \lambda\sigma_{zz}^e\tan\varphi\right) \tag{2}$$

$$N = 4\left(1 + \tan^2\varphi\right)\left[\left(\lambda\sigma_{xz}^e\right)^2 - \left(c - \lambda\sigma_{zz}^e\tan\varphi\right)^2\right] \tag{3}$$

In order to satisfy Eq. (1), one condition must be met:

$$N \leq 0 \Rightarrow \lambda \leq \frac{c}{\left|\sigma_{xz}^e\right| + \sigma_{zz}^e\tan\varphi} \tag{4}$$

The shakedown condition for the layered materials then can be written as follows:

$$\lambda_{sd} = \min\left(\lambda_{sd}^1, \lambda_{sd}^2, \lambda_{sd}^3, \ldots, \lambda_{sd}^n\right) \tag{5}$$

Then the shakedown multiplier for the layered materials is given by:

$$\lambda_{sd} = \frac{c_n}{\max\left(\left|\sigma_{xz}^e\right| + \sigma_{zz}^e\tan\varphi_n\right)} \tag{6}$$

where λ_{sd} is shakedown multiplier for the layered materials; c_n, φ_n and $\sigma_{0.2}$ are the parameters of the materials at the nth layer; $\sigma e\ ij$ and $\sigma r\ ij$ are the elastic and residual stress field, respectively.

The shakedown multiplier in Eq. 6 is dependent on material properties and elastic stresses. The elastic stress fields in the layered system are much more complicated than those in a homogeneous half-space. Therefore, FE analyses for elastic stress fields are carried out by means of the FE software ABAQUS.

Description of FE Model

A fully 3D FE model was presented in this paper to investigate the shakedown limit of the piled embankment, with the FE meshes shown in Fig. 1. A 12 m wide embankment with 1 V:1.5H is constructed on a uniform 6 m thick subsoil layer, below which a rigid layer exists. The pavement with the thickness of 0.6 m is placed above the top surface of the embankment, which includes a 0.15 m AC layer, a 0.2 m base layer and a 0.25 m subbase layer. The 6 m concrete pile, with the pile cap of 1 m width and 0.5 m thickness are assumed to be installed in a square grid pattern with the spacing of 2.5 m, and the width of the pile is 0.3 m. The horizontal length of the subsoil is taken to be 38 m so that the boundary effect can be minimized. A 7.5-m-wide section with three rows of piles beneath the embankment was selected for the analysis, so that a truly full 3D model can be obtained. The pile is modeled as linear elastic material, while a linear-elastic, perfectly plastic model with the Mohr Coulomb failure is used to model the pavement, embankment and subsoil. The 8-node brick elements (C3D8) are used in the FE model, with the total elements of approximately 145 thousands. The parameters for the materials used in the models are shown in Table 1.

The general problem of a wheel and pavement contact in this paper is idealized in terms of a half-space subjected to a surface contact loading (Hertz loads) limited to a circle of radius, a, as shown in Fig. 1. The normal and shear load distribution p and q are given as follows:
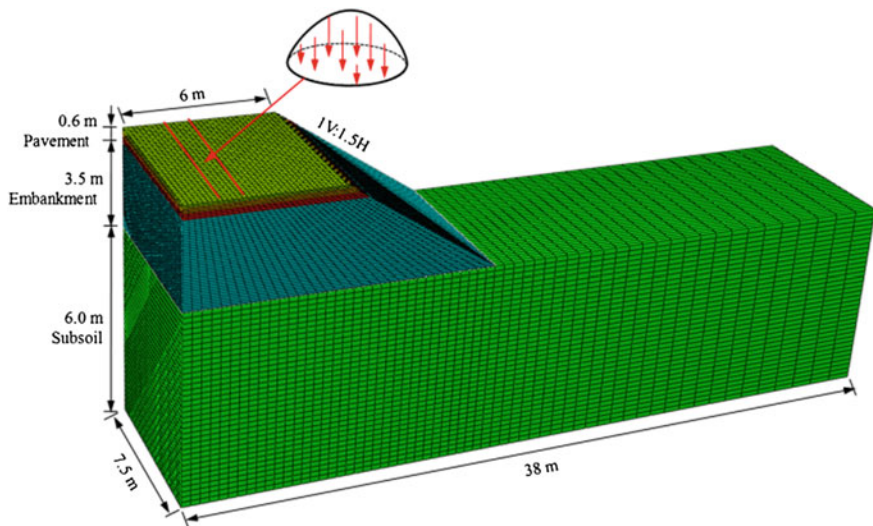
Fig. 1 3D FE model for the piled embankment under Hertz loads

Table 1 Parameters used in the FE model

	E (MPa)	v	c (kPa)	φ (°)
AC layer	3500	0.20	350	60
Base	1000	0.25	250	40
Subbase	500	0.25	200	30
Embankment	25	0.20	10	30
Subsoil	10	0.20	8	13
Pile	3,000,000	0.30	–	–

$$p = \frac{3P}{2\pi a^3} \left(a^2 - x^2 - y^2\right)^{1/2} \tag{7}$$

$$q = \frac{3Q}{2\pi a^3} \left(a^2 - x^2 - y^2\right)^{1/2} \tag{8}$$

where, P is the total normal loads applied in the vertical direction due to the wheel rolling and Q is the total shear loads applied in the travel direction due to sliding. This load distribution has a maximum compressive pressure $p_0 = 3P/2\pi a^2$ at the load center ($x = y = z = 0$). The normal and shear loads are correlated by the frictional coefficient μ as:

$$Q = \mu P \tag{9}$$

In this section, the Hertz load with the maximum compressive pressure $p_0 = 1$ kPa is applied onto the surface of the pavement to obtain the shakedown multiplier of the piled embankment.

Shakedown Limit of the Piled Embankment

As shown in Fig. 2, the shakedown limit loads decrease with the increase of the frictional coefficient μ, especially when μ is relatively large (e.g., larger than 0.2), which may be attributed to the increase of the resultant force as μ increases. The shakedown limit loads decreases by approximately 77% when increasing μ from 0.2 to 1.0.

Soil Arching Effect Under Shakedown Limit Loads

The shakedown limit loads of the piled embankment for pure rolling condition (i.e. only normal loads, $\mu = 0.0$) is 1224 kPa in Fig. 2, a Hertz load with the maximum compressive pressure $p_0 = 1200$ kPa is therefore applied onto the surface of the pavement to investigate the soil arching effect. In the FE model, the Hertz load is
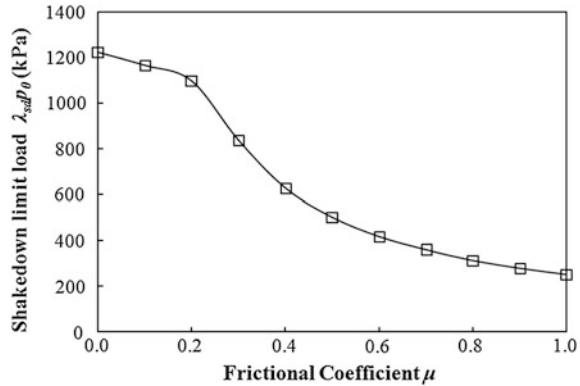
simulated to move at a speed of 60 km/h for 40 cycles since the time-consuming of the dynamic analysis is significantly large.

The settlement in Fig. 3 increases gradually within the first a few load cycles, and then approaches to approximately a steady value, indicating that the piled embankment is in the shakedown status under the Hertz load with p_0 = 1200 kPa.

The embankment settlement along the vertical profile through the midpoint of subsoil and pile cap is shown in Fig. 4, in which both the static and dynamic results are included. It shows that the settlement under dynamic loads captures approximately the same trend with that under the static loads. The embankment settlement over pile cap and the subsoil is identical above a certain plane, which terms as the plane of equal settlement, indicating that no disturb occurs above this horizontal plane. Below this plane, the embankment over the midpoint of subsoil increases to a maximum value, while that over the pile cap reduces to almost zero, implying that the soil arching still exists under dynamic loads.

Figure 5a shows the vertical stress of embankment on a vertical profile through the midpoint of subsoil. The vertical stress profile under dynamic and static loads capture similar trend, which approximately linear increases with the same gradient (equal to the unit weight of embankment fill) until reaching the maximum value at a

Fig. 3 Development of the settlement at the top surface of the pavement
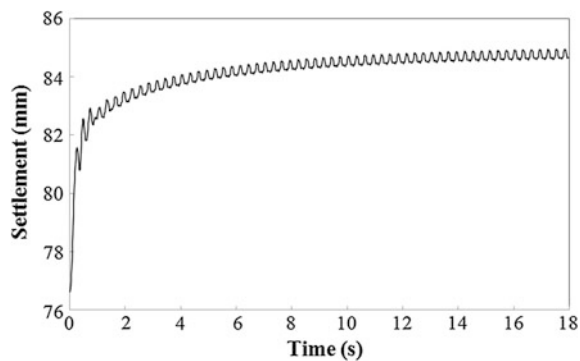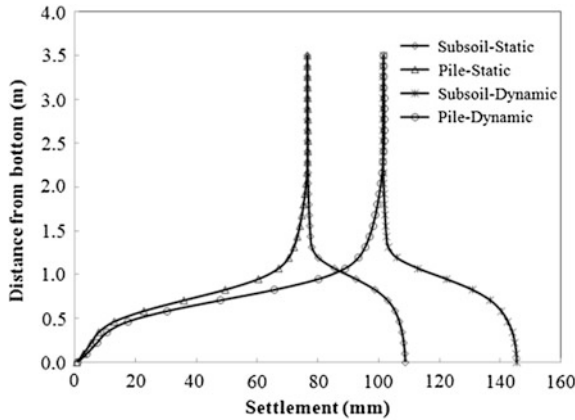
Fig. 4 Embankment settlement on a vertical profile through midpoint of subsoil and pile cap

(a)Vertical stress

(b) Earth pressure coefficient, K
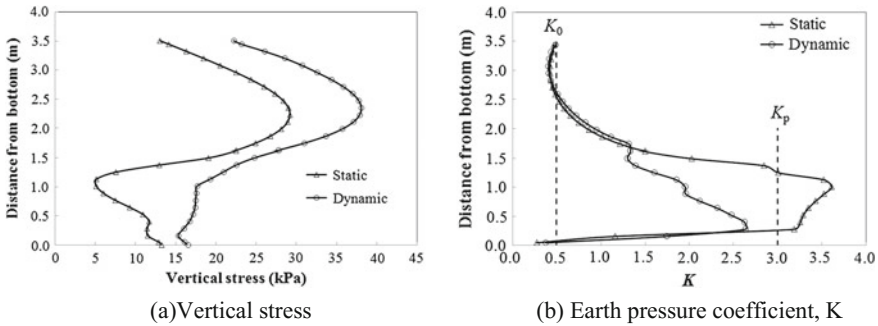
Fig. 5 Vertical stress and earth pressure coefficient of embankment on a vertical profile through the midpoint of subsoil **a** Vertical stress. **b** Earth pressure coefficient, K

certain depth (outer radius surface of arching for Hewlett and Randolph method [2]), then decreases due to the effect of soil arching and reaches to the minimum value at the inner surface of arching for Hewlett and Randolph method. Below this plane, the vertical stress again increases due to the self-weight if the infilling material beneath the inner surface of the arching. This indicates that the soil arching still exists under the dynamic loads.

The earth pressure coefficient K of embankment in Fig. 5b is defined as $K = \sigma_h/\sigma_v$, where σ_h and σ_v are the horizontal and vertical stress, respectively. The vertical dotted lines of $K_0 = 1 - \sin\varphi = 0.5$ and $K_P = (1 + \sin\varphi)/(1 - \sin\varphi) = 3$ are plotted to represent the earth pressure coefficient at rest and the Rankine passive earth pressure coefficient. As clearly seen, the value of K both under dynamic and static loads approximately equals to K_0 (i.e., no effect from arching) above a certain depth of the embankment and then gradually increases to the maximum value, and finally decreases until to the bottom of the embankment. Due to the effect of the dynamic

loads, the maximum value of earth pressure coefficient K is much smaller than that under the static loads with the difference of approximately 38%, indicating a decrease of the soil arching, which is consistent with the findings in [6].

Conclusions

Soil arching plays an important role in the load transfer of the piled embankment, and has been well investigated in the last few decades. However, most of the studies have been done are focused on the behavior of soil arching effect under static loads, while very limited research has been conducted for that under dynamic loads. This paper presented an investigation of the soil arching effect in the piled embankment under shakedown limit loads. Firstly, a 3D FE model combined with Melan's lower-bound shakedown theorem is presented, in which the elastic stress field was obtained from the FE model. The shakedown limits can therefore be calculated as the minimum shakedown multiplier among all layers of the piled embankment by means of a self-equilibrated critical residual stress field. It showed that the shakedown limit loads decreased with the increase of the frictional coefficient, which decreases by approximately 77% when increasing μ from 0.2 to 1.0. Secondly, the shakedown limit loads for the condition of $\mu = 0$ was applied onto the surface of pavement as the external traffic loads, which moved at a speed of 60 km/h for 40 cycles. The settlement at the surface of the pavement increased gradually within the first a few load cycles, and then approaches to approximately a steady value, indicating that the piled embankment in a shakedown status. Finally, the soil arching effect under the moving shakedown limit loads was investigated in terms of the settlement profile, vertical stress and earth pressure coefficient both under static and dynamic loads. It showed that the soil arching effect remained existed, while was significantly reduced under the shakedown limit loads.

References

1. Terzaghi, K. (1943). Theoretical Soil Mechanics. Wiley, New York, NY, USA.
2. Hewlett, W.J. and Randolph, M.F. (1988). Analysis of piled embankments. Ground Engineering 21(3): 12–18.
3. BS 8006-1 (2010). Code of practice for strengthened/ reinforced soils and other fills. BSI, London, UK.
4. EBGEO (2011). Recommendations for Design and Analysis of Earth Structures Using Geosynthetic Reinforcements -EBGEO. German Geotechnical Society, Berlin, Germany.

5. Van Eekelen, S.J.M., Bezuijen, A., and Van Tol, A.F. (2013). An analytical model for arching in piled embankments. Geotextiles and Geomembranes, 39(4): 78–102.

6. Heitz, C., Lüking, J., Kempfert, H.G. (2008). Geosynthetic reinforced and pile supported embankments under static and cyclic loading. Strain 1:1–5.

7. Han, J. and Bhandari, A. (2009). Evaluation of geogrid-reinforced pile-supported embankments under cyclic loading using discrete element method. In: US-China workshop on ground improvement technologies, Orlando, Florida; ASCE-GSP 188, 73–82.

8. Han, G.X., Gong, Q.M., Zhou, S.H.. Soil arching in a piled embankment under dynamic load. International Journal of Geomechanics, 2015; 15(6): 04014094.

9. Sharp, R.W., Booker, J.R. (1984). Shakedown of pavements under moving surface loads. Journal of Transportation Engineering, 110(1), 1–14.

10. Ponter, A.R.S., Hearle, A.D., Johnson, K.L.(1985). Application of the kinematical shakedown theorem to rolling and sliding point contacts. Journal of the Mechanics and Physics of Solids, 33: 339–362.

11. Krabbenhøft, K., Lyamin, A.V., Sloan, S.W. (2007). Shakedown of a cohesive-frictional half-space subjected to rolling and sliding contact. International Journal of Solids and Structures, 44(11-12): 3998–4008.

12. Yu, H.S., Wang, J. (2012). Three-dimensional shakedown solutions for cohesive-frictional materials under moving surface loads. International Journal of Solids and Structures, 49, 3797–3807.

Numerical Calculation of Reducing Negative Shaft Resistance of Group Piles with Asphalt Coats

Yanfen Wang, Yuangang Ma and Caojiong Lv

Introduction

In the late 1940s, abroad the engineering group of rock and soil gradually know negative shaft resistance of piles. In the 1960s to 1970s, it became a hotspot in engineering group of rock and soil. Researchers have done many model experiments and tests in spots, and proposed a lot of coherent theories and calculation methods. The concept of neutral point is put forward in the phase. Johanessen and Bjerrum [1], Bjerrum [2], Darvall [3], Endo [4], Fellenius [5], Clemente [6] and Bozozuk [7] have all researched the subject matter by tests, and downdrag by the negative shaft resistances are discussed in detail. In our country the research commences in 1980s. With the development of Chinese urban construction, experts and scholars gradually attach importance to the subject. The initial researches are primarily aimed at the negative shaft resistances in loess collapsible under overburden pressure area and coal pits. The next 20 years, the research for negative shaft resistances of piles continuously deepens in our country.

In recent years, numerical methods have made tremendous progresses in researches and application methods. Numerical analysis is a base trend of the design development. In principle, numerical analysis methods can consider many factors which influence negative shaft resistances of piles, such as interaction between pile

Y. Wang (✉) · Y. Ma · C. Lv
China Railway Bridge Science Research Institute Co., Ltd, Beijing, China
e-mail: 11316583@qq.com

Y. Ma
e-mail: brsi2004@126.com

C. Lv
e-mail: 411934034@qq.com

Y. Wang · Y. Ma · C. Lv
Health and Safety State Key Laboratory of Bridge Structure, Wuhan 430034, China

635

and soil, effects of group piles, etc. Finite element software is mainly used in existing researches for negative shaft resistance of piles. In this paper, the finite difference software FLAC3D is used to analyze a project example on negative shaft resistance of group piles.

Project Profile

A extra road and railroad bridge across the Yellow River, with railway bridge long 14.887 km, road main bridge long 11.575 km, segment of road and railway long 9.177 km, is the longest road and railway combined bridge in our country at present. All foundations of the bridge use piles foundation, and piles diameters are 1.2–2.0 m, and piles lengths are 70–95 m. Geologic survey and stratum reconnaissance show that the bridge spot is at the silting field where exists soft soil and unconsolidated soil. In action of deadweight, recently sedimentary soil has not consolidated. Soil gradually sinks. Conditions around piles foundations under piers of the bridge can make outstanding negative shaft resistances.

A pier locates at the north levee of the Yellow River where soft soil is thicker and piles are longer. According to geology survey, Stratified soil and mechanical parameters are listed as Table 1.

In allusion to characters of ground base, steel protected tubes are covered and asphalt coats are spouted for piles segments which belong to compressible stratums or are above neutral point.

Steel protected tubes are covered at the bottoms of cushion caps. Asphalt coats are spouted outside steel protected tubes. Steel protected tubes are wrapped by Q235 steel plates whose thicknesses are 1.4 cm, external diameters are 1.7 m and lengths are 16 m (as Fig. 1).

Modal Establishment

A quarter of modal of practice group piles are calculated. Layout of group piles are show in Fig. 2 and elements division of clays modal are show in Fig. 3. Material modal of clays use Morh-Coulomb Modal whose failure envelope line corresponds to Morh-Column criterion (shear yield function) with tension cutoff (tension yield function). The position of a stress point on this envelope is controlled by a non-associated flow rule for shear failure and an associated rule for tension failure.

Each pile length is 95 m, and the pile diameter is 1.5 m. The elastic ratio of the pile equals to 3.0×10^4 MPa and the Poisson ratio equals to 0.167. The pile is modeled by pile structure elements (pileSELs) of the finite difference software FLAC3D. PileSELs are two-noded, straight finite element with six degrees-of-freedom per node. Piles interact with the soils grid via shear and normal coupling springs in FLAC3D.

Table 1 Earth delaminations and mechanical parameters

Title	Thickness (m)	Density (g/cm³)	Moisture content (%)	Plasticity index	Cohesive strength c(kPa)	Internal friction angle (°)	Porocity ratio (e₀)	Modulus of compression Eₛ(MPa)
Accretion earth	4.0	1.96	29.5	6.1	33.0	20.0	0.783	15.63
Silt	4.0	1.95	28.8	6.5	17.75	11.55	0.804	17.82
Silty clay	2.6	1.94	30.5	4.0	18.5	24.6	0.853	7.53
Rock flour	1.0	2.00	25.6		25.4	25.1	0.696	45.57
Silty clay	2.7	1.98	28.9	12.5	26.4	13.4	0.779	14.67
Fine sand	2.4	2.06	20.2		5.1	31.2	0.600	34.56
Silty clay	2.0	2.10	25.4	15.4	45.0	20.5	0.630	26.85
Medium sand	17.3	2.14	15.3		16.0	30.3	0.447	53.67
Medium sand	12.0	2.06	19.9		6.3	36.0	0.653	52.50
Fine sand	12.5	2.02	22.9		5.1	31.2	0.65	37.38
Medium sand	3.7	2.08	18.1		10.5	34.6	0.60	60.03
Silty clay	13.3	2.06	23.7	13.9	63.03	16.07	0.63	32.55
Silt	4.4	2.00	25.1	7.3	31.35	25.7	0.67	47.07
Fine sand	13.5	1.98	15.5	12.5	5.1	31.2	0.45	58.47
Medium sand	4.0	2.06	19.9		6.2	34.2	0.55	50.16
Silty clay	3.5	2.10	22.4	13.1	45.0	20.5	0.59	30.00
Medium sand	2.6	2.06	19.9		6.2	34.2	0.55	50.16

Fig. 1 Steel shield tube layout of group piles (unit: cm)

Fig. 2 Layout of piles

The space between the bottom of platform and the soil surface is 4 m. Elements of platform use elastic model. The rule of stresses and strains are linear. Materials of platform are sameness with piles' materials. Elements of platform use entities elements whose whole parameters are sameness with piles' materials.

According to relevant documents, asphalt spouted on steel protected tubes can reduce 70–90% negative frictional resistance of piles sides. This paper uses 90% off-load ratio of asphalt coats by relevant tests. The aim is achieved by adjusting main linking parameters between soils and piles.

There are problems of original ground stresses in numerical simulations of soils and rocks. Original stresses field of stratums exist before piles foundations are constructed whose forms relate to stratums structures, stratums characters, stratums

Fig. 3 Division of model grid

bedding conditions and loads history, etc. Original ground stresses are simulated by establishing original conditions in grids of the finite difference software. Transformation of ground stresses with the depth increasing can be realized by stresses gradients.

Vertical ground stresses can be obtained by manual computation. Vertical ground stresses gradients are unit weights of corresponding soil layers. Horizontal ground stresses usually take 50–75% of vertical ground stresses, and horizontal gradients are so. In this paper, they all take 67%.

The maximum thickness of the silt located at the pier equals to 3.4 m. The unit weight of the silt is 17,300 N/m3, and stack loads of the silt is 58,820 Pa. Stack loads are divided into three levels. They are 17,300, 34,600 and 58,800 Pa. Considering design loads of combining loads of superstructures, uniform forces applied on the platform cap in the area of the pier correspond to apply the design load on each pile cap which equals to 5×106 N.

Results

Without asphalt coats, when the height of stacking loads is 3.4 m, settlements of the modal by calculated are shown in Fig. 4. Axial forces of all pile are shown in Fig. 5 (Fig. 6).
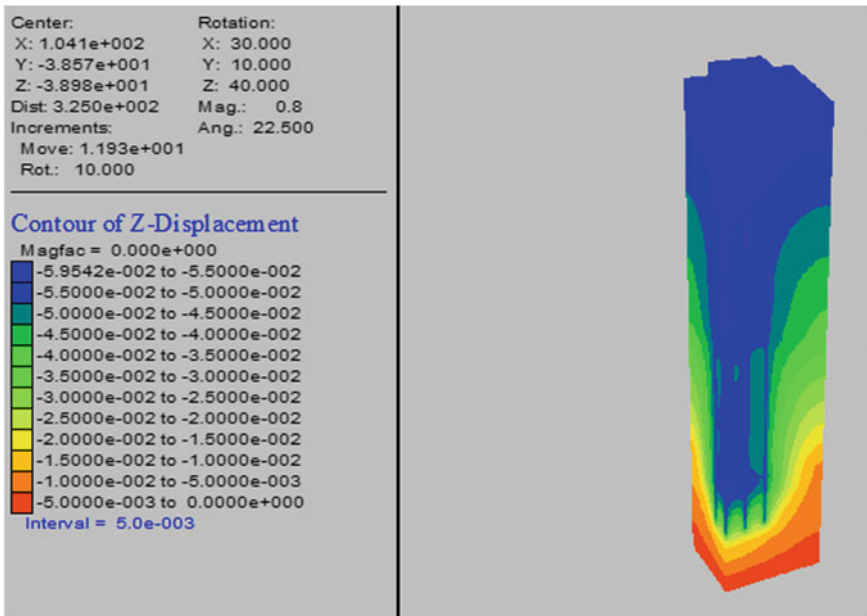
Fig. 4 Settlement of model without coat caused by heaped load

Fig. 5 Axial force distribution of piles without coat (piling height of 3.4 m)
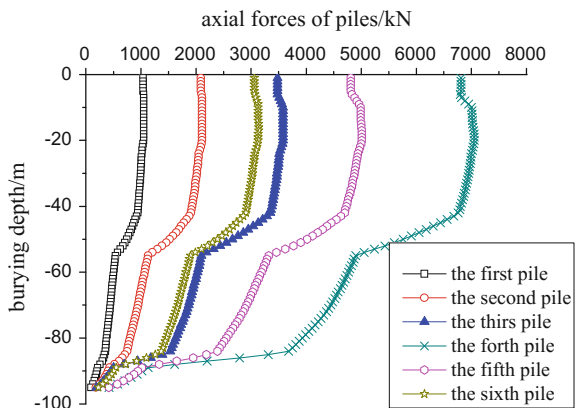
Fig. 6 Axial force distribution of the forth pile (without coat)
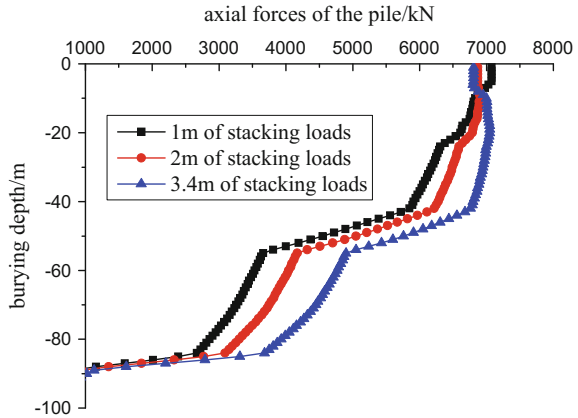
Figures 7 and 8 show axial forces, shaft resistances of piles sides and settlements caused by stacking loads of the forth pile (the angle pile) in cases of three levels stacking loads without asphalt coats.

Figure 9 show axial forces, shaft resistances of piles sides and settlements caused by stacking loads of the forth pile (the angle pile) in cases of three levels stacking loads with asphalt coats.

By the computing, it will be find that

(1) Effects of group piles are obvious. The axial force of the center pile is the least, and the axial force of the corner pile is biggest. As the second level stacking loads and the third level stacking loads, negative shaft resistances appear on all piles. The neutral point position of the corner pile is deepest which equal to 19 m.

(2) As the first level stacking loads, there are no negative shaft resistances on piles. But as the second level stacking loads, they appear. The position of the neutral point is at the lower 9 m of the piles caps. When the stacking loads are the third

Fig. 7 Settlement curve of the forth pile (without coat)
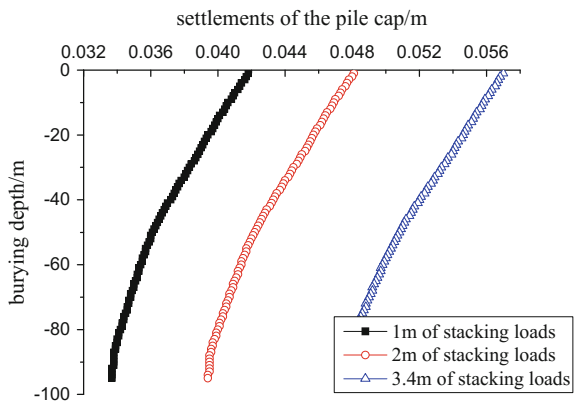
Fig. 8 Axial force distribution of the forth pile (with coat)
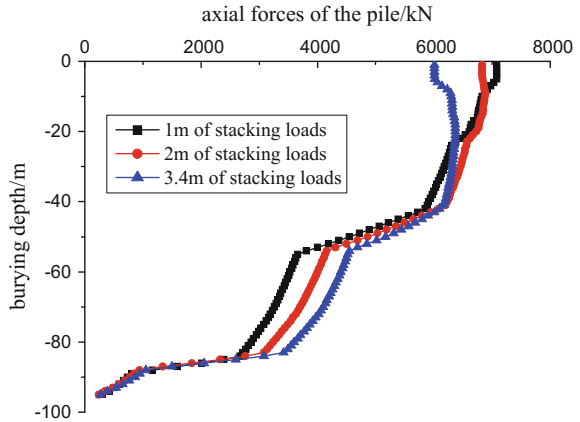
Fig. 9 Settlement curve of the forth pile (with coat)
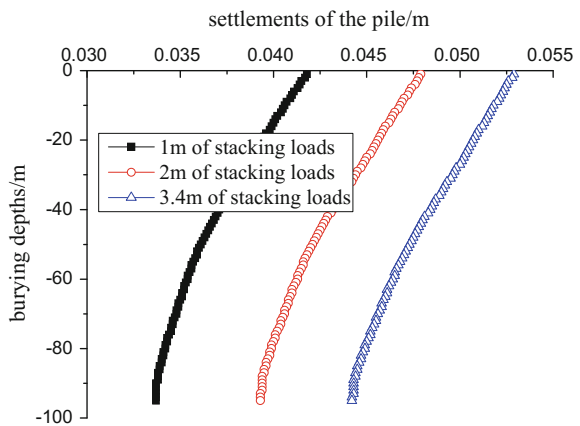
level, the position of the neutral point is at the lower 19 m of the piles caps. That along with stacking loads increasing, the area of negative frictional resistances is enlarged, and positions of neutral points are lowered. At the same time, absolute values of negative shaft resistances are bigger.

(3) The bigger stacking loads are, the more obvious differences of axial forces between with asphalt coats and without asphalt coats.

(4) Corresponding to different stacking loads, piles caps settlements of the corner pile without asphalt coats are individually 0.042, 0.048 and 0.057 m. Piles caps settlements of the corner pile with asphalt coats are individually 0.042, 0.046 and 0.057 m. Reducing ratios of settlements are 0, 0.4 and 7.2% individually. That indicates the more stacking loads are, the bigger reducing effects during to asphalt coats of settlements caused by stacking loads are.

Conclusions

Conclusions can be obtained from the above computation as follows:

(1) The finite difference software can better simulate negative shaft resistances of piles foundations.
(2) By adjusting connecting parameters, the software simulate reducing effects of asphalt coats. Computation results show that the neutral point position of the corner pile is the minimum and the area of negative shaft resistance of the corner pile is biggest, and that of the center pile is least. That matches with practice rules. It offers a new simulation method for designs and computations of practice engineering.
(3) The results also show that as stacking loads increasing, the area of negative shaft resistances extends, i.e. the position of the neutral position moves downwards, and absolute values of negative shaft resistances augment. Reducing effects of negative shaft resistances during to asphalt coats are obvious. The bigger stacking loads are, the more the settlements reducing effects of stacking loads during to asphalt coats are. Those rules have guiding significance to the practice projects.

References

1. Johannesson L J, Bjerrum L. Measurements of the Compression of a Steel Pile to Rock due to Settlement of the Surrounding clay. Proceedings 6th International Conference on Soil Mechanics and Foundation Engineering. Montreal, 1965, 2: 261–264.
2. Bjerrum L, Johannesson I J, Eide O. Reduction of Negative Skin Friction on Steel Piles to Rock. Proc 7th International Conference on Soil Mechanics and Foundation Engineering, Mexico City, 1969, 2: 27–34.
3. Walker L K, Darvall P L. Downdrag on coated and uncoated piles. Proc 8th ICSMFE, Moscow,1973, 2: 257–262.
4. Endo M, Minou A, Kawasaki T, Shibata T. Negative Skin Friction Acting on Steel Piles in Clay. Proc 7th International Conference on Soil Mechanics and Foundation Engineering, Mexico City, 1969, 2: 85–92.
5. Fellenius B H. Downdrag on Piles in Clay due to Negative Skin Friction. Canadian Geotechnical Journal. 1972, 9(4): 323–337.
6. Clemente F M. Downdrag: A Comparative Study of Bitumen Coated and Uncoated Prestressed Piles. Proceedings, Associated Pile and Fitting 7th Pile Talk Seminar. New York, 1979: 49–71.
7. Bozozuk M. Bearing Capacity of a Pile Preloaded by Download. Proc 10th International Conference on Soil Mechanics and Foundation Engineering, Stockholm. 1981, 2: 631–636.

Performance of Conductive Plastic Vertical Drainage Board Under Vacuum Preloading Combined with Electro-osmotic Consolidation

Yang Shen, Chenchen Qiu, Yande Li and Yanfeng You

Introduction

Due to the urgent demand for expressway ground improvement in coastal regions, researchers have been spending a great deal of effort and money on the dewatering of soft clay subgrade. Mention the traditional methods, the electro-osmotic dewatering method could drain water out of the low permeable soft clay and consolidate soil subgrade in a relatively short period of time. However, due to the electro-chemical reaction, metal electrode would be corroded and of which has restricted its application [1]. To avoid corrosion of mental electrodes, researchers begin to focus on the reform of new electrode materials. The researchers tried a variety of electrode materials, such as the reactive electrode (copper, iron, or aluminium) and the inert electrode (graphite or platinum). The test results showed that the reactive electrode would be corroded due to the electrolysis, and the inert electrode would also be corroded due to changes in temperature and pH [2–6].

The electro-kinetic geo-synthetics (EKG) are a technology that may be applied to mitigate the aforementioned issues. Researchers from the United Kingdom were the first to propose the concept, and their studies defined the filtration, conduction, drainage, reinforcement ability [7]. Structure-type conductive plastic but also

Y. Shen · C. Qiu (✉) · Y. Li
Key Laboratory of Ministry of Education for Geo-mechanics and Embankment
Engineering, Hohai University, Nanjing 210098, China
e-mail: ccqiu92@163.com

Y. Shen
e-mail: shenyang1998@163.com

Y. Li
e-mail: meilimeijia@126.com

Y. You
Department of Civil Engineering and Transportation, Hohai University, Nanjing, China
e-mail: yyf52308@163.com

composite conductive plastic could both be used to make the EKG electrode. In this paper, the composite conductive plastic was manufactured into the shape of a prefabricated electric vertical drainage board (e-PVD). Several researches have been carried out regarding the new materials [8–13].

Performance of the advanced e-PVD board was systematically studied in this paper. First, vertical drainage capacity from the top and bottom of the soil during the electro-osmotic dewatering process was experimentally analyzed. Furthermore, the electro-osmotic consolidation method was then combined with the vacuum preloading method to compare drainage differences among the vacuum preloading method (V-P), the vacuum preloading combined with electro-osmosis method (V-E) and the cathode straight drainage method (C-S). Parameters, such as drainage amount, moisture content, vane shear strength, current, potential change rule, vertical settlement and crack extension law, were monitored. Suggestions for the improvement of treatment efficiency were determined.

Methods and Materials

Materials

The properties of the soft clay used in these tests were showed in Table 1. Each test employed new soft clay.

The structure of the e-PVD board can be seen in Fig. 1. Both sides were covered with a groove for drainage, brass wires, and a conductive geomembrane. It contained polyethylene, carbon black, and graphite (mass ratio = 1: (0.3–0.35): (0.05–0.1)). The brass wires were protected by the electric polymer plastics and transmission electric energy during the test. The e-PVD board's resistivity was 103 Ω m. In addition, it was covered with membrane to act as reversed filter. The actual product can be seen in Fig. 2. This new kind of e-PVD board could shorten

Table 1 Basic physical properties of undisturbed soil

Specific gravity	Liquid limit (%)	Plastic limit (%)	Plasticity index	Paretical composition (%)		
				Sand	Silt	Clay
2.75	24.07	43.74	19.67	0	19.76	80.24
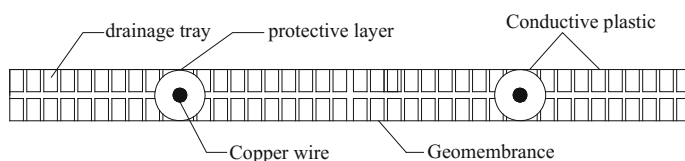
Fig. 1 Diagram for the e-PVD board

Fig. 2 Real product of the
e-PVD board

consolidation time and avoid the electrolytic reaction of metal electrode during the test, when compared with traditional metal electrode.

Experimental Design

The B-D method was applied in most of electro-osmotic (E-O) tests in laboratory, through which water could be drained out when it reached the cathode. However, this method could only simulate the electro-osmosis well-point dewatering method. It was inconsistent with practical engineering, such as the improvement of super soft clay soil. For purpose of comparing the differences on those parameters, the drainage volume and rate and the electric energy utilization, between the top drainage (T-D) and the B-D method, a comparative test was conducted.

The conductive plastic was specially tailored to look identical to the prefabricated vertical drainage board. For purpose of testing the actual ability of the e-PVD board, comparative tests on the drainage ability among the V-P method, the V-E method, the C-S method were carried out in the self-developed model tank. The vacuum pressure was set as 60 kPa in order to monitor the treatment effect at a certain depth.

Experimental Apparatus

In consideration of the research purpose, there were two sets of test apparatuses created for this experiment:

The model device was made of organic glass (L × W × D = 600 mm × 600 mm × 400 mm). There were holes in the basement of the model device for the

Fig. 3 Model tank filled with soil samples

B-D experiment to drain water away (Fig. 3). The length of the e-PVD electrode was 400 mm, and it was linked to the electric source through electric wires. The soil sample thickness was 200 mm. In order to make the soil sample denser, it was divided into four layers. Each layer was filled and compacted carefully. For the B-D experiment, the sand cushion's thickness was 50 mm, was placed under the soil. For the T-D experiment, the sand cushion was placed on the top, where a pumping pipeline was placed (Fig. 4). The pumping pipeline was wrapped by with a geotextile. When the water arrived at the pipelines, it would be drained out immediately. The water was pumped every 2 h for the first 30 h and every 4 h for the last 20 h. There were eight potential probes and the layout of which was showed in Fig. 5. They were set 2, 14, 26, and 38 cm away from the anode.

The model tank for the V-E test, which was also made of organic glass, can be seen in Fig. 6 (L × W × D = 250 mm × 200 mm × 500 mm). The length of the

Fig. 4 Model device of experiment
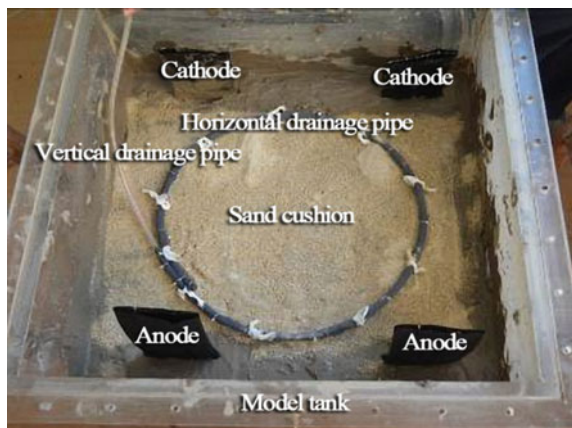
Fig. 5 The layout of the potential probes
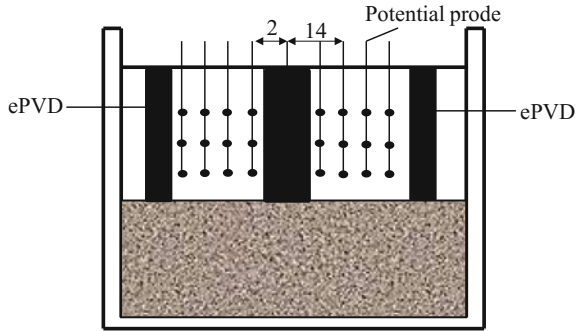
Fig. 6 Model devices for the V-P test, the V-E tests and the C-S tests
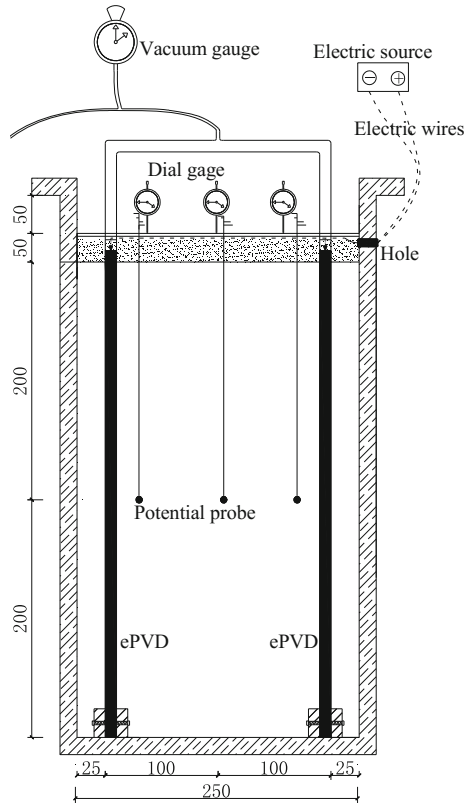
electrode was about 425 mm, and it was linked to the electric source through electric wires and the vacuum gauge at the top of the electrode. A hole which was gaged with a rubber plug was set in the model tank to make a connection between the electrodes and the electric source. Three dial gages were set at the top of the soil sample to monitor the settlement. The soil thickness was 400 mm, and a 50 mm

thick sand cushion was filled on the top of the soil. The distance between the electrodes was maintained at 200 mm with an electric voltage different of 20 V. When the electrode and the potential probe were embedded in the soil, the soil was sealed by the vacuum membrane.

Experiment Procedures

There were two different drainage methods employed (top and bottom) in the E-O test. The concrete steps are listed below:

1. The soil was filled and compacted carefully in the model device.
2. After the e-PVD board, the potential probe were embedded in the predetermined positions, the wires were then connected to the electric source.
3. The electric source was opened. The current, potential gradient, drainage amount and rate were measured periodically.
4. After the test, the shear strength and water content were measured in the predetermined positions.

In the V-P, the V-E tests and the C-S tests, the test parameters were listed in Table 2. When the soil sample was layered out and all of the monitor probes were embedded, the soil sample was sealed by geomembrane. The electric source and the vacuum pump were opened, and the discharge amount and rate, vane shear strength and water content were monitored during the test.

Table 2 Summary of contrast tests parameters

Test no.	Test code	Voltage (V)	Electrode material	Vacuum degree (kPa)
1	V-P method	0	e-PVD board	60
2	V-E method	20	e-PVD board	60
3	C-S method	20	e-PVD board	60

Results and Discussion

Discharge

The B-D method stopped drainage within 180 h, while the T-D method took only 120 h (Fig. 7). Total drainage volume of the T-D method seemed less than that of B-D method; however, it was not counted on for the water held in the sand. Water content of the sand after the test was 11.7%. Drainage volume in the sand was 3344 ml, and water discharge between two methods was roughly the same after adding this amount to the previous volume. Discharge of the B-D method was larger than that of T-D method due to gravity, but water could not be drained out from the bottom channel in the soft ground engineering treatment project. The drainage velocity (the tangent line of any point in the curve) of the T-D method at the initial phase was clearly higher than the B-D method. Accidents that may occurred during foundation treatment, for instance uneven settlement between the electrodes and shear destruction could be avoided.

The discharge is the most intuitionist control index for each drainage consolidation method. To fully demonstrate the e-PVD board's performance, the E-O method was combined with the V-P method so that water could be drained more quickly and more abundantly. The test result is presented in Fig. 8.

The total discharge of the V-E method was the largest (Fig. 8). However, the drainage velocity and discharge were roughly the same during the first 30 h for the V-P method. The useful effect of the electro-osmosis method was reflected after 30 h. This delay was due free water being drained in the early stage and bound water being drained in the late stage. As the effect from vacuum preloading lacked late stage, water moisture could still be drained out by electro-osmosis.

What's more, in the initial stages, the soil has large water content and multiple drainage channels. Therefore, the unilateral drainage method which used by the cathode straight drainage method can avoid the inhibition between the vacuum

Fig. 7 Discharge between the T-D and B-D method
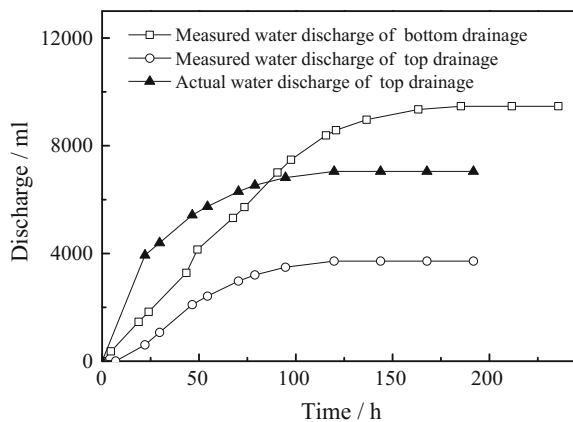
Fig. 8 Discharge of the V-E
test, the V-P test, and the C-S
test
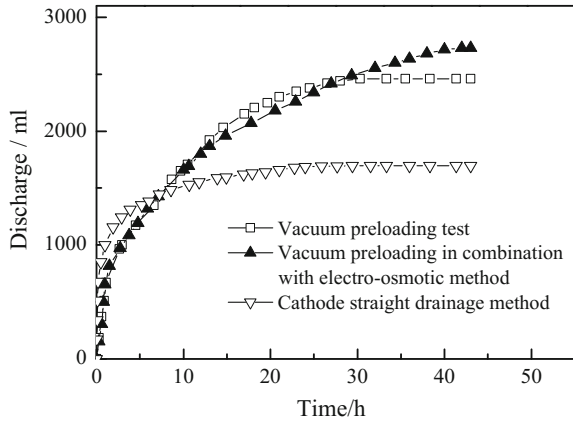
preloading and the electro-osmosis. Comparing the two sets of electro-osmosis in combination with vacuum preloading method, the drainage velocity and drainage amount of the cathode straight drainage method are larger during the first 8 h. The cathode straight drainage method has a better effect on drainage at the early period. However, the drainage ability gradually became worse in the middle-later period due to the longer drainage path.

Moisture Content

Figure 9 shows the distribution of water content of the soil for the T-D and B-D method after the test. The maximum and minimum values, between the electrodes, were at the bottom of the cathode and anode, respectively. Around the anode, the

Fig. 9 Moisture content
curves for the T-D and B-D
method
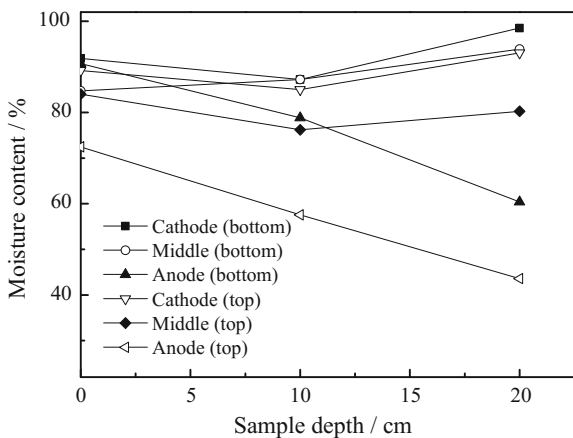
Fig. 10 Moisture content curves for the V-E test, the V-P test and the C-S test
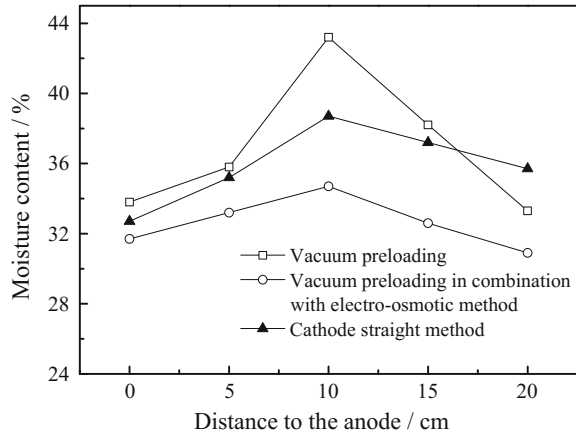
water ratio decreased with depth. Since the negative pore pressure around the anode, the water content increased from the anode to the cathode (A-C). It was later for the B-D method to lost effectiveness, compared with the T-D method. When the T-D method lost effectiveness, water would still be drained out from the cathode.

Figure 10 shows soil moisture content distribution of the V-P method, the V-E method and the C-S method after the test. The water content of the V-E method was the lowest at the same position. The water content increased gradually from the anode to the middle portion and declined gradually from the middle portion to the cathode. In addition, the moisture content around the anode was lower than that around the cathode. The uniformity of the soil moisture content of the V-E method was better than that of the V-P method.

Considering the moisture content distribution of the C-S method, Moisture content in the anode was lower than which in the cathode due to the water flowing to the cathode. This result indicated that the anode produce inhibition effect in the vacuum preloading combined with electro-osmotic method while the cathode straight method can alleviates the inhibitory effect.

Shear Strength

As shown in Fig. 11, the consolidation effect of the T-D method was better than that of the B-D method around the anode. Moreover, shear strength of the T-D method, in the middle and cathode regions, was lower than that of the B-D method, but not too much. However, vane shear strength of the T-D method exceeded that of the B-D method. In comparison with the actual acquirements in engineering, the water content was higher and the soil strength was lower in laboratory, because of the size effect. It was may be that there were no further actions, such as compaction or electrode conversion, taken to reinforce the soft clay foundation. It was
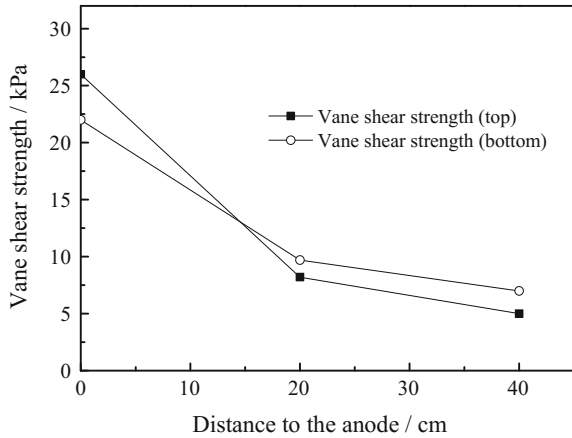
recommended that the methods referred above applied at the anaphase of the experiment. Both the water content and the vane shear strength after the test showed the superiority of T-D method around the anode.

Figure 12 demonstrates that the vane shear strength of the V-E method was larger than that of the V-P method. There was little change at different positions of the soil sample in the V-P experiment. However, the vane shear strength declined gradually from the A-C gradually in the V-E experiment. The soil strength around the anode was 26 kPa in the V-E experiment, far larger than the 14.3 kPa at the same position in the V-P experiment. The improvement ratio was 81.8%, which indicated the effectiveness of the e-PVD board for the electro-osmotic improvement of soft clay foundation.

compared with the V-E method, the moisture content in different portions was roughly the same, the uniformity of the soil moisture content of the C-S method was better than that of the V-E method, the water content distribution showed the

Fig. 12 Vane shear strength
after the treatment for the V-P
method, the V-E method and
the C-S method
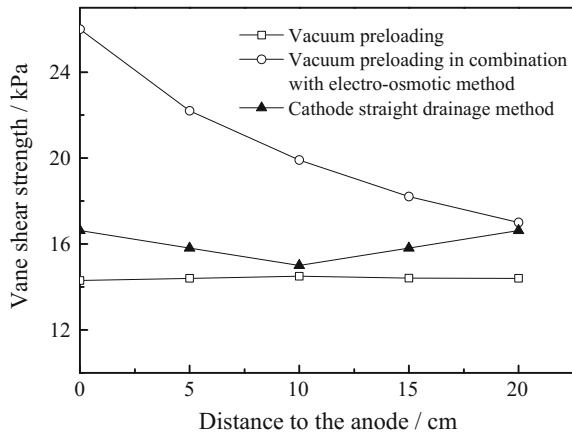
superiority of electrodes conversion. Moreover, shear strength of the C-S method around the anode and cathode regions was higher than that of the V-P method; however, drainage amount of V-P method exceeded that of the C-S method. This difference was due to the combination between the vacuum preloading and the electro-osmosis, as shown in Fig. 6, the drainage velocity and drainage amount was the largest among these tests. The effect of vacuum preloading was obviously improved in combination with the electro-osmosis, and the quickly decreasing of water content in the surficial soil contributing to the obviously increasing of the effective stress; the shear strength of the C-S method in the surficial soil exceeded that of V-P method. Meanwhile, considering the electrodes conversion of the C-S method, the precipitation generated around the anode and the cathode consolidate the soil around the drainage plate regions, and the shear strength of the soil increases. Accordingly, the V-P method in the combination with electro-osmosis improved the drainage and strength.

Accordingly, the soil strength of the T-D method was a little less than the B-D method. The E-O method could improve the treatment effect greatly on the basis of V-P method.

Potential Distribution

Figure 13 shows the change of potential gradient between the electrodes. The potential gradient decreased slowly with decreasing potential difference, simultaneously the soil resistance increased constantly as water content declined. Drainage amount and rate declined gradually, which proved that the potential gradient would greatly influence the e-PVD board drainage ability. Measures need to be taken to slow down the rising tendency of resistance. Finally, drainage ability of the e-PVD would be promoted and electric energy be saved.

Fig. 13 Potential gradients between the anode and cathode for the T-D method
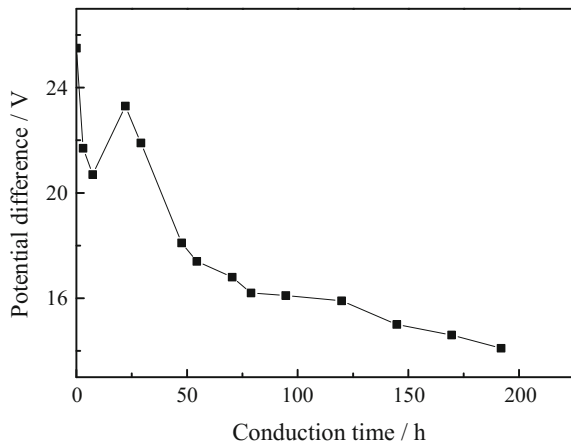
Fig. 14 Potential gradients between the anode and the cathode in the V-E experiment
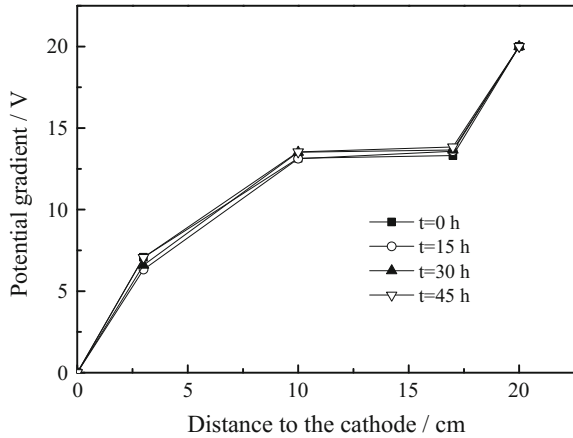
Figure 14 shows the change rule of the potential gradient between the electrodes in the V-E experiment. The potential gradient between the electrodes remained stable during the experiment. But as showed in this Figure, there was a potential gradient increase happening suddenly, this increasing can be due to the interfacial potential between the anode plate and soil. The effective potential gradient was nearly 33% of the total applied voltage. It could be identified as the control index to contrast the E-O performance of different EKG materials.

Figure 15 shows the change of potential gradient between the electrodes in the 200 mm soil depth for the C-S method. The potential value of the soil is the sum of interface potential and efficient electric potential. The sudden increase in the potential of the interface occurs after the conversion of the electrode due to the interface electric resistance increasing. As showed in the figure, the maximum value of potential curve after electrodes transition shows the trend of decreasing.

Fig. 15 Potential gradient for the C-S test
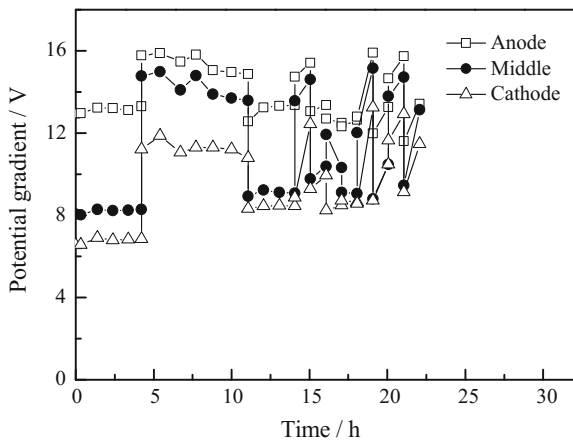
Accordingly, it can be concluded that the vacuum preloading method could attribute to reducing the potential loss on the electrode-soil interface and keep the effective potential in a stable range.

Current

Figure 16 shows the change of current. The change rules of current under the two methods were not stable for the first 40 h. After the time nodes, the currents of the two methods formed continuous decreasing trends that were similar to one another. Therefore, the electric energy consumption was similar for these two means.

Figure 17 shows the change of current for V-E test and C-S test. The drainage velocity and drainage amount of the C-S method were larger.However, the V-P method has more drainage channels, more active and higher current compared with the C-S method. Accordingly, the C-S method applied in foundation treatment alone need further study.

Fig. 16 Variation of current during test for two drainage methods
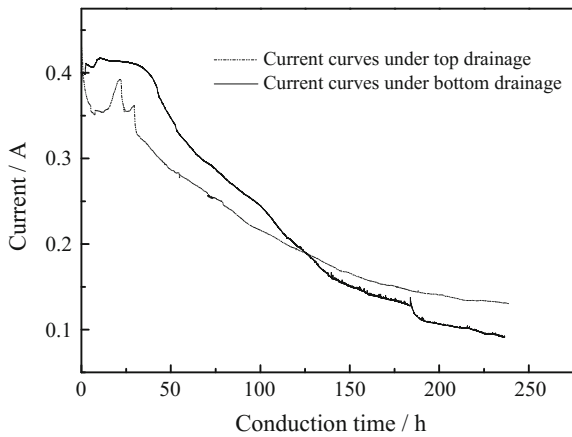
Fig. 17 Variation of current during test for V-E test and C-S test
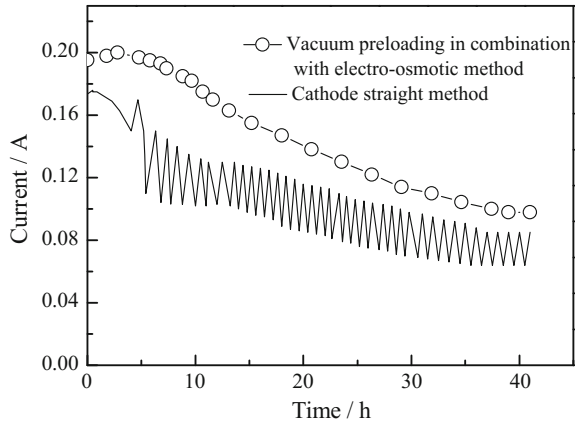
Settlement

Figure 18 demonstrates that the V-P method obtained the maximum settlement while the C-S method achieved a better uniformity of the soil surface. Whether to use the V-P method or to use V-E method, the foundation settlement in the middle portion were both the largest. Because the water is always moving toward the two electrode plate in the test process, so the settlement of the vicinity of the cathode and anode were affected. In comparison with the V-P method, the C-S method can be further improved with the analysis of drainage amount and moisture content if the effect of the vacuum preloading in the late experiment period can be improved. Therefore, considering how to improve the effect of the vacuum preloading in the V-E method was the method to optimize the V-P method.

Fig. 18 Vertical settlement after test for V-P test, V-E test and C-S test
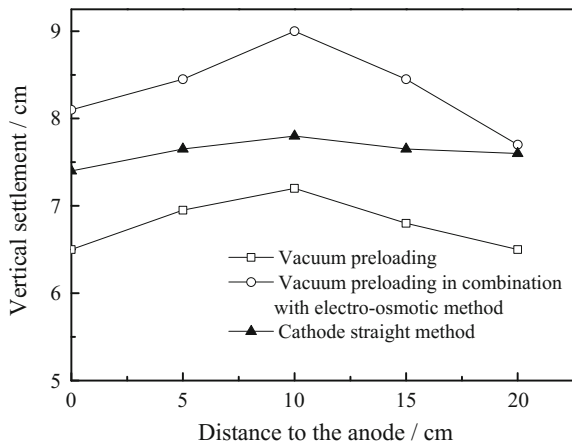
Cracks of Soil

Figures 19 and 20 show the development of cracks in the T-D and B-D methods, respectively. There are noticeable cracks on both sides of the electrode as well as at the connection between the two for the B-D method (Fig. 19), while there are nearly no cracks with the T-D method (Fig. 20). Water was discharged from the top of the sample in the T-D method. As a result, the decreasing velocity of the water drainage from the surface soil was lower than the B-D method. The cracks development tendency would be slowed in the T-D method. Therefore, cracks had difficulty emerging on soil's top surface. In addition, the sand would also prevent the cracks' extension.

Figure 21 shows the cracks development rule of the V-E method in use of the e-PVD board. The cracks accumulated in the middle portion, and stretched to the

Fig. 19 Cracks development pattern in the B-D method
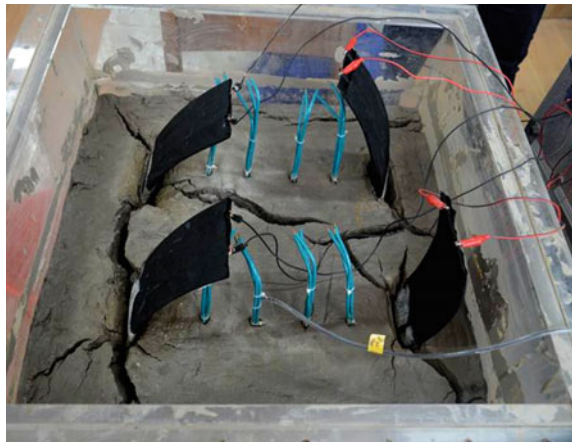
Fig. 20 Cracks development pattern in the T-D method

Fig. 21 Cracks development
rule in the V-E test

other two sides. The water was drained out along the electrode, and it flowed from the middle portion to the electrode. The soil shrank along the direction of the cross section and formed cracks along the vertical direction. Furthermore, the cracks extended from the middle section to the electrode direction with the vacuum pressure from the top surface of the soil (Fig. 21).

The formation of cracks would destroy the drainage channels, which were used for water moving. Accordingly, the water movement rate was reduced in soil and the resistance to water was increased greatly. To improve the treatment effect, it was better to take measures to hold back the development of cracks. Suggested methods for achieving this are the top drainage method or vacuum preloading method.

Conclusions

In this paper, drainage capability for the T-D method and the B-D method with usage of the e-PVD board was experimentally analyzed. The drainage effect among the V-P method alone, V-E method and the C-S method was contrasted. The results showed that the e-PVD board was efficient to drain the water out of the clay soil foundation.

Even though the drainage amount of the T-D method slightly lesser, the initial drainage rate was larger, compared with the B-D method. The consumption of electric energy was similar for these two methods. In terms of practical engineering, energy was saved, and the duration was shortened.

During the test, the T-D method was surpassing of the B-D method on some aspects, such as cracks inhibition, soil reinforcement, and water content reduction.

With the T-D method, not only the consolidation period was accelerated, but also the engineer accident risk was reduced.

The total drainage amount of the V-E method was the largest among these experiments. The beneficial effect of the E-O method was reflected when the V-P method was ineffective. The e-PVD board kept intact after the test, therefore, it is strongly recommended to be applied in engineering.

The usage of the cathode straight method in the initial experiment period can relieve inhibition effect in the anode of the V-E method at a certain extent. Meanwhile, the method that combine the vacuum preloading with the electro-osmosis makes the soil more uniform, more smooth and pH value stable.

References

1. J. Q. Shang (1997). Electro-kinetic dewatering of clay slurries as engineered soil covers. Canadian Geotechnical Journal, 34: 78–86.
2. Rittirong, A, Douglas, R S, Shang, J Q, et al (2008). Electro-kinetic improvement of soft clay using electrical vertical drains. Geo-synthetics International, 15: 369–381.
3. H Wu, L M Hu, Q B Wen (2015). Electro-osmotic enhancement of bentonite with reactive and inert electrodes. Applied Clay Science, 111: 76–82.
4. Y L Tao, J Zhou, X N Gong (2014). Experimental study on function mechanism of electrode materials upon electro-osmotic process. Journal of Zhejiang University-Science A, 48: 1618–1623.
5. Y L Tao, J Zhou, et al (2013). Comparative experiment on influence of ferrum and cuprum electrodes on electroosmotic effects. Chinese Journal of Geotechnical Engineering, 35: 388–394.
6. E T Mohamad, M Z Othman, et al (2011). The effectiveness of electrodes types on electro-osmosis of malaysian soil. The Electronic Journal of Geotechnical Engineering, 16: 887–898.
7. K Ahmad, K A Kassim, M R Taha (2005). Influence of Electrokinetic Processing of A Tropical Soil on The pHs of The Electrolytes', Jabatan Kejuruteraan Awam, 17: 39–48.
8. C J F P Jones, A Hamir, I M Nettleton (1996). Geosynthetic materials with improved reinforcement capabilities. Proceedings of the International Symposium on Earth Reinforcement, 2: 865–883.
9. J Q Shang (1998). Electro-osmosis-enhanced preloading consolidation via vertical drains. Canadian Geotechnical Journal, 35: 491–499.
10. [10] S H Chew, G P Karunaratne, V M Kuma, et al (2004). A field trial for soft clay consolidation using electric vertical drains. Geotextiles Geomembranes, 22:17–35.
11. J. Q. Shang, Q. H. Tang, Y. Q. Xu (2009). Consolidation of marine clay using electrical vertical drains. Geo-mechanics and Engineering, 4: 275–289.
12. G P Karunaratne, H K Jong, S H Chew (2004). New electrically conductive geosynthetics for soft clay consolidation. Proceeding of the 3rd Asian Regional Conference on Geo-synthetics, 277–284.
13. D T Bergado, A S Balasubramaniam, et al (2000). Electro-osmotic consolidation of oft Bangkok Clay with prefabricated vertical drains. Ground Improvement, 4: 153–163.

Stiffness Degradation and Deformation Characteristics of Soft Clay Foundation Under the Train Loads

Yang Shen, Wenhan Du, Baoguang Wang and Mingan Tao

Introduction

The variation of complex stress path of soil caused by traffic loads is different from stress path variation caused by traditional foundation excavation, machine vibration, earthquake and tides. The stress path of soil unit under traffic load is heart-shaped, which involves the coupled principal stress axis rotation and the shear stress magnitude variation [1–5].

This stress path can be expressed by dynamic stress wave. The axial dynamic stress caused by a traffic loads is a pulsing wave, instead of the sine bidirectional wave. Most typically, the axial dynamic stress wave of a traffic load can be expressed as the change of axial dynamic stress with time shown in Fig. 1.

The dynamic stress induced by a traffic load has two primary features. Firstly, the axial dynamic stress changes periodically based on a datum called the static deviator stress (Fig. 1, Note: dashed line indicates the static deviator stress). Secondly, tensile and compressive stresses can both appear in one vibration; therefore, the amplitude ratio (a) is introduced to present initial static stress status: $a = q_p/q_d$, where q_p is the amplitude of the tensile stress and q_d is the amplitude of the compressive stress.

Y. Shen (✉) · W. Du · B. Wang · M. Tao
Key Laboratory of Ministry of Education for Geomechanics
and Embankment Engineering, Hohai University, Nanjing 210098, China
e-mail: Shenyang1998@163.com

W. Du
e-mail: wenhandu2011@163.com

B. Wang
e-mail: baoguang09@126.com

M. Tao
e-mail: taomingan783@126.com

Fig. 1 Axial dynamic stress caused by traffic loading
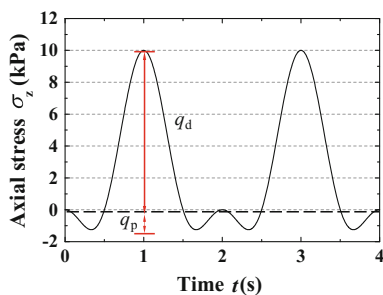
Presently, there are many studies investigating the degradation of clay under complex stress paths. The definition of degradation index is proposed, and the relationship between degradation index and vibration number is established [6, 7]. However, most studies concentrate on the influence of cyclic stress ratio, initial shear stress, over consolidation ration and frequency on the degradation of the clay based on triaxial tests, and establish mathematic models to study degradation properties [8–11]. There are little studies on the degradation index with hollow cylinder apparatus (HCA), a method that can better simulate the stress path of soil.

In this study, a HCA was used to simulate the stress paths induced in traffic-affected ground, a series of undrained shear tests were carried out, different failure modes of soils under different stress levels were discussed, effects of initial deviator stress on the soil stiffness were discussed, and a prediction model of the relation between stiffness degradation and vibration number was established.

The Equipment and Schemes of the Experiment

Samples and the Equipment of the Experiment

Remolded soft clay from Hexi area (Nanjing, China) was adopted for laboratory tests. Improved vacuum preloading technology was applied to ensure uniform properties of the remolded soft clay. The standard size of the hollow cylinder sample was 200 mm high with internal and external diameters of 60 and 100 mm, respectively. The basic physical properties of the samples are displayed in Table 1.

The testing equipment was the 5 Hz HCA developed by GDS Instruments Ltd. in conjunction with Hohai University. During the experiment, the loading process was realized by varying axial stress and torque while remaining internal and

Table 1 Physical properties of soil samples

G_s	w_L %	w_p %	I_p
2.68	42.4	24.5	17.9

external pressure constant. The intermediate stress (σ_2) was always equal to the radial stress (σ_r), and major (σ_1) and minor (σ_3) principal stresses change their directions in a plane perpendicular to the direction of σ_2.

Schemes of the Experiment

In this article, heart-shaped stress paths of remolded soft clay under traffic load were simulated by inputting self-defined wave through HCA [12]. The input wave equation of load and torque are presented as Eqs. (1) and (2).

$$W^{\text{cyc}} = W^{\text{max}}\left(\cos^2(2\pi t/T) - \cos(2\pi t/T)\right) \tag{1}$$

$$M_{\text{T}}^{\text{cyc}} = M_{\text{T}}^{\text{max}}(\sin(2\pi t/T) - 0.5\sin(4\pi t/T)) \tag{2}$$

In Eqs. (1) and (2), W^{cyc} and $M_{\text{T}}^{\text{cyc}}$ refer to load and torque cycles, respectively; W^{max} and $M_{\text{T}}^{\text{max}}$ refer to the maximum amplitudes of load and torque cycles, respectively; T refers to cycle period; and t refers to loading time.

After being assembled in HCA, samples were saturated by back pressure method and then consolidated through isotropic consolidation. Dynamic stress ratio η is introduced to indicate the dynamic stress level, which can be expressed as: $\eta = q_d/p'_0$, where the deviatoric stress amplitude is expressed as $q_d = \max[(\sigma_1 - \sigma_3)/2]$, and p'_0 refers to initial effective spherical stress. The transformation among initial effective spherical stress, axial stress, torque and effective stress can be referred to Ref. [10]. Test programs under different amplitude ratios are shown in Table 2.

Table 2 Test programs under different amplitude ratio

Number	a	η	Vibration (N)	Number	a	η	Vibration (N)
SA1010	0	0.10	10000	SD1010	1	0.10	10000
SA1020		0.20	10000	SD1020		0.20	10000
SA1023		0.23	5694	SD1023		0.23	5190
SA1030		0.30	197	SD1030		0.30	563
SB1010	0.125	0.10	10000		2		
SB1015		0.15	10000	SE1010		0.10	10000
SB1020		0.20	10000	SE1020		0.20	10000
SB1023		0.23	7945	SE1023		0.23	7834
SB1025		0.25	550	SE1030		0.30	280
SB1030		0.30	131				
SC1010	0.5	0.10	10000	SF1010	∞	0.10	10000
SC1020		0.20	10000	SF1020		0.20	10000
SC1023		0.23	5001	SF1023		0.23	582
SC1030		0.30	464	SF1030		0.30	187

Note If the number of vibration is bigger than 10,000 and the sample was still undamaged, it was treated as stable sample and the test stopped

Taking sample SA1023 as an example to explain the meanings of the serial number: S stands for Sample; A stands for $a = 0$ (B stands for $a = 0.125$, C stands for $a = 0.5$, D stands for $a = 1$, E stands for $a = 2$, F stands for $a = \infty$); 10 stands for $p'_0 = 100$ kPa; and 23 stands for $\eta = 0.23$. $f = 0.5$ Hz and $p'_0 = 100$ kPa for all tests. When $a = 0.125$, the initial deviatoric stress equals to 0. **In the article, SB series test are taken as the reference series.**

Data Analysis and Test Results

Characteristics of Generalized Shear Strain

During the test of simulating heart-shaped stress paths with HCA, the vertical, radial and tangential strain occurred at the same time. The generalized shear strain is the coupling results of three principal strains, which can reflect deformation characteristics. The equation of generalized shear strains is shown as Eq. (3):

$$\varepsilon_s = \left(\sqrt{2}/3\right)\sqrt{\left(\varepsilon_1 - \varepsilon_2\right)^2 + \left(\varepsilon_2 - \varepsilon_3\right)^2 + \left(\varepsilon_3 - \varepsilon_1\right)^2} \tag{3}$$

There is much more to the corresponding figures than I have to explain and typical findings are revealed as follows. Taking $a = 0.125$ test as an example, with the increase of η, accumulated axial compressive strain increased gradually. Among them, strain of samples SB1010 and SB1020 increased gently. It is because these samples were in a low dynamic stress level that had little influence on sample structures. However, the strain of samples SB1023 and SB1030 increased sharply after the inflection point, at which the samples' structure changed. As the value of strain exceeds 5%, the macroscopic features of samples indicate compressive failure. However, the degree of damage of sample SB1023 was less than SB1030. The strain of sample SB1023 increased slowly in the early stage of the experiment, and increased exponentially after 5000 loading cycles. This characteristic of deformation can be regarded as a transition stage between stable and sharp failure. Therefore, samples SB1010, SB1023, and SB1030, represented three distinguished deformation models: stable, critical, and destructive. The dynamic stress ratio η corresponding to the critical model can be defined as the critical dynamic stress ratio η_c. When η is smaller than η_c, the sample exhibits damage features of the stable model. When η is larger than η_c, the sample reflects damage features of the destructive model. Although the tensile stress increases with the increase of a, η_c remains stable around 0.23 when samples had compressive failure. This phenomenon indicates that when the amplitude of compressive stress is larger than tensile stress, η_c tends to be a constant, regardless of a.

With the increase of a, the characteristics of the curves can also be divided into three aforementioned models, although these samples endured tensile failures.

Thus, it can be concluded that when $a >1$, there is little compressive deformation of samples, irrespective of the level of stress. Meanwhile, η_c remains around 0.23 when the samples suffer tensile failure.

The Varying Pattern of Secant Shear Modulus

1. Characteristics of axial stress-strain relationship

The hysteretic curves of axial stress-strain relationship under different dynamic stress ratio are shown in Fig. 2. The test results indicated that the hysteretic curves of axial stress-strain have close correlation with the dynamic stress level. For same η, hysteretic curves have similar shapes regardless of a.

To illustrate curve features more clearly, the condition of pure compression (SA series) and pure tension (SF series) are used as examples. In order to compare differences regarding the shape and degree of inclination of hysteretic curves under various loading cycles, cumulative axial strain was ignored in Fig. 2, which means hysteretic curves of different vibrations were translated to the same starting point.

The hysteretic curves of stable model are shown in Fig. 2(a-1, 2) and (b-1, 2). When dynamic stress level is low ($\eta = 0.10$), hysteretic curves are long and narrow, curve shapes and degrees of inclination have little change with the increase of vibration number. When η increases ($\eta = 0.2$), the enclosed areas of hysteretic curves become larger and angle of inclination are gentler. Comparing Fig. 2(a-1)
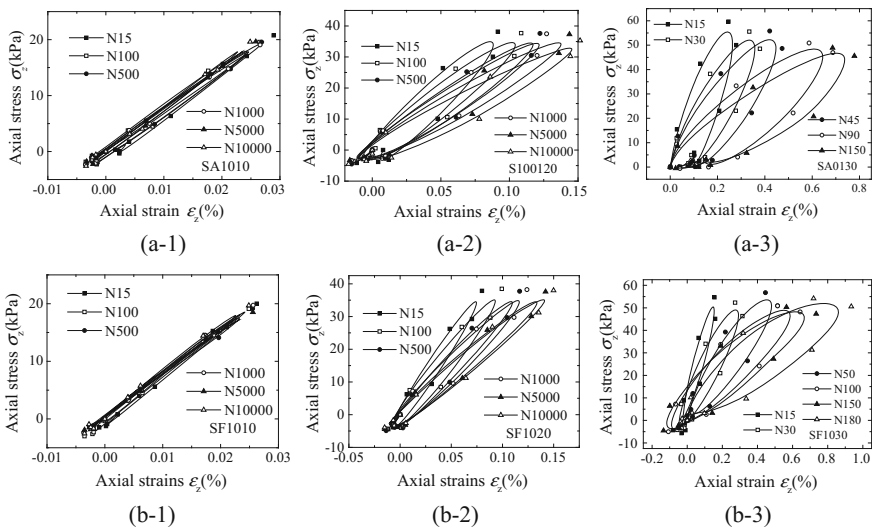
Fig. 2 Hysteretic curves of axial stress-strain under different dynamic stress ratio

and (a-2), the enclosed area and degree of inclination of hysteretic curves increase with the increase of vibration number in early vibration period, and their changes remain stable in later vibration period. For dynamic stress tests of stable model, the system energy gradually dissipates with the increase of vibration number before the accumulated plastic strain and pore water pressure reach their stable state. Moreover, with the increase of strain and pore pressure, stiffness of clay decreases.

The hysteretic curves of destructive model are shown in Fig. 2 (a-3) and (b-3). When the dynamic stress level is high ($\eta = 0.30$), hysteretic curves have large enclosed area in first several loading cycles. With the increase of vibration number, hysteretic curves are stretched and inclined. Degradation of stiffness and strength occurred until the soil was damaged. Therefore, the main difference between stable model and destructive model could be concluded: for stable model, hysteretic curves of different vibrations eventually incline to a same angle; while for destructive model, degrees of inclination of hysteretic curves decrease gradually until the soil was damaged.

The physical explanation regarding of the angle of inclination of hysteretic curves is the decrease characteristics of shear modulus. In Fig. 2, although these curves have similar shape under same dynamic stress ratio η, decrease rates of shear modulus are different, which indicates that the amplitude ratio a has great influenced on the degradation of stiffness. The influence of dynamic stress ratio η and amplitude ratio a on shear modulus are analyzed in the follows.

2. Influence of dynamic stress ratio η

A hysteretic curve consists loading and unloading paths, and it is not closed due to accumulated plastic strain. The shear modulus can be defined as the secant line of the hysteretic curve under current vibration, which is shown as follow Eq. (4):

$$G_N = \frac{q_{N,max} - q_{N,min}}{\varepsilon_{N,max} - \varepsilon_{N,min}} \tag{4}$$

where $q_{N,max}$ and $q_{N,min}$ refer to the maximum and minimum of axial loads at Nth vibration, respectively; $\varepsilon_{N,max}$ and $\varepsilon_{N,min}$ refer to the maximum and minimum of axial strains at Nth vibration, respectively.

The curves of shear modulus and vibration times under different η are shown in Fig. 3 (they are SA series, SD series, SF series). The results indicate that initial shear modulus decreases with the increase of the dynamic stress ratio. The degradation of stiffness occurs regardless of a.

3. The influence of the amplitude ratio a

The relationships between shear modulus and vibrations under different a are shown in Fig. 4. When dynamic stress level is low ($\eta = 0.10$), shear modulus is rarely influenced by a, the degradation of stiffness is not obvious. When η increases to its critical level ($\eta = 0.23$), the linearity between shear modulus and vibration time is evident. The inceptions of the curves on y axis are dispersed, but the final values are concentrated. The stiffness degrades in a faster rate with larger a. For
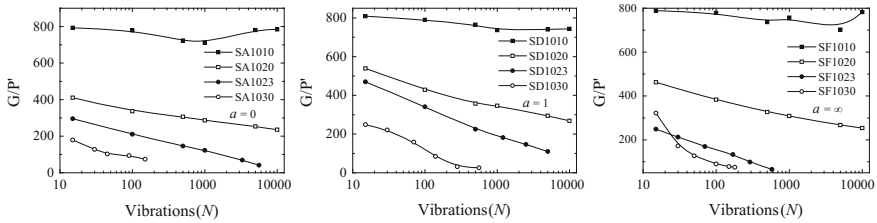
Fig. 3 Relationships between shear modulus and vibration under cyclic dynamic stress ratio
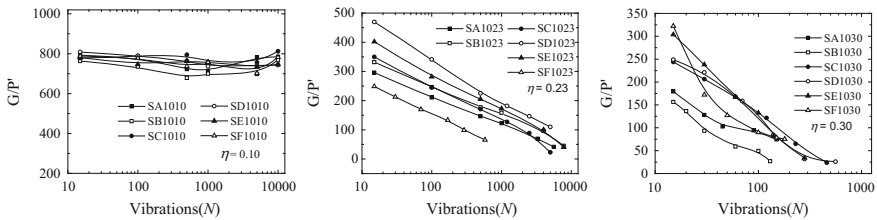
Fig. 4 Relationships between shear modulus and vibrations under different amplitude ratio

destructive model ($\eta = 0.30$), the initial shear modulus increases with the increase of a. The structure of the soil is damaged, and shear modulus decreases with the increase of vibration times.

Patterns of Stiffness Degradation and the Prediction Model

It is indicated that the train load could cause the degradation of stiffness (Fig. 2). In order to describe degradation features, the degradation index [10] is analyzed below.

$$\delta_N = \frac{G_N}{G_1} = \left(\frac{q_{max} - q_{min}}{\varepsilon_{N,max} - \varepsilon_{N,min}} \right) \Big/ \left(\frac{q_{max} - q_{min}}{\varepsilon_{1,max} - \varepsilon_{1,min}} \right) = \frac{\varepsilon_{1,max} - \varepsilon_{1,min}}{\varepsilon_{N,max} - \varepsilon_{N,min}} \qquad (5)$$

where q_{max} and q_{min} refer to maximum and minimum of axial stresses in each vibration; $\varepsilon_{N,max}$ and $\varepsilon_{N,min}$ refer to the maximum and minimum of axial strains at Nth vibration.

It is observed that the degradation is not obvious during the initial vibration because soil becomes denser. The relationship between degradation index and vibration times is described after stiffness starting to degrade, as illustrated in Fig. 5. Take SB series as an example. The degradation stiffness pattern is described by Eq. (6):

Fig. 5 Relationships between δ_N and vibrations under different stress ratios
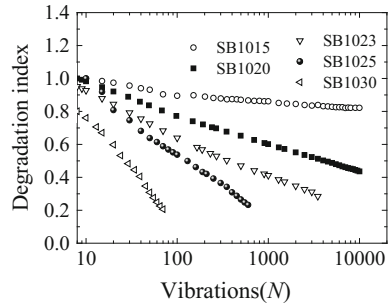
$$\delta_N = \delta_{10} - m \lg N (N > 10) \tag{6}$$

where δ_{10} refers to the degradation index at initial 10 vibrations, m refers to the slope of a curve.

The curves of stiffness degradation are fitted with Eq. (6), and fitting parameters are listed in Table 3.

In order to reveal the relationship between degradation index and dynamic stress level, slope m is further analyzed below. The relationship between slope m and dynamic stress ratio η is shown in Fig. 6. The relationship can be concluded as Eq. (7):

$$m = i + j\eta \tag{7}$$

where i and j are constants. It can be obtained from Fig. 6 that $i = -0.48271$, $j = 3.40285$. Combined with Eq. (6), Eq. (8) is obtained:

$$\delta_N = \delta_{10} - (-0.48271 + 3.40285\eta) \lg N (N > 10) \tag{8}$$

The stiffness degradation pattern under traffic load can be reflected by the prediction model presented in Eq. (8). This model can be used as the modification of stiffness of soil dynamic stress - strain relationship under complex stress paths.

Table 3 Fitting parameters of softening index model under different stress ratios

Number	δ_{10}	m	R^2
SB1015	1.0	0.05417	0.94658
SB1020	0.98276	0.1769	0.99721
SB1023	0.92773	0.24687	0.99376
SB1025	1.0	0.4049	0.99158
SB1030	0.76103	0.5435	0.9746

Fig. 6 The relationship between m and η in degradation index predicting model

$m=-0.48271+3.40285\eta$
$R^2=0.96693$
$p'=100$ kPa

- Test data
--- Predicted model
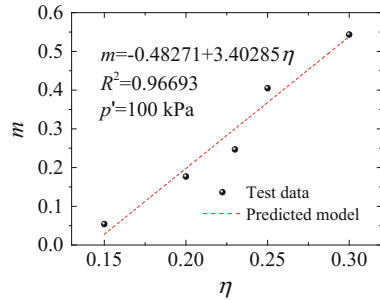
Conclusions

In this study, the hollow cylinder apparatus (HCA) was used to simulate the stress paths induced in traffic-affected ground, a series of undrained shear tests were carried out, the relationship between axial stress-strains and the stiffness degradation were analyzed, the results indicate:

(1) The hysteretic curves of stable models and destructive models have distinctive difference: the angles of inclination in stable models eventually remain constant while angles of inclination in destructive model keep decreasing until the sample is damaged;

(2) When dynamic stress level is low, the amplitude ratio a has little effect on the shear stiffness. When dynamic stress ratio is high, for critical models, the rate of stiffness degradation increases with the increases of amplitude ratio a; for destructive models, the initial shear modulus increases with the increase of amplitude ratio a, soil structure is damaged, its stiffness degrades obviously with increase of vibrations;

(3) The stiffness degradation pattern could be reflected by the prediction model established, which provides theoretical supports for future research on bearing capacity of soft clay foundations suffered from traffic loads.

References

1. Ishihara K. (1983). Soil response in cyclic loading induced by earthquakes, traffic and waves. Soil Mechanicsand Foundation Engineering, vol. 2, pp. 42–66.
2. Ishihara K, Towhata K. (1983). Sand response to cyclic rotation of principal stress directions as induced by waveloads. Soils and Foundations, vol. 23(4), pp. 11–26.

3. Ishihara K. (1996). Soil behavior in earthquake geotechnics. Oxford University Press Inc, New York.

4. Ishikawa T., Sekine E., Miura S. (2011). Cyclic deformation of granular material subjected to moving wheel loads. Geotechnical Journal, Canadian, vol. 48(5), pp. 691–703.

5. Chen Y M, Wang C J, Chen Y P, et al. (2005). Charateristics of stresses and settlement of ground induced by train. Environmental Vibration Prediction, Monitoring and Evaluation, London, Taylor and Francis/ Balkema, pp. 33–42.

6. Idriss I M, Dobry R, Singh R D. (1978). Nonlinear behavior of soft clays during cyclic loading. Journal of Geotechnical Engineering, vol. 104(12), pp. 1427–1447.

7. Yasuhara K, Hyde A F L, Toytoa N, et al. (1998). Cyclic stiffness of plastic silt with an initial drained shear stress. Proc. Geotechnique Symp. on Pre-failure Deformation of Geomterials. London:Thomas Telford Ltd, pp. 373–382.

8. Miranda E; Jorge R G. (2002). Influence of stiffness degradation on strength demands of structures built on soft soil sites. Engineering Structures, vol. 24(10), pp. 1271–1281.

9. Sharma S S; Fahey M. (2003). Degradation of stiffness of cemented calcareous soil in cyclic triaxial tests. Journal of Geotechnical and Geoenvironmental Engineering, vol. 129(07), pp. 619–629.

10. Yu Chuang, Xu Qiang, Yin Zhen-yu. (2013). Softening response under undrained compression following anisotropic consolidation. Journal of Central South University, China, vol. 20(6), pp. 1703–1712.

11. Zhang Hao, Chen Qiu-shi, Chen Jin-jian. (2015). Elasto-Plastic Modeling of Soft Soil Considering Degradation of Stiffness. Journal of Shanghai Jiaotong University (Science), China, vol. 20(6), pp. 683–689.

12. Hight D W, Gens A, Symes M J P R. (1983). The development of new hollow cylinder apparatus for investigating the effects of principal stress rotation in soils. Geotechnique, vol. 33(4), pp. 355–383.

Experimental Study on Bending-Torsional Coupled Modal Identification of Wide Viaduct

Yanwu Fang, Weiping Xie, Chao Zhang and Liangming Sun

Introduction

With the development of urban construction, road transportation is often in a busy working state, and the urban viaduct has played a more and more important role in urban transportation because of its small area, high utilization rate of space and strong capacity of traffic. The increase of the bridge width makes the dynamic characteristics of wide viaduct similar to the two-way slab, and its spatial effect is more obvious compared to the ordinary bridge. So there are coupled problem on bending-torsion in the wide viaduct, and the resulting driving comfort problem is more complicated. When the discomfortable feeling was in long duration and great intensity, it is likely to affect the driver's judgement, causing traffic accidents. Therefore, it is necessary to study this kind of problem.

In this paper, the coupled problem on bending-torsion is discussed from the modal analysis. Modal identification on bending-torsion mode about complex structure is less studied by predecessor. Ren [1, 2] has discussed such issues about modal identification of Minjiang Cable-stayed Bridge in Qingzhou, and the non-coupled modes are well matched with the finite element results. But there is a

Y. Fang
CCCC Second Harbour Engineering Co., Ltd.,
No. 6 Branch, Wuhan 430070, China
e-mail: 191481848@qq.com

W. Xie (✉) · C. Zhang · L. Sun
School of Civil Engineering and Architecture, Wuhan University
of Technology, Wuhan 430070, China
e-mail: wpxie@sina.com

C. Zhang
e-mail: 694956524@qq.com

L. Sun
e-mail: sunliangming@126.com

large error in second order lateral modes. This reason is considered that the second lateral modes are coupled with torsional mode in the finite element model. In the field test, the lateral and vertical responses are not collected at the same time, which leads to large errors. Therefore, for the urban width viaduct of large wide-span ratio characteristic, its modal identification and coupled problem on bending-torsion are worthy of further study.

To explore coupled modal identification problem on bending-torsion of the wide viaduct modal identification. The numerical example of box beam is applied to verify two kinds of identification (overall recognition and separated recognition) based on ambient excitation for bending-torsional coupled modal recognition results. Then the modal identification of wide viaduct was studied based on ambient excitation. The test scheme of 'multi reference point mutual checking' is adopted, and the round test method which validates the stability of data is adopted, two kinds of recognition method are used, peaking picking method and stochastic subspace method for modal identification and mutual authentication.

Principle of Data Driven Stochastic Subspace Identification

Stochastic Subspace Identification is based on the analysis of state space model, using linear algebra tools, the system input and noise are assumed to be white noise, Kalman Filter state matrix can be obtained according to the characteristics of white noise, the system matrix are deduced with the least square method to identify system parameters. Stochastic subspace identification includes two methods of covariance driven (SSI-COV) and data driven (SSI-DATA). The data driven stochastic subspace identification is adopted due to its relatively high accuracy.

The stability diagram is an effective method to determine the system order. If it were used in the stochastic subspace identification, it would identify the false modes [3]. The average normalized power spectrum is introduced in the stability diagram, which can help to determine the stability axis, which is advantageous to eliminate spurious modes. At the same time, the average processing of stable points near the same stable axis is beneficial to improve the identification accuracy and reduce the influence of subjective factors on the identification results. In the literature [4], it is also known as the average normalized stability graph.

Algorithm Verification of Two Kinds of Recognition Methods

A finite element model of box beam is used to verify the modal identification algorithm. For homogeneous asymmetric cross sections, the centroid and shear center is generally not coincident. Modal information must include bending-torsional coupled mode. The applicability and effectiveness of modal identification

algorithm for bending-torsional coupling mode is verified based on the numerical simulation of coupled modes.

A finite element model of box girder is established in ANSYS by shell63 element. The parameters are set such as span length L = 30 m, Poisson's ratio μ = 0.2, the density of bridge ρ = 2500 kg/m^2, bending stiffness EI = 3.45 × 1010 N/m. The Gauss white noise sequence which is not correlated with each other is generated by MATLAB. It is used to simulate environment excitation in the transient analysis and extract acceleration response for modal identification. There are a total of 31 × 2 = 62 measure points. The left eleventh point is set as the reference point. Sampling frequency is set to 200 Hz. Sampling time is set to 150 s. The Rayleigh damping ratio of the first and tenth order modes is 1%.

In order to simulate the two kinds of situations of the lateral and vertical response at the same time (i.e., the overall recognition and the separated recognition). Identification results are shown in Table 1.

From Table 1, it is indicated that the frequency error of separated recognition is quite equal to that of overall recognition. MAC of two kinds of recognition methods are all above 99%. It is shown that the numerical simulation results can meet the requirements of engineering accuracy.

Wide Viaduct Modal Identification

Test Scenarios

The cross section of the wide viaduct is shown in Fig. 1. The test equipment used is Japanese SPC-51 vibration analyzer and VSE-15-D1 servo-type single axis speed sensor. The sampling frequency is 200 Hz, gathering the acceleration responses, Limited by the length of the connecting line of the sensor, this test plan is 'Mutual check of multiple reference points'. The so-called 'Mutual check of multiple reference points' refers to the partition of all measurement points. Reference points are arranged in each area. The normalization of all measure points is carried out by the mutual check of all reference points.

Taking into account the reference point should avoid the attention of the modal nodes. The reference points are arranged at 9, 42 and 93 points respectively. There are 99 vertical measuring points, the test was divided into 33 groups, there are 4 measuring points in each group. that is, a cross section of the 3 points and the cross reference point. There are 66 horizontal measuring points, divided into 22 groups to test. Only three reference points are arranged in the longitudinal direction. The mutual check of three reference points will be carried out after the test is finished. For the reference point is very important, so the test time is extended to 30 min (Fig. 2).

Table 1 Comparison of two kinds of identification methods and FEA

Mode Num.	FE freq. (Hz)	Together				Separately			
		Freq. (Hz)	Freq. diff. (%)	MAC	Damping ratio (%)	Freq. (Hz)	Freq. diff. (%)	MAC	Damping ratio (%)
1	4.8814	4.8872	0.1178	1.00000	1.140	4.8885	0.1455	1.00000	1.505
2	13.8559	13.8632	0.0523	0.99980	1.115	13.8625	0.0476	0.99993	1.030
3	14.4937	14.4939	0.0010	0.99992	0.895	14.4971	0.0235	0.99988	0.975
4	15.4728	15.4761	0.0213	0.99952	0.875	15.5003	0.1774	0.99859	1.450
5	21.7364	21.7381	0.0078	0.99974	0.900	21.7213	-0.0695	0.99997	0.900
6	22.2824	22.2686	-0.0619	0.99630	0.835	22.3061	0.1064	0.99692	1.420
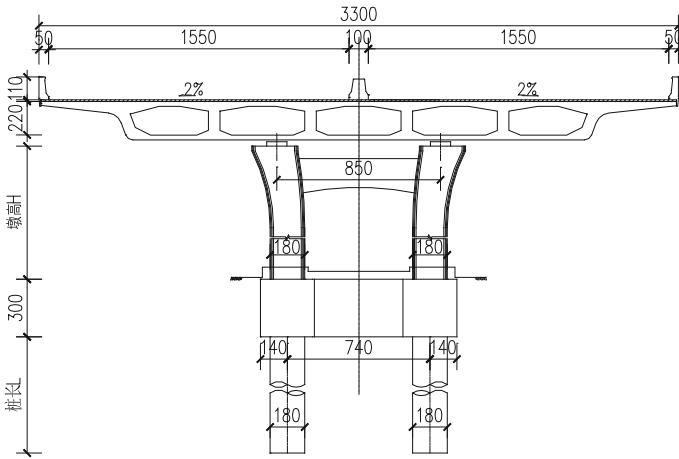
Fig. 1 Lth three span continuous steel box girder bridge
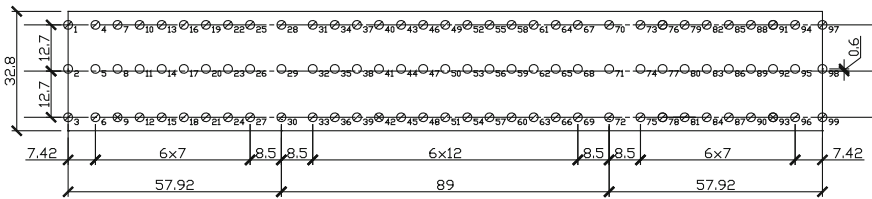
Fig. 2 Configuration of measure points on Lth bridge

Test Scenarios

This section uses 'the run test' to verify the stability of data, the basic principle of the run test refers to literature [5, 6]. In this paper, we test the stability of variance statistics. Dividing the data into 40 sections, the above sample value into time series, the variance of each interval is calculated separately. Taking the first set of test data as an example, the number of rounds of the set of data is 17, located in the interval [15, 26], so accepting the assumption of stability. That is, the data is smooth. Modal identification based on environmental excitation can be carried out. Prior to the identification of other groups of measured data, to carry out run test in the same way and operate modal identification of the run test data. On the contrary, data segment should be reselected.

Modal Identification

The peak picking method (PP) and the data-driven stochastic subspace method (SSI-DATA) both based on ambient excitation are used to identify the modal parameters and verify each other. Two kinds of identification methods are shown in Table 2. It is shown that the peak picking method can identify the 11 order modal, data-driven stochastic subspace method can identify the 12 order modal. From Table 2, the results of the method for identifying the two kinds of frequency error is below 1%, modal confidence factor (MAC value) is more than 93%. The bending-torsional coupled mode shape is illustrated in Fig. 3.

Table 2 Comparison of parameters identified

Mode number	PP	SSI-DATA		Frequency differences (%)	MAC value	Mode description
	Frequency (Hz)	Frequency (Hz)	Damping ratio (%)			
1	1.318	1.320	0.352	−0.160	0.999	1st vertical bending
2	–	1.705	1.911	–	–	1st longitudinal
3	2.053	2.064	1.286	−0.568	0.985	1st transverse bending + torsion
4	2.402	2.409	0.689	−0.299	0.994	2nd vertical bending
5	2.563	2.582	2.201	−0.726	0.943	2nd transverse bending + torsion
6	2.789	2.794	0.892	−0.175	0.971	3rd vertical bending
7	3.136	3.151	1.510	−0.465	0.993	1st torsion
8	3.656	3.683	1.705	−0.744	0.941	3rd transverse bending + torsion
9	3.775	3.787	0.803	−0.323	0.978	4th transverse bending + torsion
10	4.403	4.415	1.474	−0.281	0.969	4th vertical bending
11	4.879	4.901	2.067	−0.463	0.942	5th transverse bending + torsion
12	5.657	5.706	2.028	−0.843	0.939	2rd torsion

(a) 1st transverse bending+ torsion (2.064Hz)   (b) 2nd transverse bending+ torsion (2.582Hz)

(c) 3rd transverse bending+ torsion (3.683Hz)   (d) 4th transverse bending+ torsion (3.787Hz)
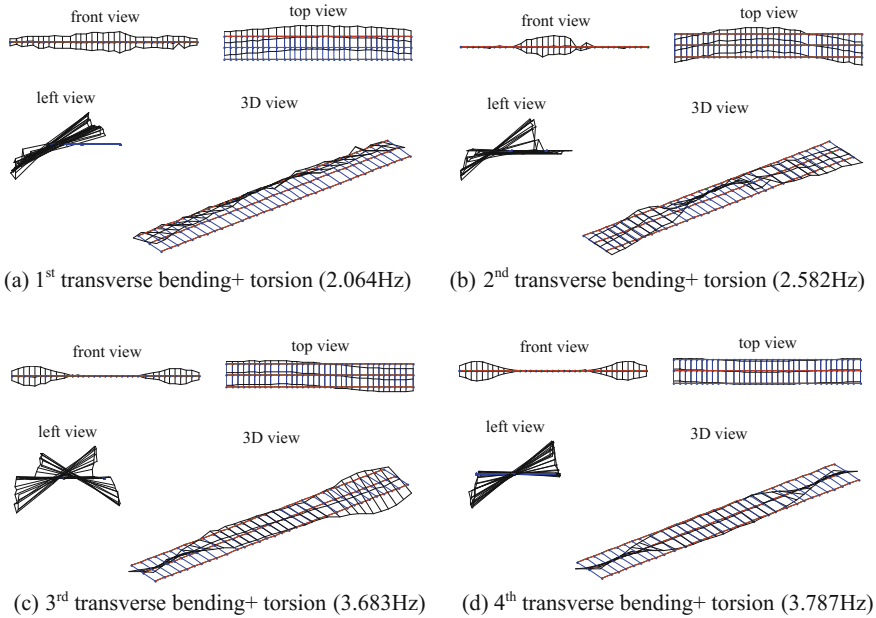
Fig. 3 SSI-DATA mode shape

Conclusions

Some conclusions are obtained as follows: Modal identification method based on ambient excitation can effectively identify the bending-torsional coupled mode. It is proved that the effects of the separation recognition and the global recognition are equivalent with an example. There are some bending-torsional coupled modes in the wide viaduct. Therefore, for this type of wide viaduct, not all modal can be regarded as unidirectional mode which is the classical beam theory. The bending-torsional coupled mode cannot be ignored. It is useful to finite element model establishment, modification and analysis for the wide viaduct. Test identification scheme of 'Mutual check of multiple reference points' is proposed to effectively solve the problems that the transmission distance of the cable test equipment is limited and the measured interval span is large.

References

1. Ren, W.X., Peng, X.L. (2005). Baseline finite element modeling of a large span cable-stayed bridge through field ambient vibration tests. Computers & Structures, 83(8-9):536–550.
2. Ren, W.X., Peng, X.L., Lin, Y.,Q. (2005). Experimental and analytical studies on dynamic characteristics of a large span cable-stayed bridge. Engineering Structures, 27(4):535–548.

3. Chang, J., Zhang, Q.W., Sun, L.M. (2007). Application of stabilization diagram for modal parameter identification using stochastic subspace method. Engineering Mechanics, 24(2):39–44.
4. Yu, D.J. (2006). Modal parameter identification of civil engineering structures- theory, implementation and applications. Fuzhou: Fuzhou University.
5. Bendat, J.S., Piersol, A.G. (1971). Random Data: Analysis and Measurement Procedures. Wiley-Interscience.
6. Xie, J.J. (2010). Bridge testing vibration signal quality evaluation based on stationary test method and SNR estimation. Changsha: Central South University.

Lateral Ground Displacement Induced by EPB Tunneling in Ningbo Soft Clay

Yaohong Zhu, Fei Gao, Junneng Ye, Xuecheng Bian, Weian Lin and Yunmin Chen

Introduction

With the rapid urbanization process, an increasing number of cities in China are building their subways, by September 2016, nearly 30 cities have over 100 lines and over 3600 km subways in operation. Not only solve the traffic jam problem the subway does, but also stimulate investment and promote economic growth, therefore China is planning to build 3000 km more subways in the next 5 years.

Stations and intervals are the two most important factors of subway. In the downtown area, most of the underground intervals, which are tunnels, are constructed by EPB (Earth Pressure Balanced) shield, especially in the soft clay area, for its quiet and efficient. However, the ground movements caused by EPB tunneling must not be overlooked. Without enough attention, the too large ground movements would make a lot of troubles, for instance, the building adjacent to the

Y. Zhu · J. Ye
Ningbo Urban Rail Transit Project Construction Headquarters,
Ningbo 315012, China
e-mail: 13336694956@189.cn

J. Ye
e-mail: yjn75@139.com

F. Gao (✉) · X. Bian · W. Lin · Y. Chen
Institute of Geotechnical Engineering, Zhejiang University,
Hangzhou 310058, China
e-mail: gf@zju.edu.cn

X. Bian
e-mail: bianxc@zju.edu.cn

W. Lin
e-mail: linweian@zju.edu.cn

Y. Chen
e-mail: chenyunmin@zju.edu.cn

tunnel may incline or even crack [1], the tubes buried into the ground may bend or even break [2], and the tunnel itself may deviate from the designed line or even make passengers feel uncomfortable during operation period [3]. Many experts and researchers have studied on the displacements for decades [4–13], Standing [4] studied the ground movements caused by the EPB in London clay, by monitoring and analyzing, it was concluded that the pressurized face of the EPB and tail-skin grouting led to outward displacements. Liu [5] investigated the disturbance to piles and pile groups caused by multiple nearby drives of a large diameter slurry shield-driven tunneling machine in Shanghai, the measured data and the numerical simulation results showed that the shield would cause the ground inwards and outwards movements during the different stages. Chen [6] studied the ground movement induced by parallel EPB tunnels in silty soils, it was suggested that the maximum horizontal displacement occurred at the depth of the tunnel axis during tail grouting, and with enough distance, the new tunnel had little effect on the existed tunnel.

This paper studied the lateral displacement caused by EPB tunneling in the Ningbo soft clay, by comprehensive monitoring in the field, the change process of the ground lateral movement was more clearly understood, which would help constructors and designers to handle the EPB tunneling more skilled and confident.

Background

Ningbo is located in the east China coast, the city was sparing no effort to construct its rail transit system in the past ten years. According to the recent planning, by the end of 2016, there would be two lines in operation, including line No. 1 (stage 1 and stage 2) and line No. 2 (stage 1). In order to explore the effect caused by EPB tunneling in the Ningbo soft clay, a comprehensive monitoring section was set and a lot of field tests were undertaken. The test sections were located at stage 2 of Line No. 1, whose total length is 25.372 km, including 2.374 km long underground line (EPB tunneling) and transition line (opening excavation) (Figs. 1 and 2).

For a detailed design of the metro tunnel, a comprehensive geotechnical investigation was conducted, which was consisted of borehole sampling, cone penetration tests, in situ vane shear tests, shear wave velocity test and so on. It was demonstrated by the geotechnical investigation that the test site had a typical quaternary stratigraphy growth along the depth 80 m under the ground. The soils were composed of very soft silty clays with high sensitivity, which meant that the soils here have a very low strength and a very strong structural.

In the shallow layers from surface to 40 m under the ground, the soils were mainly consisted of some coastal phase or Lacustrine silt, silt clay and silt sand deposited in Holocene period. According to the site investigation results, Ningbo soils can be differentiated into a number of well-defined strata based on physical properties and soil types. The soil properties of Ningbo soil strata near monitoring section (Fig. 3) are summarized in Table 1. The metro Tunnel is situated within highly compressible and very sensitive soft silty clay deposits layer 2-2 and layer 2-3.
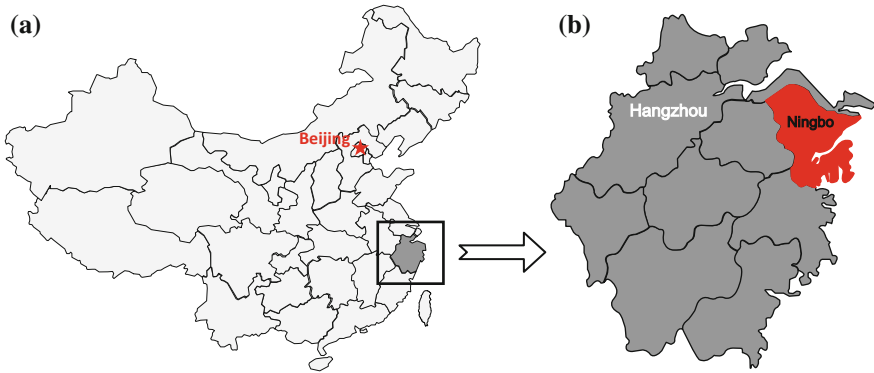
Fig. 1 **a** Zhejiang province is located in the east China coast. **b** Ningbo city is located in the east coast of Zhejiang Province Ningbo Metro line 1 is consisted of stage 1 and stage 2, the test field was located in the stage 2
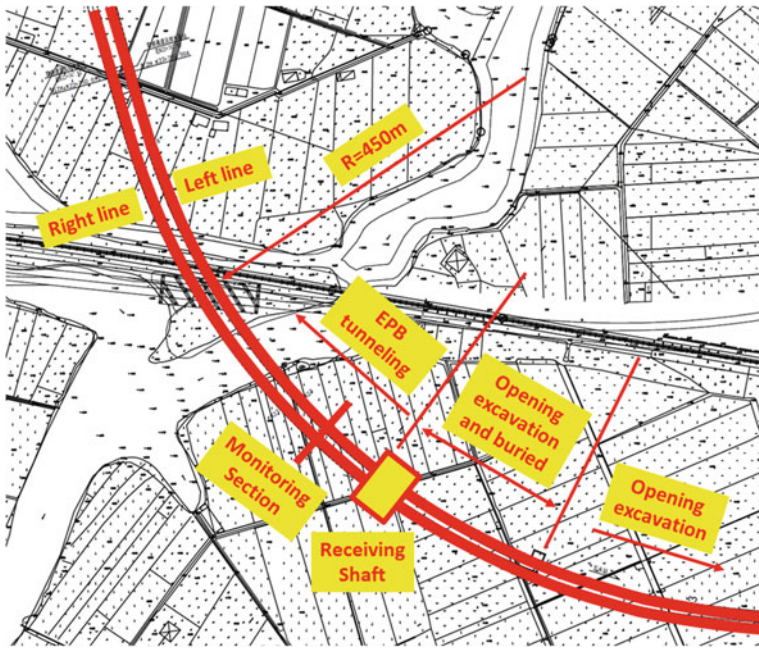
Fig. 2 Plane graph of the test field. The actual axis center line was transited by an arc of 450 m radius. The monitoring section was installed near the receiving shaft, which was the end of the EPB tunneling and the beginning of the opening excavation

The parallel tunnels include the right line tunnel (designated as RL tunnel) and the left line tunnel (designated as LL tunnel). The axes of the parallel tunnels are spaced 10 m apart and are at a depth of 8.7 m. The tunnel lining was assembled

(a) Plane graph of the monitoring section installation

(b) Transversal illustration of the monitoring section
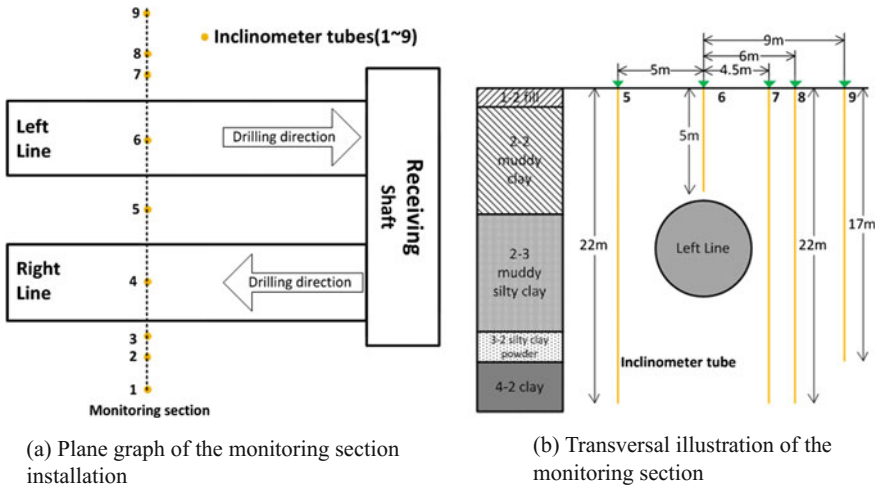
Fig. 3 The monitoring section was installed near the receiving shaft, which was the end of the EPB tunneling and the beginning of the opening excavation. The tunnel was a shallow buried tunnel and laid in the muddy clay stratum

with precast concrete segments; the outer and inner diameter of the tunnel lining is 6.2 and 5.5 m respectively, so the thickness of the lining is 0.35 m. The length of each lining ring is 1.2 m.

Monitoring Section Installation and Field Test

To better understand the performance of EPB tunneling in Ningbo soft clay, a monitoring section was installed in the area near the receiving shaft that was the end of the EPB tunneling. Several inclinometer tubes were installed around the tunnel, as Fig. 3 shows. And the displacement of the soil was measured by the inclinometer during the whole construction process.

The EPB shield was made by Komatsu in Japan, which was a big cylinder with 6340 mm diameter and 8680 mm length. The shield was employed to undertake the excavation of underground tunnel, the assembling of precast concrete segments, and the simultaneous grouting. The construction process was cycles of drilling and standing, one complete lining ring consisted of six concrete segments was accomplished during each cycle.

In this study, the left line of the parallel tunnels was first constructed, the EPB shield moved towards the receiving shaft, which was the end of the EPB tunneling, and then the shield was turned around in the shaft, after some repairing and debugging, it would leave the shaft and start to construct the right line.

Table 1 Physical properties of the soil in the test field

Soil layers	Thickness (m)	Water content (%)	Specific gravity	Natural density (kN/m³)	Natural void ratio	Saturation (%)	Liquid limit (%)	Plasticity limit (%)	Liquid index	Plasticity index
1-2 fill	1.9	45.40	2.76	17.80	1.26	99.90	46.20	23.50	0.96	22.70
2-2 muddy clay	8.1	48.23	2.73	17.28	1.34	97.80	38.13	20.90	1.58	17.23
2-3 muddy silty clay	8.5	44.47	2.74	17.45	1.27	96.08	38.60	21.20	1.34	17.40
3-2 silty clay powder	1.5	34.60	2.73	18.40	1.00	94.70	33.60	19.50	1.07	14.10
4-2 clay	11.9	41.68	2.75	17.77	1.20	95.47	41.62	22.20	1.00	19.42

Measurements and Analysis

According to Fig. 4, the lateral displacement changed as the EPB tunneling process. Initially, the EPB shield was too far away from the monitoring section that there was little effect on the soil near the monitoring section.

Gradually, the EPB moved to the section closer and closer, the face pressure of the shield was a new load on the ground, on the contrary, the excavation was unloading from the ground, however, the face pressure was larger than the unloading magnitude resulted from the excavation, therefore the superposition of the two opposite effect finally made the soil around the tunnel have an outward trend, the maximum lateral displacement was obtained when the cutter face reached the monitoring section and at a depth of 8.9 m, which was the depth of the tunnel axis. Clearly, the farther the inclinometer tube was from the tunnel, the maximum lateral displacement was smaller, the maximum lateral displacement was about 44 mm, and this data was obtained from tube 7, which was 4.5 m far away from the tunnel axis. The lateral displacement of tube 9, which was 9 m far away from the tunnel axis, was just about 5 mm, which may indicate the disturbance boundary of the EPB tunneling.
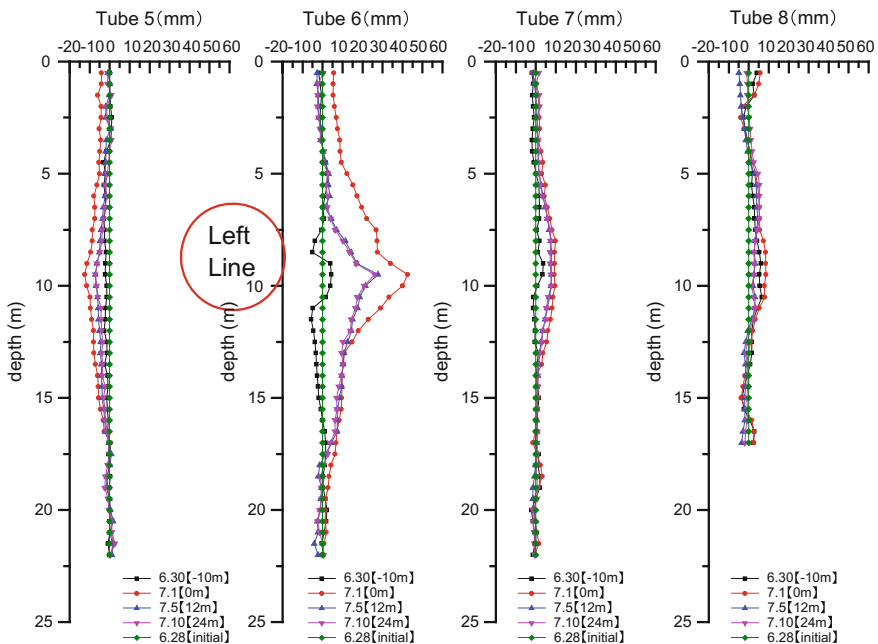

Fig. 4 The soil lateral displacement was obtained by some inclinometer tubes installed around the tunnel. Five sets of data were measured when the EPB shield moved closer, reached and *left* the monitoring section

The EPB shield kept drilling and standing periodically, and finally passed the monitoring section, however, there was a gap between the shield (diameter 6340 mm) and the concrete segments (diameter 6200 mm), so after the concrete segments moved out of the shield tail, although the synchronous grouting could fill the gap immediately, it took several day for the grouts to change from fluid to solid, the soil around the tunnel would still move inward, which was proved by the change of the lateral displacement in Fig. 4. Obviously, the soil would not recover the original state, and with the EPB shield moving farther and farther, meanwhile the grouts being stiffer and stiffer, the lateral displacement would keep a constant and not change any more.

Conclusions and Suggestions

By the detailed monitoring and analyzing the data, the effect the EPB shield had on the soil during the whole construction process was better understood, some conclusions could be drawn. With the EPB shield moving closer, reaching and leaving from the monitoring section, the soil would move outward, then inward and finally be steady. The maximum lateral displacement 44 mm was obtained where the inclinometer tube was 4.5 m far away from the tunnel axis and when the cutter face reached the monitoring section. The disturbance boundary was about 9 m far away from the tunnel axis. The lateral displacement of the soil is induced by many complex factors, including face pressure, excavation, the tail gap, synchronous grouting, supplementary grouting, and even the line design parameters etc. So the constructor should control the EPB shield very cautiously, especially the machine drivers, they must be experienced and familiar with the soil around the tunnel.

References

1. Report: structural disturbance of soft clay and the deformation control of the subway engineering.
2. http://whwb.cjn.cn/html/2015-01/03/content_5405802.htm.
3. some key technologies in civil engineering during the initial stage of the Ningbo Rail Transit.
4. J. R. STANDING, D. SELEMETAS, Greenfield ground response to EPBM tunnelling in London Clay, Geotechnique 63(2013), 989–1007.
5. Chao Liu a, Zixin Zhang, Pile and pile group response to tunnelling using a large diameter slurry shield – Case study in Shanghai Computers and Geotechnics 59 (2014), 21–43.
6. R. P. Chen, J. Zhu, Ground movement induced by parallel EPB tunnels in silty soils, Tunnelling and Underground Space Technology 26 2011. 163–171.

7. Dias D, Kastner R. Movements caused by the excavation of tunnels using face pressurized shields — Analysis of monitoring and numerical modeling results[J]. Engineering Geology, 2013, 152(1):17–25.
8. LIN Cungang Research on Shield Tunneling induced ground surface heave and subsidence and behavior of underwater shield driven tunnels subject to tidal bores[D]. Zhejiang University 2014.
9. Pinto F, Whittle A J. Ground Movements due to Shallow Tunnels in Soft Ground. I: Analytical Solutions[J]. Journal of Geotechnical & Geoenvironmental Engineering, 2014, 140(4):240–252.
10. Pinto F, Zymnis D M, Whittle A J. Ground Movements due to Shallow Tunnels in Soft Ground. II: Analytical Interpretation and Prediction[J]. Journal of Geotechnical & Geoenvironmental Engineering, 2014, 140(4):80–90.
11. Zhang Z, Huang M. Geotechnical influence on existing subway tunnels induced by multiline tunneling in Shanghai soft soil[J]. Computers & Geotechnics, 2014, 56(1):121–132.
12. González C, Sagaseta C. Patterns of soil deformations around tunnels. Application to the extension of Madrid Metro[J]. Computers & Geotechnics, 2001, 28(6-7):págs. 445–468.
13. Sagaseta C. Analysis Of Undrained Soil Deformation Due To Ground Loss[J]. Geotechnique, 1988, 38(3):301–320.

Application of Distributed Optical Fiber Sensors for Monitoring Pavement Settlement

Yifan Zhang, Chengyu Hong, Yawen Zhang and Rafique Ahmed

Introduction

Optical fiber sensors (OFS) have been widely considered as promising sensing technologies for health monitoring of structural and geotechnical infrastructures. A large number of optical fiber sensor technologies have been developed for monitoring strain and temperature variations for geotechnical structures. In recent decades, fiber Bragg grating (FBG) and Brillouin optical time domain analysis (BOTDA) based sensors have gained popularity for monitoring civil engineering structures due to the advantages such as small size, light weight, high resolution, and immune to electromagnetic interference (EMI) [1, 2]. FBG sensor, as a point sensor, only offers strain or temperature measurement at some specific "points" on structures [3]. Brillouin optical time domain analysis (BOTDA) based sensor, on the other hand, provides the measured strain or temperature over a particular length, and hence is called fully-distributed sensor, which is primarily used for monitoring average strain or temperature [4, 5].

Y. Zhang · R. Ahmed
College of Textiles, Donghua University, Shanghai 201620, China
e-mail: zhangyifan@dhu.edu.cn

R. Ahmed
e-mail: rafiqueahmed66@yahoo.com

C. Hong (✉)
Department of Civil Engineering, Shanghai University, Shanghai 200444, China
e-mail: cyhong@shu.edu.cn

Y. Zhang
Key Laboratory of Structure and Wind Tunnel of Guangdong Higher Education Institutes, Shantou 515063, China
e-mail: 2140118@mail.dhu.edu.cn

A large variety of OFS sensors based on FBG and BOTDA technologies have been proposed for monitoring geotechnical parameters such as stress, strain, pore water pressure, overburden pressure, and displacement [2, 6–9]. Monitoring the displacement is crucial and normally realized in terms of measured strain or inclined angle of a particular structural element embedded underground. Measured point strain can be transferred into displacement using specific mathematical methods such as integration method [10] or finite differential method [2], typical studies show that FBG based inclinometers offer reliable displacement monitoring, for example, low-frequency tiltmeter for real-time monitoring of structural displacement [11], FBG based inclinometers for ground movement monitoring [8, 12, 13], 2D or large deflection measurement system [14–16], and the FBG based sensor for dynamic displacement monitoring [2, 17]. These studies have proved that the FBG based sensors are reliable for reflecting the ground movement in case reliable design and protection methods were adopted.

As a fully-distributed optical fiber sensing technology, BOTDA sensors have been used for monitoring the mechanical behavior of large geotechnical structures, such as piles [18], retaining walls [19], slopes [20], etc. The monitoring of displacement for specific geotechnical structures have also been conducted, for example, pile deflection monitoring using Brillouin optical time domain reflectometry (BOTDR) technology [21], and tunnel lining monitoring system based on BOTDR [22]. These measured strain and the related calculated displacement data agree fairly well with traditional sensors (such as strain gauges), even when relatively significant ground movement occurred. Although BOTDA based sensors seem to be popular for deflection monitoring, the application for geotechnical settlement is limited. Hence a reliable settlement monitoring system based on distributed sensors (such as BOTDA or BOTDR) is required.

This paper proposed an innovative inclinometer sensor (namely large-settlement beam) based on FBG and BOTDA sensing techniques. A very simple loading case was considered in this study, that is, a simply supported beam in pure bending state. Strain data of FBG and BOTDA based strain sensors were collected and adopted for predicting the occurred large deflection along beam using finite difference method (FDM). A maximum of around 110 mm deflection was finally approached in present experiment, indicating that the settlement beam can be used for large settlement monitoring. The calculated defection data from two sensors and the occurred deflection measured by Linear Variable Differential Transformers (LVDTs) are compared to validate the monitoring data. This proposed beam is expected to be applied as a settlement sensor for monitoring possible large vertical settlement occurred below foundations, pavements, dams, etc.

Sensing Principle of Sensors and the Calculation of Settlement

Sensing Principle of FBG and BOTDA Sensors

A fiber Bragg grating (FBG) is a special distributed Bragg reflector developed in a small segment reflecting specific central wavelength via generating a periodic variation in the refractive index of fiber core [23]. The Bragg reflector can reflect specific central wavelength, which is linearly proportional to strain or temperature change, and hence enabling the measurement of occurred strain and temperature using FBG sensors. Currently FBG has been widely applied in many strain-sensing practices and the detailed introduction of sensing principle for FBG based technology can be found in many references [3, 24, 25].

BOTDA is a novel sensing technology developed for distributed strain monitoring based on stimulated Brillouin backscattering (SBS). Figure 1 shows a schematic view of the basic sensing principle of BOTDA sensors. It can be seen two light sources including pumping pulse light and continuous wave light are injected into the fiber core at the two ends of the fiber, when the frequency difference between the two lights matches the local Brillouin frequency shift of the fiber core, SBS is stimulated and the occurred Brillouin frequency shift is proportional to the change in strain or temperature. Therefore:

$$v(T) = v(0)(1 + C_T * T) \tag{1}$$

$$v(\varepsilon) = v(0)(1 + C_\varepsilon * \varepsilon) \tag{2}$$

where $v(0)$ denotes the reference frequency. T and ε are the occurred temperature and strain change. C_T and C_ε are the related coefficients for temperature and strain change, respectively. $v(\varepsilon)$ and $v(T)$ are the Brillouin frequency shift due to the

Fig. 1 Basic sensing principle of BOTDA based sensor
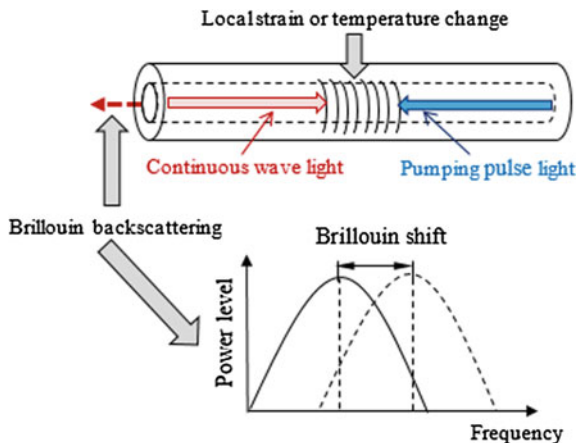
strain and temperature applied on the optic fiber sensor. Based on the above two equations, the strain can be obtained and temperature compensation can be realized.

Calculation of Deflection Based on Finite Difference Method (FDM)

Finite difference method is a mathematical discretization method deriving from Taylor's polynomial used for solving differential equations. By using this method, the continuous beam is divided into a number of small elements, and the interval between adjacent elements is assumed to be h. The first order derivatives of deflected beam at distance values x and x − h are given by:

$$f'(x) = \frac{1}{h}[f(x+h) - f(x)] \tag{3}$$

$$f'(x-h) = \frac{1}{h}[f(x) - f(x-h)] \tag{4}$$

where the first derivative of f is also the slope of deflection with respect to the length of beam element (from x + h for Eq. (3) and from x − h to x for Eq. (4)). Similarly, the second order derivative can be obtained as:

$$\begin{aligned} f'' &= \frac{1}{h}\{\frac{1}{h}[f(x+h) - f(x)] - \frac{1}{h}[f(x) - f(x-h)]\} \\ &= \frac{1}{h^2}[f(x+h) - 2f(x) + f(x-h)] \end{aligned} \tag{5}$$

Equation (5) shows the correlation between the second order derivative and the related deflection. Given the boundary conditions for example the deflection at some specific locations of a beam, the calculation of beam deflection at other locations is possible if f'' is known. Figure 2 shows a schematic view of the beam deflection resulted from external loading. As the beam deformation is small, we can obtain the approximation $Rd\theta = \Delta l \sim dx$, and gradient of the deflection curve $k = 1/R \sim d\theta/dx$ and $\theta \sim df/dx$, hence, $k \sim d^2f/dx^2 = f''$. The gradient and occurred strain follow the below relationships:

$$k = \frac{M}{EI} = f'' \tag{6}$$

$$\frac{M}{EI}\frac{D}{2} = \frac{\varepsilon_{ai} - \varepsilon_{bi}}{2} \tag{7}$$
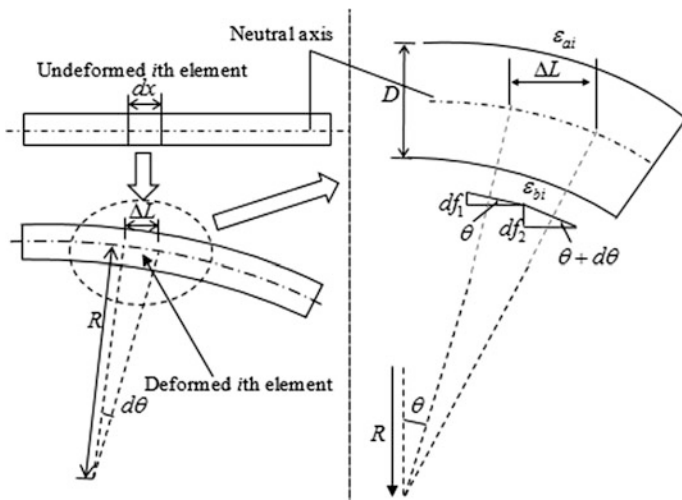
Fig. 2 Schematic views of deflection calculation for beam element

where D, E and I are the thickness, elastic modulus and moment of inertia of the beam, respectively. ε_{ai} and ε_{bi} are the occurred strain at the upper and lower beam surface, respectively (See Fig. 2). Combing Eqs. (5–7) yields:

$$\frac{1}{h^2}[f(x+2h) - 2f(x+h) + f(x)] = \frac{\varepsilon_{ai} - \varepsilon_{bi}}{D} \tag{8}$$

Given the boundary conditions and the related strain distributions, deflections at specific beam locations mounted with strain sensors can be directly calculated using Eq. (8).

Experimental Program

Laboratory test was performed to examine the strain distribution of a settlement beam with optical fiber sensors under different loading levels. This beam is expected to be applied for settlement monitoring below foundations or pavements. Figure 3 shows a schematic view of the test setup arrangement, which primarily consists of a simply supported beam subjected to loading at the two beam ends, and OFS mounted on the upper and lower precreated grooves of the beam for strain measurement. The beam was a hollow cylinder and the related internal diameter, external diameter, and length were 50 mm, 70 mm and 4 m, respectively. Four FBG sensors spaced at intervals 0.8 m and four segments of BOTDA sensors were installed for point strain and average strain measurement, respectively (See Fig. 3). It is noted that four segments of BOTDA sensors were prestressed up to
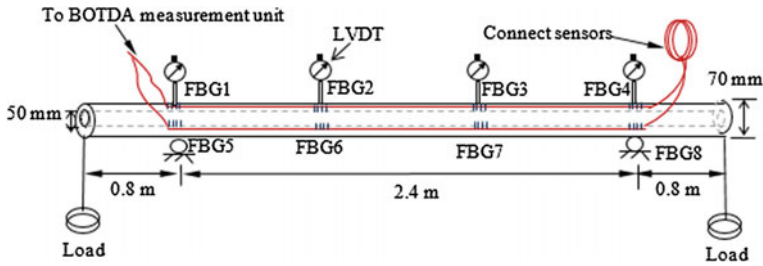
Fig. 3 Installation scheme of FBG and BOTDA sensors on settlement beam

around 4000 $u\varepsilon$ tensile strain after attaching in precreasted grooves on beam surface, in order to sense both tensile and compressive strain. LVDTs were installed at the locations where FBG sensors were mounted.

For the simulation of occurred settlement (deflection), vertical load was applied at two ends of the beam step by step at a loading increment 9.8 N for each step. A total of 49.2 N was finally approached after 5 loading steps. Then the applied load was released step by step and the released load in each step was 9.8 N. It is noted that the beam was in pure uniform bending after loading/unloading as the loads applied each end were equal. Strain data from optical fiber sensors were collected each time after loading and unloading were finished.

Experimetal Result and Discussions

Comparison of Measured Strain Between BOTDA and FBG Sensors

FBG and BTODA sensors reflect the strain variations of structures in terms of measured central wavelength change from four FBG sensors and light frequencies from four segments of BOTDA sensors, respectively. Figures 4(a) shows the relationships of light frequency of OFS attached on the upper surface of the beam against optical fiber sensor distance for different loading/unloading levels. It is seen the frequency data along the OFS distance from 55 to 66 m show significant rise compared with OFS frequency data at the two ends, indicating that the OFS was subject to significant tension. The four BTODA sensing segments were attached on the same beam locations, so that the measured strain distribution of different OFS segments should be the same, as observed from the frequency variations for the OFS distance between 55 and 65 m for the loading process. These obtained frequency data were further transferred into strain data and shown in Fig. 4(b). The monitored average strain increment for each loading step is almost constant (around 200 $u\varepsilon$), and the maximum tensile strain approached was around 900 $u\varepsilon$ after 5 loading steps.
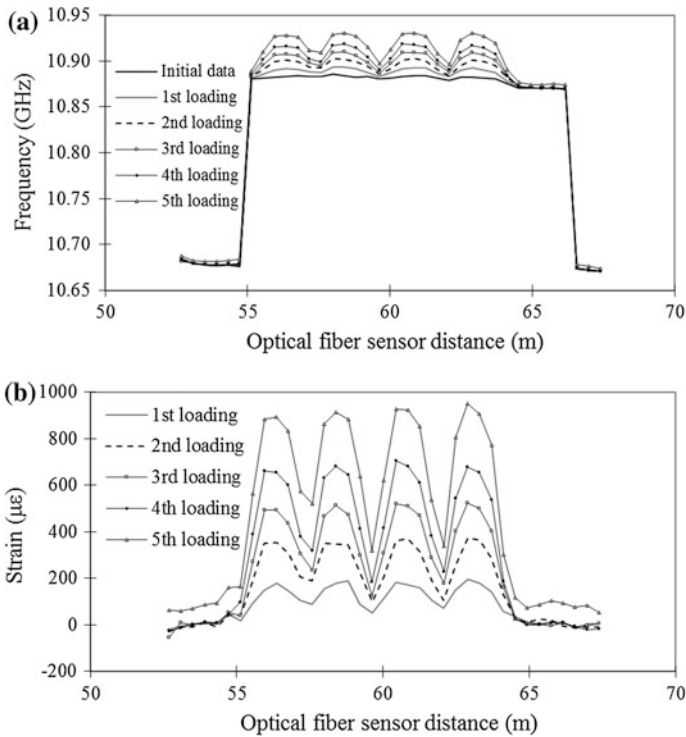
Fig. 4 **a** Measured frequency variations and **b** measured strain variations against optical fiber sensor distance for different loading levels

Average wavelength variations of four FBG strain sensors (attaching on upper beam surface) against time are summarized in Fig. 5. Locations of these FBG strain sensors (from FBG1 to FBG8) are shown in Fig. 3. It is clear from Fig. 7 that all the wavelength data increase (decrease) step by step for 5 loading (unloading) processes. All the wavelength data become very stable after around every 200 s. The measured average strain from FBG and BOTDA sensors at different loading and unloading levels are compared in Fig. 6. The monitored average strain values from two OFS agree fairly well (as the beam is in pure bending) and the strain increment for each loading step observed is around 200 $u\varepsilon$. The measured total tensile strain is about 900 $u\varepsilon$ after 5 loading steps. While around 30 $u\varepsilon$ residual strains are observed (according to the strain values measured by FBG and BOTDA strain sensors) after all vertical loads were released. The consistent measured strain values indicate that the two sensors are reliable for monitoring the average strain change of the proposed settlement beam.
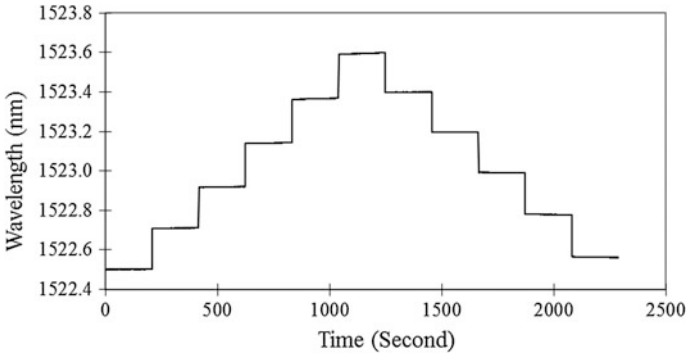
Fig. 5 Average wavelength variations against time of the four FBG strain sensors
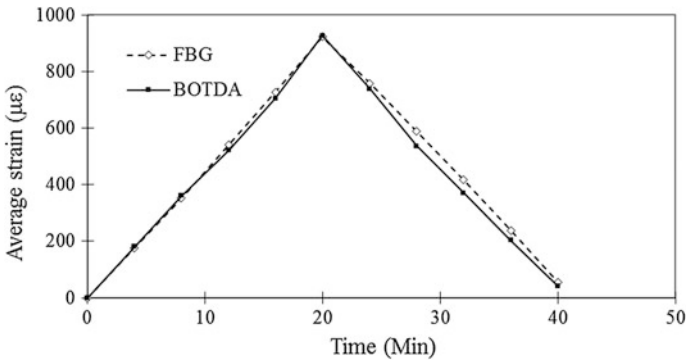
Fig. 6 Comparison of strain variations measured by FBG and BOTDA sensors

Beam Deflection Calculated from FDM

As introduced in Fig. 3 and Sect. 2.2, beam defections at different locations can be measured by LVDTs and calculated by different optical fiber strain sensors based on FDM. Figures 7 shows the calculated deflections of the settlement beam under different loading levels based on FBG and BOTDA strain data. The solid lines and dash lines marked in these figures refer to that the beam is subjected to loading and unloading, respectively. It is clear that the measured beam deflections at the middle locations of the beam are the largest, with a deflection increment around 20 mm for each loading level. The maximum beam deflection approached is around 110 mm as observed from deflection values obtained from the two OFS technologies. The maximum different between the deflection values occur at the middle location of the beam, and the deflection difference is around 5 mm, amounting to around 5%
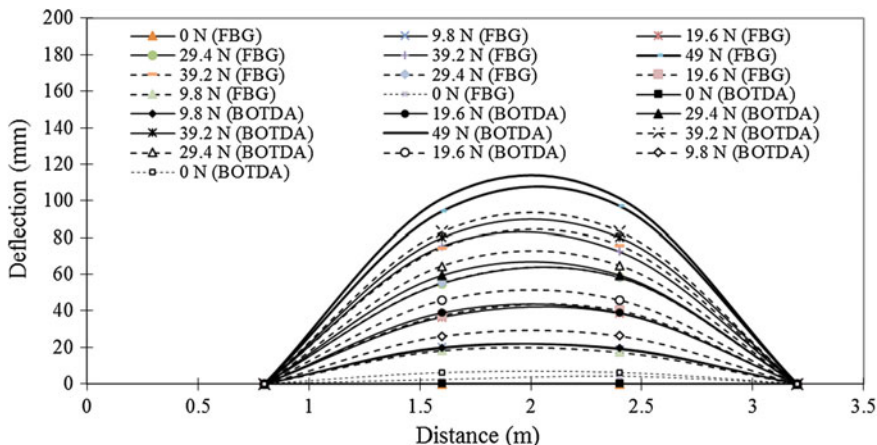
Fig. 7 Comparison of beam deflection predicted by FBG and BOTDA sensors

measurement error. In addition, the occurred significant deflection can be used to monitor the possible excessive ground settlement under pavements, foundations, dams, etc.

Potential Application as a Settlement Sensor in Practice

The large-settlement beam can be applied for real-time settlement monitoring for footings, pavements and dams by embedding itself a certain depth underground. Figure 4 shows a potential application example of the large-settlement beam in geotechnical practice. As can be seen, before the construction of the footing, the large-settlement beam (installed with different OFS) is buried at a certain depth below the footing. The footing is subjected to vertical net pressure from super-structures, causing a substantial rise of vertical soil stress/settlement, which will transfer into deeper foundation locations. Therefore, the pre-buried large settlement-beam is subjected to an increase of vertical stress and will bend espe-cially at the locations right below the footing. Hence the FOS mounted on beam surface will record the occurred strain (resulted from the vertical stress increasing) which will be further used for the calculation of the vertical settlement right below the footing with respect to the two ends of the large-settlement beam. In addition, the boundary conditions of the beam may be assumed to be simply supported if the relative movements of two beam ends are ignorable. In order to improve the sen-sitivity of the settlement beam, the system can be optimized by for example increasing the width and thickness of the beam to achieve a better coupling effect with surrounding soils, or by increasing the numbers of strain sensors mounted on beam. The beam casing can also be grouted underground in order to deform with surrounding soil under foundations.

Conclusions

An OFS based large-settlement beam was proposed for monitoring the large set-tlement for geotechnical structures, such as pavements, foundations, etc. A calibration test in lab was carried out to examine the performance of the set-tlement beam using OFS. Strain data from BOTDA and FBG sensors agree fairly well with each other for different load/unload cycles even when large defection (around 110 mm) occurred. Calculated deflection data from both BOTDA and FBG sensors are in good agreement with LVDT data, indicating the measurement of large-settlement using this proposed sensing system is reliable. Attention shall be paid to the rise of relative errors resulted from unloading process compared with loading process. These increased relative errors may be attributed to the unrecoverable plastic deformation of the beam under high level vertical loads at the two ends of the beam. Further validation tests will be carried out to examine the performance of beam for settlement monitoring under a real geotechnical structure. This paper only presents a typical case study to verify the sensor performance and some other calibration tests (such as the beam casing bends freely or placing underground for settlement measurement testing) will be carried out to verify the beam performance.

References

1. Abosh, H., Ichmoto, E., Enoki, M., Harada, K. (1979). The composer - A method to improve characteristics of soft clay by inclusion of large diameter sand columns. Proceedings of International Conference on Soil Reinforcement: Reinforced Earth and Other Techniques, Paris, vol. 1, pp. 211–216.
2. Taylor, D.W. (1948). Fundamentals of Soil Mechanics. John Wiley & Sons Inc, New York.
3. Chai, J.C., Miura, N. (1999). Investigation on some factors affecting vertical drain behavior. Journal of Geotechnical and Geoenvironmental Engineering, ASCE, 125(3): 216–226.
4. Kim, N. S. & Cho, N. S. (2004). Estimating Deflection of a Simple Beam Model Using Fiber Optic Bragg-Grating Sensors, Experimental Mechanics, 44 (4), pp. 433–439.
5. Xu, D. S., Yin, J. H., Cao, Z. Z., Wang, Y. L., Zhu, H. H. & Pei, H. F. (2013). A New Flexible Fbg Sensing Beam for Measuring Dynamic Lateral Displacements of Soil in a Shaking Table Test, Measurement, 46 (1), pp. 200–209.
6. Zhu, H. H., Yin, J. H., Yeung, A. T. & Jin, W. (2010). Field Pullout Testing and Performance Evaluation of Gfrp Soil Nails, Journal of Geotechnical and Geoenvironmental Engineering, 137 (7), pp. 633–642.

7. Kwon, I. B., Kim, C. Y. & Choi, M. Y. Distributed Strain and Temperature Measurement of a Beam Using Fiber Optic Botda Sensor. Smart Structures and Materials, 2003. International Society for Optics and Photonics, pp. 486–496.

8. Bao, X., Demerchant, M., Brown, A. & Bremner, T. (2001). Tensile and Compressive Strain Measurement in the Lab and Field with the Distributed Brillouin Scattering Sensor, Journal of Lightwave Technology, 19 (11), pp. 1698–1704.

9. Zhu, H. H., Shi, B., Yan, J. F., Zhang, J. & Wang, J. (2015). Investigation of the Evolutionary Process of a Reinforced Model Slope Using a Fiber-Optic Monitoring Network, Engineering Geology, 186, pp. 34–43.

10. Sun, Y. J., Zhang, D., Shi, B., Tong, H. J., Wei, G. Q. & Wang, X. (2014). Distributed Acquisition, Characterization and Process Analysis of Multi-Field Information in Slopes, Engineering Geology, 182, pp. 49–62.

11. Pei, H. F., Yin, J. H. & Jin, W. (2013). Development of Novel Optical Fiber Sensors for Measuring Tilts and Displacements of Geotechnical Structures, Measurement Science and Technology, 24 (9), pp. 095202.

12. Zhao, Y., Wang, Q. & Huang, H. (2010). Characteristics and Applications of Tilted Fiber Bragg Gratings, Journal of Optoelectronics and Advanced Materials, 12 (12), pp. 2343–2354.

13. Mohamad, H., Soga, K., Pellew, A. & Bennett, P. J. (2011). Performance Monitoring of a Secant-Piled Wall Using Distributed Fiber Optic Strain Sensing, Journal of Geotechnical and Geoenvironmental Engineering, 137 (12), pp. 1236–1243.

14. Meng, D. & Ansari, F. (2013). Damped Fiber Optic Low-Frequency Tiltmeter for Real-Time Monitoring of Structural Displacements, Measurement Science and Technology, 24 (12), pp. 125106.

15. Pei, H. F., Yin, J. H., Zhu, H. H. & Hong, C. Y. Development and Application of an Optical Fiber Sensor Based in-Place Inclinometer for Geotechnical Monitoring. Geo-Frontiers 2011@ sAdvances in Geotechnical Engineering, 2011. ASCE, pp. 1725–1731.

16. Ho, Y. T., Huang, A. B. & Lee, J. T. (2006). Development of a Fibre Bragg Grating Sensored Ground Movement Monitoring System, Measurement Science and Technology, 17 (7), pp. 1733–1740.

17. Bao, H. L., Dong, X. Y., Zhao, C. L., Shao, L. Y., Chan, C. C. & Shum, P. (2010). Temperature-Insensitive Fbg Tilt Sensor with a Large Measurement Range, Optics Communications, 283 (6), pp. 968–970.

18. Bao, H., Dong, X., Zhao, C., Shao, L.-Y., Chan, C. C. & Shum, P. (2010). Temperature-Insensitive Fbg Tilt Sensor with a Large Measurement Range, Optics Communications, 283 (6), pp. 968–970.

19. Bao, H. L., Dong, X. Y., Shao, L. Y., Zhao, C. L. & Jin, S. Z. (2010). Temperature-Insensitive 2-D Tilt Sensor by Incorporating Fiber Bragg Gratings with a Hybrid Pendulum, Optics Communications, 283 (24), pp. 5021–5024.

20. Au, H., Khijwania, S. K., Fu, H., Chung, W. & Tam, H. (2011). Temperature-Insensitive Fiber Bragg Grating Based Tilt Sensor with Large Dynamic Range, Journal of Lightwave Technology, 29 (11), pp. 1714–1720.

21. Klar, A., Bennett, P. J., Soga, K., Mair, R. J., Tester, P., Fernie, R., St John, H. D. & Torp-Peterson, G. (2006). Distributed Strain Measurement for Pile Foundations, Proceedings of the ICE-Geotechnical Engineering, 159 (3), pp. 135–144.

22. Li, H. N., Li, D. S. & Song, G. B. (2004). Recent Applications of Fiber Optic Sensors to Health Monitoring in Civil Engineering, Engineering Structures, 26 (11), pp. 1647–1657.

23. Habel, W. R. & Krebber, K. (2011). Fiber-Optic Sensor Applications in Civil and Geotechnical Engineering, Photonic Sensors, 1 (3), pp. 268–280.

24. Hisham, M., Peter, J., Kenichi, S., Assaf, K. & Adam, P. (2007). Distributed Optical Fiber Strain Sensing in a Secant Piled Wall. Proceedings of the Seventh International Symposium on Filed Measurements in Geomechanics, pp. 22–31.

25. Cheung, L., Soga, K., Bennett, P. J., Kobayashi, Y., Amatya, B. & Wright, P. (2010). Optical Fibre Strain Measurement for Tunnel Lining Monitoring, Proceedings of the ICE-Geotechnical Engineering, 163 (3), pp. 119–130.

Numerical Model of Widen Construct of Geogrid-Reinforced Pile-Supported Railway Embankment

Yinan Wang and Xuecheng Bian

Introduction

There are obvious differences between the requirements of railway subgrade engineering and building engineering. The foundation soil is allowed to settle clearly during the construction period in the railway subgrade project. After most of the consolidation process completed and the bearing capacity of the foundation improved, the installation of track structure starts. But the post-construction settlement, which is required quite strictly to ensure the track smooth and safety. In China, there is large area of soft soil the Four Vertical and Four Horizontal high-speed railway network plan. The soft soil comprises mainly by clay mineral leading to low strength, high compressibility, poor permeability and long consolidation time. During the process of embankment filling, the filling height is limited at one time due to potential soil damage and the road may crack due to excessive settlement and differential settlement after the embankment is put into service [1–3]. When dealing with poor foundation consisted with plastic silt or mucky soil, the GRPS design is popular because this kind of embankment will control the settlement and differential settlement effectively [4, 5]. The pile-cap is selected to replace traditional raft saving the concrete amount and the shortened construction Period. The pile-caps are covered with high-strength geogrid to constrain lateral deformation. However the behavior of GRPS design is quite complex which's load transfer mechanism mainly includes the soil arching effect and membrane effect of the geogrid and the interaction of piles and surrounding soil [6, 7]. The complexity of this kind of embankment limits theoretical analysis [8].

Y. Wang (✉) · X. Bian
Department of Civil Engineering, Zhejiang University, Hangzhou 310058, China
e-mail: 114831698@zju.edu.cn

X. Bian
e-mail: bianxc@zju.edu.cn

PLAXIS provides abundant specialized geotechnical constitutive models and reliable results widely recognized in the international geotechnical engineering community. Therefore this paper intends to choose the finite element program PLAXIS 3D to study the railway embankment widening construction. The geogrid reinforced pile supported embankment is a three-dimensional problem. Considering the asymmetry of the construct and the limitation of the plane simplification, the 3D finite element analysis is carried out.

Establishment of Finite Element Model

A length of high-speed railway is designed GRPS embankment structure. After track structure construction finished but before put into service, the railway is decided to get widen to contain four lines from two lines to better fit the high-speed network plan. In order to study the effect of the widening construction to the original lines, the numerical simulation method is used.

Engineering Geological Conditions

The project is located in the lacustrine plain which's soil is consist of lacustrine silty clay and mucky clay below which there are mud rock and argillaceous sandstone treated as base rock. Surface water system develops and river connects into networks. Underground water is pore-phreatic water which dive generally 0.4 m to 0.9 m under earth and is supplied by atmospheric precipitation and overland runoff. According to the field measured data, details are provided in Table 1.

Construction Design

According to the sequence of construction, the construction is divided into three stages: the original construction stage, the slope-cutting stage and the widening construction stage. In the original construction stage, the foundation is reinforced

Table 1 Parameters adopted for soil simulation

Soil	Depth (m)	γ_{unsat} (kN/m^3)	γ_{sat} (kN/m^3)	k (m/day)	E (kPa)	v	c (KPa)	φ (°)
(1) Mucky Silty Clay	18	17.93	18.14	1.E−04	3300	0.33	8.93	10.74
(2) Silty Clay	5	19.4	19.73	1.E−03	7800	0.33	26.58	15.08
(3) Conglomeratic Silty Clay	2	20	22	2.E−01	10000	0.3	21.3	18
(4) Argillaceous Sandstone	25	22	22.5	1.E−04	360000	0.24	60	22
(5) Sand mat	0.6	20	22	1.E+02	300000	0.25	0	40

Table 2 Numerical construction procedure

Phase	Days	Cumulative days	Phase	Days	Cumulative days
1st Embankment Filling	14	14	Track Structures	21	506
Consolidation	50	64	Consolidation	120	626
2nd Embankment Filling	14	78	Left Slope-Cutting	10	636
Consolidation	50	128	Right Slope-Cutting	10	646
3rd Embankment Filling	14	142	Barricade Arrangement	20	666
Consolidation	186	328	Left Widening	20	686
Surcharge Preload	7	335	Mutual Widening	20	706
Consolidation	143	478	Right Widening	20	726
Overload Elimination	7	485	Consolidation	360	1086

by 26.5 m length precast tube pile whose type is PHC400-95 arranged quadrate uniformly with separate distance equals 2.2 m. The pile ends crossed the whole weathered mudstone into the strong weathered mudstone layer. The pile-caps are designed 1.4 m × 1.4 m with reinforced C35 concrete. Above the caps, there is 0.5 m thick gravel +0.1 m coarse sand cushion and the high-strength geogrid lays between the sand mat. The embankment is filled 6.5 m height divided into three fillings using high quality filler. A 2.5 m height surcharge preload is arranged to accelerate consolidation process which is eliminated after soil strength grows enough. After track structure construction finished, this stage ends. In the slope-cutting stage, the slope is cut from former 1:1.5 into 1:1 to reduce the differential settlement of the widening project and to solve the problem of subgrade cracking between the new and old subgrade. The left slope is cut first and then the right one gets started, after that a L-type barricade is arranged on designed location. In the widening stage, there are three steps: the first step is called left widening in which the part I is filled; the second step is named mutual widening in which both the part II and III is filled; the third step is marked as right widening in which step, the part IV is filled and after that the full widening construct ends. Every phase is set the same as construct processes, and the duration is consistent with actual operation. The process phases are shown in the Table 2 and the model is shown as Fig. 1. Additionally the model is 2.2 m wide to simplify the simulation and Line III/IV is marked to study the deformation varying with time.

Simulation of Structures

PLAXIS 3D provides a featured embedded pile model to simulate pile-soil inter-action. The embedded pile elements can be considered to consist of a beam element which can simulate various pile section shape and an embedded interface unit to

Fig. 1 Geometric model and finite element model

Fig. 2 Deformation of model with 20 times scale factor

Table 3 Parameters adopted for structures simulation

	Length (m)	γ (kN/m^3)	E (kPa)	G (kPa)	I (m^4)	EA (kN/m)
Pile	26.5	22	3.60E+7		1.16E−3	–
Pile-Cup	0.4	22	3.15E+7	1.36E+7	–	–
Geogrid	41.1	–	–	–	–	350
L-Type barricade	–	22	–	–	–	–

simulate interaction of the pile element and the soil element including shaft resistance and tip resistance of pile which uses an elastoplastic model. As for geogrid, we choose flexible geogrid elements that can only bear tension. The pile-cap element is used to simulate pile-cap. The contact surfaces between structures is set sharing the free of degree of displacement. Parameters adopted for simulation are shown as Table 3. Figure 3 shows the simulation of piles, pile-caps and geogrid.

Fig. 3 Simulation of
structures

Analysis of Simulation Results

Deformation of the Embankment

The settlement develops with time of roadbed centre and Line III/IV shown in Fig. 4. In the original filling construct stage, the three gauge points still keep recessive in the first and second filling. So the curves start from the third filling and settlements already exist. Most of the embankment settlement occurs in the embankment filling stage and surcharge preload stage in which stages soil consolidate and strength grow. When the surcharge is unloaded, the soil rebounds partially and the roadbed has reached the state for use at this time. The soil strength has already improved leading few deformation on track construction. The settlement of stage slope-cut is similar to the remove of surcharge.

Due to the asymmetry of the filling process, we are very concerned with the differential settlement of the two lines and the embankment center during the filling phase in order to avoid the situation that the differential settlement is so large that it affect the normal operation of the line. As shown Fig. 5, it is refined to better understand what's happening in the embankment. During left widening construction, the settlement of Line IV deteriorates compared with the other two behave almost the same. When it comes to mutual widening construct, the settling rate of Line IV remains the same as left widening. The rate of the other two increase to the same as the rate of Line IV meaning that these three points are in the state of co-settlement. At last, the three rate of settling start to decrease, and the rate of Line IV get the most obvious reduction. As shown in Fig. 2, it shows the deformation after all the constructs of every part which consist the embankment. With 20 times shrinkage factor, the deformation is enlarged as we can see. The geogrid and pile-cap structures surely control the settlement of soil effectively as the soil settles as wave (Figs. 3, 4).

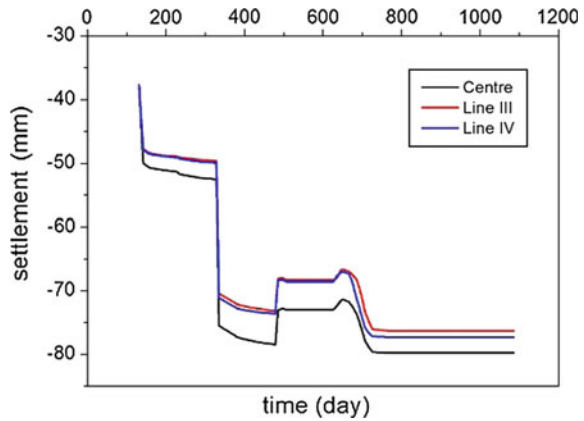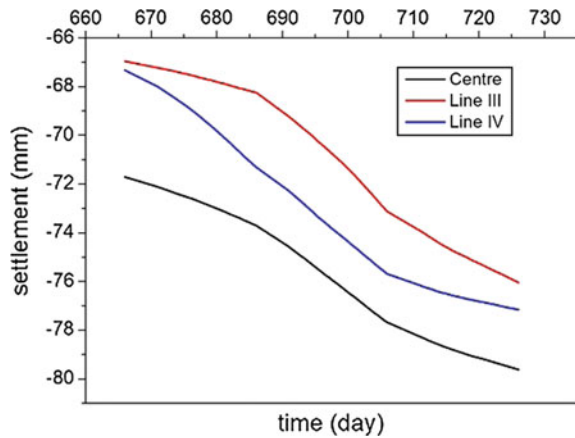**Fig. 4** Settlement of the marked points of all stages

Fig. 5 Settlement of the marked points of widening stage

The Behavior of Geogrid Tension and Deformation

The GRPS embankment design employs tension membrane effect to constrain the lateral deformation of the top of the pile and the pile-cap. Throughout the construction process, the geogrid will produce tension and deformations. The deformation of the geogrid consists of three parts, settlement, lateral deformation and total deformation. In order to verify which deformation contributes most to the tension, we chose the data of tension and deformation drawn in the same coordinate system. It make sense to point out that the value of the lateral deformation above zero means the deformation points to the right (positive direction of X axis); and the settlement of geogrid is below zero because the geogrid settles with the pile. But the total deformation is scalar, constant greater than zero and the unit of tension is also different from the deformation. So the data gets numerical method to get the data comparable, and the results are shown in Fig. 6.

Fig. 6 Correlation of
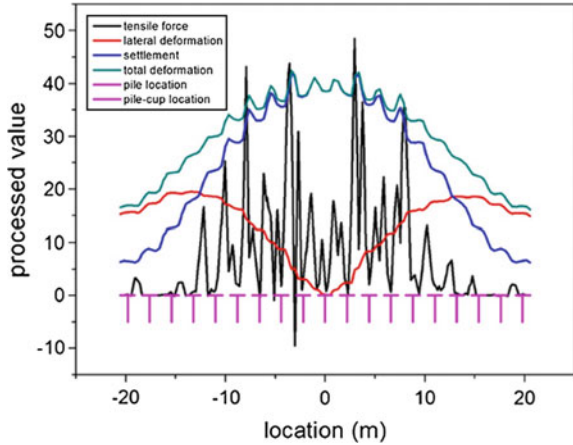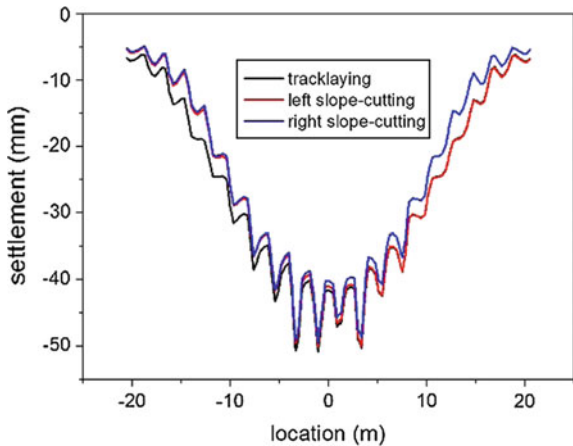geogrid's tension and
deformations

Fig. 7 Settlement of geogrid
of Stage Slope-cutting

The short lines on Y = 0 represent true location of piles and pile-caps convenient for the analysis. The tension of the geogrid shows a distinct cyclical change that it reaches the minimum at the center of each pile-cap, gets large in the gap between two pile-caps, and reaches the maximum in the center of the gap. The deformation shows obvious symmetry. Another law is detected that at the range of 9 piles of the central embankment, both the total deformation and the settlement is close to each other and tend to be slightly smaller while the lateral deformation of the geogrid develop rapidly from the center to outward of the embankment that we name this area the Coverage Area(Fig. 10). At the two sides of the coverage area, the settlement deformation declines quickly while the lateral deformation reaches its maximum and keep constant. Throughout the whole embankment area, the geogrid tension and the settlement correlate well so it is practicable to get the tension data through monitoring the settlement.

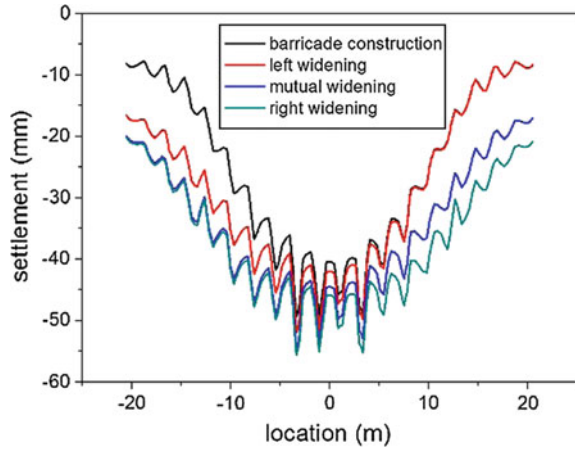Fig. 8 Settlement of geogrid
of Stage Widening

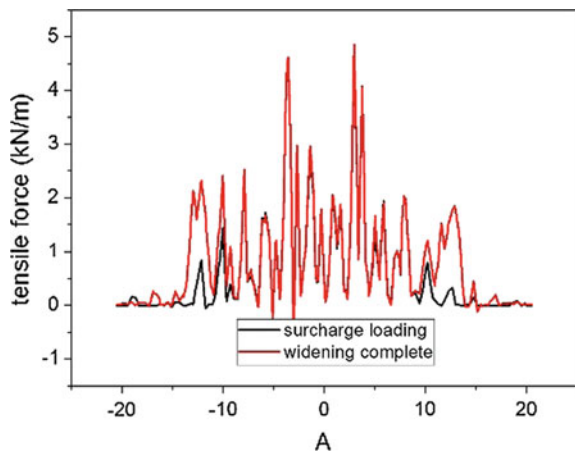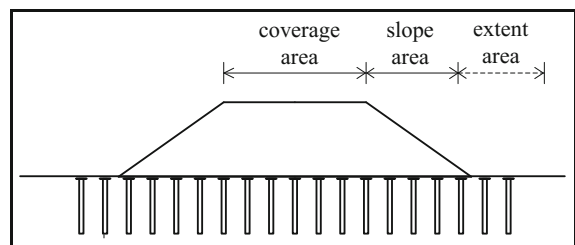Fig. 9 Comparison of tensile
force

Fig. 10 Distinction of areas

In the slope-cutting stage (Fig. 7), the slope-cutting of left affects only few piles located at the left slope. While the rebound at the top of the embankment is very small, the geogrid at the right side of the embankment is completely unaffected.

When it comes to the slope-cutting of right, the law of the geogrid deformation behaves just opposite.

On the widening stage (Fig. 8), the range that affected by the left widening contains left slope area and the whole coverage area which the topline of the embankment covers. The settlement reaches its maximum at piles 6# and 5# and the differential settlement reaches its maximum at piles 6# and 7#. In the meanwhile, the right slope is totally unaffected. At the mutual widening step, the geogrid immediately settles with the top of the pile, and also what happens in the right slope is similar to what happens in left widening. The law of right widening is opposite to the left widening while the differential settlement still happens at pile #6 and 7#.Unilateral widening construct affects the ipsilateral slope area and the whole coverage area. The pile and soil in the coverage area settles together which keeps the tension of geogrid still that verify the conclusion in the geogrid. The geogrid's tension in the range of coverage area keeps till on the stage of both surcharge preload and widening construct while the tension varies most at pile 6# and 7# as shown in Fig. 9.

The Deformation of Piles

Through the previous analysis we can distinguish the embankment into coverage area, slope area and extent area at the pile #4. The settlement of the geogrid is corresponded to the settlement of the pile at which the geogrid and the pile located together. Then the analysis comes to the distribution of the lateral deformation along the pile body (Fig. 10).

Figure 11 shows the 9 piles' lateral deformation's distribution along pile body. The lateral deformation of each pile is divided into two parts. The breakeven point in the depth of −14.5 m below which the lateral deformation point outward of the embankment and above which the lateral deformation point to the centre of the embankment. The lateral deformation which point outward increase from pile 0# to pile 4# which located in coverage area. The pile 5#, 6# and7# at slope area have the feature that the lateral deformations are similar and bigger than the other 7 piles. In the extension area, the lateral deformation of piles although the trend is reduction keeps large. In order to control the lateral deformation of whole embankment, it is necessary to arrange enough piles.

After the analysis of lateral deformation's distribution, we now focus on the lateral deformation at the top of piles as shown in Fig. 12. Because of the symmetry of subgrade before widening construction, only left half of embankment is analyzed during embankment filling and surcharge preloading but when it comes to the widening stage the symmetry is damaged, so the lateral deformation on both sides should be analyzed. But the original value should get modified to the absolute value. The lateral deformation of pile top not only verifies the law of the figure, but also shows the law more clear. In all of the three stages, the lateral deformation develop linearly from 0# to 4#. At the stage of widening, the lateral deformation of pile 6# gets more obvious than the other which consists with Fig. 10. As for the

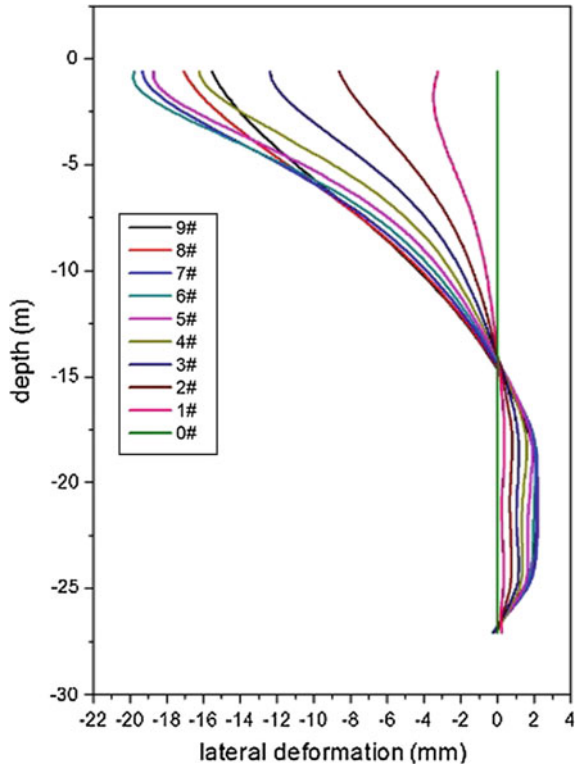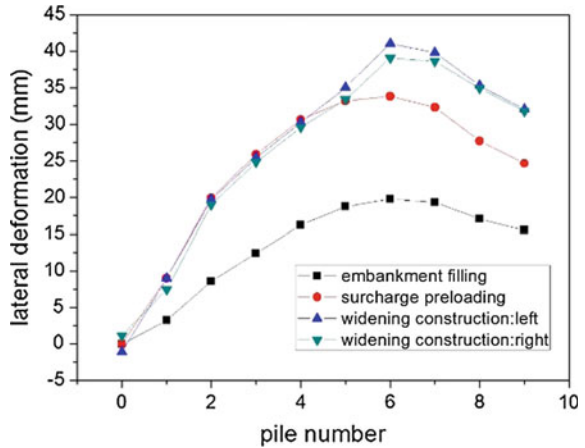**Fig. 11** Distribution of lateral deformation along pile body

Fig. 12 Lateral deformation of pile blocks

original embankment pile 6# bends most violent. Pile is treated as rod structure at theoretical calculation as a vertical bearing structure. Once it bends, the capacity decreased rapidly which explains why pile 6# get affected most at the stage of

widening construct on both settlement and lateral deformation. The lateral deformation of the two piles located at the outermost side trends reduction, but the value is still too high to ignore.

Conclusions

In this paper, the loading features and deformation behavior of the geogrid-reinforced pile-supported embankment is studied on all three stages of original construction, surcharge preloading and widening construct through the numerical simulation of a section of high-speed railway. The followings are the main conclusions of this paper:

(1) According to the model results, the embankment is distinguished into three areas: coverage area, slope area and extent area.
(2) In the Coverage Area, the topline of the embankment settles indifferently. While the settlement is obviously heavy, the lateral deformation initiates linearly.
(3) In the Slope Area, the settlement decreases rapidly and the lateral deformation reaches the maximum which strongly affect the bearing capacity of piles.
(4) In the Extent Area, the settlement of the embankment fades away and there is nearly no tension but the piles bend causing the retreat of the bearing capacity
(5) The load produced by the mound during the construction of widen couples with the bended piles leading to further reduce of the bearing capacity. In order to control the lateral deformation of GRPS embankment, it should be ensured enough piles.
(6) Rather before the widening construction, the piles located at the slope bend more violent leading to the reduction of the bearing capacity. When the load is applied in these area, the settlement caused by the filling is more serious than that of the embankment, and the piles bends further and the carrying capacity decreases again. Therefore, it should be paid more attention at the two lines lay on the original slope area to avoid potential post-construction settlement.

References

1. Han J., J. G. Collin. (2008). Geosynthetic Support Systems over Pile Foundations [J]. Geotechnical Special Publication, (130):1–5.
2. Indraratna B., A. S. Balasubramaniam, S. Balachandran. (1992). Performance of Test Embankment Constructed to Failure on Soft Marine Clay [J]. Journal of Geotechnical Engineering, 118(1):12–33.

3. Magnan Jean Pierre. (Year) Methods to Reduce the Settlement of Embankments on Soft Clay: A Review [C].Name. of 77–91.
4. Fei Kang, Han Long Liu. (2008). Advances in research on design theory of geosynthetic reinforced pile supported embankment [J]. Advances in Science & Technology of Water Resources.
5. Han J., M. A. Gabr. (2002). Numerical Analysis of Geosynthetic-Reinforced and Pile-Supported Earth Platforms over Soft Soil [J]. Journal of Geotechnical & Geoenvironmental Engineering, 128(1):44–53.
6. Ellis E. A., R. Aslam. Arching in piled embankments: Comparison of centrifuge tests and predictive methods [J]. Ground Engineering, 42(6):28–31.
7. Zdravkovic L., V. J. Potts. (2010). Finite-element study of arching behaviour in reinforced fills [J]. Proceedings of the Institution of Civil Engineers Ground Improvement, 163(4):217–229.
8. Zhou Jing, Y. E. Yangsheng, Degou Cai. (2007). Analysis of Calculation Method for Foreign Geosynthetic Reinforced Pile Supported Embankments [J]. China Railway Science.

Effects of Inhomogeneous Subgrade Settlement to Aircraft Vibration and Its Control Standard

Yun Zhao, Daosheng Ling and Bo Huang

Introduction

The airport construction in mountainous areas develops fast in China in recent years. The runway with the length of times kilometers usually passes across different geological unit, leading to complex filled and excavated forms of subgrade. Subjected to gravity stress and long-term airplane dynamic loads, inhomogeneous settlement appears in the subgrade, which influences the safety when airplane taking off or landing and passengers comfort. So, it is of great significance to study the effect of the subgrade inhomogeneous settlement to aircraft vibration and the corresponding control standard.

At present, the researches of the airplane vibration response are mainly studied by taking off, landing or taxiing models established by the traditional two-mass system method or multi-body dynamics software. With the unevenness runway input information, the body responses are solved at time domain or frequency domain [1–5]. The runway input information of the literatures above were mainly obtained by actual measurement or power spectral density function, whose emphasis points laid on the assessment and optimization of shock absorber behavior of landing gear. While, the effect of various runway input information to the body

Y. Zhao (✉) · D. Ling · B. Huang
MOE Key Laboratory of Soft Soils and Geoenvironmental Engineering,
Zhejiang University, Hangzhou 310058, China
e-mail: zhaoyun1106@163.com

D. Ling
e-mail: dsling@zju.edu.cn

B. Huang
e-mail: cehuangbo@zju.edu.cn

Y. Zhao · D. Ling · B. Huang
Institute of Geotechnical Engineering, Zhejiang University, Hangzhou 310058, China

713

vibration is researched relatively less. There are few reports about the settlement control standard of runway information which is based on passengers comfort. Shen studied the landing and taxiing responses of truck-like gear aircraft at 1-cos runways [6]. Zhao et al. studied the dynamic responses of aircraft on concave grade turn point of highway runway pavement [7]. The International Civil Aviation Organization (ICAO) suggested that 2.5–3 cm differential settlement within 45 m distance for runway pavement was acceptable [8]. The United States Federal Aviation Administration (FAA) allowed that the maximum deviation was no more than 6 mm over 5 m [9]. For China, the present control standard relies more on engineering experience. *Code for Geotechnical Engineering Design of Airport* ruled that the post-construction settlement should be no larger than 0.2–0.3 m and the differential settlement should be less than 1–1.5‰ per 50 m horizontal distance along the runway longitudinal direction [10]. The stipulation was more based on engineering experience and only gave the maximum pavement deformation value. It could not reflect the effect of single up-convex or under-concave wavelength deformation and not consider the different settlement control demand for takeoff-landing runway area and taxiing runway area.

An airplane taxiing model of six degree of freedom was established by two-mass system method to research the influence of settlement amplitude, wavelength and taxiing velocity to aircraft vibration under typical settlement model of inhomogeneous subgrade. Based on security and passenger comfort, the settlement control standard for inhomogeneous subgrade was proposed. The calculated results can have a positive significance to the settlement control or maintenance of runway in mountainous areas.

Analysis Model

Aircraft Model

Basic Assumption

Boeing737-800 was chosen since it was the main type of aircraft used in mountainous airport. In order to make the analysis model both brief and efficient, assume that:

(1) The aircraft was divided into two concentrated masses, a sprung-mass, including the mass supported by shock absorber like the body, the wing and outer cylinder of shock absorber, etc. and an unsprung-mass including landing gear piston rod and aircraft wheels, etc.
(2) The landing gear absorbing strut was simplified to air-spring and linear oleo damping.
(3) The forces and deformation of wheels at the horizontal direction was not considered.

(4) The aerodynamic lift was dealt as a concentrated force with the point of action at body centroid.

Equations of Motion

The six degree of freedom aircraft model was as shown in Fig. 1, including the body vertical movement z_0, the roll degree of freedom θ_x, the pitch degree of freedom θ_y and three vertical degree of freedom z_1, z_2 and z_3 for front wheel and the left, right posterior main landing gear tire. Build the right hand rectangular coordinate system $o - xyz$. o was the initial body centroid position. x was the heading direction. z was the vertical direction. The symbols and the corresponding parameter values were shown in Table 1. The values of each parameter refer to literature [11].

According to the rectangular coordinate system, the vibration differential equations of the system were expressed as follows:

$$m_0\ddot{z}_0 = - [k_{11}(z_4 - z_1) + c_{11}(\dot{z}_4 - \dot{z}_1)] - [k_{21}(z_5 - z_2) + c_{21}(\dot{z}_5 - \dot{z}_2)] \\ - [k_{31}(z_6 - z_3) + c_{31}(\dot{z}_6 - \dot{z}_3)] - m_0 g + L \tag{1}$$

$$m_1\ddot{z}_1 = [k_{11}(z_4 - z_1) + c_{11}(\dot{z}_4 - \dot{z}_1)] - k_{12}(z_1 - h_1) - m_1 g \tag{2}$$

$$m_2\ddot{z}_2 = [k_{21}(z_5 - z_2) + c_{21}(\dot{z}_5 - \dot{z}_2)] - k_{22}(z_2 - h_2) - m_2 g \tag{3}$$

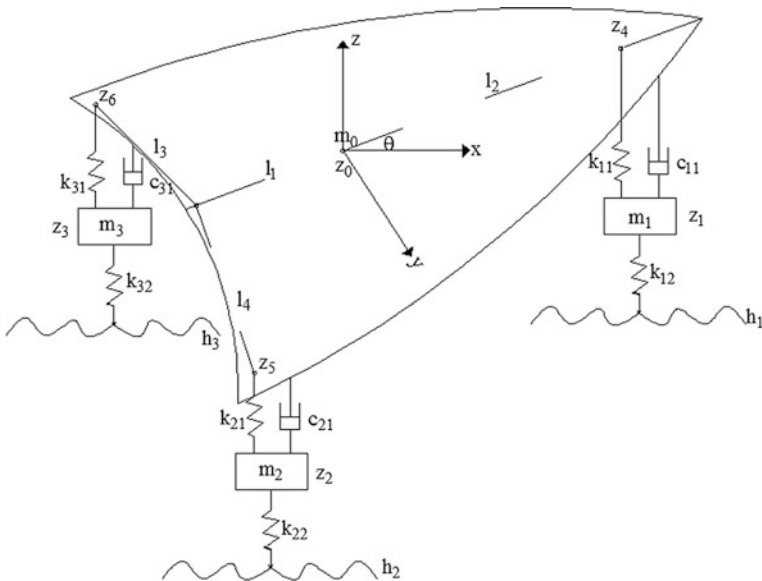$$m_3\ddot{z}_3 = [k_{31}(z_6 - z_3) + c_{31}(\dot{z}_6 - \dot{z}_3)] - k_{32}(z_3 - h_3) - m_3 g \tag{4}$$

Fig. 1 Model of Boeing737-800

Table 1 Paremeters values of Boeing737-800

Parameters	Symbol	Unit	Value
Sprung-mass	m_0	kg	32,800
Nose gear unsprung-mass	m_1	kg	2785
Posterior main landing gear unsprung-mass	m_2/m_3	kg	7455
y axis rotation inertia	I_y	kg m^2	2,000,000
x axis rotation inertia	I_x	kg m^2	720,000
Distance between main tire and body centroid	l_1	m	0.48
Distance between front tire and body centroid	l_2	m	9.02
Distance between left/right main tire and x axis	l_3/l_4	m	2.9
Nose gear air-spring stiffness	k_{11}	N/m	1,200,000
Nose gear damping coefficient	c_{11}	N s/m	5000
Nose gear tire spring stiffness	k_{12}	N/m	2,400,000
Main landing gear air-spring stiffness	k_{21}/k_{31}	N/m	4,800,000
Main landing gear damping coefficient	c_{21}/c_{31}	N s/m	20,000
Main landing gear tire spring stiffness	k_{22}/k_{32}	N/m	9,600,000
Density of air	ρ	kg m^3	1.29
Area of the wing	S	m^2	125

$$J_x \ddot{\theta}_x = -[k_{31}(z_6 - z_3) + c_{31}(\dot{z}_6 - \dot{z}_3)]l_4 + [k_{21}(z_5 - z_2) + c_{21}(\dot{z}_5 - \dot{z}_2)]l_3 \tag{5}$$

$$\begin{aligned} J_y \ddot{\theta}_y = {} & \{[k_{21}(z_5 - z_2) + c_{21}(\dot{z}_5 - \dot{z}_2)] + [k_{31}(z_6 - z_3) + c_{31}(\dot{z}_6 - \dot{z}_3)]\}l_1 \\ & - [k_{11}(z_4 - z_1) + c_{11}(\dot{z}_4 - \dot{z}_1)]l_2 \end{aligned} \tag{6}$$

$$z_4 = z_0 + l_2\theta_y \tag{7}$$

$$z_5 = z_0 - l_1\theta_y - l_3\theta_x \tag{8}$$

$$z_6 = z_0 - l_1\theta_y + l_4\theta_x \tag{9}$$

where $g = 9.8$ m s^{-2} the acceleration of gravity, L is the aerodynamic lift and expressed as $L = 1/2\rho v^2 SC_l$, v is the taxiing velocity, C_l is lift coefficient and expressed as $C_l = f(\theta_y) = 18\theta_y/\pi + 0.7$, h_1, h_2 and h_3 are the input runway information of the tires, respectively.

Settlement Model

During the life period of the runway, subjected to gravity stress and long-term airplane dynamic loads, inhomogeneous settlement appears in the filled-excavated subgrade. Due to the subgrade material difference, up-convex settlement model will

Fig. 2 Settlement models for filled and excavated subgrade
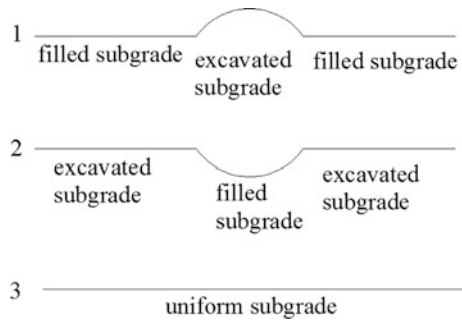
come up at filled-excavated-filled subgrade area. While under-concave settlement model will take place at excavated-filled-excavated subgrade area as shown in Fig. 2. Assume that the all the settlement models are reflected at the pavement surface. The deformation of settlement has the form of semi-wavelength sine distribution:

$$h_i(x) = \begin{cases} 0 & x < x_0, \quad x > x_0 + \lambda \\ \pm A \, \sin(\pi(x - x_0)/\lambda) & x_0 < x < x_0 + \lambda \end{cases} \tag{10}$$

where i represents 1, 2 and 3, meaning the settlement models of up-convex, under-concave and uniform, respectively. x_0 is the beginning position of settlement, λ is the length of sine settlement.

Parameters for Assessment

To evaluate the vibration response conveniently and take the influence of body static force out, define the impact coefficient Ic:

$$Ic = (F_1 - F_0)/F_0 \tag{11}$$

where F_0 represents the posterior main landing gear tire force when aircraft is taxiing at the uniform runway, F_1 represents the posterior main landing gear tire force when aircraft is taxiing at the runway with corresponding settlement model.

ISO2631 standard takes the root mean square of weighed centroid acceleration as the basic method to assess the passenger comfort [12]. The human body has a different sensitivity to aircraft vibration acceleration within a different frequency range. Through fourier transform, the time history curve of the body centroid acceleration a_0 is transformed to frequency domain curve a_1. Then weighed acceleration is obtained by filter grid of weighed function $w(f)$ at frequency domain. Root mean square of weighed centroid acceleration a is obtained as the follows:

$$a = \sqrt{\int_{0.5}^{80} (w(f) * a_1)^2 df} \tag{12}$$

where $w(f)$ has the following expression [13]:

$$w(f) = \begin{cases} 0.5 & (0.5 < f < 2) \\ f/4 & (2 < f < 4) \\ 0 & (4 < f < 12.5) \\ 12.5/f & (12.5 < f < 80) \end{cases} \tag{13}$$

Result of Vibration Response and Discussion

Effect of Settlement Model

Take the results of aircraft with taxiing velocity at 60 m/s, semi-wavelength at 20 m and settlement amplitude 0.01 m as an example to research the vibration responses at the different settlement models.

Figures 3 and 4 show the time history curves of impact coefficient for posterior main landing gear tire force Ic and centroid acceleration a_0 at different settlement models. It can be seen that the values of Ic and a_0 are around 0. The maximum values of Ic and a_0 are equivalent for up-convex and under-concave settlement
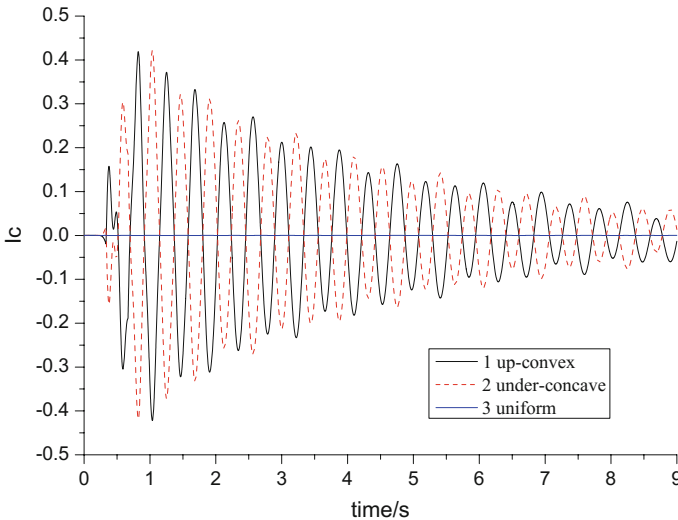

Fig. 3 Time history curves of impact factor for posterior main landing gear tire force
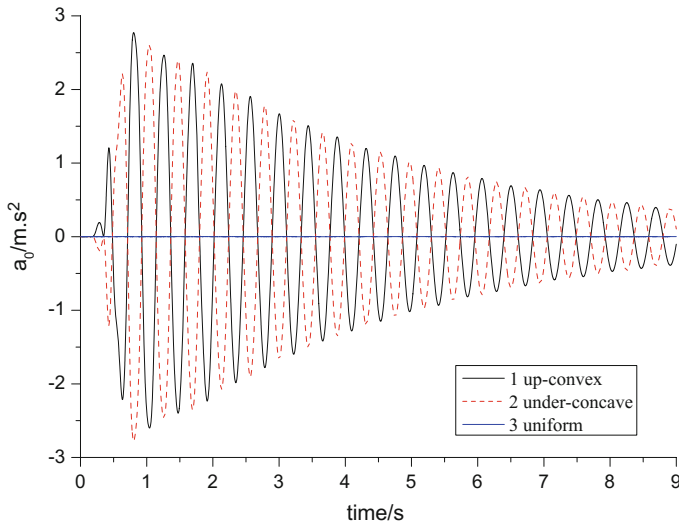
Fig. 4 Time history curves of airplane centroid acceleration

model. The time history curves are symmetrical about "0 line". For brevity, the following text only gives the calculated results of up-convex settlement model.

Effect of Settlement Amplitude

Take the results of aircraft with taxiing velocity at 30 and 60 m/s, semi-wavelength at 20 m and settlement amplitude 0.005–0.05 m as an example to research the vibration responses at the different settlement amplitude.

Figures 5 and 6 show the maximum values of impact coefficient for posterior main landing gear tire force Ic and root mean square of weighed centroid acceleration a versus settlement amplitude at taxiing velocity 30 and 60 m/s, respectively. As can be seen that the values of Ic and a increase linearly with the increase of settlement amplitude. With the increase of semi-wavelength, the ratio of Ic and a versus settlement amplitude have a decrease tendency in general. Compared the results with 30 m/s, the corresponding values of Ic and a have an apparent increase tendency at 60 m/s.

Effect of Semi-wavelength

Take the results of aircraft with settlement amplitude 0.01 m as an example to research the vibration responses at the different settlement semi-wavelength.
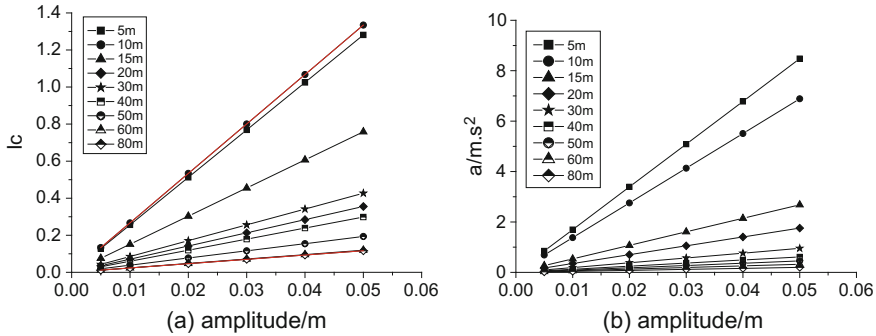
Fig. 5 Curves of **a** peak value of impact factor, **b** root mean square of weighed centroid acceleration versus settlement amplitude at 30 m/s velocity
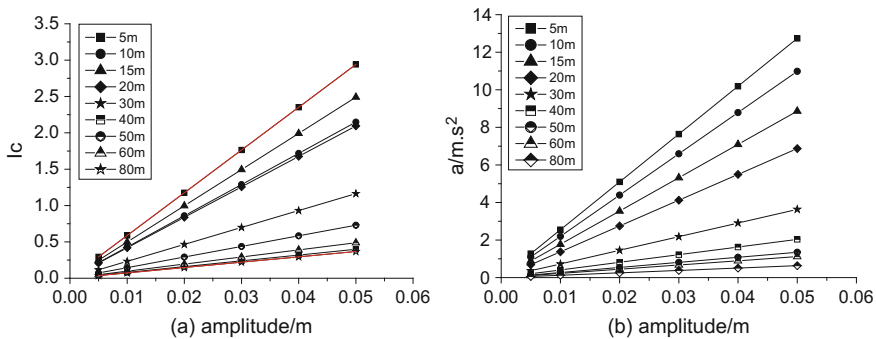

Fig. 6 Curves of **a** peak value of impact factor, **b** root mean square of weighed centroid acceleration versus settlement amplitude at 60 m/s velocity

Figures 7 and 8 show the maximum values of impact coefficient for posterior main landing gear tire force Ic and root mean square of weighed centroid acceleration a versus settlement semi-wavelength at taxiing velocity 20–80 m/s. It can be seen that with the increase of semi-wavelength, the peak values of Ic present a zigzag decrease tendency. It can be attributed to the dynamic interaction between aircraft tires and pavement reduces with the increasing semi-wavelength, leading to a relative slighter lighter impact action. Due to the influence of natural frequency, during the decrease process, salient points appear when the ratio of taxiing velocity and semi-wavelength around the natural frequency. With the increase of taxiing velocity, the dynamic interaction between aircraft tires and pavement strengthens in general, leading to larger values of Ic as a whole. The values of root mean square of weighed centroid acceleration a are not so sensitive to natural frequency. It decreases in general with the increase of semi-wavelength. Oscillating phenomenon appears when the taxiing velocity at a large stage, meanwhile, and the semi-wavelength at a short level. It is because that the vibration system has a drastic dynamic interaction with pavement at the high frequency.

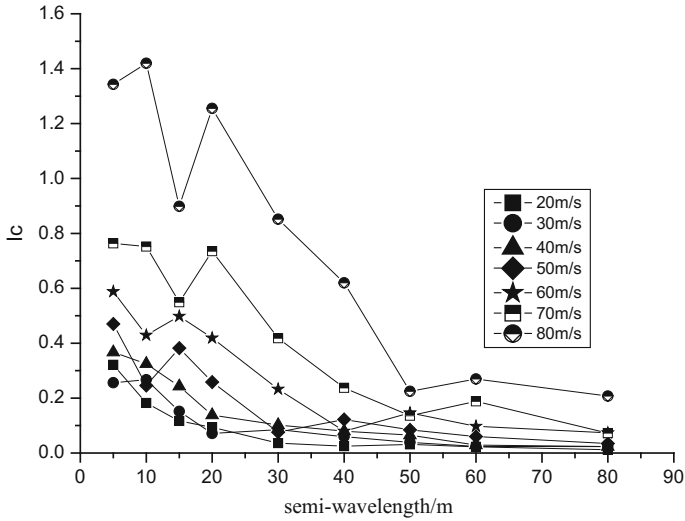**Fig. 7** Curve of peak value of impact factor versus semi-wavelength at different velocities
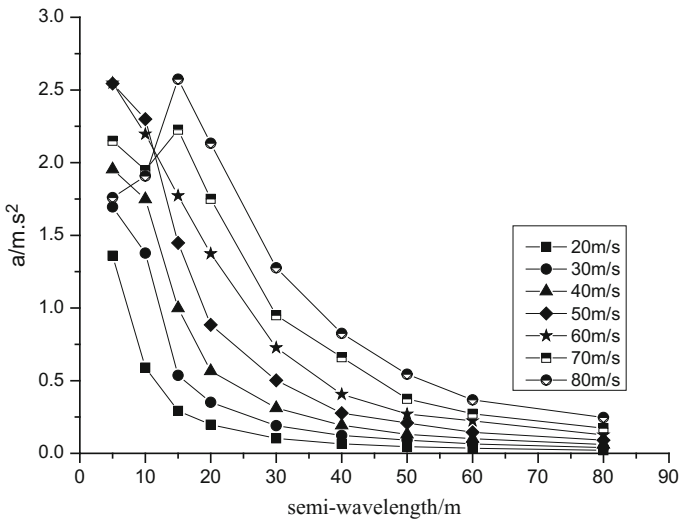

Fig. 8 Curve of root mean square of weighed centroid acceleration versus semi-wavelength at different velocities

Effect of Taxiing Velocity

Take the results of aircraft with settlement amplitude 0.01 m as an example to research the vibration responses at the different taxiing velocity.
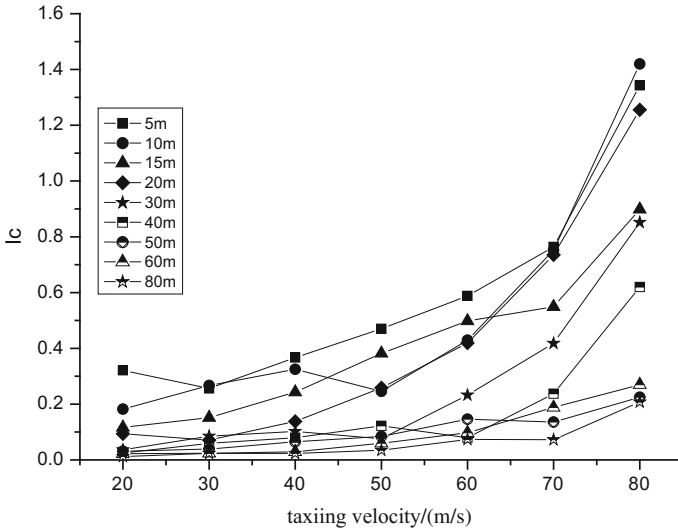
Fig. 9 Curve of peak value of impact factor versus velocity at different semi-wavelength

Figures 9 and 10 show the maximum values of impact coefficient for posterior main landing gear tire force Ic and root mean square of weighed centroid acceleration a versus taxiing velocity at settlement semi-wavelength 5–80 m. It can be seen that with the increase of taxiing velocity, the peak values of Ic present a zigzag increase tendency and the root mean square of weighed centroid acceleration a show a increase tendency in general. It can be attributed to the dynamic interaction between aircraft tires and pavement reduces with the increasing taxiing velocity. It should be pointed out that oscillating phenomenon appears since the vibration system has a drastic dynamic interaction with pavement at the high frequency.

Control Standard of Settlement

Through the discussion above, it can be seen that the differential semi-wavelength and settlement amplitude have great significance to the dynamic response of aircraft vibration and passenger comfort, which has a directly related to the safety operation of the runway. However, there is no suitable differential settlement control standard at present. The impact coefficient Ic has relation to the security of takeoff-landing and landing gear fatigue. According to literature [7], the dynamic factor of pavement is limited less than 1.25. The impact coefficient Ic defined in this article is 1 smaller than the dynamic factor. So, the control criterion value of the impact coefficient is 0.25. As there is no official root mean square of weighed centroid acceleration values to assess aircraft passengers comfort, herein, the corresponding
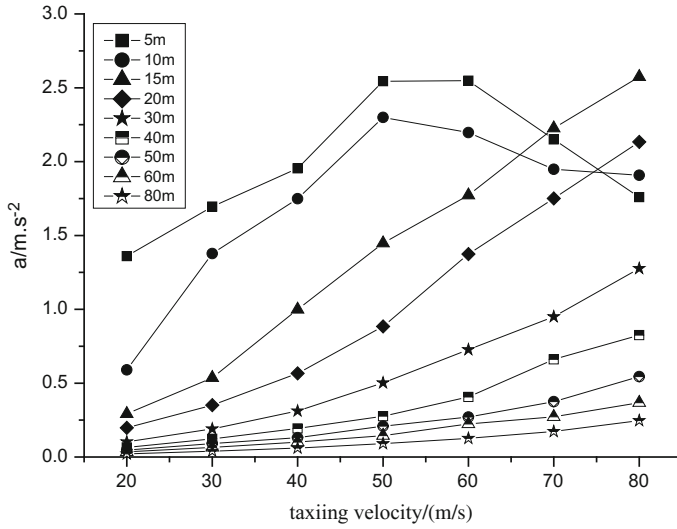
Fig. 10 Curve of root mean square of weighed centroid acceleration versus velocity at different semi-wavelength

evaluation criterion (*a* is no more than 0.13 g) used in high-speed railway, who has a similar speed with aircraft taxiing velocity, is adopted as the evaluation criterion [14]. The results of the two control standard methods are shown in Figs. 11 and 12 at different taxiing velocity.
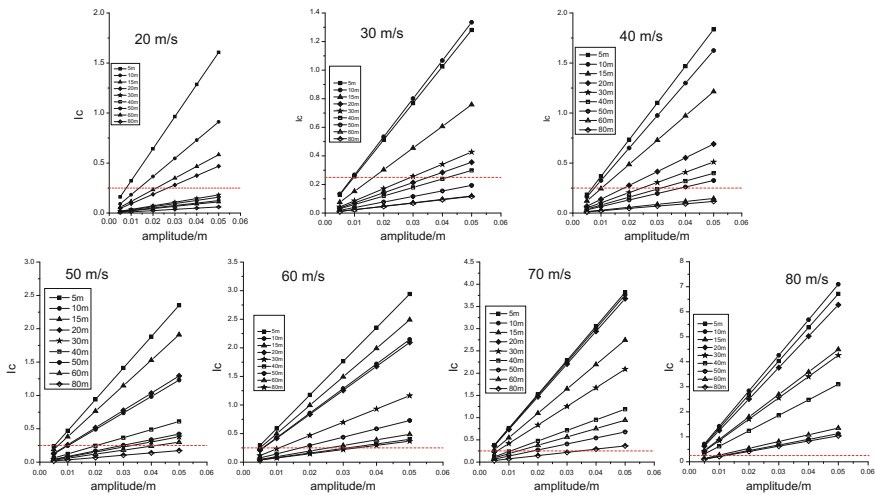
Fig. 11 Curves of the impact coefficient *Ic* versus settlement amplitude at different half-wave length at 20–80 m/s velocities
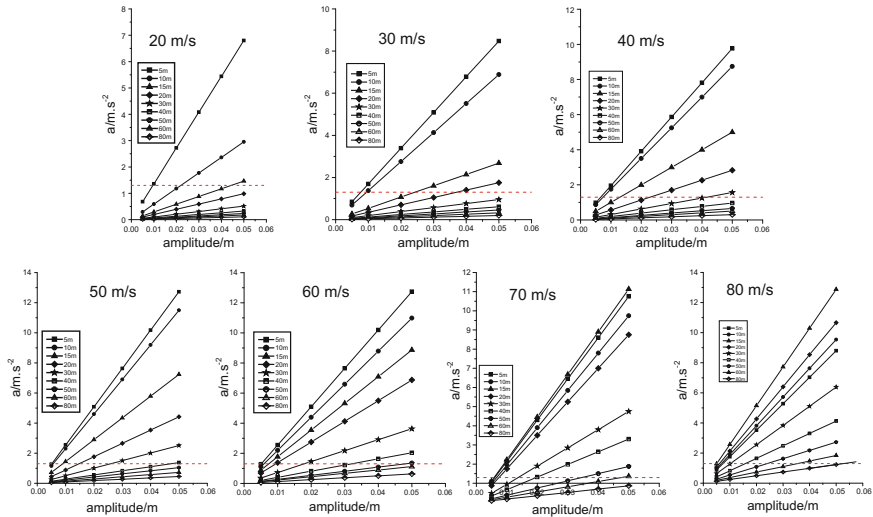
Fig. 12 Curves of root mean square of weighed centroid acceleration versus settlement amplitude at different half-wave length at 20–80 m/s velocities

Table 2 Control standard of differential settlement obtained by root mean square of weighed centroid acceleration

Velocity/semi-wavelength (m/s)	5 m	10 m	15 m	20 m	30 m	40 m	50 m	60 m	80 m
20	8	15	22	27	70	97	80	109	/
30	10	9	17	35	29	42	65	102	104
40	7	8	10	18	25	31	39	90	111
50	5	10	7	10	33	21	29	42	72
60	4	6	5	6	10	31	17	26	34
70	3	3	5	3	6	10	18	13	34
80	2	2	3	2	3	4	11	9	12

Table 3 Control standard of differential settlement obtained by root mean square of weighed centroid acceleration

Velocity/semi-wavelength (m/s)	5 m	10 m	15 m	20 m	30 m	40 m	50 m	60 m	80 m
20	10	22	44	67	122	205	271	/	/
30	8	9	24	37	68	107	144	185	292
40	7	7	13	23	42	67	99	129	204
50	5	6	9	15	26	47	62	89	137
60	5	6	7	9	19	32	48	58	100
70	6	7	6	7	14	20	35	48	75
80	7	7	5	6	10	16	24	35	53

Table 4 Control standard of differential settlement obtained by root mean square of weighed centroid acceleration

Velocity/semi-wavelength (m/s)	5 m	10 m	15 m	20 m	30 m	40 m	50 m	60 m	80 m
20	8	15	22	27	70	97	80	109	/
30	8	9	17	35	29	42	65	102	104
40	7	7	10	18	25	31	39	90	111
50	5	6	7	10	26	21	29	42	72
60	4	6	5	6	10	31	17	26	34
70	3	3	5	3	6	10	18	13	34
80	2	2	3	2	3	4	11	9	12

According to the result of Figs. 11 and 12 and the control criterion, the differential settlement control standard can be obtained as shown in Tables 2 and 3. For practical application, both the factors need to be considered. Base on more secure and strict demand. The values of settlement control standard in Table 4 are recommended for mountainous airport where Boeing737-800 aircrafts are mainly used.

Conclusions

An airplane taxiing model of six degree of freedom which can consider the effect of aerodynamic lift was established to research the influence of settlement amplitude, wavelength and taxiing velocity to aircraft vibration under typical settlement model of inhomogeneous subgrade. The conclusions are as follows:

(1) The aircraft model of six degree of freedom established here can simulate the aircraft vibration under different input runway information both briefly and efficiently.

(2) The impact coefficient for posterior main landing gear tire force and root mean square of weighed centroid acceleration increase linearly with the increase of settlement amplitude. Both values have the increasing tendency with the taxiing velocity increasing or the wavelength decreasing

(3) Based on security and passenger comfort, the settlement control standard for inhomogeneous subgrade was proposed. The calculated results can have a positive significance to the settlement control or maintenance of runway in mountainous areas.

References

1. Jin, P. (2003). Simulation analysis of dynamic behavior for airplane landing gear. MS Thesis, Nanjing University of Aeronautics and Astronautics, Nanjing, China.
2. Liu, L., Yang, G.Z., He, Q.Z. (1992). Influences of landing gear system on dynamic response in aircraft during taxiing. Acta Aeronautica et Astronautica Sinica, 13(6): B266–B273.
3. Liu, L., Yang, G.Z., He, Q.Z. (1993). Analysis of statistical vibration in aircraft during taxiing. Acta Aeronautica et Astronautica Sinica, 14(4): B126–B132.
4. Nie, H., Kortum, W. (2000). Analysis for aircraft taxiing at variable velocity on unevenness runway by the power spectral density method. Transactions of Nanjing University Aeronautics and Astronautics, 17(1): 64–70.
5. Li, S.Z. (2006). Analysis of aircraft taxiing-induced response with multiple wheels and multiple landing gears. MS Thesis, Northwestern Polytechnical University, Xian, China.
6. Shen, H. (2001). Analysis of landing-gear behavior for landing & taxiing. Chinese Journal of Applied Mechanics, SI(18): 198–202.
7. Zhao, L., Li, G.Y., Shi, B.H. (2010). Dynamic analysis on concave grade turn point of highway runway pavement used by aircraft. Journal of Chang'an University, 30(2): 44–47.
8. "International Standards and Recommended Practices, Aerodromes", International Civil Aviation Organization, Annex 14, March 1983.
9. FAA Advisory Circular, AC 150/5370-13, "Off-peak Construction of Airport Pavements Using Hot-Mix Asphalt", August 27,1990.
10. Trade Standard of People's Republic of China. MHT 5027-2013 Code for Geotechnical Engineering Design of Airport [S]. Beijing: China Civil Aviation Press, 2013.
11. Xue, H.X. (2014). Analysis on vibration frequency response of rigid pavement in conditions of aircraft taxiing. MS Thesis, Civil Aviation University of China, Tianjin, China.
12. ISO. Mechanical vibration and shock-evaluation of human exposure to whole-body vibration-Part 1: General requirements [S]. ISO 2631-1, 1997.
13. Yu, Z.S. (2009). Automotive theory [M]. Beijing: China Machine Press.
14. Cheng, C. (2015). Study on dynamic responses of irregularity ballastless track for high-speed railway. PhD Thesis, Zhejiang University, Hangzhou, China.

Experimental Study on Temperature Characteristics of CRTS I Twin-Block Ballastless Track

Zhangbo Wan and Rongshan Yang

Introduction

Ballatless tracks are widely used in high speed way of China, for the granular ballast materials, compared to traditional ballast tracks, are replaced by the concrete and asphalt with a better integrality, which have a better ability to maintain the high precision of the track geometry, meanwhile they can afford sufficient load bearing capacity. Currently, ballastless tracks are mostly made of concrete materials, mainly including CRTS I, II and III slab track, as well as CRTS I and II twin-block track [1].

Ballastless tracks are exposed to natural environment, whose properties can be easily affected by air temperature, solar radiation, rainfall, wind velocity and some other ambient factors. Periodical change measured by daily, monthly, seasonal and annual values occurs to track structure. Track slab, as superstructure of ballastless track, within its life cycle, except train cyclic loading, bears temperature loading, caused by the alternate-changing temperature, which can also lead to stretching or warping deformations. Once deformations are restrained, temperature stress occurs. During design stage, temperature loads are usually divided into two parts, including the rising and falling of temperature, as well as the temperature gradient. And the stretching and warping stress are computed for two kinds of temperature load [2]. Therefore, temperature impacts should be taken into consideration for ballastless track's design stage, meanwhile, under certain conditions, temperature acts as a controlling factor in this stage [3].

Z. Wan (✉)
Department of Civil Engineering, Zhejiang University, Hangzhou 310058, China
e-mail: wzbstudy@sina.com

R. Yang
Department of Civil Engineering, Southwest Jiaotong University, Chengdu 610031, China
e-mail: yrs@home.swjtu.edu.cn

Solar radiation represents a calculated rate related to the thermal energy that is incident upon a concrete surface. The sun's rays which are absorbed directly by the concrete surface cause the concrete surface to be heated more rapidly than the interior region of a concrete structure. This effect may contribute to a temperature gradient through the concrete, and if the boundary conditions are restrained, it will lead to different temperature stress, causing cracks in the concrete structure [4]. For the temperature issues of the hydraulic concrete, caused by sunshine and solar radiation, a lot of studies were carried out by Zhu, Gong [5, 6] and some other researchers. Yavuzturk et al. [7], based on two-dimensional finite difference method, studied impacts of environmental factors on temperature change of asphalt pavement under hot weather conditions. Yang [4] studied the influence factors of solar radiation and important parameters for the heat transfer of concrete pavement. The superstructure of ballastless track are concrete structure, however, the external conditions, such as solar radiation, angle of incidence and wind velocity, are quite different from ballastless tracks to highway pavements, bridges and dams. Therefore, the research results in this field can hardly be copied for ballastless tracks. To clarify the effect of ambient factors on temperature field of ballastless track, based on the on-site experiment, temperature of superstructure of CRTS I twin-block ballastless track and ambient factors(solar radiation intensity and air temperature) in Chengdu, were supervised and measured, and a whole year of data are acquired. Based on the field-test data, the corresponding relationship between solar radiation intensity, air temperature and temperature of track slab is analyzed, which provides an experimental basis for the study of temperature field of ballastless track.

Experimental Scheme

For having a good knowledge of temperature characteristics of superstructure of ballastless track, an actual-size model, CRTS I twin-block ballastless track, was created in Chengdu. The size of track slab is $5500 \times 2800 \times 250$ mm and base plate is $5500 \times 3400 \times 300$ mm. Along the vertical and horizontal direction of the railway, 10 testing points were arranged on the surface and each testing point was placed the temperature sensor. Inside the track slab, base plate and roadbed, the temperature sensors were just arranged at testing point 1, 2 and 6. Pt100, the thermal resistance sensor, was adopted in this test for its good thermal stability, whose measurement accuracy can reach to 0.1 °C. The automatic acquisition equipment was adopted for temperature acquisition. During the testing, temperature data were collected in every 10 or 30 min. PH AWS, an automatic weather station, was adopted for recording environmental data. The whole testing system was in natural environment, therefore, the external environmental conditions can be figured out according to the data obtained from the automatic weather station. The specific layout and place of the testing points are shown in Figs. 1 and 2, meanwhile the testing model and testing site are shown in Fig. 3.
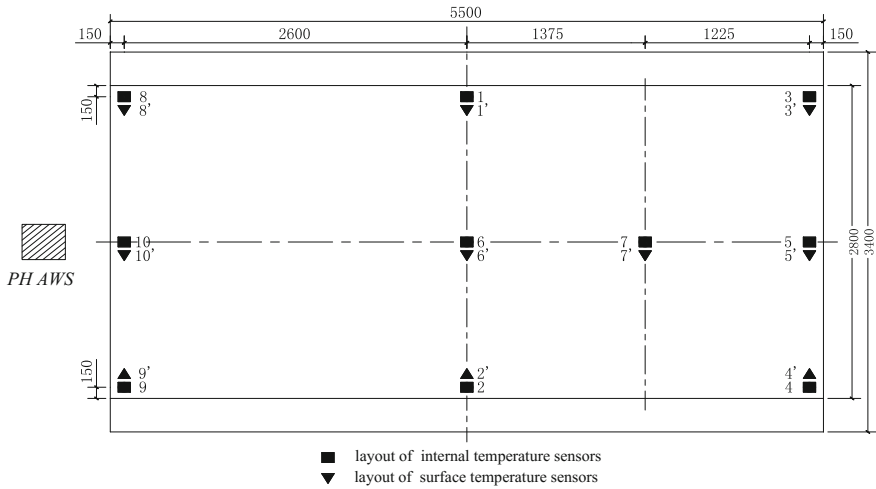
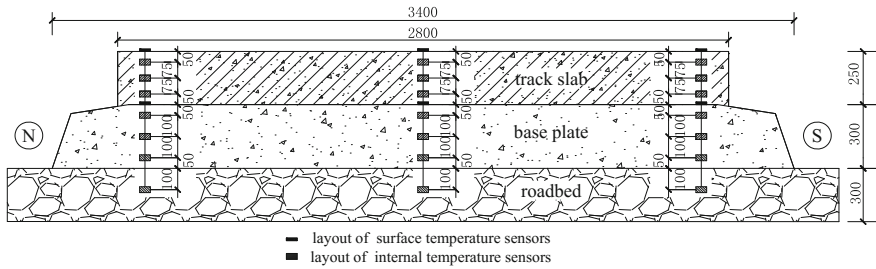**Fig. 1** Layouts of temperature testing points on the surface of track slab (unit: mm)

Fig. 2 Layouts of temperature testing points inside track structure (unit: mm)

Fig. 3 Testing model and testing site

Analysis of Temperature Characteristics
of Ballastless Track

The temperature of ballastless track structure and environmental factors are acquired through the automatic acquisition equipment, and a whole year of data are recorded. Based on this data, lots of analysis are carried out for the superstructure of ballastless track.

As is shown in Fig. 4, temperature of track slab T_i varies with y_i at different positions, therefore, the principle for calculating the average temperature of track structure(track slab and base plate) is as follows,

$$T = \frac{T_0 \cdot \frac{y_1}{2} + T_1 \cdot \frac{y_1 + y_2}{2} + T_2 \cdot \frac{y_2 + y_3}{2} + T_3 \cdot \frac{y_3 + y_4}{2} + T_4 \cdot \frac{y_4}{2}}{\sum_i^{n=4} y_i}$$
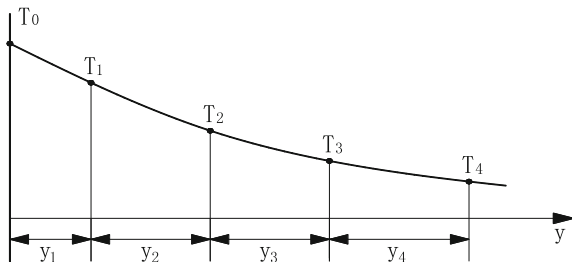
Annual Temperature Change of Track Slab

In order to observe the yearly changing regularity of track slab's temperature, air temperature and solar radiation intensity, a whole year (from Dec 2013 to Nov 2014) of data are analyzed, and the changing regularity shows in Figs. 5 and 6.

As is shown in Figs. 5 and 6, temperature of track slab, air temperature and solar radiation intensity all show a periodical change with day. Compared to air temperature, temperature of track slab is much higher in spring, summer and autumn, and lower in winter, the temperature amplitude of track slab changes seriously in late spring to early autumn than in late autumn to early spring, as well as the solar radiation intensity.

Figures 7 and 8 show that the maximum and minimum average of track slab's temperature, air temperature and solar radiation intensity are much higher in spring and summer than in autumn and winter, and the average maximum difference between track slab's temperature and air temperature is within 6 °C.

Fig. 4 Calculating method of temperature of the track slab

Fig. 5 Yearly changing curve of track slab's temperature and air temperature
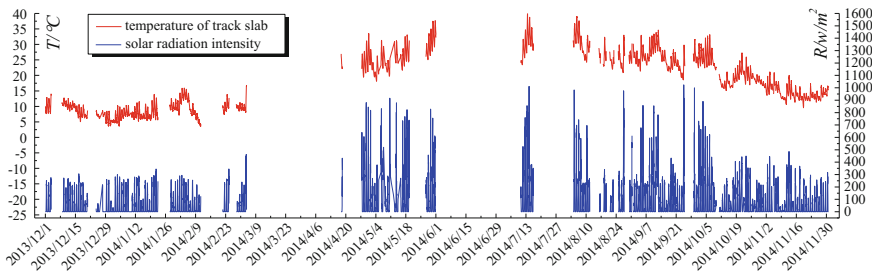
Fig. 6 Yearly changing curve of track slab's temperature and solar radiation intensity
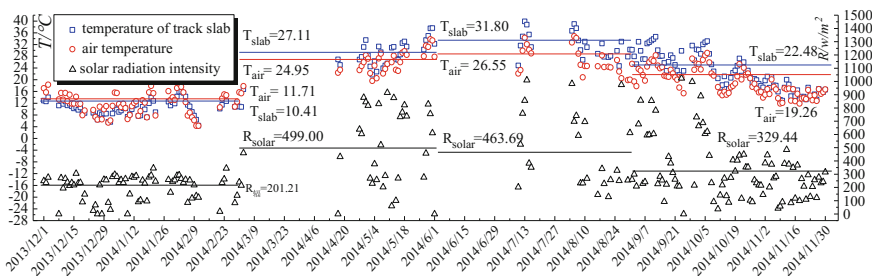
Fig. 7 A statistical analysis of the maximum average of track slab's temperature, air temperature and solar radiation intensity

Annual Temperature Change of Base Plate

Figures 9 and 10 show the yearly changing regularity of the temperature of the base plate, air temperature and solar radiation intensity.

According to Figs. 9 and 10, we can know that temperature of base plate, air temperature and solar radiation intensity show a periodical change with day, and
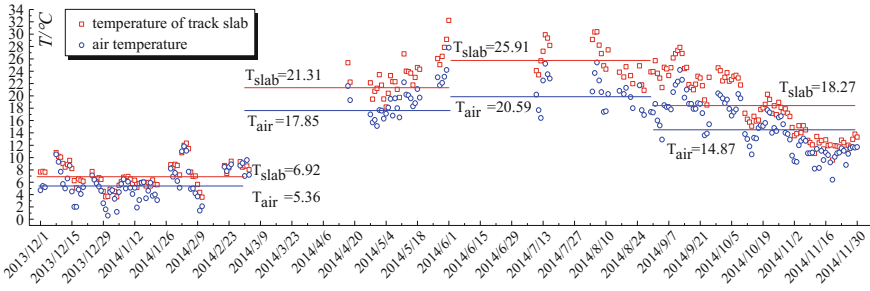
Fig. 8 A statistical analysis of the minimum of average track slab's temperature and air temperature
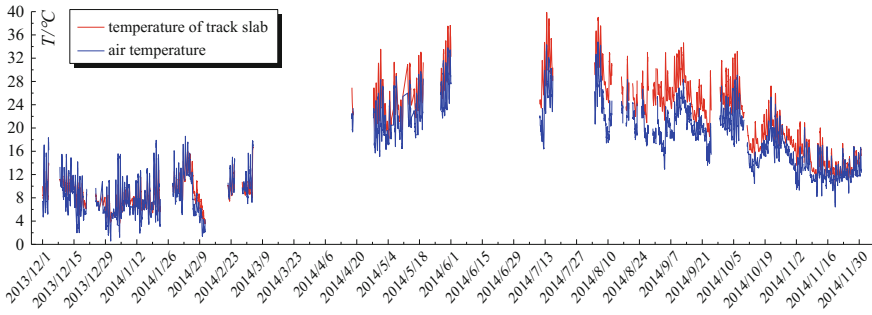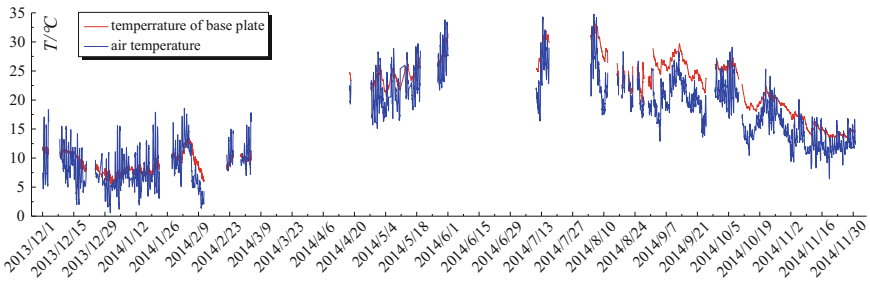

Fig. 9 Yearly changing curve of base plate's temperature and air temperature
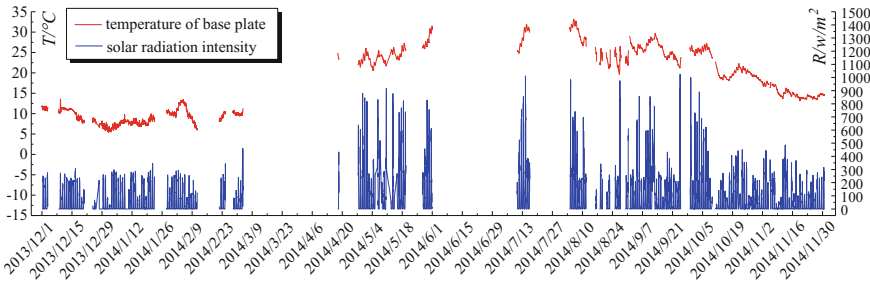
Fig. 10 Yearly changing curve of base plate's temperature and solar radiation intensity

temperature of base plate is higher than air temperature in the late summer and early autumn, however, lower in the rest of the year.

According to Fig. 11, we can know that difference between the maximum and minimum temperature of base plate is very small, and average difference is only 1.34 °C, therefore, in a whole year, the temperature of base plate changes little for the cover action of the upper structure (track slab).
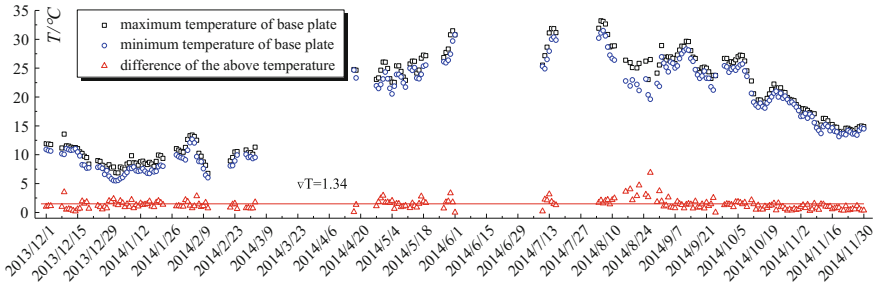
Fig. 11 Yearly changing curve of maximum and minimum temperature of base plate and the difference between two temperature

Annual Change of Temperature Gradient of Track Slab

Temperature gradient is a significant parameter in the period of ballastless track design, therefore, based on the whole year of data, temperature gradient of track slab was analyzed, showing in Figs. 12 and 13.
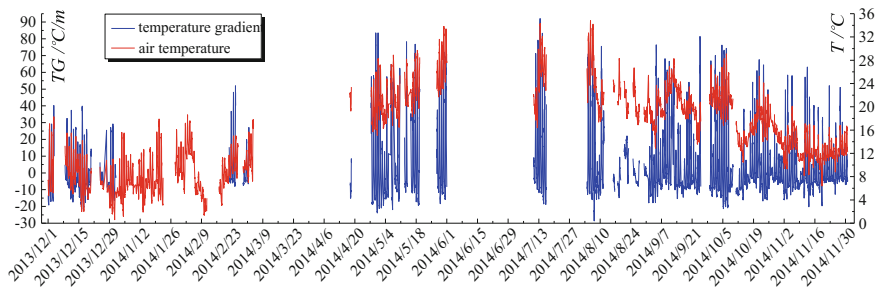
Fig. 12 Yearly changing curve of temperature gradient of track slab and air temperature
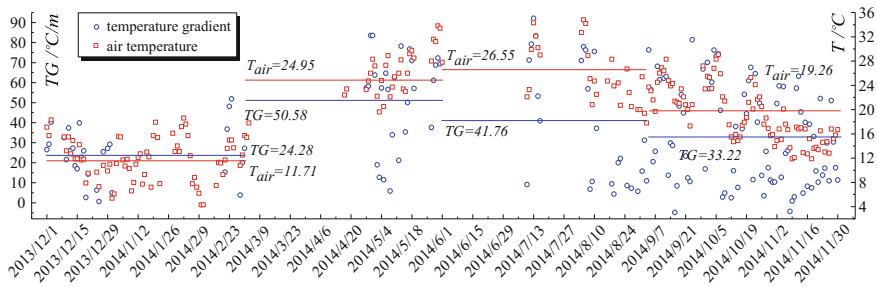
Fig. 13 A statistical analysis of the maximum of track slab's temperature gradient and air temperature

Table 1 A statistical graph of the maximum and minimum temperature gradient and the average maximum and minimum temperature gradient of track slab (°C/m)

Season	Maximum positive TG	Maximum negative TG	Average maximum positive TG	Average maximum negative TG
Spring	83.50	−16.66	50.58	−14.56
Summer	92.12	−28.55	41.76	−11.39
Autumn	81.42	−21.33	33.22	−10.90
Winter	51.88	−21.67	24.28	−12.52

According to Fig. 12, we can know that temperature gradient of track slab shows a periodical change with day, and increases with the increasing of air temperature. Meanwhile temperature gradient is apparently lower in winter than in the other 3 seasons, and seasonal change is obvious. Figure 13 shows the annual change of the maximum positive temperature gradient of track slab and the maximum of air temperature, and we can know that the average temperature gradient of track slab is more higher in spring and summer than in autumn and winter, due to the impact of ambient conditions. Based on the statistical analysis of a whole year of data, Table 1 gives the statistical results of temperature gradient of track slab.

Conclusions

The methods for on-site test of temperature field of ballastless track was put forward, and a statistical analysis for the changing relationship between the ambient factors and the temperature of the superstructure of ballastless track was conduct, the results show that temperature of track slab, air temperature and solar radiation intensity show a periodical change with day. The temperature of track slab is higher in spring, summer and autumn, and lower in winter, and the temperature amplitude of track slab changes seriously in late spring to early autumn than in late autumn to early spring as well as the solar radiation intensity. The average maximum difference between track slab's temperature and air temperature are within 6 °C. For the cover of track slab, the average difference between the maximum and minimum of base plate is only 1.34 °C. Temperature gradient of track slab shows a periodical change with day, and temperature gradient is apparently lower in winter than in the other 3 seasons, and seasonal change is obvious. The maximum positive and negative temperature gradient of track slab is 92.12 and −28.55 °C/m, and the average maximum and negative temperature gradient of track slab is 50.58 and −14.56 °C/m.

References

1. HE Hua-wu. Technology of Ballastless track [M]. Beijing: China Railway Press, 2005.
2. LIU Xue-yi, Zhao Ping-rui, Yang Rong-shan. Design Theory and Methods of Ballastless Track [M]. Chengdu, Southwest Jiaotong University Press, 2010.
3. ZHAO Ping-rui, Liu Xue-yi. Calculating method and parameter analysis of temperature stress of continuous track slab [J]. Railway Engineering, No 11, 2008, pp: 81–85.
4. SUNG CHUL Yang. A temperature prediction model in new concrete pavement and a new test method for concrete fracture parameters[D]. American, Texas A & M University, 1996.
5. ZHU Bo-fang. Temperature and temperature stress control of mass concrete [M]. Beijing: China Electric Power Press, 1999.
6. GONG Zhao-xiong. Temperature control and crack prevention of hydraulic concrete [M]. Beijing: China Electric Power Press, 1999.
7. Yavuzturk C, Ksaibati K, Chiasson A D. Assessment of temperature fluctuations in asphalt pavements due to thermal environmental conditions using a two-dimensional, transient finite-difference approach[J]. Journal of Materials in Civil Engineering, 2005, 17(4), pp: 464–475.

Experimental Study on Subway Nearby Building's Base Isolation by Sandbag Piles

Zheng Tao, Tao Sheng, Shanshan Hou, Yongjiang Guo, Jianchao Wang, Qiaoting Chen and Hongliang Jin

Introduction

The vibration induced by Urban rail transit system has an impact on buildings nearby, causing problems like decreasing quality of life and well being of inhabitants living in the vicinity of route paths, affecting the normal operation of some subtle equipment and putting some historic buildings in jeopardy. Thus, issues on reducing the vibration of urban rail transit system has received wide attention by society nowadays [1, 2].

Z. Tao · T. Sheng (✉) · S. Hou · Y. Guo · J. Wang · Q. Chen · H. Jin
Faculty of Architecture & Civil Engineering & Environmental,
Ningbo University, Ningbo 315211, China
e-mail: shengtao@nbu.edu.cn

Z. Tao
e-mail: taozheng@nbu.edu.cn

S. Hou
e-mail: houshanshan@nbu.edu.cn

Y. Guo
e-mail: guoyongjiang@nbu.edu.cn

J. Wang
e-mail: wangjianchao@nbu.edu.cn

Q. Chen
e-mail: chenqiaoting@nbu.edu.cn

H. Jin
e-mail: jinhongliang@nbu.edu.cn

T. Sheng
Department of Architecture & Civil Engineering, Zhejiang University,
Hangzhou 310058, China

Normally, one of the traditional ways to control the vibration of subway is to install disc spring, steel spring or thick laminated rubber bearing under the subway nearby building [3, 4]. By decreasing the vertical natural frequency of building structure, the vertical vibration induced by subway could be decreased. However, the hard maintenance and low damping capacity of steel springs makes them less satisfying isolation bearing. Besides, Rubber bearings' vertical stiffness discrete much [5], making the isolation layer of building hard to be designed.

Researchers have found out that when sandbags are implanted inside subgrade of highway, vertical vibration will cause relative movement between sand grains, thus friction happens, and with friction comes the reduction of ambient vibration [6, 7]. In fact, when a sandbag is under a vertical load, surface pressure can be converted to horizontal tensile stress in the bag and compression among the sand grains within, which makes the vertical stiffness of sandbags relatively small. Therefore, sandbag pile, which is stacked up by sandbags, can be used to control subway-induced building vibration as an isolation layer between the foundation and the main structure with a low vertical natural frequency. However, there're few researches conducted on this method now. In the light of sandbags' traits, like high damping [8], the easiness of controlling vertical stiffness, antiseptic properties, high durability, small construction difficulty and low price, experimental study of subway nearby building's base isolation by sandbag piles based on a scaled building model is discussed in this paper.

Building's Base Isolation Experiment

Large amount of experiments indicate that environmental vibration induced by subway is mainly high frequency vibration. And vertical vibration has the greatest impact on the human comfort of structures nearby. Some researchers indicated that some subway-induced horizontal vibration may have impacts on structures too [9, 10]. In this paper, two adjacent frames in a 5-story reinforced concrete frame structure nearby a subway line in Ningbo, China was taken as a prototype to design a 1/8 scaled model, as is demonstrated in Fig. 1. Dimensions of each component are listed in Table 1. In order to make the experiment data as truly as possible to reflect the prototype, a similarity design was conducted. Similarity ratio of experiment model is demonstrated in Table 2 below.

After the model is finished, 5 series of acceleration time history measured in the base of the office building during the passing of subways have been selected as input in the experiment. The accelerations were adjusted according to the similarity ratio of time and frequency in Table 1. A set of the adjusted vertical and horizontal accelerations is demonstrated in Fig. 2.

In order to verify the similarity of sandbag piles, 3 different dimensions of sandbags were designed: 5 cm × 5 cm × 1.25 cm, 10 cm × 10 cm × 2.5 cm, 40 cm × 40 cm × 10 cm. The compressive stiffness of sandbag piles were tested
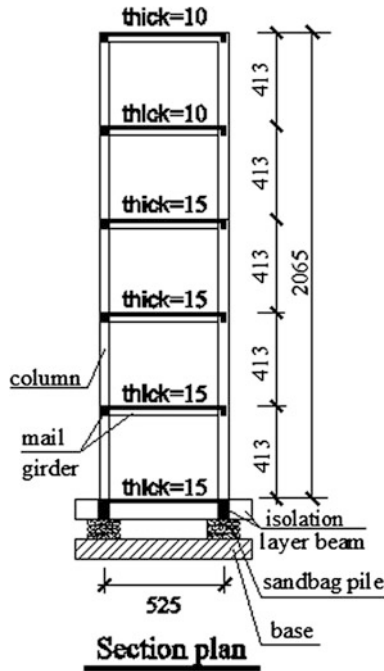
Fig. 1 1/8 scaled model for a frame structure building

Table 1 Dimensions of each component

Component	Dimensions	Reinforcement
Isolation layer beam	50 × 87.5	5Φ1.6 (longitudinal steel bars)
Main girder	31.3 × 56.3	4Φ1.6 (longitudinal steel bars)
Collumn	44 × 44	4Φ1.6 (longitudinal steel bars)
Floorslab	15 mm/10 mm	Φ0.9@20(distributing steel bars)

Table 2 Similarity ratio of the experiment model

Quantity	Similarity	Quantity	Similarity
Geometry	**0.125**	**Acceleration**	**1.0**
Mass	0.00195	Density	1.000
Elastic modulus	**0.125**	**Time**	**0.354**
Stress	0.125	Frequency	2.828

by hydraulic universal testing machine. Before the testing, vibratory compaction was conducted twice to fulfill the pores distributed in sand grains.

The testing result is demonstrated in Fig. 3. The vertical stiffness of 3 different scales, when not stacked, is 1:2.4:13.2, which indicates a direct correlation between the vertical stiffness and the size of sandbags. Thus, the requirement of vertical

(a) Vertical acceleration

(b) Power spectrum of vertical vibration

(a) Horizontal acceleration

(d) Power spectrum of horizontal vibration
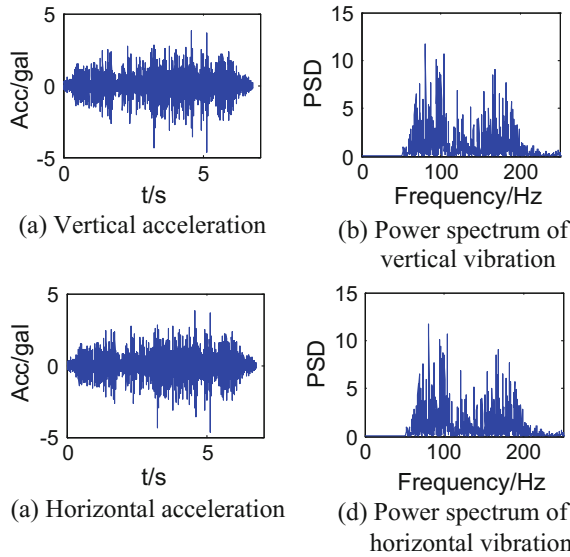
Fig. 2 Time histories and power spectrum of subway-induced vibration for input

(a) One layer sandbag

(b) Three layer sandbags
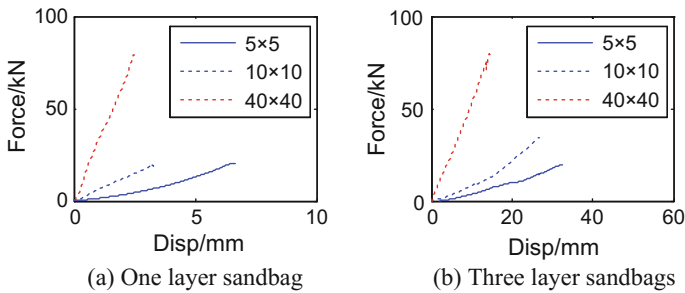
Fig. 3 Testing results of sandbags on compression stiffness

stiffness in engineering can be met by adjusting the size of sandbags. When 3 layers of sandbags was stacked, the stiffness is 6 times smaller than the stiffness of 1 layer sandbag. Therefore, scaled sandbags can validate the dynamical properties of full scale sandbags, similarity requirement is met.

Isolation Performance of Vertical Vibration

Four testing cases demonstrated in Table 2 were designed to test the vertical vibration isolation performance of sandbag piles. The total weight of the super-structure is approximately 100 kg, four sandbag piles were right beneath four

Table 3 Testing cases of vertical vibration isolation

Case	Description	Total height of sandbags	Isolation frequency
1	Fixed base	0	\
2	One layer sandbag	1.25 mm	112 Hz
3	Three layer sandbags	3.75 mm	75 Hz

Table 4 Vertical peak acceleration values in each case

Measuring site	$a_{PG,ave}/gal$		
	Case 1	Case 2	Case 3
Base	4.8	4.8	4.8
1st floor	9.2	5.2	3.6
3rd floor	9.0	5.0	3.0
4th floor	10.1	4.8	3.2
5th floor	11.2	4.2	3.1

columns. Peak acceleration values, power spectrum and 1/3 octave frequency VLs of floorslabs were analyzed in this paper.

The peak acceleration average values induced by 5 sets of different subway vibrations in 3 cases were listed in Table 3. In case 2~3, peak values of all floorslabs decreased dramatically. Especially in case 3, the decreasing ratio reached 73% (Table 4).

Take the 4th floorslab as an example, the power spectrum in different cases induced by one subway vibration was demonstrated in Fig. 4a–c. The average values of 1/3 octave frequency vibration levels is showed in Fig. 4d. The power spectrum of the other floorslabs is basically similar to the fourth floor, so it would be unnecessary to demonstrate here.

In case 2–3, the vibration frequencies is mainly distributed at the isolation frequency of structure and natural frequency of floorslab. In case 3, the isolation frequency of structure and natural frequency of floorslab differed significantly, making the vibration suppression more evident. Therefore, it's crucial to confine the vertical stiffness of sandbag piles by the first order frequency of floorslab. Moreover, in case 2–3, the maximum values of 1/3 octave frequency vibration levels decreased about 15 dB comparing with case 1, which indicated that sandbag piles have significant effect on increasing vertical human comfort inside subway nearby buildings.

Isolation Performance of Horizontal Vibration

Experiment cases on the horizontal vibration isolation performance is similar to vertical vibration demonstrated in Table 3. The tested peak values of acceleration in different cases is demonstrated in Table 5. The power spectrum and 1/3 octave frequency vibration levels is demonstrated in Fig. 5.

(a) Case 1: fixed foundation

(b) Case 2: one layer sandbag piles

(c) Case 3: three layer sandbag piles

(d) 1/3 octave frequency
vibration levels
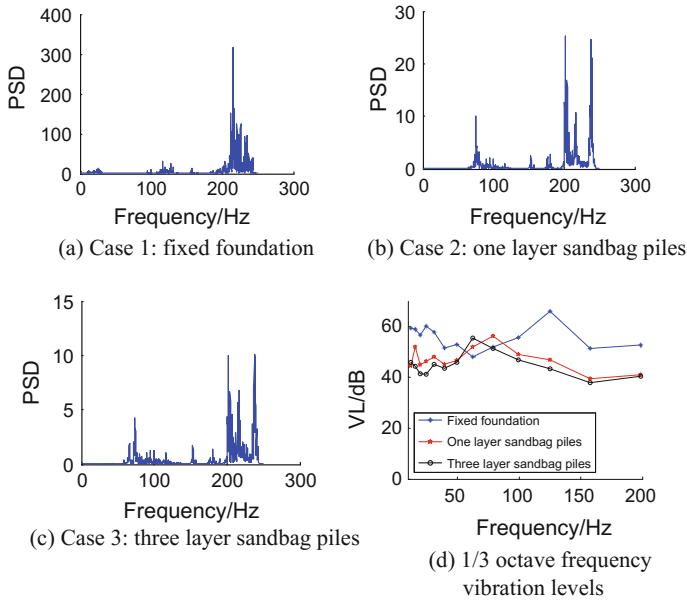
Fig. 4 Power spectrum and frequency vibration levels of vertical vibration

Table 5 Horizontal peak values of acceleration in each case

Measuring site		Base	1st floor	3rd floor	4th floor	5th floor
$a_{\mathrm{PG},ave}$ /gal	Case 1	3.0	3.2	4.8	4.2	4.5
	Case 2	3.0	2.1	2.0	2.2	1.0
	Case 3	3.0	1.0	1.2	1.2	1.4

Result in Table 5 indicates that horizontal peak values of acceleration, after applying sandbags, 70% of which decreased with a maximum damping ratio. Result in Table 5 indicates that the first order natural frequency of the structure in horizontal is 12.1 Hz. The first order natural frequency of the structure after applied 3 layer sandbag piles is 10 Hz. Although the reduction of frequency is not significant, the amplitudes at low and high frequency in power spectrum are significantly reduced. It shows that sandbag piles' high horizontal damping ratio helps to decrease the negative effect on human comfort inside subway nearby buildings.

(a) Case 1: fixed foundation

(b) Case 2: one layer sandbag piles

(c) Case 3: three layer sandbag piles

(d) 1/3 octave frequency vibration levels
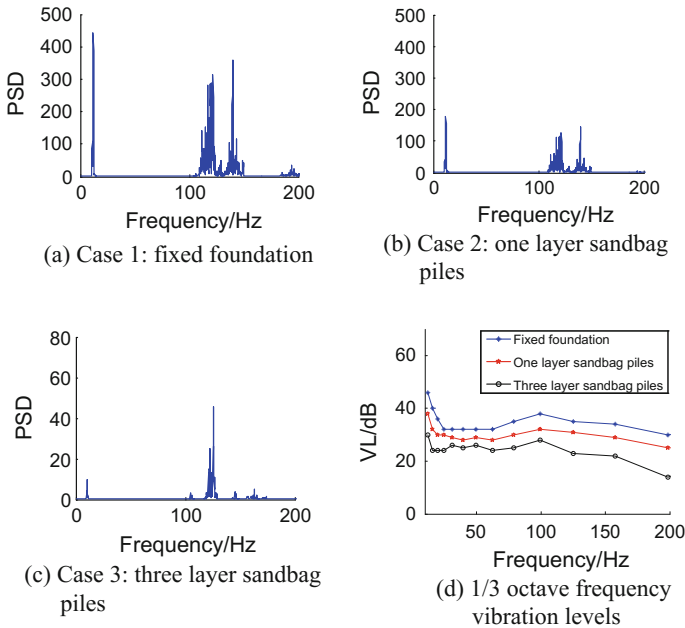
Fig. 5 Power spectrum and frequency vibration levels of horizontal vibration

Conclusions

(1) The vertical stiffness of sandbag piles is much smaller than subway nearby buildings. Applying sandbag piles for improving vertical human comfort inside subway nearby buildings is feasible and effective.

(2) Due to low horizontal stiffness and large horizontal damping ratio, it is feasible to apply sandbag piles for increasing horizontal human comfort inside subway nearby buildings.

References

1. Talbot J P, Hunt H E M. (2003). Isolation of buildings from rail-tunnel vibration: a review. Building Acoustics, 10(3): 177–192.
2. Sheng, T (2013). In-situ measurements of environmental vibration caused by urban transit and measure study on vibration isolation and reduction. PhD thesis, Tongji University: 1–2.

3. Li A, Wang W (2014). Design of a three dimensional isolation bearing and its application in building vibration control induced by underground train. Earthquake Engineering and Engineering Vibration, 34(2): 202–208.
4. Sheng T, Li Y, Zhang H, et al (2015). Field experiment study of subway nearby building's base isolation by laminated thick rubber isolator. Journal of Building Structures, 36(2): 35–40.
5. He W, Liu W, Yang Y, et al (2011). The basic mechanical properties of thick rubber isolators. Journal of PLA University of Science and Technology (Natural Science Edition),12(3): 258–263.
6. Matsuoka H, Mauramatsu D, Liu S H, et al (2005). Reduction of traffic-induced vibration by soilbags. Proceedings of 14th International Conference on Soil Mechanics and Geotechnical Engineering. Japan, pp. 1381–1384.
7. Nakagawa Y, Chen G L, Tatsui T, et al. Verification of vibration reduction characteristics with soilbag structure. Proceedings of 16th International Conference on Soil Mechanics and Geotechnical Engineering. China, 2009: 603–608.
8. Liu S, Gao J, Wang Y. (2015). Mechanism analysis and experimental study of vibration reduction and isolation effect of geotextile bag. Rock and Soil Mechanics, 36(2): 325–332.
9. Sanayei M, Maurya P, Moore J. A. (2013). Measurement of building foundation and ground-borne vibrations due to surface trains and subways[J]. Engineering Structures, 53: 102–111.
10. Sheng T, Zhang S, Shan J, et al. (2015). Environmental Vibrationsand the Effectiveness of Vibration-source Suppression Method. Journal of Vibration, Measurement & Diagnosis, 35(2): 352–358.

A Frequency Domain Solution to Vehicle Induced Vibration of Railway Bridges

Zhibin Jin, Shiling Pei, Yan Zhu and Xiaozhen Li

Introduction

Excessive vibration of railway bridges caused by high-speed trains has potential threats to the running safety of the vehicles, especially when the resonance of the bridge occurs. In current practice, the bridge vibration is dominantly evaluated using detailed vehicle–track–bridge dynamic simulations in time domain.

The dynamic vehicle–bridge simulation using computer codes can be dated back to the pioneer works of Chu [1] and Bahatti [2]. They used finite element method to model the bridge structure, and modeled vehicles as multi-body dynamic systems, then solved the equations using numerical integration method. To date, much detailed models with improvement in structural modeling, wheel–rail interactions and solving schemes have been proposed. Yang [3] proposed the VBE (vehicle–bridge interaction element) to solve the vehicle–bridge system. Xia [4] used modal decomposition method in represent the bridge structure, where both hunting motions of the wheel-sets and rail irregularities were taken as excitations. Li [5] used an iteration approach to solve the wheel-rail nonlinear interaction on bridges. Zhai [6] introduced the track structure into the vehicle-bridge system, and allowed the wheels to jump up from the rail. Li, Xu [7] and Cai [8] studied the vibration of vehicle–bridge due to cross wind.

Z. Jin (✉) · Y. Zhu · X. Li
School of Civil Engineering, Southwest Jiaotong University,
Chengdu 610031, China
e-mail: jinzhibin@swjtu.cn

X. Li
e-mail: xzhli@swjtu.cn

S. Pei
Department of Civil and Environmental Eng, Colorado School of Mines,
Golden 80401, USA
e-mail: spei@mines.edu

Although the time domain vehicle–track–bridge interaction simulation coding can give comprehensive results of the system responses, the frequency domain solution of the lateral vibration of railway bridges is still appealing because it may reveal the underlying mechanism of lateral resonance mechanism for engineering applications.

The authors gave an analytical solution of the simply-supported beam to a series of hunting forces using the Fourier transform method in [9]. In this paper, the solution is expanded to bridges with any configurations modelled by FEM (finite element method). Using the current approach, the bridge lateral responses can be obtained very efficiently aided by the fast fourier transformation (FFT) method. Further, the resonance condition can be identified in frequency domain.

Moving Hunting Forces Applied on Bridges

The bridge subjected to lateral moving hunting forces is illustrated in Fig. 1 [9]. The hunting loads applied on the bridge are harmonic forces with radius frequency ω_f. The distance between the k-th wheel-set and the first one is denoted as x_k. All hunting forces have the same frequency but have different phases. The k-th hunting force lags a time $t_k = x_k/v$ behind the first wheel-set, where v is the running speed of the train. In Fig. 1, L is the bridge span, l_a is the length of a car, l_c is the distance between two trucks of a car, and lt is the distance between two wheel-sets beneath the same truck.

The frequency of the hunting forces ω_f can be obtained from the wave length of the hunting motion L_h by $\omega_f = 2\pi v/L_h$. And L$_h$ is related to the wheel geometries through the Klingel's formula
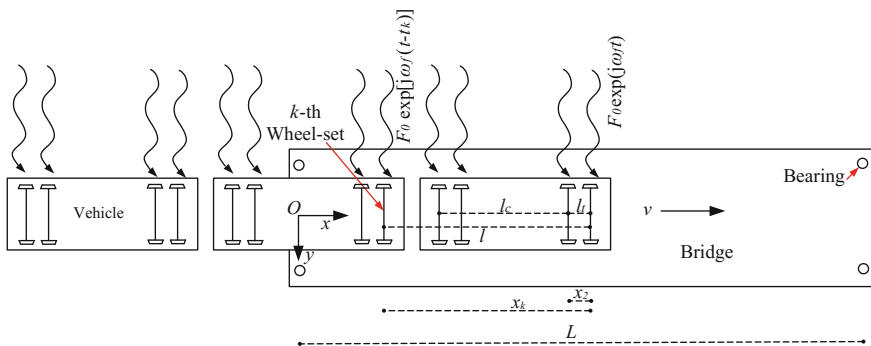
$$L_h = 2\pi \sqrt{\frac{r_0 b}{\gamma}} \tag{1}$$

Fig. 1 Moving hunting forces applied on the bridge (*Top view*)

where r_0 is the rolling radius of wheel, b is half the rail gauge and γ the conicity of the wheel tread. For a real non-conical wheel tread, an equivalent conicity can be determined from the trajectory of wheel-set motion according to the UIC code 519 (2004). Knowing the frequency of the hunting forces, the lateral force of a wheelset can be expressed as

$$F(t) = F_0 exp(I\omega_f t) \quad \text{with} \quad \omega_f = 2\pi \frac{v}{L_h} \tag{2}$$

where t denotes time, I is the imaginary unit, F_0 is the amplitude of hunting force.

Since the k-th hunting force lags a time $t_k = x_k/v$ behind the first wheel-set, the hunting force from the k-th wheel-set can be expressed as

$$F_k(t) = F_0 exp\left[I\omega_f(t - t_k)\right] \tag{3}$$

Governing Equations of the Bridge Vibration Due to Moving Hunting Forces

The dynamic equation of a bridge modeled by the finite element method (FEM) reads,

$$M_b\ddot{X}_b(t) + C_b\dot{X}_b(t) + K_bX_b(t) = P_b(t) \tag{4}$$

where M_b, C_b and K_b are the mass, damping and stiffness matrix of the bridge structure; $X_b(t)$ is the displacement vector of the bridge at time instant t; $P_b(t)$ is the load vector on the bridge from the moving hunting forces.

According to the standard mode decomposition method, the displacement vector $X_b(t)$ can be decomposed into the sum of modal displacement vectors ϕ_i as,

$$X_b(t) = \sum_i q_i(t)\Phi_i \tag{5}$$

where $q_i(t)$ is the i-th mode displacement. By Substituting Eq. (5) into Eq. (4), and left multiplying Φ_i^T to both sides, the dynamic equation of the bridge is decouple into n dynamic systems each have one degree of freedom as,

$$\ddot{q}_i + 2\zeta_i\omega_{b,i}\dot{q}_i + \omega_{b,i}^2 q_i = p_i(t) \quad \text{with} \quad i = 1, 2, \ldots, n \tag{6}$$

where ζ_i and $\omega_{b,i}$ are the damping ratio and the radius frequency of i-th mode. In derivation of Eq. (6), the mass normalized mode vector Φ_i is used, in other words, $\Phi_i^T M_b \phi_i = 1$. And $p_i(t)$ is the modal force given by

Fig. 2 Interpolation deck
mode from bridge mode
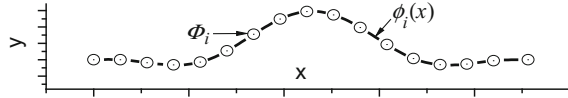
$$p_i(t) = \Phi_i^T P_b(t) \tag{7}$$

The hunting forces only act laterally on the deck elements, in other words, only the DOFs in ϕ_i representing the lateral motion of the deck receive the hunting forces. Here interpolate the lateral deck components in Φ_i as the deck mode $\phi_i(x)$ using

$$\phi_i(x) = R(x)\Phi_i \tag{8}$$

The deck mode $\phi_i(x)$ is a continuous function of x shown in Fig. 2. The deck mode is introduced for the following theoretical derivations, thus the vector $R(x)$ need not be constructed actually.

Using the deck mode, the i-th modal force induced by hunting forces can be written specifically as

$$
\begin{aligned}
p_i(t) &= \sum_{k=0}^{2N_c-1} \int_0^L F_k(t)\delta[x - v(t - t_k)]\Pi\left[\frac{v(t - t_k)}{L}\right]\phi_i(x)dx \\
&= \sum_{k=0}^{2N_c-1} \int_0^L F_0(t - t_k)\delta[x - v(t - t_k)]\Pi\left[\frac{v(t - t_k)}{L}\right]\phi_i(x)dx \qquad (9) \\
&= \sum_{k=0}^{2N_c-1} F_0(t - t_k)\Pi\left[\frac{v(t - t_k)}{L}\right]\phi_i[v(t - t_k)]
\end{aligned}
$$

where L is the bridge span, $\delta(.)$ is the Dirac function used to express concentrated forces, function $\Pi(x) = \{1, |x \in [0, 1]; 0|else\}$, indicating whether a force is in the range of the bridge or not.

For sake of concise in the following derivation, denote $\Pi\left[\frac{v(t-t_k)}{L}\right]\phi_i[v(t - t_k)]$ as $g_i(t - t_k)$. Thus the modal force reads,

$$p_i(t) = \sum_{k=0}^{2N_c-1} F_0(t - t_k)g_i(t - t_k) \tag{10}$$

Frequency Domain Solution to the Bridge Vibration

From Eqs. (9) and (10), the model responses of the bridge are governed by

$$\ddot{q}(t) + 2\zeta\omega_b\dot{q}(t) + \omega_b^2 q(t) = p(t) \tag{11}$$

where the modal force reads,

$$p(t) = \sum_{k=0}^{2N_c-1} \exp\left[I\omega_f(t - t_k)\right] \Pi\left[\frac{v(t - t_k)}{L}\right] \phi[v(t - t_k)] \tag{12}$$

Hereafter, the subscript "i" denoting the i-th mode is omitted for concise of writing.

The Fourier transformation and Inverse Fourier Transform pair of the modal force p(t) in the right hand side of Eq. (12) is

$$P(\omega) = \int_{-\infty}^{\infty} p(\omega_f, t) e^{-I\omega t} dt, \text{ and } p(\omega_f, t) = \frac{1}{2\pi} \int_{-\infty}^{\infty} P(t) e^{I\omega t} dt \tag{13}$$

The Fourier Transform $P(\omega)$ is defined here as the modal train spectrum of the $2N_c - 1$ hunting moving forces all with frequency ω_f.

Similarly, the Fourier Transform pair of the modal response $q(t)$ is

$$Q(\omega) = \int_{-\infty}^{\infty} q(t) e^{-I\omega t} dt, \text{ and } q(t) = \frac{1}{2\pi} \int_{-\infty}^{\infty} Q(\omega) e^{I\omega t} d\omega \tag{14}$$

Carryout the Fourier transform for both sides of Eq. (11), one gets

$$Q(\omega) = H(\omega)P(\omega) \tag{15}$$

where $H(\omega)$ is the frequency response function of the i-th mode as

$$H(\omega) = 1/(\omega_b^2 - \omega^2 + 2I\zeta\omega\omega_b) \tag{16}$$

It should be noted that, the Inverse Fourier Transform of Eq. (14) only gives the steady-state response. There for, the transient responses should be added to satisfy the zero initial conditions. In the end, the full solution to $q(t)$ reads,

$$q(t) = e^{-\zeta\omega_b t}[A\cos(\omega_b t) + B\sin(\omega_b t)] + \frac{1}{2\pi} \int_{-\infty}^{\infty} Q(\omega) e^{I\omega t} dt \tag{17}$$

The first term of the right hand side of Eq. (18) is the transient response, and the constants A and B satisfying the zero initial conditions read,

$$A = -\frac{1}{2\pi} \int\limits_{-\infty}^{\infty} Q(\omega)dt, \quad B = -\frac{1}{2\pi\omega_b} \int\limits_{-\infty}^{\infty} I\omega Q(\omega)dt + \zeta A \qquad (18)$$

In Eqs. (17) and (18) the difference between the damping natural frequency and the undamped frequency of the bridge was disregarded by assuming small damping ratio for most engineering problems.

Modal Train Spectrum

Decomposition of Modal Train Spectrum

By substituting the $p(t)$ of Eq. (12) into Eq. (13), the modal train spectrum $P(\omega)$ can be written as

$$P(\omega) = \int\limits_{-\infty}^{\infty} \sum_{k=0}^{2N_c-1} \exp\left[I\omega_f(t - t_k)\right] \Pi\left[\frac{v(t - t_k)}{L}\right] \phi[v(t - t_k)]e^{-I\omega t}dt \qquad (19)$$

After replacing $t - t_k$ with t', the modal train spectrum $P(\omega)$ reduces to

$$P(\omega) = C_v(\omega) \cdot \Phi_{v,\omega_f}(\omega) \qquad (20)$$

with

$$C_v(\omega) = \sum_{k=0}^{2N_c-1} \exp(Ix_k\omega/v) \qquad (21)$$

and

$$\Phi_{v,\omega_f}(\omega) = \int\limits_{0}^{L/v} \phi(vt')e^{-I(\omega-\omega_f)t'}dt' \qquad (22)$$

$C_v(\omega)$ in Eq. (32),is defined here as the load sequence spectrum, which reflects the effect of the sequence of the trucks (described by x_k). It is obvious that $C_v(\omega)$ is independent of the hunting frequency ω_f and the deck mode $\phi(x)$. If only one truck is included in a train, $C_v(\omega) = 1$ (since $x_k = 0$, $k = 0$). in this case, $\Phi_{v,\omega_f}(\omega)$ equals $P(\omega)$. Thus we define $\Phi_{v,\omega_h}(\omega)$ as the shifted modal spectrum for a single hunting force with frequency ω_f.

Equation (20) shows that the modal train spectrum is the product of the shifted modal spectrum multiplied by the load sequence spectrum.

Load Sequence Spectrum

It is easy to prove that the load sequence spectrum for different running speed satisfy the following scaling relation,

$$C_v(\omega) = C_1(\omega/v) \tag{23}$$

where $C_1(\omega)$ is the unit load sequence spectrum by substituting $v = 1$ into Eq. (21).

For typical modern railway trains whose trucks are arranged as in Fig. 3, the unit load sequence spectrum can be further simplified as

$$
\begin{aligned}
C_1(\omega) &= \sum_{k=0}^{2N_c-1} \exp(I\omega x_k) = \sum_{k=0}^{N_c-1} [\exp(I\omega x_{2k}) + \exp(I\omega x_{2k+1})] \\
&= \sum_{k=0}^{N_c-1} \{\exp(I\omega k l_c) + \exp[I\omega(k l_c + l_a)]\} \tag{24} \\
&= [1 + \exp(I\omega l_a)] \sum_{k=0}^{N_c-1} \exp(I\omega k l_c)
\end{aligned}
$$

In deriving Eq. (23) the specific $x_{2k} = k l_c$ and $x_{2k+1} = k l_c + l_a$ for the train in Fig. 3 were substituted into $C_1(\omega)$. The dimension l_c is the distance between the center of two adjacent cars, and l_a is that between the center of two trucks of the same car.

The summation factor in Eq. (24) can be simplified further. By Denoting $\sum_{k=0}^{N_c-1} \exp(I\omega k l_c)$ as Z, it is obvious that

$$Z \exp(I\omega l_c) = \sum_{k=1}^{N_c} \exp(I\omega k l_c) = Z - 1 + \exp(I\omega N_c l_c) \tag{25}$$

Then, by solving Eq. (25), the summation reads

$$Z = [\exp(I\omega N_c l_c) - 1]/[\exp(I\omega l_c) - 1] \tag{26}$$
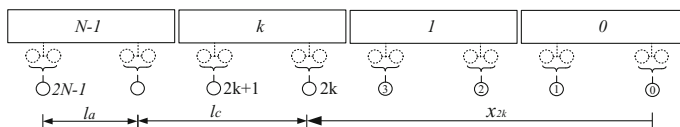

Fig. 3 Arrangement of the cars in a classical railway train

By substituting Eq. (26) into (24), the unit load sequence spectrum reads,

$$C_1(\omega) = [1 + exp(I\omega l_a)] \frac{\exp(I\omega N_c l_c) - 1}{\exp(I\omega l_c) - 1} \tag{27}$$

Shifted Modal Spectrum

Define the unit modal spectrum by letting $v = 1$ and $\omega_f = 0$ in Eq. (22),

$$\Phi_{1,0}(\omega) = \int_0^L \phi(x)e^{-I\omega x}dx \tag{28}$$

Obviously, the unit modal truck spectrum is the Fourier Transform of the deck mode $\phi(x)$.

For cases of $v \neq 1$ and $\omega_f \neq 0$, from Eq. (22), the shifted modal spectrum reads,

$$\Phi_{v,\omega_h}(\omega) = \int_0^{\frac{L}{v}} \phi(vt')e^{-I(\omega-\omega_h)t'}dt' \overset{vt'=x}{\Rightarrow}$$

$$\frac{1}{v}\int_0^L \phi(x)e^{-\frac{I(\omega-\omega_h)x}{v}}dx = \frac{1}{v}\Phi_{1,0}\left(\frac{\omega-\omega_h}{v}\right) \tag{29}$$

Equations (28) and (29) reveals that the deck mode $\phi(x)$ need only be Fourier transformed once to obtain the unit modal spectrum $\Phi_{1,0}(\omega)$, which in turn was shift by hunting frequency ω_f and scaled by the running speed v to get the shifted modal spectrum $\Phi_{v,f}(\omega)$.

Numerical Example

An prestressed concrete bridge of rigid frame type (shown in Fig. 4) was analyzed here. The bridge has two equal spans of 112 m, and the pier is 108 m high. Both the girder and the pier have box shaped section. The girder and the pier are made of C60 and C35 concrete respectively. The depth of the main girder varies from 4.8 m at the span ends to 11.3 m at the pier top. The lateral modal displacement of the bridge deck is shown in Fig. 5. Parameters of the hunting forces are listed in Table 1.

Figures 6 and 7 show that the maximum lateral vibration occurs near the center of the two spans. This indicates that the responses are consisted of higher modes other than the first one, contrary to the cases of small span simply-supported bridges.
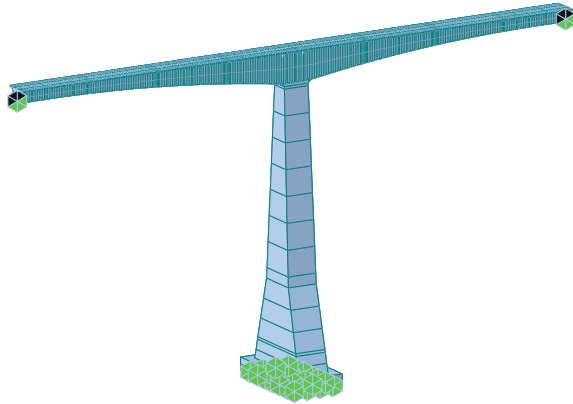
Fig. 4 FEM model of the bridge
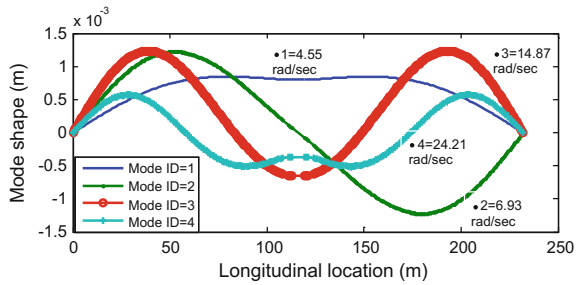
Fig. 5 Lateral modes of the bridge

Table 1 Vehicle parameters

Variable	Meaning	Value
v	Running speed of the train	100–350 km/h
N	Number of vehicles in the train	8
F_0	Amplitude of the hunting forces	17.5 kN
l_a	Length of a single vehicle	26.0 m
l_c	Distance between centers of the two trucks of in a vehicle	17.5 m
L_h	Hunting wavelength	17.0 m

Peak bridge accelerations occur as the train runs at speed 175 and 350 km/h (see Fig. 6). This resonance speed can be estimated from the resonance conditions proposed in [9]. The candidate resonance conditions are in [9] cited here,

Fig. 6 Lateral acceleration of the bridge deck

Fig. 7 Lateral displacement of the bridge deck

$$v_1 = \frac{\omega_b}{2\pi}\frac{l_c}{n_{a1}} \text{ and } v_2 = \frac{\omega_b}{2\pi}\frac{l_c}{n_{a2}}, \quad \text{with } n_{a1} = l_c/L_h \text{ and } n_{a2} = l_c/L_h \qquad (30)$$

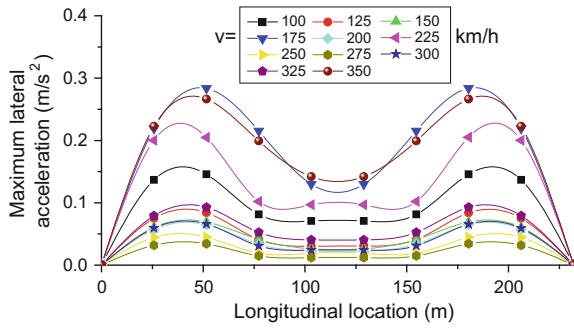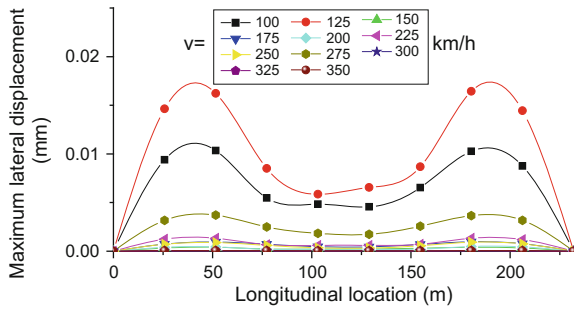By substituting the fourth frequency of the bridge parameters $\omega_{b,4}/(2\pi) = 3.85$ Hz, $l_c = 26$ m, and $L_h = 17$m into Eq. (30), the candidate resonance speeds $v_1 = 180$km/h, $v_2 = 361$km/h. These speeds are very close to the numerically calculated resonance speeds 175 and 350 km/h. The higher modes for large span bridges may contribute significantly to the vehicle induced lateral vibrations, and sometimes may induce lateral resonance.

Conclusions

A frequency domain solution to the vibration of railway bridges due to a series of hunting forces moving across is derived. The moving hunting force is took as harmonic forces. The response of the bridge is proved to be the product of three factors: the shifted modal spectrum, the load sequence spectrum and square of the bridge's modal response function. The shifted modal spectrum represents the frequency component of the modal force of the bridge due to a moving harmonic hunting force. It is obtained via shifting the unit modal truck spectrum by a distance

of the hunting frequency. The unit modal truck spectrum is the Fourier Transform of the mode shape of the bridge. And the unit modal truck spectrum represents the frequency component of the modal force of the bridge due to a moving constant hunting force.

A numerical example showed the lateral vibration of large span bridges may governed by higher modes other than the first one, and may induce the resonance of the bridge.

References

1. Chu KH, Dhar CL, Garg VK. Railway-bridge impact: Simplified train and bridge model. J. Struct 1979; 105(9): 1823–1844.
2. Bhatti M. H.. "Vertical and lateral dynamic response of railway bridges due to nonlinear vehicles and track irregularities." Ph.D. thesis, Illinois Institute of Technology, 1982, Chicago.
3. YB Yang, JD Yau, YS Wu. Vehicle–Bridge Interaction Dynamics with Applications to High-Speed Railways. Singapore: World Scientific; 2004.
4. H. Xia, N.Zhang, G.D.Roeck. Dynamic analysis of high speed railway bridge under articulated trains. Computers &Structures 2003; (81):2467–2478.
5. Y.L.Li, S.Z.Qiang, H.L.Liao, et al., Dynamics of wind–rail vehicle–bridge systems.Journal of Wind Engineering and Industrial Aerodynamics 2005; (93): 483–507.
6. Zhai, W. M., et al. High-speed train–track–bridge dynamic interactions. Part I: theoretical model and numerical simulation. Int. J. Rail Transp. 2013; (1): 3–24.
7. Y.L.Xu,W.H.Guo, Dynamic analysis of coupled road vehicle and cable-stayed bridge systems under turbulent wind. Engineering Structures 2003; (25): 473–486.
8. Cai, C.S., Hu, Jiexuan, Chen, Suren et al. A coupled wind-vehicle-bridge system and its applications: A review. Wind and Structures 2015; 20(2):117–142.
9. Jin, Z.,Pei, S.,Li, X., and Qiang, Vehicle-Induced Lateral Vibration of Railway Bridges: An Analytical-Solution Approach. J. Bridge Eng2016; (21): 1–9.

Dynamic Stability Analysis of Embankment Along the Qinghai-Tibet Railroad in Permafrost Regions

Zhijian Wu, Wei Ma, Tuo Chen and Lili Wang

Introduction

The Qinghai-Tibet Railway (QTR), as the World's highest and longest plateau railway, spans 546.41 km of permafrost. Due to the vulnerability of the permafrost environment and the unpredictability of climate change. the key to successful construction of a railway in such a region is the stability of the embankments and protecting the permafrost from warming and throwing [1]. Moreover, under the dual influence of thermal disturbances during construction and train vibration loads on the QTR, it is a scientific challenge to protect the permafrost environment and maintain the earth surface's thermal equilibrium and the embankment stability.

Z. Wu (✉) · W. Ma · T. Chen · L. Wang
Key Laboratory of Loess Earthquake Engineering, Lanzhou Institute
of Seismology, CEA, Lanzhou 730000, Gansu, China
e-mail: zhijianlz@163.com

W. Ma
e-mail: mawei@lzb.ac.cn

T. Chen
e-mail: lzchentuo@163.com

L. Wang
e-mail: wll_11539@163.com

Z. Wu · W. Ma · T. Chen · L. Wang
Geotechnical Disaster Prevention Engineering Technology Research Center
of Gansu Provence, Lanzhou 730000, Gansu, China

Z. Wu · W. Ma · T. Chen · L. Wang
State Key Laboratory of Frozen Soil Engineering, Chinese Academy
of Sciences, Lanzhou 730000, China

Z. Wu · W. Ma · T. Chen · L. Wang
State Key Laboratory for Geomechanics and Deep Underground Engineering,
China University of Mining and Technology, Xuzhou 221116, China

For this purpose, certain proactive protection measures have been adopted in embankment construction in the permafrost regions along the QTR. The observation data of ground temperature and embankment deformation in permafrost regions showed that the crushed-rock embankments, which are among the most important proactive protection measures on the QTR, are more effective for maintaining the stability of the QTR than are plain-fill embankments in permafrost areas [2–5].

Due to the lack of reliable test data, especially actual train load data [6–10], most relevant research always regarded train loads as the sinusoidal distributed loads, however, the calculated result was in short of reliable test data, especially the real vibration data. Previous researches have shown that the deformation characteristics of embankments are poor under the effects of train loads in permafrost areas. Therefore, in order to study the dynamic transfer characteristics of crushed-rock embankments under train loads, in this paper, a crushed-rock embankment on the Bailuhe River test segment of the QTR is selected to build a calculation model. At the same time, we established a comparative calculation model of a plain-fill embankment. We used the dynamic finite element method to analyze the dynamic characteristics of the embankments, the response of the displacements, and the influence of seasons to the embankment. The dynamic load data applied to the models came from field tests of the strong motions when a train was passing. The aim of this research was evaluate quantitative effects of the dynamic loads on embankment deformation of the QTR in permafrost regions.

Profile of Beilu River Segment and Strong Motion Test

Field Test Embankment

The field test embankment is a part of Bailu River segment, and this segment is located between Hoh Xil and Fenghuo Mountain in the Qinghai-Tibet Plateau, which is the main line of the QTR. The total length of this segment is 14 km. It has an arid climate, where winters last for seven to eight months, almostly from September to the following April. According to local meteorological data, the average temperature is −5.2 °C, the extreme maximum temperature is 23.2 °C, and the lowest temperature is −37.7 °C. In the whole test section, there are rich ground ice near the permafrost table.. Based on the engineering geological features, this segment is evaluated as poor to extremely poor permafrost area [1]. The natural permafrost table is approximately1.5 m to 2.0 m in depth, and the average ground temperature is about -−1.41 °C to −1.68 °C. The upper part of the stratum is a silt-sand layer, and the lower part of the active layer is brownish-red silty clay. There is a layer of soil containing ice with a thickness of 1.4–3.0 m around the permafrost table. The lower part of the stratum is mainly brownish-red, completely weathered mudstone, part of which has an interlayer of sandstone.
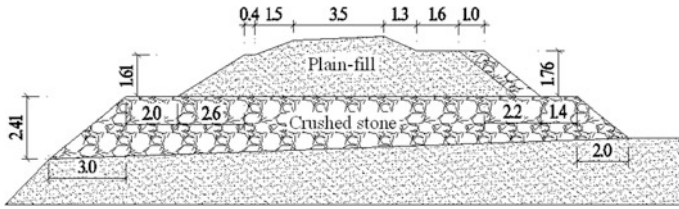
Fig. 1 Profile of the crushed-rock embankment (unit: m)

The permafrost table of the field test embankment segment is about 2.3 m deep, and the average ground temperature is −1.51 °C. The actual test segment is a composite structure of a crushed-rock embankment and crushed-rock slope protection (southern slope protection). Crushed rock is horizontally layered at the bottom, and both sides are berms (Fig. 1). The size of the crushed rocks is about 30–40 cm. According to field measurements, the center height of the embankment is 4.4 m, the left berm is 2.0 m tall, and the right berm is 1.4 m tall. An in situ borehole survey of this segment in September 2006 provided the test results on lithology, the test results showed that under 2.2 m depth, the water content of brown- red clay came to 81.4%.

Strong Motion Test

In order to study the vibration response and deformation characteristics of embankments under train loads in permafrost regions along the QTR, it is of scientific significance to obtain actual vibration data using the strong-motion monitoring method. Strong motion observation instrument, with different digital or semi-digital sensors, was widely used in engineering practice [11]. We used the ETNA strong-motion accelerometer (Kinemetrics, Inc., Pasadena, California) for testing, which has three geophones, two in the horizontal direction-CH1 and CH2, and one in the vertical direction-CH3. While testing, the CH1 was parallel of track, CH2 was vertical with CH1, and CH3 was the vertical direction. During our field tests at the embankments, the trigger acceleration was set as 0.98 cm s^{-2}, the sampling interval of each sample was 0.005 s, and the vibrating time-histories before and after train shock excitation were 20 s. Three observation points were set at the crushed-rock embankment section of the Beilu River segment for the strong-motion testing. One was at the right shoulder and the other two were at the left and right slope toes of the embankment, respectively.

The real-time vibration acceleration data of the shoulder and toes when the train was passing are shown in Fig. 2, and the Fig. 3 is the fourier spectral of the acceleration waveform. The maximum acceleration amplitude of the shoulder position reached 210 cm s^{-2}. As the vibration was transmitted along the embankment slope, the acceleration was greatly attenuated. The acceleration amplitude of

the slope toe was only 1/10 of that in the shoulder. As shown in Fig. 2, the values of vibration acceleration were very close at the two side slope toes. As can be seen from the Fig. 3, there is a rapid decrease in the amplitude of the fourier spectra, through the vibration transmission from road shoulder to slope toe, which also presents obvious attenuation at the testing section. Moreover, there are obvious changes in the spectra characteristics between the shoulder and slope toe observation points. The vibration frequency of the train mostly concentrates above 40 Hz and the high frequency components are absorbed with the transition of the vibration, while the natural frequency of the crushed-rock embankment is between 30 and 40 Hz.
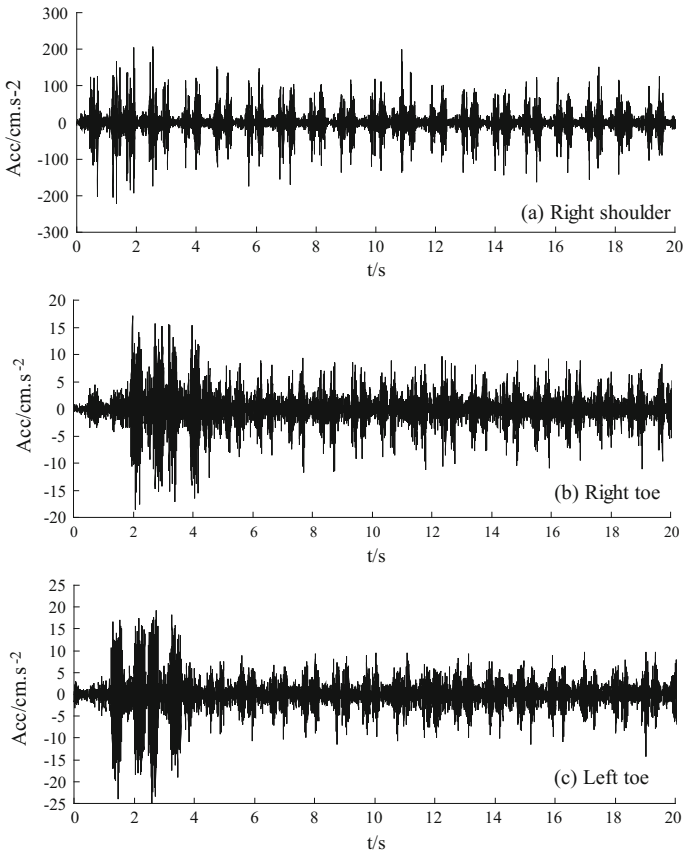

Fig. 2 Acceleration waveforms recorded at the embankment when the train was passing
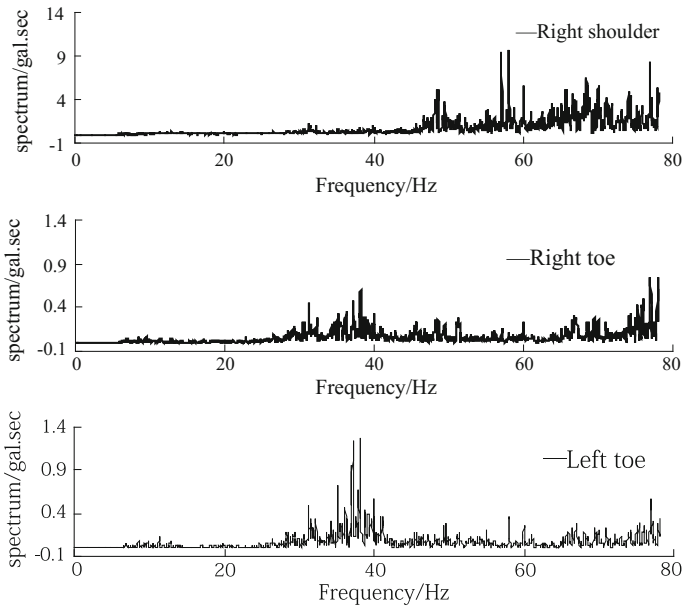
Fig. 3 Fourier spectral of the Acceleration waveform recorded at different position

Analysis of Numerical Calculation Results

Numerical Model and Mechanical Parameters

The analysis model of the crushed-rock embankment was built on the grounds of the borehole data and the railroad subgrade structure, as shown in Fig. 4a. According to the engineering geological conditions, the soil layer distribution is determined as well. The simulation is carried out with a plane strain assumption and the influence of boundary conditions is diminished by using the infinite element boundary. The lateral boundary conditions are using infinite element boundary, however, the bottom boundary is using artificial boundary condition. For a more accurate understanding of the dynamic properties of the crushed-rock embankment, a plain-fill embankment model (Fig. 4b) was also set up for comparative analysis, in which the crushed-rock layer above the ground was replaced by a plain-fill layer.
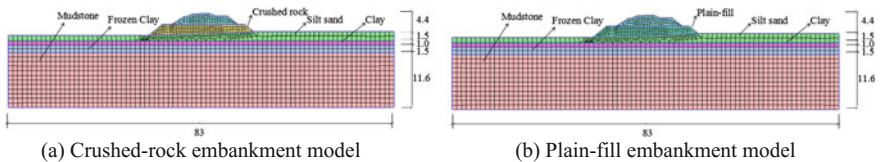

(a) Crushed-rock embankment model   (b) Plain-fill embankment model

Fig. 4 Models of finite element analysis (unit: m)

Table 1 Soil mechanics parameters at the survey area

Lithology	Frozen state	$\gamma/(kN\cdot m^{-3})$	μ	ζ	E/(MPa)	c/(MPa)	$\Phi/(°)$
Block Stone		23	0.35	0.25	500		
Silty sand	Unfrozen	16	0.35	0.3	21	0.01	34
	Frozen	16	0.35	0.3	210	0.02	36
Silty clay	Unfrozen	18	0.36	0.3	30	0.012	20
	Frozen	18	0.36	0.3	300	0.024	24
Mudstone	Frozen	21	0.32	0.4	1000	0.112	26

Before dynamic calculation, we used the one-dimensional equivalent linear method to calculate the dynamic response characteristics of free field soil. And then, its non-linear were taken into account, that the definite calculating parameters, including the equivalent shear modulus and damping ratios, were used to describe the complex changes of the soil. After the iterative calculation, the soil values of dynamic shear modulus and damping ratio were finally decided while the maximum shear strain occurred. In our two-dimensional finite element dynamic analysis, the soil was regarded as an elastic-plastic material and the Drucker–Prager yield criterion was adopted. The soil parameters of shear strength and other physical and mechanical parameters for finite element numerical calculation were obtained by triaxial tests carried out at the State Key Laboratory of Frozen Soil Engineering, and are shown in Table 1 [12]. The crushed rock material conformed to a linear elastic model [13, 14].

The real-time acceleration wave, recorded at the right shoulder of the crushed-rock embankment from the site test, was used as the input train motion and was input at the shoulder of the simulation models.

Vibration Transmission Characteristics of Train Load

In order to analyze the influences of the crushed-rock layer on the vibration-transmitting characteristics of embankments under dynamic train loads, the vibration acceleration time-history curves were picked up at the vertical central positions of the simulation models, including the embankment surface, the top, and bottom surface of the crushed-rock layer, and the permafrost table. The observation points are shown in Fig. 5.

Figure 6 shows the maximum acceleration of the two different types of embankments. The vibration transmissions in these two embankments reflected obvious attenuation effects along the vertical centers of the embankments. As the depth increased, the maximum acceleration of the plain-fill embankment decreased linearly and its vibration energy was mainly concentrated in the interior of the embankment, while the vibration value on the natural surface decreased slightly.

Fig. 5 Distribution of observation points of the crushed-rock embankment model
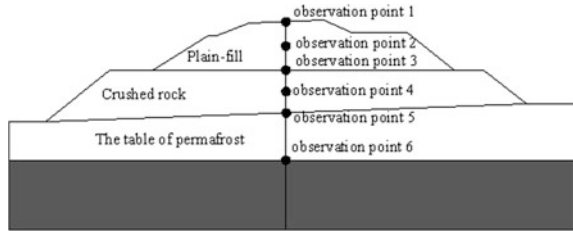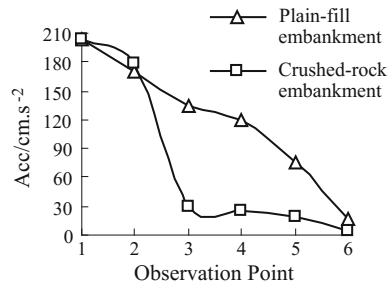

Fig. 6 Distribution of maximum acceleration along depth at different embankments

The vibration acceleration value decreased by as much as 10% when the vibration was transmitted to the permafrost table.

In the center of the embankment surface, the acceleration amplitude was slightly larger than that of the plain-fill embankment at the same position. With the attenuated transmission effect, the maximum acceleration amplitude values of the lower part of the crushed-rock layer was much less than that of the plain-fill layer. Therefore, under the same dynamic loads, the vibration attenuation effect of the crushed-rock embankment was significantly greater than that of the plain-fill embankment. For the crushed-rock embankment, when the vibration was transmitted to the permafrost table, the effects of the train load could be neglected. Because the crushed-rock layer changed the stiffness performance of the embankment, the distribution of maximum acceleration showed obvious nonlinear characteristics. Therefore, the construction of a crushed-rock layer can remarkably reduce the transmission of vibration load and can decrease the dynamic load, thus enhancing the stability of embankments in permafrost regions.

Settlement Distribution of the Embankments Under Dynamic Train Loads

Figure 7 shows the displacement distributions of the plain-fill embankment and the crushed-rock embankment, and Fig. 8 shows the distributions of the maximum settlement varying with the depth of the two embankments. The calculation results
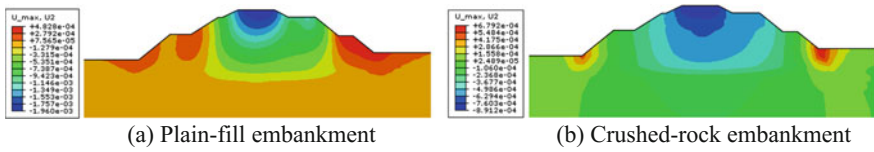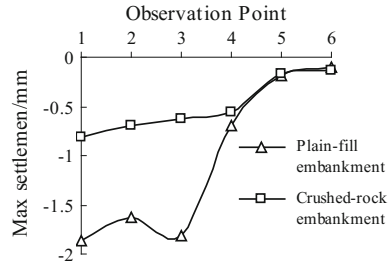
(a) Plain-fill embankment   (b) Crushed-rock embankment

Fig. 7 Displacement contours of the two embankments (unit: m)

Fig. 8 Distribution of maximum settlement of two kinds embankment along depth direction

showed that the average vertical displacement of vibration gradually increased as the train passing. The maximum settlement of both embankments appeared at the top of the embankments. The maximum settlement of the plain-fill embankment reached 1.87 mm, while that of the crushed-rock embankment was only 0.81 mm. Under the effects of the load of train, 0.5-mm surface upheavals appeared at both sides of the slope toes. The deformations caused by the train's dynamic vibration in the crushed-rock embankment were clearly less than those of the plain-fill embankment. However, the deformations of the crushed-rock embankment under the natural ground were slightly greater than that of the plain-fill embankment because of the greater density of the crushed rock. Furthermore, under the train load, the soil above the table of artificial permafrost incurred obvious deformation, while the soil under the table of artificial permafrost had little deformation. Therefore, the settlement caused by train's dynamic vibration of an upper embankment can be effectively decreased by laying a crushed-rock layer on embankments of the QTR in permafrost areas.

Figure 9 shows the displacement contour of plain-fill embankment under the train load in warm season and cold season. The results show that the influence of embankment vibration from train-induced vibrations is greater when the active layer thaws in the warm season. In cold season, the maximum displacement of the embankment is 0.09 mm, while the value reaches to 0.19 mm in warm season. The soil deformation induced by train vibrations occurs mainly above the permafrost table in summertime and above the natural surface in wintertime instead.
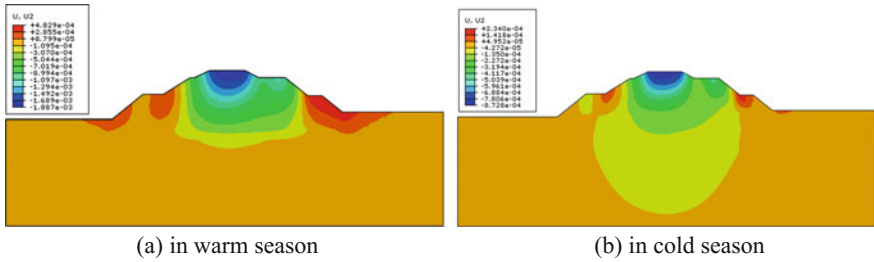
(a) in warm season   (b) in cold season

Fig. 9 The displacement contour of plain-fill embankment in different seasons(unit: m)

Conclusions

In this paper, by comparing the dynamic stability of two kinds of embankments (plain-fill embankment and crushed-rock embankment) under train load in the permafrost region of Beiluhe River section along the QTR. The dynamic stability of the two kinds of embankments are simulated. The main conclusions of this paper are as follows:

(1) There is an obvious vibration attenuation effect during the transfer process from road shoulder to slope toe and the peak acceleration drops to about 10%.

(2) The numerical simulation analysis results show that the vibration attenuation effect of a crushed-rock embankment is significantly greater than that of a plain-fill embankment. In a crushed-rock embankment, when the vibration is transmitted to the permafrost table, its effects can be neglected.

(3) Both plain-fill and crush-rock embankments, the maximum settlement of two kinds of embankments appears at the top under the effects of dynamic train loading. Also, the maximum settlement of the plain-fill embankment reaches 1.87 mm, while that of the crushed-rock embankment is only 0.81 mm. However, 0.5-mm surface upheavals appear at both sides of the slope toes.

(4) The change of seasons has a certain influence on the displacement of embankment. The amount of deformation at the same location in summertime is much more than that in wintertime. The maximum settlement of the embankment under train load appears on the pavement, which is only 0.09 mm in cold season but up to 0.19 mm in warm season.

References

1. Niu FJ, Zhang JM, Zhang Z (2002). Engineering Geological Characteristics and Evaluations of Permafrost in Beiluhe Testing Field of Qinghai -Tibetan Railway. Journal of Glaciology and Geocryology, 24(3): 264–269.
2. Ma W, Yu SS, Wu QB, et al (2006). Study on in-situ monitoring technology of cooling roadbed in permafrost regions of Qinghai-Tibet plateau. Chinese Journal of Rock Mechanics and Engineering, 25(3): 563–571.
3. Ma W, M YH, Wu QB, et al (2011). Characteristics and mechanisms of embankment deformation along the Qinghai–Tibet Railway in permafrost regions. Cold Regions Science and Technology, 67: 178–186.
4. Mu YH, Ma W, Liu YZ, et al (2010). Monitoring investigation on thermal stability of air-convection crushed-rock embankment. Cold Regions Science and Technology, 62: 160–172.
5. Mu YH, Ma W, Wu QB, et al (2012). Cooling processes and effects of crushed rock embankment along the Qinghai–Tibet Railway in permafrost regions. Cold Regions Science and Technology, 78: 107–114.
6. Kutara (1980). Settlement and countermeasures of the road with low embankment on softground. Technical Reports of Civil Engineering, 22(8): 12–16.
7. Li ZY, Gao GY, Feng SJ et al (2007). Analysis of Ground vibration induced by high-speed train. Journal of Tongji University(nature science), 35(7): 563–571.
8. Gao GY, He JF, Yang CB, et al (2011). Ground vibration induced by trains moving on saturated ground using 2.5D FEM. Chinese Journal of Geotechnical Engineering, 32(2): 234–241.
9. Dong L, Zhao CG, Cai DG, et al (2008). Method for dynamic response of subgrade subjected to high-speed Moving Load. Engineering Mechanics, 25(11): 231–240.
10. Wang LL, Liang QG, Sun W, et al (2013). Model test on dynamic response of layered slopes with different thicknesses. China Earthquake Engineering Journal, 35(3): 590–596.
11. Atkinson G.M., Boore D.M,1995. Ground motion relations for Eastern North America, Bull. Seism. Soc. Am., 85, 17–30.
12. Wu ZJ, Chen T, Ma W (2011). Characteristics of load transmission of trains in permafrost regions along Qinghai-Tibet railroad. Chinese Journal of Geotechnical Engineering, 45(5): 716–721.
13. Wang JD, Peng SJ, Ma Y, et al (2013). Dynamic tests on the cement-improved Loess under the vibratory load. China Earthquake Engineering Journal, 35(1): 35–41.
14. Che AL, Iwatate T, Ge XR (2006). Dynamic behaviors of subway structure subjected to strong earthquake motions using shaking table tests and dynamic analyses. Rock and Soil Mechanics, 27(8): 1293–1298.

Numerical Investigation on Ground Vibrations Induced by High-Speed Train and Its Mitigation

Zhixiang Sun, Xuecheng Bian and Yunmin Chen

Introduction

Vibration is one of the main environmental problems caused by urban rail transit. With the development of urban rail transit in recent years, people pay more attention to this problem. Reducing the vibration of the rail transit is important to improve the resistants' quality along the railway and make the sustainable development of the rail transit.

For environmental vibration, people are concerned about the 1–80 Hz vibration which human body is particularly sensitive to. Vibration in this range have a great impact on human organs. It also can produce a series of adverse psychological effects [1]. In order to improve people's work and life quality, a lot of research has been done. These research results gradually reflected in a series of standards for vibration comfort. British Standard Institute has released the BS standards [2]. In Germany, the DIN standards [3] and the VDI standards [4] are both for vibration comfort. ISO has released the ISO standards [5]. These standards are widely used in the fields of construction, automotive, machinery, aerospace, shipbuilding and so on.

This paper used the 2.5-dimensional finite element method to analyze the vibration isolation effect of the isolation trench, the isolation wall and the elastic foundation. ISO2631 was applied to evaluate how the parameters influence the vibration isolation effect.

Z. Sun (✉) · X. Bian · Y. Chen
Department of Civil Engineering, Zhejiang University,
Hangzhou 310058, China
e-mail: sunzhixiang1991@sina.com

X. Bian
e-mail: bianxc@zju.edu.cn

Y. Chen
e-mail: chenyunmin@zju.edu.cn

Principle of Calculation [6, 7]

In this paper, 2.5-dimensional finite element analysis method was used to solve the dynamic problem of the ground under the action of moving loads. The material and geometric properties were assumed to be constant along the load-moving direction. In the interaction model of track structure and its supporting ground, the influence of the sleeper weight was considered in orbit. The positive direction of X coordinate axis was train travel direction and the positive direction of Z coordinate axis was vertical downward. Wavenumber transformation was adopted to condense the three-dimensional problem to a plane strain problem. The motions of ground with homogeneous and isotropic media assumption can be described by the Navier's equations in the frequency domain:

$$\mu^c u_{i,jj}^t + (\lambda^c + \mu^c) u_{j,ji}^t + \omega^2 \rho u_i^t + f_i^t = 0 \tag{1}$$

where $\lambda^c = (1 + 2i\beta)\lambda$, $\mu^c = (1 + 2i\beta)\mu$, and β was the damping ratio of soil material. Based on the analytical method, the displacement along the track was transformed to the wave number:

$$u^x(\xi_x, \omega) = \int_{-\infty}^{+\infty} u(x, \omega) \exp(i\xi_x x) d\xi_x \tag{2}$$

where variables with superscript 'x' represented the components in the wave-number domain.

Then the finite element discretization of the embankment and foundation on the plane of the vertical track was carried out. The analytical model was shown in Fig. 1. By means of the wave number transformation, the degree of deformation freedom along the track was condensed to the node of the plane. It was called the 2.5-dimensional plane problem, which could express the three-dimensional problem in the two-dimensional plane. The following inverse Fourier transform was used to get the solution in three-dimensional space.

Fig. 1 Interaction model of track and ground
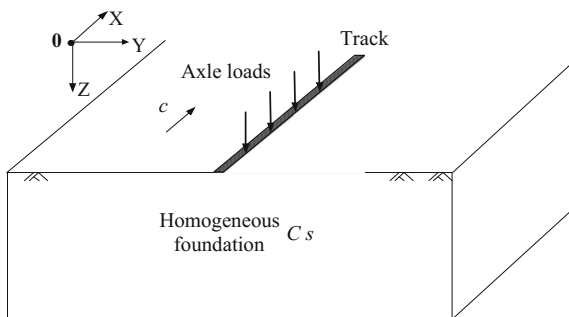
$$u(x, \omega) = \frac{1}{2\pi} \int_{-\infty}^{+\infty} u^x(\xi_x, \omega) \exp(-i\xi_x x) d\xi_x \tag{3}$$

This method greatly reduced the number of units required in computing. Maher radiation effect caused by wave propagation in three-dimensional space was also considered.

In this paper, the train movement was represented with moving vertical force at the position of the wheel shaft. The track structure on the embankment was simulated by Euler beam element. The ground was modeled by the isoparametric quadrilateral element. In the left and right sides of the model, the thin layer element was used as the transmission boundary, so that the vibration energy generated by the train could be transmitted to the infinite distance. For uniform moving loads with a velocity of c, the wave number (ξ_x) could be expressed as:

$$\xi_x = c/\omega \tag{4}$$

where ω was frequency. Two inverse Fourier transform were needed to obtain the spatial solution in the time domain before. Now only once could get the solution.

Calculation Condition

In this paper, an analysis was made on the condition of uniform foundation without embankment. Coordinate system was located in the center of the track, as shown in Fig. 2. The soil material was considered as homogeneous material. In order to compare the results of two sides, the left side did not have vibration isolation facilities while the right side had vibration isolation facilities like vibration isolation trench, vibration isolation wall and elastic foundation. The vibration isolation trench was empty trench. The material of the vibration isolation wall and the elastic foundation was concrete.

The characteristic parameters of the material in the calculation model were shown in Table 1.

The moving load was represented by the train moving load. Train load was shown in Fig. 3 by a series of wheel axle load. The number of the car number
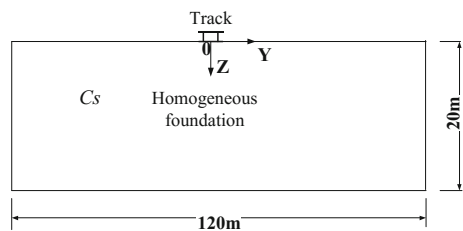
Fig. 2 Model cross section

Table 1 Parameters of foundation soil and concrete material

Material	Elastic modulus (MPa)	Density (kg/m³)	Shear wave velocity (m/s)	Damping coefficient	Poisson ratio
Soil	46	1800	100.0	0.05	0.35
Concrete	33,000	2500	2375.0	0.08	0.17
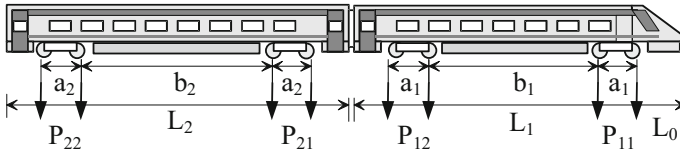
Fig. 3 Wheel axle load

Table 2 Distribution of the axle loads

Carriage number	P1(kN)	P2(kN)	a(m)	b(m)	L(m)
1	195	195	3.00	11.46	0.00
2	170	170	2.56	18.00	21.29
3	170	170	2.56	18.00	25.50
4	170	170	2.56	18.00	25.50
5	170	170	2.56	18.00	25.50
6	195	195	3.00	11.46	25.50

was M. Each car has four pairs of wheels. The velocity of the train was c. The axle weight of the train adopted the parameters of China high-speed train [8], as shown in Table 2. The train speed (c) was taken as 120 m/s. The flexural rigidity (EI_0) of the double-track rail was taken as $13.24MN/m^2$ according to the actual track conditions in China [8]. The orbital damping coefficient was 0.02 and the mass per unit length was 349 kg/m.

Analysis of Calculation Results

Vibration Isolation Trench

In order to analyze how isolation ditch width (w), groove depth (h) and distance from the orbit center of d influence vibration isolation effect, the analytical model shown in Fig. 4 was adopted. The underlying foundation was uniform half-space. Its shear wave velocity (Cs) was 100 m/s. The width of the isolation ditch in the model was 0.167B. B = 3 m in the full text referred the track width. The groove depth (h) was 1.667B, and the distance (d) was 2B. By changing the value of a
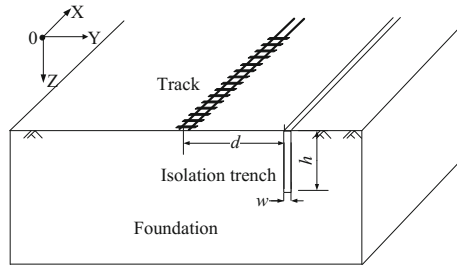
Fig. 4 Calculation model of foundation for vibration isolation trench

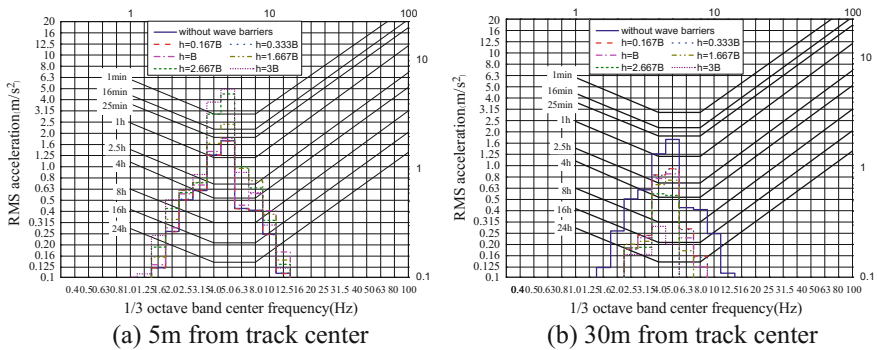(a) 5m from track center   (b) 30m from track center

Fig. 5 Influence of groove depth (*h*) on foundation vibration

certain parameter, the effect of the parameter on the vibration isolation effect was analyzed. The train moving speed (*c*) was 120 *m/s*. The calculated results were analyzed and compared with the cases without vibration isolation, and the influence of the parameters on the vibration isolation performance of the vibration isolation measures was obtained. Because the effect of the depth (*h*) was obvious, this paper only listed the calculation results of the depth *h*.

The depth of the vibration isolation trench was 0.167B, 0.333B, B, 1.667B, 2.333B, 3B respectively. ISO2631 was used to evaluate the vertical vibration under different groove depth. The calculation results were shown in Fig. 5.

Figure 5 shown that the isolation ditch had obvious amplification effect on the vibration of the soil in the front of the ditch. The phenomenon of amplification was more obvious when the ditch was deeper at some frequency. When the depth reached 3B, it can be seen that the human body would not work for more than 1 min at ground surface 5 m away from the center of the orbit under the vibration frequency of 4 Hz and 5 Hz. It would produce fatigue. For the soil behind the ditch, the vibration isolation effect was better while the ditch was deeper. When the foundation was not used vibration measures, the human body would not work for

more than 1 h at ground surface 30 m away from the center of the orbit under the vibration frequency of 4 Hz and 5 Hz. At the same frequency, the human body could work more than 8 h when the groove depth reached 3B.

Vibration Isolation Wall

In order to analyze how wall thickness (*w*), wall height (*h*) and distance from the orbit center of *d* influence vibration isolation effect, the analytical model shown in Fig. 6 was adopted. The wall thickness (w) was 0.167B. The wall height (h) was 1.667B, and the distance (*d*) was 2B. This paper only listed the calculation results of the height *h*.

The height of the vibration isolation wall was 0.167B, 0.333B, B, 1.667B, 2.333B, 3B respectively. ISO2631 was used to evaluate the vertical vibration under different wall height. The calculation results were shown in Fig. 7.

Figure 7 shown that the vibration isolation effect was better while the height was higher. When the height of the isolation wall reached 1.667B, the vibration intensity
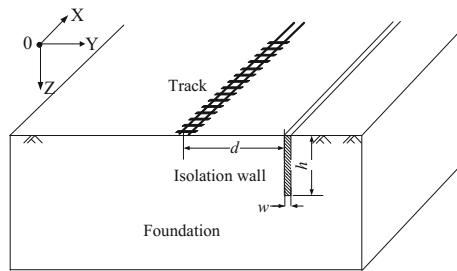

Fig. 6 Calculation model of foundation for vibration isolation wall

(a) 5m from track center

(b) 30m from track center
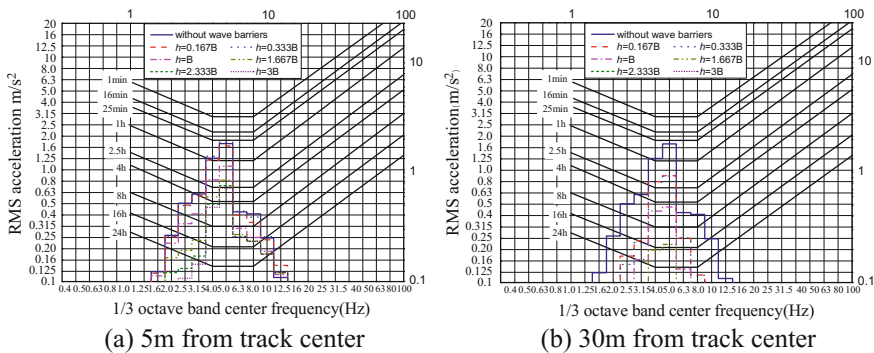
Fig. 7 Influence of wall height (*h*) on foundation vibration

of the foundation corresponding to the vibration of the ground at 30 m from the center of the track was more than 16 dB lower than that of the vibration without wave barriers under the vibration frequency of 5 Hz. At this condition, the human body could work about 16 h. When the height reached 2.333B, the human body could work more than 24 h at this position under the frequency of 5 Hz.

Elastic Foundation

In order to analyze how width (*w*) and height (*h*) of elastic foundation influence vibration isolation effect, the analytical model shown in Fig. 8 was adopted. The width (w) was 2B. The height (h) was B. This paper only listed the calculation results of the height *h*.

The height of the elastic foundation was 0.5B, B, 1.5B, 2B respectively. ISO2631 was used to evaluate the vertical vibration under different elastic foundation height. The calculation results were shown in Fig. 9. It was shown that the vibration isolation effect was better while the height of elastic foundation was higher.

Fig. 8 Calculation model of foundation for elastic foundation

(a) 5m from track center

(b) 30m from track center

Fig. 9 Influence of elastic foundation height (*h*) on foundation vibration

Conclusions

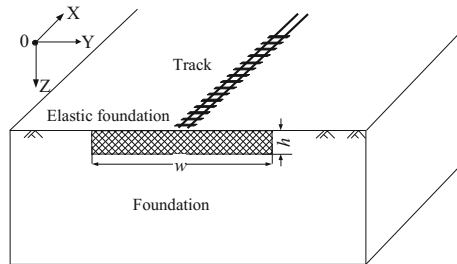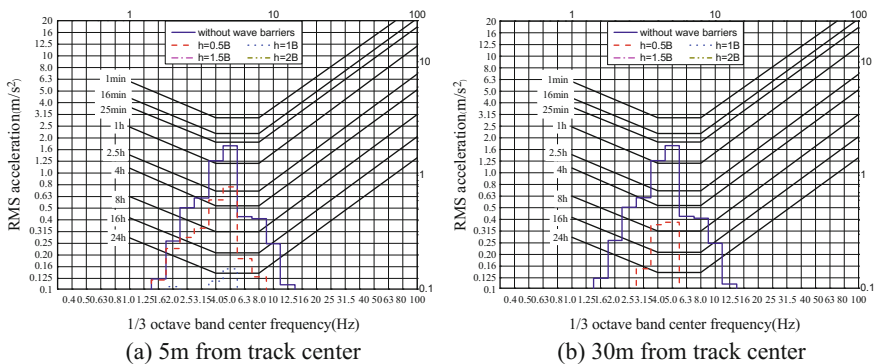Considering the harm to human body, the vibration isolation measures should be adopted while the vibration caused by the high-speed train was strong. When adopting vibration isolation measures to isolate the vibration of foundation caused by train, it is necessary to take reasonable and effective vibration isolation measures according to the different characteristics of vibration isolation measures. Before the adoption of vibration isolation measures, the reasonable vibration isolation method and its parameters should be adopted according to the damping requirements.

References

1. Zhu Guanghan, Wang Zhengling. (1992). Evaluation and standard of environmental vibration and incoming human body vibration. Journal of Vibration and Shock. 1992(3): 66–70. (in Chinese).
2. British Standard 6472. (1984). Guide to the evaluation of human exposure to vibration in building. British Standard Institute, London.
3. DIN 4150. (1975). Vibration in building. Deutsches Institut flir Normung, Berlin.
4. VDI 2057. (1986). Human exposure to mechanical vibrations. Verein Deutscher Ingenieure, Duesseldorf.
5. International Standard 2631-2. (1989). Evaluation of human exposure to whole-body vibration-Continuous and shock-induced vibration in buildings. ISO, Geneva.
6. Yang Y B, Hung H H. (2001). A 2.5D finite/infinite element approach for modelling visco-elastic bodies subjected to moving loads. International Journal For Numerical Methods in Engineering. 51(11):1317–1336.
7. Bian Xuecheng, Chen Yunmin. (2006). Analysis of ground vibration generated by train moving loads using 2.5D finite element approach. Chinese Journal of Rock Mechanics and Engineering. 25(11):2335–2342. (in Chinese).
8. Bian Xuecheng, Hu Ting. (2007). Parametric study on embankment and ground vibrations generated by train moving loads. Chinese Journal of Rock Mechanics and Engineering. 26(S2):4353–4361.(in Chinese).

Effect of Metro Excavation on Soft Clay's Displacement and Strength Behaviors Based on In-situ Tests

Zhuofeng Li, Junneng Ye, Weian Lin, Xuecheng Bian and Yunmin Chen

Introduction

It is common that the metro excavation construction in cities results in the soil displacement and its structure deformation in the surroundings, causing huge property losses [1, 2]. The influence of excavations on the surrounding environment has been studied by dozens of scholars [5–10]. However, hardly have scholars studied the influence of excavations on undrained shear strength in soil. The design at present adapts the indexes of undrained shear strength at the operation site, which is the vane shear strength, but after excavations, the stress-strain redistribution [3, 4] and vane shear strength in surrounding soil mass will change. If the vane shear strength becomes small after excavations, the foundation-pit tent to be unsecure, adverse to the service life of the foundation-pit construction.

Therefore, to investigate the influence of excavations in soil clay on soil deformation and the change of the vane shear strength, a metro excavation on-site test was launched on the typical soft clay areas of Ningbo metro excavation. And it

Z. Li (✉) · W. Lin · X. Bian · Y. Chen
Misistry of Education Key Laboratory of Soft Soils and Geoenvironmental Engineering,
Department of Civil Engineering, Zhejiang University, Hangzhou 310058, China
e-mail: lizhfg@126.com

W. Lin
e-mail: linweian@zju.edu.cn

X. Bian
e-mail: bianxc@zju.edu.cn

Y. Chen
e-mail: chenyunmin@zju.edu.cn

J. Ye
Ningbo Urban Rail Transit Project Construction Headquarters, Ningbo 315012, China
e-mail: yjn75@139.com

is discovered that the influenced areas and degrees on the surrounding environment to illuminate the life-cycle design in foundation-pit engineering.

Field Measurement of the Metro Excavation Project

Description of the Metro Excavation

The metro excavation site is located in Ningbo City, Zhejiang Province of China. It was originally open farmland with no other structures. The construction site is on the alluvial-lacustrine deposits plain in Ningbo. The ground is mainly formed by fluvial facies, lacustrine facies and marine facies and composed by a set of continental accumulation, sea-land alternating accumulation and marine accumulation stratum in accordance with decreasing age. The soil types and their properties of the metro excavation construction site are presented in Table 1. The surface of the site is miscellaneous fill of about one meter thick. The ground water mainly consists of the water in the surface fill and confined water in the gravel layer 5–6. The confined water level varies in accordance with seasons, climate and other factors and the depth of phreatic water level is 0.1 to 1.1 m.

The project was divided into two phases. The testing area sited in the first phase of 152 m. The standard segment of the station was 19.7–21.0 m and the standard depth of the excavation was 16.343–16.86 m. It adapted diaphragm wall enclosure structure. The thickness of the standard section was 800 mm. The depth of excavation is 16.66 m in testing areas. The length of diaphragm wall (crown cantilever bottom–toe of the wall) is 37.6 m. The depth of wall into the ground is 37.8 m and the insertion ratio is 1:1.27. Five struts have been set along the foundation-pit, among which the first one was 800 × 1000 (in height) mm reinforced concrete (concrete C30) struts and the rests were 16 (in diameter) × 609 mm steel struts (Q235B). The center-to-center distances of the struts from top to bottom were 3.5,

Table 1 Soils Profile and Main Geotechnical Parameters at the Construction Site

Stratum	D (m)	W (%)	γ (kN/m^3)	e_0	K_0	ν
1–2:clay	1.50	39.0	18.4	1.074	0.60	0.33
1–3:silt	3.50	54.9	16.9	1.544	0.72	0.42
2–1:clay	4.60	43.0	18.1	1.214	0.63	0.39
2–2a:silt	9.30	58.8	16.5	1.658	0.72	0.43
2–2b:mucky silty clay	14.80	43.5	17.6	1.208	0.67	0.42
3–2:silty chay	18.40	32.7	18.6	0.936	0.47	0.37
4–1:mucky silty clay	29.50	38.7	18.0	1.079	0.54	0.40
4–2:Clay	36.70	43.5	17.4	1.282	0.55	0.39
5–4:silty chay	39.00	33.8	18.3	1.021	0.47	0.35

D the bottom depth of soil, *W* water content, γ unit weight, e_0 void ratio, K_0 static lateral pressure coefficient, ν poisson ratio

Table 2 Construction Sequences of Excavation

Stage	Construction sequences	Stage	Construction sequences
1	Excavate to GL-1.0 m and construct reinforced concrete struts	4	Excavate to GL-11.4 m and install steel pipe struts
2	Excavate to GL-4.5 m and install steel pipe struts	5	Excavate to GL-13.4 m and install steel pipe struts
3	Excavate to GL-7.8 m and install steel pipe struts	6	Excavate to GL-16.7 m and cast foundation slab

GL means below ground level

3.2, 3.1, and 3.1 m accordingly. The steel struts were prestressed during installation with the powers of 370, 440, 330 and 210 kN/m from top to bottom accordingly; C30 plain concrete was cast into the bottom after excavations immediately, 250 mm thick. A tri-axial stirrring pile was used to strip-reinforce the foundation before excavations. Both of the width of the strip and the pitches were 3 m long. The weak reinforcement was used in the foundation-pit from the surface to 16 m in depth and the cement content was 8%. The strong reinforcement was used in the foundation-pit from 16 to 19 m and the cement content was 20%. The diaphragm wall was strengthened by high pressure jet grouting piles.

The foundation-pit was excavated in layers and bulks form north to south in grading. The construction on the research area included mainly six working condition (after the construction of the diaphragm wall). Specific working conditions were provided in Table 2.

Testing Methods

Before excavating the foundation-pit, inclinometers were set in the soil to test the soil deformation in the deep layers. Standard vanes were used to test vane shear strength in the soil. The profile of the arrangements of measuring points was shown in Figs. 1 and 2. Four holes were drilled to set inclinometers, one near the diaphragm wall (numbered CX0) and others kept a distance of 7.5, 15, and 30 m respectively (numbered CX7.5, CX15, CX30). For the latter three holes, two vanes were set for each hole to test the vane shear strength (numbered VST7.5, VST15, VST30) in the soil. The −1 holes were for the soil before excavation while the −2 holes were for the soil after excavation.

The displacement of soil in deep levels was tested by the inclinometer, with its data collected by every 0.5 m. The stable data from repeated tests before excavation was taken as the initial value, and the final value of soil displacement was taken from another test after the excavation.

A standard vane (5 × 10 cm) was used to test the vane shear strength in the soil, with a calibration factor of 0.02090 kPa/cm^2. The data was collected from static penetrometer KE-U310 from the data points set along the vertical direction, in 1 m
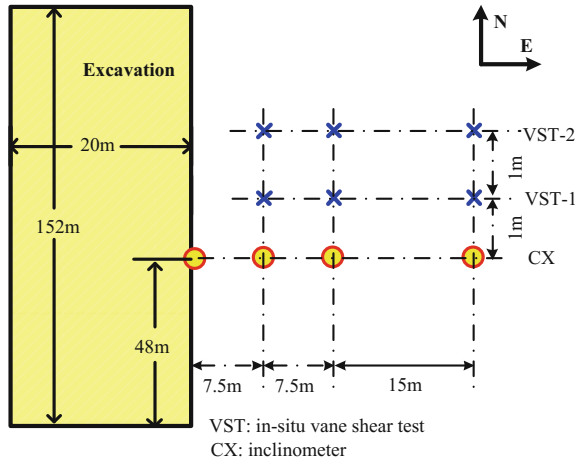
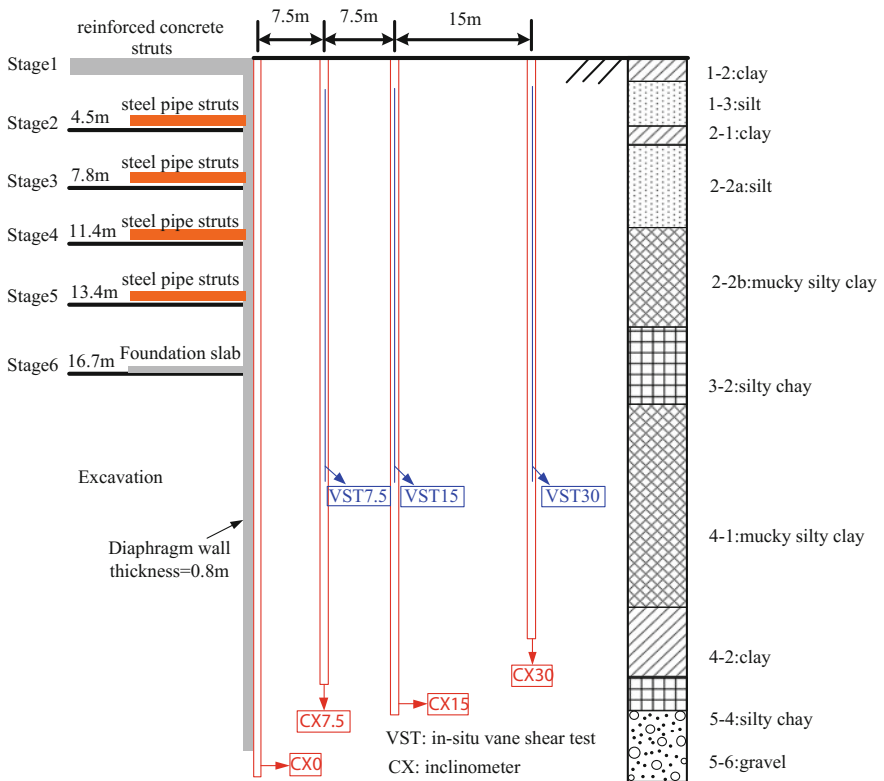**Fig. 1** Plan view of the excavation

Fig. 2 Cross section and soil profile of the excavation

interval. As the miscellaneous fill layer was established 1–2 m around the surface of the excavation, the data of the vane shear strength in the surface soil couldn't be collected.

Before the test, the surface soil was cleared away. Then, a track equipped with instruments was sent to the very holes. After that the instrument level was collected, the detector was pressed into the very depth for test in the soil and it was kept still for 2–3 min for the dissipation of excess pore water pressure. As data was collected every 10 s, during which the detector would spin 1–2 rounds, the vane would make a turn of 1°–2°. The undisturbed soil vane shear test would be stopped once the collected data went down or became stable. After that, the vane was spun quickly for six rounds. And the test of remolded soil was carried out in the similar way to the previous test of undisturbed soil. As the test data stabilized, it was stopped. The above operations were repeated before the whole tests were finished.

Monitoring and Testing Results

The Results of Lateral Soil Deformation

By testing the soil displacement in deep levels of the excavation, the conclusion of Fig. 3 was drawn, where the negative values stood for the deformation towards the inner side of the excavation. For the excavation depth of 16.7 m, the maximum value of soil deformation would be 79.40 mm. The closer the soil situated to the diaphragm wall, the bigger the deformation value would be. The deformation 30 m away from the diaphragm wall was too insignificant to claim an influence from the excavation, therefore, the influenced area of excavation could be 1.8 times of its depth. Also, the spreading points of maximum soil deformation aligned, forming the trend-line of soil damage outside the excavation. Heavy damage could be observed in the soil near the trend-line, with low values in indexes such as strength and modulus.

Figure 4 made a comparison of the maximum lateral soil deformation of soil in excavation in four areas (Boston [11, 12], Singapore [13–15], Taiwan [7, 16], Shanghai [10]). From our research, the ratio between maximum lateral soil deformation and excavation depth was 1:0.48, close to that of Shanghai and Boston.
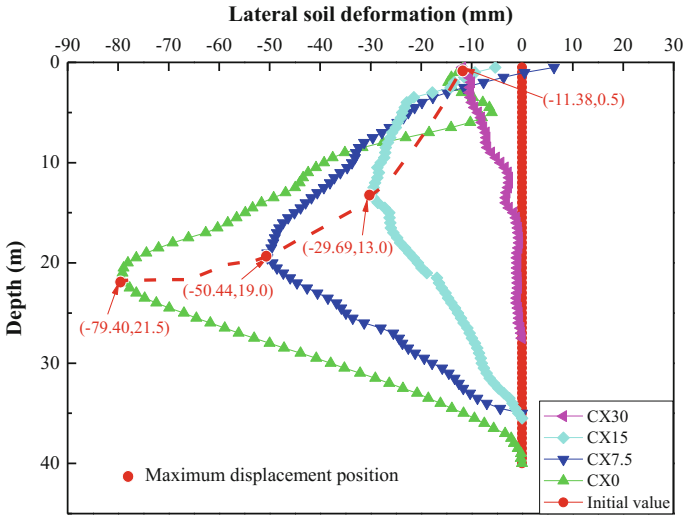
Fig. 3 Lateral soil deformation of the excavation
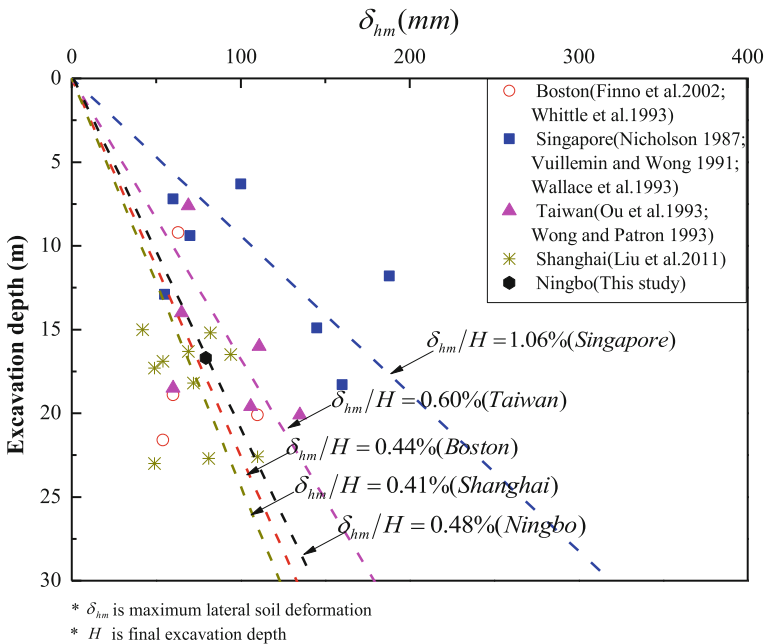
Fig. 4 Relationship between maximum lateral soil deformation and excavation depth

The Results of in Situ Vane Shear Test

Figure 5 showed the test results of vane shear strength before and after excavation. For the point 7.5 m away from the diaphragm wall, the vane shear strength after excavation plummeted, along with sensitivity, in 14–16%. For the point 15 m away, the vane shear strength after excavation dipped, along with sensitivity, in 4–6%. For the point 30 m away, the vane shear strength and sensitivity after excavation remained constant. The excavation resulted in the deformation of neighboring soil mass, and decrease in soil stress and destruction of soil structure
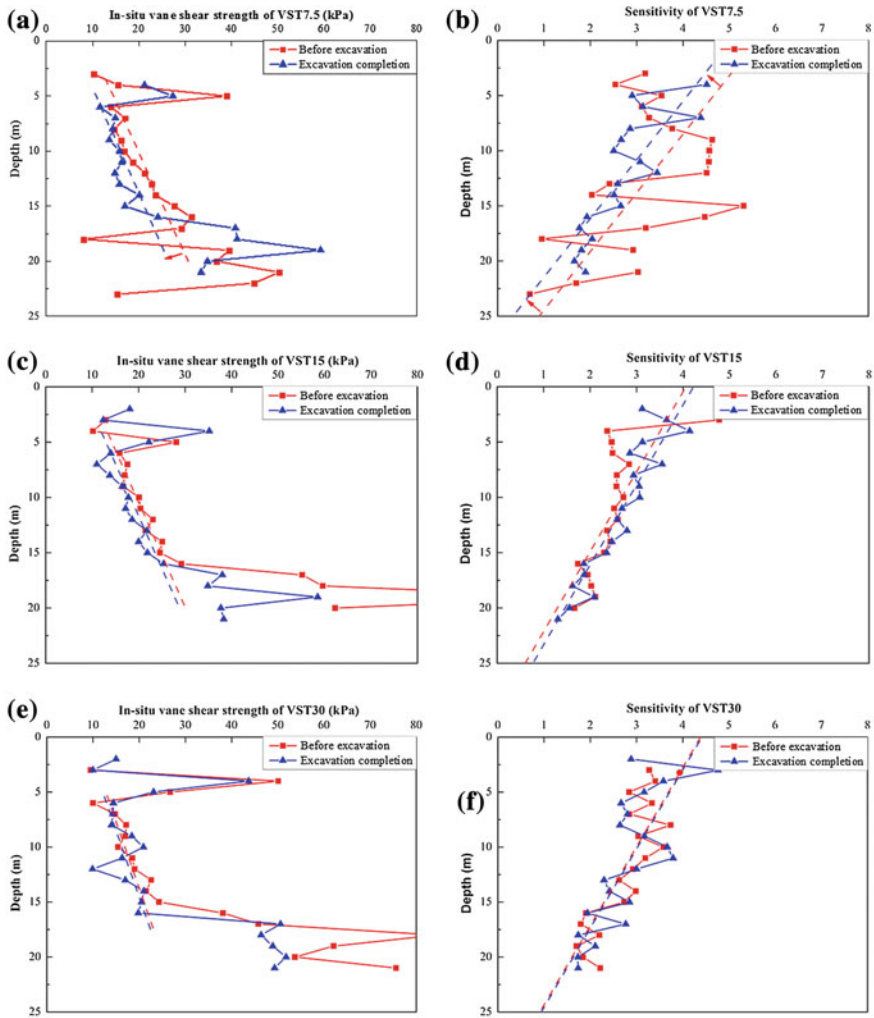
Fig. 5 In-situ vane shear strength and sensitivity values of the clay before and after excavation

contributed to the decrease in vane shear strength and sensitivity. Hence, the vane shear strength in neighboring soil mass and the soil deformation outside the excavation shared a similar pattern: the closer the soil situated to the excavation, the bigger influence the excavation could bring about on soil deformation and vane shear strength in soil. For those soil more than 30 m away from the diaphragm wall, there would be almost no influence.

Conclusions

In the research on metro excavations in areas of soft clay in Ningbo, the soil deformation and vane shear strength before and after excavation were investigated. From the analysis of the patterns of soil deformation and vane shear strength, four conclusions could be drawn:

1. The excavation would bring about influence on soil within the horizontal influence of 1.8 times of the excavation depth. The closer the soil situates to the diaphragm wall, the bigger the deformation would be. The ratio between maximum deformation and excavation depth was 1:0.48.
2. The neighboring area of maximum lateral soil deformation suffered from the severest damages in soil structure and the heaviest loss in strength.
3. After the excavation, the strength and sensitivity of vane in soil claimed a loss. For the point 0.45 times of excavation depth away from the diaphragm wall, the loss was 14–16%. For the point 0.9 times of excavation depth away, the loss was 4–6%. For the point 0.9 times of excavation depth away, there was almost no loss. This pattern was similar to that of soil deformation.
4. Life-cycle design of foundation-pits, the loss of vane shear strength in soil within the affected range should be compensated for, for the sake of the safe service of the project.

References

1. HAN Jie-hao. (2013). Analysis on impact and damage mechanism of foundation excavation upon surrounding architectural structure. Shanxi Architecture, 39(25): 61–63. (in Chinese).
2. DUAN Shao-wei, SHEN Pu-sheng. (2004). A crack analysis of concrete road with excavation of deep foundation pits. Engineering Mechanics, 21(3): 40–43.(in Chinese).

3. SUN Jun. (1999). Research on environmental soil engineering works during underground construction activities in urban area. Undergound Engineering and Tunnels, (3): 2–6. (in Chinese).

4. SUN Jun. (2000). Research on environmental soil engineering works during underground construction activities in urban area.Undergound Engineering and Tunnels, (1): 2–7. (in Chinese).

5. PECK R B. (1969). Deep excavation and tunneling in soft ground. In Proceedings of the 7th International Conference on Soil Mechanics and Foundation Engineering, Mexico City, pp. 225–290.

6. CLOUGH G W, O'ROURKE T D. (1990). Construction induced movements of in situ walls. In Proceedings, ASCE Conference on Design and Performance of Earth Retaining Structures, New York: ASCE, No. 25: 439–470.

7. OU C Y, HSIEH P G, CHIOU D C. (1993). Characteristics of ground surface settlement during excavation. Canadian Geotechnical Journal, 30(5): 758–767.

8. Zhong, W. W., Ng, C. W., & Guo, B. L. (2005). Characteristics of wall deflections and ground surface settlements in Shanghai. Canadian Geotechnical Journal, 42(42): 1243–1254.

9. Liuguo, B., Jiangrebecca, J., Ngcharles, W. W., & Hong Y. (2011). Deformation characteristics of a 38 m deep excavation in soft clay. Canadian Geotechnical Journal, 48(12): 1817–1828.

10. Zhang, H. B., Chen, J. J., Zhao, X. S., Wang, J. H., & Hu, H. (2014). Displacement performance and simple prediction for deep excavations supported by contiguous bored pile walls in soft clay. Journal of Aerospace Engineering, 28(6).

11. Finno, R.J., Bryson, L.S., and Calvello, M. (2002). Performance of a stiff support system in soft clay. Journal of Geotechnical and Geoenvironmental Engineering, 128(8): 660–671.

12. Whittle, A.J., Hashash, Y.M.A., and Whitman, R.V. (1993). Analysis of deep excavation in Boston. Journal of Geotechnical Engineering, 119(1): 69–90.

13. Nicholson, D.P. (1987). The design and performance of the retaining walls at Newton Station. In Proceedings of the Singapore Mass Rapid Transit Conference, Singapore, pp. 147–154.

14. Vuillemin, R.J., and Wong, H. (1991). Deep excavation in urban environment: examples. In Proceedings of the 10th European Conference on Soil Mechanics and Foundation Engineering, the Netherlands. Vol. 2, pp. 843–847.

15. Wallace, J.C., Ho, C.E., and Long, M.M. (1993). Retaining wall behaviour for a deep basement in Singapore marine clay. In Proceedings of the International Conference on Retaining Structures, London, pp. 195–204.

16. Wong, L.W., and Patron, B.C. (1993). Settlements induced by deep excavations in Taipei. In Proceedings of the 11th Southeast Asian Geotechnical Conference, Singapore, pp. 787–791.

An Implicit-Explicit Transition Method for Settlement Prediction of High-Speed Railway Subgrade Under High-Cycle Load

Zongqi Bi, Quanmei Gong, Zhuang Kang and Liushan Wang

Introduction

The long-term accumulated deformation of the foundation is one of the main sources of the post-construction settlement of high speed railway under the action of a large number of traffic loads. And its subgrade deformation has strict control standards, which is a high requirement for the prediction accuracy of the accumulated deformation under long-term alternating loads. But it is difficult to simulate this process quickly and accurately through general experimental or numerical method at present. For the permanent deformation of the sub rail foundation under long-term cyclic loading, a series of calculation theories and prediction methods have been proposed in recent years.

Theories and methods of prediction is mainly divided into two categories, the numerical analysis method and the empirical formula method.

The former is based on the finite element numerical analysis, which is trying to restore the actual characteristics of the soil and the cyclic loading process (we may define it as "Implicit mode"). Zheng et al. [1] studied the load - settlement relation of CFG pile composite foundation by means of 3D nonlinear finite element model; Abusharar et al. [2] established a plane strain model of the pile supported

Z. Bi (✉) · Q. Gong · Z. Kang · L. Wang
Key Laboratory of Road and Traffic Engineering of the Ministry
of Education, Tongji University, Shanghai 201804, China
e-mail: bizongqi@tongji.edu.cn

Q. Gong
e-mail: gongqm@tongji.edu.cn

Z. Kang
e-mail: jeffeykang@163.com

L. Wang
e-mail: 1334645@tongji.edu.cn

embankment, and analyzed the settlement, excess pore pressure and axial force for a period of 200 days. Chai et al. [3] considered the characteristics of soft clay and obtained the long-term settlement curve of the subgrade by the finite element simulation. Such studies generally consider the complex elastic-plastic constitutive model in the static or dynamic calculation. The effect of each cyclic load on the strain-stress relation of the soil sample unit is described by accumulation of micro increments, and the permanent deformation characteristics of soil can be reflected in the settlement-time curve. The advantage of implicit mode is that the condition of the loading and unloading of each step can be considered so the change of stress-strain process is more realistic simulated. But complex calculation parameters, limit of data capacity and computing speed have restricted its engineering practicability.

The latter quantifies the parameters of long-term settlement curve based on a large amount of data, and constructs explicit expression of empirical formula to fit and simplify the deformation law (we may define it as "Explicit formulation"). The empirical formula and initial value parameters are determined according to the laboratory test or field test data, and the strain-time curves of soil under cyclic loading are obtained by the closed total strain calculation. Li and Selig [4], Chai, Jin-Chun et al. studied the long-term deformation law of different foundation under traffic load and proposed the corresponding empirical equations. In addition, some scholars use the curve fitting method [5, 6], system theory, combined forecast method [7] and inverse analysis to get the explicit formula. This method is simple and practical, and it meets the requirements of calculation under a large number of cyclic loads without convergence problem, but the prediction accuracy is directly determined by the data quality.

The load cycle number during the life cycle of high speed railway subgrade is usually more than one million. Therefore, the state and the long-term performance of the sub rail foundation system are more stringent restricted. As the soil dynamic constitutive model is becoming increasingly sophisticated, simply using these existing "implicit" or "explicit" methods is not suitable for simulating the long-term cumulative deformation process of the subgrade. Time consuming, high computational cost and large cumulative error make it difficult to meet the needs of forecast.

In combination with the advantages of "Implicit mode" and "Explicit formulation", Niemunis et al. [8] proposed the implicit-explicit transition algorithm in the HCA (High Cyclic Accumulation) model. This method predicts the permanent deformation under high-cycle loading through the data transfer and conversion between explicit and implicit computational stages, which provides an effective solution to this problem.

As shown in Fig. 1, the implicit-explicit transition algorithm consists of two main steps: The implicit mode stages calculate the equilibrium stress field, and provide accurate parameters for the following calculation. The explicit mode stages realize the accumulation of high cycle times. The initial parameters (such as stress amplitude) in the process of explicit mode, need to be determined by the results of the implicit mode process, as the input conditions for each step. After a period of time, the dynamic parameters and the stress distribution of the whole model will be

Fig. 1 The basic idea of the implicit-explicit transition algorithm (Niemunis A, Wichtmann T, Triantafyllidis T [8], 2005)
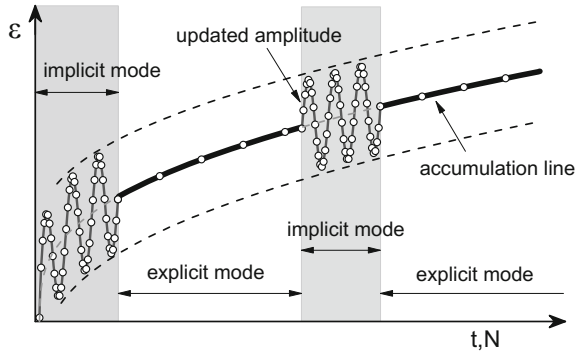
calculated and updated through the implicit mode in order to control the error between the calculation results and the actual deformation. Thus both the efficiency and the accuracy of the calculation are ensured in the prediction.

Based on the above process, the parameters of HCA model were calibrated [9] and a series of calibration work were studied by a large number of laboratory experiments of Niemunis and Wichtmann [10, 11]. The accumulative subsidence curve of a strip foundation was simulated by finite element method, and the regulations are in accord with the results of centrifugal model test. However, the method still have defects in long-term deformation prediction of high speed railway subgrade. Firstly, parameters such as the minimum cyclic deviator stress, which reflect the characteristics of the train load, are not included in the HCA model. Secondly, many parameters in the formula need to be calibrated with a large number of experimental data, and it has led to the low engineering practicability. In addition, the transition occasion between implicit and explicit mode is not explicitly stated. Its generality in numerical calculation and accuracy of simulation are to be verified. In this paper, the HCA model is simplified and improved according to the characteristics of high speed railway cyclic loading, and the criteria for the transition between calculation steps are given to improve the reliability of results.

FE Implementation and Improvement

Key Concept and Issues

The core idea of implicit-explicit transition algorithm is to synthesize the advantages of both. On the one hand, the accumulation of the number of high cycles of the load is simplified through the explicit formulation. On the other hand, the stress changes are simulated and fed back by the implicit mode. Since the stress changes with the development of the deformation, the stress field is inherited and balanced via the transition, and the corresponding stress variation curve is obtain to check the parameters in calculation.

In order to realize the implicit-explicit transition algorithm, the issues to be concerned are:

1. Applicable dynamic constitutive models for long-term deformation analysis of soil;
2. Compatibility and accuracy of data transfer between the constitutive equations;
3. Determination of termination.

Constitutive Model

Implicit mode

Under cyclic dynamic loading, the strain-stress relationship of soil in high speed railway subgrade is characterized by nonlinearity, hysteresis and accumulation [12]. Bauschinger effect of the material, homogeneous expansion effect of subsequent yield surface and the mixed hardening law need to be taken into account.

The bounding surface plasticity model is in the form of elliptical yield surface of modified Cambridge model, which is easy to be expressed in mathematics and suitable for numerical calculation. The loading surface adopts the radius mapping rule, and the proportional coefficient ψ of distance is introduced to describe the stress state of the mapping point on the bounding surface.

The bounding surface plasticity model can describe the plastic deformation of the stress state inside the boundary surface, and accurately reflect the process of loading and unloading, which meets the above requirements of implicit mode. Considering that it is more simple and practical than models like the composite yield surface model, it is used as a constitutive model for the implicit mode.

Explicit formulation

Most explicit formulations are used to establish the function relationship between the axial strain ε_1 or the settlement value s and the cyclic number N. The residual settlement of the first cyclic loading s_1 is used as the input to calculate the settlement of the N cycles $s(N)$. The formula is roughly in the form of $s(N) = s_1 N^C$ or $s(N) = s_1(1 + C\ln N)$ [13], wherein C is a material constant. The Monismith model and its modified exponential model [14, 15], which are based on the stress control test, are representative explicit formulations. The cumulative plastic strain ε^p is expressed as

$$\varepsilon^p = a\left(\frac{q_d}{q_f}\right)^m \left(1 + \frac{q_s}{q_f}\right)^n N^b \tag{1}$$

Wherein q_d, q_s and q_f denote the dynamic deviator stress, the static deviator stress and the failure deviator stress, respectively. The parameter a influences the amplitude of plastic strain, m describes the degree of development of strain along the depth, n refers to the impact of initial deviator stress and b depend on the total amount of strain accumulation and the increasing rate of cyclic loading.

Constants a, b, m, and n are determined according to the experimental data of the dynamic triaxial test.

The high-cycle accumulation model (HCA model) [16] is based on the strain controlled test, and it give an empirical formula as

$$\dot{\varepsilon}^{acc} = f_{ampl}\dot{f}_N f_e f_p f_Y f_\pi \tag{2}$$

In HCA model, strain accumulation rate $\dot{\varepsilon}^{acc}$ is represented by 6 independent control functions $f_{ampl}, \dot{f}_N, f_e, f_p, f_Y$ and f_π, which respectively represent the influence of the strain amplitude ε^{ampl}, the number of cycles N, the void ratio e, the average mean pressure p^{av}, the average stress ratio, and the change of the polarization of the strain loop. Parameters of above functions are determined by a large number of laboratory tests. And the empirical formula can be simplified by selecting influence functions with higher "sensitivity" for different soil and calculation requirements.

It can be seen that the factors considered in both models include the influences of soil dynamic stress and the number of cycles. The modified exponential model particularly includes the influence of the deviator stress, and HCA model has more advantages in analyses of the loading history and the polarization.

The train load is approximated to the form shown in Fig. 2, one periodic waveform reflects the load actions of two contiguous bogies. Results of laboratory test [17] show that the two main characteristic parameters, the cyclic dynamic stress amplitude σ_d and the minimum cyclic deviator stress σ_s (Fig. 2), obviously impact the long-term deformation of subgrade. Hence they are included in the empirical formula. The influence of cyclic loading history is reflected in the function $\dot{f}_N$ in (2), and its integral form is $f_N = C_{N1}[\ln(1 + C_{N2}N) + C_{N3}N]$. For the saturated soil, the parameters of the void ratio in function f_e are negligible. In this paper, we consider the train-induced stress characteristics in soil under K_0 consolidation [18], and the empirical formulas of the explicit mode are
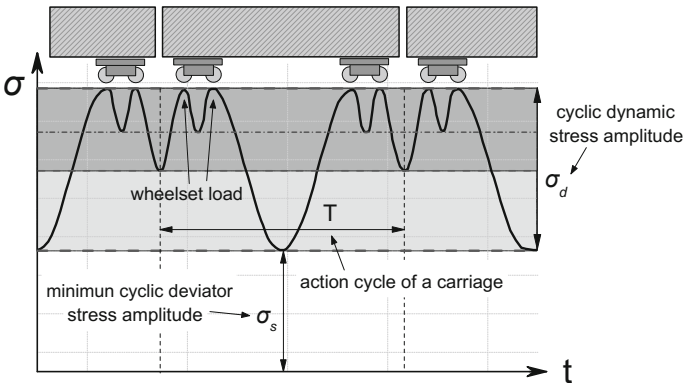

Fig. 2 Schematic diagram of simplified high speed train load

$$\varepsilon^p = a \left(1 + \frac{\sigma_s}{q_f}\right) \left(\frac{\sigma_s}{q_f}\right)^m C_1 [\ln(1 + C_2 N) + C_3 N] \tag{3}$$

$$\dot{\varepsilon}^p = a \left(1 + \frac{\sigma_s}{q_f}\right) \left(\frac{\sigma_d}{q_f}\right)^m C_1 \left(\frac{C_2}{1 + C_2 N} + C_3\right) \tag{4}$$

wherein the material parameter C_1, C_2 and C_3 are determined by fitting the experimental data curve of dynamic triaxial tests at different stress levels.

Taking the cumulative plastic strain of typical soft soil layers in Yangtze River Delta region as an example. The experimental simulation of loading frequency was 0.73 Hz, and the static deviator failure stress $q_f = 50$ kPa. The fitting parameters of (3) are shown in Table 1, and the fitting of empirical formula and experimental data of clay layer ④ is given in Fig. 3.

Table 1 Constants of the explicit formulation

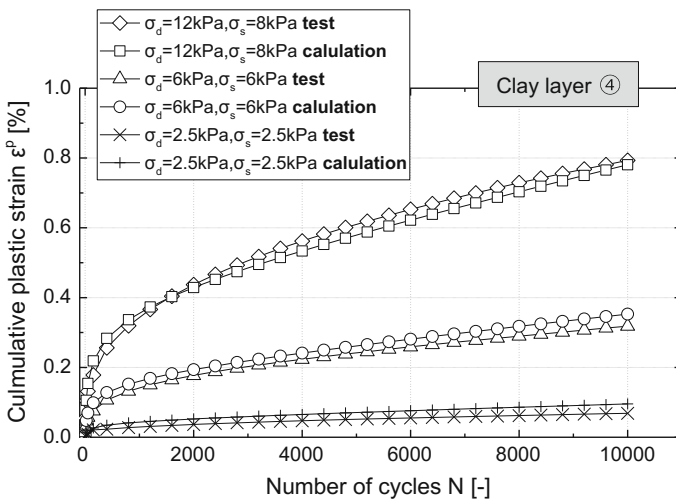| Soil samples	a [-]	m [-]	C_1 [-]	C_2 [-]	C_3 [-]	Correlation coefficients
Muddy silty clay layer ②	0.172	1.46	3	0.5	3.0×10^{-4}	0.9899
Silty clay and sand layer ③	0.075	0.93	2	0.074	1.97×10^{-4}	0.9924
Clay layer ④	0.24	1.42	2	0.25	5.5×10^{-4}	0.9972

Fig. 3 Fitting curves of empirical formula (Tests of clay layer ④, confining pressure is 85 kPa, axial pressure is 140 kPa, $K_0 = 0.6$)

Realization Process

In general finite element software platforms, constitutive models of implicit and explicit mode need to be programmed with second development through user subroutine interface. In this paper, the finite element software Abaqus is used to achieve above processes.

Bounding surface plasticity model of the implicit mode is constructed by the subroutine UMAT (User Defined Material Mechanical Behavior). When the incremental step N is finished, UMAT will calculated the stress increment $\Delta\sigma_{n+1}$ according to the incoming strain increments $\Delta\varepsilon_{n+1}$ of step $N+1$. This process is on the basis of the implicit Euler backward method proposed by Manzari and the concept of radial return algorithm, which includes the elastic prediction and the plastic correction.

The explicit formulation is realized through the creep calculation module. The nonlinear creep process is piecewise linearized with the accumulation of creep deformation under constant stress [19]. The recurrence formula of strain is expressed as (5).

$$\varepsilon_{cr}^n = \varepsilon_{cr}^{n-1} + \dot{\varepsilon}_{cr}(\sigma_{n-1}, \varepsilon_{n-1}, t_n)\Delta t \tag{5}$$

ε_{cr}^n and ε_{cr}^{n-1} are respectively the creep strain of moment t_n and t_{n-1}, σ_{n-1} denotes the stress level of moment t_{n-1} and the iterative time step $\Delta t = t_n - t_{n-1}$. The cumulative strain ε_{cr} and strain rate $\dot{\varepsilon}_{cr}$ can be obtained according to the empirical formula (3) and (4).

For the process of implicit-explicit transition, Python script is used to control the FE program kernel, realize the pre-processing and post-processing of data, read and write the result file, transmit and inherit the deformation along with the stress field of the previous step.

The procedure of a single cycle of implicit-explicit-implicit transition is shown in Table 2.

The following steps are repeated until the cycle number of the cumulative deformation prediction $N = N_1 + N_2 + N_3 + ... + N_n$ (N_i represents the number of cycles in the transition of i) is reached. And the transformation of the constitutive relations, the finite element models and the strain-stress data are realized through the process.

Need to mention that, except the first phase of calculation is started by the initial consolidation state, the following steps of explicit mode are subject to the impact of the cyclic history of previous steps. In order to reflect this process, if N_n cycles are required in step n, and the cyclic history of n-1 steps ahead is $\sum N_A$, then (3) can be expressed as

$$\varepsilon^p = a\left(1 + \frac{\sigma_s}{q_f}\right)\left(\frac{\sigma_d}{q_f}\right)^m C_1\left\{\ln[1 + C_2(N_n + \sum N_A)] + C_3(N_n + \sum N_A)\right\}f_\pi \tag{6}$$

Table 2 A single cycle process of implicit-explicit transition

	Procedure	Operation	Data transfer
1	FEM modeling	The bounding surface plasticity model is used and the boundary conditions are added.	The operation commands are record and the program code is formed.
2	Implicit mode	Equivalent train loads are applied and a number of cycles are continued.	–
3		Stress field and strain field are obtained with the cyclic dynamic stress σ_d and the minimum cyclic deviator stress σ_d as the initial parameters of the explicit mode.	Data postprocessing of stress, strain and coordinate.
4	Explicit mode	The improved empirical formula is used to establish the model of soil mass.	Data pre-processing of stress, strain and coordinate, and data updating of parameters in empirical formula.
5		Load N_n cycles.	–
6		The deformation data of the model are extracted as the initial condition of the next step.	Data postprocessing of strain and coordinate.
		The stress field generated by the last step of implicit mode is inherited as the initial stress field for the balance correction. Repeating operation from step 2.	Data pre-processing of stress, strain and coordinate.

wherein f_π denotes the polarization function [20], which can be desirable to be constant $f_\pi = 1$ in the triaxial test condition. And π represents the polarization tensor [9].

Results of simulations by the simple explicit formulation method and the implicit-explicit transition algorithm are respectively compared with the experimental data of dynamic triaxial test of clay layer ④ (Fig. 4). The initial conditions are $K_0 = 0.6$, $\sigma_d = \sigma_s = 6$ kPa, and the fitting values of the model parameters are shown in Table 1. The total number of cycles is 10,000, the cycle number for each stage is 3000, and the transition procedure is implemented for 3 times in total.

It can be seen that the slope of the curve of explicit formulation method and implicit-explicit transition algorithm appear to differ after cycle number $N > 2000$ (The deviation is about 7.5% at $N = 9000$). The average errors of the prediction and the measured data are 0.0425 and 0.0295, respectively. With the increase of the loading times, the latter shows a better fit to the variation trend of actual accumulative plastic strain.
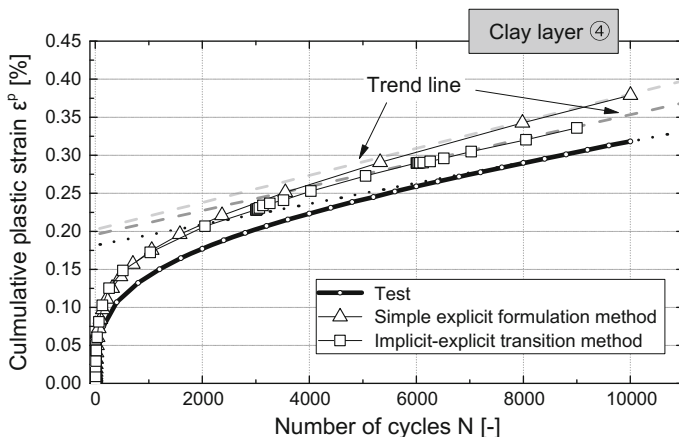
Fig. 4 Results of simulations and the experimental data of dynamic triaxial test

Control Standards of Cyclic Times

The control of cycle number in each calculation stage and the timing of the transition is the key of ensuring accuracy.

Implicit Mode

Due to the uncertainty and possible errors at the initial point and the endpoint of the cycle in implicit mode, the variation of stress and strain are generally irregular and should not be references for determining parameters. Therefore, the requirement for cycle number in each stage is: ≥ 3.

In addition, a large number of cycles in implicit mode have no significant effect on the parameters of the subsequent calculation process and the accuracy of the final results. But it may aggravate the error caused by data transmission redundancy. Thus the number of cycles should not be too large at the same time.

In conclusion, 3–4 cycles is appropriate to the loading process in the implicit mode.

Explicit Formulation

Considering the closed characteristic of the explicit formulation, the number of cycles in a stage N_n will significantly affect the calculated strain value. According to

the experimental data and the strain relationship between the adjacent stages, the following control parameters are presented.

Initial tolerable error Tol_a

On the basis of the cumulative strain curve of soil under the dynamic load in laboratory tests [17], the measured cumulative plastic strain ε_0^p which corresponds to the first stage of explicit mode can be obtained. The cycle number of the first stage is N_1, the cumulative plastic strain is $\varepsilon_1^p(N_1)$ and the tolerance Tol subjects to

$$Tol = \frac{\left|\varepsilon_1^p(N_1) - \varepsilon_0^p\right|}{\varepsilon_0^p} \leq Tol_a \tag{7}$$

wherein Tol_a is defined as the initial tolerable error, and the value of N_1 should satisfy the condition $Tol \leq Tol_a$. Tol_a should be in accordance with the accuracy requirements, the model size and the measured results.

Subsequent tolerable error Tol_n

In order to maintain the credibility of the subsequent control of errors after a certain cycles, it is required to find the correlation between the error reference system and the test data. Therefore, the subsequent tolerable errors are obtained by the recursive estimation algorithm based on the strain relationship of adjacent stages.

The cyclic dynamic stress amplitude and the dynamic deviator stress of stage n in implicit mode are respectively $\sigma_{d,n}$ and $\sigma_{s,n}$, the cycle number of stage n in explicit mode is N_n. And the cumulative plastic strain obtained in stage n-1 and stage n can be represented as

$$\varepsilon_{n-1}^p = a\left(1 + \frac{\sigma_{s,n-1}}{q_f}\right)\left(\frac{\sigma_{d,n-1}}{q_f}\right)^m C_1\left\{\ln\left[1 + C_2\left(N_{n-1} + \sum_1^{n-2} N_A\right)\right] + C_3\left(N_{n-1} + \sum_1^{n-2} N_A\right)\right\}f_\pi \tag{8}$$

$$\varepsilon_n^p = a\left(1 + \frac{\sigma_{s,n}}{q_f}\right)\left(\frac{\sigma_{d,n}}{q_f}\right)^m C_1\left\{\ln\left[1 + C_2\left(N_n + \sum_1^{n-1} N_A\right)\right] + C_3\left(N_n + \sum_1^{n-1} N_A\right)\right\}f_\pi \tag{9}$$

wherein the cumulative loading history of the former n-1 stages $\sum_1^{n-1} N_A = N_{n-1} + \sum_1^{n-2} N_A$. Then the predicted strain ratio is

$$\frac{\varepsilon_n^p}{\varepsilon_{n-1}^p} = \frac{1 + \frac{\sigma_{s,n}}{q_f}}{1 + \frac{\sigma_{s,n-1}}{q_f}}\left(\frac{\sigma_{d,n}}{\sigma_{d,n-1}}\right)^m \frac{\ln\left[1 + C_2\left(N_n + \sum_1^{n-1} N_A\right)\right] + C_3\left(N_n + \sum_1^{n-1} N_A\right)}{\ln\left(1 + C_2\sum_1^{n-1} N_A\right) + C_3\sum_1^{n-1} N_A}.$$

Parameter values of the formulation show that $C_3 < <C_2$, thus within a certain load step increment N_n, the strain ratio of adjacent stages can be approximately simplified as (10).

$$\frac{\varepsilon_n^p}{\varepsilon_{n-1}^p} = \frac{1 + \frac{\sigma_{s,n}}{q_f}}{1 + \frac{\sigma_{s,n-1}}{q_f}} \left(\frac{\sigma_{d,n}}{\sigma_{d,n-1}}\right)^m \ln(C_2 N_n) \tag{10}$$

The main idea of the following error analysis is to use the proportional relationship between ε_n^p and ε_{n-1}^p. The reference value $\varepsilon_n^{p\prime}$ of following stages is approximately expressed as a function of the measured standard value ε_0^p, thus the error between the predicted value and the estimated reference value is calculated and the decision threshold can be given.

In accordance with (10), the reference value of stage n can be approximated by

$$\varepsilon_n^{p\prime} = \frac{1 + \frac{\sigma_{s,n}}{q_f}}{1 + \frac{\sigma_{s,n-1}}{q_f}} \left(\frac{\sigma_{d,n}}{\sigma_{d,n-1}}\right)^m \ln(C_2 N_n)\varepsilon_{n-1}^{p\prime} \tag{11}$$

Note that when $n = 2$, the item on the right side of the equation $\varepsilon_1^{p\prime} = \varepsilon_0^p$. Then the subsequent calculation stages is required to meet $Tol = \frac{\left|\varepsilon_n^p(N_n) - \varepsilon_n^{p\prime}\right|}{\varepsilon_n^{p\prime}} \leq Tol_n$, wherein Tol_n denotes the subsequent tolerable error, which define the constraints of the cycle number for stage n of the explicit mode. This tolerance is proposed to be defined as the following recursive formula (12).

$$Tol_n = \frac{1}{K_n} \cdot Tol_{n-1} \tag{12}$$

The ratio coefficient of the reference values of the adjacent calculation stages is $K_n = \frac{1 + \frac{\sigma_{s,n}}{q_f}}{1 + \frac{\sigma_{s,n-1}}{q_f}} \left(\frac{\sigma_{d,n}}{\sigma_{d,n-1}}\right)^m \ln(C_2 N_n)$, and when $n = 2$, we can use the initial tolerable error to express as $Tol_2 = \frac{1}{K_1} Tol_a$.

With the control parameters Tol_a and Tol_n, the reasonable loading cycle number of each stage can be determined in the explicit mode. Take the simulation of the dynamic triaxial test of clay layer ④ as an example, the initial conditions were $K_0 = 0.6$, $\sigma_d = \sigma_s = 6$ kPa and the results are shown in Fig. 5. Controlling the number of cycles in accordance with $Tol_a = 10\%$, the loading process was required to be divided into 4 stages to complete the simulation of 10,000 cycles, cycle times were respectively 2000, 2000, 3000 and 3000. In contrast, 3 transitions were performed in the original method, with 3000 cycles in each stage.

By controlling the number of cycles and the time of transitions, the standard of deviation control for each stage in explicit mode is provided. After optimization, the relative error of the prediction was reduced to 6.49% from 10.44% (N = 9000), and the results met the experimental curves better.
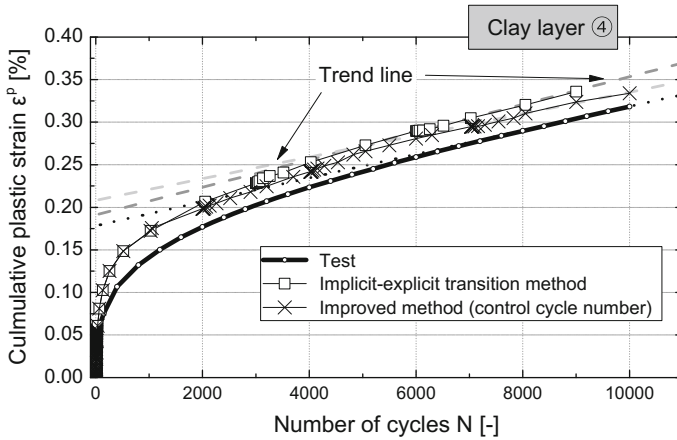
Fig. 5 Comparison between the empirical curve and the cumulative strain curves (before and after control of the cycles in each stage)

Example of FE-Calculation

The DK20 + 900.00 section of the Shanghai Nanjing Intercity High Speed Railway subgrade is shown in Fig. 6, the track structure of which is CRTS I type ballastless track plate. The foundation is reinforced with CFG piles by square arrangement, the pile diameter is 0.5 m, the pile spacing is 1.8 m and the length of the pile is 6 m. The subgrade height is 2.7 m, the thickness of the base gravel cushion is 0.6 m. The vertical settlement of the subgrade in this section has been predicted, and compared with the measured data.

Supposing that the subgrade settlement is completely caused by the deformation of the foundation, considering the attenuation characteristics of the dynamic load along with the depth, the simplified model in Fig. 6 was established, and only the vertical deformation u_z of the soil among piles within the depth of the pile length (6 m) and in the center of the cross section was analyzed. The lateral boundary of the model was a horizontal restraint, and the bottom was fixed.

The geological conditions are related to the Q_3^{al} silty clay layer ③, and the corresponding parameters in the model are shown in Tables 3 and 4.

The load action of CRH3 EMU was analyzed with pseudo-static method. The dynamic coefficient is 1.2 and the wheel load was calculated as 114 kN. Based on the Boussinesq solution for equivalent thickness conception of multi-layer structure system [21], the distribution of dynamic stress in subgrade was calculated. As a result, the dynamic stress amplitude of the pile top was 11.77 kPa, and the dynamic stress amplitude of the piles was 7.98 kPa. According to the measured data, the average dynamic stress level of the ground surface was 15 kPa. Therefore, the cyclic loading of $\sigma_d = 2 \times 7.98 = 15.96$ kPa, $\sigma_s = 15\text{-}7.98 = 7.02$ kPa (Fig. 6) was applied to the surface of the soil among piles in the model.
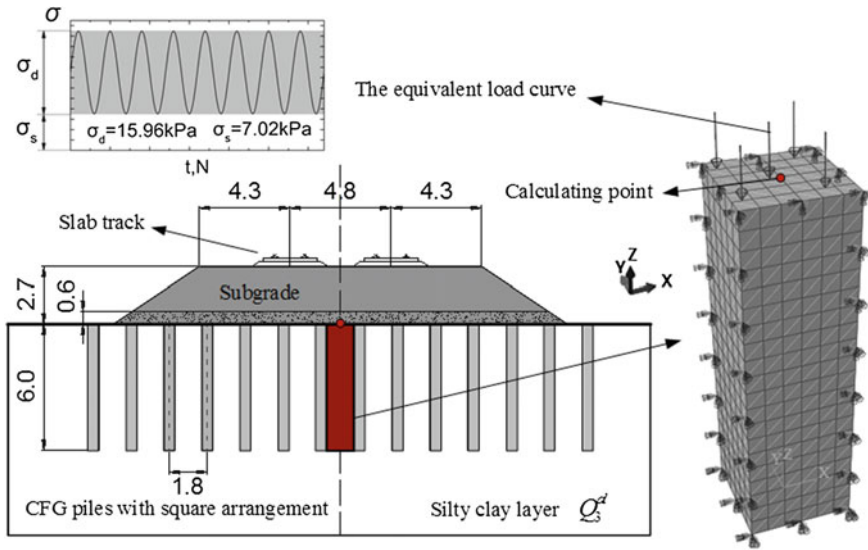
Fig. 6 Cross section of subgrade and the simplified finite element model

Table 3 Material parameters

	Dynamic elastic modulus [MPa]	γ [kN/m^3]	Poisson ratio [-]
Q_3^{al} silty clay layer ③	30	20.2	0.3

Table 4 Subprogram parameters of the bounding surface plasticity model

	The critical state line slope M	Plastic reference modulus H_c	Rebound curve slope κ	Compression curve slope λ	Poisson ratio μ
Q_3^{al} silty clay layer ③	1.1	30	0.034	0.17	0.3

119 shuttles of EMUs are operated along the line everyday according to the train operation organization, there are a total of 32 bogies corresponding to the 16 section of a train, and the cycle number of equivalent loads is $32 \times 119 \times 2 = 7616$ times in 24 h. The settlement process of the section from July 1, 2010 to July 31, 2011 (396 days) was simulated, the cumulative cycle number of which was 3,015,936.

After 20 transitions of implicit mode and explicit mode, the vertical deformation u_z-N curve of the calculating point was obtained, as shown in Fig. 7. According to the monitoring data of the section on July 31, 2011, the measured settlement of subgrade was 1.4 mm, and the predicted cumulative deformation value of the corresponding cycle number was about 0.99 mm.
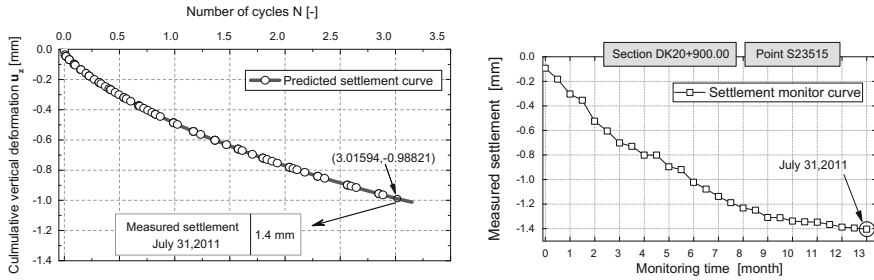
Fig. 7 The curve of vertical cumulative deformation u_z with load times N (u_z-N diagram)

It can be seen that the relative error between the predicted results and the measured results of the implicit-explicit transition method is $\Delta u_z/u_{z\text{measured}} = 0.293$, this part of the error mainly comes from the neglect of deformation in the upper part of the subgrade, as the monitoring site only reflected the settlement value of embankment surface. According to the research of literature [22], the cumulative autogenous deformation in the slab track embankment is usually 0.1–0.5 mm. If this additional settlement is taken into account, the predicted results are in agreement with the measured results.

Conclusions

Based on the bounding surface plasticity model and the improvement of semi empirical formula, the method of implicit-explicit transition algorithm is realized with second development of the finite element software, and its practicability of long term settlement prediction of the high speed railway subgrade under high-cycle loading has been confirmed. Several conclusions can be drawn from this study:

(1) The improved semi empirical formula considering the cyclic dynamic stress σ_d and the minimum cyclic deviator stress σ_s which are the significant wave parameters of the train load is well fitted to the cumulative deformation property of typical soft soil layers in Yangtze River Delta region, the average fitting correlation coefficient of which is 0.9932.

(2) The transmission and inheritance of deformation and stress field along with the updating of parameters can be realized by using Python script to control the finite element program kernel and manage the preprocessing and postprocessing of data in the implicit-explicit transition.

(3) The average error of the implicit-explicit transition method is 69.4% of simple explicit formulation method. When the number of cycles is large ($N \geq 10^3$), the predicted curve of the former shows a closer convergence trend to the experimental data.

(4) Cycle number in each stage and the transition occasion have a certain effect on the calculation accuracy of the implicit-explicit transition method. After control parameters Tol_a and Tol_n are proposed as the quantified indexes of calibration, the predicted results meet the experimental curves better.

(5) The example of FE-calculation shows that the implicit-explicit transition method can well predict the long-term post-construction settlement of the high-speed railway subgrade under high-cycle loading ($N \geq 10^6$), but there are still errors caused by the deformation of subgrade body. Thus, when the dynamic modulus of the soil is large and the deformation is relatively small, the settlement of subgrade is necessary to be revised with the autogenous deformation in the embankment.

References

1. Zheng J, Abusharar SW, Wang X. (2008). Three-dimensional nonlinear finite element modeling of composite foundation formed by CFG–lime piles. Computers and Geotechnics, 35`4):637–43.
2. Abusharar SW, Zheng J, Chen B. (2009). Finite element modeling of the consolidation behavior of multi-column supported road embankment. Computers and Geotechnics, 36(4):676–85.
3. Chai J, Igaya Y, Hino T, Carter J. (2013). Finite element simulation of an embankment on soft clay – Case study. Computers and Geotechnics, 48:117–26.
4. Li D, Selig ET. (1996). Cumulative Plastic Deformation for Fine-Grained Subgrade Soils. Journal of Geotechnical Engineering, 122(12):1006–13.
5. Wei W, Tinghao L. (2007). Study on prediction model of soft foundation settlement based on Weibull curve. Rock and Soil Mechanics, (04):803–06 [in Chinese].
6. Lihua Y, Xiaomou W, Liujun Z. (2009). Settlement prediction of embankment on soft clay ground by using Verhulst curve. Journal of Chang'an University (Natural Science Edition), (02):19–23 [in Chinese].
7. Tao L, Yiping Z, Tuqiao Z. (2005). Superior Combination Forecasting Settlement of Soft Clay Embankments. Chinese Journal of Rock Mechanics and Engineering, 24(18):3282–86 [in Chinese].
8. Niemunis A, Wichtmann T, Triantafyllidis T. (2005). A high-cycle accumulation model for sand. Computers and Geotechnics, 32(4):245–63.
9. Wichtmann T, Niemunis A, Triantafyllidis T. (2007). Strain accumulation in sand due to cyclic loading: Drained cyclic tests with triaxial extension. Soil Dynamics and Earthquake Engineering, 27(1):42–48.
10. Wichtmann T, Triantafyllidis T. (2015). Inspection of a high-cycle accumulation model for large numbers of cycles (N = 2 million). Soil Dynamics and Earthquake Engineering, 75:199–210.
11. Wichtmann T, Niemunis A, Triantafyllidis T. (2015). Improved simplified calibration procedure for a high-cycle accumulation model. Soil Dynamics and Earthquake Engineering, 70:118–32.

12. Guanghua Y (1997). The Constitutive Theory of Geotechnical Materials Should be Established in 21st Century. Chinese Journal of Geotechnical Engineering (03):119–20 [in Chinese].
13. Valanis KC, Lee CF. (1984). Endochronic Theory of Cyclic Plasticity With Applications. Journal of Applied Mechanics, 51(2):367–74.
14. Monismith CL, Ogawa N, Freeme CR. (1975). Permanent Deformation Characteristics of Subgrade Soils due to Repeated Loading. Transportation Research Record, 5(37):1–17.
15. Chai JC, Miura N. (2014). Traffic-Load-Induced Permanent Deformation of Road on Soft Subsoil. Journal of Geotechnical & Geoenvironmental Engineering, 128(11):907–16.
16. Niemunis A, Wichtmann T, Triantafyllidis T. (2005). A high-cycle accumulation model for sand. Computers and Geotechnics, 32(4):245–63.
17. Quanmei G, Zhe L, Jianyi Y. (2009). Experimental Study on Long-term Cumulative Settlement and Equivalent Cyclic Load of Speed-up Railway Subgrade Soil. Journal of The China Railway Society (02):88–93 [in Chinese].
18. Quanmei G (2011). Research on Permanent Deformation Calculation Method of Pile-Net Structure in High Speed Railway. Tongji University.
19. Peng Y, Rui Z. (2007). Analysis of Soft Soil Subgrade with Burger Creep Model. China Water Transport (10):113–14 [in Chinese].
20. Wichtmann T, Niemunis A, Triantafyllidis T. (2010). Strain accumulation in sand due to drained cyclic loading: On the effect of monotonic and cyclic preloading (Miner's rule). Soil Dynamics and Earthquake Engineering, 30(8):736–45.
21. Xiuxian L (1984). Equivalent Conversion Method of Multi Layer System in Flexible Pavement Design. Journal of Tongji University (03) [in Chinese].
22. Liang D, Degou C, Yangsheng Y, Qianli Z, Chenggang Z. (2010). A Method for Predicting the Cumulative Deformation of High-Speed Railway Subgrades under Cyclic Train Loads. China Civil Engineering Journal (06):100–08 [in Chinese].